Springer Series in
MATERIALS SCIENCE 105

Springer Series in
MATERIALS SCIENCE

Editors: R. Hull   R. M. Osgood, Jr.   J. Parisi   H. Warlimont

The Springer Series in Materials Science covers the complete spectrum of materials physics, including fundamental principles, physical properties, materials theory and design. Recognizing the increasing importance of materials science in future device technologies, the book titles in this series reflect the state-of-the-art in understanding and controlling the structure and properties of all important classes of materials.

88 **Introduction to Wave Scattering, Localization and Mesoscopic Phenomena**
By P. Sheng

89 **Magneto-Science**
Magnetic Field Effects on Materials: Fundamentals and Applications
Editors: M. Yamaguchi and Y. Tanimoto

90 **Internal Friction in Metallic Materials**
A Reference Book
By M.S. Blanter, I.S. Golovin, H. Neuhäuser, and H.-R. Sinning

91 **Time-dependent Mechanical Properties of Solid Bodies**
By W. Gräfe

92 **Solder Joint Technology**
Materials, Properties, and Reliability
By K.-N. Tu

93 **Materials for Tomorrow**
Theory, Experiments and Modelling
Editors: S. Gemming, M. Schreiber and J.-B. Suck

94 **Magnetic Nanostructures**
Editors: B. Aktas, L. Tagirov, and F. Mikailov

95 **Nanocrystals and Their Mesoscopic Organization**
By C.N.R. Rao, P.J. Thomas and G.U. Kulkarni

96 **Gallium Nitride Electronics**
By R. Quay

97 **Multifunctional Barriers for Flexible Structure**
Textile, Leather and Paper
Editors: S. Duquesne, C. Magniez, and G. Camino

98 **Physics of Negative Refraction and Negative Index Materials**
Optical and Electronic Aspects and Diversified Approaches
Editors: C.M. Krowne and Y. Zhang

99 **Self-Organized Morphology in Nanostructured Materials**
Editors: K. Al-Shamery and J. Parisi

100 **Self Healing Materials**
An Alternative Approach to 20 Centuries of Materials Science
Editor: S. van der Zwaag

101 **New Organic Nanostructures for Next Generation Devices**
Editors: K. Al-Shamery, H.-G. Rubahn, and H. Sitter

102 **Photonic Crystal Fibers**
Properties and Applications
By F. Poli, A. Cucinotta, and S. Selleri

103 **Polarons in Advanced Materials**
Editor: A.S. Alexandrov

104 **Transparent Conductive Zinc Oxide**
Basics and Applications in Thin Film Solar Cells
Editors: K. Ellmer, A. Klein, and B. Rech

105 **Dilute III-V Nitride Semiconductors and Material Systems**
Physics and Technology
Editor: A. Erol

106 **Into The Nano Era**
Moore's Law Beyond Planar Silicon CMOS
Editor: H.R. Huff

Volumes 40–87 are listed at the end of the book.

Ayşe Erol
Editor

Dilute III-V Nitride Semiconductors and Material Systems

Physics and Technology

With 373 Figures

Associated Professor Dr. Ayşe Erol
Istanbul University, Faculty of Science
Physics Department, Solid-State Physics Division
Vezneciler, 34134 Istanbul, Turkey
E-mail: ayseerol@istanbul.edu.tr

Series Editors:

Professor Robert Hull
University of Virginia
Dept. of Materials Science and Engineering
Thornton Hall
Charlottesville, VA 22903-2442, USA

Professor Jürgen Parisi
Universität Oldenburg, Fachbereich Physik
Abt. Energie- und Halbleiterforschung
Carl-von-Ossietzky-Strasse 9–11
26129 Oldenburg, Germany

Professor R. M. Osgood, Jr.
Microelectronics Science Laboratory
Department of Electrical Engineering
Columbia University
Seeley W. Mudd Building
New York, NY 10027, USA

Professor Hans Warlimont
Institut für Festkörper-
und Werkstofforschung,
Helmholtzstrasse 20
01069 Dresden, Germany

ISSN 0933-033X

ISBN 978-3-540-74528-0 Springer Berlin Heidelberg New York

Library of Congress Control Number: 2007936549

All rights reserved.
No part of this book may be reproduced in any form, by photostat, microfilm, retrieval system, or any other means, without the written permission of Kodansha Ltd. (except in the case of brief quotation for criticism or review.)
This work is subject to copyright. All rights are reserved, whether the whole or part of the material is concerned, specifically the rights of translation, reprinting, reuse of illustrations, recitation, broadcasting, reproduction on microfilm or in any other way, and storage in data banks. Duplication of this publication or parts thereof is permitted only under the provisions of the German Copyright Law of September 9, 1965, in its current version, and permission for use must always be obtained from Springer. Violations are liable to prosecution under the German Copyright Law.

Springer is a part of Springer Science+Business Media.
springer.com

© Springer-Verlag Berlin Heidelberg 2008

The use of general descriptive names, registered names, trademarks, etc. in this publication does not imply, even in the absence of a specific statement, that such names are exempt from the relevant protective laws and regulations and therefore free for general use.

Typesetting: Data prepared by SPi using a Springer TEX macro package
Cover concept: eStudio Calamar Steinen
Cover production: WMX Design GmbH, Heidelberg

Printed on acid-free paper SPIN: 12067565 57/3180/SPi 5 4 3 2 1 0

Preface

Dilute Nitride Semiconductors have been of great research interest since their development in the 1990s, both because of their unique physical properties and potential device applications. The substitution of small amounts of nitrogen atoms with group V elements in conventional III–V semiconductors such as GaAs or GaP strongly affects their electronic structure and allows one to tailor the band structure of the III–V semiconductors, leading to the development of novel optoelectronic devices such as light emitting diodes, edge emitting lasers, vertical cavity surface-emitting lasers, vertical external cavity surface-emitting lasers, semiconductor saturable absorber mirror structures, solar cells, semiconductor optical amplifiers, photodetectors, and modulators. Furthermore, dilute nitrides promise for developing novel optoelectronic integrated circuits, combining Si-based electronics with III–N–V compound semiconductor-based optoelectronics in a single chip.

In this book, leading research groups working on dilute nitrides cover growth, theory, characterization, and device applications of dilute nitrides semiconductors. Thanks to the developments in the growth techniques such as molecular beam epitaxy (MBE), metalorganic chemical vapour deposition (MOCVD), and chemical beam epitaxy (CBE), dilute nitrides could be grown with concentrations up to a few per cent of nitrogen into GaAs and GaP. In *Chap. 1*, *Yu* et al. review the synthesis of group III–V dilute nitrides by a highly non-equilibrium method – the combination of ion implantation, pulsed-laser melting, and rapid thermal annealing as an alternative growth technique – and investigate their structural, optical, and electrical properties in detail. In *Chap. 2*, *Miguel-Sánchez* et al. present the understanding of nitrogen rf plasmas in MBE process, and the effect of the ions in the chamber during growth on the optical properties of GaInNAs QWs. They use a novel in situ plasma characterization method, consisting in the use of a Bayard-Alpert gauge as a modified Langmuir probe for detecting the presence of plasma ions impinging onto the surface of the sample.

Several theoretical approaches have been used to describe the electronic band structure of nitrogen-containing III–V compounds. In *Chap. 3*, *Walukiewizc* et al. explain the band structure of dilute nitride semiconductors by the band anticrossing model (BAC) and compare the experimental data with predictions of the model. BAC model is based on an anticrossing interaction with a nearby localized level introduced by the highly electronegative impurity species which restructures the conduction band of a host semiconductor resulting in a splitting conduction band and a reduced fundamental bandgap. On the other hand, in *Chap. 4*, *Gorczyca* et al. analyse the electronic band structure of GaNAs by ab initio calculations in a supercell geometry using two different approaches based on the local density approximation (LDA) to the density functional theory and use the Perdew–Zunger parameterization of the Ceperley–Alder exchange correlation. The first approach is the plane wave method based on ab initio pseudopotentials and quantum molecular dynamics, and the second approach is the linear-muffin-tin-orbital method (LMTO). They analyse the dependence of the electronic band structure on chemical composition and hydrostatic pressure and optical properties of the alloys, and discuss the electron effective mass and its composition and pressure dependence. In *Chap. 5*, *Skierbiszewski* reviews the systematic study of the basic properties concerning giant non-parabolicity of conduction band and electron effective mass as a function of the Fermi energy, alloy composition and pressure, interband optical transitions, dielectric function, and effective g^*-factor of GaInNAs alloy. Knowledge of conduction band offset and electron effective mass is of great significance for a full exploration and optimization of dilute nitride material system for device applications. *Misiewicz* et al. investigate these parameters by using electromodulation spectroscopy in *Chap. 6*. Because this technique sheds light on the optical transitions related to the ground and excited states, the analysis of interband transitions together with theoretical calculations makes it possible to determine the energy level structure including the bandgap discontinuity at quantum interfaces.

Although the addition of small fractions of nitrogen to III–V compound results in a significant reduction of the bandgap, opening up the potential for a range of electronic and optoelectronic applications also causes deterioration at optical and structural quality of the material. In *Chap. 7*, *Mazzucato* and *Potter* give an overview of how the incorporation of nitrogen into dilute nitrides affects carrier dynamics, and discuss about the experimental evidence for exciton trapping presented in the scientific literature, such as the so-called S-shape temperature dependence of photoluminescence emission, lineshapes, and radiative decay rates. They also review the various mechanisms that have been put forward to account for the exciton trapping and discuss how/if these can be overcome. The successful performance of dilute nitride-based devices depends on the ability to grow high quality single crystalline epitaxial layers. One of the key parameters affecting quality is growth temperature, and therefore a better understanding of the behaviour of the system and, in particular, of the composition of the alloy with the growth temperature is needed to

optimize the performance of the GaInNAs optoelectronic devices. In *Chap. 8*, *Herrera* et al. address the effect of the growth temperature on the composition fluctuations of GaInNAs structures by transmission electron microscopy (TEM) in diffraction contrast mode and also approach the phase separation problem in GaInNAs theoretically.

In *Chap. 9*, *Talwar* provides an overview of the experimental and theoretical status about the dynamical behaviours of N species in III–As–N alloys and reports results of a comprehensive Green's function analyses of both infrared absorption and Raman scattering experiments on localized vibrational modes to assess the local chemical bonding of N in dilute III–As–N ternary and quaternary alloys.

The presence of nitrogen into III–V materials is known to cause a large drop in the electron mobility. In addition to the scattering from nitrogen sites and clusters, the conduction band becomes highly non-parabolic, which further affects the transport properties. In *Chap. 10*, *Vaughan* and *Ridley* explain the effect of this non-parabolicity on the mobility by using an extension to the ladder method for solving Boltzmann's transport equation. An overview of the electron spin properties in dilute nitride III–V semiconductors is given in *Chap. 11* by *Marie* et al. They present optical orientation experiments in GaNAs epilayers and GaInAsN quantum wells, which show that a strong electron spin polarization can persist at room temperature and dilute nitride materials could be used as efficient spin filters.

More recently, dilute nitride family has grown up with novel N-containing materials besides widely conventional GaNAs and GaInNAs material systems. One of the newest members of this family is GaInNP, which has recently been suggested as a promising material for GaInP/GaAs-based heterojunction bipolar transistors with a reduced offset and knee voltages. *Buyanova* and *Chen* review modelling of electronic structure of GaInNP with the effects of nitrogen on band alignment at the GaInNP/GaAs interface and origin of radiative recombination in the alloys in *Chap. 12*. On the other hand, in *Chap. 13*, Kunert et al. present GaP-based GaNAsP material system and reveal that this novel material system has a direct band structure and can be grown without the formation of extended defects on GaP and hence on silicon substrates. They prove that these materials are suitable for the intended laser application on GaP and on Si substrates in the future. In *Chap. 14*, *Güngerich* et al. compare the electronic structure of GaNAs and GaNP alloys showing the differences between $\mathrm{GaN}_x\mathrm{As}_{1-x}$ and $\mathrm{GaN}_x\mathrm{P}_{1-x}$ due to the different alignment of the N localized states relative to the conduction band minimum in the two alloys, as well as the different characters of their fundamental bandgaps.

In this book, several device applications including solar cell, quantum well laser, optoelectronic integrated circuits (OEIC), vertical cavity semiconductor optical amplifier, photodetector, modulator, and avalanche photodiode are also presented. Concerning solar cell applications, GaInNAs is a potential material having the required 1 eV bandgap for a multijunction solar cell and can be grown lattice matched to GaAs/Ge substrates. Several intrinsic

characteristics of the GaInNAs, which might influence carrier transport and hence device applications, are presented in *Chap. 15* by *Volz* et al. The chapter addresses several important topics in the framework of carrier transport in dilute nitride films. In *Chap. 16*, a very promising example of OEIC is given by *Yonezu*. The chapter reviews the growth of a structural-defect-free GaPN layer on an Si substrate by MBE. This OEIC is constructed with LEDs and Si MOSFETs, which are monolithically merged in a single chip with an Si layer and an InGaPN/GaPN double heterostructure layer lattice-matched to Si substrate, and light emission from the LED is modulated by switching the MOSFET.

In *Chapter 17* by *Alexandropoulos* et al. provides design rules for GaInNAs lasers in terms of laser parameters such as material gain, differential gain, differential refractive index, linewidth enhancement factor and investigates basic properties of GaInNAs-based semiconductor optical amplifiers. The chapter reveals that GaInNAs is a viable candidate for the near future telecom optoelectronics. *Tansu* and *Mawst* present the physics and device characteristics of high-performance strain-compensated MOCVD grown 1,200 nm GaInAs and 1,300–1,400 nm GaInNAs quantum well lasers and discuss approaches based on dilute nitride quantum wells to extend the emission wavelength up to 1,550 nm on GaAs substrate in *Chap. 18*. Current state-of-the-art GaInAsSbN quantum well lasers emitting in the 1,550 nm regime can only be realized by MBE due to the ease and efficient incorporation of Sb species into the GaInNAs material system. The pursuit of GaInAsSbN materials systems by MOCVD deposition is still immature due to the challenges in incorporating Sb- and dilute N species into GaInAs material simultaneously under optimum growth conditions. However, in *Chap. 19*, *Arif* and *Tansu* present a novel approach to realize GaInAsSbN quantum well, which allows one to circumvent the challenges present in the MOCVD epitaxy of this quinary material system and shows that combination of MOCVD and interdiffusion approach should allow realization of GaInAsSbN quantum well with emission wavelength up to 1,550 nm regime without having to grow the mixed SbN-based quinary compound directly by MOCVD.

The performance of 1,300 nm GaInNAs-based vertical-cavity semiconductor optical amplifiers (VCSOAs) under both continuous-wave and dynamic excitation is presented in *Chap. 20*, *Calvez* and *Laurand*. It has been demonstrated that monolithically grown GaInNAs-based devices can reach up 19 dB of on-chip gain with noise figures as low as 4 dB and that these devices are suitable for single channel amplification of 10 Gb s^{-1} data streams. Current material and device progress towards operation at 1,550 nm is also summarized.

The application of the GaInNAsSb compound to the design and fabrication of photodetector and modulator devices for telecommunications is reviewed in *Chap. 21* by *Héroux* and *Wang*. They present an overview of experimental results on p–i–n resonant cavity-enhanced photodetectors, heterojunction

phototransistors, avalanche photodiodes and quantum-confined Stark effect modulators.

This book brings leading scientist in the field as co-authors and reviews recent research and development of the dilute nitride semiconductors. This book is a resource for post graduate students and researchers, providing a detailed overview and current knowledge of dilute nitrides and also a reference book owing to very extensive references at the end of each chapter.

I wish to express my gratitude to all the authors who collaborated with me on this project for their invaluable contributions; it was a great pleasure working with these eminent scientists. This book would not have seen the light of day without their efforts.

I am grateful to Prof. Naci Balkan for his encouragement in the task of editing this book. I will remain indebted to him for his continuous support and invaluable contributions to my scientific life; his presence and place in my life are very important. Special thanks to him for everything.

Thanks to Prof. Çetin Arıkan for his continuous guidance, advice, and trust during my scientific life. I must also thank him for supporting me in all stages of my life. His encouragement and enthusiasm during this project was very helpful to me.

Istanbul, *Ayşe Erol*
November 2007

Contents

1 Energetic Beam Synthesis of Dilute Nitrides and Related Alloys
K.M. Yu, M.A. Scarpulla, W. Shan, J. Wu, J.W. Beeman, J. Jasinski, Z. Liliental-Weber, O.D. Dubon, and W. Walukiewicz 1
1.1 Introduction 1
1.2 Ion Beam Synthesis of Dilute Nitrides 3
1.3 Ion Implantation and Pulsed-Laser Melting 8
1.4 Synthesis of Dilute Nitrides by Ion Implantation and Pulsed-Laser Melting 10
1.5 Maximum Carrier Concentration and Mutual Passivation 17
1.6 Synthesis of Dilute II–VI Oxides by Ion Implantation and Pulsed-Laser Melting 20
1.7 Photovoltaic Applications of Highly Mismatched Alloys 26
1.8 Conclusions 29
References 30

2 Impact of Nitrogen Ion Density on the Optical and Structural Properties of MBE Grown GaInNAs/GaAs (100) and (111)B Quantum Wells
J. Miguel-Sánchez, Á. Guzmán, A. Hierro, E. Muñoz, U. Jahn, and A. Trampert 35
2.1 Introduction 36
2.1.1 Overview 36
2.1.2 Material Properties, Nitrogen Plasmas, and (111)B 36
2.2 Experimental Setup 37
2.3 Plasma Characterization 38
2.3.1 Basic Characterization 38
2.3.2 The Modified Langmuir Probe Method 40
2.3.3 Application of Magnetic Fields to Nitrogen Plasmas 44
2.4 Minimizing the Impact of the Ions 45
2.5 The Role of Ions on GaInNAs/GaAs (111)B QWs 47

2.6 The Role of Ions on GaInNAs/GaAs (100) QWs 50
2.6.1 Optical Characterization 51
2.6.2 Structural Characterization 54
2.7 Conclusions 60
References 61

3 Electronic Band Structure of Highly Mismatched Semiconductor Alloys
W. Walukiewicz, K. Alberi, J. Wu, W. Shan, K.M. Yu, and J.W. Ager III 65
3.1 Introduction 65
3.2 Localized Impurities 66
3.3 The Band Anticrossing Model 67
3.4 Experimental Investigation of Dilute III–N–V Alloys 72
3.4.1 Interband Transitions in Dilute Nitrides 73
3.4.2 Electronic Properties of Dilute Nitrides 80
3.5 Valence Band Anticrossing 82
3.6 Conclusions 86
References 87

4 Electronic Structure of GaN_xAs_{1-x} **Under Pressure**
I. Gorczyca, P. Boguslawski, A. Svane, and N.E. Christensen 91
4.1 Introduction 91
4.2 Methodology 93
4.2.1 Bandgap Adjustment 95
4.2.2 Accuracy of the Supercell Method 97
4.2.3 Group-Theoretical Discussion of Electronic States 97
4.3 Features of the GaN_xAs_{1-x} Band Structures 98
4.3.1 Effects of Lattice Relaxation 99
4.3.2 Composition Dependence of the Bandgap 100
4.3.3 Optical Transitions to E_- and E_+ 102
4.3.4 Effects of Hydrostatic Pressure 105
4.3.5 Discussion of the Origin of the E_+ Edge 108
4.4 Conduction Band Mass **vs.** Composition, Pressure, and Wavevector 109
4.5 Summary 116
References 117

5 Experimental Studies of GaInNAs Conduction Band Structure
C. Skierbiszewski 123
5.1 Introduction 123
5.2 GaInNAs Electron Effective Mass and Conduction Band Dispersion 125
5.2.1 Effective Mass Determination 125
5.2.2 Giant Nonparabolicity of the GaInNAs Conduction Band 129

5.2.3 Effective Mass at the Bottom of the Conduction Band . . . 131
5.2.4 Pressure Dependence of the Effective Mass for $k \sim 0$ 137
5.3 Interband Absorption of Free-Standing Epitaxial Layers 139
5.4 Dielectric Function and the Critical Point Transitions 142
5.5 Effective g^*-Factors for Electrons and Holes 146
5.5.1 Effective g^*-Factor for the E_- Conduction Band 151
5.5.2 Effective g^*-Factors for the E_+ Conduction Band and the Valence Bands 154
5.5.3 Electron Effective Mass at the Bottom of the E_- Band . . 155
5.6 Conclusions 157
References 158

6 Electromodulation Spectroscopy of GaInNAsSb/GaAs Quantum Wells: The Conduction Band Offset and the Electron Effective Mass Issues
J. Misiewicz, R. Kudrawiec, M. Gladysiewicz, and J.S. Harris 163
6.1 Introduction 163
6.2 Experimental Background 164
6.3 Theoretical Approach 167
6.4 Results and Discussion 171
6.4.1 Identification of Contacless Electroreflectance Resonances 171
6.4.2 Conduction Band Offset and Electron Effective Mass Determination 172
6.4.3 Influence of Remaining Parameters and Possible Errors . . 175
6.5 Summary and Outlook 176
References 177

7 The Effects of Nitrogen Incorporation on Photogenerated Carrier Dynamics in Dilute Nitrides
S. Mazzucato and R.J. Potter 181
7.1 Introduction 181
7.2 Exciton Localisation 183
7.3 Localisation in Dilute Nitrides 184
7.3.1 Photoluminescence Lineshape and S-Shape Temperature Dependence 184
7.3.2 Nearest Neighbour Configurations in Dilute Nitrides 188
7.3.3 Time Resolved Photoluminescence 188
7.3.4 Excitation Intensity Dependence 190
7.4 Reducing Localisation 191
7.4.1 Thermal Annealing 191
7.4.2 Antimony incorporation 194
7.5 Summary 194
References 195

8 Influence of the Growth Temperature on the Composition Fluctuations of GaInNAs/GaAs Quantum Wells
M. Herrera, D. Gonzalez, M. Hopkinson, H.Y. Liu, and R. Garcia 199
8.1 Introduction 199
8.2 Experimental 201
8.3 Composition Fluctuations in GaInNAs Studied by Transmission Electron Microscopy in Diffraction Contrast 201
8.4 Spinodal Decomposition in GaInNAs 209
8.5 Increase of the Composition Fluctuations with Temperature 215
8.6 Summary and Future Trends 218
References 219

9 Assessing the Preferential Chemical Bonding of Nitrogen in Novel Dilute III–As–N Alloys
D.N. Talwar 223
9.1 Introduction 223
9.2 Local Vibrational Mode Spectroscopy 225
9.2.1 Vibrational Modes of Light Impurities in GaAs 226
9.2.2 Local Vibrational Mode of Nitrogen in GaAs and InAs 227
9.2.3 Bonding of Nitrogen in $Ga_{1-x}In_xN_yAs_{1-y}$ Alloys 231
9.3 Theoretical 234
9.3.1 Ab Initio Method 235
9.3.2 Green's Function Technique 235
9.3.3 Numerical Computations and Results 237
9.4 Discussion and Conclusion 248
References 250

10 The Hall Mobility in Dilute Nitrides
M.P. Vaughan and B.K. Ridley 255
10.1 Introduction 255
10.2 Non-Parabolicity in Dilute Nitrides 257
10.3 The Hall Mobility 261
10.4 The Ladder Method 263
10.5 Ladder Coefficients in a Non-Parabolic Band 268
10.6 Elastic Scattering Processes 275
10.6.1 Alloy Scattering 275
10.6.2 Other Elastic Processes 276
10.7 Results and Conclusions 279
References 280

11 Spin Dynamics in Dilute Nitride
X. Marie, D. Lagarde, V. Kalevich, and T. Amand 283
11.1 Introduction 283
11.2 Samples and Experimental Set-Up 284
11.3 Experimental Results 285

11.4 Electron Spin Dynamics and Spin-Dependent Recombination 290
11.5 Conclusion 297
References 298

12 Optical and Electronic Properties of GaInNP Alloys: A New Material for Lattice Matching to GaAs
I.A. Buyanova and W.M. Chen 301
12.1 Introduction 301
12.2 Origin of Radiative Recombination 302
12.3 Compositional and Temperature Dependences of Bandgap Energies 305
12.3.1 Compositional Dependence 305
12.3.2 Temperature Dependence 307
12.4 Band Alignment in GaInNP/GaAs Heterostructures 308
12.4.1 PL Up-Conversion in GaInNP/GaAs Heterostructures ... 309
12.4.2 Interface-Related Emission 312
12.4.3 Band Offsets at the GaInNP/GaAs Interface 313
12.5 Summary 314
References 314

13 Properties and Laser Applications of the GaP-Based GaNAsP-Material System for Integration to Si Substrates
B. Kunert, K. Volz, and W. Stolz 317
13.1 Introduction 317
13.2 Growth and Structural Properties 320
13.2.1 GaInNAsP Growth 320
13.2.2 Structural Properties of GaInNAsP/GaP 324
13.3 Optical Properties and Band Structure 330
13.4 Laser Devices 337
13.5 Summary 339
References 341

14 Comparison of the Electronic Band Formation and Band Structure of GaNAs and GaNP
M. Güngerich, P.J. Klar, W. Heimbrodt, G. Weiser, A. Lindsay, C. Harris, and E.P. O'Reilly 343
14.1 History of Dilute-N III–V Semiconductor Alloys and Corresponding Optoelectronic Devices 344
14.2 Luminescence Characteristics of GaN_xAs_{1-x} and GaN_xP_{1-x} 347
14.3 Electronic Density of States in GaN_xAs_{1-x} and GaN_xP_{1-x} 351
14.4 Theory of Band Formation in Dilute Nitride Semiconductors 358
14.5 Conclusions 363
References 364

15 Doping, Electrical Properties and Solar Cell Application of GaInNAs
K. Volz, W. Stolz, J. Teubert, P.J. Klar, W. Heimbrodt, F. Dimroth, C. Baur, and A.W. Bett 369
15.1 Introduction 369
15.2 GaInNAs Growth and Doping 371
15.3 Carrier Transport Properties 378
15.3.1 Hall Measurements 378
15.3.2 Magnetoresistance Measurements 381
15.3.3 Thermopower Measurements 386
15.4 Annealing Effects on Structural and Optical Properties 388
15.4.1 Structural Properties 388
15.4.2 Optical Properties 395
15.5 Solar Cell Characteristics 400
15.6 Summary 401
References 402

16 Elemental Devices and Circuits for Monolithic Optoelectronic-Integrated Circuit Fabricated in Dislocation-Free Si/III–V-N Alloy Layers Grown on Si Substrate
H. Yonezu 405
16.1 Introduction 405
16.2 Growth of Structural Defect-Free Si/(In)GaPN Layers on Si Substrate 406
16.3 Optical and Electrical Properties of GaPN and InGaPN 408
16.4 Monolithic Implementation of Elemental Devices for Optoelectronic-Integrated Circuits 412
16.5 Summary 416
References 417

17 Analysis of GaInNAs-Based Devices: Lasers and Semiconductor Optical Amplifiers
D. Alexandropoulos, M.J. Adams, and J. Rorison 419
17.1 Introduction 419
17.2 Band Structure 420
17.2.1 General Considerations 420
17.2.2 Parameterization of the Band Anticrossing Model 422
17.2.3 Band Lineup 423
17.2.4 Implementation of the Band Structure Model 423
17.3 Optical Properties of GaInNAs Alloys 424
17.3.1 GaInNAs Material Gain 425
17.3.2 N-Positional Dependence of Material Gain 426
17.3.3 Comparison of GaInNAs and GaInAsP Material Gain 428
17.3.4 Differential Gain 428

17.3.5 Differential Refractive Index ... 431
17.3.6 Linewidth Enhancement Factor ... 431
17.4 Laser Design Considerations ... 433
17.4.1 Effect of In and N Composition on the Transition Wavelength ... 434
17.4.2 Effect of In and N Composition on the Optical Properties ... 436
17.5 GaInNAs Based Semiconductor Optical Amplifiers ... 439
17.5.1 Polarization Sensitive GaInNAs Semiconductor Optical Amplifiers ... 439
17.5.2 Polarization Insensitive GaInNAs SOAs ... 444
17.6 Conclusion ... 446
References ... 446

18 Dilute Nitride Quantum Well Lasers by Metalorganic Chemical Vapor Deposition
N. Tansu and L.J. Mawst ... 449
18.1 Introduction ... 449
18.2 Metalorganic Chemical Vapor Deposition-Grown GaIn(N)As Quantum Well ... 451
18.3 Lasing Characteristics of 1,200 nm GaInAs ... 453
18.4 Lasing Characteristics of GaInNAs Quantum Well Lasers ... 458
18.5 1,300 nm GaInNAs Multiple Quantum Well Lasers ... 463
18.6 1,300 nm GaInNAs Single Quantum Well Lasers with Higher N Content ... 464
18.7 1,320 nm GaInNAs Quantum Well Lasers with GaNAs Barriers ... 466
18.8 Comparison of Metalorganic Chemical Vapor Deposition GaInNAs with Other GaInNAs in 1,300 nm Regimes ... 471
18.9 Single-Mode Ridge Waveguide 1,300 nm GaInNAs Quantum Well Lasers ... 472
18.10 Extension of GaInNAs Quantum Well Lasers Beyond 1,320 nm ... 475
18.11 Temperature Analysis of the GaInNAs QW Lasers ... 480
18.12 Thermionic Emission Lifetime of GaInNAs Quantum Wells Lasers ... 485
18.13 Experimental Evidence of the Existence of Carrier Leakages ... 490
18.14 Extending the Emission Wavelength to 1,550 nm Regimes ... 495
18.15 Conclusions ... 496
References ... 497

19 Interdiffused GaInNAsSb Quantum Well on GaAs for 1,300–1,550 nm Diode Lasers
R.A. Arif and N. Tansu ... 503
19.1 Introduction ... 504
19.2 Design of the Interdiffused GaInAsNSb Quantum Well ... 505
19.3 Band Lineups of GaInNAsSb Material Systems ... 507

19.4 Computational Model of Sb–N Quantum Well Intermixing 508
19.4.1 Sb–N Interdiffusion Model ... 508
19.4.2 Ga(N)As–GaInNAs–GaIn(N)AsSb Energy Band Lineup .. 509
19.5 Interdiffused GaInAsSb–GaInNAs Quantum Well Structure 514
19.6 Optimization for Interdiffused GaInNAsSb Quantum Well at 1,550 nm Regime ... 515
19.7 Strain-Compensated Interdiffused GaInAsSb–GaNAs Quantum Well Structure ... 516
19.8 Experiments on the Interdiffusion of Sb- and N-Species in GaAs ... 518
19.9 Summary ... 521
References ... 522

20 Vertical Cavity Semiconductor Optical Amplifiers Based on Dilute Nitrides
S. Calvez and N. Laurand ... 525
20.1 Introduction ... 525
20.2 Device Description and Theory ... 526
20.2.1 Device Description ... 526
20.2.2 Amplification Analysis Using Rate Equations ... 528
20.3 Continuous-Wave Experimental Demonstrations ... 534
20.3.1 Devices ... 534
20.3.2 Amplification Characterization Setup ... 535
20.3.3 Reflective 1,300 nm GaInNAs Vertical Cavity Semiconductor Optical Amplifier in Operation ... 537
20.3.4 Optimization and Noise of 1,300 nm GaInNAs Vertical Cavity Semiconductor Optical Amplifiers ... 540
20.3.5 Tunability ... 543
20.3.6 Material Parameter Extraction ... 547
20.4 Gain Dynamics ... 550
20.4.1 Measurement Method and Associated Theoretical Remarks ... 551
20.4.2 Experimental Setup ... 552
20.4.3 VCSOA Dynamics Measurement ... 553
20.5 Extension to the 1,550 nm Band ... 555
20.6 Conclusion ... 559
References ... 560

21 Dilute Nitride Photodetector and Modulator Devices
J.B. Héroux and W.I. Wang ... 563
21.1 Introduction ... 563
21.2 GaInNAsSb Material Properties for Detector and Modulator Devices ... 566
21.2.1 Material Growth ... 566
21.2.2 Band Structure ... 567

21.3 p–i–n Photodetectors 570
21.3.1 GaInNAs:Sb Resonant Cavity-Enhanced Photodetector Operating at 1.3 μm 570
21.3.2 Subsequent Results 574
21.3.3 Alternatives Devices 575
21.4 Photodetectors with Gain 576
21.4.1 Heterojuntion Phototransistors 576
21.4.2 Avalanche Photodiodes 580
21.5 Modulators 581
References 584

Index 587

Contributors

Mike J. Adams
Department of Electronics
Systems Engineering
University of Essex
Wivenhoe Park
Colchester, CO4 3SQ
UK
adamm@essex.ac.uk

Joel W. Ager III
Electronic Materials Program
Materials Sciences Division
Lawrence Berkeley National
Laboratory
Berkeley, CA 94720, USA
JWAger@lbl.gov

Kirstin Alberi
Electronic Materials Program
Materials Sciences Division
Lawrence Berkeley National
Laboratory
Berkeley, CA 94720
and
Department of Materials Science
and Engineering
University of California
Berkeley, CA 94720, USA
kalberi@berkeley.edu

Dimitris Alexandropoulos
Department of Informatics and
Telecommunications
University of Athens
Panepistimiopolis, Ilisia
Athens, 15784
Greece
dalexa@di.uoa.gr

Thierry Amand
Laboratoire de Nanophysique
Magnétisme et Optoélectronique
INSA 135 avenue de Rangueil
31077 Toulouse, France
amand@insa-toulouse.fr

Ronald A. Arif
Center for Optical Technologies
Department of Electrical and
Computer Engineering
Lehigh University
7 Asa Drive, Bethlehem
PA 18015, USA
Raa4@Lehigh.Edu

Carsten Baur
Fraunhofer Institute for Solar
Energy Systems
79110 Freiburg, Germany
carsten.baur@ise.fraunhofer.de

Jeffrey W. Beeman
Materials Sciences Division
Lawrence Berkeley National Laboratory
Berkeley, CA 94720, USA
JWBeeman@lbl.gov

Andreas W. Bett
Fraunhofer Institute for Solar Energy Systems
79110 Freiburg, Germany
andreas.bett@ise.fhg.de

Piotr Boguslawski
Institute of Physics
Polish Academy of Sciences
al. Lotnikow 6/42
02-668 Warsaw, Poland
bogus@ifpan.edu.pl

Irina A. Buyanova
Department of Physics
Chemistry and Biology
Linköping University
S- 58183 Linköping, Sweden
irb@ifm.liu.se

Stephane Calvez
Institute of Photonics
University of Strathclyde
106 Rottenrow, Glasgow
G4 0NW, United Kingdom
s.calvez@strath.ac.uk

Weimin M. Chen
Department of Physics
Chemistry and Biology
Linköping University
S- 58183 Linköping, Sweden
wmc@ifm.liu.se

Niels E. Christensen
Department of Physics and Astronomy
University of Aarhus
DK-8000 Aarhus C, Denmark
nec@phys.au.dk

Frank Dimroth
Fraunhofer Institute for Solar Energy Systems
79110 Freiburg, Germany
frank.dimroth@ise.fraunhofer.de

Rafael Garcia
Department of Electronic and Electric Engineering
University of Sheffield
Mapping Street
Sheffield S1 3JD. United Kingdom
rafael.garcia@uca.es

Marta Gladysiewicz
Institute of Physics
Wroclaw University of Technology
Wroclaw, Poland
gladys@rainbow.if.pwr.wroc.pl

David Gonzalez
Departamento de Ciencia de los Materiales e I. M. y Q. I.,
Universidad de Cadiz
Apdo. 40, 11510 Puerto Real
Cadiz, Spain
david.gonzalez@uca.es

Izabela Gorczyca
Institute of High Pressure Physics
Polish Academy of Sciences
ul. Sokolowska 29/37
01-142 Warsaw, Poland
iza@unipress.waw.pl

Martin Güngerich
Department of Physics and Material Sciences Center
Philipps-University
D-35032 Marburg, Germany
martin.guengerich@physik.uni-marburg.de

Álvaro Guzmán
Institute for Systems based on Optoelectronics and Microtechnology (ISOM) and Dept. Ingeniería Electrónica.
Universidad Politécnica de Madrid
ETSI Telecomunicación
28040 Madrid, Spain
guzman@die.upm.es

Clive Harris
Tyndall National Institute
Lee Maltings
Cork, Ireland
clive.harris@tyndall.ie

James S. Harris
Solid State and Photonics Laboratory
Stanford University
California, USA
harris@snowmass.stanford.edu

Wolfram Heimbrodt
Department of Physics and Material Sciences Center
Philipps-University
D-35032 Marburg, Germany
wolfram.heimbrodt@physik.uni-marburg.de

Jean Benoit Héroux
Department of Applied Physics
The University of Tokyo
Tokyo, Japan
jbh14@columbia.edu

Miriam Herrera
Departamento de Ciencia de los Materiales e I. M. y Q. I.,
Universidad de Cadiz
Apdo. 40, 11510 Puerto Real
Cadiz, Spain
miriam.herrera@uca.es

Adrián Hierro
Institute for Systems based on Optoelectronics and Microtechnology (ISOM) and Dept. Ingeniería Electrónica.
Universidad Politécnica de Madrid
ETSI Telecomunicación
28040 Madrid, Spain
ahierro@die.upm.es

Mark Hopkinson
Department of Electronic and Electric Engineering
University of Sheffield
Mapping Street
Sheffield S1 3JD. United Kingdom
m.hopkinson@sheffield.ac.uk

Uwe Jahn
Paul-Drude-Institur for Solid State Electronics
Hausvogteiplatz 5-7
10117 Berlin, Germany
ujahn@pdi-berlin.de

Jacek Jasinski
School of Engineering
University of California, Merced
Merced, CA 95344
jjasinski@ucmerced.edu

Vladimir Kalevich
A.F. Ioffe Physico-Technical Institute
194021 St-Petersburg
Russia
kalevich@solid.ioffe.rssi.ru

Peter J. Klar
Institute of Experimental Physics I
Justus-Liebig University
Heinrich-Buff-Ring 16
D-35392 Giessen, Germany
peter.klar@physik.uni-giessen.de

Robert Kudrawiec
Institute of Physics
Wroclaw University of Technology
Wroclaw, Poland
robert.kudrawiec@pwr.wroc.pl
and
Solid State and Photonics Laboratory
Stanford University
California, USA
kudrawie@if.pwr.wroc.pl

Bernardette Kunert
Material Sciences Center and Faculty of Physics
Philipps University
35032 Marburg, Germany
Bernardette.Kunert@physik.uni-marburg.de

Delphine Lagarde
Laboratoire de Nanophysique Magnétisme et Optoélectronique
INSA 135 avenue de Rangueil
31077 Toulouse, France
delphine.lagarde@insa-toulouse.fr

Nicolas Laurand
Institute of Photonics
University of Strathclyde
106 Rottenrow, Glasgow
G4 0NW, United Kingdom
nicolas.laurand@strath.ac.uk

Zuzanna Liliental-Weber
Electronic Materials Program
Materials Sciences Division
Lawrence Berkeley National Laboratory
Berkeley, CA 94720, USA
Z_Liliental-Weber@lbl.gov

Andrew Lindsay
Tyndall National Institute
Lee Maltings
Cork, Ireland
andrew.lindsay@tyndall.ie

Hui Yun Liu
Department of Electronic and Electric Engineering
University of Sheffield
Mapping Street
Sheffield S1 3JD. United Kingdom
h.liu@sheffield.ac.uk

Xavier Marie
Laboratoire de Nanophysique Magnétisme et Optoélectronique
INSA 135 avenue de Rangueil
31077 Toulouse, France
marie@insa-toulouse.fr

Simone Mazzucato
Dipartimento di Scienze Chimiche
Università di Padova
Via Marzolo 1
35131 Padova, Italy
s_mazzucato@yahoo.it

Luke J. Mawst
Reed Center for Photonics
Department of Electrical and Computer Engineering
University of Wisconsin-Madison
1415 Engineering Drive
Madison, WI 53706
mawst@engr.wisc.edu

Jan Misiewicz
Institute of Physics
Wroclaw University of Technology
Wroclaw, Poland
jan.misiewicz@pwr.wroc.pl

Javier Miguel-Sánchez
Institute for Systems based on Optoelectronics and Microtechnology (ISOM) and Dept. Ingeniería Electrónica.
Universidad Politécnica de Madrid
ETSI Telecomunicación
28040 Madrid, Spain
Now with:
Isofoton S.A.
C/Severo Ochoa 50
29590 Malaga, Spain
j.miguel@isofoton.com

Elías Muñoz
Institute for Systems based on Optoelectronics and Microtechnology (ISOM) and Dept. Ingeniería Electrónica.
Universidad Politécnica de Madrid
ETSI Telecomunicación
28040 Madrid, Spain
elias@die.upm.es

Eoin P. O'Reilly
Tyndall National Institute
Lee Maltings
Cork, Ireland
eoin.oreilly@tyndall.ie

Richard J. Potter
Department of Material Science and Engineering
The University of Liverpool
George Holt Building
Liverpool
L69 3BX, UK
rjpott@liverpool.ac.uk

Brian K. Ridley
Department of Electronic Systems Engineering
University of Essex
Wivenhoe Park
Colchester CO4 3SQ
United Kingdom
bkr@essex.ac.uk

Judy Rorison
Department of Electrical & Electronic Engineering
University of Bristol
Merchant Venturers Building
Woodland Road, Bristol
BS8 1UB, UK
Judy.Rorison@bristol.ac.uk

Wei Shan
Intematix Inc.,
46410 Fremont Blvd.,
Fremont, CA 94538, USA
wshan@intematix.com

Czeslaw Skierbiszewski
Institute of High Pressure Physics
Polish Academy of Sciences
Sokołowska 29/37
01-142 Warszawa, Poland
czeslaw@unipress.waw.pl

Wolfgang Stolz
Material Sciences Center and Faculty of Physics
Philipps University
35032 Marburg, Germany
wolfgang.stolz@physik.uni-marburg.de

Axel Svane
Department of Physics and Astronomy
University of Aarhus
DK-8000 Aarhus C, Denmark
svane@phys.au.dk

Devki N. Talwar
Department of Physics
Indiana University of Pennsylvania
975 Oakland Avenue
56 Weyandt Hall, Indiana
Pennsylvania 15705-1087, USA
Talwar@iup.edu

Nelson Tansu
Center for Optical Technologies
Department of Electrical and
Computer Engineering
Lehigh University
7 Asa Drive, Bethlehem
PA 18015, USA
Tansu@Lehigh.Edu

Jörg Teubert
Material Sciences Center and
Faculty of Physics
Philipps University
35032 Marburg, Germany
joerg.teubert@physik.
uni-marburg.de

Achim Trampert
Paul-Drude-Institur for Solid
State Electronics
Hausvogteiplatz 5-7
10117 Berlin, Germany
trampert@pdi-berlin.de

Martin P. Vaughan
Department of Electronic
Systems Engineering
University of Essex
Wivenhoe Park
Colchester CO4 3SQ
United Kingdom
mpvaug@essex.ac.uk

Kerstin Volz
Material Sciences Center and
Faculty of Physics
Philipps University
35032 Marburg, Germany
kerstin.volz@physik.
uni-marburg.de

Wladek Walukiewicz
Electronic Materials Program
Materials Sciences Division
Lawrence Berkeley National
Laboratory
Berkeley, CA 94720
W_Walukiewicz@lbl.gov

Wen I. Wang
Department of Electrical Engineering
Columbia University
New York, NY 10027
wiw1@columbia.edu

Gerhard Weiser
Department of Physics and
Material Sciences Center
Philipps-University
D-35032 Marburg, Germany
gerhard.weiser@physik.
uni-marburg.de

Junqiao Wu
Electronic Materials Program
Materials Sciences Division
Lawrence Berkeley National
Laboratory
Berkeley, CA 94720, USA
and
Department of Materials Science
and Engineering
University of California
Berkeley, CA 94720
wuj@berkeley.edu

Hiroo Yonezu
Department of Electrical and Electronic Engineering
Toyohashi University of Technology
Tempaku-cho, Toyohashi
Aichi, 441-8580, Japan
yonezu@eee.tut.ac.jp

Kin Man Yu
Electronic Materials Program
Materials Sciences Division
Lawrence Berkeley National Laboratory
Berkeley, CA 94720, USA
kmyu@lbl.gov

Michael A. Scarpulla
Materials Department
University of California, Santa Barbara
CA 93106-5050
mikes@engineering.ucsb.edu

Oscar D. Dubon
Electronic Materials Program
Materials Sciences Division
Lawrence Berkeley National Laboratory
Berkeley, CA 94720
and
Department of Materials Science and Engineering
University of California
Berkeley, CA 94720
oddubon@berkeley.edu

Abbreviations

AFM	Atomic Force Microscopy
AM	Amplitude Modulation
APD	avalanche photodiode
AR	anti-reflective
ASA	Atomic-Spheres-Approximation
ASE	Amplified Spontaneous Emission
BAC	Band Anticrossing
BL	Buffer layers
BOM	Bond Orbital Model
BS	beam splitter
BZ	Brillouin Zone
CB	Conduction Band
CBE	chemical beam epitaxy
CBM	Conduction Band Minimum
CER	Contactless Electroreflectance
CFE	correlated function expansion
CCD	Charged Coupled Device
CL	Cathodoluminescence
CP	Critical Point
Cp_2Mg	Dicyclopentadienylmagnesium
CPA	Coherent Potential Approximation
c-RBS	Channelling Rutherford Back-Scattering
CS	Cluster States
CV	Capacitance Voltage
cw	continuous wave
DBR	Distributed Bragg Reflector
dc	direct-current
DET	diethyltellurium
DETe	Diethyl tellurium
DEZn	diethyl zinc
DG	Differential gain

DitBuSiH	ditertiarybutyl silane
DLP	Delta Lattice Parameter
DLTS	Deep Level Transient Spectroscopy
DOS	Density of States
DQW	Double Quantum Well
EA	Electromodulated absorption
ECR	Electron Cyclotron Resonance
ECV	Electrochemical capacitance-voltage profiling
EDX	Energy Dispersive X-ray
EELS	Electron Energy Loss Spectroscopy
EPM	Empirical Pseudopotential Method
fcc	Face centred cubic
FFP	far field pattern
FFT	Fast Fourier transform
FM	Frequency Modulation
FP	Full-Potential
FP-LMTO	Full-Potential - Linear-Muffin-Tin-Orbital Method
FTIR	Fourier Transform Infrared
FWHM	Full width at half maximum
GSMBE	Gas Source Molecular Beam Epitaxy
HAADF	High Angle Annular Dark Field
HH	Heavy Hole
HMA	Highly mismatched Alloy
HPT	Heterojunction Bipolar Transistors
HR	high reflective
HRXRD	High Resolution X-Ray Diffraction
IBS	Ion Beam Synthesis
IBSC	Intermediate band solar cell
II-PLM	Ion Implantation Pulsed-Laser Melting
IQE	internal quantum efficiencies
IR	Infrared
LAN	Local Area Networks
LL	Landau level
LCINS	Linear Combination of Isolated Nitrogen States
LDA	Local Density Approximation
LE	Localized Excitons
LED	light-emitting diode
LH	Light Hole
LAPW	Linear Augmented Plane Wave
LMTO	Linear-Muffin-Tin-Orbital
LN_2	Liquid Nitrogen
LT	Low Temperature
LK	Luttinger-Kohn
LVM	Localized Vibrational Mode
LW-VCSEL	Long Wavelength Vertical Cavity Surface Emitting Lasers

MBE	Molecular Beam Epitaxy
MME	Momentum Matrix Element
MOCVD	Metal Organic Chemical Beam Epitaxy
MOVPE	Metal Organic Vapour Phase Epitaxy
MQW	Multiple Quantum Well
MQWH	multi-quantum well heterostructure
MR	magnetoresistance
MSM	Metal-Semiconductor-Metal
NBE	Near-Bandedge
NF	noise figure
NIR	Near-InfraRed
NN	Nearest-Neighbour
OB	Optical Bistability
ODCR	Optically Detected Cyclotron Resonance
OED	Optical Emission Detector
OPA	Optical Parametric Amplifier
OSA	Optical Spectrum Analyzer
pBN	pyrolithic boron nitride
PC	Photoconductivity, Photocurrent
PECVD	plasma enhanced chemical vapour deposition
PHS	Perturbed Host States
PITS	Photo-Induced Transient Spectroscopy
PL	Photoluminescence
PLE	photoluminescence excitation
PLM	Pulsed-Laser Melting
PLU	PL Up-Conversion
PR	Photomodulated Reflectance
PT	Photomodulated Transmission
QCSE	Quantum-Confined Stark Effect
QD	Quantum Dot
QW	Quantum Well
RCE	resonant cavity-enhanced
rf	radio frequency
RHEED	Reflection High Electron Energy Diffraction
RIM11	11-parameter rigid-ion-model
RMS	Root Mean Square
RS	Regular Solution
RTA	Rapid Thermal Annealing
RWG	ridge waveguide
sc	simple cubic
sccm	standard cubic centimeter per minute
SCH	Separate Confinement Heterostructure
SDR	Spin Dependent Recombination
SE	Spectroscopic Ellipsometry
SEM	Scanning Electron Microscopy

STEM	Scanning Transmission Electron Microscopy
SIMS	Secondary Ion Mass Spectrometry
sig-sp	signal-spontaneous
SK	Stranski-Krastanow
SLD	super-luminescent diode
SO	Spin Orbit
SOA	Semiconductor Optical Amplifiers
sp-sp	spontaneous
SQW	Single Quantum Well
SQWH	Single Quantum Well Heterostructure
TB	Tight binding
TBA	tertiarybutylarsine
TBAs	Tertiarybutyl arsine
TBP	Tertiarybutyl phosphine
TDFF	Third Derivate Functional Form
TEGa	triethylgallium
TEM	Transmission Electron Microscopy
TMAl	trimethyl aluminium
TMGa	trimethylgallium
TMIn	trimethylindium
TO	transverse optical
TR-PL	Time Resolved PhotoLuminescence
TRR	Time Resolved Reflectivity
TS-TPA	Two Step Two-Photon Absorption
U-DMHy	U-dimethylhydrazine
UDMHy	unsymmetric dimethyl hydrazine
UDMHy	unsymmetric dimethyl hydrazine
UHV	Ultra High Vacuum
VB	Valence Band
VBAC	Valence Band Anticrossing
VBM	Valence Band Maximum
VCA	Virtual Crystal Approximation
VCSEL	Vertical Cavity Surface Emitting Laser
VCSOA	Vertical Cavity Semiconductor Optical Amplifier
VFF	Valence Force Field
WDM	wavelength division multiplexed
XRD	X-Ray Diffraction

1

Energetic Beam Synthesis of Dilute Nitrides and Related Alloys

K.M. Yu, M.A. Scarpulla, W. Shan, J. Wu, J.W. Beeman, J. Jasinski,
Z. Liliental-Weber, O.D. Dubon, and W. Walukiewicz

Group III–V dilute nitrides, III-N_x–V_{1-x} (with x up to 0.10) have exhibited many unusual properties as compared to conventional semiconductor alloys. Here we review studies on the synthesis of group III–V dilute nitrides by a highly nonequilibrium method: the combination of ion implantation, pulsed-laser melting (PLM), and rapid thermal annealing (RTA). Using this method, the formation of a wide variety of III-N_x–V_{1-x} alloys including GaN_xAs_{1-x}, InN_xP_{1-x}, $Al_yGa_{1-y}N_xAs_{1-x}$, and $GaN_xAs_{1-x-y}P_y$ has been synthesized and their optical properties investigated. In particular, ion implantation followed by PLM has been successful in forming thermally stable thin films of GaN_xAs_{1-x} with x as high as 0.016 and structural and optical properties comparable to films grown by epitaxial deposition techniques with similar substitutional N content. Using the implantation, PLM technique group II–VI dilute oxide (II–O–VI) semiconductors, a direct analogue of the III–V diluted nitrides, have also been formed. In $Zn_{1-x}Mn_xTe$, where the O level lies below the conduction band edge, it was demonstrated that incorporation of a small amount of oxygen leads to the formation of a narrow, oxygen-derived band of extended states located well below the conduction band edge of the ZnMnTe matrix. The three absorption edges of this material (∼0.73, 1.83, and 2.56 eV) cover the entire solar spectrum providing a material envisioned for the multiband, single junction, high-efficiency photovoltaic devices.

1.1 Introduction

Recently a novel class of compound semiconductors – the highly mismatched alloys (HMAs), whose fundamental properties are dramatically modified through the substitution of a relatively small fraction of host atoms with a very different element, has attracted much attention. Among these HMAs are dilute III–V nitrides, notably GaN_xAs_{1-x}, which exhibits a reduction of the band gap by as much as 180 meV per N mole fraction, x [1–5]. Comparably large band gap reductions have also been observed in other III-N_x–V_{1-x}

alloys such as GaInNAs [6,7], GaNP [8,9], InNP [10], and AlGaNAs [11,12]. The strong dependence of the band gap on the N content has made these dilute III–V nitrides important materials for a variety of applications, including long wavelength optoelectronic devices [13,14] and high-efficiency hybrid solar cells [15,16].

The unusually strong dependence of the fundamental gap on the N content in the group III–N–V alloys has been the subject of many theoretical investigations [17–19]. The observation of an additional feature above the fundamental gap in the optical spectrum of GaInNAs alloys [1,20,21] as well as the unusual pressure dependence of the band gap and this high-energy transition led to the development of a band anticrossing (BAC) model (see Chap. 3, Sect. 1.3). The BAC model takes into account an anticrossing interaction between localized N states and the extended states of the host semiconductor matrix. Such interaction splits the conduction band into two subbands, E_- and E_+ [1,2,22]. The downward shift of the lower subband (E_-) is responsible for the reduction of the fundamental band gap and the optical transition from the valence band to the upper subband (E_+) accounts for the high energy edge. The model has been successfully used to quantitatively describe the dependencies of the upper and lower subband energies on hydrostatic pressure and on N content of $Ga_{1-y}In_yN_xAs_{1-x}$, $Ga_{1-y}Al_yN_xAs_{1-x}$, InN_xP_{1-x}, and GaN_xP_{1-x} alloys [1,11,12,23–25]). In the BAC model, the dispersion relations for E_+ and E_- conduction subbands of GaN_xAs_{1-x} are given by:

$$E_\pm(k) = \frac{1}{2}\left[E_\mathrm{N} + E_\mathrm{M}(k) \pm \sqrt{(E_\mathrm{N} - E_\mathrm{M}(k))^2 + 4C_\mathrm{NM}^2 x}\right], \qquad (1.1)$$

where E_N is the energy of the N level, $E_\mathrm{M}(k)$ is the dispersion relation for the host semiconductor matrix, and C_NM is the matrix element describing the coupling between N states and the extended states. For GaN_xAs_{1-x}, the downward shift of the lower subband E_- can account well for the reduction of the fundamental band gap using a value of $E_\mathrm{N} = 1.65\,\mathrm{eV}$ above the valence band maximum derived from photoluminescence (PL) measurements in N-doped GaAs [26] and $C_\mathrm{NM} = 2.7\,\mathrm{eV}$ from fitting data on the variation of the band gap with N content [1,22,27]. Recently, the BAC model has been extended to describe the electronic structure of other HMAs including ZnS_xSe_{1-x}, ZnS_xTe_{1-x}, $ZnSe_xTe_{1-x}$ [2,28,29] and the dilute II–VI oxides (e.g., ZnO_xTe_{1-x}) [30–32].

The BAC model not only explains the band gap reduction in III-N_x–V_{1-x} alloys but it also predicts that the N-induced modifications of the conduction band may have profound effects on the transport properties of this material system [27]. In particular, the downward shift of the conduction band edge and the enhancement of the density of state effective mass in GaInNAs [33] may lead to much enhanced maximum electron concentration n_max. Recent experiments have confirmed such prediction and showed that the modified conduction band in GaN_xAs_{1-x} enables a large enhancement in the maximum achievable free electron concentration n_max as compared to GaAs [34,35].

The dilute nitrides (and HMAs in general) are materials of extreme compositions that extend far beyond the thermodynamically allowed solubility and exist at the limit of kinetic stability. Thus, the epitaxial growth of dilute nitrides is still a formidable task even when using the most advanced nonequilibrium deposition processes such as molecular beam epitaxy (MBE). Here we review our work on the synthesis of a variety of HMAs (see Chap. 3), namely dilute III–V nitrides and the analogous dilute II–VI oxides by ion implantation followed by either RTA (conventional ion beam synthesis (IBS)) or PLM techniques. In the following, we will first briefly review the synthesis of dilute nitrides using conventional IBS method. A detailed review of the synthesis of dilute nitrides using ion implantation and PLM (II-PLM) will follow a brief description of the PLM process. Recent development on the application of II-PLM for the synthesis of other HMAs – the dilute II–VI oxides, which are analogous to the dilute III–V nitrides, will also be described. Finally, results on the formation of a new multiband quaternary III–V nitride, the GaNAsP will be presented.

1.2 Ion Beam Synthesis of Dilute Nitrides

Dilute nitride thin films were typically grown by either metal organic vapor phase epitaxy (MOCVD) with dimethylhydrazine as nitrogen source or gas-source molecular beam epitaxy (GSMBE) using a RF plasma nitrogen radical beam source [3,4]. Alternative synthesis methods have also been investigated. For example, Hung et al. [36,37] attempted to synthesize GaN_xAs_{1-x} using pulsed-laser ablation (PLD) of GaAs in NH_3 atmosphere and laser nitridation of GaAs. In this context, because only a small amount of N (<1%) can lead to a large reduction in the energy band gap of III-N_x-V_{1-x} materials, conventional IBS – ion implantation followed by thermal annealing is an attractive alternative approach to synthesize these alloys. Several attempts have been reported on the formation of thin film as well as nanostructure of diluted III–N–V alloys using the IBS technique [12,25,38–41]. The fundamental band gap energy for the ion beam synthesized thin films of GaN_xAs_{1-x}, InN_xP_{1-x}, and $Al_yGa_{1-y}N_xAs_{1-x}$ after N^+ implantation into GaAs, InP, and $Al_yGa_{1-y}As$ was found to decrease with increasing N implantation dose in a manner similar to that observed in epitaxially grown thin films. In GaN_xAs_{1-x} the highest value of x achieved using conventional IBS technique was 0.006 [38]; this corresponds to an N activation efficiency of only ∼15%. In the course of optimizing the annealing conditions in these studies, it was also found that, in GaN_xAs_{1-x} formed by IBS, the substitutional N_{As} is thermally unstable at temperatures higher than 850°C and will precipitate to form N-related voids [42].

In our work on the IBS of dilute nitride, typically multiple energy nitrogen ions were implanted into bulk GaAs crystals, creating ∼2,000–3,500 Å thick layers with roughly uniform N atomic concentration. The N dose was varied to

obtain diluted nitride layers with implanted N concentrations corresponding to N mole fractions of $x_{\rm imp} = 0.005 - 0.05$. RTA was performed on the implanted samples in a flowing N_2 ambient in the temperature range of 560–950°C for 5–120 s with the sample surface protected by a blank GaAs wafer.

The band gaps of the films were measured using photomodulated reflectance (PR) at room temperature. The PR experiment utilized radiation from a 300 W halogen tungsten lamp that was dispersed by a 0.5 m monochromator. The monochromatized beam focused on the samples as a probe beam. A chopped HeCd laser beam ($\lambda = 442$ or 325 nm) provided the photomodulation. PR signals were detected by a Si or Ge photodiode using a phase-sensitive lock-in amplification system. The values of the band gap and the line width were determined by fitting the PR spectra to the Aspnes third-derivative functional form [43].

The structural damage of GaAs by N^+ implantation was studied by channeling Rutherford back-scattering RBS (c-RBS). Figure 1.1 shows the c-RBS spectra from unimplanted GaAs and N^+-implanted GaAs samples with $x_{\rm imp}$ in the range of 1–4%. Notice that for the <100> aligned spectra from the N^+-implanted GaAs sample performed at room temperature, the channeling yields do not reach the "random" (nonchanneling) level. This suggests that the sample is highly damaged yet still crystalline even for the sample with $x_{\rm imp} = 4\%$. This is consistent with the high dynamic annealing rate of GaAs at room temperature during implantation [44]. For the samples with $x_{\rm imp} = 1$ and 2%, dechanneling (change in slope in the c-RBS spectrum) is observed in the spectra with no observable direct scattering peak, indi-

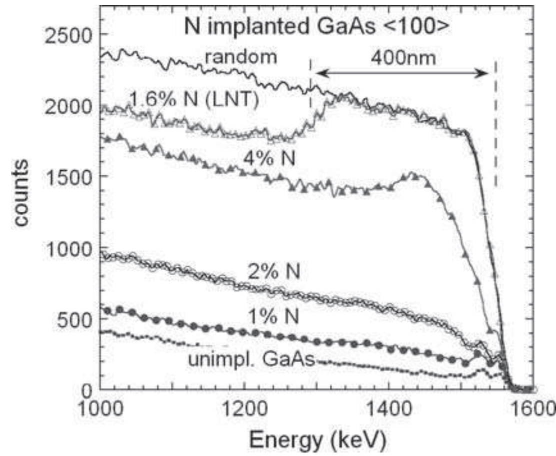

Fig. 1.1. Channeling Rutherford back-scattering (c-RBS) spectra from unimplanted and N^+-implanted GaAs samples performed at room temperature with $x_{\rm imp} = 1$, 2, and 4% taken in the $\langle 100 \rangle$ axial direction. The $\langle 100 \rangle$ aligned spectra from a LNT temperature 1.6% N-implanted GaAs sample is also shown

cating that the majority of the damage present in the top 200 nm layer of the sample consists of extended crystalline defects [45]. For the sample with $x_{\mathrm{imp}} = 4\%$, a direct scattering peak is observed at ∼150 nm below the surface. This can be attributed to the presence of either displaced Ga and As atoms or amorphous regions in the sample. On the other hand, when the implantation was performed at liquid nitrogen temperature (LNT) dynamic annealing was suppressed and an amorphous layer is formed. This is illustrated in the <100> c-RBS spectrum from the LNT N^+-implanted sample also shown in the Fig. 1.1. While the projected range of 80 keV N^+-implant (the highest energy used in this implantation series) in GaAs is ∼160 nm, the amorphous layer of the LNT sample extends to 400 nm.

Figure 1.2 shows the PR spectra from an unimplanted GaAs and a series of N^+-implanted GaAs samples with $x_{\mathrm{imp}} \approx 0.018$, 0.02, and 0.036 after RTA at 800°C for 10 s. The PR spectra shown in Fig. 1.2 exhibit well-resolved spectral features related to the fundamental band gap transitions. It should be pointed out that no optical transition is detected without thermal annealing from these samples. The significant broadening of the features in the implanted samples can be attributed mainly to the tails in the distribution of N and remaining damage due to implantation. The reduction of the band gap transition in the N-implanted GaAs is a direct result of the formation of GaN_xAs_{1-x} alloy layers. The mole fraction of “active” N, x_{act} in these IBS GaN_xAs_{1-x} layers

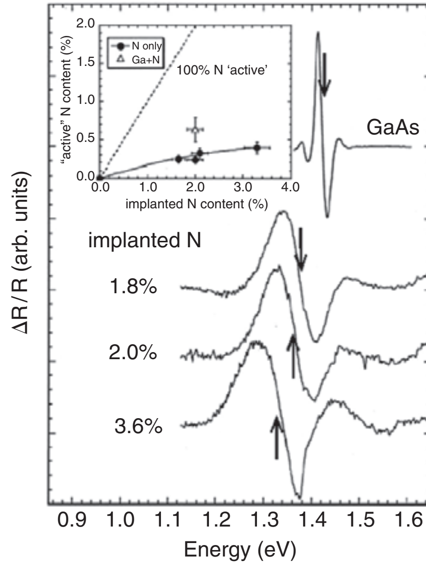

Fig. 1.2. A series of PR spectra from N^+-implanted GaAs with implanted N^+ doses of 1.8%, 2.0%, and 3.6% after 10 s RTA at 800°C. The *inset* shows the mole fraction of N incorporated in the As sublattice calculated from the band gap reduction as observed by the PR measurements using (1.1)

can be derived from the observed reduction in band gap ΔE values by using the BAC model (1.1) and is shown in the inset of Fig. 1.2. An activation efficiency ($x_{\mathrm{act}}/x_{\mathrm{imp}}$) of about 10–15% has been achieved for $x_{\mathrm{imp}} < 0.036$. The highest x_{act} achieved using this method is ≈0.004 for an implanted N $x_{\mathrm{imp}} \approx 0.036$.

Investigation on the effect of RTA temperature on the incorporation of N in GaAs shows that ΔE decreases as the RTA temperature increases, especially above 800°C. In fact, only a negligible band gap reduction (∼10 meV) was observed when the RTA temperature was raised to above 870°C, indicating that less than 0.1% of N remained substitutional in the As sublattice. Secondary ion mass spectroscopy (SIMS) measurements showed that the N did not diffuse out of the implanted region even after RTA at 900°C for 20 s. The results indicate that the substitutional configuration of the N_{As} in IBS GaN_xAs_{1-x} is thermally unstable.

Transmission electron micrographs (TEM) obtained for N-implanted GaAs samples after RTA at 800°C for 10 s are shown in Fig. 1.3. In addition to typical implantation-induced defects, void-like defects were also present in the samples. Figure 1.3 shows that the region extending from just below the surface and continued to a depth of about 0.6–0.7 μm contains a very high density of small voids, with an average size of about 2–3 nm [42]. Such void-like defects are not observed in samples implanted with S and are present only in N-implanted samples. This strongly suggests that these voids are related to N and are likely formed by the segregation of N during annealing. The formation of these voids may be the result of the presence of a high-vacancy concentration in the GaAs samples due to the N implantation. During RTA,

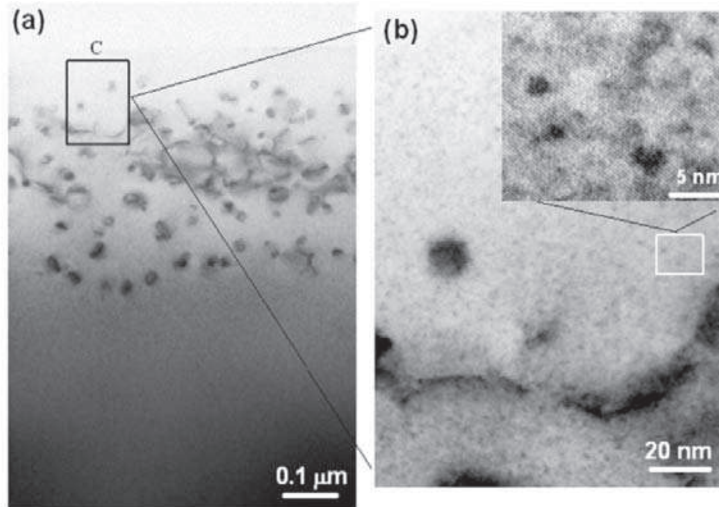

Fig. 1.3. TEM micrographs of GaAs implanted with N after RTA at 800°C 10 s

the N atoms have a strong tendency to diffuse via these vacancies and form strong N–N bonds and eventually become bubbles. Such N bubbles, therefore, may account for the low N activation efficiency in these samples.

In many III–V semiconductors, coimplantation of a matrix element (e.g., Ga in GaAs) to restore the local stoichiometry has been used successfully to enhance incorporation of electrically active dopants on the opposite lattice sites [46–48]. Attempts to increase the activation efficiency in the N-implanted GaAs samples by Ga ion coimplantation were also made. Equal amount of Ga ions coimplanted with N in GaAs in such a way that their atomic profiles overlapped results in a more than a factor of two enhancements in the activation efficiency. This is apparently due to the creation of a locally nonstoichiometric (Ga-rich) region with a high concentration of As vacancies available for N substitution. After RTA at 800°C for 10 s, with Ga coimplantation, $x_{\mathrm{act}} \approx 0.0065$ has been achieved (see inset, Fig. 1.2).

Moreover, the $\mathrm{N_{As}}$ in the $\mathrm{GaN}_x\mathrm{As}_{1-x}$ layers formed by Ga and N coimplantation in GaAs are thermally more stable. TEM results on the Ga + N coimplanted sample show that the voids are larger (with an average diameter of about 5–6 nm) but their density is much lower. They are located in a relatively narrow layer at depths between about 0.1 and 0.4 µm. These two effects indicate that less N is trapped in the voids and could account for the measured higher (by a factor of two) N activation and thermal stability in the Ga + N coimplanted samples.

Similar to the $\mathrm{GaN}_x\mathrm{As}_{1-x}$, large band gap reduction was also observed in dilute $\mathrm{InN}_x\mathrm{P}_{1-x}$ alloys grown by GSMBE [10]. The optical transitions from $\mathrm{InN}_x\mathrm{P}_{1-x}$ formed by N^+ implantation with increasing N dose in InP after RTA at 800°C for 10 s are shown in Fig. 1.4. A monotonic decrease in the band gap is observed as the implanted N dose increases. For the highest $x_{\mathrm{imp}} \approx 0.048$ the band gap is estimated to be 1.17 eV, corresponding to $\Delta E = 180$ meV with reference to an unimplanted InP sample ($E_{\mathrm{g}} = 1.35$ eV) [25].

The experimental band gap energies for epitaxial $\mathrm{InN}_x\mathrm{P}_{1-x}$ thin films grown by GSMBE method can also be described using the BAC model, (1.1) with a coupling matrix element $C_{\mathrm{NM}} = 3.5$ eV [25]. Using this fitted parameter the x_{act} in $\mathrm{InN}_x\mathrm{P}_{1-x}$ layers formed by N^+ implantation is calculated from the ΔE values obtained by the PR measurements; the results are presented in the inset of Fig. 1.4. The amount of N incorporated on the P sublattice $\mathrm{N_P}$ in the $\mathrm{InN}_x\mathrm{P}_{1-x}$ layers is $x_{\mathrm{act}} = 0.005$, 0.0065, and 0.012 for samples implanted with $x_{\mathrm{imp}} \approx 0.008$, 0.016, and 0.048, respectively. Notice that the maximum value achieved for x, 0.012, exceeds that reported to date ($x = 0.009$) [10] for $\mathrm{InN}_x\mathrm{P}_{1-x}$ thin films grown by the GSMBE technique. For the N implantation dose corresponding to x_{imp} in the range of 0.01–0.02, the activation efficiency is ∼40%, much higher than that in N^+-implanted and RTA GaAs.

Unlike in the IBS $\mathrm{GaN}_x\mathrm{As}_{1-x}$ layers where the N atoms substituting As sites is found to be thermally unstable, the N atoms in the P sublattice in the IBS $\mathrm{InN}_x\mathrm{P}_{1-x}$ layers are thermally stable. Only a small decrease in ΔE (<20 meV) is observed for the highest annealing temperature used in this

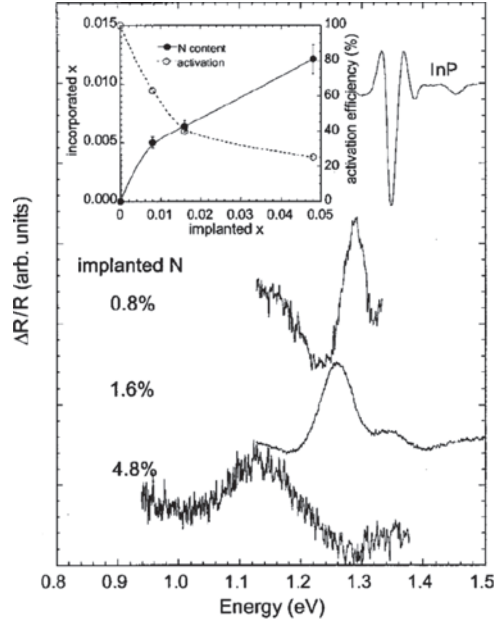

Fig. 1.4. PR spectra from N^+-implanted InP with $x_{\mathrm{imp}} \approx 0.008$, 0.016, and 0.048 after 10 s RTA at 800°C. The *inset* shows the mole fraction and activation efficiency of N incorporated on the P sublattice calculated from the band gap reduction

study (850°C). The high-activation efficiency and the good thermal stability of N in InP may be due to the smaller size difference between the N and P atoms compared to that between the N and As atoms.

Similar N incorporation was also achieved in $\mathrm{Al}_y\mathrm{Ga}_{1-y}\mathrm{As}$ with AlAs content y as high as 0.6 using the conventional IBS method [12, 38]. The active N contents in the IBS $\mathrm{Al}_y\mathrm{Ga}_{1-y}\mathrm{N}_x\mathrm{As}_{1-x}$ layers estimated using the known composition dependence for the Γ band edge, E_{M} (y), the localized N level, E_{N} (y) and the measured values of E_+ and E_- are ∼0.002–0.003. This corresponds to an activation efficiency in the range of 10–16%, similar to the case of $\mathrm{GaN}_x\mathrm{As}_{1-x}$.

1.3 Ion Implantation and Pulsed-Laser Melting

The utility of laser radiation to incorporate implanted dopants in semiconductors was identified in the late 1970s and remains an ongoing topic of research today. As in the semiconductor industry in general, most studies have focused on Si, where the incorporation of dopants like B, P, and As at concentrations larger than 10^{21} cm^{-3} has been realized [49–53] (this is not necessarily the *active* dopant concentration). The formation of supersaturated substitutional alloys of Si and group III and V elements by ion implantation and PLM

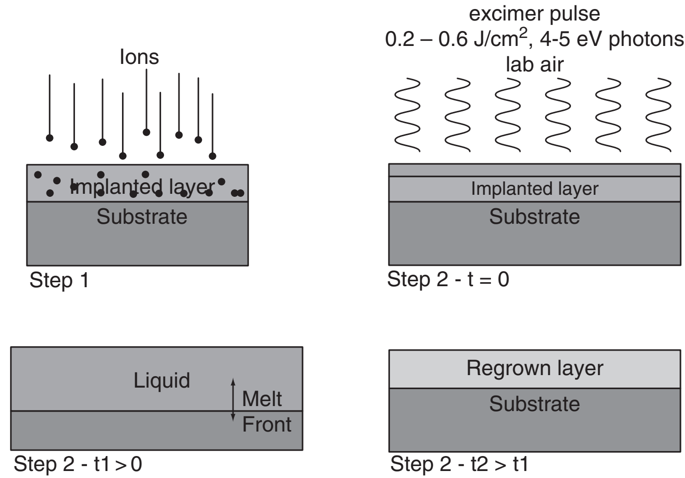

Fig. 1.5. The steps involved in II-PLM processing

has also been studied [51]. Similar results have been reported for dopants in GaAs [49, 54–56]. PLM has also been used to synthesize equilibrium phases such as transition metal silicides formed by irradiation of deposited stacks of the appropriate metal and Si [57, 58]. Recently synthesis of dilute ferromagnetic $Ga_{1-x}Mn_xAs$ and $Ga_{1-x}Mn_xP$ with Curie temperature as high as 130 and 60 K, respectively, using the PLM process has been demonstrated [59–62]. In these studies, it was established that the incorporation of concentrations of impurities higher than the solubility limit at ambient temperatures without precipitation or the formation of secondary phases is due to fast quenching during the laser-induced transient heat flow.

Figure 1.5 shows a schematic time sequence of the stages of a typical ion implantation-pulsed laser melting (II-PLM) experiment: First the semiconductor wafer is implanted with the desired species and then the implanted sample is irradiated using a single pulse from an excimer laser. The laser photons are absorbed close to the surface and converted rapidly to heat [57, 63] which causes the implanted region to melt for times on the order of a few hundred nanoseconds. As the heat flows into the underlying substrate, epitaxial solidification begins from the underlying crystalline template and the liquid–solid interface. The solidification front moves at velocities of a few meters per second and the quench rate can reach 10^9 K s^{-1} – parameters that are extraordinary in materials processing. This process results in an epitaxial film of the desired semiconductor alloy as the implanted atoms remain after solidification.

Both ion implantation and PLM occur far enough from thermodynamic equilibrium to be governed by kinetics (as opposed to thermodynamic equilibrium). Ion implantation produces nonuniform spatial distributions of implanted species which are quenched in due to near-negligible diffusion

distances at room temperature. The subsequent PLM exploits the transient regime of heat flow following a near-impulse deposition of energy to drive a rapid liquid-phase epitaxial growth which maintains the supersaturation induced by ion implantation while reinstating crystalline order. These departures from thermodynamic equilibrium have also been exploited to form homogeneous dilute nitride semiconductors with N ~ 2 orders of magnitude higher than equilibrium solubility limits [64, 65].

In the work presented in Sect. 1.4, the PLM process is carried out using either a KrF laser ($\hbar\omega = 5\,\text{eV}$, $\lambda = 248\,\text{nm}$, $\sim$16 ns FWHM pulse) or XeCl excimer laser ($\hbar\omega = 4\,\text{eV}$, $\lambda = 308\,\text{nm}$, $\sim$30 ns FWHM) with single pulse energy fluence $F = 0.1$–$0.6\,\text{J cm}^{-2}$ directed onto an implanted sample after being spatially homogenized. The transient melting and solidification process is understood to be governed by heat flow into the substrate. The absorption length for 5 eV photons in amorphous GaAs is approximately 10 nm [66]; thus most of the laser energy is deposited in the near surface region and converted to heat. This initial temperature profile can have temperature gradients on the order of $10^9\,\text{km}^{-1}$; thus heat flows very rapidly. As the heat flows into the substrate, the melt interface moves through the sample and consumes the ion damaged region. The melt duration (τ_{melt}) was determined by monitoring the time resolved reflectivity (TRR) of the samples using an argon-ion laser. When solidification begins from the underlying crystalline substrate, a process of single crystalline liquid-phase epitaxial growth occurs as the front returns to the surface at velocities of a few meters per second. The high-solidification velocity results in what is known as solute trapping, whereby impurity atoms are essentially buried in the growing crystal at concentrations far in excess of the solid solubility because it grows faster than they can diffuse out [58, 66].

1.4 Synthesis of Dilute Nitrides by Ion Implantation and Pulsed-Laser Melting

Similar to the conventional IBS of dilute nitride, a layer of GaAs (200 nm thick) with uniform nitrogen concentration of 1–4 mol% (2×10^{20}–$8 \times 10^{20}\,\text{cm}^{-3}$) was created in GaAs substrate by multiple energy N implantations [64, 65]. Typically to create a $\sim$200-nm thick layer with $x_{\text{imp}} = 0.01$ two N^+ implants with energies of 80 and 33 keV with doses of 3.5×10^{15} and $1.2 \times 10^{15}\,\text{cm}^{-2}$ were used. All implantations were carried out at room temperature.

Figure 1.6 shows a series of c-RBS spectra from a 2% N^+-implanted GaAs samples after PLM with increasing energy fluence. The threshold energy fluence for melting GaAs was determined by TRR to be $\sim 0.2\,\text{J cm}^{-2}$. From the onset of the high-dechanneling slope in the c-RBS spectra, we estimate the melt-regrown layers for samples subjected to 0.24 and $0.34\,\text{J cm}^{-2}$ laser pulses to be $\sim$0.12 and 0.18 μm, respectively. For energy fluences $>0.47\,\text{J cm}^{-2}$, the dechanneling slope in the c-RBS spectra is no longer observable, indicating

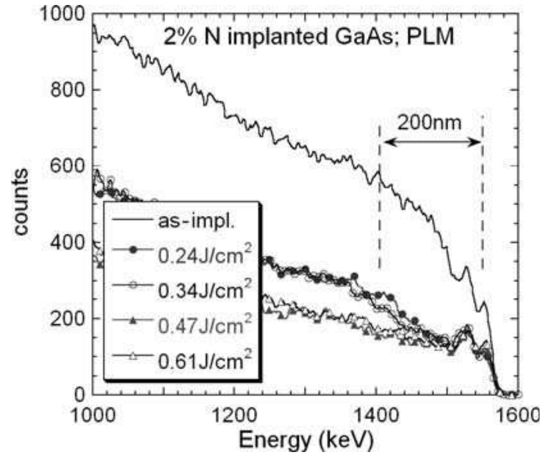

Fig. 1.6. A series of c-RBS spectra from a 2% N^+-implanted GaAs samples after PLM with increasing energy fluence

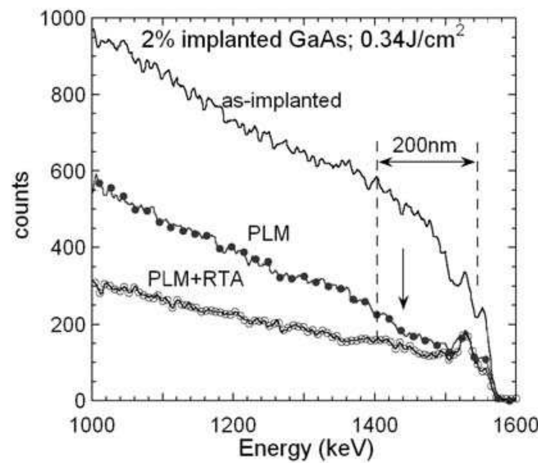

Fig. 1.7. c-RBS spectra from a 2% N^+-implanted GaAs samples as-implanted, after PLM at an energy fluence of 0.34 J cm^{-2}, and after PLM followed by RTA at 950°C for 10 s

that the laser-melted layer exceeds the regions with significant amounts of implant-damage (≥0.3 µm).

The effects of RTA after the PLM process is illustrated in Fig. 1.7 where the c-RBS spectra from a N^+-implanted GaAs sample with $x_{\mathrm{imp}} = 0.02$ for the as-implanted condition, after PLM with 0.34 J cm^{-2}, and after PLM followed by RTA at 950°C for 10 s are shown. The <100> aligned spectrum from the sample exposed to a pulse fluence of 0.34 J cm^{-2} alone shows complete recrystallization of the implanted layer with a normalized yield χ (the ratio of

channeled to random yields) ∼0.08, slightly higher than that for perfect unimplanted GaAs ($\chi = 0.04$). This suggests that the epitaxially regrown layer is still defective after PLM, likely containing extended crystalline defects. A high dechanneling slope is noticeable at ∼0.18 µm below the surface (indicated by the arrow), suggesting that the region above this point melted and epitaxially regrew from the liquid phase at this energy fluence. Since the underlying GaAs was still defective due to the end-of-range implantation damage, a high concentration of defects accumulates at the regrowth interface. Additional RTA at 950°C for 10 s removed these interfacial defects. c-RBS measurements on the PLM–RTA sample shows much improved crystalline quality, approaching that for unimplanted GaAs.

Figure 1.8 shows a two-beam cross-sectional TEM image of the GaAs sample with $x_{\mathrm{imp}} = 2\%$ after PLM at an energy fluence of 0.34 J cm^{-2} followed by RTA at 950°C for 10 s. In contrast to the RTA-only sample (Fig. 1.2) the TEM image of the PLM–RTA sample shows that the subsurface layer is free from structural defects. Close examination of Fig. 1.8 reveals a sharp interface at ∼0.2 µm below the surface separating two regions indicated by arrows in the Fig. 1.8. The high-resolution image of this interfacial region shown in the inset shows that there is much less crystalline disorder/clustering in the area above than in the area below this interface. However, small bubble-like defects typically less than 5 nm in size are still present but the density of these bubbles is much reduced. We note that some "end-of-range" defects remain below this interface. TEM images from PLM samples with 0.61 J cm^{-2} reveals that the laser-melted region extended to >0.3 µm. This is in perfect agreement with the channeling results presented earlier.

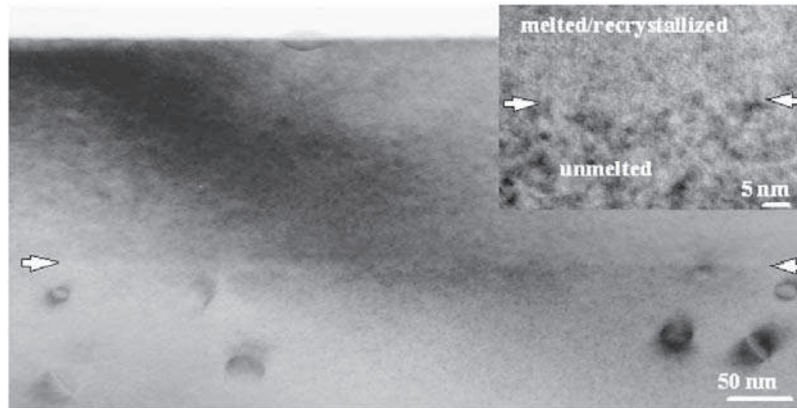

Fig. 1.8. Bright-field two-beam cross-sectional TEM images of N^{+}-implanted GaAs samples with $x_{\mathrm{imp}} = 2\%$ after PLM at an energy fluence of 0.34 J cm^{-2} followed by RTA at 950°C for 10 s The *inset* shows a high resolution image of the interface region. Note the much higher disorder/clustering in the area below the interface

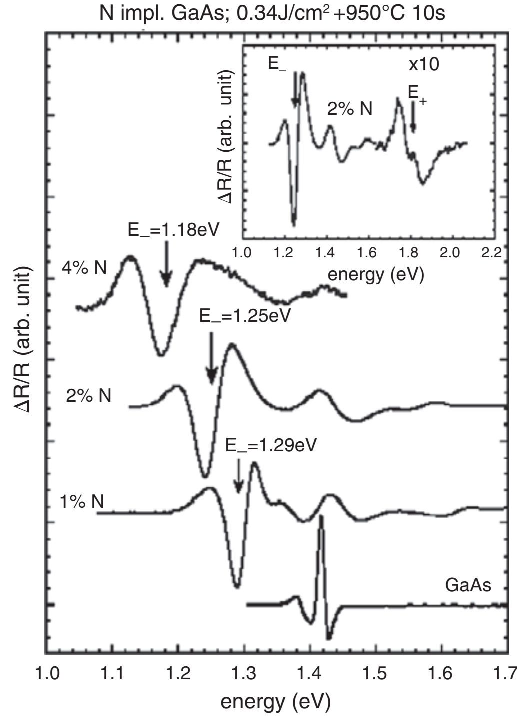

Fig. 1.9. PR spectra measured from a series of samples implanted with increasing levels of N (x_{imp}) and processed by PLM at an energy fluence of $0.34\,\mathrm{J\,cm^{-2}}$ and subsequent RTA at 950°C for 10 s. The *inset* shows a PR spectrum from GaAs sample with $x_{\mathrm{imp}} = 2\%$ taken over a wide photon energy range (1–2.2 eV) showing both the E_{-} and E_{+} transitions

Figure 1.9 shows a series of PR spectra from samples implanted with increasing amounts of N processed by PLM with energy fluence of $0.34\ \mathrm{J\ cm^{-2}}$ and subsequently RTA at 950°C for 10 s. Such PLM–RTA post-implantation treatments represent the "optimum" conditions giving rise to good crystalline quality of the nitride layer as well as to clear, sharp optical transitions. PR spectra from all of the PLM–RTA samples shown in Fig. 1.9 exhibit distinct optical transitions across the fundamental band gap of the material. The optical transition energies of the various samples are indicated in the Fig. 1.9. A monotonic decrease in the band gap with increasing implanted N content x_{imp} is clearly observed, indicating an increasing fraction of N is incorporated in the As sublattice with increasing x_{imp}.

In addition to the E_{-} level, the BAC model also predicts an upper subband E_{+} as a result of the anticrossing interaction of the localized N states and the extended conduction band states of GaAs. This electronic transition to the E_{+} level has been observed in $\mathrm{GaN}_x\mathrm{As}_{1-x}$ thin films grown by epitaxial

techniques for $x > 0.008$ when it becomes resolvable from the spin–orbit transition ($E_0 + \Delta$) [1, 24]. The inset of Fig. 1.9 shows a PR spectrum taken over a wide photon energy range (1–2.2 eV) from the 2% N^+-implanted GaAs followed by optimum PLM–RTA processing where $x_{act} \approx 0.009$. In addition to the fundamental band gap transition at 1.25 eV, a transition at 1.8 eV is observed. This high energy transition is in excellent agreement with transition to the E_+ level as calculated using (1.1) (1.81 eV). The observation of the E_+ transition further confirms the successful formation of GaN_xAs_{1-x} thin films by II-PLM process.

The band gap transitions from the valence band maximum to the lower subband E_- of the GaN_xAs_{1-x} layers synthesized by II-PLM are plotted in Fig. 1.10 as a function of implanted N. The band gap transitions from GaN_xAs_{1-x} layers formed by conventional IBS method are also plotted for comparison. The amount of N incorporated in the As sublattice ("active" N) for these GaN_xAs_{1-x} layers was calculated using the BAC model (1.1) and the N activation efficiencies for the various samples are indicated the Fig. 1.10.

Figure 1.10 demonstrates that using the II-PLM method, the N incorporation efficiency varies with x_{imp}: ~60% for $x_{imp} < 0.02$ and ~40% for $x_{imp} > 0.02$. For high x_{imp}, this represents a five times higher N activation than that observed in samples synthesized by conventional IBS. This can be attributed to the extremely short melt duration (~200 ns) and regrowth process that promotes N substitution in the As sublattice and inhibits the formation of nitrogen related voids, which have been observed in samples formed by N^+-implantation followed by RTA only [42].

The effect of laser energy fluence on N incorporation in GaAs samples with $x_{imp} = 1,\ 2$, and 4% is displayed in Fig. 1.11. For x_{imp} of 1 and 2% increasing

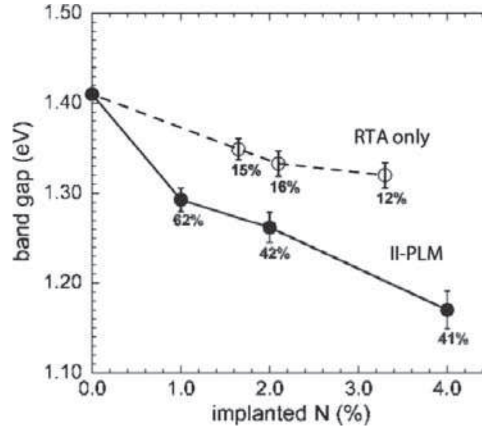

Fig. 1.10. Band gap energies of GaN_xAs_{1-x} layers synthesized by II-PLM (Fig. 1.9) are compared with those by conventional IBS. The N incorporation efficiencies for the various samples are also indicated

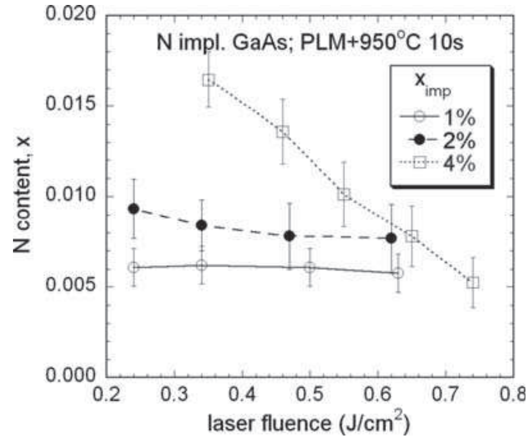

Fig. 1.11. Active N concentration (x_{act}) determined from PR spectra as a function of PLM energy fluence. The samples were annealed at 950°C for 10 s following the PLM process

the energy fluence does not influence the N incorporation in the film. Since the melt depth exceeds the implanted GaAs layer thickness for the high-laser energy fluence (>0.5 J cm^{-2}), one might expect a decrease in the incorporated N concentration if the N atoms are free to redistribute in the melted layer. The fact that the incorporation of N atoms does not depend on energy fluence in these cases suggests that they do not diffuse significantly in the short melt duration of hundreds of nanoseconds. On the other hand, for samples with $x_{\mathrm{imp}} = 4\%$ the N incorporation depends strongly on the energy fluence of the laser pulse. Increasing the energy fluence in this case results in an increase in the band gap and a decrease in the amount of incorporated N. At a fluence of 0.61 J cm^{-2}, a similar amount of incorporated N (∼0.8%) is found for both the 2 and 4% N-implanted samples. This can be attributed to the high N content in the GaAs that exceeds the kinetic limit of solubility even for the short melt duration. Hence the longer duration of the melt associated with the higher fluence enables the N atoms to migrate to the surface or to coalesce and form bubbles (i.e., N-related voids).

It should also be pointed out that distinct optical transitions in N^+-implanted GaAs followed by PLM are observable only after RTA at temperatures higher than 700°C. This is consistent with the c-RBS measurements on the PLM samples that showed the presence of structural defects after the PLM process. Studies on the effects of RTA temperature on II-PLM samples with $x_{\mathrm{imp}} = 2\%$ show a slight, gradual increase in the band gap with increasing RTA temperature. Figure 1.12 shows the band gaps and the linewidth of the E_- transitions measured by PR from N^+-implanted GaAs samples with $x_{\mathrm{imp}} = 0.02$ after PLM at an energy fluence of 0.34 J cm^{-2} as a function of the subsequent 10 s RTA temperature. For RTA at 950°C, the band gap increases

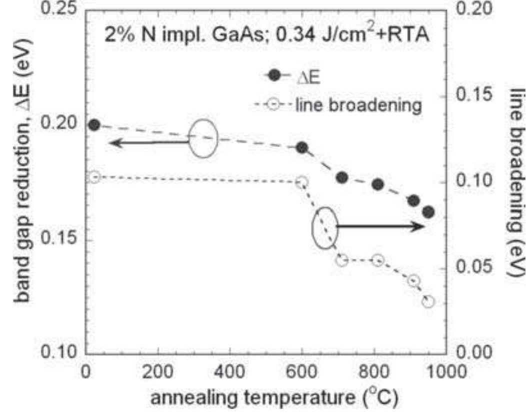

Fig. 1.12. The band gaps and the linewidth of the transitions measured by PR from N^+-implanted GaAs samples with $x_{\mathrm{imp}} = 0.02$ after PLM at an energy fluence of 0.34 J cm^{-2} are plotted as a function of the subsequent 10 s RTA temperature

by 20 meV with respect to the sample not treated by RTA. This change in the band gap, although observable, accounts to only ∼10% of the total band gap reduction and corresponds to a reduction in active N incorporated in the layer from $x_{\mathrm{act}} = 0.0107$ to 0.0093.

As a comparison, for IBS $\mathrm{GaN}_x\mathrm{As}_{1-x}$ samples annealing above 870°C resulted in less than 0.1% N incorporation in GaAs [38]. We believe that this is due to the presence of a high concentration of vacancies in the N-implanted samples. Upon RTA these vacancies recombine and also act as sinks for the N atoms, promoting the clustering of N into voids. In the case of PLM the process of rapid melting and solidification may result in the annihilation of implantation-induced vacancies as well as a complete local rearrangement of the atom sites leading to the formation of strong Ga–N bonds, thus stabilizing N atoms on the anion sites. The subsequent, lower temperature RTA cannot break these bonds but can improve the overall crystal quality by short range atomic diffusion and rearrangement. In MOCVD grown $\mathrm{GaN}_x\mathrm{As}_{1-x}$ layers, N atoms on As sites are also found to be thermally stable at RTA at 950°C, similar to the $\mathrm{GaN}_x\mathrm{As}_{1-x}$ layers formed by II-PLM.

A narrowing of the linewidth of optical transitions observed in PR measurement occurs as the RTA temperature is increased. This is also depicted in the Fig. 1.12. Increasing the RTA temperature is more effective in removing structural imperfections that are still present after the PLM process. The improved crystal quality of the implanted layer leads to sharper optical transitions. For samples synthesized by PLM and RTA at 950°C, the linewidth of the optical transition becomes comparable to that from $\mathrm{GaN}_x\mathrm{As}_{1-x}$ thin films with similar N composition that were epitaxially grown by MOCVD (<30 meV) [11].

1.5 Maximum Carrier Concentration and Mutual Passivation

In addition to the lowering of the fundamental gap, the anticrossing interaction between the N impurity level and the GaAs conduction band also leads to a considerable flattening of the lower subband E_- near its minimum which in turn results in a large increase of the electron effective mass [27, 33]. These N-induced modifications of the conduction band were expected to have profound influences on the transport properties of GaN_xAs_{1-x} [27]. Shown in Fig. 1.13 are the electron concentrations in Se doped MOCVD-grown $Ga_{1-3x}In_{3x}N_xAs_{1-x}$ films with $x = 0$–0.033 measured by Hall effect and electrochemical capacitance–voltage (ECV) technique. Since the Se atomic concentrations in these films are in the range of 2–7×10^{20}cm^{-3}, the measured free electron concentration should be regarded as the maximum achievable free electron concentration, $n_{\max}$. The result shown in Fig. 1.13 indicates that the $n_{\max}$ increases strongly with the N concentration. A maximum value of $7 \times 10^{19}\,\mathrm{cm}^{-3}$ was observed for $x = 0.033$. This value is $\sim$20 times higher than that found in a GaAs film ($3.5\times10^{18}\,\mathrm{cm}^{-3}$) grown under the same conditions. The much-enhanced $n_{\max}$ in $Ga_{1-3x}In_{3x}N_xAs_{1-x}$ films can be explained by considering the conduction band modifications by N-induced anticrossing interaction within the framework of the amphoteric defect model [67]. The amphoteric defect model suggests that the maximum free carrier concentration in a semiconductor is determined by the Fermi energy with respect to

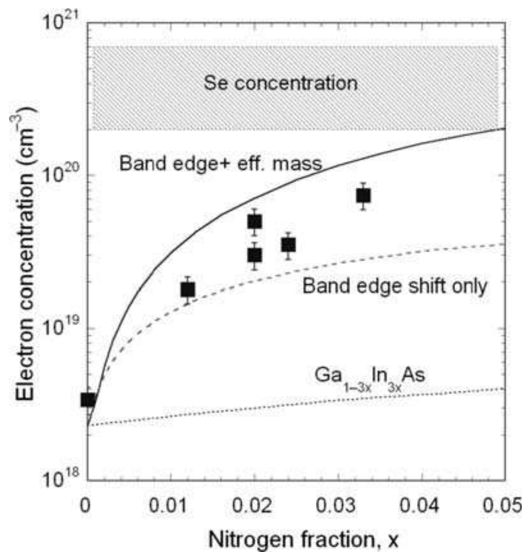

Fig. 1.13. Comparison of the measured maximum electron concentration with the calculated values as a function of N fraction in $Ga_{1-3x}In_{3x}N_xAs_{1-x}$. The shaded area indicates the range of Se concentration in these samples

the Fermi stabilization energy E_{FS} – a universal energy reference 4.9 eV below vacuum level [67]. Since the position of the valence band in GaInNAs is independent of N concentration, the downward shift of the conduction band edge toward E_{FS} and the enhancement of the density of states (DOS) effective mass in GaInNAs lead to much larger concentration of uncompensated, electrically active donors for the same location of the Fermi energy relative to E_{FS}.

The calculated n_{max} as a function of x for $Ga_{1-3x}In_{3x}N_xAs_{1-x}$ due to the downward shift of the conduction band only, as well as that including the increase in the effective mass are also shown in Fig. 1.13. Comparison of the experimental data with the calculation shows that in order to account for the large enhancement of the doping limits in $Ga_{1-3x}In_{3x}N_xAs_{1-x}$ alloys both the effects of band gap reduction and the increase in the effective mass have to be taken into account [34]. The increase in n_{max} has also been observed in GaN_xAs_{1-x} doped with S, another group VI donor [35]. Surface layer with high electron concentration has been formed by coimplanting N and S followed by RTA [68]. In contrast, Si and N coimplantation in GaAs only resulted in a highly resistive layer. This disparity in the behavior of group VI and IV donors can be explained by an entirely new effect in which an electrically active substitutional group IV donor and an isovalent N atom passivate each other's electronic effects [69, 70]. This *mutual passivation* occurs in Si doped GaN_xAs_{1-x} through the formation of nearest neighbor Si_{Ga}–N_{As} pairs. Consequently, Si doping in GaN_xAs_{1-x} under equilibrium conditions results in a highly resistive GaN_xAs_{1-x} layer with the fundamental band gap governed by a net "active" N, roughly equal to the total N content minus the Si concentration.

Recent pesudopotential large-supercell calculations show that for a group-IV impurity such as Si, the formation of the nearest-neighbor Si–Ga–N–As defect complex creates a deep donor level below the conduction band minimum (CBM). The coupling between this defect level with the CBM pushes the CBM upward, thus restoring the GaAs band gap; the lowering of the defect level relative to the isolated Si–Ga shallow donor level is responsible for the increased electrical resistivity [71].

The general nature of the mutual passivation effect in dilute nitride materials has also been demonstrated in Ge doped GaN_xAs_{1-x} [72] synthesized by II-PLM method. Ge doped GaN_xAs_{1-x} layers were synthesized by sequential implantation of Ge and N ions into GaAs followed by a combination PLM and RTA.

The passivation of the N activity by the Ge atoms is illustrated in the series of PR spectra presented in Fig. 1.14 from 2% Ge+2% N implanted GaAs followed by PLM at 0.45 J cm^{-2} with increasing RTA duration at 950°C. The band gap energies obtained from the PR spectra are shown in the inset as a function of the duration of 950°C RTA treatment. A fundamental band gap transition at 1.24 eV is observed for GaAs samples implanted with 2% N alone after PLM–RTA at 950°C for 10–120 s, corresponding to a GaN_xAs_{1-x} layer with $x \sim 0.01$. In contrast, the band gap of the 2% N + 2% Ge samples after

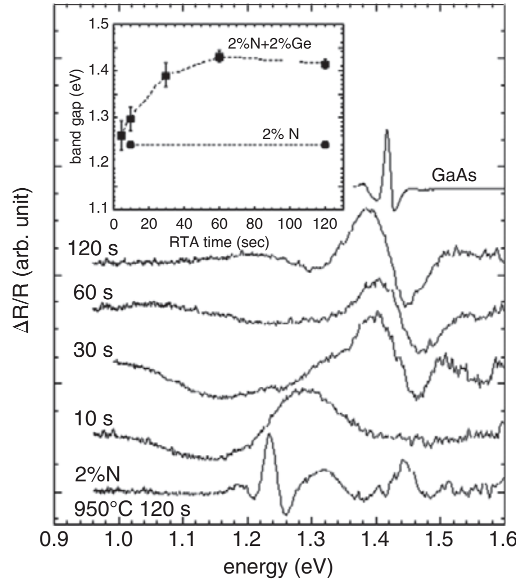

Fig. 1.14. PR spectra from GaAs samples implanted with 2% N + 2% Ge followed by PLM–RTA at 950°C for a duration of 5–120 s. PR spectra from a GaAs wafer (*top spectrum*) and a GaAs sample implanted with 2% N only after PLM–RTA at 950°C for 120 s (*bottom spectrum*) are also shown. The *inset* shows the band gap energies of the samples after PLM–RTA at 950°C for durations of 5–120 s

PLM increases from 1.24 to 1.42 eV (band gap of GaAs) as the RTA duration increases to 60 s, revealing that all N_{As} sites are passivated by Ge. The gradual increase in the band gap of the 2% N + 2% Ge sample as a function of RTA temperature and/or time duration can be attributed to the passivation of N_{As} by Ge_{Ga} through the formation of nearest neighbor Ge_{Ga}–N_{As} pairs.

Figure 1.15 shows a comparison of the electron concentration of the 2% N + 2% Ge and 2% Ge samples followed by PLM–RTA for 10 s in the temperature range of 650–950°C. The electron concentration of both samples approaches 10^{19} cm^{-3} after PLM. This high electron concentration exceeding the equilibrium $n_{\max}$ results from the highly nonequilibrium rapid melting and solidification in the PLM process. For the 2% Ge sample, thermal annealing after PLM drives the system toward equilibrium with an electron concentration of $\sim 1 \times 10^{18}$ cm^{-3} which is consistent with the amphoteric nature of Ge in GaAs. The electron concentration of the 2% N + 2% Ge samples, on the other hand, drops over two orders of magnitude to less than 10^{17} cm^{-3} as the samples are subjected to RTA at temperatures higher than 650°C. The changes in the band gap and the electrical behavior in the Ge doped GaN_xAs_{1-x} sample show that the activities of Ge donors and isovalent N mutually passivate each other via the formation of N_{As}–Ge_{Ga} pairs, just as was the case in Si doped GaN_xAs_{1-x}.

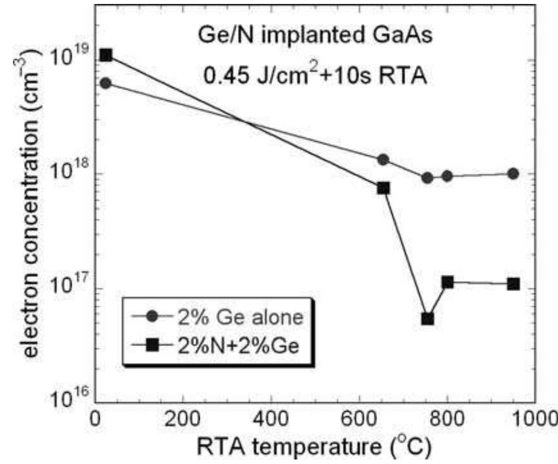

Fig. 1.15. Free electron concentrations of the 2% Ge and 2% N + 2% Ge samples after PLM+RTA at increasing temperature for 10 s obtained by Hall effect measurements

The ability to use PLM for a spatially controlled passivation provides a unique opportunity for the fabrication of novel planar and three-dimensional structures by the selective implantation of either one or both species. The mutual passivation effect described here may therefore be exploited for electrical isolation, band gap engineering, and quantum confinement.

1.6 Synthesis of Dilute II–VI Oxides by Ion Implantation and Pulsed-Laser Melting

Dilute nitrides are only a subgroup of a much broader class of materials, HMAs whose electronic structure is determined by the anticrossing interaction. Group II–VI dilute oxide (II–O–VI) semiconductors with the anions partially replaced by highly electronegative isoelectronic O atoms are a direct analogue of the III–V diluted nitrides. It has recently been demonstrated that group II–O–VI alloys in which highly electronegative O partially replaces the group VI element show behaviors that are similar to those of III–N–V alloys. For example, a dramatic O-induced reduction of the band gap has been reported in $Cd_{1-y}Mn_yO_xTe_{1-x}$ and ZnO_xSe_{1-x} [30, 73, 74]. The electronic band structure of the dilute oxides is determined by an anticrossing interaction between localized states of O and the extended states of the semiconductor matrix. Although similar or even more pronounced effects are also expected in II–O–VI HMAs [2], much less work has been done on these materials because of the difficulties in the synthesis of the alloys with large enough O content [30, 73].

Conventional IBS technique has been used as our first approach to form II–O–VI HMAs [73]. For all the CdTe samples implanted with O^+ followed by RTA, no significant band gap reduction can be observed. This indicates that the implanted O does not reside in the Te sublattice, but possibly agglomerates to form O bubbles, similar to the case of N in N^+-implanted GaAs after RTA at temperatures higher than 950°C. In CdTe crystals alloyed with >2% Mn ($Cd_{1-y}Mn_yTe$ with $y > 0.02$), small amounts of O up to $x \sim 0.004$ can be incorporated in the Te sublattice after 600°C 10 s RTA, causing a sizable decrease in the band gap (∼70 meV). The band gap reduction increases with y; the largest value observed is 190 meV in O^+-implanted $Cd_{0.38}Mn_{0.62}Te$.

Much enhanced band gap reduction in O^+-implanted CdTe is observed when PLM is used as a post-implantation process instead of RTA. This is illustrated in the series of PR spectra in Fig. 1.16 from CdTe with increasing implanted O dose followed by PLM with an energy fluence of 40 mJ cm^{-2}. PR spectra from a CdTe substrate and an unimplanted CdTe after PLM (0% O) are also included for direct comparison. A large band gap reduction (ΔE) is immediately evident in the O^+-implanted CdTe samples after PLM. For the CdTe sample implanted with 2% of O after PLM, the fundamental gap is 1.37 eV, corresponding to a band gap reduction $\Delta E = 140$ meV. This large

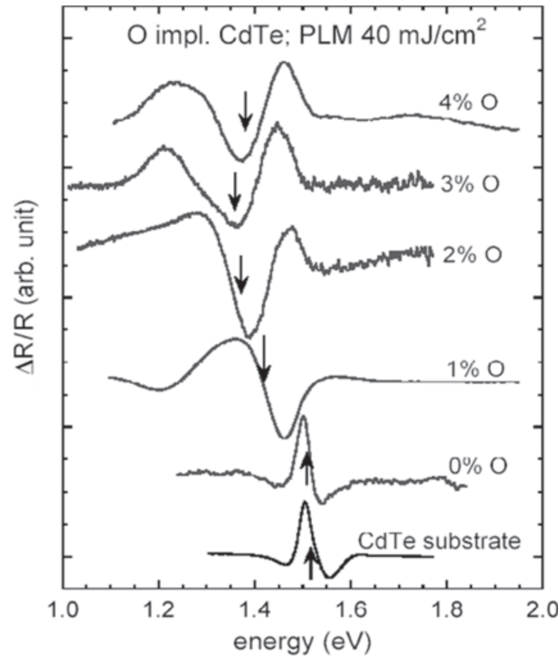

Fig. 1.16. PR spectra of O^+-implanted CdTe samples followed by PLM with an energy fluence of 40 mJ cm^{-2}. The samples were implanted with O with total dose corresponding to 0–4 mol.% of O in CdTe

reduction in the band gap is a clear indication of O incorporation in the Te sublattice, forming CdO_xTe_{1-x} alloys. Contrary to the case of PLM of N^+-implanted GaAs where an optical transition can only be observed after RTA following PLM, O^+-implanted CdTe samples show clear, sharp optical transitions after PLM without additional thermal annealing. This can be attributed to the higher resistance of CdTe (and II–VI alloys in general) to the formation of structural defects due to the more ionic nature of the crystals.

Figure 1.16 also shows that the band gap reduction (or O incorporation) increases as the implanted O content increases up to 2%. However, a further increase in the implanted O concentration leads to a saturation of the band gap at $\sim$1.37 eV. This suggests that there is a maximum in the amount of O that can be incorporated in the Te sublattice in CdTe under the present PLM conditions. Notice that there is no reduction in the band gap energy for an unimplanted CdTe sample after PLM (0% O). This clearly shows that the band gap reduction indeed arises from the O incorporation in the Te sublattice but not from the laser melting process. It should be pointed out that for all the CdO_xTe_{1-x} alloys synthesized by the II-PLM process, no transition from the valence band to the upper subband E_+ has been observed. This can be explained by the fact that the E_+ subband edge in this case is formed from states of largely localized-like character. Since the dipole interaction for optical transitions couples much more strongly to extended states than localized ones, the transition related to E_+ is inherently weak.

Figure 1.17 summarizes the band gap energies of the CdO_xTe_{1-x} alloys formed by II-PLM with laser energy fluence in the range of 40–100 mJ cm^{-2} as a function of the implanted O^+ concentration. No band gap reduction is found in O^+-implanted CdTe followed by PLM with energy fluence lower than

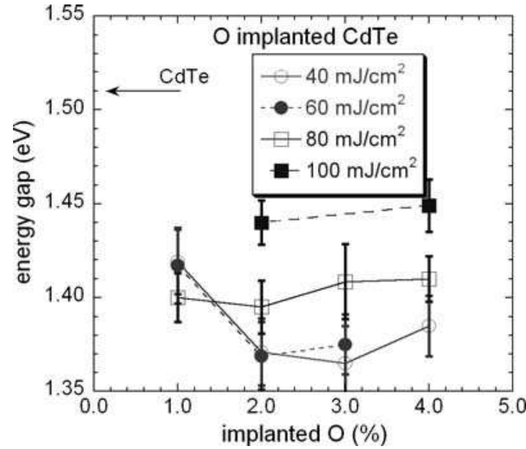

Fig. 1.17. The band gap energies of the CdO_xTe_{1-x} alloys formed by O^+-implantation in CdTe followed by PLM with laser energy fluence in the range of 40–100 mJ cm^{-2} as a function of implanted O^+ concentration

30 mJ cm^{-2}, suggesting that under the present PLM conditions the threshold for melting the implanted CdTe region is between 30–40 mJ cm^{-2}. This is in agreement with the recently reported melting threshold energy fluence for CdTe determined by TRR [75].

For O$^+$-implanted CdTe samples PLM at 40 and 60 mJ cm^{-2}, the band gap follows a similar trend. It is reduced for the implanted O range from 1 to 2% and then it saturates at ∼1.37 eV when more O atoms is introduced into the substrate. This saturation can be attributed to the O content exceeding the kinetic solubility limit even for the short melt duration of ∼300 ns. On the other hand, the band gap of samples melted at energy fluence higher than 60 mJ cm^{-2} becomes insensitive to the total implanted O dose. Moreover, for fixed implanted O content, an increase in the band gap is observed as the PLM energy fluence increases. This indicates that for high O content, less O is incorporated in the Te sublattice as the O$^+$-implanted CdTe samples are exposed to laser pulse with higher energy fluences. This can be understood since increasing the energy fluence increases the melt depth in the sample and consequently also prolongs the duration of the melt/crystallization process, driving the system closer to the equilibrium state. For CdTe implanted with 1–4% of O and irradiated with energy fluence greater than 150 mJ cm^{-2}, no band gap reduction was detected. This is consistent with the reported ablation threshold of ∼0.12 J cm^{-2} for CdTe using a 248 nm KrF laser pulse [75].

The amount of O incorporated in the Te sublattice in CdO_xTe_{1-x} HMAs can be determined using the BAC model (1.1). The location of the O level E_O in CdTe was determined to be ∼1.9 eV above the valence band maximum by PL studies in ZnTe [76] and the known band offsets between ZnTe and CdTe. These positions of the E_O with respect to the valence band in CdTe and ZnTe are in good agreement with recent calculations using first-principles band structure method and supercells up to 4,096 atoms per cell [77], despite discrepancies on the band offset obtained from the calculation. From the dependence of the coupling parameter C_{OM} in the various II–VI HMA systems on the anion electronegativity difference, we make the reasonable assumption that $C_{OM} \approx 2.2$ eV in II–O–Te alloys [78]. Using $C_{OM} \approx 2.2$ eV and (1.1), the "active" O mole fractions incorporated in the Te sublattice for CdO_xTe_{1-x} HMAs using a laser fluence of 40 and 80 mJ cm^{-2} as a function of implanted O concentration are calculated and shown in Fig. 1.18. The x values shown in Fig. 1.18 reveal that for the lower implanted O$^+$ concentration of 1% the O activation efficiency is close to 100%. Moreover, the kinetic limit of solubility of O in CdTe for PLM at 40 mJ cm^{-2} is ∼0.015. For a PLM fluence of 80 mJ cm^{-2} this limit decreases to ∼0.01 because of the prolonged melt/crystallization duration.

Thermal stability of the CdO_xTe_{1-x} alloys formed by implantation and PLM was also studied by subjecting the alloy to RTA for 10 s in the temperature range of 300–500°C. A reduction in the energy shift of the fundamental gap at RTA temperature higher than 300°C was observed. This again suggests that the Cd–O bonds are relatively weak and these CdO_xTe_{1-x} alloys

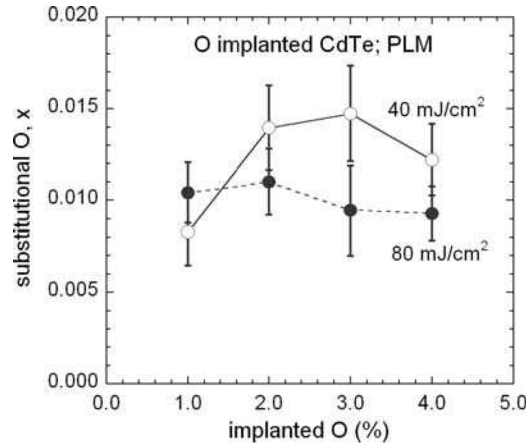

Fig. 1.18. The "active" O mole fractions incorporated in the Te sublattice for CdO_xTe_{1-x} synthesized by II-PLM using laser fluence of 40 and 80 mJ cm^{-2} as a function of implanted O concentration

are thermally less stable than GaNAs. At an RTA temperature of 400°C, only the original E_M transition is observed, suggesting that most of the implanted O atoms that resided in the Te sites after PLM diffused out of the Te sites, possibly forming O bubbles when subjected to the RTA process.

For the cases of N in GaAs or O in CdTe, the localized states are located within the conduction band and consequently a relatively wide lower subband is formed through the anticrossing effect. The conduction band states associated with the E_- edge retain the extended E_M-like character and those at the E_+ edge have a more localized E_N (E_O)-like character. A narrow lower band can be formed only if the localized states lie well below the conduction band edge. In this case the E_- subband states are of highly localized character and the E_+ subband states become more extended. This situation occurs when O is introduced into the II–VI semiconductors ZnTe, MnTe, and MgTe.

Figure 1.19 shows PR spectra from a $Zn_{0.88}Mn_{0.12}Te$ substrate and two $Zn_{0.88}Mn_{0.12}Te$ samples implanted with 3.3% of O followed by PLM with laser energy fluence of 0.15 and 0.3 J cm^{-2}. Two optical transitions in the vicinity of ∼1.8 and 2.6 eV are clearly observed from the O^+-implanted samples after PLM. These transitions occur at energies distinctly different from the fundamental band gap transition at $E_M = 2.32$ eV of the $Zn_{0.88}Mn_{0.12}Te$ matrix, and can be attributed to transitions from the valence band to the two conduction subbands, E_+(∼2.6 eV) and E_-(∼1.8 eV) formed as a result of the hybridization of the localized O states and the extended conduction band states of ZnMnTe. The strong photomodulated transition signals indicate the extended nature of these electronic states and the substantial oscillator strength for the transitions. Optical absorption shows that the intermediate band (E_-) has a relatively large absorption coefficient

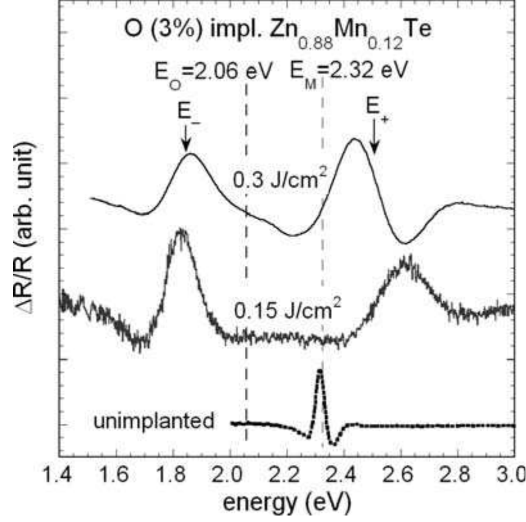

Fig. 1.19. PR spectra obtained from $Zn_{0.88}Mn_{0.12}Te$ samples as-grown and implanted with 3.3% O^+ followed by PLM with energy fluence of 0.15 and 0.3 J cm^{-2}

($\alpha \sim 10^5\,cm^{-1}$); similar to that obtained above the band gap in direct gap materials. PLM of O^+-implanted ZnMnTe samples with energy fluence in the range of 0.02–0.3 J cm^{-2} indicates that the threshold for melting through the implanted region in ZnMnTe is between 0.04 and 0.08 J cm^{-2} under the current PLM conditions [32].

The substitutional mole fractions of O for the $Zn_{0.88}Mn_{0.12}O_xTe_{1-x}$ layers synthesized by II-PLM are calculated using the BAC model with the assumed value of $C_{OM} = 2.2\,eV$ and estimated to be $x \sim 0.024$. X-ray diffraction (XRD) shows only extra diffraction peaks at higher diffraction angle of the (002) and (004) diffraction peaks of the substrate ZnTe. This confirms the formation of epitaxial ZnO_xTe_{1-x} layer with a smaller lattice parameter and no polycrystalline secondary phase.

Furthermore, photomodulated transmission (PT) measurements of a II-PLM $Zn_{0.88}Mn_{0.12}O_xTe_{1-x}$ sample under hydrostatic pressure showed that the pressure-induced energy shift of the E_- transition of $Zn_{0.88}Mn_{0.12}O_xTe_{1-x}$ is much weaker (initial slope $\approx 2\,meV\,kbar$) and nonlinear as compared to the change of the direct band gap of $Zn_{0.88}Mn_{0.12}Te$ [31]. This weak pressure dependence of the E_- transition can be fully understood with the BAC model. The fact that E_- is located much closer to the energy level of the localized O states gives its wavefunction a pronounced O-like character. The best fits to the data yield the energy position of the O level (relative to the top of the valence band) $E_O = E_V + 2.0 \pm 0.1\,eV$ at atmospheric pressure with a pressure dependence of $0.6 \pm 0.1\,meV\,kbar^{-1}$. It is also observed that the pressure dependence of E_- is slightly stronger than that of the O level as expected

from the admixture of extended conduction-band Γ_C states of the matrix to the E_- band edge states.

Similar behavior of the E_- subband edge under applied pressure was previously observed in GaN_xAs_{1-x} at the pressures high enough to shift the Γ conduction-band edge of GaAs matrix above the localized N level [1, 2, 22]. Although it can only be explained by the BAC model as a pressure-induced transformation of the nature of the E_- subband from an extended to highly localized state GaN_xAs_{1-x}, the pressure dependence of E_- conduction band edge along with the origin of the E_+ transitions as well as its pressure dependence have been a subject of debate due to the complexity of the conduction band structure of GaAs, the close proximity of the localized N level to the L conduction-band edges in particular. Here, the $Zn_{1-y}Mn_yO_xTe_{1-x}$ system serves well as a test case for the BAC model since the conduction-band L and X edges are located far away from the Γ edge (>1.0 eV) in the $Zn_{1-y}Mn_yTe$. The much simpler band structure makes it much easier to directly evidence that the E_- and E_+ transitions are the results of a BAC interaction between the extended Γ conduction band states and highly localized states in HMAs.

1.7 Photovoltaic Applications of Highly Mismatched Alloys

In addition to the unconventional conduction band structure, the $Zn_{1-y}Mn_y O_xTe_{1-x}$ alloys represent an interesting case of a semiconductor with multiple direct gaps that has technological potential for photovoltaic applications. To date, the highest power conversion efficiency of ∼33% has been achieved with multijunction solar cells based on standard semiconductor materials [79–81]. It was recognized over 30 years ago that the introduction of states in a semiconductor band gap presents an alternative to multijunction designs for improving the power conversion efficiency of solar cells [82–85]. It was argued that deep impurity or defect states could play the role of the intermediate states for this purpose. Detailed balance calculations indicate that a single junction cell with one and two properly located bands of intermediate states (intermediate band solar cell, IBSC) could achieve maximum power conversion efficiencies up to 62% [83] and 71.7% [84], respectively. However, difficulties in controlling the incorporation of high concentrations of impurity or defect states have thwarted prior efforts to realize such materials [85].

The three absorption edges of the II-PLM $Zn_{0.88}Mn_{0.12}O_xTe_{1-x}$ alloy: $E_+(k=0) - E_V(k=0) = 2.56\,\text{eV}$, $E_-(k=0) - E_V(k=0) = 1.83\,\text{eV}$, and $E_+(k=0) - E_-(k=0) = 0.73\,\text{eV}$ span much of the solar spectrum; thus these alloys are good candidates for the multiband semiconductors envisioned for high efficiency IBSC. Calculations based on detailed balance theory [83,84,86] for this material yield an ideal power conversion efficiency of 45%. Even with this nonoptimal band gap configuration the ideal power conversion efficiency is higher than that of any solar cell based on a single junction in a single gap

semiconductor and is comparable to the efficiency of a tandem cell (~55%) with two semiconductors of optimal band gaps (0.7 and 1.5 eV) [83].

The potential technological importance of the multiband semiconductors raises the question if they can also be realized in group III-$N_x - V_{1-x}$ HMAs as well. In most III–V compounds the localized N level lies above the conduction band edge. An exception is the $GaAs_{1-y}P_y$ alloy system in which N-level falls below the conduction band edge for $y > 0.3$. Consequently the anticrossing interaction of the N states with the extended conduction band states in these GaAsP alloys is expected to result in the formation of a narrow band of intermediate states. This is supported by the observation that the fundamental band gap in GaN_xP_{1-x} is transformed from indirect to direct for $x > 0.005$. [24, 87, 88]. However, the novel band structure of $GaN_xAs_{1-x-y}P_y$ alloys has not been explored [89, 90].

Synthesis of quaternary $GaN_xAs_{1-x-y}P_y$ alloys using the II-PLM method has also been explored [91]. Figure 1.20 shows a series of PR spectra from MOCVD grown $GaAs_{1-y}P_y$ epitaxial layers (~0.5 μm thick) on GaAs with $0 \leq y \leq 0.38$ implanted with 2% of N followed by PLM with 0.4 J cm^{-2} laser pulse and RTA at 950°C for 10 s. The energy gap, E_M of as-grown $GaAs_{1-y}P_y$ and the N level E_N are indicated in the Fig. 1.20. The PR spectrum from the N^+-implanted GaAs sample after PLM and RTA exhibit a strong, well-resolved interband transition from the valence band maximum to the lower

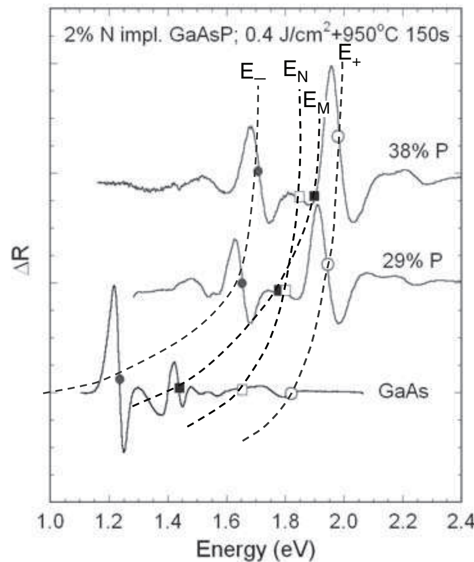

Fig. 1.20. PR spectra from 2% N^+-implanted $GaAs_{1-y}P_y$ ($y = 0$–0.4) PLM at 0.4 J cm^{-2} followed by 950°C 10 s RTA. Positions of the E_- and E_+ transitions as well as the energy levels of the conduction band minimum of the substrate E_M and the N level E_N are also indicated

subband E_- at ∼1.24 eV. This location of E_- corresponds to ∼1% of substitutional N incorporated in the GaAs lattice, similar to the result shown above.

PR spectra from the N$^+$-implanted GaAs$_{1-y}$P$_y$ samples ($y > 0$) show two well-resolved optical transitions E_- and E_+, distinctly different from the band gap transitions of the corresponding GaAs$_{1-y}$P$_y$ substrates. The locations of E_+ and E_- vary as the P content increases. It is also important to note the change in the relative strength of these two transitions. In GaAs and in As-rich GaAs$_{1-y}$P$_y$ the E_- transition is much stronger than E_+ transition. However as seen in Fig. 1.20 the relative strength of the E_+ transitions increases with increasing P content and becomes stronger than E_- for $y > 0.25$. This behavior is similar to the case of ZnO$_x$Te$_{1-x}$ alloys and can be easily explained by the BAC model, taking into account the much weaker dipole optical coupling of the valence band to E_N compared with the coupling between the valence band and E_M. As is shown in Fig. 1.21 the energy values of the E_- transitions follow E_M at low and E_N at high P contents. On the other hand E_+ transitions mostly follow E_N at low and E_M at larger y. The character of the wavefunctions and thus also the strength of the optical transitions depend on the location of the E_- and E_+ states relative to E_N and E_M.

Figure 1.21 also shows the calculated values of E_+ and E_- transitions using the BAC model assuming an N concentration of 0.3, 1, and 2% in the

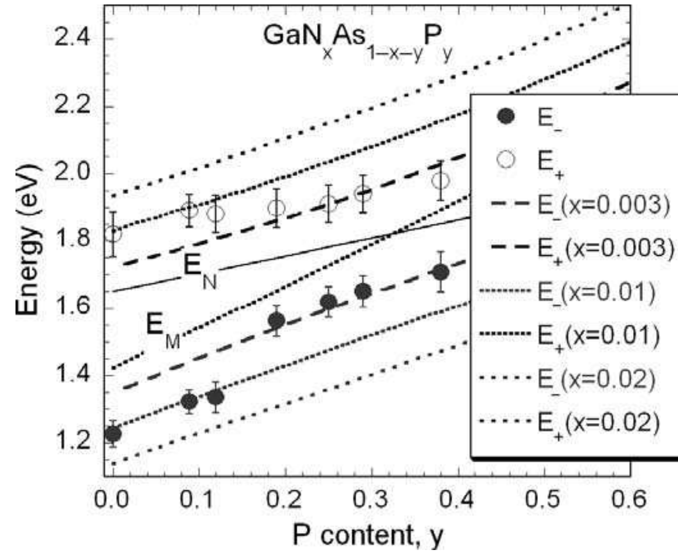

Fig. 1.21. Measured values of the E_- and E_+ transitions in GaNAsP are shown as *closed* and *open circles*, respectively. The positions of the conduction band minimum at the Γ point E_M for the GaAs$_{1-y}$P$_y$ substrate and the N level E_N are also shown as a function of P content, y. Calculated values of the E_- and E_+ transitions based on the BAC model for $x = 0.003$, 0.01, and 0.02 are also shown

$GaN_xAs_{1-x-y}P_y$ layers. Comparison between the calculated and measured E_+ and E_- values in Fig. 1.21 shows that for $GaAs_{1-y}P_y$ layers with $y \leq 0.12 \sim 1\%$ of N is incorporated in the film ($\sim$50% of the total implanted N). This is similar to the N activation efficiency observed for II-PLM GaN_xAs_{1-x}. For $GaAs_{1-y}P_y$ layers with $y > 0.12$, the incorporated N concentration is smaller ($x \sim 0.003$), and corresponds to an activation efficiency of 15% of the implanted N. This may be due to the high density of the misfit dislocations in $GaAs_{1-y}P_y$ epitaxial layers coming from the large lattice mismatch with the GaAs substrate (>0.4% for $y > 0.12$). These dislocations may act as a sink for the preferential segregation of N during the PLM and RTA processing steps.

As shown in Fig. 1.21, at a P content $y \geq 0.3$, E_N, lies below the direct CBM E_M of the $GaAs_{1-y}P_y$ alloy; these are precisely the conditions that are required to make the narrow intermediate band required for a multiband solar cell. An upper limit to the P content is set by the appearance of an indirect band gap ($E^X < E^\Gamma$) at $y > 0.5$. Although only small fraction of N ($x = 0.003$) is incorporated in $GaAs_{1-y}P_y$ layers with $y > 0.2$ using the present II-PLM conditions, strong and distinctive optical transitions are indeed observed. As illustrated by the BAC calculation shown in Fig. 1.21, for a $GaN_xAs_{1-y}P_y$ multiband semiconductor with $y = 0.4$ and an $x = 0.02$, a N derived narrow band of extended states E_- is separated from the upper subband E_+ by about 0.8 eV. Three types of optical transitions are possible in this band structure: 0.8 eV ($E_- \rightarrow E_+$), 1.5 eV ($E_V \rightarrow E_-$), and 2.3 eV ($E_V \rightarrow E_+$). A theoretical maximum efficiency of between 55% and 60% is expected for IBSCs fabricated using this alloy. It should be emphasized that unlike the dilute II–VI oxides, $GaN_xAs_{1-y}P_y$ with significant N content (>4%) can be grown using the MBE technique [89, 90, 92, 93].

1.8 Conclusions

In this chapter we have reviewed our works on the synthesis of HMAs using both conventional IBS and ion implantation followed by PLM (II-PLM) methods. The synthesis of III–V dilute nitrides and their structural, optical, and electrical properties are discussed in detail. Using II-PLM thermally stable GaN_xAs_{1-x} thin films with N content up to 1.6% with fundamental band gap of 1.16 eV was obtained. N activation efficiency in II-PLM GaN_xAs_{1-x} thin films is as much as a factor of five higher than that in GaN_xAs_{1-x} thin films synthesized by N^+ implantation and RTA only. The II-PLM method was also exploited to study the mutual passivation effect of group IV donors and isovalent N in GaN_xAs_{1-x}.

Moreover, group II–VI dilute oxide (II–O–VI) semiconductors, a direct analogue of the III–V diluted nitrides, with the anions partially replaced by highly electronegative isoelectronic O atoms have been successfully synthesized by II-PLM. Specifically, in the case of $Zn_{1-x}Mn_xTe$, where the O

level lies below the conduction band edge, incorporation of a small amount of oxygen by II-PLM leads to the formation of a narrow, oxygen-derived band of extended states located well below the conduction band edge of the ZnMnTe matrix. The three absorption edges of this material (∼0.73, 1.83, and 2.56 eV) cover the entire solar spectrum providing a material envisioned for the multiband, single junction, high-efficiency photovoltaic devices. Finally, recent work on the quaternary $GaN_xAs_{1-x-y}P_y$ (with $y > 0.3$) alloys that is another three band semiconductor with potential applications for high-efficiency intermediate band solar cells is also discussed.

Acknowledgments. The authors acknowledge I.D. Sharp, R. Farshchi, and E.E. Haller at UC Berkeley, J.F. Geisz, D.J. Friedman, and J.M. Olson at NREL, H.P. Xin and C.W. Tu at UC San Diego, M.R. Pillai and M.J. Aziz at Harvard University and M.C. Ridgway at the Australian National University for their contributions on some of the experimental works presented in this review. One of the authors (MAS) acknowledges support from a National Science Foundation Graduate Research Fellowship. This work was supported in part by the Director's Innovation Initiative Program, National Reconnaissance Office and the Director, Office of Science, Office of Basic Energy Sciences, Division of Materials Sciences and Engineering, of the U.S. Department of Energy under Contract No. DE-AC02-05CH11231.

References

1. W. Shan, W. Walukiewicz, J.W. Ager III, E.E. Haller, J.F. Geisz, D.J. Friedman, J.M. Olson, S.R. Kurtz, Phys. Rev. Lett. **82**, 1221 (1999)
2. W. Walukiewicz, W. Shan, K.M. Yu, J.W. Ager III, E.E. Haller, I. Miotlowski, M.J. Seong, H. Alawadhi, A.K. Ramdas, Phys. Rev. Lett. **85**, 1552 (2000)
3. For a review see: III-N-V Semiconductor Alloys 2002, special Issue of Semiconductor Science and Technology 17, 741–906
4. I. Buyanova, W. Chen (Eds.) *Physics and Applications of Dilute Nitrides*, (Taylor & Francis, New York, 2004)
5. K. Uesugi, N. Marooka, I. Suemune, Appl. Phys. Lett. **74**, 1254 (1999)
6. M. Kondow, K. Uomi, K. Hosomi, T. Mozume, Jpn. J. Appl. Phys. **33**, L1056 (1994)
7. J.F. Geisz, D.J. Friedman, J.M. Olson, S.R. Kurtz, B.M. Keyes J. Cryst, Growth **195**, 401 (1998)
8. J.N. Baillargeon, K.Y. Cheng, G.E. Hofler, P.J. Pearah, K.C. Hsieh, Appl. Phys. Lett. **60**, 2540 (1992)
9. W. Shan, W. Walukiewicz, K.M. Yu, J. Wu, J.W. Ager, E.E. Haller, H.P. Xin, C.W. Tu, Appl. Phys. Lett. **76**, 3251 (2000)
10. W.G. Bi, C.W. Tu, J. Appl. Phys. **80**, 1934 (1996)
11. W. Shan, W. Walukiewicz, K.M. Yu, J.W. Ager III, E.E. Haller, J.F. Geisz, D.J. Friedman, J.M. Olson, Kurtz, R. Sarah, K. Nauka, Phys. Rev. B **62**, 4211 (2000)
12. W. Shan, K.M. Yu, W. Walukiewicz, J.W. Ager III, E.E. Haller, M.C. Ridgway, Appl. Phys. Lett. **75**, 1410 (1999)

13. M. Kondow, T. Kitatani, S. Nakatsuka, M.C. Larson, K. Nakahara, Y. Yazawa, M. Okai, K. Uomi, IEEE J. Sel. Topics in Quantum Elect. **3**, 719 (1997)
14. M. Kondow, T, Kitatani, M.C. Larson, K. Nakahara, K. Uomi, H. Inoue, J. Cryst. Growth **188**, 255 (1998)
15. D.J. Friedman, J.F. Geisz, S.R. Kurtz, D. Myers, J.M. Olson, J. Cryst. Growth **195**, 409 (1998)
16. S.R. Kurtz, A.A. Allerman, E.D. Jones, J.M. Gee, J.J. Banas, B.E. Hammons, Appl. Phys. Lett. **74**, 729 (1999)
17. P.R.C. Kent, L. Bellaiche, A. Zunger, Semicond. Sci. Technol. **17**, 851 (2002)
18. E.P. O'Reilly, A. Lindsay, S. Tomic, M. Kamal-Saadi, Semicond. Sci. Technol. **17**, 870 (2002)
19. A. Lindsay, E.P. O'Reilly, Phys. Rev. Lett. **93**, 196402 (2004)
20. J.D. Perkins, A. Masceranhas, Y. Zhang, J.F. Geisz, D.J. Friedman, J.M. Olson, S.R. Kurtz, Phys. Rev. Lett. **82**, 3312 (1999)
21. P. Perlin, P. Wisniewski, C. Skierbiszewski, T. Suski, E. Kaminska, S.G. Subramanya, E.R. Weber, D.E. Mars, W. Walukiewicz, Appl. Phys. Lett. **76**, 1279 (2000)
22. J. Wu, W. Shan, W. Walukiewicz, Semicond. Sci. Technol. **17**, 860 (2002)
23. W. Shan, W. Walukiewicz, K.M. Yu, J. Wu, J.W. Ager III, E.E. Haller, H.P. Xin, C.W. Tu, Appl. Phys. Lett. **76**, 3251 (2000)
24. W. Shan, W. Walukiewicz, J.W. Ager III, E.E. Haller, J.F. Geisz, D.J. Friedman, J.M. Olson, S.R. Kurtz, J. Appl. Phys. **86**, 2349 (1999)
25. K.M. Yu, W. Walukiewicz, J. Wu, J. Beeman, J.W. Ager III, E.E. Haller, W. Shan, H.P. Xin, C.W. Tu, M.C. Ridgway, Appl. Phys. Lett. **78**, 1077 (2001)
26. D.J. Wolford, J.A. Bradley, K. Fry, J. Thompson in *Proceedings of the 17th International Conference on the Physics of Semiconductors*, ed. by J.D. Chadi, W.A. Harrison (Springer, Berlin Heidelberg New York, 1984), p. 627
27. W. Walukiewicz, W. Shan, J.W. Ager III, D.R. Chamberlin, E.E. Haller, J.F. Geisz, D.J. Friedman, J.M. Olson, S.R. Kurtz, in *Photovoltaics for the 21st Century*, ed. by V.K. Kapur, R.D. McDonnell, D. Carlson, G.P. Ceasar, A. Rohatgi, (Electrochemical Society Press, Pennington, 1999) p. 190
28. J. Wu, W. Walukiewicz, K.M. Yu, W. Shan, J.W. Ager III, E.E. Haller, I. Miotkowski, A.K. Ramdas, and Su Ching-Hua, Phys. Rev. B **68**, 033206 (2003)
29. J. Wu, W. Walukiewicz, K.M. Yu, J.W. Ager III, E.E. Haller, I. Miotkowski, A.K. Ramdas, Su Ching-Hua, I.K. Sou, R.C.C. Perera, J.D. Denlinger, Phys. Rev. B **67**, 035207 (2003)
30. W. Shan, W. Walukiewicz, J.W. Ager III, K.M. Yu, J. Wu, E.E. Haller, Y. Nabetani, T. Mukawa, Y. Ito, T. Matsumoto, Appl. Phys. Lett. **83**, 299 (2003)
31. W. Shan, K.M. Yu, W. Walukiewicz, J. Wu, J.W. Beeman, J.W. Ager III, M.A. Scarpulla, O.D. Dubon, E.E. Haller, Appl. Phys. Lett. **84**, 924 (2004)
32. K.M. Yu, W. Walukiewicz, J. Wu, W. Shan, J.W. Beeman, M.A. Scarpulla, O.D. Dubon, P. Becla, Phys. Rev. Lett. **91**, 246203 (2003)
33. C. Skierbiszewski, P. Perlin, P. Wišniewski, W. Knap, T. Suski, W. Walukiewicz, W. Shan, K.M. Yu, J.W. Ager, E.E. Haller, J.F. Geisz, J.M. Olson, Appl. Phys. Lett. **76**, 2409 (2000)
34. K.M. Yu, W. Walukiewicz, W. Shan, J.W. Ager III, J. Wu, E.E. Haller, J.F. Geisz, D.J. Friedman, J.M. Olson, S.R. Kurtz, Phys. Rev. B **61**, R13337 (2000)

35. K.M. Yu, W. Walukiewicz, W. Shan, J. Wu, J.W. Ager III, E.E. Haller, J.F. Geisz, M.C. Ridgway, Appl. Phys. Lett. **77**, 2858 (2000)
36. W.K. Hung, M.Y. Chern, J.C. Fan, T.Y. Lin, Y.F. Chen, Appl. Phys. Lett. **74**, 3951 (1999)
37. W.K. Hung, M.Y. Chern, Y.F. Chen, Semicond. Sci. Tehnol. **15**, 892 (2000)
38. K.M. Yu, W. Walukiewicz, J. Wu, J. Beeman, J.W. Ager III, E.E. Haller, W. Shan, H.P. Xin, C.W. Tu, M.C. Ridgway, J. Appl. Phys. **90**, 2227 (2001)
39. K.M. Yu, Semicond. Sci. Technol. **17**, 785 (2002)
40. X, Weng, S.J. Clarke, W. Ye, S. Kumar, R.S. Goldman, V. Rotberg, J. Holt, J. Sipowska, A. Francis, A. Daniel, R. Clarke, J. Appl. Phys. **92**, 4012 (2002)
41. M. Reason, H.A. McKay, W. Ye, S. Hanson, R.S. Goldman, V. Rotberg, Appl. Phys. Lett. **85**, 1692 (2004)
42. J. Jasinski, K.M. Yu, W. Walukiewicz, Z. Liliental-Weber, J. Washburn, Appl. Phys. Lett. **79**, 931 (2001)
43. D.E. Aspnes, Surf. Sci. **37**, 418 (1973)
44. R.A. Brown, J.S. Williams, J. Appl. Phys. **81**, 7681 (1997)
45. L.C. Feldman, J.W. Mayer, S.T. Picraux, *Materials Analysis by Ion Channeling* (Academic Press, New York, 1982)
46. R. Heckingbottom, T. Ambridge, Rad. Eff. **17**, 31 (1973)
47. A.J. Moll, K.M. Yu, W. Walukiewicz, W.L. Hansen, E.E. Haller, Appl. Phys. Lett. **60**, 2383 (1992)
48. K.M. Yu, M.C. Ridgway, Appl. Phys. Lett. **73**, 52 (1998)
49. J.S. Williams, in *Laser Annealing of Semiconductors*, ed. by J.M. Poate, J.W. Mayer (Academic Press, New York 1982), p. 385
50. C.W. White, P.S. Peercy, (eds.), *Laser and Electron Beam Processing of Materials* (Academic Press, New York, 1980)
51. C.W. White, S.R. Wilson, B.R. Appleton, F.W. Young Jr., J. Appl. Phys. **51**, 738 (1980)
52. A. Herrera-Gómez, P.M. Rousseau, G. Materlik, T. Kendelewicz, J.C. Woicik, P.B. Griffin, J. Plummer, W.E. Spicer, Appl. Phys. Lett. **68**, 3090 (1996)
53. Y. Takamura, S.H. Jain, P.B. Griffin, J.D. Plummer, J. Appl. Phys. **92**, 230 (2002)
54. P.A. Barnes, H.J. Leamy, J.M. Poate, S.D. Ferris, J.S. Williams, G.K. Celler, Appl. Phys. Lett. **33**, 965 (1978)
55. J.A. Golovchenko, T.N.C Venkatesan, Appl. Phys. Lett. **32**, 147 (1978)
56. D.H. Lowndes, *Pulsed Laser Processing of Semiconductors*, ed. by R.F. Wood et al. (Academic Press, Orlando, FL, 1984), p. 472
57. M. Von Allmen, S.S. Lau, in *Laser Annealing of Semiconductors*, ed. by J.M. Poate, J.W. Mayer (New York, Academic Press, 1982), p. 439
58. M. Von Allmen, A. Blatter, *Laser-Beam Interactions with Materials: Physical Principles and Applications*, 2nd edn. (Springer, Berlin Heidelberg New York, 1995)
59. M.A. Scarpulla, K.M. Yu, O.P.M. Monteiro, M.C. Ridgway, M.J. Aziz, O.D. Dubon, Appl. Phys. Lett. **82**, 1251 (2003)
60. O.D. Dubon, M.A. Scarpulla, K.M. Yu, W. Walukiewicz, Proc. Inst. Phys. Conf. Ser. **184**, 399 (2005)
61. M.A. Scarpulla, B.L. Cardozo, R. Farshchi, W.M. Hlaing Oo, M.D. McCluskey, K.M. Yu, O.D. Dubon, Phys. Rev. Lett. **95**, 207204 (2005)

62. P.R. Stone, M.A. Scarpulla, R. Farshchi, I.D. Sharp, E.E. Haller, O.D. Dubon, K.M. Yu, J.W. Beeman, E. Arenholz, J.D. Denlinger, H. Ohldag, Appl. Phys. Lett. **89**, 012504 (2006)
63. M. Von Allmen, *Laser Annealing of Semiconductors*, ed. by J.M. Poate, J.W. Mayer (New York, Academic Press, 1982), p. 43
64. K.M. Yu, W. Walukiewicz, J.W. Beeman, M.A. Scarpulla, O.D. Dubon, M.R. Pillai, M. Aziz, Appl. Phys. Lett. **80**, 3958 (2002)
65. K.M. Yu, W. Walukiewicz, M.A. Scarpulla, O.D. Dubon, J. Jasinski, Z. Liliental-Weber, J. Wu, J.W. Beeman, M.R. Pillai, M.J. Aziz, J. Appl. Phys. **94**, 1043 (2003)
66. C.W. White, in *Pulsed Laser Processing of Semiconductors*, ed. by R.F. Wood et al. (Orlando, Fla., Academic Press), p. 44
67. W. Walukiewicz, Physica B **302–303**, 123 2001
68. K.M. Yu, W. Walukiewicz, W. Shan, J. Wu, J.W. Beeman, J.W. Ager III, E.E. Haller, App. Phys. Lett. **77**, 3607 (2000)
69. K.M. Yu, W. Walukiewicz, J. Wu, D. Mars, D.R. Chamberlin, M.A. Scarpulla, O.D. Dubon, J.F. Geisz, Nat. Mater. **1**, 185 2002
70. J. Wu, K.M. Yu, W. Walukiewicz, G. He, E.E. Haller, D.E. Mars, D.R. Chamberlin, Phys. Rev. B **68**, 195202 (2003)
71. J. Li, P. Carrier, Wei Su-Huai, Li Shu-Shen, Xia Jian-Bai, Phys. Rev. Lett. **96**, 035505 (2006)
72. K.M. Yu, W. Walukiewicz, J. Wu, W. Shan, J.W. Beeman, M.A. Scarpulla, O.D. Dubon, M.C. Ridgway, D.E. Mars, D.R. Chamberlin, Appl. Phys. Lett. **83**, 2844 (2003)
73. K.M. Yu, W. Walukiewicz, J. Wu, J.W. Beeman, J.W. Ager III, E.E. Haller, I. Miotkowski, A.K. Ramdas, P. Becla, Appl. Phys. Lett. 80, 1571 (2002)
74. Y. Nabetani, Mater. Res. Soc. Symp. Proc. **744**, M3.4 (2003)
75. V.A. Gnatyuk, T. Aoki, O.S. Gorodnychenk, Y. Hatanaka, Appl. Phys. Lett. **83**, 307704 (2003)
76. M.J. Seong, H. Alawadhi, I. Miotkowski, A.K. Ramdas, S. Miotkowska, Phys. Rev. B **60**, R16275 (1999)
77. J. Li, S.-H. Wei, Phys. Rev. **B73**, 041201(R) (2006)
78. K.M. Yu, W. Walukiewicz, J. Wu, W. Shan, J.W. Beeman, M.A. Scarpulla, O.D. Dubon, P. Becla, J. Appl. Phys. **95**, 6232 (2004)
79. P.K. Chiang, J.H. Ermer, W.T. Nishikawa, D.D. Krut, D.E. Joslin, J.W. Eldredge, B.T. Cavicchi, J.M. Olson in *Proceedings of 25th IEEE Photovoltaic Specialists Conference* (IEEE, New York, 1996) p. 183
80. S.R. Kurtz, D. Myers, J.M. Olson, in *Proceedings of 26th IEEE Photovoltaic Specialists Conference*, (IEEE, New York, 1997) p. 875
81. R.R. King, P.C. Colter, D.E. Joslin, K.M. Edmondson, D.D. Krut, N.H. Karam, S. Kurtz, in *Proceedings of 29th IEEE Photovoltaic Specialists Conference*, (IEEE, New York, 2002) p. 852
82. M. Wolf, Proc. IRE **48**, 1246 (1960)
83. A. Luque, A. Marti, Phys. Rev. Lett. **78**, 5014 (1997)
84. A.S. Brown, M.A. Green, R.P. Corkish, Physica E **14**, 121 (2002)
85. L. Cuadra, A. Marti, A. Luque, Thin Solid Films **451–452**, 593 (2004)
86. W. Shockley, H.J. Queisser, J. Appl. Phys. **32**, 510 (1961)
87. H.P. Xin, C.W. Tu, Y. Zhang, A. Mascarenhas, Appl. Phys. Lett. **76**, 1267 (2000)

88. J. Wu, W. Walukiewicz, K.M. Yu, J.W. Ager III, E.E. Haller, Y.G. Hong, H.P. Xin, C.W. Tu, Phys. Rev. B **65**, 241303 (2002)
89. Y. Fujimoto, H. Yonezu, A. Utsumi, K. Momose, Y. Furukawa, Appl. Phys. Lett. **79**, 1306 (2001)
90. K. Momose, H. Yonezu, Y. Furukawa, A. Utsumi, Y. Yoshizumi, S. Shinohara, J. Cryst. Growth, **251**, 443 (2003)
91. K.M. Yu, W. Walukiewicz, J.W. Ager III, D. Bour, R. Farshchi, O.D. Dubon, S.X. Li, I.D. Sharp, E.E. Haller, Appl. Phys. Lett. **88**, 092110 (2006)
92. W.G. Bi, C.W. Tu, Appl. Phys. Lett. **69**, 3710 (1996)
93. C.W. Tu, W.G. Bi, Inst. Phys. Conf. Ser. **155**, 213 (1996)

2

Impact of Nitrogen Ion Density on the Optical and Structural Properties of MBE Grown GaInNAs/GaAs (100) and (111)B Quantum Wells

J. Miguel-Sánchez, Á. Guzmán, A. Hierro, E. Muñoz, U. Jahn,
and A. Trampert

The impact of nitrogen ion density, present in the chamber during molecular beam epitaxial growth of the GaInNAs quantum wells, on their structural and optical properties is presented. The growth on two different substrate orientations, GaAs (100) and (111)B has been studied. The quantum well optical emission was found to be strongly increased when the nitrogen ion density was reduced during the growth, as determined by photoluminescence experiments. Cathodoluminescence mappings of quantum wells grown under different ion densities are compared, showing a stronger compositional modulation depth, and thus a higher structural disorder, when a higher ion density is present during the growth. This technique was also used to study the optical activity of defects found in GaAs (111)B samples. We applied deflecting magnetic fields to tune the amount of nitrogen ion density in the chamber during growth. Atomic force microscopy (AFM) measurements in similar epilayers showed that ions cause an important structural disorder of the layers, showing approximately twice the root mean square (RMS) roughness when the density of ions is not reduced by external magnetic fields. Additionally, transmission electron microscopy (TEM) measurements of buried GaInNAs quantum wells is presented, showing that lateral compositional fluctuations of In and N are suppressed when the quantum wells are protected from the ions. Finally, we have found that quantum wells exposed to higher ion densities during the growth show deeper localization levels and higher delocalization temperatures. These results clearly show that the structural properties such as the roughness and the compositional modulation, as well as the optical properties, such as the optical emission and localization energies are strongly dependent on the density of nitrogen ions present in the chamber during the growth of GaInNAs quantum wells. Rapid thermal annealing (RTA) experiments are also consistent with this hypothesis.

2.1 Introduction

2.1.1 Overview

In this chapter, we describe in detail our research concerning the impact of the nitrogen plasma parameters on the optical and structural properties of dilute nitrides. We performed an extensive characterization of this plasma. Optimum parameters for the growth of high quality GaInNAs quantum wells, and a method to decrease the damage produced by such plasma ionic species are presented.

2.1.2 Material Properties, Nitrogen Plasmas, and (111)B

It is known from the literature that the addition of small concentrations of nitrogen to GaInAs layers (typically N mole fractions lower than 5%), cause a strong reduction of the optical quality of quantum wells, due to the formation of nonradiative defects, mainly due to the creation of Ga vacancies [1], interstitial incorporation of nitrogen [2] and damage caused by the ionized nitrogen species from the plasma [3–7]. The formation of the first two types of defects is directly related to the growth dynamics and can be controlled by using the proper growth conditions. In this work, we study the latter type of defects, i.e., those formed by ions generated in the nitrogen plasma, and their impact on the GaInNAs quantum wells (QWs) grown on GaAs (111)B and (100) has been assessed.

In order to incorporate nitrogen in the dilute nitride QW an atomic nitrogen source is needed. The most extended method to achieve this goal in molecular beam epitaxy (MBE) systems is to create a plasma from ultra-pure nitrogen. In these plasmas, different species coexist simultaneously: electrons (e^-), atomic nitrogen (N), diatomic nitrogen (N_2) and their excited species (${N_2}^+$, etc) [6–8]. The ratio of the ionized species to the atomic species is called ionization factor. The lower this ionization factor, the higher the quality of the plasma for epitaxial growth applications, as we will show in the following sections.

Since electron cyclotron resonance (ECR) plasma sources show high ionization factors [8,9], the most extended nitrogen sources for the growth of nitrides and diluted nitrides are radio frequency (rf) plasmas and direct current (dc) plasmas. In this work, we used an Oxford applied rf source.

To precisely control the amount of atomic nitrogen in the plasma, we used an optical emission detector (OED) that detects the characteristic emission of atomic nitrogen. This device gives an in situ and real-time value proportional to the amount of atomic nitrogen in the plasma. It consists of an optical detector, capped with a narrow band pass optical filter tuned to the emission energy of the photons emitted from excited nitrogen atoms in the plasma.

In the following sections, different ways for in situ characterization of plasmas allowing to determine optimum working conditions for epitaxial growth are described.

In the literature, almost each work devoted to the study of the GaInNAs material refers to the (100) orientation [10–12]. In the present chapter we additionally propose the study of dilute nitride materials grown on the GaAs (111)B substrates. Our motivation is due to the interesting properties of heterostructures grown along this orientation. First of all, the presence of a piezoelectric field in strained heterostructures grown on (111) surfaces of zincblende structures [13]. These properties have been extensively studied in the literature for the well-known GaInAs/GaAs (111)B system and an excellent descriptions can be found in [14–17]. With this material system, laser emission up to 1.1 μm has been reached, with low thresholds [18–21]. Additionally, this piezoelectric field has been used for the design of nonlinear devices and optical modulators based on GaInAs/GaAs [22–26]. Recently, the first GaInNAs laser diode grown on GaAs (111)B and working at room temperature was demonstrated by our group [27].

Another interesting property refers to the critical layer thickness on this orientation. Several publications claim that the theoretical critical layer thickness is greater than for GaAs (100) [28, 29]. However, some experimental results seem to indicate that the critical layer thickness is approximately the same [30, 31].

Apart from above features, an additional interesting property of the GaAs (111)B surface is the difficulty to find a transition from the 2D to the 3D Stranski–Krastanov growth mode. There is some controversy in the literature about this point, since some authors could not find any 3D growth mode [31–33], but on the other hand, some authors reported the growth of quantum dots on GaAs (111)B [34–39]. This problem could be interesting for the growth of dilute nitrides to avoid the transition to 3D growth mode reported in the literature for GaInNAs on GaAs (100), under certain growth conditions. Additionally, if the critical layer thickness is higher, higher In mole fraction could be incorporated in the QWs without relaxation, so longer wavelengths with high-optical quality material could be achieved.

2.2 Experimental Setup

Samples characterized in this chapter were grown by MBE in a Riber 32 machine equipped with a rf plasma source. The structure of the GaAs (111)B samples is a p–i–n diode, unless otherwise stated in the text. It consists of a 500 nm intrinsic region between 300-nm thick p^+ and n^+ regions doped with beryllium and silicon, respectively. In the middle of the intrinsic region, a 7-nm thick GaInNAs quantum well was grown.

Photoluminescence (PL) characterization was performed using a He–Ne laser, with samples cooled in a cryogenic system down to 16 K. Light was collected and focused by two lenses, dispersed by a computer-controlled monochromator, and finally detected by a cooled Ge detector.

RTA were performed in a conventional RTA oven under a 1.3 bar nitrogen pressure with samples sandwiched between two dummy GaAs pieces.

2.3 Plasma Characterization

2.3.1 Basic Characterization

To achieve an accurate control of the plasma properties we can tune two different external parameters: the molecular nitrogen flux and the applied rf power. In this section, we will show techniques, which are suitable to characterize nitrogen plasmas in an effective manner. So, plasma conditions can be achieved allowing for the fabrication of GaInNAs QWs with optimum optical emission properties.

The basic plasma characterization is to determine the amount of atomic nitrogen found in the plasma cavity for each applied power and nitrogen flux. For that purpose, we measured the OED intensity as a function of the applied power, for several nitrogen fluxes. Additionally, this basic measurement is valid to perform a calibration of the system, in order to know the amount of nitrogen for each pair of rf power and nitrogen flux. The OED characterization of the plasma used in this work is shown in Fig. 2.1 for three different nitrogen fluxes: 0.3, 0.5, and 1.0 standard cubic centimeter per minute (sccm).

For low rf powers (lower than 70 W), no stable plasma could be ignited in our system, which is the reason for the absence of data points for that range of powers in the curves shown in Fig. 2.1. By increasing the applied power, the OED output increases. For powers between 70 and 200 W the difference for the three nitrogen fluxes is almost negligible. This difference increases as the applied rf power is increased, specifically for rf powers higher than 200 W, approximately. Thus, at the highest applied powers, there is an increment of

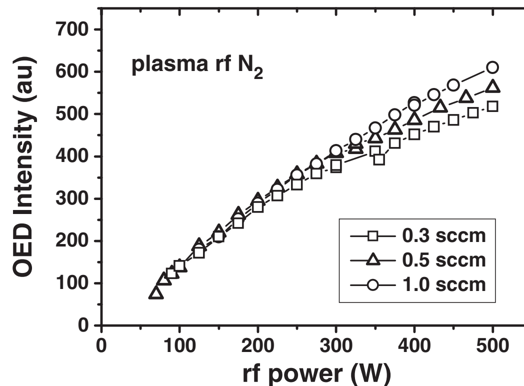

Fig. 2.1. OED characterization as a function of the applied rf power for three different nitrogen fluxes

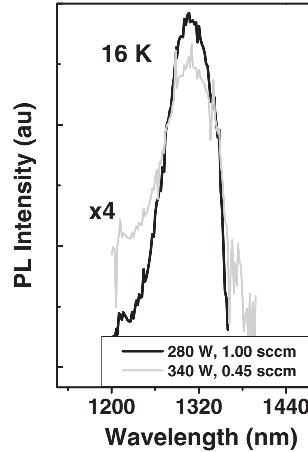

Fig. 2.2. Low-temperature (16 K) PL spectra of two GaInNAs QWs, grown under the same conditions, except for plasma parameters: 280 W and 1 sccm (*black line*) as well as 340 W and 0.45 sccm (*grey line*). OED intensity was the same for both samples

active nitrogen (OED) of up to 20% when the nitrogen flux is increased from 0.3 to 1.0 sccm.

To effectively verify that the OED signal is strongly correlated to the nitrogen content incorporated in the dilute nitride samples, the following experiment was performed: Two p–i–n structure samples were grown on GaAs (111)B (exhibiting the previously described structure), using exactly the same growth conditions for both samples (substrate temperature, growth rate, As flux, and OED intensity). The only difference between both samples was the plasma conditions to achieve the same OED intensity. We used two different powers, 280 and 340 W applied to two different nitrogen fluxes of 1.00 and 0.45 sccm, respectively, to achieve exactly the same OED value. In Fig. 2.2, low-temperature PL spectra of both samples are shown.

Both spectra are vertically shifted for clarity. The PL peak emission from both samples is exactly at the same wavelength (within measurement errors). As the In contents from both samples are nominally the same, we can finally conclude that the OED output is a reliable parameter for the accurate control of the nitrogen mole fraction in GaInNAs QWs grown by MBE. Additionally, in this figure, it is shown that the emission from the sample grown with the lower rf power (280 W) is stronger than the emission from the sample grown with the higher rf power (340 W). Thus, we may conclude that it is the rf power and not the flux that determines the optical quality of GaInNAs QWs. A lower structural quality of samples grown with higher nitrogen fluxes is expected, since high nitrogen fluxes strongly decreases the mean free paths of atoms and molecules in the chamber and over the surface. For this reason, further experimental parameters, apart from rf power and nitrogen flux, must

be taken into account to control the optical quality of GaInNAs QWs, as it will be shown in following sections.

2.3.2 The Modified Langmuir Probe Method

In order to characterize rf plasmas, electrical methods were commonly used in the past. The most spread one is based on Langmuir and consists of a narrow metallic wire (probe) introduced in an ignited plasma. By biasing this wire, current–voltage measurements were obtained, from which important plasma parameters can be extracted to characterize the plasma [8]. For dilute nitrides growth, the plasma characterization found in the literature was almost exclusively optical [6,7,40]. By a careful inspection of the optical emission coming from the plasma, radiative transitions of various species (atomic, excited, molecular, etc.) could be detected and measured in the plasma. This method is very accurate, but requires the presence of complex optical equipment near the plasma source, which is sometimes not possible due to the position of the cells in the growth chambers. Additionally, the characterization of the plasma performed in this way gives information about the plasma inside the nitrogen source, in which completely different conditions may hold when compared to the plasma impinging onto the sample.

In this section we present an easy and novel electric method for in situ plasma characterization at the sample position, where the conditions must be accurately known to control the epitaxial growth process, since it is in this region where growth dynamics and thermodynamics determine the characteristics of the grown material [41].

This novel method is based on the use of a Bayard–Alpert vacuum gauge as a modified Langmuir probe. Bayard–Alpert gauges are found in almost every ultra-high vacuum system (UHV system) and in MBE systems, due to the need of accurate pressure measurements in the 1×10^{-5} to 1×10^{-11} Torr range. The operation of these gauges is as follows: a tungsten filament is heated producing electrons due to the thermionic effect. A biased grid accelerates these electrons. When these electrons travel through an effective cross section of the atomic or molecular species in the vacuum, ionization occurs by the lost of an electron from the outer shells of these gaseous species. Finally, ionized species impinge onto a narrow metallic wire (collector), being collected and generating an electric current directly proportional to the amount of particles in the chamber that is proportional to the pressure at every moment. In standard MBE chambers, this gauge can be moved to exactly the same position of the growing surface. This allows the precise characterization of the incident flux that combined with precise reflection high electron energy diffraction (RHEED) observations permit an accurate calibration of the growth rate for several material systems [41].

On the other hand, the Langmuir probe consists of a short metallic wire introduced in the plasma cavity. Charged species impinge onto the probe

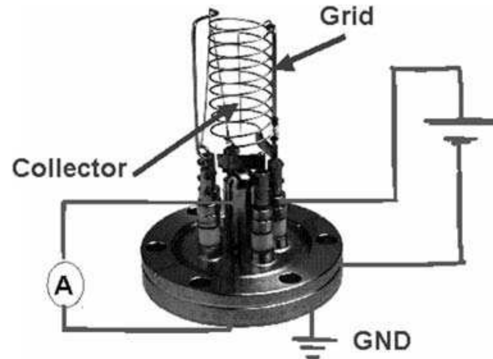

Fig. 2.3. Schematic view of the biasing of a Bayard–Alpert gauge to be used as a modified Langmuir probe

generating a current in an external circuit proportional to their density. Typically, these probes are biased to obtain I–V characterization of the plasma, as stated above [8]. The proposed method takes the advantages from both the gauge and the probe: the plasma has to be characterized at the sample position, to obtain an accurate measurement of the ions impinging onto it during growth. For this purpose, we propose a vacuum-gauge triode-like configuration for the Bayard–Alpert gauge to work as a modified Langmuir probe (Fig. 2.3), with the plasma acting as a cathode. A precision electrometer is connected in series with the probe collector. This will work as the anode. Thus, the different charged species impinging onto it will generate a positive or negative current, depending on the charge of the incident particles. The grid of the probe will act as the deflection grid found in electronic vacuum valves. A voltage source is connected in series with the grid to bias it. Thus, if the bias voltage is negative, negatively charged species from the plasma will be deflected, and therefore a positive current will be measured. In the literature, this is called ion saturation region. On the other hand, when a positive bias is applied to the grid, positively charged species (ionized atoms and molecules) will be deflected, which will yield a negative current, the electron saturation region. Thus, by using this technique we could directly measure the I–V characteristics of the generated plasma in our system, as shown in Fig. 2.4.

Using this setup, the typical characteristics expected from a conventional Langmuir probe are obtained [8]. In our system, by applying bias voltages lower than -60 V, a positive current is obtained in the ion saturation region. As reducing the bias voltage, the measured current turns negative due to the reduction of the electron shielding: the amount of electrons deflected is reduced. For bias voltages higher than 50 V, the I–V characteristics show another plateau, the electron saturation region, where ions are deflected and electrons attracted toward the collector. With the proposed model, we have

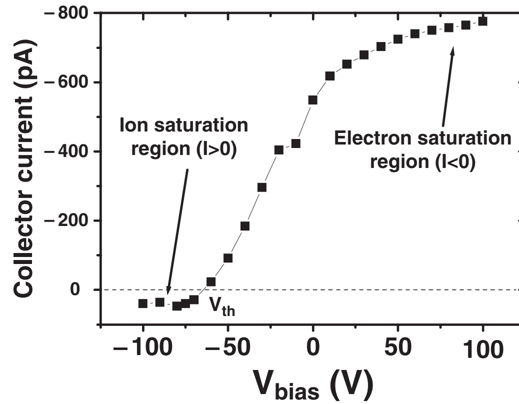

Fig. 2.4. Typical *I–V* characteristics of our nitrogen plasma, obtained with the modified Langmuir probe. In the figure, ion and electron saturation regions are shown

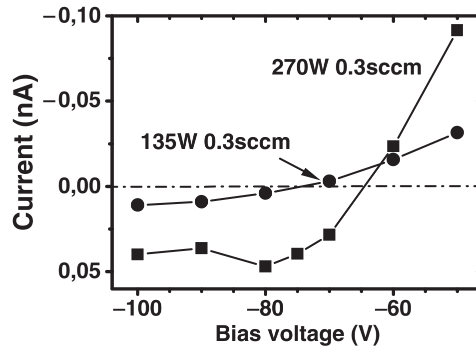

Fig. 2.5. Detail from the ion saturation region of the *I–V* characteristics from two plasmas generated using the same nitrogen flux (0.3 sccm) and two different rf powers, 135 W (*circles*) and 270 W (*squares*)

detected a positive current generated in the probe that could be only due to positively charged species impinging onto the collector. Thus, we have measured a nonnegligible amount of ionic nitrogen species coming from the plasma during the growth of dilute nitrides.

To assess this point, we performed the *I–V* plasma characterization for the same nitrogen flux, but using two different applied rf powers, 135 and 270 W (giving rise to different OED intensities, 195 and 356 a.u.). A detail of the ion saturation region from the measured *I–V* characteristics is shown in Fig. 2.5. According to this data, the application of higher rf powers to the same nitrogen flux yields a more positive current. Thus, we can conclude that the positively charged species measured using this novel modified Langmuir probe method originate from the ignited plasma and are not due to the self-ionization of

the gas due to the grid biasing (these biases are still much lower than the usual bias voltage applied to typical Bayard–Alpert gauges, around 150 V). The objective of the modified Langmuir probe method is the detection and the quantification of ions arriving at the position of the sample. To use this method for an exact quantization of the ion density (charged particles per unit surface in a time unit), impinging onto the surface, a detailed theoretic treatment, a more accurate knowledge of the geometry of the system, and an exact measurement of the area of the collector are needed. On the other hand, this method can be readily used for the optimization of the plasma parameters, to minimize the generated amount of ions, for a given amount of active nitrogen. This is the main objective, since, as previously stated, ionic nitrogen species strongly damage the optical properties of the grown materials [3–5, 42]. To choose the optimum conditions, a set of measurements have been performed, as described below. The first experiment consists of the measurement of the collector current (directly correlated with the amount of ions found in the chamber) for different applied rf powers for three different nitrogen fluxes. The results of these measurements are depicted in Fig. 2.6.

For a given rf power typically used in the growth experiments (below 350 W, in our system), we observe that the lower the nitrogen flux, the lower the measured collector current. If we now measure the amount of nitrogen atoms by reading the OED intensity for several fluxes (Fig. 2.7), it is also observed that the lower the nitrogen flux the lower the OED intensity, for a given applied rf power. This variation is almost negligible (around 3% for a given OED intensity). We can thus conclude that for a given amount of nitrogen to be incorporated in the samples (a given OED, for given growth conditions) the amount of ions is minimized by using a lower nitrogen flux. This nitrogen flux cannot be reduced indefinitely, since there is a minimum flux, for which ignited plasma turns unstable and eventually disappears. Other groups [43] have drawn the same conclusions using other techniques.

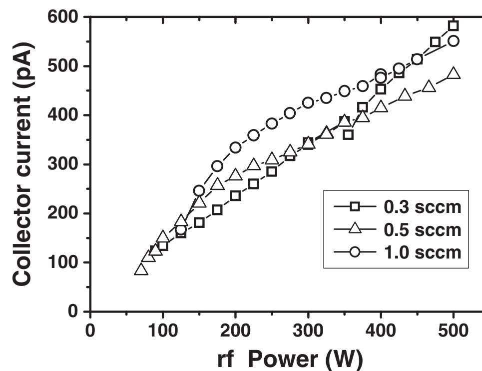

Fig. 2.6. Collector current measured by the modified Langmuir probe as a function of the applied rf power, for three different nitrogen fluxes, 0.3 (*squares*), 0.5 (*triangles*), and 1.0 sccm (*circles*)

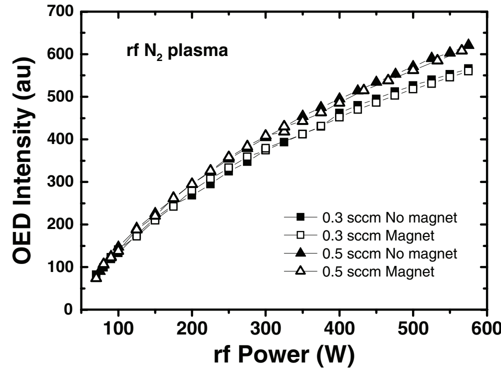

Fig. 2.7. OED intensity as a function of applied rf power for two different nitrogen fluxes, 0.3 sccm (*squares*) and 0.5 sccm (*triangles*), with and without the application of a magnetic field (*filled and hollow symbols*, respectively)

2.3.3 Application of Magnetic Fields to Nitrogen Plasmas

Previously, basic measurements allowed us to easily find the optimum conditions to minimize the amount of ions in the MBE chamber during the growth of dilute nitrides. As we are dealing with ions, we must note that these charged species can interact with electromagnetic fields. Other authors proposed in the past the application of electromagnetic fields to deflect ions generated in DC [3] and ECR [44] plasmas. In our case, we will use static magnetic fields to deflect the ionic species. With the measurement setup proposed in Sect. 2.2, we will check the effect on the QWs of the ion deflection by the magnetic field.

The first step is to check the effect of the magnetic field in the normal operation of the plasma source. In practice, to apply this static magnetic field, a 0.2 T magnet was used, placed under an extension tube between the plasma source and the growth chamber. In this position, the magnetic field lines are perpendicular to the flux of nitrogen species from the source to the sample. The position was chosen by minimizing the current measured by the modified Langmuir probe. The OED intensity, for two different nitrogen fluxes, and the effect of the application of a magnetic field are shown in Fig. 2.7. For comparison purposes, measurements carried out with no magnetic field are also shown in Fig. 2.7. We can observe that the OED intensity obtained by applying the magnetic field is slightly higher than the OED intensity when no field is present. This effect could be due to an enhancement of the confinement of the plasma due to the magnetic field. On the other hand, this difference is almost negligible for the applications used in this work, lower than 2% and comparable to the 1% resolution of our OED measurement system. Thus, we can conclude that the operation of the nitrogen source is not significantly altered by the presence of the magnetic field.

We can now use the modified Langmuir probe to check the effect of the magnetic field on the ions (Fig. 2.8). It is clear from this figure that the

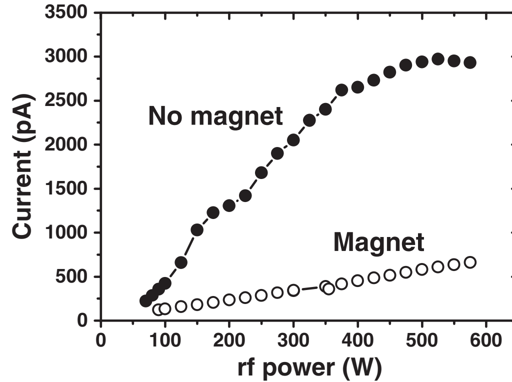

Fig. 2.8. Measured current by the modified Langmuir probe as a function of the applied power (W), for a given nitrogen flux (1 sccm). *Hollow* and *filled symbols* represent the date with and without the application of the magnetic field

application of a magnetic field reduces the collected current, and thus, it reduces the amount of ions reaching the sample. In the following sections we will show how the ion density present during the growth, impinging onto the sample, strongly affects the optical and structural properties of the GaInNAs quantum wells grown on GaAs (111)B and (100), and how the reduction of this density by the application of magnetic fields strongly reduces the damage introduced in the quantum wells during growth.

2.4 Minimizing the Impact of the Ions

In this section we will briefly describe how the ratio of the incorporated nitrogen atoms and the density of ions in the chamber can be tuned. Using these techniques, different samples with different $[N]/[N_{ion}]$ ratio can be grown [42], to check whether the reduction of the ions effectively enhances or not the optical sample quality.

The nitrogen concentration [N] incorporated to the samples was deduced from QW photoluminescence measurements. Additionally, $[N_{ion}]$ is proportional to the collected current using the modified Langmuir probe, as stated in previous sections. Thus, as we are dealing with a plasma, two approaches can be used to modify the $[N]/[N_{ion}]$ ratio: using the nitrogen cell shutter and by the application of a magnetic field. By the combination of the two techniques, we grew three equivalent samples, on GaAs (100), using the same growth conditions, with the only difference in the $[N]/[N_{ion}]$ ratio, as described below and in Fig. 2.9.

The three samples were 7-nm thick single GaInNAs single QWs, with a 100 nm GaAs cap and barrier layer. A first sample was grown (sample A, Fig. 2.9a), under the application of a magnetic field in the way explained in

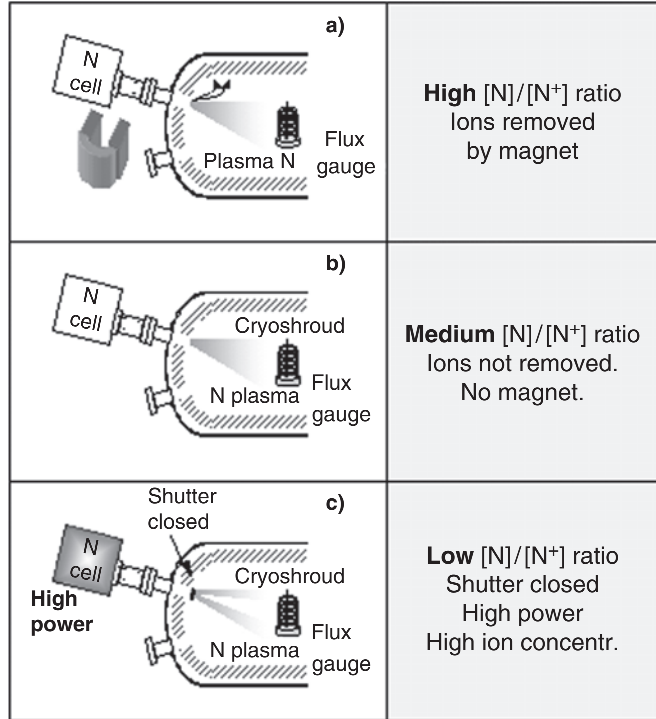

Fig. 2.9. Schematic diagram of the growth procedures for samples A, B, and C, described in the text, with low, medium, and high ion concentrations during the growth, respectively

Sect. 2.3.3. The following sample was grown exactly under the same conditions, using no magnetic field deflection (sample B, Fig. 2.9b). The third sample was grown with the nitrogen cell shutter closed (sample C, Fig. 2.9c). In order to achieve a similar N incorporation in the sample a higher rf power was applied, since the shutter does not interrupt but strongly reduces the flow of atomic and ionic species toward the sample.

Due to this high power, the current measured by the modified Langmuir probe, when the cell shutter was closed, was still very high. For this reason, sample C has the lowest $[N]/[N_{ion}]$ ratio of the three samples. Sample A has the highest ratio, since exactly the same N contents are found for this and for sample B, but the ion density was strongly reduced by the magnetic deflection. For the three samples, low-temperature photoluminescence measurements were carried out to compare their optical properties. The results are shown in Fig. 2.10.

In Fig. 2.10a, the low-temperature (16 K) PL peak intensity is shown as a function of the $[N]/[N_{ion}]$ ratio. As seen in this figure, the higher this ratio, the higher the PL intensity, which implies a lower concentration of

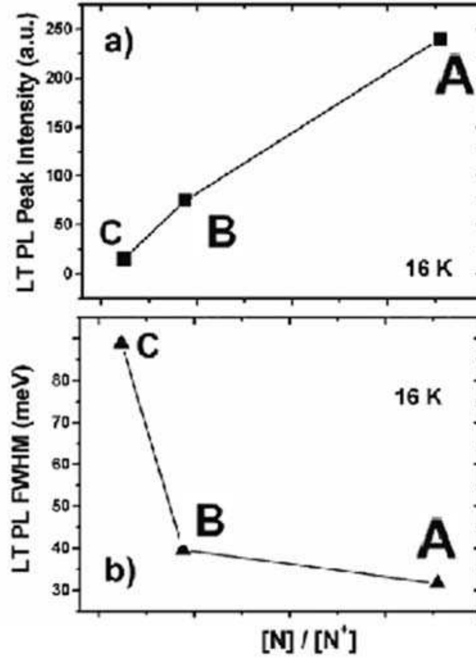

Fig. 2.10. PL peak intensity (**a**) and FWHM (**b**) of the A, B, and C samples described in the text, for several ion contents

nonradiative recombination centers. Full width at half maximum (FWHM) from the same measurements is shown in Fig. 2.10b. There we can clearly observe that this FWHM is wider (lower optical quality) when the $[N]/[N_{ion}]$ decreases. From these experiments we can conclude that the utilization of higher powers combined with a closed cell shutter is not a reliable procedure for the development of good quality dilute nitride-based optoelectronic devices. For this reason, this method was not employed in this work. We will focus on the growth of quantum wells with and without the application of magnetic fields, thus varying the $[N]/[N_{ion}]$ ratio, and studying the effect of these ions on the optical and structural properties of dilute nitride quantum wells in the following sections.

2.5 The Role of Ions on GaInNAs/GaAs (111)B QWs

To study the impact of these ionic species on the optical properties of GaInNAs/GaAs (111)B QWs two equivalent samples were grown, with the only difference that the first of the samples (IM1) was grown under the application of a magnetic field, and the second sample (NIM1) was grown conventionally. The structure of both samples is the p–i–n diode described in previous sections. There is an evident difference between the photoluminescence

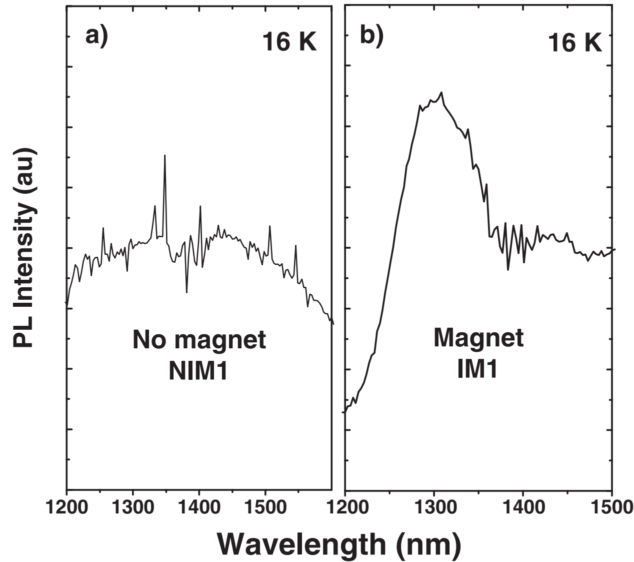

Fig. 2.11. (**a**) PL spectrum (16 K) of the NIM1 sample, grown with no magnet. (**b**) Low-temperature (16 K) PL spectrum of the IM1 sample, grown with the magnetic deflection

spectra from both samples. In Fig. 2.11 the low-temperature (16 K) photoluminescence spectra of both samples are shown. We can observe how the IM1 sample shows a well-defined peak at 1,300 nm, with the usual energy tail related to the formation of low energy states below the band gap. On the other hand, the sample grown without the magnet, and thus with a higher ion density present in the chamber during growth, shows no clear peak emission, but a very broad emission. The impact of the ions on the optical properties of GaInNAs is thus shown: higher ion densities degrade the optical properties of the QWs like in the case of GaAs (100) (see Sect. 2.4).

As widely reported, a RTA cycle maximizes the optical emission of QWs [3, 11, 12, 15]. We describe now some results regarding the behavior of both samples IM1 and NIM1 after different RTA cycles. In Fig. 2.12, we show how after RTA annealing (30 s at 850°C) both samples show a well-defined peak.

The cycle used in this experiment was chosen based on results of our previous experiments. For each sample (growth conditions) this optimum cycle has to be studied, since it strongly depends on the structural quality of the as-grown material [45]: The lower the structural quality of the GaInNAs quantum wells (compositional modulation, undulation of the interfaces), the higher the optimum RTA temperature, for a given dwell time. For these reasons, we performed a detailed RTA characterization of samples IM1 and NIM1, to extract indirectly structural information from the QWs. The results of such experiments are shown in Fig. 2.13.

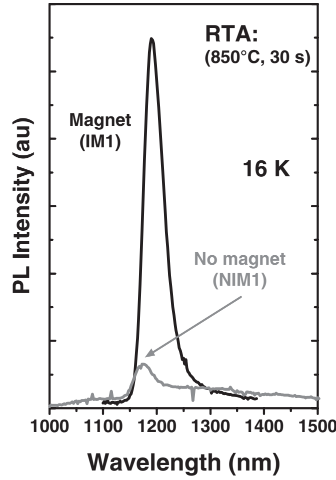

Fig. 2.12. Low temperature, 16 K, PL spectrum of the sample NIM1 (*grey line*) and IM1 (*black line*), after a RTA process (30 s at 850°C)

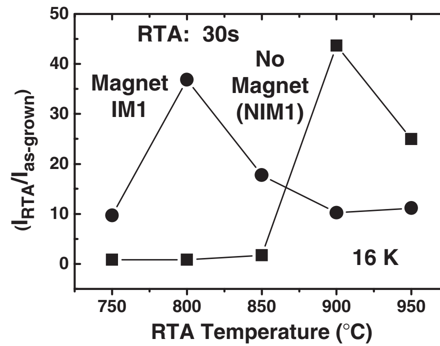

Fig. 2.13. Relative increment of the PL intensity after RTA annealing, for a dwell time of 30 s. No magnet: *squares*, magnet: *circles*

There we have plotted the relative increase of the measured intensity after annealing when compared to its as-grown value. 30 s was the annealing time for all the experiments. We can clearly observe that the optimum annealing temperature is much lower for the IM1 sample than for NIM1 sample, what is consistent with a higher structural quality of the GaInNAs quantum well sample grown under the lower density of ions.

Another effect produced by the RTA annealing is the shift of the quantum well emission toward higher energies (blueshift). If we compare this shift from both samples, as a function of the annealing temperature (Fig. 2.14), we observe a strong difference in blueshifts from both samples assuming that IM1 and NIM1 samples contain the same nominal N mole fraction: In that case, for the sample IM1 the blueshift would be much lower than for sample NIM1. We

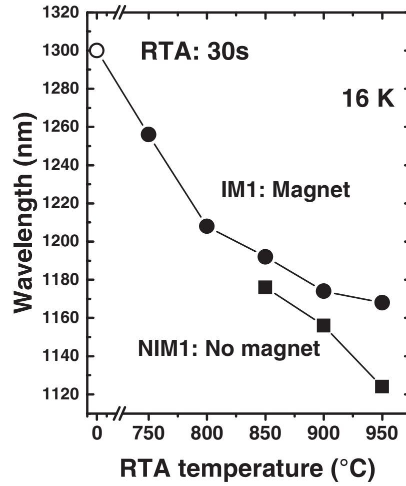

Fig. 2.14. Peak wavelength of the low-temperature PL spectra after RTA annealing, for a dwell time of 30 s. No magnet: *squares*, magnet: *circles*

will see in the following section that this reduced blueshift using ion deflection is confirmed in the case of GaInNAs/GaAs (100) QWs. In this figure, the absence of data for the as-grown sample and for the lower temperature annealing is due to the fact that no clear peak emission could be measured from this sample. This is an important result, since we have determined a method to reduce blueshifts in dilute nitride samples for given nitrogen contents. Thus, to achieve a given wavelength in the design of the optoelectronic device, a slightly lower nitrogen contents have to be incorporated into the quantum wells when using the magnetic deflection. This effect will give rise to an enhanced emission from the QW, since it is known in the literature that an increase in nitrogen content in the GaInNAs QWs yields to a reduction in their optical quality. As shown in Sect. 2.6, similar results are found for the GaInNAs/GaAs (100) system. Therefore, we can tentatively conclude that the reduction of nitrogen ions during the growth enhances the formation of In–N bonds, more favorable energetically [46], what would explain the reduced blueshift and the stronger emission from these samples [47, 48].

2.6 The Role of Ions on GaInNAs/GaAs (100) QWs

The observations and measurements found in Sect. 2.5 for the GaInNAs on GaAs (111)B quantum wells are not exclusive for this material system. In this section we will describe the impact of the ions on the optical and structural quality of GaInNAs quantum wells grown on GaAs (100).

2.6.1 Optical Characterization

For this purpose, we studied the optical properties of two equivalent samples, consisting of 7-nm thick GaInNAs QWs (nominal In and N mole fractions of 30% and 1.7%, respectively). A 100-nm thick GaAs barrier and cap layer was grown over both QWs. As described in the previous section, the only difference between both samples is again the application of magnetic fields during the growth of one of the samples (IM2), whereas the second sample (NIM2) was grown conventionally, with no ion deflection. Thus, to achieve a given wavelength in the design of the optoelectronic device, a slightly lower nitrogen contents have to be incorporated into the quantum wells when using the magnetic deflection. This effect will give rise to an enhanced emission from the QW, since it is known in the literature that an increase in nitrogen content in the GaInNAs QWs yields to a reduction in their optical quality. As shown in the following section, similar results are found for the GaInNAs/GaAs (100) system. Therefore, we can tentatively conclude that the reduction of nitrogen ions during the growth enhances the formation of In–N bonds, more favorable energetically [46], what would explain the reduced blueshift and the stronger emission from these samples [47, 48].

Photoluminescence Measurements

Low-temperature PL measurements are shown in Fig. 2.15. As seen in this figure, and as it was found for GaInNAs on GaAs (111)B, sample IM2, grown with the lower ion density, shows a stronger luminescence (four times higher) and a 10 meV narrower FWHM. This comparison was performed at room

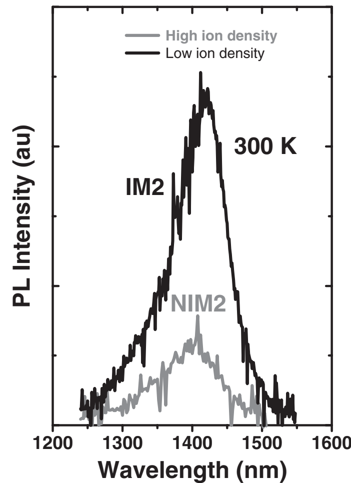

Fig. 2.15. Room Temperature PL measurements of the IM2 (*black line*) and NIM2 (*grey line*)

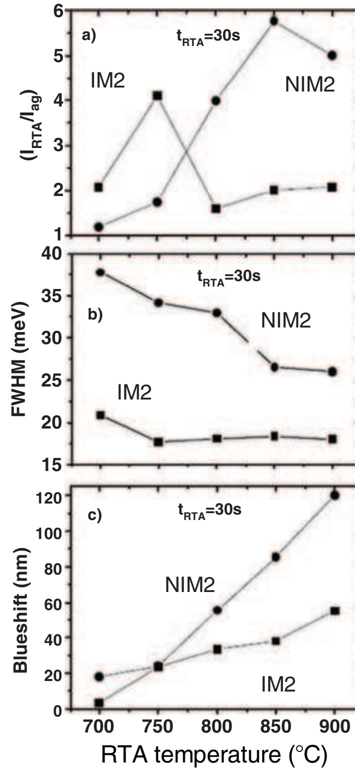

Fig. 2.16. PL (16 K) experiments for different annealings of the IM2 and NIM2 samples (*squares* and *circles*, respectively) (**a**) Increment of the PL intensity relative to the as-grown intensity. (**b**) FWHM. (**c**) Blueshift after annealing. The annealing time was 30 s in all the cycles

temperature, where localization effects are almost negligible for these two samples. The impact of the ion nitrogen density on the optimum annealing temperature was also measured for these samples, similarly to what we did for the (111)B orientation. In Fig. 2.16a, we show the ratio of the peak intensity after annealing to the as-grown intensity. We clearly observe that the optimum temperature for the sample grown without the magnet is much higher than for the sample IM2. Thus, to achieve a given wavelength in the design of the optoelectronic device, a slightly lower nitrogen contents have to be incorporated into the quantum wells when using the magnetic deflection. This effect will give rise to an enhanced emission from the QW, since it is known in the literature that an increase in nitrogen content in the GaInNAs QWs yields to a reduction in their optical quality. As shown in the following section, similar results are found for the GaInNAs/GaAs (100) system. Therefore, we can tentatively conclude that the reduction of nitrogen ions during the growth enhances the formation of In–N bonds, more favourable

energetically [46], what would explain the reduced blueshift and the stronger emission from these samples [47, 48].

If we measure the blueshift of the PL emission, we observe how for annealing temperatures greater than 750°C this blueshift is lower for the samples grown under a lower ion density. This is again a positive result for the development of optoelectronic devices based on dilute nitrides: the application of magnetic fields implies that a lower blueshift will appear after annealing. Thus, in the design of the GaInNAs QW-based optoelectronic devices lower nitrogen mole fraction should be incorporated in the growth process to achieve a given final (after annealing) emission wavelength of the device. The introduced procedure yields to a double enhancement of the emission of the QWs: ion deflection reduces nonradiative centers and the lower nitrogen content to be incorporated additionally improves optical quality.

Cathodoluminescence Measurements

Although cathodoluminescence (CL) at these wavelengths is a powerful tool for the analysis of GaInNAs material, only very few reports have been published about this topic [12, 49]. We obtained CL mappings at 10 K. Some results are shown in Fig. 2.17.

The darker area shown in the sample grown with no magnetic field, NIM2 (Fig. 2.17a), is caused by a dust particle on the surface, as observed in the corresponding SEM image (not shown). Both figures show a rather homogeneous lateral distribution of the luminescence intensity, but a slight granularity is detected in both images. To analyze this CL distribution quantitatively, we performed CL intensity profiles or line scans.

Results of such measurements are shown in Fig. 2.18 performed at the same energy as the CL mappings of Fig. 2.17. The intensity fluctuations visible in this figure show areas of different brightness of around 4 μm in diameter. These were previously observed in GaInNAs material by Kitatani et al. [12], who reported similar granularity in the same scale. To directly compare both

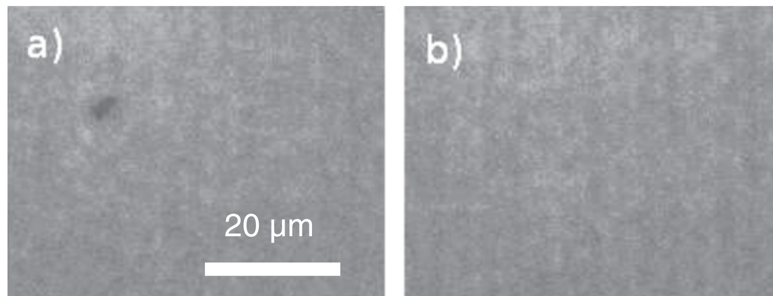

Fig. 2.17. (×2,000) CL images of (**a**) NIM2 sample (no magnet) at 1,330 nm and (**b**) IM2 sample (magnet) at 1,300 nm. Scale is indicated by the *white line*

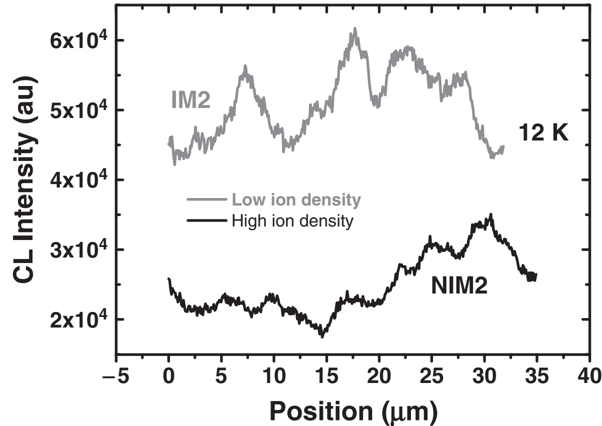

Fig. 2.18. CL emission from samples IM2 and NIM2, (*grey* and *dark lines*, respectively), at 12 K

line scans, we used the RMS modulation depth, as defined in [50]. We can then directly compare both samples. Calculations of this parameter yield values of 17.3% and 9.7% for samples NIM2 and IM2, respectively. The modulation depth reveals the underlying disorder of the GaInNAs QW [50, 51] and indicates a higher degree of disorder for the sample grown without magnetic field. This conclusion is consistent with the previous experiments (RTA annealing and photoluminescence). In Sect. 2.6.2 we will describe structural measurements that corroborate our hypothesis of a better quality of the GaInNAs QWs grown under an applied magnetic field.

2.6.2 Structural Characterization

To complement the optical measurements presented in Sect. 2.6.1, we performed some structural analysis, using two different microscopy techniques, AFM and TEM.

Atomic Force Microscopy

To use this powerful characterization tool for the analysis of GaInNAs material, we grew two equivalent 7-nm thick epilayers, with the same composition than NIM2 and IM2 QWs, and which we will call NIM3 and IM3, for the conventionally grown epilayer and under the application of a magnetic field, respectively. These epilayers were grown under exactly the same conditions of IM2 and NIM2 QWs. Plasma and nitrogen flux were immediately stopped after the completion of the epilayer.

Figure 2.19a, b show two 500 × 500 nm regions for both samples. Figure 2.19c, d show the same region with a higher detail (180 × 180 nm).

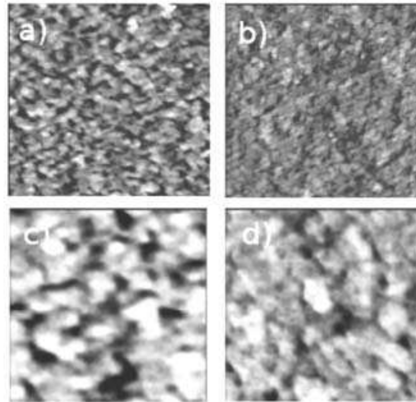

Fig. 2.19. Atomic force microscope scans of samples NIM3 (no magnet, figures a and c) and IM3 (magnet, figures b and d). Scan scales: (**a**) 500 × 500 nm. (**b**) 500 × 500 nm. (**c**) 180 × 180 nm. (**d**) 180 × 180 nm

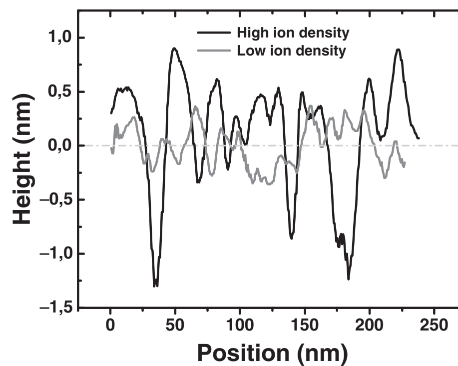

Fig. 2.20. Height profiles from the surfaces shown in Figs. 2.19a, b. *Grey* and *black lines* represent the section profiles of IM3 (magnet) and NIM3 (no magnet) samples, respectively

In Fig. 2.19a the NIM3 epilayer is shown, grown under the usual ion density in the chamber. This image shows a great modulation of the surface, and the presence of holes tens of nanometers wide. The formation of such holes has been observed by other groups previously [52].

The depth of some holes is higher than ten atomic monolayers. In the scanned area the RMS roughness of this surface is 0.53 nm. Figure 2.20 shows profiles of a random section from both surfaces. In these profiles, the fluctuations of the surface can be easily observed. Undulations of the same magnitude have been observed for GaInNAs QWs by other groups [53].

On the other hand, if we observe the IM3 surface (Fig. 2.19b), grown with a lower ion density, we can clearly see a flatter, more homogeneous, and compact

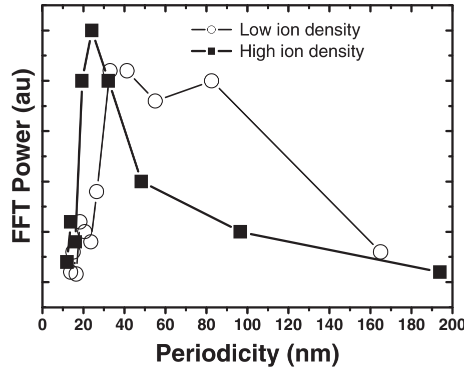

Fig. 2.21. Normalized fast Fourier transform of a mean section (shown in Fig. 2.20) of the surfaces from samples IM3 (magnet) and NIM3 (no magnet), represented by *white circles* and *dark squares*, respectively

layer, with a RMS roughness of only 0.35 nm, almost half that of NIM2. The profile measurements show that only fluctuations from one to four monolayers are found. Thus, we can conclude from these measurements that the application of the magnetic fields strongly reduces the roughness of the upper layer from GaInNAs QWs, for given growth conditions. The statistical analyses of every section of the images give rise to similar results. In Fig. 2.21 we show the mean fast Fourier transform (FFT) taken from several profiles from the surfaces. We obtain from this transform information about the periodicity of the features of the surfaces. Continuous lines are interpolations between the points, representing the data. As seen in this figure, we observe a clear periodicity in patterns (holes) in the sample grown with no magnetic deflection (black squares), with strong components with periods between 20 and 50 nm. On the other hand, if we repeat the analysis for sample IM3, we obtain different results: a wide band (white circles) is obtained, which indicates a more flat surface, with no apparent periodicity due to surface modulation.

Transmission Electron Microscopy

Structural properties of GaInNAs material are quite sensitive to the growth parameters [54] and to the growth temperature in particular [55]. This growth temperature must be low (compared to the optimum growth temperatures for materials such as GaInAs, around 450°C), to suppress 3D or Stranski–Krastanov growth mode and minimize the formation of undulations from the upper quantum well interface. Additionally, an intermediate step between 2D and 3D modes was described in the literature, consisting of the 2D growth mode, with the formation of a lateral composition modulation from In and N mole fractions, with modulations periods in the range of 10–50 nm, typically [56–58]. These modulation fluctuations are directly related to the incorporation of N, since these variations have not been found such strongly in GaInAs

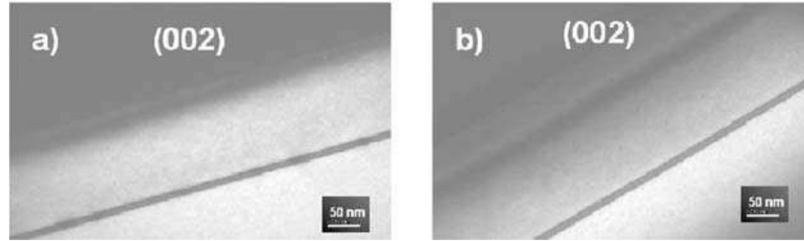

Fig. 2.22. TEM micrographs ($g = 002$) from NIM2 (**a**) and IM2 (**b**). The growth direction was from the *bottom* to the *top* of the figures

QWs, and as shown in [53]. In this section we show how this lateral composition modulation is strongly reduced if the ion density in the growth chamber is reduced. For this reason, we studied samples IM2 and NIM2 by TEM.

Figure 2.22a, b show TEM photographs taken with a diffraction vector $g = 002$, sensible to the material composition [53, 56]. As observed in this figure, we only see slight fluctuations in the upper interface of the QW, indicating that no 3D growth mode occurred. This is consistent with the streaky patterns observed in the RHEED during the growth. A slight modulation of the upper interface is observed for sample NIM2 (Fig. 2.22a). In addition to this fluctuation, a lateral composition modulation is also observed. This fluctuation is caused by the simultaneous incorporation of In and N, as shown in [56]. This modulation has not been observed for InGaAs. These composition fluctuations are spaced apart between 20 and 100 nm, as depicted in Fig. 2.22a. The period of this fluctuation is in the same range than that found in the previously showed AFM measurements. Analyzing sample IM2, shown in Fig. 2.22b, we cannot now appreciate fluctuations in QW thickness, which is consistent with a perfect 2D growth mode. Additionally, no compositional modulation was found along the QW. With this experiment, we have a direct evidence of the strong correlation of the ion density present in the chamber during the growth and the lateral composition modulation of the GaInNAs QWs: When this density is reduced by the application of magnetic fields this lateral composition modulation is suppressed for QWs grown under exactly the same conditions.

Figure 2.23 shows a high-resolution TEM micrograph from sample IM2. Here we can appreciate the high quality of the quantum well and its interfaces. Upper and lower interfaces are almost undistinguishable. Only variations of very few monolayers are to be seen in the micrograph.

Effect of Plasma Ions on Carrier Localization

The incorporation of small nitrogen quantities in GaInNAs QWs shifts the gap of the material toward lower energies [10]. But additionally, a nonnegligible density of localized states is formed below the GaInNAs conduction band

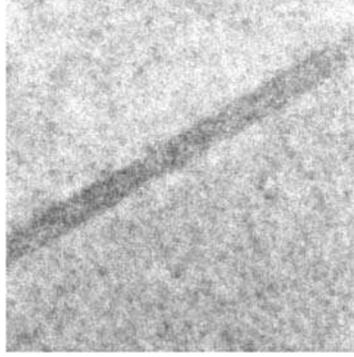

Fig. 2.23. High-resolution TEM micrograph of IM2 sample, grown with the low-ion density

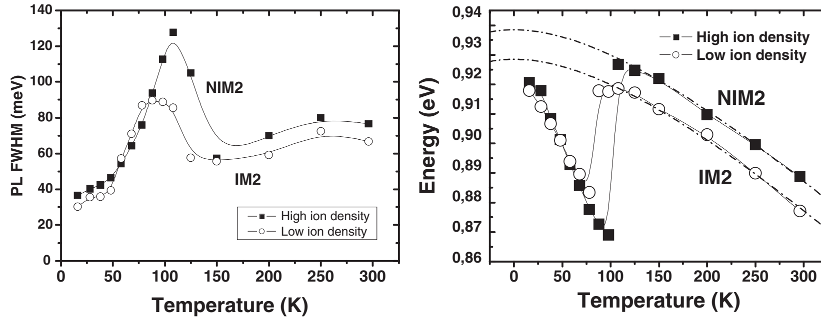

Fig. 2.24. *Left*: PL peak energy as a function of the temperature for samples IM2 and NIM2, *white circles* and *black squares*, respectively. The *continuous lines* are β-spline interpolations between the data. *Dashed-dotted lines* are Varshni fits to the data. *Right*: evolution of the FWHM of the PL spectra as a function for the temperature for the same samples IM2 and NIM2

[56]. Several experiments have been made to detect and characterize them. In photoluminescence at different temperatures we can observe S-shape behavior of the QW peak emission [59,60]. PL spectra from IM2 and NIM2 QWs, similar results are shown in Fig. 2.24.

The peak energy emission from both samples is plotted in this figure by white circles and black squares, for samples IM2 and NIM2, respectively. Solid lines are β-spline interpolations between experimental data, drawn as a guide for the eye. Dashed-dotted lines are fittings to the Varshni model, which describes the variation of the gap with temperature. These fittings were also performed by other authors for GaInNAs QWs with good results [60]. Varshni's formula, to be fitted, is

$$E(T) = E(0) - \frac{\alpha T^2}{T + \beta}. \tag{2.1}$$

Table 2.1. Parameters used in Varshni fits for the single quantum well GaInNAs samples IM2 and NIM2, shown in Fig. 2.24

Parameter	IM2	NIM2
α	3.4×10^{-4} eV K^{-1}	3.4×10^{-4} eV K^{-1}
B	296 K	296 K
$E(0)$	0.9285 eV	0.9385 eV

Table 2.2. Localization parameters measured for the single quantum well GaInNAs samples IM2 and NIM2, shown in Fig. 2.24

Parameter	IM2	NIM2
T_{loc}	77 K	100 K
E_{loc} (16 K)	10 meV	18 meV
E_{loc} @ T_{loc}	34 meV	60 meV

Fitting parameters are listed in Table 2.1. These are very close to those found in the literature [60]. At lower temperatures, the optical emission is mainly due to transitions from localized states. In this region, it is observed that the transition energy is linearly reduced as the temperature is increased. After reaching the delocalization temperature (T_{loc}), if the temperature is increased, carriers are thermally activated, and the conduction band population is increased. If the delocalization temperature is exceeded, the optical emission observed is mainly due to transitions from the conduction band. As observed in the figure, the fitting of the data with Varshni model is quite satisfactory for temperatures higher than 100 K for both samples, where localization effects are almost negligible.

To make an estimation of the localization energy, we can study different parameters [45]. First of all, a comparison of the delocalization temperatures can be made. In Fig. 2.24 we can clearly observe how the delocalization temperature T_{loc} is lower for the low-ion density QW (${T_{loc}}^{IM2} = 77\,K$) than for the other sample, with a higher ${T_{loc}}^{NIM2}$ of 100 K. Another estimation for the localization energy is the difference from localized states measured from the PL experiments and the simulated gap energy. At the lowest temperature from our experimental setup, 16 K, the localization energy is (${E_{loc}}^{IM2} = 10\,meV$), again lower than the localization energy of the sample with higher ion density, ${E_{loc}}^{NIM2} = 18\,meV$. If this energy is estimated at the delocalization energy, the difference is higher, as shown in Table 2.2.

Additionally, we can observe the FWHM of the PL emission of the same samples NIM2 and IM2 (Fig. 2.24, right). We see in this image how the maximum of the FWHM occurs at higher temperatures in the NIM2 sample. This is again consistent with a deeper localization energy in the case of the sample grown conventionally with no ion deflection.

We thus conclude that the observed localization energy from GaInNAs QWs is strongly dependent on the ion density present in the chamber during

growth. The higher ion density causes the deeper the localized states. This effect could also be due to the structural properties discussed in the previous subsection, since it is known that QW morphology plays a fundamental role on the localization energy [45].

2.7 Conclusions

In this chapter, our contributions to the characterization and understanding of nitrogen rf plasmas, and the effect of the ions on the optical properties of GaInNAs QWs grown by MBE have been presented.

A novel in situ plasma characterization method, consisting in the use of a Bayard–Alpert gauge as a modified Langmuir probe, has been proposed and demonstrated. We used this technique to perform a reliable characterization of the ignited plasma. This proposed setup can be used for the characterization of plasma parameters exactly at the sample position. Combining this method with other widely extended standard plasma characterization techniques (as for example the OED), optimum plasma parameters (Nitrogen flux, rf applied power) can be chosen for the growth of high-quality quantum wells.

Using the modified Langmuir probe method, the presence of plasma ions impinging onto the surface of the sample was detected. Since the presence of these ions during growth reduces the quality of the QWs, the application of external static magnetic fields was proposed to deflect the flux of ions flowing from the nitrogen source toward the growing surface, thus reducing the density of charged particles impinging onto the surface. With the modified Langmuir probe an effective reduction of the ion current at the position of the sample was measured, assessing the effectiveness of the deflection method.

The effects of the ion density impinging onto the sample during the growth of GaInNAs layers grown on GaAs (111)B and (100) were presented. The results for both orientations are similar: It was found that samples grown under a higher ion density showed poorer optical (reduced intensity and broader emission) and structural quality (compositional fluctuations, QW undulation), as shown by combined experiments of microscopy (AFM and TEM), and luminescence techniques (PL and CL).

We found that using the proposed magnetic deflection, the ion density is effectively reduced and the overall quality of the GaInNAs quantum wells is therefore strongly increased. Particularly, on GaAs (100) it was shown that the application of a deflecting magnetic field during the growth yielded a strong reduction of lateral compositional modulation of the GaInNAs quantum wells. Finally, we found from PL experiments that the samples grown with higher ion density showed a more pronounced and a deeper localization energy than the optimal samples grown under the magnetic deflection.

Acknowledgments. Based on the research carried out over several years, this work has been supported by several sources: Spanish Ministerio de Educación

y Ciencia, FPU grant program (first author); European Union, Project No. IST-2000-26478-GINA1.5; Comunidad Autónoma de Madrid; and by the Spanish Ministerio de Educación y Ciencia, projects CICYT TIC2001-4950-E and CICYT TIC2001-3849.

References

1. W. Li, M. Pessa, T. Ahlgren, J. Decker, Appl. Phys. Lett. **79**, 1094 (2001)
2. S.G. Spruytte, M.C. Larson, W. Wampler, C.W. Coldern, H.E. Petersen, J.S. Harris, J. Crys. Growth **227–228**, 506 (2001)
3. Z. Pan, L.H. Li, W. Zhang, Y.W. Lin, R.H. Wu, W. Ge, Appl. Phys. Lett. **77**, 1280 (2000)
4. J. Miguel-Sánchez, A. Guzmán, E. Muñoz, Appl. Phys. Lett. **85**, 1940 (2004)
5. J. Miguel-Sánchez, A. Guzmán, J.M. Ulloa, A. Hierro, E. Muñoz, J. Crys. Growth **278**, 234 (2005)
6. H. Carrère, A. Arnoult, A. Ricard, X. Marie, T.H. Amand, E. Bedel-Pereira, Sol. State Elect. **47**, 419 (2003)
7. H. Carrère, A. Arnoult, A. Ricard, E. Bedel-Pereira, J. Crys. Growth **243**, 295 (2002)
8. A. Grill, *Cold Plasma in Materials Fabrication: From Fundamentals to Applications* (Wiley-IEEE Press, New York 1994)
9. M.R. Wertheimer, M. Moisan, (1994) Pure and Appl. Chem. **66**, 1343
10. M. Kondow, K. Uomi, A. Niwa, T. Kitatani, S. Watahiki, Y. Yazawa, Jpn. J. Appl. Phys. Part 1 **35**, 1273 (1996)
11. I.A. Buyanova, W.M. Chen, B. Monemar, MRS Internet J. Nitride Semicond. Res. **6**, 2 (2001)
12. T. Kitatani, K. Nakahara, M. Kondow, K. Uomi, T. Tanaka, J. Cryst. Growth **209**, 345 (2000)
13. D.L. Smith, Solid. State. Commun. **57**, 919 (1986)
14. J.L. Sánchez-Rojas (1995) Contribución a la caracterización y aplicaciones de heteroestructuras piezoeléctricas de InGaAs, Doctoral Thesis, Universidad Politécnica de Madrid
15. J.M. Ulloa (2005) Diseño, fabricación y caracterización de diodos láser basados en pozos cuánticos de InGaAs(N)/GaAs', Doctoral Thesis, Universidad Politécnica de Madrid
16. J. Hernando (2002) Crecimiento por MBE, fabricación y caracterización de detectores de infrarrojos de pozo cuántico de InGaAs/GaAs, Doctoral Thesis, Universidad Politécnica de Madrid
17. J.J. Sánchez (2000) Crecimiento por MBE, fabricación y caracterización de láseres de AlGaAs/GaAs/InGaAs/GaAs (111)B para..., Doctoral Thesis, Universidad Politécnica de Madrid
18. I.W. Tao, W.I. Wang, Electron. Lett. **28**, 705 (1992)
19. A. Ishihara, H. Watanabe, Jpn. J. Appl. Phys. **33**, 1361 (1994)
20. T. Takeuchi, K. Muraki, Y. Hanamaki, S. Fukatsu, N. Yamada, N. Ogasawara, N. Mikoshiba, Y. Shiraki, J. Cryst. Growth **150**, 1338 (1995)
21. T. Fleischmann, M. Moran, M. Hopkinson, H. Meidia, G.J. Rees, J.L. Sanchez-Rojas, I. Izpura, J. Appl. Phys. **89**, 4689 (2001)

22. K.W. Goosen, E.A. Caridi, T.Y. Chang, J.B. Stark, D.A.B Miller, R.A. Morgan, Appl. Phys. Lett. **56**, 715 (1990)
23. E.A. Khoo, A.S. Pabla, J. Woodhead, J.P.R David, R. Grey, G.J. Rees IEE Proc.-Optoelectron. **145**, 62 (1999)
24. E.A. Khoo, J. Woodhead, J.P.R David, R. Grey, G.J. Rees Electron. Lett. **35**, 150 (1999)
25. V. Ortiz, N.T. Pelekanos, Appl. Phys. Lett. **77**, 788 (2000)
26. T. Fleischmann, J.M. Ulloa, M. Moran, G.J. Rees, J. Woodhead, M. Hopkinson, Microelectron. J. **33**, 547 (2002)
27. J. Miguel-Sánchez, A. Guzmán, J.M. Ulloa, A. Hierro, M. Montes, E. Muñoz, Photon. Technol. Lett. **17**, 2271 (2005)
28. T. Anan, K. Nishi, S. Sugou, Appl. Phys. Lett. **60**, 3159 (1992)
29. H.G. Colson, D.J. Dunstan, J. Appl. Phys. **81**, 2898 (1997)
30. S.P. Edirisinghe, A.E. Staton-Bevan, R. Grey, J. Appl. Phys. **82**, 4870 (1997)
31. M. Gutiérrez, D. González, G. Aragón, R. García, M. Hopkinson, J.J. Sánchez, I. Izpura, Appl. Phys. Lett. **80**, 1541 (2002)
32. H. Yamaguchi, M.R. Fahy, B.A. Joyce, Appl. Phys. Lett. **69**, 776 (1996)
33. M. Henini, S. Sanguinetti, L. Brusaferri, E. Grilli, M. Guzzi, M.D. Upward, P. Moriarty, P.H. Beton, Microelectron. J. **28**, 933 (1997)
34. F.Y. Tsai, C.P. Lee, J. Appl. Phys. **84**, 2624 (1997)
35. S. Sanguinetti, M. Gurioli, M. Henini, Microelectron J. **33**, 583 (2002)
36. P.P. González-Borrero, D.I. Lubyshev, E. Petitprez, N. La Scala Jr, E. Marega Jr., P. Basmaji, Brazilian J. Phys. **27**, 65 (1997)
37. W. Jiang, H. Xu, B. Xu, W. Zhou, Q. Gong, D. Ding, J. Liang, Z. Wang, J. Vac. Sci. Technol. B **19**, 197 (2001)
38. S.L. Tyan, P.A. Shields, R.J. Nicholas, F.Y. Tsai, C.P. Lee, Jpn. J. Appl. Phys. **39**, 3286 (2000)
39. F.Y. Tsai, C.P. Lee, Jpn. J. Appl. Phys. **38**, 558 (1999)
40. A.J. Ptak, K.S. Ziemer, M.R. Millecchia, C.D. Stinespring, T.H. Myers, MRS Internet J. Nitride Semicond. Res. **4S1**, G3.10 (1999)
41. M.A. Herman, H. Sitter, (1989) Molecular Beam Epitaxy: Fundamentals and Current Status, Springer, Berlin Heidelberg New York
42. J. Miguel-Sanchez, A. Guzman, J.M. Ulloa, A. Hierro, E. Muñoz IEE Proc. Optoelectron. **151**, 305 (2004)
43. J.M. Reifsnider, M.M. Oye, S. Govindaraju, A.L. Holmes Jr., J. Crys. Growth **280**, 7 (2005)
44. R.J. Molnar, T.D. Moustakas, J. Appl. Phys. **76**, 4587 (1994)
45. A. Hierro, J.M. Ulloa, J.M. Chauveau, A. Trampert, M.A. Pinault, E. Tournié, A. Guzmán, J.L. Sanchez-Rojas, E. Calleja, J. Appl. Phys. **94**, 2319 (2003)
46. K. Kim, A. Zunger, Phys. Rev. Lett. **86**, 2609 (2001)
47. S. Karirinne, E.M. Pavelescu, J. Kontinnen, T. Jouhti, M. Pessa New J. Phys. **6**, 192 (2004)
48. K. Uno, M. Yamada, I. Tanaka, O. Ohtsuki, T. Takizawa, J. Crys. Growth **278**, 214 (2005)
49. M. Kondow, T. Kitatani, S. Shirakata, J. Phys. Condens. Matter **16**, S3229 (2004)
50. E. Runge, J. Menniger, U. Jahn, R. Hey, H.T. Grahn, Phys. Rev. B **52**, 12207 (1995)
51. U. Jahn, O. Brandt, A. Trampert, P. Waltereit, R. Hey, K.H. Ploog, Mat. Sci. Eng. B, **91–92**, 329 (2002)

52. Y. Park, M.J. Cich, R. Zhao, P. Specht, H. Feick, E.R. Weber Phys. B: Condens. Matter, **308–310**, 98 (2001)
53. A. Trampert, J.M. Chauveau, K.H. Ploog, E. Tournié, A. Guzmán, J. Vac. Sci. Technol. B **22**, 2195 (2004)
54. H.F. Liu, S. Karirinne, C.S. Peng, T. Jouhti, J. Konttinen, M. Pessa, J. Cryst. Growth **263**, 171 (2004)
55. M.O. Fischer, M. Reinhardt, A. Forchel, IEEE J. Sel. Top. Quantum Electron. **7**, 149 (2001)
56. J.M. Chauveau, A. Trampert, K.H. Ploog, M.A. Pinault, E. Tournié, Appl. Phys. Lett. **82**, 3451 (2003)
57. J.M. Chauveau, A. Trampert, M.A. Pinault, E. Tournié, K. Du, K.H. Ploog, J. Crys. Growth **251**, 383 (2003)
58. M. Albrecht, V. Grillo, T. Remmele, H.P. Strunk, A.Y. Egorov, G.H. Dumitras, H. Riechert, A. Kaschner, R. Heitz, A. Hoffmann, Appl. Phys. Lett. **81**, 2719 (2002)
59. I.A. Buyanova, W.M. Chen, C.W. Tu, Semicond. Sci. Technol. **17**, 815 (2002)
60. M.A. Pinault, E. Tournié, Appl. Phys. Lett. **78**, 1562 (2001)

3

Electronic Band Structure of Highly Mismatched Semiconductor Alloys

W. Walukiewicz, K. Alberi, J. Wu, W. Shan, K.M. Yu, and J.W. Ager III

The large changes in the electronic structure in dilute III–V nitrides and other semiconductor alloys containing isoelectronic impurities of high electronegativity or low ionization energy can be explained by the band anticrossing model. Interaction between the localized levels introduced by a highly electronegative impurity, such as N in GaN_xAs_{1-x}, and the delocalized states of the host semiconductor causes a restructuring of the conduction band into E_+ and E_- subbands, which in this case effectively lowers the conduction band edge of the alloy. This restructuring is not only responsible for the reduction of the fundamental band gap energy but also accounts for the direct band gap nature in GaN_xP_{1-x} and the enhanced electron effective mass observed in GaN_xAs_{1-x}. Conversely, the incorporation of large-sized isoelectronic impurities with low ionization energy into III–V and II–VI compounds is found to induce a restructuring of the host valence band by the same anticrossing mechanism. Integration of the conduction and valence band anticrossing models provides an accurate description of the electronic structure of these alloys across their entire composition range.

3.1 Introduction

Alloying offers the ability to tailor the band gap as well as the conduction and valence band edge positions of a semiconductor through the manipulation of its composition, enabling the use of these materials in a wide variety of applications, including power transistors, lasers, light emitting diodes, photodetectors, and solar cells. It is well known that alloys composed of two compounds of similar character can be treated within the virtual crystal approximation (VCA), where the potential of the periodic crystal is taken as an average of the atomic potentials of the constituents [1–3]. Thus, the band gaps of these alloys may be well described through the quadratic relationship

between the band gaps ${E_g}^A$ and ${E_g}^B$ of the endpoint compounds A and B and is given by [1]

$$E_g^{AB}(x) = xE_g^A + (1-x)E_g^B - bx(1-x). \tag{3.1}$$

Here, x is the fraction of compound B mixed in compound A, and b is the bowing parameter, which represents the divergence of the band gap energy from the linear interpolation. Alloys of mixed cation species, such as $Al_xGa_{1-x}As$ or $B_xGa_{1-x}As$, typically fit this trend quite well, as do alloys containing anion species of similar character, including $GaAs_xP_{1-x}$ [4–6]. For these materials, the atomic potentials of the two elements occupying either the cation or anion sublattice are substantially similar, and the bowing parameter in (3.1) is much smaller than the band gaps of the endpoint compounds.

With advances in thin film growth techniques, it is now possible to fabricate single-phase alloys from constituents that are highly "mismatched" with respect to electronegativity, size, and/or ionization energy. The VCA approach to modeling the band gaps of these alloys is not applicable due to the localized nature of the impurity, and a single bowing parameter can no longer adequately describe the trend in the band gap. The dilute III–N–V alloys fall into this category of moderately or highly mismatched alloys (HMA) [7–11]. Instead, a more advanced theory is required to calculate the electronic structure of these alloys in order to explain the composition dependence of the band gap as well as other optical and transport properties that cannot be accounted for by a simple bowing parameter. This chapter details the band anticrossing theory, which was developed to explain the anomalous characteristics observed in dilute nitrides and similar alloys and highlights some of the major experimental findings achieved to date.

3.2 Localized Impurities

Although isovalent impurities behave as electrically neutral components within a host semiconductor, they may differ in properties such as electronegativity or size from the atoms they are substituting. When the differences are large, these impurities act as deep centers with localized potentials. Because the wavefunctions of these centers are localized in real space, they are comprised of Bloch functions originating from many bands in a wide region of k-space. For this reason, the impurity energy levels are not sensitive to the positions of the conduction and valence band edges and thus are not expected to shift significantly in energy with a change in composition or pressure.

The behavior of deep centers in semiconductors has been extensively treated by Hjalmarson and Vogl [12]. The presence of an impurity atom alters the bonding–antibonding energy of the host crystal, introducing an impurity-related deep trap state. Deep trap states with A_1 symmetry tend to lie in a range of energies relative to the vacuum level that happens to be near the conduction band edges of most semiconductors, while those with T_2 symmetry are

located near the valence band edges. Assessment of the relative energy levels of these deep states can be carried out within the Koster–Slater model using a tight-binding basis [12]. This generalized theory is intended to identify the broad chemical trends in the localized levels of the impurities and is therefore effective in predicting the approximate behavior of an impurity within a host crystal. The calculations consider the interaction of the host semiconductor with a localized potential introduced by the impurity and can be determined by solving the subsequent Schrödinger equation. When the defect potential is restricted to nearest neighbor distances, the problem is simplified to a difference in *s*-orbital energies of the impurity and host for A_1 symmetries and *p*-orbital energies for T_2 symmetries.

The nature of the impurity within the host will ultimately determine the symmetry of the deep center and consequently its location within the bandstructure of the host semiconductor. Highly electronegative isoelectronic impurities, such as N in III–V compounds, act as weak acceptors and localize electrons in A_1 states near the conduction band edge of the host. For example, the Koster–Slater theory predicts that the N defect level is resonant with the conduction band in GaAs, while it is bound just below the conduction band minimum (CBM) of GaP [12]. These calculations correspond quite well with experimental observations [13, 14]. Oxygen in II–VI compounds behaves in a similar manner and is a bound A_1 state in ZnTe [15]. Likewise, C is expected to lie within the conduction band of both Si and Ge [12]. Metallic impurities, on the other hand, act as weak donors and localize holes in a T_2 state near the valence band of the host semiconductor. For example, the As defect level lies just above the valence band edge of GaN [16, 17]. Antimony and Bi have a lower ionization energy than As as well, and their defect levels are also predicted to lie near or within the valence bands of other III–V compounds [18, 19]. These approximate trends serve as a guide to the behavior of dilute nitrides and other moderately and highly mismatched alloys.

3.3 The Band Anticrossing Model

A number of theoretical approaches have been applied to explain the optical bowing in dilute nitride alloys. First-principles local density approximation (LDA) calculations, carried out by Wei and Zunger, utilized a composition dependent bowing parameter to explain the large band gap reduction in GaN_xAs_{1-x} [20]. Due to band gap errors introduced in the LDA method, this model was replaced by empirical pseudopotential calculations that increasingly focus on the interactions of N-clusters [21–23]. Alternatively, a band anticrossing (BAC) model has been proposed to explain the properties of III–V dilute nitrides as well as other mismatched alloys. The BAC model describes the electronic structure of HMAs by considering the interaction between the delocalized states of the host semiconductor and the localized states of the impurity. In the case of highly electronegative impurities, localization

of electrons occurs at A_1 states, inducing a restructuring of the conduction band of the host. This situation can be handled in a straightforward manner by considering a two-band anticrossing situation carried out within the many-impurity Anderson model [24]. The Hamiltonian describing a system of randomly dispersed impurity atoms within a host crystal can be written as [25, 26],

$$H = \sum_k E_k^c c_k^+ c_k + \sum_j E_j^d d_j^+ d_j + \frac{1}{\sqrt{N}} \sum_{j,k} \left(e^{\mathrm{i}k \cdot j} V_{kj} c_k^+ d_j + h.c. \right). \quad (3.2)$$

The first term in (3.2) corresponds to the Hamiltonian of the electrons in the delocalized band states of dispersion E_k^c, while the second term refers to the localized electrons at the jth impurity site with energy E_j^d. The third term expresses the change in energy of a single electron induced by the hybridization of the band and localized states. The hybridization strength of this dynamic mixing is determined by the parameter V_{kj}, which is defined as [24]

$$V_{kj} = \sum_l \mathrm{e}^{\mathrm{i}k(l-j)} \int a^*(r-l) H_{\mathrm{HF}}(r) \varphi_d(r-j)\, \mathrm{d}r. \quad (3.3)$$

The term $a(r-l)$ is the Wannier function of the delocalized band, $\varphi_d(r-j)$ is the localized wavefunction of the impurity at the jth site, and $H_{\mathrm{HF}}(r)$ is the energy of a single electron in the Hartree–Fock approximation [24]. Solutions may be obtained through the use of Green's function methods. Dilute alloys follow a many-impurity Anderson model, in which $0 < x << 1$, and consequently the coherent potential approximation (CPA) must be applied to address the issue of random impurity placement [27–29]. Configurational averaging while neglecting correlations between the positions of the impurities leads to the partial restoration of the space translational invariance, and k can again be considered a good quantum number. Green's function now takes the form [25, 27–29]

$$G_{kk}(E) = \left[E - E_k^c - \frac{V^2 x}{E - E^d - \mathrm{i}\pi\beta V^2 \rho_0 \left(E^d\right)} \right]^{-1}. \quad (3.4)$$

The dispersion relations are then determined by the poles of $G_{kk}(\mathrm{E})$, and the approximate solutions are ascertained from the two-state-like eigenvalue problem:

$$\begin{vmatrix} E_k^c - E(k) & V\sqrt{x} \\ V\sqrt{x} & E^d + \mathrm{i}\Gamma_d - E(k) \end{vmatrix}. \quad (3.5)$$

The term $\Gamma_d = \pi\beta V^2 \rho_0 \left(E^d\right)$ is the broadening parameter of E^d in the single-impurity Anderson model. The unperturbed density of states (DOS) of E_k^c, ρ_0, is evaluated at E^d and is then multiplied by an experimentally determined prefactor, β. From (3.5), it is evident that the BAC model predicts the splitting of the conduction band into two subbands. In the event that $\Gamma_d = 0$, the dispersion relation of these bands is given as [30]

$$E_{\pm}(k) = \frac{1}{2}\left[\left(E_k^c + E^d\right) \pm \sqrt{\left(E_k^c - E^d\right)^2 + 4V^2x}\right]. \quad (3.6)$$

However, if Γ_d is nonzero, but obeys the relationships $2V\sqrt{x} >> \pi\beta V^2\rho_0\,(E^d)$ and $\left|E_k^c - E^d\right| >> \pi\beta V^2\rho_0\,(E^d)$, then the approximate analytical solution is given as

$$E_{\pm}(k) = E_{\pm}(k) + \mathrm{i}\Gamma_d \frac{[E_{\pm}(k) - E_k^c]}{[E_{\pm}(k) - E_k^c] + [E_{\pm}(k) - E^d]} = [E_{\pm}(k) + \mathrm{i}\Gamma_{\pm}(k)]\,. \quad (3.7)$$

The dispersion relation in (3.7) is an extension of the BAC model, with the real part defined in (3.6). The addition of the imaginary part accounts for the hybridization induced uncertainty in electron energy, which is proportional to the fraction of the localized states ($|d>$) in the restructured wavefunctions ($|E_{\pm}(k)>$). In the two-state-like perturbation situation it is described by (3.6) [29]:

$$\Gamma_{\pm}(k) = |\langle d|E_{\pm}(k)\rangle|^2 \cdot \Gamma_d. \quad (3.8)$$

The dispersion relations of the restructured E_+ and E_- bands calculated using (3.7) are shown in Fig. 3.1 for the alloy $\mathrm{GaN_{0.005}As_{0.995}}$ [30]. Notice that the broadening is most pronounced in the regions of the dispersion relations located near the unperturbed N defect level, E_d. The E_- band now constitutes the conduction band edge and determines the band gap of the alloy. Figure 3.2 displays the composition dependence of the band gap energy for $\mathrm{GaN}_x\mathrm{As}_{1-x}$ as calculated by the BAC model. Agreement with the

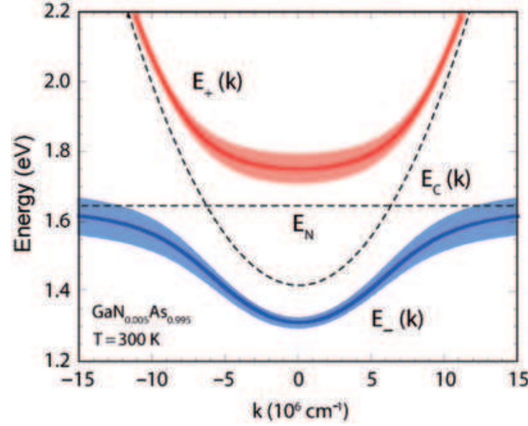

Fig. 3.1. Dispersion relations for the restructured conduction E_+ and E_- subbands of $\mathrm{GaAs_{0.995}N_{0.005}}$. The broadening of the curves (*shaded regions*) illustrates the energy uncertainties defined in (3.8). The dashed lines represent the unperturbed conduction band dispersion curves of the GaAs conduction band, E_C, and the localized N defect level, E_N

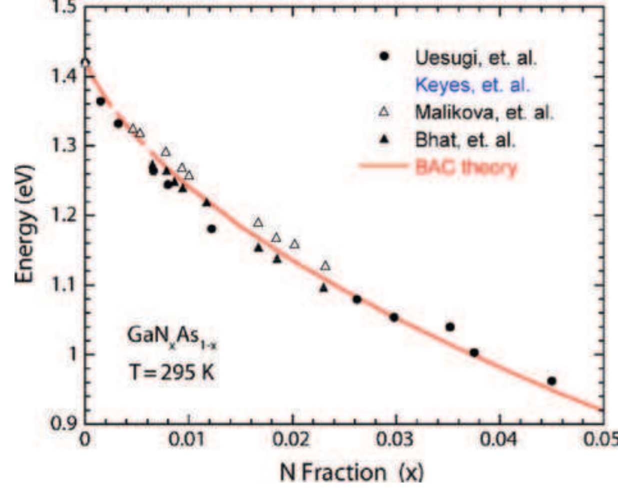

Fig. 3.2. Composition dependence of the GaN_xAs_{1-x} band gap. The BAC model accurately fits the trend in the experimentally determined values [31–34]

experimentally measured values was achieved with a single coupling parameter of $V = 2.7\,\mathrm{eV}$ [31–34].

The hybridization-induced modification of the electronic structure influences other properties of HMAs as well. The density-of-states electron effective mass for the lowest conduction subband, $E_-(k)$, can be evaluated from the dispersion relations displayed in (3.6) as [35, 36]

$$m_-^*(k_\mathrm{F}) = \hbar^2 \left| \frac{k}{\mathrm{d}E_-(k)/\mathrm{d}k} \right|_{k=k_\mathrm{F}} = m_0^* \left[1 + \frac{V^2 x}{\left(E^d - E_-(k_\mathrm{F})\right)^2} \right], \qquad (3.9)$$

where m_0^* is the electron effective mass of the unperturbed dispersion E_k^c. The relationship between the free electron concentration (n) and the Fermi energy, $E_\mathrm{F} = E_-(k_\mathrm{F})$, is given by

$$n(E_\mathrm{F}) = \int \frac{\rho(E)\,\mathrm{d}E}{1 + e^{\frac{E-E_\mathrm{F}}{k_\mathrm{B}T}}}, \qquad (3.10)$$

where $\rho(E)$ is the restructured density of states [37].

The original density of states for a parabolic conduction band assumes the following form:

$$\rho_0(\varepsilon) = 4\pi\sqrt{\varepsilon - E_0^c}/\varepsilon_b^{3/2}, \qquad (3.11)$$

where $\varepsilon_b = \hbar^2 (2\pi/b)^2/(2m^*)$ is on the order of the conduction band width, b is the lattice constant of the unit cell, and m^* is the effective mass. The new density of states associated with the restructured bands is determined by the imaginary part of the Green's function, given as

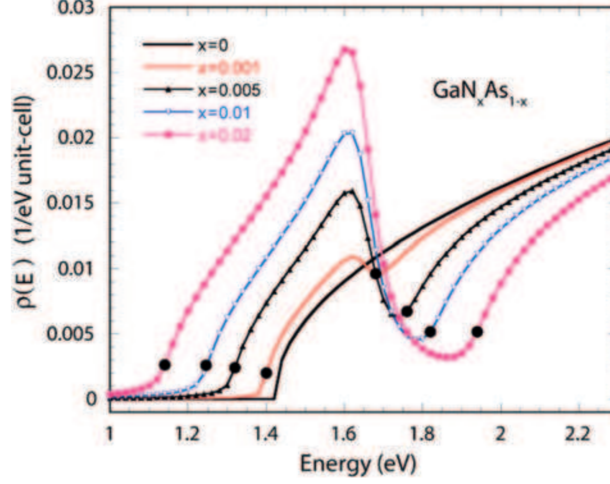

Fig. 3.3. Density of states of $\mathrm{GaN}_x\mathrm{As}_{1-x}$ predicted by the BAC model for several compositions. The black dots correspond to the band edge of E_+ and E_- defined by (3.12)

$$\rho(E) = \frac{1}{\pi}\mathrm{Im}\sum_k G_{kk}(E) = \frac{1}{\pi}\int \rho_0\left(E_k^c\right)\mathrm{Im}\left[G_{kk}(E)\right]\mathrm{d}E_k^c. \tag{3.12}$$

The integration in (3.12) converges rapidly with E_k^c over a small range that is proportional to x. The perturbed DOS derived from (3.12) for various compositions of $\mathrm{GaN}_x\mathrm{As}_{1-x}$ is shown in Fig. 3.3. The anticrossing interaction redistributes the electronic states in the conduction band between the E_- and E_+ states and produces a widening of the gap between the two as the N concentration increases.

The enhancement of the density-of-states electron effective mass and the finite lifetime for the E_- band defined by the broadening parameter also affect the mobility of electrons within the band, imposing the limit [38]

$$\mu = \frac{e\tau\left(k_\mathrm{f}\right)}{m_-^*\left(k_\mathrm{f}\right)} \approx \frac{e\hbar}{m_-^*\left(k_\mathrm{f}\right)\cdot\Gamma_-\left(k_\mathrm{f}\right)} \tag{3.13}$$

Finally, the k-dependence of the interaction term V_{kj} can be obtained assuming that the Hartree–Fock energy changes slowly in space and therefore it can be replaced by a constant, ε_HF. With this assumption (3.3) can now be expressed as

$$V_k = \varepsilon_\mathrm{HF}\sum_l \mathrm{e}^{\mathrm{i}k\cdot l}\int a^*\left(r-l\right)\varphi_d(r)\,\mathrm{d}r. \tag{3.14}$$

The localized nature of $a(r)$ and $\varphi_d(r)$ substantially reduces the overlap integral when they are separated by a sizeable distance. Consequently, the

integral in (3.14) can be replaced with an exponentially decaying function $\approx \exp(-l/l_d)$ to produce

$$V_k = \varepsilon_{\mathrm{HF}} \sum_l \mathrm{e}^{\mathrm{i}k\cdot l - l/l_d} = \frac{V_0}{\left(1 + l_d^2 k^2\right)^2}. \tag{3.15}$$

Experimental evidence suggests that the value of V_k at the L-point in GaN_xAs_{1-x} and the X-point in GaN_xP_{1-x} are approximately three to four times smaller than the value at the Γ-point [39, 40]. This ratio indicates a localized wavefunction decay length, l_d, of roughly a lattice constant, implying that the anticrossing interaction appreciably involves the off-zone-center conduction band minima only when their energies are close to the localized level. This result is consistent with measurements of the optical properties of $Ga_{1-y}In_yN_xAs_{1-x}$ alloys, in which the high energy transitions at large k-vector depend only weakly on the N concentration [36].

3.4 Experimental Investigation of Dilute III–N–V Alloys

The BAC theory presented in Sect. 3.3 has been successfully applied to explain the optical and electronic properties of a wide variety of III–V and II–VI HMAs with highly electronegative impurities. This section highlights the major results and findings obtained from investigations carried out on dilute III–N–V alloys. The thin films used in these studies were mostly grown by molecular beam epitaxy (MBE) using a rf plasma nitrogen source, or by metalorganic vapor phase epitaxy (MOVPE) operated with a dimethylehydrazine nitrogen gas source. Alternatively, thin films can be fabricated by an ion implantation and pulsed laser melting (II-PLM) method, which is detailed in Chap. 1. The compositions of the samples were determined by secondary ion mass spectrometry (SIMS) and x-ray diffraction (XRD) analysis. The optical properties were primarily characterized by photomodulated reflectance spectroscopy, which is a differential detection method utilizing modulation of the built-in E-field on the surface of a semiconductor material through photo-injected carriers by a periodically modulated light beam, such as a chopped laser beam. It is generally conducted in reflection geometry and is thus referred to as photomodulated reflectance (PR). The modulation-induced changes in both the real and imaginary parts of the dielectric function of a material produce third-derivative-like spectral features associated with the band-to-band transitions in a PR spectrum ($\Delta R/R$) of the material, which correspond to the critical points in the band structure. Photoluminescence (PL), optical absorption, and Hall measurements were also used to characterize the samples.

3.4.1 Interband Transitions in Dilute Nitrides

The restructuring of the conduction band of both GaN_xAs_{1-x} and $Ga_{1-y}In_y N_xAs_{1-x}$ due to the presence of N has been explicitly observed by PR measurements [30, 41, 42]. The PR spectra of several GaN_xAs_{1-x} thin films of various N concentrations are displayed in Fig. 3.4, which reveal three distinct interband transitions in N-containing samples [41]. The E_0 transition corresponds to the fundamental band gap at 1.42 eV in GaAs ($x = 0$). The introduction of N into GaAs to form GaN_xAs_{1-x} alloy films induces a splitting of the conduction band into E_- and E_+ subbands, which diverge in energy as the N concentration increases. The band gap (E_- transition), now defined as the transition from the valence band maximum (VBM) to the conduction band minimum, decreases as the E_- band is pushed downward in energy. The reduction in the band gap energy by approximately 180 meV for 1% of N incorporated onto the As sublattice, as shown in Fig. 3.5, can be fitted with the BAC model using a coupling parameter of $V = 2.7$ eV and correlates quite well with the previously reported values displayed in Fig. 3.2 [41]. Likewise, the spin–orbit split-off band to E_- band transition ($E_- + \Delta_0$) decreases by roughly the same energy as well, indicating that the spin–orbit splitting energy, Δ_0, remains constant. This result suggests that the valence band structure is not appreciably affected by the presence of N. Finally, the valence band to E_+ transition increases in energy according to (3.6).

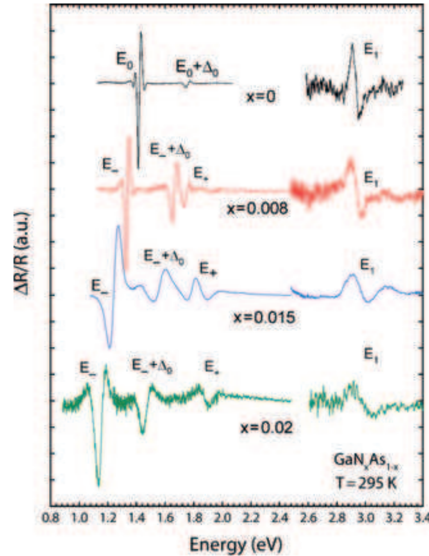

Fig. 3.4. Photoreflectance spectra of $GaAs_{1-x}N_x$ films with $0 < x < 0.02$. The splitting of the E_0 transition from the valence band to the conduction band into two transitions, E_- and E_+, is evident in the alloy films. The position of the E_1 transition does not split significantly with x

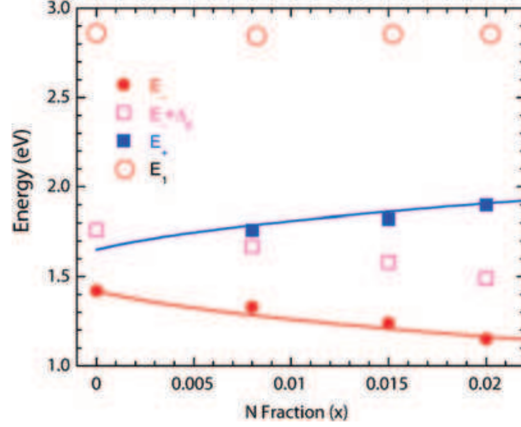

Fig. 3.5. $GaAs_{1-x}N_x$ critical point energies determined from the PR measurements shown in Fig. 3.4. The composition dependencies of the E_+ and E_- bands predicted by the BAC model are also shown

The alloy $Ga_{1-y}In_yN_xAs_{1-x}$ exhibits a similar trend in the restructuring of the conduction band [42–44]. Indium is known to be insufficiently mismatched with Ga to induce any band anticrossing effects and instead affects the positions of the conduction and valence band edges of GaAs in a manner well predicted by the VCA. Therefore, the effects of In and N on the band gap of $Ga_{1-y}In_yN_xAs_{1-x}$ are completely separable, and thus the valence and conduction band edges of the alloy only need to be adjusted slightly within the BAC model to account for the effects of In. Figure 3.6 displays the corresponding positions of the E_- and E_+ subbands relative to the VMB of GaN_xAs_{1-x} and $Ga_{1-3x}In_{3x}N_xAs_{1-x}$ lattice matched to GaAs [41, 45]. Here, the E_- and E_+ bands are simultaneously shifted downward in energy due to the In-induced upward shift in the VBM and downward shift in the CBM of the alloy. The splitting of the conduction band, however, is entirely the result of the anticrossing of the delocalized $Ga_{1-y}In_yAs$ conduction band states and the localized N states.

The effects of state broadening on the optical properties of $Ga_{1-y}In_yN_x$ As_{1-x} have also been observed through absorption measurements [37, 46]. From the DOS expression in (3.12), the optical absorption coefficient can be written as

$$\alpha(E) \propto \frac{1}{E}\sum_{\nu}\int \rho_0(E_k^c)\mathrm{Im}\left[G_{kk}\left(E+E_k^{\nu}\right)\right]\mathrm{d}E_k^c \qquad (3.16)$$

The sum over ν represents the contributions from the heavy hole, light hole, and spin–orbit split-off valence bands. The contributions from the individual bands along with the total absorption are displayed in Fig. 3.7. The theoretical prediction is in good agreements with the experimental data taken from a $Ga_{0.96}In_{0.04}N_{0.01}As_{0.99}$ film when a broadening parameter $\beta = 0.22$ in the

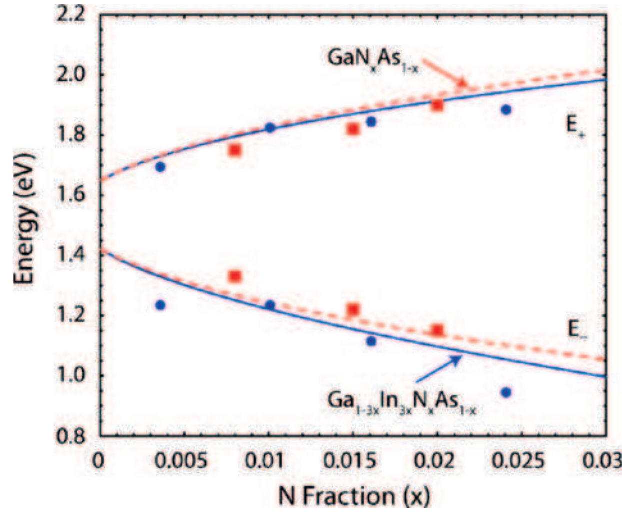

Fig. 3.6. Composition dependence of the E_+ and E_- subbands of $GaAs_{1-x}N_x$ and $Ga_{1-y}In_yN_xAs_{1-x}$. The dashed and solid lines show the composition dependence of the BAC-predicted E_+ and E_- transitions for GaN_xAs_{1-x} and $Ga_{1-3x}In_{3x}N_xAs_{1-x}$, respectively. The squares and circles represent the experimentally determined transition energies in GaN_xAs_{1-x} [41] and $Ga_{1-3x}In_{3x}N_tAs_{1-x}$ [45], respectively

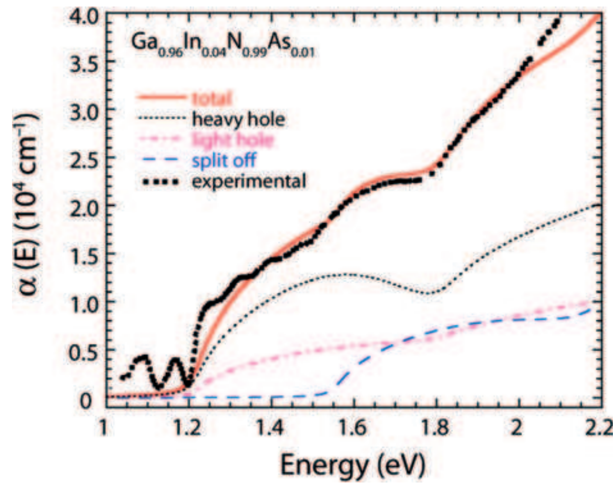

Fig. 3.7. Absorption spectrum of a free standing $In_{0.04}Ga_{0.96}As_{0.99}N_{0.01}$ film. Also shown are the theoretically determined contributions from the heavy hole, light hole, and spin–orbit split-off valence band-related transitions [37]

Green's function in (3.16) is applied. The initial rapid rise in α at 1.2 eV corresponds to the band gap (VBM to E_- band edge transition), while the additional increase in the absorption at this energy is attributed to the exciton continuum absorption effect, which is not considered in the theoretical calculations. The subsequent rise at 1.5 eV correlates with the spin–orbit split-off valence band to E_- band transition, and the increase at 1.8 eV results from the VBM to E_+ band edge transition.

The band anticrossing interaction depends on the energy separation between the localized nitrogen levels and the conduction band edge. This is why hydrostatic pressure experiments in which one can change the relative positions of those two sets of levels played such a crucial role in the discovery of the BAC phenomena in $Ga_{1-y}In_yN_xAs_{1-x}$, and consequently the development of the BAC model. Figure 3.8 displays the pressure dependencies of the E_- and E_+ transitions in GaN_xAs_{1-x} as measured with PR [47]. As indicated in the graph, the localized nature of the N impurity level significantly reduces its related pressure coefficient as compared to that of the GaAs matrix at the Γ-point. At low pressures, the E_- transition has a strong pressure dependence

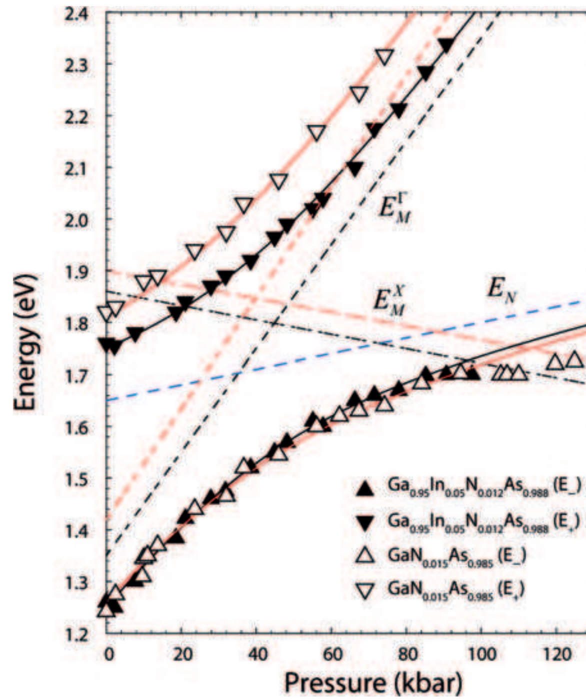

Fig. 3.8. Pressure dependencies of the E_- (*up arrow*) and E_+ (*down arrow*) transitions in $GaN_{0.015}As_{0.985}$ (*open symbol*) and $Ga_{0.95}In_{0.05}N_{0.012}As_{0.988}$ (*filled symbol*). Pressure dependence of the conduction band edge at the X and Γ-points for $Ga_{1-y}In_yAs$ as well as the localized N-level are also shown

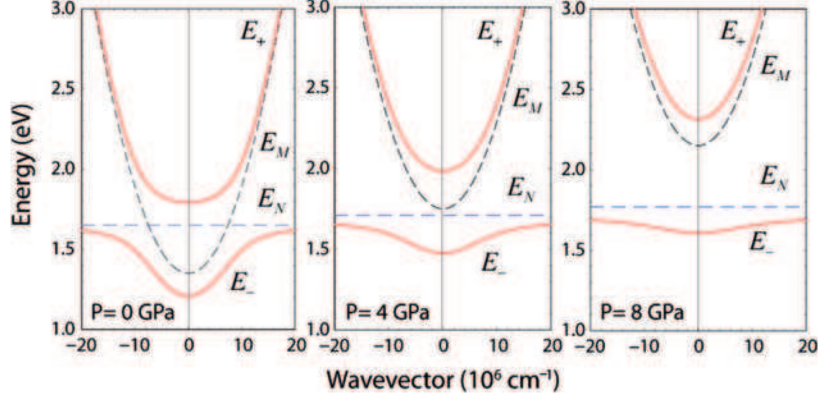

Fig. 3.9. Calculated $E_{-}(k)$ and $E_{+}(k)$ dispersion relations of $GaN_{0.012}As_{0.988}$ for three different hydrostatic pressures

and closely follows the E_M^{Γ} trend. However, at higher pressures, the delocalized host level and the localized N level interact strongly, and as a result its pressure dependence decreases. The E_{+} transition, on the other hand, follows the opposite trend. At low pressures it has a weak dependence resembling that of the N level and then converts to a much stronger dependence at high pressures. The results obtained from the $Ga_{0.95}In_{0.05}N_{0.012}As_{0.988}$ sample further demonstrate the distinct effects that both the In and N constituents have on the alloy, as In only slightly translates E_M^{Γ} downward in energy.

The behavior of both subbands may be further verified by examining the dispersion relations of the $E_{-}(k)$ and $E_{+}(k)$ bands shown in Fig. 3.9, as calculated by the BAC model for three different pressures [43]. The pressure dependencies of the subbands most closely approximate that of the nearest lying unperturbed band (E_{M} or E_{N}). This result suggests that the E_{-} subband edge transitions from a delocalized host-like to a localized impurity-like nature with a gradual increase in pressure, where the E_{+} subband edge evolves from a localized impurity-like to a delocalized host-like character.

Similar band anticrossing behavior has been observed in comparable alloys containing dilute concentrations of highly electronegative isovalent impurities. The band edge bowing exhibited by III–V materials including InN_xP_{1-x} [9,43, 48], $GaAs_xSb_{1-x}$ [37], $InAs_xSb_{1-x}$, InN_xSb_{1-x} [49], and GaP_xSb_{1-x} can be well explained by the BAC model, as can II–VI alloys, such as ZnO_xTe_{1-x} [15], CdO_xTe_{1-x} [49], ZnS_xTe_{1-x} and $ZnSe_xTe_{1-x}$ [50]. Further discussion on the processing and properties of these materials may be found in Chap. 1.

So far, the discussion of band anticrossing has been limited to examining the restructuring of the conduction band at the Γ-point in direct band gap alloys. However, the BAC model applies to indirect gap semiconductors with dilute concentrations of mismatched impurities as well. The GaN_xP_{1-x} system provides a good example, in which the localized N level lies roughly 0.1 eV

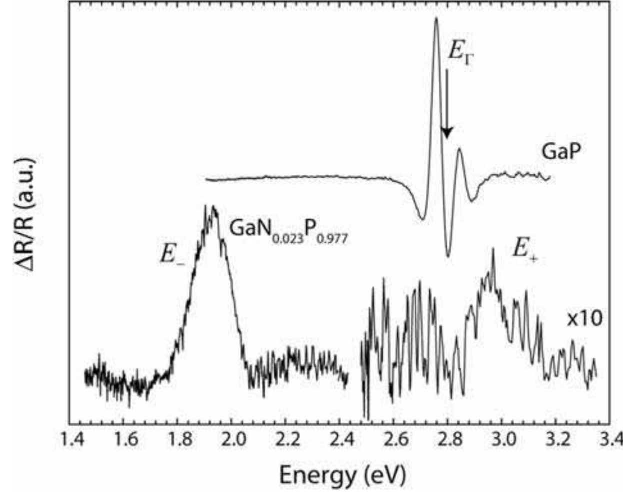

Fig. 3.10. PR spectra of GaP and $GaN_{0.023}P_{0.977}$ demonstrating the direct band gap nature of GaN_xP_{1-x}

below the CBM (X_c) and about 0.6 eV below the Γ-point edge. Experimental investigation suggests that the strength of anticrossing interaction between the localized and delocalized states varies across the different conduction band minima (X, L, Γ-points), changing the fundamental nature of the gap [51]. The PR spectra shown in Fig. 3.10 demonstrate how the transition energies at the Γ-point change as N is added to GaP. In contrast to the spectrum of GaP, which contains only one transition at 2.78 eV, two transitions are now present in the $GaN_{0.023}P_{0.977}$ film. The low energy transition below the indirect band gap (E_{gX}) at 1.96 eV corresponds to the newly formed E_- subband and the high energy feature above the direct band gap (E_Γ) at 2.96 eV is attributed to the E_+ subband. The strong nature of the E_- transition indicates that the addition of N to GaP produces a new subband of extended states at the Γ-point and changes the nature of the band gap from indirect to direct.

One salient feature of the BAC model is that the impurity-induced downward movement of the E_- subband is matched by an equivalent upward movement of the E_+ subband. Figure 3.11 displays the experimentally determined subband energies relative to the VBM of GaP as a function of the N concentration along with the theoretically calculated trends obtained with a coupling parameter of $V = 3.05$. Also shown are the positions of the X-point (E_X) and Γ-point (E_Γ) minima and the localized N level (E_N). Notice that the E_- and E_+ subbands originate from the unperturbed E_N and E_Γ levels, respectively, and diverge in a symmetrical manner.

The influence of the anticrossing interactions on the bandstructure of GaN_xP_{1-x} has been further elucidated by examining the effects of hydrostatic pressure on the PL energies. The pressure dependencies of three GaN_xP_{1-x} samples of various compositions are shown in Fig. 3.12 along with

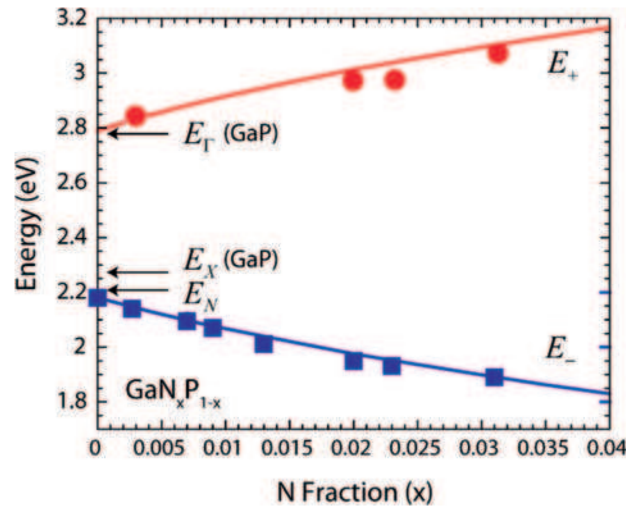

Fig. 3.11. Composition dependencies of the E_- and E_+ transitions in GaN_xP_{1-x}

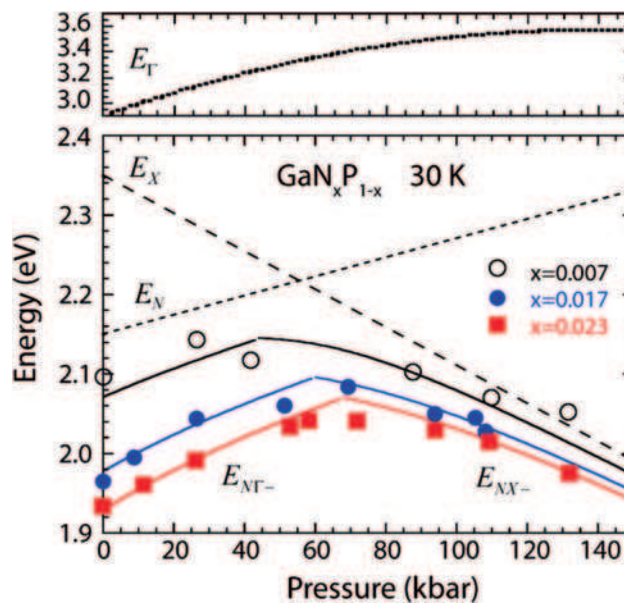

Fig. 3.12. Pressure dependence of the band edge in GaN_xP_{1-x} measured by photoluminescence. The dashed lines show the pressure dependencies of the Γ and X band minima in GaP as well as the localized N level. The solid curves indicate the lowest conduction band energies of the three N concentrations calculated with the BAC model

the dependencies of the Γ (E_Γ) and X (E_X) conduction band minima and localized N level (E_N) [40]. The upward shift in the PL energy at low pressures clearly opposes the pressure dependence of the indirect transition and instead is more consistent with the expected movement of the direct gap. The measured pressure coefficients of the samples are much smaller than the pressure coefficient of the E_Γ conduction band edge ($dE_\Gamma/dP = 10\,\text{meV kbar}^{-1}$) of GaP but are slightly larger than the pressure coefficient of the highly localized N level ($dE_N/dP = 1.5\,\text{meV kbar}^{-1}$) [52]. This behavior arises from the more localized nature of the E_- subband, as it mostly derives from the E_N level. At higher pressures, the X-point again becomes the lowest conduction band edge, and the trend in the experimental data reverses direction to follow E_X instead.

3.4.2 Electronic Properties of Dilute Nitrides

The impurity-induced restructuring of the conduction band in these HMAs not only affects the optical properties but has stark implications for the electronic properties as well. As stated in the previous section, the electron effective mass will change significantly due to the hybridization of extended states of the matrix with the localized states of the impurities. This effect has been confirmed by measuring the PR transitions in GaN_xAs_{1-x}/GaAs multiple quantum well (MQW) samples of various well thicknesses [53]. Figure 3.13

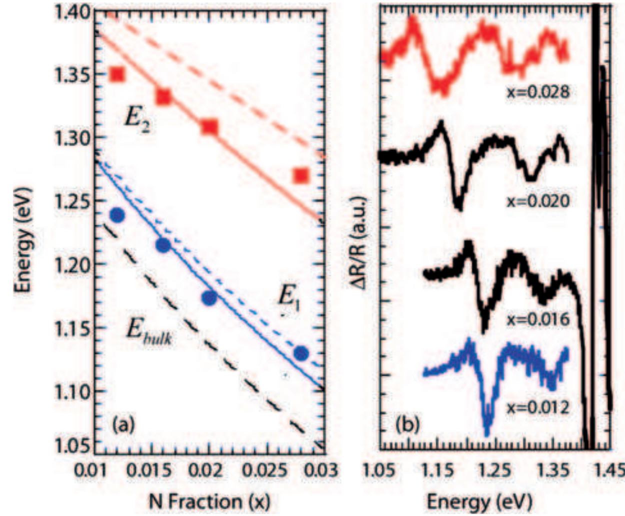

Fig. 3.13. (**a**) Composition dependencies of the E_- and E_+ transitions in GaN_xAs_{1-x} multiple quantum wells determined from the PR spectra shown in (**b**). Also displayed are the theoretical fits of the BAC model using the effective mass of GaAs (*dashed lines*) and an enhanced effective mass determined by (3.17). The GaN_xAs_{1-x}/GaAs MQW structures consisted of a repeat of 7 nm GaN_xAs_{1-x} QW with a 20 nm GaAs barrier

displays the energy levels of the two confined levels in the conduction band of the GaN_xAs_{1-x} wells, denoted E_1 and E_2, as a function of N concentration [54]. The decrease in the energy of these two levels results from the band gap reduction in the alloy caused by anticrossing effects. Also shown in Fig. 3.13 are the expected energies of E_1 and E_2 calculated with a finite-depth square well confinement model assuming an electron effective mass equal to that of GaAs ($m^*_{\mathrm{GaAs}} = 0.067m^*$). These expected values overestimate the experimental data. The BAC model predicts a nonparabolic electron dispersion relation for the E_- band, and therefore the effective mass now conforms to the following relation [54]:

$$m^* = \hbar^2 \left| \frac{k}{\mathrm{d}E_-(k)/\mathrm{d}k} \right|_{k=0} = 2m^*_{\mathrm{GaAs}} \Big/ \left[1 - \frac{E^c(0) - E^d}{\sqrt{\left(E^c(0) - E^d\right)^2 + 4V^2 x}} \right] \quad (3.17)$$

The experimental data fits quite well with the BAC-determined effective mass, suggesting an enhanced electron effective mass due to the flattening of the E_- band. It has also been demonstrated that the application of hydrostatic pressure also induces an increase in the electron effective mass [54].

It is also well known that the electron mobilities of GaAs and $Ga_{1-y}In_yAs$ are reduced by 1–2 orders of magnitude upon the incorporation of N [55, 56]. Figure 3.14 displays the electron mobility in a $Ga_{0.93}In_{0.07}N_{0.017}As_{0.983}$:Si film as a function of electron concentration [47]. At high concentrations, the Fermi level is pushed upward toward the unperturbed localized N level, and the homogeneous broadening caused by the resulting anticrossing interaction becomes the dominant scattering mechanism that limits the mobility. In this region, the theoretically calculated electron mobility, μ_1, fits the experimental data quite well. At low electron concentrations, the mobility also drops. In this regime, electron scattering is now caused by the potential fluctuations that occur from the structural and compositional disorder in the alloy. The estimate of electron mobility dominated by alloy disorder scattering, μ_2, is also shown in Fig. 3.14. The experimental data agrees well with the calculated values when taking these two factors into account ($1/\mu_{\mathrm{total}} = 1/\mu_1 + 1/\mu_2$).

Reviewing the band anticrossing-induced novel phenomena, it is apparent that the optical and electrical properties of these HMAs can be manipulated by controlling the amount of active isoelectronic impurities as well as the electron concentration. Mutual passivation of an impurity on the anion sublattice with a donor residing on the cation sublattice provides a means of restricting the anticrossing interaction [57]. On the other hand, the maximum electron concentration of the alloy may be enhanced through the restructuring of the conduction band and the correct choice of donor dopant species [58,59]. These two effects will be explored in further detail in Chap. 1.

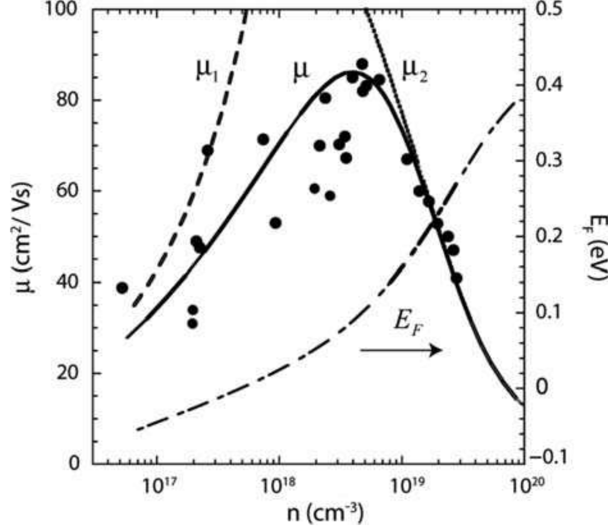

Fig. 3.14. Room temperature of mobility of $Ga_{0.93}In_{0.07}N_{0.017}As_{0.983}$:Si as a function of electron concentration. The conduction band-broadening (μ_1) and alloy scattering (μ_2) limited mobilities as well as the final fit are also displayed. The Fermi level is also shown

3.5 Valence Band Anticrossing

Large isoelectronic impurities behave in an analogous manner to highly electronegative impurities if they are sufficiently mismatched in ionization energy from the host anion. The localized T_2 states of these metallic impurities often lie near the valence band edge of the host matrix, resulting in a band anticrossing-induced restructuring of the valence band. The hybridization of the localized impurity states with the extended host states can be analyzed with a valence band anticrossing (VBAC) model. The conventional $6 \times 6\, \boldsymbol{k} \cdot \boldsymbol{p}$ matrix describing the six delocalized states of the host valence band is augmented with the localized impurity states of the same six momentum-decoupled wave functions as the basis, producing a 12×12 Hamiltonian matrix [19]. The energy levels of the impurity atoms are divided into three doubly degenerate pairs, corresponding to the heavy and light hole states of energy E_{Imp}, and the spin–orbit split-off states of energy $E_{\mathrm{Imp\text{-}so}}$, which are determined from the atomic spin–orbit splitting energy of the impurity. Finally, the hybridization energy between the localized and extended states is defined as

$$V = \left\langle P_X^{\mathrm{A}} \left| U \right| X \right\rangle = \left\langle P_Y^{\mathrm{A}} \left| U \right| Y \right\rangle = \left\langle P_Z^{\mathrm{A}} \left| U \right| Z \right\rangle , \tag{3.18}$$

where U is the localized potential of the impurity species in the host crystal, P^{A} represents the wavefunction of impurity A, and X, Y, and Z refer

to the Bloch wavefunctions of the host. Configurational averaging over the randomly distributed impurity atoms with fraction x yields the following simplified expression:

$$V = C_{\mathrm{A}}\sqrt{x} \tag{3.19}$$

The term, C_{A}, is the coupling parameter that describes the strength of the interaction and depends on the difference in ionization energy of the two anion elements. The restructuring of the valence band can now be understood as a function of three anticrossing interactions; those between the localized and extended heavy hole states, light hole states, and spin–orbit split-off states, respectively.

As a natural extension to the discussion on conduction band anticrossing in dilute nitrides, the valence band anticrossing model has been applied to $GaN_{1-x}As_x$, in which As is now the minority species replacing the N anion [17]. Photomodulated transmission (PT) measurements on $GaN_{1-x}As_x$ thin-film samples with various compositions ($0 < x < 0.06$) reveal a discontinuous decrease in the band gap, resulting from the formation of an As-related impurity band located 0.6 eV above the valence band edge of GaN. The downward shift in the energy of this transition with increasing x can be well explained with the VBAC model, as shown in Fig. 3.15. Hybridization produces a set of three E_+ and E_- bands. The heavy and light hole (HH/LH) E_+ and E_- bands derive from the As impurity heavy and light hole levels and the host crystal, respectively, while the corresponding spin–orbit split-off (SO) E_+ and E_- bands originate from the host and As levels, respectively, as shown in Fig. 3.16.

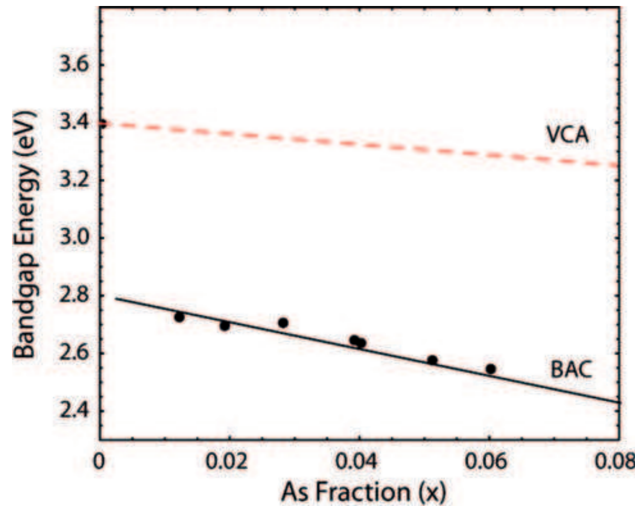

Fig. 3.15. Experimentally measured band gap values of $GaN_{1-x}As_x$ as well as the VCA- and BAC-determined trends.

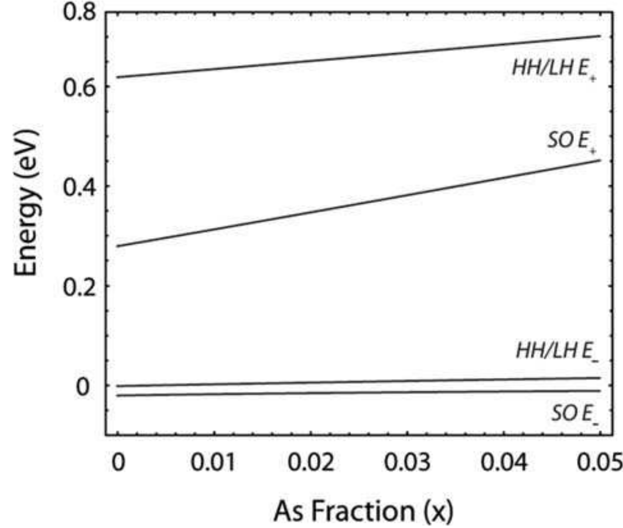

Fig. 3.16. Composition dependence of the heavy hole (HH), light hole (LH), and spin–orbit split-off (SO) related E_- and E_+ band edges in $GaN_{1-x}As_x$

Valence band anticrossing effects have also been observed in other III–V and II–VI alloys. The localized T_2 level of Te is located just above the valence band edges of ZnSe and ZnS. Alloying ZnTe with either ZnSe or ZnS produces an abrupt decrease in the band gap of each alloy as well as a significant increase in the spin–orbit splitting energy, suggesting hybridization between the localized Te states with the delocalized host valence band states [60]. Recently, the incorporation of dilute concentrations of Sb and Bi into GaAs have also been shown to lead to a decrease in the band gap energy [61–65]. The VBAC model can explain these trends as well [19].

By understanding how impurities of high electronegativity and low ionization energy influence the bandstructure of a host semiconductor, the band gap of a highly mismatched III–V or II–VI alloy can be characterized by a linear interpolation between the two extremes. The final composition dependence of the band gap can be expressed as

$$E_{\mathrm{g}}(x) = (1-x)\,E_{\mathrm{g}}^{\mathrm{N-rich}}(x) + xE_{\mathrm{g}}^{\mathrm{As-rich}}(x) \tag{3.20}$$

This scheme weights the two band anticrossing effects according to the majority component. Shown as an example, Fig. 3.17 displays the band gap of $GaN_{1-x}As_x$ across the entire composition range. Note that the experimentally determined values within both the N-rich and As-rich extremes are approximated quite well by the weighted BAC model, while they deviate significantly from the trends predicted by the VCA or a simple quadratic relationship containing a bowing parameter.

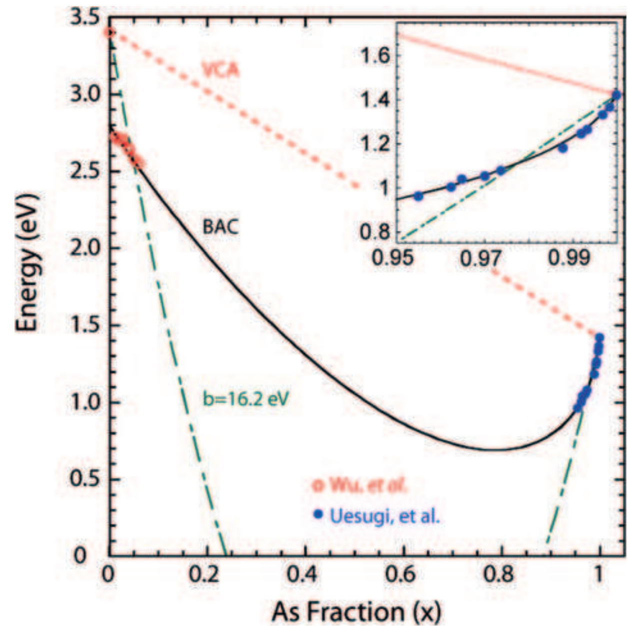

Fig. 3.17. Composition dependence of the band gap of $GaN_{1-x}As_x$ determined by the VCA, quadratic bowing parameter, and BAC methods. The BAC calculations provide the best fit to the experimental data [17]

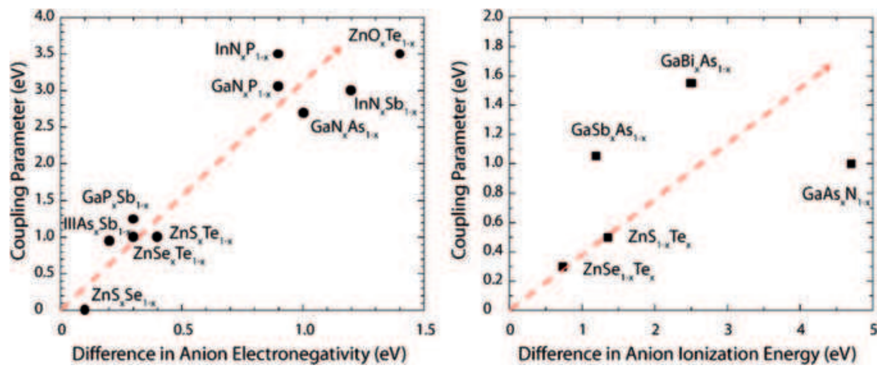

Fig. 3.18. Coupling parameters used in the conduction and valence band anticrossing models of various HMAs as a function of electronegativity and ionization energy, respectively. The dashed lines represent the general trend

As discussed in the previous sections, the coupling parameter in the conduction and valence band anticrossing models depends on the mismatch in electronegativity and ionization energy, respectively, between the two anion elements. Comparison of the alloy systems examined here, shown in Fig. 3.18, reveals that C increases with an increase in the mismatch in either

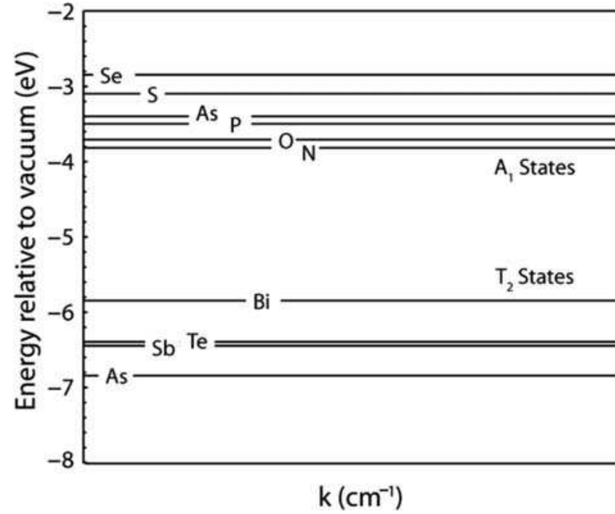

Fig. 3.19. The A_1 and T_2 defect level positions relative to the vacuum level for the common group V and IV impurities

electronegativity or ionization energy between the two anion species in III–V and II–VI HMAs. This suggests a direct correlation between the coupling parameter and mismatch and is entirely expected considering that a greater disparity in either the electronegativity or ionization energy will lead to an enhanced spatial localization of carriers at the isoelectronic impurity sites and thus a greater strength of the anticrossing interaction.

The universal positions of the isoelectronic impurity A_1 and T_2 defect states are summarized in Fig. 3.19. They follow a general trend as well. The A_1 states of impurities with high electronegativities tend to lie at comparatively low energies relative to the vacuum level. This places them close to the conduction band edges of host compound semiconductors, allowing them to interact strongly with those delocalized states. Likewise, the T_2 states of the impurities with low ionization energies are located near the valence band edges of the host compounds, inducing a similar effect.

3.6 Conclusions

The BAC model has been successfully applied to describe the electronic structure of highly mismatched alloys including dilute III–V nitrides. An anticrossing interaction with a nearby localized level introduced by the highly electronegative impurity species restructures the conduction band of a host semiconductor, resulting in a split conduction band and a reduced fundamental band gap. Composition and pressure dependence studies carried out on GaN_xAs_{1-x}, $Ga_{1-y}In_yN_xAs_{1-x}$, GaN_xP_{1-x}, and other alloy systems confirm

that the unusual optical and electronic properties observed in these materials can be attributed to the band anticrossing behavior of the restructured conduction subbands. This model has recently been extended to III–V and II–VI HMAs with dilute species of low ionization energy, which induces a restructuring of the valence band of a host material. These two models can be simultaneously applied to describe the band gap across the entire composition range of an alloy system with two very dissimilar binary constituents, as has been demonstrated for $GaN_{1-x}As_x$. Full understanding of the effects of the valence band anticrossing phenomenon, such as its dispersion in k-space and its chemical trend compared with ab initio calculations, requires further investigation into the mechanisms of these interactions.

Acknowledgment. This work was supported in part by the Director's Innovation Initiative Program, National Reconnaissance Office and the Director, Office of Science, Office of Basic Energy Sciences, Division of Materials Sciences and Engineering, of the U. S. Department of Energy under Contract No. DE-AC02-05CH11231. KA acknowledges support from an NSF IGERT traineeship.

References

1. M. Cardona, Phys. Rev. **129**, 67 (1963)
2. J.A. Van Vechten, T.K. Bergstresser, Phys. Rev. B **1**, 3351 (1970)
3. D. Richardson, J. Phys. C: Solid State Phys. **4**, L289 (1971)
4. H.C. Casey, M.B. Panish, J. Appl. Phys. **40**, 4910 (1969)
5. W. Shan, W. Walukiewicz, J. Wu, K.M. Yu, J.V. Ager III, S.X. Li, E.E. Haller, J.F. Geisz, D.J. Friedman, S.R. Kurtz, J. Appl. Phys. **93**, 2696 (2003)
6. A.G. Thompson, M. Cardona, K.L. Shaklee, J.C. Woolley, Phys. Rev. **146**, 601 (1966)
7. M. Weyers, M. Sato, H. Ando, Jpn. J. Appl. Phys. **31**, L853 (1992)
8. N. Baillargeon, K.Y. Cheng, G.F. Hofler, P.J. Pearah, K.C. Hsieh, Appl. Phys. Lett. **60**, 2540 (1992)
9. W.G. Bi, C.W. Tu, J. Appl. Phys. **80**, 1934 (1996)
10. J.C. Harmand, J. Ramos, E.V.K. Rao, G. Saint-Girons, R. Teissier, G. Le Roux, L. Largeau, G.J. Patriarche, J. Cryst. Growth **227–228**, 553 (2000)
11. B.N. Murdin, M. Karmal-Saadi, A. Lindsay, E.P. O'Reilly, A.R. Adams, G.J. Nott, J.G. Crowder, C.R. Pidgeon, I.V. Bradley, J.P.R. Wells, T. Burke, A.D. Johnson, T. Ashley, Appl. Phys. Lett. **78**, 1568 (2001)
12. H.P. Hjalmarson, D.J. Wolford, J.D. Dow, Phys. Rev. Lett. **44**, 810 (1980)
13. D.J. Wolford, J.A. Bradley, K. Fry, J. Thompson, in *Physics of Semiconductors*, ed. by J.D. Chadi, W.A. Harrison (Springer, Berlin Heidelberg New York, 1984)
14. D.G. Thomas, J.J. Hopfield, C.J. Frosch, Phys. Rev. Lett. **15**, 857 (1965)
15. K.M. Yu, W. Walukiewicz, J. Wu, W. Shan, J.W. Beeman, M.A. Scarpulla, O.D. Dubon, P. Becla, Phys. Rev. Lett. **91**, 246404 (2003)
16. T. Mattila, A. Zunger, Phys. Rev. B **58**, 1367 (1998)
17. J. Wu, W. Walukiewicz, K.M. Yu, J.D. Denlinger, W. Shan, J.W. Ager III, A. Kimura, H.F. Tang, T.F. Kuech, Phys. Rev. B **70**, 115214 (2004)

18. F.A. Trumbore, M. Gershenzon, D.G. Thomas, Appl. Phys. Lett. **9**, 4 (1966)
19. K. Alberi, J. Wu, W. Walukiewicz, K.M. Yu, O.D. Dubon, S.P. Watkins, C.X. Wang, X. Liu, Y.J. Cho, J. Furdyna, Phys. Rev. B, **75**, 045203 (2007)
20. S.H. Wei, A. Zunger, Phys. Rev. Lett. **76**, 664 (1996)
21. T. Mattila, A. Zunger, Phys. Rev. B **60**, R11245 (1999)
22. Y. Zhang, A. Mascarenhas, H.P. Xin, C.W. Tu, Phys. Rev. B **63**, 161303 (2001)
23. P.R.C. Kent, L. Bellaiche, A. Zunger, Semicond. Sci. Technol. **17**, 851 (2002)
24. P.W. Anderson, Phys. Rev. **124**, 41 (1961)
25. A.N. Kocharyan, Soc. Phys. Solid State **28**, 6 (1986)
26. M.A. Ivanov, Y.G. Pogorelov, Sov. Phys. JETP **61**, 1033 (1985)
27. F. Yonezawa, K. Morigaki, Suppl. Prog. Theor. Phys. **53**, 1 (1973)
28. R.J. Elliott, J.A. Krumhans, P.L. Leath, Rev. Mod. Phys. **46**, 465 (1974)
29. J. Wu, W. Walukiewicz, E.E. Haller, Phys. Rev. B. **65**, 233210 (2002)
30. W. Shan, W. Walukiewicz, J.W. Ager III, E.E. Haller, J.F. Geisz, D.J. Friedman, J.M. Olson, S.R. Kurtz, Phys. Rev. Lett. **82**, 1221 (1999)
31. R. Bhat, C. Caneau, L. Salamanca-Riba, W.G. Bi, C.W. Tu, J. Cryst. Growth **195**, 427 (1998)
32. L. Malikova, F.H. Pollak, R. Bhat, J. Electron. Mater. **27**, 484 (1998)
33. B.M. Keyes, J.F. Geisz, P.C. Dippo, R. Reedy, C. Kramer, D.J. Friedman, S.R. Kurtz, AIP Conf. Proc. **462**, 511 (1999)
34. K. Uesugi, N. Marooka, I. Suemune, Appl. Phys. Lett. **74**, 1254 (1999)
35. K.M. Yu, W. Walukiewicz, W. Shan, J.V. Ager III, J. Wu, E.E. Haller, J.F. Geisz, D.J. Friedman, J.M. Olson, Phys. Rev. B **61**, R13337 (2000)
36. C. Skierbiszewski, P. Perlin, P. Wisniewski, T. Suzuki, J.F. Geisz, K. Hingerl, W. Jantsch, D. Mars, W. Walukiewicz, Phys. Rev. B **65**, 035207 (2001)
37. J. Wu, W. Shan, W. Walukiewicz, Semicond. Sci. Technol. **17**, 860 (2002)
38. J. Wu, K.M. Yu, W. Walukiewicz, G. He, E.E. Haller, D.E. Mars, D.R. Chamberlin, Phys. Rev. B **68**, 195202 (2003)
39. J.D. Perkins, A. Mascarenhas, J.F. Geisz, D.J. Friedman, Phys. Rev. B **64**, 121301 (2001)
40. J. Wu, W. Walukiewicz, K.M. Yu, J.W. Ager III, E.E. Haller, Y. Hong, H.P. Xin, C.W. Tu, Phys. Rev. B **65**, R241303 (2002)
41. W. Shan, W. Walukiewicz, J.W. Ager III, E.E. Haller, J.F. Geisz, D.J. Friedman, J.M. Olson, S.R. Kurtz, J. Appl. Phys. **86**, 2349 (1999)
42. W. Walukiewicz, W. Shan, J. Wu, J.W. Ager III, D.R. Chamberlin, E.E. Haller, J.F. Geisz, D.J. Friedman, J.M. Olson, S.R. Kurtz, in *Proceedings of 195th Mtg. of Electrochemical Society*, vol. 99, 1999, p. 190
43. K.M. Yu, W. Walukiewicz, J. Wu, J.W. Beeman, J.W. Ager III, E.E. Haller, W. Shan, H.P. Xin, C.W. Tu, M.C. Ridgway, J. Appl. Phys. **90**, 2227 (2001)
44. J.D. Perkins, A. Mascarenhas, Y. Zhang, J.F. Geisz, D.J. Friedman, J.M. Olson, S.R. Kurtz, Phys. Rev. Lett. **82**, 3312 (1999)
45. C. Skierbiszewski, Semicond. Sci. Technol. **17**, 803 (2002)
46. P. Perlin, P. Wisniewski, C. Skierbiszewski, T. Suski, E. Kaminska, S.G. Subramanya, E.R. Weber, D.E. Mars, W. Walukiewicz, Appl. Phys. Lett. **76**, 1279 (2000)
47. W. Walukiewicz, W. Shan, J. Wu, K.M. Yu, in *Physics and Applications of Dilute Nitrides*, ed. by I. Buyanova, W. Chen (Taylor & Francis, New York, 2004) p. 23
48. K.M. Yu, W. Walukiewicz, J. Wu, J.W. Beeman, J.W. Ager III, E.E. Haller, W. Shan, H.P. Xin, C.W. Tu, M.C. Ridgway, Appl. Phys. Lett. **78**, 1077 (2001)

49. K.M. Yu, J. Wu, W. Walukiewicz, J.W. Beeman, J.W. Ager III, E.E. Haller, I. Miotkowski, A. Ramdas, J. Electron. Mater. **31**, 754 (2002)
50. W. Walukiewicz, W. Shan, K.M. Yu, J.W. Ager III, E.E. Haller, I. Miotkowski, M.J. Seong, H. Alawadhi, A.K. Ramdas, Phys. Rev. Lett. **85**, 1552 (2000)
51. W. Shan, W. Walukiewicz, K.M. Yu, J. Wu, J.W. Ager III, E.E. Haller, H.P. Xin, C.W. Tu, Appl. Phys. Lett. **76**, 3251 (2000)
52. G. Martinez, in *Optical Properties of Solids*, ed. by M. Balkanski (North-Holland, Amsterdam, 1980)
53. H.P. Xin, C.W. Tu, Appl. Phys. Lett. **72**, 2442 (1998)
54. J. Wu, W. Shan, W. Walukiewicz, K.M. Yu, J.W. Ager III, E.E. Haller, H.P. Xin, C.W. Tu, Phys. Rev. B **64**, 085320 (2001)
55. J.F. Geisz, D.J. Friedman, J.M. Olson, S.R. Kurtz, B.M. Keyes, J. Cryst. Growth **195**, 401 (1998)
56. S.R. Kurtz, A.A. Allerman, C.H. Seager, R.M. Sieg, E.D. Jones, Appl. Phys. Lett. **77**, 400 (2000)
57. K.M. Yu, W. Walukiewicz, J. Wu, D.E. Mars, D.R. Chamberlin, M.A. Scarpulla, O.D. Dubon, J.F. Geisz, Nat. Mater. **1**, 185 (2002)
58. K.M. Yu, W. Walukiewicz, W. Shan, J. Wu, J.W. Ager III, E.E. Haller, J.F. Geisz, M.C. Ridgway, Appl. Phys. Lett. **77**, 2858 (2000)
59. K.M. Yu, W. Walukiewicz, W. Shan, J. Wu, J.W. Beeman, J.W. Ager III, E.E. Haller, Appl. Phys. Lett. **77**, 3607 (2000)
60. J. Wu, W. Walukiewicz, K.M. Yu, W. Shan, J.W. Ager III, E.E. Haller, I. Miotkowski, A.K. Ramdas, C.H. Su, Phys. Rev. B **68**, 033206 (2003)
61. R. Teissier, D. Sicault, J.C. Harmand, G. Ungaro, G. Le Roux, L. Largeau, J. Appl. Phys. **89**, 5473 (2001)
62. S. Tixier, M. Adamcyk, T. Tiedje, S. Francoeur, A. Mascarenhas, P.W. Wei, F. Schiettekatte, Appl. Phys. Lett. **82**, 2245 (2003)
63. S. Francoeur, M.J. Seong, A. Mascarenhas, S. Tixier, M. Adamcyk, T. Tiedje, Appl. Phys. Lett. **82**, 3874 (2003)
64. W. Huang, K. Oe, G. Feng, M. Yoshimoto, J. Appl. Phys. **98**, 053505 (2005)
65. B. Fluegel, S. Francoeur, A. Mascarenhas, S. Tixier, E.C. Young, T. Tiedje, Phys. Rev. Lett. **97**, 067205 (2006)

4

Electronic Structure of GaN_xAs_{1-x} Under Pressure

I. Gorczyca, P. Boguslawski, A. Svane, and N.E. Christensen

The electronic band structures of GaN_xAs_{1-x} alloys are examined within the density functional theory. The calculations, including structural optimizations, are performed by means of full-potential linear muffin-tin-orbital and pseudopotential methods. The effects of applying external pressure and of varying the composition, x, are examined.

The host conduction states near X and L in the Brillouin zone are modified by addition of N. Their interaction with the lowest conduction bands induce a pronounced nonparabolicity of this band and affect strongly the value of the effective electron mass and its pressure and composition dependences. The origin of the additional E_+ optical transition is elucidated.

4.1 Introduction

GaN_xAs_{1-x} and $Ga_{1-y}In_yN_xAs_{1-x}$ alloys with a small content of nitrogen have attracted a substantial attention during the last few years due to their technological potential for device applications in fabrication of infrared diode lasers, light detectors operating in the 1.3–1.5 µm wavelength regime, efficient multijunction solar cells [1], and possibly the most important application nowadays: vertical cavity surface emitting lasers (VCSELs) [2].

Quaternary alloys offer the possibility of independent tuning of the lattice constant and the energy bandgap [3], which creates an additional flexibility desired in many applications. For example, the $Ga_{1-y}In_yN_xAs_{1-x}$ alloy for $x = 0.01$ and $y = 0.03$ has an energy bandgap which is ≈ 0.2 eV lower than that of GaAs, but has the same lattice constant, leading to reduced strain in $Ga_{1-y}In_yN_xAs_{1-x}$/GaAs heterostructures.

Beside the technological importance, the GaNAs alloys are very interesting from the scientific point of view due to their peculiar properties related to the large lattice mismatch between GaAs and GaN (or, alternatively, the large difference of atomic radii of As and N), as well as large differences of electronegativities of As and N. Due to these features, GaN_xAs_{1-x} and

$Ga_{1-y}In_yN_xAs_{1-x}$ alloys belong to a new class of semiconductors, the so-called highly mismatched alloys, whose properties are dramatically modified through the substitution of a small fraction of host atoms with an element of very different electronegativity. To the same class belong $ZnTe_{1-x}O_x$ and $Mn_yZn_{1-y}Te_{1-x}O_x$ alloys with small values of x and y, which were recently investigated and also look promising from the application point of view [4].

The first experimental investigations of N impurities in GaAs were performed by Wolford et al. [5], Liu et al. [6], and Leymarie et al. [7]. In all cases, N concentrations were lower than $10^{18}\,cm^{-3}$. The energy of the N-induced state was assessed from luminescence under hydrostatic pressure up to 3 GPa [6], 6 GPa [7], and 7 GPa [5], respectively. It was demonstrated that N, in this extremely diluted limit, introduces a resonance about 150 meV above the conduction band (CB) minimum, which is labeled $a_1(N)$ in the following. Since the pressure coefficient of the $a_1(N)$ level is lower than that of the CB, the $a_1(N)$ state becomes a deep state in the bandgap for pressures higher than 2 GPa. For pressures higher than about 6 GPa, the energy of the secondary minimum at the X point of the Brillouin zone (BZ) is lower than $a_1(N)$, which consequently becomes a resonance degenerate with the conduction band at X. The picture above is valid only in the impurity limit, in the alloy regime the nitrogen incorporation leads to quite different features. The $a_1(N)$ state moves rapidly to very high energies as x is increased, as shown by Mattila et al. [8].

Progress in epitaxy have allowed to overcome the low solubility of N in GaAs, and to obtain GaNAs alloys with compositions up to 15% of N [9, 10]. Experimentally, adding a few per cent of N to GaAs leads to unexpectedly strong modifications of the electronic structure. The most important features observed in the typical nitrogen concentration regime ($x = 0.005$–0.03) are the following:

(1) A significant reduction of the bandgap with increasing N content [11–19]. This demonstrates a strongly nonlinear dependence of the fundamental bandgap on the alloy composition, i.e., the bandgap bowing, since the bandgap of GaN is larger than that of GaAs by about 2 eV. Moreover, in most III–V alloys the composition dependence of the bandgap is quadratic. This relation is not obeyed in GaNAs, indicating that N induces very strong perturbations of the GaAs band structure, which cannot be described within the virtual crystal approximation and the second-order perturbation theory.
(2) The pressure dependence of the bandgap is sublinear and weaker as compared to that of GaAs, and it exhibits a tendency to saturate at high pressures [13, 15, 19, 20]. The magnitude of the effect depends on the alloy composition.
(3) Electroreflectance and absorption measurements have revealed the appearance of a new transition called E_+. For samples with $x \geq 0.008$ its energy is about 0.4 eV higher than the bandgap, denoted as E_-, and increases with the N content [13, 14, 16, 18, 19, 21–23]. These results show that the

states close to the CB minimum at the Γ point are drastically modified. In contrast, optical transitions at other points of the GaAs BZ are almost unaffected by the presence of N [18].

(4) Large and strongly composition-dependent values of the electron effective mass, which increase further as the wavevector is shifted away from the center of the BZ [16, 21]. Moreover, for low N concentrations (0.1–0.2%) the pressure coefficient of the electron effective mass is reported to be almost an order of magnitude larger than that observed in GaAs [24].

From the theoretical side, several calculations [8, 15, 25–33] of the electronic structure of GaNAs have been performed. It has been found that the addition of nitrogen strongly modifies the CBs, and has a negligible effect on the valence bands. A good agreement between theory and experiment is found for the composition and pressure dependence of the bandgap. In particular, the results reveal a very important role played by the lattice relaxations around N atoms. An analysis of the results complemented by a group theoretical approach also explains the presence and the nature of the E_+ state. The separation between the E_- and E_+ edges as a function of the composition is well described [26], as well as the relative oscillator strengths of the optical transitions involving these levels. Finally, the dependence of the effective mass on both the pressure and the composition is well accounted for [32].

Here, we present such detailed analyses of the GaN_xAs_{1-x} energy bands obtained by ab initio calculations, examining the nature of individual states, calculating the electron effective masses, as well as studying the pressure effects on these quantities.

4.2 Methodology

The electronic structures of GaN_xAs_{1-x} alloys have been analyzed by ab initio calculations in a supercell geometry using two different approaches. Both are based on the local density approximation (LDA) [34] to the density functional theory, and use the Perdew–Zunger [35] parameterization of the Ceperley–Alder exchange correlation [36].

The first approach is the plane wave method based on ab initio pseudopotentials [37–39] and quantum molecular dynamics [37, 38]. We have employed the standard pseudopotentials [39]. A cutoff energy of 30 Ry for the plane wave basis set was sufficient to obtain converged results.

The second approach used is the linear-muffin-tin-orbital method (LMTO) [40]. A full-potential (FP) version was applied in order to allow structural optimizations. The version is based on the code developed by Methfessel [41, 42], modified by van Schilfgaarde [43] and Novikov et al. [44]. It allows for a simultaneous optimization of lattice axial ratios, angles, and atomic coordinates by total-energy minimization. A so-called *triple-κ* basis set was used (κ refers here to the decay constant of the LMTOs outside the muffin-tin spheres). For

Ga, As, and N angular momenta up to $\ell = (2,\ 2,\ 1)$ were included in the three κ channels. The semicore Ga-3d states were included as local orbitals [45]. As usual, in open structures, empty spheres (muffin-tin spheres without nuclear charge) were included for the accuracy of interpolation of the charge density [46]. No orbitals were associated with these, but the "E-spheres" used in the full-potential version play a somewhat different role from those of the atomic-spheres-approximation (ASA) [40,46], where orbitals must be included at these sites. The k-space integrations used up to 1,728 k-points in the BZ. All (nonoverlapping) muffin-tin spheres are chosen to have the same size.

In both approaches, we relax the atomic positions in order to find the equilibrium atomic configuration. As we show in the following, the inclusion of atomic displacements in the vicinity of N atoms is necessary for a proper description of the electronic structure of GaNAs.

In the following, presenting the results obtained by the two methods we show that they lead to the same picture of the GaNAs properties. The first method, pseudopotentials, is well suited for calculations of the atomic relaxations in the whole supercell by applying quantum molecular dynamics. The second method, FP-LMTO, allows for the gap adjustment, as will be described later. For example, the band structures presented in Fig. 4.1 were obtained by FP-LMTO method with adjusting potentials to get the

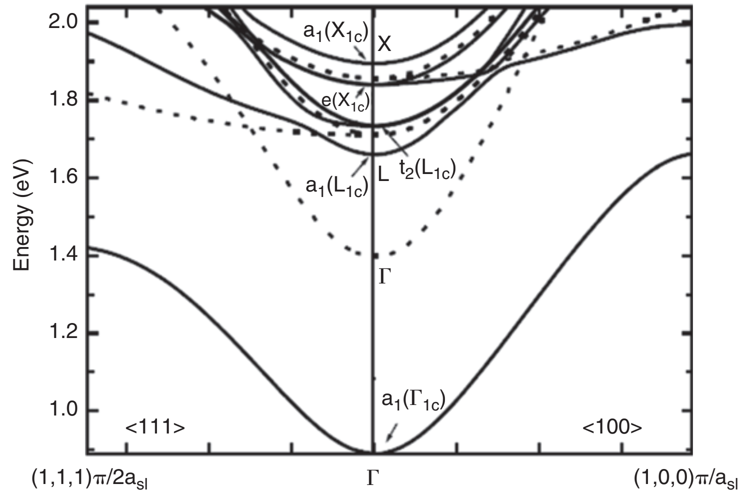

Fig. 4.1. Band structure of GaN_xAs_{1-x} for $x = 0.031$ (64 atoms) – *solid lines*, in comparison with the GaAs band structure – *dashed lines*, for the wavevectors along the (111) and (100) directions in the BZ of a cubic supercell. The point $(1,1,1)\pi/2a_{\mathrm{sl}}$ is only halfway toward the BZ edge (a_{sl} is the supercell lattice constant, i.e., twice the "normal" lattice constant of GaAs). FP-LMTO with gap adjusting potentials; scalar-relativistic calculation, i.e., spin–orbit coupling is omitted

bandgaps in agreement with experimental data. Similar band structure calculations were performed by means of the pseudopotential method, without adjustment, leading to comparable relative values of energies and similar pressure and composition dependences. Consequently, the conclusions related to the features of GaNAs alloy were drawn on the basis of both kinds of calculations.

The nitrogen concentrations, $x = 0.062$, 0.031, 0.016, and 0.009, have been realized by substituting one As atom by N in a supercell with $n = 32$, 64, 128, and 216 atoms, respectively. Energy levels at the high-symmetry points X and L in the BZ of the face-centered cubic lattice for zinc-blende (ZB) GaAs, specifically L_{1c} and X_{1c}, fold into states at the Γ point of the BZ of the structure built from n-atom supercells. The experimental lattice constants of the end compounds were assumed, together with the alloy lattice constants chosen according to Vegard's law.

4.2.1 Bandgap Adjustment

It is well known that the LDA underestimates the bandgaps of semiconductors. Compared to experiment, the values of the bandgaps of GaAs at Γ, L, and X are underestimated by about 1 eV. Moreover, close to the Γ point, the LDA gap errors are **k**-dependent, which leads to errors in the derived effective masses, see [47] and Table II in [48]. On the other hand, the wavefunctions of the CB are well described by LDA. Consequently, the pressure dependence of both the bandgap and of the effective mass, as well as the momentum matrix elements (which determine the oscillator strengths of optical transitions), are expected to be correct as discussed in [26, 47, 49, 50].

In order to perform a more detailed analysis of the effective mass (see Sect. 4.4) as a function of x and compare it with the experimental data we have included a semiempirical correction scheme for the LDA gap errors and thereby obtained results for gaps, effective masses as well as pressure coefficients which are quantitatively more reliable. One should note that it is necessary to correct not only the fundamental gap, but also the dispersion of the CB, so that the effective mass at the Γ point is affected. For this reason a correction using a "scissors operator" (a rigid shift of the CBs [51]) is useless, since it does not change the dispersion of the CB and the value of the effective CB mass.

There are well-established methods for correcting the LDA bandgaps. The so-called GW method [52, 53] is based on fundamental theoretical principles (G and W are the Green's function and the screened Coulomb potential, respectively), and we would have preferred to use this for the present work. A combination of the GW theory with methods of including electron–hole correlations, see for example [54–56], would be very interesting, but at present we cannot implement any of these schemes for supercells containing as many atoms as considered here. We therefore apply the ad hoc method of [47], which was successfully applied to superlattices [57]. This is a simple procedure for

correcting the bandgaps and dispersion by introducing additional external potentials of the form [47]:

$$V(r) = V_0 \frac{r_0}{r} \exp\left[-\left(\frac{r}{r_0}\right)^2\right], \tag{4.1}$$

where V_0 and r_0 are adjustable parameters. At the (real) atomic sites V_0 (positive) is usually chosen to be very large, and the range parameter, r_0, small. In this way the potentials become sharply peaked at the nuclear positions, and they produce "artificial Darwin shifts," i.e., they push s-states, which have nonzero density at the nuclei ($r = 0$), upward in energy.

In compound semiconductors we choose different parameters at anion and cations sites, but the fact that for the relatively open zinc-blende structure we need to insert the interstitial "empty spheres" (E-spheres) implies additional flexibility in the adjustment of the lowest CB. By using extra potentials also on the E-sites we can make gap corrections at several points in the BZ, for example at Γ, X, and L. In that way we correct not only the fundamental gap, but also the dispersion of the CB, and the effective mass at the Γ point. On E-sites smaller values of V_0 and larger range parameters r_0 must be chosen because the charge density in the interior of the E-spheres is small. The potentials are transferable [47, 58] in the sense that they can be determined at ambient conditions by adjusting to experimental gap values, and then used unchanged while the volume is varied, i.e., in pressure studies as performed in this work. They can be determined for different compounds (e.g., GaAs and AlAs) and subsequently be applied, with the same parameters, to systems where the two compounds are combined, for example superlattices and heterojunctions [57]. In spite of the simplicity in this ad hoc method for correcting the LDA "gap-errors," it requires knowledge of reliable experimental values of gaps in the pure bulk materials. The gaps in GaAs are very well known, but since here we study alloys of GaAs and GaN, we would have preferred to extract also parameters for bulk β-GaN (ZB type). However, reliable gap values for β-GaN have been published only for the zone center, see [59]. In addition, the above-mentioned transferability cannot be safely applied in this case, where there is one single nitrogen atom in a large GaAs cell. Ambiguity in nature of the N-neighbors (i.e., are the closest E-sites of "GaAs type" or "GaN type"? etc.) complicates the choice of the parameters. Therefore we simply used one set for all cations, one for all anions (As as well as N), one set for all E_1 and one for all E_2 kinds [47] of empty sites. These parameters were determined for pure GaAs at zero pressure. The resulting values in GaAs for the bandgaps and electron effective mass at the CB minimum are given in Table 4.1, together with the experimental values [60], and the unadjusted gaps obtained in the previous work [29].

Table 4.1. GaAs – bandgaps (in eV) and electron effective mass (in units of the free-electron mass) calculated without (unadjusted case) and with the adjusting potentials in comparison with the experimental data [60]

	Theory unadjusted	Theory adjusted	Experiment
Γ	0.21	1.40	1.42
L	0.80	1.70	1.71
X	1.33	1.84	1.90
M^*	0.01	0.08	0.07

4.2.2 Accuracy of the Supercell Method

In principle we wish to examine the electronic properties of the substitutionally disordered $GaAs_{1-x}N_x$ alloy. There are two ways of performing ab initio calculations for such materials. The first one is based on the coherent potential approximation (CPA) [61, 62], also in the LMTO implementation [63]. The second one uses "representative" supercells with various atomic configurations and periodic boundary conditions. Whereas the CPA methods describe well the effects of the random occupation of the atomic sites in the alloy and provide electronic structures as appropriately broadened spectral density functions, the supercell calculations provide usual band structures allowing a detailed analysis of individual states in the k-space. This is convenient, but we stress that discussion of "folded-in" host states should be considered as approximative. Exact folding of fcc-zone edge states is only obtained for certain choices of supercell dimensions. In particular, for the sake of simplicity we describe here the E_+ state as a state derived from and dominated by the folded-in L_{1c}, but states from the vicinity of L_{1c} contribute to E_+ as well. However, as discussed in the following, the resulting inaccuracies are small in the limit of very small x, and since the use of larger supercells allows us to extend the calculations to lower nitrogen concentrations (we mainly consider N concentrations less than 3%) useful results are obtained by the supercell method. Moreover, we estimated effects of varying the arrangement of the N atoms in the GaAs host crystal. To this end additional calculations for $x = 0.062$ and 0.031 were made by substituting two atoms in a 64- and a 128-atom cell, respectively. This procedure provides error limits on various properties calculated by means of the supercell method (see Sect. 3.2).

4.2.3 Group-Theoretical Discussion of Electronic States

Before analyzing the GaNAs electronic band structures as a function of composition and pressure, we provide a group-theoretical discussion of electronic states in the considered alloys.

We begin by the case of pure GaAs, and observe that its point symmetry is T_d. The standard convention assumes the origin on the anion. With this assumption, the lowest conduction state at the X point in GaAs has the X_1

symmetry, and is composed of the s orbitals of anions, s_{anion}, and the p orbitals of cations, p_{cation} [64] (to simplify the discussion, the contribution of d states is neglected). The second state at X, situated 0.3 eV above the first one, has the X_3 symmetry, and it is a combination of s_{cation} and p_{anion}.

Introduction of an impurity has three effects. First, after the substitution of a host atom by an impurity the symmetry of the system is still T_{d}, provided that the origin is fixed at the impurity and the lattice relaxation is symmetric (which is the case of N impurity). Consequently, the site of substitution determines the origin of the coordinate system, and therefore the symmetry of states at the X point. Second, some of the degenerate states split. Finally, the impurity potential may couple states from various points of the BZ, e.g., the CB minima at Γ, X, and L. The coupling is allowed or forbidden depending on the actual symmetry of the two states in question.

The relevant selection rules will be discussed later. Considering the band splitting effects, there are three X minima, and the band states are threefold degenerate. The impurity potential splits the X_1-derived triplet into an $a_1(X_1)$ singlet and an $e_2(X_1)$ doublet (we use the molecular notation appropriate for diluted alloys). The X_3-derived triplet is not split, and its symmetry is $t_2(X_3)$. The L_1-derived quadruplet is split into an $a_1(L_1)$ singlet and a $t_2(L_1)$ triplet (see Fig. 4.1). The Γ_1 state becomes an $a_1(\Gamma_1)$ singlet. We obtain at zero pressure the $a_1(L_{1c})$–$t_2(L_1)$ splitting in GaNAs with 3% of N to be about 0.07 eV, and the $a_1(X_1)$–$e_2(X_1)$ splitting of the second CB at X to be 0.05 eV. In this reciprocal-space picture, the impurity-induced coupling of states from various points of the BZ is monitored by projecting the states of the alloy onto the states of pure GaAs. We find that the bottom of the CB, $a_1(\Gamma_{1c})$, contains a strong admixture (31%) of the L_{1c} states. The contribution of X_{1c} is an order of magnitude smaller (about 2%), indicating a weak Γ_{1c}–X_{1c} interaction in the alloy at zero pressure.

4.3 Features of the GaN_xAs_{1-x} Band Structures

The energy band structures of GaN_xAs_{1-x} were calculated for four N concentrations, $x = 0.009$, 0.016, 0.031, and 0.062, and for a few values of the hydrostatic pressure (from 0 to 3.2 GPa). The first observation resulting from the analysis of band structure is that a small amount of nitrogen strongly modifies conduction states, whereas the valence bands are only slightly affected. To analyze the changes in the CBs caused by the alloying of GaAs with GaN, recalling the limitations of using a supercell representation of the alloy (see Sect. 4.2.2), we compare the results for pure GaAs and GaN_xAs_{1-x}. In Fig. 4.1 we present the CB structure of both pure GaAs (dotted lines) and GaN_xAs_{1-x} with $x = 0.031$ (solid lines) calculated using the 64-atom supercell.

The following main features can be observed:

1. The bandgap decreasing by 0.50 eV with respect to that of pure GaAs. This finding is in a very good agreement with the experimental results,

which show that the bandgap reduction is ~0.16 eV per 1% of nitrogen content [16].

2. Splitting of host states induced by the impurity potential. Splitting of the L conduction edge: In GaN_xAs_{1-x} the fourfold degenerate lowest L conduction level, according to the symmetry rules, is split into a singlet and a triplet. The singlet, $a_1(L_{1c})$, is lying below, and the triplet, $t_2(L_{1c})$, slightly above the unperturbed host state. The calculated value of the splitting is ~0.07 eV for $x = 0.031$. Taking into account its character, energy position, pressure, and composition dependence (to be discussed in the following sections) we can identify the L_{1c} derived singlet state with the experimentally observed E_+ state, and from now it will be denoted E_+. The bottom of the CB will be called consequently E_-.
3. A band repulsion resulting from hybridization of bands of the same symmetry ($a_1(\Gamma_{1c})$ and $a_1(X_{1c})$, $a_1(L_{1c})$). Along the [111] direction, a strong interaction between the two lowest CBs of a_1 symmetry is visible: the crossing of the folded-in host GaAs bands is replaced by Γ–L and L–X anticrossings in the band structure of the GaN_xAs_{1-x} alloy. In particular, it causes a change of the shape of the lowest CB and enhances the nonparabolicity of this band.

4.3.1 Effects of Lattice Relaxation

Before going into details of the band structure properties we analyze the impact of atomic relaxation on the electronic structure. The results for the GaN_xAs_{1-x} with $x = 0.031$ are summarized in Table 4.2.

Table 4.2. Effects of atomic displacements around N in GaAs: ΔE_g^r is the total (i.e., calculated for the relaxed lattice) change of the bandgap induced by nitrogen inclusion, ΔE_g^{nr} is the bandgap change calculated without relaxations of the bond length Δl between the impurity and its neighbors

ΔE_g^r (eV)	−0.50
ΔE_g^{nr} (eV)	−0.26
Δl (%)	14
Q^{nr} (%)	9
Q^r (%)	12
$\alpha^{nr}(L_{1c})$ (%)	38
$\alpha^r(L_{1c})$ (%)	31

Q is the probability amplitude obtained by projection of the $a_1(\Gamma_{1c})$ state onto the s(N) orbital states before (nr) and after (r) the lattice relaxation. Similarly, α is the projection onto the L_{1c} host states of the $a_1(\Gamma_{1c})$ [64]

According to the calculations, the presence of 3% of N reduces the gap by about 0.50 eV. Half of this reduction involves effects of structural relaxations. More specifically, atomic displacements around the impurity consist in a fully symmetric decrease of the bond lengths between N and its nearest Ga neighbors Δl by 14%. Their impact on the electronic structure is quite big: the relaxation reduces the gap by 0.24 eV. In order to analyze the origin of the relaxation-induced effects, we have projected wavefunctions from the bottom of the CB onto atomic orbitals [64]. The analysis of the conduction states shows that the electron transfer induced by the lattice relaxation is large. In ideal GaAs the bottom of the CB is composed of 49% of s(Ga) and 51% of s(As) [64]. Consequently, in a 64-atom unit cell, the contribution of s(Ga) of one Ga atom to the bottom of the CB is 1.5%. In the case of GaAs:N the relaxation increases the contribution of s(N) from 9 to 12%. The contribution of N is thus almost an order of magnitude larger than that of Ga atoms. As is shown later (Fig. 4.5a), the electron wavefunction is localized on N, and the localization increases with the inward displacement of Ga neighbors. The electron transfer is one of the sources of the calculated changes of bandgap. In fact, since the energy of s(N) is lower than that of s(Ga), the increasing contribution of s(N) to the bottom of the CB decreases its energy, and reduces the bandgap. Furthermore, the analysis reveals that the only conduction state with an appreciable localization on the nitrogen atom is the bottom of the CB. In particular, there is no resonance localized on N up to about 1 eV above the CB (see also Sect. 4.3.5).

4.3.2 Composition Dependence of the Bandgap

The main features of the GaN_xAs_{1-x} band structure as a function of composition and pressure are summarized in Table 4.3.

Table 4.3. Calculated parameters of $GaAs_{1-x}N_x$ band structures as functions of composition, x

x (%)	$-\Delta E_g$ (eV)	$E_+ - E_-$ (eV)	dE_g/dp (meV/GPa)	m^* (m_0)	dm^*/dp (TPa^{-1})
0	–	0.30	107	0.082	5.6
0.9	0.20	0.46	71	0.126	36
1.6	0.27	0.53	63	0.120	28
3.1	0.3–0.5	0.6–0.8	54–60	0.10–0.12	11–12
6.2	0.5–0.9	0.8–1.2	49–57	0.09–0.12	10–12

For $x = 0.031$ and 0.062 ranges of the parameters are given. They indicate uncertainties due to variations in the N-atom arrangement in the host. The free-electron mass is called m_0. E_+ for pure GaAs is the bulk L_{1c} state

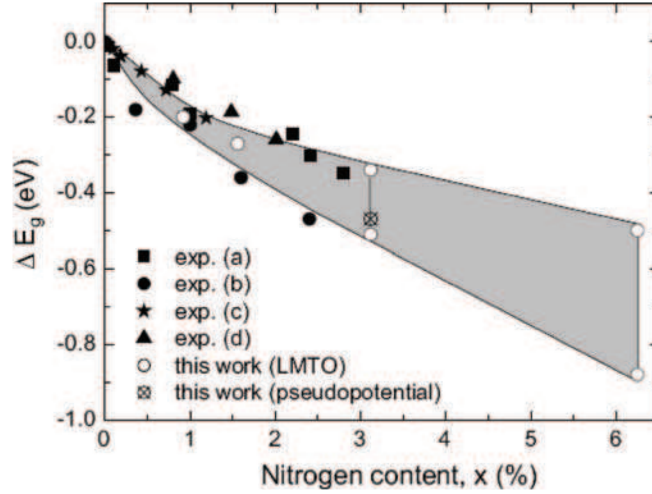

Fig. 4.2. The calculated (present: *open circles* and *shaded range*) change of the bandgap of GaN_xAs_{1-x} as a function of the nitrogen concentration (x) in comparison with experimental results from: (**a**) [14], (**b**) [21], (**c**) [28], and (**d**) [65]. The lines forming the borders of the *shaded region* illustrate the estimated range of the calculated values if random substitution of As by N had been taken into account

The changes in the bandgap of the GaN_xAs_{1-x} with respect to pure GaAs are listed in the second column of Table 4.3 and shown in Fig. 4.2 together with the experimental data [14, 21, 28, 65].

The calculated reductions of the bandgap agree well with those measured up to 3% of N. On the other hand, a comparison with experiment should be performed with caution because in the supercell method the N atoms form a superlattice, and their potential is coherent, while in a real alloy both their locations and the alloy potential are random. The long-range order reduces the bandgap of alloys [66, 67], i.e., overestimates the bowing, and in our case the nonlinear pressure dependence of the bandgap. The results discussed above demonstrate a strong bowing of the GaN_xAs_{1-x} bandgap, since the linear interpolation between GaAs and GaN predicts an increase of E_- by 0.06 eV for $x = 0.031$.

We have also investigated the bowing of the bandgaps at wavevectors other than the Γ point. Interestingly, we find that the bowing strongly depends on the k-vector. In particular, contrary to the fundamental bandgap, both the E_1 and E_2 gaps that give rise to strong optical transitions in the vicinity of the L and X points, respectively, are only slightly changed by the presence of N. From Fig. 4.1 we can see, that final states are changed no more than 0.03 eV for the N composition, $x = 0.031$. Assuming that presence of N does not influence the valence band, this result is in agreement with the recent optical measurements reported in [19, 21]. The nonsensitivity of the minima

at L and X to the chemical perturbation reflects the very small contributions of the impurity orbitals to these states.

Finally, we comment on the effects of changes in the geometry of the arrangement of N impurities. To estimate the influence of this factor, additional calculations for $x = 0.062$ and 0.031 were made by substituting two As atoms by N in a 64- and a 128-atom cell, respectively. The shaded area in Fig. 4.2 illustrates the estimated uncertainty in the calculations due to variations in the arrangement of the nitrogen atoms. Bentoumi et al. [28] performed optical near-gap absorption measurements as well as ab initio calculations using both plane-wave pseudopotentials and the full-potential linear augmented plane wave (LAPW) method. They compared the bandgaps calculated in fcc-like and sc-like (face-centered cubic and simple cubic) arrangements of the N-atoms, and they also found a significant geometry dependence. The effect of N clustering was examined in [68] by considering a linear array of four N atoms directed along the [100] and [110] directions, respectively. For a nitrogen concentration of 1.6% the latter work cites the range of $-\Delta E_{\mathrm{g}}$ to be 0.19–0.40 eV, [28] gives: 0.30–0.41 eV, and we get (see Fig. 4.2): 0.2–0.3 eV. Taking all three calculations into account, it appears that our shaded areas are somewhat too narrow, and that the uncertainty of the supercell method in predicting the alloy gap is even larger than our shaded areas indicate. The large theoretical spread of the bandgap values caused by spatial distribution of nitrogen implies that the optical absorption threshold of GaNAs is strongly smeared out compared to that of pure GaAs, and that one should expect a large redshift of the fundamental emission.

4.3.3 Optical Transitions to E_- and E_+

The coupling of the CB-minimum $\Gamma_{1\mathrm{c}}$ with the secondary minima at L and X strongly influences the optical properties of the alloy, which will now be discussed. Optical investigations of GaNAs have shown that at energies higher than the fundamental bandgap there is an additional transition denoted E_+ [14, 65]. The pressure dependences of the two dominant optical transitions to E_- (conventionally called the E_0 transition in the pure material) and E_+, calculated by the pseudopotential method, are shown in Fig. 4.3.

To understand the character of the E_+ transition in the supercell geometry, we have analyzed the optical transition rate, which is proportional to the square of the interband momentum matrix element, $|P_{\mathrm{vc}}|^2$. The normalized matrix elements as a function of pressure are given in Fig. 4.3; the value of $|P_{\mathrm{vc}}|^2$ for the E_0 transition at zero pressure is taken as 100.

The calculations reproduce two main experimental findings [14, 65]. First, we identify two dominant transitions, E_- and E_+. Their intensities are at least five times bigger than those of other transitions, not shown in the figure. Second, the relative intensity of E_+ compared to E_- increases with pressure, in agreement with the observation by Perkins et al. [14]. Both effects stem from the N-induced modifications of the conduction states. In particular, optical

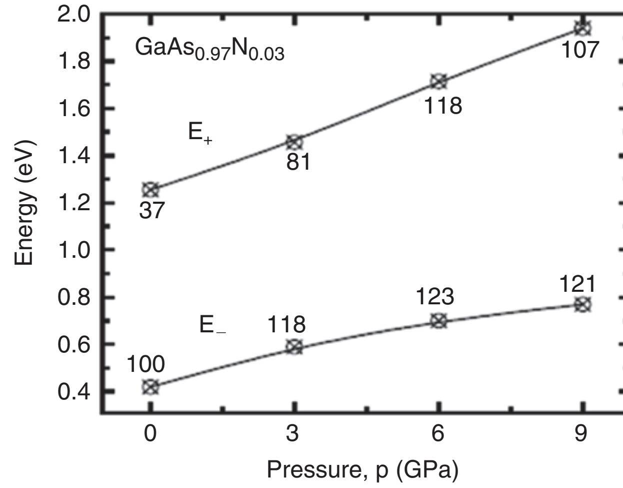

Fig. 4.3. The calculated pressure dependence of two dominant optical transitions in GaNAs. The numbers give the normalized square of the interband matrix elements. The lines are only guides for the eye. Pseudopotential calculations, no gap adjustment, i.e., straight LDA

transitions from the top of the valance band to $a_1(\mathrm{L}_{1c})$ and $a_1(\mathrm{X}_{1c})$, which are forbidden in pure GaAs, become allowed. At zero pressure, the E_+ feature is due to the transition to $a_1(\mathrm{L}_{1c})$, while the transition to $a_1(\mathrm{X}_{1c})$ is a few times weaker.

The energy difference between E_- and E_+ strongly depends on the composition. Our calculated values of the energy separation between $a_1(\mathrm{L}_{1c})$ identified with E_+ and $a_1(\mathrm{L}_{1c}) = E_-$ levels are given in the third column of Table 4.3, and a comparison of our results with other calculations and experimental data, [8, 14, 15, 18, 19, 26, 65] is presented in Fig. 4.4.

The agreement between various experimental and theoretical data is satisfactory. Extrapolation of E_+–E_- to the dilute limit yields the value 0.30 eV, which is close to the separation between the Γ and L CB minima in pure GaAs (see Table 4.3 and Fig. 4.4). The E_+-E_- separation increases almost linearly with x in the considered concentration range. The observed increase of the separation between the E_+ and E_- states with nitrogen concentration is caused mainly by the large bandgap reduction, since an upshift of E_+ is less pronounced.

The excellent agreement between experimental and theoretical values supports the identification of $a_1(\mathrm{L}_{1c})$ as the level involved in the E_+ feature. Again, the supercell results are estimated to have error bars due to ambiguity in the locations of the N atoms. Also this scatter is sizable at high concentrations. Different characters of the states involved in the N-induced coupling, i.e., $a_1(\mathrm{N})$, $a_1(\Gamma_{1c})$, $a_1(\mathrm{L}_{1c})$, and $a_1(\mathrm{X}_{1c})$, and their relations to E_- and E_+ states were first discussed by Mattila et al. [8] on the basis of

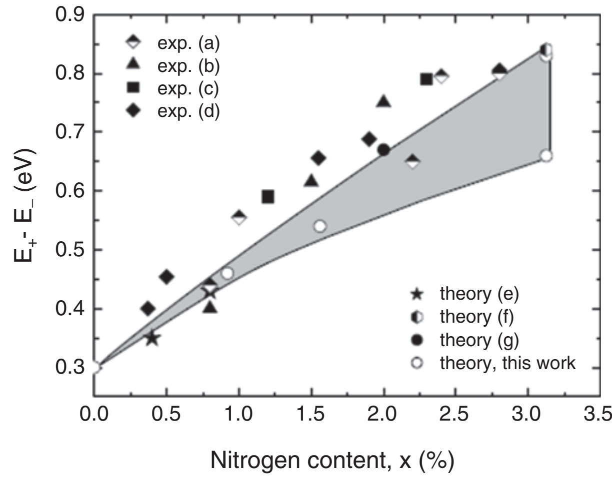

Fig. 4.4. The calculated (FP-LMTO with gap adjusting potentials: *open circles* and *shaded range*) change of separation between the E_+ and E_- levels in GaN_xAs_{1-x} as a function the nitrogen concentration (x) in comparison with experimental results and other calculations. Experiments: (**a**) [13], (**b**) [19], (**c**) [14], (**d**) [15]. Other theory: (**e**) [18], (**f**) [8], and (**g**) [26]

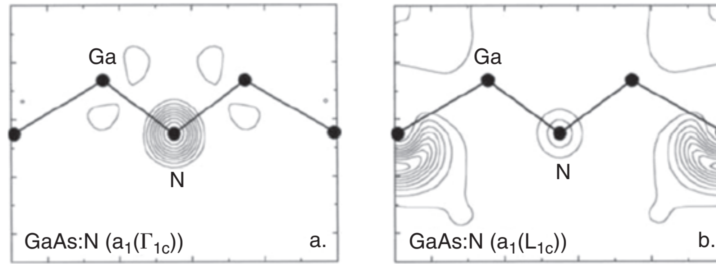

Fig. 4.5. Wavefunctions density (**a**) of the bottom of the conduction band, and (**b**) of the second band $a_1(\mathrm{L}_{1c})$ in GaAsN

pseudopotential-supercell calculations. Subsequently their conclusions were supported by our pseudopotential and FP-LMTO calculations [26, 29].

In Fig. 4.5a, b we show the wavefunctions of the two CB states that are involved in the E_- and E_+ transitions, respectively, for GaNAs containing 3% of nitrogen. The first one is the state at the bottom of the CB. This state is an antibonding combination of cation and anion s orbitals, like the Γ_{1c} state of pure GaAs, but its localization on N atoms is pronounced, see the discussion in Sect. 4.3.1. The wavefunction of the second conduction state in GaNAs, $a_1(\mathrm{L}_{1c})$, is shown in Fig. 4.5b. We see that this state, which is induced by the presence of N, is clearly not localized on N, but rather on its third neighbors.

4.3.4 Effects of Hydrostatic Pressure

The presence of N atoms not only affects band energies, but also induces coupling of states from various points of the Brillouin Zone. As a result of the coupling, the pressure coefficients of alloy bands are drastically reduced compared to those of pure GaAs [29,31], and the effect is composition dependent. We analyze the E_- $(= E_g)$ and E_+ behavior, applying hydrostatic pressure and varying the nitrogen concentration. Different characters of the bands should be reflected in their behavior under pressure. The pressure dependence of the bandgap (E_-) and the E_+ level for $x = 0.031$ calculated by the pseudopotential method is shown in Fig. 4.3. The pressure dependencies of these levels for $x = 0.009$ obtained by the FP-LMTO method with bandgaps corrected by adjusting potentials, are presented in Fig. 4.6.

Generally, as we can see from the figures, the dependence of the energy gap in GaN_xAs_{1-x} on hydrostatic pressure is nonlinear (the pressure coefficient of the bandgap decreases at higher pressures) and weaker than in GaAs. The corresponding values of the deformation potential for GaAs ($\mathrm{d}E_g/\mathrm{d}\ln V = -8.5\,\mathrm{eV}$) and for GaNAs with 3% of N ($\mathrm{d}E_g/\mathrm{d}\ln V = -4.6\,\mathrm{eV}$) differ almost by a factor of two, confirming the results of two other theoretical works [5,8].

With increasing pressure, the oscillator strength of E_+ increases (see Fig. 4.3), since the corresponding state becomes progressively more Γ_{1c}-like. The nonmonotonic dependence of the oscillator strength of E_+ is due to the fact that we have added contributions of transitions with energies differing by

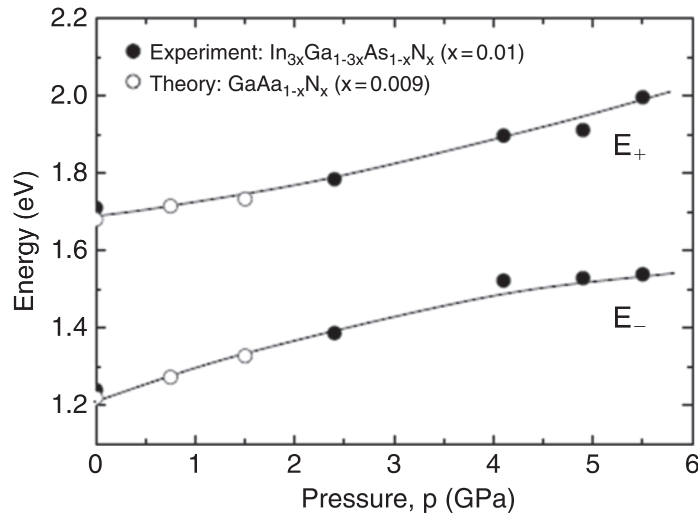

Fig. 4.6. The calculated (FP-LMTO with gap adjusting potentials: *open circles*) E_- and E_+ levels as functions of applied pressure. The *filled circles* are experimental results from [70]. The lines represent least-squares fits to the experimental data. See also the very detailed set of experimental values vs. pressure in Fig. 4 of [13]

less than 0.1 eV. Namely, the value of $|P_{\rm vc}|^2$ increases from 100 at zero pressure to 120 at 9 GPa. An analogous symmetry-induced effect has been investigated by Morgan [69] for the indirect bandgap in GaP. He has pointed out that zero-phonon interband optical transitions become allowed in the presence of impurities, but they are much stronger for the anion-substituting (as it is in our case) than for the cation-substituting donors because of the different symmetry of the conduction states at the X point.

Theoretical results for $\rm GaN_xAs_{1-x}$ with $x = 0.009$ are compared in Fig. 4.6 with the experimental pressure dependence of both the E_- and E_+ transitions [70] for $\rm GaInN_xAs_{1-x}$ for $x = 0.01$. We observe good agreement, although the calculations were performed only for low pressures. According to experiment, the pressure dependence of the bandgap is sublinear with a tendency to saturate at high pressures. The second conduction state $a_1(\rm L_{1c})$, which is the final state of the E_+ transition, exhibits a nonlinear pressure dependence as well. The influence of hydrostatic pressure on the E_+ band edge is weaker near $p = 0$ and the experimental data behave superlinearly. This different character of the pressure dependence of E_- and E_+ states is clearly seen in Fig. 4.3, where the calculated results are presented for a larger range of pressure (up to 9 GPa).

The nonlinear behavior of E_- and E_+ states with pressure can be explained as follows. From the analysis (see Sect. 4.3.3) of the wavefunction for the Γ-, L- and X-derived states in $\rm GaN_xAs_{1-x}$ with N concentration about 3% we obtain that the bottom of the CB $a1(\Gamma_{\rm 1c})$ contains a strong admixture of the $a_1(\rm L_{1c})$ state of pure GaAs. The contribution of $\rm X_{1c}$ is an order of magnitude smaller, indicating a weak $\Gamma_{\rm 1c}$–$\rm X_{1c}$ interaction in the alloys at zero pressure. With increasing pressure, the relative energies of the GaAs host conduction states change, which also changes the interaction between them. Consequently, at low pressures the nonlinear pressure behavior of the bandgap is due to the increasing coupling between the bottom of the conduction band $a_1(\Gamma_{\rm 1c})$ and the $a_1(\rm L_{1c})$ state. For higher pressures, the effect stems from the increasing coupling between $a_1(\Gamma_{\rm 1c})$ with the singlet $a_1(\rm X_{1c})$, which adds to the nonlinearity of the pressure dependence of the bandgap. A comparison of Figs. 4.3 and 4.6 shows that the discussed effects are composition dependent.

A more detailed study of the pressure effects can be performed by analyzing the calculated values of the pressure derivatives of the E_- for different nitrogen compositions quoted in Table 4.3. The pressure derivatives of the E_- and E_+ states as functions of the composition are illustrated in Figs. 4.7 and 4.8, respectively.

As one can see from Fig. 4.7 and Table 4.3, the pressure derivative of the $\rm GaN_xAs_{1-x}$ bandgap ($E_{\rm g} = E_-$) decreases with x; the pressure coefficients being in the range from about 70 meV GPa^{-1} for $x = 0.009$ to about 50 meV GPa^{-1} for $x = 0.062$. On the other hand (see Fig. 4.8) the pressure derivative of the E_+ level increases with pressure. The above effects result from the increase in $\Gamma_{\rm 1c}$–L mixing with increasing nitrogen admixture, and simply reflect the difference in deformation potentials of the lowest conduction states

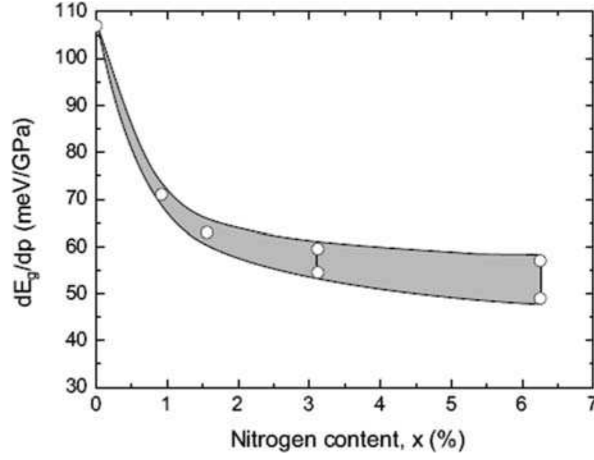

Fig. 4.7. The calculated (*open circles* and *shaded range*) pressure coefficient of the minimum gap, $E_g(= E_-)$, as a function of the nitrogen concentration (x)

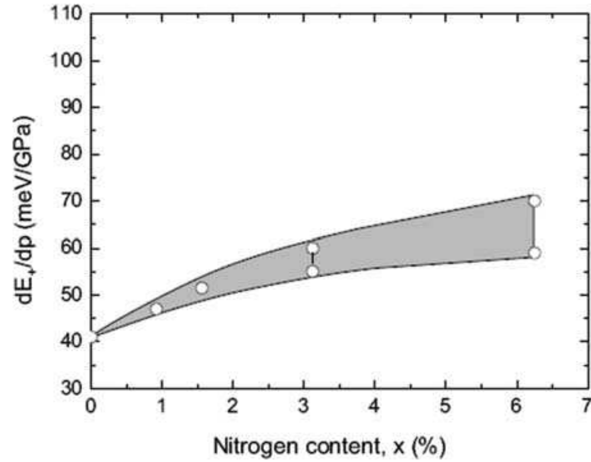

Fig. 4.8. The calculated (*open circles* and *shaded range*) pressure coefficient of the E_+ level at the zone center (supercell representation) as a function of the nitrogen concentration (x)

at Γ and L in GaAs. The pressure coefficient of the GaAs bandgap at the L point, $\sim$40 meV GPa^{-1}, is considerably smaller than that at the Γ-point, $\sim$110 meV GPa^{-1}. Therefore, increasing admixture of the L_{1c} into the E_- state lowers its pressure coefficient, and, analogically, increasing admixture of the Γ-conduction character into the E_+ state increases its pressure coefficient.

The next observation is that the L splitting is reduced with pressure (with a rate $\sim -20\,\mathrm{meV\,GPa^{-1}}$), while the X splitting is slightly increased with pressure, (at a rate $\sim 5\,\mathrm{meV\,GPa^{-1}}$), for N concentrations about 3%. The pressure coefficients of the new low-energy states, $a_1(\mathrm{L_{1c}})$ and $a_1(\mathrm{X_{1c}})$ are different from the split-off triplet $t_2(\mathrm{L_{1c}})$ and doublet $e(\mathrm{X_{1c}})$ states. The pressure behavior of the $a_1(\mathrm{X_{1c}})$ state is similar to that of the X state in pure GaAs.

4.3.5 Discussion of the Origin of the E_+ Edge

The so-called band anticrossing (BAC) model proposed by Shan et al. (see Chap. 3) has provided a simple model band structure of $\mathrm{GaN}_x\mathrm{As}_{1-x}$ which describes well several experimental data in terms of a few adjustable parameters. In the BAC model, the nitrogen impurity state $a_1(\mathrm{N})$, located 0.15–0.18 eV above the CB minimum [5, 6], and the CB minimum interact. As a result, two states, E_- and E_+ are formed. However, in spite of its apparent successes, the BAC model is based on assumptions which cannot be supported by a more stringent theory. Early model calculations [71] show that the impurity state $a_1(\mathrm{N})$ is an antibonding combination of $s(\mathrm{N})$ with sp^3 orbitals of the nearest neighbors, and it is localized mainly on the neighbors. Extensive calculations [8] confirm this picture and find $a_1(\mathrm{N})$ at 0.18 eV above the CB bottom. But with increasing x (into the alloy regime) its energy rises so rapidly that Mattila et al. [8] conclude that "$a_1(\mathrm{N})$ is too far to act as a principal source of the low-energy anticrossing observed by Shan et al." The more recent large-cell calculations by Wang [72] show that the energy of $a_1(\mathrm{N})$ is essentially independent on x in the impurity regime ($x \leq 0.4\%$). If we assume that "$a_1(4)$" or maybe "$a_1(3)$" in Fig. 4.4 of [72] should be assigned to $a_1(\mathrm{N})$, then Wang's results agree extremely well with those of [8]. Further, both calculations then also agree with our calculated $a_1(\mathrm{N})$ levels for $x = 1.6$ and 3.1%. This is illustrated in Fig. 4.9.

Consequently, it has again been demonstrated that $a_1(\mathrm{N})$ in the alloy regime is too high in energy to be responsible for the formation of the E_+ edge through the BAC mechanism. Rather it results from an N-induced perturbation of host states around the secondary minimum at L [8, 15]. This state, $a_1(\mathrm{L_{1c}})$, is induced by the presence of N, but it is not localized on N (see Fig. 4.5b), and it is not the $a_1(\mathrm{N})$ resonance. Based on the facts that (1) the calculated momentum matrix elements reflect the experimental features of E_+, (2) the theoretical composition-dependent energy separation between $a_1(\mathrm{L_{1c}})$ and $a_1(\Gamma_{1c})$ agrees well with the experimental difference between E_+ and E_-, see Fig. 4.4, and (3) the pressure dependences of $a_1(\mathrm{L_{1c}})$ (theoretical) and E_+ (experimental) are very similar (see Fig. 4.6), we support the interpretation [8] that $a_1(\mathrm{L_{1c}})$ gives rise to the E_+ transition. The L-related character of E_+ is also suggested by recent experiments [17].

In summary of this section, we have studied the influence of nitrogen on the energy band structure of $\mathrm{GaN}_x\mathrm{As}_{1-x}$. We have shown the strong modification of the CBs. The Γ, L, and X conduction states mix, forming new, low-energy

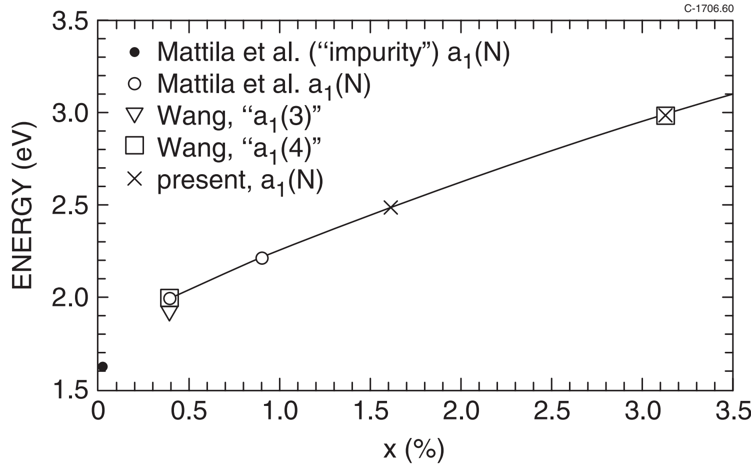

Fig. 4.9. Calculated energies (relative to the valence band maximum) of states which are $a_1(N)$ as obtained by Mattila et al. [8] and us (*crosses*). Further, the levels called $a_1(3)$ and $a_1(4)$ as given by Wang [72] in his Fig. 4 are marked

states. We found an additional optical transition involving an L_{1c}-derived state and we support its identification with the E_+ transition.

4.4 Conduction Band Mass vs. Composition, Pressure, and Wavevector

As mentioned in the previous section, the calculations for GaN_xAs_{1-x} with $x = 0.031$ exhibited (see Fig. 4.1) a strong nonparabolicity of the lowest CB caused by Γ–L mixing. Figure 4.10 further shows the calculated dispersion of the lowest CB for $x = 1.6$ and 0.9% together with the results for pure GaAs and with experimental [21] data.

The comparison between theory and experiment was realized by applying the following procedure. The experiment has been performed using a $Ga_{1-y}In_yN_xAs_{1-x}$ sample with $y = 0.03$ and $x = 0.01$, whereas we performed calculations for $y = 0$ and $x = 0.009$ and 0.016. However, the calculation have been made for lattice constants corresponding to inclusion of indium with $y = 0.03$. Therefore, the two theoretical curves in Fig. 4.10 are labeled $Ga_{0.97}In_{0.03}N_{0.009}As_{0.0991}$ and $Ga_{0.97}In_{0.03}N_{0.016}As_{0.0984}$, respectively. These two curves are rigidly shifted in energy in such a way that the experimental CB minimum is located between the two "theoretical" bandgaps as given by a linear interpolation between the values for $x = 0.009$ and 0.016. Both the experiment and the calculations show that the lowest CB of the alloy is more flat than that of pure GaAs, i.e., electrons in the alloy have a larger effective mass. At first sight this might seem surprising since in conventional semiconductors the electron effective mass is proportional to the bandgap. This follows

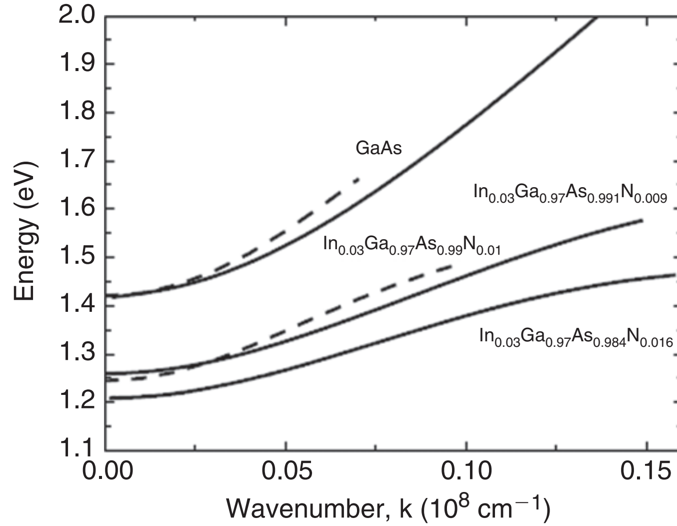

Fig. 4.10. The calculated (*full lines*) lowest conduction bands (along [100] for GaAs and $Ga_{1-y}In_yN_xAs_{1-x}$ for two different nitrogen concentrations in comparison with experiments (*dashed lines*) from [21]. The approximate ways of taking the nonzero indium concentration into account in the theoretical curves and to adjust them on the energy scale are described in the text

in particular from $\boldsymbol{k}\cdot\boldsymbol{p}$ theory, see [73]. In GaInNAs, the coupling between the N-induced levels and the bottom of the CB modifies the electron mass.

The calculated values of electron effective masses for different concentrations of nitrogen are summarized in column 5 of Table 4.3, and in Fig. 4.11 our results are compared with the results of other calculations [25, 74] and masses obtained from the BAC model fitted to experimental photoluminescence [70] (PL) and photoreflectance [75] (PR) data obtained for quantum well structures. The model which was used is an extension [76] of the version used for bulk materials (see also [77] for a refinement of this scheme and application to the regime of very low nitrogen concentrations). Further, the figure contains the results of experiments from [78–82].

All calculations and experiments agree in finding that the effective masses of the CB minimum in the alloys are considerably larger than the value $m^* = 0.067m_0$ of pure GaAs. We have no calculations for $x < 0.009$. An extrapolation of our results down to $x \approx 0.001$ agrees well with the masses derived from the experiments by Masia et al. [79] ((b) in Fig. 4.11), but the relevance of our type of calculations in the range of N concentrations toward the very dilute region is questionable, for example due to the influence of cluster formation and localized states [83, 84].

Even within a simple alloy model, like the one assumed in this work, it is not clear whether the transition to $x = 0$, pure GaAs, is accompanied by

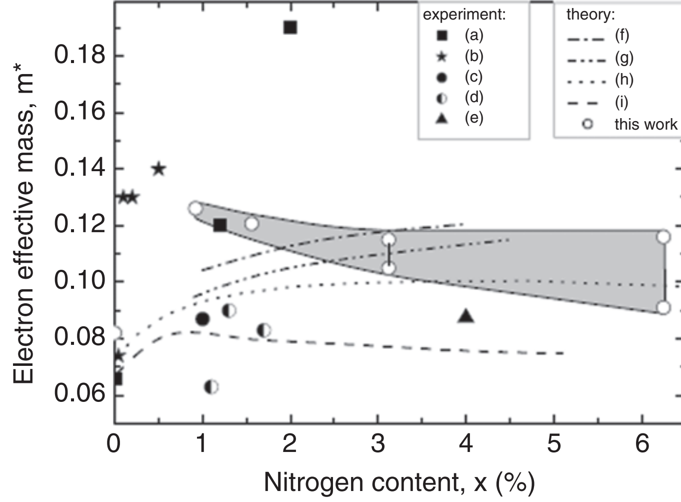

Fig. 4.11. The calculated (*open circles* and *shaded* "error area"; FP-LMTO with gap adjusting potentials) effective conduction band mass (in units of the free-electron mass) for GaN_xAs_{1-x} vs. nitrogen content. Also, experimental data and the results of other theoretical calculations are included in the figure: Experiments: (**a**) [78], (**b**) [79], (**c**) [80], (**d**) 81, (**e**) [82]. Other theory: (**f**) [70] (BAC model fitted to PL data), (**g**) [70] (BAC model fitted to quantum well energies measured in [75]) (**h**) [25] ($\boldsymbol{k} \cdot \boldsymbol{p}$ theory), and (**i**) [74] (tight-binding calculation)

a continuous variation of $m^*(x)$ or there would be an abrupt drop to $m^* = 0.067m_0$. In that context the experimental point $(x,\ m^*) = (0.00043, 0.074m_0)$ (lowest lying asterisk in Fig. 4.11) obtained in [79] is interesting. It is noted that the magneto-PL experiments of [79] yield one of few direct measurements of the CB-minimum masses in GaN_xAs_{1-x}. For a sample with $x = 0$ the value $0.065m_0$ was found, i.e., very close to the well-established GaAs CB-minimum mass.

For x larger than 0.009 our calculated masses decrease with x, and a similar trend is found in the tight-binding calculations by Shtinkov et al. [74] ((i) in Fig. 4.11). The values of the masses obtained in their scheme, however, are considerably lower than those of the other calculations and also smaller than the various experimental results. In the same concentration regime the $\boldsymbol{k} \cdot \boldsymbol{p}$ theory of [25] predicts the CB-minimum mass to increase quite slowly with x, maybe reaching a wide maximum around $x = 0.04$.

However, in the simple $\boldsymbol{k} \cdot \boldsymbol{p}$ scheme the sign of $\mathrm{d}m^*(x)/\mathrm{d}x$ depends on the ratio between the x-dependent coupling matrix element P and the x-dependent gaps. Thus a small adjustment of the $P^2(x)$ function can reproduce our calculated trend. The masses derived in [70] by fitting the $\boldsymbol{k} \cdot \boldsymbol{p}$ model to PL and PR data increase with nitrogen concentration. The masses presented in the paper by Zhang et al. [75] decrease with x, but the values

are too large (see discussion in [70]). The two alloy data points from [78] ((a) in Fig. 4.11) probably are insufficient to demonstrate a clear trend. The result at $x = 0.02$ is surprisingly large, but details in sample preparation may affect the properties of the materials substantially. The value obtained for x near 0.01 agrees well with our calculations. The work by Wang et al. [81] cites three experimental masses ((d) in Fig. 4.11), but a clear trend cannot be deduced. The single data point (c) in Fig. 4.11 was obtained [80] from Faraday rotation experiments, which however only yields information about the reduced effective mass of the electron and the hole. Therefore, the electron mass can only be determined if the mass of the relevant hole in the $Ga_{1-y}In_yN_xAs_{1-x}$ sample [80] is accurately known. The inclusion of In changed [80] slightly the bands at the valence band maximum so that it was the light hole which is relevant, and the value $m_h = 0.082$ of GaAs was used in the analysis. Thus, the experimental data do not clearly indicate whether the CB mass decreases or increases with x for N concentrations above 0.01. It is indeed difficult to measure the effective masses in this material, and the authors of [80] describe the situation in this way: "*A systematic study of the effective mass at the bottom of the E-band in GaInNAs is still missing.*"

The strong nonparabolicity of the lowest CB is reflected in the wavevector dependence of the electron effective mass. In order to quantify this we calculated the k-dependent effective mass, $m^*(k)$:

$$m^*(k) = \hbar^2 k (\mathrm{d}E/\mathrm{d}k)^{-1}, \qquad (4.2)$$

which in fact is the "optical mass" (or "slope effective mass"), which may differ from the band-curvature effective mass, m_c^*, (in scalar form):

$$m_c^*(k) = \hbar^2 (\mathrm{d}^2E/\mathrm{d}k^2)^{-1}. \qquad (4.3)$$

At the extremum ($k = 0$, here the CB minimum) these two masses are identical. The values of m^* presented below are "optical" effective masses (4.2) in order to be consistent with the work by Spitzer and Fan [85]. For the lowest CB of GaAs the two definitions yield similar values (see for example the compilation in Table 13 of [60]), but in GaN_xAs_{1-x} there are stronger nonparabolicity effects in the CB, and the two kinds of masses differ more. In Fig. 4.12 we compare the k-dependence of the electron effective masses as determined experimentally [21] (see also the note, [86], and [87]) for $Ga_{1-3x}In_{3x}N_xAs_{1-x}$ (for $x = 0.01$) and theoretically for GaN_xAs_{1-x} for $x = 0.009$, as well as for pure GaAs. The data referred to as "experimental" for GaAs ($x = 0$) are from Blakemore's review (Table 13 in [60]) and are based on experiments (see also [88, 89]) reported in [90–93].

The theoretical values of the effective mass are systematically higher than the experimental ones. For GaAs, the calculated mass is $m^* = 0.082m_0$, whereas the experimental value is $m^* = 0.067m_0$, and similar errors are probably in the calculations for the alloys. In order to illustrate the effects of nonparabolicity and to compare it to the experimental data, we show in

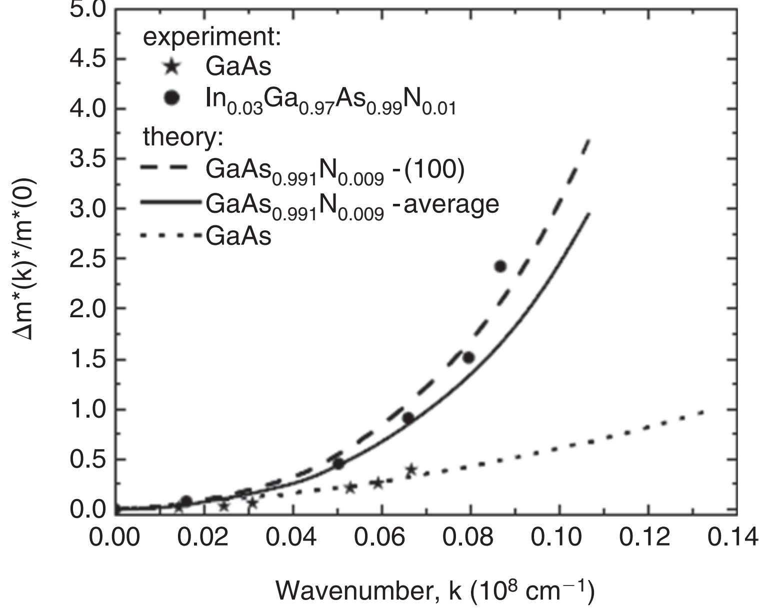

Fig. 4.12. The calculated (FP-LMTO with gap adjusting potentials) relative variation with k of the conduction band mass ("optical effective mass," (4.2)) in GaN_xAs_{1-x} for $x = 0.009$ for k-vectors along (100) (*long dashes*) and obtained as a weighted average (*full line*) over (100), (110), and (111) directions, in comparison with experiments (*filled circles*) from [21]. (See also the note, [86]). The calculated mass variation for GaAs was obtained along a (100) direction. For "experimental" data for pure GaAs (asterisk), see [60] and the main text

Fig. 4.12 the increase of the mass $\Delta m^*(k)$ relative to the CB-minimum mass m^* $(k = 0)$. It is clearly seen that the masses increase considerably faster with k in the alloy than in pure GaAs. The strong nonparobolicity of CB in the GaN_xAs_{1-x} also implies that $\Delta m^*(k)$ for nonzero k exhibits a significant anisotropy. This is illustrated in Fig. 4.12, where the curve shown with long dashes was obtained by restricting the wavevector to a (100) direction, whereas the full curve is a weighted average between (100), (110), and (111) directions. Although these two calculations differ, they both agree with the experiments.

The comparison between calculated masses and these extracted from experiments should be made with some caution. The experimental mass for a certain k, which is considered as a *Fermi radius* (k_F) of a degenerate gas of conduction electrons [21, 29, 70, 86], is obtained using the relation [94]:

$$m^*(k_F) = \frac{n_e(k_F)e^2}{\omega_p^2 \varepsilon_0 \varepsilon(\infty)}, \tag{4.4}$$

where e is the electron charge, ε_0 the vacuum permittivity, and $\varepsilon(\infty)$ is the high-frequency dielectric constant [95,96], introduced to describe the screening in the infrared reflectivity measurement of the plasma frequency, $\omega_{\rm p}$. The electron concentration, $n_{\rm e}(k_{\rm F})$, was determined by Hall effect measurements, and it also yields $k_{\rm F}$ through an isotropic band model:

$$n_{\rm e}(k_{\rm F}) = k_{\rm F}^3/3\pi^2. \tag{4.5}$$

As mentioned in [29], the samples used by Skierbiszewski et al. are highly doped so that the electron gas is degenerate and the Fermi level is well defined. (Note that this way of analyzing data for free carriers in heavily doped semiconductors is also used in cases, where the condition for existence of a Fermi surface is not satisfied; see for example [85, 96]). But a difficulty in applying the method still remains. The relation given in (4.4) between $m^*(k_{\rm F})$ and $n_{\rm e}(k_{\rm F})$ through the plasma frequency (defined by $\epsilon_1(\omega_{\rm p}) = 0$) is only obvious if m^* is k-independent. The reflectivity measurement detects a plasma edge, but the specific relation, (4.4), may be disputed. In view of these problems, it is surprising that the data deduced from the experiments are as close to the calculations as the figures show. Further, the expression derived in [85] for the susceptibility showed that the relevant effective mass is the optical one, (4.2). We have estimated the k-dependence of the "curvature mass" and find that both for GaN_xAs_{1-x} and pure GaAs it increases significantly faster with k than the optical mass, i.e., by far the best agreement between theory and experiment is indeed obtained with the calculations using (4.2).

Transport measurements of Skierbiszewski et al. [70] for GaN_xAs_{1-x} with $x = 0.014$ show that the electron mobility strongly decreases with hydrostatic pressure. This indicates that m^* increases with pressure. To verify this we performed band structure calculations for different values of pressure. The results for $x = 0.009$ and 0.016 in comparison with the pressure dependence of m^*, as deduced from the experiment [70, 97, 98], are presented in Fig. 4.13.

The pressure-induced changes in calculated and experimentally determined masses are very similar, and thus the pressure coefficients agree well: $\mathrm{d}(m^*/m_0)/\mathrm{d}p = 34\,\mathrm{TPa}^{-1}$ from the experiment for 1.4% nitrogen and 36 and $28\,\mathrm{TPa}^{-1}$ as obtained theoretically for $x = 0.009$ and 0.016, respectively. The calculated values of the pressure derivatives of the electron effective mass in GaN_xAs_{1-x} for different values of x are given in the last column of Table 4.3, and further illustrated in Fig. 4.14. A rapid decrease of $\mathrm{d}(m^*/m_0)/\mathrm{d}p$ with x in the range between 0.009 and 0.02 is followed by a "saturation" regime with almost no effects of varying the nitrogen concentration. Similarly, the pressure coefficients of the bandgaps for higher N concentrations are almost composition-independent (see Fig. 4.7). As for the CB-minimum mass itself we also find for its pressure coefficient, Fig. 4.14, that the GaAs value is much lower than the value for $x = 0.009$. Again, the regime for x between 0 and 0.009 was not explored by our calculations. The experimental data points (asterisks) in Fig. 4.14 correspond to the results of the same experiment [70] as presented in Fig. 4.13.

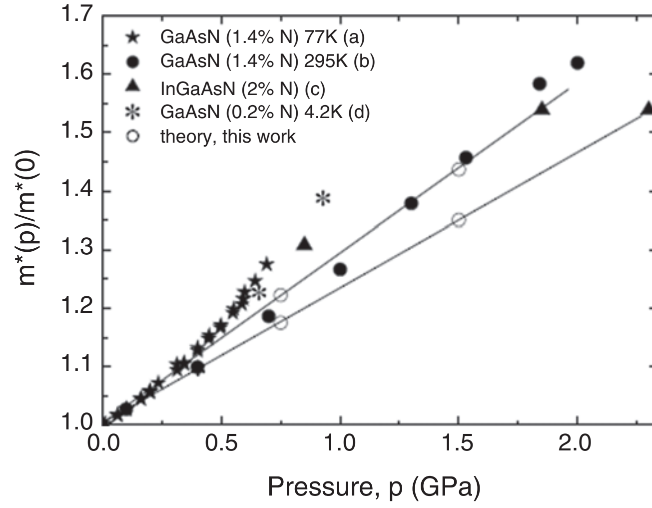

Fig. 4.13. The calculated pressure-induced mass enhancements (*open circles*: FP-LMTO with gap adjusting potentials) at the CBM in GaN_xAs_{1-x} for $x = 0.016$ (*lower open circles*) and 0.009 (*upper open circles*) as functions of pressure in comparison with experiments (**a**) for $x = 0.014$ at $T = 77\,K$ [97], (**b**) room temperature data from [70], (**c**) $x = 0.001$–0.002 at $T = 4.2\,K$

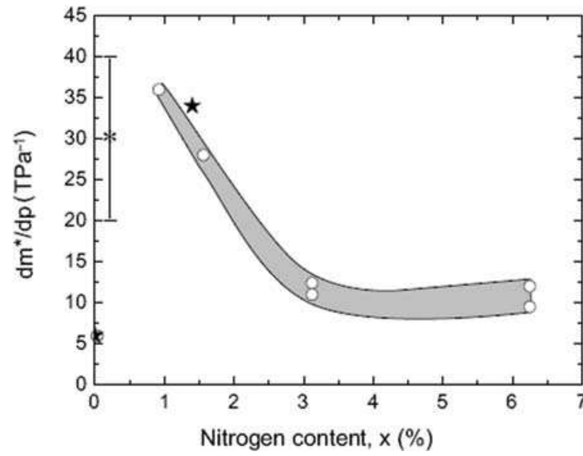

Fig. 4.14. The pressure coefficient of the effective conduction band mass (in units of m_0) of GaN_xAs_{1-x} *vs.* x (*open circles* and *shaded area*; FP-LMTO with bandgap adjusting potentials). The asterisks represent experimental values from [70], the star represents the experimental value from [24]

4.5 Summary

We have studied the electronic structure of GaNAs and its pressure dependence using two ab initio approaches, FP LMTO and plane waves with pseudopotientials. The agreement between the results of the two approaches is excellent. We have shown that alloying GaAs with small amounts of GaN strongly modifies the CBs. The Γ, L, and X conduction states of GaAs mix, forming new, low-energy states. The results obtained explain the strong reduction of the gap with the increasing N content, and demonstrate an important role played by the lattice relaxations. Energy gaps at other points of the BZ are much less affected by N. In particular, the calculations reproduce the characteristic feature observed in the experiment, i.e., the presence of the additional E_+ absorption edge.

The identification of the $a_1(\mathrm{L}_{1c})$ state as the E_+ state was proposed and then confirmed by analyzing the energy positions of the E_+ and E_- states and their pressure and composition dependencies. In particular, the calculated momentum matrix elements reflect the experimental features of E_+, and the theoretical composition-dependent energy separation between $a_1(\mathrm{L}_{1c})$ and $a_1(\Gamma_{1c})$ agrees well with the experimental difference between states E_- and E_+.

It is repeated that discussions about E_+ in a supercell band structure refer to transitions to a specific perturbed host level from cells where the L points fold into Γ -point of the superlattice BZ. In reality several levels in the relevant energy regime contribute to the "E_+" structure in the optical spectrum. The supercell geometry does not describe accurately the disordered alloy, as our error bars also show. But the basic picture given by the ab initio calculations is quite different from the BAC model. Further, our results agree with experimental data in [99], although we do not fully support the analysis of the theoretical data made in that work.

The different character of E_+ and E_- states is reflected in their behavior under pressure. Both states exhibit nonlinear pressure dependences, which have opposite characters (E_--sublinear, and E_+-superlinear). Also the composition dependencies of their pressure derivatives are strongly nonlinear in both cases, but have opposite signs ($\mathrm{d}E_-/\mathrm{d}p$ -decreases and $\mathrm{d}E_+/\mathrm{d}p$ -increases with composition). The above effects have been correctly interpreted based on the N-induced coupling between the states derived from Γ, L, and X points of the BZ, which increases with N-composition and pressure. The increase in $\Gamma_{1c} - \mathrm{L}$ mixing lowers the pressure coefficient of the E_- state, and makes the pressure coefficient of the E_+ level higher, reflecting the difference in the pressure coefficients of the lowest conduction states at Γ ($\sim$110 meV GPa^{-1}) and L ($\sim$40 meV GPa^{-1}) in pure GaAs. For higher pressures the increasing coupling between $a_1(\Gamma_{1c})$ and the singlet $a_1(\mathrm{X}_{1c})$ is observed, which increases the effect of nonlinearity in the pressure behavior of the E_+ and E_- states.

The lowest CB exhibits strong nonparabolicity, which is reflected in the dependence of the electron effective mass on k. The calculated variation of the

mass with k agrees well with experimental data, although some details of the method used to extract the masses from the reflectivity measurements may be disputed. It has been found that hydrostatic pressure strongly influences the electronic properties of GaN_xAs_{1-x}. In particular, it affects the electron effective masses and their dependence on nitrogen concentration. The dependence of the effective mass and its pressure coefficients on the concentration of nitrogen is strongly nonlinear. These effects are in the calculations caused by the anticrossing of folded-in CBs in the supercell band structures.

A conclusive comparison of the calculated x-dependence of the effective mass at the CB minimum to experiments has not been possible. The calculations agree with experiments in finding that for x above 0.01 the alloys have CB-minimum masses which are significantly larger than that of pure GaAs. The present calculations further suggest that the CB-minimum mass in the range considered should decrease with x. The difficulties in obtaining reliable experimental values of the masses lead to a large scatter in the published values, and therefore it cannot be concluded whether the suggested trend is correct.

Finally, considering the BAC model, we find that for the alloy compositions above 1% of N the a_1(N) is at too high energies to be responsible for the E_+ transition. In the impurity limit the N-induced resonance, a_1(N), is lying about 0.15–0.18 eV above the bottom of the CB. With increasing concentration of N the energy of a_1(N) rises steeply, and a new state, $a_1(L_{1c})$, emerges, induced by nitrogen, but not localized on N, and not to be identified with the a_1(N) resonance.

Acknowledgments. The work was partially supported by the project of Polish Ministry of Higher Education and Science (No. 1P03B 037 29) and the European Commission project "GaNano" STREP No. 505641-1. We also thank the Danish Centre for Scientific Computing (DCSC) for financial support.

References

1. J. Wu, W. Walukiewicz, K.M. Yu, W. Shan, J.W. Ager III, E.E. Haller, L.U Hai, W.W. Schaff, W.K. Metzger, S.R. Kurtz, Appl. Phys. Lett. **94**, 6477 (2003)
2. M.A. Wistley, S.R. Bank, H.B. Yuen, L.L. Goddard, J.S. Harris, J. Vac. Sci. Tech. B **22**, 1562 (2004)
3. P. Perlin, I. Gorczyca, T. Suski, P. Wisniewski, S. Lepkowski, N.E. Christensen, A. Svane, M. Hansen, S.P. DenBaars, B. Damilano, N. Grandjean, J. Massies, Phys. Rev. B **64**, 115319 (2001)
4. K.M. Yu, W. Walukiewicz, J. Wu, W. Shan, J.W. Beeman, M.A. Scarpula, O.D. Dubon, P. Becla, Phys. Rev. Lett. **91**, 246403 (2003)
5. D.J. Wolford, J.A. Bradley, K. Fry, J. Thompson, in *Physics of Semiconductors*, ed. by J.D. Chadi, J.D. Harrison (Springer, Berlin Heidelberg New York, 1984), p. 627

6. X. Liu, M.E. Pistol, L. Samuelson, S. Schwetlick, W. Seifert, Appl. Phys. Lett. **56**, 1451 (1990)
7. J. Leymarie, M. Leroux, G. Neu, Semicond. Sci. Technol. **4**, 235 (1988)
8. T. Mattila, S.H. Wei, A. Zunger, Phys. Rev. B **60**, 11245 (1999)
9. W.G. Bi, C.W. Tu, Appl. Phys. Lett. **70**, 1608 (1997)
10. U. Tisch, E. Finkman, J. Salzman, Appl. Phys. Lett. **81**, 463 (2002)
11. M. Weyers, M. Sato, Jpn. J. Appl. Phys. Part 2 **31**, L853 (1992)
12. M. Kondow, K. Uomi, K. Hosomi, T. Mozume, Jpn. J. Appl. Phys. Part 2 **33**, L1056 (1994)
13. W. Shan, W. Walukiewicz, J.W. Ager III, E.E. Haller, J.F. Geisz, D.J. Friedman, J.M. Olson, S.R. Kurtz, Phys. Rev. Lett. **82**, 1221 (1999)
14. S.R. Perkins, A. Mascarenhas, Y. Zhang, J.F. Geisz, J.F. Friedman, J.F. Olson, S.R. Kurtz, Phys. Rev. Lett. **82**, 3312 (1999)
15. E.D. Jones, N.A. Modine, A.A. Allerman, S.R. Kurtz, A.F. Wright, S.T. Tozer, X. Wei, Phys. Rev. B **60**, 4430 (1999)
16. C. Skierbiszewski, P. Perlin, P. Wisniewski, W. Knap, T. Suski, W. Walukiewicz, W. Shan, K.M. Yu, J.V. Ager III, E.E. Haller, J.F. Geisz, J.M. Olson, Appl. Phys. Lett. **76**, 2409 (2000)
17. H.M. Cheong, Y. Zhang, A. Mascarenhas, J.F. Geisz, Phys. Rev. B **61**, 13687 (2000)
18. P.J. Klar, H. Grüning, W. Heimbrodt, J. Koch, F. Höhnsdorf, W. Stolz, P.M.A. Vicente, J. Camassel, Appl. Phys. Lett. **76**, 3439 (2000)
19. W. Shan, W. Walukiewicz, K.M. Yu, J.V. Ager III, E.E. Haller, J.F. Geisz, D.J. Friedman, J.M. Olson, S.R. Kurtz, C. Nauka, Phys. Rev. B **62**, 4211 (2000)
20. P. Perlin, S.G. Subramanya, D.E. Mars, J. Kruger, N.A. Shapiro, H. Siegle, E.R. Weber, Appl. Phys. Lett. 73: 3703 (1998)
21. C. Skierbiszewski, P. Perlin, P. Wisniewski, T. Suski, J.F. Geisz, K. Hingerl, W. Jantsch, D. Mars, W. Walukiewicz, Phys. Rev. B **65**, 35207 (2002)
22. M. Kondow, T. Kitatani, M.C. Larson, K. Nakahara, K. Uomi, H. Inoue J. Cryst. Growth **188**, 255 (1998)
23. I.A. Buyanova, W.M. Chen, B. Monemar, MRS Internet J. Nitride Semicond. Res. **6**, 2 (2001)
24. J. Endicot, A. Patane, D. Maude, L. Eaves, M. Hopkinson, G. Hill, Phys. Rev. B **72**, 041306(R) (2005)
25. A. Lindsay, E.P. O'Reilly, Solid State Commun. **112**, 443 (1999)
26. N.G. Szwacki, P. Boguslawski, Phys. Rev. B **64**, 161201 (2001)
27. A. Zunger, Phys. Stat. Sol. b **216**, 117 (1999)
28. G. Bentoumi, V. Timoschevskii, N. Madini, M. Cote, R. Leonelli, J.N. Beaudry, P. Desjardins, R.A. Masut, Phys. Rev. B **70**, 35315 (2004)
29. I. Gorczyca, C. Skierbiszewski, T. Suski, N.E. Christensen, A. Svane, Phys. Rev. B **66**, 081106 (2002)
30. N.G. Szwacki, P. Boguslawski, I. Gorczyca, N.E. Christensen, A. Svane, Acta Phys. Pol. A **102**, 633 (2002)
31. N.E. Christensen, I. Gorczyca, A. Svane, N.G. Szwacki, P. Boguslawski, Phys. Stat. Sol. b **235**, 374 (2003)
32. I. Gorczyca, N.E. Christensen, A. Svane, Solid State Commun. **136**, 439 (2005)
33. I. Gorczyca, N.E. Christensen, A. Svane, Phys. Stat. Sol. b **234**, 1599 (2006)
34. R.O. Jones, O. Gunnarsson, Rev. Mod. Phys. **61**, 681 (1989) and references therein

35. J.P. Perdew, A. Zunger, Phys. Rev. B **23**, 5048 (1981)
36. D.M. Ceperley, B.J. Alder, Phys. Rev. Lett. **45**, 566 (1980)
37. R. Car, M. Parrinello, Phys. Rev. Lett. **55**, 2471 (1985)
38. C. Wang, Q.M. Zhang, J. Bernholc, Phys. Rev. Lett. **69**, 3789 (1992)
39. G.B. Bachelet, D.R. Hamann, M. Schlüter, Phys. Rev. B **26**, 4199 (1982)
40. O.K. Andersen, Phys. Rev. B **12**, 3060 (1975)
41. M. Methfessel, Phys. Rev. B **38**, 1537 (1988)
42. M. Methfessel, C.O. Rodriguez, O.K. Andersen, Phys. Rev. B **40**, 2009 (1989)
43. M. Van Schilfgaarde, private communication
44. D.L. Novikov, private communication, and N.E. Christensen, D.L. Novikov, Solid State Commun. **119**, 477 (2001) and references therein
45. D. Singh, Phys. Rev. B **43**, 6388 (1991)
46. D. Glötzel, B. Segal, O.K. Andersen, Solid State Commun. **36** 403 (1980)
47. N.E. Christensen, Phys. Rev. B **30**, 5753 (1984)
48. N.E. Christensen, in *High Pressure in Semiconductor Physics I*, ed. by T. Suski, W. Paul and *Semiconductors and Semimetals V*, vol. 54, ed. by R.K. Willardson, E.R. Weber (Academic Press, New York, 1998), p. 49
49. N.E. Christensen, I. Gorczyca, Phys. Rev. B **50**, 4397 (1994)
50. I. Gorczyca, A. Svane, N.E. Christensen, Phys. Rev. B **60**, 8147 (1999)
51. J.F. Muth, J.H. Lee, I.K. Shmagin, R.M. Kolbas, H.C. Casey, B.P. Keller, U.K. Mishira, S.P. Den Baars, Appl. Phys. Lett. **71**, 2572 (1997)
52. L. Hedin, S. Lundqvist, Solid State Phys. **23**, 1 (1969)
53. M.S. Hybertsen, S.G. Louie, Phys. Rev. B **34**,: 5390 (1986)
54. M. Rohlfing, S.G. Louie, Phys. Rev. Lett. **82**, 1959 (1999)
55. P. Puschnig, C. Ambrosch-Draxl, Phys. Rev. Lett. **89**, 056405 (2002)
56. R. Laskowski, N.E. Christensen, C. Ambrosch-Draxl, Phys. Rev. B **72**, 035204 (2005)
57. M. Alouani, S. Gopalan, S. Garriga, N.E. Christensen, Phys. Rev. Lett. **61**, 1643 (1988)
58. I. Gorczyca, N.E. Christensen, M. Alouani, Phys. Rev. B **39**, 7705 (1989)
59. In fact we did try to use adjusting potentials which reproduce the value of the direct gap at Γ in GaN, but the lack of experimental data for the gaps at L and X made the adjustment at the points poorer. The results obtained for GaN_xAs_{1-x} in this way differed insignificantly from the calculations with GaAs parameters throughout the supercell, the choice described in the main text
60. J.S. Blakemore, J. Appl. Phys. **53**, R123 (1982)
61. K.C. Hass, H. Ehrenreich, B. Velický, Phys. Rev. B **27**, 1088 (1983)
62. J. Kudrnovský, V. Drchal, J. Mašek, Phys. Rev. B **35**, 2487 (1987)
63. J. Kudrnovský, V. Drchal, M. Šob, N.E. Christensen, O.K. Andersen, Phys. Rev. B **40**, 10029 (1989)
64. P. Bogusławski, I. Gorczyca, Semicond. Sci. Technol. **9**, 2169 (1994)
65. W. Shan, W. Walukiewicz, J.W. Ager III, E.E. Haller, J.F. Geisz, D.J. Friedman, J.M. Olson, S.R. Kurtz, J. Appl. Phys. **86**, 2349 (1999)
66. P. Bogusławski, A. Baldereschi, Solid Stat. Commun. **66**, 679 (1988); Phys. Rev. B **39**, 8055 (1989)
67. L. Bellaiche, S.H. Wei, A. Zunger, Phys. Rev. B **54**, 17568 (1996)
68. A. Al-Yacoub, L. Bellaiche, Phys. Rev. B **62**, 10847 (2000)
69. T. Morgan, Phys. Rev. Lett. **21**, 819 (1968)
70. C. Skierbiszewski, Semicond. Sci. Technol. **17**, 803 (2002)

71. H.P. Hjalmarson, P. Vogl, D.J. Wolford, J.D. Dow, Phys. Rev. Lett. **44**, 810 (1980)
72. W. Lin-Wang, Phys. Rev. Lett. **88**, 256402 (2002)
73. M. Cardona, J. Phys. Chem. Solids **24**, 1543 (1963); ibid. **26**, 1351 (1965) (Erratum)
74. N. Shtinkov, P. Desjardins, R.A. Masut, Phys. Rev. B **67**, 81202 (2003)
75. Y. Zhang, A. Mascarenhas, H.P. Xin, C.W. Tu, Phys. Rev. B **61**, 7479 (2000)
76. J. Hader, S. Koch, J.V. Moloney, E.P. O'Reilly, Appl. Phys. Lett. **76**, 3685 (2000)
77. E.P. O'Reilly, A. Lindsay, S. Tomic, P.J. Klar, Phys. Stat. Sol. B **241**, 3099 (2004)
78. P.N. Hai, W.M. Chen, I.A. Buyanova, H.P. Xin, C.W. Tu, Appl. Phys. Lett. **77**, 1843 (2000)
79. F. Masia, A. Polimeni, G. Baldassarri Höger von Högersthal, M. Bissiri, M. Capizzi, P.J. Klar, W. Stolz, Appl. Phys. Lett. **82**, 4474 (2003)
80. C. Skierbiszewski, J. Lusakowski, J. Phys. Condens. Matter **16**, S3319 (2004)
81. Y.J. Wang, X. Wei, Y. Zhang, A. Mascarenhas, H.P. Xin, Y.G. Hong, C.W. Tu, Appl. Phys. Lett. **82**, 4453 (2003)
82. J. Toivonen, T. Hakkarainen, M. Sopanen, H. Lipsanen, J. Crys. Growth **221**, 456 (2000)
83. P.R.C Kent, A. Zunger, Phys. Rev. Lett. **86**, 2613 (2001)
84. P.R.C Kent, A. Zunger, Appl. Phys. Lett. **82**, 559 (2003)
85. W.G. Spitzer, H.Y. Fan, Phys. Rev. **106**, 882 (1957)
86. The experimental values for the k-dependence of the effective mass in the CB are usually obtained by a combination of Hall effect and infrared reflectivity measurements. In the analysis of the data a Fermi radius is deduced from the electron concentration obtained in the Hall measurement by application of a free-electron like relation between density and Fermi radius. Thus, it is implicitly assumed that the sample has been heavily doped, and that the doping levels are above the CB minimum, so that the electron gas is degenerate (metal, in fact). See also: ref. 87
87. M. Corti, A. Gabetta, M. Fanciulli, A. Svane, N.E. Christensen Phys. Rev. B **67**, 064416 (2003)
88. R.K. Willardson, A.C. Beer (eds.), *Semiconductors and Semimetals, V 8* (Academic Press, New York, 1972)
89. R.K. Willardson, A.C. Beer (eds.), *Semiconductors and Semimetals, V 12* (Academic Press, New York, 1977)
90. M. Cardona, Phys. Rev. **121**, 752 (1961)
91. H. Piller, J. Phys. Soc. Jpn. Suppl. **21**, 206 and [88], p. 103 (1966)
92. G.E. Stillman, C.M. Wolfe, J.O. Dimmock, in [89], p. 169
93. A. Raymond, J.L. Robert, C. Bernard, J. Phys. C **12**, 2289 (1979)
94. P. Perlin, E. Litwin-Staszewska, B. Suchanek, W. Knap, J. Camassel, T. Suski, R. Piotrzkowski, I. Grzegory, S. Porowski, E. Kaminska, J.C. Chervin, Appl. Phys. Lett. **68**, 1114 (1996)
95. For GaAs $\varepsilon(\infty) = 10.9$ (see for example [96], p. 337), but it is maybe not obvious that this is relevant to the case of GaN_xAs_{1-x}. However, if only rather small nitrogen concentrations are considered the screening of the electron system caused by the ions may not be significantly different from that of pure GaAs. Thus the value used in the analyses made by Skierbiszewski et al.

was $\varepsilon(\infty) = 10.9$, [97]. The argument for using the dielectric constant for the semiconductor host, although the "free carriers" created by the doping is that the electron concentrations are low, $\approx 10^{19}\,\text{cm}^{-3}$, compared to the density of ions

96. P.Y. Yu, M. Cardona, *Fundamentals of Semiconductors*, 3rd edn. (Springer, Berlin Heidelberg New York, 2001)
97. C. Skierbiszewski, private communication
98. E.D. Jones, N.A. Modine, A.A. Allerman, I.J. Fritz, S.R. Kurtz, A.F. Wright, S.T. Torez, X. Wei, Proc. SPIE **3621**, 52 (1999)
99. P.H. Tan, X.D. Luo, Z.Y. Xu, Y. Zhang, A. Mascarenhas, H.P. Xin, C.W. Tu, W.K. Ge, Phys. Rev. B **73**, 205205 (2006)

5

Experimental Studies of GaInNAs Conduction Band Structure

C. Skierbiszewski

In this chapter comprehensive review of the nitrogen-induced modifications of the electronic structure of GaInNAs alloys is carried out. We study behavior of conduction band effective mass as a function of Fermi energy, nitrogen content, and pressure. From analysis of the effective mass for different electron concentrations we have determined the energy dispersion relation for conduction band. We have investigated also optical absorption spectra on GaInNAs thin films and determined the absorption coefficients for E_- and E_+ transitions. Spectroscopic ellipsometry measurements performed in a wide photon energy range 1.5–5.5 eV have been used to determine energy dependence of the dielectric function as well as energies of E_1, E_0, and E_2 critical point transitions. From the magneto absorption experiments we have obtained the values of the Zeeman splitting and the effective g^* factors for the conduction and valence bands in GaInNAs alloys. Experiments have shown profound changes of the GaInNAs conduction band close to the Γ point, conduction band splitting, and giant conduction band nonparabolicity. Much less effect have been observed for X and L minima as well as for valence band states.

5.1 Introduction

Dilute nitrides attracted recently considerable interest due to their unusual physical properties and variety of optoelectronic applications. The GaAs and GaN have an energy gap equal to 1.4 and 3.4 eV, respectively, and one can assume that the energy gap of the GaN_xAs_{1-x} alloy will be in between these values depending on the alloy content x. However, it was found that alloying GaAs with N leads to giant bowing of the band gap energy – unlike to the conventional alloys, e.g., AlGaAs GaInAs GaInP where band gap energy changes almost linearly according to the virtual crystal approximation model. Band gap reductions as large as 0.18 eV have been observed in $GaAs_{1-x}N_x$ with only 1% of N [1–4]. Similar effects were also observed in GaNP [5, 6], InNP [7,8], GaNSbAs [9], and InNSb [10] alloys. On the other hand, by adding

In or Sb to GaN_xAs_{1-x} one can compensate the N-induced contraction of the lattice parameter. This also reduces the band gap making possible to grow $Ga_{1-y}In_yN_xAs_{1-x}$ or $GaN_xSb_yAs_{1-x-y}$ quaternaries that are lattice matched to GaAs or InP and have energy gaps in the 1.3–1.55 μm spectral range. All these findings opened an interesting possibility of using group $IIIN_xV_{1-x}$ alloys for a variety of optoelectronic applications [11–14] and generated a considerable interest to investigate its electronic structure [15–42].

The turning point that accelerated the investigation of diluted nitrides was related with discoveries of the highly nonlinear pressure dependencies of the energy gap [20, 21] and conduction band (CB) splitting into two subbands E_- and E_+ [21, 23]. The GaInNAs CB peculiarities were explained by Shan and Walukiewicz within framework of the band anticrossing (BAC) model [see Chap. 3]. In this approach, the CB splitting results from an anticrossing interaction between nitrogen induced, localized, a_1 symmetry state and the extended conduction band states of the semiconductor matrix [21, 24, 25]. On the other hand, ab initio calculations by Kent and Zunger [39, 40], Gonzales Szwacki et al. [38] and Gorczyca et al. [41, see Chap. 4], confirming the CB splitting, showed quite different role of nitrogen in GaInNAs band formation. Presence of N atoms causes breaking of the T_d symmetry of the lattice and leads to a mixing of the electronic states from Γ, X, and L points of the Brillouin zone and subsequent formation of the E_+ and E_- bands without any significant admixture of N-related wavefunctions. Bellaiche et al. [19] point out two ranges of N content in discussion of the GaNAs conduction band structure peculiarities. The first one covers N content less than 0.6%; when, in addition to the deep a_1 state, resonant with the CB [43, 44], the deep states related to N pairs and other N complexes located below the CB edge appears. These states, so called cluster states (CS), were observed experimentally [45]. The CS disappear (replaced by perturbed host states (PHS)) when the nitrogen content in GaNAs is higher than 0.6%, i.e., in the second range of N content when GaNAs alloy is formed [39, 45]. Another description of the GaNAs peculiarity was proposed by Zhang et al. [46] where impurity band inside the forbidden gap is created as a result of interaction of different N related states.

Since explanation of available experimental data can be made on the basis of different models, an intense theoretical debate on the microscopic origin of the CB structure of the GaInNAs and the role played by N in its formation is still going on [21, 22, 28, 35–42].

In this chapter we provide systematic study of the basic properties of GaInNAs alloys. We concentrate only on the alloy limit – for N content higher than 0.8%. We discuss the following:

(a) The giant nonparabolicity of conduction band and electron effective mass as a function of the Fermi energy, alloy composition, and pressure in the Sect. 5.2
(b) The interband optical transitions in the Sect. 5.3

(c) The dielectric function in the Sect. 5.4
(d) The effective g^*-factors of the conduction and valence bands in the Sect. 5.5

Our results are compared with other existing data obtained, e.g., by photomodulated reflectance or photoluminescence measurements. The important electronic parameters are analyzed using the BAC, $\boldsymbol{k} \cdot \boldsymbol{p}$, tight binding models as well as an ab inito calculations.

5.2 GaInNAs Electron Effective Mass and Conduction Band Dispersion

In this section we are focused on the experimental determination of the effective mass as a function of the Fermi energy, nitrogen content, and pressure. The dispersion of the conduction band is inferred from the energy dependence of the effective mass.

5.2.1 Effective Mass Determination

Because of the low electron mobility (100–400 $\mathrm{cm^2\,V^{-1}\,s^{-1}}$), determination of the effective mass, m^*, in GaNAs alloys is very difficult. From this reason, the well known and precise methods of measurements of the m^*, like cyclotron resonance or Shubnikov de Haas oscillations, can not be applied. In that case, the effective mass at the Fermi level, $m^*(k_\mathrm{F})$, can be inferred from the plasma edge frequency, ω_p [47, 48]. In heavily doped semiconductor the well known expression for ω_p yields

$$m^*(k_\mathrm{F}) = \frac{n_\mathrm{e}(k_\mathrm{F})e^2}{\omega_\mathrm{p}^2 \varepsilon_0 \varepsilon_\infty}, \tag{5.1}$$

where $n_\mathrm{e}(k_\mathrm{F})$ is the electron density, k_F is the wave vector at the Fermi surface, e is the electron charge, ε_∞ is the high frequency dielectric constant, and ε_0 is a vacuum permittivity. For an isotropic conduction band k_F is related to the electron concentration n_e through the relation, $n_\mathrm{e}(k_\mathrm{F}) = (k_\mathrm{F})^3/3\pi^2$.

We used Fourier Transform Infrared spectrometer to determine the plasma edge frequency. Experiments were done for series of 1–3 μm thick MOCVD grown samples doped with Se, which had the electron concentration in the range 1×10^{17}–$6 \times 10^{19}\,\mathrm{cm^{-3}}$ (in order to vary the Fermi energy) [13]. The electron concentration n_e was determined by the Hall effect in the Van der Pauw configuration and/or with electrochemical capacitance–voltage (C–V) profiler measurements. The layer thickness for all samples was determined by the scanning electron microscopy (SEM). All experiments were performed at room temperature.

An example of reflectivity data is shown in Fig. 5.1. We analyze this spectrum using the Drude model for the dielectric function to determine the

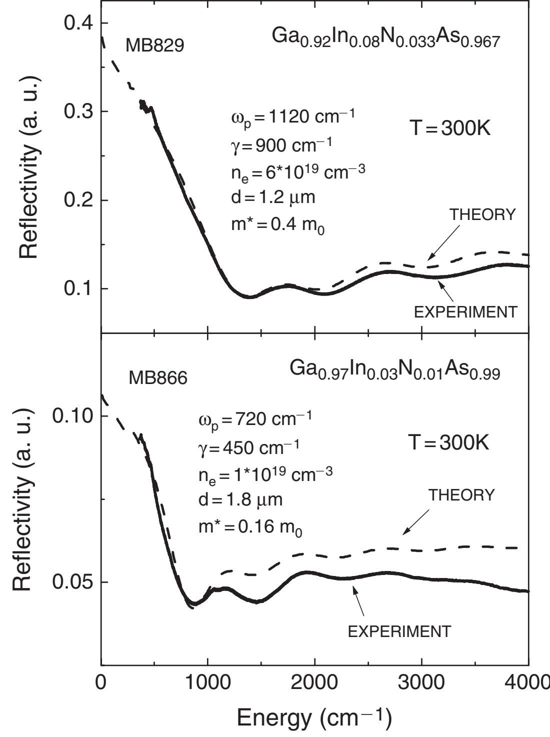

Fig. 5.1. Reflectivity spectra (*solid lines*) for two $Ga_{1-y}In_yN_xAs_{1-x}$:Se samples with distinctly different electron concentrations. The *dashed lines* show the theoretical fit with set of parameters indicated in figure

plasma frequency ω_p [30, 48]. The reflectivity of a semi-infinite medium is described by the following formula:

$$R = \frac{(n-1)^2 + \kappa^2}{(n+1)^2 + \kappa^2}, \tag{5.2}$$

where n is a real part of the refractive index and κ is the extinction coefficient. The link between n and κ is given by complex dielectric function $\varepsilon(\omega) = (n - i\kappa)^2$. If only the free carrier contribution is taken into account, the dielectric function has following form:

$$\varepsilon(\omega) = \varepsilon_\infty \left(1 - \frac{\omega_\mathrm{p}^2}{\omega\,(\omega + \mathrm{i}\gamma)}\right), \tag{5.3}$$

where γ is the electron damping constant, related to the electron mobility μ. The plasma frequency can be obtained by fitting reflectivity R to the experimental data (see dashed lines in Fig. 5.1). The reflectivity fringes (Fabry–Perot oscillations) observed at energies above plasma edge are well reproduced by

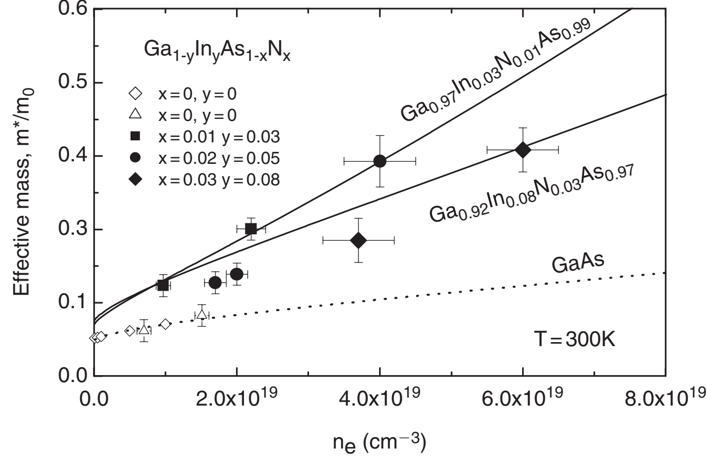

Fig. 5.2. The experimental electron effective mass, m^*, vs. electron density, n_e, for $Ga_{1-y}In_yN_xAs_{1-x}$ samples with different alloy compositions x and y. Open diamonds represent data from [49]. The solid lines are the predictions of the band anticrossing model for the indicated compositions. The dashed line represents the much smaller enhancement predicted for GaAs due to nonparabolicity of the conduction band

taking the layer thickness measured in SEM and assuming that high frequency dielectric constant is the same as for GaAs ($\varepsilon_\infty = 10.9$). This indicates that in the energy range from 1,000–4,000 cm^{-1}, the dielectric function of GaInNAs is not affected by the small amount of N and In in our samples. To illustrate the dependence of the effective mass on the electron energy and the N content we have shown in Fig. 5.2 values of the experimental effective masses for different electron concentrations.

We find a very large increase of the effective mass for all investigated GaInNAs samples. Almost sixfold increase of the effective mass ($m^* = 0.4\,m_0$) in the heavily doped $Ga_{0.92}In_{0.08}N_{0.03}As_{0.97}$ sample (with $n_e = 6\times10^{19}\,\mathrm{cm}^{-3}$) was detected. This can be compared with a slight increase of the effective mass in GaAs. The small increase of effective mass in GaAs can be understood in terms of the $\boldsymbol{k}\cdot\boldsymbol{p}$ interaction between the Γ_6 conduction band and Γ_8 valence band. Equally important is a fact that it was easy to obtain very high electron densities – up to $6 \times 10^{19}\,\mathrm{cm}^{-3}$, which can be used as independent indication of the profound change of the conduction band density of states. For GaAs such electron densities are not available due to the electron transfer to the L minimum.

We analyzed these results in a framework of a phenomenological, two-level BAC model, which describes the electronic structures of GaInNAs alloys in terms of an anticrossing interaction between localized a_1 symmetry state induced by nitrogen and the extended conduction band states of the semiconductor matrix [21,24,25]. The significant, practical advantage of the BAC

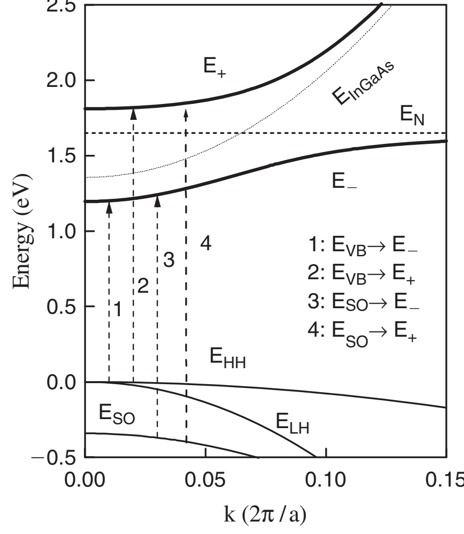

Fig. 5.3. Conduction band splitting and dispersion in $Ga_{0.96}In_{0.04}N_{0.01}As_{0.99}$ according to band anticrossing model [21]. Arrows indicate different optical transitions

model is that it provides simple analytic expressions for the conduction band dispersion and allows easily to calculate, e.g., strength of the optical transitions [26] in bulk material, transition energies between electronic states in quantum wells (QWs), or gain in laser structures [27]. The BAC model predicts splitting of the CB into two subbands, E_- and E_+ (see Fig. 5.3).

The formula for the lower E_- and upper E_+ conduction subbands is given by

$$E_{\pm}(k) = \frac{1}{2}\left[(E_{\mathrm{M}}(k) + E_{\mathrm{N}}) \pm \sqrt{(E_{\mathrm{M}}(k) - E_{\mathrm{N}})^2 + 4xC_{\mathrm{MN}}^2}\right], \tag{5.4}$$

where $E_{\mathrm{M}}(k)$ is the energy of the conduction band of the semiconductor matrix, E_{N} is the energy position of the nitrogen related level with a_1 symmetry, x is the nitrogen molar fraction, and C_{MN} is the hybridization matrix element.

In general, the inverse density of states effective mass at the Fermi level is defined as

$$\frac{1}{m^*(k)} = \frac{1}{\hbar^2 k}\left|\frac{\partial E(k)}{\partial k}\right|. \tag{5.5}$$

Therefore, one can easily derive the analytic expression for effective mass at the Fermi level from (5.4) and (5.5):

$$\frac{1}{m^*(k)} = \frac{1}{2m_{\mathrm{M}}(k)}\left[1 - \frac{(E_{\mathrm{M}}(k) - E_{\mathrm{N}})}{\sqrt{(E_{\mathrm{M}}(k) - E_{\mathrm{N}})^2 + 4xC_{\mathrm{MN}}^2}}\right], \tag{5.6}$$

Table 5.1. Parameters used for calculations within framework of the BAC model

C_{MN}	2.7 eV
E_{N} (300 K)	1.65 eV
$\mathrm{d}E_{\mathrm{N}}/\mathrm{d}p$	$0.015\,\mathrm{eV\,GPa^{-1}}$
$\mathrm{d}E_{\mathrm{N}}/\mathrm{d}T$	$-0.00025\,\mathrm{eVK^{-1}}$
$\mathrm{d}E_{\mathrm{M}}/\mathrm{d}p$	$0.105\,\mathrm{eV\,GPa^{-1}}$
E_{g} ($\mathrm{Ga_{1-y}In_yAs}$)	$1.512 - 1.337y + 0.27y^2$ (eV)
E_{M} (T)	$E_{\mathrm{g}}^{\mathrm{GaInAs}} - \alpha T^2/(\beta + T)$
	$\alpha = 5.408 \times 10^{-4}\,\mathrm{eVK^{-1}}$
	$\beta = 204\,\mathrm{K}$

where $m_{\mathrm{M}}(k)$ is the energy dependent electron effective mass of the semiconductor matrix obtained within three-band $\boldsymbol{k} \cdot \boldsymbol{p}$ model [49].

In Fig. 5.2 we present calculations of the effective mass according the BAC model for two alloy compositions $x = 0.01$, $y = 0.03$ and $x = 0.033$, $y = 0.08$ (see solid lines). We have gathered in Table 5.1 all parameters necessary for modeling [29]. The BAC model well predicts giant increase of the effective mass, indicating that nitrogen strongly modifies the conduction band of GaInNAs. Much less effect is predicted by 3-band $\boldsymbol{k} \cdot \boldsymbol{p}$ model [49] for effective mass dependence of GaAs (see dotted line in Fig. 5.2).

5.2.2 Giant Nonparabolicity of the GaInNAs Conduction Band

To test in more details the conduction band dispersion, we have measured the effective mass for different electron density in GaInNAs samples containing 1% of N and 3% of In [50]. The dependence of the electron effective mass on the Fermi wavevector, k_{F}, for these samples is shown in Fig. 5.4. Also, a literature data on the effective mass in GaAs is presented there.

When the $m^*(k)$ dependence is known from an experiment, the $E(k)$ can be derived by the numerical integration of (5.5),

$$E(k) = \hbar^2 \int_0^k \frac{x}{m^*(x)}\, dx + E(k = 0), \tag{5.7}$$

where E $(k = 0)$ is the energy gap.

With the experimentally determined $m^*(k_{\mathrm{F}})$ for $\mathrm{Ga_{0.97}In_{0.03}As_{0.99}N_{0.01}}$ and GaAs we use (5.7) to calculate $E(k)$ dependence for the conduction band – see solid lines in Fig. 5.5. For GaAs we used E $(k = 0) = 1.42\,\mathrm{eV}$ [49] and for $\mathrm{Ga_{0.97}In_{0.03}N_{0.01}As_{0.99}}$, $E(k = 0) = 1.24\,\mathrm{eV}$, determined in optical transmission measurements for undoped sample. Our experimental data demonstrate giant nonparabolicity of the GaInNAs conduction band. We analyzed these results using the full-potential version of ab initio linear-muffin-tin-orbital (LMTO) method and the BAC model [51–54]. First we tested the LMTO approach describing GaAs conduction band (dashed line in Fig. 5.5). Since

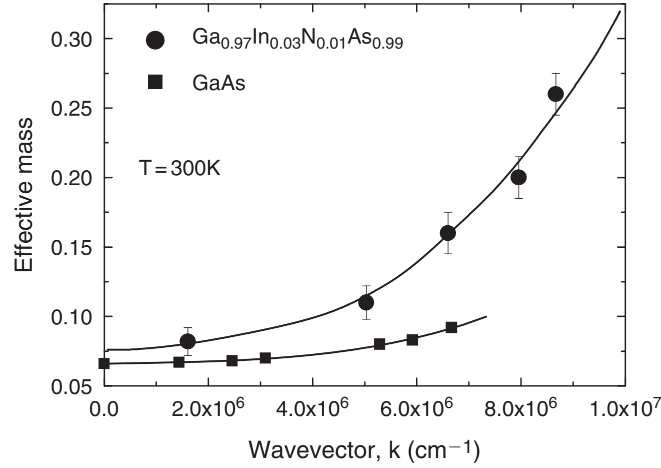

Fig. 5.4. The effective mass, m^*, vs. Fermi wavevector for $Ga_{0.97}In_{0.03}$ $N_{0.01}As_{0.99}$ (*dots*), this work, and GaAs (*squares*) after [49]

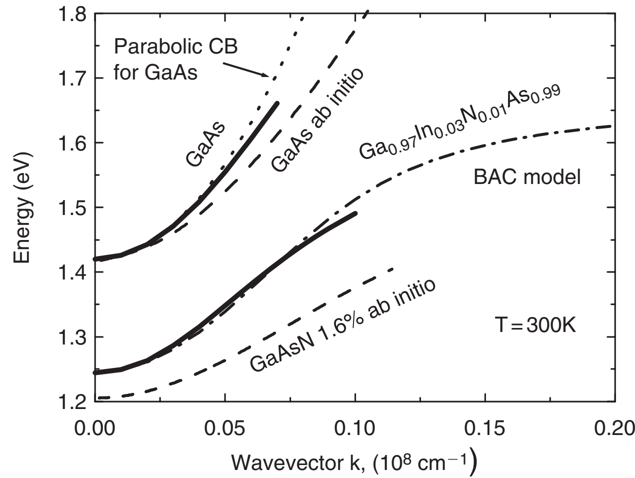

Fig. 5.5. Experimentally determined $E(k)$ for GaAs and $Ga_{0.097}In_{0.03}N_{0.01}As_{0.99}$ bulk crystals (*solid lines*). The *dashed lines* – ab initio LMTO calculations for GaAs and $GaN_{0.016}As_{0.984}$. *Dash-dotted line* – the BAC model for $Ga_{0.097}In_{0.03}N_{0.01}As_{0.99}$. *Dotted line* – parabolic GaAs conduction band

it worked well, we applied this procedure for GaN_xAs_{1-x} alloys. The LMTO calculations predict a strong nitrogen-induced modification of the GaNAs CB structure. In particular, the lowest conduction band is found to be strongly nonparabolic – see the dashed line in Fig. 5.5 calculated for $GaN_{0.016}As_{0.984}$.

The dash–dot line presented in Fig. 5.5 shows the $E(k)$ within a framework of the BAC model (for $C_{\mathrm{MN}} = 2.7\,\mathrm{eV}$ and $E_{\mathrm{N}} = 1.65\mathrm{eV}$ with respect to the

valence band maximum). From Fig. 5.5 one can see that the BAC (dash–dot line) and the ab initio (dashed line) give a very similar degree of GaInNAs nonparabolicity describing well experimental results (solid line), in spite of the profound differences in microscopic pictures behind theoretical models. Therefore, as far as nonparabolicity of CB is investigated, there is no apparent indication about microscopic nature of N-induced changes of the CB in GaInNAs alloys. We stress here that in ab inito calculations, the E_- and E_+ bands arise due to the mixing of host wavefunctions from Γ, X, and L points of the Brillouin zone and no nitrogen wavefunctions forming the E_- and E_+ bands was found [38–41, 51]. The difficulties with detection of the nitrogen related wavefunctions component within E_+ and E_- bands in ab initio calculations probably can be linked with the properties of the localized a_1 state in GaAs:N. This state was very difficult to identify, but finally it was done in photoluminescence experiments under hydrostatic pressure by Liu et al. [43]. Liu et al. showed that the localized a_1 symmetry state in GaAs:N has very similar properties to the most interesting, nitrogen related a_1 state in GaP:N, responsible for the efficient green luminescence. Hjalmarson et al. [44] pointed out within defect molecule model that the N-related, impurity-like state (in semiconductors like GaP or GaAs) is a *hyperdeep bonding state*, located in the valence band and the properties of the localized a_1 state are controlled by its orthogonality to the hyperdeep state. Therefore, the a_1 state (which enters to the BAC model) is a *host-like antibonding state*, i.e., its wavefunctions are predominantly host-like and not impurity-like, similar to wavefunctions of a deep-trap related to Ga dangling bonds. It is probably a reason why no states related directly to nitrogen wavefunctions is found in ab initio calculations in the energy range of interest.

The independent experiments probing the GaNAs CB density of states was done by Patane et al. [55]. The CB dispersion was determined from magneto-tunneling spectroscopy in resonant tunneling devices based on $GaAs/Al_{0.4}Ga_{0.6}As/GaN_xAs_{1-x}$ heterostructures. They found that for very low nitrogen content (0.08% of N in GaNAs), CB is strongly nonparabolic and interpreted its behavior in the framework of the BAC model.

5.2.3 Effective Mass at the Bottom of the Conduction Band

The energy of interband optical transitions observed in the photoreflectance (PR) or photoluminescence (PL) experiments in QWs allows to calculate effective mass, due to the fact that the energy of the electric subbands in QWs depends on m^*. In earlier interpretation, Zhang et al. [46] adjusted the PR peak energy by increasing the m^* values to fit the PR transition energy with a parabolic (GaAs-like) dispersion of the CB in QWs. From that procedure the m^* at the bottom of the CB was inferred to be as large as $0.55\, m_0$ for $x = 0.01$ and decreased to $0.15\, m_0$ for $x = 0.045$. We mention these values here because they were used as an argument supporting theoretical models, e.g., by Kent and Zunger [39].

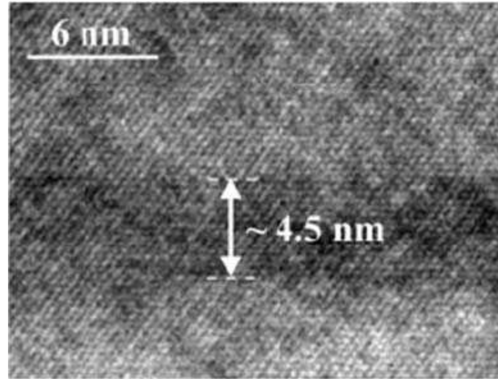

Fig. 5.6. High resolution transmission electron microscopy image of 4.5 nm wide GaAs/GaNAs single quantum well

We will show that a strong nonparabolicity of the CB of a material that builds the well (here, GaNAs) has a profound effect on the position of electric subbands in QWs. When the degree of nonparabolicity increases, the electric levels are pushed towards the bottom of the QW. For the parabolic CB, the similar effect can be obtained by an increase of the effective mass.

First, we study the interband transitions in the PL experiments for GaN_xAs_{1-x}/GaAs single quantum wells (SQWs) with different alloy content x. Then, description of the interband transitions for two-dimensional QWs system within a framework of the BAC model is given.

For the PL experiments we used MOCVD grown GaN_xAs_{1-x}/GaAs SQWs with $0.009 < x < 0.04$. The GaNAs well and GaAs barriers had 4.5 and 50 nm, respectively [56]. After growth, the samples were annealed at 700°C for 10 min. The information about the nitrogen content was obtained from X-ray diffraction on 500 nm thick reference GaNAs layers. The thickness of the SQWs was determined by the transmission electron microscopy (TEM). Figure 5.6 presents TEM picture of GaN_xAs_{1-x}/GaAs SQW with $x = 0.02$. In Fig. 5.7 we show temperature dependence of the PL for the SQW with $x = 0.009$ and $x = 0.02$ [51]. For temperatures below 70 K, the S-shape behavior of the PL line position is observed. It originates from the fact that the PL emission takes place from localized states well below the CB edge. This is indicative for localization effects due to potential fluctuations [57].

The giant nonparabolicity of the bulk GaNAs CB determined experimentally triggered our attention to study the influence of this effect on the position of the electronic states and its energy dispersion in QWs. We transformed the BAC model to the form suitable to describe the CB states in two-dimensional systems like GaNAs/GaAs QWs. This can be done, for a QW lying in xy plane, by replacing the k_z component of the bulk wavevector by $-id/dz$ [58]. Then the following 2×2 conduction band Hamiltonian for GaNAs/GaAs QWs gives

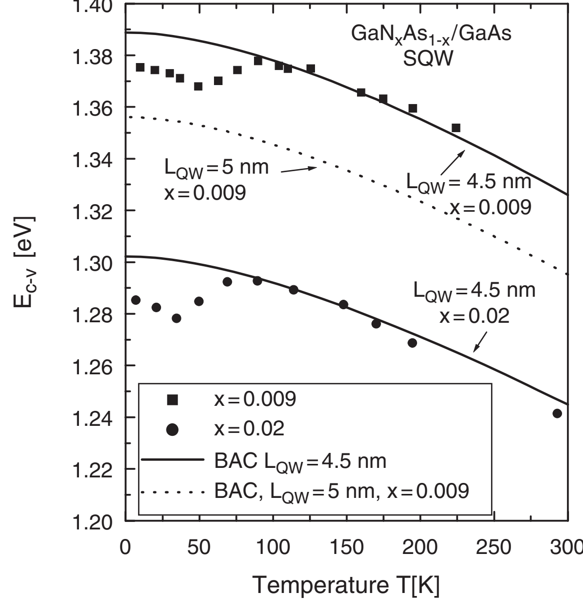

Fig. 5.7. Temperature dependence of the fundamental interband transition energy in 4.5 nm-wide $GaN_{0.009}As_{0.991}$/GaAs (*squares*) and $GaN_{0.02}As_{0.98}$/GaAs (*dots*) SQWs. *Solid lines* – the 2D BAC model calculations for 4.5 nm-wide QWs. *Dotted line* – the 2D BAC for $GaN_{0.009}As_{0.991}$/GaAs with 5 nm-wide well

$$\begin{pmatrix} E_{\mathrm{N}} & C_{\mathrm{MN}}\sqrt{x(z)} \\ C_{\mathrm{MN}}\sqrt{x(z)} & E_0 + \frac{\hbar^2 k_{II}^2}{2m^*} - \frac{\hbar^2 \mathrm{d}^2}{2m^* \mathrm{d}z^2} \end{pmatrix}, \tag{5.8}$$

where $x(z)$ denotes z-dependent nitrogen concentration, $E_0 = 1.428\,\mathrm{eV}$ is the energy gap of the bulk GaAs, $m^* = 0.067m_0$ is the CB edge effective mass of GaAs, and k_{II} is the component of k-vector in the xy plane. The values of the E_{N} and C_{MN} are the same as used previously for 3D system (see Table 5.1). It is interesting to note that contrary to the effective mass models used for a typical QW with the parabolic CB dispersion, in the case of the 2D BAC model the band offset of the CB is not an explicit parameter. It can be calculated as a difference between the energy gaps E_0(GaAs) and E_0(GaNAs) for the bulk GaAs and GaNAs materials, respectively. It is related with the fact that nitrogen in GaNAs changes conduction band predominantly, while valence band remains N-independent. The N content independent valence band offset in GaInNAs/GaAs QWs was recently confirmed experimentally by Gallupi et al. [59]. To compute the conduction band states for considered QWs we transformed the Hamiltonian (5.8) to a discrete form using the finite element method and then solved the resulting algebraic eigenvalue problem applying the Householder transformation and the QL method [60].

The conduction band structure of confined states was obtained by performing calculations for various values of k_{II}. We compared the fundamental transition energies calculated within the 2D BAC model (solid lines in Fig. 5.7) with the temperature dependence of the PL data for $x = 0.009$ (squares) and $x = 0.02$ (dots) $\mathrm{GaN}_x\mathrm{As}_{1-x}$/GaAs SQWs. We would like to stress here that the precise knowledge of the QW thickness (for narrow QWs, like in this work) plays the crucial role in a detailed theoretical description because the value of the transition energy is very sensitive to the QW thickness. As an example, we show in Fig. 5.7 the calculated PL energy vs. temperature for a 4.5 nm (solid line) and a 5 nm (dotted line) wide QW with $x = 0.009$. For the 4.5 nm-wide SQWs the 2D BAC model works well and describes PL data. The discrepancies between the experimental data and the BAC model predictions for temperatures lower than 70 K are due to the localization effects mentioned above. This is why for a quantitative analysis of the transition energy in SQWs, x, in order to derive the electron effective mass, higher temperatures were chosen. The dots in Fig. 5.8 show positions of the PL peaks at 80 K as a function of the N content in GaNAs SQWs, while the solid line results from the 2D BAC model for 4.5 nm-wide SQWs.

As an example of the 2D BAC model predictions of the energetic dispersion, $E_{\mathrm{c}}(k)$, for the 5 nm-wide SQW containing 4% N is shown in Fig. 5.9a (for four subbands, E_{c1}, E_{c2}, E_{c3}, and E_{c4}, respectively). For higher values of k_{II}, a strong nonparabolicity is clearly visible. We calculated the electron effective mass for each electric subband in the QW from Fig. 5.9a according to (5.5) (replacing k by k_{II}) and plotted it in Fig. 5.9b.

We would like to stress that a strong nonparabolicity of GaNAs changes positions of the electronic levels in QWs and the effective mass for $k_{\mathrm{II}} = 0$ strongly increases with the electric subband number (see Fig. 5.9b). The

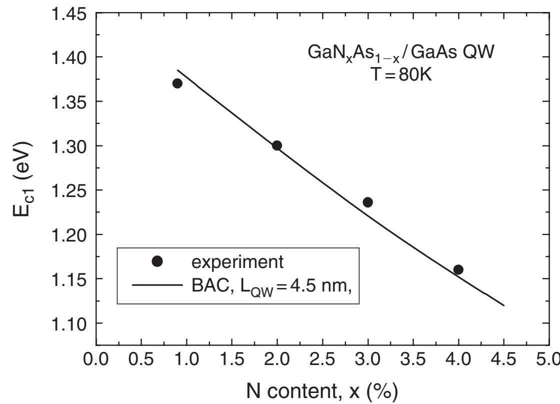

Fig. 5.8. Fundamental interband transition energies in 4.5 nm-wide $\mathrm{GaN}_x\mathrm{As}_{1-x}$/GaAs SQWs (*dots*) at 80 K. The *solid line* – 2D BAC model calculations for 4.5 nm-wide well

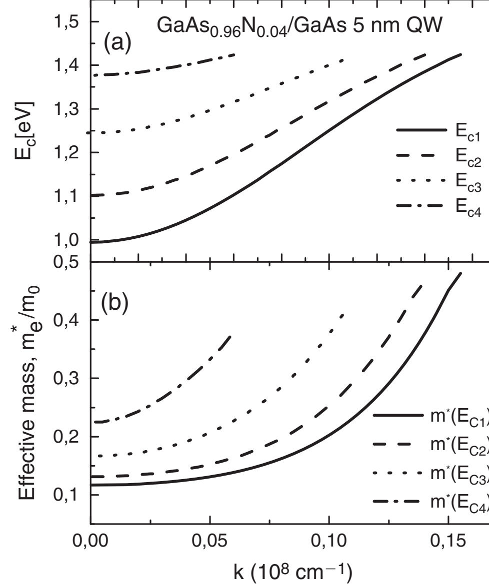

Fig. 5.9. Energy dispersion for the electric subbands in 5 nm-wide well $GaN_{0.04}As_{0.96}$/GaAs SQW (**a**) and effective mass for these subbands (**b**)

insight what is a difference in quantum confinement between the "conventional" QWs (like GaInAs/GaAs or GaAs/GaAlAs) and GaNAs based QWs is given below. For the infinite barrier width and the parabolic dispersion, the energy of nth quantum number state is given by the simple equation,

$$E(k_{II}) = \frac{\pi^2 \hbar^2 n^2 + L_{\mathrm{QW}}^2 \hbar^2 k_{II}^2}{2m_{\mathrm{e}}^* L_{QW}^2}, \tag{5.9}$$

where L_{QW} is the well width.

In Fig. 5.10 we show schematically an influence of the nonparabolicity and the effective mass value on the energy of the first electric subband. For the parabolic CB dispersion and effective mass equal to $0.067\,m_0$, the first electric level is located above the bottom of the QW as it is shown in Fig. 5.10a. An increase of the effective mass, e.g., to values of $0.55\,m_0$, causes a decrease of the confinement energy of the electric subband as it is depicted in Fig. 5.10b. For strong nonparabolicy of $E(k)$, like in the BAC model, the same effect can be obtained for the m^* equal to $0.095\,m_0$ at the CB bottom (Fig. 5.10c).

It is interesting to point out that values of the m^* for different electric subbands are constant for the parabolic CB case (e.g., for GaAs/GaAlAs QWs) and is in apparent disagreement with our results for GaNAs/GaAs QWs, where the m^* strongly depends on the electronic subband number (see Fig. 5.9b). This can result in a much higher effective mass observed in experiment when higher electric subband are populated. Finally, we plot

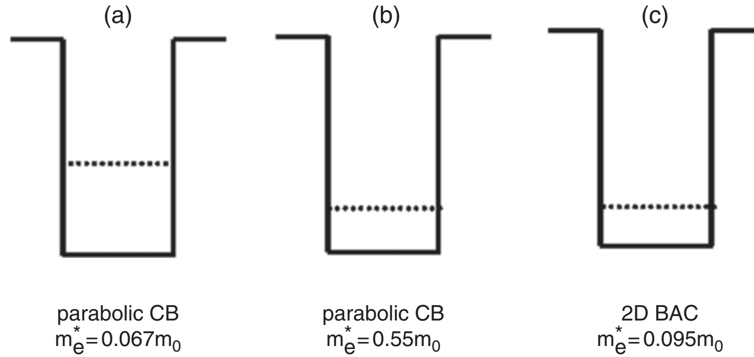

Fig. 5.10. The schematic diagram of the position of the first electric subband (*dotted lines*) in a QW for the parabolic CB with effective mass equal to $0.067m_0$ (**a**), $0.55m_0$ (**b**), and for 2D BAC model with the $m_e^* = 0.095m_0$ (**c**)

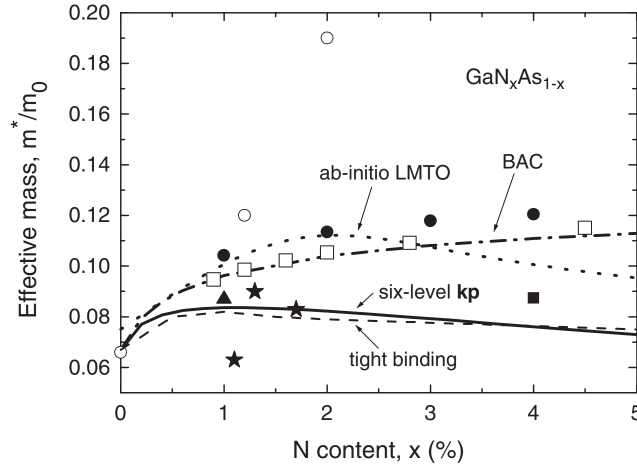

Fig. 5.11. Conduction band edge effective mass, m^*, in GaN_xAs_{1-x}. Experimental data: *solid dots* – obtained from the PL fitting with the 2D BAC model (80 K); *open squares* – recalculated PR data from [46] (300 K); *open circles* – from ODCR [66]; *solid triangle* – from the Faraday rotation [62]; *square* – from the energy loss spectroscopy [70]. Stars from [63]. Lines show theoretical predictions: *Dotted line* – ab initio LMTO [51], *dash-dotted line* - 3D BAC model, *dashed line* – tight binding calculations [72], *solid line* – six-level $\boldsymbol{k} \cdot \boldsymbol{p}$ theory [71]

the values of the m^* (solid dots – see Fig. 5.11) of the first conduction subband (E_{c1}) in the vicinity of the band edge for 4.5 nm wide GaNAs SQWs at $T = 80$ K. Our results show that in GaNAs the effective mass at the bottom of the CB increases from $0.067\,m_0$ for GaAs to $0.12\,m_0$ for $GaN_{0.04}As_{0.96}$. We also recalculated the PR data obtained by Zhang et al. [46] within the 2D BAC model [61]. The resulting effective mass followed our data from PL (see

open squares in Fig. 5.11). The systematic difference between dots and open squares in Fig. 5.11 is related with the temperature dependence of the effective mass [51]. In contrast to a strong *decrease* of the m^* obtained within the impurity band model (where parabolic CB dispersion is assumed) reported in [46], we get an *increase* of the effective mass, from $m^* = 0.095\,m_0$ for $x = 0.008$ to $m^* = 0.115\,m_0$ for $x = 0.045$.

The other existing experimental data where the m^* at the bottom of CB was determined are scattered in the range from $0.05\,m_0$ to $0.2\,m_0$. From analysis of the Faraday rotation experiments for bulk $GaN_{0.014}As_{0.986}$, $m^* = 0.08\,m_0$ was inferred [62]. The high magnetic field PL yields effective mass around $0.063\,m_0, 0.09\,m_0$, and $0.083\,m_0$ for nitrogen molar fraction $x = 0.011$, $x = 0.013$, and $x = 0.017$, respectively [63]. Also for ultra dilute limit (i.e., for $x = 0.002$–0.006) the increase of the effective mass up to $0.15\,m_0$ was reported [64, 65]. For GaN_xAs_{1-x}/GaAs QWs, in optically detected cyclotron resonance (ODCR) an increase of m^* from $0.1\,m_0$ to $0.2\,m_0$ was found for $0.01 < x < 0.02$ [66]. In PR spectroscopy, the values of m^* up to $0.11\,m_0$ were obtained [67–69] and finally in the energy loss spectroscopy, where $m^* = 0.0874\,m_0$ was obtained for $x = 0.04$ and $y = 0.1$ in $Ga_{1-y}In_yN_xAs_{1-x}$/GaAs [70].

In Fig. 5.11 we also plot the result of different theoretical calculations. Dashed-dotted, dotted, and solid lines present results of the BAC, ab initio LMTO and six-level $\boldsymbol{k}\cdot\boldsymbol{p}$ theory, respectively. It is interesting that the $\boldsymbol{k}\cdot\boldsymbol{p}$, LMTO, and tight binding calculations predict maximum of the effective mass for 1–2% of N [42, 51, 71, 72].

The effective mass at the bottom of GaInNAs CB changes with the N alloy content in rather moderate way. Except ODCR experiments, all data is in the range $0.05\,m_0 - 0.12\,m_0$. In addition, experimental points are scattered probably due to the difference in electron concentration (and Fermi energies) for different measurements. Therefore, the precise determination of the $m^*(\mathrm{N})$ at the bottom of CB will require careful planning of experiments since any increase of the Fermi energy can create experimental error difficult to estimate.

5.2.4 Pressure Dependence of the Effective Mass for $\boldsymbol{k} \sim 0$

In this section we report briefly on studies of the pressure dependence of the effective mass for a low electron concentration ($n_e = 1.6 \times 10^{17}\,\mathrm{cm}^{-3}$) $GaAs_{0.986}$ $N_{0.014}$ sample [73]. We measured the electron concentration and electron mobility as a function of applied hydrostatic pressure, p, up to $p = 2\,\mathrm{GPa}$ at $T = 295\,\mathrm{K}$ and $T = 77\,\mathrm{K}$ (see Fig. 5.12). At temperatures below 115 K we observed metastable behavior of electron conductivity. Above 115 K we were able to change electron concentration under hydrostatic pressure, while below 115 K the electron concentration remained constant. Such effects are related with electron population/depopulation of deep traps or localized metastable states (DX centres) and were observed in GaAs doped with Si, Se, Te, or Ge. This behavior allowed us to apply pressure at 77 K without changing electron

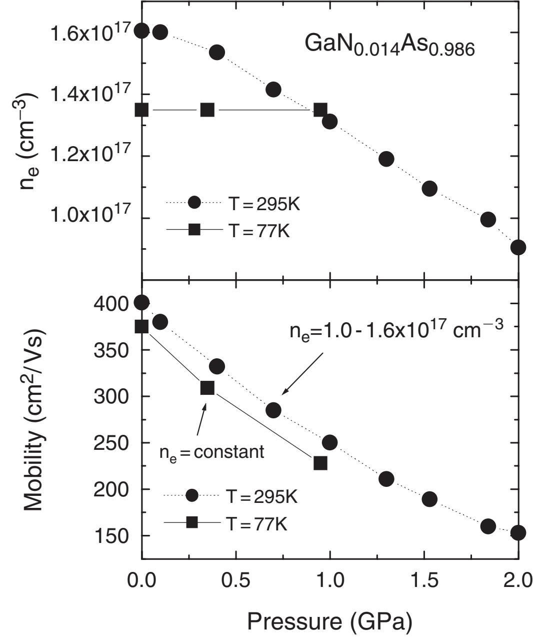

Fig. 5.12. The pressure dependence of the electron concentration and mobility in $GaN_{0.014}As_{0.986}$

concentration (see squares in Fig. 5.12). Important message from the experiments at 295 and 77 K is that the electron mobility, μ, strongly depends on hydrostatic pressure, and is much less sensitive to the temperature or change of the electron concentration. This leads us to conclusion that there is one dominant scattering mechanism – alloy scattering – which limits the mobility in GaNAs. In that case the mobility is inversely proportional to the square of the effective mass [42].

Within above assumptions the pressure changes of the mobility values can be estimated as

$$\frac{\mu(p)}{\mu(p=0)} \propto \left(\frac{m^*(p=0)}{m^*(p)}\right)^2 . \tag{5.10}$$

In Fig. 5.13 we show by squares the pressure induced changes of the m^* obtained from mobility behavior (making use of (5.10)). One should notice a much weaker pressure dependence of the electron effective mass (and therefore mobility) in GaAs (dashed line). Our results quantitatively agree (at least in the pressure range up to 2 GPa) with data obtained by Jones et al. [74] from exciton diamagnetic shift in QWs (circles in Fig. 5.13). Also very recently, Wu et al. [67] demonstrated large pressure induced increase of the m^* (from $m^* = 0.11\, m_0$ at $p = 0$ GPa to $m^* = 0.28\, m_0$ at $p = 7$ GPa) for 1.6% N containing GaNAs/GaAs QWs. Solid line in Fig. 5.13 indicate the BAC model predictions. The increase of the effective mass under pressure, stronger than

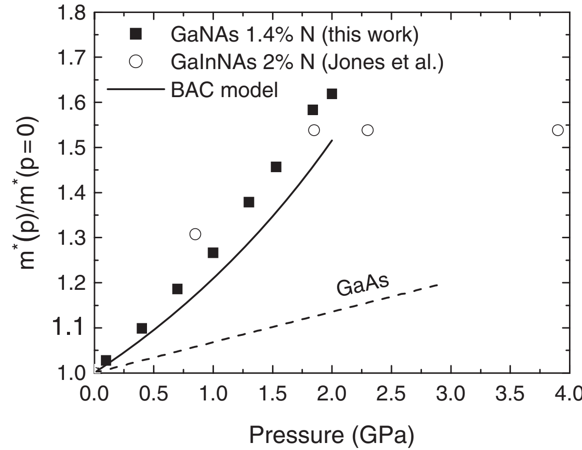

Fig. 5.13. The relative changes of electron effective mass, m^*, vs. pressure. *Squares* – values inferred from mobility drop for $GaN_{0.014}As_{0.986}$, *open circles* – data from [74]. *Dashed* and *solid lines* are predictions for GaAs and BAC model for $GaN_{0.014}As_{0.986}$, respectively.

that for GaAs (and quantitative the same like the BAC), is also predicted by ab initio calculations [41, 75].

5.3 Interband Absorption of Free-Standing Epitaxial Layers

To get more insight to the optical properties of GaInNAs alloys, the interband transmission on free standing $Ga_{1-y}In_yN_xAs_{1-x}$ with $0 \leq x \leq 0.025$ and $0 \leq y \leq 0.09$ layers in the energy range 0.8–2.4 eV was measured. This type of experiment allowed us to investigate the absorption coefficient and positions of the E_- and E_+ bands. Samples were grown by MBE [20] and MOCVD [13] technique and were not intentionally doped. The thin films were closely lattice matched to GaAs substrates by maintaining the In to N composition ratio $y = 3x$. To measure the absorption coefficient in a wide photon energy range a special structure that allowed separation of the layer from the substrate have been grown.

Figure 5.14 shows the cross-section of an MBE GaInNAs sample grown on a semi-insulating GaAs substrate. The structure consists of 0.1 μm thick GaAs buffer followed by a 50 nm AlAs etch stop layer, and then by 1.87 μm GaInNAs having ∼4% In and 1% N. The etching procedure used to remove the substrate and to secure the thin GaInNAs layers to sapphire or glass is described in [26] and [76]. Both the glass and sapphire substrates are well transparent in the spectral range of 0.8–2.5 eV, where the transmission experiments were performed. The absorption coefficient measured on thin, free-standing

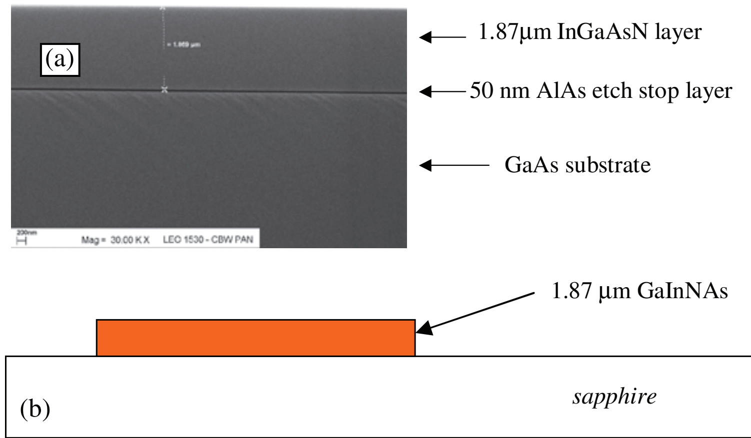

Fig. 5.14. (**a**) Scanning electron microscope image of 1,87 μm MBE grown GaInNAs layer on GaAs substrate with AlAs etch stop layer and (**b**) fixing of the thin layer on sapphire for transmission experiments

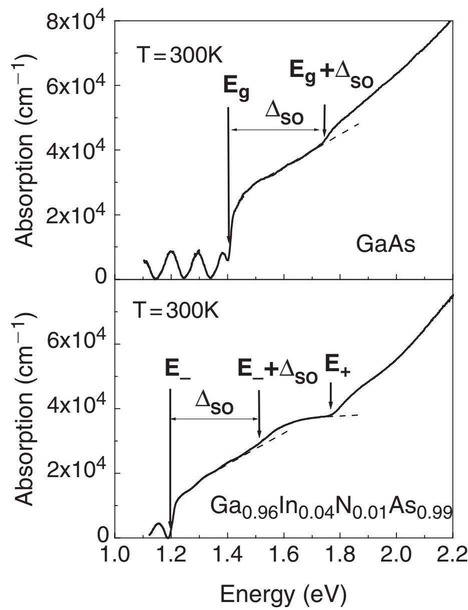

Fig. 5.15. Absorption of free-standing GaAs and GaInNAs layers. Positions of the energy gap E_g, $E_\mathrm{g} + \Delta_\mathrm{so}$ for GaAs, and E_-, $E_- + \Delta_\mathrm{so}$, E_+ for GaInNAs are indicated by the arrows

GaAs and $Ga_{0.96}In_{0.04}N_{0.01}As_{0.99}$ layers are compared in Fig. 5.15. At the low energy range, below energy gap values, Fabry–Perot oscillations were observed (similar to those measured in infrared reflectivity – see Fig. 5.1). Period of these oscillations allow to confirm the layer thickness. The calculated layer

thicknesses were equal to those obtained by SEM (with assumption of GaAs dielectric function in this energy rage).

We found that the fundamental absorption edge shifts towards lower energies for GaInNAs. The arrows in Fig. 5.15 indicate the band gap of GaAs, E_g, and GaInNAs, E_-. The higher energy transitions from the spin orbit split-off valence band to the CB, denoted as $E_g + \Delta_{so}$ and $E_- + \Delta_{so}$ are also evidenced in absorption experiments. What is most important additional absorption edge, denoted by E_+, was clearly observed. The absorption edges related with transition to E_- and E_+ bands have square root dependence as a function of photon energy, which is indicative for direct energy gap (for more details see [50]). This is strong argument that the minima of the E_- and E_+ bands are located at Γ point of Brillouin zone. All transitions observed in our experiments are schematically depicted in Fig. 5.3. As it is seen in Fig. 5.15 we observed a significant reduction of the absorption coefficient, $\alpha(E)$, at the absorption edge of GaInNAs related to E_- in comparison to GaAs.

This reduction of the value of α can be understood within the BAC model. The anticrossing interaction admixes localized N-induced wavefunctions of the a_1 state to the lowest conduction band edge states. The localized state component is only very weakly optically coupled to the valence band states, resulting in a reduced absorption coefficient. We analyzed quantitatively absorption data taken at $T = 10\,\mathrm{K}$ for $Ga_{0.96}In_{0.04}N_{0.01}As_{0.99}$ layer (see dots in Fig. 5.16) [50].

The solid line represents $\alpha(E)$ calculated within a framework of the BAC model with $E_N = 1.65\,\mathrm{eV}$ and $C_{MN} = 2.7\,\mathrm{eV}$. The model quite well describes the spectral dependence of the absorption coefficient in the wide photon energy range. The discrepancies between the experimental data and theoretical calculations is evident for the photon energies close to the $E_{VB} \rightarrow E_+$ transitions

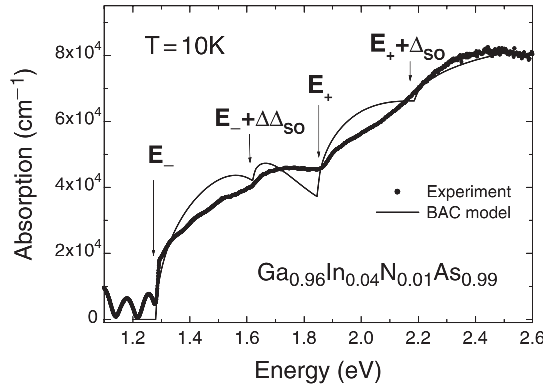

Fig. 5.16. Absorption spectrum of $Ga_{0.96}In_{0.04}N_{0.01}As_{0.99}$ layer at $T = 10\,\mathrm{K}$ (*points*) and calculation based on the BAC model (*line*). The calculated curves show contributions from the transitions between three valence bands and two conduction subbands

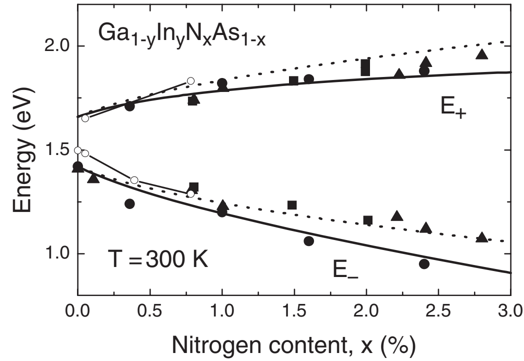

Fig. 5.17. Nitrogen composition dependence of the E_- and E_+ transitions. *Dots* – transmission experiments for lattice matched $Ga_{1-y}In_yN_xAs_{1-x}$ layers ($x \sim 3y$). *Triangles and squares* – PR data from [23] and [77], respectively. *Solid and dotted lines* – BAC model predictions for $Ga_{1-y}In_yN_xAs_{1-x}$ ($x = 3y$) and GaN_xAs_{1-x}, respectively. *Circles* – EPM calculations [35]

and underscores a need for a more accurate description of the optical coupling matrix element for the higher energy transitions.

Our experimental results on the interband optical transitions obtained from the optical absorption for different nitrogen content are shown by dots in Fig. 5.17. We combine it with other experimental data obtained by Perkins et al. [23] (triangles) and Shan et al. [77] (squares). The E_- and E_+ transitions show a very strong, nonlinear dependence of the N content. This dependence can be well explained by the BAC model. The solid lines in Fig. 5.17 indicate the calculated dependencies for E_- and E_+ using 5.4 (with $E_N = 1.65\,\text{eV}$ and $C_{MN} = 2.7\,\text{eV}$) for $Ga_{1-y}In_yN_xAs_{1-x}$ ($x = 3y$), while the dotted lines are for GaN_xAs_{1-x} alloys.

It is important that the nitrogen content evolution of E_- and E_+ can be also well described by ab initio empirical pseudopotential method (EPM), (see open circles in Fig. 5.17 [35]), molecular dynamics [38], or supercell LMTO [75] calculations. For 3% N content these calculations predict the difference $E_+ - E_- = 0.8\,\text{eV}$, which agree well with experimental data. We note here that the E_+ according to [35] consist of several different optical transitions, while we observe one: well resolved single band absorption edge. On the other Gonzalez Szwacki et al. [38] identify the E_+ as a state derived mainly from L minimum.

5.4 Dielectric Function and the Critical Point Transitions

The results of the absorption experiments and the effective mass determination indicated a large effect of N on the optical transition close to the lowest minimum of the conduction band. All these effects can be explained by the

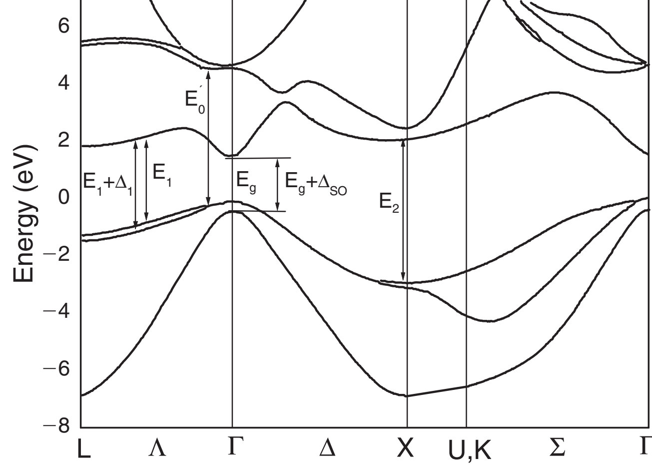

Fig. 5.18. The GaAs conduction band structure

BAC model or by ab initio calculations. For theoretical description of the GaInNAs band structure, information about evolution of other conduction and valence bands is also important.

We used spectroscopic ellipsometry (SE) to determine the optical transitions to higher bands, at the energies $E_1,\ E_1+\Delta_1,\ E_0'$, and E_2 in strain free $Ga_{1-3x}In_{3x}N_xAs_{1-x}$ films. The location of the critical point (CP) transitions corresponding to different van Hove singularities ($E_1,\ E_1+\Delta_1,\ E_0'$, and E_2) in the case of GaAs are schematically shown in Fig. 5.18.

The SE measurements were performed with an automatic and commercially available spectroscopic ellipsometer using a photoelastic modulator. The sampling distance was 10 meV in the photon energy range of 1.5–5.5 eV. All the spectra were taken at an angle of incidence θ of 70.4°. We used the same samples as for transmission experiments (described in Sect. 5.3). The dielectric function ε has been determined from the measured ellipsometric angles by standard procedure described by us in details elsewhere [50]. The real and imaginary part of the bulk dielectric function ε of GaAs and of three GaInNAs samples are shown in Fig. 5.19.

It is seen that with increasing N content, the structures around 2.9–3 eV (E_1 and $E_1+\Delta_1$ transitions) are smeared out due to a disorder in the quaternary compounds. The broadening is much less pronounced for the E_0' and E_2 transitions around 4.5 and 4.9 eV. To resolve the spectroscopic features close to the CPs, we have numerically calculated the second derivative of the experimental complex dielectric function with respect to energy.

The results are fitted with $\frac{\partial^2\varepsilon}{\partial E^2}$ given by the expressions

$$\frac{\partial^2\varepsilon}{\partial E^2} = -n(n-1)A\mathrm{e}^{\mathrm{i}\phi}(E - E_{\mathrm{CP}} + \mathrm{i}\Gamma_{\mathrm{CP}})^{n-2} \text{ for } n \neq 0, \tag{5.11}$$

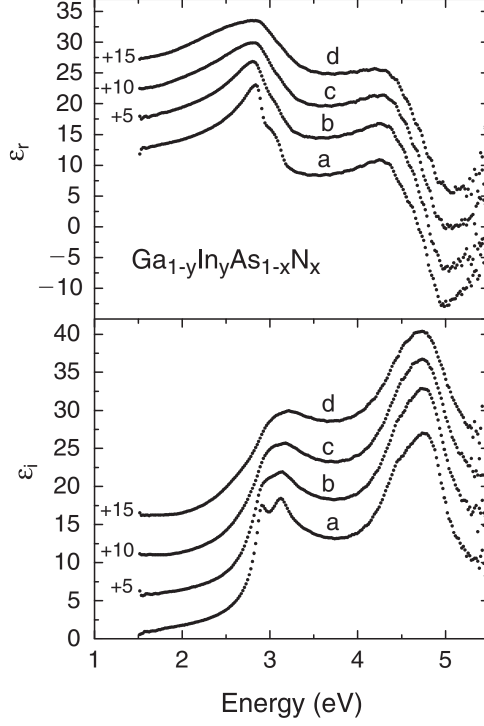

Fig. 5.19. Real (ε_{r}) and imaginary (ε_{i}) part of the dielectric function in GaInNAs alloys after numerical removal of the influence from the oxide layer: (**a**) GaAs; (**b**) $x = 0.004$, $y = 0.07$; (**c**) $x = 0.0164$, $y = 0.05$; (**d**) $x = 0.0247$, $y = 0.08$. The curves (**b**), (**c**), and (**d**) are shifted by 5, 10, and 15, respectively

and,

$$\frac{\partial^2 \varepsilon}{\partial E^2} = A\mathrm{e}^{\mathrm{i}\phi}(E - E_{\mathrm{CP}} + \mathrm{i}\Gamma_{\mathrm{CP}})^{-2} \text{ for } n = 0. \tag{5.12}$$

The only free parameters in the fitting procedure were Γ_{CP} and E_{CP}. The exponent n and the phase angle ϕ were chosen using arguments of [78]. If the conduction and valence bands are strictly parallel, the E_1 and $E_1 + \Delta_1$ transitions are two-dimensional (2D) CPs with $n = 0$. The corresponding phase angle at RT is $\pi/2$. It should be emphasized, however, that, as has been shown in [78], fitting of the E_1 transition with an excitonic lineshape ($n = 1$) results only in minor changes less than 10 meV in the resonance energies of the critical points. Therefore, we adopted this procedure also for fitting spectra in the samples with the N contents up to 2.5% and we determine E_{CP} at the E_1, $E_1 + \Delta_1$, E_0', and E_2 transitions with the n and ϕ parameters of GaAs and GaInNAs. Figure 5.20 shows an example of the second derivative of the imaginary part of ε for GaAs and GaInNAs, respectively. The dots indicate experimental results while the solid lines are the fitting curves. The arrows

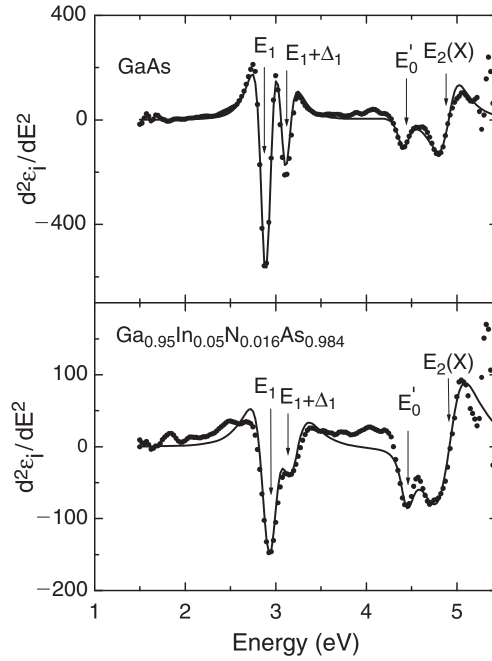

Fig. 5.20. Second derivative of the imaginary part of the dielectric function for a reference GaAs layer and an GaInNAs layer – the appropriate critical points transitions are indicated by arrows. *Dots* – experimental data. *Solid lines* – fits according to the critical point analysis

indicate the various transitions. To determine the transition energies more carefully we fitted both the real and imaginary part of dielectric function ε independently.

The experimental results of interband transitions obtained from the SE measurements and from absorption experiments are combined in Fig. 5.21. For E_1, $E_1 + \Delta_1$, E_0', E_2 transitions our experimental data are similar to those reported in [33, 79–81]. In a strong contrast to the behavior of E_- and E_+ absorption edges, the higher energy E_1, $E_1 + \Delta_1$, E_0', and E_2 transitions show a very weak linear dependence on the N content. This behavior can be well understood within virtual crystal approximation that accounts for the small gradual shift of the transition energy with the N content. The linear extrapolations of the energies of E_1 and E_2 transitions agree reasonably well with the energies of about 6 eV predicted for the both transitions in cubic GaN [82]. Also the energy positions of the valence bands are unchanged. We found that the values of the Δ_{so} (the spin–orbit splitting) and Δ_1 (the Γ_8 valence band splitting in direction to L minimum) remain constant with the N content and are equal to the 0.34 eV and 0.25 eV, respectively.

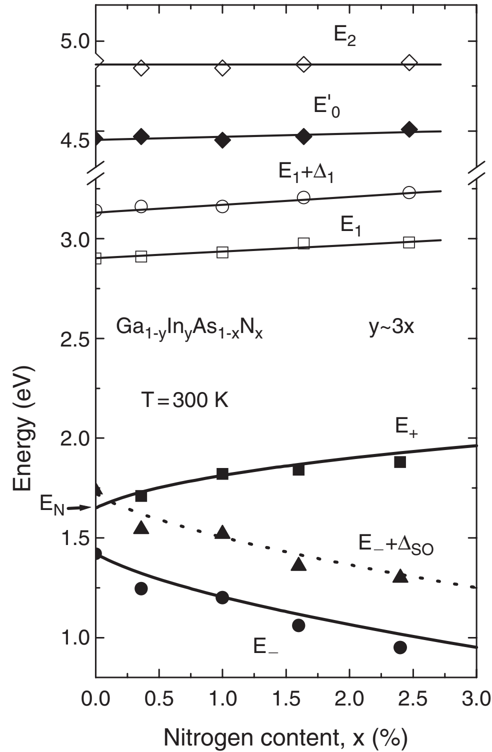

Fig. 5.21. Composition dependence of E_-, $E_- + \varDelta_{\mathrm{so}}$, and E_+ transitions measured in transmission and E_1, $E_1 + \varDelta_1$, E_0^*, E_2 obtained from spectroscopic ellipsometry

5.5 Effective g^*-Factors for Electrons and Holes

Application of the magnetic field allows obtaining information about the spin splitting of the conduction and valence bands of GaInNAs. The spin splitting of the conduction and valence bands is described by their g^*-factors. The knowledge of the band g^*-factors is highly interesting for a theoretical description and for practical applications (like spintronics). In this section, we present the experimental data of the Zeeman splitting determination and the Landé effective g^*-factors for conduction (E_- and E_+) and valence (Γ_7 and Γ_8) bands in GaInNAs alloys in magnetic fields up to 6 T [62, 71]. We analyzed the experimental results within the new six-level $\boldsymbol{k} \cdot \boldsymbol{p}$ model, which accounts for the nitrogen-induced E_- and E_+ bands. Our model describes the band structure in the external magnetic field, which allows to calculate the spin splitting of the conduction and valence bands in GaInNAs.

For magneto-optical experiments we used the same set of free – standing samples as for transmission (described in Sect. 5.3). The magneto absorption experiments were carried out in an optical cryostat supplied with a

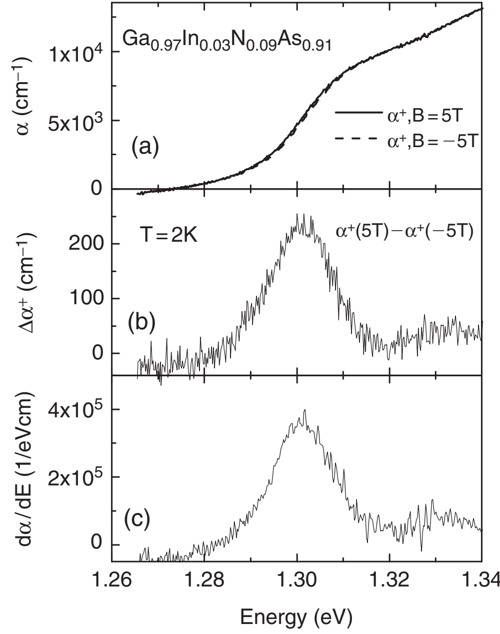

Fig. 5.22. (**a**) Absorption of the GaInNAs for circular polarized light for magnetic fields 5 T and −5 T, respectively; (**b**) difference between circular polarized light absorption for 5 T and −5 T; (**c**) derivative of the absorption coefficient

6 T superconducting split coil and a spectrometer with a charged coupled device (CCD) detector. The samples were immersed directly in the pumped liquid helium at $T = 2$ K and sample surface was perpendicular to the direction of the magnetic field. A beam of the incident light, polarized circularly in the magneto absorption experiment, was directed parallel to the magnetic field. A quartz linear polarizer was combined with a Fresnel $\lambda/4$ rhomb and both circular polarizations were detected by inversion of the magnetic field.

Figure 5.22a shows the absorption coefficient of $Ga_{0.97}In_{0.03}N_{0.09}As_{0.91}$ for a circularly polarized light, α^+, for the magnetic field strength of $B = 5$ T and $B = -5$ T, respectively. This type of experiment is equivalent to measurements of the absorption coefficient of the right, α^+, and the left, α^-, circularly polarized light without changing the orientation of the magnetic field. As it is evidenced, there is a small energy shift between these spectra. It is a result of the spin splitting of the conduction and the valence bands induced by the magnetic field. The energy shift, ΔE_Z, between the two spectra is given by

$$\Delta E_z = (g_e^* + g_v^*)\,\mu_B B, \tag{5.13}$$

where $g_e{}^*$ and $g_v{}^*$ are g-factors describing the spin splitting of the CB (E_- band) and the valence band (Γ_8), respectively. The Zeeman splitting, ΔE_Z,

Table 5.2. Zeeman splitting, ΔE, and the effective g-factor, $g_e{}^* + g_v{}^*$, for the fundamental transition in GaInNAs with different In and N content

N content (%)	In content (%)	ΔE (meV T^{-1})	$g_e^* + g_v^*$
0	0	–	$-2,1^{[*]}$
0.4	3	$-0.11 \pm 0,01$	-1.9 ± 0.2
0.9	3	-0.128 ± 0.01	-2.2 ± 0.2
1	4	-0.132 ± 0.01	-2.3 ± 0.2
1.6	5	-0.15 ± 0.01	-2.6 ± 0.2

[*] Data for GaAs – after Ref. 83.

can be calculated according to the following expression:

$$\Delta E_Z = \frac{\alpha^+(B) - \alpha^+(-B)}{d\alpha^+/dE}, \tag{5.14}$$

where $d\alpha^+/dE$ is the derivative of the absorption coefficient, $\alpha^+(B)$ and $\alpha^+(-B)$ is the absorption for the magnetic field B and $-B$, respectively. As it is seen in Figs. 5.22b,c, for energies around 1.3 eV, i.e., in the energy range corresponding to the maximum splitting between the absorption edges, $\alpha^+(5\text{T})$ and $\alpha^+(-5\text{T})$, we observe a maximum of $\Delta\alpha^+ = \alpha^+(B) - \alpha^+(-B)$ and $d\alpha^+/dE$. The value of $|\Delta E_Z|$ for $Ga_{0.97}In_{0.03}N_{0.09}As_{0.91}$ obtained from $\Delta\alpha^+/(d\alpha^+/dE)$ for $E = 1.30$ eV is $0.64 \pm 0,05$ meV. Determination of ΔE_Z is discussed in a more details in [62, 71].

Experimental results for different N content (up to 1.6%) are collected in Table 5.2. We indicated there also the value obtained for GaAs in [83] ($g^*_{\text{eff}} = g_e{}^* + g_v{}^* = -2.1$). We will consequently assume that the energy splitting of the fundamental transition in GaInNAs compounds, in N and In content of interest, is described by a negative effective g^*-factor, g^*_{eff}, as it is in the case of GaAs. The sign of ΔE_Z was deduced from the fact that it is negative for GaAs, and in the case of GaInNAs with low N and In content, the main contribution to g^*_{eff} comes from the negative valence band g-factor, $g_v{}^*$.

To have some insight to the effective g-factors for other optical transitions (see Figs. 5.3 and 5.24), we performed similar experiments on a thin (1.87 µm) $Ga_{0.96}In_{0.04}N_{0.01}As_{0.99}$ layer in a wide range of energies (from 1.2 up to 2 eV). This layer was attached to a sapphire holder with glue. In Fig. 5.23 we present the absorption spectra together with $\Delta\alpha(E)$ and $d\alpha^+/dE$. To make observed effects more visible, we multiplied $\Delta\alpha$ by the factor of 5 in the energy range 1.7–2 eV. We would like to stress two striking features observed in $\Delta\alpha(E)$ (Fig. 5.23b):

I. $\Delta\alpha$ around 1.87 eV (for transition $\Gamma_8 \rightarrow E_+$) has the opposite sign in comparison with $\Delta\alpha$ for transitions around 1.3 eV ($\Gamma_8 \rightarrow E_-$) and 1.64 eV ($\Gamma_7 \rightarrow E_-$). This means that g^*-factor for E_+ has the *opposite sign* than that for E_-

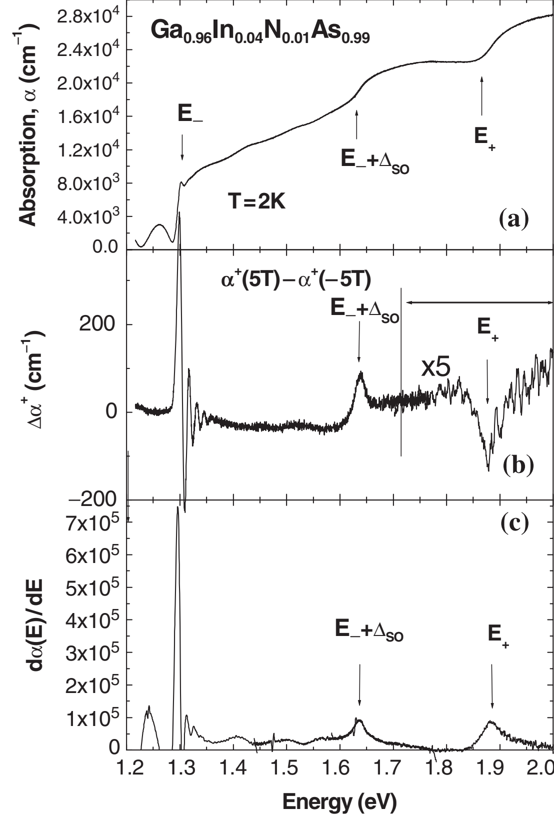

Fig. 5.23. (**a**) Absorption of thin $Ga_{0.96}In_{0.04}N_{0.01}As_{0.99}$ layer. Positions of the energy gap E_-, transition from Γ_7 valence band to E_-, $E_- + \Delta_{so}$, and transition from Γ_8 to E_+ for GaInNAs are indicated by the arrows, (**b**) difference between absorption for 5 T and −5 T, (**c**) derivative of the absorption coefficient

II. For the fundamental transition around 1.3 eV, oscillations of $\Delta\alpha$ appear. This effect is related with transitions between Landau levels from the valence and conduction bands (it is discussed in detail in [62]).

For the theoretical description, we introduced into the $\boldsymbol{k}\cdot\boldsymbol{p}$ Hamiltonian the interaction due to the N-related a_1 resonant states. The energy of electron states in GaInNAs is calculated using a six-level $\boldsymbol{k}\cdot\boldsymbol{p}$ model, which couples the five-level $\boldsymbol{k}\cdot\boldsymbol{p}$ model with terms connected with N related band. The applied five-level $\boldsymbol{k}\cdot\boldsymbol{p}$ model (derived in [84]) includes exactly the Γ_7^v, Γ_8^v, Γ_6^c, Γ_7^c, Γ_8^c levels in the $\boldsymbol{k}\cdot\boldsymbol{p}$ description and involves approximately, as second order terms of perturbation theory, far-level contributions. These additional elements are based on F, N_1, and modified Luttinger ($\gamma^{L_i} \rightarrow \gamma_i$) parameters, which result from far-level interaction with Γ_8^c conduction and Γ_8^V valence level, respectively. Below we show the scheme of transition from five-level to six-level $\boldsymbol{k}\cdot\boldsymbol{p}$ model for B = 0.

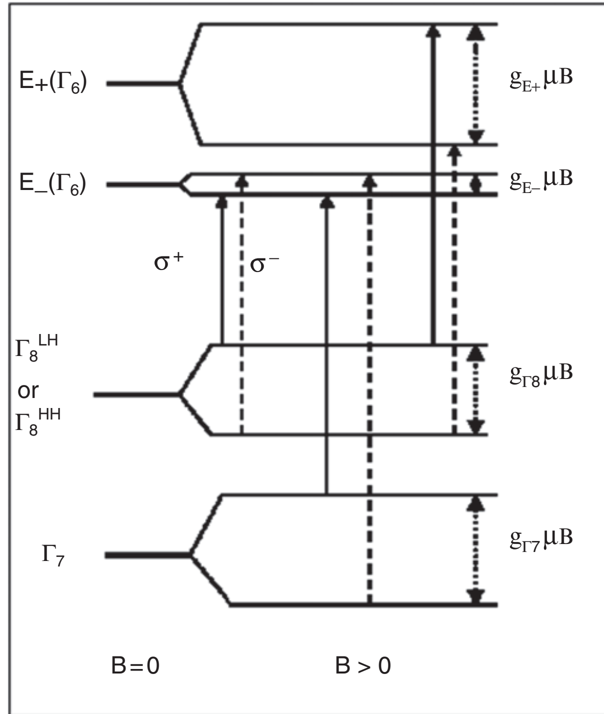

Fig. 5.24. Schematic diagram of GaInNAs band near $k = 0$ without and with magnetic field B. Solid and dashed arrows indicate the optical transitions for left and right circularly polarized light. $\Gamma_8{}^{LH}$ and $\Gamma_8{}^{HH}$ stands for light and heavy hole Γ_8 valence band

$$\left(\begin{array}{cccccccccccccc|cc}
 & & & & & & & & & & & & & & 0 & 0 \\
 & & & & & & & & & & & & & & 0 & 0 \\
 & & & & & & & & & & & & & & 0 & 0 \\
 & & & & & & & & & & & & & & A_{4,15}(N) & 0 \\
 & & & & & & & & & & & & & & 0 & 0 \\
 & & & & & & & & & & & & & & 0 & 0 \\
 & & & & & & 14\times 14 & & & & & & & & 0 & 0 \\
 & & & & & & & & & & & & & & 0 & 0 \\
 & & & & & & & & & & & & & & 0 & 0 \\
 & & & & & & & & & & & & & & 0 & 0 \\
 & & & & & & & & & & & & & & 0 & A_{11,16}(N) \\
 & & & & & & & & & & & & & & 0 & 0 \\
 & & & & & & & & & & & & & & 0 & 0 \\
 & & & & & & & & & & & & & & 0 & 0 \\
\hline
0 & 0 & 0 & A_{15,4}(N) & 0 & 0 & 0 & 0 & 0 & 0 & 0 & 0 & 0 & 0 & A_{15,15}(N) & 0 \\
0 & 0 & 0 & 0 & 0 & 0 & 0 & 0 & 0 & 0 & A_{16,11}(N) & 0 & 0 & 0 & 0 & A_{16,16}(N)
\end{array}\right) \tag{5.15}$$

The 14×14 matrix for five-level $\boldsymbol{k} \cdot \boldsymbol{p}$ model (see [84]) completed by the terms connected with the N band is resulting in the 16×16 matrix, where

$$A_{15,15} = A_{16,16} = E_{\mathrm{N}} + \hbar^2 k^2 / 2m_0$$

and

$$A_{15,4} = A_{16,11} = A_{4,15} = A_{11,16} = C_{\mathrm{MN}}\sqrt{x}.$$

To find electron energy in the presence of the magnetic field we use, starting from the initial matrix, the method of Evtuhov [85], which means that for $\mathbf{B}||[001]$ and $k_{\mathrm{z}} = 0$ the calculation amounts to diagonalization of 40×40 matrices for both spins of conduction states, respectively. The 40×40 matrix is created by 8×8 matrices, each one for the different set of spin and Landau level (LL) number, coupled by terms proportional to $\gamma_2 - \gamma_3$ or matrix element Q. The basic 8×8 matrix of six-level $\boldsymbol{k} \cdot \boldsymbol{p}$ model includes (see scheme below) matrix 7×7 (five-level $\boldsymbol{k} \cdot \boldsymbol{p}$ model, [84]) and N terms.

$$\left(\begin{array}{ccccccc|c} & & & & & & & 0 \\ & & & & & & & 0 \\ & & & & & & & 0 \\ & & & 7\times7 & & & & \mathrm{A}_{4,8}(\mathrm{N}) \\ & & & & & & & 0 \\ & & & & & & & 0 \\ & & & & & & & 0 \\ \hline 0 & 0 & 0 & \mathrm{A}_{8,4}(\mathrm{N}) & 0 & 0 & 0 & \mathrm{A}_{8,8}(\mathrm{N}) \end{array}\right) \tag{5.16}$$

The presence of the nitrogen band E_{N} states in the basic 8×8 matrix (which accounts for the isotropic approximation and is soluble in terms of eight harmonic oscillator functions) is introduced as the term $A_{8,8}$, $A_{8,8} = E_{\mathrm{N}} + \mu_{\mathrm{B}} B(2n+1) + s\mu_{\mathrm{B}} B$, which interacts by the term $A_{4,8} = C_{\mathrm{MN}}\sqrt{x}$, with s-type functions of the conduction band, i.e., with the term $A_{4,4}$, $A_{4,.4} = (2F+1)\mu_{\mathrm{B}} B(2n+1) + s(2N_1+1)\mu_{\mathrm{B}} B$, where s, $s = \pm 1$, depends on the conduction states spin and n is LL number. The values of parameters for $\mathrm{Ga}_{0.96}\mathrm{In}_{0.04}\mathrm{NAs}$ used in the calculations are given in Table 5.3.

To introduce the band anticrossing interaction in our model we took established values of C_{MN} and E_{N} parameters, which well describe the CB peculiarities observed in PL or PR experiments (see Table 5.1). Other parameters are as the same as for GaInAs. We would like to stress here that presence of nitrogen influences mostly the Γ_6 band leaving other bands almost unchanged.

5.5.1 Effective g^*-Factor for the E_- Conduction Band

In our experiments we determined the effective g^*_{eff}-factor that is the sum of the electron and hole g^*-factors, $g^*_{\mathrm{eff}} = g^*_{\mathrm{e}} + g^*_{\Gamma_8}$. We showed already that the presence of nitrogen does not affect the valence bands, e.g., the valence-band spin–orbit splitting does not depend on N content [50]. This enables us to

Table 5.3. The values of parameters for $Ga_{0.96}In_{0.04}NAs$ used in the calculations

E_{P_0}	27.592 eV
E_{P_1}	2.128 eV
E_Q	15.56 eV
F	−1.257
N_1	−0.0036
γ_1^L	6.85
γ_2^L	2.1
γ_3^L	2.9
χ^L	1.105
E_0	−1.458 eV
$E_0 + \Delta_0$	−1.8006 eV
E_1	3.011 eV
$E_1 + \Delta_1$	3.182 eV
Δ^-	−0.061 eV
E_N	1.72 eV (relative to Γ_8 VB edge)
C_{MN}	2.7 eV

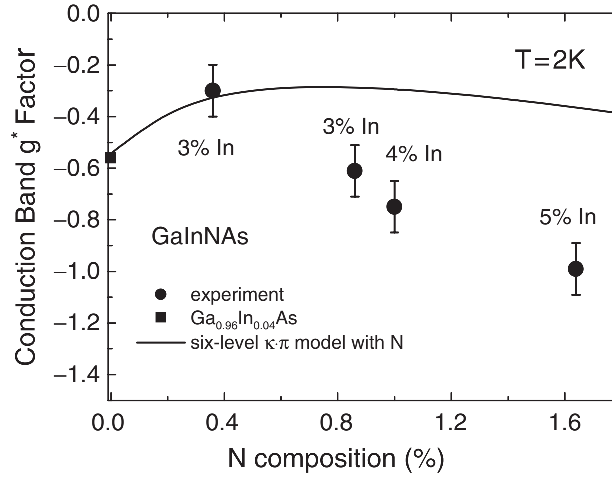

Fig. 5.25. The conduction band g^*_{E-}-factor for GaInNAs as a function of N content. *Dots* – experimental data. Near each point, the In content is indicated. Solid line shows the behavior of conduction band g-factor calculated in six-level $\boldsymbol{k} \cdot \boldsymbol{p}$ model for $Ga_{0.96}In_{0.04}N_xAs_{1-x}$

assume that $g^*_{\Gamma_8}$ does not depend on N (up to 1.6%) and In (up to 5%) content and $g^*_{\Gamma_8} = -1.6$ (i.e., is equal to that of Γ_8 heavy holes in GaAs [83, 86]). The dots in Fig. 5.25 present the values of the effective electron g^*-factor for the E_- band, $g^*_{E_-}$, extracted from the Zeeman splitting in GaInNAs (with the assumption that $g^*_{\Gamma_8} = -1.6$). We observe an increase and then a decrease

of the $g^*_{E_-}$ as a function of the N content. Also our six-level $\boldsymbol{k}\cdot\boldsymbol{p}$ model reproduces this unusual behavior – see solid line in Fig. 5.25.

To give a deeper insight into the physical meaning of our results we plot the electron effective $g^*_{E_-}$ factor as a function of the energy gap (dots in Fig. 5.26). In general, according to three- or five-level $\boldsymbol{k}\cdot\boldsymbol{p}$ models, the electron g^*_{e} factor in conventional III–V (or II–VI) compounds is defined by the following equation:

$$g^*_{\mathrm{e}} = g_0 + A_{\mathrm{so}} + C, \tag{5.17}$$

where g_0 ($g_0 = 2$) is the free-electron Landé g-factor; A_{so} and C are terms related to the spin–orbit interaction within three- (five-) level $\boldsymbol{k}\cdot\boldsymbol{p}$ model and far bands, respectively. The A_{so} term depends on relative positions of the conduction and valence bands and in all III–V (and II–VI) compounds is always negative [87, 88]. The C constant, negligible in comparison with A_{so}, in most semiconductors is equal to -0.04 [87, 88].

According to the above arguments, the effective g^*_{e}-factor in III–V compounds is smaller than 2 (e.g., $g^*_{\mathrm{e}} = 1.26$ for InP [88]) and becomes smaller, and even negative, as the fundamental gap is shrinking (e.g., $g^*_{\mathrm{e}} = -0.51$ for InSb [88]). For a small energy gap material, the spin–orbit interaction is more effective and therefore A_{so} term (which is negative) becomes more dominant. Indeed, when we plot results of the five-level $\boldsymbol{k}\cdot\boldsymbol{p}$ model vs. energy gap (see dashed line in Fig. 5.26) the strong decrease of the g^*_{e} factor ($g^*_e = -3.25$ for the energy gap of 1.2 eV) is observed. Such behavior (i.e., a monotonic decay) of the g^*_{e} factor was found for GaInAs compound [89] – see squares in Fig. 5.26. On the other hand, our six-level $\boldsymbol{k}\cdot\boldsymbol{p}$ model with the additional E_+ band shows that the value of the effective electron $g^*_{E_-}$ factor in GaInNAs

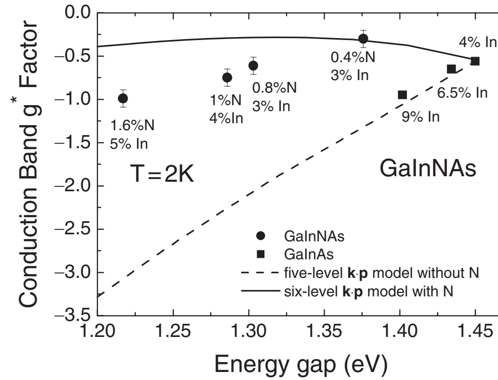

Fig. 5.26. The conduction band $g^*_{E_-}$-factor for GaInNAs (*dots*) and for GaInAs (*squares*; after [89]) vs. energy gap. The N and In content for these alloys is indicated near each experimental point. *Solid line* – $g^*_{E_-}$-factor behavior of $\mathrm{Ga_{0.96}In_{0.04}N_{\mathit{x}}As_{1-\mathit{x}}}$ CB from six-level $\boldsymbol{k}\cdot\boldsymbol{p}$ model (with N). *Dashed line* – g^*-factor behavior from five-level $\boldsymbol{k}\cdot\boldsymbol{p}$ model (with parameters of $\mathrm{Ga_{0.96}In_{0.04}As}$) where energy gap was varied in the range 1.2–1.45 eV.

(for E_- band) increases when the energy gap is decreasing down to about 1.3 eV (see solid line in Fig. 5.26). This means that the $g^*_{E_-}$ is influenced by an additional term (we named it B_{BAC}):

$$g^*_{E_-} = g_0 + A_{\mathrm{so}} + B_{\mathrm{BAC}} + C \tag{5.18}$$

The B_{BAC} term is related to the band anticrossing interaction and *increases* the value of the effective $g^*_{E_-}$ factor. Both effects, the spin–orbit (A_{so}) and the band anticrossing (B_{BAC}) interactions having the same strength and the opposite sign, result together in moderate changes of $g^*_{E_-}$ observed in the experiment. On the basis of our $\boldsymbol{k} \cdot \boldsymbol{p}$ model, we are able to explain quantitatively the behavior of the CB Zeeman splitting in GaInNAs. We notice here that in addition to an unusual CB g^*-factor behavior, the BAC interaction in GaInNAs *increases* the value of the m^* at the bottom of CB while *decreases* the fundamental energy gap – contrary to the common rule that lower energy gap material has a lower CB effective mass [84]. At this context, the experimental results for the electron effective $g^*_{E_-}$-factor, which is unusual for "normal" semiconductors, becomes more understandable since both $g^*_{E_-}$ and m^* depend on a combination of the same matrix elements [87]. We will return to this point in the paragraph where the CB edge effective mass in connection with effective g^*-factor is discussed.

5.5.2 Effective g^*-Factors for the E_+ Conduction Band and the Valence Bands

For free standing GaInNAs layer we were able to measure not only the fundamental energy gap optical transition ($\Gamma_8 \rightarrow E_-$), but other transitions as well, namely $\Gamma_8 \rightarrow E_+$, $\Gamma_7 \rightarrow E_-$, as shown in Fig. 5.23. In Table 5.4 the experimental data resulting from the Zeeman splitting for different optical transitions for (001) $\mathrm{Ga_{0.96}In_{0.04}N_{0.01}As_{0.99}}$ are presented.

The values for $g^*_{\Gamma_8}$ (HH) + $g^*_{E_-} = -2.3 \pm 0.2$ and $g^*_{\Gamma_7}$ (HH) + $g^*_{E_-} = -5.6 \pm 0.4$ are very close to the experimental data obtained for GaAs ($g^*_{\Gamma_8}$ (HH) is the g^*-factor for heavy hole (HH) Γ_8 valence band) [83, 86, 90]. Taking $g^*_{\Gamma_8} = -1.6$, $g^*_{\Gamma_7} = -4.9$ the effective g^*-factor for E_- band is equal to -0.7, which well fits to the $g^*_{E_-}$ dependence vs. N content (see Fig. 5.25). From

Table 5.4. Zeeman splitting, ΔE, and the effective g-factor, $g_{\mathrm{e}}{}^* + g_{\mathrm{v}}{}^*$, for different optical transitions observed in magneto absorption experiment in $\mathrm{Ga_{0.96}In_{0.04}N_{0.01}As_{0.99}}$

Optical transition	ΔE (meV T^{-1})	$g_{\mathrm{e}}{}^* + g_{\mathrm{v}}{}^*$
Γ_8 (HH) $\rightarrow E_-$	-0.136 ± 0.01	-2.3 ± 0.2
$\Gamma_7 \rightarrow E_-$	-0.33 ± 0.02	-5.6 ± 0.4
Γ_8 (HH) $\rightarrow E_+$	$+0.07 \pm 0.03$	$+1.2 \pm 0.6$

Table 5.4 we can extract the electron g^*-factor for E_+ bands, $g^*_{E_+} = +2.8 \pm 0.8$. Surprisingly, its value is positive and very large. From our six-level $\boldsymbol{k} \cdot \boldsymbol{p}$ model this value is around 1.54. The positive value of the g^*-factor for the E_+ band originates from a large distance of this band to the valence band (and therefore A_{so} term is small) and an additional B_{BAC} interaction due to presence of nitrogen. The experimental values of the g^*-factors for the conduction E_+, E_- and valence Γ_7, Γ_8 bands in GaInNAs together with available literature data for $Ga_{0.96}In_{0.04}As$ and GaAs are collected in Table 5.5. We calculated the effective g^*-factors for all bands using five- and six-level $\boldsymbol{k} \cdot \boldsymbol{p}$ models. First, we tested the five-level $\boldsymbol{k} \cdot \boldsymbol{p}$ model on GaAs and $Ga_{0.96}In_{0.04}As$ conventional semiconductors. Since the agreement between experimental data is sound, we therefore use parameters of the five-level model in the six-level $\boldsymbol{k} \cdot \boldsymbol{p}$ model (with $E_{\text{N}} = 1.72\,\text{eV}$, and $C_{\text{MN}} = 2.7\sqrt{x}$ eV). Table 5.5 contains data for g^*-factors calculated according the six-level (for GaInNAs) and five-level (for GaAs and GaInAs) $\boldsymbol{k} \cdot \boldsymbol{p}$ models for magnetic field $B = 0.01\,\text{T}$ and $B = 5\,\text{T}$.

5.5.3 Electron Effective Mass at the Bottom of the E_- Band

In general, within the framework of $\boldsymbol{k} \cdot \boldsymbol{p}$ perturbation theory, the effective mass and the Landé g^*-factor at a given band minimum depend on the same energy gaps and matrix elements [86–88]; e.g., for a cubic semiconductor, at $k = 0$, the x component of the CB effective mass m_x^* is given by

$$\frac{m_0}{m_x^*} = 1 + \sum_i \frac{\left|\langle S\,|p_x|\,P_i\rangle\right|^2}{E_{\text{c}} - E_i}, \tag{5.19}$$

where m_0 is the free electron mass, E_{c} and S are the CB energy and wave function, P_i is the ith wave function at the band edge related to E_i energy state, p_x is the x component of the momentum operator [87]. The Landé g^*-factor for the same conditions is given by

$$\frac{g^*}{g_0} = 1 + \frac{1}{\mathrm{i}m_0} \sum_i \frac{\langle S\,|p_x|\,P_i\rangle\,\langle P_i\,|p_y|\,S\rangle - \langle S\,|p_y|\,P_i\rangle\,\langle P_i\,|p_x|\,S\rangle}{E_{\text{c}} - E_i}, \tag{5.20}$$

where $g_0 = 2$ is the free electron Landé factor [87].

Since our six-level $\boldsymbol{k} \cdot \boldsymbol{p}$ model well describes the g^*-factor behavior we decided to calculate (with the same parameters as for the g^*-factor calculations) the effective mass behavior at the bottom of the CB and compare it with the recent experimental and theoretical findings. In Fig. 5.11 (see Sect. 5.2) we show the effective mass dependence as a function of the N content calculated from the six-level $\boldsymbol{k} \cdot \boldsymbol{p}$ models as a solid line. The six-level $\boldsymbol{k} \cdot \boldsymbol{p}$ model qualitatively agrees with ab initio calculations [51] (i.e., predicts a decrease of the electron effective mass for N composition higher than 2%) and gives almost the same N dependence as the tight binding model [72].

To give more insight to the effect of the BAC interaction on the effective mass enhancement at the bottom of the CB we plot in Fig. 5.27 the effective

Table 5.5. Effective g^*-factors in $Ga_{0.96}In_{0.04}N_{0.01}As_{0.99}$ for the conduction E_- ($g^*_{E_-}$), E_+ ($g^*_{E_+}$) and valence Γ_7 ($g^*_{\Gamma_7}$), Γ_8 ($g^*_{\Gamma_8}$) bands determined with an assumption that $g^*_{\Gamma_8}$ is equal to -1.6 (i.e., the same as for GaAs)

	$Ga_{0.96}In_{0.04}N_{0.01}As_{0.99}$			$Ga_{0.96}In_{0.04}As$			GaAs		
	Exp. $B = 5\,T$	Theory $B = 0.01\,T$	Theory $B = 5\,T$	Exp.	Theory $B = 0.01\,T$	Theory $B = 5\,T$	Exp. $B = 0.01\,T$	Theory $B = 5\,T$	Theory
g^*_{E+}	$+2.8 \pm 0.8$	$+1.547$	$+1.54$	–	–	–	–	–	–
g^*_{E-}	-0.7 ± 0.2	-0.284	-0.19	-0.58^a	-0.62	-0.48	-0.44^b	-0.44	-0.37
$g^*_{\Gamma 8}$(HH)	-1.6	-2.27	-2.2	–	-2.2	-2.17	-1.6^c	-2.2	-2.2
$g^*_{\Gamma 8}$(LH)	–	-14.9	-14.6	–	-14.5	-14.2	–	-14.5	-14.2
$g^*_{\Gamma 7}$	-4.9 ± 0.6	-4.35	-4.87	–	-4.2	-4.6	-4.3^d	-4.3	-4.8

The effective g^* factors were calculated according to six-level (for GaInNAs) and five-level (for GaAs and GaInAs) $\boldsymbol{k} \cdot \boldsymbol{p}$ models for magnetic field $B = 0.01$ and $5\,T$, respectively.

The existent experimental data for $Ga_{0.96}In_{0.04}As$ and GaAs is also given.

[a] After [89].

[b] After [86].

[c] After [83] ($g^*_e + g^*_{\Gamma_8} = -2.1$) and [86].

[d] After [90] ($g^*_e + g^*_{\Gamma_7} = -4.9$) and [86].

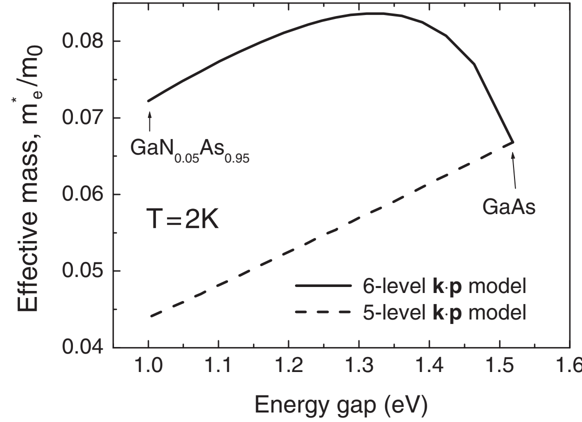

Fig. 5.27. The effective mass, $m_e{}^*$, at the bottom of conduction band in GaN_xAs_{1-x} as a function of the energy gap. *Solid line* – six-level $\boldsymbol{k}\cdot\boldsymbol{p}$ model for GaN_xAs_{1-x}. *Dashed line* – five-level $\boldsymbol{k}\cdot\boldsymbol{p}$ model (with parameters of GaAs) where energy gap was varied in the range 1–1.54 eV

mass dependence (solid line) as a function of the energy gap for GaN_xAs_{1-x} derived from the six-level $\boldsymbol{k}\cdot\boldsymbol{p}$ model (the energy gap of GaN_xAs_{1-x} changes from 1 eV for $GaN_{0.05}As_{0.95}$ to 1.54 eV for GaAs). Dashed line in this figure shows a result from the five-level $\boldsymbol{k}\cdot\boldsymbol{p}$ model (with GaAs parameters) where the energy gap was varied in the range 1–1.54 eV. Similar to the effective g^*-factor dependence (see Fig. 5.26), the effective mass first increases and then gradually decreases for the energy gap smaller than 1.3 eV. The difference between the solid and dashed lines is the effective mass enhancement due to the BAC interaction. Below 1.3 eV (i.e., for N content higher than 1%) this difference saturates at the level of $0.028\,m_0$. This means that for N composition higher than 1%, the BAC interaction starts to be compensated by spin–orbit term and the effective mass is equal to $m^*(E_g) + 0.028\,m_0$, where $m^*(E_g)$ can be approximated by the effective mass for a conventional semiconductor with energy gap E_g (like for GaInAs).

5.6 Conclusions

In this chapter we provided systematic study of technological important parameters of GaInNAs alloys, like energy gap, effective mass, effective g^*-factors, intensity of the interband transitions, positions of conduction, and valence bands. Our experimental results show that incorporation of few percent of N in GaInNAs alloys lead to drastic modification of the conduction band density of states close to the Γ point of Brillouin zone. We found highly nonparabolic behavior of conduction band leading to giant increase of the effective mass (as large as $0.4\,m_0$) for high electron densities. The moderate

(and nonmonotonic, with the maximum of $0.12\,m_0$ for 1–2% of N) dependence of the effective mass as a function of N content at the bottom of CB is postulated. A clear evidence in absorption experiments for additional density of states, responsible for E_+ transition, is given. In contrast, the energies of the higher lying L and X minima are not significantly affected by these small amounts of nitrogen. The variation of the energies of L and X minima with N-content can be well understood within the virtual crystal approximation for GaInNAs alloys. The results also show that incorporation of N does not have any significant effect on the valence band structure as exemplified by a constant N-independent value of the $\Delta_{\rm so}$ (spin–orbit splitting) and Δ_1. We found that presence of N in GaInNAs introduces an interaction, which increases the value of effective g^* factor for E_- band, $g^*_{E_-}$. We developed the six-level $\boldsymbol{k}\cdot\boldsymbol{p}$ model, which can be used for a description of the experimental data for diluted nitrides with and without the magnetic field. This model confirmed quantitatively the unusual $g^*_{E_-}$ dependence on N content and also accounts for the effective mass enhancement when the energy gap is shrinking (or N content is increasing) in GaInNAs. A very high and positive g^* factor was found for the E_+ band: $g^*_{E_-} = +2.8 \pm 0.8$ (experiment) $g^*_{E+} = 1.54$ (six-level $\boldsymbol{k}\cdot\boldsymbol{p}$ theory). We attribute it to a small contribution of the spin–orbit interaction to the $g^*_{E_+}$ for the E_+ band. We demonstrated that for alloy limit of GaInNAs (i.e., N content higher than 0.6%) variety of experimental data can be successfully described by ab initio calculations and by the two-level band anticrossing phenomenological model (and its generalizations, like the six-level $\boldsymbol{k}\cdot\boldsymbol{p}$ theory). This will require further studies in understanding the microscopic origin of the GaInNAs band structure formation and interpretation of the nature of the nitrogen induced a_1 symmetry state in GaAs:N.

Acknowledgments. I am grateful to P. Perlin, P. Wiśniewski, T. Suski, J. Łusakowski, W. Knap, A. Witowski, J. Borysiuk, K. Hingerl, W. Jantsch, W. Shan, K. M. Yu, J.W. Ager, and E.E. Haller for help in experimental part of this work. I thank P. Pfeffer, S. Łepkowski, and I. Gorczyca for their contribution in theoretical calculations. I express my special thanks to W. Walukiewicz, J. Majewski, P. Bogusławski, and J. Gaj for stimulating discussions. I am also extremely grateful to J. Geisz, J.M. Olson, S.R. Kurtz, J. Toivonen, and D. Mars for MOVPE and MBE samples.

References

1. M. Weyers, M. Sato, H. Ando, Jpn. J. Appl. Phys. **31**, L853 (1992)
2. W. Su-Huai, A. Zunger, Phys. Rev. Lett. **76**, 664 (1996)
3. M. Kondow, K. Uomi, K. Hosomi, T. Mozume, Jpn. J. Appl. Phys. **33**(Part 2), L1056 (1994)
4. K. Uesugi, N. Marooka, I. Suemune, Appl. Phys. Lett. **74**, 1254 (1999)
5. N. Baillargeon, K.Y. Cheng, G.F. Hofler, P.J. Pearah, K.C. Hsieh, Appl. Phys. Lett. **60**, 2540 (1992)

6. W.G. Bi, C.W. Tu, Appl. Phys. Lett. **69**, 3710 (1996)
7. W.G. Bi, C.W. Tu, J. Appl. Phys. **80**, 1934 (1996)
8. K.M. Yu, W. Walukiewicz, J. Wu, J.W. Beeman, J.W. Ager, E.E. Haller, W. Shan, H.P. Xin, C.W. Tu, Appl. Phys. Lett. **78**, 1077 (2001)
9. J.C. Harmand, G. Ungaro, J. Ramos, E.V.K. Rao, G. Saint-Girons, R. Teissier, G. Le Roux, L. Largeau, G. Patriarche, J. Cryst. Growth **227–228**, 553 (2001)
10. B.N. Murdin, M. Karmal-Saadi, A. Lindsay, E.P. O'Reilly, A.R. Adams, G.J. Nott, J.G. Crowder, C.R. Pidgeon, I.V. Bradley, J.P.R. Wells, T. Burke, A.D. Johnson, T. Ashley, Appl. Phys. Lett. **78**, 1558 (2001)
11. S.R. Kurtz, A.A. Allerman, E.D. Jones, J.M. Gee, J.J. Banas, B.E. Hammons, Appl. Phys. Lett. **74**, 729 (1999)
12. A. Wagner, C. Ellmers, F. Hohnsdorf, J. Koch, C. Agert, S. Leu, M. Hofmann, W. Stolz, W.W. Ruhle, Appl. Phys. Lett. **76**, 271 (2000)
13. J.F. Geisz, D.J. Friedman, J.M. Olson, S.R. Kurtz, B.M. Keyes, J. Cryst. Growth **195**, 401 (1998)
14. I.A. Buyanova, W.M. Chen, B. Monemar, MRS Internet J. Nitride Semicond. Res. **6** 2 (2001)
15. S. Sakai, Y. Ueta, Y. Terauchi, Jpn. J. Appl. Phys. **32**(Part 1), 4413 (1993)
16. M.A. Ivanov, Y.G. Pogorelov, Zh. Eksp. Teor. Fiz. **76**, 1010 (Sov. Phys. JEPT **49**, 510) (1979)
17. A. Rubio, M.L. Cohen, Phys. Rev. B **51**, 4343 (1995)
18. J. Neugebauer, C.G. Van de Walle, Phys. Rev B **51**, 10568 (1995)
19. L. Bellaiche, S.H. Wei, A. Zunger, Phys. Rev. B **54**, 17568 (1996)
20. P. Perlin, S.G. Subramanya, D.E. Mars, J. Kruger, N.A. Shapiro, H. Siegle, E.R. Weber, Appl. Phys. Lett. **73** 3703 (1998)
21. W. Shan, W. Walukiewicz, J.W. Ager III, E.E. Haller, J.F. Geisz, D.J. Friedman, J.M. Olson, S.R. Kurtz, Phys. Rev. Lett. **82**, 1221 (1999)
22. E.D. Jones, N.A. Modine, A.A. Allerman, S.R. Kurtz, A.F. Wright, S.T. Tozer, X. Wei, Phys. Rev. B **60**, 4430 (1999)
23. J.D. Perkins, A. Mascarenhas, Y. Zhang, J.F. Geisz, D.J. Friedman, J.M. Olson, S.R. Kurtz, Phys. Rev. Lett. **82**, 3312 (1999)
24. W. Walukiewicz, W. Shan, J.W. Ager III, D.R. Chamberlin, E.E. Hailer, J.F. Geisz, D.J. Friedman, J.M. Olson, S.R. Kurtz, in *Proceedings of 195th Mtg. of the Electrochemical Society*, Seattle, WA, 1999, p. 190
25. W. Shan, W. Walukiewicz, K.M. Yu, J.W. Ager III, E.E. Haller, J.F. Geisz, D.J. Friedman, J.M. Olson, S.R. Kurtz, H.P. Xin, C.W. Tu, Phys. Status Solidi B **223**, 75 (2001)
26. P. Perlin, P. Wisniewski, C. Skierbiszewski, T. Suski, E. Kaminska, S.G. Subramanya, E.R. Weber, D.E. Mars, W. Walukiewicz, Appl. Phys. Lett. **76**, 1279 (2000)
27. J. Hader, S.W. Koch, J.V. Moloney, E.P. O'Reilly, Appl. Phys. Lett. **76**, 3685 (2000)
28. E.P. O'Reilly, A. Lindsay, Phys. Status Solidi B **216**, 131 (1999)
29. C. Skierbiszewski, Semicond. Sci. Technol. **17**, 803 (2002)
30. C. Skierbiszewski, P. Perlin, P. Wiśniewski, W. Knap, T. Suski, W. Walukiewicz, W. Shan, K.M. Yu, J.W. Ager, E.E. Haller, J.F. Geisz, J.M. Olson, Appl. Phys. Lett. **76**, 2409 (2000)
31. K.M. Yu, W. Walukiewicz, W. Shan, J.W. Ager III, J. Wu, E.E. Haller, J.F. Geisz, D.J. Friedman, J.M. Olson, Phys. Rev. B **61**, R13 337 (2000)

32. W. Shan, W. Walukiewicz, K.M. Yu, J. Wu, J.W. Ager III, E.E. Haller, H.P. Xin, C.W. Tu, Appl. Phys. Lett. **76**, 3251 (2000)
33. W. Shan, W. Walukiewicz, K.M. Yu, J.W. Ager III, E.E. Haller, J.F. Geisz, D.J. Friedman, J.M. Olson, S.R. Kurtz, C. Nauka, Phys. Rev. B **62**, 4211 (2000)
34. W. Walukiewicz, W. Shan, K.M. Yu, J.W. Ager III, E.E. Haller, I. Miotkowski, M.J. Seong, H. Alawadhi, A.K. Ramdas, Phys. Rev. Lett. **85**, 1552 (2000)
35. T. Mattila, S.-H. Wei, A. Zunger, Phys. Rev. B **60**, R11245 (1999)
36. L. Bellaiche, N.A. Modine, E.D. Jones, Phys. Rev. B **62**, 15311 (2000)
37. L.-W. Wang, Appl. Phys. Lett. **78**, 1565 (2001)
38. N. Gonzalez Szwacki, P. Bogusławski, Phys. Rev. B **64**, 161201 (2001)
39. P.R.C. Kent, A. Zunger, Phys. Rev. Lett. **86**, 2609 (2001)
40. A. Zunger, Phys. Status Solidi B **216**, 117 (1999)
41. I. Gorczyca, C. Skierbiszewski, T. Suski, N.E. Christensen, A. Svane, Phys. Rev. B **66**, 81106(R) (2002)
42. E.P. O'Reilly, A. Lindsay, S. Fahy, J. Phys. Condens. Matter **16**, S3257 (2004)
43. X. Liu, M.E. Pistol, L. Samuelson, S. Schwetlick, W. Seifert, Appl. Phys. Lett. **56**, 1451 (1990)
44. H.P. Hjalmarson, P. Vogl, D.J. Wolford, J.D. Dow, Phys. Rev. Lett. **44**, 810 (1980)
45. S. Francoeur, S.A. Nikishin, C. Jin, Y. Qiu, H. Temkin, Appl. Phys. Lett. **75**, 1538 (1999)
46. Y. Zhang, A. Mascarenhas, H.P. Xin, C.W. Tu, Phys. Rev. B **61**, 7479 (2000)
47. W.G. Spitzer, H,Y. Fan, Phys. Rev. **106**, 882 (1957)
48. P. Perlin. E. Litwin Staszewska, B. Suchanek, W. Knap, J. Camassel, T. Suski, R. Piotrzkowski, I. Grzegory, S. Porowski, E. Kaminska, J.C. Chervin, Appl. Phys. Lett. **68**, 1114 (1996)
49. J.S. Blackmore, J. Appl. Phys. **53**, R123 (1982)
50. C. Skierbiszewski, P. Perlin, P. Wisniewski, T. Suski, J. Geisz, K. Hingerl, W. Jantsch, D. Mars, W. Walukiewicz, Phys. Rev. B **65**, 35207 (2001)
51. C. Skierbiszewski, I. Gorczyca, S.P. Łepkowski, J. Łepkowski, J. Borysiuk, J. Toivonen, Semicond. Sci. Technol. **19**, 1189 (2004)
52. M. Methfessel, Phys. Rev. B **38**, 1537 (1988)
53. O.K. Andersen, Phys. Rev. B **12**, 3060 (1975)
54. I. Gorczyca, A. Svane, N.E. Christensen, Phys. Rev. B **60**, 8147 (1999)
55. A. Patane, J. Endicott, J. Ibanez, L. Eaves, J. Phys. Condens. Matter **16**, S3171 (2004)
56. J. Toivonen, T. Hakkarainen, M. Sopanen, H. Lipsanen, J. Cryst. Growth **221**, 456 (2000)
57. M.A. Pinault, E. Tournie, Appl. Phys. Lett. **78**, 1562 (2001)
58. J. Hader, S.W. Koch, J.V. Moloney, E.P. O'Reilly, Appl. Phys. Lett. **76**, 3685 (2000)
59. M. Galluppi, L. Geelhaar, H. Riechert, Appl. Phys. Lett. **86**, 131925 (2005)
60. W.H. Press, B.P. Flannery, S.A. Teukolsky, W.T. Vetterling, "Numerical Recipes, the Art of Scientific Computing" (Cambridge University Press, UK, 1986)
61. C. Skierbiszewski, S.P. Łepkowski, P. Perlin, T. Suski, W. Jantsch, J. Geisz, Physica E **13**, 1078 (2002)
62. C. Skierbiszewski, J. Lusakowski, J. Phys. Condens. Matter **16**, S3319 (2004)
63. Y.J. Wang, X. Wei, Y. Zhang, A. Mascarenhas, H.P. Xin, Y.G. Hong, C.W. Tu, Appl. Phys. Lett. **82**, 4453 (2003)

64. F. Masia, A. Polimeni, G. Baldassarri Hoger von Hogersthal, M. Bissiri, M. Capizzi, P.J. Klar, W. Stolz, Appl. Phys. Lett. **82**, 4474 (2003)
65. A. Polimeni, G. Baldassarri Hoger von Hogersthal, F. Masia, A. Frova, M. Capizzi, S. Sanna, V. Fiorentini, P.J. Klar, W. Stolz, Phys. Rev. B **69**, 41201 (2004)
66. P.N. Hai, W.M. Chen, I.A. Buyanova, H.P. Xin, C.W. Tu, Appl. Phys. Lett. **77**, 1873 (2000)
67. J. Wu, W. Shan, W. Walukiewicz, K.M. Yu, J.W. Ager III, E.E. Haller, H.P. Xin, C.W. Tu, Phys. Rev. B **64**, 85320 (2001)
68. P.J. Klar, H. Gruning, W. Heimbrodt, J. Koch, W. Stolz, S. Tomic, E.P. O'Reilly, Solid State Electron. **47**, 437 (2003)
69. R. Kudrawiec, K. Ryczko, J. Misiewicz, H.B. Yuen, S.R. Bank, M.A. Wistey, H.P. Bae, J.S. Harris Jr., Appl. Phys. Lett. **86**, 141908 (2005)
70. M.H. Gass, A.J. Papworth, T.B. Joyce, T.J. Bullough, P.R. Chalker, Appl. Phys. Lett. **84**, 1453 (2004)
71. C. Skierbiszewski, P. Pfeffer, J. Łusakowski, Phys. Rev. B **71**, 205203 (2005)
72. N. Shtinkov, P. Desjardins, R.A. Masut, Phys. Rev. B **67**, 81202(R) (2003)
73. C. Skierbiszewski, C. Perlin, P. Wisniewski, T. Suski, W. Walukiewicz, W. Shan, J.W. Ager, E.E. Haller, J.F. Geisz, D.J. Friedman, D.J. Olson, S.R. Kurtz, Phys. Status Solidi B **216**, 135 (1999)
74. E.D. Jones, N.A. Modine, A.A. Alerman, I.J. Fritz, S.R. Kurtz, A.F. Wright, S.T. Torez, X. Wei, Proc. SPIE **3621**, 52 (1999)
75. I. Gorczyca, N.E. Christensen, A. Svane, Solid State Comm. **136**, 439 (2005)
76. S. Kurtz, J.F. Geisz, D.J. Friedman, J.M. Olson, A. Duda, N.H. Karam, R.R. King, J.H. Ermer, D.E. Joslin, in *Proceedings of the 28th IEEE Photovoltaic Specialists Conference*, 2000, p. 1210
77. W. Shan, W. Walukiewicz, J.W. Ager, E.E. Haller, J.F. Geisz, D.J. Friedman J.M. Olson, S.R. Kurtz, J. Appl. Phys. **86**, 2349 (1999)
78. P. Lautenschlager, M. Garriga, S. Logothetidis, M. Cardona, Phys. Rev. B **35**, 9174 (1987)
79. H. Gruning, L. Chen, T. Hartman, P.J. Klar, W. Heimbrodt, F. Hohnsdorf, J. Koch, W. Stolz, Phys. Status Solidi B **215**, 39 (1999)
80. W.K. Hung, M.Y. Chern, Y.F. Chen, Z.L. Yang, S. Huang, Phys. Rev. B **62**, 13028 (2000)
81. G. Leibiger, V. Gottschalch, B. Rheinlander, J. Sik, M. Schubert, Appl. Phys. Lett. **77**, 1650 (2000)
82. A. Rubio, J.L. Corkill, M.L. Cohen, E.L. Shirley, S.G. Louie, Phys. Rev. B **48**, 11810 (1993)
83. M. Zwara, Phys. Status Solidi **36**, 785 (1969)
84. P. Pfeffer, W. Zawadzki, Phys. Rev. B **53**, 12813 (1996)
85. V. Evtuhov, Phys. Rev. **125**, 1869 (1962)
86. M. Oestreich, W.W. Ruhle, Phys. Rev. Lett. **74**, 2315 (1995)
87. L.M. Roth, B. Lax, S. Zwerdling, Phys. Rev **114**, 90 (1959)
88. C. Herman, C. Weisbuch, Phys. Rev. B **15**, 823 (1977)
89. C. Weisbuch, C. Herman, Phys. Rev. B **15**, 816 (1977)
90. M. Reine, R.L. Aggarwal, B. Lax, C.M. Wolfe, Phys. Rev. B **2**, 458 (1970)

6

Electromodulation Spectroscopy of GaInNAsSb/GaAs Quantum Wells: The Conduction Band Offset and the Electron Effective Mass Issues

J. Misiewicz, R. Kudrawiec, M. Gladysiewicz, and J.S. Harris

In the past few years, GaInNAsSb has been found to be a potentially superior material to GaInNAs for long wavelength laser applications. Since GaInNAsSb is relatively new, there has not been any detailed study of the band properties of GaInNAsSb/GaAs quantum wells. In this chapter the electromodulation spectroscopy to measure energies of quantum well transitions and one band approach to calculate the energy levels in these quantum wells are presented. The advantages of this simple approach are discussed in details. The conduction band offset in GaInNAsSb/GaAs quantum wells can be easily controlled by the change in the content of the quinary alloy is shown there. It means that GaInNAsSb/GaAs quantum wells are very promising for bandgap engineering since the bandgap discontinuity, strains, and the bandgap energy in this system can be controlled more independently than in ternary or quaternary quantum wells. Moreover, N-related increase in the electron effective mass is discussed in this work.

6.1 Introduction

The demonstration of bandgap narrowing in GaInAs with the introduction of nitrogen by Kondow et al. [1] has promoted intense research toward high-performance GaAs-based lasers for the fiber optic telecommunications windows (1.3 and 1.55 μm) [2, 3]. Recent progress on the use of GaInNAs for laser applications has succeeded in producing devices operating at 1.3 μm wavelength. Extending the operating wavelength to the C- and L-bands (1.53–1.6 μm) is very desirable but requires larger N and In concentrations in the quantum well (QW) compared with 1.3 μm-emitting QWs [4]. More recently, GaInNAsSb has been found to be potentially superior to GaInNAs for these applications [5–9], since higher quality material can be grown over QW compositions covering the entire telecommunications wavelength range and particularly at the longest wavelengths that were previously unattainable. The performances of GaInNAsSb lasers have been successfully developed

at Stanford University [10–13] and Gupta and coworkers at Institute for Microstructural Sciences of National Research Council of Canada [14, 15] as well as other researchers [16].

Despite strong progress in the development of devices, many fundamental material parameters, including the conduction band offset (Q_C) and the electron effective mass (m_e), remain unknown or are not fully understood. Knowledge of these parameters is of great significance for a full exploration and optimization of this material system for device applications. Electromodulation spectroscopy [photomodulated reflectance (PR) or contactless electroreflectance (CER)] [17–19] is an excellent tool for investigating both the conduction band offset and the electron effective mass. This technique, due to its absorption-like character and high sensitivity, probes optical transitions related to the ground and excited states even at room temperature, i.e., the typical operating temperature of electronic devices. The analysis of interband transitions together with theoretical calculations makes it possible to determine the energy level structure including the bandgap discontinuity at QW interfaces [17, 19]. In addition, the electron effective mass can be treated as a free parameter during the calculations and hence this parameter can be also determined. Such procedures have been often applied in PR and CER studies for different semiconductor structures including GaNAs/GaAs [20, 21], GaInNAs/GaAs [19, 22, 23], and GaNAsSb/GaAs QWs [24, 25]. In the case of dilute nitride QWs, three-, six-, eight-, and ten-band $\boldsymbol{k}\cdot\boldsymbol{p}$ methods as well as simple one band method have been applied to calculate the band structure [20, 23, 26–28]. GaInNAsSb/GaAs quantum wells are more difficult for calculations due to poor knowledge about the GaInNAsSb bandgap energy and other parameters necessary for $\boldsymbol{k}\cdot\boldsymbol{p}$ calculations. In this chapter it is shown that both the bandgap discontinuity and the electron effective mass can be quite accurately determined for these QWs using electromodulation spectroscopy and a simple approach based on one band model.

This chapter is organized as follows. In Sect. 6.2, experimental setup for CER measurements is described and advantages of CER spectroscopy are explained. In Sect. 6.3, the theoretical approach used to calculate energies of optical transitions in QWs is introduced. Also, in this section material parameters used for calculations are given and discussed. Matching of experimental data with theoretical calculations for example samples is shown in Sect. 6.4. Obtained results are discussed in the contexts of bandgap discontinuity tuning in QW structures by alloying of different III–V binary compounds. Our conclusions and outlook are given in Sect. 6.5.

6.2 Experimental Background

The GaInNAsSb/GaAs QW samples used in this study were grown on n-type (100) GaAs substrates by solid-source molecular beam epitaxy (MBE) in a Varian Mod Gen-II system at Stanford University. Gallium and indium

were supplied by SUMO effusion cells. A valved-arsenic cracker supplied As_2 and an unvalved-antimony cracker supplied monomeric antimony. The GaInNAsSb QWs were grown at a substrate temperature of 440°C measured by pyrometry. An arsenic-to-gallium overpressure of 20× and an antimony flux of 1.0×10^{-7} Torr beam equivalent pressure were supplied during the GaInNAsSb QW growth. Nitrogen was supplied by a modified SVT Associates plasma cell operating at a rf of 13.56 MHz. Nitrogen gas of 5N (99.999%) purity was filtered through a <1 ppb Pall Mini-Gaskleen purifier to minimize oxygen contamination. The cell was operated with 300 W input power and a nitrogen gas flow of 0.5 sccm. Nitrogen incorporation into (In)GaAs is directly controlled by the group-III growth rate [29]. The total group-III flux (gallium and indium) was held constant such that the nitrogen composition remained the same for all samples in this series. Different indium compositions were obtained by changing the ratio of indium and gallium fluxes. The structure for all samples consists of a 7.5 nm GaInNAsSb QW grown on a 300 nm GaAs buffer and capped by a 50 nm GaAs layer. The compositions of the samples were determined by high resolution X-ray diffraction (HRXRD) and secondary ion mass spectrometry (SIMS) [30]. HRXRD was obtained with a Philips X'Pert Pro four crystal high-resolution X-ray diffractometer and SIMS analysis from a Physical Electronics ADEPT 1010 quadrupole analyzer. Relevant details of the grown conditions can be found in [30]. In this work two samples with different content are discussed: $Ga_{0.84}In_{0.16}N_{0.025}As_{0.925}Sb_{0.05}$/GaAs (sample A) and $Ga_{0.68}In_{0.32}N_{0.025}As_{0.965}Sb_{0.01}$/GaAs (sample B).

The CER measurements were performed in the so-called "bright configuration" [31] where the sample was illuminated by white light instead of monochromatic light as it takes place in the standard configuration, i.e., so-called "dark configuration." A schematic diagram of the CER setup is shown in Fig. 6.1. The sample mounted in a semitransparent capacitor is illuminated by light from a halogen lamp (100 W) at normal incidence as it is shown in Fig. 6.1. The reflected light was dispersed through a 0.55 m focal length single grating monochromator and detected by thermoelectrically cooled InGaAs photodiode. The signal measured by photodiode has two components (1) the DC component which is proportional to I_0R and (2) AC component which is proportional to $I_0\Delta R$. Both DC and AC components are measured with a lock-in amplifier (I_0 is the intensity of reflected light). A computer divides the AC signal by the DC component giving the photoreflectance spectrum, $\frac{\Delta R}{R}(E)$, where E is the photon energy of the incident beam. The capacitor system is built of a top electrode made of a copper mesh and the bottom electrode made of a copper solid block. The semitransparent top electrode was kept at a distance of approx. 0.1–0.4 mm from the sample surface while the sample itself was glued to the bottom copper electrode. A home made generator of square AC voltage was used to generate the AC field inside the capacitor. A maximum peak-to-peak alternating voltage of 1.8 kV with frequency of 280 Hz was used for the modulation.

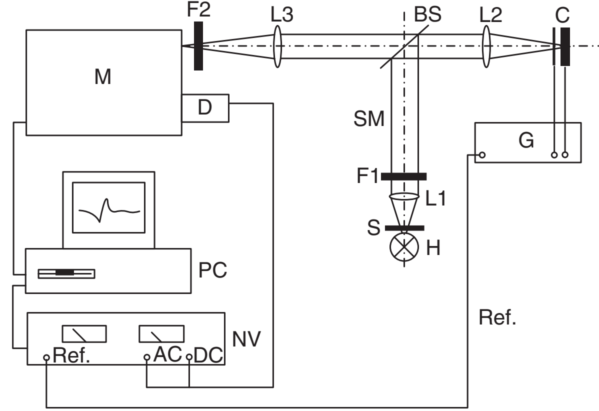

Fig. 6.1. Experimental setup for CER measurements in the so-called "bright configuration." H, halogen lamp; S, slit; L1, L2, L3, lenses; F1, F2, filters; SM, small mirror; BS, beam splitter; C, capacitor; M, monochromator; D, detector; NV, nanovoltmeter (lock-in); G, generator; PC, personal computer

In CER, relative changes in the reflectivity coefficient are measured. These changes are related to the perturbation of the dielectric function ($\varepsilon = \varepsilon_1 + \mathrm{i}\varepsilon_2$) expressed as [17]

$$\frac{\Delta R}{R} = \alpha\left(\varepsilon_1, \varepsilon_2\right)\Delta\varepsilon_1 + \beta\left(\varepsilon_1, \varepsilon_2\right)\Delta\varepsilon_2, \tag{6.1}$$

where α and β are the Seraphin coefficients, related to the dielectric function, and $\Delta\varepsilon_1$ and $\Delta\varepsilon_2$ are related by Kramers–Kronig relations. In general, electromodulation can be classified into three categories depending on the relative strengths of characteristic energies [17]. Electroreflectance spectra of simple, lightly doped systems, measured under low-field conditions, can often be modeling using Aspnes' third-derivate functional form (TDFF) [17,32], the so-called Lorentzian line shape

$$\frac{\Delta R}{R}\left(E\right) = \mathrm{Re}\left[\sum_{j=1}^{n} C_j \mathrm{e}^{\mathrm{i}\vartheta_j}\left(E - E_j + \mathrm{i}\mathit{\Gamma}_j\right)^{-m_j}\right] + f\left(E\right), \tag{6.2}$$

where n is the number of the optical transitions and spectral functions used in the fitting procedure, C_j and ϑ_j are the amplitude and phase of the line shape, and E_j and $\mathit{\Gamma}_j$ are the energy and the broadening parameter of the transitions, respectively. The function $f(E)$ is a parabolic function and simulates the background related to below bandgap oscillations [33, 34] or other phenomena. The term m refers to the type of CPs, i.e. the nature of optical transitions, namely $m = 2, 2.5$, and 3 for an excitonic transition, a three-dimensional one-electron transition and a two-dimensional one-electron transition, respectively. This formula is appropriate at low temperatures for

a high-quality structures. Usually at room temperature and/or for a sample with high inhomogeneities first-derivate Gaussian line shape is more appropriate. In the case of (Ga,In)(N,As,Sb)/GaAs QWs, Lorentzian line shape with $m = 3$ is acceptable at room temperature since this line corresponds to one electron transition and quite well simulates Gaussian line shape.

The moduli of CER resonances related to individual optical transitions are expressed by (6.3)

$$\Delta\rho_j(E) = \frac{|C_j|}{\left[(E - E_j)^2 + \mathit{\Gamma}_j^2\right]^{m_j/2}}. \tag{6.3}$$

There is worth to notice that the plot of the modulus of individual resonances helps to decide if the fit is correct. Moreover, the integrated modulus of CER resonance can be interpreted as the oscillator strength of the optical transition while E_0 and $\mathit{\Gamma}$ are the transition energy and the transition broadening, respectively. The broadening is related to the sample quality and temperature.

6.3 Theoretical Approach

The calculations of QW energy levels have been performed within the framework of the effective mass approximation. The influence of strain on the band structure is taken into account, but excitonic effects are neglected. The biaxial strain was calculated based on the Pikus–Bir Hamiltonian [35]. For the E_0 critical point in GaInNAsSb ($\boldsymbol{k} = 0$) the hydrostatic component of the strain, δE_{H}, shifts the valence and conduction bands. This total shift corresponds to the change in the bandgap energy due to a hydrostatic deformation, which is proportional to the deformation potential a, that is measured. The total shift should be divided between the valence and conduction bands proportionally to the potential constants a_{V} and a_{C}, where $a = a_{\mathrm{V}} + a_{\mathrm{C}}$. The shear component, δE_{S}, removes the valence band degeneracy, giving a separate E_{HH} (related to heavy holes) and E_{LH} (related to light holes). For highly strained QWs, such as GaInNAsSb/GaAs QWs with high indium content, the strain-induced coupling with the spin–orbit split band cannot be neglected. Thus taking into account the coupling, the energy of conduction and valence bands can be expressed in terms of the unstrained value as

$$E_{\mathrm{C}}^{*} = E_{\mathrm{C}} + \delta E_{\mathrm{H}}^{\mathrm{C}}, \tag{6.4a}$$

$$E_{\mathrm{V}}^{\mathrm{HH}} = E_{\mathrm{V}} + \delta E_{\mathrm{H}}^{\mathrm{V}} + \delta E_{\mathrm{S}}, \tag{6.4b}$$

$$E_{\mathrm{V}}^{\mathrm{LH}} = E_{\mathrm{V}} + \delta E_{\mathrm{H}}^{\mathrm{V}} + \frac{1}{2}\left(\mathit{\Delta} - \delta E_{\mathrm{S}} - \mathit{\Delta}\sqrt{1 + 2\frac{\delta E_{\mathrm{S}}}{\mathit{\Delta}} + 9\left(\frac{\delta E_{\mathrm{S}}}{\mathit{\Delta}}\right)^2}\right), \tag{6.4c}$$

where E_{C} and E_{V} correspond to energy of the conduction and valence bands at $\boldsymbol{k} = 0$, respectively. The values of the $\delta E_{\mathrm{H}}^{\mathrm{C}}$, $\delta E_{\mathrm{H}}^{\mathrm{V}}$, and δE_{S} are given by following formulas

$$\delta E_{\mathrm{H}}^{\mathrm{C}} = 2a^{\mathrm{C}}\left(1 - \frac{C_{12}}{C_{11}}\right)\varepsilon, \tag{6.5a}$$

$$\delta E_{\mathrm{H}}^{\mathrm{V}} = 2a^{V}\left(1 - \frac{C_{12}}{C_{11}}\right)\varepsilon, \tag{6.5b}$$

$$\delta E_{\mathrm{S}} = b\left(1 - 2\frac{C_{12}}{C_{11}}\right)\varepsilon, \tag{6.5c}$$

where ε is the in-plane strain, C_{11} and C_{12} are elastic stiffness constants, and b is the shear deformation potential. Δ is the energy between the valence and spin–orbit split bands and is 0.34 eV for GaAs. The value of Δ changes for GaInNAsSb and a linear interpolation between the Δ of the binary compounds does not work correctly (as is the case for the linear interpolation for the bandgap energy and the electron effective mass). However, a linear interpolation for this parameter can be accepted as a first-order approximation, especially since an exact value of this parameter is not important for QWs with low indium content (samples with low strain since $\frac{\delta E_{\mathrm{S}}}{\Delta} \ll 1$). Also for samples with high indium content, this parameter is not crucial in the calculations. Please note that this parameter influences energies of light-hole transitions only.

The material parameters necessary in the calculations conform with Vegard's law with good accuracy, contrary to the behavior mentioned for the bandgap energy and the electron effective mass. Therefore, all the material parameters for $\mathrm{Ga}_{1-x}\mathrm{In}_x\mathrm{N}_y\mathrm{As}_{1-y-z}\mathrm{Sb}_z$ have been obtained by linear interpolation between the parameters of a relevant binary semiconductor [36, 37] according to (6.6).

$$\begin{aligned} Q(x,y,z) = {} & (1-x)\,yQ_{\mathrm{GaN}} + (1-x)\,(1-y-z)\,Q_{\mathrm{GaAs}} + (1-x)\,zQ_{\mathrm{GaSb}} \\ & + xyQ_{\mathrm{InN}} + x\,(1-x-y)\,Q_{\mathrm{InAs}} + xzQ_{\mathrm{InSb}}, \end{aligned} \tag{6.6}$$

where $Q_{\mathrm{i}} = b_{\mathrm{i}}$ or $C_{12\mathrm{i}}$ (i = GaN, GaAs, GaSb, InN, InAs, and InSb). The parameters of binary compounds used in the calculations are listed in Table 6.1.

The conduction- and valence-band offsets, Q_{C} and Q_{V}, are defined by (6.7a) as

$$Q_{\mathrm{C}} = \frac{\Delta E_{\mathrm{C}}}{(\Delta E_{\mathrm{C}} + \Delta E_{V})} \times 100\%, \tag{6.7a}$$

$$Q_{V} = (1 - Q_{\mathrm{C}}) \times 100\%, \tag{6.7b}$$

where ΔE_{C} and ΔE_{V} are the conduction- and valence band discontinuities at the heterojunction for unstrained materials, as illustrated in Fig. 6.2.

Table 6.1. Binary material parameters used to calculate the strained quinary GaInNAsSb material parameters

Parameter (unit)	GaN	GaAs	GaSb	InN	InAs	InSb
Heavy-hole mass m_{hh}/m_0	0.85	0.35	0.25	0.83	0.33	0.26
Light-hole mass m_{lh}/m_0	0.24	0.09	0.044	0.16	0.027	0.015
CB hydrostatic deformation potential a_{C} (eV)	−6.71	−7.17	−7.5	−2.65	−5.08	−6.94
VB hydrostatic deformation potential a_{V} (eV)	−0.69	−1.16	−0.8	−0.7	−1.0	−0.36
Shear deformation potential b (eV)	−2.2	−2.0	−2.0	−1.2	−1.8	−2.0
Elastic constant C_{11} (GPa)	293	1,221	884.2	187	832.9	684.7
Elastic constant C_{12} (GPa)	159	566	402.6	125	452.6	373.5

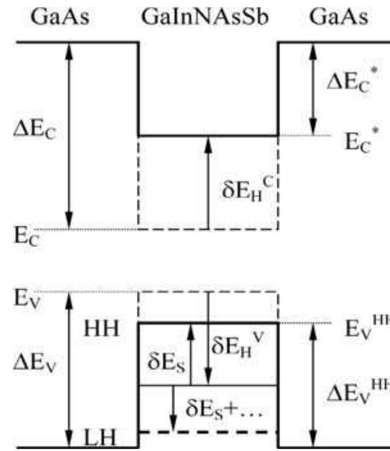

Fig. 6.2. Energy-band diagram in real space for compressively strained GaInNAsSb/GaAs QWs

They are designated unstrained because they are the "natural" band offset corresponding to the ab initio calculations [38] and the experimental values extracted from X-ray photoemission measurements. From a laser device perspective, the most interesting values are the bandgap discontinuities with the strain corrections, shown in Fig. 6.2 as $\Delta E_{\mathrm{C}}^{*}$ and $\Delta E_{\mathrm{V}}^{\mathrm{HH}}$. Generally, the most

appropriate approach to heterojunction band offsets is to determine the Q_C (or Q_V) since a GaInNAsSb/GaAs QW can be grown on both GaAs and InP substrates. For identical QWs grown on different substrates, the Q_C does not vary whereas the ΔE_C^* and ΔE_V^{HH} discontinuities vary due to different lattice strains. Moreover, the value of ΔE_C^* and ΔE_V^{HH} discontinuities can be calculated if the unstrained natural offset, Q_C, is known. Thus the Q_C value is more universal parameter. In this chapter, both the Q_C and ΔE_C^* and ΔE_V^{HH} discontinuities are determined.

In the calculations, the Q_C and electron effective mass are treated as free parameters. The bandgap energy of the GaInNAsSb layer has been adjusted to the experimental value of the QW ground state transition on the basis of a series of calculations with various Q_C and m_e. It was observed that the energy of the ground state transition does not vary significantly with the change in the Q_C. In addition, the energy difference between the QW levels (the most important criterion for the electron effective mass determination) is insensitive to small changes in the bandgap energy. For example, the change in the GaInNAsSb bandgap energy from 800 to 790 meV, at $Q_C = 70\%$ and $m_e = 0.09\, m_0$, changes the energy difference between the first and the second electron levels less than 1 meV. Thus the bandgap energy can be easily adjusted in the calculations. An error associated with the GaInNAsSb bandgap energy exists, but this error does not influence the conclusion concerning the $\Delta E_C^*, \Delta E_V^{HH}$, and m_e because this error is compensated by errors associated with hydrostatic coefficients and elastic stiffness constants of the binary compounds. Note that with this approach, $\Delta E_C^*, \Delta E_V^{HH}$ can be precisely determined despite the fact that a five-element alloy is considered.

This situation is possible since, to solve the Schrödinger equation given by (6.8a),

$$-\frac{\hbar^2}{2}\frac{\partial}{\partial z}\left[\frac{1}{m^*(z)}\frac{\partial f_n(z)}{\partial z}\right] + V(z)\, f_n(z) = E_n f_n(z)\,, \tag{6.8a}$$

$$V(z) = \begin{cases} 0 & |z| < \frac{L_Z}{2}, \\ V_0 & |z| > \frac{L_Z}{2}, \end{cases} \tag{6.8b}$$

we only need to know three parameters: the QW depth (V_0), the effective mass in the (100) direction (m^*), and the QW width (L_Z). The E_n and f_n in (6.8a) are, respectively, the energy and the wavefunction related to n subband. V_0 corresponds to $\Delta E_C^*, \Delta E_V^{HH}$, and ΔE_V^{LH} for electrons, heavy and light holes, respectively. The V_0 is calculated by using several material parameters after (6.4)–(6.6). The adjustment of the GaInNAsSb bandgap energy to the ground state transition compensates for errors from (6.4)–(6.6), which are from inaccuracies of the material parameters for binary compounds. It should be noted that the Q_C extracted from the analysis possesses an error higher than $\Delta E_C^*, \Delta E_V^{HH}$, and m_e.

6.4 Results and Discussion

To determine the conduction band offset and electron effective mass for GaInNAsSb/GaAs QWs, energies of CER resonances have to be extracted from CER spectra. In general, the number of CER resonances necessary to simulate experimental data is decided arbitrary analyzing individual CER spectra by nagged eye (note that preliminary calculations help to make a reasonable decision). It is obvious that larger number of CER resonances better simulate experimental data but each resonance has to be justified since imaginary transitions can be generated if too many resonances were used to simulate CER spectrum. Therefore, the moduli of individual CER resonances are plotted and evaluated. The evaluation means a comparison of transition intensities and the energy difference between individual resonances. Usually the allowed transitions are much stronger than partially allowed ones. Moreover, broadening of each CER resonances should be comparable. Also it is acceptable that broadening of CER resonances is higher for excited state transitions, e.g., the partially allowed transitions. Next energies of CER resonances are compared with theoretical calculations for various Q_C and m_e. This procedure allows us to identify CER resonances and to determine the conduction band offset and the electron effective mass.

6.4.1 Identification of Contacless Electroreflectance Resonances

Figure 6.3a,b shows the room temperature CER spectra for sample A and B, respectively. The strongest CER signal is observed at an energy of $\sim$1.42 eV. This signal origins from the band-to-band absorption in the GaAs barrier and cap layers. Below the GaAs signal, CER features associated with optical transitions in GaInNAsSb/GaAs SQW are clearly observed. These features are fitted by using (6.2). The fitting curves are shown in Fig. 6.3 as thick solid grey lines. In addition, the moduli of individual resonances (dashed lines) obtained according to (6.3) are shown in this figure.

As was mentioned the identification of CER resonances is possible due to a series of calculations with various Q_C and m_e. The notation klH(L) denotes the transition between the kth heavy-hole (light-hole) valence subband and the lth conduction subband. The resonance at the lowest energy originates from the 11H transition, which is a fundamental transition for the two samples. In addition to the 11H transition, the CER spectra show an 11L transition (the lowest energy transition for light holes) and transitions between excited QW states such as 22H, 33H, and 22L. The partially forbidden transitions, such as the 31H transition, were also considered. However, it was concluded that they are weak in comparison with the allowed transitions and they can be neglected in the fitting procedure. In this manner, the number of CER resonances was reduced to the number of allowed transitions. Finally, for the sample A (GaInNAsSb/GaAs QW with 16% In content) four resonances have been resolved in the CER spectrum. With the indium content increase, all QW

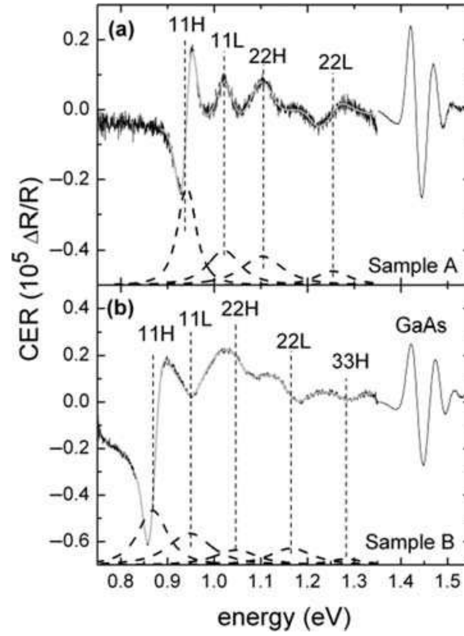

Fig. 6.3. Room temperature CER spectra of the sample A (GaInNAsSb/GaAs SQW with 16% In) and sample B (GaInNAsSb/GaAs SQW with 32% In) content (*solid line*) together with the fitting curves (*thick grey lines*) and the moduli of individual CER resonances (*dashes lines*)

transitions shift to the red. For the sample B (GaInNAsSb/GaAs QW with 32% In content) an additional CER resonance related to the 33H transition appears between 22L and GaAs transitions.

The procedure for correlating measured data with theory is illustrated in Figs. 6.4–6.6. For the identification of CER resonances a plot as the one shown in Fig. 6.4 is sufficient. In this figure, the experimental transition energies are shown as horizontal-dashed lines while those calculated are shown as solid curves. Using this method, the optimal match between theory and experiment can be determined by comparing the experimental data with calculated energies. The value of Q_{C} can be determined from this plot if the value of the electron effective mass is well known. If the electron effective mass is treated as a second free parameter, since its value is unknown, the calculations have to be performed for various Q_{C} and m_{e}.

6.4.2 Conduction Band Offset and Electron Effective Mass Determination

The energy difference between electron levels is quite strong sensitive to changes in the electron effective mass. Therefore the analysis of the energy

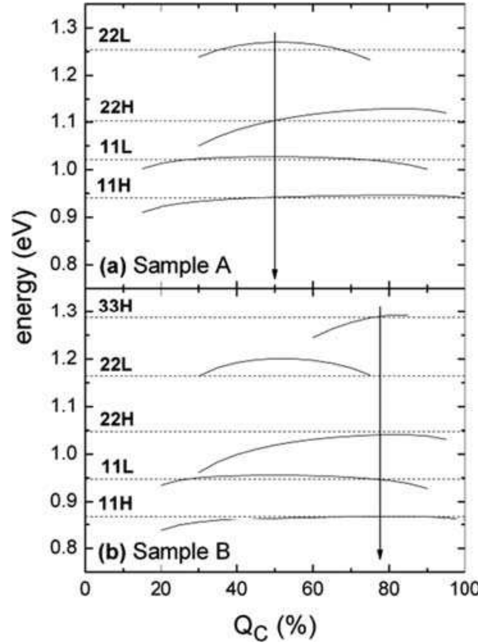

Fig. 6.4. Comparison of experimental data and theoretical calculations performed for various Q_C and $m_e = 0.09m_0$

difference between QW transitions (e.g., the difference between 22H and 11H transitions) is a good criterion for matching experimental data with theoretical calculations. Figures 6.5 and 6.6 show the energy difference between the 22H and 11H transitions obtained from experimental data (horizontal dashed lines) and theoretical calculations performed for various Q_C and m_e. It is clearly visible that the conclusion concerning the conduction band offset depends on the electron effective mass, which is the second free parameter in our calculations. Note that an increase in the electron effective mass, in comparison to N free QWs, is expected for this system. This high value of the electron effective mass in GaInNAsSb is related to the incorporation of nitrogen atoms. In the samples A and B, the nitrogen content does not vary. Therefore, it can be assumed that the nitrogen-related increase for the electron effective mass is the same for all samples. Any possible differences in the electron effective mass are small since they are related to changes in the indium and antimony concentrations. Based on data from literature [36], it has been estimated that the differences in the electron effective mass for the nitrogen-free samples are <10%. Therefore, for the samples investigated in this chapter, it can be assumed that the electron effective mass decreases less than 10% with a rise in indium content from 16 to 32%. This assumption leads to a narrow window of acceptable m_e for the two samples. An agreement between experimental data and theoretical predictions should appear for each

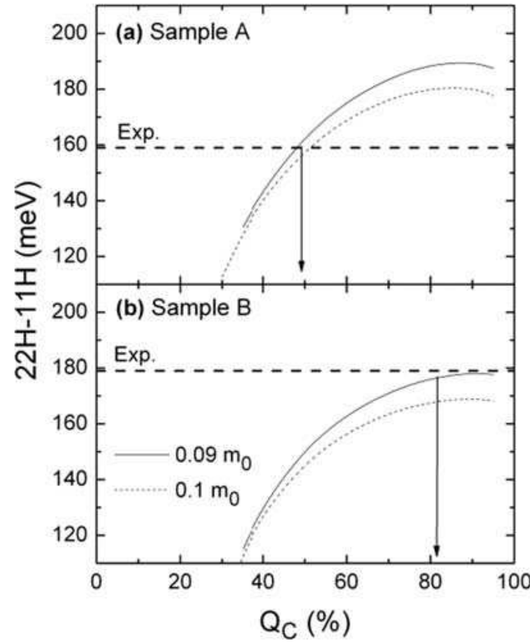

Fig. 6.5. Method used to analyze the Q_{C} in GaInNAsSb/GaAs SQWs with (**a**) 16% In and (**b**) 32% In. The *horizontal-dashed lines* correspond with the energy difference between the 22H and 11H transitions taken from experimental data. *Solid and dashed curves* correspond with the energy difference between the 22H and 11H transitions obtained from the theoretical calculations with the electron effective mass of $0.09m_0$ and $0.1m_0$, respectively

sample at the same value of the m_{e}. This value is easy to locate in Fig. 6.6. It is clearly visible that the electron effective mass should be close to $0.09\,m_0$ for each sample. It is also apparent that the high value of the electron effective mass ($m_{\mathrm{e}} > 0.12\,m_0$) is not appropriate for GaInNAsSb. This conclusion is consistent with the literature, since it can be assumed that the upper limit for the electron effective mass in GaInNAsSb, with 2.5% N content, corresponds to the electron effective mass in $\mathrm{GaN_{0.025}As_{0.975}}$ (0.1–0.12 m_0 according to the band anticrossing model proposed by Walukiewicz and coworkers [39, 40, and see Chap. 3] and [21, 41–43]). Incorporation of indium and antimony atoms leads to a decrease of the electron effective mass. Its value should be smaller than $0.1\,m_0$. If we assume that with 16% In content has an electron effective mass of 0.1 m_0, then the 10% change in the electron effective mass leads to a shift of $\Delta m_{\mathrm{e}} = 0.01\,m_0$. For the sample with 32% In content, the electron effective mass should be close to $0.09\,m_0$. The expected trend toward lower electron effective masses with increasing indium content has been shown in [44].

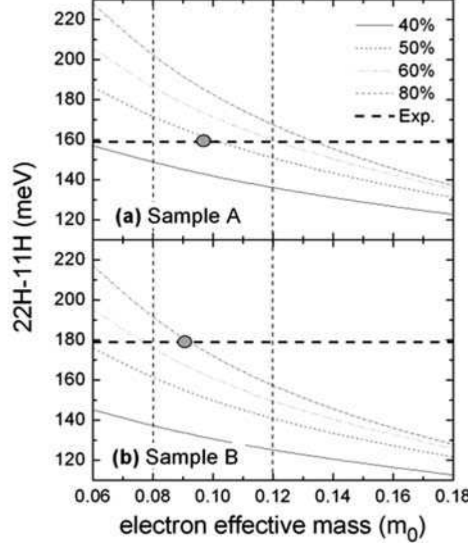

Fig. 6.6. Method used to analyze the m_e in GaInNAsSb/GaAs SQWs with (**a**) 16% In (**b**) 32% In. The *horizontal dashed lines* correspond to the energy difference between the 22H and 11H transitions taken from experimental data. The *vertical thin dashed lines* show the recommended range of the electron effective mass for these samples whereas the *dots* mean the expected change in the electron effective mass

6.4.3 Influence of Remaining Parameters and Possible Errors

The errors of $Q_C(\Delta E_C^*, \Delta E_V^{HH})$ and m_e are due to (1) a limit of the applied theoretical model, (2) an accuracy of fitting of CER data (3) an error of QW width and content and (4) an accuracy of material parameters of binary compounds. Usually, the two first contributions to the total error of Q_C and m_e are smaller than the contribution associated with the accuracy of QW width and content. Thus to minimize the error, both the QW width and content have to be determined as precisely as possible. In our case the QW width and content were determined on the basis of XRD and SIMS measurements [30]. Since the QW width can be determined with the accuracy better than 5%, the error associated with QW width can be significantly reduced. Remaining errors are related to the GaInNAsSb alloy content and the accuracy of material parameters for binary compounds. As was mentioned in Sect. 6.2, the ΔE_C^* and ΔE_V^{HH} are determined with better accuracy than Q_C. It is possible since the bandgap discontinuities can be determined neglecting strain-related shifts (4–6) by adjusting the GaInNAsSb bandgap energy to the fundamental transition in QW. To calculate Q_C, which is more universal than the ΔE_C^* and ΔE_V^{HH}, strain-related shift has to be taken into consideration. For quinary alloys these shifts could have significant errors ($\sim$50%) and hence the error

of Q_C increases. Note that the strain-related contribution to total error of Q_C is more important for highly strained QWs where the strains are very important. Finally it has been estimated that within the presented approach the Q_C can be determined with ∼5 and ∼10% accuracy for weakly and highly strained GaInNAsSb/GaAs QWs, respectively, if the electron effective mass was treated as a known parameter. For unknown electron effective mass there appears a range of acceptable Q_C (and m_e). This range can be significantly reduced by analyzing a set of QWs with various widths.

6.5 Summary and Outlook

In summary, the experimental method to investigate the number of confined states in GaInNAsSb/GaAs QWs as well as a simple approach to analyze the band structure of these QWs have been discussed. It has been shown that the CER spectroscopy is a very powerful technique to study energies of QW transitions related to both the ground and excited states. Knowing energies of QW transitions the band structure can be found via matching of experimental data with theoretical calculations performed for various Q_C. In this work the theoretical calculations were performed within the effective mass approximation.

In addition, it has been shown that GaInNAsSb/GaAs QWs are a system where the Q_C varies significantly with the alloy content. In this work it has been shown that the Q_C changes from 50% (sample A) to 80% (sample B). In general, it is expected that from the bandgap engineering viewpoint quinary alloys, such as GaInNAsSb, should have significant advantages over ternary and quaternary alloys (InGaAs, GaNAs, or GaInNAs) since the Q_C for the quinary/GaAs system can be tuned better than for ternary/GaAs or quaternary/GaAs systems. Moreover, it is very important to control independently three parameters (1) bandgap energy, (2) strains, and (3) bandgap discontinuities. Note that such independent control is impossible for ternary/GaAs and quaternary/GaAs systems whereas it is possible for quinary/GaAs system if the Q_C is strongly sensitive to the content of quinary alloys. In the case of GaInNAsSb alloys results shown in this work and our previous investigations as well as literature data show that the bandgap discontinuity (band offset) tuning is very promising in this system. The content dependent Q_C for (Ga,In)(N,As,Sb)/GaAs structures can be summarized in following conclusions:

1. *GaInNAsSb/GaAs with vary N content.* According to the BAC model (see Chap. 3) the incorporation of N atoms into GaInAsSb/GaAs QWs mostly influences the conduction QW. Therefore at the first approximation it can be assumed that all N-related redshift appears in the electron QW. Recent studies for GaNAs/GaAs QWs show that the Q_C for this system is ∼70–90% [20, 21]. It means that the incorporation of N atoms into

GaAs also influences the deepness of hole QWs. However, the influence of N atoms on the valence band discontinuity is small in comparison to changes in the conduction band discontinuity. Therefore, it is concluded that incorporation of N atoms into GaInNAsSb/GaAs mostly increases the conduction bandgap discontinuity (i.e., increases the Q_{C}).
2. *GaInNAs/GaAs with vary In content.* GaInNAs/GaAs QWs with high In content (In $>$ 20%) were studies many times [19, 22, 23, 44–48] and there is a general agreement that the Q_{C} for such QWs is close to 80%. A fever investigations were devoted for GaInNAs/GaAs QWs with lower In content (In $<$ 20%) [22, 44]. For such QWs the Q_{C} is smaller than 80%. It means that change in In content can tune both the conduction and valence band discontinuities.
3. *GaNAsSb/GaAs with vary Sb content.* The Q_{C} for this system was investigated in [24, 25]. There has been shown that the incorporation of Sb atoms into GaNAs/GaAs QWs increases the valence band discontinuity and it almost does not change the conduction band discontinuity. It means that an increase in Sb content in this system decreases the Q_{C}.
4. *GaInNAsSb/GaAs with vary In content.* For this system, similarly as for Sb-free system, it has been observed that an increase in In content leads to an increase in the Q_{C}. Such a behavior is observed for samples shown in this work and also is reported in [44].
5. *GaInNAsSb/GaAs with vary Sb content.* It has been shown that the Q_{C} decreases with the increase in Sb content for GaInNAsSb/GaAs QWs with low In content (In = 10%, N = 2.5%) [49]. Like for the indium free system (GaNAsSb/GaAs QWs) it has been observed that the incorporation of Sb atoms increases the valence bandgap discontinuity and almost does not change the conduction band discontinuity.

In addition, N-related increase in the electron effective mass has been observed for samples shown in this work. It can be summarized that after incorporation of 2.5% N atoms into GaInAsSb the m_{e} increases by ~50% in comparison to nitrogen free alloys. Also it is expected that changes in the m_{e} due to changes in In and Sb contents are significantly smaller than N-related changes in the m_{e}.

Acknowledgments. We acknowledge the support from the Foundation for Polish Science through a Subsidy 8/2005. R.K. acknowledges support from the Foundation for Polish Science.

References

1. M. Kondow, K. Uomi, A. Niwa, T. Kitatani, S. Watahiki, Y. Yazawa, Jpn. J. Appl. Phys. Part 1 **35**, 1273 (1996)
2. I.A. Buyanova, W.M. Chen (eds.), *Physics and Applications of Dilute Nitrides*, (Taylor & Francis, New York, 2004)

3. M. Henini (ed.), *Dilute nitride Semiconductors*, (Elsevier, Oxford, 2005)
4. G. Jaschke, R. Averbeck, L. Geelhaar, H. Riechert, J. Cryst. Growth **278**, 224 (2005)
5. X. Yang, M.J. Jurkovic, J.B. Heroux, W.I. Wang, Appl. Phys. Lett. **75**, 178 (1999)
6. G. Ungaro, G. Le Roux, R. Teisser, J.C. Harmand, Electron. Lett. **35**, 1246 (1999)
7. H. Shimizu, K. Kumada, S. Uchiyama, A. Kasukawa, Electron. Lett. **36**, 1379 (2000)
8. X. Yang, J.B. Heroux, L.F. Mei, W.I. Wang, Appl. Phys. Lett. **78**, 4068 (2001)
9. V. Gambin, W. Ha, M.A. Wistey, H.B. Yuen, S.R. Bank, S.M. Kim, J.S. Harris, IEEE J. Sel. Top. Quantum Electron. **8**, 795 (2002)
10. S.R. Bank, M.A. Wistey, H.B. Yuen, L.L. Goddard, W. Ha, J.S. Harris, Electron. Lett. **39**, 1445 (2003)
11. M.A. Wistey, S.R. Bank, H.B. Yuen, L.L. Goddard, J.S. Harris, Electron. Lett. **39**, 1822 (2003)
12. S.R. Bank, H.P. Bae, H.B. Yuen, M.A. Wistey, L.L. Goddard, J.S. Harris, Electron. Lett. **42**, 156 (2006)
13. M.A. Wistey, S.R. Bank, H.P. Bae, H.B. Yuen, E.R. Pickett, L.L. Goddard, J.S. Harris, Electron. Lett. **42**, 282 (2006)
14. J.A. Gupta, P.J. Barrios, X. Zhang, G. Pakulski, X. Wu, Electron. Lett. **41**, 71 (2005)
15. J.A. Gupta, P.J. Barrios, X. Zhang, J. Lapointe, D. Poitras, G. Pakulski, A. Delage, Electron. Lett. **41**, 1060 (2005)
16. Z.C. Niu, S.Y. Zhang, H.Q. Ni, D.H. Wu, H. Zhao, H.L. Peng, Y.Q. Xu, S.Y. Li, Z.H. He, Z.W. Ren, Q. Han, X.H. Yang, Y. Du, R.H. Wu, Appl. Phys. Lett. **87**, 231121 (2005)
17. F.H. Pollak, in *Modulation Spectroscopy of Semiconductors and Semiconductor Microstructures Handbook on Semiconductors*, vol. 2, ed. by T.S. Moss (Elsevier Science, Amsterdam, 1994), pp. 527–635
18. X. Yin, F.H. Pollak, Appl. Phys. Lett. **59**, 2305 (1991)
19. J. Misiewicz, R. Kudrawiec, K. Ryczko, G. Sęk, A. Forchel, J.C. Harmand, M. Hammar, J. Phys. Cond. Mat. **16**, 3071 (2004), and references there in
20. S. Tomic, E.P. O'Reilly, P.J. Klar, H. Gruning, W. Heimbrodt, W.M. Chen, I.A. Buyanova, Phys. Rev. B **69**, 245305 (2004)
21. R. Kudrawiec, M. Motyka, M. Gladysiewicz, J. Misiewicz, J.A. Gupta, G.C. Aers, Solid State Commun. **138**, 365 (2006)
22. J.B. Heroux, X. Yang, W.I. Wang, J. Appl. Phys. **92**, 4361 (2002)
23. S.A. Choulis, T.J.C. Hosea, S. Tomic, M. Kamal Saadi, A.R. Admas, E.P. O'Reilly, B.A. Weinstein, P.J. Klar, Phys. Rev. B **66**, 165321 (2002)
24. R. Kudrawiec, K. Ryczko, J. Misiewicz, H.B. Yuen, S.R. Bank, M.A. Wistey, H.P. Bae, J.S. Harris, Appl. Phys. Lett. **86**, 141908 (2005)
25. R. Kudrawiec, M. Gladysiewicz, J. Misiewicz, H.B. Yuen, S.R. Bank, M.A. Wistey, H.P. Bae, J.S. Harris, Phys. Rev. B **73**, 245413 (2006)
26. H. Carrere, X. Marie, J. Barrau, T. Amand, S. Ben Bouzid, V. Sallet, J.C. Harmand, J. Phys. Cond. Mater. **16**, 3215 (2004)
27. M. Giehler, R. Hey, P. Kleinert, H.T. Grahn, Phys. Rev. B **73**, 085322 (2006)
28. S.T. Ng, W.J. Fan, S.F. Yoon, S.Z. Wang, Y. Qu, C.Y. Liu, S.G. Ma, S. Yuan, J. Appl. Phys. **96**, 4663 (2004)

29. S.G. Spruytte, M.C. Larson, W. Wampler, C.W. Coldren, H.E. Petersen, J.S. Harris, J. Cryst. Growth **227–228**, 506 (2001)
30. H.B. Yuen, S.R. Bank, H.P. Bae, M.A. Wistey, J.S. Harris, J. Appl. Phys. **99**, 073504 (2006)
31. R. Kudrawiec, J. Misiewicz, Appl. Surf. Sci. **253**, 80 (2006)
32. D.E. Aspnes, Surf. Sci. **37**, 418 (1973)
33. R. Kudrawiec, P. Sitarek, J. Misiewicz, S.R. Bank, H.B. Yuen, M.A. Wistey, J.S. Harris, Appl. Phys. Lett. **86**, 091115 (2005)
34. R. Kudrawiec, M. Motyka, M. Gladysiewicz, P. Sitarek, J. Misiewicz, S.R. Bank, H.B. Yuen, M.A. Wistey, J.S. Harris, Appl. Surf. Sci. **253**, 266 (2006)
35. G.L. Bir, G. Pikus, *Symmetry and Strain-Induced Effects in Semiconductors* (Wiley, New York, 1974)
36. I. Vurgaftman, J.R. Meyer, L.R. Ram-Mohan, J. Appl. Phys. **89**, 5815 (2001)
37. I. Vurgaftman, J.R. Meyer, J. Appl. Phys. **94**, 3675 (2003)
38. S.H. Wei, A. Zunger, Appl. Phys. Lett. **72**, 2011 (1998)
39. W. Shan, W. Walukiewicz, J.W. Ager III, E.E. Haller, J.F. Geisz, D.J. Friedman, J.M. Olson, S.R. Kurtz, Phys. Rev. Lett. **82**, 1221 (1999)
40. W. Shan, W. Walukiewicz, K.M. Yu, J.W. Ager III, E.E. Haller, J.F. Geisz, D.J. Friedman, J.M. Olson, S.R. Kurtz, H.P. Xin, C.W. Tu, Phys. Stat. Sol. B **223**, 75 (2001)
41. C. Skierbiszewski, P. Perlin, P. Wisniewski, W. Knap, T. Suski, W. Walukiewicz, W. Shan, K.M. Yu, J.W. Ager III, E.E. Haller, J.F. Geisz, J.M. Olson, Appl. Phys. Lett. **76**, 2409 (2000)
42. P.H. Hai, W.M. Chen, I.A. Buyanova, H.P. Xin, C.W. Tu, Appl. Phys. Lett. **77**, 1843 (2000)
43. J. Wu, W. Shan, W. Walukiewicz, K.M. Yu, J.W. Ager III, E.E. Haller, H.P. Xin, C.W. Tu, Phys. Rev. B **64**, 085320 (2001)
44. R. Kudrawiec, H.B. Yuen, M. Motyka, G. Gladysiewicz, J. Misiewicz, S.R. Bank, H.P. Bae, M.A. Wistey, J.S. Harris, J. Appl. Phys. **101**, 103504 (2007)
45. M. Hetterich, M.D. Dawson, A.Y. Egorov, D. Bernklau, H. Riechert, Appl. Phys. Lett. **76**, 1030 (2000)
46. Z. Pan, L.H. Li, Y.W. Lin, B.O. Sun, D.S. Jiang, W.K. Ge, Appl. Phys. Lett. **78**, 2217 (2001)
47. G.H. Dumitras, H. Riechert, J. Appl. Phys. **94**, 3955 (2003)
48. M. Galluppi, L. Geelhaar, H. Riechert, Appl. Phys. Lett. **86**, 131925 (2005)
49. R. Kudrawiec, M. Motyka, M. Gladysiewicz, J. Misiewicz, H.B. Yuen, S.R. Bank, H.P. Bae, M.A. Wistey, J.S. Harris, Appl. Phys Lett. **88**, 221113 (2006)

7

The Effects of Nitrogen Incorporation on Photogenerated Carrier Dynamics in Dilute Nitrides

S. Mazzucato and R.J. Potter

The addition of small fractions of nitrogen to GaAs-based materials results in a significant reduction of the bandgap, opening up the potential for a range of electronic and optoelectronic applications. However, the addition of nitrogen also has a large impact on the carrier dynamics, often resulting in a considerable increase in shallow traps, which readily capture excitons. A number of mechanisms have been proposed to explain the creation of shallow traps, which give rise to localised states. Many of these are associated with deposition problems, such as well width fluctuations and compositional inhomogeneities, caused by the large miscibility gap associated with the incorporation of nitrogen. However, some of these growth issues are not intrinsic to dilute nitrides and advances in deposition technology have shown that these associated problems can be significantly reduced. In this chapter, we will give an overview of how the incorporation of nitrogen into dilute nitrides affects carrier dynamics. This will include detailed discussion about the experimental evidence for exciton trapping presented in the scientific literature, such as the so-called S-shape temperature dependence of photoluminescence emission, lineshapes and radiative decay rates. We will also review the various mechanisms which have been put forward to account for the exciton trapping and discuses how/if these can be overcome.

7.1 Introduction

The discovery that adding small fractions of nitrogen to GaAs [1] or GaInAs [2] results in a rapid reduction in the fundamental bandgap has attracted significant interest from both industry and academia. These materials have offered the tantalising prospect of producing a range of narrow bandgap electronic and optoelectronic devices without many of the problems encountered with InP-based materials [3, 4]. The main drive behind dilute nitride research has been to produce economical, uncooled vertical cavity surface emitting lasers (VCSELs) operating in the low loss (1.26–1.68 μm) [5, 6] telecommunications

window. Low cost transceivers operating in this window would facilitate the widespread introduction of "last mile" high-speed optical links. These could replace traditional copper wire links used to transmit data over medium and short haul distances, such as in local area networks (LANs). However, several other appealing applications for dilute-nitride-based devices are currently under deep investigation [7–13].

The small atomic radius and large electronegativity of nitrogen compared to the arsenic that it replaces in dilute nitrides, result in a large miscibility gap between the arsenides and nitrides. While these atomic differences give rise to the interesting physical properties exhibited by dilute nitrides, they also make it extremely difficult to deposit high-quality epitaxial layers. The large miscibility gap inhibits the smooth mixing of constituents within the alloy, which can result in compositional inhomogeneities, 3D growth and generation of defects. As with all quantum well (QW) structures, compositional and structural inhomogeneities in the dilute nitride layers cause localised potential fluctuations in the band structure, resulting in an undulating energy landscape. Free excitons travelling through this landscape are perturbed by these potential fluctuations and can become trapped in regions of low potential, particularly at low temperatures. If this occurs, then the excitons become spatially trapped (localised) within the potential dips or valleys. The localisation of excitons has a significant impact on carrier dynamics within the material and may inhibit the performance of electronic or optoelectronic devices.

In many early dilute nitride studies, the observed localisation phenomena were attributed to growth related problems. It was believed that the rapid improvements in growth and post-growth processing would eventually lead to high quality dilute nitrides and effectively eliminate exciton localisation. While it is clear that significant improvements to material quality have been made over recent years, it is now widely believed that localisation is an intrinsic property of all dilute nitrides. By their very nature, dilute nitrides only contain a small fraction of nitrogen; hence the nitrogen acts more like an impurity than a true alloy constituent. At best this implies that dilute alloys can only form semi-crystalline structures rather than true periodic crystals. Even in this best case, the relatively sparse distribution of nitrogen sites in the lattice will result in some degree of potential fluctuation. In reality, it is likely that the electronegativity, atomic radius and hence the large miscibility will result in energetically preferred atomic configurations in the vicinity of each nitrogen atom. This nearest neighbour cluster can significantly affect the local potential and is therefore a prime candidate for the cause of exciton localisation in dilute nitrides.

In this chapter, we will provide an overview of the causes and effects of carrier localisation in dilute nitride materials. In Sect. 7.2, we give a brief introduction to the topic of carrier localisation in semiconductors. In Sect. 7.3 we review the published experimental evidence for carrier localisation in dilute nitrides and we discuss the possible causes, and in Sect. 7.4 we illustrate some of the methods used to reduce localised energy states.

7.2 Exciton Localisation

The optical properties of quantum well structures are strongly influenced by disorder due to alloy fluctuations, interface roughness and defects. In each case these create random potential fluctuations, which broaden the electronic density of states. So, instead of sharp conduction and valance band edges, we are left with exponential tails in the density of states (Fig. 7.1a). To visualise this we can picture the conduction (or valance) band edge as a landscape, which is essentially flat in a perfect QW, but in disordered QWs it will contain "hills" and "valleys". The undulating potential landscape will have a significant effect on free excitons as they travel through the material. This is particularly true for excitons with low thermal energy as they can easily fall into low energy states but have insufficient energy to escape. Excitons with sufficient thermal energy can readily be de-trapped and are less likely to be trapped in the first place. In many cases localisation potentials are only a few tens of meV below the band edges, and therefore, localisation tends to dominate carrier dynamics only at relatively low temperatures.

In general, disorder in QW structures and the resulting localisation is undesirable as it results in poor device performance. For devices that rely on good carrier mobility, the process of trapping, de-trapping and scattering by the potential fluctuations reduces mobility and hence performance. The localisation of excitons also affects the radiative recombination dynamics of the system, as translational symmetry parallel to the well plane is broken, leading to the violation of the $\boldsymbol{k}$-selection rule ($k_{\mathrm{ex}} \approx k_{\mathrm{photon}}$) [14]. This can result in relatively short carrier lifetimes as the whole population of localised

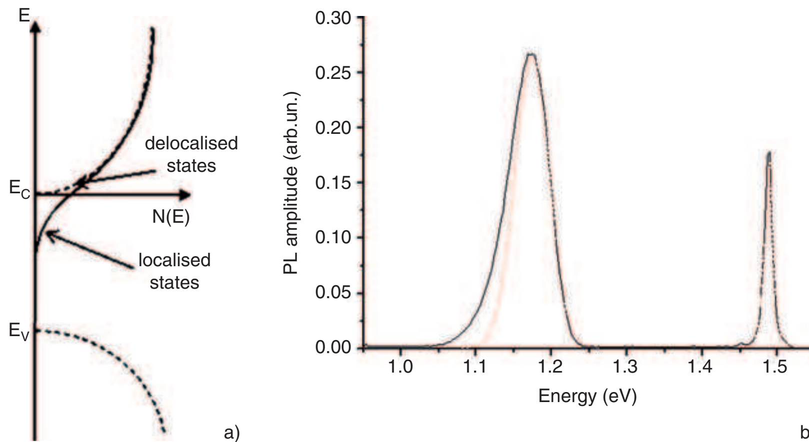

Fig. 7.1. (**a**) Schematic view of the density of states in QWs containing localised states. (**b**) Typical PL spectrum from a GaNAs/GaAs QW structure (*solid lines*) with Gaussian fits applied to the GaNAs and GaAs peaks (*dashed lines*). Note that the GaNAs peak is highly asymmetry compared to the GaAs feature

excitons can radiatively recombine [15]. Short carrier lifetimes will clearly inhibit the performance of devices such as lasers, which require long carrier lifetimes.

However, localisation can also be exploited to enhance device performance. In the case of III-nitrides materials with high densities of non-radiative centres, exciton localisation improves luminescence efficiency by preventing migration of carriers towards the defects.

7.3 Localisation in Dilute Nitrides

7.3.1 Photoluminescence Lineshape and S-Shape Temperature Dependence

Photoluminescence (PL) emission from high-quality QW samples is generally characterised by symmetric Gaussian-shaped peaks, whose energy position varies with temperature (T) following the empirical Varshni law [16] (or equivalently the Bose–Einstein relation [17]):

$$E_{\mathrm{g}}(T) = E_{\mathrm{g}}(0) - \frac{\alpha T^2}{\beta + T}, \qquad (7.1)$$

where $E_{\mathrm{g}}(0)$ is the emission energy at $T = 0\,\mathrm{K}$, α and β are fitting parameters, which are material specific.

In many dilute nitride studies, both the lineshape and temperature dependence of emission deviate from this ideal behaviour. Dilute nitride emission peaks tend to be asymmetric, having sharp high energy cut-offs and exponential low-energy tails [18, 19]. The low energy tail emission originates from radiative recombination of localised excitons trapped in potential fluctuations in the QW. This means that either the band edges are not well defined or that there are a number of highly radiative states available in the forbidden gap, both implying a strong spatial carrier localisation (Fig. 7.1a). The effect of this localisation on the spectral lineshape can be seen in Fig. 7.1b. While the GaAs-related feature (at around 1.48 eV) is clearly symmetrical, the GaNAs feature (at around 1.17 eV) is highly asymmetric.

The temperature dependence of the peak emission from dilute nitrides is often observed to deviate from the Varshni-like behaviour at low temperatures, as it can be clearly seen with standard temperature dependent PL spectroscopy. This behaviour has been observed in several nitrogen-containing ternary and quaternary alloys, such as AlGaN [20–22], GaInN [20,23], GaInNP [24] and GaInNAs [25–27] and can be explained in terms of recombination of excitons localised at potential fluctuations induced by the presence of nitrogen. In dilute nitrides, the small quantities of incorporated nitrogen results in strong carrier localisation, which leads to a characteristic S-shape feature, composed of three distinct regions (redshift–blueshift–redshift). At very low

temperatures, the peak emission energy decreases due to exciton thermalisation into the lowest localised states. Radiative recombination of these states results in the initial redshift, however, this is not always visible [28]. As temperature increases further, trapped excitons, first in shallow and then deeper potentials, acquire sufficient thermal energy to allow activation into higher localised states or de-trapping. This results in a blueshift of the peak as tail state emission is suppressed. When the temperature is further increased, excitons become completely delocalised and the emission peak energy decreases as expected from bandgap shrinkage with temperature. PL emission energy redshifts again and follows the Varshni curve. A mathematical interpretation of this behaviour has been recently proposed by Li et al. [29] through the relation:

$$E_{\mathrm{g}}(T) = E_{\mathrm{g}}(0) - \frac{\alpha T^2}{\beta + T} - x(T)\, k_{\mathrm{B}} T. \tag{7.2}$$

This equation completes the empirical Varshni relation for the emission energy temperature dependence of perfect semiconductors with the contribution of a third-term, which represents the effect of thermal redistribution of localised carriers. The dimensionless coefficient $x(T)$ can be obtained numerically as described in [30], where the reader can find additional details about this theoretical fit. From a more qualitative investigation, the carrier localisation energy can be estimated from the difference between Varshni-fitted energies and measured PL emission energies:

$$E_{\mathrm{loc}}(T) = E_{\mathrm{Var}}(T) - E_{\mathrm{PL}}(T). \tag{7.3}$$

The parameters characterising the S-shape trend are clearly related to this difference, and are shown in Fig. 7.2 for a GaNAs QW sample. In this figure $E_{\mathrm{loc}}^{0\mathrm{K}}$ and $E_{\mathrm{loc}}^{\mathrm{Max}}$ represent the localisation energies at $T = 0\,\mathrm{K}$ and at the temperature T_{Max} corresponding to the maximum initial redshift. Finally T_{deloc} gives the temperature corresponding to full delocalisation: above this temperature the curve follows the standard Varshni fit [31].

The observation and explanation of S-shape trend in dilute nitrides have been the source of much discussion in the literature, but have always been related to the influence of nitrogen. However, Pinault et al. [26] presented results, which indicate that S-shape behaviour occurs in GaInNAs QW samples but not in GaInAs or GaNAs QWs. These results would seem to indicate that localisation is induced by the simultaneous presence of both indium and nitrogen in the QW. Such behaviour would seem to favour a nearest neighbour interpretation (discussed in Sect. 3.2) of the localisation mechanism in GaInNAs. However, other groups, including the current authors, not only observe S-shape trends in GaInNAs, but also in indium free GaNAs QW samples [32, 33]. In these studies, the degree of localisation is clearly related to the quantity of nitrogen incorporated. Moreover as with all quantum well structures, the growth conditions have also an important effect.

Misiewicz et al. [34] demonstrated that increasing N content in GaInNAs QW systems, at fixed growth parameters, leads to a higher density of

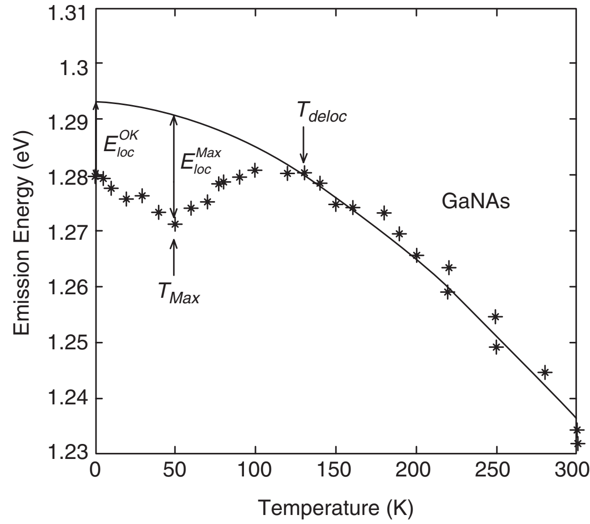

Fig. 7.2. Diagram illustrating S-shape parameter for a GaNAs QW sample

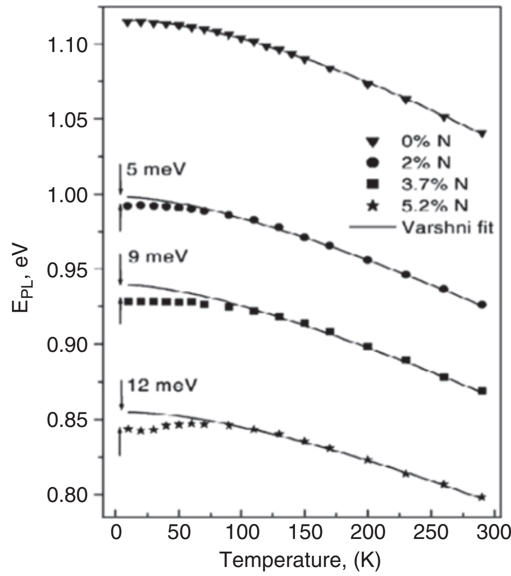

Fig. 7.3. Temperature dependence of the peak emission energy for GaInNAs/GaAs SQW structures, with estimated localisation energies at 10 K (courtesy Misiewicz [35])

defects coming from compositional and structural inhomogeneities. The primary effect is an increase in the carrier localisation energy, which goes from zero in N-free samples to 12 meV for structures with 5.2% N incorporated (Fig. 7.3).

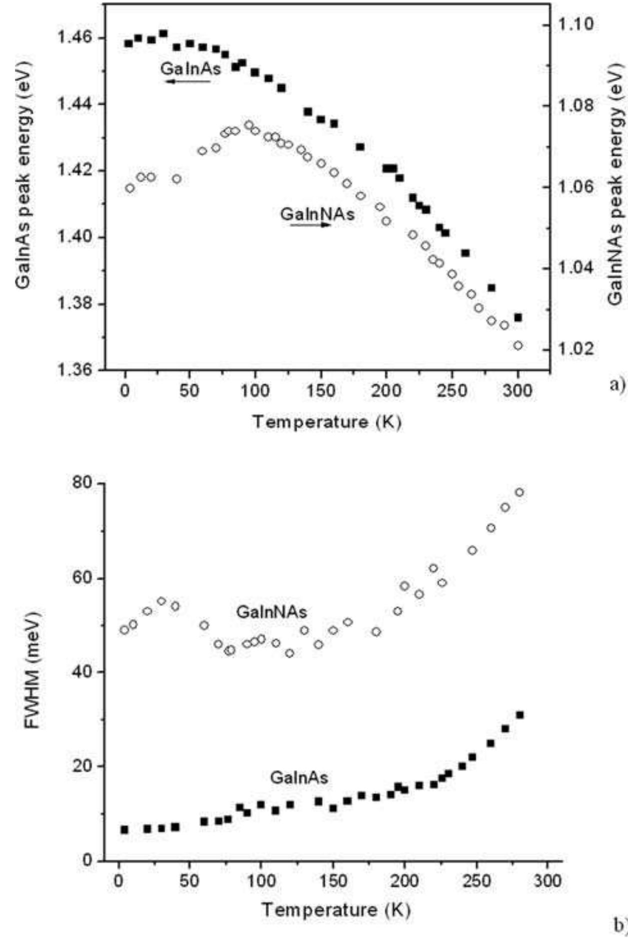

Fig. 7.4. Temperature dependence of PL peak emission (**a**) and spectral width (**b**) for a sequentially grown GaInNAs and GaInAs/GaAs QW sample

The effect of N incorporation on carrier localisation is clearly illustrates in Fig. 7.4a, this shows emission from GaInNAs and GaInAs QWs of a double quantum well sample [36]. In addition to the S-shape peak emission trend, localisation also affects the temperature dependence of spectral linewidth for nitrogen containing QWs. While the linewidth (full width at half maximum, FWHM) of GaInAs emission essentially increases monotonically with temperature due to thermal broadening, the linewidth of GaInNAs emission follows an S-shape style trend (Fig. 7.4b).

At low increasing temperatures, the linewidth broadens rapidly due to the increased population of tail states. It then narrows as de-trapping occurs, which suppresses the low energy emission tail, and finally broadens again in keeping with the expected thermalisation of carriers.

7.3.2 Nearest Neighbour Configurations in Dilute Nitrides

Recent work using tight binding calculations [37] suggests that each nitrogen site in GaInNAs may be surrounded by one of five nearest neighbour (NN) configurations; four gallium atoms (4Ga), three gallium plus one indium (3Ga), and so on, up to four indium atoms (0Ga). The indium-rich NN configurations are energetically favoured in the lattice, so it is likely that GaInNAs deposited by MBE will favour these. In contrast, Ga–N bonds are favoured during MOCVD of GaInNAs: hence Ga-rich NN configurations are preferred. With appropriate post-deposition annealing, the NN configurations can undergo phase changes. In the case of Ga-rich NN configurations, this transformation causes an increase in the bandgap, in keeping with the emission blueshift commonly observed after annealing. The NN environments can have a significant effect on the bandgap, with a maximum energy difference of more than 100 meV between 4Ga and 0Ga environments [37]. Additional experimental [38] and theoretical work based on Monte Carlo simulation [39] supports the NN interpretation. While it is likely that any given sample of GaInNAs will contain a favoured NN-configuration, it is also likely that other closely related NN-configurations will be present. The presence of multiple NN-configurations will result in some degree of carrier localisation within GaInNAs.

7.3.3 Time Resolved Photoluminescence

Time-resolved photoluminescence (TR-PL) is one of the techniques available for studying fast transient carrier dynamics in direct bandgap semiconductors. To date, relatively few TR-PL studies have been carried out on dilute nitride materials [19, 31, 40–43]. However, in most cases the low temperature TR-PL results are dominated by the effects of localisation.

At very short timescales (sub ns) after excitation, the population of localised excitons is low due to the finite time required for exciton trapping. In the work of Potter et al. [31] this finite exciton trapping time is thought to be responsible for the observed temporal evolution of GaInNAs emission peaks. While peak emission from GaInAs QWs was observed to remain essentially constant, emission from GaInNAs QWs shifted rapidly after excitation (Fig. 7.5). In a time period of less than half a nanosecond after excitation, the peaks redshifted by up to 20 meV converging towards the steady-state emission. The magnitudes of the redshifts were found to be similar to localisation energies calculated from the S-shape steady-state PL analysis.

In the work carried out by Nakayama et al. [40] the low temperature (10 K) TR-PL decay time from GaInNAs QWs at energies close to the emission peak was found to be around 1 ns, which is comparable to other typical QW structures. However, decay times were found to increase dramatically with decreasing detection energy, i.e. the tail state region. In addition, the decay

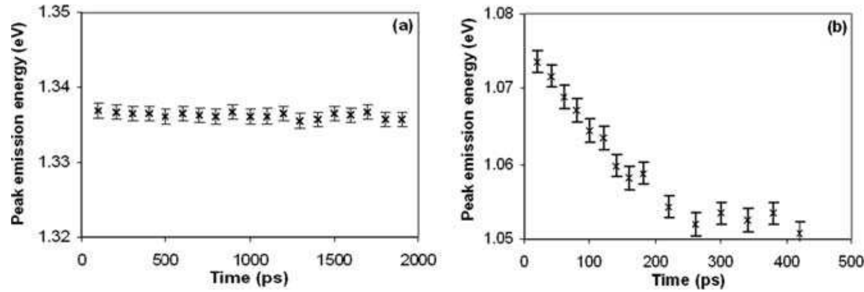

Fig. 7.5. Peak emission energy versus time at 10 K with 5 mW pumping, (**a**) GaInAs peak and (**b**) GaInNAs peak

profiles were found to exhibit non-exponential features, which required fitting using the following stretched exponential form [44]:

$$I\left(t\right)=I_{\mathrm{o}}\exp\left[-\left(\frac{\mathrm{t}}{\tau}\right)^{\beta}\right], \tag{7.4}$$

where τ corresponds to a mean decay time, and β is a dispersion factor (between 0 and 1). This stretched exponential decay behaviour is often encountered in systems which have some degree of disorder and is considered to be a result of dispersive diffusion of excited carriers. The physical meaning of β is rather complex and interested readers are referred to [44] for more details. For the current discussion, β is taken to be a measure of the dispersion, so that dispersion decreases as β approaches one and the decay curve tends towards being a single exponential. The effect of dispersive diffusion is that electrons and holes become spatially separated, temporarily suppressing radiative recombination. Dispersive diffusion of carriers may be due to excitation of carriers from localised to extended states, multiple trapping–detrapping or hopping between different localised states. In the first case, the localised states act as traps and disorder within the system results in a distribution of rates and energies. The decay times of the GaInNAs samples were found to decrease as sample temperature increased to 80 K, leading to β approaching to unity (i.e. less stretched). The temperature dependence of the decay times and the decay profiles indicate an enhancement of detrapping from localised states by thermal activation. From these results, Nakayama et al. [40] concluded that the PL decay dynamics in the GaInNAs SQWs is dominated by the carrier localisation and that the decay profile exhibits the stretched exponential peculiar to a disordered system.

Hoffmann et al. [41] have performed TR-PL measurements on GaInNAs QW samples using resonant excitation. They observe that increasing excitation energy results in decreasing rise times and increasing decay times. This is typical behaviour when capture and recapture processes occur between different localised states. In materials where localised energy states do not dominate

this behaviour, both rise and decay times generally decrease with increasing excitation energy.

Both Hoffmann et al. [41] and Mair et al. [19] have found that the emission energy dependence of low-temperature PL decay rates for GaInNAs samples is characterised by a distribution of localised excitons. They both fit their decay data with Gourdon and Lavaillard's model using functions of the form [45]

$$\tau(E) = \frac{\tau_{\mathrm{rad}}}{1 + \exp\left[\left(E - E_{\mathrm{me}}\right)/E_0\right]}, \tag{7.5}$$

where τ_{rad} is the maximum radiative lifetime, $\mathrm{E_{me}}$ is the energy for which the radiative lifetime equals the lateral transfer time and E_0 is a characteristic energy for the density of states. This model includes mechanisms for both exciton recombination and transfer out of the localised state. The decay process for the lowest energy, strongly localised excitons ($E < E_{\mathrm{me}}$), is predominantly radiative, and hence at low temperatures decay times are long. While higher energy excitons ($E > E_{\mathrm{me}}$) are more likely to transfer out of their sites, hence decay times rapidly decrease with increasing emission energies (Fig. 7.6). The fitted values of E_{me} seem to be correlated with localisation energies determined from PL lineshape analysis [19]. Also, as nitrogen fraction is increased, both τ_{rad} and E_0 increase [41], which is indicative of increased localisation.

7.3.4 Excitation Intensity Dependence

From the above discussion, it is clear that localised carrier effects are visible at low temperature, and are related to localised excitons. Of course there are a finite number of available localised states, hence at low temperatures it is possible to fill them via increased excitation. A blueshift in the emission peak

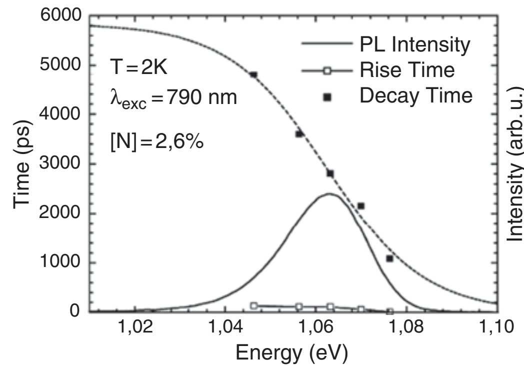

Fig. 7.6. Time-integrated PL of the GaInNAs MQW with 2.6% nitrogen content. The decay and rise times as functions of the detection energy recorded at 2 K. (7.5) was applied to determine the parameters $\tau_{\mathrm{rad}} = 5800\,\mathrm{ps}$, $E_{\mathrm{me}} = 1.078\,\mathrm{eV}$ and $E_0 = 10.6\,\mathrm{meV}$ (courtesy Hoffmann [46])

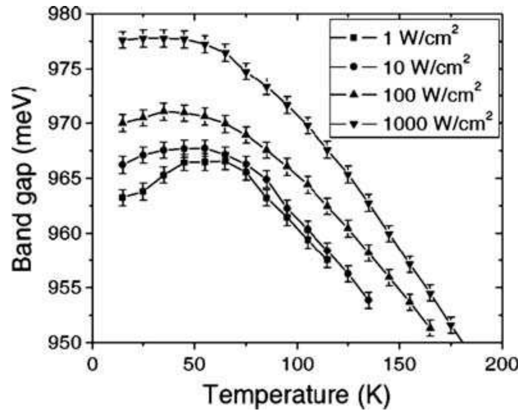

Fig. 7.7. Bandgap shift with temperature for a GaInNAs QW at different excitation densities (courtesy Bank [48])

with increasing PL excitation intensity is therefore common in systems with a population of localised states [18]. This reflects a progressive saturation of the localised energy states until emission becomes dominated by band-edge transitions. As the excitation intensity increases, the S-shape characteristic of emission temperature dependence becomes less pronounced and eventually disappears (Fig. 7.7) [47].

7.4 Reducing Localisation

7.4.1 Thermal Annealing

In situ or post-growth thermal annealing has been extensively investigated as a method of enhancing the optical properties of GaNAs and GaInNAs-based samples. This annealing process allows migration of atoms within the QW and eliminates some of the various defects formed in the material during the growth process [49–51]. Intrinsic point defects have been identified in GaIn(N)As as As_{Ga} antisites [52], N interstitials [53,54] and Ga vacancies [55].

In most cases, annealing of dilute nitride samples results in enhanced emission intensity, a higher quenching temperature and a narrowing in the FWHM. However, it also leads to an undesirable blueshift in the emission, which is believed to be related to defect-assisted interdiffusion, due to defects and compositional inhomogeneities at the interfaces [49,56]. While the magnitude of these effects depends largely on annealing parameters (time, temperature and atmosphere), they also seem to relate to the growth conditions. A full discussion of how annealing affects the characteristics of dilute nitride emission is beyond the scope of this chapter. However, recent studies on GaNAs QW samples show that annealing can reduce the S-shape emission behaviour,

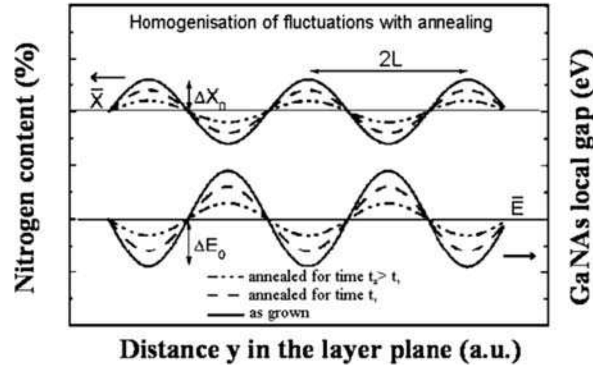

Fig. 7.8. Schematic view of N composition fluctuations, and their homogenisation after annealing, in the layer's plane of a GaNAs QW. The effect on the local gap is also shown (courtesy Grenouillet [59])

which implies that it suppresses localised states [57]. It is believed that the post-growth annealing process improves the homogeneity of nitrogen within the layer. The N preferentially reorganises in the Ga(In)NAs layers rather than diffuse into GaAs barriers.

Rapid-thermal annealing (RTA) induces a decrease of N composition fluctuations in GaNAs. An observed blueshift of the alloy bandgap much greater at low temperature than at room temperature is indicative of this reduction of alloy disorder and therefore of localisation effects. A decrease of the FWHM further confirms this conclusion, and a graphical explanation is schematically shown in Fig. 7.8. The effect is the decrease of the potential fluctuations induced by a reorganisation of nitrogen inside the well, improving the N uniformity [58].

Several other studies also indicate that carrier localisation can be suppressed by annealing. Shirakata et al. [60] show that the crystal quality of GaInNAs SQW samples can be greatly improved via rapid-thermal annealing. They observe a suppression of the S-shape behaviour, a significant reduction in spectral linewidth and a greatly enhanced (∼100 times) emission intensity. Zhao et al. [61] investigated the optical properties of GaNAs QW structures grown at different temperatures and subsequently annealed. They found that carrier localisation is strongly affected by both growth and annealing temperatures. By optimising them, they effectively remove the localisation effects. A significant reduction in the S-shape feature, attributed to a reduced compositional fluctuation inside the QW, was also reported by Kovsh et al. [62], and by Erol et al. [63] In the latter work, PL and spectral photoconductivity (PC) experiments were performed on a GaInNAs QW, before and after RTA (Figs. 7.9 and 7.10). The PL emission before annealing clearly shows strong S-shape features in both the peak emission and FWHM. However, after annealing the S-shapes are significantly reduced, indicating a reduction

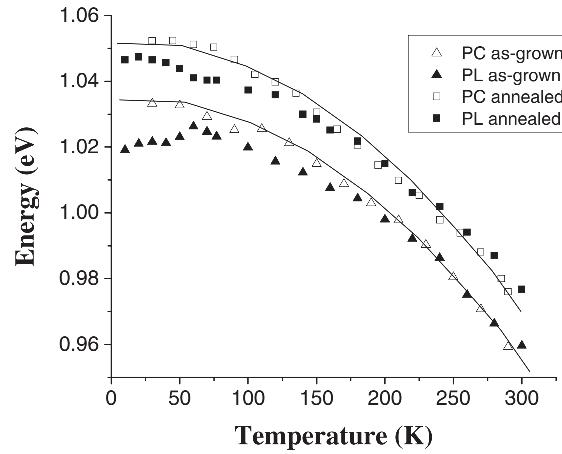

Fig. 7.9. PC and PL bandgap energy evolution with temperature, for a GaInNAs QW, as-grown and after in situ RTA process The *continuous lines* represent the theoretical Varshni fit

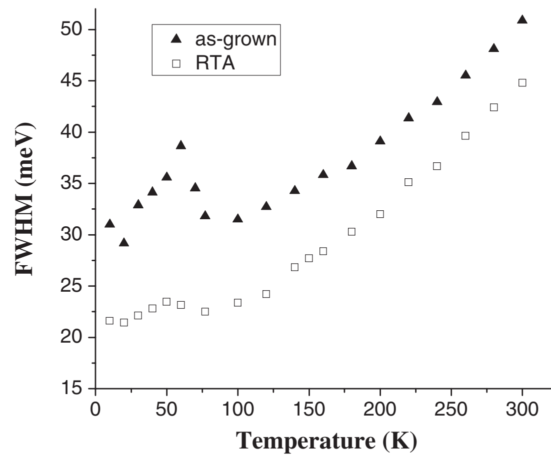

Fig. 7.10. PL linewidth evolution with temperature for a GaInNAs QW, as-grown and after in situ RTA process

in localisation all be it at the cost of a slight blueshift. In contrast, both the before and after annealing PC results follow Varshni-like curves. While PL is an emission-based technique, PC is an absorption-based technique and is, therefore, most sensitive to absorption at the band edge. Similar studies, which compare band-edge behaviour with localisation effects, have been carried out by Uesugi et al. [64, 65] using absorption spectroscopy.

Removal of the S-shape feature in dilute nitrides has been reported also by other means, for example adding GaInNAs barriers in the sample structure [66] or adding antimony into the material, as described in Sect. 7.4.2.

7.4.2 Antimony incorporation

The incorporation of antimony during dilute nitride deposition was first reported by Yang et al. [67]. Sb acts in a surfactant-like manner lowering surface free energy, suppressing diffusion and preventing 3D growth, island formation and phase separation [68]. It has been demonstrated that an excess flux of antimony introduced in the growth process enhances the optical properties of dilute nitrides [69]. Emission wavelengths above 1.4 μm have been demonstrated, which are difficult to achieve without Sb due to the large amount of either In or N required and hence a large miscibility gap. The enhanced crystal and optical properties achievable via the use of Sb results in a significant reduction in carrier localisation. Again, this improvement can be pushed further by an accurate optimisation of growth parameters such as the growth temperature [70], or using both thermal annealing and ion deflection plates [47].

7.5 Summary

In this chapter, we have given an overview of how the incorporation of small fractions of nitrogen affects carrier dynamics in dilute nitrides. Particular emphasis is placed on the formation of localised states due to the addition of nitrogen. Drawing on our own research as well as that of the wider dilute nitride research community, we discuss the experimental evidence for localisation, and the possible causes and methods employed to reduce this. Experimentally, a number of low temperature methods have been used to study and quantify the localised states. Steady-state PL has been extensively used to study spectral lineshape and the so-called "S-shape" emission energy temperature dependence. In addition, time resolved PL, absorption and spectral PC measurements have also been employed to provide further information about these states. In many early dilute nitride studies, it is likely that growth related issues played a significant part in the generation of excessive localisation in QW samples. Recent advances in dilute nitride growth techniques have resulted in enhanced quantum efficiencies and reductions in localisation. In this area of research the addition of antimony is particularly note worthy and certainly deserves further investigation. While advances in dilute nitride growth and in situ or post-growth thermal annealing have clearly helped reduce potential fluctuations, we believe that the dilute nature of these alloys will intrinsically result in some degree of localisation. It is clear that more work is required to fully understand and minimise the localisation in dilute nitrides.

Acknowledgments. We are deeply grateful to Prof. Naci Balkan for his support and guidance in producing this chapter.

References

1. M. Weyers, M. Sato, H. Ando, Jpn. J. Appl. Phys., **31**, L853 (1992)
2. M. Kondow, K. Uomi, A. Niwa, T. Kitatani, S. Watahiki, Y. Yazawa Jpn. J. Appl. Phys., **35**, 1273 (1996)
3. M. Kondow, T. Kitatani S. Nakatsuka, M.C. Larson, K. Nakahara, Y. Yazawa, M. Okai, IEEE J. Sel. Top. Quantum Electron. **3**, 719 (1997)
4. J.S. Harris, IEEE J. Sel. Top. Quantum Electron., **6**, 1145 (2000)
5. J.J. Refi, Bell Lab. Tech. J., **4**, 246 (1999)
6. H. Riechert, A. Ramakrishnan, G. Steinle Semicond. Sci. Technol., **17**, 892 (2002)
7. Q. Han, X.H. Yang, Z.C. Niu, H.Q. Ni, Y.Q. Xu, S.Y. Zhang, Y. Du, L.H. Peng H. Zhao C.Z. Tong, R.H. Wu, Q.M. Wang, Appl. Phys. Lett., **87**, 111105 (2005)
8. C.Y. Liu, S.F. Yoon, Z.Z. Sun, K.C. Yew, Appl. Phys. Lett., **88**, 081105 (2006)
9. A.J. Ptak, D.J. Friedman, S. Kurtz, R.C. Reedy, J. Appl. Phys., **98**, 094501 (2005)
10. Y.Q. Wei, Y. Fu, X.D. Wang, P. Modh, P.O. Hedekvist, Q.F. Gu, M. Sadeghi, S.M. Wang, A. Larsson, Appl. Phys. Lett., **87**, 081102 (2005)
11. R. Grange, A. Rutz, V. Liverini, M. Haiml, S. Schn, U. Keller, Appl. Phys. Lett., **87**, 132103 (2005)
12. P.C. Chang, A.G. Baca, N.Y. Li, P.R. Sharps, H.Q. Hou, J.R. Laroche, F. Ren, Appl. Phys. Lett., **76**, 2788 (2000)
13. T. Kato, Y. Mizuno, M. Hirotani, T. Saka, H. Horinaka, J. Appl. Phys., **89**, 2907 (2001)
14. J. Christen, M. Krahl, D. Bimberg, Superlatt. Microstruct., **7**, 1 (1990)
15. X. Marie, F. Lephay, T. Amand J. Barrau F. Voillot, M. Brousseau, Superlatt. Microstruct., **10**, 415 (1991)
16. Y.P. Varshni, Physica, **34**, 149 (1967)
17. L. Via, S. Logothetidis, M. Cardona, Phys. Rev. B, **30**, 1979 (1984)
18. I.A. Buyanova, W.M. Chen, G. Pozina, J.P. Bergman, B. Monemar, H.P. Xin, C.W. Tu, Appl. Phys. Lett., **75**, 501 (1999)
19. R.A. Mair, J.Y. Lin, H.X. Jiang, E.D. Jones, A.A. Allerman, S.R. Kurtz, Appl. Phys. Lett., **76**, 188 (2000)
20. Y.H. Cho, G.H. Gainer, J.B. Lam, J.J. Song, W. Yang, W. Jhe, MRS Int. J. Nitr. Semicond. Res., **5S1**, W11.57 (2000), http://nsr.mij.mrs.org/5S1/W11.57/
21. L. Bergman, M. Dutta, M.A. Stroscio, S.M. Komirenko, R.J. Nemanich, C.J. Eiting, D.J.H. Lambert, H.K. Kwon, R.D. Dupuis, Appl. Phys. Lett., **76**, 1969 (2000)
22. A. Bell, S. Srinivasan, C. Plumlee, H. Omiya, F.A. Ponce, J. Christen, S. Tanaka, A. Fujioka, Y. Nakagawa, J. Appl. Phys., **95**, 4670 (2004)
23. A. Kaschner, J. Holst, Von U. Gfug, A. Hoffmann, F. Bertram, T. Riemann, D. Rudloff, P. Fischer, J. Christen, R. Averbeck, H. Riechert, MRS Int. J. Nitr. Semicond. Res., **5S1**, W11.34 (2000), http://nsr.mij.mrs.org/5S1/W11.34/
24. Y.G. Hong, A. Nishikawa, C.W. Tu, Appl. Phys. Lett., **83**, 5446 (2003)

25. A. Kaschner, T. Luttgert, H. Born, A. Hoffmann, A.Y. Egorov, H. Riechert, Appl. Phys. Lett., **78**, 1391 (2001)
26. M.A. Pinault, E. Tournié, Appl. Phys. Lett., **78**, 1562 (2001)
27. L. Grenouillet, C. Bru-Chevallier, G. Guillot, P. Gilet, P. Duvaut, C. Vannuffel, A. Million, A. Chenevas-Paule, Appl. Phys. Lett., **76**, 2241 (2000)
28. S. Mazzucato, R.J. Potter, A. Erol, N. Balkan, P.R. Chalker, T.B. Joyce, T.J. Bullough, X. Marie, H. Carrere, E. Bedel, G. Lacoste, A. Arnoult, C. Fontaine, Physica E, **17**, 242 (2003)
29. Q. Li, S.J. Xu, M.H. Xie, J. Phys.: Cond. Matt., **17**, 4853 (2005)
30. Q. Li, S.J. Xu, Cheng, W.C. M.H. Xie, S.Y. Tong, C.M. Che, H. Yang, Appl. Phys. Lett., **79**, 1810 (2001)
31. R.J. Potter, N. Balkan, J. Phys: Cond. Matt., **16**, S3387 (2004)
32. R.J. Potter, N. Balkan, H. Carrere, A. Arnoult, E. Bedel, X. Marie, Appl. Phys. Lett., **82**, 3400 (2003)
33. I.A. Buyanova, W.M. Chen, B. Monemar, MRS Int. J. Nitr. Semicond. Res., **6**, 2 (2001), http://nsr.mij.mrs.org/6/2/
34. J. Misiewicz, P. Sitarek, K. Ryczko, R. Kudrawiec, M. Fischer, M. Reinhardt, A. Forchel, Microelectron. J., **34**, 737 (2003)
35. Reprinted from Microelectron. J. **34**, J. Misiewicz, P. Sitarek, K. Ryczko, R. Kudrawiec, M. Fischer, M. Reinhardt, A. Forchel, "Influence of nitrogen on carrier localization in InGaAsN/GaAs single quantum wells", pp. 737–739, Copyright (2003), with permission from Elsevier
36. S. Mazzucato, R.J. Potter, A. Erol, N. Balkan, P.R. Chalker, S. Thomas, T.B. Joyce, T.J. Bullough, Solid State Electron., **47**, 483 (2003)
37. P.J. Klar, H. Gruning, J. Koch, S. Schafer, K. Volz, W. Stolz, W. Heimbrodt, Kamal A.M. Saadi, A. Lindsay, E.P. O'Reilly, Phys. Rev. B, **64**, 121203[R] (2001)
38. S. Kurtz, J. Webb, L. Gedvilas, D. Friedman, J. Geisz, J. Olson, R. King, D. Joslin, N. Karam, Appl. Phys. Lett., **78**, 748 (2001)
39. K. Kim, A. Zunger, Phys. Rev. Lett., **86**, 2609 (2001)
40. M. Nakayama, K. Tokuoka, K. Nomura, T. Yamada, A. Moto, S. Takagishi, Phys. Stat. Sol. B, **240**, 352 (2003)
41. A. Hoffmann, R. Heitz, A. Kaschner, T. Luttgert, H. Born, A.Y. Egorov, H. Riechert, Mater. Sci. Eng. B, **93**, 55 (2002)
42. K.T. Tsen, W. Liang, D.K. Ferry, H. Lu, W.J. Schaff, U. Ozgur, Y. Fu, Y.T. Moon, F. Yun, H. Morkoc, H.O. Everitt, Superlatt. Microstruct., **38**, 77 (2005)
43. Z. Sun, Z.Y. Xu, X.D. Yang, B.Q. Sun, Y. Ji, S.Y. Zhang, H.Q. Ni, Z.C. Niu, Appl. Phys. Lett., **88**, 011912 (2006)
44. L. Pavesi, M. Ceschini, Phys. Rev. B, **48**, 17625 (1993)
45. C. Gourdon, P. Lavallard, Phys. Stat. Sol. B, **153**, 641 (1989)
46. Reprinted from Mater. Sci. Eng. B, **93**, A. Hoffmann, R. Heitz, A. Kaschner, T. Luttgert, H. Born, A.Y. Egorov, H. Riechert "Localization effects in InGaAsN multi-quantum well structures", pp. 55–59, Copyright (2002), with permission from Elsevier
47. S.R. Bank, M.A. Wistey, H.B. Yuen, V. Lordi, V.F. Gambin, J.S. Harris Jr., J. Vac. Sci. Technol. B, **23**, 1320 (2005)
48. Reprinted with permission from J. Vac. Sci. Technol. B, **23**, S.R. Bank, M.A. Wistey, H.B. Yuen, V. Lordi, V.F. Gambin, J.S. Harris Jr., pp. 1320–1323, Copyright (2005), AVS The Science & Technology Society

49. Z. Pan, T. Miyamoto, D. Schlenker, F. Koyama, K. Iga, Jpn. J. Appl. Phys., **38**, 1012 (1999)
50. T. Kitatani, K. Nakahara, M. Kondow, K. Uomi, T. Tanaka, J. Cryst. Growth, **209**, 345 (2000)
51. T. Kitatani, M. Kondow, K. Nakahara, K. Uomi, T. Tanaka, Mater. Res. Soc. Symp. Proc., **579**, 33 (2000)
52. N.Q. Thinh, I.A. Buyanova, P.N. Hai, W.M. Chen, H.P. Xin, C.W. Tu, Phys. Rev. B, **63**, 033203 (2001)
53. S.G. Spruytte, C.W. Coldren, J.S. Harris Jr., W. Wampler, P. Krispin, K. Ploog, M.C. Larson, J. Appl. Phys., **89**, 4401 (2001)
54. T. Ahlgren, E. Vainonen-Ahlgren, J. Likonen, W. Li, M. Pessa, Appl. Phys. Lett., **80**, 2314 (2002)
55. W. Li, M. Pessa, T. Ahlgren, J. Dekker, Appl. Phys. Lett., **79**, 1094 (2001)
56. M.C.Y. Chan, C. Surya, P.K.A. Wai, J. Appl. Phys., **90**, 197 (2001)
57. L. Grenouillet, C. Bru-Chevallier, G. Guillot, P. Gilet, P. Ballet, P. Duvaut, G. Rolland, A. Million, J. Appl. Phys., **91**, 5902 (2002)
58. I.A. Buyanova, G. Pozina, P.N. Hai, N.Q. Thinh, J.P. Bergman, W.M. Chen, H.P. Xin, C.W. Tu, Appl. Phys. Lett., **77**, 2325 (2000)
59. Reprinted with permission from J. Appl. Phys. **91**, L. Grenouillet, C. Bru-Chevallier, G. Guillot, P. Gilet, P. Ballet, P. Duvaut, G. Rolland, A. Million, pp. 5902–5908, Copyright (2002), AIP American Institute of Physics
60. S. Shirakata, M. Kondow, T. Kitatani, Appl. Phys. Lett., **80**, 2087 (2002)
61. Q.X. Zhao, S.M. Wang, Y.Q. Wei, M. Sadeghi, A. Larsson, M. Willander, Appl. Phys. Lett., **86**, 121910 (2005)
62. A.R. Kovsh, J.S. Wang, L. Wei, R.S. Shiao, J.Y. Chi, B.V. Volovik, A.F. Tsatsul'nikov, V.M. Ustinov, J. Vac. Sci. Technol. B, **20**, 1158 (2002)
63. A. Erol, N. Akcay, M.C. Arikan, S. Mazzucato, N. Balkan, Semicond. Sci. Technol., **19**, 1086 (2004)
64. K. Uesugi, I. Suemune, T. Hasegawa, T. Akutagawa, T. Nakamura, Appl. Phys. Lett., **76**, 1285 (2000)
65. I. Suemune, K. Uesugi, W. Walukiewicz, Appl. Phys. Lett., **77**, 3021 (2000)
66. H.D. Sun, A.H. Clark, H.Y. Liu, M. Hopkinson, S. Calvez, M.D. Dawson, Y.N. Qiu, J.M. Rorison, Appl. Phys. Lett., **85**, 4013 (2004)
67. X. Yang, M.J. Jurkovic, J.B. Heroux, W.I. Wang, Electron. Lett., **35**, 1082 (1999)
68. X. Yang, J.B. Heroux, M.J. Jurkovic, W.I. Wang, Appl. Phys. Lett., **76**, 795 (2000)
69. J.C. Harmand, A. Caliman, E.V.K. Rao, L. Largeau, J. Ramos, R. Teissier, L. Travers, G. Ungaro, B. Theys, I.F.L. Dias, Semicond. Sci. Technol., **17**, 778 (2002)
70. S.R. Bank, H.B. Yuen, M.A. Wistey, V. Lordi, H.P. Bae, J.S. Harris Jr., Appl. Phys. Lett., **85**, 021908 (2005)

8

Influence of the Growth Temperature on the Composition Fluctuations of GaInNAs/GaAs Quantum Wells

M. Herrera, D. Gonzalez, M. Hopkinson, H.Y. Liu, and R. Garcia

In this chapter, we review our investigations on the composition fluctuations of GaInNAs/GaAs(001) quantum wells and on the effect of the growth temperature in this feature. For this, we have analyzed GaInNAs quantum well samples grown at different temperatures in the range 360–460°C by transmission electron microscopy in diffraction contrast mode. Our results show a variation of the contrast as bright and dark regions along the quantum well, related to phase separation in the alloy. This variation becomes more severe on increasing the growth temperature, showing that the composition fluctuations are stimulated with this growth parameter. From the analysis of the structure factor of GaInNAs for the g002DF reflection, it is proposed that the observed compositional inhomogeneity of GaInNAs is due firstly to a fluctuation of the indium content and secondly to an out of phase N fluctuation, the latter occurring since nitrogen bonds preferentially to Ga-rich regions in the alloy. With regard to the thermodynamics of the process, we have used several models from the literature for the calculation of the critical temperatures of spinodal decomposition. This analysis shows that N has a higher tendency to phase separation than In, and that the introduction of nitrogen into the ternary alloy GaInAs can also stimulate the composition fluctuations of indium in the alloy. Regarding the kinetics of the process of phase separation, we have calculated the energy of activation for surface diffusion in the alloy. The results suggest that the diffusion of indium controls the process of formation of phase separation.

8.1 Introduction

Since Kondow et al. [1] proposed and created the GaInNAs alloy in 1995, many efforts have been devoted to the research and development of this semiconductor alloy with the aim to use it in optoelectronic devices, such as those in the optical fiber field. The principal characteristic of this system is that it shows

an extremely large negative band gap bowing [2] that allows a redshift of the emission wavelength through the incorporation of low-N contents in GaAs or GaInAs structures. GaInNAs can be grown pseudomorphically on GaAs substrates with a type-I band line up, offering the advantages of established GaAs device technology, such as lower substrate cost, ease of fabrication, and the advantageous refractive index properties of the GaAlAs ternary alloy. The GaInNAs material system has been used for transverse lasers [3–5], with laser emission at 1.3 μm produced from quantum wells of GaInNAs with 30% of In and a N composition as low as ∼2%. Other optoelectronic applications include vertical cavity surface-emitting lasers (VCSELs) [6] as well as solar cells [7] and heterojunction bipolar transistors [8].

The successful performance of such devices depends on the ability to growth of high-quality single crystalline epitaxial layers of these materials. Using molecular beam epitaxy (MBE), which is predominantly considered here, the growth temperature appears to be one of the key parameters. On the one hand, a growth temperature too high limits the incorporation of N in the GaInAs alloy [9], whilst, on the other hand, low growth temperatures degrade the efficiency of light emission due to an increase of point defects [10]. Moreover, as we will show in the following, this growth parameter also influences drastically the composition in the alloy [11, 12]. Although, in principle, a random atomic distribution in the layers could be supposed, in practice a temperature-dependent miscibility gap exists in most solid solutions, leading to the apparition of composition fluctuations. The difficulties in the growth of homogeneous layers are more complex in quaternary alloys because two compositional degrees of freedom are present. In GaInNAs, the phase separation problem can be overcome to some extent by growing the layer at low temperature followed by a postgrowth annealing process at high temperature [13], during which the degradation of the luminescence properties [14] is partially recovered. However, a better understanding of the behavior of the system and, in particular, of the composition of the alloy, with the growth temperature, is needed to optimize the performance of the GaInNAs optoelectronic devices.

This work addresses the effect of the growth temperature on the composition fluctuations of GaInNAs structures. For this study, the samples of GaInNAs quantum wells described below have been studied by transmission electron microscopy (TEM) in diffraction contrast mode. We have also approached the phase separation problem in GaInNAs theoretically, firstly through the calculation of the critical temperatures of spinodal decomposition according to several models proposed in the literature. However, these models cannot explain the results obtained experimentally. This has led us to consider kinetic parameters such as the diffusion of the different species in the alloy to obtain a better understanding the behavior of the system.

8.2 Experimental

The GaInNAs samples studied in this work have been grown by MBE on (001) GaAs substrates in a VG V80H MBE system equipped with an Oxford Applied Research HD25 radiofrequency plasma source for N. The N flux was controlled by monitoring the intensity of the atomic N plasma emission with a photodiode. The nitrogen content in the epilayers was calibrated from the X-ray diffraction analysis of bulk samples and GaNAs quantum wells grown using similar plasma emission intensities. Three different sets of samples have been studied. The first one consists of four structures with 8 nm thick $Ga_{0.62}In_{0.38}N_{0.023}As_{0.977}$ single quantum wells embedded between $GaN_{0.007}As_{0.993}$ barrier layers with thickness 52 nm. The growth temperature of these samples was 360, 400, 440, and 460°C, respectively. With regard to the second set of samples, the design of the structures is similar to the previous set, but with the difference that buffer layers (BLs) of $Ga_{0.88}In_{0.12}N_{0.019}As_{0.981}$ were inserted before and after each well. This set of samples comprises five structures, grown at 375, 385, 400, 410, and 420°C, respectively. Finally, for comparison, 8 nm thick GaInAs QWs with nominal In content of $x = 0.3$ were also grown at two different temperatures; 460 and 515°C.

Specimens were thinned to electron transparency by mechanical polishing followed by low-voltage Ar^+ ion milling at a liquid nitrogen cooled stage for the cross-sectional TEM analysis. TEM studies were performed in JEOL EX1200 and JEOL 2011 microscopes operating at 120 and 200 kV, respectively.

8.3 Composition Fluctuations in GaInNAs Studied by Transmission Electron Microscopy in Diffraction Contrast

Analysis by TEM of the GaInNAs samples grown at $T \leq 440$°C has shown that these structures present a good crystal quality, with no dislocations or any other structural defects, and exhibiting perfectly flat wells. When increasing the growth temperature to 460°C, however, an undulation of the wells and the presence of threading dislocations are observed [15, 16]. Therefore, it seems that the growth temperature is a key parameter to obtain high-quality GaInNAs structures.

Despite the good structural quality, a variation of the contrast with g220BF reflection along the well has been observed in all samples, showing dark and light fringes with periodic character. For the structures grown at the lower temperatures, the variation of the contrast is relatively slight, but we have found that on increasing the growth temperature the change of contrast gets progressively more pronounced. The dark and light fringes observed have been associated to the existence of a phase separation in the alloy, as it will be shown later. To quantify the differences found between the samples grown at different temperatures, the intensity profiles of the g220BF images taken

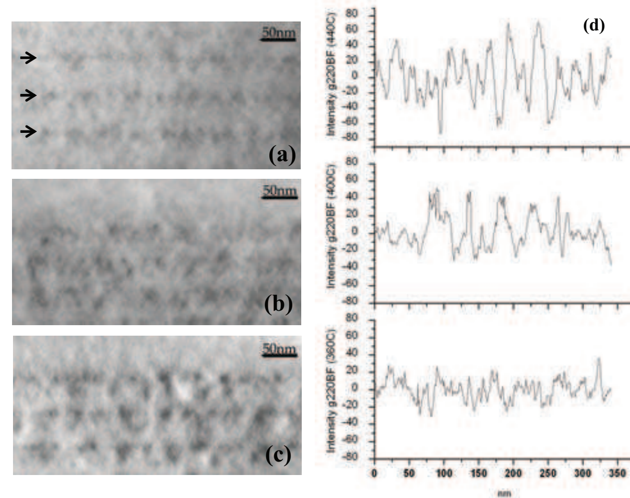

Fig. 8.1. g220BF images of the samples grown at 360°C (**a**), 400°C (**b**), and 440°C (**c**), and (**d**) the intensity profiles taken in the upper well of each structure

in the upper well of each sample and normalized with the GaAs substrate have been considered. Figure 8.1 shows g220BF micrographs of the samples grown at 360, 400, and 440°C, where the intensity profiles taken from the upper well of both micrographs and normalized to the GaAs substrate have been included. In these profiles, an increase in the amplitude when raising the growth temperature is clearly observed.

To try to separate the contribution of the In and the N atoms to the structural features found in these samples, quantum wells of the ternary alloy GaInAs were grown at different temperatures. The composition of these samples was chosen in such a way that the lattice mismatch is similar to that in the GaInNAs structures described above. The analysis with g002DF reflection of the $Ga_{0.7}In_{0.3}As$ structure grown at 460°C has shown that the well is perfectly flat; however, very slight stress contrasts have been observed in g220BF. This is in contrast to the behavior of the GaInNAs structures, where more pronounced contrasts were found in samples grown at even lower temperatures. This result suggests that the addition to N to the ternary GaInAs alloy has a strong influence in the formation of the observed contrasts, as will be further discussed later. Increasing the growth temperature to 515°C, the $Ga_{0.7}In_{0.3}As$ QW is strongly undulated, as it can be observed in Fig. 8.2. Thus, both alloys GaInAs and GaInNAs show the same behavior with regard to the 3D growth mode, but in GaInAsN this behavior takes place at a significantly lower temperature.

Figure 8.3 shows a summary of the results obtained with the g220BF reflection in the present work. In this figure, the average amplitude of the intensity profiles taken from g220BF images in the samples with GaNAs barrier layers

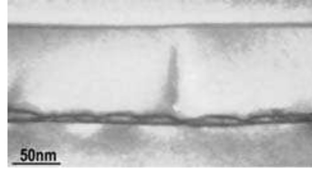

Fig. 8.2. g002DF micrograph of the GaInAs structure grown at 515°C

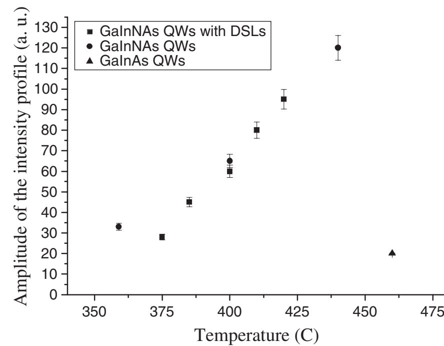

Fig. 8.3. Graph of the amplitude of the intensity profile taken from g220BF micrographs in the upper well of each structure vs. the growth temperature

and with BLs is plotted vs. the growth temperature. It should be noted that the amplitude of the strain contrasts in both sets of samples presents a similar tendency with temperature; therefore, the insertion of BL seems not to affect drastically the phase separation in the alloy. The insertion of BL between the GaInNAs quantum well and the GaNAs barrier has been proposed to improve the optoelectronic properties of this alloy, extending the emission wavelength in quantum wells mainly due to a reduction in the potential barrier. In this work, we have not found significant evidences that this improvement is due to a variation in the composition fluctuations in the alloy. With regard to the graph in Fig. 8.3, we have fitted the experimental data to a line using the minimum squares method. From this graph, we have obtained a value of approximately 330°C for the temperature at which the amplitude of the contrasts would become zero, suggesting that, at this temperature, the growth of a homogeneous GaInNAs layer would be expected. This experimental result is of great technological importance, given that the phase separation affects the optoelectronic properties of the alloy. In the same figure, we add the intensity of the contrast amplitude for the $Ga_{0.7}In_{0.3}As$ sample growth at 460°C. As we can observe, the extent of composition modulation for the GaInNAs samples is remarkably high with respect to the $Ga_{0.7}In_{0.3}As$ sample, the latter being only comparable to the GaInNAs grown at the lowest growth temperature (360°C).

To clarify the origin of the contrasts observed with the stress-sensitive g220BF reflection in our samples, we need to consider electron scattering in a deformed crystal, a phenomenon that can be treated by means of the dynamical theory of diffraction contrast. Thus, the intensity of the incident and scattered waves is related to the displacement field ($\boldsymbol{R}(r)$) of the atoms in a nonperfect crystal [17]. The variation in intensity of the electron beams gives rise to the contrasts observed in TEM images. The displacement field $\boldsymbol{R}(r)$ can be produced by lattice defects such as dislocations as well as by the distortion of the atomic planes of a coherent thin layer. In our samples, the lattice mismatch between the GaInNAs quantum wells and the substrate is identical for the different structures, given that they all have the same composition. Therefore, in the absence of lattice defects, similar contrasts are expected. However, we have observed in our study that the contrasts are stronger on increasing the growth temperature of the quantum well, despite the fact that all the samples have the same composition. Moreover, although the structure obtained at 460°C shows 3D growth, the other samples do not exhibit any structural defect that could be responsible for such contrasts. Therefore, the cause of the displacement field responsible for the contrasts observed with g220BF reflection needs to be treated as an atomic plane distortion in the $\langle 110 \rangle$ directions. According to Vegard's law, the lattice parameter of any material system is directly related to its composition. Consequently, variations of composition inside a particular alloy would result in a modulation of its lattice parameter and hence in the apparition of a displacement field in the atomic planes. We believe that the contrasts observed with g220BF reflection are due to composition fluctuations in the wells as a consequence of interdiffusion at increasing growth temperature. If we compare these contrasts with those found with g220BF reflection in the GaInAs structure grown at 460°C and with the same lattice mismatch than the GaInNAs samples, we can see that in the quaternary alloy the contrasts are much more pronounced. This means that the introduction of N in the ternary alloy plays an important role in the formation of the observed contrasts.

It should be mentioned that, although our reasoning about the existence of composition fluctuations is based on the stress-sensitive g220BF reflection, the g002DF reflection is usually considered as a "composition-sensitive" reflection. The g002DF reflection is associated with composition because its intensity depends on the difference in the atomic structure factors of the constituent atoms, whereas in g220BF it depends on the sum of these factors. The GaInNAs samples considered have also been studied with the g002DF reflection. However, this reflection does not show variations in the contrast along the wells in any of the samples, independently of the growth temperature and of the insertion of BLs. Figure 8.4a shows a micrograph of the structure grown at 440°C, and in Fig. 8.4b the intensity profile taken from this micrograph in the central part of the well and normalized with the GaAs substrate is shown. As can be observed, no major fluctuations of the amplitude in this profile are observed.

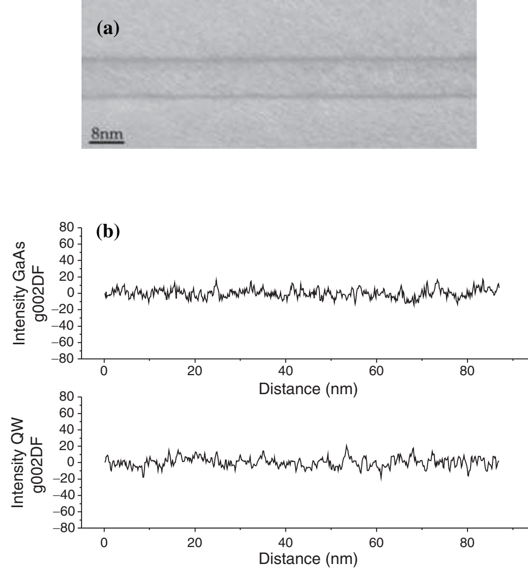

Fig. 8.4. (**a**) g002DF image of the sample grown at 360°C and (**b**) intensity profiles taken inside the quantum well and in the GaAs substrate from the picture in (**a**)

Up to now, several authors have already reported experimental evidence of lateral composition modulations in the GaInNAs QWs using g002DF image analysis [18–20], although this has been only attributed to In segregation. Albrecht et al. reported In-concentration fluctuations of ∼5% whilst Patriarche et al. found a fluctuation of ∼7% between In-depleted and In-rich zones in a similar quaternary alloy using normalized g002DF intensity profiles for the as-grown samples. In both reports, there was no indication of lateral fluctuations of N-concentration. For the annealed samples, they also do not observe fluctuations in the g002DF profiles. The experimental results by TEM show that no modulation contrasts appear with the chemical-sensitive g002DF reflection, whereas a high degree of lateral deformation with g220BF reflection is observed. As we are showing in the following, both results can only be explained if nitrogen and indium segregation occurs [21].

The chemically sensitive g002DF reflection under kinematical conditions depends mainly on differences between the atomic scattering factors of III and V elements, being relatively independent of sample thickness for these contents. The intensity of the g002DF reflection (I_{002}) for a zinc-blende structure is given by

$$I_{002} \approx C\,|F|^2 = 4C(f_{\mathrm{III}} - f_{\mathrm{V}})^2 = 4C[xf_{\mathrm{In}} + (1-x)\,f_{\mathrm{Ga}} - yf_{\mathrm{N}} - (1-y)f_{\mathrm{As}}]^2, \quad (8.1)$$

where C is a factor that depends on thickness and imaging conditions, F is the structure factor, and f are the atomic scattering factors. For a sample with nonuniform composition, a region of the material A, where the In and

N contents are increased by an arbitrary quantity Δx and Δy, respectively, implies a region B nearby in which these compositions are decreased in the same proportion. To obtain the same dark field intensity in the two different regions A and B, we need that

$$I_{002}^{A}(x+\Delta x, y+\Delta y) = I_{002}^{B}(x-\Delta x, y-\Delta y). \tag{8.2}$$

Solving, we obtain

$$\Delta x = -\frac{f_{\mathrm{As}} - f_{\mathrm{N}}}{f_{\mathrm{In}} - f_{\mathrm{Ga}}}\Delta y = -2.208\Delta y. \tag{8.3}$$

Therefore to obtain the invariant g002DF intensity profiles in GaInNAs QWs that we have observed experimentally, it is necessary that an increase in the N composition Δy must be accompanied of a simultaneous decrease in the In content Δx in the proportion $\Delta x \approx -2.21\Delta y$. The formation of N-rich regions with a depletion of In content into In-rich and N-depleted regions obeying the rule $\Delta x \approx -2.2\Delta y$ could explain the absence of contrast modulation with the g002DF reflection. Consequently, we suggest that there are two compositional modulation profiles, one for N and another for In, which are 90° out of phase to the In distribution. In addition, the uncoupling of In and N composition profiles could also explain the high-strain fields that appear with g220BF reflection. For this reflection, the image is dominated by the strain field contrast ($\boldsymbol{g} \cdot \boldsymbol{R}$), where $\boldsymbol{R}$ is the displacement vector regarding the regular position of the atoms. In a simplified form, if we consider two close coherent regions with different composition, for example A and B, the displacement field for this situation is

$$\boldsymbol{R} = \frac{3K\delta}{3K + 2E(1-\nu)}, \tag{8.4}$$

where K is the bulk modulus for the phase A, E and ν are, respectively, the elastic modulus and Poisson's ratio of phase B, and δ is the lattice misfit. Although the compositional profile follows a sinusoidal form, we can calculate the maximum δ that corresponds to the higher contrast as

$$\delta = \frac{a^{A}(x+\Delta x, y+\Delta y) - a^{B}(x-\Delta x, y-\Delta y)}{a^{B}(x-\Delta x, y-\Delta y)}, \tag{8.5}$$

where a^{A} and a^{B} are the lattice parameters of regions A and B, respectively. If we imposed the condition derived in (8.2), we can obtain the lattice misfit amongst regions with the same chemical contrast in the g002DF condition (see Fig. 8.5).

In the same figure, we also show the lattice misfit for the GaInAs case ($y = 0$) with the same Δx. As we can see, the lattice misfit for the same amplitude of In modulation, Δx, is always higher in the GaInNAs samples than GaInAs samples. This result is in agreement with the contrast amplitude

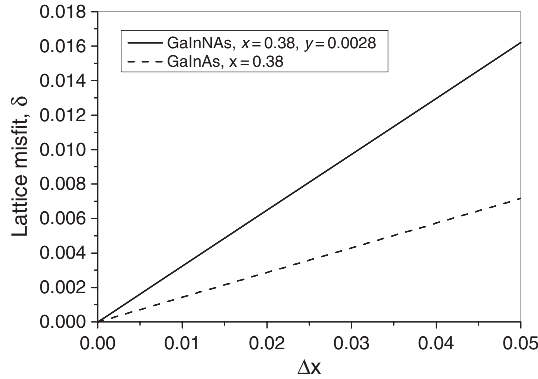

Fig. 8.5. Lattice misfit among GaInNAs regions with the same chemical contrast in the g002DF condition. In the same figure, we also show the reticular misfit for the GaInAs case ($y = 0$) with the same Δx

ratio experimentally measured with the g220BF reflection (see Fig. 8.1). The system would show homogeneous contrasts with the g220BF (no strain fields) if the In and N composition profiles were in phase (matched conditions, $\Delta x \sim 3\Delta y$), i.e., to say, the N-rich regions coincide with In-rich regions. Only the formation of separate In-rich and N-rich regions could explain the higher strain fields observed with the g220BF and the absence of fluctuation contrast with the g002DF reflection.

We should point out that the proportion $\Delta x \approx -2.21\Delta y$ need not to be precisely followed to observe an absence of contrast with the g002DF reflection. Probably there exists a range of proportions of indistinguishable contrasts for which the image is not sensitive to. The use of g002DF intensity contrasts has been studied in detail for GaInAs. Cagnon [22], Glas [23], or Patriarche [20], using different models for g002DF image analysis, have shown that there does not exist a perfect agreement between experimental and theoretical results, although their experimental results indicate that the relative g002DF contrasts are more sensitive than theoretical predictions when In contents are in the 30–40% range. As example, Patriarche et al., using an experimental fit of normalized contrast, propose contrast sensitivity for Indium measurement of 0.02%. With regard to the effect on the g002DF contrast of N incorporation, there have been no experimental studies in the bibliography from which we can estimate the relative sensitivity of the technique. However, if we use the kinetical model and compare this to known observations, we believe that we should be able to detect differences of 0.5% of N for the same In content (relative intensities higher than 10%). The large difference between the N atomic factor and the other atoms (Ga, In, and As) explains this relatively high sensitivity. These predictions are confirmed experimentally through g002DF TEM analysis of GaAsN/GaAs QWs with ~1% of nitrogen which show remarkably strong contrast with respect to the

GaAs barriers. In addition, in the same way that elastic strain raises the experimental g002DF contrast with regard to theoretical predictions [22], we suppose that the nitrogen g002DF analysis could be more sensitive because the inhomogeneity of N incorporation introduces a higher strain field. However, it should be noted that we do not propose exact measurement of composition modulation amplitude in our work, but rather we think that contrast differences should be more appreciable for this N and In composition.

There are few works in the literature concerning measurements of In and N in QWs with the required compositional sensitivity on a nanometer scale. Using electron energy loss spectroscopy (EELS) [24] or annular dark field scanning transmission electron microscopy (STEM) [25], there have been no studies reported which can resolve the N distribution to the required compositional and spatial sensitivity. However, for N-rich samples, the existence of a composition profile, which is 90° out phase, has been confirmed using STEM energy dispersive X-ray (EDX) elemental maps. Bullough et al. [26] confirm the presence of differentiated cells rich in In, Ga, and As atoms that tend to become In-rich toward the cell center separated by thin second phase regions, and show an increase in the Ga and N contents, and a deficiency in In and As. These results are consistent with our experimental findings.

On the other hand, and in relation to the results obtained with g002DF reflection, some comments should also be made on the differences found with regard to the 3D growth between the GaInAs and the GaInNAs samples studied. The Stranski–Krastanow (SK) growth mode observed in our study shows a similar tendency in both GaInAs and GaInNAs alloys. Whereas growing at relatively low temperature the wells appear perfectly flat, on increasing the temperature the growth mode changes from 2D to 3D. However, the temperature at which the bidimensionality is lost is different in both systems. At 460°C the GaInAs wells remain flat, but in comparison the GaInNAs ones show well-defined islands. The SK growth mode [27] has been demonstrated to take place in highly mismatched systems [28, 29], as a mechanism to relax the strain in the epilayer [30]. Thermodynamic models have been widely used to predict its stability by considering the balance of strain and surface energies [31]. However, as the growth process is a nonequilibrium process, other factors such as deposition rate [32], temperature [33], and diffusion [33] must also be considered. Our results have shown that, although in both $Ga_{0.7}In_{0.3}As$ and $Ga_{0.62}In_{0.38}N_{0.023}As_{0.977}$ alloys the SK growth process is thermodynamically favored, but kinetically limited by growth temperature, in GaInNAs quantum wells the critical temperature for this to take place is lower. Therefore, it should be an N-related phenomenon which promotes the 3D growth at lower temperatures and not the strain difference.

Classical theories of SK growth consider that an initially flat epilayer would evolve into 3D islands only when the first nuclei of material reach a particular critical size [34], otherwise these nuclei dissolve back into the 2D layer. This implies that an energetic barrier is present which needs to be overcome for the stabilization of the first islands. As our results have shown, whilst the GaInAs

structures are quite homogeneous, the GaInNAs quantum wells show phase separation. The presence of composition fluctuations is expected to produce nonuniformities in the surface strain of the structure. These variations in surface strain could locally reduce the energy barrier for the transformation into stable islands, favoring the 3D growth at lower temperature in the GaInNAs structures. This mechanism is analogous to that acting in stacked quantum dots, in which stress from underlying dots promotes subsequent layers to stack above this position.

Recently it has been proposed theoretically and demonstrated experimentally that the segregation of In from the flat wetting layer to the surface of the structure controls island formation [35, 36]. Taking into account this theory and according to our results, a possible mechanism would be that In segregation toward the surface is more favored in the GaInNAs system than in GaInAs. Increased In segregation in the nitrogen-containing alloy would seem reasonable if we consider the high elastic strain in the nitride. In the GaInNAs alloy, there is a big difference in atomic size between the constituent atoms (as mentioned earlier). Placing the small N atoms in the atomic sites of the larger As atoms should produce local stresses in the structure. Diffusion toward the surface of the structure of an atom of large size as In could be enhanced because of these stresses in the alloy, then favoring the formation of islands according to the model mentioned above [35, 36].

The two mechanisms considered could contribute up to a point to the Stranski–Krastanow growth in GaInNAs alloys. However, we believe that the main reason for the transition 2D–3D taking place at lower temperature in GaInNAs than in GaInAs could be the nonuniformities in the surface of the nitride structure because of the phase separation. Lowering the energy barrier for the formation of the first nuclei would result in the apparition of islands at lower temperature, as our results have shown. In addition, we know of no data on increased In segregation in GaInNAs QWs and therefore favor the former model.

8.4 Spinodal Decomposition in GaInNAs

Cross section and planar view of TEM specimens reveal that strong composition contrasts are aligned to the ⟨110⟩ directions. It is well known that the lateral composition modulation can line up in the ⟨100⟩ direction in which the elastic strain energy is minimum or in the ⟨110⟩ directions where the atomic diffusion is faster [37]. This fact highlights the importance of the surface diffusion process and therefore the deposition variables for this system, but also reinforces our hypothesis that the profiles obtained in the ⟨110⟩ cross-section micrographs can offer a good and realistic image of the strength of composition modulation in the alloy. For all of the samples, except the highest temperature (460°C) sample, compositional modulation occurs without undulations in the QW structure. It has been reported that morphological instabilities are in

many cases the origin of phase separation due to a different size or mobility of the atoms in the alloy [38–40]. Although the sample grown at 460°C shows that a higher composition modulation is coupled with a surface modulation, the samples grown at lower temperatures present perfectly flat interfaces with a well-defined composition modulation. This is evidence to support the intrinsic trend of GaInNAs alloys toward phase separation. In the last years, the problem of the phase separation has been often approached theoretically by the calculation of the critical temperatures of spinodal decomposition. Although it is true that kinetic factors such as growth rate must be included in a more realistic model and that it is probable that phase separation occurs within a few monolayers close the surface, it is also clear that thermodynamic aspects such as the chemical interactions between atoms play an important role in the description of phase separation in this system [41].

Following Cahn [42,43], who proposed a theoretical model for bulk binary metal alloys, several authors have extended the theory of spinodal decomposition to semiconductor alloys [44, 45]. However, the predicted critical temperatures were abnormally low. Since then, several authors have applied theoretical calculations to epitaxial layers, considering also the elastic energy that results from the lattice mismatch of a layer grown on a substrate [46,47]. Nowadays, theoretical models tend to include specific characteristics of the epitaxial growth, such as the atom adsorption from the vapor to the surface, surface diffusion instead of bulk diffusion, or surface morphological undulation. From the earlier treatment of Malyshkin [48], several models that introduce different kinetic instabilities coupled with morphological instabilities have been developed. However, as pointed by Millunchick [49], compositional modulations can occur even in the absence of morphological modulations if the semiconductor alloy shows a tendency for phase separation or spinodal decomposition.

According to the exposed above, we believe that the spinodal decomposition models can be very useful to obtain a first estimation of the tendency toward phase separation of the different components of the alloy. Therefore, we have applied some of the models found in the literature to the alloy under the study of GaInNAs.

Several factors are usually included in the calculation of the miscibility gap for epitaxial semiconductor layers, mainly the chemical energy, the coherency strain energy, and the gradient energy, although often the last one is considered negligible with respect to the other two. With regard to the chemical energy, two approaches are normally used for its calculation: the regular solution (RS) model and the delta lattice parameter (DLP) [44]. The expressions for the chemical energy according to these models read, respectively, as follows

$$\begin{aligned} G_{\mathrm{chem}}^{\mathrm{RS}} &= xy\mu_{\mathrm{InN}}^{0} + x(1-y)\mu_{\mathrm{InAs}}^{0} + (1-x)y\mu_{\mathrm{GaN}}^{0} \\ &\quad + (1-x)(1-y)\mu_{\mathrm{GaAs}}^{0} + x(1-x)y\alpha_{\mathrm{InN\text{–}GaN}} \\ &\quad + xy(1-y)\alpha_{\mathrm{InAs\text{–}InN}} + x(1-x)(1-y)\alpha_{\mathrm{InAs\text{–}GaAs}} \\ &\quad + (1-x)y(1-y)\alpha_{\mathrm{GaAs\text{–}GaN}} + A \end{aligned} \tag{8.6}$$

and

$$G_{\text{chem}}^{\text{DLP}} = -K(\Delta a)^2 a^{-4.5} + A, \tag{8.7}$$

where

$$A = RT\left[x\ln(x) + (1-x)\ln(1-x) + y\ln(y) + (1-y)\ln(1-y)\right], \tag{8.8}$$

μ^0 is the chemical potential of the pure binaries, a is the lattice constant, α is the interaction parameter between the binary compounds, K is a constant for all systems, R is the universal gas constant, and x and y are the In and N composition, respectively.

As it can be seen, the expression of the regular solution model includes the calculation of the chemical potentials and the interaction parameters of the pure binaries. The DLP, on the other hand, allows us to simplify the calculation, approximating these terms by the expression $K(\Delta a)^2 a^{-4.5}$. We are going to evaluate the validity of this approximation for our alloy GaInNAs.

For the RS model we have used the approximation proposed by Asomoza [50], where the chemical potentials of the pure binaries are estimated using the expression

$$\mu_{AB}^0 = H_{AB} - TS_{AB} + \int_{298.15}^{T} C_{\text{p}}^{AB}\,\mathrm{d}T - T\int_{298.15}^{T} C_{\text{p}}^{AB}\,\mathrm{d}T/T, \tag{8.9}$$

where H and S are the enthalpy and the entropy at the standard state, respectively, and C_{p} is the specific heat capacity at constant pressure.

We have taken the experimental dependences of the specific heat capacity with the temperature from a different source [51, 52] than the ones [53] used by Asomoza [50]. This has produced deviations in the slope of the curve of the critical temperature with regard to that proposed by this author. Moreover, we have found a high sensitivity in the calculated critical temperatures when changing slightly the expressions considered by us for the specific heat capacity. This means that we should be very careful with the absolute values of the critical temperatures obtained in this calculation, given that the expressions for C_{p} have been obtained experimentally and could be affected by some errors. However, these variations do not affect the main tendencies and conclusions obtained in the present work.

The second term included in these models of spinodal decomposition is the elastic energy due to the lattice mismatch with the substrate, which in this case is

$$G_{\text{strain}} = \Omega(C_{11} - C_{12})(C_{11} + 2C_{12})\varepsilon^2/C_{11}, \tag{8.10}$$

where Ω is the molar volume, C_{11} and C_{12} are the elastic constants, and ε is the elastic strain. Then, for the calculation of the critical temperatures, the condition of the spinodal for quaternary alloys [54]

$$\frac{\partial^2 F(x,y)}{\partial x^2}\frac{\partial^2 F(x,y)}{\partial y^2} - \left(\frac{\partial^2 F(x,y)}{\partial x \partial y}\right)^2 = 0 \tag{8.11}$$

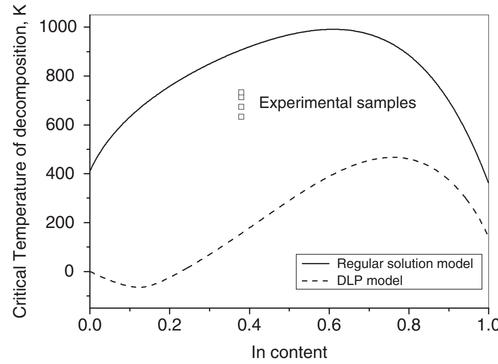

Fig. 8.6. Critical temperatures for spinodal decomposition using DLP and RS models in $Ga_xIn_{1-x}As_{0.977}N_{0.023}$/GaAs structures. Our experimental results are included

is used, where F is the global free energy of the alloy, which is the sum of the chemical energy (G_{chem}) and the strain energy (G_{strain}).

Figure 8.6 shows a plot of the theoretical calculations of critical temperatures for spinodal decomposition from DLP and RS models. Our experimental results are also included. As can be clearly seen, the curve using the DLP model shows critical temperatures for spinodal decomposition considerably lower than that corresponding to our samples. Therefore, this model predicts that our GaInNAs quantum wells should be homogeneous, a conclusion that differs from our experimental observations. On the other hand, the RS model is in good agreement with our results, showing that spinodal decomposition should have taken place in our samples. It follows that the DLP model of Stringfellow [44] is not appropriate for the calculation of the miscibility gap in GaInNAs alloys.

In view of the results above, we focus only on the RS model in the subsequent discussion. Figure 8.7 exhibits a plot of the critical temperatures for spinodal decomposition vs. variations in In (keeping the N content constant at the value of our samples, 0.023) and N (keeping the In content constant at 0.38). As can be observed, the curve corresponding to the N is much higher than that for the In. Higher critical temperatures in the miscibility gap mean higher instability with regard to spinodal decomposition. In this way, it seems that N is the alloy constituent which will show a higher tendency to suffer spinodal decomposition and phase separation.

The experimental results obtained with g002DF also point at the fact that N has higher tendency to phase separation than In. Our calculations on the structure factor of the g002DF reflection for the GaInNAs alloy have shown that the studied samples should be a fluctuation in In close to double the fluctuation in N ($\Delta x \approx -2.2\Delta y$). If we consider a fluctuation of In of 1% as has been proposed by Albrecht et al. [55], then the variation in the N composition should be approximately 0.4%. Although it could be seen that these results

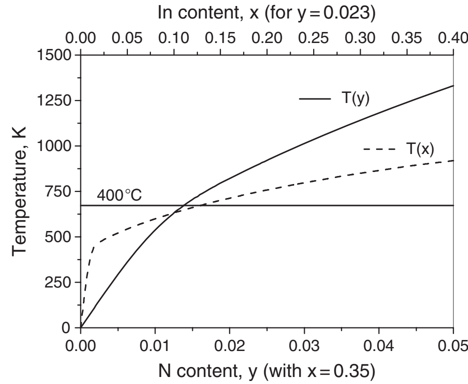

Fig. 8.7. Critical temperatures for spinodal decomposition of GaInAsN/GaAs samples using the RS model for In composition (keeping the N content constant at the value of our samples, $y = 0.023$) and N composition (keeping the In content constant at $x = 0.38$)

point at In as the main element responsible for the phase separation of the alloy, if we consider the fluctuation of each element in relation to its absolute content in the alloy, the conclusion would be the opposite. A variation of 1% of In with regard to the 35% existing in the alloy supposes a 3.5% difference in composition from some regions to others inside the well; for N, however, a variation of 0.4% with respect to the global N content of 2.3% results in a 18% of N fluctuation in the structure. This result shows a very high tendency of N toward phase separation, much higher than In. This finding appears reasonable considering the extremely low solubility of N in the GaAs alloy [56].

It should be noted that the fact that the critical temperatures for N are higher than that for In are a direct consequence of the higher interaction parameter of InAs–InN and GaAs–GaN with regard to the other combinations [50]. The higher interaction parameters of $\alpha_{\mathrm{GaAs-GaN}}$ (2.16×10^5 J mole^{-1}) and $\alpha_{\mathrm{InAs-InN}}$ (1.46×10^5 J mole^{-1}) regarding $\alpha_{\mathrm{InN-GaN}}$ (4.53×10^4 J mole^{-1}) and $\alpha_{\mathrm{InAs-GaAs}}$ (1.89×10^4 J mole^{-1}) explain the trend of nitrogen to separate into GaN and other phases. Following this reasoning, the RS model predicts a separation into N-rich regions (Ga**N**) and In-rich regions (**In**As). This is in good agreement with the conclusions obtained from the analysis of the results found with g002DF reflection, reinforcing the hypothesis that the GaInNAs alloy is constituted by alternate In-rich and N-rich regions. Moreover, the analysis of the critical temperatures with the RS model has also shown that the N, besides forming an independent composition profile, could also influence on the behavior of In. Figure 8.8 shows a graph of the critical temperatures calculated with the RS model for In for the GaInAs alloy and the GaInNAs one. As it can be observed, the critical temperatures are higher in the quaternary system than in the ternary. This means that the introduction of N in the GaInAs alloy increases the tendency to phase separation in the

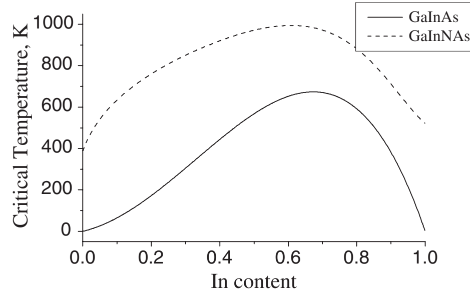

Fig. 8.8. Critical temperatures for spinodal decomposition of In in GaInAs (*continuous line*) and GaInNAs (*dotted line*)

group III sublattice, therefore the magnitude of the composition fluctuations regarding In atoms is expected to be higher in the quaternary alloy.

Some comments should also be made with regard to the mechanism of formation of the 90° out of phase compositional profile in the GaInNAs alloy. It is well known that In modulation occurs in GaInAs structures and also the existence of N modulation in GaNAs [57, 58] has been observed. One possible explanation is that, during the growth process, chemical bonding aspects are dominating at the growing surface, which favor Ga–N bonds instead of In–N bonds [59] and this state is then frozen-in during the nonequilibrium epitaxial growth process. The natural trend of In atoms to form a modulation at the surface of GaInAs structures could produce nitrogen accumulation in the Ga-rich phase. However, local strain effects have higher importance in bulk, favoring In-rich nearest-neighbor configurations of N. Therefore, the frozen nonequilibrium bulk state can be moved toward the equilibrium bulk state by certain annealing processes [60]. The diffusion of N to In-rich regions decreases the elastic N-induced perturbation, leading to reduced band structural modification. This behavior explains very well the blueshift produced by the annealing of GaInNAs structures, although the very low bulk diffusion coefficients ($\sim 10^{-19}\,\mathrm{cm}^2\,\mathrm{s}^{-1}$) limit this process and therefore high postgrowth annealing temperatures are required (typically ∼800°C).

Finally, it should be noted that a discrepancy can be found between our experimental results and critical temperature curves for spinodal decomposition. We have observed an increase in the intensity of the strain contrasts when raising the growth temperature of the GaInNAs quantum wells, a fact that has been related to an increase in the magnitude of composition fluctuations in the alloy for higher growth temperatures. However, theoretical models predict a higher stability with regard to spinodal decomposition for higher growth temperatures. This disagreement occurs because here we do not consider the kinetics of the spinodal model. Thus, kinetic factors, such as the influence of growth temperature on the surface diffusion of the different constituents of the alloy, play an essential role in the development

of composition fluctuations, and could explain the experimentally observed enhancement of the phase separation when raising the growth temperature. Therefore, in the following we consider the kinetics of the phase separation in the GaInNAs alloys.

8.5 Increase of the Composition Fluctuations with Temperature

Our experimental results with g220BF reflection have shown an increase in the intensity of the strain contrasts when raising the growth temperature, related to an increase in the magnitude of the composition fluctuations in the alloy. As shown above, the composition fluctuations in the alloy GaInNAs should consist of alternate fringes due to regions enriched in In and N linked coherently. The changes in the growth temperature should produce variations in the composition fluctuation of the two alloy constituents in a similar proportion, in such a way that although the magnitude of the fluctuations in both In and N increases with temperature, the relation $\Delta x \approx -2\Delta y$ should remain satisfied. Following this, a measurement of the variations in the intensity of the strain contrasts with temperature could constitute a good estimation of the evolution of the amplitude of the phase separation.

A relation between the amplitude of phase separation produced by diffusion and the temperature of the process has been previously proposed by Cahn [61]. The evolution with time t of the composition c of an alloy exhibiting a periodic phase separation can be described by

$$\frac{\partial c}{\partial t} = M\left\{\left(\frac{\partial^2 F}{\partial c^2}\right)\nabla^2 c\right\} + \text{nonlinear terms}, \tag{8.12}$$

where M is the diffusion mobility and F is the free energy of the system.

This equation has a simple sine wave solution [62]

$$c - c_0 = \mathrm{e}^{R(\bar{\beta}t)} \cos \bar{\beta}\bar{r}, \tag{8.13}$$

where $R(\bar{\beta})$ is obtained by substituting this solution back into the diffusion equation, as

$$R(\bar{\beta}) = -M\beta^2\left(\frac{\partial^2 f}{\partial c^2}\right). \tag{8.14}$$

The mobility M can be expressed as a function of the growth temperature as [63]

$$M = M_0\mathrm{e}^{-Q/RT}, \tag{8.15}$$

where Q is the activation energy of the diffusion process and M_0 is the preexponential factor.

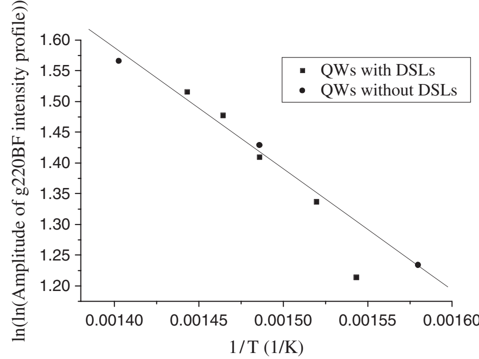

Fig. 8.9. Double logarithm of the amplitude of strain contrasts measured in g220BF images vs. the inverse of the growth temperature for the simple quantum wells and the wells with strain relief layers

According to these equations, the amplitude in the composition profile is related to the growth temperature by

$$c - c_0 \propto \mathrm{e}^{\mathrm{e}^{-Q/RT}}. \tag{8.16}$$

Figure 8.9 shows a plot of the double logarithm of the amplitude of the intensity profile taken from g220BF micrographs vs. the inverse of the absolute growth temperature for the GaInNAs quantum wells with and without BL. A linear fit of this data is also included. From the slope of these graphs, we have obtained an activation energy for adatom diffusion in GaInNAs of $0.19 \pm 0.04\,\mathrm{eV}$. In the literature, a value of 0.35 eV has been reported for the activation energy of In surface diffusion on (001) GaAs with A (2×4) surface reconstruction, 0.25 eV for (111)A, and 0.29 eV for (111)B [64]. There have also been published values of 0.22 eV for the diffusion of In in InAs quantum dots [65] and 0.13 and 0.29 eV for the diffusion of In on $\mathrm{Ga_{0.34}In_{0.66}As}$ (001)-2×3 for the directions $[1\bar{1}0]$ and [110] [66], respectively. In the present work, we have not found differences between the (110) directions, although an asymmetry could exist within the experimental errors of the measurements. As can be observed, the energy of activation for GaInNAs structures calculated in this work is of the same order of magnitude as the values found in the literature for indium in GaInAs alloys. Moreover, it should be mentioned that the quantum well studied contains 38% In but only 2.3% N. Therefore the behavior of In is expected to have a much greater effect on the microstructure of the GaInNAs quantum wells than that of N. On the other hand, the existence of the same proportion between the composition fluctuations of In and N, independent of the growth temperature (as observed with g002DF reflection), indicates that the kinetics of the composition profile could be controlled just by one of the alloy constituents, with the second one becoming adapted to it. We have not found in the literature diffusion data for N in GaInNAs to

be compared with our experimental results, but the obtained values suggest that it is the surface diffusion of In atoms that controls the phase separation in the GaInNAs alloy.

With regard to the samples with the quantum wells sandwiched between BLs, it should be mentioned that this design has been proposed to improve the luminescence properties of this alloy [67–69]. The introduction of these intermediate composition layers may be expected to reduce the average lattice mismatch of the epitaxial layers with the substrate, allowing wider quantum wells, an enhancement of the carrier confinement, and a redshift of the emission [70]. In relation to the structural changes that these layers induce in the system, Peng et al. [71] have observed that the introduction of BL reduces drastically the diffusion of In and N along the growth direction (out of the quantum well). However, no indications of structural changes inside the quantum wells have been reported. Our study has shown that the composition fluctuations of GaInNAs quantum wells are not significantly affected by the introduction of $Ga_{0.88}In_{0.12}N_{0.019}As_{0.981}$ strain reduction layers. Variations in the local elastic strain of an epitaxial layer have been found to influence the surface diffusion process during growth [72–74], but evidence of the effect of a change in the average lattice mismatch with the substrate on this process has not been found. The use of BLs is therefore not expected to cause local changes in the layers during growth, and therefore the diffusion process should not be affected. This would explain the similarities in the results of composition fluctuations for structures with and without BLs.

According to the experimental and theoretical results obtained in the present work, we can describe the mechanism of formation of the phase separation in GaInNAs as follows. Due to the higher concentration of In with regard to N in the GaInNAs structures studied (more than one order of magnitude higher) and according to the experimental values of activation energy for surface diffusion obtained in the present work, it is likely that the composition profile found experimentally is determined firstly by In atoms. During the MBE process, group III atoms are expected to suffer phase separation into Ga-rich and In-rich regions at the growing surface. In the GaInNAs alloy, these composition fluctuations are further stimulated with regard to the ternary alloy GaInAs because of the introduction of N in the alloy. While this composition profile is being developed, N atoms are attracted preferably toward the Ga-rich areas, clustering in these regions. This produces an independent composition profile for N. The resulting compositional profile presents an out of phase periodic enrichment in In and N in the alloy. However this grown-in distribution can partially reverse through diffusion either at the MBE growth temperature or by postgrowth annealing. This diffusion is favored by the strain energy decrease which accompanies the formation of N–In bonds in the GaAs host crystal. Further investigation is needed to know the degree of this diffusion process and the final distribution which might be obtained due to optimal thermal annealing. Further work is also required to quantify the effect

of this compositional inhomogeneity on the photoluminescence characteristics to result in optimal quantum wells required by optical device industries.

8.6 Summary and Future Trends

Our investigations on the structural properties of the dilute nitrides of GaInAs have shown that the growth temperature is one of the key growth parameters for obtaining epitaxial layers with good crystal quality. As has been described in the present chapter, the introduction of N in the ternary alloy leads to composition fluctuations in the quantum wells, which are stimulated on increasing the growth temperature. With regard to the composition profile, the analysis of our TEM results with the chemical-sensitive g002DF reflection and the strain-sensitive g220BF reflection indicates that the phase separation in this alloy consists of regions enriched alternately in In and N. The thermodynamics of the phase separation has been analyzed and we have applied several models of spinodal decomposition from the literature to understand this in the GaInNAs alloy. Our calculations show that the critical temperatures for spinodal decomposition for N are higher than that of In, indicating a higher tendency to phase separation for this element due to the low solubility of N in the GaInAs alloy. Also, it has been found that the introduction of N in the alloy increases the tendency to phase separation in the group III sublattice. Finally, the rate of increase in the composition fluctuations with temperature suggests that In atoms could be the primary atomic species controlling the evolution of this process.

Despite the rapid pace of progress in the development of GaInNAs since the first results about a decade ago, additional studies are required to take advantage of its potential capabilities. Future work should undoubtedly include analyses at the atomic scale of the distribution of N and In in the lattice. The low solubility of N in the GaInAs lattice likely causes a deviation from the ideal incorporation of this element in As lattice sites, and indeed, the existence of N interstitials under certain growth conditions has been reported. Although some theoretical studies on the energetically favorable incorporation sites for N have been published, experimental evidence by techniques with atomic resolution, such as high angle annular dark field (HAADF) STEM, is still lacking. The importance of these analyses stems from the fact that the atomic environment of In and N atoms is likely to have a major influence on the optical properties of this system. Therefore to understand and improve the emission characteristics of this alloy, detailed studies at atomic scale are needed. In this sense and as shown in the present chapter, the growth temperature has been proved to change significantly the composition profile in the quantum wells, and thus it should cause a considerable variation in the environment of N/In atoms. The role that this main growth parameter plays in the performance of the alloy should necessarily be investigated by analytical techniques. On the other hand, the application of a postgrowth thermal annealing is a common

practice to improve the emission efficiency of the system, but clear evidence of the reasons for this behavior in relation to the changes of the microstructure of the system with this process has not been reported yet, and will definitely constitute the main objective of our further studies. Yet despite the demand for additional work to optimize the properties of the GaInNAs alloy, it should be highlighted that this system already exhibits a huge potential to become one of the leading alloys for long wavelength telecommunications.

Acknowledgments. Financial supports from CICYT project MAT2001-3362 (Spain) and EPSRC (UK) are gratefully acknowledged. One of us (Miriam Herrera) acknowledges the EU for financial support through a Marie Curie Fellowship.

References

1. M. Kondow, K. Uomi, A. Niwa, T. Kitatani, S. Watahiki, Y. Yazawa, Jpn. J. Appl. Phys. **35**, 1273 (1996)
2. S.H. Wei, A. Zhunger, Phys. Rev. Lett. **76**, 664 (1996)
3. K. Nakahara, M. Kondow, T. Kitatani, M. Larson, K. Uomi, IEEE Photon. Technol. Lett. **10**, 487 (1998)
4. M. Reinhardt, M. Fischer, M. Kamp, J. Hofmann, A. Forchel, IEEE Photonics Technol. Lett. **12**, 239 (2000)
5. A. Egorov, D. Bernklau, D. Livshits, V. Ustinov, Z. Alferov, H. Riechert, Electron. Lett. **35**, 1643 (1999)
6. H. Riechert, L. Geelhaar, G. Ebbinghaus, A. Lima, A. Ramakrishnan, G. Steinle, in *Conference Proceedings of Indium Phosphate*, 2003, p. 3
7. J.F. Geisz, D.J. Friedman, Semicond. Sci. Technol. **17**, 769 (2002)
8. P.C. Chang, A.G. Baca, N.Y. Li, X.M. Xie, H.Q. Hou, E. Armour, Appl. Phys. Lett. **76**, 2262 (2000)
9. D. Gotthold, S. Govindaraju, J. Reifsnider, G. Kinsey, J. Campbell, A. Holmes, J. Vac. Sci. Technol. B **19**, 1400 (2001)
10. M.R. Gokhale, J. Wei, H. Wang, S.R. Forrest, Appl. Phys. Lett. **74**, 1287 (1999)
11. M. Herrera, D. González, M. Hopkinson, P. Navaretti, M. Gutiérrez, H.Y. Liu, R. García, Semicond. Sci. Technol. **19**, 813 (2004)
12. M. Herrera, D. Gonzalez, J.G. Lozano, M. Gutierrez, R. Garcia, M. Hopkinson, H.Y. Liu, Semicond. Sci. Technol. **20**, 1096 (2005)
13. W.G. Bi, C.W. Tu, Appl. Phys. Lett. **70**, 1608 (1997)
14. H.P. Xin, C.W. Tu, Appl. Phys. Lett. **72**, 2442 (1998)
15. M. Herrera, D. González, R. García, M. Hopkinson, P. Navaretti, M. Gutiérrez, H.Y. Liu, Thin Solid Films **483**, 185 (2005)
16. M. Herrera, D. González, R. García, M. Hopkinson, P. Navaretti, M. Gutiérrez, H.Y. Liu, IEEE Proc.: Optoelectron., **151**, 301 (2004)
17. A. Howie, M. Whelan, J. Proc. R. Soc. London A **263**, 217 (1961)
18. V. Grillo, M. Albrecht, T. Remmele, H.P. Strunk, A.Y. Egorov, H. Riechert, J. Appl. Phys. **90**, 3792 (2001)
19. M. Albrecht, V. Grillo, T. Remmele, H.P. Strunk, A.Y. Egorov, G.H. Dumitras, H. Riechert, A. Kaschner, R. Heitz, A. Hoffmann, Appl. Phys. Lett. **81**, 2719 (2002)

20. G. Patriarche, L. Largeau, J.C. Harmand, D. Gollub, Appl. Phys. Lett. **84**, 203 (2004)
21. M. Herrera, D. González, M. Hopkinson, M. Gutiérrez, P. Navaretti, H.Y. Liu, R. García, J. Appl. Phys. **97**, 073705-1 (2005)
22. J. Cagnon, P.A. Buffat, P.A. Stadelmann, K. Leifer, Inst. Phys. Conf. Ser. **169**, 37 (2001)
23. F. Glas, Inst. Phys. Conf. Ser. **180**, 191 (2003)
24. M.H. Gass, A.J. Papworth, T.J. Bullough, P.R. Chalker, Ultramicroscopy **101**, 257 (2004)
25. P.R. Chalker, H. Davock, S. Thomas, T.B. Joyce, T.J. Bullough, R.J. Potter, N. Balkan, J. Cryst. Growth **233**, 1–4 (2001)
26. S. Davies, S. Thomas, T.B. Joyce, P.R. Chalker, Solid-State Electron. **47**, 407 (2003)
27. I.N. Stranski, L. Krastanow, Sitzungsber. Akad. Wiss. Wien, Math.-Naturwiss. Kl., Abt. 2B **146**, 797 (1938)
28. G. Capellin, M. De Seta, J. Appl. Phys. **93**, 291 (2003)
29. A. Rosenauer, W. Oberst, D. Litvinov, D. Gerthsen, Phys. Rev. B **61**, 8276 (2000)
30. J. Tersoff, F.K. LeGous, Phys. Rev. Lett. **72**, 3570 (1994)
31. V.A. Shchukin, N.N. Ledentsov, P.S. Kopèv, D. Bimberg, Phys. Rev. Lett. **75**, 2968 (1995)
32. J. Johansson, W. Seifert, J. Cryst. Growth **234**, 139 (2002)
33. A.V. Osipov, S.A. Kukushkin, F. Schmitt, P. Hess, Phys. Rev. B **64**, 205421 (2001)
34. J. Tersoff, F.K. LeGous, Phys. Rev. Lett. **72**, 3570 (1994)
35. T. Walther, A.G. Cullis, D.J. Norris, M. Hopkinson, Phys. Rev. Lett. **86**, 2381 (2001)
36. A.G. Cullis, D.J. Norris, T. Walther, M.A. Migliorato, M. Hopkinson, Phys. Rev. B **66**, 081305 (2002)
37. T.L. McDevitt, S. Mahajan, D.E. Laughlin, W.A. Bonner, V.G. Keramidas, Phys. Rev. B **45**, 6614 (1992)
38. J.E. Guyer, P.W. Voorhees, J. Cryst. Growth **187**, 150 (1998)
39. B.J. Spencer, P.W. Voorhees, J. Tersoff, Phys. Rev. B **6423**, 235318 (2001)
40. F. Leonard, R.C. Desai, Phys. Rev. B **57**, 4805 (1998)
41. D González, G. Aragón, D. Araújo, R. García, Appl. Phys. Lett. **76**, 3236 (2000)
42. J.W. Cahn, Acta Met. **9**, 795 (1961)
43. J.W. Cahn, Trans. Met. Soc. **242**, 166 (1967)
44. G.B. Stringfellow, J. Cryst. Growth **58**, 194 (1982)
45. K. Onabe, Jpn. J. Appl. Phys. **21**, L323 (1982)
46. P. Ipatova, V.G. Malyshkin, V.A. Shchukin, J. Appl. Phys. **74**, 7198 (1993)
47. F. Glas, Phys. Rev. B **62**, 7393 (2000)
48. V.G. Malyshkin, V.A. Shchukin, Semiconductors **27**, 1062 (1993)
49. J.M. Millunchick, D.J. Srolovitz (eds.), *Encyclopedia of Materials: Science and Technology* (Elsevier, Amsterdam, 2004), p. 1
50. R. Asomoza, V.A. Elyukin, R. Peña-Sierra, Appl. Phys. Lett. **81**, 1785 (2002)
51. I. Barin, O. Knacke, O. Kubaschewski (eds.) *Thermochemical Properties of Inorganic Substances*, (Springer, Berlin Heidelberg New York, 1977)
52. J.S. Blakemore, J. Appl. Phys. **53**, R123 (1982)
53. M. Shulz, H. Weiss (eds.), *Landolt–Börnstein, New Series*, vol. 17d (Springer, Berlin Heidelberg New York, 1984)

54. B. de Cremoux, J. Phys., **12**, C5 (1982)
55. M. Albrecht, V. Grillo, T. Remmele, H.P. Strunk, A. Yu Egorov, Gh. Dumitras, H. Riechert, A. Kaschner, R. Heitz, A. Hoffmann, Appl. Phys. Lett. **81**, 2719 (2002)
56. I. Ho, G.B. Stringfellow, J. Cryst. Growth **178**, 1 (1997)
57. R.S. Goldman, R.M. Feenstra, B.G. Brine, M.L. O'Steen, R. Hauenstein, J. Appl. Phys. Lett. **69**, 3698 (1996)
58. L. Grenouillet, C. Bru-Chevallier, G. Guillot, P. Gilet, P. Ballet, P. Duvaut, G. Rolland, A. Million, J. Appl. Phys. **91**, 5902 (2002)
59. T. Matsuoka, T. Sasaki, A. Katsui, Optoelectron. Devices Technol. **5**, 53 (1990)
60. P.J. Klar, Progr. Solid State Chem. **31,** 301 (2003)
61. J.W. Cahn, Trans. Metall. Soc. AIME **242**, 166 (1968)
62. J.W. Cahn, Acta Met. **9**, 795 (1961)
63. J.W. Cahn, Trans. Metall. Soc. AIME **242**, 166 (1968)
64. C.C. Matthai, G.A. Moran, Appl. Surf. Sci. **123–124**, 653 (1998)
65. K. Shiramine, T. Itoh, S. Muto, T. Kozaki, S. Sato, J. Cryst. Growth **242**, 332 (2002)
66. C.C. Matthai, G.A. Moran, Appl. Surf. Sci. **123–124**, 653 (1998)
67. Y. Fedorenko, T. Jouhti, E.M. Pavelescu, S. Karirinne, J. Kontinnen, M. Pessa, Thin Solid Films, **440,** 195 (2003)
68. L.F. Bian, D.S. Jiang, S.L. Lu, J.S. Huang, K. Chang, L.H. Li, J.C. Harmand, J. Cryst. Growth **250**, 339 (2003)
69. L.H. Li, G. Patriarche, A. Lemaitre, L. Largeau, L. Travers, J.C. Harmand, J. Cryst. Growth **251**, 403 (2003)
70. E.M. Pavelescu, C.S. Peng, T. Jouhti, J. Konttinen, W. Li, M. Pessa, M. Dumitrescu, S. Spanulescu, Appl. Phys. Lett. **80**, 3054 (2002)
71. C.S. Peng, E.M. Pavelescu, T. Jouhti, M. Pessa, Solid-State Electron. **47**, 431 (2003)
72. M.I. Larsson, R.F. Sabiryanov, K. Cho, B.M. Clemens, Surf. Sci. **536**, L389 (2003)
73. P. Roura, A. Vila, J. Bosch, M. López, A. Cornet, J.R. Morante, D.I. Westwood, J. Appl. Phys. **82,** 1147 (1997)
74. C. Roland, G.H. Gilmer, Phys. Rev. B **46**, 428 (1992)

9

Assessing the Preferential Chemical Bonding of Nitrogen in Novel Dilute III–As–N Alloys

D.N. Talwar

To assess the local chemical bonding of N in dilute III–As–N ternary and quaternary alloys, we have reported results of a comprehensive Green's function analyses of both infrared absorption and Raman scattering experiments on localized vibrational modes. Contrary to the recent report in GaInNAs multiple-quantum well structures, our results of impurity modes are found to be in good agreement with earlier experimental data – providing strong corroboration to the fact that upon annealing and/or by increasing In composition there occur structural changes causing N environment to transform from the tetrahedral $N_{As}Ga_4$ to a preferred $N_{As}InGa_3$ and/or $N_{As}In_2Ga_2$ configuration. Theoretical results of impurity modes presented for dilute In(Al)AsN and high-In(Ga) content GaInNAs (GaAlNAs) alloys are compared and discussed with the existing infrared absorption and Raman scattering data.

9.1 Introduction

In the recent years, dilute ternary and quaternary III–As–N alloys have received a great deal of attention [1–9] both from a fundamental point of view as well as for applications in technology (e.g., photodetectors, modulators, amplifiers, and long wavelength vertical cavity surface-emitting lasers (LW-VCSELs), etc.). Dilute nitrides can be derived from the conventional III–V semiconductors (viz., GaAs, GaInAs or GaAsP) by the insertion of N into the group V sublattice – causing profound effects on the electronic properties of the resulting alloys [10–14]. Contrary to the general trends in the conventional alloy semiconductors where a smaller lattice constant generally increases the band gap, the smaller covalent radius and larger electronegativity of N cause a very strong bowing parameter in III–V–N compounds. Consequently, the addition of N to GaAs or GaInAs decreases the band gap (E_g) dramatically (see Fig. 9.1). This strong dependence of E_g on the N content in III–As–N has provided opportunities to engineer material properties suitable for the

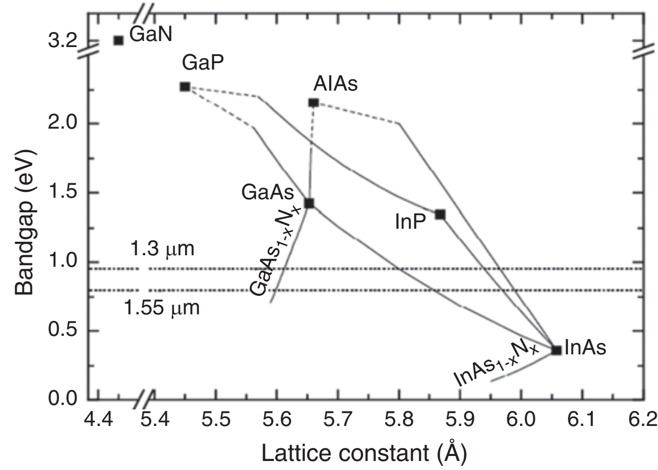

Fig. 9.1. Band gaps vs. lattice constants of binary III–V semiconductors (*squares*). The *continuous and dashed lines* indicate direct and indirect band gaps of ternary compounds, respectively. The areas between lines represent quaternary compounds. The Ga- and In-rich GaInNAs materials can be grown lattice matched to GaAs and InP [3], respectively, to reach the fibre-optical communication wavelengths of 1.3 and 1.55 μm

fibre-optical communications at 1.3 and 1.55 μm wavelengths as well as high efficiency hybrid solar cells [15].

In the past decade while major efforts have been focused on Ga-rich GaInNAs, little work has been devoted to other alloys such as In-rich GaInNAs or Ga/Al-rich GaAlNAs and GaAsNSb, etc. By choosing the appropriate In/N ratio, GaInAsN layers, with unusual electronic properties, have been grown [10–14] lattice matched and/or strained on GaAs or InP substrates – allowing not only for the realization of GaAs-based diode lasers and long wave length photodetectors [2, 3] in the ≥1.3 μm range, but also for use in the solar cells with record power (∼38%) efficiencies [15]. More recently Ga-rich GaAlNAs/GaAs [12, 16] and In-rich GaInNAs/InP [17] alloys have been prepared by MBE using rf-nitrogen plasma source. Despite the commercial production of GaInAsN/GaAs-based laser diodes, the optical quality of the ternary GaAs(In)N and quaternary GaIn(Al)AsN layers is still poor [1–3]. The III–As–N alloys have shown the evidence of inhomogeneities with broad photoluminescence (PL) line widths, variable PL decay times, and short minority carrier diffusion lengths. Fortunately, with high-temperature anneals of 600–900°C, the non-radiative recombination sites can be removed. Although the annealing does improve the PL intensity it causes, however, an undesired blueshift of the emission [2,3]. These observations are often taken as an indicator of the compositional fluctuations requiring structural characterization to monitor the carrier distribution and defect properties [7]. Clearly, the nature of

defects associated with N incorporation in III–As is very contentious and the precise mechanisms of their removal by annealing are still not well understood.

To improve the material quality for device applications [2, 5], it is highly desirable to have experimental characterization techniques available to examine the role of various nitrogen species, their atomic structures, and preferential chemical bonding (i.e., the redistribution of In–N, Ga–N(Al–N) bonds with the increase of In (Al) contents) that might occur upon rapid thermal annealing (RTA) [3, 9]. Although X-ray diffraction (XRD) spectroscopy with synchrotron radiation [8, 18] has been used for examining the local structures, the relative dispositions of cations and anions in the sublattices of the dilute $Ga_{1-x}In_x(Al_x)N_yAs_{1-y}$ alloys have not been uniquely determined. The problems of carrier distribution associated with composition disorder have also been studied by using frequency-dependent capacitance-voltage (CV) [19, 20], transmission electron microscopy (TEM) [21], photo-induced transient spectroscopy (PITS) [22], and deep level transient spectroscopy (DLTS) [19]. A highly sensitive localized vibrational mode spectroscopy, which addresses directly the force constants of the bonds, has been proven quite successful in probing the local bonding of isolated light impurities as well as complex defect centres [23–29] in the conventional III–V compounds. In the recent years, there has been a renewed interest for studying the local modes using infrared (IR) absorption [30, 31] and Raman scattering [32–35] spectroscopy to assess the preferential chemical bonding of nitrogen in $Ga_{1-x}In_x(Al_x)N_yAs_{1-y}$ alloys.

In this chapter, we have attempted to provide an overview of the experimental (Sect. 9.2) and theoretical (Sect. 9.3) status about the dynamical behaviours of N species in III–As–N alloys. Starting with the existing spectroscopic data of vibrational modes (Sect. 9.2.1) for several light impurities in GaAs, we have summarized the experimental information available for the N-related impurity modes in GaAs and GaIn(Al)As. We focussed our discussion primarily on the dilute GaN_yAs_{1-y} and $Ga_{1-x}In_xN_yAs_{1-y}$ alloys (for $0 \leq x \leq 1$ with $y \leq 0.04$) to which a large amount of experimental (IR absorption and Raman scattering) data on local modes exist (Sects. 9.2 and 9.3). By using a realistic lattice dynamical approach, in the framework of a comprehensive Green's function theory (Sect. 9.3), we have critically analysed the data on impurity modes and assessed the preferential N bonding in these alloys. Comparison of theoretical results with discussion on the existing data has provided a firm corroboration (Sect. 9.4) to some of the observed N-related modes to specific bonding (micro-clusters) configurations.

9.2 Local Vibrational Mode Spectroscopy

The addition of impurities (intentional or accidental) during the growth of bulk or epitaxial semiconductors generally affects the electrical properties by the introduction of energy levels in their band gaps. Besides altering the electronic properties, impurities also destroy the translational symmetry of the

host lattices and modify their vibrational characteristics as well. If the impurity atoms are sufficiently light compared to the host atoms, then some of the modified modes may occur at frequencies above the maximum normal mode frequency (ω_{max}) of the perfect lattice. These new high frequency modes cannot propagate through the lattice and are highly localized spatially around the impurity site. Because of the spatial localization of the vibrational energies of such impurity modes, they are called "localized vibrational modes", hereafter designated by LVMs. If the modified modes occur between the phonon branches of the perfect lattices where the phonon density of states is zero, then they are also spatially localized and are called "gap modes". Of special interest here are the high frequency LVMs since, as will be shown, they occur in the material systems being studied. In general, these modes have a nonzero dipole moment associated with them, and are, therefore, infrared active. Besides IR absorption, Raman scattering spectroscopy [23–29] has been considered equally powerful technique with strong ability to sense not only the electronic properties but also to identify the nature of impurities and their bonding mechanisms in semiconductors.

9.2.1 Vibrational Modes of Light Impurities in GaAs

In GaAs ($\omega_{\mathrm{max}} \sim 295\,\mathrm{cm}^{-1}$ [36]) comprehensive spectroscopic measurements of LVMs in the spectral region from ω_{max} to $2\omega_{\mathrm{max}}$ have been reported (see Table 9.1) for several isolated defects (mass ranging between 6 and 31 amu) occupying either the gallium (say $\mathrm{Be_{Ga}}$) or the arsenic (say $\mathrm{C_{As}}$) site. The impurities listed in Table 9.1 vary from simple isoelectronic (i) to charged one, i.e. acceptor (a^{-}) and donor (d^{+}). These impurities have already played significant roles in determining the fundamental properties of GaAs as well as in evaluating their potentials for device applications. Generally, the LVMs are detected by IR absorption spectroscopy, but Raman scattering has also been used. If the impurity with a mass greater than 31 amu is present in GaAs, the modified lattice modes involving significant displacement of the impurity atom may fall within the bands of its optic or acoustic modes ($\omega < \omega_{\mathrm{max}}$) – causing broad IR absorption features – resulting in a low sensitivity for its detection. About nitrogen in GaAs very little was known until recently except that it might be an isoelectronic trap [10–14] with electronic level lying in the conduction band.

Besides LVMs of isolated light defects in GaAs, the modes caused by pairing of light impurity atoms with native (say $\mathrm{As_{Ga}}$) or compensated impurities (say $\mathrm{Cu_{Ga}}$) have also been observed – providing strong spectroscopic evidence for the presence of a second impurity atom even if it has a heavier mass. Like many other semiconductors, hydrogen in GaAs forms complex centres (hydrogen acceptor and hydrogen donor) with other impurities or defects and passivates their electrical activity [28, 29]. Oxygen in GaAs generally occurs interstitially or as an off-centre substitutional atom lying close to the As-lattice site. Measurements of Ga-isotopic fine structures of LVMs for $\mathrm{C_{As}}$,

Table 9.1. Experimental data on localized vibrational modes (LVMs) of various isolated defects in GaAs

System	Local modes (cm^{-1})[a]
*Ga*As:^{6}Li	482
*Ga*As:^{7}Li	450
*Ga*As:^{9}Be	482
*Ga*As:^{10}B	540
*Ga*As:^{11}B	517
*Ga*As:^{24}Mg	331
*Ga*As:^{25}Mg	326
*Ga*As:^{26}Mg	322
*Ga*As:^{27}Al	362
*Ga*As:^{28}Si	384
*Ga*As:^{29}Si	379
*Ga*As:^{30}Si	373
Ga*As*:^{10}B	628
Ga*As*:^{11}B	602
Ga*As*:^{12}C	582
Ga*As*:^{13}C	561
Ga*As*:^{14}N	480
Ga*As*:^{28}Si	399
Ga*As*:^{30}Si	389
Ga*As*:^{31}P	355

[a]See [27]

B_{As}, and Si_{As} in GaAs have also been reported by using the high-resolution Fourier transform infrared (FTIR) spectroscopy [27].

All these studies with improved accuracies in the experimental results have provided strong spectroscopic "fingerprints" for the site selectivity of impurity atoms and contributed to the fundamental understanding of lattice dynamics as well as impurity–host interactions (i.e. chemical bonding) in the cases of both isolated and complex defect centres in semiconductors. Experimental results have also been tested and interpreted rigorously in the framework of realistic lattice dynamical schemes by using sophisticated Green's function and other methods [37].

9.2.2 Local Vibrational Mode of Nitrogen in GaAs and InAs

Until recently, the information about the LVMs of nitrogen in III–V compounds was rather sparse. In GaAs or InAs the addition of a small amount of nitrogen occupying the anion site (N_{As}) acts as an isoelectronic impurity [10–14]. For a light N atom on the heavier As site, one expects to observe an LVM of N_{As} by using either IR absorption or Raman scattering spectroscopy.

Infrared Absorption

In GaAs, the first spectroscopic evidence of nitrogen local mode was reported by Kachare et al. [38] who observed a broad absorption band near 480 cm^{-1} after implanting high energy $^{14}N^{+}$ ions into semi-insulating GaAs. More recently, it has been shown that the N_{As} local mode can be observed in epitaxial layers of $GaAs_{1-x}N_x$ with thickness as small as of 10 nm, in the alloying range, for the N fraction of $x < 0.03$. IR measurements performed in nitrogen-doped GaAs prepared by vapour phase epitaxy as well as in $GaAs_{1-x}N_x$ layers grown by liquid source MBE have revealed N_{As}-related LVM near ∼470 cm^{-1} [31]. This assignment has now been confirmed, with the implantation of ^{15}N in GaAs and observing shift of the local mode towards lower ∼458 cm^{-1} frequency. It is worth mentioning that in an earlier study [30] the N_{As} local mode near ∼471 cm^{-1} was detected in a nominally undoped bulk GaAs crystal where nitrogen was a contaminant (∼10^{15} cm^{-3}) coming from either the N_2 gas or the pyrolithic boron nitride (pBN) crucible used for the crystal growth.

In Fig. 9.2, we have displayed the FTIR absorption spectrum (77 K) [30] of a $GaAs_{0.983}N_{0.017}$ film grown by MOCVD on a semi-insulating GaAs substrate. Clearly, the absorption spectrum after subtracting the reference spectra of semi-insulating GaAs has revealed a relatively broad (∼13 cm^{-1}) band of the N_{As} local mode near ∼472.5 cm^{-1}. At the same time the N-related mode exhibited some very peculiar behaviour. If comparison is made with the LVMs of closest mass $^{11}B_{As}$ and $^{12}C_{As}$ in GaAs (a) the frequency of the N_{As} local mode is relatively lower (Table 9.1) and (b) since the nearest-neighbour atoms

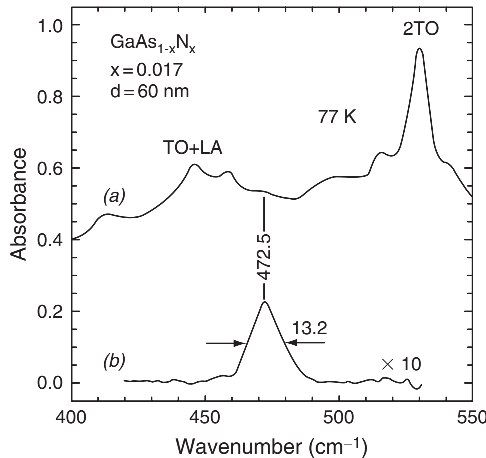

Fig. 9.2. FTIR absorption spectrum of a GaNAs film grown by MOCVD on a semi-insulating GaAs substrate. (**a**) Uncorrected spectrum showing multi-phonon absorption caused by the GaAs substrate. (**b**) Difference spectrum after subtraction of the substrate spectrum [30]

of N_{As} are gallium atoms, the local mode does not reveal the fine structure splitting [30] due to Ga-isotopic (^{69}Ga and ^{71}Ga) masses [39, 40]. Again, the observed broad bandwidth of N_{As}-mode is likely to be caused by the reduced lifetime of the vibrational state and it is assumed that elastic scattering [41] of the lattice phonons might be a dominant process.

In InAs, the FTIR measurements performed on ^{14}N- and ^{15}N-implanted bulk materials have also revealed LVM frequencies near ∼443 and 429 cm^{-1}, respectively [30].

Raman Scattering

In dilute $GaAs_{1-x}N_x$ layers ($x < 0.032$) Raman scattering measurements in the back scattering configurations have been performed to extract information about the N-related defect modes. Figure 9.3 shows a typical Raman spectra [35] of low-N content $GaAs_{0.99}N_{0.01}$ layer revealing a single N-related LO_2 vibrational mode around ∼472 cm^{-1}. Again, the resonance profile of Raman scattering by N-related mode – showing pronounced maximum for the incident photon energy approaching the N-related E_+ transition – broadens substantially with the increase of N contents.

By increasing the N concentration, a gradual blueshift of the N-mode [33] is seen with an increase in the LVM intensity (I_{LVM}) as well as a rapid deterioration of the sharp second-order Raman features of the GaAs near 513 and 540 cm^{-1} [32]. The increase of I_{LVM} with the addition of N content has provided us a reliable calibration method for determining the N composition in GaN_xAs_{1-x} ternary alloys [33].

In Fig. 9.4, the results of Raman scattering [34] are shown from a single GaNAs layer of 200 nm followed by a 5 nm GaAs cap layer, grown by solid

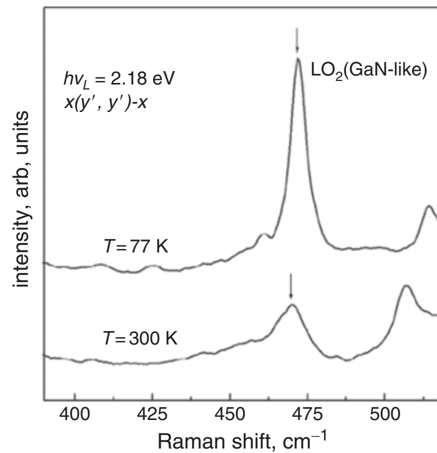

Fig. 9.3. Raman spectra of $GaAs_{0.99}N_{0.01}$ layer on GaAs recorded at 77 and 300 K [35]

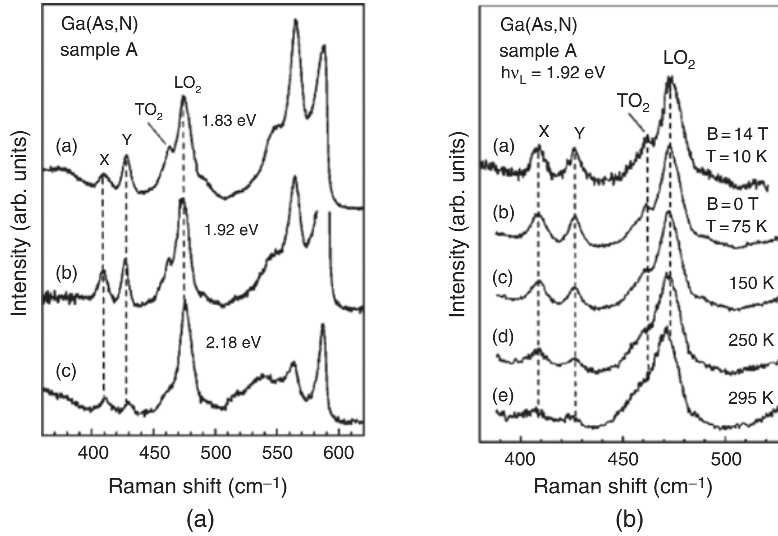

Fig. 9.4. (**a**) Raman spectra in diluted $GaAs_{1-x}N_x$/GaAs(001) layers ($x < 0.015$), sample A excited at different photon energies, (**b**) Same as (a) but at different temperatures with a constant 1.92 eV excitation energy; spectrum (a) with and spectra (b)–(e) without application of an external magnetic field $B = 14$ T [34]

source MBE at 500°C, where rf-plasma source is used for the nitrogen supply. The spectra, excited at three different incident photon energies (1.83, 1.92, and 2.18 eV), are displayed in Fig. 9.4a, where as in Fig. 9.4b the effects of the external magnetic fields and temperatures at a fixed excitation energy of 1.92 eV are revealed.

It is worth mentioning that the defect-induced Raman scattering efficiency is stronger only for the excitation at photon energies in the range between 1.8 and 2.2 eV. From Fig. 9.4a, one can note the expected GaN-like LO_2 phonon line near $\sim$472 cm^{-1} superimposed on the background of the second-order phonon scattering. A similar resonance behaviour of the LO_2 phonon signal in the energy range between 1.9 and 2.0 eV has previously been attributed to the enhancement of the Raman efficiency for photon energies approaching the localized E_+ transition in GaNAs [35]. Based on the selection rules, the peak near 463 cm^{-1} can be assigned to either the scattering by GaN-like TO_2 phonon or two GaAs-like $2LA_1$ phonons. The Raman features at frequencies higher than $\sim$500 cm^{-1} are related to the second-order scattering by GaAs-like TO_1 and LO_1 phonons. Two additional peaks, observed in Fig. 9.4a near $\sim$409 cm^{-1} (line X) and 427 cm^{-1} (line Y), are attributed to the N-related vibrational modes (possibly N dimers on Ga and As sites, respectively) as the external magnetic fields up to 14 T (see Fig. 9.4b) do not cause any split or shift to these lines. Similar to GaAsN, Wagner et al. [42], while analysing the bonding of nitrogen by Raman spectroscopy in InAsN, not only observed (see

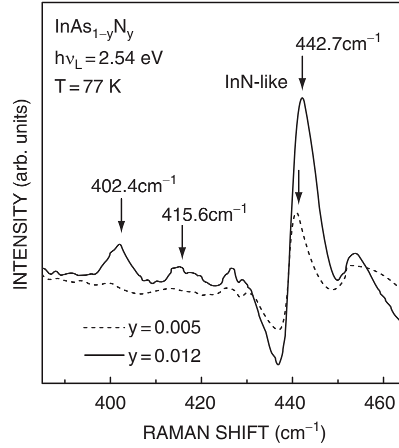

Fig. 9.5. Raman spectra in MBE-grown dilute $InAs_{1-y}N_y$ layers for the excitation at 2.54 eV with $0 \leq y \leq 0.012$ [42]

Fig. 9.5) the $^{14}N_{As}$ LVM $\sim 443\,cm^{-1}$ but also detected two additional modes possibly due to N dimers near 402 and $416\,cm^{-1}$, respectively.

9.2.3 Bonding of Nitrogen in $Ga_{1-x}In_xN_yAs_{1-y}$ Alloys

It is well known that the electronic and optical properties of dilute quaternary $Ga_{1-x}In_xN_yAs_{1-y}$ alloys strongly depend upon the microscopic spatial arrangement of its constituent elements. Unlike various other techniques (e.g. PL, XRD) used for assessing the incorporation of nitrogen in semiconductors, the local mode spectroscopy has been considered to be very well suited for addressing the key issues of the local N bonding in GaAs (InAs)-based low-In (Ga) content dilute $Ga_{1-x}In_xN_yAs_{1-y}$ alloys. This is simply because the transverse optical phonon (TO) in cubic GaN, which is the symmetry for the dilute Ga–N bonds in zinc-blende GaInAs-like host matrix, is nearly dispersion less. Consequently a small fluctuation in the Ga–N frequency can give rise to phonon localization, i.e. to different signals corresponding to the many zone-centre modes. In other words, the phonon frequencies in low-In (Ga) content dilute $Ga_{1-x}In_xN_yAs_{1-y}$ alloys will be strongly dependent on the local bond arrangement related to the large differences in the bond strengths and bond lengths between the Ga–N and (Ga,In)–As bonds.

Infrared Studies in Dilute $Ga_{1-x}In_xN_yAs_{1-y}$ Quaternary Alloys

In the recent years, several FTIR measurements on $Ga_{1-x}In_xN_yAs_{1-y}$/GaAs materials ($0 \leq x \leq 1$ and $y < 0.02$) grown by MOCVD and gas source MBE techniques have been reported in the literature [30, 31, 43, 44]. Despite a general consensus on the N_{As} local mode in GaAs and InAs, the results

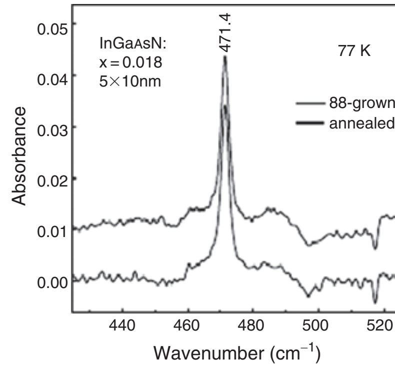

Fig. 9.6. Low-temperature FTIR absorption spectra in a $Ga_{1-x}In_xN_yAs_{1-y}$ MQW structure before and after annealing [30]

on the vibrational spectra in Ga- and/or In-rich GaInNAs quaternary alloys are either scarce or at variance. For instance, a recent low-temperature (77 K) absorption measurement [30] (see Fig. 9.6) in a $Ga_{1-x}In_xN_yAs_{1-y}$ multiple-quantum well (MQW) structure ($y = 0.018$ and $x = 0.35$, with five quantum wells of thickness 10 nm each) has reported the observation of only one sharp band identical to the position of an isolated N_{As} in GaAs near $\sim$471.4 cm^{-1}. The full width at half-maximum (FWHM) of the band was about $\sim$3 cm^{-1} – smaller than the one seen in a dilute ternary GaNAs alloys (see Fig. 9.2) with no change in its position or strength after annealing at 750°C. This observation has clearly suggested that, in the MBE-grown GaInAsN MQW structure, nitrogen is bonded only to gallium atoms with no effect of indium.

On the contrary the FTIR study reported earlier by Kurtz et al. [31] on thick $Ga_{1-x}In_xN_yAs_{1-y}$ sample (with $y = 0.002$ and $x = 0.025$) grown by MOCVD has revealed two additional LVMs near $\sim$457 and 487 cm^{-1} after RTA. Quite recently, Alt and Gomeniuk [44] have recorded the FTIR spectra on indium and nitrogen co-implanted samples of GaAs after RTA at 800°C (see Fig. 9.7). In addition to the well-known $^{14}N_{As}$-mode near 472 cm^{-1}, the authors of [44] are able to resolve two new bands near 460 and 492 cm^{-1}. When heavier ^{15}N isotope with In (see Fig. 9.7b) is co-implanted in GaAs, the absorption spectra provided shift of the $^{15}N_{As}$ local mode to a lower frequency $\sim$458 cm^{-1} along with the observation of two additional bands near 478 and 447 cm^{-1}.

It is worth mentioning that the nitrogen-related isotopic shift of LVMs $\sim$14 cm^{-1} seen earlier in GaAs [30] after the implantation of ^{14}N or ^{15}N is found to be the same for all the bands observed in the N and In co-implanted GaAs samples [44]. Moreover, the growth of newer bands with the increase of In has provided an unambiguous identification that these new modes are to be related to indium. Again, it is to be noted that a band near $\sim$489 cm^{-1} has been detected earlier [43] by FTIR in GaInNAs material containing 5%

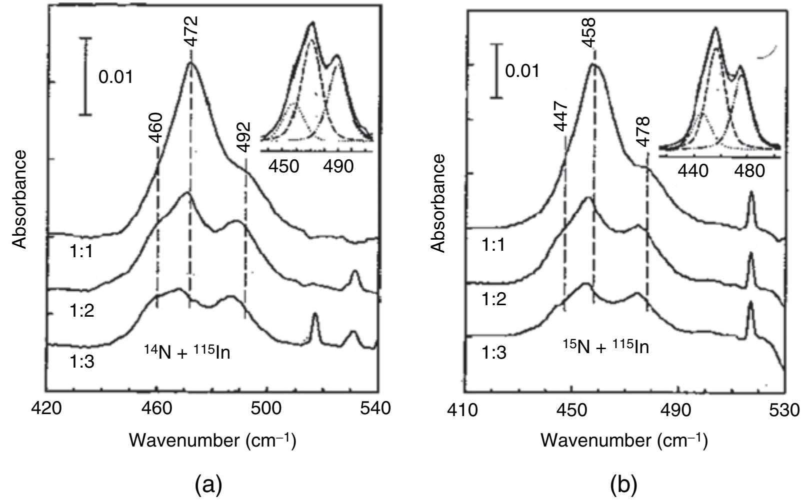

Fig. 9.7. FTIR absorption spectra [44] of GaAs samples co-implanted with indium and nitrogen isotopes (^{14}N and ^{15}N) after rapid thermal annealing at 800°C: (**a**) co-implantation of ^{14}N and ^{115}In and (**b**) co-implantation of ^{15}N and ^{115}In

of indium and 2% of nitrogen. This is probably the same for indium-related feature recently observed by independent researchers near 487 cm^{-1} [31] or 492 cm^{-1} [44] after RTA – providing strong evidence of the formation of In–N bonds.

Raman Scattering in Dilute $Ga_{1-x}In_xN_yAs_{1-y}$ Quaternary Alloys

Vibrational modes in epitaxially grown ternary $Ga(In)N_yAs_{1-y}$ [28–30] and quaternary $Ga_{1-x}In_xN_yAs_{1-y}$ layers ($y \leq 0.04$ and $x \leq 1$) as well as MQWs [31] by MBE on GaAs (on InP for high-In content) substrates have also been studied recently by Raman spectroscopy to gain additional insight into the resonance behaviour of Raman scattering by N-related LVMs as well as to assess the effects of In on the local chemical bonding of N in GaInAsN.

Figure 9.8a shows Raman scattering [35] covering the range of nitrogen-induced LVMs. The spectrum (1) has been recorded from an as-grown $GaN_{0.01}As_{0.99}$/GaAs MQW (i.e. 1% N in the wells) serving as a reference; spectrum (2) is recorded from an as-grown sample with 3% of In content; while spectrum (3) shows the same sample as of (2) after RTA for 15 s at 950°C. The change induced by annealing is clearly visible in spectrum (4) which is the difference of (3) and (2). Again, the $GaN_{0.01}\,As_{0.99}$/GaAs MQW sample shows the N-induced local mode (LO_2) – observed previously both by infrared absorption [30, 31] and Raman spectroscopy [32–35] – and assigned to the vibration of isolated nitrogen atom bonded to four Ga neighbours ($N_{As}Ga_4$) of T_d symmetry. The addition of In to GaNAs leaves the GaN-like LO_2-mode

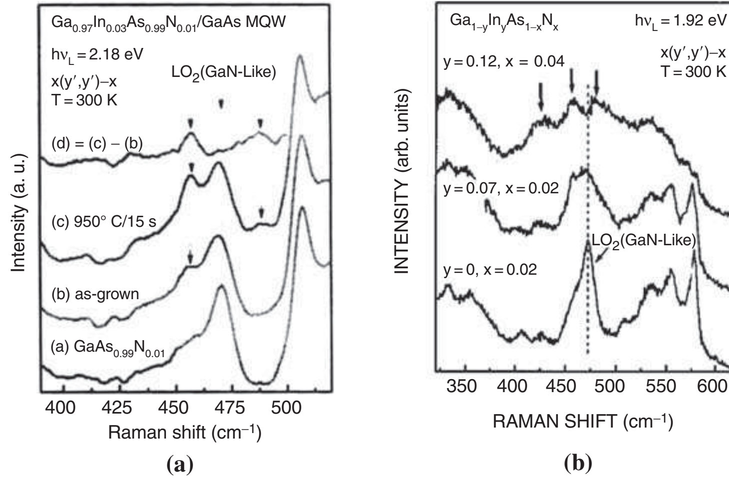

Fig. 9.8. (**a**) Room temperature Raman spectra of (*1*) an as-grown $GaAs_{0.99}N_{0.01}$/GaAs MQW; (*2*) an as-grown $Ga_{0.97}In_{0.03}As_{0.99}N_{0.01}$/GaAs MQW; (*3*) same as (*2*) but after RTA at 950°C for 15 s, and (*4*) the difference spectrum (*3*)−(*2*). (**b**) Raman spectra of $Ga_{1-y}In_yN_xAs_{1-x}$ layers on GaAs recorded for on-resonance excitation at 1.92 eV with different In and N compositions [35]

practically unchanged close to $\sim$470 cm^{-1}, with an additional shoulder emerging at 457 cm^{-1}, accompanied by a second peak on the high frequency side centred around $\sim$488 cm^{-1}.

Figure 9.8b shows the on-resonance Raman spectra recorded from $GaN_{0.02}As_{0.98}$ and from nearly lattice matched layers of $Ga_{0.93}In_{0.07}N_{0.02}As_{0.98}$ and $Ga_{0.88}In_{0.12}N_{0.04}As_{0.96}$ grown on GaAs substrates. Once again, there is a significant broadening of the Ga(In)N-like LO_2 phonon mode spectrum with increasing N(In) contents, resulting in a resolved splitting into three peaks centred at 425, 458, and 480 cm^{-1} for the $Ga_{0.88}In_{0.12}N_{0.04}As_{0.96}$ layer. Once again, these results have provided strong indications that the incorporation of In into GaNAs alters the chemical bonding of the N and/or the local strain state of the immediate environment of the N atoms. More recently, the Raman scattering studies [42] performed on In-rich $Ga_{1-x}In_xN_yAs_{1-y}$ alloys grown on InP have shown similar behaviours.

9.3 Theoretical

There are two main theoretical methods available for the calculations of impurity modes in semiconductors (1) the super-cell approach [45, 46] and (2) the crystalline Green's functions method [47,48]. These techniques differ primarily in the treatments of the surrounding atoms of the defective region. In the ab initio super-cell approach, one considers a large unit cell containing the defect

with atoms of periodic repetitions. In the Green's function method, however, one divides the crystal into two regions (1) an inner region containing the defect – called the "defect space" where the atoms are allowed to vibrate and (2) an outer region in which the atoms do not sense the presence of the defect.

9.3.1 Ab Initio Method

In the ab initio super-cell approach [45, 46], the selected number of atoms in the large unit cell are displaced to all three Cartesian directions. After each displacement the electronic structure for the new configuration is optimized and the resulting Hellmann–Feynman forces are calculated. This is done for all the atoms which are a priori considered important for the description of the impurity modes of the defect structure. The dynamical matrix is then calculated by finite difference using the forces and displacements. The normal modes and the corresponding vibrational frequencies are then obtained by diagonalizing the dynamical matrix.

9.3.2 Green's Function Technique

The vibrational properties of crystalline lattices with point defects involving Green's function method generally describe the displacement response of the imperfect lattice to sinusoidal driving forces [44–48]. The advantage of Green's function approach over the ab initio method is that it allows the coupling of the vibrations of the defect to the bulk crystal – permitting one to visualize which types of vibrational modes remain localized around the defect. We find Green's function method to be quite sensitive for monitoring the changes in the impurity mode frequencies in GaIn(Al)NAs alloys by the variations in the local bond configurations [49]. It is worth mentioning that, while the Green's function approach may be superseded by ab initio calculations [45, 46], its simplicity and ease of interpretation, however, strongly suggest that it still has an important role to play in assigning the observed local mode frequencies to specific defect configurations in the alloys of current interest.

The general procedure of calculating impurity modes in the Green's function framework is done in two stages. Firstly, the Green's functions of the perfect lattice $\mathbf{G}^{o}$ are obtained numerically by exploiting the translational symmetry and calculating the normal modes (eigenvalues and eigenvectors) from a reliable lattice dynamical scheme (see "Phonons" section). Secondly, the elements of the perturbation matrices $\mathbf{P}$ are obtained by defining the "impurity space" and restricting it to a small region around a specific defect configuration (see "Defect Configurations" section) and using the scaling properties and chemical trends found in the short-range interactions of the host crystal's dynamical matrix. The local distortions caused by substitutional impurities occupying either the cation or the anion sites are obtained from *first principles* using a bond-orbital model (BOM) [50] (from the minimum of total

change in bond energy, i.e. $\partial\Delta E_{\rm b}/\partial\Delta d = 0$) to estimate the nearest-neighbour force constant change parameters for the perturbation matrix $\mathbf{P}$. The frequencies of impurity vibrations are then obtained by setting the determinant of the dynamical matrix equal to zero [47, 48], i.e.

$$|\mathbf{I} + \mathbf{G}^{\rm o}\mathbf{P}| = 0. \tag{9.1}$$

Phonons

In the Green's function theory, one requires a realistic lattice dynamical scheme for gaining information of the microscopic structures related to the incorporation of N in dilute III–As–N. The choice of a lattice dynamical model should be such that (1) it must provide accurate values of phonons (eigenvalues and eigenvectors) for the host (GaAs, InAs, and AlAs) crystals and (2) to the Green's function theory it should be extended in a straightforward manner for treating the impurity vibrations. For these reasons, we have selected a relatively simple 11-parameter rigid-ion model (RIM11) [51] – adapted earlier for studying the dynamical properties of both perfect and imperfect compound semiconductors [52]. In zinc-blende-type crystals, the model provides adequate representations of the perturbation matrices for both isolated and complex defect centres. In this scheme, the local basis set required by the Green's function theory is simply the x, y, and z vibrations of the "rigid ions" and there is no need for introducing additional degrees of motion. Certainly, this is not the case in "shell" and "bond-charge" models [53] where one does require additional degrees of motion between "electron shells" and "rigid cores" and between "bond charge" and "ions", respectively.

Defect Configurations

To comprehend the observed FTIR [30, 31, 44] and Raman [35, 42, 43] scattering data on LVMs in $\mathrm{Ga}_{1-x}\mathrm{In}_x(\mathrm{Al}_x)\mathrm{N}_y\mathrm{As}_{1-y}$ quaternary alloys ($y \le 0.03$ and $0 \le x \le 1$), one can select five defect configurations involving isolated elementary tetrahedrons related to the incorporation of nitrogen (see Fig. 9.9, viz., $\mathrm{NIn}_m(\mathrm{Al}_m)\mathrm{Ga}_{4-m}$ with $m = 0$, 1, 2, 3, and 4: $\mathrm{NGa}_4(T_d)$, $\mathrm{NIn}_1(\mathrm{Al}_1)\mathrm{Ga}_3(C_{3v})$, $\mathrm{NIn}_2(\mathrm{Al}_2)\mathrm{Ga}_2(C_{2v})$, $\mathrm{NIn}_3(\mathrm{Al}_3)\mathrm{Ga}_1(C_{3v})$, and $\mathrm{NIn}_4(\mathrm{Al}_4)(T_d)$). In GaIn(Al)NAs alloys, as the symmetry of the defect configurations is changing from $T_d \to C_{3v} \to C_{2v} \to C_{3v} \to T_d$, one anticipates from group theoretical arguments a total of nine optically active impurity modes.

Generally, the frequencies of impurity modes in mixed configurations fall between the values of LVMs of the two end members, i.e. between the local modes of N_{As} in GaAs (with $x = 0$ for In(Al)-free case) and In(Al)As (with $x = 1$ for Ga-free case). Notable exceptions can occur, however, if the new equilibrium positions of the defect centres in the alloy systems are associated with significant variations in the force constants, as might be the case, in our choice of $\mathrm{Ga}_{1-x}\mathrm{In}_x(\mathrm{Al}_x)\mathrm{N}_y\mathrm{As}_{1-y}$ quaternary alloys.

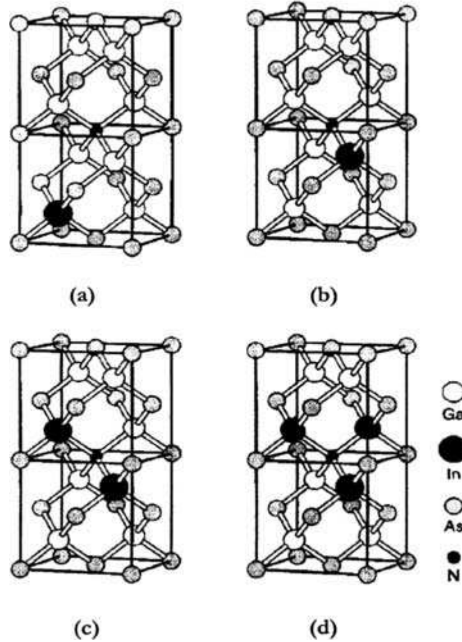

Fig. 9.9. Representation of the zinc-blende GaAs lattice with isolated NAs and InGa defects (**a**), NAsInGa(1)Ga_3 nearest-neighbour pair (**b**), NAsInGa(2)Ga_2 next nearest-neighbour pair (**c**), and NAsInGa(3)Ga_1 complex centre (**d**)

It is therefore quite challenging to carefully examine the force constant variations caused by isolated N_{As}, $In_{Ga}(Al_{Ga})(Ga_{In}(Ga_{Al}))$ defects in GaAs (InAs (AlAs)). For complex centres (viz., N_{As}–$In_{Ga}(1)$ and N_{As}–$In_{Ga}(2)$), the task of estimating force constant changes is even more exigent. In the Green's function theory using RIM11, the estimation of force constant variations is relatively straightforward – illustrating the significance of the methodology for defining the perturbation matrices and thus calculating impurity modes.

9.3.3 Numerical Computations and Results

Lattice Dynamics

The host crystal phonons are described by an RIM11 [51] in which the force constants are written as the sum of a short-range bonding-type interactions and a long-range interaction due to the Coulomb field. The short-range forces are assumed to be zero after the second nearest neighbours, which when combined with the zinc-blende symmetry conditions, restrict parameters to ten [A, B (nearest neighbour); C_i, D_i, E_i, and F_i; $i = 1, 2$ (second nearest neighbour)] force constants. The long-range interaction is derived by assuming that

Table 9.2. Rigid-ion model force constants and Szigeti effective charge used for the lattice dynamical (phonon) calculations of GaAs, AlAs, and InAs

Parameters	GaAs[a]	AlAs[b]	InAs[c]
A	−40.71	−40.83	−34.57
B	−16.64	−8.06	−25.00
C_1	−1.77	−3.59	−1.95
C_2	−4.61	−1.69	−0.75
D_1	2.48	1.112	1.13
D_2	−12.33	−10.07	−5.9
E_1	9.12	3.94	−5.3
E_2	8.34	−3.49	5.5
F_1	−11.72	1.15	−7.7
F_2	20.08	14.61	9.93
Z_{eff}	0.6581	0.7548	0.756

The units (in the notations of Kunc et al. [51]) are Nm^{-1} for force constants (A, B, C_i, D_i, E_i, and F_i; $i = 1, 2$) and electron charge for Z_{eff}
[a] [51], [b] [54], [c] [48]

atoms behave like rigid ions with an effective Szigeti charge Z_{eff}. All the model parameters are calculated by using a non-linear least-square fitting procedure with constrained parameters and weighting to the available data on phonon frequencies at critical points (Γ, X, L, and K) and elastic constants. The parameters used (see Table 9.2) here for GaAs are those of Kunc et al. [51] which model the phonon dispersions relatively well, providing an excellent agreement with the neutron scattering data [36]. For AlAs and InAs, however, we have chosen the set of parameters from [54] and [48], respectively, obtained by fitting to the existing IR and Raman scattering data.

As a representative case, we have displayed (see Fig. 9.10) the calculated one-phonon density of states and the phonon dispersions of GaAs (using the parameter set from Table 9.2) compared with the neutron scattering data of Strauch and Dorner [36]. This serves to illustrate the level of agreement obtained by our lattice dynamical model (RIM11). Moreover, we find a very good concurrence in the phonon frequencies at high-symmetry points when comparison is made with the values obtained by more sophisticated ab initio methods [55]. It is worth mentioning, however, that a set of force constants in a phenomenological scheme providing good agreement to the neutron scattering IR and Raman data of phonon frequencies of a perfect crystal is not necessarily a guarantee for the accuracy of the model.

The point that compels recognition to a lattice dynamical scheme demand simultaneously correct eigenvalues and eigenvectors. Although the impetus for examining the phenomenological models comes from ab initio [45, 46] methods, the later approaches have not yet replaced the former schemes completely. The simple reason is that the ab initio methods deal only with the phonons at a few high-symmetry points while the efficiency of phenomenological models

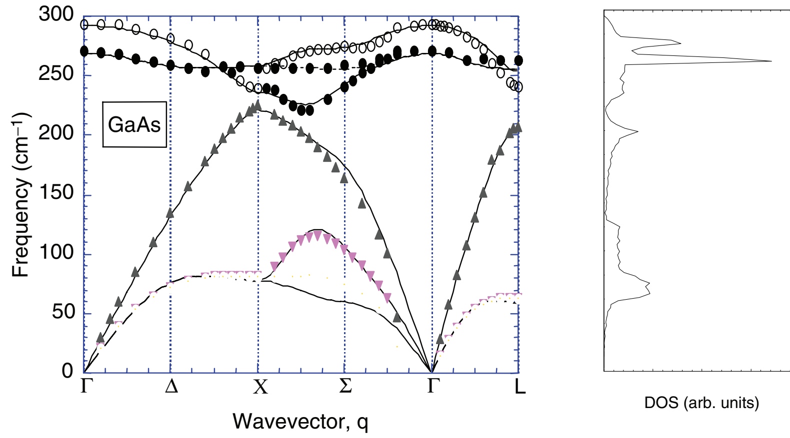

Fig. 9.10. Rigid-ion model calculations for the phonon dispersions along high-symmetry directions compared with the neutron scattering data [36] and one-phonon density of states obtained with the parameter values of Table 9.2 for GaAs

comes to profit when different Brillouin zone averages are evaluated, viz., in the calculations of Green's functions used for studying the impurity vibrations [37]. Our earlier investigation of LVMs for identifying the microscopic lattice structures of silicon in $Ga_{1-x}Al_xAs$ alloys [48] for low-Al composition (x) has provided indirect support for the reliability of the calculated phonons of GaAs using RIM11.

Lattice Distortion

A semi-empirical method of Harrison [50] is used to study the lattice relaxation around impurity atoms and its effect on the dynamical properties in dilute III–V–N. In terms of the Hartree–Fock atomic term values, this method provides simple analytical expressions [56] for the change in impurity–host and host–host bond energies and suggests a computationally efficient and reasonable way to estimate the bond-length distortions. In the notation of Harrison, the gain in the impurity–host bond energy per bond connected with a distortion Δd ($\Delta d > 0$ outwards and $\Delta d < 0$ inwards) can be calculated as

$$\Delta E_{\mathrm{b}} = \Delta E_{\mathrm{b}}^{1} + \Delta E_{\mathrm{b}}^{2}, \tag{9.2}$$

where $\Delta E_{\mathrm{b}}^{1}$ and $\Delta E_{\mathrm{b}}^{2}$ are the changes in the energy of the bonds caused by distortion in the nearest-neighbour and next nearest-neighbour atom positions, respectively. The local distortion is then calculated by taking, $\partial \Delta E_{\mathrm{b}} / \partial \Delta d = 0$. For Ga$As$:N, the calculated variations of impurity–host $\Delta E_{\mathrm{b}}^{1}$, host–host $\Delta E_{\mathrm{b}}^{2}$, and total ΔE_{b} change in bond energies as a function of distortion $\Delta d/d_{\mathrm{o}}$ is displayed in Fig. 9.11.

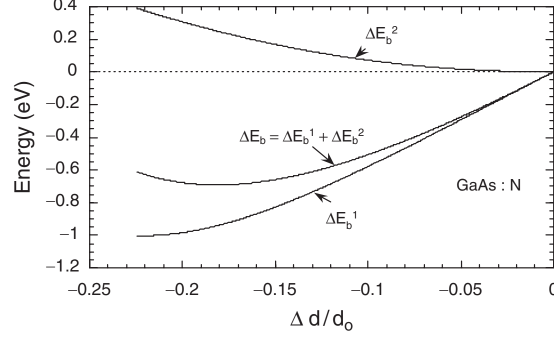

Fig. 9.11. The variation of change in impurity–host $\Delta E_{\rm b}^1$, host–host $\Delta E_{\rm b}^2$, and total $\Delta E_{\rm b}$ bond energy vs. $\Delta d/d_{\rm o}$ for GaAs:N

The BOM calculation of $\Delta d/d_{\rm o}(= -0.18)$ for N_{As} in GaAs (see Fig. 9.11), estimated at the minimum of total change in bond energy, is used to evaluate the stiffening in the force constant variation parameter for the perturbation matrix **P** of the Green's function theory. Similar calculations were performed for Al*As*:N, In*As*:N, *Ga*As:In, etc.

Localized Vibrational Modes of Isolated Defects

If the impurity space is confined to its nearest neighbours, then the simplest case of an isolated N occupying the As site (N_{As}) in GaAs (InAs or AlAs) with T_d symmetry (see Fig. 9.9a) would involve only five atoms. In the framework of an RIM11, the two nearest-neighbour force constants A and B will be modified to $A'(\equiv A + \Delta A)$ and $B'(\equiv B + \Delta B)$ or A'' and B'', if the impurity $M_1^{\rm I}$ (or $M_2^{\rm I}$) occupies the Ga (or the As) site in GaAs, respectively. The changes are described by the parameters [48]

$$\varepsilon_1 = (M_1 - M_1^{\rm I})/M_1 \quad \text{and} \quad t = (A - A')/A = (B - B')/B \tag{9.3}$$

or

$$\varepsilon_2 = (M_2 - M_2^{\rm I})/M_2 \quad \text{and} \quad u = (A - A'')/A = (B - B'')/B. \tag{9.4}$$

The displacements involving impurity atom and its four nearest neighbours can be classified by the irreducible representations of the defect point group T_d, i.e. $\Gamma_{T_d} \equiv A_1 \oplus E \oplus F_1 \oplus 3F_2$. Transformation to the symmetry-adapted displacements can be used to reduce the defect and the Green's functions matrices to block diagonal form. We then solve (9.1) in the A_1, E, F_1, and F_2 irreducible representations of the T_d point group, as a function of the force constant change parameter t or u for isolated defects occupying either the Ga (In or Al) or the As site, respectively.

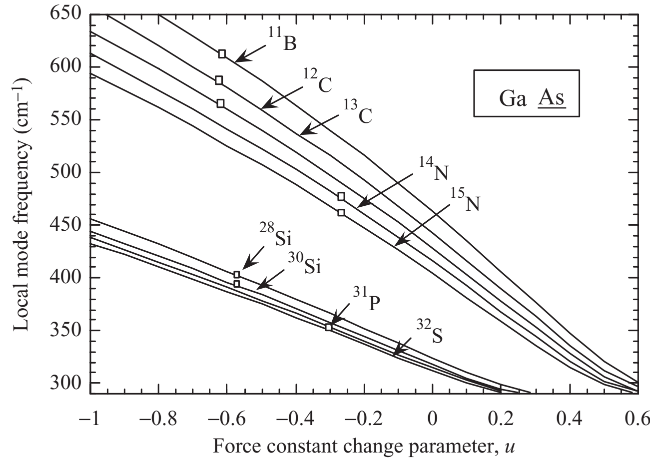

Fig. 9.12. Green's function calculation of localized vibrational mode frequencies (cm^{-1}) as a function of force constant change parameter u for various isolated defects occupying the As site in GaAs

In N-implanted GaAs sample, the force constant variation u between N and Ga bond is assessed (see Fig. 9.12) from the tetrahedral T_d configuration by simulating the triply degenerate F_2 local mode ($\sim$471 cm^{-1}) of $^{14}\mathrm{N}_{\mathrm{As}}$. Despite the simplicity of the perturbation model, the magnitude and splitting of the calculated isotopic shifts of LVMs due to C_{As}, N_{As}, and B_{As}, defects in GaAs are found to be in very good agreement with the experimental data. Similar calculations of LVMs are also performed for isolated light substitutional defects in InAs and AlAs. It is worth mentioning, however, that the accurate force constant variation parameters t for the heavier Ga or In isoelectronic substituents in *In*As or *Ga*As are rather difficult to obtain from the in-band modes of $\mathrm{Ga}_{1-x}\mathrm{In}_x\mathrm{N}_y\mathrm{As}_{1-y}$ alloys ($y = 0$ and $x < 0.3$).

In Table 9.3, we have reported the results of our Green's function calculations for local modes in the F_2 representation of a selected group of substitutional (isoelectronic (i), acceptor (a^-), and donor (d^+)) impurities in AlAs, GaAs, and InAs. In each case, the last column of Table 9.3 lists the relative change in force constants between impurity and its nearest neighbours which reproduces the experimental local mode frequency. In contrast to the earlier findings [57], our results for isolated defects suggest the relative force constant variation to be independent of the size of the impurity–host atoms – larger for isoelectronic impurities and quite appreciable for charged defects. The evidence that the size of substitutional defects does not dominate the bond strength is quite obvious from the results of N_{As} and C_{As} in III–As, both of which have similar radii but smaller than that of the As (cf. Table 9.3) atom.

Table 9.3. Comparison of the calculated localized vibrational modes due to closest mass N (*isoelectronic*) and C (*acceptor*) (Be (*acceptor*), B (*isoelectronic*) defects) occupying *As*, *P*, and *Sb* site (*Ga*, *In*) in various III–V compound semiconductors

System	Symmetry	Local modes (cm^{-1})		Force constant
		Calculated	Experimental[a]	variation t, u
Al*As*:^{12}C	T_d	630	630[b]	−0.60
Al*As*:^{14}N	T_d	510	–	−0.25
Al*As*:^{15}N	T_d	499	–	−0.25
Ga*As*:^{11}B	T_d	601	601	−0.60
Ga*As*:^{12}C	T_d	582	582	−0.61
Ga*As*:^{14}N	T_d	471	471.4[c]	−0.26
Ga*As*:^{15}N	T_d	457	458.0[c]	−0.26
Ga*As*:P	T_d	355	355	−0.31
Ga*As*:Si	$\mathrm{T_d}$	399	399	−0.54
*Ga*As:^{9}Be	T_d	482	482.4	0.63
*Ga*As:^{10}B	T_d	540	540	0.33
*Ga*As:^{11}B	T_d	517	517	0.33
*Ga*As:^{27}Al	T_d	362	362	0.18
*Ga*As:Mg	T_d	331	331	0.5
*Ga*As:Si	T_d	384	384	−0.03
In*As*:^{12}C	T_d	527	527[d]	−0.15
In*As*:^{14}N	T_d	443	443[e]	0.2
In*As*:^{15}N	T_d	428	429[e]	0.2
In*As*:P	T_d	303	303	0.2
In*As*:Si	T_d	328	328	0.08
*In*As:^{9}Be	T_d	435	435	0.1

[a] [27], [b] [58], [c] [30], [d] [59], [e] [44]

Several interesting trends are noted in the force constant variations for closest mass $C_V(a^-)$ and $N_V(i)$ occupying the V site; and $Be_{III}(a^-)$ and $B_{III}(i)$ occupying the III site in III–V compounds:

(a) For C_{As} acceptors in III–As, we find an increase in the force constant of around 35% with respect to the closest mass isoelectronic N_{As} while for Be_{III} and Mg_{III} acceptors, there is a decrease in the values of force constants by ∼30% from those of the closest mass isoelectronic B_{III} and Al_{III} impurities, respectively.
(b) For Si_{III} donors in III–V compounds, on the other hand, we have found an increase in the force constant (∼20%) with respect to the closest mass isoelectronic Al_{III}.

It is worth mentioning that the above trends in the force constant variations are found independent of the long-range Coulomb interactions. We strongly believe, however, that the charged impurities in semiconductors affect only the short-range forces via lattice relaxations and by the redistribution of the bond electron charge density. The increase (decrease) in the bonding force constant

corresponds to the charge on the impurity, whether donor or acceptor, being of opposite (similar) sign to the charge on the host nearest-neighbour atoms. Again, the redistribution of electron density in the bond caused by the charge on the impurity atom is responsible for the modification of the covalency (ionicity) and hence the strength of the bond.

These results are supported by the calculations of electronic charge density contours [60] in perfect/imperfect semiconductors. For iso-row Ge–GaAs–ZnSe compounds, the electronic charge density in the "covalent" Ge (group IV) lies midway between the two Ge atoms. For "partially covalent" GaAs (III–V compound), the electron charge density is displaced towards the As atom as there is a positive static charge on the Ga (group III) atoms and a negative charge on the As (group V) atoms. In the case of a "partially ionic" ZnSe (II–VI), nearly all the charge density is located near the Se atoms (see Fig. 9.13a).

Stiffening in the force constant arises (see Fig. 9.13b) when the charge on the impurity atom and its neighbours have *opposite* signs (e.g. $\mathrm{Si_{Ga}}(d^+)$ and $\mathrm{C_{As}}(a^-)$) – causing electronic charge density to move towards the middle of the bond and making it more covalent. On the other hand, softening in the force constant arises when the charged impurity and its neighbours have *similar* signs (e.g. $\mathrm{Be_{Ga}}(a^-)$ and $\mathrm{S_{As}}(d^+)$) – causing electronic charge density to move towards the anion site and making the bond weaker, i.e. less covalent (or more ionic). In semiconductors, the present simple physical understanding of the bonding mechanism in terms of the general magnitude of "impurity–host parameter" has played an important role in establishing and identifying the microstructure features of defects and their relationship to the optical experiments [52]. Moreover, these intuitive ideas have also been verified by ab initio calculations [61] on GaAs with Si impurities in different charge states where an increase in the negative charge localized on a $\mathrm{Si_{Ga}}$ impurity leads to decrease in the covalency of the bond and hence a reduction in the local mode frequency.

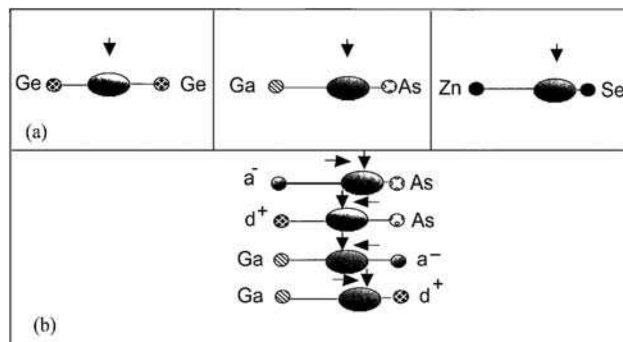

Fig. 9.13. (**a**) Force constant variation correlation with bond covalency (ionicity) in iso-row Ge–GaAs–ZnSe semiconductors and (**b**) charged impurities occupying the cation and anion sites in GaAs

Again, from the analysis of LVM for B_{As} in GaAs (see Table 9.3), our Green's function calculations provided force constant variation similar to C_{As}. Since B_{As} is expected to act as a double acceptor (a^{2-}) while C_{As} is a single acceptor (a^-), this result seems a little odd. A possible explanation for this result might be that the extra charge on the B_{As} atom in GaAs is widely distributed so that as far as the force constant with the nearest neighbours is concerned, any adjustment by the redistribution of electron charge density between the B_{As} and Ga bond is similar to C_{As}–Ga bond. Again, since the gallium neighbours of the B_{As} and C_{As} atoms have different combinations of ^{69}Ga and ^{71}Ga isotopes, nine LVM frequencies are expected [52] from five different isotopic centres for each impurity configuration. High-resolution FTIR spectroscopy [62], carried out at 4.2 K for B_{As} in Ga-rich GaAs after a small dose of 2 MeV electron irradiation, has allowed five lines to be detected, of which two are not fully resolved. Similar observation of Ga-isotopic fine structures of C_{As} LVMs provided strong corroboration for the site selectivity of C in GaAs [39] and was successfully analysed by the Green's function theory. Finally, it is worth mentioning that the present Green's function analysis of LVMs for isolated substitutional defects in semiconductors is not applicable for defects occupying the off-centre sites (e.g. oxygen in GaAs [63, 64]).

Nearest-Neighbour Pair Defects in $\mathbf{Ga_{1-x}In_xN_yAs_{1-y}}$

In Ga-rich (In-rich) $Ga_{1-x}In_xN_yAs_{1-y}$ layers with $x \leq 0.12$ ($x \geq 0.9$), one can realize the possibility of a nearest-neighbour pair-defect $^{14}N_{As}$–In_{Ga} (or $^{14}N_{As}$–Ga_{In}) of trigonal symmetry (C_{3v}) (see Fig. 9.9b), in which one of the four Ga (In) atoms in the neighbourhood of $^{14}N_{As}$ at site 2 (say) is replaced by a larger size and heavier In, i.e. In_{Ga} (or a smaller size and lighter Ga_{In}) atom at site 1. From group theoretical arguments, the vector spaces formed by the displacement of "impurity centre" and its nearest neighbours in the $^{14}N_{As}In_{Ga}(1)Ga_3$($^{14}N_{As}Ga_{In}(1)In_3$) configuration will be transformed according to the irreducible representations: $\Gamma_{C_{3v}} = 6A_1 \oplus 2A_2 \oplus 8E$. As the nearest-neighbour pair defect does not move in the A_2 representation, only A_1 and E types of modes are optically active. Clearly, defining the perturbation matrix to study the vibrational modes of a pair defect of C_{3v} symmetry is more challenging than the T_d case. In this configuration, one needs a minimum of two (u and t) perturbation parameters. To make the $\mathbf{P}$ matrix more meaningful, one may also consider a direct interaction Γ_{12} between the two impurities in terms of the force variation $F_{12}(\equiv u + t - ut + \Gamma_{12})$.

For the $^{14}N_{As}$–In_{Ga} pair defect in Ga-rich GaInNAs layers grown on (100) GaAs, we have defined the appropriate parameters by including corrections to the force constants of isolated defects after studying lattice relaxation of $^{14}N_{As}$ and In_{Ga} in GaAs, respectively. In the framework of a first principle BOM, we estimated ∼5% increase in the N–In (N–Ga) bond lengths from that of the pure InN 2.14 Å (GaN 1.95 Å) bond, in good agreement with the results obtained by an empirical pseudo-potential method using large atomistically

relaxed super-cells [65]. The effects of lattice relaxation lead to 2.7% softening in the N–In bond, a negligible change in the In–As and 8.6% stiffening in the N–Ga bond, respectively. Although the effects of mismatch strain in the GaInNAs layers are difficult to incorporate, we have chosen, however, in our study $u = \Gamma_{12}$ to keep the number of force constant parameters a minimum. For the $^{14}N_{As}$–In_{Ga} pair, our results of Green's function calculations have clearly revealed the splitting of a triply degenerate $^{14}N_{As}$$\sim$471 cm^{-1} (In-free) F_2 band into a non-degenerate $\sim$462 cm^{-1} (A_1) and a doubly degenerate $\sim$490 cm^{-1} (E) local mode in good agreement with the FTIR [31] (457 and 487 cm^{-1}) and Raman [35] scattering (462 and 492 cm^{-1}) data (see Table 9.4).

It is to be noted that the doubly degenerate E-mode describes the vibration in the plane orthogonal to the N–In bond and is mainly affected by the force constant between the N and Ga atoms, whereas the non-degenerate A_1-mode represents the vibration of N atom along the bond of the defect pair and is primarily influenced by the force constant between the N and In bond. Since the N–Ga bond stretching force constant is larger than the force constant

Table 9.4. Comparison of the calculated local vibrational modes with the experimental data of N_{As} involving In and Ga atoms in different configurations of Ga- and In-rich $Ga_{1-x}In_xN_yAs_{1-y}$ alloys

System	Symmetry	Local vibrational modes (cm^{-1})	
		Calculated	Experimental
[a]*$Ga_xIn_{1-x}As_{1-y}N_y$ Ga-rich*			
$^{14}N_{As}$–In_{Ga}(1)Ga_3	C_{3v}	490(E), 462(A_1)	487, 457[a], 492, 462[b]
$^{15}N_{As}$–In_{Ga}(1)Ga_3	C_{3v}	476(E), 448(A_1)	478, 447[b]
$^{14}N_{As}$–In_{Ga}(2)Ga_2	C_{2v}	481(B_1), 457(A_1), 429(B_2)[c]	480, 458, 425[b]
		499(B_1), 479(A_1), 458(B_2)[d]	521, 480, 454[e]
$^{15}N_{As}$–In_{Ga}(2)Ga_2	C_{2v}	468(B_1), 444(A_1), 417(B_2)[c]	–
		485(B_1), 465(A_1), 445(B_2)[d]	
[b]*$Ga_xIn_{1-x}As_{1-y}N_y$ In-rich*			
$^{14}N_{As}$–Ga_{In}(1)In_3	C_{3v}	496(A_1), 445(E)	471, 443[f] 510, 447[e]
$^{15}N_{As}$–Ga_{In}(1)In_3	C_{3v}	482(A_1), 430(E)	

[a] See [31]
[b] See [35]
[c] With 3.6% softening in the N–In and 9.6% stiffening in the N–Ga bond
[d] With 3.6% softening in the N–In and 16% stiffening in the N–Ga bond
[e] See [66]
[f] See [42]

between the In and N bond, the frequency of the E-mode is found higher for the In–N pair in the $^{14}N_{As}In_{Ga}(1)Ga_3$ configuration than the A_1-mode. The lower value of the A_1-mode frequency is caused by the collective effects of larger indium mass and weaker force constant between the N and In bonds. Again by changing the N-isotopic mass and keeping the same force constant variations in the perturbation matrix, our Green's function calculations for the $^{15}N_{As}In_{Ga}(1)Ga_3$ configuration predicted a non-degenerate A_1-mode near $448\,cm^{-1}$ and a doubly degenerate E-mode near $476\,cm^{-1}$, respectively.

Results of similar calculations performed for the LVMs of N_{As}–Ga_{In} pair in In-rich (Ga-rich) $Ga_{1-x}In_xN_yAs_{1-y}$ alloys are also included in Table 9.4. It is to be noted that a low-temperature Raman study by Wagner et al. [42] has revealed only Ga–N and In–N like modes near 470 and $443\,cm^{-1}$, respectively, on high-In content $Ga_{1-x}In_xN_yAs_{1-y}$ (with $y \leq 0.012$ and $x \geq 0.92$) grown by rf-nitrogen plasma source MBE on InP substrate. More recent FTIR study [66] at 77 K of the local modes in ^{14}N-implanted $In_{0.26}Ga_{0.74}As$ layers annealed at 700–900°C has observed a weaker band near $510\,cm^{-1}$ (A_1) in addition to the two modes detected in the Raman spectroscopy near 472 and $447\,cm^{-1}$. Unlike $^{14}N_{As}$–In_{Ga} pair modes in Ga-rich material, the solution of (9.1) for the LVMs of $^{14}N_{As}$–Ga_{In} pair in In-rich GaInNAs provided lower value of InN-like doubly degenerate mode and a higher GaN-like non-degenerate mode [37] in good agreement with the recent FTIR [66] and Raman scattering [67] data.

Other Complex Centres in $\mathbf{Ga_{1-x}In_xN_yAs_{1-y}}$

In Ga- (In-) rich $Ga_{1-x}In_xN_yAs_{1-y}$ alloys with In (Ga) contents ranging between 0.1 and 0.3, one may speculate the possibility of the formation of a second nearest-neighbour complex $N_{As}In_{Ga}(2)Ga_2$ ($N_{As}Ga_{In}(2)In_2$) of orthorhombic symmetry (C_{2v}). For such a defect centre in GaAs (say), we consider replacing two of the four Ga atoms (at sites 1 and 6) by two larger size and heavier In_{Ga} atoms in the vicinity of N_{As} (on site 2) (or in InAs substituting two of the four In atoms by smaller size and lighter Ga_{In} atoms; see Fig. 9.9c). In this configuration, the vector spaces formed by the displacements of impurity atoms and their nearest neighbours transform according to the irreducible representations: $\Gamma_{C_{2v}} = 10A_1 \oplus 6A_2 \oplus 8B_1 \oplus 9B_2$, where A_1, B_1, and B_2 type of vibrations are optically active. For studying the vibrational modes of such a defect centre ($N_{As}In_{Ga}(2)Ga_2$), by the Green's function theory, we require at least two u, t $(= v)$ force constant change parameters. To make the perturbation matrix $\mathbf{P}$ meaningful, one may also consider direct interactions between impurities at sites 1–2 (Γ_{12}) and 2–6 (Γ_{26}) via the additional force variation parameters F_{12} $(\equiv u + t - ut + \Gamma_{12})$ and F_{26} $(\equiv u + v - uv + \Gamma_{26})$, respectively.

From the sparse data of N-related modes in Ga-rich GaInNAs and recognizing the fact that the observed Raman bands at frequencies higher than

500 cm^{-1} are associated with the second-order scattering of GaAs-like optical modes, we first choose only two (u and $t = v$) perturbation parameters for the complex centre of C_{2v} symmetry. In the framework of BOM, our study of lattice relaxation for the $N_{As}In_{Ga}(2)Ga_2$ centre provided 3.6% softening in the N–In bonds and a small stiffening 9.6% in the N–Ga bonds, respectively. With appropriate adjustments of force constants ($t = v$ and u) in the **P** matrix, the Green's function theory provided a complete lifting of the degeneracy of the $^{14}N_{As}$ ($^{15}N_{As}$) local mode – predicting three distinct bands near 481 (B_1), 457 (A_1), and 429 (B_2) cm^{-1} (468, 444, and 417 cm^{-1}) for $^{14}N_{As}In_{Ga}(2)Ga_2$ ($^{15}N_{As}In_{Ga}(2)Ga_2$), respectively. Theoretical results (see Table 9.4) are found to be in good agreement with the Raman scattering [42] data as well as with two FTIR [66] bands observed near 480 and 454 cm^{-1}. In the B_1- and B_2-modes as N–Ga or N–In bonds are involved, we find their frequencies lower than the values in the C_{3v} case for the present choice of parameters. The reason for the lower values is believed to be the combined effects caused by the involvement of a second heavier In mass in the $N_{As}In_{Ga}(2)Ga_2$ cluster and by the weakening of force constant between the N and In bonds.

It is worth mentioning, however, that the frequencies of impurity modes for this configuration are found strongly dependent on the choice of the force constant change parameters especially the values between Ga and N bonds. For instance by retaining the same set of force constant change parameter t ($= v$) between In and N bonds, and increasing the force constant u ($= \varGamma_{12} = \varGamma_{26}$) between the N and Ga bonds from 9.6 to 16%, our Green's function theory for the $^{14}N_{As}In_{Ga}(2)Ga_2$ ($^{15}N_{As}In_{Ga}(2)Ga_2$) cluster has provided shifts to the LVM frequencies to 499 (B_1), 479 (A_1), and 458 (B_2) cm^{-1} (485 (B_1), 465 (A_1), and 445 (B_2) cm^{-1}) in accord with at least two of the observed Raman [42] and FTIR bands near 480 and 454 cm^{-1} [66]. Although the calculated local mode at 499 cm^{-1} falls near the frequency range dominated by the second-order GaAs-like optical phonons, a broad IR band recently observed near 521 cm^{-1} after annealing at 900°C [66] has been assigned as a B_1-mode. If one accepts the feature near 521 cm^{-1} to be a true local mode and not as an artefact, then in In-rich GaInNAs one should have also observed an A_1-mode near 500 cm^{-1} for the nearest-neighbour $^{14}N_{As}$–Ga_{In} pair of C_{3v} symmetry.

Accepting such a scenario requires an additional 7% stiffening in the Ga–N bond for defining the perturbation matrix in the Green's function theory for the $^{14}N_{As}Ga_{In}(1)In_3$ ($^{15}N_{As}Ga_{In}(1)In_3$) nearest-neighbour pair in the InAs lattice. This additional stiffening in the Ga–N bond shifts the LVMs of $^{14}N_{As}Ga_{In}(1)In_3$ ($^{15}N_{As}Ga_{In}(1)In_3$) pair to 496 cm^{-1} ($A_1$) and 445 cm^{-1} ($E$) (482 cm^{-1} ($A_1$) and 430 cm^{-1} ($E$): see Table 9.4), respectively. For the $^{14}N_{As}Ga_{In}(2)In_2$ ($^{15}N_{As}Ga_{In}(2)In_2$) C_{2v} cluster in In-rich materials, our study required even larger stiffening (10%) in the Ga–N force constants for matching the LVMs modes closer to those of the $^{14}N_{As}In_{Ga}(2)Ga_2$ ($^{15}N_{As}In_{Ga}(2)Ga_2$) in Ga-rich GaInNAs alloys.

9.4 Discussion and Conclusion

In dilute III–As–N alloys, we have reviewed the experimental (FTIR and Raman scattering) data on N-related local vibrational modes and presented a comprehensive Green's function analyses to investigate the microscopic lattice structures related to the incorporation of N in Ga- (In-) rich $Ga_{1-x}In_xN_yAs_{1-y}$ alloys. Nine LVMs are calculated from the five [N_{As}–Ga_4 (T_d), N_{As}–$In_{Ga}(1)Ga_3$ (C_{3v}), N_{As}–$In_{Ga}(2)Ga_3$ (C_{2v}), N_{As}–$Ga_{In}(1)In_3$ (C_{3v}), and N_{As}–In_4 (T_d)] different possible clusters in GaInNAs alloys (see Table 9.4).

Based on the assessed force constant variations u between N–In and N–Ga bonds from the triply degenerate F_2-modes of $^{14}N_{As}$ in InAs and GaAs, we are able to accurately predict the isotopic shift of LVM for $^{15}N_{As}In_4$ ($^{15}N_{As}Ga_4$) to 428 cm^{-1} (457 cm^{-1}) in excellent agreement with the FTIR data. Similar calculation for the F_2 local mode of $^{14}N_{As}$ in AlAs near 510 cm^{-1} is found to be in good accord with the IR absorption AlN-like feature observed by Hashimoto et al. [68] in Ga-rich AlGaAsN. As compared to GaAs and InAs, the upward shift of the $^{14}N_{As}$ local mode in AlAs is expected due to the higher ω_{max} 404 cm^{-1} of AlAs than that of GaAs ($\omega_{max} \sim 296$ cm^{-1}) and InAs ($\omega_{max} \sim 254$ cm^{-1}). The observation of a Raman line near 500 cm^{-1}, not resolved in an earlier room temperature study due to underlying background from second-order phonon scattering, has provided further corroboration to our findings.

By using the estimated force constants of isolated defects with appropriate corrections caused by lattice relaxations in Ga- (In-) rich GaInNAs, we are able to construct perturbation matrices involving $^{14}N_{As}$ and In_{Ga} (Ga_{In}) atom(s) in different (C_{3v} and C_{2v}) configurations. Contrary to the FTIR results on multiple-quantum well structures [30], our Green's function theory in Ga-rich alloys has accurately revealed the splitting of $^{14}N_{As}$ local mode into a doublet (490 (E) and 462 (A_1) cm^{-1}) for the $^{14}N_{As}In_{Ga}(1)Ga_3$ (C_{3v}: see Fig. 9.9b) cluster. This result is in very good agreement with the infrared [31] and Raman scattering [35] data obtained earlier after RTA. Relative to $^{14}N_{As}$-mode in GaAs (470 cm^{-1}), the frequency shifts of new bands are attributed to the preferential In–N bonding and by the associated strength in the Ga–N bonds. Since N has a lighter mass than As and In is heavier than Ga, our study revealed that the higher frequency of E-mode is mainly influenced by the force constant between N and Ga atoms which in turn is affected by the Ga–N bond length. In the MOCVD-grown $Ga_{1-x}In_xN_yAs_{1-y}$ samples with $y = 0.002$ and $x = 0.025$, the appearance of two modes (457 and 487 cm^{-1}) in the absorption spectra after RTA has provided further credible testimony to the change in bonding configuration in the N-nearest-neighbour bonds towards the In–N bonding.

As the composition of In increases, one expects the formation of complex centres – most likely of C_{2v} symmetry (see Fig. 9.9c) – involving two In_{Ga} atoms in the vicinity of N_{As}. In GaInAsN/GaAs samples with 12% In and 4%

N, three new Raman lines were detected earlier near 425, 458, and 480 cm^{-1}. Although the origin of 425 cm^{-1} feature was not fully understood, the authors of [42] speculated it, however, either to the involvement of a nitrogen dimer, i.e. NN on the As site (NN_{As}), or to a Ga–N mode in the N-rich domain. The other two lines observed near 458 and 480 cm^{-1} were thought to be related to the nearest-neighbour $^{14}N_{As}In_{Ga}(1)Ga_3$ pair of C_{3v} symmetry [42]. More recently, two modes in ^{14}N-implanted $Ga_{0.84}In_{0.16}As$ layers observed near 454 and 480 cm^{-1} by infrared spectroscopy [66] after RTA treatment at 700 and 800°C are attributed to the $^{14}N_{As}In_{Ga}(2)Ga_2$ pair of C_{2v} symmetry. Again after annealing at 900°C, the intensities of lines near 454 and 480 cm^{-1} are found to decrease with the emergence of a new broadband at 521 cm^{-1}.

From a theoretical stand point and using a simplified BOM, we have estimated qualitatively the lattice relaxation effects caused by $^{14}N_{As}In_{Ga}(2)Ga_2$ in GaAs lattice. The study provided a small softening (3.6%) and stiffening (9.6%) in the N–In and N–Ga bonds, respectively. By including appropriate force variations in the perturbation matrix for the $^{14}N_{As}In_{Ga}(2)Ga_2$ centre, our Green's function theory predicted three distinct local modes near 429 (B_2), 457(A_1), and 481 (B_1) cm^{-1} in good agreement with the Raman data [42]. We have also noted, however, that the mode frequencies of the C_{2v} centre are strongly dependent on the choice of force constants between the N and Ga bonds. By increasing the N–Ga bond strength from 9.6 to 16% and retaining the N–In value as before, our calculations provided shifts in the LVMs (458 (B_2), 479 (A_1), and 499 (B_1) cm^{-1}). Although two of the three modes (B_2 and A_1) are in conformity with the recent FTIR [66] and Raman data [42], the highest calculated frequency of B_1-mode (499 cm^{-1}) falls in the spectral range dominated by the second-order optical phonons of GaAs. In N-implanted InGaAs layers, we believe that the feature observed near 521 cm^{-1} after RTA at 900°C is too broad and higher in frequency to be associated with the B_1-mode. However, if it is a true local mode and not an artefact, as suggested [66], then the large width caused by the shortening of lifetime is probably related to its strong interaction with the lattice phonons. To check the validity of our theoretical conjectures and to test the experimental [66] claims of the true local modes near or above $\geq$500 cm^{-1}, we strongly feel the need of more sophisticated calculations by first principle methods as well as the necessity of additional experiments by using Raman scattering and/or IR spectroscopy.

Similar to Ga-rich $Ga_{1-x}In_xN_yAs_{1-y}$ alloys, we have also anticipated the formation of nearest-neighbour pairs $^{14}N_{As}Ga_{In}(1)In_3$ of C_{3v} and $^{14}N_{As}Ga_{In}(2)In_2$ complexes of C_{2v} configurations in In-rich materials ($1.0 > x \geq 0.7$, $y > 0.005$). As compared to $^{14}N_{As}In_{Ga}(1)Ga_3$ cluster of C_{3v} symmetry where $E > A_1$, the role of A_1- and E-modes is, however, reversed (i.e. $E < A_1$) in $^{14}N_{As}Ga_{In}(1)In_3$. The A_1-mode in $^{14}N_{As}Ga_{In}(1)In_3$ – caused by the vibration of nitrogen along the N–Ga axis – is influenced by a strong N–Ga bond and three weak N–In bonds. The E-mode – influenced by the vibration of nitrogen atom perpendicular to the axis – is dependent upon

the weaker N–In bonds. Therefore, one suspects the frequency of E-mode to fall near 443 cm^{-1} and the A_1-mode to lie at a value close to or higher than ≥470 cm^{-1} (see Table 9.4). Quite recently, low-temperature studies of local modes have been reported in $Ga_{1-x}In_xN_yAs_{1-y}$ with $y \leq 0.012$ and $x \geq 0.92$ using Raman scattering [42] and by FTIR in N-implanted $In_xGa_{1-x}As$ layers (with $x = 0.26$, 0.53, 0.75, and 1) annealed at 700–900°C [66]. Although the two experimental results have provided different values of LVMs, both have confirmed the preferential bonding with a significant fraction of substitutional nitrogen attached at least to one Ga neighbour.

In summary, our comprehensive Green's function analyses of the Raman and FTIR data on thermally annealed Ga- (In-) rich GaInNAs samples have provided a strong support for the creation of preferential N–In (N–Ga) bonding beyond what is statistically expected from a random alloy. By using simple perturbation models, we have predicted nine local vibrational modes for five different N–$Ga_{4-m}In_m$ clusters with $m = 0, 1, 2, 3, 4$. In Raman studies, although no evidence of N-centred clusters involving more than one In (Ga) atoms is found, the possibility of N–In_2Ga_2 clusters cannot be completely ruled out, however, in GaInNAs samples with higher In (Ga) contents and/or upon RTA at 600–900°C [66]. In the MBE-grown low-In content layers of $Ga_{1-x}In_xN_yAs_{1-y}$ with $x = 0.058$ and $y = 0.028$, the annealing-induced blueshift of the band gap has been suggested to the changes in recent photo-reflectance resonances [69] associated with three different N-centred short-range order clusters (N–Ga_4, N–Ga_3In_1, and N–Ga_2In_2). The mechanism for the redistribution of N environment from Ga- (In-) ligand rich sites to In- (Ga-) ligand rich sites is not well understood, the hopping of N or vacancy-assisted migration of In and Ga atoms at elevated temperatures is speculated for the rearrangement of group III–N–As bonding. To check our theoretical conjectures, more systematic work on the impurity vibrational modes is necessary by using sophisticated first principle methods as well as spectroscopic techniques by using Raman and FTIR methods to elucidate the local coordination of N and In (Ga) in Ga- (In-) rich dilute GaInNAs alloys under different growth conditions with varied In (Ga) contents and annealing procedures.

Acknowledgements. The work performed at Indiana University of Pennsylvania was supported in part by the grants from National Science Foundation (NSF: ECS-9906077) and Research Corporation (Cottrell College Science Award No. CC4600).

References

1. For recent reviews, please see: "Special issue: III–V–N Semiconductor Alloys", J.W. Ager, W. Walukiewicz (eds.), Semicond. Sci. Technol. **17** (2002); and "Special issue: The Physics and Technology of Dilute Nitrides", N. Balkan (ed.), J. Phys. Condens. Matter **16** (2004)

2. M. Kondow, K. Uomi, A. Niwa, T. Kitatani, S. Watahiki, Y. Yazawa, Jpn. J. Appl. Phys. 1, Regul. Pap. Short Notes **35**, 1273 (1996); *ibid.*, Electron. Lett. **32**, 2244 (1996); *ibid.*, IEEE J. Sel. Top. Quantum Electron. **3**, 719 (1997); *ibid.*, J. Phys. Condens. Matter **16**, S3229 (2004)
3. J.S. Harris Jr., Semicond. Sci. Technol. **17**, 1 (2002); *ibid.*, GaInNAs and GaInNAsSb: Long wavelength lasers, in CRC LLC, Boca Raton, FL (Taylor & Francis London, UK), Chap. 14, p. 395 (2004)
4. D.A. Louderback, M.A. Fish, J.F. Klem, D.K. Serkland, K.D. Choquette, W.G. Pickrell, R.V. Stone, P.S. Guilfoyle, IEEE Photon. Technol. Lett. **16**, 963 (2004)
5. S.R. Bank, M.A. Wistey, H.B. Yuen, L.I. Goddard, W. Ha, J.S. Harris Jr., Electron. Lett. **39**, 20 (2003)
6. W. Li, J. Konttinen, T. Jouhti, C.S. Peng, E.M. Pavelescu, M. Suominen, M. Pessa, *Advanced Nanomaterials and Nanodevices* (IUMRS-ICEM, Xi'an, China, 10–14 June 2002), p. 252; *ibid.*, Appl. Phys. Lett. **79**, 1094 (2001); *ibid.*, Appl. Phys. Lett. **79**, 3386 (2001)
7. I.A. Buyanova, W.M. Chen, B. Bonemar, MRS Internet J. Nitride Semicond. Res. **6**, 1 (2001)
8. G. Ciatto, F. Boscherini, J. Phys. Condens. Matter **16**, S3141 (2004)
9. K. Kim, A. Zunger, Phys. Rev. Lett. **86**, 2609 (2001)
10. W.G. Bi, C.W. Tu, Appl. Phys. Lett. **70**, 1608 (1997)
11. L. Bellaiche, S.H. Wei, A. Zunger, Appl. Phys. Lett. **70**, 3558 (1997)
12. W. Shan, W. Walukiewicz, J.W. Ager, E.E. Haller, J.F. Geisz, D.J. Friedman, J.M. Olson, S.R. Kurtz, Phys. Rev. Lett. **82**, 1221 (1999); *ibid.*, Phys. Rev. B: Condens. Matter **62**, 4211 (2000); *ibid.*, J. Appl. Phys. **90**, 2227 (2001)
13. I. Vurgaftman, J.R. Meyer, L.R. Ram-Mohan, J. Appl. Phys. **89**, 5815 (2001)
14. P.J. Klar, H. Grüning, J. Koch, S. Schäfer, K. Volz, W. Stolz, W. Heimbrodt, A.M. Kamal Saadi, A. Lindsay, E.P. O'Reilly, Phys. Rev. B: Condens. Matter **64**, 121203 (2001)
15. J.F. Geisz, D.J. Friedman, J.M. Olson, S.R. Kurtz, B.M. Keyes, J. Cryst. Growth **195**, 401 (1998)
16. J.O. Maclean, D.J. Wallis, T. Matrin, M.R. Houlton, A.J. Simons, J. Cryst. Growth **231**, 31 (2001)
17. K. Köhler, J. Wagner, P. Ganser, D. Serries, T. Geppert, M. Maier, L. Kirste, J. Phys. Condens. Matter **16**, S2995 (2004)
18. D.C. Koningsberger, R. Prins (eds.), *X-Ray Absorption: Principles, Applications, Techniques of EXAFS, SEXAFS and XANES* (Wiley, New York, 1988)
19. J.-F. Chen, R.-S. Hsiao, P.-C. Hsieh, Y.-C. Chen, J.-S. Wang, J.-Y. Chi, Jpn. J. Appl. Phys. **45**, 5662 (2006)
20. P. Krispin, V. Gambin, J.S. Harris, K.H. Ploog, J. Appl. Phys. **99**, 6095 (2003)
21. H.P. Xin, K.L. Kavanagh, Z.Q. Zhu, C.W. Tu, Appl. Phys. Lett. **74**, 2337 (1999)
22. A. Erol, S. Mazzucato, M.Ç. Arikan, H. Carrère, A. Arnoult, E. Bedel, N. Balkan, Semicond. Sci. Technol. **18**, 968 (2003)
23. A.S. Barker, A.J. Sievers, Rev. Mod. Phys. **47**, S1 (1975)
24. Please see: J.I. Pankove, N.M. Johnson (eds.), *Semiconductor and Semimetals*, vol. 34 (Academic, New York, 1991)
25. S.K. Estreicher, Mater. Sci. Eng. R **14**, 319 (1995)
26. E.E. Haller, in *Handbook on Semiconductors*, ed. by S. Mahajan, vol. 3b (North-Holland, Amsterdam, 1994) p. 1515

27. R.C. Newman, Adv. Phys. **18**, 545 (1969); *ibid.*, Semicond. Semimet. **38**, 117 (1993); *ibid.*, Semicond. Sci. Technol. **9**, 1749 (1994)
28. M. Stavola, Semicond. Semimet. B **51**, 153 (1999)
29. M.D. McCluskey, Appl. Phys. Rev. **87**, 3593 (2000)
30. H.C. Alt, J. Phys. Condens. Matter **16**, S3037 (2004); *ibid.*, H.C. Alt, Y.V. Gomeniuk, B. Wiedemann, Phys. Rev. B **69**, 125214 (2004); *ibid.*, Semicond. Sci. Technol. **18**, 303 (2003); *ibid.*, Appl. Phys. Lett. **77**, 3331 (2000); *ibid.*, Mat. Sci. Forum **258–263**, 867 (1997)
31. S. Kurtz, J. Webb, L. Gedvilas, D. Friedman, J. Geisz, J. Olsen, R. King, D. Joslin, N. Karam, Appl. Phys. Lett. **78**, 748 (2001)
32. T. Prokofyeva, T. Sauncy, M. Seon, M. Holtz, Y. Qiu, S. Nikishin, H. Temkin, Appl. Phys. Lett. **73**, 1409 (1998)
33. M.J. Seong, M.C. Hanna, A. Mascarenhas, Appl. Phys. Lett. **79**, 3974 (2001); *ibid.*, Semicond. Sci. Technol. **17**, 823 (2002)
34. M.S. Ramsteiner, D.S. Jiang, J.S. Harris, K.H. Ploog, Appl. Phys. Lett. **84**, 1859 (2004)
35. K. Köhler, J. Wagner, P. Gesner, D. Serries, T. Geppert, M. Maier, L. Kirste, IEE Proc. Optoelectron. **151**, 247 (2004); *ibid.*, J. Appl. Phys. **90**, 2576 (2004); *ibid.*, Solid State Electron. **47**, 461 (2003); *ibid.*, Mater. Res. Symp. Proc. **744**, 627 (2003); *ibid.*, Appl. Phys. Lett. **83**, 2799 (2003); *ibid.*, Appl. Phys. Lett. **80**, 2081 (2002); *ibid.*, J. Appl, Phys. **90**, 5027 (2001); *ibid.*, Appl. Phys. Lett. **77**, 3592 (2000)
36. D. Strauch, B. Dorner, J. Phys. Condens. Matter **2**, 1457 (1990)
37. D.N. Talwar, J. Appl. Phys. **99**, 123505 (2006); *ibid.*, IEE Proc. Circuits Devices Syst. **150**, 529 (2003)
38. A.A. Kachare, W.G. Spitzer, W.G. Kahan, F.K. Euler, T.A. Whatley, J. Appl. Phys. **44**, 4393 (1973)
39. W.M. Theis, K.K. Bajaj, C.W. Litton, W.G. Spitzer, Appl. Phys. Lett. **41**, 70 (1982)
40. G.A. Gledhill, S.B. Upadhyay, M.J.L. Sangster, R.C. Newman, J. Mol. Struct. **247**, 313 (1991)
41. R.J. Elliot, W. Hayes, G.D. Jones, H.F. MacDonald, C.T. Sennett, Proc. R. Soc. A **289**, 1 (1965)
42. J. Wagner, K. Köhler, P. Ganser, M. Maier, Appl. Phys. Lett. **87**, 051913 (2005)
43. T. Kitatani, M. Kondow, M. Kudo, Jpn. J. Appl. Phys. **40**, L750 (2001)
44. H.C. Alt, Y.V. Gomeniuk, Phys. Rev. B **70**, 161314 (2004)
45. S. Baroni, S. De Girnocoli, A. Dal Corso, P. Gianozzi, Rev. Mod. Phys. **73**, 515 (2001)
46. R. Jones, P.R. Briddon, in *Identification of Defects in Semiconductors*, ed. by M. Stavola. Semiconductors and Semimetals, vol. 51A, Chap. 6 (Academic, Boston, 1998)
47. A.A. Maradudin, E.W. Montroll, C.H. Weiss, I.P. Ipatova, in *Solid State Physics*, ed. by F. Seitz, D. Turnbull, H. Ehrenreich (Academic, New York, 1971)
48. D.N. Talwar, M. Vandevyver, Phys. Rev. B **40**, 9779 (1989)
49. D.N. Talwar, Phys. Stat. Solidi C **4**, 674 (2006)
50. W.A. Harrison, *Electronic Structure and the Properties of Solids – The Physics of Chemical Bond* (Dover, New York, 1980)
51. K. Kunc, M. Balkanski, N. Nusimovici, Phys. Stat. Solidi B **72**, 229 (1975)
52. D.N. Talwar, M. Vandevyver, W. Theis, K.K. Bajaj, Phys. Rev. B **33**, 8525 (1986)

53. B.D. Rajput, D.A. Browne, Phys. Rev. B **53**, 905 (1996)
54. S.F. Ren, H. Chu, Y.C. Chang, Phys. Rev. B **37**, 8899 (1988)
55. Z.V. Popovic, M. Cardona, E. Richter, D. Strauch, L. Tapfer, K. Ploog, Phys. Rev. B **41**, 5904 (1990); *ibid.*, Phys. Rev. B **40**, 1207 (1989)
56. D.N. Talwar, K.S. Suh, C.S. Ting, Philos. Mag. B **54**, 93 (1986)
57. L. Bellomonte, J. Phys. Chem. Solids **38**, 59 (1977)
58. M.D. McCluskey, E.E. Haller, P. Becla, Phys. Rev. B **65**, 045201 (2001)
59. S. Najmi, X. Zhang, X.K. Chen, M.L.W. Thewalt, S.P. Watkins, Appl. Phys. Lett. **88**, 041908 (2006)
60. J.R. Chelikowsky, M.L. Cohen, Phys. Rev. B **14**, 556 (1976)
61. R. Jones, S. Öberg, Phys. Rev. B **44**, 3407 (1989); *ibid.*, Semicond. Sci. Technol. **7**, 855 (1992)
62. G.A. Gledhill, R.C. Newman, J. Woodhead, J. Phys. C: Solid State Phys. **17**, L301 (1984)
63. J. Schneider, B. Dischler, H. Seelewind, P.M. Mooney, J. Lagowski, M. Matsui, D.R. Beard, R.C. Newman, Appl. Phys. Lett. **54**, 1442 (1989)
64. H.C. Alt, Semicond. Sci. Technol. **6**, B121 (1991)
65. P.R. Kent, A. Zunger, Phys. Rev. B **64**, 115208 (2001)
66. H.C. Alt, Y.V. Gomenuik, G. Mussler, Semicond. Sci. Technol. **21**, 1425 (2006)
67. M. Ramsteiner, G. Mussler, P. Kleinert, K.H. Ploog, Appl. Phys. Lett. **87**, 111907 (2005)
68. A. Hashimoto, T. Kitano, K. Takahashi, H. Kawanishi, A. Patane, C.T. Foxon, A. Yamamoto, Phys. State Solidi B **228**, 283 (2001); *ibid.*, Phys. State Solidi B **234**, 915 (2002)
69. R. Kudrawiecz, J. Misiewicz, E.M. Pavelescu, J. Konttinen, M. Pessa, Acta Phys. Pol. A **106**, 249 (2004)

10

The Hall Mobility in Dilute Nitrides

M.P. Vaughan and B.K. Ridley

The introduction of dilute concentrations of nitrogen into III–V materials is known to cause a large drop in the electron mobility. In addition to the scattering from nitrogen sites and clusters, the conduction band becomes highly non-parabolic, which further affects the transport properties. The effect of this non-parabolicity on the mobility can be dealt with using an extension to the ladder method for solving Boltzmann's transport equation. The ladder method was developed to deal realistically with the highly inelastic nature of polar-optical phonon scattering, which limits the high temperature mobility in most III–V semiconductors. Here, we detail this extension and discuss the theoretical models of electron scattering from nitrogen centres.

10.1 Introduction

The transport properties of III–V semiconductors are now well known to be greatly affected by the introduction of small concentrations of nitrogen. In particular, the mobility is seen to drop quite dramatically from that of the matrix III–V semiconductor. Skierbiszewski et al. [1] investigated Si doped GaN_xAs_{1-x} with $x = 0.014$ and carrier density $1.6 \times 10^{17}\,cm^{-3}$, finding a mobility at 295 K of $400\,cm^2V^{-1}s^{-1}$. Kurtz et al. [2] performed measurements on a series of n-type GaInNAs samples ($x \sim$ 0.016–0.019) doped with Sn in the range $2 \times 10^{16}\,cm^{-3}$ to $6 \times 10^{17}\,cm^{-3}$. These samples indicated a thermally activated mobility, with activation energy decreasing with increasing dopant concentration (and hence Fermi energy). This would be consistent with an electron relaxation time that increased monotonically in energy, which would yield a mobility with the same dependence in temperature. The high temperature mobility of all these samples tended to converge around $\sim 300\,cm^2\,V^{-1}s^{-1}$. Other workers have reported similar mobilities for n-type GaInNAs [3,4] in the range 100–300 $cm^2V^{-1}s^{-1}$ for $x \sim 0.02$.

The causes of this mobility drop appear to be twofold. Firstly, the introduction of nitrogen is known to have a profound effect on the conduction band,

manifesting most obviously in the large redshift of the energy gap [5]. This phenomenon is well explained by the band-anticrossing (BAC) model due to Shan et al. [6, see Chap. 3], which predicts a splitting of the conduction band around a localised nitrogen energy level. The dispersion relations predicted by this model show a considerable flattening of the band edge in **k** (wavevector) space, hence giving rise to an enhanced effective mass, as well as a pronounced non-parabolicity quite low in the band. This non-parabolicity is discussed in Sect. 10.2, where we also address the problematic issue of the density of states.

Secondly, whilst polar-optical phonon scattering is usually the dominant scattering process at room temperature in polar semiconductors, it has been predicted by Fahy and O'Reilly [7] that it is scattering from nitrogen complexes that will limit the mobility in dilute nitrides. Existing theories are based mostly on some kind of alloy scattering model. We shall briefly review these models in Sect. 10.6. For the time being, we note that a common feature of these theories is the predicted temperature dependence of the mobility, which varies as $T^{-1/2}$. However, Hall measurements of GaNAs structures by Mouillet et al. [8] tend to show a mobility that varies more like $T^{1/2}$ at low temperature. This is not quite like ionised impurity scattering, which varies as $T^{3/2}$ (although such processes may well be present) but is more reminiscent of dislocation scattering. This suggests that, at low temperature, the mobility is being limited by some kind of defect scattering and/or trapping.

Whilst the observed mobility seems to exhibit features characteristic of disordered systems, the residual low temperature mobility seems too high to be due to hopping conduction, so low energy electrons may only be weakly localised. This has been proposed by Teubert et al. [4], who observed a negative magnetoresistance in GaInNAs samples. One way of explaining this is in terms of a quantum correction due to enhanced backscattering of the electron. At low temperature, the elastic relaxation time can be much smaller than the inelastic relaxation time. This means that the electron may be scattered elastically many times before losing its phase coherence. When adding the amplitudes for these scattering events, it is found that there is an enhanced amplitude for the scattering from **k** to $-\mathbf{k}$. This gives rise to a decrease in the conductivity. Applying a magnetic field shifts the relative phases of the interfering paths and hence reduces this effect so that, initially, a decrease in the resistivity is observed. An alternative explanation can be given in terms of Zeeman splitting of degenerate states in the potential traps. If the states are close to the top of the potential barriers, one state may be raised above it in energy and thus able to freely take part in conduction.

A problem with applying a model of weak localisation (using the former explanation) is that we need to know the elastic and inelastic relaxation times. The latter would naturally be taken to be due to phonon scattering but the former would require knowledge of the potential seen by the electron. If this is predominantly due to lattice imperfections at low temperature, an accurate model will be difficult to devise. Moreover, improvements in material fabrication may obviate the problem. We shall therefore focus on the more

readily tractable scattering mechanisms. At room temperature, these will be polar-optical phonon scattering and some kind of alloy scattering.

Polar-optical phonon scattering is a highly inelastic process. This causes problems when trying to determine the mobility using the relaxation time approximation since, as we shall see, no unique relaxation time can be defined. Instead we solve the Boltzmann equation using the ladder method, originally due to Delves [9]. The name refers to the fact that scattering into and out of phonon mode at a particular electron energy is coupled to the scattering rates at energies separated by the phonon energy $\hbar\omega$. This invokes a picture of an energy 'ladder' with rungs $\hbar\omega$ apart.

The method was further developed by Fletcher and Butcher [10] for bulk material in an arbitrary magnetic field and applied to GaAs. It has since been applied to bulk GaN by Ridley [11] and further developed by Anderson et al. [12, 13] for application to 2D electron mobility in GaN-based quantum wells. These treatments all assumed that the electron energy is parabolic. In light of the non-parabolicity implied by the BAC model, we shall extend the method to non-parabolic bands in 3D and 2D.

As we shall find, incorporating elastic scattering processes into the ladder method is straightforward, provided that the form of the scattering rates are known. This leaves us with our final task of establishing the nature of these scattering processes. In Sect. 10.6, we review the possible models and give scattering rates for other elastic processes.

10.2 Non-Parabolicity in Dilute Nitrides

The energy dispersion relations in dilute nitrides can be expressed using the BAC model. This gives for the energy in the upper (+) and lower (−) conduction band

$$E_{\pm}(\mathbf{k}) = \frac{1}{2}\left\{E_{\mathrm{N}} + E_{\mathrm{M}}(\mathbf{k}) \pm \left([E_{\mathrm{N}} - E_{\mathrm{M}}(\mathbf{k})]^2 + 4\beta^2 x\right)^{1/2}\right\}, \tag{10.1}$$

where E_{M} is the energy of the matrix semiconductor

$$E_{\mathrm{M}}(\mathbf{k}) = \frac{\hbar^2 k^2}{2m^*} + E_{\mathrm{C}}, \tag{10.2}$$

where x is the nitrogen concentration and β determines the coupling strength between the nitrogen and matrix states. According to tight-binding calculations [14], the matrix band edge should also have an x dependence given by

$$E_{\mathrm{C}} = E_{\mathrm{C}}(0) - \alpha x. \tag{10.3}$$

Typical values for these parameters are $\alpha = -1.45\,\mathrm{eV}$ and $\beta = 2.45\,\mathrm{eV}$ [7].

Now for a non-parabolic band, we can write the dispersion relations in the form

$$\frac{\hbar^2 k^2}{2m^*} = \gamma(E), \tag{10.4}$$

from which we can find the 3D and 2D densities of states

$$N_{\mathrm{3D}}(E) = \frac{(2m^*)^{3/2}}{4\pi^2\hbar^3}\gamma^{1/2}(E)\frac{\mathrm{d}\gamma(E)}{\mathrm{d}E}, \tag{10.5}$$

and for a single subband,

$$N_{\mathrm{2D}}(E) = \frac{m^*}{2\pi\hbar^2}\frac{\mathrm{d}\gamma\,(E)}{\mathrm{d}E}. \tag{10.6}$$

Using (10.1) and (10.2), if we write γ as in (10.4) (where m^* is the *matrix* semiconductor effective mass), we obtain

$$\gamma(E) = \frac{\beta^2 x}{E_{\mathrm{N}} - E} + E - E_{\mathrm{C}}. \tag{10.7}$$

This can be written with E relative to the dilute nitride band edge by defining $\Delta E_{\mathrm{N}} = E_{\mathrm{N}} - E_{-}(0)$ and $\Delta E_{\mathrm{C}} = E_{\mathrm{C}} - E_{-}(0)$ and noting that, from (10.1), $\Delta E_{\mathrm{C}}\Delta E_{\mathrm{N}} = \beta^2 x$:

$$\gamma(E) = \left(\frac{\Delta E_{\mathrm{C}}}{\Delta E_{\mathrm{N}}}\frac{1}{1 - E/\Delta E_{\mathrm{N}}} + 1\right)E. \tag{10.8}$$

This has the derivative

$$\frac{\mathrm{d}\gamma(E)}{\mathrm{d}E} = \frac{\Delta E_{\mathrm{C}}}{\Delta E_{\mathrm{N}}}\frac{1}{(1 - E/\Delta E_{\mathrm{N}})^2} + 1. \tag{10.9}$$

Casual inspection of (10.7) or (10.8) will reveal that we now have a problem: as the energy approaches E_{N}, γ (and its derivative) approaches infinity. In particular, the integrals of the densities of states (DOS) (10.5) and (10.6) imply that the number of states with energy less that E becomes infinite as E approaches E_N. This is clearly not a physically valid result.

A possible solution to the problem has been provided by Wu et al. [15], who have derived the BAC model using the Green's functions of Anderson's many-impurity model [16] in the coherent potential approximation. The Green's function for the system can be written

$$G\,(E, E_{\mathrm{M}}) = \left\{E - E_{\mathrm{M}}\,(\mathbf{k}) - \frac{\beta^2 x}{E - E_{\mathrm{N}} + \mathrm{i}\Delta}\right\}^{-1}. \tag{10.10}$$

The dispersion relations can now be found from the poles of (10.10) with the difference that now E_{N} becomes $E_{\mathrm{N}} + \mathrm{i}\Delta$ and hence $E_{\pm}(\mathbf{k})$ develops an

imaginary component, interpreted as an energy broadening. The density of states can now be found from the imaginary part of the Green's function

$$N(E) = -\frac{1}{\pi}\mathrm{Im}\int G\left(E, E_{\mathrm{M}}\right) N_0\left(E_{\mathrm{M}}\right) \mathrm{d}E_{\mathrm{M}}, \tag{10.11}$$

where $N_0(E_{\mathrm{M}})$ is the matrix semiconductor density of states. Integrating (10.11) using the appropriate forms for N_0, we obtain the 3D and 2D DOS

$$N_{3\mathrm{D}}(E) = -\frac{\left(2m^*\right)^{3/2}}{4\pi^2\hbar^3} g(E) \left\{2\left[\left(h^2(E) + g^2(E)\right)^{1/2} - h(E)\right]\right\}^{-1/2} \tag{10.12}$$

and, for a single subband

$$N_{2\mathrm{D}}(E) = \frac{m^*}{2\pi\hbar^2}\left\{\frac{1}{2} - \frac{1}{\pi}\arctan\left(\frac{h(E)}{g(E)}\right)\right\}, \tag{10.13}$$

where we have employed the auxiliary functions

$$g(E) = -\frac{\beta^2 x \Delta}{\left(E - E_{\mathrm{N}}\right)^2 + \Delta^2},$$
$$h(E) = E - \frac{\left(E - E_{\mathrm{N}}\right)}{\Delta}\left|g(E)\right|.$$

Note that in (10.12)–(10.13), E is relative to E_{C}. Taking the limit of (10.12) as $\Delta \to 0$, we have

$$\lim_{\Delta\to 0} N_{3\mathrm{D}}(E) = \frac{\left(2m^*\right)^{3/2}}{4\pi^2\hbar^3}\left(\frac{\beta^2 x}{E_{\mathrm{N}} - E} + E\right)^{1/2}. \tag{10.14}$$

However, comparing this to (10.7), we see that we have just obtained

$$\lim_{\Delta\to 0} N_{3\mathrm{D}}(E) = \frac{\left(2m^*\right)^{3/2}}{4\pi^2\hbar^3}\gamma^{1/2}(E). \tag{10.15}$$

This is almost in the same form as (10.5), except that the derivative of γ has disappeared. However, this new form has the advantage that its integral over energy does converge. In Fig. 10.1, calculated 3D DOS using the Green's function approach for energy broadenings of 0 and 100 meV are shown.

In the 2D case, we find that taking the limit $\Delta \to 0$, the argument of the *arctan* function in (10.13) tends to $\pm\infty$, and therefore the value of the bracketed term becomes 0 or unity, depending on the value of E.

Specifically, we have

$$\lim_{\Delta\to 0} N_{2\mathrm{D}}(E) = \begin{cases} \frac{m^*}{2\pi\hbar^2}, & E_-\left(0\right) < E < E_{\mathrm{N}} \text{ or } E > E_+\left(0\right), \\ 0 & \text{otherwise.} \end{cases} \tag{10.16}$$

In other words, the 2D density of states is the same as in the parabolic case over the $E_\pm$ bands and 0 elsewhere. Now from (10.1), we find that $E_{\mathrm{C}} - E_-(0) = E_+(0) - E_{\mathrm{N}}$, so integrating over the 2D DOS, we find that

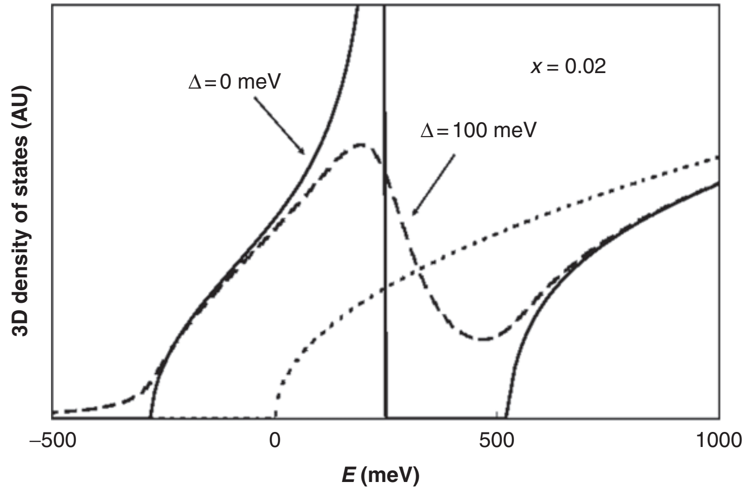

Fig. 10.1. The 3D density of states (DOS) calculated using the Green's function approach. Here, E_{N} is 250 meV above the matrix semiconductor band edge ($E = 0$). The *solid line* shows the DOS in the limit of the energy broadening taken to 0. Note that this approaches infinity close to E_{N}. The *dashed line* is for a broadening of 100 meV. Both these graphs are calculated using $x = 0.02$. The *dotted line* shows the unperturbed DOS ($x = 0$) for comparison

there is the *same* number of states with energy less than E for any energy greater than $E_+(0)$ in both the matrix semiconductor and the dilute nitride. The calculated 2D DOS for a subband using the Green's function approach for energy broadenings of 0 and 100 meV are shown in Fig. 10.2. Note that the singularity seen in the 3D DOS at E_N reappears when we perform a summation over subbands. This is due to an increasing number of higher subband states being pushed below the nitrogen energy (see [17]).

These new forms for the DOS should not give us too much cause for concern when calculating the mobility, since, at low energies, the major effect of the increased effective mass arises through the electron group velocity. Since in the limit $\varDelta \to 0$ we still obtain the dispersion relations given by (10.1), it is reasonable to assume that we can continue to use the group velocity obtained from them:

$$v\left(\mathbf{k}\right) = \left(\frac{\mathrm{d}\gamma(E)}{\mathrm{d}E}\right)^{-1}\left(\frac{2\gamma(E)}{m^*}\right)^{1/2}. \tag{10.17}$$

A couple of points should be emphasised here. Firstly, the effective mass appearing in this expression and elsewhere in the DOS is still that of the *matrix* semiconductor. Secondly, care must be taken whenever the derivative of γ arises. In (10.17), the derivative emerges from the dispersion relations, which we take to be valid, so we must keep this. In other derivations, the derivative may arise through the density of states. In this case, if we are to employ the modified DOS derived using the Green's function, we must reject

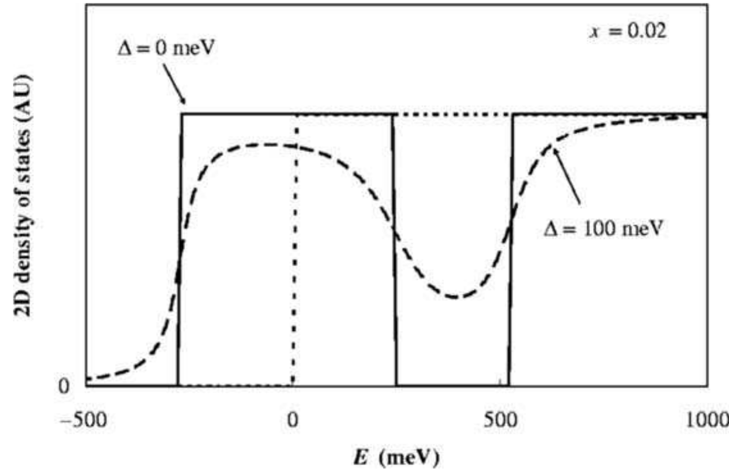

Fig. 10.2. The 2D density of states for a single subband calculated using the Green's function approach. The *solid line* shows the DOS in the limit of the energy broadening taken to 0. Note that this has the same magnitude as the unperturbed DOS (*dotted line*) with the band just shifted down in energy. The *dashed line* is for a broadening of 100 meV. The nitrogen concentration in both cases is $x = 0.02$

these derivatives. For the time being, we shall derive all our formulae in the most general case and indicate within the derivation where modifications may need to be made.

10.3 The Hall Mobility

The current density is given by the integration of the electron group velocity $\mathbf{v}(\mathbf{k})$ over all states, weighted by the distribution function $f(\mathbf{k})$

$$\mathbf{j} = -2\frac{e}{(2\pi)^3}\int \mathbf{v}(\mathbf{k})f(\mathbf{k})\mathrm{d}^3\mathbf{k}, \tag{10.18}$$

where the factor of 2 accounts for spin. Here, e is the electronic charge and the negative sign has been inserted for consistency since, by convention, $\mathbf{j}$ is in the opposite direction to the electron flow. If the distribution function is displaced by $\boldsymbol{\delta}\mathbf{k}$ in $\mathbf{k}$ space due to the application of a vanishing small electric field, we can expand $f(\mathbf{k})$ to first order as

$$f(\mathbf{k}) = f_0(\mathbf{k} - \boldsymbol{\delta}\mathbf{k}) \approx f_0(\mathbf{k}) - \nabla_{\mathbf{k}} f_0(\mathbf{k}) \cdot \boldsymbol{\delta}\mathbf{k}, \tag{10.19}$$

where the equilibrium distribution $f_0(\mathbf{k})$ is given by the Fermi factor

$$f_0(\mathbf{k}) = \frac{1}{1 + \exp\left([E_{\mathbf{k}} - E_{\mathrm{F}}]/k_{\mathrm{B}}T\right)}. \tag{10.20}$$

Here, $E_{\mathbf{k}}$ is the energy of the state, E_{F} is the Fermi energy, k_{B} is Boltzmann's constant and T is the absolute temperature. Equation (10.19) is in the form $f_0(\mathbf{k}) + f_1(\mathbf{k})$, where $f_0(\mathbf{k})$ and $f_1(\mathbf{k})$ have even and odd parity in $\mathbf{k}$, respectively, and, by assumption, $f_0(\mathbf{k}) \gg f_1(\mathbf{k})$.

Since the electron group velocity $\mathbf{v}(\mathbf{k})$ is

$$\mathbf{v}\left(\mathbf{k}\right) = \nabla_{\mathbf{k}}\omega = \frac{1}{\hbar}\nabla_{\mathbf{k}}E_{\mathbf{k}}, \tag{10.21}$$

using the chain rule and writing $f_0(\mathbf{k})$ as a function of E (dropping the $\mathbf{k}$ subscript), we have

$$f(\mathbf{k}) = f_0(E) - \hbar\frac{\mathrm{d}f_0(E)}{\mathrm{d}E}\mathbf{v}\left(\mathbf{k}\right)\cdot\boldsymbol{\delta}\mathbf{k}. \tag{10.22}$$

In the presence of both electric and magnetic fields ($\mathbf{E}$ and $\mathbf{B}$), the total force on an electron is given by the Lorentz law

$$\mathbf{F} = -e\left(\mathbf{E} + \mathbf{v}\times\mathbf{B}\right). \tag{10.23}$$

Following Fletcher and Butcher [10], we take $\mathbf{B}$ to be in the z-direction and define the vector function

$$\varPhi(E) = -e\left\{\tau_1(E)\mathbf{v}_t + \tau_2(E)(\hat{\mathbf{z}}\times\mathbf{v}_t) + \tau_3(E)\mathbf{v}_z\right\}, \tag{10.24}$$

where

$$\begin{aligned}\mathbf{v}_t &= v_x\hat{\mathbf{x}} + v_y\hat{\mathbf{y}},\\ \mathbf{v}_z &= v_z\hat{\mathbf{z}}\end{aligned} \tag{10.25}$$

and the hat notation indicates a unit vector. The τ_i are energy dependent relaxation times. We can now write $f(\mathbf{k})$ as

$$f(\mathbf{k}) = f_0(E) - \frac{\mathrm{d}f_0(E)}{\mathrm{d}E}\varPhi(E)\cdot\mathbf{E}. \tag{10.26}$$

When we substitute this into (10.18) for the current density, the even part f_0 disappears due to the odd parity of $\mathbf{v}(\mathbf{k})$ so that $\mathbf{j}$ is directly proportional to $\mathbf{E}$. Comparing with the macroscopic form $\mathbf{j} = \sigma\mathbf{E}$, we find that the components of the conductivity tensor σ are

$$\sigma_{ij} = 2\frac{e}{(2\pi)^3}\int v_i\varPhi_j\frac{\mathrm{d}f_0(E)}{\mathrm{d}E}\mathrm{d}^3\mathbf{k}. \tag{10.27}$$

The Cartesian components of $\varPhi(E)$ are

$$\begin{aligned}\varPhi_x &= -e\left\{\tau_1(E)v_x - \tau_2(E)v_y\right\},\\ \varPhi_y &= -e\left\{\tau_1(E)v_y + \tau_2(E)v_x\right\},\\ \varPhi_z &= -e\tau_3(E)v_z.\end{aligned} \tag{10.28}$$

Note that when (10.28) are inserted into (10.27), the cross-terms involving $v_i v_j$ where $i \neq j$ disappear due to negative parity. The conductivity tensor then reduces to

$$\sigma = \begin{bmatrix} \sigma_{xx} & \sigma_{xy} & 0 \\ -\sigma_{xy} & \sigma_{xx} & 0 \\ 0 & 0 & \sigma_{zz} \end{bmatrix}. \tag{10.29}$$

Changing (10.27) to an integral over energy, the components of σ can be written as

$$\begin{aligned} \sigma_{xx} &= \sigma_1, \\ \sigma_{xy} &= \sigma_2, \\ \sigma_{zz} &= \sigma_3, \end{aligned} \tag{10.30}$$

where

$$\sigma_i = -\frac{2e^2}{3} \int v^2 \frac{\mathrm{d}f_0(E)}{\mathrm{d}E} \tau_i(E) N_{3\mathrm{D}}(E) \mathrm{d}E \tag{10.31}$$

in 3D and

$$\sigma_i = -\frac{e^2}{L} \int v^2 \frac{\mathrm{d}f_0(E)}{\mathrm{d}E} \tau_i(E) N_{2\mathrm{D}}(E) \mathrm{d}E \tag{10.32}$$

in 2D for a quantum well of width L.

Now the Hall factor is given by

$$R_\mathrm{H} = -\frac{\mathbf{j} \times \mathbf{B}}{|\mathbf{j} \times \mathbf{B}|^2} \cdot \mathbf{E}. \tag{10.33}$$

With $\mathbf{B}$ parallel to the z-axis, using (10.29), this reduces to

$$R_\mathrm{H} = \frac{\sigma_{xy}}{\left(\sigma_{xy}^2 + \sigma_{xx}^2\right) B}, \tag{10.34}$$

whilst the Hall mobility is given by

$$\mu_\mathrm{H} = -R_\mathrm{H} \sigma_{zz}. \tag{10.35}$$

10.4 The Ladder Method

Having established our basic transport formulae, we now need to find the forms of the relaxation times τ_i. As we have seen, for low-field transport, these are proportional to the perturbation of the distribution function $f(\mathbf{k})$, which can be found by solving the Boltzmann equation. The first-order treatment allows us to linearize the Boltzmann equation and find an exact solution.

In the absence of any temperature or carrier concentration gradient, the steady state Boltzmann equation for a driving force $\mathbf{F}$ is

$$\frac{\mathbf{F}}{\hbar} \cdot \nabla_\mathbf{k} f(\mathbf{k}) = \left(\frac{\partial f(\mathbf{k})}{\partial t}\right)_\mathrm{scat}. \tag{10.36}$$

The right-hand side of (10.36) is the temporal rate of change of $f(\mathbf{k})$ due to scattering and can be written

$$\left(\frac{\partial f(\mathbf{k})}{\partial t}\right)_{\text{scat}} = \int s(\mathbf{k}', \mathbf{k}) f(\mathbf{k}') \left[1 - f(\mathbf{k})\right] - s(\mathbf{k}, \mathbf{k}') f(\mathbf{k}) \left[1 - f(\mathbf{k}')\right] \mathrm{d}^3\mathbf{k}', \tag{10.37}$$

where $s(\mathbf{k}', \mathbf{k})$ and $s(\mathbf{k}, \mathbf{k}')$ are the intrinsic scattering rates for some general scattering process from $\mathbf{k}'$ to $\mathbf{k}$ and vice versa (strictly, these are not rates since they have the dimensions of length^3 $\times$ time^{-1}, however we refer to them as rates for convenience). We note that the rates inside the integral are multiplied not only by the probability that the initial state is occupied but also, since electrons are fermions, the probability that the final state is *not* occupied.

The perturbation to $f(\mathbf{k})$ is

$$f_1(E) = -\frac{\mathrm{d}f_0(E)}{\mathrm{d}E} \Phi(E) \cdot \mathbf{E}. \tag{10.38}$$

Note that the derivative of the Fermi factor can be written

$$\frac{\mathrm{d}f_0(E)}{\mathrm{d}E} = -\frac{1}{k_{\mathrm{B}}T} f_0(E) \left\{1 - f_0(E)\right\}. \tag{10.39}$$

Using this, putting $\mathbf{F}$ equal to the Lorentz force (10.23) and neglecting second-order terms in $\mathbf{E}$, the left-hand side of (10.36) is

$$\frac{\mathbf{F}}{\hbar} \cdot \nabla_{\mathbf{k}} f(\mathbf{k}) = e\mathbf{E} \cdot \left\{\mathbf{v} + \frac{1}{\hbar} \left[\mathbf{B} \cdot (\mathbf{v} \times \nabla_{\mathbf{k}})\right] \Phi(E)\right\} \frac{f_0(E) \left\{1 - f_0(E)\right\}}{k_{\mathrm{B}}T}. \tag{10.40}$$

Turning our attention to the other side of the Boltzmann equation, we substitute $f(\mathbf{k}) = f_0(E) + f_1(E)$ into the scattering integral (10.37). Making use of the equilibrium condition

$$s(\mathbf{k}', \mathbf{k}) f_0(E') \left\{1 - f_0(E)\right\} = s(\mathbf{k}, \mathbf{k}') f_0(E) \left\{1 - f_0(E')\right\} \tag{10.41}$$

and neglecting products of the first-order components of $f(\mathbf{k})$, a little algebra leads to

$$\left(\frac{\partial f(\mathbf{k})}{\partial t}\right)_{\text{scat}} = \int s(\mathbf{k}', \mathbf{k}) \left\{f_1(E') \frac{1 - f_0(E)}{1 - f_0(E')} - f_1(E) \frac{f_0(E')}{f_0(E)}\right\} \mathrm{d}^3\mathbf{k}'. \tag{10.42}$$

Substituting for $f_1(E)$ using (10.38) and (10.39) then gives

$$\left(\frac{\partial f(\mathbf{k})}{\partial t}\right)_{\text{scat}} = \frac{1}{k_{\mathrm{B}}T} \int s(\mathbf{k}', \mathbf{k}) f_0(E') \left[1 - f_0(E)\right] \left\{\Phi(E') - \Phi(E)\right\} \cdot \mathbf{E} \, \mathrm{d}^3\mathbf{k}'. \tag{10.43}$$

Equating this with (10.40), we arrive at

$$-e \left(\mathbf{v} + \frac{1}{\hbar} \left[\mathbf{B} \cdot (\mathbf{v} \times \nabla_{\mathbf{k}})\right] \Phi(E)\right) = \int s(\mathbf{k}', \mathbf{k}) \frac{f_0(E')}{f_0(E)} \left\{\Phi(E) - \Phi(E')\right\} \mathrm{d}^3\mathbf{k}'. \tag{10.44}$$

Note that the electric field has now dropped out of the equation. Expressed in component form, (10.44) is

$$-e\left(v_i + \frac{B}{\hbar}\left(v_x\frac{\partial}{\partial k_y} - v_y\frac{\partial}{\partial k_x}\right)\Phi_i(E)\right)$$
$$= \int s(\mathbf{k}',\mathbf{k})\frac{f_0(E')}{f_0(E)}\left\{\Phi_i(E) - \Phi_i(E')\right\}\mathrm{d}^3\mathbf{k}'. \qquad (10.45)$$

Since on the left-hand side of (10.45) we take the derivative of $\Phi_i(E)$, which is a function of group velocity, with respect to k_j, we need to express $\mathbf{v}$ in terms of $\mathbf{k}$. For non-parabolic energy bands, the group velocity is

$$\mathbf{v} = \frac{\mathrm{d}E}{\mathrm{d}\gamma}\frac{\hbar\mathbf{k}}{m^*}. \qquad (10.46)$$

On the right-hand side of (10.45) we have sums of terms of the form

$$v_x\int s(\mathbf{k}',\mathbf{k})\frac{f_0(E')}{f_0(E)}\left(\tau_i(E) - \tau_i(E')\frac{v_x{}'}{v_x}\right)\mathrm{d}^3\mathbf{k}'. \qquad (10.47)$$

The ratios of the components of the group velocity can be expressed in terms of the velocity magnitudes and α, the angle between $\mathbf{v}$ and $\mathbf{v}'$. Now, for each integral (in either 2D or 3D), we may always transform to a set of axes such that $\mathbf{v}$ lies along the x-axis and $\mathbf{v}'$ lies in the $x-y$ plane. Then

$$\frac{v_x{}'}{v_x} = \frac{v'}{v}\cos\alpha \qquad (10.48)$$

and similarly for the other components of $\mathbf{v}'$ and $\mathbf{v}$. Applying these considerations, the components of (10.44) can be written out in full as

$$v_x + \frac{\mathrm{d}E}{\mathrm{d}\gamma}\omega_\mathrm{c}\left[v_x\tau_2(E) + v_y\tau_1(E)\right] = v_xL\left(\tau_1(E)\right) - v_yL\left(\tau_2(E)\right),$$
$$v_y - \frac{\mathrm{d}E}{\mathrm{d}\gamma}\omega_\mathrm{c}\left[v_x\tau_1(E) - v_y\tau_2(E)\right] = v_yL\left(\tau_1(E)\right) + v_xL\left(\tau_2(E)\right),$$
$$v_z = v_zL\left(\tau_3(E)\right), \qquad (10.49)$$

where

$$L\left(\tau_i(E)\right) = \int s(\mathbf{k}',\mathbf{k})\frac{f_0(E')}{f_0(E)}\left(\tau_i(E) - \tau_i(E')\frac{v'}{v}\cos\alpha\right)\mathrm{d}^3\mathbf{k}' \qquad (10.50)$$

and ω_c is the cyclotron frequency

$$\omega_\mathrm{c} = \frac{eB}{m^*}. \qquad (10.51)$$

Eliminating the components of $\mathbf{v}$ from (10.49), we then have

$$L(\tau_1(E)) = 1 + \frac{\mathrm{d}E}{\mathrm{d}\gamma}\omega_\mathrm{c}\tau_2(E),$$
$$L(\tau_2(E)) = -\frac{\mathrm{d}E}{\mathrm{d}\gamma}\omega_\mathrm{c}\tau_1(E),$$
$$L(\tau_3(E)) = 1 \tag{10.52}$$

In reality, there will be many different scattering processes. Assuming that these are independent of each other, we may then write $s(\mathbf{k}', \mathbf{k})$ as

$$s(\mathbf{k}', \mathbf{k}) = \sum_i s_i(\mathbf{k}', \mathbf{k}), \tag{10.53}$$

where the $s_i(\mathbf{k}', \mathbf{k})$ are particular scattering processes. Equation (10.51) can then be written

$$\sum_i L_i(\tau_j(E)) = \sum_i \int s_i(\mathbf{k}', \mathbf{k}) \frac{f_0(E')}{f_0(E)} \left(\tau_j(E) - \tau_j(E') \frac{v'}{v} \cos\alpha \right) \mathrm{d}^3\mathbf{k}'. \tag{10.54}$$

For elastic processes, we may put

$$s_i(\mathbf{k}', \mathbf{k}) \to s_i(\mathbf{k}', \mathbf{k}) \delta(E' - E). \tag{10.55}$$

On insertion of this into the integral on the right-hand side of (10.54), the action of the delta function means that the τ_j take the same value of E whilst the f_0 and v cancel out, leaving

$$L_i(\tau_j(E)) = \tau_j(E) \int s_i(\mathbf{k}', \mathbf{k}) (1 - \cos\alpha) \mathrm{d}^3\mathbf{k}'. \tag{10.56}$$

Note that, since α is the angle between $\mathbf{k}'$ and $\mathbf{k}$, in the absence of a magnetic field this gives us the definition of a momentum relaxation time $\tau_\mathrm{m}(E)$ as the reciprocal of the elastic scattering rate $w_i(E)$ for a given process:

$$\left(\frac{1}{\tau_\mathrm{m}(E)} \right)_i = w_i(E) = \int s_i(\mathbf{k}', \mathbf{k}) (1 - \cos\alpha) \mathrm{d}^3\mathbf{k}'. \tag{10.57}$$

These results can be summarised in a concise form by writing

$$\sum_i L_i(\tau_j(E)) = \tau_j(E) \sum_i w_i. \tag{10.58}$$

For polar-optical phonon scattering, we must allow that the process can no longer be modelled as elastic. Consider the case of scattering from a single optical mode of energy $\hbar\omega$. The intrinsic rate from an initial state $\mathbf{k}$ to a final state $\mathbf{k}'$ can be written formally as

$$s(\mathbf{k},\mathbf{k}') = s_{\mathrm{A}}\delta\,(E' - E - \hbar\omega) + s_{\mathrm{E}}\delta\,(E' - E + \hbar\omega), \tag{10.59}$$

where s_{A} and s_{E} are the intrinsic scattering rates for absorption (final energy $E' = E + \hbar\omega$) and emission ($E' = E - \hbar\omega$), respectively. However, we have written the integrals for the scattering rates (10.50) in terms of $s(\mathbf{k}',\mathbf{k})$, i.e. the intrinsic rate from the final state $\mathbf{k}'$ to the initial state $\mathbf{k}$. Hence, the rate multiplying the first delta function in (10.59) must be the *emission* rate (going from $E' = E + \hbar\omega$ to E) and that multiplying the second delta function the *absorption* rate (going from $E' = E - \hbar\omega$ to E). Thus

$$s(\mathbf{k}',\mathbf{k}) = s_{\mathrm{E}}\delta\,(E' - E - \hbar\omega) + s_{\mathrm{A}}\delta\,(E' - E + \hbar\omega). \tag{10.60}$$

When (10.60) is inserted into (10.50), the effect of the delta functions is to introduce values of the τ_i at energies $E - \hbar\omega,\ E$ and $E + \hbar\omega$, which can then be taken outside the integrals. The result is an expression of the form

$$L\,(\tau_i(E)) = A(E)\tau_i(E - \hbar\omega) + B(E)\tau_i(E) + C(E)\tau_i(E + \hbar\omega), \tag{10.61}$$

where

$$\begin{aligned}
A(E) &= -\theta(E - \hbar\omega)\int s_{\mathrm{A}}\frac{f_0(E')}{f_0(E)}\frac{v'}{v}\cos\alpha\delta(E' - E + \hbar\omega)\mathrm{d}^3\mathbf{k}',\\
B(E) &= \theta(E - \hbar\omega)\int s_{\mathrm{A}}\frac{f_0(E')}{f_0(E)}\delta(E' - E + \hbar\omega)\mathrm{d}^3\mathbf{k}'\\
&\qquad + \int s_{\mathrm{E}}\frac{f_0(E')}{f_0(E)}\delta(E' - E - \hbar\omega)\mathrm{d}^3\mathbf{k}',\\
C(E) &= -\int s_{\mathrm{E}}\frac{f_0(E')}{f_0(E)}\frac{v'}{v}\cos\alpha\delta(E' - E - \hbar\omega)\mathrm{d}^3\mathbf{k}',
\end{aligned} \tag{10.62}$$

Here, we have introduced the step function

$$\theta(E) = \begin{cases} 0, & E \le 0,\\ 1, & E > 0, \end{cases} \tag{10.63}$$

since for an electron with energy $E < \hbar\omega$ there can be no phonon emission, hence the scattering rate for this process must be zero. On substitution of (10.61) into (10.52), we find that scattering time at any particular energy E is correlated with the times at $E \pm \hbar\omega$. This suggests the picture of the phonon energy 'ladder' with rungs $\hbar\omega$ apart: the scattering rate on any particular rung being related to the rates on adjacent rungs. We can make this more explicit by writing the energy as $\varepsilon + n\hbar\omega$, where $0 \le \varepsilon < \hbar\omega$, and rewriting (10.52) as a system of linear equations:

$$\begin{aligned}
L\,(\tau_1(\varepsilon + n\hbar\omega)) &= 1 + \frac{\mathrm{d}E}{\mathrm{d}\gamma}\omega_{\mathrm{c}}\tau_2(\varepsilon + n\hbar\omega),\\
L\,(\tau_2(\varepsilon + n\hbar\omega)) &= -\frac{\mathrm{d}E}{\mathrm{d}\gamma}\omega_{\mathrm{c}}\tau_1(\varepsilon + n\hbar\omega),\\
L\,(\tau_3(\varepsilon + n\hbar\omega)) &= 1,\\
n &= 0, 1, \ldots.
\end{aligned} \tag{10.64}$$

If we require any τ_i at a particular level E, we need to solve for all the values of τ_i separated by integral multiples of $\hbar\omega$. In practice, we may only solve for a finite number of rungs, which we may do by using a matrix inversion technique such as Gaussian elimination. To minimize any truncation error incurred from only solving for a finite number of rungs, it is assumed that as $n \to \infty$, $\tau_i(\varepsilon + n\hbar\omega) \to \tau_i(\varepsilon + [n+1]\hbar\omega)$. Hence, for the last rung N, we put

$$B(\varepsilon + N\hbar\omega) \to B(\varepsilon + N\hbar\omega) + C(\varepsilon + N\hbar\omega). \tag{10.65}$$

In reality, of course, there will only be a finite number of rungs in an energy band. In GaN_xAs_{1-x} the width of the lower band E_- depends on temperature and nitrogen concentration but at 300 K can be as narrow as six rungs for ultra-dilute N concentrations. Even for such a narrow band, the boundary condition given in (10.65) may still be reasonable, although strictly speaking, we ought to modify (10.62) by imposing the condition

$$C(E) \to \theta(E_\mathrm{B} - E)\, C(E), \tag{10.66}$$

where E_B is the band width and then just solving for $E_\mathrm{B}/\hbar\omega$ rungs (rounded down to the nearest integer).

To include elastic scattering processes in our calculations, we just make the substitution

$$B(E) \to B(E) + \sum_i w_i. \tag{10.67}$$

10.5 Ladder Coefficients in a Non-Parabolic Band

The general form of $s(\mathbf{k}', \mathbf{k})$ for phonon scattering is

$$s(\mathbf{k}', \mathbf{k}) = W(\mathbf{k}, \mathbf{k}', \omega)\left\{n(\omega) + \tfrac{1}{2} \mp \tfrac{1}{2}\right\}\delta_{\mathbf{k}', \mathbf{k} \mp \mathbf{q}}\,\delta(E' - E \pm \hbar\omega), \tag{10.68}$$

where $n(\omega)$ is the phonon occupation number, given by the Bose–Einstein factor, $\mathbf{q}$ is the phonon wavevector and the Kronecker delta imposes the conservation of momentum. $W(\mathbf{k}, \mathbf{k}', \omega)$ is given by

$$W(\mathbf{k}, \mathbf{k}', \omega) = I^2(\mathbf{k}, \mathbf{k}')\,|G(q_z)|^2\,\frac{V}{8\pi^2 NM}\frac{C_\mathbf{q}^2}{\omega}, \tag{10.69}$$

where $I(\mathbf{k}, \mathbf{k}')$ is a factor of order unity arising out of the overlap of the electron wavefunctions over the unit cell, $G(q_z)$ is a 2D form factor (equal to unity in 3D), N is the number of unit cells in the crystal volume V, M is a characteristic mass and $C_\mathbf{q}^2$ is a coupling strength for the particular process. For polar optical scattering $C_\mathbf{q}^2$ is given by [18]

$$C_\mathbf{q}^2 = \frac{e^2 M\omega^2}{V_0 q^2 \varepsilon_\mathrm{p}}, \tag{10.70}$$

where V_0 is the volume of the unit cell and we have defined

$$\frac{1}{\varepsilon_{\rm p}} = \frac{1}{\varepsilon_0}\left(\frac{1}{\kappa_\infty} - \frac{1}{\kappa_0}\right), \tag{10.71}$$

in terms of the permittivity of free space ε_0 and the high- and low-frequency dielectric constants κ_∞ and κ_0, respectively. Substituting (10.70) into (10.69), we get

$$W\left(\mathbf{k},\mathbf{k}',\omega\right) = I^2(\mathbf{k},\mathbf{k}')\frac{W_0}{2}\frac{\hbar}{\pi}\left(\frac{\hbar\omega}{2m^*}\right)^{1/2}\frac{\left|G(q_z)\right|^2}{q^2}, \tag{10.72}$$

where we have defined a characteristic rate for polar-optical phonon scattering

$$W_0 = \frac{e^2}{4\pi\hbar\varepsilon_{\rm p}}\left(\frac{2m^*\omega}{\hbar}\right)^{1/2}. \tag{10.73}$$

Substituting these expressions into in our formal equations for the ladder coefficients (10.62), we obtain

$$\begin{aligned}
A(E) &= -\theta(E-\hbar\omega)\frac{W_0}{2}\frac{\hbar}{\pi}\left(\frac{\hbar\omega}{2m^*}\right)^{1/2} n(\omega)\frac{f_0(E-\hbar\omega)}{f_0(E)}I_1^+,\\
B(E) &= \frac{W_0}{2}\frac{\hbar}{\pi}\left(\frac{\hbar\omega}{2m^*}\right)^{1/2}\Bigg(\theta(E-\hbar\omega)n(\omega)\frac{f_0(E-\hbar\omega)}{f_0(E)}I_2^+\\
&\qquad\qquad + \left(n(\omega)+1\right)\frac{f_0(E+\hbar\omega)}{f_0(E)}I_2^-\Bigg),\\
C(E) &= -\frac{W_0}{2}\frac{\hbar}{\pi}\left(\frac{\hbar\omega}{2m^*}\right)^{1/2}\left(n(\omega)+1\right)\frac{f_0(E+\hbar\omega)}{f_0(E)}I_1^-,
\end{aligned} \tag{10.74}$$

where we have extracted the $f_0(E')/f_0(E)$, after allowing for the action of the delta functions, from the integrals $I_i^\pm$

$$\begin{aligned}
I_1^\pm &= I^2(\mathbf{k},\mathbf{k}')\int\frac{\left|G(q_z)\right|^2}{q^2}\frac{v'}{v}\cos\alpha\,\delta(E'-E\pm\hbar\omega)\mathrm{d}^3\mathbf{k}',\\
I_2^\pm &= I^2(\mathbf{k},\mathbf{k}')\int\frac{\left|G(q_z)\right|^2}{q^2}\delta(E'-E\pm\hbar\omega)\mathrm{d}^3\mathbf{k}'.
\end{aligned} \tag{10.75}$$

Note that we have omitted the Kronecker delta from the above, as the conservation of momentum will be taken to be implicit.

In 3D, analytical solutions for the ladder coefficients (10.74) in a non-parabolic band have been found [19] by changing to an integral over energy. However, this approach proves intractable in the 2D case. Instead, we adopt the alternative strategy of exploiting the one-to-one correspondence between **k** and phonon wavevector **q** and integrate over **q**. This gives the same result as integrating over energy in the 3D case. Unfortunately, in 2D our final

expressions for the ladder coefficients are no longer in an analytical form and we are left with integrals that we must solve numerically.

We now make use of the one-to-one mapping between $\mathbf{k}'$ and $\mathbf{q}$ to change to an integral over $\mathbf{q}$

$$\mathrm{d}^3\mathbf{k}' \to \mathrm{d}^3\mathbf{q} = \begin{cases} 2\pi q^2 \mathrm{d}q\, \mathrm{d}(-\cos\beta), & \text{3D}, \\ 2\frac{q_{||}}{\sin\beta}\mathrm{d}q_{||}\, \mathrm{d}q_z \mathrm{d}(-\cos\beta), & \text{2D}, \end{cases} \tag{10.76}$$

where β is the angle between $\mathbf{k}$ and $\mathbf{q}$ in 3D or the angle between $\mathbf{k}_{||}$ and $\mathbf{q}_{||}$ in 2D (the '$||$' subscript denotes the component of the wavevector in the plane of the quantum well). Note that the factor of 2 for the 2D expression accounts for the fact that β is the azimuthal angle in this case and so we need to double the integration to account for $\pi \leq \beta \leq 2\pi$. We take the factor of $1/q^2$ in (10.75) into the integration over q_z in the 2D case and use the form factor

$$F(q_{||}) = \frac{q_{||}}{\pi}\int_{-\infty}^{\infty} \frac{|G(q_z)|^2}{q_z^2 + q_{||}^2}\mathrm{d}q_z. \tag{10.77}$$

We can write the integrals for both 3D and 2D in an analogous form by defining

$$F\left(q\right) = 1, \tag{10.78}$$

in 3D. Dropping the '$||$' notation, the integrals can then be written using a common q dependent factor:

$$2\pi F\left(q\right)\mathrm{d}q. \tag{10.79}$$

The argument of the delta function can be rewritten in terms of the inverse of γ:

$$E' - E \pm \hbar\omega = \gamma^{-1}\left(\frac{\hbar^2 k'^2}{2m^*}\right) - E \pm \hbar\omega. \tag{10.80}$$

Note that the existence of $\gamma^{-1}(E)$ requires that γ is a monotonically increasing function of E. Physically; this means that we are constrained to $\mathbf{k}$ values in a single energy band.

The conservation of momentum gives us

$$k'^2 = k^2 + q^2 + 2kq\cos\beta, \tag{10.81}$$

which allows us to substitute for k' in (10.80). We can now integrate over $-\cos\beta$ using the property of the delta function

$$\int_{x_\mathrm{A}}^{x_\mathrm{B}} f(x)\delta\left\{g(x)\right\}\mathrm{d}x = \sum_i \frac{f(x_i)}{|\mathrm{d}g(x_i)/\mathrm{d}x|}, \tag{10.82}$$

where x_i is a point on the interval $[x_\mathrm{A},\ x_\mathrm{B}]$ and $g(x_i) = 0$. In our case, we have

$$g(\cos\beta) = \gamma^{-1}\left(\frac{\hbar^2}{2m^*}\left[k^2 + q^2 + 2kq\cos\beta\right]\right) - E \pm \hbar\omega,$$
$$f(\cos\beta) = \begin{cases} 1, & \text{3D}, \\ \left(1 - \cos^2\beta\right)^{-1/2}, & \text{2D}, \end{cases} \tag{10.83}$$

where we have used the identity $\sin\beta = (1 - \cos^2\beta)^{1/2}$. Now, the derivative of $g(\cos\beta)$ is

$$\frac{\mathrm{d}g(\cos\beta)}{d\cos\beta} = \frac{\hbar^2 kq}{m^*}\frac{\mathrm{d}\gamma^{-1}(X)}{dX}, \tag{10.84}$$

where X is the argument of γ^{-1} in (10.83). But, when $g(\cos\beta) = 0$, we have

$$X = \gamma\,(E \mp \hbar\omega) = \gamma\,(E'). \tag{10.85}$$

Consequently, from the definition of an inverse function, we have

$$\gamma^{-1}(\gamma') = E',$$
$$\frac{\mathrm{d}\gamma^{-1}(\gamma')}{\mathrm{d}\gamma'} = \frac{\mathrm{d}E'}{\mathrm{d}\gamma'} = \left(\frac{\mathrm{d}\gamma\,(E')}{\mathrm{d}E}\right)^{-1}. \tag{10.86}$$

Had we been integrating over energy (in 3D), it is this derivative that would have emerged from making the substitution

$$\mathrm{d}k' = \frac{(2m^*)^{1/2}}{2\hbar}\gamma^{-1/2}(E')\,\frac{\mathrm{d}\gamma\,(E')}{\mathrm{d}E}\mathrm{d}E'. \tag{10.87}$$

That is, this derivative arises out of the density of states derived from the dispersion relations rather than the Green's function (that this is the case when integrating over $\mathbf{q}$ is not supposed to be obvious). For the time being, we shall retain it as it will be straightforward to remove from our final results when we wish to specialise to dilute nitrides.

In the 2D case we have the $(\sin\beta)^{-1}$ function to deal with. When $g(\cos\beta) = 0$, we have

$$\cos\beta = \frac{1}{2}\left(\frac{2m^*}{\hbar^2}\right)\frac{1}{kq}\left(\gamma\,(E \mp \hbar\omega) - \frac{\hbar^2k^2}{2m^*} - \frac{\hbar^2q^2}{2m^*}\right),$$
$$= \frac{1}{2}\left(\frac{2m^*}{\hbar^2q^2}\right)^{1/2}\frac{1}{\gamma^{1/2}(E)}\left(\gamma\,(E \mp \hbar\omega) - \gamma(E) - \frac{\hbar^2q^2}{2m^*}\right). \tag{10.88}$$

Putting these results together, we find that integration over $-\cos\beta$ introduces a factor

$$\frac{(2m^*)^{1/2}}{2\hbar\gamma^{1/2}(E)}\frac{\mathrm{d}\gamma(E \mp \hbar\omega)}{\mathrm{d}E}\frac{H_\pm(E,q)}{q}, \tag{10.89}$$

where we have substituted for k in terms of γ and

$$H_{\pm}(E,q) = \begin{cases} 1, & \text{3D,} \\ \left[1 - \frac{1}{4}\frac{2m^*}{\hbar^2 q^2}\frac{1}{\gamma(E)}\left(\gamma(E \mp \hbar\omega) - \gamma(E) - \frac{\hbar^2 q^2}{2m^*}\right)^2\right]^{-1/2}, & \text{2D.} \end{cases} \tag{10.90}$$

A further consequence of this integration is the imposition of limits on q due to the condition that $\cos\beta$ must lie between -1 and 1. Setting $g(\cos\beta) = 0$ with $\cos\beta = \pm 1$ in (10.83), we obtain a quadratic equation in q. Imposing the condition $q \geq 0$, we find that the limits for absorption (integrals involving $\delta(E' - E - \hbar\omega)$) are

$$\begin{aligned} q_1^- &= \frac{(2m^*)^{1/2}}{\hbar}\gamma^{1/2}(E)\left\{\left(\frac{\gamma(E+\hbar\omega)}{\gamma(E)}\right)^{1/2} - 1\right\} \\ q_2^- &= \frac{(2m^*)^{1/2}}{\hbar}\gamma^{1/2}(E)\left\{\left(\frac{\gamma(E+\hbar\omega)}{\gamma(E)}\right)^{1/2} + 1\right\} \end{aligned} \tag{10.91}$$

and for emission (integrals involving $\delta(E' - E + \hbar\omega)$) are

$$\begin{aligned} q_1^+ &= \frac{(2m^*)^{1/2}}{\hbar}\gamma^{1/2}(E)\left\{1 - \left(\frac{\gamma(E-\hbar\omega)}{\gamma(E)}\right)^{1/2}\right\} \\ q_2^+ &= \frac{(2m^*)^{1/2}}{\hbar}\gamma^{1/2}(E)\left\{1 + \left(\frac{\gamma(E-\hbar\omega)}{\gamma(E)}\right)^{1/2}\right\}. \end{aligned} \tag{10.92}$$

Using these results, the integrals in (10.75) become

$$\begin{aligned} I_1^{\pm} &= I^2(\mathbf{k},\mathbf{k}')\frac{\pi}{\hbar}\left(\frac{2m^*}{\gamma(E)}\right)^{1/2}\frac{\mathrm{d}\gamma(E\mp\hbar\omega)}{\mathrm{d}E}\int_{q_1^{\pm}}^{q_2^{\pm}}\frac{F(q)}{q}H_{\pm}(E,q)\frac{v_{\pm}}{v}\cos\alpha_{\pm}\mathrm{d}q, \\ I_2^{\pm} &= I^2(\mathbf{k},\mathbf{k}')\frac{\pi}{\hbar}\left(\frac{2m^*}{\gamma(E)}\right)^{1/2}\frac{\mathrm{d}\gamma(E\mp\hbar\omega)}{\mathrm{d}E}\int_{q_1^{\pm}}^{q_2^{\pm}}\frac{F(q)}{q}H_{\pm}(E,q)\mathrm{d}q. \end{aligned} \tag{10.93}$$

Note that in the first integral, we have rewritten v' and $\cos\alpha$ with $\pm$ subscripts. This is to allow for the effect of the delta function on these factors after the integration over $-\cos\beta$.

From the conservation of momentum, $\cos\alpha$ can be written

$$\cos\alpha = \frac{k'^2 + k^2 - q^2}{2k'k}. \tag{10.94}$$

Hence, using (10.17) for the group velocity in a non-parabolic band, we have

$$\frac{v'}{v}\cos\alpha = \frac{\mathrm{d}E/\mathrm{d}\gamma'}{\mathrm{d}E/\mathrm{d}\gamma}\left(\frac{\gamma(E')}{\gamma(E)}\right)^{1/2}\frac{\gamma(E') + \gamma(E) - \hbar^2 q^2/(2m^*)}{2\gamma^{1/2}(E')\gamma^{1/2}(E)}, \tag{10.95}$$

so $I_1^{\pm}$ is

$$I_1^{\pm} = I^2(\mathbf{k},\mathbf{k}')\frac{\pi}{2\hbar}\frac{(2m^*)^{1/2}}{\gamma^{3/2}(E)}\frac{\mathrm{d}\gamma(E)}{\mathrm{d}E} \times \int_{q_1^{\pm}}^{q_2^{\pm}} \frac{F(q)}{q} H_{\pm}(E,q)\left\{\gamma(E\mp\hbar\omega)+\gamma(E)-\frac{\hbar q^2}{2m^*}\right\}\mathrm{d}q. \tag{10.96}$$

In the 3D case, these integrals reduce to

$$I_1^{\pm} = I^2(\mathbf{k},\mathbf{k}')\frac{\pi}{2\hbar}\frac{(2m^*)^{1/2}}{\gamma^{3/2}(E)}\frac{\mathrm{d}\gamma(E)}{\mathrm{d}E}\int_{q_1^{\pm}}^{q_2^{\pm}} \frac{\gamma(E\mp\hbar\omega)+\gamma(E)}{q} - \frac{\hbar q}{2m^*}\mathrm{d}q,$$
$$I_2^{\pm} = I^2(\mathbf{k},\mathbf{k}')\frac{\pi}{\hbar}\left(\frac{2m^*}{\gamma(E)}\right)^{1/2}\frac{\mathrm{d}\gamma(E\mp\hbar\omega)}{\mathrm{d}E}\int_{q_1^{\pm}}^{q_2^{\pm}}\frac{\mathrm{d}q}{q}, \tag{10.97}$$

which can be solved analytically. Using the limits on q ((10.91) and (10.92)) and the identities

$$\tanh^{-1}(x) = \tfrac{1}{2}\ln\left(\tfrac{1+x}{1-x}\right),$$
$$\coth^{-1}(x) = \tfrac{1}{2}\ln\left(\tfrac{x+1}{x-1}\right), \tag{10.98}$$

we finally obtain, after substituting the $I_i^{\pm}$ back into (10.74),

$$A(E) = -\theta(E-\hbar\omega)I^2(\mathbf{k}',\mathbf{k})W_0(\hbar\omega)^{1/2}n(\omega)\frac{f_0(E-\hbar\omega)}{f_0(E)}\frac{\mathrm{d}\gamma(E)}{\mathrm{d}E}\frac{\gamma^{1/2}(E-\hbar\omega)}{\gamma(E)} \times\frac{1}{2}\left\{\frac{\gamma(E-\hbar\omega)+\gamma(E)}{\gamma^{1/2}(E-\hbar\omega)\gamma^{1/2}(E)}\tanh^{-1}\left(\frac{\gamma(E-\hbar\omega)}{\gamma(E)}\right)^{1/2}-1\right\},$$

$$B(E) = I^2(\mathbf{k}',\mathbf{k})W_0\left(\frac{\hbar\omega}{\gamma(E)}\right)^{1/2} \times\left[\theta(E-\hbar\omega)n(\omega)\frac{f_0(E-\hbar\omega)}{f_0(E)}\frac{\mathrm{d}\gamma(E-\hbar\omega)}{\mathrm{d}E}\tanh^{-1}\left(\frac{\gamma(E-\hbar\omega)}{\gamma(E)}\right)^{1/2} + \{n(\omega)+1\}\frac{f_0(E+\hbar\omega)}{f_0(E)}\frac{\mathrm{d}\gamma(E+\hbar\omega)}{\mathrm{d}E}\coth^{-1}\left(\frac{\gamma(E+\hbar\omega)}{\gamma(E)}\right)^{1/2}\right],$$

$$C(E) = -I^2(\mathbf{k}',\mathbf{k})W_0(\hbar\omega)^{1/2}\{n(\omega)+1\}\frac{f_0(E+\hbar\omega)}{f_0(E)}\frac{\mathrm{d}\gamma(E)}{\mathrm{d}E}\frac{\gamma^{1/2}(E+\hbar\omega)}{\gamma(E)} \times\frac{1}{2}\left\{\frac{\gamma(E+\hbar\omega)+\gamma(E)}{\gamma^{1/2}(E+\hbar\omega)\gamma^{1/2}(E)}\coth^{-1}\left(\frac{\gamma(E+\hbar\omega)}{\gamma(E)}\right)^{1/2}-1\right\}. \tag{10.99}$$

In the parabolic limit, it can be shown that (10.99) reduce to the formulae given by Fletcher and Butcher [10]. Forms for (10.99) in which the dependence on the group velocity and density of states is made explicit can be found in [20].

For the 2D case, the integrals cannot be performed analytically and we must leave the expressions for the ladder coefficients in the form:

$$
\begin{aligned}
A(E) &= -\theta(E-\hbar\omega) I^2(\mathbf{k},\mathbf{k}') \frac{W_0}{4} (\hbar\omega)^{1/2}\, n(\omega) \frac{f_0(E-\hbar\omega)}{f_0(E)} \\
&\quad \times \frac{1}{\gamma^{3/2}(E)} \frac{\mathrm{d}\gamma(E)}{\mathrm{d}E} \int_{q_1^+}^{q_2^+} \frac{F(q)}{q} H_+(E,q) \left\{ \gamma(E-\hbar\omega) + \gamma(E) - \frac{\hbar q^2}{2m^*} \right\} \mathrm{d}q, \\
B(E) &= I^2(\mathbf{k},\mathbf{k}') \frac{W_0}{2} \left(\frac{\hbar\omega}{\gamma(E)} \right)^{1/2} \\
&\quad \times \left(\theta(E-\hbar\omega) n(\omega) \frac{f_0(E-\hbar\omega)}{f_0(E)} \frac{\mathrm{d}\gamma(E-\hbar\omega)}{\mathrm{d}E} \int_{q_1^+}^{q_2^+} \frac{F(q)}{q} H_+(E,q) \mathrm{d}q \right. \\
&\quad \left. + \{n(\omega)+1\} \frac{f_0(E+\hbar\omega)}{f_0(E)} \frac{\mathrm{d}\gamma(E+\hbar\omega)}{\mathrm{d}E} \int_{q_1^-}^{q_2^-} \frac{F(q)}{q} H_-(E,q) \mathrm{d}q \right), \\
C(E) &= -I^2(\mathbf{k},\mathbf{k}') \frac{W_0}{4} (\hbar\omega)^{1/2} \{n(\omega)+1\} \frac{f_0(E+\hbar\omega)}{f_0(E)} \\
&\quad \times \frac{1}{\gamma^{3/2}(E)} \frac{\mathrm{d}\gamma(E)}{\mathrm{d}E} \int_{q_1^-}^{q_2^-} \frac{F(q)}{q} H_-(E,q) \left\{ \gamma(E+\hbar\omega) + \gamma(E) - \frac{\hbar q^2}{2m^*} \right\} \mathrm{d}q,
\end{aligned}
\tag{10.100}
$$

Having obtained these general expressions, we must remember that if we are to use the modified DOS we must divide the appropriate terms by $\mathrm{d}\gamma(E \mp \hbar\omega)/\mathrm{d}E$. Simpler forms for (10.101) in terms of the group velocity and density of states and in which the numerical integrals are free from singularities can be found in [20]. We also require explicit forms for the $F(q)$. The exact form used will depend on the choice of electron wavefunction in the confinement direction. For a triangular quantum well, a common choice is the Fang–Howard wavefunction [21]. For an electron in the first subband, the form factor is then [13, 22]

$$
F(q_{||}) = \left(1 + \frac{q_{||}}{b}\right)^{-3} \left(1 + \frac{9}{8}\frac{q_{||}}{b} + \frac{3}{8}\frac{q_{||}^2}{b^2}\right), \tag{10.101}
$$

where b is a parameter chosen to minimise the electron energy. For an electron in the nth subband of an infinite quantum well, we have

$$
F_n(q_{||}) = \left\{ \frac{2}{q_{||}L} + \frac{q_{||}L}{q_{||}^2 L^2 + 4\pi^2 n^2} - \frac{32\pi^4 n^4 \left[1 - \exp(-q_{||}L)\right]}{q_{||}^2 L^2 \left(q_{||}^2 L^2 + 4\pi^2 n^2\right)^2} \right\}. \tag{10.102}
$$

10.6 Elastic Scattering Processes

10.6.1 Alloy Scattering

For III–V semiconductors, the conventional model of alloy scattering is due to Harrison and Hauser [23], building on the work of Flinn [24], Hall [25] and Asch [26]. According to this model, the alloy is treated in the virtual crystal approximation [27] in which the potential seen by the electron is a linear interpolation of the binary constituents. The scattering rate is then ascribed to random fluctuations in the potential and calculated using time-dependent perturbation theory. The scattering rate, in the form of (10.57), is found to be

$$w(E) = \frac{3\pi^3 x(1-x)\Delta V^2 a_0^3}{8\hbar} N(E), \tag{10.103}$$

where a_0 is the lattice constant, $N(E)$ is the appropriate density of states and ΔV is the difference in the binary potentials. The actual nature of this potential is still an open question. Harrison and Hauser take this to be the difference in electron affinity and calculate the scattering rate using the Born approximation. Subsequently, it was suggested by Ferry [28] that the potential used by Van Vechten and Bergstresser [29] in their dielectric method treatment of bandgap bowing in alloys should be a better choice. The magnitude of this potential for an alloy $A_xB_{1-x}C$ where A and B have the same valence Z is given by

$$\Delta V = Be^2 Z \left|1/r_\mathrm{B} - 1/r_\mathrm{A}\right| \exp\left(-k_\mathrm{s} R\right), \tag{10.104}$$

where

$$R = \tfrac{1}{2}\left[x r_\mathrm{A} + (1-x)\, r_\mathrm{B} + r_\mathrm{C}\right], \tag{10.105}$$

the r_i are Philips' rationalised covalent radii [30], k_s is the Thomas–Fermi screening wave number and B is a parameter of order unity (take to be 1.5) used to adjust to compensate for the error in the Thomas–Fermi factor. This model would certainly produce a large scattering rate in dilute nitrides due to the much smaller radius of the nitrogen atom compared to the other group V atoms it might substitute for.

Alternatively, a phenomenological approach was suggested by Auslender and Hava [31], who used the Hellman–Feynman theorem to show that the difference in the binary potentials could be expressed in terms of the derivative of the virtual crystal potential with alloying and hence in terms of the rate of change of the band edges. However, whether this method can be used to find the scattering rate from optical bowing data depends on two factors: Firstly, the model is based on band-edge bowing and not band-gap bowing. This may not be a critical objection if the rate of change of the valence band-edge is negligible compared to that of the conduction band. For dilute nitrides, this seems a reasonable approximation. Secondly, and perhaps more crucially, the model is derived from the rate of change of the virtual crystal potential, which

does not explicitly involve bowing. The model may then not relate directly to the observed variation of the bandgap at all.

More recently, a similar result to that of Auslender and Hava's for an isolated impurity has been derived by Fahy and O'Reilly [7] using S-matrix theory. These authors subsequently developed their model to incorporate scattering from nitrogen complexes [32]. This has become the most commonly cited model in the literature for the mobility in dilute nitrides.

In Fahy and O'Reilly's original work, a scattering cross section was derived from the S-matrix element, which was shown to be proportional to the rate of change of the band edge E_0 with the number of impurities per unit volume N_I

$$\langle\psi_0|\,\Delta V\,|\phi_0\rangle = \frac{1}{V}\frac{\mathrm{d}E_0}{\mathrm{d}N_\mathrm{I}}. \tag{10.106}$$

Here, ΔV is the perturbation in the potential due to the presence of the impurity, ψ_0 and ϕ_0 are the eigenfunctions at $\mathbf{k} = 0$ for the perturbed and unperturbed Hamiltonians, respectively, and V is the crystal volume. For our purposes, we again require a scattering rate in the form of (10.57)

$$\begin{aligned} w(E) &= N_\mathrm{I} V \frac{2\pi}{\hbar}\int |\langle\psi_0|\,\Delta V\,|\phi_0\rangle|^2 \left(1-\cos\theta\right)\delta\left(E'-E\right)\frac{V}{8\pi^3}\mathrm{d}^3\mathbf{k}', \\ &= \frac{\pi}{2}\frac{x a_0^3}{\hbar}N(E)\left(\frac{\mathrm{d}E_0}{\mathrm{d}x}\right)^2, \end{aligned} \tag{10.107}$$

where $N(E)$ is the appropriate density of states and we have used $N_\mathrm{I} = 4x/a_0^3$. This expression can be adapted to the case of different nitrogen environments (such as N–N clusters) with concentrations x_i by making the substitution

$$\left(\frac{\mathrm{d}E_0}{\mathrm{d}x}\right)^2 \rightarrow \sum_i \left(\frac{\mathrm{d}E_0}{\mathrm{d}x_i}\right)^2 x_i. \tag{10.108}$$

For isolated nitrogen states, the rate of change of the lower E_- band can be calculated from the BAC model

$$\frac{\mathrm{d}E_-}{\mathrm{d}x} = -\frac{1}{2}\left\{\alpha + \frac{\alpha\left(E_\mathrm{N}-E_\mathrm{C}\right)+2\beta^2}{\left[\left(E_\mathrm{N}-E_\mathrm{C}\right)^2+4\beta^2 x\right]^{1/2}}\right\}. \tag{10.109}$$

More recent theoretical models of scattering in dilute nitrides can be found in [17, 33].

10.6.2 Other Elastic Processes

Although, as discussed earlier, the predominant scattering processes in dilute nitrides are likely to be polar-optical phonon and alloy scattering, we briefly summarise other possible processes here. We start with acoustic phonon scattering, which we take to be elastic.

Deformation Potential Phonon Scattering

In 3D, the rate for deformation potential phonon scattering is [18]

$$w(E) = I^2(\mathbf{k}', \mathbf{k}) \frac{2\pi\ \Xi_{\mathrm{d}}^2 k_{\mathrm{B}} T}{\hbar c_{\mathrm{L}}} N_{3\mathrm{D}}(E), \tag{10.110}$$

where Ξ_{d} is the deformation potential for pure dilation and c_{L} is the average elastic constant for longitudinal modes, given in terms of the components of the elastic stiffness constants c_{ij} by

$$c_{\mathrm{L}} = c_{11} + \tfrac{2}{5}\left(c_{12} + 2c_{44} - c_{11}\right). \tag{10.111}$$

In 2D, we find

$$w(E) = I^2(\mathbf{k}', \mathbf{k}) \frac{\Xi^2 k_{\mathrm{B}} T m^*}{2\pi\ c_{\mathrm{L}} \hbar^3} \frac{\mathrm{d}\gamma(E)}{\mathrm{d}E} F_0, \tag{10.112}$$

where F_0 is a form factor given by

$$F_0 = \int_{-\infty}^{\infty} |G(q_z)|^2\, \mathrm{d}q_z. \tag{10.113}$$

For an infinite square well of width L, this is

$$F_0 = \frac{3\pi}{L}. \tag{10.114}$$

Note that the derivative of γ in (10.112) again arises through the density of states, so that if we reject this factor, the scattering rate is the same as that for found for a parabolic band [13].

Piezoelectric Phonon Scattering

For piezoelectric phonon scattering, we must incorporate screening. In 3D, we have

$$w_{\mathrm{pe}} = I^2(\mathbf{k}', \mathbf{k}) \frac{\pi e^2 K_{\mathrm{av}}^2 \hbar k_{\mathrm{B}} T}{2\varepsilon m^*} \frac{N(E)}{\gamma(E)} H(E), \tag{10.115}$$

where

$$H(E) = 1 - \frac{\hbar^2 q_0^2}{4m^*\gamma(E)} \log\left[\frac{8m^*\gamma(E)}{\hbar^2 q_0^2} + 1\right] + \frac{1}{8m^*\gamma(E)/\hbar^2 q_0^2 + 1}, \tag{10.116}$$

q_0 is the reciprocal Debye screening length and $\varepsilon = \kappa_0 \varepsilon_0$. K_{av}^2 is an average electromechanical coupling coefficient given in terms of the piezoelectric coefficient e_{14} and the average longitudinal and transverse elastic constants c_{L} and c_{T} by

$$K_{\mathrm{av}}^2 = \frac{e_{14}^2}{\varepsilon}\left(\frac{12}{35c_{\mathrm{L}}} + \frac{16}{35c_{\mathrm{T}}}\right) \tag{10.117}$$

and

$$c_{\mathrm{T}} = c_{44} - \tfrac{1}{5}\left(c_{12} + 2c_{44} - c_{11}\right). \tag{10.118}$$

Once again, we find that a closed form for the 2D case is not obtainable. Using the form factor (10.77), we have

$$\begin{aligned} w(E) = I^2(\mathbf{k}', \mathbf{k}) \frac{e^2 K_{av}^2 k_{\mathrm{B}} T m^*}{4\pi\varepsilon\hbar^3 k_{||}^3} \\ \times \frac{\mathrm{d}\gamma(E)}{\mathrm{d}E} \int_0^{2k_{||}} \frac{F(q_{||})}{\left(1 + q_{\mathrm{s}}/q_{||}\right)^2 \left\{1 - \left(q_{||}/2k_{||}\right)^2\right\}^{1/2}} q_{||} \mathrm{d}q_{||}, \end{aligned} \tag{10.119}$$

which reduces in the parabolic limit (or use of the Green's function density of states) to the result of [34].

Ionized Impurity Scattering

The rate for ionized impurity scattering is based on the Brooks–Herring approach [35] in which the scattering cross section is limited by electron screening:

$$w(E) = \frac{\pi Z^2 e^4 N_{\mathrm{II}} \hbar^3}{16\varepsilon^2 m^{*2} \gamma^2(E)} N(E) \left\{ \log\left[\frac{8m^*\gamma(E)}{\hbar^2 q_0^2} + 1\right] - \frac{1}{1 + \hbar^2 q_0^2/8m^*\gamma(E)} \right\}, \tag{10.120}$$

where Z is the ionisation number (taken to be unity) and N_{II} is the number density of ionised impurities. From the hydrogenic impurity model, the donor ionization energy used to calculate N_{II} is given by

$$E_{\mathrm{d}}(x) = \left.\frac{\mathrm{d}\gamma}{\mathrm{d}E}\right|_{k=0} E_{\mathrm{d}}(\mathrm{matrix}) \tag{10.121}$$

(the acceptor impurities are all assumed to be occupied).

Neutral Impurity Scattering

An expression for the scattering rate due to neutral impurity scattering can be found based on the Erginsoy formula [36] in which the effective mass is modified by multiplying it by the derivative of the γ function:

$$w(E) = \frac{80\pi\varepsilon\hbar^3 N_{\mathrm{NI}}}{e^2 \left(m^* \mathrm{d}\gamma/\mathrm{d}E\right)^2}, \tag{10.122}$$

where N_{NI} is the number density of neutral impurities.

10.7 Results and Conclusions

The model presented here has been implemented for the 3D, using the additional elastic scattering processes detailed above [19]. These calculations assumed n-type doping with a compensation ratio of 0.5. The Fermi energy was then calculated from the charge neutrality condition. Scattering from nitrogen centres was modelled using (10.107).

The results given in Fig. 10.3 showed that for $x = 0.02$, nitrogen scattering does indeed dominate over polar-optical phonon scattering, pining the high temperature mobility to around $720\,\mathrm{cm^2\,V^{-1}s^{-1}}$. At low temperatures, neutral impurity and then, between around 10 and 100 K, ionised impurity scattering dominates. A quirk of the model was that the low temperature mobility seemed to be improved with increasing x due to the reciprocal dependence of neutral impurity scattering on effective mass. However, we do not wish to place too much confidence in this result, (10.122) being only a rough model. Moreover, the low temperature mobility did not reflect experimental results [8] well, although these data are for 2D. We attribute this, in part, to not having modelled defect scattering, which probably gives rise to the observed thermally activated mobility.

It should be pointed out that the calculations in [19] were performed using the density of states given by (10.5), rather than the modified density of states derived using the Green's function. The authors were aware of the problem of the density of states and addressed it by imposing a Lorentzian broadening of

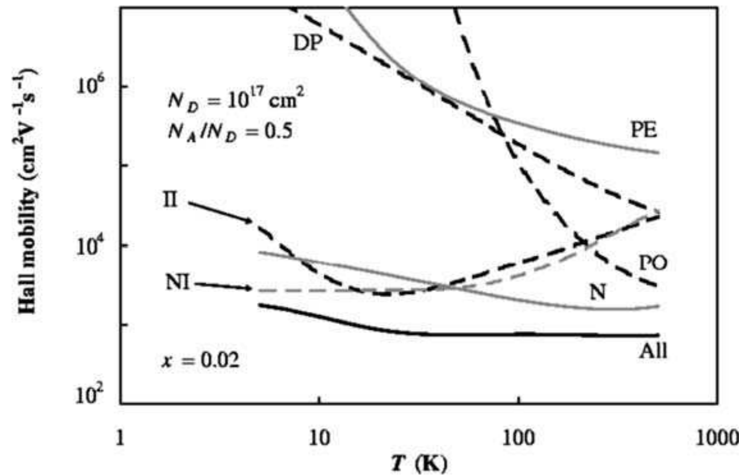

Fig. 10.3. Calculated mobilities showing the contribution of individual processes: polar optical (PO), deformation potential (DP) and piezoelectric (PE) phonon scattering; ionized (II) and neutral (NI) impurity scattering and nitrogen (N) scattering. N_D and N_A are the donor and acceptor concentrations, respectively. The *bottom solid line* shows the resultant mobility due to all processes

the nitrogen level, chosen so that the integral of the modified density of states equalled the integral of the parabolic density of states plus the number of nitrogen states per unit volume. No significant difference was found, although this is unsurprising, since the discrepancies arise quite high in the band where the Fermi factor is small.

Where the choice of density of states does make a difference is in the determination of the relaxation times. Reference [19] indicated that the relaxation times all tended to zero at the nitrogen energy E_{N}, suggesting that this is because the electron becomes immobile at this point. This is not quite correct, however. Even using modified density of states, in 3D the relaxation time will still converge to zero at E_{N} since it will be inversely proportional to $N_{\mathrm{3D}}(E)$. However, this should be interpreted as being due to the density of states, and hence the scattering rate, becoming infinite at this point. In 2D, using (10.13) for the density of states, this is no longer the case. Instead, the immobility of the electron at E_{N} emerges through the group velocity, which is zero at this point. This would enter the calculations through the mobility integrals (10.31) rather than being intrinsic to the relaxation time.

In conclusion, the high temperature mobility does appear to be limited by nitrogen scattering for $x > 0.02$, with the calculated values being close to that observed. However, the low temperature mobility exhibits a different temperature dependence to any form of alloy scattering and is probably due to material defects rather than scattering from nitrogen sites.

Acknowledgements. One of the authors (M.P.V.) would like to acknowledge the support of this research by an Engineering and Physical Sciences Research Council grant. We would also like to thank Prof. Eoin O'Reilly for many useful discussions.

References

1. C. Skierbiszewski, P. Perlin, P. Wisniewski, T. Suski, W. Walukiewicz, W. Shan, J.W. Ager, E.E. Haller, J.F. Geisz, D.J. Friedman, J.M. Olson, S.R. Kurtz, Phys. Status Solidi B Basic Res. **216**, 135 (1999)
2. S.R. Kurtz, A.A. Allerman, C.H. Seager, R.M. Sieg, E.D. Jones, Appl. Phys. Lett. **77**, 400 (2000)
3. W. Li, M. Pessa, J. Toivonen, H. Lipsanen, Phys. Rev. B **64**, 113308 (2001)
4. J. Teubert, P.J. Klar, W. Heimbrodt, K. Volz, W. Stolz, IEE Proc. Optoelectron. **151**, 357 (2004)
5. M. Weyers, M. Sato, H. Ando, Jpn. J. Appl. Phys. Pt. 2., **31**, L853 (1992)
6. W. Shan, W. Walukiewicz, J.W. Ager III, E.E. Haller, J.F. Geisz, D.J. Friedman, J.M. Olson, S.R. Kurtz, Phys. Rev. Lett. **82**, 1221 (1999)
7. S. Fahy, E.P. O'Reilly, Appl. Phys. Lett. **83**, 3731 (2003)
8. R. Mouillet, L.A. de Vaulchier, E. Deleporte, Y. Guldner, L. Travers, J.C. Harmand, Solid State Commun. **126**, 333 (2003)
9. R.T. Delves, Proc. Phys. Soc. **73**, 572 (1959)
10. K. Fletcher, P.N. Butcher, J. Phys. C: Solid State Phys. **5**, 212 (1972)

11. B.K. Ridley, J. Phys.: Condens. Matter. **10**, 6717 (1998)
12. D.R. Anderson, N.A. Zakhleniuk, M. Babiker, B.K. Ridley, C.R. Bennet, Phys. Rev. B **63**, 245313 (2001)
13. D.R. Anderson, Ph.D. Thesis, University of York, 2002
14. A. Lindsay, E.P. O'Reilly, Solid State Commun. **112**, 443 (1999)
15. J. Wu, W. Walukiewicz, E.E. Haller, Phys. Rev. B **65**, 233210 (2002)
16. P.W. Anderson, Phys. Rev. **124**, 41 (1961)
17. M.P. Vaughan, B.K. Ridley, Phys. Rev. B **75**, 195205 (2007)
18. B.K. Ridley, in *Quantum Processes in Semiconductors*, 4th edn. (Oxford, 1999)
19. M.P. Vaughan, B.K. Ridley, Phys. Rev. B **72**, 075211 (2005)
20. M.P Vaughan., Ph.D. Thesis, University of Essex, 2007
21. F.F. Fang, W.E. Howard, Phys. Rev. Lett. **16**, 797 (1966)
22. P. Tripathi, B.K. Ridley, Phys. Rev. B **66**, 195301 (2002)
23. J.W. Harrison, J.R. Hauser, Phys. Rev. B **13**, 5347 (1976)
24. P.A. Flinn, Phys. Rev. **104**, 350 (1956)
25. G.L. Hall, Phys. Rev. **116**, 604 (1959)
26. A.E. Asch, G.L. Hall, Phys. Rev. **132**, 1047 (1963)
27. Nordheim L, Ann. Phys. (Leibz.) **9**, 607 (1931)
28. D.K. Ferry, Phys. Rev. B **17**, 912 (1978)
29. J.A. Van Vechten, T.K. Bergstresser, Phys. Rev. B **1**, 3351 (1970)
30. J.C. Phillips, Phys. Rev. Lett. 20: 550 (1968); in *Bands and Bonds in Semiconductors* (Academic Press, 1973)
31. M. Auslender, S. Hava, Solid State Commun. **87**, 335 (1993)
32. S. Fahy, E.P. O'Reilly, Physica E **21**, 881 (2004)
33. S. Fahy, A. Lindsay, H. Ouerdane, E.P. O'Reilly, Phys. Rev. B **74**, 035203 (2006)
34. B.K. Ridley, B.E. Foust, L.F. Eastman, Phys. Rev. B **61**, 16862 (2000)
35. H. Brooks, Adv. Electron. Electron. Phys. **7**, 85 (1955)
36. C. Erginsoy, Phys. Rev. **79**, 1013 (1950)

11

Spin Dynamics in Dilute Nitride

X. Marie, D. Lagarde, V. Kalevich, and T. Amand

An overview of the electron spin properties in dilute nitride III–V semiconductors is given. We present optical orientation experiments in GaNAs epilayers and GaInNAs quantum wells, which show that a strong electron spin polarisation can persist at room temperature. Introducing about 1% of nitrogen in the binary (GaAs) or the ternary (GaInAs) alloy modifies drastically the electron spin dynamics. We demonstrate that the spin dynamics in dilute nitride structures is governed by a spin-dependent recombination process of free conduction electrons on deep paramagnetic centres. A non-linear theory of the spin dynamics in the coupled system of spin-polarised free and localised carriers is presented.

11.1 Introduction

The spin properties of carriers in semiconductors have been the subject of extensive studies for about 40 years [1–3]. Nevertheless, the longest spin relaxation times of electrons reported so far at room temperature in direct gap bulk semiconductors are rather short, typically a few hundreds of picoseconds [4–8]. The spin properties of dilute nitride semiconductors have attracted less attention probably due to the special features of this new class of materials. Recent works have indeed shown that the substitution of small amounts of nitrogen at anion sites in certain III–V semiconductors (GaAs, GaInAs, GaP) drastically modifies the optical and electronic properties of these materials, which are important for optoelectronic device applications [9–13]. A reduction of the band gap by more than 100 meV per atomic percentage of nitrogen was for instance observed in GaNAs and GaInNAs alloys. These modifications, which are still under investigation, result from the ability of N to form isoelectronic localised states that are resonant with the conduction band (CB) and strongly coupled to the extended CB states. Promising advances have recently been reported for 1.3 and 1.55 µm telecommunication quantum well lasers that employ this intriguing class of alloy materials [14–16]. Because

of the unusual characteristics of these alloys (nitrogen induced band structure modifications, presence of very localised electronic states), we can expect significant changes of the electron spin properties compared to nitrogen-free structures. We present in this chapter a review of experimental results and theoretical investigations of the electron spin dynamics in GaNAs and GaInNAs structures.

The chapter is organised as follows: In Sect. 11.2, we present the characteristics of the samples we have analysed (bulk and quantum well structures); we also describe briefly the experimental setups and recall the basis of optical orientation experiments. In Sect. 11.3, the experimental results on the circular polarisation dynamics of the photoluminescence (PL) in the bulk and quantum well samples are presented in detail. We demonstrate that a strong electron spin polarisation can persist at room temperature and the apparent electron spin relaxation time is longer than 2 ns. Finally the dependence of the total luminescence intensity dynamics as a function of the polarisation of the excitation laser is investigated in Sect. 11.4. Either the change of photoexcitation polarisation from circular to linear or the application of a transverse magnetic field (∼0.8 T) results in a decrease of the PL intensity decay time. We explain all these effects by a spin-dependent recombination process of free conduction electrons on deep paramagnetic centres.

11.2 Samples and Experimental Set-Up

The samples studied are grown by molecular beam epitaxy on (001) semi-insulating GaAs substrates. We have investigated the spin properties in two sets of samples.

The first one consists of a 100-nm thick GaN_yAs_{1-y} epilayer surrounded by GaAs layers on each side. The N content is $y = 0.021$ and $y = 0.012$ in sample A and sample B, respectively.

The second set of samples is composed of quantum well structures. Sample C consists of five $Ga_{1-x}In_xN_yAs_{1-y}$ QWs with a well width $L_W = 7$ nm, separated by 25 nm GaAs barriers. The indium and nitrogen compositions, determined from in situ intensity oscillations of Reflection High Energy Electron Diffraction and X-ray measurements, are $x = 0.33$ and $y = 0.0075$. To explore the role of nitrogen on the carrier spin properties, we also studied sample D, which contains two QWs grown under exactly the same conditions (same well width $L_W = 8$ nm, same indium content $x = 0.34$) separated by a 130 nm GaAs barrier. The first QW contains a nitrogen fraction $y = 0.006$, whereas the second QW is nitrogen free. In samples B, C and D, the N containing layers (as well as the GaInAs QW of sample D) were grown at 400°C, a relatively low temperature, to prevent alloy phase separation; the other epilayers were grown at 580°C, and no subsequent annealing was applied. Sample A was grown at 430–450°C, and a subsequent annealing at 700–720°C during 3 min was applied. All the samples are nominally undoped.

We have investigated the spin properties in these structures by time-resolved optical orientation experiments [17]. The principle is to transfer the angular momentum of the excitation photons using circularly polarised light to the photogenerated electronic excitations. If the carriers do not loose their spin polarisation during their lifetime, the luminescence will also be circularly polarised and will give information on both the symmetry of the carrier wavefunction and the spin relaxation time [2].

If the growth direction Oz is chosen as the quantization axis for the angular momentum, the conduction band in these GaAs type structures is s-like, with two spin states $s_{\mathrm{e},z} = \pm 1/2$; the upper valence band is split into a heavy-hole band with the angular momentum projection $j_{\mathrm{h},z} = \pm 3/2$ and a light-hole band with $j_{\mathrm{h},z} = \pm 1/2$ at the centre of the Brillouin zone.

Because of the lattice mismatch between GaAs and GaNAs, the GaNAs epilayers studied here are elastically strained: Because of the biaxial tension, the top of the light-hole band lies above the heavy-hole band. Conversely, the GaInAs(N)/GaAs samples studied here are under biaxial compression (because of the Indium content): the top of the heavy-hole sub-band lies above the light-hole sub-band [14–16].

The samples are excited by 1.5 ps pulses generated by a mode-locked Ti-doped sapphire laser with a repetition frequency of 80 MHz. The time resolved PL is then recorded using a S1 photocathode Hamamatsu Streak Camera with an overall time-resolution of 8 ps. The excitation pulses are circularly polarised (σ^+) using a Soleil Babinet compensator. The luminescence intensity components co-polarised (I^+) and counter-polarised (I^-) with the excitation laser are recorded. The circular polarisation degree of the luminescence is defined as $P_\mathrm{c} = (I^+ - I^-)/(I^+ + I^-)$. Since the spin relaxation times of the photogenerated holes is less than 1 ps at room temperature [18], it appears that the circular polarisation degree of the luminescence corresponds directly to the electron spin polarisation degree defined as $P_\mathrm{s} = (n^+ - n^-)/(n^+ + n^-)$; $n^+(n^-)$ is the spin-down (spin-up) electron population [1, 2].

11.3 Experimental Results

Figure 11.1a presents the time-integrated PL spectrum co-polarized (I^+) and counter-polarised (I^-) with the excitation laser measured in sample A at room temperature. The excitation laser energy ($E_\mathrm{exc} = 1.392\,\mathrm{eV}$) corresponds to the photogeneration of carriers in the GaNAs epilayer, slightly below the GaAs gap. Very similar results are obtained for an excitation energy above GaAs.

We clearly see that the circular polarisation P_c is negative (opposite to the helicity of the excitation laser) in the low energy part of the spectrum (long wavelength), whereas it is positive on the high energy part. This effect is due to the thermal population at room temperature of both the heavy-hole and light-hole bands in GaNAs: the splitting of the heavy hole and light hole due to the biaxial tension is about 24 meV, i.e. close to $k_\mathrm{B}T$ [19]. The

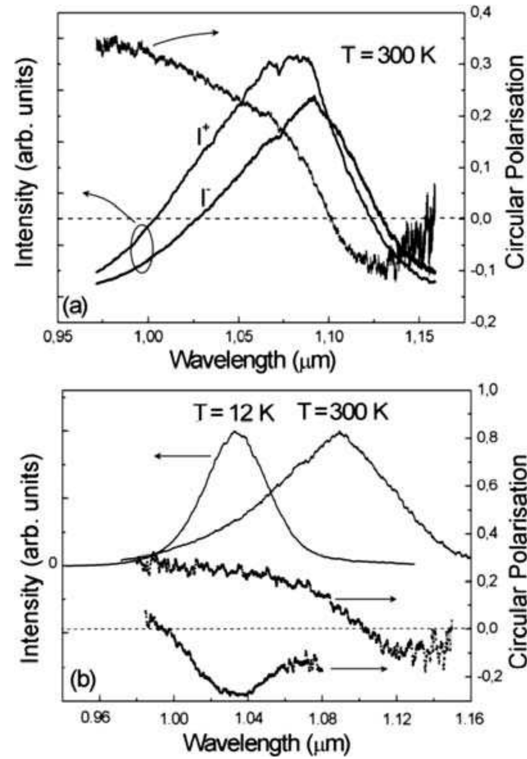

Fig. 11.1. Sample A: (a) Time-integrated PL spectra of $GaAs_{1-y}N_y$ epilayer ($y = 2.1\%$) co-polarised (I^+) and counter-polarised (I^-) with the circularly polarised (σ^+) excitation laser. The dots display the corresponding circular polarisation. (b) Total PL intensity spectra ($I^+ + I^-$) for two temperatures $T = 12$ K and $T = 300$ K. The dots display the PL circular polarisation; the PL intensity spectra have been normalised

positive (negative) circular polarisation on the high (low) energy part of the spectrum comes respectively from the recombination of conduction electrons with heavy (light) holes as expected by the well-known selection rules in III–V semiconductors [2].

In Fig. 11.1b, the time-integrated PL spectra of sample A and the corresponding circular polarisation are displayed for two temperatures: $T = 12$ K and $T = 300$ K. The laser excitation energy is 1.44 eV. At low temperature ($T = 12$ K), only the light-hole band is populated and the circular polarisation is negative in the all spectrum, in contrast to the spectrum at $T = 300$ K where a clear reversal of the helicity of the PL circular polarisation is observed.

In all these time-integrated spectra, we measure a rather high absolute value of the circular polarisation. This indicates that the spin relaxation time of electrons is close to or longer than their lifetime. The circular polarisation

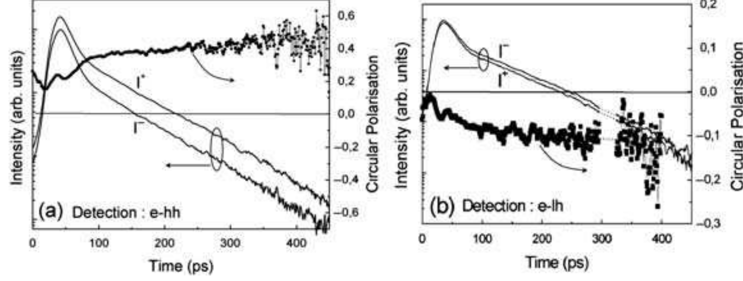

Fig. 11.2. Sample A: Time evolution of the circular luminescence components (I^+) and (I^-) after a (σ^+) polarised excitation. The circular polarisation (right axis) is also displayed. The detection wavelength is (**a**) $\lambda_{\mathrm{det}} = 1\,\mu\mathrm{m}$(*e-hh*) and (**b**) $\lambda_{\mathrm{det}} = 1.12\,\mu\mathrm{m}$(*e-lh*). The absence of data around $\sim$300 ps in (b) is due to a problem of detector

dynamics of sample A is presented in Figs. 11.2a and 11.2b for two detection energies $E_{\mathrm{det}} = 1.24\,\mathrm{eV}$ (*e-hh*) and $E_{\mathrm{det}} = 1.127\,\mathrm{eV}$ (*e-lh*) respectively (the corresponding wavelengths are $\lambda_{\mathrm{det}} = 1\,\mu\mathrm{m}$ and $\lambda_{\mathrm{det}} = 1.12\,\mu\mathrm{m}$); the experimental conditions are the same as in Fig. 11.1a. In both cases, we observe almost no decay of the circular polarisation during the PL lifetime. This indicates that the relaxation time τ of the average electron spin $\langle S_{\mathrm{z}} \rangle$ at room temperature in these structures is much longer than the electron lifetime. From Fig. 11.2, we can infer that τ is longer than 2 ns.

This strong electron spin memory we measured in epilayers is a general feature of dilute nitride GaNAs or GaInNAs structures since we have observed it also in quantum wells as presented below [20, 21].

Figure 11.3a displays, for instance, the time-integrated PL spectrum co-polarized (I^+) and counter-polarized (I^-) with the excitation laser at room temperature in sample C (five GaInNAs/GaAs quantum wells). The excitation laser energy ($E_{\mathrm{exc}} = 1.44\,\mathrm{eV}$) corresponds to the photogeneration of carriers in the bulk GaAs barrier. Because of the well-known optical selection rules in bulk semiconductors, the relative concentration of optically generated spin-down to spin-up electrons is 3:1, leading to a maximum spin polarisation of electrons $P_{\mathrm{s}} = 50\%$ [2]. Remarkably we see in Fig. 11.3a that the electron spin polarisation in the GaInNAs QWs (where $P_{\mathrm{s}} = P_{\mathrm{c}}$) is about 40% compared to the photogenerated electron spin polarisation in the barrier $P_{\mathrm{s}} = 50\%$, as if almost no spin relaxation occurred during the energy relaxation and the subsequent radiative recombination in the QWs.

Figure 11.3b presents the corresponding circular polarisation dynamics after a picosecond laser excitation pulse in the GaAs barrier. As in the epilayers, we find here that the high circular polarisation degree remains almost constant with no measurable decay on the luminescence lifetime scale. We can infer that the apparent spin relaxation time is again longer than 2 ns, i.e. 50 times longer than the decay time of the luminescence intensity.

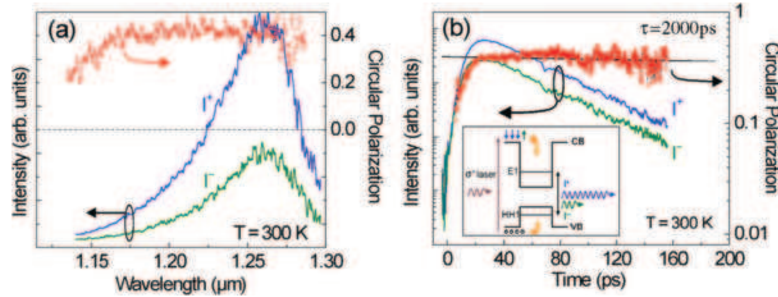

Fig. 11.3. Sample C. Nitrogen fraction in the QWs: $y = 0.0075$. (**a**) Time-integrated PL spectra of the QW luminescence components co-polarized (I^+) and counter-polarised (I^-) with the circularly polarised laser excitation (left axis). The dots represent the corresponding circular polarisation (right axis). (**b**) Time evolution of the circular luminescence components (I^+) and (I^-) after a (σ^+) polarised picosecond excitation pulse (left axis). The circular polarisation dynamics is also displayed (right axis in logarithmic scale); the full line is an exponential fit with a decay time $\tau \sim 2{,}000$ ps. The inset presents the schematic of the optical generation of carriers in the bulk barrier and the detection of the polarized components of the QW luminescence. The laser excitation energy is $h\nu = 1.44$ eV, i.e. above the GaAs energy gap

Most striking is the contrast between the spin dynamics of a single GaInAs QW and that of a single GaInNAs QW. Figure 11.4a presents the circular polarisation of the time-integrated PL in a GaInNAs QW and in the same QW without N (sample D) for the same excitation conditions at room temperature. One can see a much stronger electron spin memory ($P_s \sim 30\%$) in the dilute nitride QW compared to the one in the N-free layer ($P_s \sim 5\%$). We found in Fig. 11.4b that the electron spin relaxation time τ in the dilute nitride QW is at least 20 times longer than the one in the N-free QW: $\tau(\text{GaInNAs}) > 1{,}000$ ps and τ (InGaAs) ~50 ps. It is important to note that the nitrogen content in the GaInNAs QW is a mere 0.6%. The decay time of the luminescence intensity is $\tau_{\text{lum}} \sim 140$ ps (60 ps) in the GaInAs (GaInNAs) QW. Let us recall that spin relaxation time of the order of 100 ps at room temperature is typical in undoped III–V semiconductors [8,22,23]. This means that the relaxation time of the electron spin polarisation degree in dilute nitride QW is more than 10 times longer than in N-free structures.

It should be stressed that we observe long $\langle S_z \rangle$ relaxation times at room temperature whatever the strain value of the structure is: in samples C and D, the QW are compressively strained, whereas in sample A and B the GaNAs epilayers are under elastic tension [15,16,24,25].

We believe that the strong electron spin memory observed here is due to the unusual electronic properties of dilute nitride III–V structures. It has been shown that the introduction of nitrogen in GaAs or GaInAs strongly modifies the CB, whereas it does not affect the Valence Band (VB). Substitutional

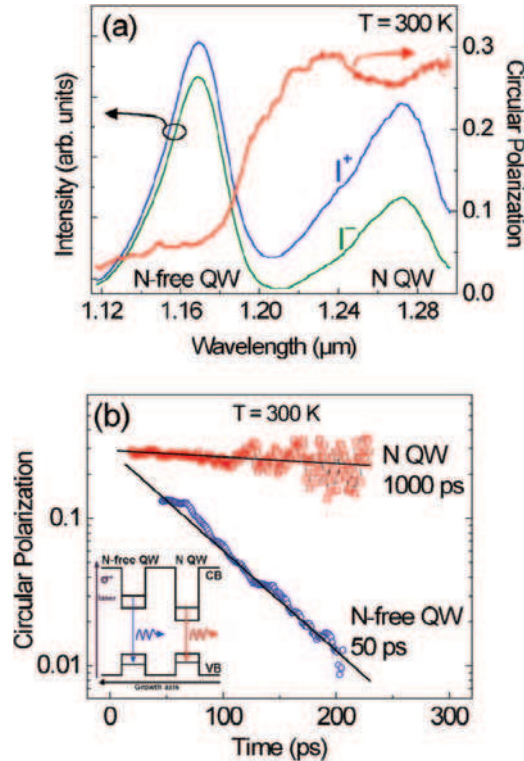

Fig. 11.4. Sample D. nitrogen fraction in the N-QW: $y = 0.006$. (**a**) Time-integrated spectra of the luminescence components co-polarised (I^+) and counter-polarised (I^-) with the circularly polarised laser excitation. The dots represent the corresponding circular polarisation. (**b**) Time evolution of the circular polarisation of the luminescence components of the N-QW (open squares) and the N-free QW (open circles). The full lines are exponential fits of the decays. The laser excitation energy is $h\nu = 1.44\,\text{eV}$

nitrogen atoms form perturbed host states inside the CB, whereas small nitrogen aggregates form localised cluster states in the band gap [24–26]. For typical nitrogen content of the order of $\sim 1\%$, there is a coexistence of localised states overlapping with delocalised ones. It has been shown that the localised–delocalised duality of the conduction band leads to anomalous temperature and pressure effects in optical spectroscopy experiments [26,27]. The introduction of nitrogen also leads to the formation of defects that trap the free carriers yielding rather short luminescence decay times at room temperature ($<\sim 100\,\text{ps}$) [27, 28]. The strong electron spin memory at room temperature observed here could be interpreted as arising from the quenching of the classical spin relaxation mechanisms due to the strongly localised character of the electron wavefunction. The interpretation is in fact more complicated. In

the next section, we show that the electron spin dynamics in dilute nitride structures is strongly affected by a Spin-Dependent Recombination (SDR) process, which explains the apparent long spin memory of conduction electrons at room temperature.

11.4 Electron Spin Dynamics and Spin-Dependent Recombination

It turns out that the very long conduction electron average spin lifetime measured at $T = 300\,\mathrm{K}$ in GaNAs is strongly linked to the special features of the recombination processes of free electrons. We demonstrate in this section that both the giant value of the circular polarisation observed at room temperature and its persistence over 2 ns can be explained by the spin-dependent capture of photogenerated conduction electrons on deep paramagnetic centres.

The experimental evidence of this SDR mechanism is shown in Fig. 11.5a for sample A, where we have recorded the total luminescence intensity $(I^+ + I^-)$ as a function of time for a circularly polarised (σ^+) or linearly polarized (σ^x) excitation laser. The laser excitation energy is $E_{\mathrm{exc}} = 1.44\,\mathrm{eV}$ (i.e. above the GaAs barriers); very similar results are again observed for an excitation energy below the GaAs gap. The remarkable feature in Fig. 11.5a is that the total PL intensity decay time is *four times* shorter for a linearly polarised excitation laser compared to the one for circularly polarised excitation. We measure $\tau_{\mathrm{lum}}^{\sigma^x} \sim 20\,\mathrm{ps}$ and $\tau_{\mathrm{lum}}^{\sigma^+} \sim 85\,\mathrm{ps}$. We present here the data at room temperature but we have observed this effect from $T = 10\,\mathrm{K}$ to $T = 350\,\mathrm{K}$.

It is well known that (a) the introduction of nitrogen in GaAs yields the formation of a large density of non-radiative defects [29] and (b) the PL intensity decay time at $T = 300\,\mathrm{K}$ is not controlled by the intrinsic radiative recombination time but by the non-radiative recombination time on these

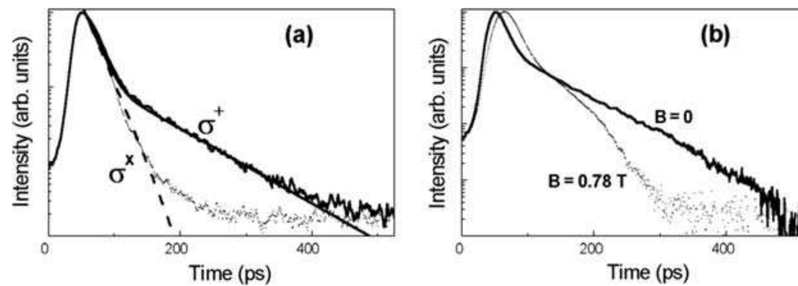

Fig. 11.5. Sample A: $T = 300\,\mathrm{K}$ Total PL intensity dynamics (**a**) under circular (σ^+) and linear (σ^x)-polarised excitation for an applied magnetic field $B = 0$ and (**b**) under circular (σ^+)-polarized excitation with $B = 0$ or $B = 0.78\,\mathrm{T}$. Solid and dashed curves in (a) correspond to the calculated PL intensity dynamics (see text)

defects [27,28]. The data in Fig. 11.5a show that this capture time depends on the spin polarisation of the photogenerated free electrons. This effect, called Spin-Dependent Recombination, has been observed 30 years ago in Si, GaAs and GaAlAs at low temperatures [30–33]. The SDR mechanism is due to the well known Pauli principle, which states that two electrons cannot have the same spin orientation in the same orbital state. The key point in SDR is the existence of a deep centre that possesses an unpaired electron before trapping a conduction electron: this centre is thus paramagnetic. As a consequence, if the photogenerated electron in the CB and the resident electron on the deep centre have the same spin, the photogenerated electron cannot be captured by the centre [34]. On the contrary, when the photogenerated electron and the resident electron on the deep centre have antiparallel spins, the capture will be efficient. In other words, the recombination time of photocreated electrons depends on the relative spin orientation of the free electron and of the electron resident on the centre.

In the SDR model developed initially by Weisbuch and Lampel in GaAlAs, the electrons resident on the deep centres are assumed to be unpolarised in the absence of light; they become polarised after the photogeneration of free spin-polarised electrons in the CB [31]. The mechanism is the following:

1. The centre can only capture a photogenerated electron from the CB with a spin antiparallel to the spin of the electron already present.
2. When two electrons of opposite spins occupy a centre, one of them (of either spin) can recombine radiatively or not with a photogenerated hole in the VB, leaving the centre again with a single resident electron (if this recombination is radiative, we do not detect it since it occurs at much lower energy than the detected interband PL [33]).
3. Since the capture on the centre is spin-dependent but the recombination process of the electrons trapped on the centre does not depend on the spin, this leads to a dynamic polarisation of the centres: after a few cycles, they become spin-polarised. This mechanism is schematically presented in Fig. 11.6

In Fig. 11.5a, the SDR effect is clearly observed. When the excitation laser is linearly polarized, i.e. the photogenerated electrons have random spin orientation, the average capture time on the centres (measured by the PL decay time) is short (Fig. 11.6c). On the contrary, when the laser is circularly polarised, i.e. the photogenerated electrons are spin polarised, the capture of the electrons in the same spin state as the one of the centre is blocked and the overall capture time will be longer (Fig. 11.6b).

An alternative way to characterise the SDR effect is to compare the ratio $R_{\mathrm{SDR}} = I_{\mathrm{PL}}(\sigma^+)/I_{\mathrm{PL}}(\sigma^x)$, where $I_{\mathrm{PL}}(\sigma^+)$ and $I_{\mathrm{PL}}(\sigma^x)$ are the total PL intensity under circularly (σ^+) or linearly (σ^x) polarised laser excitation [35]. If the SDR effect occurs, $I_{\mathrm{PL}}(\sigma^+)$ will be larger than $I_{\mathrm{PL}}(\sigma^{\mathrm{x}})$ since the total PL intensity decay time (due to the electron capture on the paramagnetic centres) is larger for (σ^+) excitation compared to (σ^{x}) excitation.

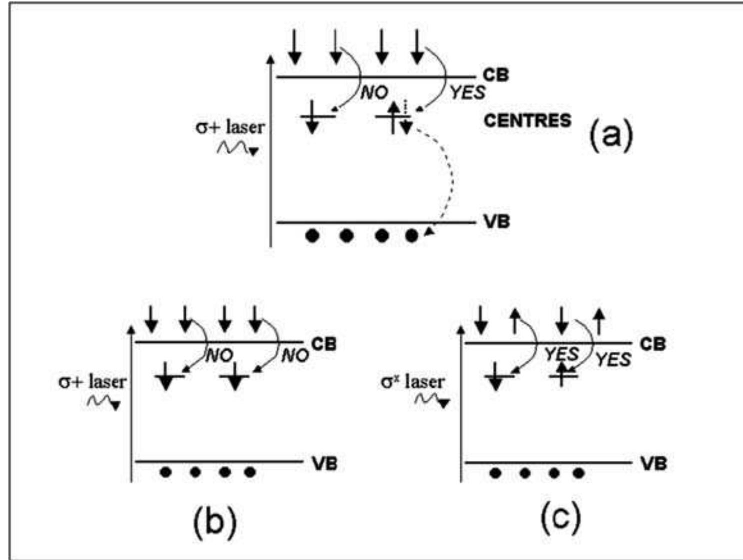

Fig. 11.6. Schematic representation of the spin states of free photogenerated electrons and deep centres (**a**) at $t = 0$ just after the (σ^+)-polarised excitation laser; for simplicity we assume here that the photogenerated electron spin polarisation is 100%. In (**b**) and (**c**) the spins configurations are presented for a (σ^+)-polarised excitation (once the centres have been dynamically polarised) or for a (σ^x) excitation (see text)

Weisbuch and Lampel measured for instance $R_{\mathrm{SDR}} \sim 230\%$ in GaAlAs at $T = 10\,\mathrm{K}$ [31]. Miller et al. got a SDR ratio of 140% in GaAs superlattices at $T = 10\,\mathrm{K}$ [32]. According to Paget the SDR effect in these materials were observed in a very small number of samples. Paget managed to observe a small SDR effect (R_{SDR} slightly larger than 100%) in bulk GaAs at $T = 5\,\mathrm{K}$ [33]. Figure 11.7a shows the total time integrated PL intensity spectra in sample A after (σ^+) or (σ^x)-polarised excitation. The SDR ratio measured here is $R_{\mathrm{SDR}} \sim 175\%$ at $T = 300\,\mathrm{K}$. Note that Kalevich et al. measured $R_{\mathrm{SDR}} \sim 300\%$ in the same sample in cw PL experiments (using a very different photogenerated density) [36]. The observation of such strong effect in Figs. 11.5a and 11.7a means that the photogenerated electron density is much larger than the density of deep centres. Figure 11.7b displays the dependence of R_{SDR} as a function of the excitation power. As expected, the SDR vanishes at low excitation power when the photogenerated carrier density is close or smaller than the paramagnetic centre density. Taking into account the absorption volume and coefficient of GaNAs, we can estimate that the photogenerated carrier density at the point of disappearance of the SDR effect ($\mathrm{P} = 2.5\,\mathrm{mW}$) is $N_{\mathrm{carriers}} \approx 1.6 \cdot 10^{16}\mathrm{cm}^{-3}$. From the above discussion we can thus infer that the density of the deep centres is of the same order of magnitude.

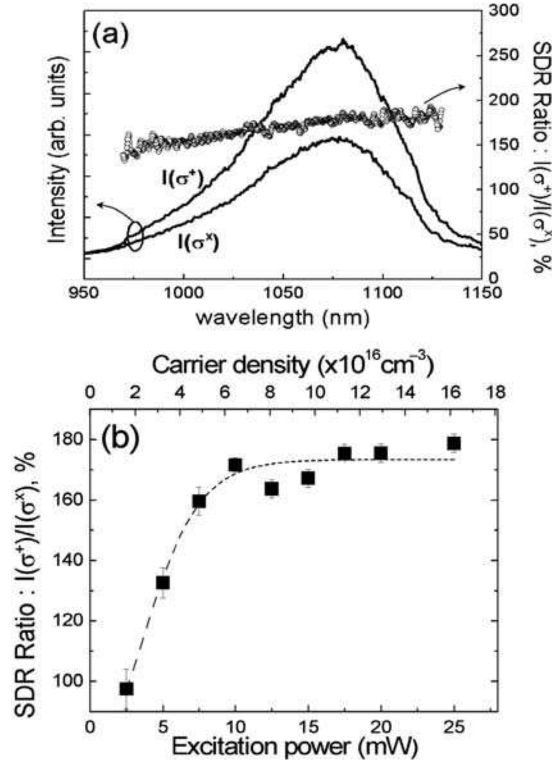

Fig. 11.7. Sample A: (**a**) Ratio between the total time-integrated PL intensity under circular (σ^+) and linear (σ^{x}) excitation as a function of the emission wavelength. The excitation power is 20 mW. (**b**) Excitation power dependence of the SDR Ratio. The excitation energy is $E_{\mathrm{exc}} = 1.392\,\mathrm{eV}$, i.e. below the GaAs gap

To our knowledge the SDR effect in GaNAs is the first one observed (i) at room temperature in III–V semiconductor and (ii) in a structure of intrinsic conductivity type (undoped material).

We observed the SDR effect in 6 different GaNAs samples with nitrogen fractions varying from 0.6 to 3.4%. These samples were grown in two MBE machines from two different laboratories. No SDR effect is observed in GaAs material grown at the same temperature as GaNAs. We thus strongly believe that the SDR process is due to a paramagnetic centre, directly related to the introduction of nitrogen in GaAs.

The SDR effect has also a great impact on the electron spin dynamics. The time evolution of the average spin of free electrons will depend on the spin polarisation of the centres. As the polarised centres do not capture electrons of opposite spin with the same speed, this produces an accumulation of electrons with a given spin ($s_z = -1/2$ if the excitation laser is (σ^+) polarised), as shown in Fig. 11.6b. Paget observed this effect in bulk GaAs

at low temperature where the polarized centres act as a 'spin filter' for the conduction electrons (note that the SDR effect measured in GaAs was very small, i.e. a few percents) [33].

A similar phenomenon is measured here in GaNAs at room temperature: the large value of the circular polarisation and its long decay time observed in Fig. 11.2 can be understood in terms of the formation of a coupled spin-system of free and localised electrons. Since (a) the capture of a photogenerated electron in the same spin state as the one of the resident electron is blocked and (b) the spin relaxation of the resident electron on the deep centre is slow, the dynamic polarisation of deep centres causes an initial increase of the polarisation of conduction electrons. This effect is clearly observed in Fig. 11.2a: the circular polarisation degree increases from 20 to 40% from $t = 0$ to $t = 100$ ps.

For longer delays, the PL circular polarisation dynamics is not controlled by the spin relaxation time of conduction electrons but by the spin relaxation of the electron on the deep centres. This can be explained qualitatively as follows. If a conduction electron experiences a spin flip once the centres have been dynamically polarised, this electron will then have a spin antiparallel to one of the centre. It will thus be quickly captured on the centre. As a consequence, this spin flip of the conduction electron does not affect the average spin of the conduction electrons (one electron has just disappeared from the CB), see Fig. 11.6. There will thus be no effect on the value of the PL circular polarisation. On a longer time scale, the average spin of the conduction electrons could be affected by the spin relaxation of the electrons on the centres. Experimentally, we observe in Fig. 11.2 no decay of the PL circular polarisation on the timescale of the luminescence decay time. This means that the spin flip of electrons on the centre is longer than 2 ns [36].

An important finding of this study is that the spin flip of conduction electrons does not yield a decay of the PL circular polarisation but we predict in this interpretation that it leads to a decay of the conduction electron density and thus a decay of the total PL intensity. We see in Figs. 11.2a and 11.2b that the PL intensity dynamics is characterised by a bi-exponential decay.

The scenario can be presented in the following way when the density of photoinjected carriers is larger than the deep centres density. After the photogeneration of carriers, the electron capture on the centres is initially very fast (almost not resolved in the experiments) but it stops quickly when all the centres are occupied by two electrons. The fast electron capture is then blocked and the further capture is controlled by the photogenerated hole non-radiative recombination with one of the two electrons localised on the centre. As a consequence, the first decay of the luminescence intensity in Figs. 11.2a and 11.2b corresponds to the hole lifetime due to the recombination of deep centres occupied by 2 electrons (singlet): $I \propto \exp(-2t/\tau_h)$; we measure $\tau_{\mathrm{h}} \sim 30$ ps. This first regime ends at the moment when the spin minority photoelectrons disappear from the conduction band. As described above, the second decay time of the total PL intensity is then the spin relaxation time of free electrons: we find $\tau_{\mathrm{s}} \sim 130$ ps.

It is interesting to note that the measurement of a spin relaxation time through the analysis of the total PL intensity decay time was already performed in GaAs and GaInAs quantum wells [37, 38]. In these systems the single particle hole spin flip at $T = 4\,\mathrm{K}$ is accompanied by a drop of the total luminescence intensity because of the transfer from optically active excitons to non-optically active excitons; this hole spin flip had no consequence on the spin polarisation of the optically active excitons. This situation is very similar to the GaNAs system: the deep centres simply play the role of the non-optically active excitons.

To confirm the qualitative interpretation presented above, we have developed a non-linear theory of the spin dynamics in the coupled system of spin-polarised free and trapped electrons [36].

In this model, the density of free electrons and paramagnetic centres with spins $s_z = \pm 1/2$ is labelled $n_\pm$ and $N_\pm$ respectively; p corresponds to the hole density (we recall that the holes are not spin polarized [18]). The density of centres occupied by two electrons is noted $N_{\uparrow\downarrow}$. The rate of free electrons capture on the centre is written: $(\mathrm{d}n_\pm/\mathrm{d}t)_{\mathrm{cap}} = -\gamma_e n_\pm N_\mp$. We neglect in this model the radiative recombination time in the interband transition since it is much longer than the non-radiative capture time on the deep centres. The time evolution of $n_\pm$, $N_\pm$, $N_{\uparrow\downarrow}$ and p is governed by the following rate equations:

$$\begin{cases} \frac{\mathrm{d}n_\pm}{\mathrm{d}t} = -\gamma_e n_\pm N_\mp - \frac{n_\pm - n_\mp}{2\tau_{\mathrm{s}}} + G_\pm \\ \frac{\mathrm{d}N_\pm}{\mathrm{d}t} = -\gamma_e n_\mp N_\pm - \frac{N_\pm^- N_\mp}{2\tau_{\mathrm{sc}}} + \frac{1}{2}\gamma_h p N_{\uparrow\downarrow} \\ \frac{\mathrm{d}N_{\uparrow\downarrow}}{\mathrm{d}t} = \gamma_e \left(n_- N_+ + n_+ N_-\right) - \gamma_h p N_{\uparrow\downarrow} \\ \frac{\mathrm{d}p}{\mathrm{d}t} = -\gamma_h p N_{\uparrow\downarrow} + G_+ + G_- \end{cases} \tag{11.1}$$

where τ_{s} and τ_{sc} are the spin relaxation time of free and localised electron on the centre respectively; $G_\pm$ is the photogeneration rate of electrons with spin $s_z = \pm 1/2$; $\gamma_e(\gamma_h)$ is the electron (hole) recombination coefficient. These equations have been solved numerically.

Figure 11.8 displays the time-resolved total PL intensity and circular polarisation in sample A at $T = 300\,\mathrm{K}$. The excitation and detection conditions are similar to the ones of Fig. 11.2b. The dashed curves are the result of the calculation based on (11.1). The agreement between the experiments and the calculations is very good.

The parameters are the effective hole lifetime $\tau_h = 1/\gamma_h N_{\uparrow\downarrow} = 35\,\mathrm{ps}$ and the spin relaxation time of the free electrons $\tau_{\mathrm{s}} = 130\,\mathrm{ps}$. As indicated above, these two parameters correspond to the two decay times of the total PL intensity. The calculation is done for a ratio between the photogenerated electron density and the centre density of 30. The last parameter is the ratio $\gamma_e/\gamma_h = 10$. The calculations are done for a spin relaxation time of the centres of $\tau_{\mathrm{sc}} = 2{,}000\,\mathrm{ps}$ but the fit is not very sensitive to this parameter since the circular polarisation experiences almost no decay during the PL intensity decay time.

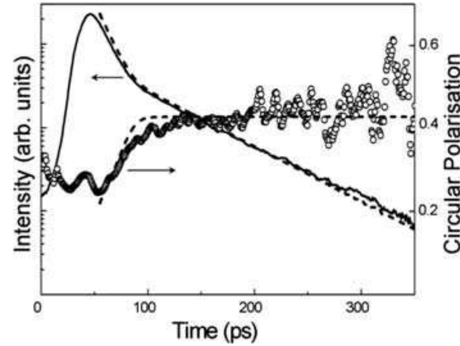

Fig. 11.8. Sample A: $T = 300\,\mathrm{K}$ Time-resolved total PL intensity (solid line) and circular polarisation (circles). Dashed curves are the results of the calculations (see text)

We used the same model to calculate the total PL intensity dynamics after a circularly polarised σ^+ or a linearly polarised σ^x excitation. The dashed lines in Fig. 11.5a display the results of the calculations. We see again that the agreement between the experimental results and the theory is very satisfactory.

The validity of the SDR interpretation in GaNAs is further confirmed by the measurement of the electron spin dynamics in a transverse magnetic field B_x (Voigt geometry). Figure 11.9 presents the time evolution of the luminescence intensity component co-polarised (I^+) and counter-polarised (I^-) with the (σ^+) polarised excitation laser in a transverse magnetic field $B_x = 0.78\,\mathrm{T}$. The (I^+) and (I^-) oscillations reflect the electron spin precession around B_x [39, 40]. Figure 11.5b displays the total PL intensity under (σ^+) polarised laser excitation for $B = 0$ and $B_x = 0.78\,\mathrm{T}$; the excitation energy is $1.392\,\mathrm{eV}$ (below the GaAs gap). We observe a shorter decay time when the transverse magnetic field is applied.

This is a direct consequence of the spin-dependent capture of electrons on deep centres. The electron spin precession due to the magnetic field cancels the dynamic polarisation of the centres and hence the accumulation of polarised free electrons in the CB. As observed by Kalevich et al. in cw experiments, the same total PL intensity is measured under circularly (σ^+) excitation in a transverse magnetic field and under linearly (σ^x) excitation for $B_x = 0$ [36].

The oscillation period T of the PL circular polarisation in Fig. 11.9 yields in principle the direct evaluation of the free electron g factor since $T = h/\left(g\mu_B B_x\right)$, μ_B is the Bohr magneton. This would give $|\mathrm{g}(\mathrm{GaN}_{0.021}\mathrm{As}_{0.979})| \sim 0.6$ [41]. Let us recall that the electron g factor in bulk GaAs is $g = -0.44$ [2]. However the interpretation of the oscillations observed in Fig. 11.9 must be done more carefully because of the SDR effect. The particular features of the coupled system of spin-polarised free and localised electrons have to be taken into account. As a matter of fact the magnetic field induces both a precession

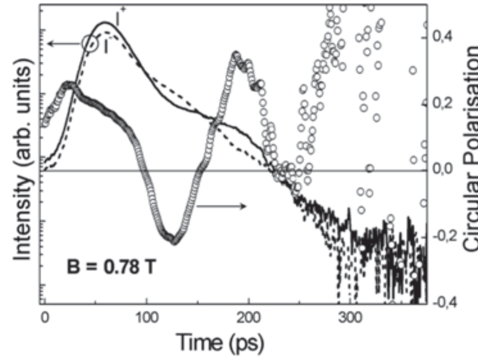

Fig. 11.9. Sample A: $T = 300\,\mathrm{K}$ Time evolution of the circular luminescence components I^+ (solid line) and I^- (dashed line) under (σ^+)-polarised excitation in a transverse magnetic field $B = 0.78\,\mathrm{T}$. The dots correspond to the circular polarisation

of the free electron in the CB and a precession of the single electron localised on the paramagnetic centre (when the centre is occupied by a singlet, no precession occurs).

This precession of the electron on the paramagnetic centre may have consequences on the time evolution of the polarised luminescence components measured in Fig. 11.9. A model taking into account both the SDR effect and interaction of the electrons (free and localised) with the transverse magnetic field is under development [42].

11.5 Conclusion

In summary, we have shown that the spin properties of dilute nitride semiconductor alloys are markedly different to that of conventional alloys. A very large PL circular polarisation is observed at room temperature in optical orientation experiments both in bulk epilayers and in quantum well structures.

It turns out that the spin dynamics in dilute nitride structures is governed by a spin-dependent recombination process of free conduction electrons on deep paramagnetic centres. As the dynamic polarisation of deep centres causes an increase of the polarisation of conduction electrons, these dilute nitride materials could thus be used as efficient spin-filters.

Acknowledgments. The authors wish to thank L. Lombez, A. Balocchi, P.F. Braun, P. Renucci, H. Carrère, E. Egorov, A. Shirayev, A. Egorov, E. Ivchenko, V. Ustinov and J.C. Harmand for their contributions to this work. X.M. is grateful to Institut Universitaire de France for financial support.

References

1. G. Lampel, Phys. Rev. Lett. 20, 491 (1968)
2. F. Meier, B.P. Zakharchenya, *Optical Orientation* (North-Holland, New York, 1984)
3. I. Zutic, J. Fabian, S. Das Sarma, Rev. Mod. Phys. 76, 323 (2004)
4. J.M. Kikkawa, D.D. Awschalom, Phys. Rev. Lett. 80, 4313 (1998)
5. B. Murdin, L. Litvinenko, J. Allam, C. Pidgeon, M. Bird, K. Morrison, T. Zhang, T. Clowes, W. Branford, J. Harris, L. Cohen, Phys. Rev. B 72, 85346 (2005)
6. J.M. Kikkawa, I.P. Smorchkova, N. Samarth, D.D. Awschalom, Science 277, 1284 (1997)
7. R. Dzhioev, K. Kavokin, V. Korenev, M. Lazarev, B. Meltser, M. Stepanova, B. Zakharchenya, D. Gammon, D. Katzer, Phys. Rev. B 66, 245204 (2002)
8. T. Boggess, J. Olesberg, C. Flatté, W. Lau, Appl. Phys. Lett. 77, 1333 (2000)
9. M. Kondow, T. Kitatani, S. Nakatsuka, M. Larson, K. Nakahara, Y. Yazawa, M. Okai, IEEE J. Sel. Top. Quantum Electron. 3, 719 (1997)
10. P. Kent, A. Zunger, Phys. Rev. B 64, 115208 (2001)
11. A. Lindsay, E. O'Reilly, Phys. Rev. Lett. 93, 196402 (2004)
12. L. Grenouillet, C. Bru-Chevallier, G. Guillot, P. Gilet, P. Duvaut, C. Vannuffel, A. Million, A. Chenevas-Paule, Appl. Phys. Lett. 76, 2241 (2000)
13. P. Klar, H. Gruning, J. Koch, S. Shafer, L. Volz, W. Stolz, H. Heimbrodt, A. Kamal Saadi, A. Lindsay, E. O'Reilly, Phys. Rev. B 64, 121203 (2001)
14. M. Kondow, T. Kitatani, K. Nakahara, T. Tanaka, Jpn. J. Appl. Phys. 38, L1355 (1999)
15. M. Hofmann, A. Wagner, C. Ellmers, C. Schlichenmeier, S. Schafer, F. Hohnsdorf, J. Koch, W. Stolz, S.W. Koch, W.W. Rühle, J. Hader, J.V. Moloney, E.P. O'Reilly, B. Borchert, A.Y. Egorov, H. Riechert, Appl. Phys. Lett. 78, 3009 (2001)
16. H. Carrere, X. Marie, T. Amand, J. Barrau, Appl. Phys. Lett. 86, 71116 (2005)
17. B. Dareys, X. Marie, T. Amand, J. Barrau, Y. Shekun, I. Razdobreev, R. Planel, Superlattices Microstr. 13, 353 (1993)
18. Because of the fourfold degeneracy of the valence band in $k = 0$ and the large spin-orbit coupling in III–V semiconductors, the hole spin relaxation time at $T = 300\,\mathrm{K}$ is shorter than 1 ps. In GaAs, see for instance D.J. Hilton, C.L. Tang, Phys. Rev. Lett. 89, 146601 (2002)
19. A. Egorov, V. Kalevich, M. Afanasiev, A. Shiryaev, V. Ustinov, M. Ikezawa, Y. Masumoto, J. Appl. Phys. 98, 13539 (2005)
20. L. Lombez, P.F. Braun, H. Carrere, B. Urbaszek, P. Renucci, T. Amand, X. Marie, J.C. Harmand, V. Kalevich, Appl. Phys. Lett. 87, 252115 (2005)
21. We also measured electron spin relaxation times longer than 2 ns in a GaNAs sample with a controlled n-type doping ($n \sim 10^{17}\,\mathrm{cm}^{-3}$)
22. K. Jarasiunas, R. Aleksiejunas, V. Gudelis, L. Subacius, M. Sudzius, S. Iwamoto, T. Shimura, K. Kuroda, Y. Arakawa, Semicond. Sci. Technol. 19, S339 (2004)
23. A. Malinowski, R.S. Britton, T. Grevatt, R.T. Harley, D.A. Ritchie, M.Y. Simmons, Phys. Rev. B 62, 13034 (2000)
24. K. Kim, A. Zunger, Phys. Rev. Lett. 86, 2609 (2001)
25. R.J. Potter, N. Balkan, X. Marie, H. Carrere, E. Bedel, G. Lacoste, Physica Stat. Sol. (a) 187, 623 (2001)
26. W. Shan, W. Walukiewicz, J.W. Ager, E.E. Haller, J.F. Geisz, D.J. Friedman, J.M. Olson, S.R. Kurtz, Phys. Rev. Lett. 82, 1221 (1999)

27. R.J. Potter, N. Balkan, X. Marie, M. Senes, H. Carrere, A. Arnoult, C. Fontaine, IEE Proc. Optoelectron. 150, 75 (2003)
28. A. Markus, A. Fiore, J.D. Ganiere, U. Oesterle, J.X. Chen, B. Deveaud, M. Ilegems, H. Riechert, Appl. Phys. Lett. 80, 911 (2002)
29. A. Erol, S. Mazzucato, M. Arikan, H. Carrere, A. Arnoult, E. Bedel, N. Balkan, Semicond. Sci. Technol. 18, 968 (2003)
30. D. Lepine, Phys. Rev. B 6, 436 (1972)
31. C. Weisbuch, G. Lampel, Solid State Com. 14, 141 (1974)
32. R.C. Miller, W.T. Tsang, W.A. Nordland, Phys. Rev. B 21, 1569 (1980)
33. D. Paget, Phys. Rev. B 30, 931 (1984)
34. It is generally assumed that the triplet levels are not bound
35. The same ratio is measured for (σ^+) or (σ^-) polarised excitation laser: $R_{SDR} = I_{PL}(\sigma^+)/I_{PL}(\sigma^x) = I_{PL}(\sigma^-)/I_{PL}(\sigma^x)$].
36. V. Kalevich, E. Ivchenko, M. Afanasiev, A. Egorov, A. Shiryaev, V. Ustinov, B. Pal, Y. Masumoto, JETP Lett. 82, 455 (2005)
37. B. Baylac, X. Marie, T. Amand, M. Brousseau, J. Barrau, Y. Shekun, Surface Science 326, 161 (1995)
38. A. Vinattieri, J. Shah, T. Damen, D. Kim, L. Pfeiffer, M. Maialle, L. Sham, Phys. Rev. B 50, 10868 (1994)
39. A. Heberle, W. Ruhle, K. Ploog, Phys. Rev. Lett. 72, 3887 (1994)
40. T. Amand, X. Marie, P. Le Jeune, M. Brousseau, T. Robart, J. Barrau, R. Planel, Phys. Rev. Lett. 78, 1355 (1997)
41. C. Skierbiszewski, P. Pfeffer, J. Lusakowski, Phys. Rev. B 71, 205203 (2005)
42. K. Kalevich, A. Shiryaev, E. Ivchenko, A. Egorov, L. Lombez, D. Lagarde, X. Marie, T. Amand, JETP Lett. 85, 174 (2007)

12

Optical and Electronic Properties of GaInNP Alloys: A New Material for Lattice Matching to GaAs

I.A. Buyanova and W.M. Chen

Alloying of nitrogen with conventional III–V compounds has recently attracted substantial research efforts ignited by unusual fundamental physical properties of the formed dilute nitride materials as well as their great potential for various applications in optoelectronics and photonics. Among the newest members of the dilute nitrides family are $Ga_{0.5}In_{0.5}N_xP_{1-x}$ alloys lattice matched to GaAs. They have recently been suggested as promising materials for GaInP/GaAs-based heterojunction bipolar transistors, e.g., in blocked hole heterojunction bipolar transistors with a reduced offset and knee voltages. In this chapter we will review our present knowledge on the basic electronic and also material-related properties of GaInNP alloys. Issues to be addressed include: modeling of electronic structure of GaInNP, effects of nitrogen on band alignment at the GaInNP/GaAs interface, origin of radiative recombination in the alloys.

12.1 Introduction

Alloying of nitrogen with conventional III–V compounds has lately attracted substantial research efforts ignited by unusual fundamental properties of the formed dilute nitride materials as well as their great potential in various applications in optoelectronics and photonics [1,2]. Among the newest members of the dilute nitrides family are $Ga_{0.5}In_{0.5}N_xP_{1-x}$ alloys for lattice matching to GaAs. This material system was first suggested in 2000 by Welty et al. [2] as a suitable material for an emitter and collector in GaInP/GaAs-based heterojunction bipolar transistors (HBTs), e.g., in blocked hole HBTs, with reduced offset and knee voltages [3,4]. The materials can also be suitable for optoelectronic devices based on GaInP/GaAs [4].

In this chapter we will review our present understanding of electronic structure and key material-related properties of these new alloys. The chapter is organized as follows. We will first discuss origin of radiative recombination in GaInNP in relation to structural properties of the alloys. We will then address

electronic properties of GaInNP/GaAs including modeling of the N-induced modifications in the band structure of GaInNP, as well as band alignment at the GaInNP/GaAs heterointerface.

12.2 Origin of Radiative Recombination

A price to pay for the novel fundamental properties of dilute nitrides is pronounced degradation of material quality to varying degrees, which has a strong impact on transport properties and also recombination processes in these materials. To evaluate material quality altered by N incorporation, highly sensitive optical spectroscopy has often been employed. For example, previous optical studies of Ga(In)NAs alloys [5–7] have demonstrated that low-temperature (LT) photoluminescence (PL) from these materials is dominated by recombination of excitons localized at band tail states and have, therefore, revealed unusually strong potential fluctuations at the band edges induced by nonuniformities in N compositions.

Localization effects were also found to be important for GaInNP [8, 9], as the near-band edge (NBE) emission in these alloys at LT exhibits all properties characteristic for the optical transition involving localized carriers/excitons. These include:

1. A very asymmetric PL lineshape with a sharp high-energy cutoff and a long exponential tail at low energies, which reflects a distribution of band tail states (see Fig. 12.1).
2. The so-called "S-shape" dependence of the PL maximum position on the measurement temperature, due to thermal activation of localized carriers/excitons to extended states (see Fig. 12.2).

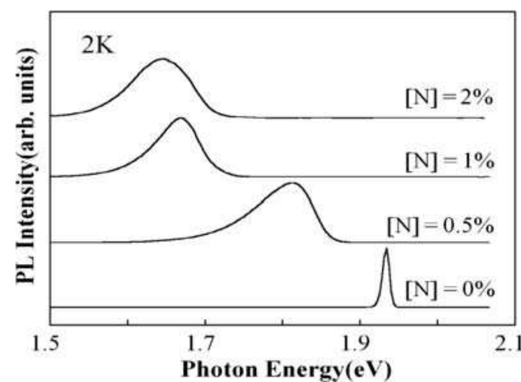

Fig. 12.1. Effect of N incorporation on the NBE PL from the $Ga_yIn_{1-y}N_xP_{1-x}$ epilayers at 2 K. The spectra are normalized to the same peak intensity and are vertically shifted for clarity

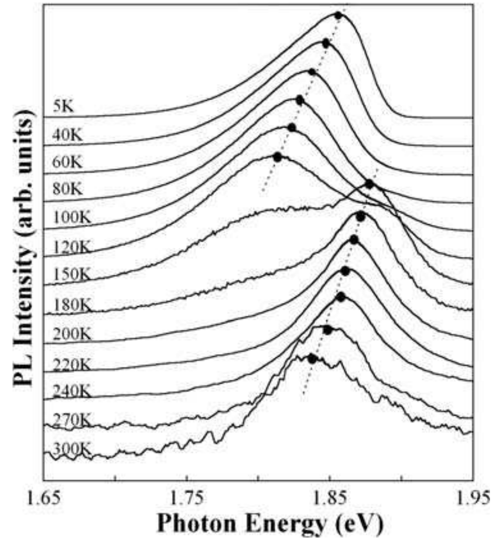

Fig. 12.2. Temperature-dependent PL spectra measured from the $Ga_{0.49}In_{0.51}N_{0.005}P_{0.995}$ epilayer. The dependence of the PL maximum position on measurement temperature is indicated by the *dash-dotted line* (The localization effects become less important at room temperature, where PL is dominated by the recombination of free carriers, evident from the observed changes in the PL lineshape, and also its dependence on the excitation power [9])

3. A significant blueshift of the LT PL with increasing excitation power at a rate of approximately 12 meV per decade [9], due to filling of the tail states at high excitation densities.

Potential fluctuations of the band edges, which lead to carrier localization at LT, are typical for all semiconductor alloys, e.g., due to compositional nonuniformities. In dilute nitrides, however, these fluctuations are largely enhanced because of the giant bowing effect of the bandgap energy, which translates minor variations in N content into pronounced changes in the bandgap energy. As N incorporation predominantly influences the conduction band (CB) edge of the alloys, the nonuniformities in N composition mainly cause fluctuations of the CB edge whereas the edge of the valence band (VB) remains practically flat. This has led to the fact that the LT radiative recombination in the direct bandgap dilute nitrides (e.g., Ga(In)NAs) is governed by recombination of localized excitons (LE) [5–7].

Quite unexpectedly, this scenario does not apply to the GaInNP alloys, as has recently been revealed by our transient PL studies [9]. Typical decays of the NBE emission from the GaInNP alloys are shown in Fig. 12.3. For the N-free GaInP alloy, the PL decay (shown by the dotted line in Fig. 12.3) can be described by a biexponential function with a characteristic time of around 1.1 ns for the slow decay component, i.e., typical for a radiative excitonic

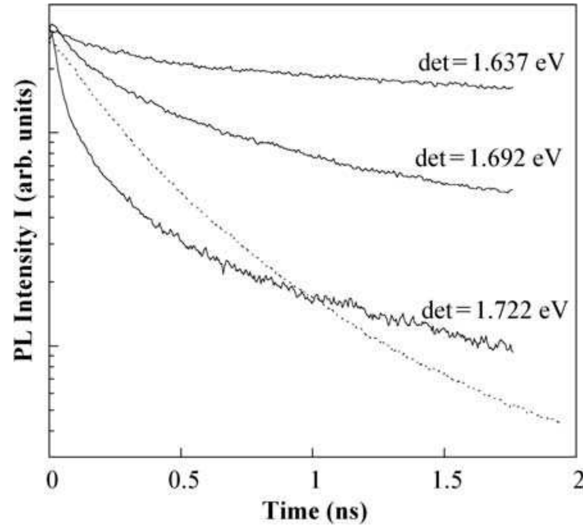

Fig. 12.3. PL decays measured at 2 K from the RTA-treated $Ga_{0.49}In_{0.51}N_{0.01}P_{0.99}$ epilayer at the specified detection energies. The *dashed line* shows the PL decay measured from the reference N-free $Ga_{0.49}In_{0.51}P$ epilayer, detected at the PL maximum position of 1.937 eV

transition in a direct bandgap semiconductor. N incorporation, however, causes a substantial slow-down of the PL decay. The characteristic decay times for the slow decay component are now about 3–22 ns (depending on detection energies). Even longer PL decays of around 1–2 μs were revealed within the time interval of 10 μs. This by far exceeds maximum LE lifetime, which is ∼1–8 ns, limited by the radiative lifetime. The observed long PL decays imply that the LT PL in the GaInNP alloys is largely governed by the recombination of the localized e–h pairs that are spatially separated. (The LE emission may be responsible for the fast components of the PL decays). A significantly lower recombination rate of the corresponding transitions is expected due to a weak overlap of the wave functions of the recombining carriers. Moreover, the recombination rate should be especially suppressed for optical transitions at low PL energies, as they correspond to the recombination of strongly localized carriers trapped within the deepest localization potentials, consistent with the experimental findings.

We should point out that this recombination mechanism is rather unusual for dilute nitrides with a direct bandgap and seems to be specific for the GaInNP alloys. A dramatic increase of the PL lifetime in these materials suggests an additional localization mechanism which leads to a spatial separation of the photoexcited carriers. Even though the exact physical mechanism behind is still not certain, a possible origin could be CuPt ordering which is often observed in the parental GaInP alloys and correlates with an appearance of the slow component of the PL decay [10].

It is worth mentioning that the CuPt ordering is usually observed in the GaInP alloys grown within a rather limited temperature range of around 650°C [11]. Therefore, it is not expected for the studied GaInNP epilayers grown at the substantially lower temperature of 460°C. Indeed, the disordered GaInP alloy was formed in the reference N-free structure, judging from the energy position of the LT PL maximum and the observation of the fast PL decay. Therefore, the long-range ordering in GaInNP should be solely facilitated by the presence of N. Weak ordering effects in GaInNP promoted by N incorporation were also concluded from the recent polarized piezoreflectance measurements [12], supported by the high-resolution transmission electron microscopy, as well as by the Raman studies [13].

12.3 Compositional and Temperature Dependences of Bandgap Energies

Exploration of a new material system requires detailed knowledge of its electronic band structure and related parameters, e.g., bandgap energy and its temperature dependence, CB dispersion and effective mass values, etc. For GaInNP alloys, such information has become available only most recently as will be briefly summarized hereafter.

12.3.1 Compositional Dependence

Bandgap energies of GaInNP alloys with In compositions of 51–56% (as required to satisfy lattice matching with a GaAs substrate) were evaluated based on PL [8, 14, 15] and reflectance [14] measurements. As usually observed for dilute nitrides, N incorporation has been found to cause a dramatic decrease in the bandgap energies indicating the giant bowing effect. This is demonstrated in Fig. 12.4, taking as an example the 235-nm thick GaInNP epilayers grown on a GaAs substrate by gas source molecular beam epitaxy (GSMBE).

In order to model the observed compositional dependence of the fundamental bandgap as well as to accurately evaluate band structure parameters of GaInNP, we have employed [15] the so-called band anticrossing (BAC) approach [16, 17, and see Chap. 3]. This empirical approach models electronic structure of dilute nitrides in terms of an anticrossing interaction between the localized a_1 symmetry state of the substitutional N atom and the extended Γ_c CB states of the host semiconductor matrix. The conduction band subbands are given as:

$$E_{\pm}(k) = \frac{1}{2}\left[\left((E_{\Gamma}(k) + E_{\mathrm{N}}) \pm \sqrt{(E_{\Gamma}(k) - E_{\mathrm{N}})^2 + 4xC_{\mathrm{NM}}^2}\right)\right]. \qquad (12.1)$$

Here $E_{\Gamma}(k)$ is the energy dispersion of the Γ_c CB edge of the semiconductor matrix, E_{N} is the energy position of the nitrogen-related level with a_1 symmetry, and x is the N molar fraction. All energies are measured relative to

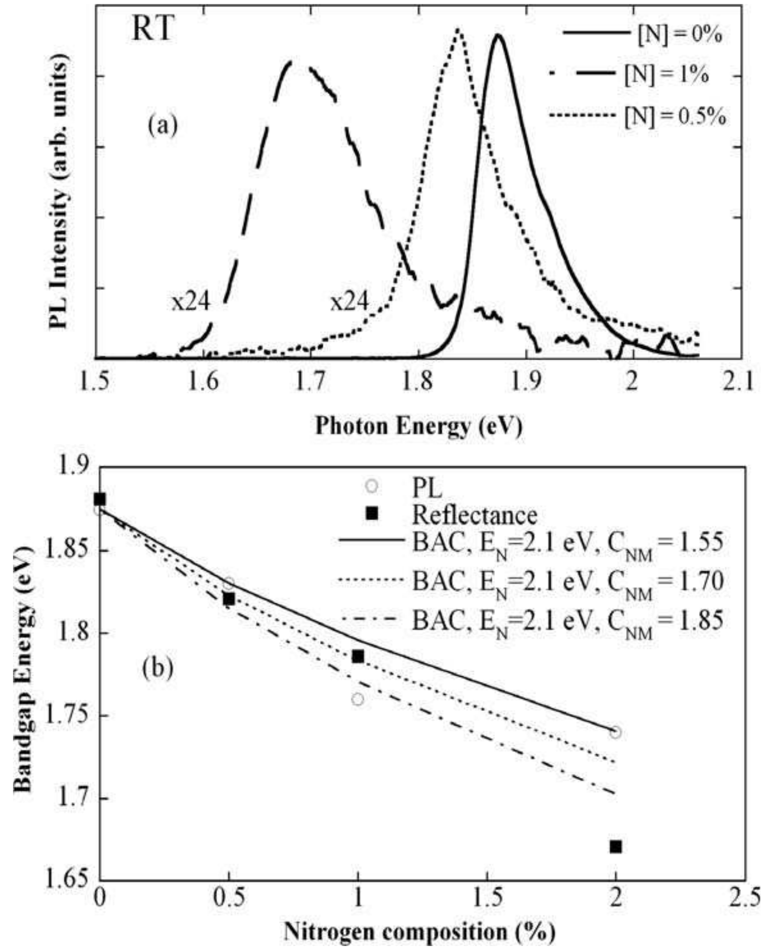

Fig. 12.4. (**a**) Room temperature PL spectra measured from GaInNP epilayers as a function of N composition. The values of In composition in the samples were: [In] = 51% for [N] = 0% and 0.5%; and [In] = 56% for [N] = 1%. (**b**) Compositional dependence of the bandgap energies of the $Ga_{0.49}In_{0.51}N_xP_{1-x}$ alloys. The *open circles* represent values obtained from room temperature PL measurements. The data were corrected to the same In composition of 51%, based on the known compositional dependence of the bandgap energies in GaInP [18]. The *filled squares* are results from the reflectance measurements of [14]. Lines are the BAC fitting curves with the specified parameters

the VB edge. $C_{\rm NM}$ is an adjustable coupling parameter which depends on the host semiconductor and reflects interaction strength between the N-related state and the host matrix. The bandgap energy is given by the energy of the lower subband edge, $E_-(0)$. Practical advantage of the BAC approach is that it allows to easily predict all important band structure parameter of dilute nitrides, such as compositional, temperature and pressure dependences of the

CB states in the alloys, their dispersion, oscillator strength of related optical transitions, etc.

The coupling parameter can be determined by fitting compositional dependence of the fundamental bandgap of the alloys. The results of such fitting for GaInNP are shown in Fig. 12.4b. The energy position of the N-related level E_N was chosen as 2.1 eV, based on [19]. Taking into account all available data, the BAC parameters for the InGaNP alloys with In compositions around 50% can be deduced as $E_N = 2.1 \pm 0.1$ eV and $C_{NM} = 1.7 \pm 0.2$ eV [15].

12.3.2 Temperature Dependence

Based on the previous studies for Ga(In)NAs [20, 21] and GaNP alloys [22], alloying with nitrogen can also affect thermal variation of the bandgap energies in dilute nitrides. The extent of the effect, which is of importance for device applications of the alloys, depends on the semiconductor matrix. For GaInNP, effects of N on the thermally induced changes in the bandgap were investigated in [15]. A slow-down of the $E_g(T)$ dependence upon N incorporation was observed (Fig. 12.5) from about 91 meV (within the temperature range of 4–300 K) for the N-free $Ga_{0.59}In_{0.51}P$ down to 74 meV for the $Ga_{0.59}In_{0.51}N_{0.005}P_{0.995}$ alloy. This accounts to a modifications by about

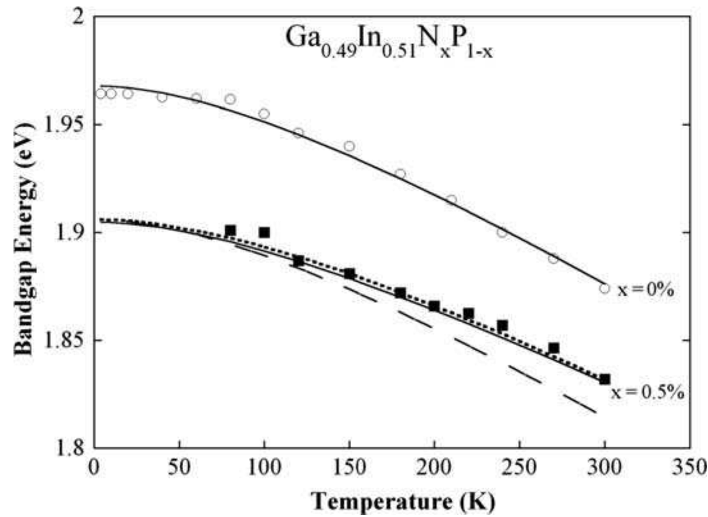

Fig. 12.5. Temperature dependence of the bandgap energies for the $Ga_{0.49}In_{0.51}N_xP_{1-x}$ epilayers with the specified N compositions. The bandgap values were obtained based on the measured maximum positions of the PL emission related to free carriers/excitons. The *dots* represent experimental data. The *solid lines* are fitting curves using the Varshni equation with fitting parameters as specified in Ref. [15]. The *dotted* (*dashed*) lines are fitting curves based on the BAC model assuming a constant (temperature dependent) energy position of the N level (From [15])

20% and is therefore less pronounced than that reported for GaNAs, where about 35% changes were observed for the similar N compositions [20].

The slow-down of the E_g variation with temperature can be described by the BAC model. In fact, such fitting provides a complementary experimental tool for estimating the coupling parameter C_{NM}. The results of the fitting with $C_{NM} = 1.55$ eV are shown in Fig. 12.5 by the dotted line, and are in very good agreement with the experimental data for the $Ga_{0.59}In_{0.51}N_{0.005}P_{0.995}$ alloy. During fitting, the $E_{\Gamma}(0)$ value was set equal to the $E_g(T)$ dependence measured for the N-free GaInP epilayer, whereas the E_N was assumed to be independent of T. We would like to point out, that this assumption has been commonly used for the BAC analysis of the $E_g(T)$ dependences in the Ga(In)NAs alloys [20, 21]. On the other hand, it was found to be invalid in GaNP [22], where the N level follows the bandgap variation with temperature. Assuming similar $E_{\Gamma}(0)$ and $E_N(T)$ dependences in the studied structures, the predicted changes of the GaInNP bandgap are shown by the dashed line and clearly contradict to the experimental data. Apparently, the assumption of the constant E_N position with T is critical to account for a slow-down of the $E_g(T)$ dependence in the studied alloys within the framework of the BAC model, similar to the case of GaInNAs alloys [20, 21]. It is presently not clear whether this difference in the $E_N(T)$ behavior in various host matrixes reflects the real difference in a character of the N state when it is resonant with the CB states (as in the case of Ga(In)NAs and GaInNP alloys) or lies within the bandgap of the host material (as in the case of GaNP). Further theoretical efforts are required to clarify this issue.

It is worth mentioning that the coupling coefficient in the GaInNP alloys is very close to the value of $C_{NM} = 1.7$ eV obtained for the GaInNAs alloys with high In contents of 25–40% [21]. On the other hand, it is substantially smaller than the values deduced for the In-free dilute nitrides, e.g., $C_{NM} = 2.3$–2.7 eV for GaNAs [16,20,23] or $C_{NM} = 2.76$ eV for GaNP [22]. This leads to relatively smaller values of the bowing coefficient in the alloys [14], as well as weaker effects of N on the thermal variation of the bandgap energy. The observed reduction of the coupling parameter seems to indicate a reduction of the interaction strength between the N-related localized state and the extended host states because of the presence of In. A possible reason could be short range ordering effects leading to correlation in spatial locations of In and N atoms, as predicted for GaInNAs [24].

12.4 Band Alignment in GaInNP/GaAs Heterostructures

Knowing band alignment is of vital importance for full exploration of the bandgap engineering. Alloying of GaInP with nitrogen is expected to change the band alignment with GaAs due to the downshift of the CB edge of GaInNP [25, 26]. Detailed analysis of N-induced effects on the CB and VB states of

GaInNP alloys was performed in [27, 28]. The type-II band alignment at the $Ga_{0.46}In_{0.54}N_xP_{1-x}$/GaAs interface was concluded for the alloys with $x \geq 0.5\%$ based on (1) highly efficient PL up-conversion (PLU) observed in the N-containing samples; and (2) appearance of a near infrared (NIR) PL emission attributed to the spatially indirect type II transitions.

12.4.1 PL Up-Conversion in GaInNP/GaAs Heterostructures

PLU is a process in which photon emission occurs at energies higher than that of an excitation photon. In the case of the GaInNP/GaAs system, the PLU process was found to be largely facilitated by the presence of nitrogen [28]. This can be seen from Fig. 12.6 where spectra of the NBE PL emission from GaInNP are shown upon optical excitation with energy below the bandgap of GaInNP. We need to point out that PLU in the GaInNP/GaAs system is very efficient and can be detected for the excitation power density as low as $0.1\,\mathrm{Wcm^{-2}}$.

The spatial location of the PLU process, as being within the GaAs layers close to the GaInNP/GaAs interface, was singled out from dependences of the up-converted PL emission on the excitation photon energy – see Fig. 12.6. Substantial enhancement of the PLU efficiency was observed at the excitonic

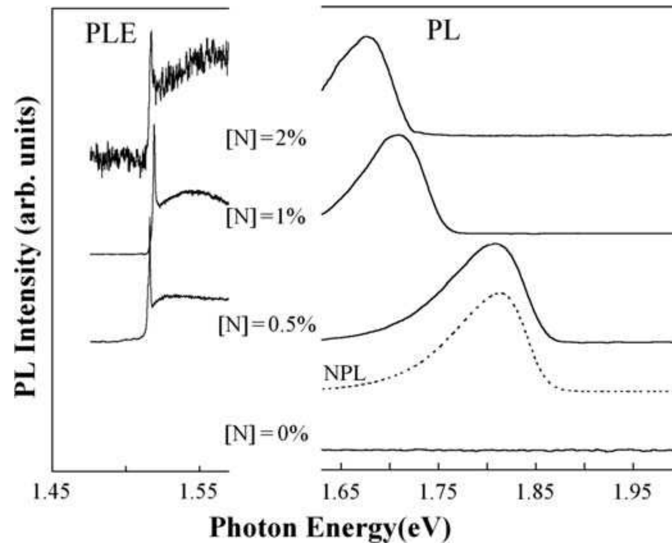

Fig. 12.6. PL (*right panel*) and PL excitation (*left panel*) spectra of the PLU emissions detected from the GaInNP/GaAs structures with the specified N compositions. The excitation photon energy during the PL measurements was set at 1.59 eV. The spectra are normalized to the same intensity and are shifted in the y-direction, for clarity. For comparison, also shown is the spectrum of the NBE emission under optical excitation at 2.41 eV, i.e., above the GaInNP bandgap energy (the *dotted line*)

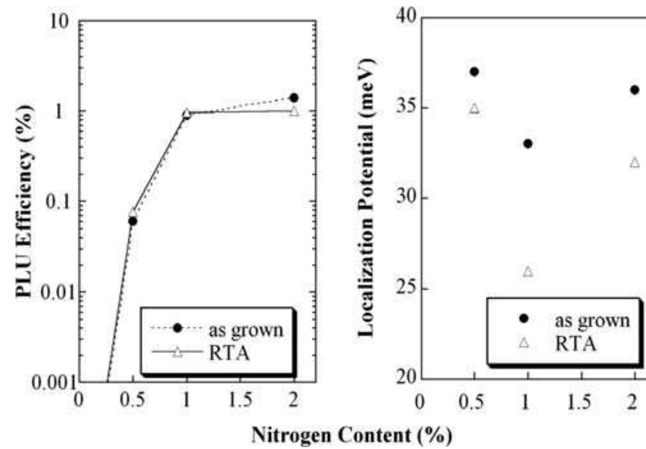

Fig. 12.7. Compositional dependence of the PLU efficiency (**a**) and of the localization potential (**b**) measured from the as-grown (*dots*) and the RTA-treated (*open triangles*) structures, respectively

bandgap of GaAs which indicated light absorption within the GaAs layers. Proximity of the light absorption process to the GaInNP/GaAs interface was obvious from variations in the spectral position of the GaAs excitonic line between the GaInNP/GaAs samples with different In and N compositions, which indicated a slightly different strain in the GaAs layers involved in the PLU process.

Interestingly, efficiency of this PLU process critically depends on the N content in GaInNP – Fig. 12.7a. For example, no PLU emission could be detected in the N-free GaInP/GaAs structure in spite of the high intensity of the NBE emission observed under the above GaInP excitation. On the other hand, the PLU efficiency dramatically increases to 0.06% for [N] = 0.5% and practically saturates at around 1% for higher N compositions.

Let us now discuss a possible origin of the efficient PLU observed in the N-containing structures and a role of nitrogen in facilitating this process. Several effects have previously been shown to dramatically improve the PLU efficiency in semiconductor heterostructures and quantum wells. These include (1) lifting of momentum conservation restrictions by the presence of a heteroboundary which allows no-phonon (or "cold") Auger processes [29, 30]; (2) existence of localized or bound exciton states in the narrow bandgap semiconductor which participate in two step two-photon absorption (TS-TPA) [31, 32]; (3) carriers localization in the wide bandgap region of the type I heterostructures, which prevents a back flow of carriers to the narrow bandgap semiconductor [33, 34] – Fig. 12.8a; and (4) the type II band alignment at a heterointerface which assists transport of one of the photoexcited carries to the wide bandgap material [35–37] – Fig. 12.8b. The first two mechanisms are expected to be independent of the N presence in the GaInP alloy and, therefore, can not

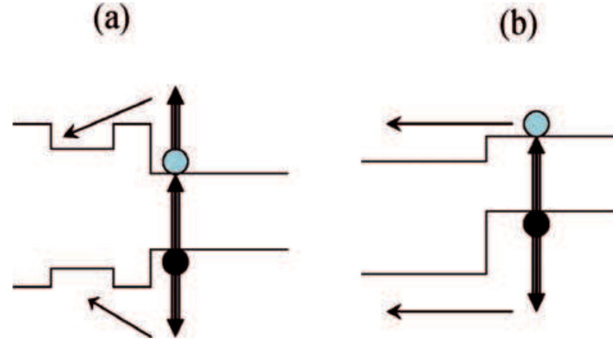

Fig. 12.8. Possible effects improving the PLU efficiency in heterostructures: (**a**) carriers localization in the wide bandgap region of the type I heterostructures, which prevents a back flow of carriers to the narrow bandgap semiconductor, (**b**) the type II band alignment at a heterointerface which assists transport of one of the photoexcited carries to the wide bandgap material

account for the experimentally observed enhancement of the PLU efficiency in the N-containing samples. On the other hand, the last two conditions can be assisted by the presence of nitrogen as it increases localization in the wide bandgap GaInNP and can also induce the type II alignment at the heterointerface, due to the downshift of the CB edge.

Even though dramatic enhancement of band tailing effects is typical for dilute nitrides [38], this mechanism cannot be chiefly responsible for the enhanced efficiency of the PLU process in the N-containing structures. Indeed, judging from the line shape of the NBE emissions and its dependence on measurement temperature [9], the localization potential in the investigated structures does not significantly depend on the N content – Fig. 12.7b. On the other hand, the PLU efficiency increases from 0.06% for the structure with [N] = 0.5% up to 1–1.5% for the higher N compositions – Fig. 12.7a. Moreover, suppression of the localization by postgrowth thermal annealing does not affect the PLU efficiency.

We, therefore, attribute the observed dramatic increase in the PLU efficiency to a N-induced change in the band alignment at the GaInNP/GaAs interface from the type I for [N] = 0% to the type II for [N] $>$ 0.5%, which eliminates the energy barrier for electron transport from GaAs to GaInNP – Fig. 12.9b. Such modification of the band lineup is not surprising as the N-induced dramatic reduction in the bandgap energy of the forming alloys is predominantly caused by a downshift of the CB edge. The band lineup should be close to flat for [N] = 0.5%, to account for the lower PLU efficiency. This is consistent with the stronger dependence of the PLU intensity on the excitation power observed for the $GaInN_{0.005}P_{0.995}$/GaAs structure [28], as participation of the second photon may be required to compensate for a possible back flow of the carriers from GaInNP to GaAs.

12.4.2 Interface-Related Emission

Further evidence towards the type II band line-up at the GaInNP/GaAs heterointerface was obtained based on the observation of the spatially indirect type II recombination across the GaInNP/GaAs interface within the NIR spectral range [27], see Fig. 12.9. N incorporation was found to cause an appearance of a new NIR PL band (marked by arrows in Fig. 12.9). This new NIR emission strongly downshifts in energy with increasing N content which implies involvement of the CB states of the GaInNP alloys in the corresponding optical transition. Moreover, the PLE spectra of the NIR PL band measured within the energy range below the GaInNP bandgap (see the insert in Fig. 12.9) show a pronounced enhancement at the GaAs exciton energy and closely resemble those measured either for the GaAs-related emissions or for the PLU emission. This rules out free-to-bound transitions at some deep centres in GaInNP as a possible origin of the observed NIR PL and confirms the suggested mechanism for this emission as being due to the spatially indirect type II recombination between the GaInNP electrons and the GaAs holes.

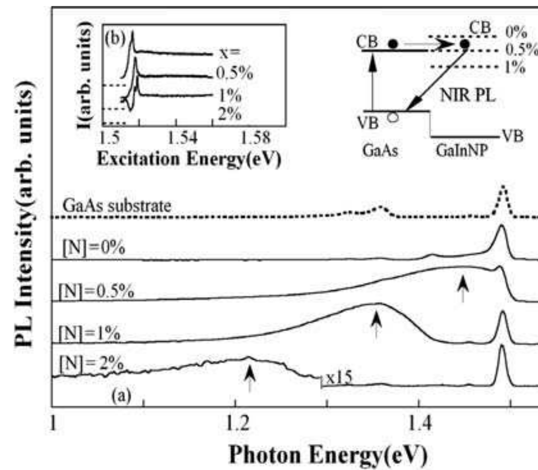

Fig. 12.9. (**a**) Typical PL spectra detected at 4 K within the NIR spectral range from the $GaInN_xP_{1-x}$/GaAs structures. The PL spectrum related to the GaAs substrate is also shown by the *dotted line*, for comparison. Identical PL transitions were observed for the excitation photon energies above and below the GaInNP bandgap. The spectra shown in the figure were recorded under the photoexcitation at 1.59 eV, below the GaInNP bandgap. The N-induced changes in the band alignment at the GaInNP/GaAs interface leading to the appearance and shift of the NIR PL are schematically illustrated in the upper part of the figure. (**b**) PLE spectra of the interface-related emissions. The spectra are vertically offset for clarity. The detection energies during the PLE measurements were set at the peak position of the NIR emission, as indicated by the *arrows* (from [27])

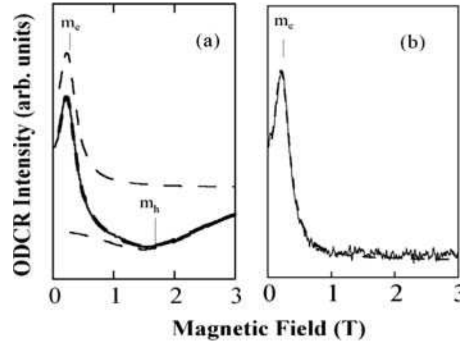

Fig. 12.10. ODCR spectra (*solid lines*) measured from the $Ga_{0.44}In_{0.56}N_{0.02}P_{0.98}$ epilayer and detected via the interface-related PL (**a**) or via the GaAs emission (**b**). The spectra were measured under magnetic fields perpendicular to the interface plane. The *dashed lines* represent the fitting curves according to [39] with $m_e = 0.067\,m_0$ and $m_h = 0.46\,m_0$ (from [27])

The same conclusion also followed from the optically detected cyclotron resonance (ODCR) measurements [27], where spatial locations of carriers involved in the NIR emission was directly determined. In the ODCR experiments, an intensity change of light emission induced by carrier heating upon the cyclotron resonance absorption of the microwave radiation is detected. Since the cyclotron resonance condition $\omega_c = qB/m^*$ is determined by the effective mass of the involved free carrier, its spatial location within a multilayer heterostructure can be identified [39]. Here ω_c is the cyclotron frequency, q is the elementary charge, m^* is the effective mass of the carriers, and B is an applied magnetic field. For the GaInNP/GaAs structures, the ODCR spectra (see Fig. 12.10) contained two peaks related to the free carriers with effective masses of $0.067\,m_0$ and $0.46\,m_0$, i.e., typical for a free electron and hole in GaAs. High intensity of the hole-related ODCR peak indicated direct involvement of the GaAs holes in the corresponding optical transitions. On the other hand, weak intensity of the GaAs electron resonance pointed towards the secondary character of the signal, e.g., due to an increasing supply of electrons from GaAs to the GaInNP layer under the CR conditions. Such behavior is expected for the type II transitions, where the main contributions to the ODCR should be from the carriers directly involved in the radiative recombination, i.e., a GaAs hole and a GaInNP electron. (The ODCR peak related to the GaInNP electron is not seen in the experiments due to low electron mobility in the GaInNP layer).

12.4.3 Band Offsets at the GaInNP/GaAs Interface

Compositional dependences of the band offsets at the GaInNP/GaAs interface were estimated by comparing spectral positions of the NBE ($E_c^{GaInNP} - E_v^{GaInNP}$) and the NIR ($E_c^{GaInNP} - E_v^{GaAs}$) emissions [27]. (To account for

strong potential fluctuations in the CB edge, all energies were measured as the high energy cutoff of the PL spectra). Almost flat alignment of the CB edge was concluded for the structures with [N] = 0.5%, whereas for the higher N compositions $0.5\% \leq [N] \leq 2\%$ a practically linear change of the CB offset with a slope of −0.10 eV per percentage was observed. The valence band offset with GaAs was found to be of about 0.4 eV, independent of the N content in GaInNP.

12.5 Summary

In summary, we have reviewed presently known electronic and material-related properties of the GaInNP alloys for lattice matching to GaAs, which is a new material system promising for a variety of electronic applications. We have shown that N incorporation in these alloys induces a variety of changes in their structural properties as well as of the electronic structure. The main structural changes include (1) increasing carrier localization, which is typical for all dilute nitrides, and (2) N-induced long range ordering effects, specific for GaInNP. Even though the exact role of nitrogen in promoting ordering is not yet well understood, the existence of the ordering seems to be rather reliably established from various structural (transmission electron microscopy), as well as optical (Raman scattering, polarized reflectance, and time resolve photoluminescence) characterization measurements. N induced modifications of the electronic structure of GaInNP and applicability of the BAC model for their description were also discussed. From the analysis of the relevant BAC parameters, a somewhat weak coupling between the localized N state and the extended host states is concluded, which may be related to the high In content and to correlations in spatial locations of In and N atoms.

Acknowledgments. The authors wish to thank Y.G. Hong and C.W. Tu for the growth of the studied GaInNP/GaAs structures. We also gratefully acknowledge M. Izadifard, I. Vorona, and T. Mtchedlidze for their contribution to the experimental results discussed in this chapter. This work was supported by the Swedish Research Council and Wenner–Gren Foundations.

References

1. For a review see e.g., I.A. Buyanova, W.M. Chen, B. Monemar, MRS Internet J. Nitride Semicond. Res. **6**, 2 (2001)
2. I.A. Buyanova, W.M. Chen (eds.), *Physics and Applications of Dilute Nitrides* (Taylor & Francis, New York, 2004)
3. R.J. Welty, Y.G. Hong, H.P. Xin, K. Mochizuki, C.W. Tu, P.M. Asbeck, in *Proceedings of 2000 IEEE/Cornell Conference on High Performance Devices*, Piscataway, NJ, 2000, pp. 33–40

4. C.W. Tu, J. Phys: Condens. Matter. **13**, 7169 (2001)
5. I.A. Buyanova, W.M. Chen, G. Pozina, J.P. Bergman, B. Monemar, H.P. Xin, C.W. Tu, Appl. Phys. Lett. **75**, 501 (1999)
6. R.A. Mair, J.Y. Lin, H.X. Jiang, E.D. Jones, A.A. Allerman, S.R. Kurtz, Appl. Phys. Lett. **76**, 188 (2000)
7. L. Grenouillet, C. Bru-Chevallier, G. Guillot, P. Gilet, P. Duvaut, C. Vannuffel, A. Million, A. Chenevas-Paule, Appl. Phys. Lett. **76**, 2241 (2000)
8. Y.G. Hong, A. Nishikawa, C.W. Tu, Appl. Phys. Lett. **83**, 5446 (2003)
9. M. Izadifard, J.P. Bergman, W.M. Chen, I.A. Buyanova, Y.G. Hong, C.W. Tu, Appl. Phys. Lett. **88**, 011919 (2006)
10. M.C. DeLong, W.D. Ohlsen, I. Viohl, P.C. Taylor, J.M. Olson, J. Appl. Phys. **70**, 2780 (1991)
11. M.C. DeLong, P.C. Taylor, J.M. Olson, Appl. Phys. Lett. **57**, 520 (1990)
12. Y.K. Su, C.H. Wu, S.H. Hsu, S.J. Chang, W.C. Chen, Y.S. Huang, H.P. Hsu (2004) Appl. Phys. Lett. **84**, 1299
13. K.I. Lin, J.Y. Lee, T.S. Wang, S.H. Hsu, J.S. Hwang, Y.C. Hong, C.W. Tu, Appl. Phys. Lett. **86**, 211914 (2005)
14. Y.K. Su, C.H. Wu, Y.S. Huang, H.P. Hsu, W.C. Chen, S.H. Hsu, S.J. Chang, J. Cryst. Growth **264**, 357 (2004)
15. I.A. Buyanova, M. Izadifard, W.M. Chen, Y.G. Hong, C.W. Tu, Appl. Phys. Lett. **88**, 031907 (2006)
16. W. Shan, W. Walukiewicz, J.W. Ager III, E.E. Haller, J.F. Geisz, D.J. Griedman, J.M. Olson, S.R. Kurtz, Phys. Rev. Lett. **82**, 1222 (1999)
17. W. Walukiewicz, W. Shan, J. Wu, K.M. Yu, in *Physics and Applications of Dilute Nitrides*, ed. by I.A. Buyanova, W.M. Chen (Taylor & Francis, New York, 2004), pp. 23–64
18. P. Merle, D. Auvergne, D. Mathieu, J. Chevallier, Phys. Rev. B **15**, 2032 (1977)
19. H.M. Macksey, N. Holonyak Jr., R.D. Dupuis, J.C. Campbell, G.W. Zack, J. Appl. Phys. **44**, 1333 (1973)
20. I. Suemune, K. Uesugi, W. Walukiewicz, Appl. Phys. Lett. **77**, 3021 (2000)
21. A. Polimeni, M. Capizzi, M. Geddo, M. Fischer, M. Reinhardt, A. Forchel, Phys. Rev. B **63**, 195320 (2001)
22. I.A. Buyanova, M. Izadifard, A. Kasic, H. Arwin, W.M. Chen, H.P. Xin, Y.G. Hong, C.W. Tu, Phys. Rev. B **70**, 085209 (2004)
23. P.J. Klar, H. Gruning, W. Heimbrodt, J. Koch, F. Höhnsdorf, W. Stolz, P.M.A Vicente, J. Camassel, Appl. Phys. Lett. **76**, 3439 (2000)
24. K. Kim, A. Zunger, Phys. Rev. Lett. **86**, 2609 (2001)
25. Y.G. Hong, R. Andre, C.W. Tu, J. Vac. Sci. Technol. B **19**, 1413 (2001)
26. J.S. Hwang, K.I. Lin, H.C. Lin, S.H. Hsu, K.C. Chen, Y.T. Lu, Y.G. Hong, C.W. Tu, Appl. Phys. Lett. **86**, 061103 (2005)
27. M. Izadifard, T. Mtchedlidze, I. Vorona, W.M. Chen, I.A. Buyanova, Y.G. Hong, C.W. Tu, Appl. Phys. Lett. **86**, 261904 (2005)
28. M. Izadifard, J.P. Bergman, W.M. Chen, I.A. Buyanova, Y.G. Hong, C.W. Tu, J. Appl. Phys. **99**, 073515 (2006)
29. G.G. Zegrya, V.A. Kharchenko, Sov. Phys. JETP **74**, 173 (1992)
30. W. Seidel, A. Titkov, J.P. Andre, P. Voisin, M. Voos, Phys. Rev. Lett. **73**, 2356 (1994)
31. R. Hellmann, A. Euteneuer, S.G. Hense, J. Feldmann, P. Thomas, E.O. Göbel, D.R. Yakovlev, A. Wagg, G. Landwehr, Phys. Rev. B **51**, 18053 (1995)

32. J. Zeman, G. Martinez, P.Y. Yu, K. Uchida, Phys. Rev. B **55**, R13428 (1997)
33. F.A.J.M. Driessen, Appl. Phys. Lett. **67**, 2813 (1995)
34. H.M. Cheong, B. Fluegel, M.C. Hanna, A. Mascarenhas, Phys. Rev. B **58**, R4254 (1998)
35. Z.P. Su, K.L. Teo, P.Y. Yu, K. Uchida, Solid State Commun. **99**, 933 (1996)
36. Y.H. Cho, D.S. Kim, B.D. Choe, H. Lim, J.I. Lee, D. Kim, Phys. Rev. B **56**, R4375 (1997)
37. J. Zeman, G. Martinez, P.Y. Yu, K. Uchida, Phys. Rev. B **55**, R13428 (1997)
38. I.A. Buyanova, W.M. Chen, in *Physics and Applications of Dilute Nitrides*, ed. by I.A. Buyanova, W.M. Chen (Taylor & Francis, New York, 2004), pp. 255–280
39. M. Godlewski, W.M. Chen, B. Monemar, Crit. Rev. Solid State Mater. Sci. **19**, 241 (1994)

13

Properties and Laser Applications of the GaP-Based (GaNAsP)-Material System for Integration to Si Substrates

B. Kunert, K. Volz, and W. Stolz

Multiquantum well heterostructures in the GaInNAsP/GaP material system were grown pseudomorphically strained on GaP substrates. This class of dilute nitride material system has a tremendous application potential in silicon photonics, as the novel material system is shown to have a direct band structure and as it can be grown without the formation of extended defects on GaP and hence on silicon substrates.

This chapter summarizes our present understanding of metalorganic vapor phase epitaxial growth as well as of structural characteristics of this class of metastable material systems. We will discuss the optical properties as well as give an estimate on the modification of the band structure of the host material altering the composition. The proof of concept will be demonstrated at the end of the chapter, where electrical injection lasing for this material system will be shown at low and room temperatures.

13.1 Introduction

The monolithic integration of optoelectronic circuits with Si-based microelectronics would tremendously increase the functionality of Si-microelectronics and open-up completely new fields of applications. Light, for example, could provide chip-to-chip or even on-chip communications within high-bandwidth data transfer, no signal latency, and without heat dissipation. Therefore, silicon photonics can combine the advantages of optical data processing with the highly developed expertise of Si-based integrated electronics and revolutionize future chip design.

The key element for this integration scheme is an efficient light source based on Si-substrate. Because of Si indirect electronic band gap, however, light emission is phonon-mediated and has very low internal quantum efficiency. Furthermore, free carrier absorption hinders population inversion essential for stimulated light emission and Auger recombination reduces the emitted photon density, see Fig. 13.1. Hence, researchers have been exploring

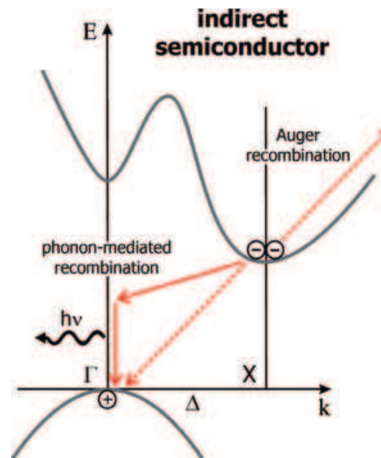

Fig. 13.1. Schematic drawing of an indirect band structure. Excited carriers can combine by phonon-mediated recombination or Auger recombination, which are indicated by the arrows

novel techniques, e.g., Si-nanocrystals [1] or Er-doped Si [2], to circumvent the weak luminescence efficiency since early 1990s, but even intense luminescence was found to be very difficult to achieve yet. The first optical pumped all-silicon based laser was demonstrated by stimulated Raman scattering in silicon waveguides in 2004 [3] followed by the demonstration of a continuous wave (CW) laser in 2005 [4]. Although this achievement enables novel applications including optical amplifiers and wavelength converters, there is still the basic necessity of an optical pump source for the nonlinear Raman process. So far, Raman lasers are incapable of being electrically pumped.

Another approach to realize a Si-based electrical injection laser is heteroepitaxy. Standard direct band gap III–V compound semiconductor like GaAs [5] or InP are deposited on Si-substrate to merge their sophisticated optical properties with Si. Because of the large lattice mismatch of these standard materials to Si, high densities of threading dislocations are formed in the epitaxial III–V film. This obstacle becomes obvious in Fig. 13.2, which summarizes the energy gap plotted vs. the lattice constant of the most common III–V semiconductors in comparison to Si. GaAs as well as InP have a lattice constant larger than Si by more than 4%. The technological challenge is to optimize the epitaxial growth conditions to suppress the formation of dislocations in the complete III–V layer. Although III–V laser diodes were realized [5], the high densities of misfit dislocations are still preventing any long-term stable lasing operation of optical device structures until now.

A view at the properties of different III-V compound semiconductors as plotted in Fig. 13.2 reveals that the indirect semiconductor GaP has a lattice constant almost equal to that of Si. In addition, the ternary crystal system Ga(NP) can be grown lattice-matched to Si-substrate with a N-content of 2%.

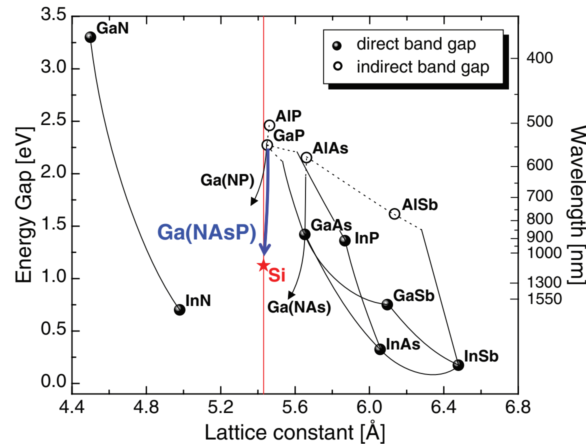

Fig. 13.2. Energy gap vs. the lattice constant of the most common III–V semiconductors in comparison to Si

Chap. 16 reviews the pseudomorphical growth of Ga(NP)/Ga layer sequences on Si-substrate with high structural perfection and without the formation of misfit dislocations and antiphase domains.

Based on this fact our approach is the development of the direct band gap material, which can be grown lattice-matched to GaP and therefore transferred in a straight forward way to Si-substrate.

To achieve this goal it is obvious to consider the application of the ternary materials system Ga(NP). The incorporation of a few percent of N into the indirect semiconductor GaP changes the fundamental band characteristics and particularly increases the luminescence efficiency significantly, as discussed in detail in Chap. 14. Whether this modification indicates a transition of an indirect to direct band structure is still under controversial discussion. Nevertheless, the material system Ga(NP) was only applied in light emitting diodes so far and the direct band gap character appears not be pronounced enough to realize population inversion and material gain essential for laser operation.

The incorporation of In and As into GaP results in a common transition of a indirect semiconductor to a direct one at relatively high concentration (unstrained Ga(AsP) at 53% As and (GaIn)P at 31% In). However, the large lattice mismatch hinders a pseudomorphic growth of these ternary materials systems on GaP-substrate.

However, the incorporation of N in combination with In or As allows for the necessary adjustment of the lattice constant of the quaternary material system (GaIn)(NP) and (GaNAsP) to GaP-substrate. The challenge is to find the right material composition of GaInNAsP, which enables the pseudomorphic growth of high quality films on GaP-substrate and reveals a direct band structure and a high luminescence efficiency, respectively, at the same time.

Recently, we introduced the novel As-rich dilute nitride material system (GaNAsP), which fulfils both requirements [6, 7]. Compressively strained (GaNAsP) multiquantum well heterostructures (MQWHs) were grown pseudomorphically on GaP-substrates by metalorganic vapor phase epitaxy (MOVPE) without any formation of misfit dislocation. Furthermore, the unique band gap formation of this dilute nitride leads to a strong reduction of the band gap energy and hence to a pronounced direct band gap of the quaternary material system. This novel material system acts as a sufficient light emitter and the capability for electrical pumped laser diodes was proven in first device structures [6,8]. Therefore, this realization of a direct semiconductor on GaP-substrate might lead to the real monolithic integration of III/V-based optoelectronics and Si-based microelectronics in the near future.

The focus of the chapter is to describe the heteroepitaxial growth of GaP-based dilute nitride materials, which have excellent structural properties and will be shown to have a direct band gap structure. Hence, these materials are suitable for the intended laser application on GaP and on Si substrates in the future.

13.2 Growth and Structural Properties

13.2.1 GaInNAsP Growth

In the following, selected MOVPE growth experiments will be presented with the aim of understanding the nitrogen incorporation in the mixed group-V material and with the aim of investigating the influence of nitrogen on structural characteristics in the GaP-based materials.

(GaNAsP)/GaP structures were grown in a commercially available AIX200 MOVPE reactor using Pd-purified H_2 as carrier gas at a reduced reactor pressure of 50 mbar [9]. Because of the metastability also of this dilute nitride system, growth temperatures were chosen in the range of 500–700°C, using all-liquid group-V MO precursors because of their better decomposition characteristics at these low temperatures. Tertiarybutyl arsine (TBAs), tertiarybutyl phosphine (TBP), and the unsymmetric dimethyl hydrazine (UDMHy) were the sources for arsenic, phosphorous, and nitrogen, respectively. Triethyl gallium (TEGa) was used as Ga precursor. As one deals with a material, containing three group-V elements, composition determination is not as straight-forward as in the case of GaInNAs, and several Secondary Ion Mass Spectrometry (SIMS) investigations were undertaken to support the results of X-ray diffraction (XRD).

One of the most important dependencies in the MOVPE growth is the nitrogen incorporation on growth temperature, as depicted in Fig. 13.3. Two sample sets, Ga(NP) grown on GaP and GaNAs grown on GaAs, are shown together in Fig. 13.3. Both ternary materials exhibit tensile strain with respect to their substrates, hence, strain-induced nitrogen desorption should – at a

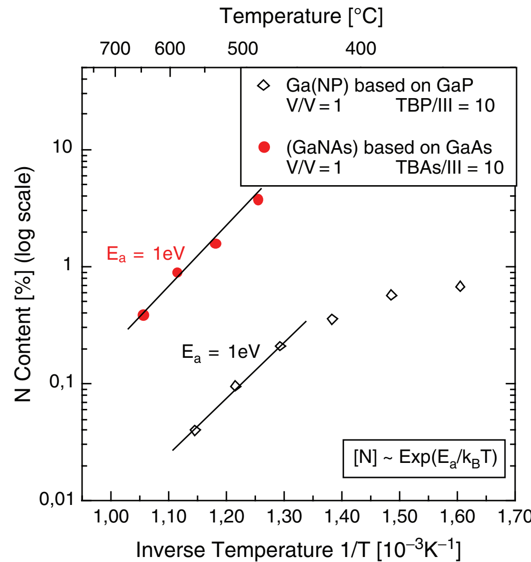

Fig. 13.3. Arrhenius plot of the dependence of the nitrogen content in GaNAs/GaAs and Ga(NP)/GaP on the growth temperature

similar lattice mismatch – be expected to a similar extent. The growth conditions for both sample sets shown in Fig. 13.3 were additionally chosen in a way that direct comparability of the data is possible. The V/V as well as V/III ratios were identical for the GaAs- and GaP-based materials, respectively. If one neglects differences in the temperature-dependence of the TBAs and TBP decomposition, respectively, which is at least true in the high-temperature-regime, direct comparability is given. It is known for MOVPE-grown GaInNAs and GaNAs that the nitrogen incorporation in GaNAs/GaAs is determined by both surface chemistry and strain constraints as well as gas-phase reactions of the MO precursors. Both aspects are confirmed when taking the GaP-based data into account. It can be seen that under comparable growth conditions, one order of magnitude more nitrogen is incorporated in Ga(NP)/GaP than in GaNAs/GaAs. One evident explanation takes the strain energies of nitrogen in GaP and GaAs into account. The strain energy, calculated by valence force field (VFF) methods, of a single N-atom in GaP is only 1.25 eV, whereas it was 1.69 eV in GaAs. This difference might well be responsible for the significant difference in nitrogen incorporation and convincingly confirms that there is a strong driving force by the crystal for the maximum N-content possible under certain growth conditions. Despite the difference in total nitrogen content achieved under equivalent growth conditions, the temperature dependence for the nitrogen incorporation shows the same activation energy for both materials, Ga(NP) and GaNAs. This underlines that in the case of ternary dilute nitrides gas-phase reactions resulting in a loss of reactive nitrogen species also

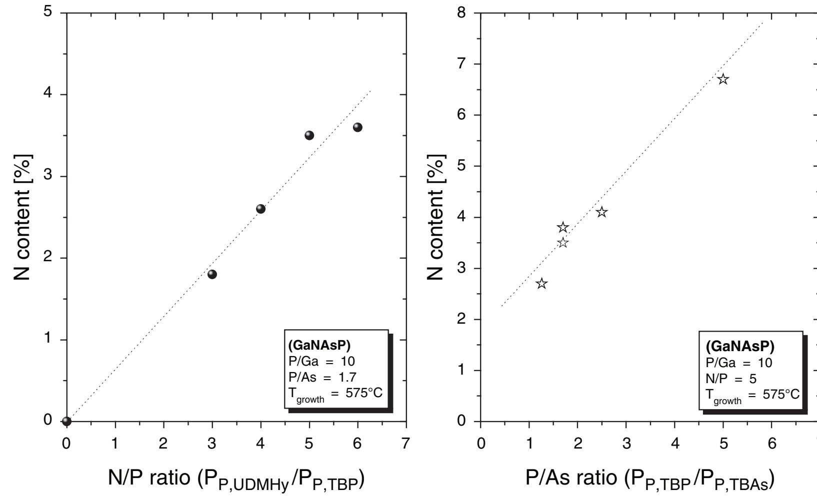

Fig. 13.4. Nitrogen incorporation into $GaNAs_{<0.75}P$ depending on different V/V ratios

play a large role and are present to the same extent in the growth of Ga(NP) as well as GaNAs.

The N-incorporation in the quaternary material system generally takes place by group-V competition on the surface of the growing crystal. These dependencies are elucidated in Fig. 13.4. Here, the N-content in quaternary layers with As-contents below 75% is plotted in dependence of the UDMHy/TBP gas-phase ratio (left graph). The other growth conditions were hold constant. The nitrogen content was determined by SIMS measurements in this case.

To vary the N/P ratio, the partial pressure of the UDMHy was varied, keeping the TBP partial pressure constant. It can be seen that the N-incorporation increases linearly with increase in UDMHy partial pressure. Hence, the nitrogen content in this alloy could most easily be adjusted by just varying the UDMHy partial pressure.

Fixing $P_{\mathrm{P,UDMHy}}$ and $P_{\mathrm{P,TBP}}$ and varying the partial pressure of TBAs, one gets the dependence shown as the right graph in Fig. 13.4. It can be seen that the N-content is influenced by the gas-phase ratio of the other two group-V constituents of the crystal in that way that it decreases with increasing $P_{\mathrm{P,TBAs}}$. There are two possible reasons for this behavior. First, when decreasing $P_{\mathrm{P,TBAs}}$ to increase the TBP/TBAs ratio one reduces the competition for the reactive nitrogen species at the surface and hence might increase the nitrogen incorporation, as already seen from the previous discussion. On the other hand, it had also been shown that the nitrogen incorporation into GaP is significantly larger than into GaAs under identical growth conditions. Consequently, the decreasing As-fraction in the crystal might induce an increased nitrogen content. Hence, the nitrogen content should decrease, the

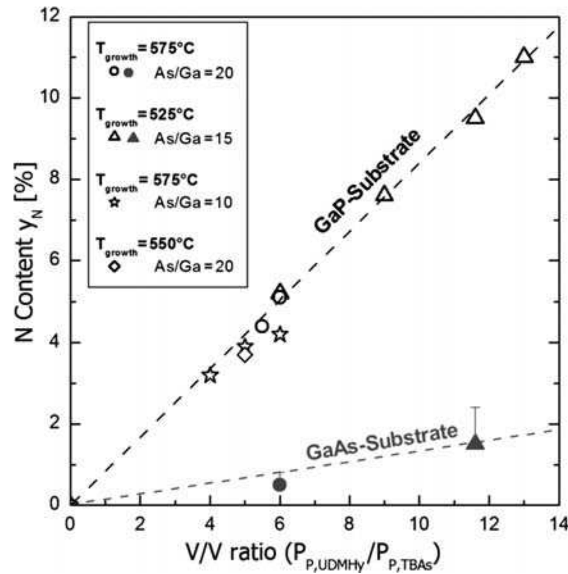

Fig. 13.5. Dependence of the N-content in GaNAs grown on GaP and GaAs substrates on the V/V gas-phase ratio. The different symbols belong to different growth parameters

more As-rich a mixed (GaNAsP) crystal becomes, if other growth conditions are not changed.

In this conjunction, it is instructive to examine the difference in nitrogen incorporation characteristics in GaNAs grown on GaP and GaAs substrates, respectively, as shown in Fig. 13.5. For N-contents below 18%, GaNAs is compressively strained when grown on GaP, whereas it grows tensilely strained with respect to GaAs over the complete composition regime. In the first case, the addition of nitrogen reduces the compressive strain of the layer, while it increases the tensile strain in the latter case.

The nitrogen content increases, as mentioned before, with increasing UDMHy/TBAs ratio. The different data points belong to samples grown on GaAs (solid symbols) and on GaP substrates (open symbols) under different conditions, e.g., with different growth rate, TBAs/TEGa ratios or even at different temperatures in the case of GaNAs/GaP growth. The nitrogen incorporation is about a factor of 10 lower in GaNAs/GaAs than in GaNAs/GaP. This is an excellent example of strain-driven incorporation of – in this case – nitrogen in GaAs. As one builds up tensile strain with incorporating N in GaAs when growing on GaAs substrates, the crystal desorbs nitrogen. On the other hand, driven by the reduction of the compressive strain, the crystal incorporates additional N in GaAs, when grown on GaP substrates.

It is interesting to note that the GaNAs/GaP samples, which go into this figure, were grown at temperatures between 525 and 575°C. From

Fig. 13.3 the nitrogen content strongly depends on the growth temperature for GaNAs/GaAs as well as for Ga(NP)/GaP. This seems not to be the case for GaNAs/GaP. If temperature dependence would be similar to that of the other material combinations, the N-content should decrease by a factor of 2.5 when increasing the temperature by 50°C. As the data falls on one line, this reflects no temperature dependence in the growth window chosen. This might be traced back to the fact that the strong strain-induced incorporation of the nitrogen in GaNAs/GaP overshades all other possible N-incorporation effects.

Already from these few examples it becomes clear that the growth of (GaNAsP) on GaP substrate is highly complex and that the resulting nitrogen content in the quaternary layers is the result of Chap. 15, a difficult interplay of all growth parameters as well as the crystal composition. In the remainder of this chapter, material of different composition will be characterized structurally and the structure will be correlated to optical properties with the objective of deriving optimum compositions for potential device applications.

13.2.2 Structural Properties of GaInNAsP/GaP

It is well known for dilute nitrides grown on GaAs substrates that increasing the amount of nitrogen in the layers, structural degradation takes place. The following paragraph summarizes results on structural investigations by means of transmission electron microscopy (TEM) and XRD. The aim was to study structure in dependence on quinary alloy composition to pinpoint compositions favorable from the structural point of view.

To examine the structural quality of the samples, TEM investigations, using strain and composition sensitive reflections, as also applied to the GaAs based materials, were undertaken.

Influence of Nitrogen on Structural Characteristics

In Fig. 13.6 cross-section TEM dark field micrographs of GaNAs/GaP quantum wells having different nitrogen concentrations are shown under chemical- (left column) and strain-sensitive (right column) imaging conditions.

The nitrogen content as well as the strained lattice mismatch of the respective quantum wells with respect to the GaP substrates are also given in the Fig. 13.6. The samples having the lowest nitrogen content have the largest lattice mismatch with respect to the GaP substrate and hence are highly compressively strained. The chemical composition is homogeneous in the growth plane for all N-contents investigated here, indicating that N-clustering with N-variations exceeding ±0.5% does not play a role. With increasing nitrogen content one observes an increased roughening of the upper quantum well interface with the GaP barrier, despite the reduction in macroscopic compressive strain, when increasing N. This modulation is typical for layers that undergo a Stranski–Krastanov growth mode transition, which can, however, not be the case here, as increasing the N-content shifts the overall strain more towards the

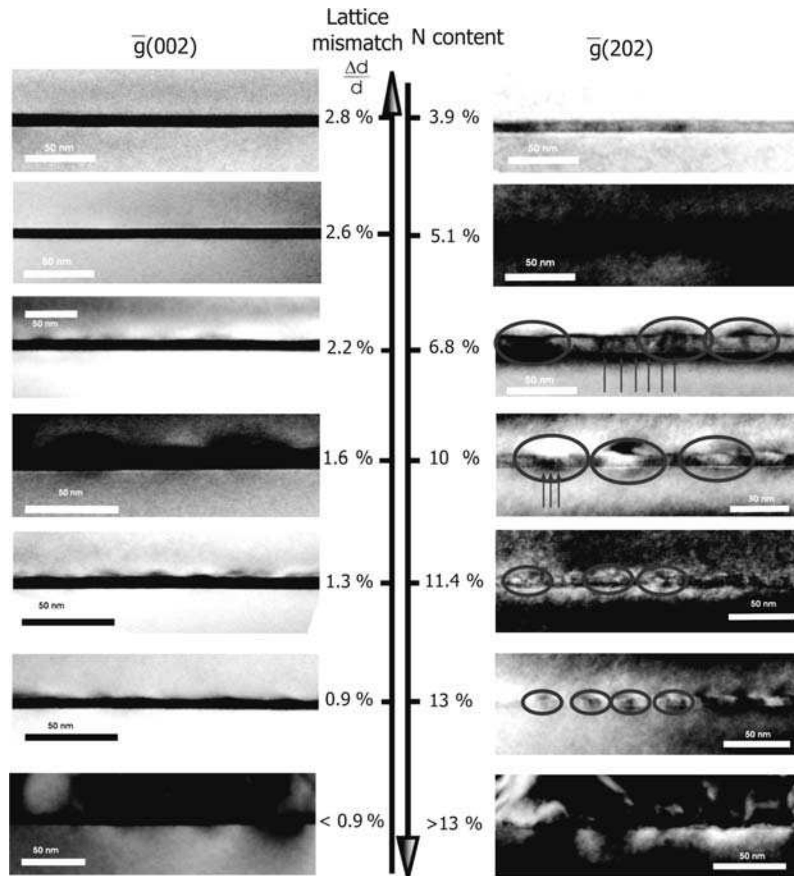

Fig. 13.6. Cross-sectional dark field TEM micrographs of GaNAs/GaP quantum wells with different nitrogen contents, taken under composition-sensitive (*left-hand side*) and strain-sensitive (*right-hand side*) conditions. The nitrogen content incorporated in the quantum wells as well as their respective lattice mismatch to the GaP-substrate is given in the center column. The arrows indicate strain fields, which are originated by N-ordering. Accumulation of these strain fields leads to larger scale strain fluctuations, which are encircled

lattice-matched conditions. We also do not observe clustering of the elements, which would be characteristic of Stranski–Krastanov transitions, which result at the end in quantum-dot formation. A similar roughening transition had already been observed when investigating GaAs-based materials and when increasing the nitrogen content in GaInNAs/GaAs above a certain critical value [10, 11].

One can attribute this morphological phase transition, which is now observed for the GaP-based material as well, to the inhomogeneous microscopic strain in the samples, introduced by the chain-like ordering of nitrogen in

growth direction. This ordering is energetically favorable also in the GaP-based GaNAs, as shown by VFF calculations, which also take the strain with respect to the substrate into account. The number of the N-induced strain fields increases with increase in N-content in GaNAs and GaInNAs [12]. nitrogen chains as proposed here are a strong source of tensile strain in the host materials. The strain field they introduce penetrates several nanometers into the surrounding material, as shown by VFF calculations [13]. As their distance decreases with increase in number, they might be close enough at a certain concentration to act collectively and have a roughening effect on the material grown on top. This is also what one observes under strain sensitive imaging conditions for GaNAs/GaP quantum wells with increasing N-concentration (right column Fig. 13.6). For N-contents below 5% one observes inhomogeneous strain fields in the material, as also seen in GaNAs/GaAs. The density of the strain fields increases, and at N-contents in the range of 7%, one already observes an accumulation of the strain fields together with a roughening of the quantum well interface. As the strain fluctuations in the material become more pronounced with increasing nitrogen content and decreasing macroscopic strain, one observes more and more degraded morphology of the dilute nitride material. This morphological degradation, which goes along with increasing nitrogen content and increasing inhomogeneous strain, is an intrinsic property of the dilute nitride materials, as this phenomenon had been observed in material grown with different growth techniques, under a wide range of growth conditions and irrespective of the strain state, the N-containing material has with respect to the substrate material. Despite the morphological degradation, the crystalline quality of the metastable materials and the barriers grown on top remains excellent. This is proven by high-resolution imaging GaNAs/GaP having N-contents of 3.9 and 13%, respectively (Figs. 13.7 and 13.8).

The quality of the lower GaP/GaNAs interface is remarkable. Despite the high N-content incorporated in the structure shown in Fig. 13.8 the transi-

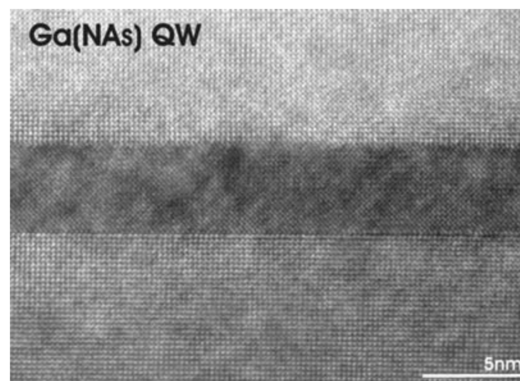

Fig. 13.7. High resolution TEM micrograph of a GaNAs/GaP quantum well, having a nitrogen content of 3.9%

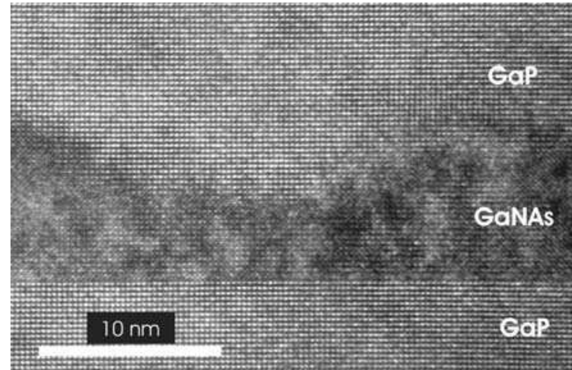

Fig. 13.8. High-resolution TEM micrograph of a GaNAs/GaP quantum well, having an N-content of 13%

tion between the GaP- and GaNAs-based materials is abrupt within a few (1–2) monolayers without the sign of any additional roughness. This confirms that the group-V exchange sequence from phosphorous to arsenic as applied here yields smooth interfaces. The upper interface of the GaNAs quantum well containing 3.9% nitrogen is rather smooth, exhibiting a roughness of 3–4 monolayers. In contrast to that, the morphology of the quantum well having an N-content of 13% is completely changed. There are regions where the material is significantly thicker than the nominal thickness and on the other hand also areas where the nominal quantum well thickness significantly exceeds the observed one. This is again the manifestation of the morphological phase transition, described for GaInNAs before [10,11]. Up to now there is no viable way of circumventing this structural degradation, which goes along with increasing the N-content. Hence, the influence of adding phosphorous and reducing the compressive strain by growing a three group-V element containing alloy (GaNAsP)/GaP was checked and the structure of these films will be shown in the following. Introducing this quaternary material, one is able to reduce the compressive strain with the addition of phosphorous instead of nitrogen.

Influence of Phosphorous on Structural Characteristics

Dark-field TEM micrographs of a (GaNAsP)/GaP quantum well are shown in Fig. 13.9. The quaternary material has a nitrogen content of $(5 \pm 1)\%$ and a phosphorous content of $(9 \pm 6)\%$. Consequently, the structure can be compared with the GaNAs/GaP sample shown second from the top of Fig. 13.6 with respect to the nitrogen content and with the sample shown third from the top in the same figure from the point of view of lattice mismatch with respect to the substrate.

The dark field micrograph taken using the $g = (002)$ reflection (left image), which exhibits chemical sensitivity, proves that the elements are also distributed homogeneously in this quaternary alloy. In the strain-sensitive image

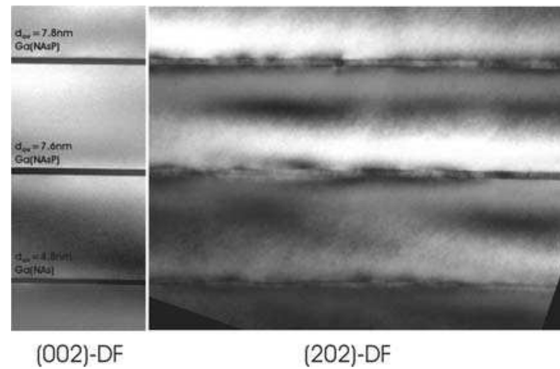

Fig. 13.9. Cross-section dark-field TEM micrographs of a (GaNAsP) quantum wells, taken under chemically sensitive (*left image*) and strain-sensitive (*right image*) conditions

shown on the right one observes N-induced strain fluctuations, which are present in an extent one would expect from the nitrogen content of 5%. The morphology of the quantum well also resembles that of samples having similar N-content, not strain. Compared with ternary structures having similar strain and higher N-content, the morphology of the quaternary sample is superior. Hence, replacing nitrogen by phosphorous for strain compensation yields better structural quality. However, inhomogeneous strain fields, caused by nitrogen ordering, are also found in the quaternary (GaNAsP) structures and cannot be dissolved upon annealing.

Influence of Indium on Structural Characteristics

As one can assume that the inhomogeneous strain fields detected in all dilute nitride materials are carrier traps and thus significantly deteriorate electronic and optical properties of the material, it is of importance to find possibilities to also dissolve them in the GaP-based material. A possibility to remove the N-induced strain fields in the case of GaInNAs was the annealing of In-containing material and the nearest neighbor change of the nitrogen from a Ga-rich environment adopted during growth in an In-rich, taken after the annealing. In context with the growth of GaInNAs solar cell material – as detailed in Chap. 15 – it had, however, been shown that a certain minimum Indium concentration is necessary to have the possibility at all to rearrange the nitrogen atoms.

Following this approach, Indium was incorporated into the (GaNAsP) layers. As the lattice mismatch for already 4% nitrogen in GaNAs/GaP still amounts to almost 3%, incorporation of In, which further adds compressive strain to the crystal, will be a challenge. In Fig. 13.10 strain-sensitive dark-field TEM micrographs of a GaInNAsP quantum well having an In-content of 3% as well as a N-content of (4 ± 1)% are shown. The upper micrograph had been

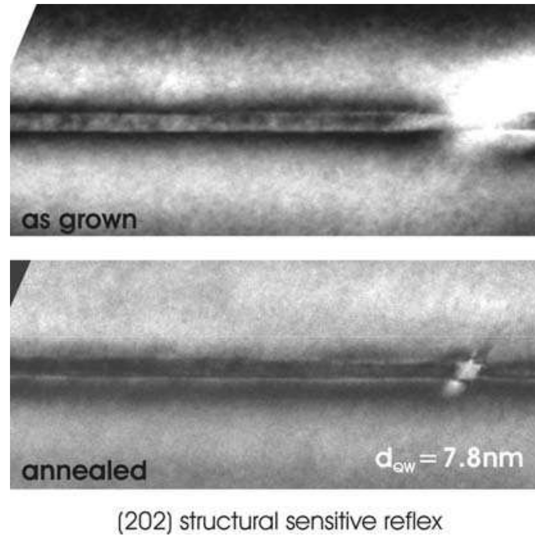

Fig. 13.10. Structurally sensitive dark-field TEM images of a $(GaIn_{0.03})(NAsP)$ quantum well before (*upper micrograph*) and after (*lower micrograph*) annealing for 1 h at 800°C under TBP stabilization

taken before annealing the sample at 800°C for 1 h under TBP stabilization, and the lower micrograph after doing so. The contrast fluctuation, proving the existence of inhomogeneous strain fields caused by the nitrogen, is clearly visible in the grown sample. However, after annealing, the contrast structure throughout the quantum well is a lot more homogeneous, pointing to the fact that it had been possible to dissolve a large amount of the strain fields. What one, however, always observes under the growth conditions chosen at present is the formation of defects as well as a significant roughening of the quantum wells as soon as small amounts of Indium are added. This might underline that the transition to Stranski–Krastanov growth, which had been shifted towards larger lattice mismatches when growing a mixed group-V alloy, again shifts towards lower strains when a second group-III element is mixed into the crystal. These findings emphasize that it will be necessary in future to optimize growth conditions in a way to allow for the growth of highly compressively strained material that is mixed on the group-V as well as group-III sublattice.

Structural Properties upon Annealing

Annealing had been shown to be necessary also in this dilute nitride material system to remove defect and enhance PL intensity as well as to structurally improve the material. High-resolution X-ray diffraction (HRXRD) ω-2ϑ scans of a GaNAs/GaP multiquantum well structure around the (004) reflection of GaP are shown in Fig. 13.11. The profiles were taken from the same sample before and after annealing at 800°C for 1 h under TBP stabilization.

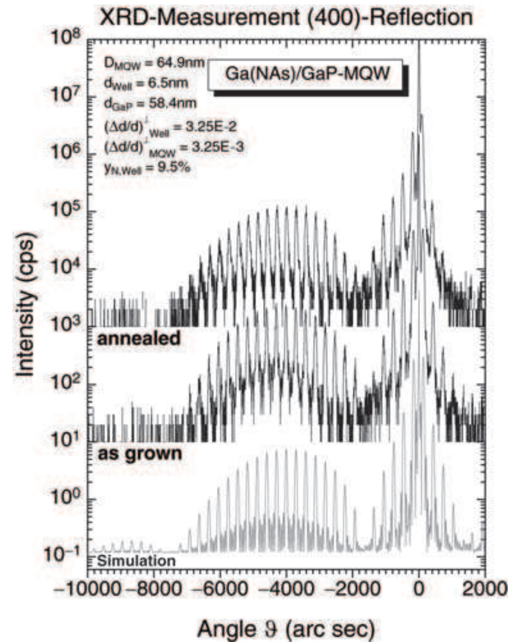

Fig. 13.11. High resolution XRD ω-2ϑ scans around the (004) GaP reflection of a GaNAs/GaP multiquantum well structure before and after annealing (1 h, 800°C, TBP stabilized). The dynamical simulation matching the experimental profiles is shown in grey.

There is no significant difference between the structures before and after annealing. The Pendellösung fringes are well resolved in both cases, and their position as well as the envelope, which gives the compressive strain of the quantum wells, did not shift upon annealing. This is a clear indication that neither quantum well thickness nor nitrogen content did change upon annealing. Hence, nitrogen out-diffusion can be ruled out to happen under the annealing conditions chosen here. The simulation to the experimental HRXRD profiles using dynamical theory gives a nitrogen content of 9.5%. The other layer parameters derived from the simulation are indicated in the inset of the figure. Adding phosphorous to the quantum well and annealing these samples does not lead to any observable change in HRXRD profiles either.

13.3 Optical Properties and Band Structure

The following paragraph describes the optical characteristics of selected samples in the (GaNAsP)/GaP material system and depicts their direct band gap, which makes them suitable for laser applications, as will be shown in the

following paragraph. An estimate of the modification of the conduction band structure of the alloy in dependence on its composition will also be given.

Photoluminescence (PL) measurements were carried out under direct excitation of the QWs using a CW Ti:sapphire laser at an emission wavelength of 800 nm or applying an Ar-ion laser at the wavelength of 514 nm. The samples were mounted on a cold finger liquid helium cryostat in order to allow for temperature dependent measurements. The PL signal was dispersed in a 1 m grating monochromator (THR 1000, Jobin-Yvon) and collected by a cooled germanium detector applying standard lock-in technique. First PL investigations of a grown and annealed MQW structures had shown that a post growth annealing step of 1 h at 800°C under TBP stabilization leads to a significant increase of the luminescence intensity. Therefore, all samples discussed in following are annealed accordingly.

The photoluminescence excitation (PLE) (full line) and the PL (dotted line) spectra at low temperature of the annealed (GaNAsP)/GaP-MQWH with 4% N and 6% P are given in Fig. 13.12 [7]. A sharp and intense emission band of the quaternary material system at a peak emission wavelength of 905 nm and a line width of 38 meV (FWHM) is obtained under direct excitation of the QWs using a CW excitation wavelength of 800 nm. Here carriers are only excited in the QWs whereas the GaP barrier is transparent for the photon energy of 1.55 eV, respectively. The energetic overlap of the PL and PLE spectra proves that the (GaNAsP)/GaP-MQWH exhibits a direct band gap,

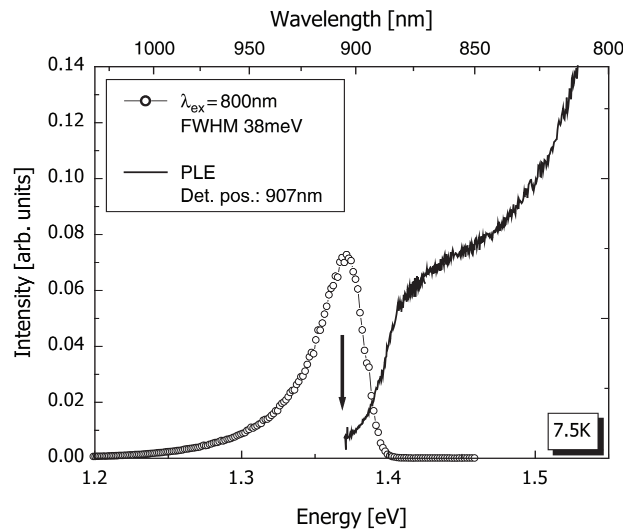

Fig. 13.12. Optical spectroscopy of a 8-periode sample (GaNAsP)/GaP-MQWH at temperature of 7 K (*dotted line*: PL spectrum, *solid line*: PLE spectrum). The PL-spectrum was excited at a wavelength of 800 nm, the detection wavelength of the PLE-spectrum is 907 nm (*black arrow*)

where the PL emission results from carrier recombination out of the respective band tails of the direct energy gap in this material system. The pronounced shoulder in the PLE spectrum models the expected two-dimensional step-like density of states of the direct band gap, which is broadened due to the intrinsic quaternary alloy disorder. The spectral features reported here [7] for the quaternary (GaNAsP)-MQW structure are significantly sharper as compared to the first spectroscopic reports for the ternary GaNAs/GaP-QWH in the literature [14, 15].

With increasing sample temperature the luminescence intensity of the (GaNAsP)-MQWH is decreasing as reviewed in Fig. 13.13. The inset in this figure displays the temperature quenching of the integrated intensity. This decline in the PL intensity observed also for the GaAs-based diluted nitride GaInNAs system [16] can be modeled by the interplay between radiative and nonradiative recombination and hopping dynamics of excitations in the manifold of localized states created by the disorder potential [17]. In addition, the energetic PL peak position follows an S-shape in the low to intermediate temperature range and converges towards a standard Varshni-type characteristic of direct semiconductors at high temperatures. This S-shape behavior is typical for dilute nitrides [18] and also an evidence for the pronounced degree

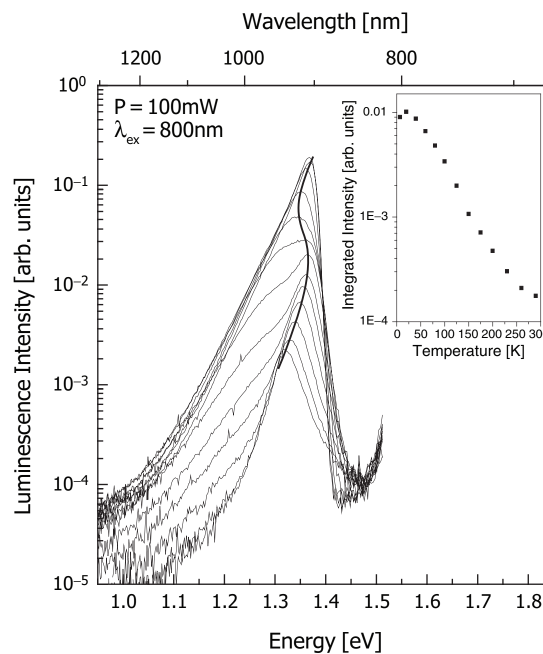

Fig. 13.13. Temperature dependent PL measurements of a 8-periode (GaNAsP)/GaP MQWH. The QWs were directly excited with a wavelength of 800 nm and a power of 100 mW. As a guide to the eye the S-shape behavior of the PL peak position is indicated by a solid line. The inset gives the integrated luminescence intensity vs. sample temperature

of disorder due to alloy fluctuation and/or imperfect interfaces, which leads to carrier localizations (see Chap. 7). Nevertheless, efficient PL is observed even at room temperature with a peak wavelength of 942 nm and a line width of 56 meV.

The above mentioned studies verified the direct band gap characteristic of the novel (GaNAsP)/GaP-MQWH system. In the following we briefly exploit the concentration range for which we expect a direct energy gap of the (GaNAsP)-material system. For this estimate we consider first the variations of the Γ- and X-levels with chemical composition and strain, then introduce the energetic position of the N-level and model the obtained energy gap by the simple band anticrossing (BAC) model. It is important to note that also physical parameters are used, which are not yet known precisely for this materials system. The energy position of the Γ- and X-energy levels of Ga(AsP) ($x_{\mathrm{As}} > 50\%$) are plotted in Fig. 13.14 as function of the As-concentration, taking also the modification of these levels as a function of macroscopic strain into account. For clarity we fixed the N-concentration at 4% for the pseudomorphically strained (GaNAsP)-layer in the following.

The relative changes $\Delta E^{\mathrm{CB}}(\Gamma)$ and $\Delta E^{\mathrm{CB}}(\mathrm{X})$ of the two extrema in the conduction band with the strain ε were evaluated using the hydrostatic deformation potential constants $a_i(a_\Gamma$ or $a_{\mathrm{X}})$ listed in the inset of Fig. 13.14 and the following equation [19]:

$$\Delta E^{\mathrm{CB}}(\Gamma, \mathrm{X}) = -2a \left(\frac{c_{11} - c_{12}}{c_{11}} \right) \varepsilon, \qquad (13.1)$$

with the elastic stiffness constants c_{ik}. Any modifications of the band structure due to biaxial strain of the X-states and the valence bands are neglected. The N was considered as an electronic impurity N-band, the energy level E_{N} of which was extrapolated from the ternary composition endpoints of the window in Fig. 13.14 (GaAs:N and GaP:N). In literature an increasing pressure dependence of the N-level with rising N-concentration was reported for the diluted nitride Ga(NP) [20]; thus, we used a value of $45\,\mathrm{meV\,GPa^{-1}}$ for the strain induced shift of the N-level [21].

In order for the $\mathrm{Ga(N_{0.04}As_xP_{1-x})}$-material system to exhibit a real direct energy gap, the Γ-level has to be lowest in energy with the N-level positioned in between the Γ- and the X-level. This condition is fulfilled for a relative broad concentration range for As-concentrations in excess of about 70%, see Fig. 13.14. The band gap energy can be extracted out of PL/PLE spectra within a certain error bar at room temperature. Experimental data points (squares) of three samples with varying compositions are added to the theoretical estimate in Fig. 13.14. All samples contain a maximum of about 4% N and different P-fractions between 16% and 0%. The energy positions of the experimental band gaps are very much redshifted compared with the position of the Γ-level at corresponding composition. This indicates a strong BAC coupling of Γ- and N-levels also in the GaP-based (GaNAsP) material system.

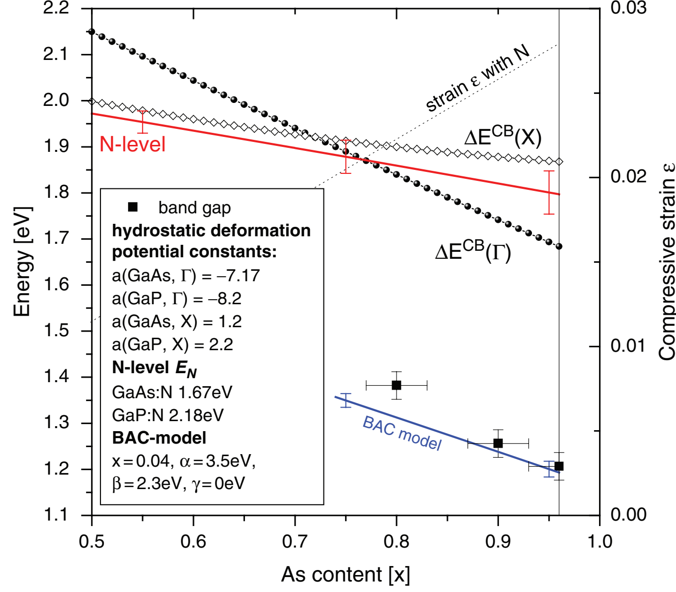

Fig. 13.14. Estimation of the relative modification $\Delta E^{\mathrm{CB}}(\Gamma, \mathrm{X})$ of the conduction band extrema of (GaNAsP)/GaP-MQW structures as a function of As-concentration for a fixed N-content of 4% (*full circles*: Γ-level, *open diamonds*: X-level, *solid line*: N-level). The squares mark the band gap energy of three investigated samples. The energetic position of the E_- subband calculated by the BAC model is shown as a solid line, whereas the error bars are related to the uncertainty of the N-level. The value of the compressive strain ε of the (GaNAsP) individual quantum well layers with respect to GaP (right hand axis) as a function of the As-concentration is indicated as a dotted line

In the two-band BAC model, the modification of the conduction band is explained as an anticrossing interaction between highly localized A_1 states of the substitutional N atoms and the extended states of the host semiconductor matrix [22]. This model was first applied to parameterize the strong band gap bowing of GaAs-based materials system like GaNAs and GaInNAs, respectively [23, 24], and is described in detail in Chap. 3. According to this model the newly formed lowest subband position E_- is given by

$$E_- = \frac{1}{2}\left[(E_N - \gamma x) + (E_\Gamma - \alpha x) - \sqrt{[(E_N - \gamma x) - (E_\Gamma - \alpha x)]^2 + 4\beta^2 x}\right], \tag{13.2}$$

x is the N concentration and is kept constant at 0.04. As the values of the parameters α, β, and γ are not known yet for the (GaNAsP)-material system, they were adopted from the GaAs-based material system $\mathrm{Ga(N}_x\mathrm{As}_{1-x})$ out of [23]. The energetic position of the E_- level (solid line in Fig. 13.14) agrees

favorably well with the experimental values for the GaP-based (GaNAsP) material system. The best coincidence is observed for low P contents whereas a certain deviation develops with increasing P concentration. As the parameters α, β, and γ were taken from the P-free material system GaNAs, this slight deviation, however, is not surprising.

For a more precise and sophisticated description of the band structure formation a polymorphous model is necessary, which considers the perturbation of the host states and the effects of the random N-distribution leading to a disordered alloy. Zunger and coworkers are using an empirical pseudopotential method and large atomistically relaxed supercells to describe the evolution of the electronic structure of diluted nitrides [21]. The application of this more advanced theory will lead to more detailed description of the direct band structure of (GaNAsP)-MQWH based on GaP-substrate in the future.

For the discussion of the As-composition range regarding the direct band structure formation, the N-content was fixed to 4%. To investigate the N-dependence of the luminescence characteristic a series of P-free GaNAs/GaP-MQW samples were grown pseudomorphically strained on GaP-substrate. This allows for a straight forward way to determine the N-concentration by XRD measurements of the ternary material system. The structural characteristics of these samples were already described in the preceding section (see Fig. 13.6). Room temperature PL spectra of GaNAs/GaP MQWHs with different N-content are compared in Fig. 13.15. An excitation wavelength of 514 nm was chosen for these experiments.

The luminescence intensity of the sample series is decreasing with rising N-concentration in the active material significantly. For N-concentrations above 10% only a weak luminescence signal is observed for the applied excitation conditions. The incorporation of high amounts of N yields presumably to the formation of a large number of nonradiative recombination centers. This behavior was also observed for GaAs-based diluted nitrides. The origin might be the N-correlated incorporation of impurity atoms and/or the defect formation due to agglomerations of N [12, 13]. Furthermore, the PL peak position is shifting toward longer emission wavelength with increasing N-incorporation. This redshift is a typical phenomenon for dilute nitrides [23]. The increasing N-content leads to a stronger repulsion between the extended Γ-states and the N-impurity band, resulting in a pronounced N-dependence of the band gap bowing. These first experiments show that the emission wavelength of the novel GaP-based (GaNAsP) material system can be pushed beyond 1,100 nm possibly allowing for laser devices with emission energies below the indirect band gap of Si at 1.124 eV in the future. However, it is essential to improve the crystal quality and emission efficiency by careful optimization of the epitaxial growth process further to realize efficient laser device structures.

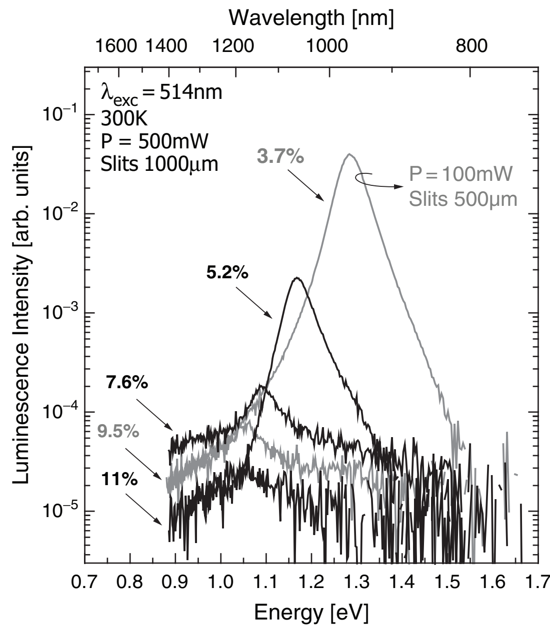

Fig. 13.15. Room temperature PL measurements of GaNAs/GaP-MQWHs varying composition. The samples have been excited with a wavelength of 514 nm

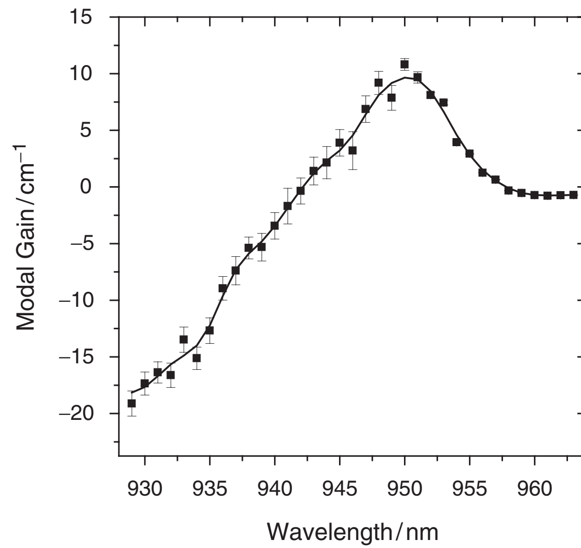

Fig. 13.16. Modal gain at room temperature according to the stripe-length method. The standard deviation of the data points are shown in arrow bars [25]

13.4 Laser Devices

To test also possible device applications of this novel class of materials, various (GaNAsP)/GaP-MQWH were embedded in doped and undoped $(Al_{0.25}Ga_{0.75})P$/GaP-separate confinement heterostructures (SCH). The SCH layers were grown by MOVPE using trimethyl gallium (TMGa) and trimethyl aluminum (TMAl) in combination with TBP at growth temperatures of 675–725°C. The layer thickness of the nominally undoped GaP-separate confinement layer was chosen to 400 nm. Diethyl tellurium (DETe) and diethyl zinc (DEZn) were used as n- and p-type dopant. To exclude possible prereactions between the Al- and N-precursors the laser structures were realized in separate MOVPE-systems connected via a common glove box. After epitaxial growth of the active (GaNAsP)/GaP-single quantum well heterostructure (SQWH), the sample was annealed at 750°C for 1 h under TBP-stabilization to improve the luminescence efficiency.

Depending on the investigations the grown laser structures were cleaved into bars with cavity lengths in the range from 500 μm to several millimeter. In first experiment undoped laser bars were optically pumped applying a femtosecond Ti-Sapphire based amplifier system with a pulse center wavelength of 800 nm. A clear threshold behavior as a function of pump intensity and a longitudinal mode spectrum characteristic for laser action were detected for temperatures even up to room temperature [25]. In a second series of experiments the bars were excited using a nanosecond frequency doubled Nd:YAG laser system at an excitation wavelength of 532 nm at room temperature. Optical gain has been obtained by applying the spectrally resolved variable stripe length method [26]. The values of the determined modal gain as a function of emission wavelength are summarized in Fig. 13.16. The spectral dependence of the modal gain curve in the novel (GaNAsP)/GaP-MQWH resembles that of standard III/V-compound semiconductor systems with respect to both spectral width as well as peak modal gain. A peak modal gain of $10\,cm^{-1}$ has been measured for a sample structure with a relatively small optical confinement factor due to the low Al-content in the $(Al_{0.25}Ga_{0.75})P$/GaP-SCH. This is an indication for a relatively high material gain of the novel dilute nitride (GaNAsP)/GaP.

The processing of broad laser structures allows for electrical injection of the active material system. Fifty micrometer wide Au/Cr-metal stripes were deposited for the p-contact layer and an Au/Ni/AuGe-based full backside n-contact. For part of the laser bars the cleaved facets were coated with standard high reflection coatings. The finished laser bars were mounted p-side up in a variable temperature cryostat for temperature-dependent measurements under pulsed injection conditions (pulse length 440 ns, duty cycle 0.1%). The emission of the laser facets was either focused on a power meter or dispersed in a 1 m grating monochromator for evaluation of the spectral characteristics.

The optical output characteristics in Fig. 13.17 indeed demonstrate the lasing operation of these very first GaP-based laser devices. For this laser

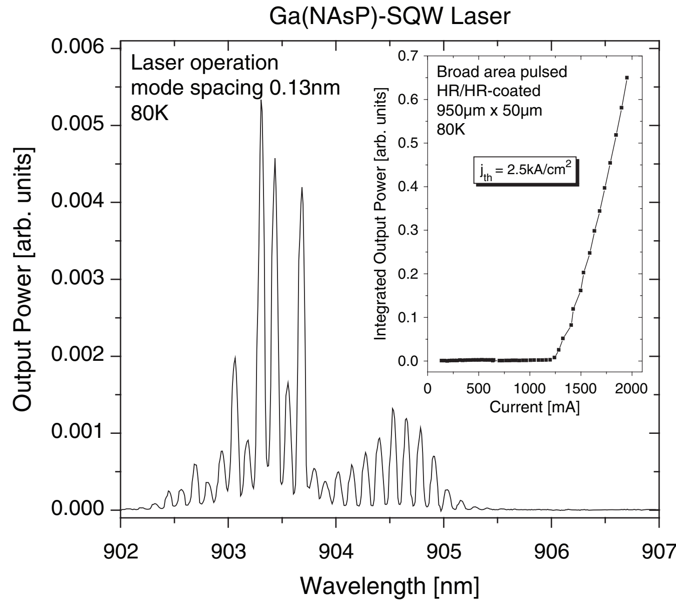

Fig. 13.17. Spectrum of an electrically pumped (GaNAsP)/GaP-SQWH laser structure with stripe width of 50 μm and a cavity length of 950 μm under pulsed operation at 80 K. The facets have been coated by standard high reflection coatings. The inset shows the threshold type output characteristic as a function of current [6]

structure the p^+-GaP:Zn contact layer has not been etched off, thus, a considerable current spreading is expected. As an inset in Fig. 13.17 the optical output power is shown as a function of current under pulsed operation. Defined threshold behavior of the output power is observed. In addition, the optical output spectrum as a function of emission wavelength clearly exhibits the expected modal characteristic of laser emission. The observed mode spacing of 0.13 nm agrees favorably well with the cavity length of 950 μm for this laser stripe [6]. For laser bars, where the top p^+-GaP:Zn contact has been selectively etched off, we observe threshold current densities of $1.5\,\mathrm{kA\,cm^{-2}}$ at 80 K. With increasing temperature an increase in the threshold current density is observed. Laser action under electrical injection conditions is obtained for temperatures up to 150 K, limited by the maximum current of 2 A under pulsed conditions in the variable temperature cryostat in our present experimental set-up.

At room temperature a clear threshold type behavior is observed for a current of about 20 A, resulting in a threshold current density of $42\,\mathrm{kA\,cm^{-2}}$ for these first SQWH laser diode [8], see Fig. 13.18. These high threshold current densities as well as the detected heating effects of the device with an increase in repetition frequency are due to significant nonradiative recombination processes still present in the structures studied. Future work will

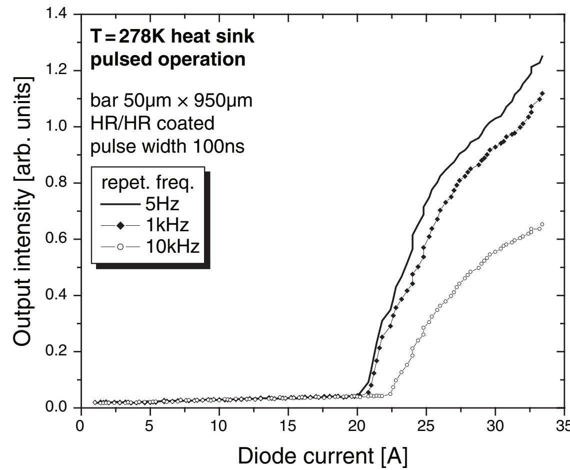

Fig. 13.18. Light/current characteristics of a (GaNAsP)/GaP-SQWH laser diode under pulsed operation at a heat sink temperature of 278 K for different repetition frequencies [8]

focus on the optimization of the MOVPE growth and annealing conditions of the novel (GaNAsP)/GaP-material system as well as in improvements of the optical confinement factor and in the electrical confinement by applying an optimized design for the waveguide structures.

The spectral emission characteristics of the (GaNAsP)/GaP-SQWH laser diode below and above threshold are summarized in Fig. 13.19 for a heat sink temperature of 278 K under pulsed electrical injection conditions. The electroluminescence spectrum (lower trace in Fig. 13.19) peaks at an emission wavelength of 943 nm with an emission line width of 66 meV (FWHM). Above threshold the emission spectrum (upper trace in Fig. 13.19) narrows drastically and a clear mode spectrum is detected (inset of Fig. 13.19), which proves the successful realization of an electrical injection laser in this novel (GaNAsP) material system around room temperature.

13.5 Summary

A material, which possesses a direct band structure and can be grown pseudomorphically strained on Si substrates, would have the potential to revolutionize today's semiconductor market. We propose the novel dilute nitride material system GaInNAsP/GaP to be a candidate to fulfil these aims.

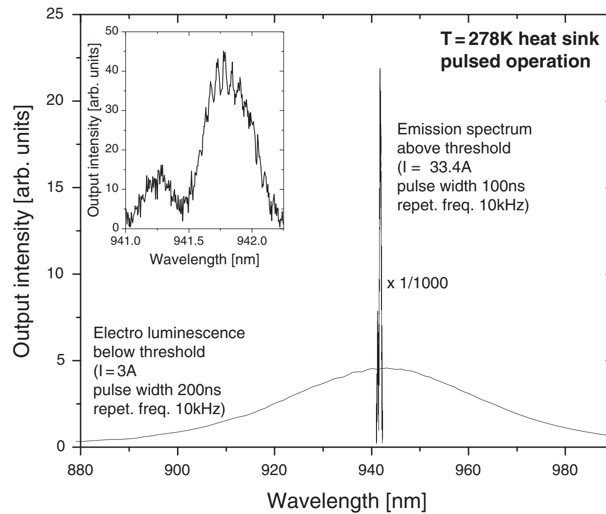

Fig. 13.19. Spectral emission characteristics of the (GaNAsP)/GaP-SQWH laser diode under pulsed operation at a heat sink temperature of 278 K for currents below threshold (electroluminescence spectrum lower trace) and above threshold (laser spectrum upper trace). The inset depicts the mode structure of the laser diode above threshold [8]

High quality, compressively strained GaInNAsP/GaP multiquantum well heterostructures were grown without the formation of misfit dislocations on GaP substrates by metalorganic vapor phase epitaxy. Photoluminescence and photoluminescence excitation measurements prove the direct band structure of this class of material systems for a wide range of compositions. This direct band gap character is in the first place due to the high As fraction incorporated into the crystal and secondly due to the effect of N, which introduces a further pronounced redshift of the direct energy gap. This can be understood in the framework of the band anticrossing model that was used to describe the band structure formation, which is similar to the one of other dilute nitride materials.

The proof of concept is given by demonstrating gain in this novel material system as well as by showing electrical injection lasing at low and at room temperature for the first time.

Acknowledgements. The authors gratefully acknowledge financial support from the Deutsche Forschungsgemeinschaft in the framework of the Topical Research Group on Metastable compound semiconductor systems and heterostructures and form $NAsP_{III/V}$ GmbH, Marburg.

References

1. L. Pavesi, L. DalNegro, C. Mazzoleni, G. Franzo, F. Priolo, Nature **408**, 440 (2000)
2. G. Franzo, F. Priolo, S. Coffa, A. Polman, A. Carnera, Appl. Phys. Lett. **64**, 2235 (1994)
3. O. Ozda, B. Jalali, Optics Express **12**, 5269 (2004)
4. H. Rong, R. Jones, A. Liu, O. Cohen, D. Hak, A. Fang, M. Paniccia, Nature **433**, 725 (2005)
5. S.F. Fang, K. Adomi, S. Iyer, H. Morkoc, H. Zabel, C. Choi, N. Otsuka, J. Appl. Phys. **68**, R31 (1990)
6. B. Kunert, S. Reinhard, J. Koch, M. Lampalzer, K. Volz, W. Stolz, Phys. Status Solidi C **3**, 614 (2006)
7. B. Kunert, K. Volz, J. Koch, W. Stolz, Appl. Phys. Lett. **88**, 182108 (2006)
8. B. Kunert, A. Klehr, S. Reinhard, K. Volz, W. Stolz, Elect. Lett. **42**, 601 (2006)
9. B. Kunert, K. Volz, J. Koch, W. Stolz, J. Cryst. Growth **298**, 121 (2007)
10. K. Volz, A.K. Schaper, A. Hasse, T. Weirich, F. Höhnsdorf, J. Koch, W. Stolz, Mater. Res. Soc. Symp. Proc. **619**, 271 (2000)
11. P.J. Klar, K. Volz, J. Phys. Condens. Matter. **16**, 3053 (2004)
12. K. Volz, T. Torunski, W. Stolz, J. Appl. Phys. **97**, 14306 (2005)
13. O. Rubel, K. Volz, T. Torunski, S.D. Baranovskii, F. Grosse, W. Stolz, Appl. Phys. Lett. **85**, 5908 (2004)
14. M. Kondow, K. Uomi, T. Kitatani, S. Watahiki, Y. Yazawa, J. Cryst. Growth **164**, 175 (1996)
15. W.G. Bi, C.W. Tu, Appl. Phys. Lett. **70**, 1608 (1997)
16. S. Shirakata, M. Kondow, T. Kitatani, Appl. Phys. Lett. **80**, 2087 (2002)
17. O. Rubel, S.D. Baranovskii, K. Hantke, B. Kunert, W.W. Rühle, P. Thomas, K. Volz, W. Stolz, Phys. Rev. B **73**, 233201 (2006)
18. R.J. Potter, N. Balkan, J. Phys. Condens. Matter **16**, S3387 (2004)
19. H. Asai, K. Oe, J. Appl. Phys. **54**, 2052 (1983)
20. W. Shan, W. Walukiewicz, K.M. Yu, J. Wu, J.V. Ager III, E.E. Haller, H.P. Xin, C.W. Tu, Appl. Phys. Lett. **76**, 3251 (2000)
21. P.R.C. Kent, A. Zunger, Phys. Rev. B **64**, 115208 (2001)
22. W. Shan, W. Walukiewicz, J.V. Ager III, Phys. Rev. Lett. **82**, 1221 (1999)
23. P.J. Klar, H. Grüning, W. Heimbrodt, J. Koch, F. Höhnsdorf, W. Stolz, P.M.A. Vicente, J. Camassel, Appl. Phys. Lett. **76**, 3439 (2000)
24. J. Wu, W. Shan, W. Walukiewicz, Semicond. Sci. Technol. **17**, 860 (2002)
25. S. Borck, S. Chatterjee, B. Kunert, K. Volz, W. Stolz, J. Heber, W.W. Rühle, Appl. Phys. Lett. **89**, 031102 (2006)
26. K.L. Shaklee, R.F. Leheny, Appl. Phys. Lett. **18**, 475 (1971)

14

Comparison of the Electronic Band Formation and Band Structure of GaNAs and GaNP

M. Güngerich, P.J. Klar, W. Heimbrodt, G. Weiser, A. Lindsay, C. Harris, and E.P. O'Reilly

III–N–As as well as III–N–P materials have been successfully employed in optoelectronic devices. Nitrogen impurities in the dilute range have been investigated in the indirect gap semiconductor GaP since the 1960s, where they were used to produce green light-emitting diodes. In recent years new developments in molecular beam epitaxy and metalorganic vapour phase epitaxy growth methods have made it possible to introduce up to a few percent of nitrogen into direct gap GaAs and indirect gap GaP. GaInNAs with N concentrations of about 1% has been used as the active material in vertical cavity surface emitting laser (VCSEL) devices operating at telecommunication wavelengths. However, GaAs:N and GaP:N differ considerably in terms of their electronic structure. In GaNAs the nitrogen impurity states in the doping regime lie resonantly in the conduction band. With increasing N-content a strong redshift of the GaAs-like fundamental band gap (referred to as E_-) occurs. It is accompanied by the formation of an N-induced E_+ band, which blueshifts with increasing N. This repulsion behaviour of E_- and E_+ can be well parameterized by a simple two-level band-anticrossing model, which forms the basis of the 10 band $\boldsymbol{k}\cdot\boldsymbol{p}$ model successfully employed for describing the electronic states of III–N–As layers in laser structures in the vicinity of the GaAs-like E_- band gap. The situation in GaP is somewhat different because the N levels in the doping regime are situated in the band gap close to the X conduction band states (corresponding to the indirect gap), i.e. well below the Γ conduction-band states of GaP (corresponding to the direct gap). In other words, the order of the N states and the Γ conduction band states is reversed. With increasing N content, the lowest conduction band must then evolve from the N-like states in GaNP. The question then arises as to whether the band-anticrossing model yields a good description of the lowest conduction band E_- in this case. If so, the lowest band gap will in a two-level band-anticrossing model acquire a large Γ-like density of states comparable to a direct semiconductor, which is a prerequisite for employing GaNP based heterostructures in the active region of laser devices. In this review, we compare the electronic structure of GaNAs and GaNP, demonstrating that, in GaNP, the Γ character

in the energy range of the N localized states is spread over a broad variety of transitions. This situation cannot be properly parameterized by the simple band-anticrossing model and indicates that, in contrast to GaNAs, the lowest conduction band states are not suitable to promote laser action in GaNP alloys.

14.1 History of Dilute-N III–V Semiconductor Alloys and Corresponding Optoelectronic Devices

The substitution of a small fraction of the group V atoms in GaP, GaAs, or GaSb by nitrogen leads to the introduction of isoelectronic impurities, which form localized electronic states in the doping regime, i.e. at small N concentrations. Figure 14.1 depicts schematically the energetic positions of the N localized levels relative to the band gaps of GaAs and GaP as well as the N-induced band formation taking place in GaNAs when N concentrations are increased to a few percent, i.e. into the alloying regime, as discussed in detail further.

The main difference between the two binary zinc-blende semiconductors is that GaAs possesses a direct gap at the Γ point of the Brillouin zone as the lowest band gap, whereas GaP has an indirect lowest gap, with the valence band maximum at Γ and the lowest conduction band states at X. The lowest Γ conduction band in GaP, which forms the direct gap, is over 0.5 eV above the lowest conduction band at X. Furthermore, the localized N-levels in GaAs are resonant with the conduction band states, whereas in GaP they are situated below the host conduction bands. The $GaAs_{1-y}P_y$ alloy can be formed

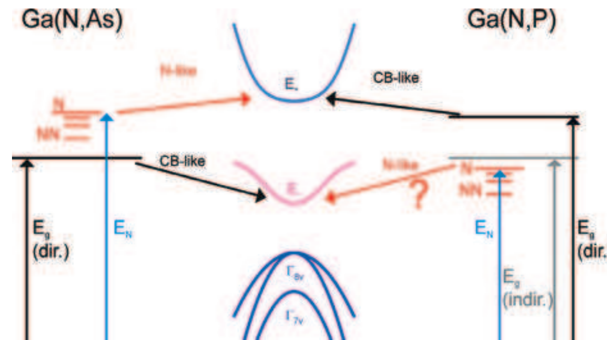

Fig. 14.1. Energy scheme of the N localized levels relative to the host band gaps in GaNAs and GaNP. N denotes the isolated N level while NN stands for N pairs or clusters. The N-induced formation of E_- and E_+ bands in GaNAs and GaNP is symbolized in the centre of the figure with arrows linking these bands with the states they originate from in the framework of the BAC model. The question mark for GaNP reflects the discussion presented later as to the applicability of this BAC model to GaNP

over the entire composition range y. Varying the amount of phosphorus y in the ternary alloy allows one to continuously tune the electronic band structure between those of the two binaries. The lowest band gap of $GaAs_{1-y}P_y$ becomes indirect for $y > 0.45$ ([1] and references therein). Nitrogen remains an isolectronic impurity over the entire composition range. The isolated N state changes from being resonant in the conduction band to being located below the conduction band at $y > 0.35$ and then follows the lowest conduction band at higher y [2–9].

The technological potential of $GaAs_{1-y}P_y$:N was soon realized and first steps towards optoelectronic devices were undertaken. Starting in the 1960s, when only equilibrium methods for crystal growth were known, nitrogen-doped GaP was used as the active material for green light-emitting diodes (LEDs) because electrons can be excited electrically into the localized N states and the radiative recombination of excitons bound to N impurities is very efficient [10]. This behaviour arises from the fact that the N impurity states in GaP are situated within the band gap of the host and therefore can be regarded as the lowest conduction band states. A large variety of N-induced impurity states was discovered with the help of photoluminescence spectroscopy and assigned to isolated N atoms as well as to NN pairs of different interatomic distances [2, 3]. At about the same time, $GaAs_{1-y}P_y$:N was also used for fabricating LEDs with emission energies peaking at 1.8–2.2 eV, i.e. in the red to yellow spectral range [11]. Optically pumped laser action (stimulated emission) out of N-related states was reported in $GaAs_{1-y}P_y$:N, both in the direct gap ($y < 0.45$) and in the indirect gap ($y > 0.45$) regimes [12–15], but always in the vicinity of the cross-over point of $y = 0.45$. However, no stimulated emission of the N states and no gain was observed in GaP:N in a similar experiment [16].

Nitrogen doping of GaAs had to wait longer for its application in optoelectronics. This is mainly due to the fact that under ambient conditions the isolated N level in GaAs lies resonantly in the host conduction band, about 200 meV above the conduction band minimum and therefore does not contribute significantly to luminescence in this material [4]. N pair and N-cluster states are formed in a range of 200 meV below the isolated N-state, i.e. also above the band edge. Additionally, GaAs, in contrast to GaP, shows a high efficiency of intrinsic luminescence because of the direct band gap. Consequently, N concentrations in GaAs have to exceed the doping range to substantially modify the emission characteristics and to offer new possibilities for optoelectronic devices. Nitrogen incorporation at concentrations sufficient to observe modifications of the light emission compared with GaAs became possible in the early 1990s, when advanced non-equilibrium growth techniques using molecular beam epitaxy (MBE) and metalorganic vapour phase epitaxy (MOVPE) were employed to push the N content x in GaN_xAs_{1-x} alloys up to a few percent [17, 18]. It was shown that GaNAs, in contrast to the well-known amalgamation-type semiconductor alloys such as (Al,Ga)As, (In,Ga)As or Ga(As,P), exhibits a huge band gap bowing with increasing N

incorporation [17–24]. Although the band gap of GaN is nearly 2 eV larger than that of GaAs [25, 26], N incorporation into GaAs up to several percent leads to a significant redshift of the band gap instead of the blueshift, which would be expected from a linear interpolation between the corresponding binary materials. This behaviour was interpreted in terms of a repulsive interaction between the lower-lying Γ-like conduction band minimum (E_- band) and the higher-lying N-induced impurity band (E_+ band). A simple two-level band-anticrossing (BAC) model was successfully applied to parameterize the dependence of the energies of these two bands on the N concentration x ([27], see Chap. 3). Soon after the first reports of the successful growth of GaN_xAs_{1-x} and the observation of the extensive tunability of the fundamental band gap by N incorporation (by about 150 meV per percent of N for $x \leq \sim 0.03$) it was realized that the GaNAs system and the related GaInNAs system are interesting for applications in optoelectronic devices [28]. Indeed, GaInNAs has now been demonstrated to be suitable as the active material of vertical-cavity surface-emitting lasers and edge-emitting lasers emitting at the 1.3 and 1.55 μm wavelengths suitable for long-distance signal transmission through optical fibers [28–43]. The models used to calculate the electronic states of the GaInNAs quantum wells employed in the active region of these laser devices are all based on the simple BAC model, and its extension to a 10 band $\boldsymbol{k} \cdot \boldsymbol{p}$ Hamiltonian, including the interactions between the conduction bands and highest valence states. These models describe well many of the major features of this new class of semiconductor alloys, including the low pressure coefficients of the band gap energy, the optical gain spectra and the fact that there is a N-induced increase of the electron effective mass [44–50], although the BAC model underestimates the experimentally observed increase in effective mass across a wide range of GaNAs samples [51, 52].

In parallel with the efforts to obtain GaN_xAs_{1-x} alloys with x of a few percent, the same non-equilibrium growth techniques were also successfully employed to raise the N-content x in the GaN_xP_{1-x} alloy to a similar level [53, 54]. This successful growth and the application of GaInNAs in optoelectronic devices, in particular lasers, immediately renewed the interest in GaNP as a material for optoelectronics. LED structures with GaN_xP_{1-x} with x up to 1% in the active region were soon fabricated [55,56]. Immediately, the question was raised as to whether GaNP is also suitable as the active material for laser structures on Si substrates (GaP is almost lattice-matched to Si). As a precondition for this, the indirect gap semiconductor GaP would have to change into a direct gap material with a high joint density of states at the energy of the lowest transition between the conduction band and the valence band. It is still under controversial discussion whether this desirable effect really occurs in GaN_xP_{1-x} with increasing N content x. Recent results of modulation spectroscopy and band structure calculations imply that no such indirect-to-direct transition takes place with increasing x but that instead the Γ character of transitions stays distributed over a large variety of energy gaps originating from the localized states of N atoms in different spatial configurations [57].

The GaNP system can consequently not be expected to be suitable as an active material for laser applications and other ways need to be explored to achieve a III–V-based laser on a Si substrate.

14.2 Luminescence Characteristics of GaN_xAs_{1-x} and GaN_xP_{1-x}

Substantial differences in luminescence characteristics are expected to arise between the two material systems due to the different characters of their fundamental host band gaps, as well as the different alignments of the N localized states relative to their conduction band minima (see again Fig. 14.1). Binary GaAs has a direct lowest band gap of 1.52 eV at low temperature [25] and consequently shows a strong photoluminescence (PL) band at that energy. Early studies of the N resonant level in GaAs were performed in the doping regime using hydrostatic pressure, as at ambient pressure the PL spectrum of lightly doped GaAs:N does not reveal any N-related features. Because of the low pressure shift of the N-impurity level, the latter moves into the band gap at a pressure of about 24 kbar, which dramatically changes the shape of the PL spectra [4]. The emission is then dominated by a doublet of sharp zero-phonon lines from the N level itself together with corresponding acoustic and optical phonon replica. The weak pressure dependence of the N level expresses the strong perturbation of the crystal by the incorporation of N. From an extrapolation to ambient pressure the energy of the N level was found to be about 180 meV above the Γ conduction band edge at low temperatures. In GaN_xAs_{1-x} with N concentrations around $10^{17}\,cm^{-3} (x \approx 5 \times 10^{-6})$ N-pair and cluster states are formed in an energy range about 150 meV below the isolated N level [58]. Several phonon replica of those states extend into the band gap and are visible in PL spectra at ambient pressure. However, there is no shift of the band gap related PL of the GaAs host distinguishable at these ultra-low concentrations.

Increasing the N concentration above $10^{18}\,cm^{-3} (x \geq 5 \times 10^{-5})$ leads to a redshift of the band gap [17–24], as demonstrated in the main graph of Fig. 14.2. The samples with the two lower N concentrations ($x = 0.043$ and 0.095%) exhibit additional sharp lines originating from the LO-phonon replica of the N-cluster states [58]. In contrast, the spectrum of the sample with $x =$ 0.21% merely consists of a broad emission at the GaN_xAs_{1-x} band gap energy. A group of three major peaks is repeated in the spectra of the low-x samples, each time shifted by a multiple n of the GaAs LO-phonon energy of 35 meV, as indicated by the horizontal bars in the figure. These groups are labeled as $(n+1)$LO, nLO, $(n-1)$LO, respectively, although the assigned n may not be equal for the three peaks due to the 150 meV broad energy range covered by the N-related states, in particular different N pairs. The N pair states in GaNAs and GaNP are commonly labelled as NN_i where $i = 1$ is assumed to correspond to the N atoms located on nearest-neighbour anion sites. The spatial separation

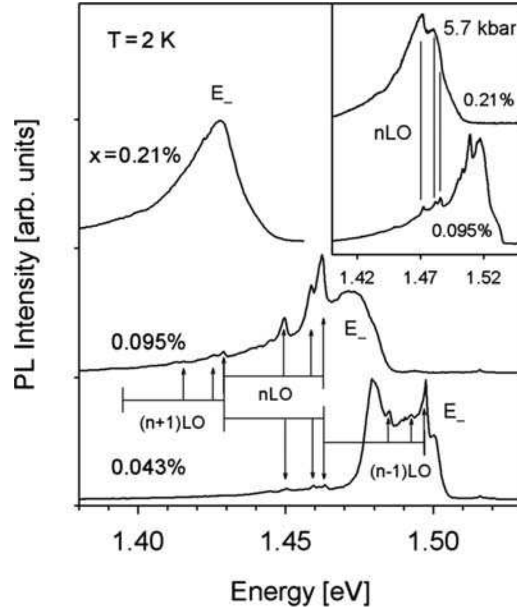

Fig. 14.2. PL spectra of three GaN_xAs_{1-x} samples with different x taken at $T = 2$ K and 718 nm (1.73 eV) laser excitation. *Inset*: Comparison of the PL spectra ($T = 2$ K and 515 nm (2.41 eV) excitation) of the $x = 0.095$ and 0.21% samples at a hydrostatic pressure of 5.7 kbar

tends to become greater with increasing i such that the line energies converge towards that of isolated N. The peak energies of the replica are the same for the two samples, but the intensities vary from sample to sample as well as for different n. This supports the interpretation that the three features originate from different zero-phonon lines and therefore from different N pair states. The redshift of the E_- related PL band starts at a concentration where the structure of the N-related states appears to be still unchanged, i.e. no variations in peak energies and line widths are observed. The localization of the N-related states even persists at concentrations higher than $x = 0.1\%$, as was demonstrated by hydrostatic pressure experiments. PL spectra recorded at hydrostatic pressure of 5.7 kbar of the two samples with $x = 0.095$ and 0.21% are compared in the inset of Fig. 14.2. The phonon replica in the sample with $x = 0.21\%$ are shifted into the band gap by the pressure and appear at the same energies as in the sample with $x = 0.095\%$, but significantly broadened. It is worth noting that the alloy E_- bands for $x = 0.095\%$ and $x = 0.21\%$ shift with pressure at a rate of 8 meV kbar^{-1}, which is considerably smaller than the 12 meV kbar^{-1} of binary GaAs [24, 58–60]. Weinstein et al. demonstrated recently in PL experiments under high hydrostatic pressures that there are exceptions and certain types of N-clusters (e.g. NN_3 for $x = 0.004$) seem to become delocalized, i.e. incorporated into the conduction band continuum for

symmetry reasons [61]. This result is supported by recent pseudo-potential studies employing very large supercells [62]. A similar experiment was also performed by Ma et al. [60].

As described in the Sect. 14.1, the incorporation of N into GaP strongly changes the luminescence even in the very dilute range. Binary GaP, exhibiting an indirect fundamental band gap, has a low radiative recombination efficiency and N forms efficient recombination centres within the band gap. Therefore, the structure of the N impurity states could already be studied extensively at ambient pressure. It turns out that the structure and the spread of the N-related localized states (e.g. isolated N state, various N pair states and higher N clusters) is essentially the same for both hosts, GaP and GaAs [58].

The PL intensity increases by orders of magnitude even when much less than 0.1% of P is substituted by N. Figure 14.3 depicts the low-temperature PL spectrum of a GaN_xP_{1-x} epitaxial layer with $x = 0.3\%$, grown by MOVPE. A large variety of emission lines is detected, of which the one with the highest energy (2.32 eV, 'A-line') originates from the transition between the electronic state of an isolated N atom and the host valence band maximum [2], with lines of lower energies emitted by NN_i pairs with different separations between the two constituents. In general, the closer the two N atoms are, the deeper is the potential well formed and the lower is the energy of the corresponding electronic state. Basically, with increasing i the line energies converge towards that of the A-line. Although this trend is generally reasonable, Gil et al. showed that this 'classical' labelling of the PL lines is not completely correct [63]. They showed that unusual properties of the NN_2

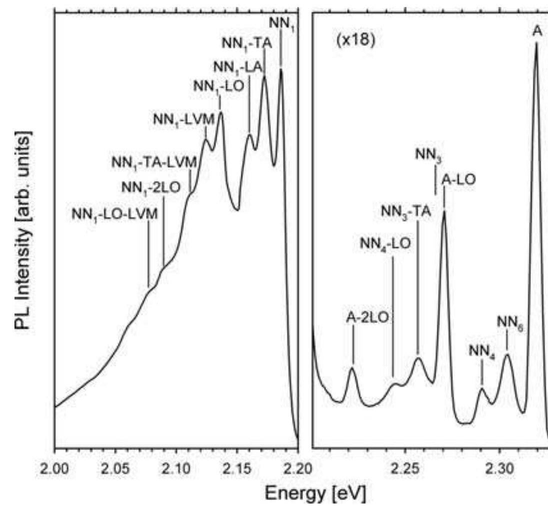

Fig. 14.3. PL spectrum of a $GaN_{0.003}P_{0.997}$ epitaxial layer taken at $T = 10\,K$ with 442 nm (2.8 eV) laser excitation. N-related emission lines are assigned according to Thomas and Hopfield [2].

trap regarding, e.g. its pressure-induced shift [64] and its stress-induced splitting [65] are best explained theoretically by assuming it to be a complex of three N atoms. Additional emission lines arise from phonon replica of the N pair states, involving optic and acoustic phonons as well as the local vibrational mode (LVM) of the N impurities. The occurrence of an LVM is also observed in the vibrational spectra (e.g. Raman spectra) of GaN_xP_{1-x} and GaN_xAs_{1-x}, and is typical of impurity atoms that are considerably lighter than the host atoms and whose vibrations therefore couple weakly to the extended host phonon modes ([66], [67], see Chap. 9).

Felici et al. studied in detail the contributions of different energy transfer processes between the different NN_i centres [68]. They found by PL excitation and temperature-dependent PL measurements that the contribution of exciton tunnelling from isolated N atoms to the pairs decreases with decreasing emission energies of the pairs, while the probability for a subsequent capture of a hole and an electron increases.

A series of PL spectra from epitaxial layers with concentrations ranging between $x = 0.15\%$ and $x = 2.1\%$ is depicted in Fig. 14.4a. Up to $x = 0.3\%$, the N-related emission lines show no change in their energies and only a slight broadening. At higher concentrations the features get strongly broadened and lower-energy signals gain intensity at the expense of those at higher energies. This behaviour can be understood as a consequence of the spatial distribution of N atoms in a random alloy. With increasing concentration, an increasing

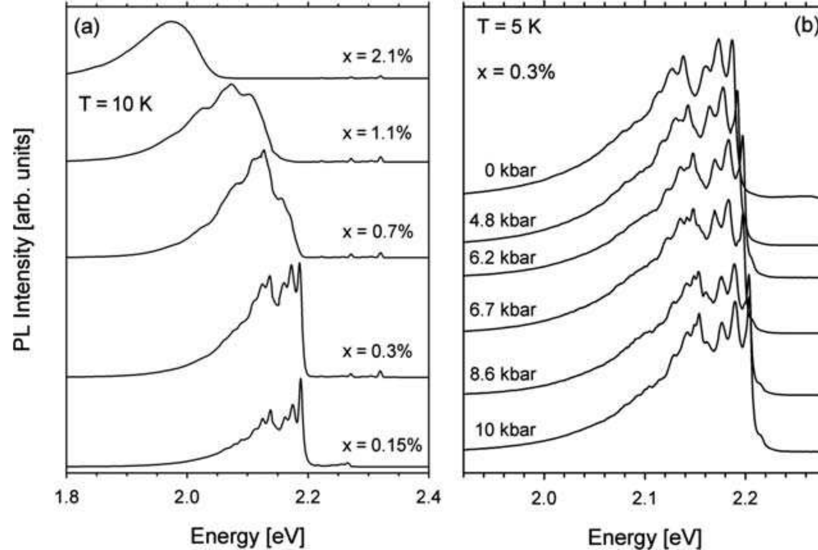

Fig. 14.4. (**a**) PL spectra of a series of GaN_xP_{1-x} epitaxial layers with x varying between 0.15 and 2.1% recorded at $T = 10$ K with 442 nm (2.8 eV) laser excitation. (**b**) PL spectra of a $GaN_{0.003}P_{0.997}$ layer taken at $T = 5$ K with 355 nm (3.5 eV) laser excitation under hydrostatic pressures ranging up to 10 kbar

proportion of the N atoms are bound in configurations where other N atoms are nearby and therefore emitting at lower energies. It is worth noting that in all spectra up to $x = 2.1\%$ the A-line of the isolated N atom as well as several lines of distant N pairs are still visible although at such high concentrations only a negligible proportion of N atoms is expected to be spatially isolated. This feature may therefore originate from the top of the GaP substrates, into which N atoms from the epitaxial layer may diffuse during the growth process. This view is supported by the observation that these signals are suppressed when using a UV laser as the excitation source, whose light has a smaller penetration depth. From $x = 0.7\%$ upwards, features are formed that lie even lower in energy than the phonon replica of the NN_1 state. At least parts of these features arise from N clusters consisting of more than two N atoms. At $x = 2.1\%$, the spectrum is dominated by a broad band located about 150 meV below the NN_1 transition energy. Overall, the maximum of the PL spectrum redshifts with increasing x. At a first glance, this behaviour of GaN_xP_{1-x} resembles that observed for GaN_xAs_{1-x}, but one has to keep in mind that the lowest conduction states in the former case are mainly impurity-like, while they are host-like in the latter alloy. From the PL characteristics at ambient pressure it cannot be decided if the broad emission band forming at higher x is due to interacting N cluster states, or if there is a new direct band gap forming below the energy of the N localized levels, as some authors have suggested [69–72]. PL spectroscopy under hydrostatic pressure has shed more light on this question. Figure 14.4b depicts the PL spectra from a GaN_xP_{1-x} sample with $x = 0.3\%$ for a series of different hydrostatic pressures. It can be seen that the emission lines blueshift with increasing pressure, but the rate of pressure shift is only about 1.5 meV kbar^{-1}, which is typical of transitions involving strongly localized states and which was previously observed for ultra-dilute GaP:N [64]. The lowest direct band gap of GaP shifts at a much higher rate of 9.7 meV kbar^{-1} [73]. Unlike GaN_xAs_{1-x} where the different shift rates of localized states and band states are reflected in a drastic variation in the shape of the PL profile, the GaN_xP_{1-x} emission does not show any significant changes in its shape up to at least 10 kbar. Consequently, no direct band gap seems to be superimposed on the emission from the impurity states. This view is also supported by time-resolved PL spectroscopy on nanosecond time scales [74].

14.3 Electronic Density of States in GaN_xAs_{1-x} and GaN_xP_{1-x}

In the alloy regime of N concentrations, i.e. from about $x = 0.2\%$ upwards, the redshift of the fundamental E_- band gap of GaN_xAs_{1-x} is accompanied by the formation of a new E_+ band at higher energy. An experimental method sensitive to the electronic density of states is required to detect such higher-energy

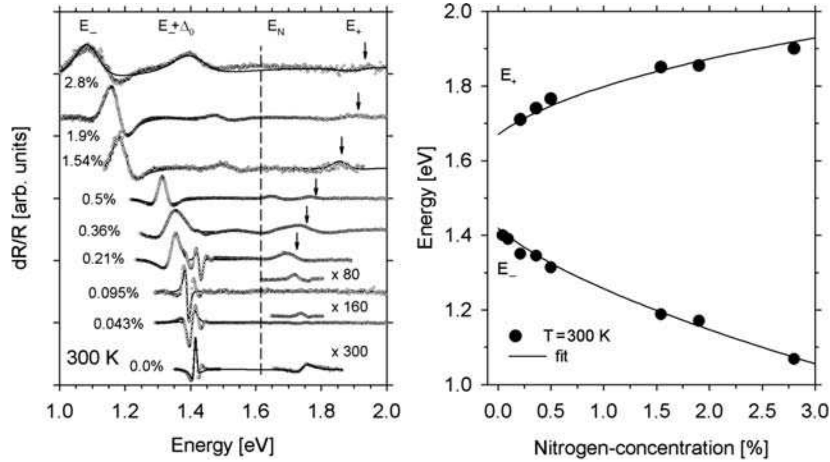

Fig. 14.5. *Left panel*: Series of PR spectra of GaN_xAs_{1-x} layers with x varying between 0.0 and 2.8% recorded at room temperature using 442 nm (2.8 eV) laser modulation. The solid lines are least-squares fits to the spectra using standard lineshape models. *Right panel*: Variation of the E_- and E_+ energies with N concentration, obtained from the fits to the PR spectra. The solid lines are fits obtained using the two-level BAC model

transitions. Modulation spectroscopy has been shown to provide a powerful tool for this purpose in dilute nitride alloys.

Photomodulated reflectance (PR) spectra taken at room temperature of a series of GaN_xAs_{1-x} epitaxial layers with x up to 2.8% are shown in the left panel of Fig. 14.5 [24]. Three main features originating from the GaN_xAs_{1-x} layers can be identified in these spectra: the GaN_xAs_{1-x} E_- band gap, the $E_- + \Delta_0$ band (where Δ_0 is the spin–orbit split-off energy) and the new E_+ band [23]. The signal strength of $E_- + \Delta_0$ increases by several orders of magnitude from $x = 0$ to 0.21%, whereas at higher concentration it only varies slightly. The valence bands seem to be less affected by N incorporation than the conduction bands, as the spin–orbit split-off energy Δ_0 does not depend on x.

The E_+ transition is detected from $x = 0.21\%$ upwards, initially as a subtle shoulder on the high-energy side of the $E_- + \Delta_0$ signal. At higher x it can be seen as a distinct feature, as the two signals shift in opposite directions. The position of E_+ is indicated for each composition by a vertical arrow in Fig. 14.5. No such signal is seen in the spectra for $x \leq 0.21\%$. Thus, the transition from nitrogen acting as isoelectronic impurities towards N-induced band formation takes place around $x = 0.2\%$. The blueshift of the E_+ feature and the corresponding redshift of the E_- band take place in a generally symmetric manner. They can be parameterized in a simple way by assuming a level repulsion between the E_0 host band edge and a band of N-related states situated at E_N, the energy of the isolated N level, for $x = 0\%$ [27, 75]. At

$k = 0$, one obtains the following equation for $E_{\pm}$ as a function of x:

$$E_{\pm}(x) = \frac{1}{2}(E_{\mathrm{N}} + E_{\mathrm{C}}) \pm \frac{1}{2}\sqrt{(E_{\mathrm{N}} - E_{\mathrm{c}})^2 + 4V_{\mathrm{Nc}}^2}, \qquad (14.1)$$

where we assume $E_{\mathrm{N}}(x) = E_{\mathrm{N0}} - \gamma x$, $E_{\mathrm{c}}(x) = E_{\mathrm{c0}} - \alpha x$ and $V_{\mathrm{Nc}}(x) = \beta\sqrt{x}$. $E_{\mathrm{N}}(x)$ and $E_{\mathrm{c}}(x)$ are the energies of the isolated N level and the conduction band edge relative to the valence band of $\mathrm{GaN}_x\mathrm{As}_{1-x}$ [24, 44, 76]. The right panel of Fig. 14.5 depicts the energies of the E_- and E_+ bands extracted from the PR spectra as a function of x. The data in Fig. 14.5 were fitted by assuming $E_{\mathrm{N0}} = 1.67\,\mathrm{eV}$, $E_{\mathrm{c0}} = 1.42\,\mathrm{eV}$, $\alpha = 3.5\,\mathrm{eV}$, $\gamma = 0.0\,\mathrm{eV}$, $\beta = 1.67\,\mathrm{eV}$. Because of the large number of parameters, this choice is not unique and a good fit can be obtained for a range of parameter sets. However, the parameters predicted from tight-binding calculations are of comparable magnitude to the fitting parameters used for the curves in Fig. 14.5 [44]. The assumption that the E_+ level is due to interaction with a single N level considerably simplifies the description of the band structure by omitting the detail of the energy distribution of the states associated with different N configurations. We shall see below that this assumption is reasonable when describing some but not all of the properties of dilute nitride alloys.

We note that a good description of the E_- band is all that is usually required when describing many of the properties of interest in III(N,V) optoelectronic devices. The host-like E_- band in GaInNAs is in general well parameterized by the BAC model, and the deviations occurring from the E_+ band are in most cases of minor importance, as the latter band is located significantly above the conduction band edge. Because the localized N levels are situated above the host conduction band minimum, the conduction band edge in $(\mathrm{Ga, In})\mathrm{N}_x\mathrm{As}_{1-x}$ maintains a strong Γ-like character for all accessible values of x. The BAC model can then be used for $\mathrm{GaN}_x\mathrm{As}_{1-x}$ and $\mathrm{Ga}_{1-y}\mathrm{In}_y\mathrm{N}_x\mathrm{As}_{1-x}$ to give a good quantitative description of many of the material properties, such as the E_- band gap, electronic states in quantum wells and the optical gain [44–50]. There are, however, several properties where the distribution of N state energies needs to be taken into account explicitly in $\mathrm{GaN}_x\mathrm{As}_{1-x}$. These include the low temperature variation of electron effective mass and electron g-factor with composition [51, 52], as well as the very low electron mobility values experimentally observed in GaInNAs alloys. For many N concentrations the E_- band and some localized N states are close in energy in $\mathrm{GaN}_x\mathrm{As}_{1-x}$ [77]. This near-degeneracy of the E_- band and localized states strongly affects the properties of the extended band states leading to anomalies in the electronic g-factor, the effective mass and the k-dispersion of the conduction band, as well as a marked reduction in the theoretically predicted electron mobility values [52, 78–82].

In $\mathrm{GaN}_x\mathrm{P}_{1-x}$, the evolution of the lowest conduction states becomes considerably more complex than in $\mathrm{GaN}_x\mathrm{As}_{1-x}$ because the order of localized and host-like conduction states in the former is reversed compared with the latter.

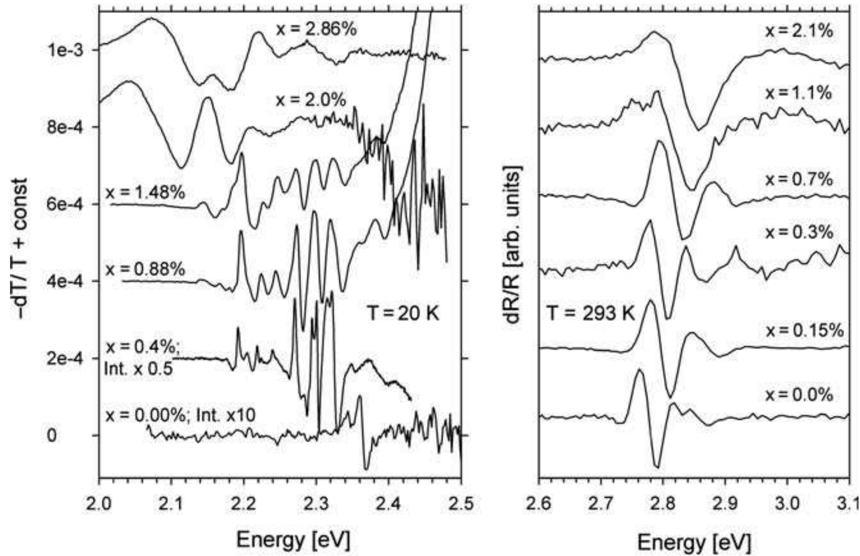

Fig. 14.6. *Left panel*: Electromodulated absorption spectra of a series of GaN_xP_{1-x} samples with x varying between 0.0 and 2.86% recorded at $T = 20\,K$. dT/T denotes the relative change in transmission. *Right panel*: Room temperature CER spectra of a series of GaN_xP_{1-x} layers with x ranging between 0.0 and 2.1%

As PL spectra cannot provide a direct measure for the electronic density of states, modulation spectroscopy has been applied for this purpose.

Electromodulated absorption (EA) spectra taken at 20 K in the energy range of the N localized levels and of the lowest GaP indirect band gap (at 2.35 eV) are presented in the left panel of Fig. 14.6. The spectrum of binary GaP exhibits very weak features only, from phonon-assisted transitions at the indirect gap between 2.34 and 2.38 eV [83]. When N is incorporated in the alloying regime, sharp features appear, which are several orders of magnitude higher in intensity than the indirect gap features of binary GaP and which lie in a spectral range of about 150 meV in width, located just below the GaP indirect band gap. Increasing the N concentration from $x = 0.4$ to 1.48% causes signals at lower energies to gain intensity at the expense of the ones at higher energies. This is obvious if one compares, for example, the features at around 2.32 eV and just below 2.2 eV with respect to their strength. For $x = 0.4\%$ the amplitude of the former is larger by a factor of about 3 compared to the amplitude of the latter. For $x = 1.48\%$ this relation becomes nearly inverted. The energies of the EA features hardly change with increasing x, but the features are observed to broaden significantly. The main EA signals coincide well with the spectral positions of the emission lines observed in the PL spectra, implying that essentially the same transitions are observed with both techniques. The EA amplitude serves as a rough measure of the Γ character at each transition energy. Therefore, these spectra show that with

increasing x direct transitions between close pair or cluster states and the valence band maximum gain probability, while those from more isolated N atoms lose probability. This behaviour suggests that, first, an increase of x leads to an increased number of N atoms bound in configurations where other N atoms are close enough to interact and that, second, the anticrossing interaction mixes band states of Γ character with the lowest energy N states, as discussed further below. An increase of x causes inhomogeneous broadening but keeps the energies of the N states roughly constant up to $x = 1.48\%$. This broadening reflects an increase in alloy disorder, due to interactions between the N atoms. For the two highest x (2.0 and 2.86%), only broad signals remain in the spectra. This may be related to significant strain relaxation of the layers as observed by X-ray diffraction measurements. If there existed, as proposed by other authors [69–72], a single N-related band gap obeying the BAC model, the EA spectra would be expected to contain a dominant signal showing a continuous redshift with increasing x. None of the spectra exhibits such a feature. The spectra rather reflect that the Γ character of transitions is distributed over a multiplicity of states due to N atoms in different configurations. In this respect GaN_xP_{1-x} differs considerably from GaN_xAs_{1-x}, where the lowest band gap retains a significant Γ character and shows a clear redshift with increasing x. While the simple level repulsion model provides a satisfactory description for a fundamental band gap mainly formed by the host bands, as in GaN_xAs_{1-x}, InN_xAs_{1-x} and InN_xSb_{1-x} [84], it fails here when the lowest transitions are due to multiple impurity states. Nevertheless, optical investigations in the spectral range of the GaP direct band gap show that there is indeed a repulsive interaction between the multiplicity of N-related states and the Γ conduction band minimum [71, 72, 85]. To demonstrate this, contactless electroreflectance (CER) spectra are depicted in the right panel of Fig. 14.6. These were recorded at room temperature and therefore are not directly comparable to the low temperature EA spectra in the left panel, as the energy of the direct gap redshifts by approximately 70 meV when heating from low to room temperature [86]. Additionally, a different series of layers was used for the CER measurements, for which there is no need for metallic contacts on top of the layers or for doped substrates. Two features of the GaN_xP_{1-x} electronic structure are observed in these spectra: the E_+ transition and the corresponding spin–orbit split-off transition $E_+ + \Delta_0$. Because of the relatively small signal strengths and the small spin–orbit split-off energy of GaP compared to GaAs [87], the latter is only seen as a distinct feature for $x \leq 0.3\%$, while at higher x the broadening and weakening of the signals make the split-off feature more difficult to distinguish. Nevertheless, a clear blueshift of the E_+ signal can be observed. Its magnitude is significantly smaller than the one observed in GaN_xAs_{1-x}. While in GaN_xAs_{1-x} the total shift between $x = 0$ and 2% is over 200 meV, the GaN_xP_{1-x} direct gap only shifts by about a quarter of this value. Such a behaviour is expected because the difference in energy between the isolated N state and the lowest Γ conduction band state is larger in GaN_xP_{1-x} than in GaN_xAs_{1-x} (480 meV vs. 250 meV at room

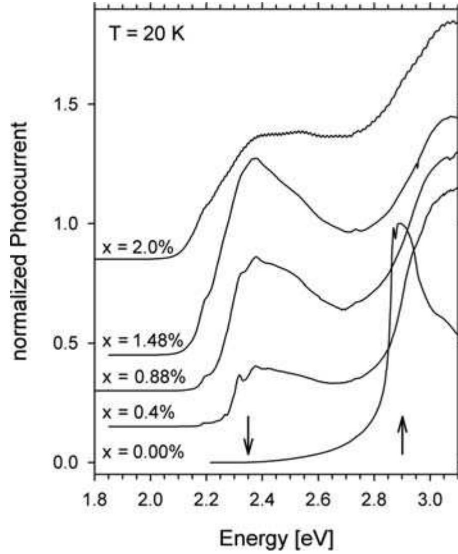

Fig. 14.7. Normalized and response-corrected PC spectra for the series of GaN_xP_{1-x} samples with x up to 2.0% recorded at $T = 20\,K$. Arrows indicate the GaP indirect and direct band gaps

temperature), leading to a weaker repulsive interaction between these levels in GaN_xP_{1-x}. The observed blueshift is also in concordance with theoretical investigations applying the tight-binding model [77].

Figure 14.7 shows photocurrent (PC) spectra for the series of samples up to $x = 2\%$. These spectra are normalized to the incident photon flux. The PC spectrum of GaP exhibits a strong signal from the direct band gap at Γ (2.85 eV) with a corresponding sharp excitonic feature (2.82 eV) and a weak onset of photocurrent at 2.35 eV, where the weak absorption across the indirect gap from the Γ valence band states to the X conduction band states sets in. Incorporating N leads to three major changes: (1) The intensity of the broad main features corresponding to the signals of the GaP-like direct and indirect gap changes, i.e. the indirect gap feature becomes more significant compared to the direct gap feature, but basically does not change in energy. We attribute this to a weakening of the k selection rule with increasing N-induced disorder. (2) Additional sharp features develop in the range of the localized N states (below 2.4 eV) which then broaden on increasing x further, showing again that the transition probability is distributed over a range of localized states. (3) The maximum of the PC feature at the direct gap is blueshifted even at low x.

Relating the blueshift of the PC feature to a shift of the actual GaN_xP_{1-x} conduction band edge at Γ is somewhat difficult as the PC signal arises from contributions of the GaN_xP_{1-x} layer as well as the GaP substrate. The differences in carrier–diffusion length between the two layers and the variation

of the penetration depth into the heterostructure as a function of energy impede a quantification of the blueshift of the Γ conduction band edge of the GaN_xP_{1-x} layer. However, the PC results in this energy range are in concordance with the observation of a blueshift in CER as well as in PL excitation studies [71]. This result suggests that there is indeed a BAC-like behaviour present in GaNP, although a simple two-band model is not able to describe it properly in the energy range of the localized N-states.

In contrast to the E_- and E_+ transitions, the influence of N incorporation is small on the energies of higher optical transitions such as E_1 and $E_1 + \Delta_1$ at L, E'_0 at Γ and E_2 and $E_2 + \Delta_2$ at X in both material systems. A strong broadening of these transitions is found in GaN_xAs_{1-x}, which reflects the massive perturbation introduced into the crystal due to the impurity character of N in GaAs. In GaN_xP_{1-x} the broadening is found to be less pronounced. This can be qualitatively explained by the difference in atomic size between N and P atoms being smaller than the one between N and As, which causes the perturbation due to N in GaP to be smaller than in GaAs.

These results have been obtained by different techniques sensitive to density of states, such as ER, spectroscopic ellipsometry and reflection measurements [22, 85, 88–91]. As an example, reflection spectra of GaN_xAs_{1-x} and GaN_xP_{1-x} recorded at 80 K are presented in Figs. 14.8 and 14.9, respectively. For GaN_xP_{1-x} the $E_1 + \Delta_1$ transition cannot be resolved in contrast to GaN_xAs_{1-x}, because in the former the spin–orbit split-off energy Δ_1 is only about a third of the one in the latter. A blueshift small compared to the width of the transitions is visible for the L-point transitions while the

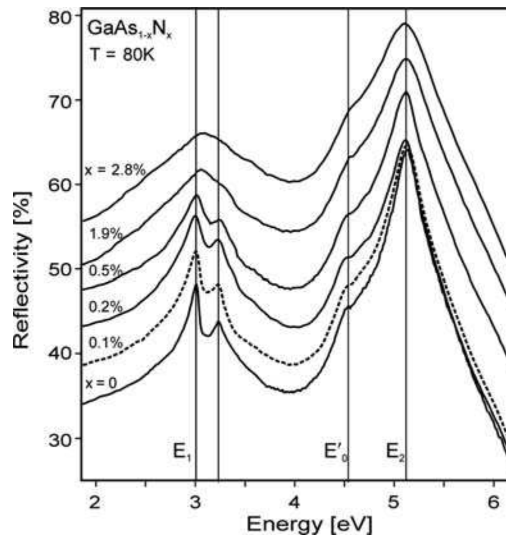

Fig. 14.8. Series of reflectance spectra of GaN_xAs_{1-x} layers with x varying between 0.0 and 2.8%, recorded at $T = 80\,K$

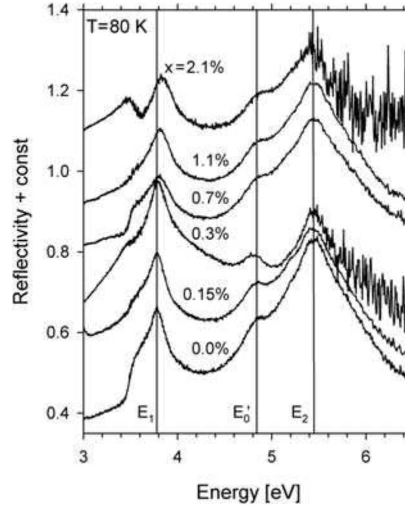

Fig. 14.9. Series of reflectance spectra of GaN_xP_{1-x} samples with x varying between 0.0 and 2.1%, recorded at $T = 80\,K$.

X-point transitions maintain a constant energy. The structures below E_1 in the spectra of Fig. 14.9 are most likely measurement artefacts arising from the line spectrum of the deuterium lamp used.

14.4 Theory of Band Formation in Dilute Nitride Semiconductors

As mentioned above, the two-level BAC model empirically describes the large band gap reduction in direct gap III–N–V alloys where the isolated N state is resonant with the conduction band. A BAC interaction between the bulk III–V conduction band edge state Ψ_{c0} at energy E_{c0} and a higher-lying band of N resonant defect levels Ψ_{N0} at energy E_N yields the III–N–V conduction band minimum energy E_- as the lower eigenvalue of [27]:

$$H = \begin{pmatrix} E_N & V_{Nc} \\ V_{Nc} & E_{c0} \end{pmatrix}, \tag{14.2}$$

where the interaction V_{Nc} between the quasi-localized N states and the GaAs conduction band edge scales with N composition x as $V_{Nc} = \beta x^{1/2}$, with $\beta \sim 2.04\,eV$ in GaNAs [44].

The redshift of the band gap obtained from the BAC model agrees well with the behaviour observed in tight-binding calculations for ordered supercells with a single N atom per cell. However, we found when we carried out calculations on 1,000-atom $Ga_{500}N_MAs_{500-M}$ supercells containing a random

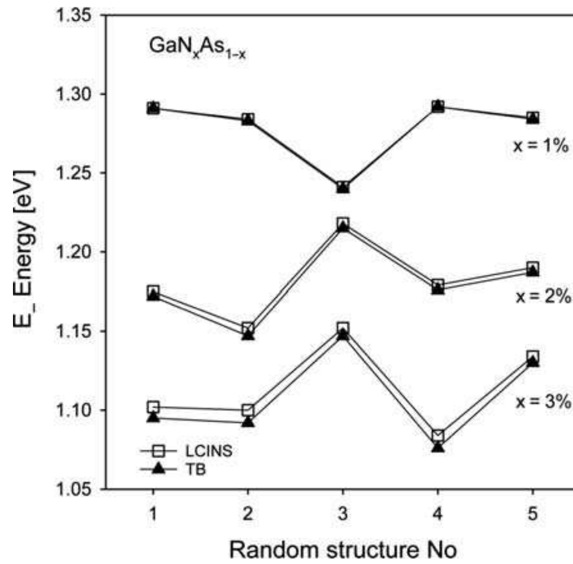

Fig. 14.10. Variation in the conduction band edge over several different random $Ga_{500}N_MAs_{1-M}$ supercell structures calculated using the full tight-binding (*solid triangles*) and LCINS (*open squares*) methods for M = (1) 5, (2) 10 and (3) 15

distribution of M N-atoms that the calculated conduction band edge energy depends strongly on the distribution of N atoms in the supercell. This is illustrated in Fig. 14.10 where the solid data points show the calculated conduction band minimum energy in five different supercells with $M = 5$, 10 and 15 N atoms (N composition $x = 1$, 2, 3% respectively). The calculated E_- energy varies by as much as 70 meV between the different structures with $x = 3\%$, due to the different random N configurations in the structures considered. This emphasises the importance of the local N distribution and of choosing a sufficiently large supercell to average out the effects of the different N environments.

We have therefore introduced an extension of the simple BAC model which treats explicitly the interactions between the different N atoms and the conduction band edge. The open data points in Fig. 14.10 show that the conduction band edge energy calculated using this technique is in excellent agreement with the results of the full tight-binding calculations for the 1,000-atom supercells considered, confirming the validity of the approach. We can therefore explicitly account for the statistical spatial distribution of the N atoms by using ultra-large supercells containing several 1,000 N atoms. In this model, the anticrossing interaction between the Linear Combination of Isolated Nitrogen States (LCINS) and the host Γ conduction band minimum is evaluated. Because of the large size of the supercells virtually all possible N pair and cluster configurations are accounted for. Figure 14.11 confirms the

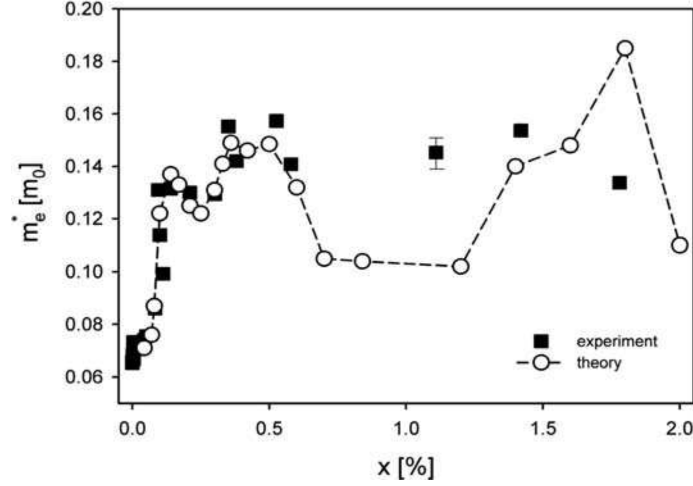

Fig. 14.11. Measured values of the electron effective mass as a function of N composition x (*full squares*). The error bar indicates the typical experimental uncertainty on the mass values. Open circles are the effective mass values calculated using the LCINS model.

value of this approach, comparing the experimentally measured variation of electron effective mass in GaN_xAs_{1-x} with the theoretically predicted variation using the LCINS model [52]. We find that when the conduction band edge E_- passes through N pair and/or cluster states, it hybridises with these states, leading to an increase in the measured band edge mass, m_e, in excellent agreement with the theoretically predicted mass enhancement.

Turning to GaNP, the energy of the GaP Γ_{1c} conduction band minimum E_{c0} lies about 0.57 eV higher in energy than the isolated N defect state. We expect in a 2-level BAC model that the lowest conduction levels in GaNP will therefore have predominantly N character, Ψ_{N0}, with just a small admixture of the GaP host Γ state, Ψ_{c0}. We have used a sp^3s^* tight-binding (TB) Hamiltonian to explicitly calculate the evolution of the lowest conduction band state

$$\Psi = \alpha_\mathrm{N}\Psi_{\mathrm{N}0} + \alpha_\mathrm{c}\Psi_{\mathrm{c}0} \tag{14.3}$$

in ordered $Ga_MN_1P_{M-1}$ supercells [92] with $32 \leq M \leq 864$ (composition $0.12\% \leq x \leq 3.1\%$), following the approach that we used above for ordered GaNAs supercells [75]. We can extract a single, N-related level below the GaP conduction band edge for each of these ordered supercells, and find that the evolution of the band structure is well described by a BAC interaction between this N-related state and the GaP Γ conduction band minimum. The calculated matrix element linking the N and Γ states varies with x as $\beta x^{1/2}$, where $\beta = 1.7$ eV, smaller than the value calculated for GaNAs, with the lower β value reflecting the smaller difference in size and electronegativity between N and P compared to that between N and As. The TB calculations for these

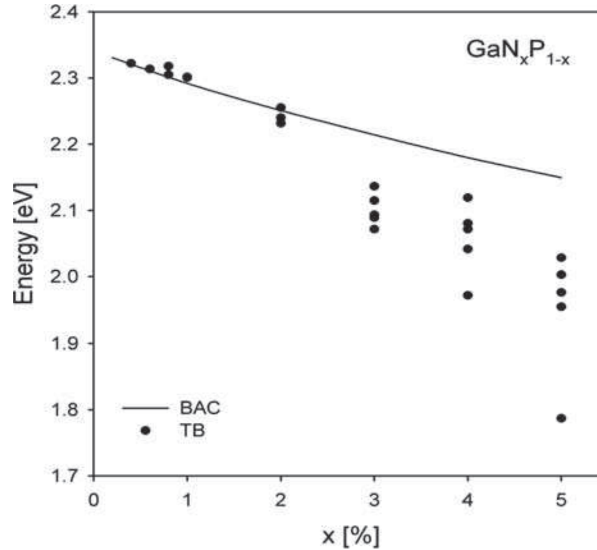

Fig. 14.12. E_{-} energies of GaN_xP_{1-x} for different supercells with random N distributions calculated using the TB method (*full circles*) are plotted vs. x together with the predicted variation of energy gap using a BAC model (*line*) fitted to the band structure of ordered GaNP supercells

ordered structures also show a clear redshift of the lowest conduction band state and a general upward shift of the higher-lying Γ states, consistent with the 2-level BAC model.

The simple 2-level BAC model breaks down when we use the TB method to calculate the electronic structure of large (1,000-atom) disordered GaN_xP_{1-x} supercells containing a random distribution of N atoms. Figure 14.12 shows that for a given x, the energy of the lowest conduction band state now depends explicitly on the relative positions and interactions between the N atoms. In fact, the variation of the lowest N-induced level due to different configurations at a given $x \geq 2\%$ is now larger than the variation of the gap predicted by the BAC model when increasing x from 0 to 5%. Also, in contrast to the ordered case, the Γ character is shown to be distributed over several lower-lying N levels in the disordered supercells, with the Γ distribution also varying significantly between different supercell calculations.

We need to choose significantly larger supercells to minimize the effects of different random distributions of N atoms. We model the effects of the random N distribution by placing $L = 5{,}000$ nitrogen atoms at random on the group V sites in a $Ga_MN_LP_{M-L}$ supercell with $2M$ total atoms, and with composition $x = L/M$. We follow the same approach we have used previously for GaNAs [77], using a TB Hamiltonian to calculate the energies ϵ_l and wavefunctions $\Psi_{Nl}(l = 1, \ldots, L)$ due to the interactions between the random distribution of nitrogen atoms considered.

The strength of the interaction between the GaP Γ host conduction band state Ψ_c and the lth state Ψ_{Nl} of the N-related defect states is given by $V_{Nl} = <\Psi_{Nl}|H|\Psi_c>$, with the alloy conduction band energy levels E_i and wavefunctions φ_i found by diagonalising the $(L+1)\times(L+1)$ Hamiltonian $H_{ij}\varphi_i = E_i\varphi_i$, where $H_{ll} = \varepsilon_l,\ l = 1,\ldots,L;\ H_{L+1,L+1} = E_{c0},\ H_{l,L+1} = H_{L+1,l} = V_{Nl}$ and $H_{ij} = 0$ otherwise.

The black lines in Fig. 14.13 display the calculated evolution with N concentration of the interaction $V_N(E)$ between the GaP Γ conduction band state

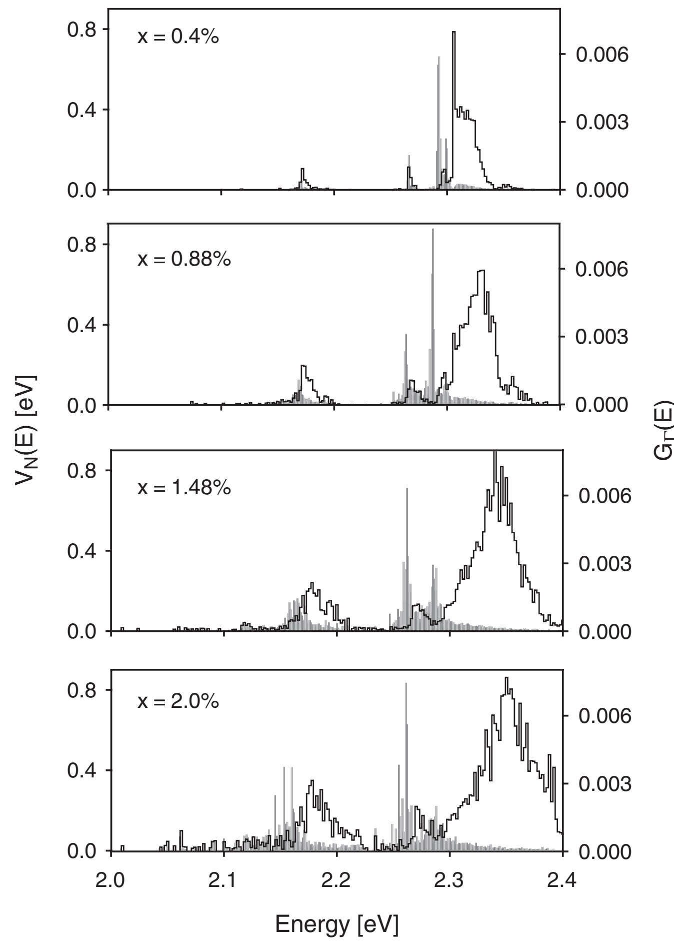

Fig. 14.13. *Black lines*: calculated N state energies of GaN_xP_{1-x} weighted by the square of their interaction with the Γ conduction band minimum. *Gray filled histograms*: $G_\Gamma(E)$, the projection of the N state spectrum onto the unpertubed GaP Γ state

and the N defect states ε_l close to the GaN_xP_{1-x} conduction band edge, where $V_N(E)$ is given by

$$V_{\mathrm{N}}(E) = \sum_l \left|V_{\mathrm{N}l}\right|^2 T(E - \varepsilon_l), \qquad (14.4)$$

with $T(x)$ a top-hat function of width 2 meV and unit area. For low N composition, most of the interaction arises from states that lie close to the isolated N defect level ($E_N = 2.306$ eV). A feature due to N-N (110) pairs is observed about 2.180 eV, as well as other calculated features at 2.282 and 2.298 eV due to N-N (220) and (221) pairs, respectively. These calculated energies correlate reasonably well with the main peaks in the photoluminescence spectra of GaN_xP_{1-x} samples with very low x (0.05%) [68], confirming that our approach gives a good description of the N defect states.

The gray filled histograms in Fig. 14.13 show $G_\Gamma(E) = \sum_l |\langle \varphi_i \mid \Psi_c \rangle|^2 \delta(E - E_i)$, the projection of the N-related band edge states onto the GaP Γ conduction band edge state. The evolution of these states closely matches the evolution of the EA (see Fig. 14.6) and PL spectra (see [68]). Because the GaP Γ state is interacting with a distribution of N levels, we do not find a single N-related level undergoing a strong redshift. Instead, many levels each experience a small redshift, and the overall distribution of Γ-related states both broadens and shifts towards lower energy with increasing x, as also observed experimentally.

14.5 Conclusions

We have presented comparative experimental and theoretical studies concerning the optoelectronic properties of the dilute nitride semiconductors GaN_xAs_{1-x} and GaN_xP_{1-x} with x up to a few percent. A basic similarity between the two materials is reflected by the fact that both in GaAs and in GaP the N atom introduces a strong perturbation of the periodic crystal potential. This leads to highly localized electronic (and vibrational) states in both host materials and to a breakdown of the virtual crystal approximation where the alloy band gap is obtained by a linear interpolation between the binaries. On the other hand, marked differences are observed between GaN_xAs_{1-x} and GaN_xP_{1-x}, due to the different alignment of the N localized states relative to the conduction band minimum in the two alloys, as well as the different character of their fundamental band gaps. In contrast to GaAs, where the N states, including pair and cluster states, are resonant with the conduction band of the host, these states are situated in the band gap in GaP, just below the X-conduction band minimum and more than 0.5 eV below the Γ-conduction band minimum. These fundamental differences in the energy schemes imply a substantially different character for the lowest conduction band states formed in the alloying range, when the N states interact with the conduction band states. In GaN_xAs_{1-x} the lowest conduction band states are host-like, i.e. mainly formed by the GaAs Γ conduction band minimum, for

the range of x considered (i.e. $\leq\sim 5\%$). This leads to a high and still almost square-root-like joint density of states at the energy of the alloy band gap E_-, enabling the application of this material in laser devices. The redshift of E_-, as well as the corresponding blueshift of the N-derived density of states (E_+), can be well parameterized by the simple band anticrossing model. In GaN_xP_{1-x} on the other hand the lowest conduction band states (corresponding to E_-) predominantly retain N impurity character, i.e. they are derived from localized states. As in GaN_xAs_{1-x}, these states do not have a single energy but are instead distributed over a range of approximately 200 meV due to the different spatial configurations of the impurity atoms. Consequently, there is not a single conduction band edge, but instead the density of states is distributed over a large variety of energy levels, each of which experiences only a small redshift. The latter behaviour can be accounted for by an extension of the BAC model to investigate ultra-large supercells, which include a random distribution of N atoms. This technique has previously been used to explain the large electron effective mass and its non-monotonic variation with x in GaN_xAs_{1-x}. The technique is used here to show that the apparently strong redshift of the lowest conduction band states observed in PL and absorption measurements in GaN_xP_{1-x} is mainly due to the increasing contributions of N atoms bound in close pairs or cluster configurations with increasing x. As there is no sharp conduction band edge and no formation of a parabolic band dispersion at the conduction band minimum, GaN_xP_{1-x} and related materials are not expected to fulfill the requirements for lasing applications, despite their success as an active material for light emitting diodes. Recent studies show that highly strained As-rich Ga(N,As,P) quantum wells with GaP barriers can be excited to lasing action near room temperature [93, 94]. As the lattice constant of the GaP barrier material closely matches the one of Si this material system can in principle be grown on Si substrates and therefore has a great potential to deliver lasing devices compatible with conventional silicon-based electronics.

References

1. M. Bugajski, A.M. Kontkiewicz, H. Mariette, Phys. Rev. B **28**, 7105 (1983)
2. D.G. Thomas, J.J. Hopfield, C.J. Frosch, Phys. Rev. Lett. **15**, 857 (1965)
3. D.G. Thomas, J.J. Hopfield, Phys. Rev. **150**, 680 (1966)
4. D.J. Wolford, J.A. Bradley, K. Fry, J. Thompson, in *Proc. of the* 17*th International Conference on the Physics of Semiconductor* (Springer, New York, 1984)
5. M. Altarelli, Phys. Rev. B **11**, 5031 (1975)
6. H.P. Hjalmarson, P. Vogl, D.J. Wolford, J.D. Dow, Phys. Rev. Lett. **44**, 810 (1980)
7. H. Mariette, J. Chevallier, P. Leroux-Hugon, Phys. Rev. B **21**, 5706 (1980)
8. D.R. Scifres, N. Holonyak Jr, C.B. Duke, G.G. Kleinman, A.B. Kunz, M. Crawford, W.O. Groves, A.H. Herzog, Phys. Rev. Lett. **27**, 119 (1971)

9. D.J. Wolford, B.G. Streetman, W.Y. Hsu, J.D. Dow, R.J. Nelson, N. Holonyak Jr, Phys. Rev. Lett. **36**, 1400 (1976)
10. R.A. Logan, H.G. White, W. Wiegmann, Appl. Phys. Lett. **13**, 139 (1968)
11. W.O. Groves, A.H. Herzog, M.G. Crawford, Appl. Phys. Lett. **19**, 184 (1971)
12. N. Holonyak Jr, D.R. Scifres, R.D. Burnham, M.G. Crawford, W.O. Groves, A.H. Herzog, Appl. Phys. Lett. **19**, 254 (1971)
13. N. Holonyak Jr, D.R. Scifres, M.G. Crawford, W.O. Groves, D.L. Keune, Appl. Phys. Lett. **19**, 256 (1971)
14. N. Holonyak Jr, R.D. Dupuis, H.M. Macksey, M.G. Crawford, W.O. Groves, J. Appl. Phys. **43**, 4148 (1972)
15. D.J. Wolford, B.G. Streetman, R.J. Nelson, N. Holonyak Jr, Appl. Phys. Lett. **28**, 711 (1976)
16. R.F. Leheny, J. Shah, Phys. Rev. B **12**, 3268 (1975)
17. M. Kondow, K. Uomi, K. Hosomi, T. Mozume, Jpn. J. Appl. Phys. **33**, L1056 (1994)
18. M. Weyers, M. Sato, H. Ando, Jpn. J. Appl. Phys. **31**, L853 (1992)
19. T. Makimoto, H. Saito, T. Nishida, N. Kobayashi, Appl. Phys. Lett. **70**, 2984 (1997)
20. G. Pozina, I. Ivanov, B. Monemar, J.V. Thordson, T.G. Andersson, J. Appl. Phys. **84**, 3830 (1998)
21. W.G. Bi, C.W. Tu, Appl. Phys. Lett. **70**, 1608 (1997)
22. H. Grüning, L. Chen, T. Hartmann, P.J. Klar, W. Heimbrodt, F. Höhnsdorf, J. Koch, W. Stolz, Phys. Status Solidi B **215**, 39 (1999)
23. J.D. Perkins, A. Mascarenhas, Y. Zhang, J.F. Geisz, D.J. Friedman, J.M. Olson, Phys. Rev. Lett. **82**, 3312 (1999)
24. P.J. Klar, H. Grüning, W. Heimbrodt, J. Koch, F. Höhnsdorf, W. Stolz, P.M.A. Vicente, J. Camassel, Appl. Phys. Lett. **76**, 3439 (2000)
25. M.D. Sturge, Phys. Rev. **127**, 768 (1962)
26. M.R. Lorenz, G.D. Pettit, R.C. Taylor, Phys. Rev. **171**, 876 (1968)
27. W. Shan, W. Walukiewicz, J.W. Ager III, E.E. Haller, J.F. Geisz, D.J. Friedman, J.M. Olson, S.R. Kurtz, Phys. Rev. Lett. **82**, 1221 (1999)
28. M. Kondow, K. Uomi, A. Niwa, S. Watahiki, Y. Yazawa, Jpn. J. Appl. Phys. **35**, 1273 (1996)
29. S.R. Bank, H.P. Bae, H.B. Yuen, M.A. Wistey, L.L. Goddard, J.S. Harris, J. Electron. Lett. **42**, 156 (2006)
30. K.D. Choquette, J.F. Klem, A.J. Fischer, O. Blum, A.A. Allerman, I.J. Fritz, S.R. Kurtz, W.G. Breiland, R. Sieg, K.M. Geib, J.W. Scott, R.L. Naone, Electron. Lett. **36**, 1388 (2000)
31. S.A. Choulis, T.J.C. Hosea, P.J. Klar, M. Hofmann, W. Stolz, Appl. Phys. Lett. **79**, 4277 (2001)
32. C.W. Coldren, M.C. Larson, S.G. Spruytte, J.S. Harris, Electron. Lett. **36**, 951 (2000)
33. M. Fischer, M. Reinhardt, A. Forchel, Electron. Lett. **36**, 1208 (2000)
34. J. Hader, S.W. Koch, J.V. Moloney, E.P. O'Reilly, Appl. Phys. Lett. **76**, 3685 (2000)
35. J. Hader, S.W. Koch, J.V. Moloney, E.P. O'Reilly, Appl. Phys. Lett. **77**, 630 (2000)
36. J.S. Harris, S.R. Bank, M.A. Wistey, H.B. Yuen, IEEE Proc. Optoelectron. **151**, 407 (2004)

37. M. Hofmann, A. Wagner, C. Ellmers, C. Schlichenmeier, S. Schäfer, F. Höhnsdorf, J. Koch, W. Stolz, S.W. Koch, W.W. Rühle, J. Hader, J.V. Moloney, E.P. O'Reilly, B. Borchert, A.Y. Egorov, H. Riechert, Appl. Phys. Lett. **78**, 3009 (2001)
38. M. Kawaguchi, E. Gouardes, D. Schlenker, T. Kondo, T. Miyamoto, F. Koyama, K. Iga, Electron. Lett. **36**, 1776 (2000)
39. M. Kondow, S. Natatsuka, T. Kitatani, Y. Yazawa, M. Okai, Electron. Lett. **32**, 2244 (1996)
40. M.C. Larson, C.W. Coldren, S.G. Spruytte, H.E. Petersen, J.S. Harris, IEEE Photon. Technol. Lett. **12**, 1598 (2000)
41. A. Ramakrishnan, G. Steinle, D. Supper, C. Degen, G. Ebbinghaus, Electron. Lett. **38**, 322 (2002)
42. H. Riechert, A. Ramakrishnan, G. Steinle, Semicond. Sci. Technol. **17**, 892 (2002)
43. S. Sato, S. Satoh, J. Cryst. Growth **192**, 381 (1998)
44. A. Lindsay, E.P. O'Reilly, Solid State Commun. **112**, 443 (1999)
45. S. Tomić, E.P. O'Reilly, P.J. Klar, H. Grüning, W. Heimbrodt, W.M. Chen, I.A. Buyanova, Phys. Rev. B **69**, 245305 (2004)
46. S. Tomić, E.P. O'Reilly, Phys. Rev. B **71**, 233301 (2005)
47. A. Thränhardt, S. Becker, C. Schlichenmaier, I. Kuznetsova, T. Meier, S.W. Koch, J. Hader, J.V. Moloney, W.W. Chow, Appl. Phys. Lett. **85**, 5526 (2004)
48. A. Thränhardt, I. Kuznetsova, C. Schlichenmaier, S.W. Koch, L. Shterengas, G. Belenky, J.Y. Yeh, L.J. Mawst, N. Tansu, J. Hader, J.V. Moloney, W.W. Chow, Appl. Phys. Lett. **86**, 201117 (2005)
49. C. Schlichenmaier, A. Thränhardt, T. Meier, S.W. Koch, W.W. Chow, J. Hader, J.V. Moloney, Appl. Phys. Lett. **87**, 261109 (2005)
50. C. Skierbiszewski, P. Pfeffer, J. Łusakowski Phys. Rev. B **71**, 205203 (2005)
51. A. Lindsay, E.P. O'Reilly, Physica E **21**, 901 (2004)
52. F. Masia, G. Pettinari, A. Polimeni, M. Felici, A. Miriametro, M. Capizzi, A. Lindsay, S.B. Healy, E.P. O'Reilly, A. Cristofoli, G. Bais, M. Piccin, S. Rubini, F. Martelli, A. Franciosi, P.J. Klar, K. Volz, W. Stolz, Phys. Rev. B **73**, 073201 (2006)
53. J.N. Baillargeon, K.Y. Cheng, G.E. Hofler, P.J. Pearah, K.C. Hsieh, Appl. Phys. Lett. **60**, 2540 (1992)
54. S. Miyoshi, H. Yaguchi, K. Onabe, R. Ito, Y. Shiraki, Appl. Phys. Lett. **63**, 3506 (1993)
55. H.P. Xin, R.J. Welty, C.W. Tu, Appl. Phys. Lett. **77**, 1946 (2000)
56. T. Sato, M. Imai, J. Appl. Phys. **91**, 6266 (2002)
57. M. Güngerich, P.J. Klar, W. Heimbrodt, G. Weiser, J.F. Geisz, C. Harris, A. Lindsay, E.P. O'Reilly, Phys. Rev. B **74**, 241202(R) (2006)
58. X. Liu, M.E. Pistol, L. Samuelson, S. Schwetlick, W. Seifert, Appl. Phys. Lett. **56**, 1451 (1990)
59. X. Liu, M.E. Pistol, L. Samuelson, Phys. Rev. B **42**, 7504 (1990)
60. B.S. Ma, F.H. Su, K. Ding, G.H. Li, Y. Zhang, A. Mascarenhas, H.P. Xin, C.W. Tu, Phys. Rev. B **71**, 045213 (2005)
61. B.A. Weinstein, S.R. Stambach, T.M. Ritter, J.O. Maclean, D.J. Wallis, Phys. Rev. B **68**, 035336 (2003)
62. P.R.C. Kent, A. Zunger, Appl. Phys. Lett. **82**, 559 (2003)
63. B. Gil, H. Mariette, Phys. Rev. B **35**, 7999 (1987)
64. B. Gil, M. Baj, J. Camassel, H. Mathieu, C.B. à la Guillaume, Phys. Rev. B **29**, 3398 (1984)

65. B. Gil, J.P. Albert, H. Mathieu, Phys. Rev. B **33**, 2690 (1986)
66. I.A. Buyanova, W.M. Chen, E.M. Goldys, H.P. Xin, C.W. Tu, Appl. Phys. Lett. **78**, 3959 (2001)
67. T. Prokofyeva, T. Sauncy, M. Seon, M. Holtz, Y. Qiu, S. Nikishin, H. Temkin, Appl. Phys. Lett. **73**, 1409 (1998)
68. M. Felici, A. Polimeni, A. Miriametro, M. Capizzi, H.P. Xin, C.W. Tu, Phys. Rev. B **71**, 45209 (2005)
69. W. Shan, W. Walukiewicz, K.M. Yu, J.W. Ager III, E.E. Haller, H.P. Xin, C.W. Tu, Appl. Phys. Lett. **76**, 3251 (2000)
70. H.P. Xin, C.W. Tu, Y. Zhang, A. Mascarenhas, Appl. Phys. Lett. **76**, 1267 (2000)
71. I.A. Buyanova, M. Izadifard, A. Kasic, H. Arwin, W.M. Chen, H.P. Xin, Y.G. Hong, C.W. Tu, Phys. Rev. B **70**, 085209 (2004)
72. I.A. Buyanova, M. Izadifard, W.M. Chen, H.P. Xin, C.W. Tu, Phys. Rev. B **69**, 201303(R) (2004)
73. S. Ves, K. Strössner, C.K. Kim, M. Cardona, Solid State Commun. **55**, 327 (1985)
74. T. Niebling, T. Lapp, J. Kampmann, P.J. Klar, W. Heimbrodt, B. Kunert, K. Volz, W. Stolz, Physica E **32**, 222 (2006)
75. A. Lindsay, E.P. O'Reilly, Solid State Commun. **118**, 313 (2001)
76. E.P. O'Reilly, A. Lindsay, Phys. Status Solidi **216**, 131 (1999)
77. A. Lindsay, E.P. O'Reilly, Phys. Rev. Lett. **93**, 196402 (2004)
78. J. Endicott, A. Patane, J. Ibáñez, L. Eaves, M. Bissiri, M. Hopkinson, R. Airey, G. Hill, Phys. Rev. Lett. **72**, 041306R (2005)
79. J. Endicott, A. Patanè, D. Maude, L. Eaves, M. Hopkinson, G. Hill, Phys. Rev. B **71**, 195307 (2005)
80. S. Fahy, A. Lindsay, E.P. O'Reilly, IEEE Proc. Optoelectron. **151**, 352 (2004)
81. S. Fahy, A. Lindsay, E.P. O'Reilly, Phys. Rev. B **74**, 035203 (2006)
82. A. Patanè, J. Endicott, J. Ibáñez, P.N. Brunkov, L. Eaves, S.B. Healy, A. Lindsay, E.P. O'Reilly, M. Hopkinson, Phys. Rev. B **71**, 195307 (2005)
83. P.J. Dean, D.G. Thomas, Phys. Rev. **150**, 690 (1966)
84. B.N. Murdin, A.R. Adams, P. Murzyn, C.R. Pidgeon, I.V. Bradley, J.P.R. Wells, Y.H. Matsuda, N. Miura, T. Burke, A.D. Johnson, Appl. Phys. Lett. **81**, 256 (2002)
85. G. Leibiger, V. Gottschalch, M. Schubert, G. Benndorf, R. Schwabe, Phys. Rev. B **65**, 245207 (2002)
86. S.E. Stokowski, D.D. Sell, Phys. Rev. B **5**, 1636 (1972)
87. A.G. Thompson, M. Cardona, K.L. Skaklee, J.C. Wooley, Phys. Rev. **146**, 601 (1966)
88. J.D. Perkins, A. Mascarenhas, J.F. Geisz, D.J. Friedman, Phys. Rev. B **64**, 121301(R) (2001)
89. W.K. Hung, M.Y. Chern, Y.F. Chen, Z.L. Yang, Y.S. Huang, Phys. Rev. B **62**, 13028 (2000)
90. G. Leibiger, V. Gottschalch, B. Rheinländer, J. Sik, M. Schubert, Appl. Phys. Lett. **77**, 1650 (2000)
91. J. Wagner, K. Köhler, P. Ganser, N. Herres, Appl. Phys. Lett. **77**, 3592 (2000)
92. C. Harris, A. Lindsay, E.P. O'Reilly, unpublished yet
93. B. Kunert, K. Volz, J. Koch, W. Stolz, Appl. Phys. Lett. **88**, 182108 (2006)
94. B. Kunert, A. Klehr, S. Reinhard, K. Volz, W. Stolz, Electron. Lett. **42**, 601 (2006)

15

Doping, Electrical Properties and Solar Cell Application of GaInNAs

K. Volz, W. Stolz, J. Teubert, P.J. Klar, W. Heimbrodt, F. Dimroth,
C. Baur, and A.W. Bett

The present chapter addresses several important topics in the framework of carrier transport in dilute nitride films, having a potential application in multi-junction solar cells. Minority carrier devices are sensitive to carrier localization and trapping. Hence, in a complex material system like GaInNAs results of transport, optical and structural properties should be interpreted together to obtain a picture of the intrinsic and the growth-related properties of the material system.

The metastable GaInNAs was grown as bulk layers on GaAs under non-equilibrium conditions at low temperatures by metal organic vapour phase epitaxy with high structural quality using all-liquid MO precursors. Results on doping with various elements and their transport properties, as determined by Hall-measurements in van der Pauw geometry as well as by magnetoresistance measurements are discussed. Because of the low growth temperature, the post-growth annealing procedure is of key importance to establish opto-electronic properties in these metastable dilute N-containing materials with improved device performance via removing of defects. These defects are – if not removed – shown to have a significant influence on minority carrier devices like solar cells. The annealing conditions were varied systematically and the related changes in the microstructural N-environment were quantified. In addition, the correlation of these characteristics with improvements in 1 eV solar cell performance is established.

15.1 Introduction

Aside from laser applications, GaInNAs with a band gap of 1.0 eV is an interesting material for the use in 4-junction solar cells to increase the efficiency under the space solar AM0-spectrum as well as for terrestrial applications. The GaInP/GaAs/Ge 3-junction cell is now successfully in production for space photovoltaic applications and yields efficiencies well above 30% under the extraterrestrial AM0 spectrum [1]. However, to increase the efficiency

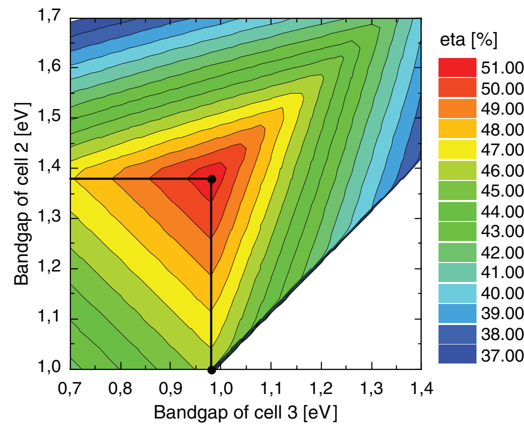

Fig. 15.1. Iso-efficiency plot of a multijunction III/V solar-cell on Germanium substrate, varying the band gaps of cells 2 and 3

further, a 4-junction solar cell has to be developed [2,3]. Calculations with the computer code "etaOpt" [4] were carried out in [5,6] to give both, the thermodynamic limit of photovoltaic energy conversion and the optimum structure of a 4-junction device in case of the AM0 spectrum. The band gap of the top and bottom cell are fixed, while the band gap of cell 2 and cell 3 are varied. The thermodynamic limit efficiency for this structure is 51.7% as shown in Fig. 15.1. Cell 2 and cell 3 can be realized with GaInAs and GaInNAs, respectively. Hence, the limiting efficiencies increase from about 40% for a standard GaInP/GaAs/Ge 3-junction cell to almost 52% for the 4-junction-structure using a material with a band gap of 1.0 eV as third junction material.

The aim of the present chapter is to discuss the lattice-matched growth of the quaternary alloy on GaAs and hence on Ge substrates as well as to present several doping characteristics of GaInNAs. As one deals with a metastable material system, intrinsic structural properties, as element clustering or local atomic ordering, might play an important role and influence carrier transport and device properties, especially also of solar cells. Consequently, a large part of this chapter is devoted to structural properties of the material with special emphasis put on the influence of different quaternary alloy compositions on the microstructure of the material. In this regard, high-In-containing $Ga_{0.7}In_{0.3}(N_{0.015}As_{0.985})$ laser material (for example 1.3 μm telecommunication applications) is compared with the low-In-containing $Ga_{0.92}In_{0.08}(N_{0.03}As_{0.97})$ solar cell material. The minority carrier properties are determined by photoluminescence investigations. Majority carrier properties are examined via Hall transport and magnetoresistance measurements. The understanding of structural as well as carrier transport properties is applied to optimize solar cell device structures at the end.

15.2 GaInNAs Growth and Doping

In the following results on the growth of GaInNAs, lattice matched to GaAs and having an 1 eV band gap will be summarized together with the doping characteristics of selected elements.

Because of the metastability of the class of materials under investigation here, growth techniques far from thermodynamical equilibrium have to be applied. The two techniques normally used are metal organic vapour phase epitaxy (MOVPE) and molecular beam epitaxy (MBE). To incorporate nitrogen into the samples, the substrate temperatures of choice are usually low, around 500–550°C for MOVPE and 400–450°C in MBE. Thermal annealing of the samples takes place either in situ or ex situ. After MOVPE growth, in situ annealing is mostly used where the sample is kept in the reactor under arsenic stabilization for several minutes at about 700°C. Rapid thermal annealing (RTA) is mainly used after MBE growth of the samples and takes place ex situ at temperatures between 700°C and 800°C for several seconds to minutes, using a second GaAs wafer as a proximity cap. Unstabilized annealing is sometimes applied without arsenic stabilization of the surface in a hydrogen or nitrogen atmosphere at reduced temperatures. There are plenty of reports in literature on MOVPE and MBE growth of GaInNAs and the incorporation characteristics of N, which is quite different for both techniques [7–15].

As results on doping and majority carrier mobility depend significantly on growth and annealing conditions, it is challenging to present intrinsic results at this point. Hence, some data from literature are compiled on these subject before referencing own results.

Different elements like selenium, silicon, tin, and tellurium were tested for their suitability for n-type doping of GaInNAs in a various range of N- and In-compositions [16–19, 25]. Silicon doping results in general in a low activation level of the donors, irrespective of the growth technique, MOVPE [18, 25] or MBE [19]. Except in [25] comparatively low electron mobilities in the range of 100–300 $cm^2 V^{-1} s^{-1}$ were reported with the exact value depending on carrier concentration, growth and annealing temperature and Nitrogen composition [16–19]. As p-type dopant zinc was mainly employed [16, 18]. Magnesium was also shown to be a suitable p-dopant [25] as well as beryllium in the case of MBE growth [19]. The hole mobility was found to be in the expected range of 50–200 $cm^2 V^{-1} s^{-1}$.

At this place, it is important to note that mobilities as well as carrier concentrations will depend strongly on the quaternary composition, more precisely on the energetic position of the conduction band edge with respect to the position of the N-cluster state as well as e.g. post-growth annealing procedures. This annealing procedure might have a significant influence on In- as well as N-distribution. It was shown that the degradation of mobility by N is suppressed by In [20] and that mobility can be maximized by randomizing the N-distribution [21]. Comparative studies between MBE and MOVPE grown material [22] show that there are different levels of the contaminants,

carbon and hydrogen, in GaInNAs grown with the two techniques. MOVPE grown samples generally exhibit larger carbon and hydrogen levels than MBE grown samples, also influencing the background carrier concentration, which is larger in the case of MOVPE growth. Nevertheless, similar defect structures, which are concluded to be related to Nitrogen and not related to the growth technique, are found in material grown with both techniques.

All GaInNAs bulk structures or multi quantum well samples used for this study were grown on (001) GaAs substrates in a commercially available horizontal reactor system (AIX200) by MOVPE using hydrogen carrier gas at a low reactor pressure of 50 mbar. Because of the large difference in covalent radius between Nitrogen and Arsenic, the material system under investigation is metastable and low substrate temperatures have to be chosen to achieve significant N incorporation. Substrate temperatures were usually fixed to 550°C for bulk films with a growth rate of $1\,\mu m\,h^{-1}$ in this case. The substrate temperatures were calibrated to the Al/Si eutectic formation occurring at 577°C. As a consequence of the low growth temperatures, MO sources efficiently decomposing at lower temperatures like the group V sources tertiarybutylarsine (TBAs) and the unsymmetric dimethylhydrazine (UDMHy) have to be used. As group III sources, trimethylgallium (TMGa) as well as triethylgallium (TEGa) and trimethylindium (TMIn) were applied. For solar cell device structures Te (from diethyltellurium (DETe)) was used as n-type dopant and Mg (from dicyclopentadienylmagnesium (Cp_2Mg)) as p-dopant, respectively. Si (from ditertiarybutyl silane, DitBuSiH) and Zn (from diethyl zinc, DEZn) were additionally tested for their suitability to dope GaInNAs.

To reduce the defect density in the as-grown quaternary, metastable material, which dramatically influence minority carrier properties, it needs to be thermally treated at elevated temperatures after growth. These annealing procedures were varied systematically in this study. We applied annealing steps consisting of a 5–120 min TBAs stabilized anneal at 700–800°C and a subsequent unstabilized annealing step in H_2-ambient at 625–700°C for 25 min in the MOVPE reactor.

In the following, ways to achieve the two prerequisites, lattice matching to GaAs and Ge substrates and a 1 eV band gap, will be described. This will be followed by results on doping of the quaternary alloy.

To incorporate GaInNAs in a stack of solar cells on Ge substrate, besides the 1 eV band gap lattice matching to the substrate is mandatory. Both conditions are only fulfilled at a certain quaternary composition. The energy gaps of quaternary as well as ternary GaInNAs films are depicted in dependence on the Nitrogen content for different In-contents in Fig. 15.2. The strain state of the layers was verified performing high-resolution X-ray diffraction (HRXRD) either for the bulk films or for multi-quantum well reference samples, grown under identical conditions as the bulk structures.

There is a significant bowing of the GaInAs band gap when introducing small amounts of Nitrogen, depending on the In-content of the material. The band gap bowing becomes weaker as one increases the In-content in the

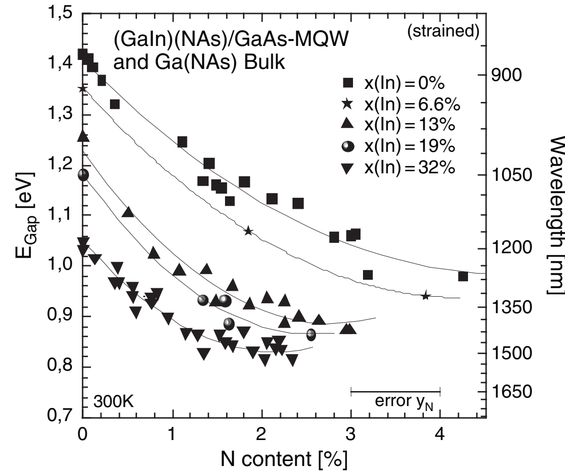

Fig. 15.2. Bowing of the band gap for GaInNAs in dependence on the Indium as well as Nitrogen composition. These data are not corrected for the strain of the quantum well

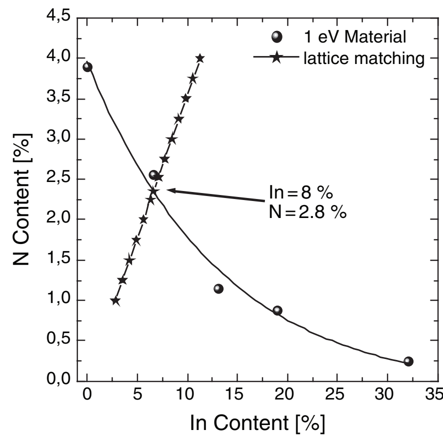

Fig. 15.3. Dependence of the lattice matching condition as well as a 1 eV bandgap on the composition of GaInNAs

material, as was also theoretically predicted. The desired 1 eV band gap can be achieved by using several different compositions, which are plotted as spheres in Fig. 15.3.

Additionally, lattice matching conditions to GaAs substrate were calculated assuming Vegard's law (stars in Fig. 15.3). At the composition, where both curves intersect, lattice matching conditions as well as the 1 eV band gap of the quaternary alloy are fulfilled. This material has a composition of 8% In and 2.8% N [25].

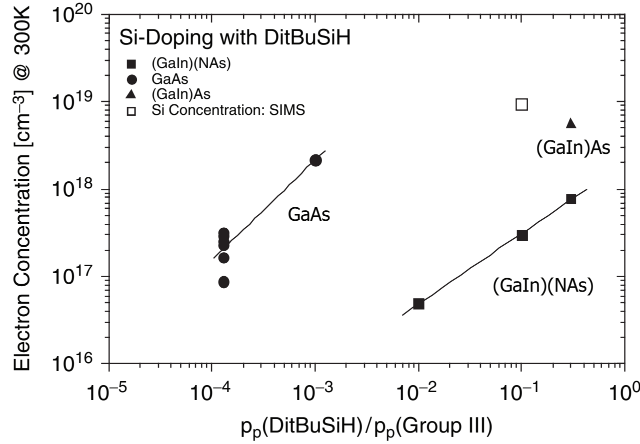

Fig. 15.4. Si incorporation in GaInNAs in dependence on the DitBuSiH source partial pressure

In the following, the incorporation of the individual dopants in GaInNAs, obtained from electrical measurements, will be compared with their incorporation in comparable GaAs samples. In the subsequent section, the mobility of the donors and acceptors will be shown in dependence on the dopant's concentrations.

For van der Pauw-Hall measurements 1–2 μm thick test films were grown and measured as grown and after annealing at 77 K and 300 K. Secondary ion mass spectrometry (SIMS) analysis was performed on selected samples to examine the actual incorporation of the dopants in comparison to the activated amount, measured by Hall effect measurements.

Figure 15.4 shows the doping characteristics of Si from DitBuSiH as a function of the partial pressure of the Si source over the partial pressure of the growth determining group III sources.

It can be seen that the electron concentration at 300 K in GaInNAs is considerably lower as the one achieved in GaAs or GaInAs under comparable growth conditions. A very high partial pressure for the Si source has to be chosen, to yield any doping. These high partial pressures are not desirable for dopant sources, particularly as doping levels of only $10^{18}\,\mathrm{cm}^{-3}$ can be achieved for a considerable high flow of DitBuSiH in the reactor. Si could be incorporated amphoteric in GaInNAs, resulting in a low net doping efficiency. Another possibility for this low doping efficiency, which is generally observed when using Si-doping for GaInNAs [18,19,25], is an influence of the very stable N–Si bond on the incorporation of Si. Comparing the electrically active donor concentration with the Si concentration in the quaternary crystal, as derived from SIMS analysis, confirms that Si is not a suitable dopant for dilute N-containing material systems. The Si-content in the layers exceeds the donor concentration by two orders of magnitude.

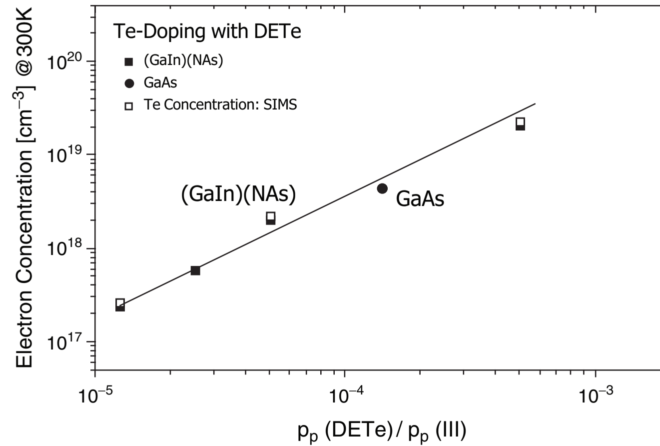

Fig. 15.5. Te incorporation in GaInNAs in dependence on the DETe source partial pressure

The efficiency of tellurium (from DETe) as an n-type dopant in GaInNAs is shown in Fig. 15.5. It can be seen that the Te donor exhibits very good incorporation behaviour in the quaternary material. Carrier concentrations above $10^{19}\,\mathrm{cm}^{-3}$ were achieved. Even at these high donor concentrations, the carrier concentration depends still linearly on the partial pressure of the DETe. The doping efficiency in the quaternary material is comparable to that in GaAs grown at the same temperature. This is due to the fact that for the GaInNAs growth As-deficient growth conditions have to be chosen in order to incorporate high amounts of N. These As-deficient conditions favour the incorporation of Te on a group V lattice site. The activation of the Te-donor in GaInNAs is close to 100%, what can be derived from the SIMS Te-concentration data. On the basis of these results, Te was chosen as n-type dopant for the solar cell structures.

In the following, own results of the experiments of p-type doping of the quaternary alloy are summarized. Figure 15.6 shows the carrier concentration for DEZn in dependence of the source partial pressure for GaInNAs and GaInAs and GaAs bulk films, grown under comparable conditions.

The incorporation behaviour of Zn seems to be similar for the quaternary alloy as for GaInAs and for GaAs, carrier concentration still increases linearly as a function of source flow, even for high concentration values. However, in contrast to GaAs and GaInAs, Zn is not incorporated into GaInNAs on the lattice site, resulting in p-type conductivity, but all Zn-doped quaternary films showed n-type conductivity in Hall measurements, both, before and after annealing in all our experiments. The donor concentration measured also corresponds to the actual zinc concentration in the samples. To exclude possible interface layers, which would influence the results of Hall-measurements, differently thick Zn-doped samples were grown, which showed

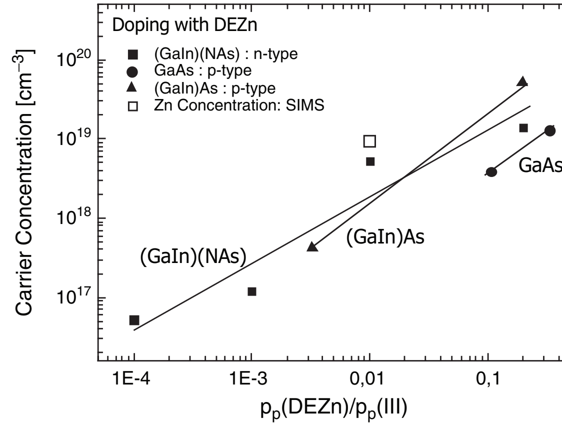

Fig. 15.6. Zn incorporation in GaInNAs in dependence on the DEZn source partial pressure

all identical carrier concentrations and type, irrespectively of the layer thickness. One possible explanation for Zn acting as a donor in GaInNAs would be the incorporation on an interstitial instead of a substitutional lattice site. These results are the more stunning, as literature reports p-type doping for MOVPE grown GaInNAs with DEZn [16].

However, Leibiger et al. [18] also reported on a very low incorporation coefficient of acceptors from DEZn compared with the DEZn/Ga ratio adjusted. It should be noted that several of the layers, which show n-type carriers in Hall-measurements, exhibit p-type conductivity, when measuring them using CV-depth profiling. This phenomenon is known from amorphous Silicon; however, there is no explanation yet, also for this well-established material system [23, 24].

Figure 15.7 shows the carrier concentration for the magnesium (from Cp_2Mg) acceptor in GaInNAs and GaAs. Extremely high acceptor concentrations were obtained from the Cp_2Mg source. Concentrations above $10^{19}\,cm^{-3}$ are achieved in the quaternary material and even one order of magnitude higher in GaAs with no sign of saturation of the carrier concentration for increasing Cp_2Mg partial pressures. This dopant was the only one, for which carrier concentrations and mobilities considerably changed after annealing. The carrier concentration increased by two orders of magnitude upon annealing. SIMS analysis has shown that this is related to the passivation of the acceptor with hydrogen, which diffuses out upon unstabilized annealing. Activation levels of the Mg-acceptor in GaInNAs are in the range of 50–60% after annealing.

Another issue when p-type doping might be the lowering of the Fermi level by the p-doping and linked to that a possible change in the N incorporation behaviour as N distorts mostly the conduction band. Indeed, an increased

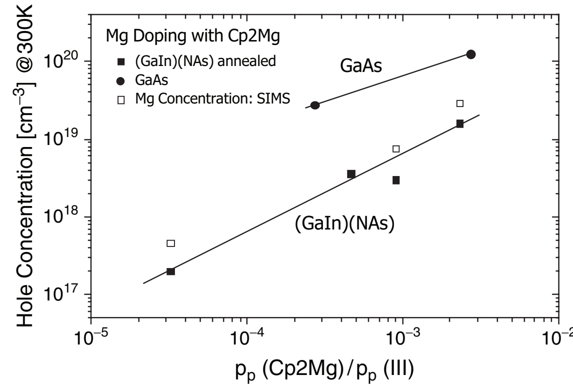

Fig. 15.7. Mg incorporation in GaInNAs in dependence on the Cp2Mg source partial pressure

N incorporation was observed in Mg-doped samples grown under otherwise unchanged conditions as the undoped or n-doped samples. In addition to the PL analysis of the structures, it was verified by HRXRD that in fact the N content in the samples is increased. In the p-doped region of the devices, the TBAs/III ratio has to be increased significantly if lattice matching and an 1 eV band gap are still to be achieved [25].

Hence, controlling the growth conditions precisely, Mg is a controllable p-type dopant for GaInNAs, exhibiting a good incorporation behaviour – without deteriorating the crystal quality. As a result of the above-mentioned study, Te and Mg were chosen as dopants for the later solar cell devices.

Dopant diffusion during growth or during subsequent annealing is a considerable issue in the solar cell community. As a result of the low growth temperatures, the Mg- and Te-profiles in the final solar cells exhibit sharp flanks with no diffusion going on.

A further important point using MOVPE growth is possible carbon incorporation from the different MO precursors. Because of the C–N bond strength, GaInNAs is a special case in the class of III/V semiconductors, as carbon impurities are incorporated together with the N upon growth [26]. In this framework, TEGa and TMGa were both applied to grow GaInNAs. The nominally undoped GaInNAs films, grown using TEGa or TMGa, respectively, show different majority carrier properties: Van der Pauw - Hall measurements yield p-type carrier concentrations in the range of $5–10 \times 10^{15}\,\mathrm{cm}^{-3}$ for samples grown using TEGa. Using TMGa as source, the carrier type is – from both Hall as well as CV measurements – n-type with a concentration of $5–10 \times 10^{16}\,\mathrm{cm}^{-3}$. Upon annealing for 5 min at 700°C, carrier concentration does not change for the n-type sample, whereas carrier concentration increases by one order of magnitude for the p-type, TEGa grown sample. This is presumably due to hydrogen incorporation, which passivates the acceptor upon growth, but diffuses out upon annealing. SIMS measurements of TEGa and TMGa grown

samples show similar Carbon levels in both samples. It is, however, possible that for the TEGa- grown samples – because of the low growth temperature and the not completely activated β-hydride elimination reaction of the MO source at these low temperatures – the ethyl group is incorporated together with the Nitrogen. Using TMGa, solely the methyl group of the group III molecule could be incorporated together with the N. This would result in a significantly different defect structure using both Ga molecules, as an ethyl-like contamination would act as a deep centre in the material. As a consequence of these findings, TMGa was used as Ga-precursor for the later solar cells.

15.3 Carrier Transport Properties

The following chapter summarizes own results on transport properties of MOVPE grown samples. An overview on results from literature was given in the preceding sections.

15.3.1 Hall Measurements

An issue predicted in literature for the quaternary alloy is alloy scattering from N producing random alloy fluctuations resulting in intrinsic localizations and mobility edges, which would limit the band mobilities to 100–500 $cm^2\,V^{-1}\,s^{-1}$ at 300 K [17]. Fahy and O'Reilly [5] also suggested that well-established models, based on the Born-approximation [28], underestimate the alloy scattering cross-section in dilute N-alloys significantly due to strong scattering due to N atoms.

There are several special features of the conduction band electronic structure, which should affect, in particular, the electron transport in GaInNAs: (1) strong localization of the electrons in the conduction band due to disorder. This might originate from the strong dependence dE_-/dx of the conduction band edge E_- on the N-content x [31], from the competition between localized N-states and extended host-like states [42] as well as from the effects of different nearest-neighbour environments of N and N-clusters on the band edge [43, 44]. These effects vary locally according to the N-distribution in the lattice and thus give rise to disorder. (2) At the Γ-point, the electron effective mass $m_c{}^*$ increases considerably with x (at constant In-content y). This effect is most significant for $x < 1\%$. For higher x, like in the samples under study, $m_c{}^*$ tends to saturate as a function of x. On the other hand, $m_c{}^*$ will decrease again with increasing y (at constant x). (3) A strong conduction band non-parabolicity occurs. For example, Skierbiszewski et al. observed strong increase of $m_c{}^*$ at the Fermi level in $Ga_{0.92}In_{0.08}(N_{0.033}As_{0.967})$:Se with increasing electron concentration up to a value of $0.4 \times m_0$ for $n = 6 \times 10^{19}\,cm^{-3}$ [45].

Fahy and O'Reilly derived the following expression for the mobility (ignoring N-clustering and different N-environments):

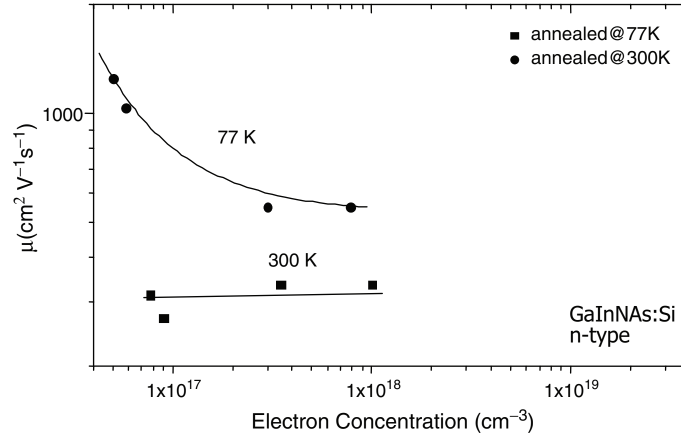

Fig. 15.8. Mobilities of the Si-donor in GaInNAs from Hall measurements in dependence on the carrier concentration and on the measurement temperature

$$\mu = \frac{e}{\pi a_0^3 x \sqrt{3m_c^* kT}} \left(\frac{2\pi\hbar^2}{m_c^*}\right)^2 \left[\frac{dE_-}{dx}\right]^{-2}, \tag{15.1}$$

where a_0 is the GaInNAs lattice constant, e is the electron charge, and dE_-/dx is the derivative of the conduction band edge energy with respect to N-content x. Maximum mobilities for electrons predicted for GaInNAs in the composition range, where the material is interesting for solar cell applications, are according to their study of the order of $1{,}000\,\mathrm{cm^2\,V^{-1}\,s^{-1}}$.

It should be noted that the mobility results presented in the following were carefully checked, by growing differently thick samples for Hall measurements, which should exhibit different mobilities, if highly charged regions at possible interfaces would be present. Figure 15.8 depicts the dependence of the mobility of the Si donor on the carrier concentration, measured at liquid nitrogen and room temperature. Here, only annealed samples are compared, as annealing of the GaInNAs bulk films has no influence on neither the carrier concentration nor the mobility for Si-doping. A strong dependence of the mobility on the temperature is observed here for all carrier concentrations possibly due to phonon scattering at room temperature. The low mobilities at room temperature, which show no dependence on the carrier concentrations, could be a sign for Si-N induced cluster scattering or compensation effects. From the SIMS measurements presented in the preceding section, it is known that the actual Si concentration in the crystal is of two orders of magnitude larger than the measured donor concentration.

Figure 15.9 points out that the mobilities measured for the Te donor are very high. For carrier concentrations in the $10^{17}\,\mathrm{cm^{-3}}$ mobilities of $2{,}000\,\mathrm{cm^2\,V^{-1}\,s^{-1}}$ are measured. These mobilities are approximately five times

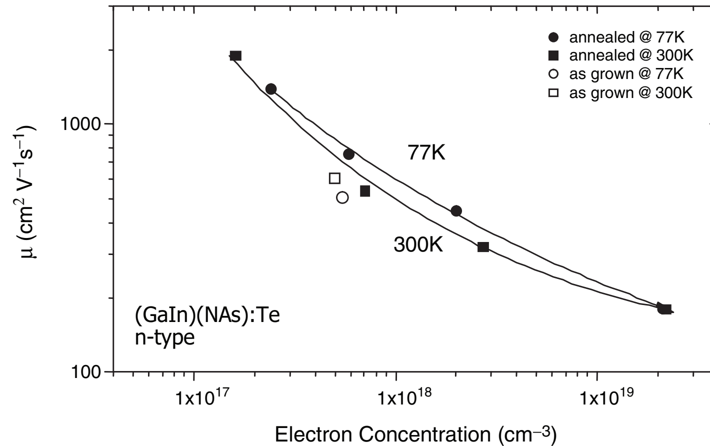

Fig. 15.9. Mobilities of the Te-donor in GaInNAs from Hall measurements in dependence on the carrier concentration and on the measurement temperature

higher than the best values for electrons in GaInNAs reported by other authors in literature, but correspond to what had been calculated to be the maximum theoretical limit for electron mobility in dilute nitrides [5]. The mobilities and carrier concentration for the Te donor do hardly depend on the temperature in range between 80 and 300 K. Also for this dopant, no difference in carrier concentration or mobility is observed before and after annealing of the GaInNAs bulk films, evidencing that all donors are already activated during growth.

A decrease of the mobility is found at temperatures below 80 K. Figure 15.10 depicts plots of the mobility vs. temperature in the full range between 2 and 300 K for GaInNAs samples of various Te-doping levels. The decrease of the mobility with decreasing temperature is very much pronounced at low doping levels. This temperature behaviour deviates from that calculated by Fahy and O'Reilly, who had predicted an increase of the mobility toward lower temperatures. However, this is understandable as the calculations only account for elastic scattering by N atoms and neglect other relevant scattering mechanisms. At low temperatures, this is, in particular, scattering by ionized donor impurities. The almost constant mobilities in the high temperature range indicate that inelastic scattering by LO-phonons, which usually leads to strong reduction of the mobility in conventional III–V semiconductors above 100 K, is less important in GaInNAs:Te than the elastic scattering by N atoms.

In summary, Te exhibits several advantages over Si, if used as a donor in GaInNAs. Among them are the app. 100% activation of the incorporated atoms on the group V lattice sites and the comparatively high mobility.

The mobilities for the Mg acceptor are shown in Fig. 15.11 and are considerably lower than the values found for the donors in GaInNAs, reflecting

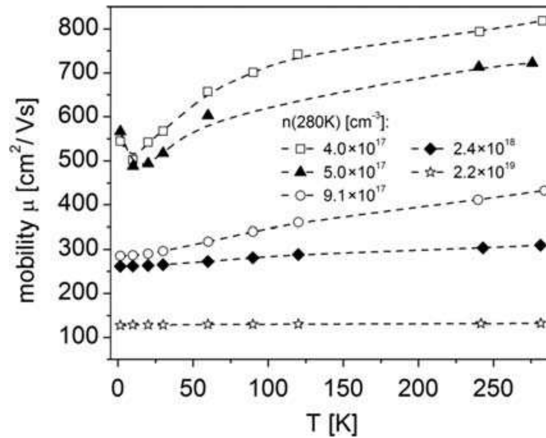

Fig. 15.10. Electron mobility measurements in the temperature range from 1.6 K to 280 K of typical GaInNAs:Te solar cell material of various doping levels

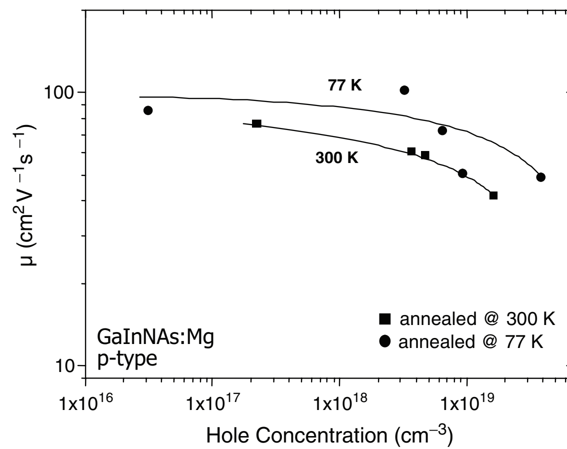

Fig. 15.11. Mobilities of the Mg-acceptor in GaInNAs from Hall measurements in dependence on the carrier concentration and on the measurement temperature

the higher hole effective mass. The dependence of the mobility on the carrier concentration and on the temperature is weak.

15.3.2 Magnetoresistance Measurements

The magnetoresistance (MR) behaviour of the p-type GaInNAs (see right graph of Fig. 15.12) is similar to that observed in semiconductors and amalgamation-type alloys of comparable doping levels [34, 35] whereas the negative MR effect of n-type GaInNAs (see left graph of Fig. 15.12) are unusually large for a doping level of about 10^{18}cm^{-3} [29]. Such large negative

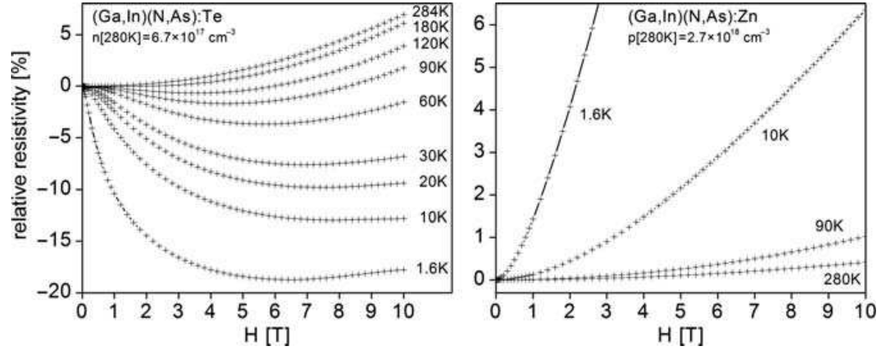

Fig. 15.12. Magnetoresistance measurements in the temperature range from 1.6 K to 280 K of typical n-type (*left*) and p-type (*right*) GaInNAs solar cell material

MR effects are commonly observed in undoped or lightly doped semiconductors only [36–38]. The negative MR effects in conventional diamagnetic III–V and group IV semiconductors are explained in the framework of weak Anderson localization [39–41]. In the regime of Anderson localization, the dominant scattering process has to be elastic (i.e. it holds $\tau_{\mathrm{elastic}} \ll \tau_{\mathrm{inelastic}}$ for the elastic and inelastic scattering times).

In this case the back-scattering of an electron state with momentum k into the state with $-k$ at zero-magnetic field will be strongly enhanced because of constructive quantum interference of the amplitudes of a given scattering path (comprising several elastic scattering events) with its time-reversed one. Applying a magnetic field H shifts the relative phase of these two contributions and thus reduces the back-scattering i.e. the resistance decreases. This negative MR effect is a quantum correction to the resistance and referred to as weak localization effect. In conventional III–V semiconductors it is only observed at low temperatures because with increasing temperature inelastic scattering by LO-phonons becomes the dominant scattering process and $\tau_{\mathrm{elastic}} \ll \tau_{\mathrm{inelastic}}$ is no longer fulfilled.

The observed MR effects in GaInNAs can be understood qualitatively as a superposition of a weak localization MR contribution and a classical transverse quadratic contribution:

$$\left(\frac{\Delta\rho}{\rho_0}\right) \propto H^2 \tag{15.2}$$

Both MR contributions are affected by the peculiarities of the GaInNAs band structure, as discussed later. As mentioned earlier, the incorporation of N into GaInNAs strongly modifies the conduction band of the alloy giving it its non-amalgamation type character [30–32, 42, 43] whereas the effect of N on the valence band can be considered as “normal alloying”. Therefore, the p-type samples where the valence band is probed in the MR experiment behave like conventional III–V semiconductors. The MR effects in the n-type samples, on the other hand, must reflect the unusual conduction band structure of the

GaInNAs alloy. The electron transport is considerably altered by the incorporation of N into GaInAs as the elastic scattering by N-impurities becomes a dominant scattering process for electrons in the entire temperature range up to 300 K [5]. The scattering cross section of an isolated N-atom is given by:

$$\sigma = \frac{\pi}{4}\left(\frac{m_{\mathrm{c}}^{*}}{2\pi\hbar^{2}}\right)^{2}\left[\frac{\mathrm{d}E_{-}}{\mathrm{d}x}\right]^{2} a_{0}^{6}. \tag{15.3}$$

As $\mathrm{d}E_{-}/\mathrm{d}x$ decreases with increasing x, σ decreases strongly with x [5,46] and, consequently, the total scattering cross section $\sigma_{\mathrm{tot}} = x \times \sigma$ is not necessarily proportional to x. The efficient elastic scattering of electrons by the disorder related to the N-atoms causes the observed enhancement of the weak localization effects in the n-type GaInNAs samples. Furthermore, as $\tau_{\mathrm{elastic}} \ll \tau_{\mathrm{inelastic}}$ at all temperatures the negative MR effects even persist up to 300 K.

The variation of these negative MR-effects with free-carrier concentration shows a clear trend in n-type GaInNAs alloys as shown in Fig. 15.13, where the absolute values of the minimum of the MR curves at 1.6 K are plotted vs. n on a double logarithmic scale. It can be seen that the negative MR effects is less pronounced with increasing n, which can be understood within the weak Anderson localization picture as a result of state filling and screening effects.

In the qualitative discussion of the origin of strong negative MR effects in GaInNAs, we ignored so far the existence of the broad energy distribution of N-related cluster states and instead used a representative single N level interacting with the host conduction band (CB) states. However, recent theoretical calculations by Fahy et al. show that this is an over-simplification

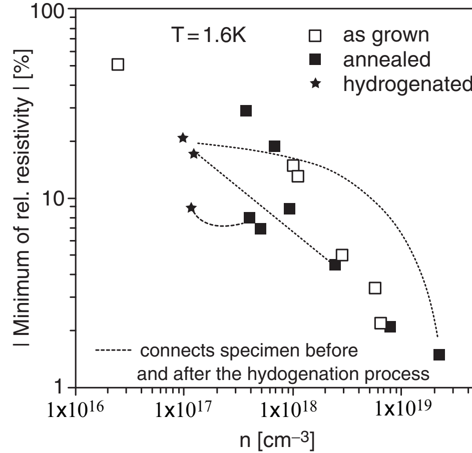

Fig. 15.13. Absolute value of the minimum of the MR curves at 1.6 K for n-type GaInNAs as a function of carrier density. The *open symbols*, *full symbols*, and *stars* denote annealed, as grown and hydrogenated samples, respectively

since all the N-related states interact with the conduction band states and the strength of this interaction depends on the energy difference between the CB edge and the individual state energy [46, 47]. In what follows we will show that taking into account the different N related states and their energy distribution allows one to refine the qualitative picture and to consistently explain all observations.

The discussion above made it clear that the transport properties, in particular, of n-type GaInNAs are strongly dependent on the subtle interplay of host-like extended band states, of localized N-related states and of the free-electron concentration due to doping. The interplay of these three quantities within the same sample can be tuned in controlled ways by either hydrogenation or by the application of hydrostatic pressure [48–50].

Hydrogenation can have significant effects on the electronic properties of semiconductors [51]. Because of a high chemical reactivity, hydrogen binds to and neutralizes dangling bonds in the lattice, thus wiping out non-radiative recombination centres and deep defect energy levels from the gap of crystalline semiconductors. In the case of dilute nitrides such as Ga(NAs) and GaInNAs, hydrogen surprisingly also affects the isoelectronic impurity N. It was shown that hydrogenation leads to an effective removal of the N-related perturbation and virtually reestablishes the GaAs band structure due to the formation of N–H complexes in undoped samples (see ref. [52] and references therein). However, in GaInNAs:Te hydrogenation mainly causes a significant passivation of the Te-donor leading to an effective reduction of the free-electron concentration n. Furthermore, it was found that the formation of $N–H_2{}^*$ complexes, which are responsible for full N-passivation, is suppressed despite the high H-doses used [48]. The effect of hydrogenation on the MR is shown in Fig. 15.14 where the MR-curves measured at 1.6 K of three GaInNAs:Te samples of different Te-doping level measured before and after hydrogenation are depicted. In all three samples, the strong negative contributions to the MR increase after hydrogenation. The corresponding absolute values of the minimum of the MR curves are also plotted in Fig. 15.13 and agree well with the general trend confirming that the magnitude of the negative MR effect in n-type GaInNAs of comparable alloy composition is mainly determined by the free-carrier concentration n in the conduction band.

Hydrostatic pressure experiments were used from the beginning for studying the interplay between localized N-related states and extended host-like band states in III-N-V alloys, because the N levels and the conduction band edge shift at different rates under hydrostatic pressure, which allows one to continuously tune the interaction between N-states and the conduction band edge [30]. In GaInNAs with solar cell compositions, the distribution of the localized N-states extends below or close to the band gap of the quaternary alloy at low temperatures [50, 53, 54].

The left graph of Fig. 15.15 depicts MR curves of the GaInNAs:Te epitaxial layer taken at 1.6 K for various hydrostatic pressures up to 13.4 kbar. Again the strong negative contribution to the overall MR effect dominates. This negative

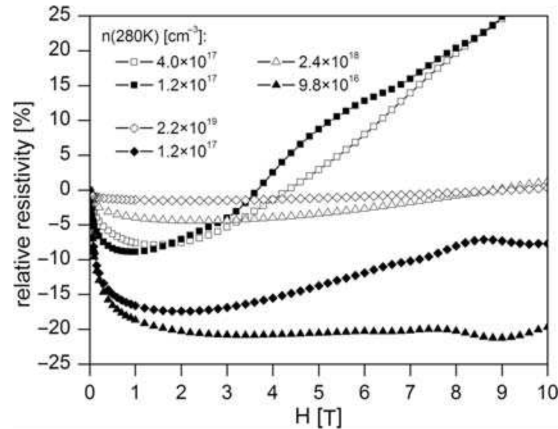

Fig. 15.14. Magnetoresistance measurements at 1.6 K n-type GaInNAs:Te solar cell material of different doping levels before (*open symbols*) and after hydrogenation (*full symbols*)

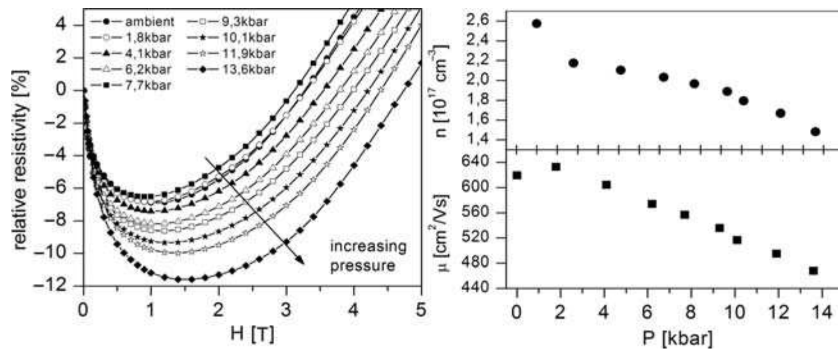

Fig. 15.15. *Left*: Magnetoresistance measurements of a GaInNAs:Te sample at various hydrostatic pressures taken at 1.6 K. *Right*: Corresponding dependence of carrier density and mobility on hydrostatic pressure

MR contribution increases with increasing hydrostatic pressure. Already at ambient pressure, it leads to a minimum in the MR curve of −6% at a magnetic field of about 1 T. At the highest pressure, the minimum value is even smaller, −12%, and the minimum position is shifted to higher fields, to about 1.5 T. The right graph depicts mobility μ and free-carrier concentration n extracted from the Hall and resistivity data taken at various hydrostatic pressures at $T = 1.6\,\mathrm{K}$. The carrier concentration and the mobility drop with increasing pressure.

A consistent explanation of all the transport results under hydrostatic pressure, i.e. the behaviour of the negative MR effect, of the mobility and of the carrier concentration, can be given only when resonance effects in the

scattering process and the energy distribution of the localized N-impurity states are taken into account. As discussed earlier, a qualitative understanding of the negative MR behaviour under pressure can already be given in the approximation of an effective single N-state. The maximum pressure shift of the band gap realized in the experiment is about 150 meV. This reduces the relative energy difference ΔE between the band edge and the effective impurity state by about 20% for GaInNAs. As the scattering cross-section roughly scales with $(\Delta E)^{-2}$ [46,47] this leads to an increase of the negative MR under hydrostatic pressure. It also explains the drop of the mobility under pressure. Similar arguments hold taking into account the full distribution of localized states [46, 47]. There is a considerable density of N-cluster states above the conduction band edge in GaInNAs. The hypothesis that the full distribution of localized cluster states needs to be accounted for is supported by the pressure dependence of the free-carrier concentration determined by Hall measurements as shown in the right graph of Fig. 15.15. The measurements show a significant decrease of the free-carrier concentration by about a factor of 2. Such results were qualitatively explained previously in GaInNAs as due to an increase of the potential fluctuations under hydrostatic pressure due to strong level repulsion effects and to different nearest neighbour environments [49]. An alternative reason for the reduction of the free-carrier concentration is a trapping of donor electrons at some of the localized N-cluster states that cross the CB edge under pressure. Both effects may contribute to the reduction of the free-carrier concentration n. Further work is required to evaluate the contributions of the two effects to the reduction of n under pressure, but it is worth noting that both effects arise within the same consistent picture of the conduction band transport in GaInNAs.

15.3.3 Thermopower Measurements

Many experiments on dilute nitride III-N-V semiconductor systems exhibit significant similarities with disordered semiconductor systems such as amorphous semiconductors. Examples are strong localization effects observed in luminescence e.g. the S-shape dependence of the photoluminescence peak position as a function of temperature, the photoluminescence-linewidth behaviour or the large Stokes shifts between photoluminescence peak and absorption peak. In disordered semiconductors such as amorphous silicon, useful information about the disorder potential and other disorder-related properties of the carrier transport can be obtained by a combined analysis of zero-field resistivity and thermopower measurements. However, it is a prerequisite of this analysis that the Seebeck coefficient is solely determined by the electronic system [55]. In conventional crystalline semiconductors, this prerequisite is not fulfilled because of the extended phonon states that contribute significantly to the Seebeck effect (and, thus, also to the Peltier effect) at low temperatures leading to the so called "phonon drag" effect. The proposed origin of this effect is that in the presence of an electric current the scattering of the charge

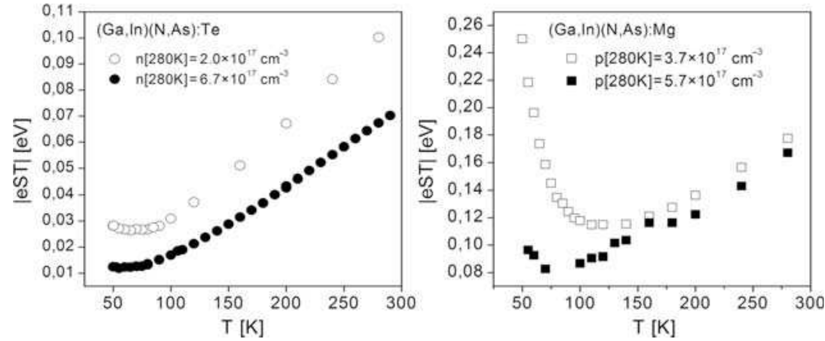

Fig. 15.16. Thermopower measurements as a function of temperature of n-type (*left*) and p-type (*right*) GaInNAs before (*full symbols*) and after annealing (*full symbols*)

carriers by phonons tends to increase the amplitudes of the phonons travelling in the same direction as the carriers and to decrease the amplitudes of those moving in the opposite direction. This results in a net-transport of energy by the phonons in the direction of the carrier flow, thus increasing the Seebeck coefficient with respect to the "interaction-free" case [56]. The phonon drag effect is most pronounced at low temperatures (where phonon umklapp-processes do not play a role) and low carrier densities (where carrier–carrier and carrier–dopant ion scattering are less significant than carrier–phonon scattering).

Figure 15.16 shows typical temperature dependence of the Peltier heat presented by the product $|eST|$ where S is the Seebeck coefficient for n-type (GaInNAs:Te (left) and p-type GaInNAs:Mg (right) before and after annealing. At first sight surprisingly, even for the n-type samples the curves resemble those of crystalline semiconductors exhibiting phonon drag at low temperatures. The occurrence of the phonon-drag effect in these samples despite the significant amount of disorder in the electronic potential of the conduction band reflects the phonon structure of GaInNAs. Basically, the incorporation of the much lighter N-atoms into the GaInAs host hardly affects the extended phonon modes instead additional localized vibrational modes occur where the N atom vibrates in the potential formed by its four nearest neighbour cations of Ga or In [57]. Thus, the N-induced disorder from a vibrational point of view is rather small, i.e. the GaInAs-like phonon dispersions remain intact, i.e. extended phonon modes with a defined wavevector that contribute to heat transport exist. In contrast, amorphous semiconductors only possess localized vibrational modes those contribution to the heat transport in response to a temperature gradient is negligible. The observed differences between annealed and as grown samples in Fig. 15.16 are mainly caused by the increase of the free-carrier concentration after annealing, which is more pronounced in the p-type samples.

15.4 Annealing Effects on Structural and Optical Properties

15.4.1 Structural Properties

As a metastable material is grown, phase separation effects, elemental clustering or local atomic ordering might be an issue influencing carrier transport and, thus, nanoanalytical studies are necessary to characterize the structures. At this point, it is very instructive to compare high-In-containing $Ga_{0.7}In_{0.3}(N_{0.015}As_{0.985})$ laser material, typically used for 1.3 μm emission, to low-In-containing $Ga_{0.92}In_{0.08}(N_{0.03}As_{0.97})$ solar cell material, as a lot on the structure formation mechanisms can be learnt studying the material in two different composition regimes. Transmission electron microscopy (TEM) at an acceleration voltage of 300 kV with a special dark field technique [58] was used to image the distribution of the elements as well as of the strain in GaInNAs. To explain the observed strain contrast in the samples, we calculated the strain energy of the crystal for different N-III-N as well as N-In arrangements in the framework of the valence force field (VFF) model [59].

In transmission electron microscopy, the (002) reflection of cubic zinc blende materials is sensitive for the chemical composition. It was shown that deviations from a homogeneous In depth profile would be detectable, if they are larger than ±10% of the amount of In present in the structure, hence in the range of ±0.8% for an 8% In containing solar cell. The sensitivity of this reflection to small variations in the N depth profile is low, as a result of which imaging with the (202) reflection was also performed in order to be able to detect possible inhomogenieties of the N depth distribution rather by the strain fluctuation they would introduce than by their chemical contrast. Dark field images ($g = (002)$ (a) and $g = (202)$ (b)) taken from a GaInNAs sample with an In-content of 30% and a N-content of 2.4% are shown in Fig. 15.17. The micrograph taken with the chemically sensitive reflection (a) shows a uniform contrast distribution in the growth planes throughout the complete thickness of the quantum well. From the uniform contrast in the $x - y$ plane, it can be concluded that there is no elemental clustering in the growth plane. Hence, we conclude that the In is homogeneously distributed in the growth planes of the quantum wells as the contrast characteristics also do not change with specimen thickness. The strain sensitive image (b), taken with the (202) reflection, shows that there exist columnar regions with an inhomogeneous strain distribution throughout the 7-nm thick quantum well. They extend through the complete well and have a lateral distance in the range of 10 nm as will be shown in more detail later.

A plan view TEM (202) dark field micrograph of a $Ga_{0.7}In_{0.3}(N_{0.015}As_{0.985})$ quantum well – as shown in Fig. 15.18 – makes the distribution of the strain fields on the quantum well surface clear. The strain fields can be seen as dark contrast under the imaging conditions used for this micrograph. One recognizes once more that they are homogeneously distributed, but do not form an

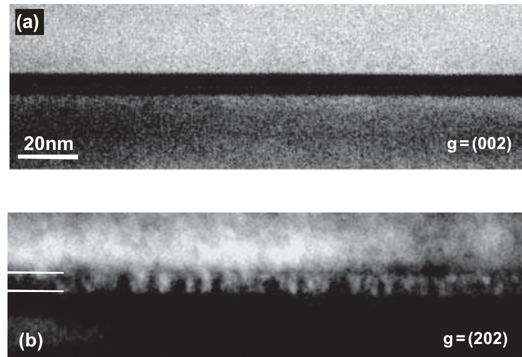

Fig. 15.17. Cross-sectional dark field TEM images of a $Ga_{0.7}In_{0.3}(N_{0.015}As_{0.985})$/ GaAs quantum well, using the chemically sensitive (002) (**a**) and the strain sensitive (202) (**b**) reflection

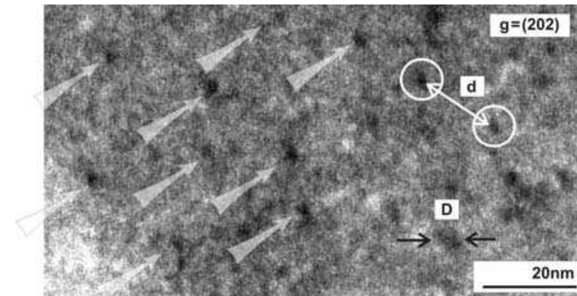

Fig. 15.18. Plan view dark field TEM micrograph of a $Ga_{0.7}In_{0.3}(N_{0.015}As_{0.985})$ quantum well using the strain sensitive (202) reflection

ordered lattice. Their extension D, which can be concluded from the diameter of the black regions – and of course depends on the imaging conditions used – is identical for all of them. Their average distance d was determined by Fourier filtering the TEM images. It depends on the N-content of the samples [58] and is for 3% N-containing GaInNAs solar cell material in the range of 10–20 nm. This is very close to what was reported to be the surprisingly short minority carrier diffusion length of electrons in the quaternary material [17].

The inhomogeneous strain fields are found in GaInNAs as well as Ga(NAs) irrespective of the growth technique, MBE or MOVPE. Hence, they are an intrinsic property of the material and in the following section a possible explanation on the origin of them will be given.

An arrangement of N-atoms quite consistent with that expected from random occupation was found in scanning tunnelling microscopic investigations of Ga(NAs) samples with an enhanced occurrence of N nearest-neighbour pairs [60]. Those N-nearest-neighbour pairs would certainly not show up in (002) TEM dark field imaging because of their low contribution to the

structure factor. They, however, might show up in strain-sensitive images because of the large lattice distortion, they introduce. As the N was identified to be the source of those strain fields, VFF calculations of different next nearest-neighbour configurations of N in GaAs and GaInAs were performed.

The VFF supercell method previously suggested by Kent, Zunger and Kim [42, 43] was used to calculate the strain energies [59]. Following this method, one or more substitutional N or In atoms are placed in a large supercell and relaxed with respect to the total strain energy.

The supercell size used was $5\times5\times8.5\,\text{nm}^3$, containing almost 11,000 atoms. This supercell showed adequate convergence of the total strain energy. The energy functional depends on the atomic positions $\boldsymbol{R}_i$ and on the chemical composition as follows:

$$E_i = E_{\text{strain}}(R_i) + 0.5\sum_{j=1}^{4} E_{\text{chemij}}. \tag{15.4}$$

With E_{chemij} being the cohesive energy for bonds of type *ij*. The values used for these energies are compiled in [59]. The strain energy E_{strain} was evaluated in the framework of Keating's VFF model. The bond-stretching and bond-bending coefficients were derived from the elastic constants and from equilibrium bond lengths of the binary cubic zinc-blende solids, which are known experimentally or from density functional theory, respectively [61–63]. Bond-bending coefficients for asymmetric bonds were calculated assuming linear additive contribution of both bonds. For Ga(NAs) first principle calculations were reported in the literature [42, 64]. The values for the strain of the different N-configurations of our VFF calculations are summarized in Table 15.1 and fit very well to the values reported in literature so that we conclude that our VFF model for Ga(NAs) agrees with the first principle calculations and, thus, can be applied to calculate further configurations also in In-containing material. Strain fields of the extent observed cannot be explained by the lattice distortion of a single N-atom in GaAs. Therefore, we concentrated on different N - N next nearest-neighbour configurations, as schematically shown in Fig. 15.19, and find that [011] oriented N-pairs (b) have even higher strain energy than two separated N-atoms in GaAs. Therefore, this configuration should not be adopted from the crystal upon growth. In contrast to that, we find – in accordance with [42, 64] – that N-ordering in [001] (c) reduces the strain energy of the crystal by 0.10 eV when compared

Table 15.1. Strain energies of various nitrogen arrangements in GaAs

Local configuration	$\boldsymbol{E}_{\text{strain}}$[eV]	ΔE_{strain}[eV]
Isolated N in GaAs	1.69	–
2N in [110]-direction	3.75	0.37
2N in [001]-direction	3.28	−0.10
3N in [001]-direction	4.85	−0.22

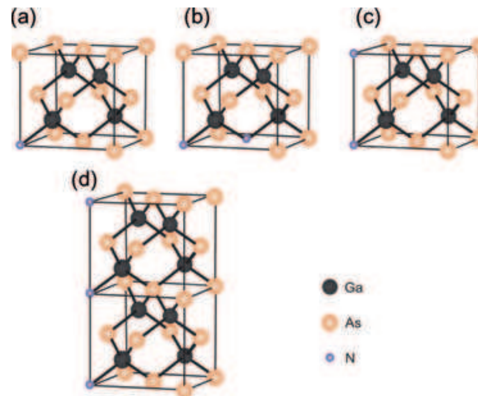

Fig. 15.19. Ball and stick models of nitrogen in different pair configurations. (**a**) Isolated N in GaAs, (**b**) N nearest-neighbour pair in [110] direction, (**c**) pair on [001] direction and (**d**) a chain of three nitrogen atoms in [001] direction

with putting two isolated N-atoms in GaAs. This strain energy is even further reduced, when longer [001] oriented N-chains (Fig. 15.19d) in GaAs are formed. We attribute the columnar strain fields, which have the tendency to extend in growth direction and which we find in as-grown Ga(NAs) as well as GaInNAs samples of different composition to this chain like ordering of N upon growth into the thermodynamically stable configuration on the surface. If the supposed nitrogen chains have a length equal to the quantum well thickness, a maximum of 10% of the entire nitrogen concentration would be contained in the chains.

The energy balance of crystal structures with nitrogen in different group-III environments was also calculated by VFF methods, to quantitatively judge on whether there are more stable configurations for the nitrogen than the chain-like ordered one. When bulk constraints play a larger role – as after growth – not on the free surface, these configurations might be taken.

The schematic crystal models of nitrogen in different group-III environments, which underlie the VFF calculations, are depicted in Fig. 15.20. As one goes to a weaker binding energy when reducing the number of GaN bonds and increasing the number of InN bonds, the difference in chemical binding energy has also to be taken into account when calculating the energy balance for the proposed change in local environment of the nitrogen. The strain energies together with the differences in chemical energy and the total energy balance is summarized in Table 15.2. As expected, it can be seen that the strain energy of the crystal considerably decreases when putting N from a four Ga to a four In-environment. The energy gain when doing so is about 0.5 eV per additional one In-environment. The energy one loses when adopting the weaker In–N bonds compared with the Ga–N bonds is about 0.25 eV per additional one In-environment. In summary, if the proposed place-change happens, one gains 0.2–0.3 eV per one In-environment. Thus, one can gain a maximum of almost 1 eV in total energy, when moving a nitrogen atom

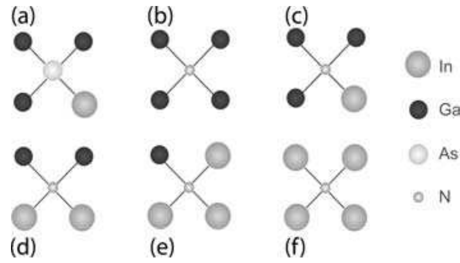

Fig. 15.20. Ball and stick models of different group-III next nearest-neighbour configurations of a nitrogen atom on a group-V lattice site

Table 15.2. Strain energies, chemical energies and resulting interaction energies of various N-III nearest-neighbour configurations

Local configuration	E_{strain}(eV)	ΔE_{strain}(eV)	ΔE_{chem}(eV)	ΔE(eV)
N-Ga_4In_0 (Fig. 15.20b)	1.69	–	–	
N-Ga_3In_1 (Fig. 15.20c)	1.28	−0.55	0.23	0.32
N-Ga_2In_2 (Fig. 15.20d)	0.92	−1.05	0.46	−0.59
N-Ga_1In_3 (Fig. 15.20e)	0.61	−1.50	0.69	−0.81
N-Ga_0In_4 (Fig. 15.20f)	0.39	−1.86	0.92	0.94

Models of the different nearest-neighbour configurations are shown in Fig. 15.20

from a four Ga-environment to a four In-environment, strongly supporting the above-explained model.

This place-change, together with the different band gaps the varying local N-III arrangements have [44], is a unique property of the dilute N-containing III/V-semiconductors.

The TEM micrographs, which were taken under strain-sensitive diffraction conditions, of the sample (high-In content laser material) annealed for 1 h under TBAs stabilization at 725°C and annealed for 25 min in H_2-atmosphere at 625°C are shown in Figs. 15.21 and 15.22, respectively. The As-stabilized annealing does not result in dissolution of the strain fields, which can be clearly seen in Fig. 15.21. The alternating white/dark contrast, which hints to strong strain fluctuations, is still present. However, annealing conditions in H_2-ambient – even at lower temperature – result in the complete dissolution of the strain fields and hence of the N-ordering (Fig. 15.22). This hints to a process, which is strongly driven by the presence of As-vacancies, which are generated to a larger extent, when annealing less As-stabilized, i.e. under extreme conditions without TBAs stabilization at higher temperatures.

The dissolution of the nitrogen chains upon annealing in laser material, thus, is caused by the change in N-nearest-neighbour environment from a Ga-rich to an In-rich one, which is driven by a significant energy gain due to low strain energy of the In-rich configurations.

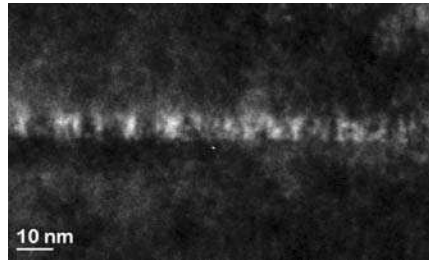

Fig. 15.21. Strain-sensitive ($g = (202)$) cross-sectional TEM micrographs of a GaInNAs/GaAs laser quantum well annealed TBAs-stabilized at 700°C for 5 min

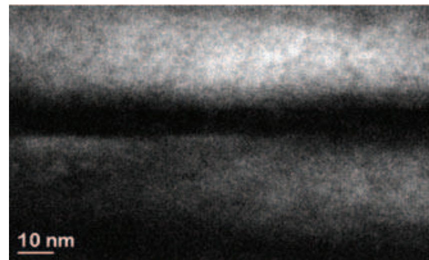

Fig. 15.22. Strain-sensitive ($g = (202)$) cross-sectional TEM micrographs of GaInNAs/GaAs laser material annealed unstabilized at 625°C in H_2-atmosphere

From this model, it is also possible to explain, why the dissolution of the strain fields in high In-containing material should be easier compared with low In-containing solar cell material. The probability for different In-rich environments of the N as a function of the In-content is shown in Fig. 15.23.

For structures having an In-content of 30%, the probability for N to have one In- nearest-neighbour is >40%, for two In-nearest-neighbours 27%, three In-nearest-neighbours 7% and four In-nearest-neighbours <1%, respectively. Concerning material with an In-content of only 8%, the probability for N to have one In-nearest-neighbour is 25%, for two In-nearest-neighbours 3%, the probability for more In in the neighbourhood is negligible in this case. Hence, upon annealing of high In-content material, the N needs only to hop 0.5 nm to find an environment of two In atoms or more. In contrast to that, the N needs to cover a longer distance (1.2 nm), to reach an environment of two In atoms in the low In-content material. Consequently, this diffusion process takes either longer or only occurs at higher temperatures in low In-containing material. Therefore, the annealing conditions have to be adjusted for the solar cell material to allow for a longer diffusion of the N.

The inhomogeneous strain fields detected in quaternary GaInNAs, which are caused by chain-like nitrogen ordering in [001]-direction, might play an important role in solar cell devices as they might scatter carriers efficiently and hence deteriorate solar cell performance. One can hence speculate that

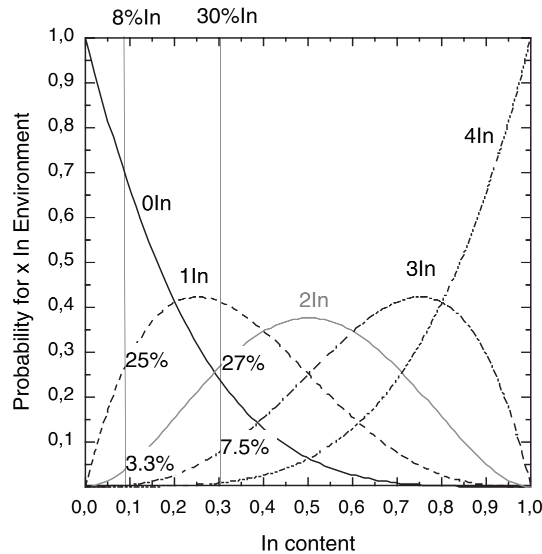

Fig. 15.23. Probability for different In-nearest neighbour environments of nitrogen in dependence on the In content in the quaternary material

the strain fields act as carrier traps limiting minority carrier lifetime. How far these defects are also identical to the ones described in ref. [27] is still to be shown. It is reported that a N-correlated defect lies 0.25 eV below the band gap and traps electrons very efficiently [27]. This defect is also responsible for the reduction of the open-circuit-voltage of the devices as soon as nitrogen is mixed to the crystal.

In the following the possibility to remove those strain fields also in low-Indium containing solar cell material – as was observed for high In-containing laser material – will be elucidated. (002) dark field imaging of a complete p on n solar cell structure after growth confirmed a homogeneous In-depth distribution in the solar cell material. The corresponding strain-sensitive TEM (202) dark field micrograph of an entire GaInNAs solar cell structure after growth is shown in Fig. 15.24a. Large columnar strain fields are clearly observed in the TEM dark field micrograph. The strain fields have a distance of 10–20 nm from each other and are elongated in growth direction to about 50 nm. The strain undulations are found in the complete quaternary structure, independent from the carrier type and concentration. The source for the strong strain undulations in the material is again the chain-like nitrogen ordering.

After annealing the sample for 5 min under As-stabilization at 700°C and subsequently for 25 min at 625°C in H_2 atmosphere, only a slight reduction of the inhomogeneous strain contrast is observed, as can be seen from the (202) dark field micrograph of the annealed sample, which is shown in

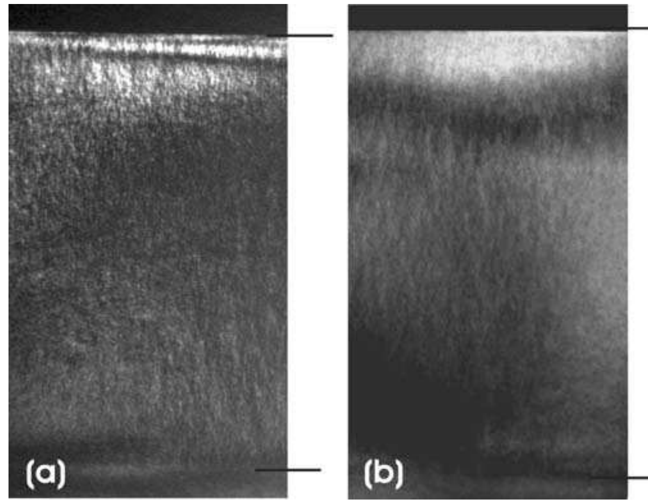

Fig. 15.24. Cross-sectional TEM dark field images of a 1 μm thick $Ga_{0.92}In_{0.08}(N_{0.03}As_{0.97})$ solar cell structure

Fig. 15.24b. These annealing conditions did result in the dissolution of the nitrogen ordering in GaInNAs laser material, as had been shown in Fig. 15.22.

15.4.2 Optical Properties

As the N-chains might act as non-radiative carrier traps and/or recombination centres in this material system, photoluminescence spectroscopy (PL) was chosen as suitable measurement to judge on the dissolution of the N-ordering in GaInNAs. The PL intensity is a complex function of carrier lifetime, interface recombination rates and carrier concentration; however, PL intensity is correlated to the minority carrier properties.

Photoluminescence measurements were performed at room temperature, exciting the samples using a cw Ar ion laser, operating at 514 nm. The excitation density was chosen to be similar to what one would expect for a III/V solar cell under concentration. The following discussion summarizes the results of PL investigations on GaInNAs solar cell and laser material with the aim of improving the material quality for optimized solar cell and laser structures. Concomitant Hall measurements were performed to be able to decide whether the change in PL intensity should be attributed to a change in carrier concentration or a change in minority carrier lifetime.

The blueshift of the energy gap in GaInNAs alloys, i.e. a decrease in PL wavelength after annealing, is a property of the quaternary, In- and N-containing material. The ternary base materials Ga(NAs) and GaInAs do not show a comparable increase of the band gap as a consequence of thermal treatment [44], always paying special attention to not alter composition –

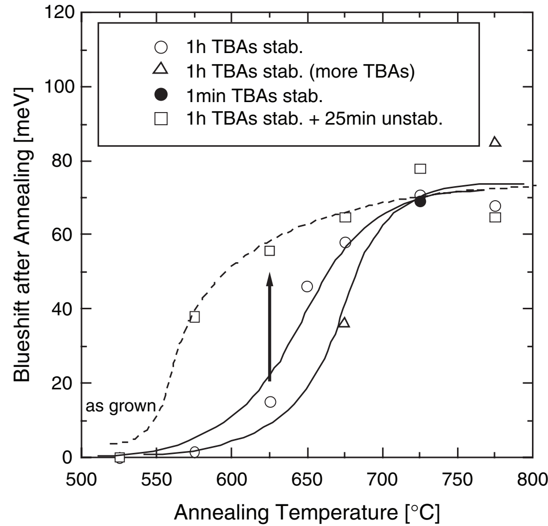

Fig. 15.25. Blueshift of the bandgap of GaInNAs as a function of the anneal temperature and the As stabilizing conditions

also not locally – or e.g. quantum well width during the anneal. It should also be mentioned that the blueshift of the energy-gap is observed for quaternary bulk-material as well as thin quantum well structures, indicating that one deals with a bulk-material effect. In Fig. 15.25, the blueshift of the photoluminescence peak position is plotted as a function of the annealing temperature for GaInNAs applying different annealing ambients. At room temperature, where the PL data of Fig. 15.25 had been taken, the PL signal originates from band-to-band transitions, which is also confirmed by the negligible Stokes-shift observed between PL and photomodulated reflectance measurements (PR) in this material system. The progression of the curve shown here is characteristic for the process. One observes an increase in band gap upon increasing the annealing temperature, which saturates at a certain value. Annealing at significantly higher temperatures neither improves PL intensity further nor results in a further blueshift of the emission, but results in the structural degradation and compositional phase-separation of the samples.

There is no change in PL peak position below an annealing temperature of 580–600°C, indicating that there is a certain activation energy involved in the process leading to this phenomenon. What one also observes is that the onset-temperature as well as the absolute value of the blueshift are functions of the quaternary alloy composition. Lower In-contents in the samples require higher temperatures for the same blueshift. In-line with that lower In-contents also result in a smaller maximum blueshift achievable. This finding is summarized in Fig. 15.26, where experimentally measured blueshifts of the band gap are plotted in dependence on the In-content in the quaternary layers.

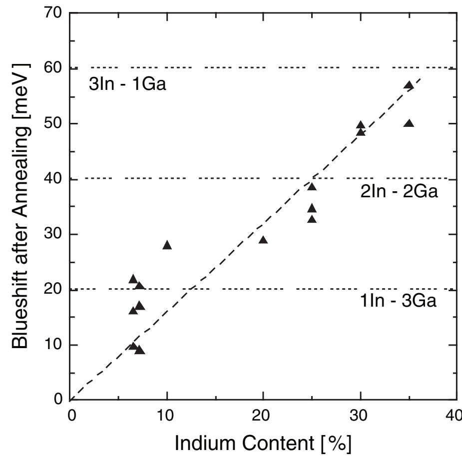

Fig. 15.26. Blueshift of the bandgap of GaInNAs as a function of the In-content in the material

It can be clearly seen that the maximum blueshift of the band gap is for low In-concentrations in the range of 10–20 meV, while it can reach up to 60 meV for In-concentrations used for laser-material, which are in the range of 30–35%. Maximum blueshifts mentioned in literature amount up to 80–100 meV, depending on the composition of the alloy, which can reach up to 40% In.

What becomes also obvious from Fig. 15.26 is that the blueshift depends linearly on the In-content of the samples. Dependencies on the N-content were also predicted and observed [44]. For low In-contents under 10%, it is in the range of 20 meV, and it increases to a value around 40 meV, when increasing the In-content to below 30%. Further increase in In to values above 30% results in an increase in maximum blueshift to 60 meV. A further parameter influencing the amount of blueshift at a given annealing temperature is the TBAs stabilization as well as the duration of the annealing, as also outlined in Fig. 15.25. This behaviour points to a strong influence of As-vacancies on the process, as their concentration can be altered when changing the stabilizing conditions. Decreasing the anneal time from 1 h under certain TBAs stabilization conditions (open circles) to 1 min (filled circle) does not change the amount of blueshift, indicating that a diffusion-controlled process over long distances is not the cause of the blueshift. This can, however, be tailored by varying the amount of As-stabilization during the annealing. Using higher stabilization results in an onset of the blueshift at higher temperatures (open triangles), adjusting lower As-stabilizing conditions – as done when offering no additional TBAs at all (open squares) – results in a low-temperature onset of a significant blueshift. This confirms that the amount of blueshift increases with increasing temperature as well as decreasing As-stabilization, proving that an

increase in the amount of As-vacancies driven into the crystal increases the value of the blueshift of the PL wavelength.

The band gap in the quaternary material and its shift upon annealing gives information on the change in the group III neighbourhood of the nitrogen atoms from Ga-rich ones upon growth to In-rich ones upon annealing. This change in the nearest neighbour configuration of the N-atoms is driven by the minimization of the total energy of the crystal. As described in the preceding section, upon growth a Ga-rich configuration is adopted, as the crystal can relax freely on the surface and the Ga-N bond is the strongest one in the quaternary alloy. Upon annealing, bulk constraints play a larger role and the N-place-change into an In-rich environment becomes favourable from the point of view of minimizing strain energy.

One should also look into the change in PL-intensity upon annealing, as this yields information on the dissolution of the N-chains, which act as non-radiative centres in the material. The onset of their dissolution is linked – but not directly correlated – to the blueshift, as nitrogen in chain-like configuration exhibits an even more stable state than nitrogen in a Ga-rich environment. Hence, more "aggressive" annealing conditions might be needed to dissolve the N-ordering. The integrated PL intensity is depicted in dependence on the anneal temperature – for different surface As-stabilizations – in Fig. 15.27.

The data were normalized to the PL intensity of the as-grown sample (point at 525°C). It can be seen that for samples annealed under TBAs stabilization (circles) as well as for the samples annealed in H_2-ambient (squares) the integrated PL intensity increases with increasing anneal temperature up to

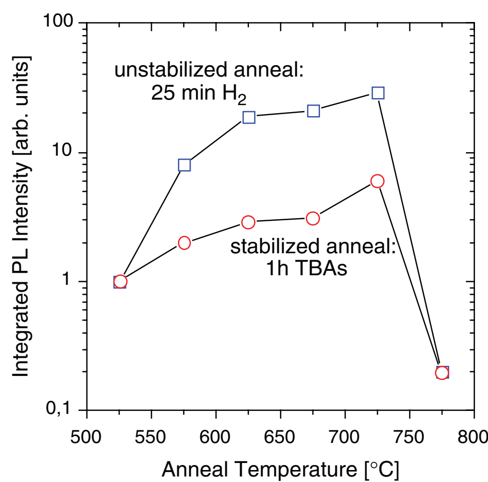

Fig. 15.27. Integrated room-temperature photoluminescence (PL) intensity of GaInNAs/GaAs multi-quantum well (MQW) heterostructures annealed in different environments as a function of anneal temperature. The data were normalized to the PL intensity of the as-grown sample

a temperature of 725°C. Above this value, the PL intensity drastically drops for all annealing conditions studied, indicating a strong structural degradation, presumably a phase separation of the quaternary alloy treated above this temperature. This increase in PL intensity upon annealing, which is observed by many groups, is usually attributed to the removal of defects, which are incorporated into the metastable alloy during growth. The annealing in H_2-ambient results in a much larger increase in PL intensity when compared with the As-stabilized anneal at the same temperature. The PL signal is about one order of magnitude more intense, if no As – except the As that is desorbing from the GaAs covered susceptor – is offered to the epitaxial surface. Annealing under As supply at 725°C, it is not even possible to achieve the same PL intensity as the sample annealed in H_2-ambient at a temperature 150°C lower.

The PL intensity increase upon annealing goes along with a decrease in linewidth of the PL signal. The linewidth of samples annealed under different As-stabilization at different temperatures are plotted in Fig. 15.28.

The linewidth, measured at room temperature, of the sample annealed in H_2-ambient continuously decreases with increasing anneal temperature from a value of 70 meV to a value of 40 meV, indicating an improved compositional homogeneity upon annealing. Also for the PL linewidth, the in H_2-ambient annealing conditions are more effective than the As-stabilized ones, which result in similar linewidths, however, only at higher annealing temperatures. This discussion shows – together with the findings concluded from Figs. 15.21 and 15.22 – that the chain-like N-ordering can be dissolved in high-In-containing laser material applying annealing under low-As-stabilization. These annealing conditions create the As-vacancies necessary to mediate the N-place change from a Ga-rich environment into an In-rich one as well as out

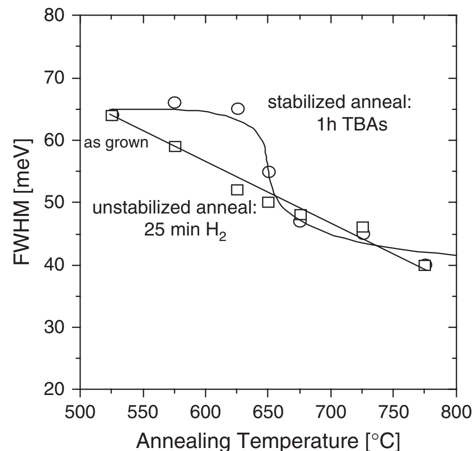

Fig. 15.28. Full width at half maximum (FWHM) of the room-temperature PL peak of a GaInNAs/GaAs MQW heterostructure annealed under different conditions

of the N-chains into In-rich environments. This goes along with dissolution of non-radiative centres and carrier scattering centres in the material, which also should drastically influence minority carrier properties and solar cell device performance, as will be shown in the subsequent section.

15.5 Solar Cell Characteristics

GaInNAs solar cells with an area of 0.25 cm^2 and 1 cm^2 were processed. Photolithography was used to define the front grid structure of the solar cells. Ti/Pd/Ag (30/30/100 nm) contacts were evaporated sequentially and annealed at 360°C for 2 min. The backside contact is made of Ni/AuGe/Ni (12% Ge) (10/130/10 nm). The contacts are reinforced by electroplated Au. For simplicity no anti-reflection coating was applied during processing, but the EQE results were corrected for surface reflectivity, which had been measured.

The internal quantum efficiencies (IQE) of identical n-on-p solar cell layer structures annealed for different times and at different temperatures is depicted in Fig. 15.29.

The solar cell consists of a 50-nm thick Mg-doped back surface field region underneath the 100-nm thick Mg-doped base region, which is separated from the 300-nm thick Te-doped emitter by a 500-nm thick, nominally intrinsic region. The 700-nm thick GaAs-cap absorbers – as the above-laying GaInAs-solar-cell will do in a multijunction-stack – the light above the band-edge of GaAs. It can be seen from the IQE dependence on the annealing conditions that one can already significantly improve the IQE, when going from a 5 min anneal under TBAs to a 60 min long anneal at the same temperature. One has seen previously [65] that the nearest neighbour change of N into an In-rich

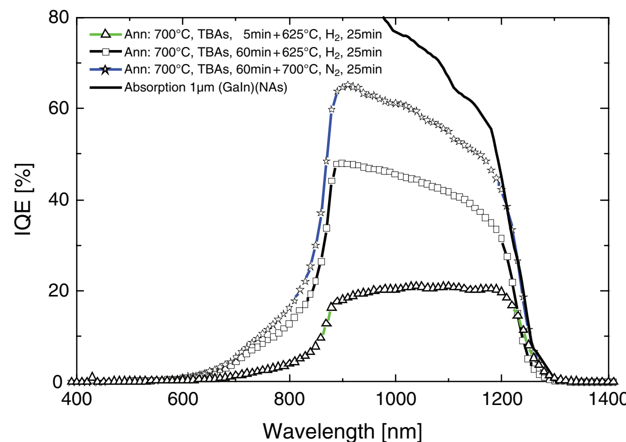

Fig. 15.29. Internal quantum efficiencies of n-on-p GaInNAs solar cells that were annealed under different conditions

environment was only finished after the longer anneal for low In-containing solar cell material.

On the other hand, One can still significantly improve IQE, when increasing the temperature of the unstabilized anneal from 625°C to 700°C. These are conditions that maximize the amount of As-vacancies in the crystal when compared with the low-temperature anneal. The complete dissolution of the N-induced strain-fields consequently needs that further activation. As only 10% of the entire nitrogen incorporated into the crystal is in the chains, there might well be two annealing steps necessary, one optimized for the nearest neighbour change of nitrogen in a Ga-rich environment, but not in a chain-configuration, and a second one that needs to be optimized for dissolving the N-chains. This is in agreement with what one had observed for the GaInNAs laser material: that the TBAs stabilized anneal is responsible for the blueshift of the energy-gap and the nearest neighbour change in nitrogen environment, but the subsequent unstabilized anneal results in the dissolution of the N-ordering. This step also has to be adjusted to the low In-contents in solar cell material, as at the end the driving force for both processes is the same, namely the nitrogen place change into an environment with lower strain energy. Using a not yet fully optimized annealing process, already almost absorption limited solar cell stacks were realized as confirmed by comparison of the IQE results with the absorption of a 1 μm thick GaInNAs structure.

15.6 Summary

Several intrinsic characteristics of the dilute nitride material system GaInNAs, which might influence carrier transport and hence device applications, were presented in the preceding chapter. Concerning solar cell applications, for which GaInNAs is a potential material for the introduction into a multijunction stack, the metastable material system can be grown lattice matched to GaAs/Ge substrates and having the required 1 eV band gap. Majority carrier electron transport is still controversially discussed in literature and might be strongly influenced by the quaternary composition, resulting in different band gaps as well as by post-growth annealing procedures, resulting in different distribution of the alloying elements. Minority carrier transport might be governed by intrinsic structural characteristics of the dilute nitride material systems, namely a chain-like ordering of N in growth direction upon growth. This configuration, which reduces the strain energy of the crystal, might act as a non-radiative recombination centre and/or a carrier trap. Dissolution of this N-ordering by annealing in quaternary material, via altering the N-neighbour environment to an In-rich one, results in improved minority carrier properties. This is reflected in a strong increase in PL intensity as well as solar cell device structures, which are then nearly absorption limited.

Acknowledgements. The authors gratefully acknowledge financial support from the European Community (IP "*FULLSPECTRUM*" SES6-CT-2003-502620) and the Deutsche Forschungsgemeinschaft in the framework of the Topical Research Group on *Metastable compound semiconductor systems and heterostructures*.

References

1. R.R. King, C.M. Fetzer, P.C. Colter, K.M. Edmondson, J.H. Ermer, H.L. Cotal, H. Yoon, A.P. Stavrides, G. Kinsey, D.D. Krut, N.H. Karam, Proc. of 29th IEEE Photovoltaic Specialists Conference, New Orleans, USA, 776, 2002
2. D.J. Friedman, J.F. Geisz, S.R. Kurtz, J.M. Olson, Proc. of 2nd World Conference and Exhibition on Photovoltaic Solar Energy Conversion, Vienna, Austria, 3, 1998
3. H.Q. Hou, K.C. Reinhardt, S.R. Kurtz, J.M. Gee, A.A. Allerman, B.E. Hammons, C.E. Chang, E.D. Jones, Proc. of 2nd World Conference and Exhibition on Photovoltaic Solar Energy Conversion, Vienna, Austria, 3600, 1998
4. G. Létay, A.W. Bett, Proc. of 17th European Photovoltaic Solar Energy Conference and Exhibition, Munich, Germany, 178, 2001
5. S. Fahy, E.P. O'Reilly, Appl. Phys. Lett. **83**, 3731 (2003)
6. C. Baur, A.W. Bett, F. Dimroth, S. Riesen, B. Kunert, M. Traversa, K. Volz, W. Stolz, Proc. of 3rd World Conference on Photovoltaic Energy Conversion, Osaka, Japan 677 (2003)
7. Z. Pan, T. Miyamoto, D. Schlenker, S. Sato, F. Koyama, K. Iga, J. Appl. Phys. **84**, 6409 (1998)
8. H.P. Xin, C.W. Tu, Appl. Phys. Lett. **72**, 2442 (1998)
9. F. Höhnsdorf, J. Koch, C. Agert, W. Stolz, J. Cryst. Growth **195**, 391 (1998)
10. J.C. Harmand, G. Ungaro, L. Largeau, G. Le Roux, Appl. Phys. Lett. **77**, 2482 (2000)
11. A.Y. Egorov, D. Bernklau, B. Borchert, S. Illek, D. Livshits, A. Rucki, M. Schuster, A. Kaschner, A. Hoffmann, Gh Dumitras, M.C. Amann, H. Riechert, J. Cryst. Growth **227**, 545 (2001)
12. Z. Pan, L. Li, W. Zhang, X. Wang, Y. Lin, R. Wu, J. Cryst. Growth **227**, 516 (2001)
13. S.G. Spruytte, M.C. Larson, W. Wampler, C.W. Coldren, H.E. Petersen, J.S. Harris, J. Cryst. Growth **227**, 506 (2001)
14. M. Kondow, T. Kitani, Semicond. Sci. Technol. **17**, 746 (2002)
15. T. Kitatani, M. Kondow, T. Tanaka, J. Cryst. Growth **227**, 521 (2001)
16. J.F. Geisz, D.J. Friedman, J.M. Olson, S.R. Kurtz, B.M. Keyes, J. Cryst Growth **195**, 401 (1998)
17. S.R. Kurtz, A.A. Allerman, C.H. Seager, R.M. Sieg, E.D. Jones, Appl. Phys. Lett. **77**, 400 (2000)
18. G. Leibiger, C. Krahmer, J. Bauer, H. Herrnberger, V. Gottschalch, J. Cryst. Growth **272**, 732 (2004)
19. W. Li, M. Pessa, J. Toivonen, H. Lipsanen, Phys. Rev. B. **64**, 113308 (2001)
20. T. Suzuki, T. Yamaguchi, A. Yamamoto, A. Hashimoto, Phys. Stat. Sol. (c) 0, 2769 (2003)

21. A. Hashimoto, T. Yamaguchi, T. Suzuki, A. Yamamoto, J. Cryst. Growth **278**, 532 (2005)
22. A.J. Ptak, S.W. Johnston, S. Kurtz, D.J. Friedman, W.K. Metzger, J. Cryst. Growth **251**, 392 (2003)
23. H. Overhof, P. Thomas, *Transport Properties of Amorphous Semiconductors*, (Springer, Berlin Heidelberg New York, 1984)
24. S.D. Baranovski, O. Rubel, in *Theory of Charge Transport in amorphous Semiconductors*, ed. by S.D. Baranovki. Electrical Conductivity in disordered Materials with Applications in Electronics (Wiley, London, 2006)
25. K. Volz, J. Koch, B. Kunert, W. Stolz, J. Cryst. Growth **248**, 451 (2003)
26. K. Volz, T. Torunski, B. Kunert, O. Rubel, S. Nau, S. Reinhard, W. Stolz J. Cryst Growth 272, 739 (2004)
27. S. Kurtz, S. Johnston, H.M. Branz, Appl. Phys. Lett. **86**, 113506 (2005)
28. J.W. Harrison, J.R. Hauser, Phys. Rev. B. **13**, 5347 (1976)
29. J. Teubert, P.J. Klar, W. Heimbrodt, K. Volz, W. Stolz, P. Thomas, Appl. Phys. Lett. **84**, 747 (2004)
30. W. Shan, W. Walukiewicz, J.W. Ager III, E.E. Haller, J.F. Geisz, D.J. Friedman, M. Olson, S.R. Kurtz, Phys. Rev. Lett. **82**, 1221 (1999)
31. P.J. Klar, H. Grüning, W. Heimbrodt, J. Koch, F. Höhnsdorf, W. Stolz, P.M.A. Vicente, J. Camassel, Appl. Phys. Lett. **76**, 3439 (2000)
32. J. Wu, W. Shan, W. Walukiewicz, Semicond. Sci. Technol. **17**, 860 (2002)
33. E.P. O'Reilly, A. Lindsay, Tomic, A.M. Kamal-Saadi, Semicond. Sci. Technol. **17**, 870 (2002)
34. H. Roth, W.D. Straub, W. Bernard, J.E. Mulhern Jr., Phys. Rev. Lett. **11**, 328 (1963)
35. J.M. Monsterleet, B. Capoen, G. Biskupski, J. Phys. Condens. Matter **9**, 8657 (1997)
36. L. Halbo, R.J. Sladek, Phys. Rev. **173**, 794 (1968)
37. J.F. Woods, C.Y. Chen Phys. Rev. **135**, A1462 (1964)
38. M. Benzaquen, D. Walsh, K. Mazuruk Phys. Rev. **B38**, 10933 (1988)
39. P.W. Anderson, Phys. Rev. **109**, 1492 (1958)
40. G. Bergmann, Phys. Rev. B. **28**, 2914 (1983)
41. B.L. Altshuler, A.G. Aronov (1985) in *Electron-Electron Interactions in Disordered Systems* vol. 1, ed. by A.L. Efros, M. Pollak, (Elsevier, Amsterdam) pp. 2–153
42. P.R.C. Kent, A. Zunger, Phys. Rev. B. **64**, 115208 (2001)
43. K. Kim, A. Zunger, Phys. Rev. Lett. **86**, 2609 (2001)
44. P.J. Klar, H. Grüning, J. Koch, S. Schäfer, K. Volz, W. Stolz, W. Heimbrodt, A.M. Kamal Saadi, A. Lindsay, E.P. O'Reilly, Phys. Rev. B. **64**, 121203(R) (2001)
45. C. Skierbiszewski, P. Perlin, P. Wisniewski, W. Knap, T. Suski, W. Walukiewicz, W. Shan, K.M. Yu, J.W. Ager, E.E. Haller, J.F. Geisz, J.M. Olson, Appl. Phys. Lett. **76**, 2409 (2000)
46. S. Fahy, A. Lindsay, E.P. O'Reilly, IEE Proc. Optoelectron. **151**, 352 (2004)
47. S. Fahy, A. Lindsay, H. Ouerdane, E.P. O'Reilly, Phys. Rev. B. **74**, 035203 (2006)
48. J. Teubert, P.J. Klar, W. Heimbrodt, K. Volz, W. Stolz, A. Polimeni, M. Capizzi, Physica E. **32**, 218 (2006)
49. J. Teubert, P.J. Klar, W. Heimbrodt, K. Volz, W. Stolz, IEE Proc. Optoelectron. **151**, 357 (2004)

50. J. Teubert, P.J. Klar, W. Heimbrodt, V. Gottschalch, A. Lindsay, E.P. O'Reilly, Phys. Stat. Sol. (b) **244**, 431 (2006)
51. J.I. Pankove, N.M. Johnson *Hydrogen in Semiconductors in Semiconductors & Semimetals*, (Academic Press, New York, 1991) p. 34
52. P.J. Klar, H. Grüning, M. Güngerich, W. Heimbrodt, J. Koch, T. Torunski, W. Stolz, A. Polimeni, M. Capizzi, Phys. Rev. B **67**, 121206 (2003)
53. S.B. Healy, A. Lindsay, E.P. O'Reilly, Physica E. **32**, 249 (2006)
54. P.J. Klar, J. Teubert, M. Güngerich, T. Niebling, H. Grüning, W. Heimbrodt, K. Volz, W. Stolz, A. Polimeni, M Capizzi, E.P. O'Reilly, A. Lindsay, M. Galuppi, L. Geelhaar, H. Riechert, Tomic, Phys. Stat. Sol. (b) **244**, 24 (2006)
55. H. Overhof, P. Thomas, in *Springer Tracts in Modern Physics*, vol. 114, (Springer, Berlin Heidelberg New York, 1989)
56. C. Herring, Phys. Rev. **96**, 1163 (1954)
57. J Wagner, T. Geppert, K. Köhler, P. Ganser, N. Herres, J. Appl. Phys. **90**, 5027 (2001)
58. K. Volz, T. Torunski, W. Stolz, J. Appl. Phys. **97**, 014306 (2005)
59. O. Rubel, K. Volz, T. Torunski, S.D. Baranovskii, F. Grosse, W. Stolz, Appl. Phys. Lett. **85**, 5908 (2004)
60. H.A. McKay, R.M. Feenstra, T. Schmidtling, U.W. Pohl, Appl. Phys. Lett. **78**, 82 (2001)
61. Y.A. Burenkov, S.Y. Davidov, S.P. Nikanorov, Sov. Phys. Solid State **17**, 1446 (1975)
62. Y.A. Burenkov, Y.M. Burdukov, S.Y. Davidov, S.P. Kikanorov, Sov. Phys. Solid State **15**, 1175 (1973)
63. F. Grosse, J. Neugebauer, Phys. Rev. B. **63**, 085207 (2001)
64. C. Persson, A. Zunger, Phys. Rev. **68**, 035212, (2003)
65. K. Volz, T. Torunski, D. Lackner, O. Rubel, W. Stolz, C. Baur, S. Müller, F. Dimroth, A.W. Bett, J. Solar Energy Eng. **129**, 266 (2007).

16

Elemental Devices and Circuits for Monolithic Optoelectronic-Integrated Circuit Fabricated in Dislocation-Free Si/III–V-N Alloy Layers Grown on Si Substrate

H. Yonezu

Basic technologies for realizing a monolithic optoelectronic-integrated circuits have been developed, in which light-emitting diodes and metal oxide semiconductor field effect transistors were merged in a single chip. Structural defect-free GaPN and InGaPN layers were grown on a Si substrate. Point defects in these layers were reduced by reducing N ions and rapid thermal annealing. The carrier concentrations of the GaPN layer were controlled by doping S and Mg. InGaPN/GaPN double heterostructure light-emitting diodes were fabricated by integrating these technologies.

Light-emitting diodes and metal oxide semiconductor field effect transistors, which are elemental devices for optoelectronic-integrated circuits, were fabricated merged in a single chip with a Si layer and an InGaPN/GaPN double heterostructure layer lattice-matched to Si grown on a Si substrate. The developed processing flow was based on a conventional metal oxide semiconductor field effect transistor processing flow. All light-emitting diodes and metal oxide semiconductor field effect transistors operated normally. Light emission from the light-emitting diode was modulated by switching the metal oxide semiconductor field effect transistor. The growth and fabrication process technologies could be effective for the realization of monolithic optoelectronic-integrated circuits for massively parallel processing systems and optical interconnections.

16.1 Introduction

It has been a dream to realize novel optoelectronic-integrated circuits (OEIC) in which light-emitting devices are implemented into Si large-scale-integrated circuits (LSI) consisted of metal oxide semiconductor field effect transistors (MOSFET) [1]. However, following three problems have been preventing such novel monolithic OEICs, although a few trials have been proposed [2, 3].

The first problem is the generation of a large number of structural defects such as dislocations and stacking faults at the growth of radiative III–V

compounds on Si substrates due to the difference of material parameters. The second problem is the control of electrical and optical properties of GaPN and InGaPN for fabricating light-emitting devices. The third problem is the mismatch of fabrication processes between Si LSI and III–V compound devices. In addition, it should be avoided that the number of process steps is increased by fabricating the Si LSI and light-emitting devices sequentially [2] since it leads to a nonrealistic poor yield, as reported on a three dimensional LSI [4].

The first problem was overcome by applying GaPN-based III–V-N alloys which was lattice-matched to Si [5–7]. In addition, (In)GaPN light-emitting diodes (LED) were fabricated since (In)GaPN is radiative although a host material of GaP is an indirect-transition type [8, 9]. Thus, a Si LSI and an (In)GaPN LED could be formed in Si/GaPN-based layers grown on a Si substrate [10]. We have tried to develop the technologies for overcoming the second and third problems [11]. As a result, elemental devices of Si MOSFETs and GaPN-based LEDs for monolithic OEICs were fabricated in Si/GaPN-based epitaxial layers grown on a Si substrate [12]. In this chapter, the details of the fabrication and characterizations of these novel monolithic OEICs are described.

16.2 Growth of Structural Defect-Free Si/(In)GaPN Layers on Si Substrate

The epitaxial growth of III–V compound semiconductors on Si substrates contains the specific following problems:

(1) The difference in the number of valence electrons
(2) The difference in lattice parameters
(3) The difference in thermal expansion coefficients

Problem (1) causes the generation of antiphase domains (APDs) [10, 13]. A Si (100) surface forms monolayer steps covered with P atoms in the growth of GaP. Then continuing atomic layers form different domains called APDs on each terrace, in which P and Ga layers are shifted by one monolayer (ML) between adjacent domains. Wrong bonds of P–P and Ga–Ga are formed at a boundary between adjacent domains. These boundaries are called antiphase boundaries (APBs). This problem was overcome by using a vicinal Si (100) substrate since a terrace length was short [14]. APDs were annihilated at an early growth stage within 10 nm thickness when a thin GaP layer was grown on the Si (100) substrate misoriented by 4 degree towards a [011] direction at 450°C by migration-enhanced epitaxy (MEE). Ga and P_2 fluxes were supplied by evaporating elemental Ga and InP polycrystals respectively with conventional Knudsen cells. The initial formation of APDs would be related to the charge imbalance at the heterointerface which could principally cause the mixture of group III and V atoms and Si [15, 16].

Problem (1) causes the generation of stacking faults and threading dislocations as well. A part of P atoms is desorbed from a P layer adsorbed on a topmost surface of the Si substrate at 590°C in conventional molecular beam epitaxy (MBE). This leads to the formation of stacking faults and threading dislocations [17]. This problem was overcome by MEE at relatively low temperature for suppressing the desorption of P atoms on the Si surface. A stacking fault-free and dislocation-free GaP layer was obtained when the thickness of the GaP initial layer was less than a critical thickness of about 50 nm [18]. A 20 nm thick GaP initial layer was grown on the Si (100) substrate misoriented by 4 degree towards a [011] direction at 450°C by MEE. There were no structural defects of misfit dislocations and threading dislocations as well as stacking faults in the GaP initial layer and at the heterointerface between the GaP initial layer and the Si substrate. Thus, a Si surface is converted to a GaP surface without the structural defects. It is noted that the lateral lattice parameter of the GaP initial layer is the same as that of Si.

Problem (2) causes the generation of misfit dislocations and threading dislocations in lattice relaxation process [19, 20]. This problem was overcome by lattice-matched growth using GaPN, GaAsPN and InGaPN [5, 6]. A lattice parameter decreases with the increase in N contents x in the III–V-N alloys, while the band gap (E_g) decreases, as shown in Fig. 16.1 [13, 21–24]. It has been estimated that $GaP_{0.98}N_{0.02}$ is lattice-matched to Si [21]. The GaPN layers were grown at 590°C by MBE. Radical nitrogen was supplied with an rf-plasma source flowing N_2 gas. Before the growth, the 20-nm thick GaP initial layer was grown on the Si (100) substrate misoriented by 4° towards the [011] direction at 450°C by MEE. The lattice parameters and N contents x

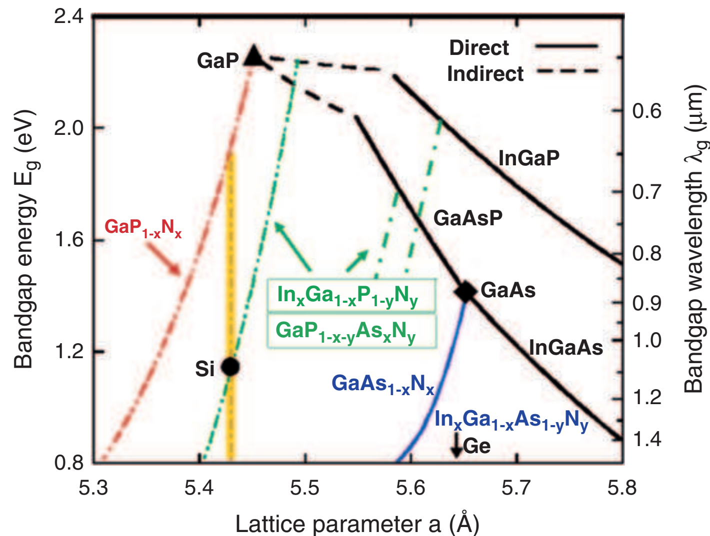

Fig. 16.1. Lattice parameter and band gap energy of III–V-N alloys [13, 21–24]

of the $GaP_{1-x}N_x$ layer were estimated with peak angles measured by (400) and (511) X-ray diffraction (XRD), lattice parameters of GaP and cubic GaN, elastic parameters of GaP and Vegard's law. The threading and misfit dislocations were investigated with a tilted cross-sectional transmission electron microscopy (X-TEM) image.

Neither threading dislocations nor misfit dislocations were observed in the 200-nm thick $GaP_{0.98}N_{0.02}$ layer [5,13]. On the other hand, misfit dislocations were observed in a 200-nm thick GaP layer grown on the Si substrate. Thus, it was clarified that dislocation-free GaAsPN and InGaPN layers can be grown on the Si substrate covered with the GaP initial layer [6, 9].

Problem (3) causes a tensile strain in III–V compound semiconductors grown on Si substrates during cooling process since the thermal expansion coefficients of the III–V compound semiconductors are larger than those of Si. In the $GaP_{0.98}N_{0.02}$ layer grown on the Si substrate at 590°C, the tensile strain of the order of 10^8 Pa cm^{-2} is contained. When the tensile strain is increased above a critical value at a relatively high temperature, edge dislocations are introduced from a grown surface [25, 26]. The edge dislocations glide on a (111) plane and remain at the heterointerface along <110> directions.

A Si capping layer is ideal since its lattice parameter is almost the same as that of the Si substrate. Thus, the tensile strain is negligibly small. A 100-nm thick Si capping layer following a 400-nm thick $GaP_{1-x}N_x$ layer was grown on the Si substrate covered with the 20-nm thick GaP initial layer [7]. For Si epitaxy, a Si flux was supplied by evaporating a polycrystalline Si with an electron beam evaporator. A small lattice-mismatch of 0.13% was obtained between the $GaP_{1-x}N_x$ layers and Si substrate, which is almost the same as that between AlAs and GaAs. The N content x was estimated to be 2.9%. No threading dislocations and no misfit dislocations were observed in any of the epitaxial layers and heterointerfaces, as shown in Fig. 16.2 [7, 10]. No stacking faults or APDs were observed either; that is to say, a structural defect-free Si/GaPN layers were realized on a Si substrate.

16.3 Optical and Electrical Properties of GaPN and InGaPN

Possible LEDs that can be lattice-matched to Si substrate are InGaPN/GaPN and GaAsPN/GaPN double heterostructure (DH), as seen in Fig. 16.1. The other LEDs are strained $GaP_{1-y}N_y/GaP_{1-x}N_x (y > x)$ DH LEDs and strained InGaPN/GaPN and GaAsPN/GaPN DH or quantum well (QW) LEDs. Thus, the optical and electrical properties of GaPN, InGaPN and GaAsPN should be evaluated.

It has been argued that GaPN contains a factor of direct transition since it is radiative and its absorption edge is steep while GaP is an indirect-transition type [27–29]. However, the crystalline quality and the photoluminescence (PL) efficiency of the GaPN layer deteriorate markedly with the increase in N

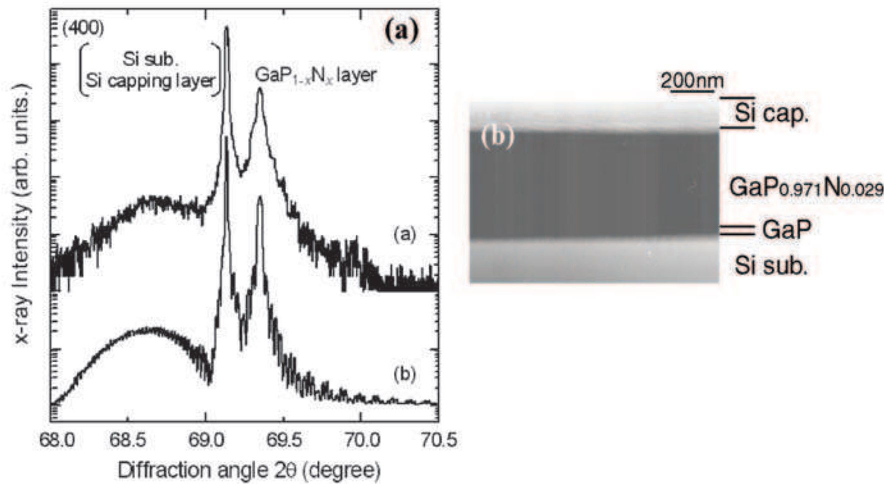

Fig. 16.2. Structural defect-free Si/GaPN layers grown on a Si substrate [7, 10]. (**a**) XRD profile, and (**b**) X-TEM image of the structure

contents [30, 31]. Thus, GaPN layers were evaluated whose N contents ranged from about 1 to 2%. To investigate the effects of nitrogen ions during growth process on the crystalline quality, an ion collector, constructed of two parallel deflection plates at the head of the rf-plasma cell, was used. The ions, which were generated in the rf-plasma cell, could be deflected by applying a high voltage of 500 V between the deflection plates. 100-nm thick GaPN layers were grown with and without an ion collector on a 200-nm thick GaP buffer layer grown on a GaP (100) substrate at 590°C. Then a 100-nm thick GaP capping layer was grown. Post-growth rapid thermal annealing (RTA) was carried out at 900°C for 60 s in order to improve quality of the sample. The PL-integrated intensity of the $GaP_{0.986}N_{0.014}$ layer grown with the ion collector was two times higher than that without the ion collector at 18 K, as shown in Fig. 16.3 [32]. No difference between the PL line shapes was observed.

The thermal quenching of the PL intensity of the GaPN layer grown with the ion collector was less than that of the GaPN layer grown without the ion collector. The PL-integrated intensity was increased by RTA for both GaPN layers grown with and without the ion collector. PL peak wavelengths showed blueshift after RTA [33]. These results indicated that as-grown GaPN layers contained point defects with high concentration caused by ion damage and N atoms. The point defects were reduced by applying the ion collector and RTA although the defects were not completely eliminated.

To investigate electrical properties of n- and p-type GaPN layers, in which the N content was smaller than 2%, 100–500-nm thick GaPN layers were grown at 590°C by MBE with the ion collector. The thickness is less than the critical thickness of the GaPN layer grown on a GaP (100) substrate. Sulphur and magnesium were used as n-type and p-type dopants, respectively, evaporating

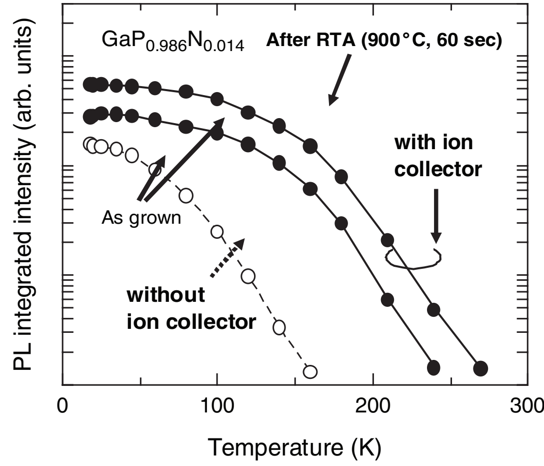

Fig. 16.3. Temperature dependence of photoluminescence intensity of $GaP_{0.986}$-$N_{0.014}$ layers [32]. PL intensity was increased by reducing ion damage and applying RTA. Samples were pumped with a YAG laser with a wavelength of 532 nm and an optical power density of 16 W cm^{-2}

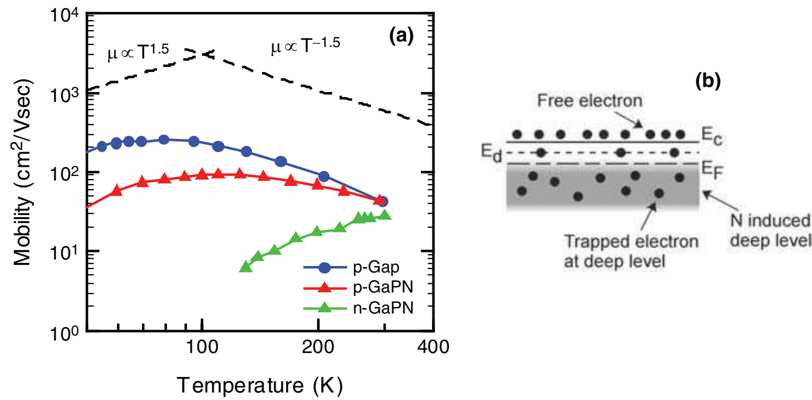

Fig. 16.4. (**a**) Carrier mobility vs. temperature, and (**b**) electron scattering mechanism of n-$GaP_{0.994}N_{0.006}$ layers [34]. The electron concentration of the n-GaPN layer is 4.3×10^{17} cm^{-3} and the hole concentration of the p-GaPN layer is 1.1×10^{18} cm^{-3}

from a GaS compound and elemental Mg by conventional Knudsen cells. n- and p-GaP layers were grown as well for reference.

The electron concentration in the n-GaPN layer was ten times lower than that in a S-doped GaP layer. The temperature dependence of mobility (μ) in the n-and p-GaPN layers are shown in Fig. 16.4a [34]. In general, mobility is restricted by phonon scattering ($\propto T^{-1.5}$) at around room temperature and by ionized impurity scattering ($\propto T^{1.5}$) at low temperature, as indicated in Fig. 16.4a. The n-$GaP_{0.994}N_{0.006}$ layer with electron concentration

of $4.3 \times 10^{17}\,\mathrm{cm}^{-3}$ showed extraordinary temperature dependence of electron mobility although the n-GaP layer showed normal temperature dependence similar to that of the p-GaP layer, as shown in Fig. 16.4a. The electron mobility was decreased as the temperature was decreased even at around room temperature. On the other hand, the n-$GaP_{0.994}N_{0.006}$ layer with hole co ncentration of $1.1 \times 10^{18}\,\mathrm{cm}^{-3}$ showed normal temperature dependence of hole mobility.

We proposed a scattering model as shown in Fig. 16.4b [34]. A low-energy tail in photoluminescence caused by deep levels was supposed to be related to the N–N pairs and the N clusters [35]. In addition, S and N atoms might form complex point defects. In the n-GaPN layer, the N atoms at the low-energy tail could trap electrons and be negatively charged since the Fermi level E_F is close to the conduction bandedge E_c and donor level E_d is shallow. As a result, negatively charged N atoms could act as a Coulomb scattering centre. Thus, the electron mobility of the n-GaPN layer follows the ionized impurity scattering mechanism. On the other hand, such scattering does not occur in the p-GaPN layer since the Fermi level is far below the low-energy tail.

In general, the increase in N content causes severe deterioration of crystalline quality and PL efficiency. A promising range of the N content is smaller than about 4% at the present time. When the condition of lattice-match to Si is satisfied, the In content is limited below about 8%. Thus, such InGaPN could be an indirect-transition type since a host material of InGaP is indirect for the In content smaller than 27%. In order to realize a direct-transition type, large In contents are needed. A strained InGaPN/GaPN QW is promising, whose well width is smaller than a critical thickness. The dislocation-free growth condition and electronic properties were investigated for the InGaPN layers with small and large In contents. InGaPN is used to an active layer of the InGaPN/GaPN DH or QW LEDs. A 500-nm thick $In_{0.041}Ga_{0.959}P_{0.982}N_{0.018}$ layer was grown at 460°C following the growth of a 200 nm thick GaP buffer layer at 590°C on a GaP (100) substrate by MBE. A $GaP_{0.982}N_{0.018}$ was grown at 460°C for comparison. No threading dislocations were observed in the InGaPN layer and no misfit dislocations at the heterointerface between the InGaPN and GaP buffer layers. The temperature dependence of PL peak energy showed a dip below 50 K for the InGaPN layer although no dip was observed for the GaPN layer [36]. This effect indicates the spatial variation of band gap energy related to the spatial variation of In and N contents in the InGaPN layer. The PL-integrated intensity of the InGaPN layer increased after RTA at 700°C for 30 s in a N_2 ambient as for the GaPN layer.

$In_{0.33}Ga_{0.67}P_{0.984}N_{0.016}/GaP_{0.982}N_{0.012}$ QWs were grown at 500°C following the growth of a 200-nm thick GaP buffer layer at 590°C on a GaP (100) substrate by MBE. Five-period QWs contained 3-nm thick InGaPN wells and 25-nm thick GaPN barriers. Their thicknesses were smaller than their critical thicknesses. The XRD curve is shown in Fig. 16.5a [37]. The zeroth-order satellite peak of the InGaPN/GaPN QWs was shifted to the right-hand side of a substrate peak. It means that the lattice parameter of the InGaPN/GaPN

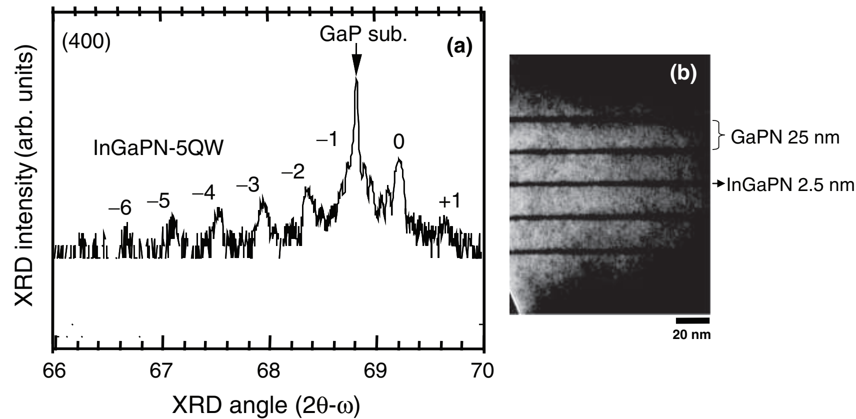

Fig. 16.5. $In_{0.33}Ga_{0.67}P_{0.984}N_{0.016}/GaP_{0.988}N_{0.012}$ 5QWs grown on a GaP substrate [37]. (**a**) XRD profile, and (**b**) X-TEM image of the structure

QWs is smaller than that of the GaP substrate. No structural defects such as threading and misfit dislocations were observed by X-TEM, as shown in Fig. 16.5b [37].

The InGaPN wells and the GaPN barriers were grown coherently. Thus, the InGaPN wells were strained compressively and the GaPN barriers contained tensile strain. The integrated PL intensity of the InGaPN layer increased after RTA up to 800°C for 30 s in a N_2 ambient.

16.4 Monolithic Implementation of Elemental Devices for Optoelectronic-Integrated Circuits

Structural defect-free Si/GaPN layers are realized on a Si substrate, as mentioned in Sect. 16.2. The GaPN layer can be replaced with GaPN-based layers for light-emitting devices with a DH and a QW structure lattice-matched to Si. Thus, a structural defect-free Si/GaPN-based layers could provide monolithic OEICs in which an LSI is formed in the Si layer and light-emitting devices are in the GaPN-based layer [10, 11].

Elemental devices for the monolithic OEIC are typically a Si MOSFET and an LED [11]. In principle, the LSI is composed of the Si MOSFETs and the LED is driven by the MOSFET, as shown in Fig. 16.6a [12]. Operated results in MOSFET circuits are obtained as the light output of the LEDs. We have tried to fabricate the elemental devices of the Si MOSFETs in the topmost Si layer and the LEDs in the InGaPN/GaPN DH layer.

The Si/InGaPN/GaPN DH layers in Fig. 16.6b were grown by MBE following the structural defect-free growth processes mentioned in Sect. 16.2. The 20-nm thick GaP initial layer was grown on a p-Si (100) substrate misoriented by 4° towards a [011] direction at 450°C by MEE. Then the DH

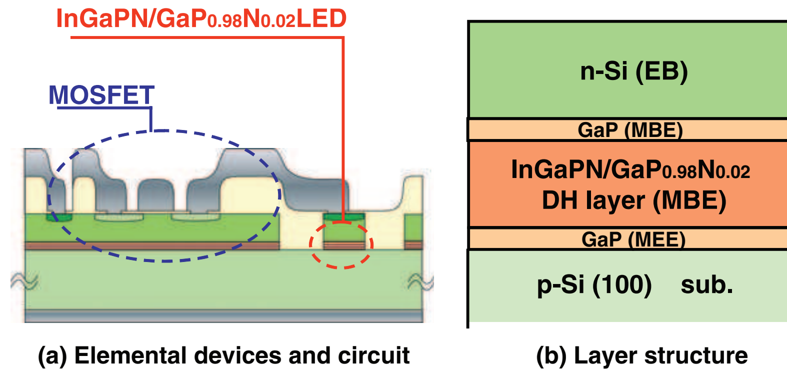

Fig. 16.6. Elemental devices and circuit for monolithic OEICs [12]

layer was grown at 500°C which was constructed with a 600-nm thick p-$GaP_{0.98}N_{0.02}$ cladding layer, a 100-nm thick p-$In_{0.03}Ga_{0.97}P_{0.96}N_{0.04}$ active layer and a 600-nm thick n-$GaP_{0.98}N_{0.02}$ cladding layer. Sulphur and magnesium were doped in the n- and p-$GaP_{0.98}N_{0.02}$ cladding layers, respectively. An InGaPN/GaPN DH LED with a similar layer structure was fabricated on a Si (100) substrate before this trial [9]. The layers were structural defect-free and a peak wavelength was around 650 nm at room temperature. Then a 10-nm thick GaP layer was grown at 500°C for preventing a subsequent Si layer from reacting with nitrogen in the n-GaPN cladding layer. The substrate was transferred to another chamber through a high-vacuum tunnel. A 1-µm thick Si layer was grown at 590°C with an electron beam evaporator. The electron concentration of the Si layer was measured to be $4 \times 10^{17}\,\text{cm}^{-3}$.

The LEDs and the MOSFETs should be fabricated in a conventional processing flow for MOSFETs. The fabrication processes are shown in Fig. 16.7, by which p-MOSFETs and InGaPN/GaPN DH LEDs were formed [11]. Firstly, a p–n junction around the LED was etched off by reactive ion etching. A 1-µm thick SiO_2 film, which was utilized as a field oxide for the p-MOSFET and passivation for the LED, was deposited by chemical vapour deposition at 550°C. After forming the active region of the p-MOSFETs, boron ions were implanted at 30 kV for forming a source and a drain. Phosphorous ions were implanted at 30 kV for forming a contact to the Si layer. A 16-nm thick SiO_2 film for forming a gate oxide was grown in a wet O_2 ambient at 900°C for 10 min. This thermal process provided thermal annealing after ion implantation as well as the increase in the light emission efficiency of the InGaPN active layer. An aluminium metal gate was formed instead of a conventional polycrystalline Si gate in order to simplify the processing flow. As a result, the number of process steps was smaller than that for a conventional MOSFET. The LEDs were simultaneously fabricated through the MOSFET fabrication process.

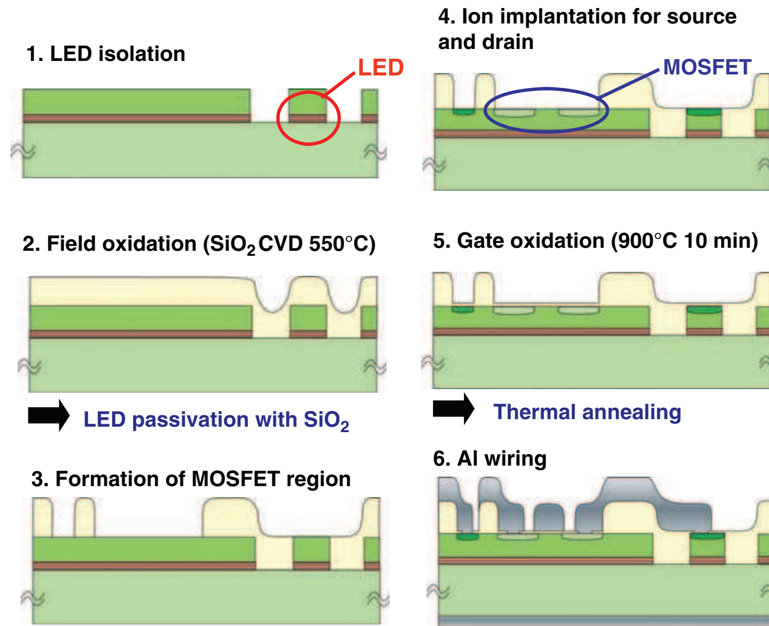

Fig. 16.7. Processing flow for elemental devices and circuit for OEIC [11]

The gate length L_g of the p-MOSFET was fixed to 10 μm. The gate widths W_g of the p-MOSFETs were varied from 30 to 400 μm. The active regions of the LEDs were varied from 20 × 45 μm to 300 × 300 μm.

The photograph of the fabricated test chip is shown in Fig. 16.8, in which four LEDs with an active area of 100 × 100 μm emitted red light at 10 mA applied through a metal probe [12]. All p-MOSFETs and LEDs in the chip operated. Drain current I_{ds} vs. drain voltage V_{ds} curves of the p-MOSFET with W_g of 30 μm were inserted with a parameter of gate-source voltage V_{gs} in Fig. 16.8 [12]. All LEDs with different active areas showed mostly linear current *vs.* optical output curves. The spectra were obtained through the Si layer at 2–10 mA at room temperature for the LED with an active area of 20 × 45 μm, as inserted in Fig. 16.8 [12]. The peak wavelength was about 640 nm. The cathode of the LED with an active area of 300 × 300 μm was connected to the source of the p-MOSFET with $\mathrm{W_g}$ of 400 μm by the metal probes. The optical output of the LED was switched by applying a pulsed voltage to the gate of the p-MOSFET.

A high threshold voltage V_T of −3.1 V could be attributed to a rough surface and a high electron concentration of $4 \times 10^{17}\,\mathrm{cm^{-3}}$ in the Si layer. A leak current through the thin gate oxide was in the order of 10^{-14} A. This small leak current means the high quality of the gate oxide and of the interface between the oxide and the Si layer.

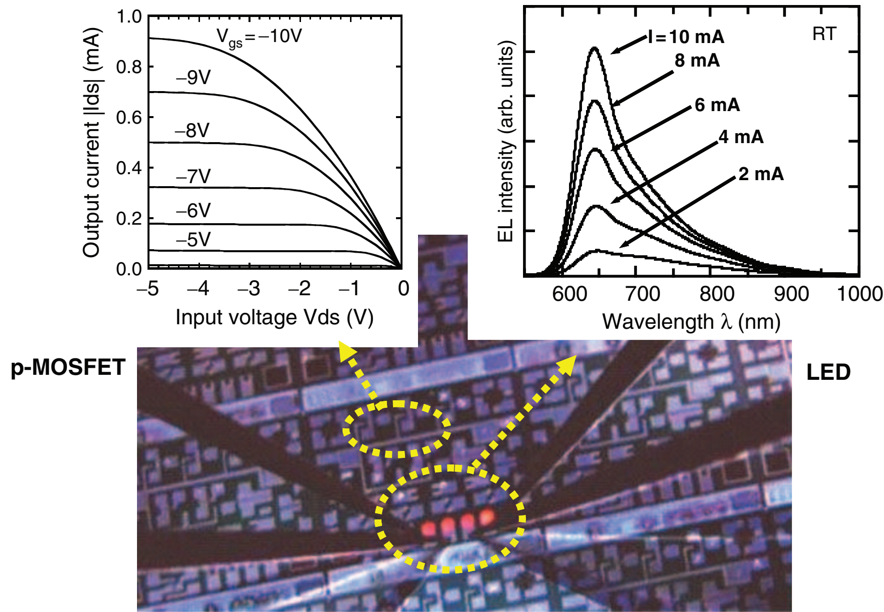

Fig. 16.8. Photograph of a wafer containing several chips [12]. Four LEDs with an active area of $100 \times 100\,\mu\text{m}$ emitted red light in the centre chip. LEDs and p-MOSFETs with various sizes were contained in a single chip. The *upper left inset* is drain current (output current) I_{ds} vs. drain voltage V_{ds} curves of p-MOSFET with W_{g} of $30\,\mu\text{m}$. The *upper right inset* is the spectra of the LED with an active area of $20 \times 45\,\mu\text{m}$

The current *vs.* optical output curves of the LEDs were super-linear at a small current region [9]. These performances mean that saturable nonradiative recombination centres related to point defects were contained in the active layer [38, 39]. It was confirmed by XRD profiles that no apparent structural deterioration occurred in the LED layer at the thermal process for the growth of the gate oxide at 900°C for 10 min. From these results, this thermal process condition at the gate oxide growth can be matched with an optimum condition for increasing the light emission efficiency of the LED [33].

OEICs in which LSIs containing LEDs could be realized when the threshold voltage of MOSFETs is controlled and the small-size LEDs are fabricated. For high performance, point defects should be reduced and InGaP or GaAsP, in which N is incorporated, should be of a direct transition for an active layer.

A specific application of novel OEICs is massively parallel information processing which is performed in biological sensors and brains. We have designed and fabricated a bioinspired vision chip, in which the edge pattern of an input pattern ("A") was obtained, as shown in Fig. 16.9a [11].

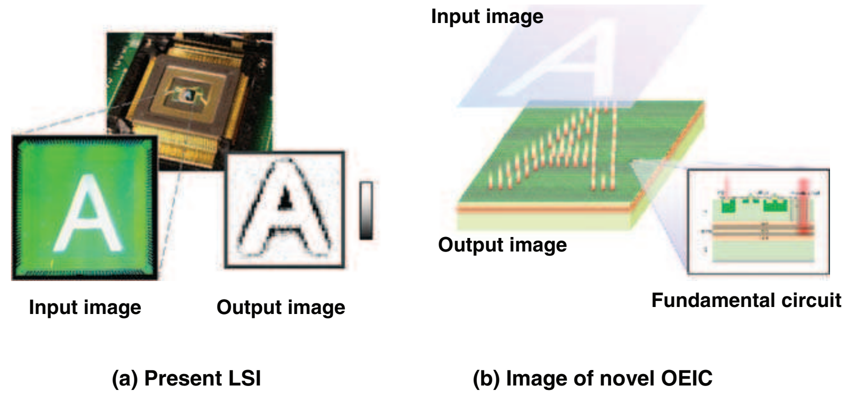

Fig. 16.9. Application of the novel OEIC to massively parallel information processing [11]

42 × 42 pixels in the chip operated in parallel. However, the edge pattern must be displayed sequentially by using a shift resistor. When a light-emitting device is contained in each pixel, the edge pattern could be obtained instantaneously as an optical output pattern in the chip (Fig. 16.9b). Such massively parallel information processing can be realized by implementing light-emitting devices into each fundamental circuit although it is impossible in present time-sequential processing. Moreover, the light emission would be useful to transfer signals in a single chip and between chips instead of electrons. Thus, optical interconnections would be also realized in the OEIC.

16.5 Summary

Structural defect-free GaPN and InGaPN layers were grown on a Si substrate. Point defects in these layers were reduced by reducing N ions and by applying RTA. The carrier concentrations of the GaPN layer were controlled by doping S and Mg, and an electron scattering mechanism was clarified. InGaPN/GaPN DH LEDs were fabricated by integrating these technologies.

LEDs and Si MOSFETs, which are elemental devices for OEICs, were monolithically merged in a single chip with a Si layer and an InGaPN/GaPN DH layer lattice-matched to Si grown on a Si substrate. The developed processing flow was based on a conventional MOSFET processing flow. All LEDs and MOSFETs operated normally. Light emission from the LED was modulated by switching the MOSFET. The growth and fabrication process technologies could be effective for the realization of monolithic OEICs for massively parallel processing systems and optical interconnections.

Acknowledgements. This work was supported by the Ministry of Education, Science, Sports and Culture Scientific Research in Priority Areas, Specially Promoted

Research, the 21st Century COE Program "Intelligent Human Sensing", the Venture Business Laboratory and the Research Center for Future Technology of Toyohashi University of Technology.

References

1. I. Hayashi, Jpn. J. Appl. Phys. **32**, 266 (1993)
2. H.K. Choi, H.K. Mattia, G.W. Turner, B.Y. Tsaur, IEEE Electron Device Lett. **9**, 512 (1998)
3. R.N. Ghosh, B. Griffing, J.M. Ballantyne, Appl. Phys. Lett. **48**, 370 (1986)
4. Y. Inoue, K. Sugahara, S. Kusunoki, M. Nakaya, T. Nishimura, Y. Horiba, Y. Akasaka, H. Nakata, IEEE Electron Device Lett. **7**, 327 (1986)
5. Y. Furukawa, H. Yonezu, K. Ojima, K. Samonji, Y. Fujimoto, K. Momose, Y. Aiki, Jpn. J. Appl. Phys. **41**, (2002)
6. Y. Fujimoto, H. Yonezu, A. Utsumi, K. Momose, Y. Furukawa, Appl. Phys. Lett. **79**, 1306 (2001)
7. K. Momose, H. Yonezu, Y. Fujimoto, Y. Furukawa, Y. Motomura, K. Aiki, Appl. Phys. Lett. **79**, 4151 (2001)
8. H.P. Xin, R.J. Welty, C.W. Tu, IEEE Photonics Technol. Lett. **12**, 960 (2000)
9. S.Y. Moon, H. Yonezu, Y. Furukawa, S.M. Kim, Y. Morita, A. Wakahara, Jpn. J. Appl. Phys. **44**, 1752 (2005)
10. H. Yonezu, Semicond. Sci. Technol. **17**, 762 (2002)
11. H. Yonezu, Y. Furukawa, H. Abe, Y. Yoshikawa, S.Y. Moon, A. Utsumi, Y. Yoshizumi, A. Wakahara, M. Ohtani, Opt. Mater. **27**, 799 (2005)
12. Y. Furukawa, H. Yonezu, Y. Morisaki, S.Y. Moon, S. Ishiji, A. Wakahara, Jpn. J. Appl. Phys. **45**, L290 (2006)
13. H. Yonezu, in *Dilute Nitride Semiconductors*, ed. by M. Henini. (Elsevier, Oxford, 2005) p. 451
14. M. Kawabe, T. Ueda, Jpn. J. Appl. Phys. **26**, L944 (1987)
15. W.A. Harrison, E.A. Kraut, J.R. Waldrop, R.W. Grant, Phys. Rev. **B18** 4402 (1978)
16. H. Kroemer, J. Cryst. Growth **81**, 193 (1987)
17. Y. Takagi, H. Yonezu, K. Samonji, T. Tuji, N. Ohshima, J. Cryst. Growth **187**, 42 (1998)
18. N. Momose, H. Yonezu, Y. Fujimoto, K. Ojima, Y. Furukawa, A. Utsumi, K. Aiki, Jpn. J. Appl. Phys. **41**, 7301 (2002)
19. M. Tamura, A. Hashimoto, N. Sugiyama, J. Appl. Phys. **70**, 4770 (1991)
20. N. Hayafuji, N. Miyashita, T. Nishimura, K. Kadoiwa, H. Kumabe, T. Murotani, Jpn. J. Appl. Phys. **29**, 2371 (1990)
21. M. Kondow, K. Uomi, K. Hosomi, T. Mozume, Jpn. J. Appl. Phys. **33**, L1056 (1994)
22. M. Kondow, K. Uomi, T. Kitatani, S. Watahiki , Y. Yazawa, J. Cryst. Growth **164**, 175 (1996)
23. W.G. Bi, C.W. Tu, Appl. Phys. Lett. **69**, 3710 (1996)
24. J.F. Geisz, D.J. Freidman, Semicond. Sci. Technol. **17**, 769 (2002)
25. T. Nishioka, Y. Itoh, A. Yamamoto, M. Yamaguchi, Appl. Phys. Lett. **51**, 1928 (1987)
26. K. Nozawa, Y. Horikoshi, Jpn. J. Appl. Phys. **29**, L540 (1990)

27. H.P. Xin, C.W. Tu, Y. Zhang, A. Mascarenhas, Appl. Phys. Lett. **76**, 1267 (2000)
28. L. Bellaiche, S.H. Wei, A. Zunger, Appl. Phys. Lett. **70**, 3558 (1977)
29. I. Vurgaftman, J.R. Meyer, L.R. Ram-Mohan, J. Appl. Phys. **89**, 5815 (2001)
30. H.P. Xin, C.W. Tu, Appl. Phys. Lett. **77**, 2180 (2000)
31. K. Momose, H. Yonezu, Y. Furukawa, A. Utsumi, Y. Yoshizumi, S. Shinohara, J. Cryst. Growth **251**, 443 (2003)
32. A. Utsumi, Y. Furukawa, H. Yonezu, Y. Yoshizumi, Y. Morita, A. Wakahara, Phys. Stat. Sol. A **202**, 758 (2005)
33. A. Utsumi, H. Yonezu, Y. Furukawa, K. Momose, K. Kuroki, Phys. Stat. Sol. C 2741 (2003)
34. Y. Furukawa, H. Yonezu, A. Wakahara, Y. Yoshizumi, Y. Morita, A. Sato Appl. Phys. Lett. **88**, 142109 (2006)
35. I.A. Buyanova, G.Y. Rudko, W.M. Chen, H.P. Xin, C.W. Tu, Appl. Phys. Lett. **80**, 1740 (2002)
36. S.M. Kim, Y. Furukawa, H. Yonezu, K. Umeno, A. Wakahara, Jpn. J. Appl. Phys. **44**, 8309 (2005)
37. S.M. Kim, Y. Furukawa, H. Yonezu, K. Umeno, A. Wakahara, J. Cryst. Growth **293**, 359 (2006)
38. W. Li, M. Pessa, J. Likonen, Appl. Phys. Lett. **78**, 2864 (2001)
39. N.Q. Thinh, I.P. Vorona, I.A. Buyanova, W.M. Chen, S. Limpijumnong, S.B. Zhang, Y.G. Hong, H.P. Xin, C.W. Tu, A. Utsumi, Y. Furukawa, S. Moon, A. Wakahara, H. Yonezu, Phys. Rev. B, **71**, 125209 (2005)

17

Analysis of GaInNAs-Based Devices: Lasers and Semiconductor Optical Amplifiers

D. Alexandropoulos, M.J. Adams, and J. Rorison

An analysis of GaInNAs for optoelectronic device applications is performed. Design rules are provided for GaInNAs lasers in terms of laser parameters such as material gain, differential gain, differential refractive index, and linewidth enhancement factor. The study is extended to semiconductor optical amplifiers whose basic properties are investigated and issues related to polarization insensitivity are addressed.

17.1 Introduction

Since the original suggestion of GaInNAs as an alternative to InP-based optoelectronics by Kondow and coworkers [1], dilute nitride research has exhibited considerable progress that extends from material physics to device applications and this is reflected by the range of topics in the chapters of the book in hand. Indicative of the fast development in the research is the fact that although GaInNAs optoelectronic applications were limited by material crystalline quality to 1.3 μm emission wavelength [2], now this has been extended to the 1.55 μm telecommunications wavelength [3, 4].

The reader so far has been introduced to the physical properties of dilute nitrides; working from these we deal here with GaInNAs from the application viewpoint. This formulates the scope of the present chapter, i.e., the manipulation of the unusual physics of GaInNAs alloys for practical optoelectronic devices.

Until recently laser applications in the published work on GaInNAs [5–7] focused on the superior temperature characteristics. However, GaInNAs possesses features that can prove beneficial for other optoelectronic device applications, thus making the use of the material more versatile. For example, the high electron mass and the reduced transition matrix element can be used to tune the properties of the structure, depending on the application of interest. In addition, it is desirable from the fabrication point of view

that optoelectronic devices of different functionality are based on the same material substrate, in this case GaAs.

Few researchers initially acknowledged the potential of GaInNAs for nonlaser applications [8–12] but gradually the list of nonlaser GaInNAs applications is expanding [13].

Here we highlight the potential for GaInNAs-based semiconductor optical amplifiers (SOAs) and also address design issues related to GaInNAs lasers. The rest of the chapter is organized as follows. In Sect. 17.2 we establish the band structure model, which is implemented in Sect. 17.3 to study N- effects on the optical properties of GaInNAs alloys. In Sect. 17.4 we provide design maps for optimal laser performance. Finally in Sect. 17.5 we deal with GaInNAs for optical amplification under both polarization sensitive and insensitive conditions.

17.2 Band Structure

17.2.1 General Considerations

The requirements from the band structure model for the modeling of GaInNAs-based optoelectronic devices are (1) to describe accurately the physics and (2) be computationally accessible. This implies the use of phenomenological parameters that are calibrated against complicated approaches. These include full pseudopotential calculations [14] and super-shell tight-binding calculations [15]. Both build the physics of the crystal on an atom-by-atom basis and therefore the requirement of phenomenological parameters is minimal if nonexistent. Hence they can be of predictive value and at the same time provide estimations of parameters that are otherwise calculated implicitly from experiment. However, their complexity and the demanding computational requirements make them unsuitable for laser modeling.

An alternative approach to account for the nitrogen-induced modification of the band structure is the band anticrossing model (BAC) [16] already presented in Chap. 3. For the sake of completeness, here we only present a brief account of the mathematical formalism of the BAC model that serves the scope of the present analysis, highlighting the aspects of the model that are important for the modeling of practical devices. For a more informative analysis along with an experimental verification of the model, the reader is referred to Chap. 3.

The BAC model explains the anticrossing behavior of GaInNAs conduction band energy levels with pressure. In the context of BAC the incorporation of N into GaInAs (or GaAs) alloys leads to a strong interaction between the conduction band and a narrow resonant band formed by the N states, because of the highly localized nature of the perturbation induced by the N atoms. The overall effect is the splitting of the conduction band, with a consequent reduction of the fundamental band gap due to the lowering of the conduction

band edge. The states of the subbands are represented by functions that are a mixture of extended GaInNAs (or GaAs) conduction band and localized nitrogen states.

The mathematical formalism of the model is derived as follows: the interaction between the extended conduction states of the matrix semiconductor (GaInAs) and the localized N states is treated as a perturbation that leads to the following eigenvalue problem [16]:

$$\begin{vmatrix} E - E_{\mathrm{M}} & -V_{\mathrm{MN}} \\ -V_{\mathrm{MN}} & E - E_{\mathrm{N}} \end{vmatrix} = 0 \tag{17.1}$$

where E_{M} is the conduction states of the matrix semiconductor, E_{N} is the localized states of the nitrogen, and V_{MN} is the matrix element describing the interaction between the E_{M} and E_{N}. It is the V_{MN} that leads to the mixing and anticrossing of these two states. The functional form for V_{MN} and the E_{N} parameters reads [15]

$$\begin{aligned} V_{\mathrm{MN}} &= C_{\mathrm{MN}}\sqrt{x} \\ E_{\mathrm{N}} &= 1.675 - \gamma x \end{aligned} \tag{17.2}$$

In the above x is the nitrogen concentration and C_{MN} is a parameter that depends on the matrix semiconductor and hence the In composition, and a typical value for γ is 2.52. It is obvious that the calculation is very sensitive to the values of E_{N} and C_{MN}; we deal with this in more detail in Sect. 17.2.2.

The BAC model, despite its simplicity, manages to explain and provide useful insight into the physics of the material. An obvious drawback of its simplicity is that it is heavily dependent upon experimentally determined parameters, thus limiting the ability of the model to provide quantitative results except for specific samples. This approach, however, can benefit from the more detailed band structure models in terms of analytical expressions for the parameters otherwise provided by experiment. Thus it can be extended to give relatively reliable estimates for any sample, irrespective of experiment. The valence band structure is primarily determined by the matrix semiconductor (in the case of GaInNAs, this being GaInAs) [16,17]. It is assumed that the valence bands and the conduction bands are decoupled. We only consider the coupling between all valence bands, namely heavy hole (HH), light hole (LH), and Spin–Orbit (SO) [18]. This is essential since the spin–orbit coupling has significant effects on the band structure especially for highly strained quantum wells [19], as is indeed the case for GaInNAs/GaAs quantum wells when aiming for the emission wavelength of 1.3 μm.

The dispersion relations of the energy levels are delivered by diagonalizing the Luttinger–Kohn (LK) Hamiltonian [20]. For the LK Hamiltonian we have followed standard procedures for ensuring the Hermitian properties of the operators and for accommodating the quantum size effect. The additional mixing due to strain is also accounted for through the Pikus–Bir Hamiltonian, while the conduction band states of the strained structure are shifted by the hydrostatic deformation energy [21].

The Hamiltonian matrix gives rise to six coupled differential equations. This can be further simplified if the axial approximation is applied, which transforms the six rate equations to a system of three. The resulting system of three coupled differential equations is solved using the finite difference method [22].

17.2.2 Parameterization of the Band Anticrossing Model

The correct parameterization in terms of E_{N} and C_{MN} is imperative for the predictability of the model [23]. The work of Klar and coworkers [24] is a significant contribution towards this end. Their experimental and theoretical work proved that a set of discrete band gaps exist in GaInNAs depending on the nearest-neighbor (NN) configuration around the N site. This can be 4Ga, 3Ga, 2Ga, or 4In. An oscillator strength is associated with the transition corresponding to each NN and the experimentally observable band gap is the outcome of the overlapping contributions of each NN environment. The existence of NN distributions in GaInNAs and GaInNAsSb has also been observed experimentally by Lordi and coworkers [25].

Depending on the growth technique and the post-growth treatment, different environments are favored. In this way, the blueshift observed during annealing is attributed to the enhancement of the oscillator strength for the NN configuration with the biggest band gap [24]. For each environment the parameterization of the band structure is different. In particular the E_{N} is calculated to vary depending on In composition and the possible NN configuration. Using supercell calculations of the conduction band structure of $\mathrm{Ga}_x\mathrm{In}_{1-x}\mathrm{N}_y\mathrm{As}_{1-y}$ the In-concentration dependence of the E_- state and the localized N-level for different (Ga,In)-nearest neighbor environments of the N-center can be determined. The functional form of these can be expressed as

$$\begin{aligned} E_{\mathrm{N(4In)}} &= 2.31x10^{-5}y^2 - 0.0062y + 1.8918 \\ E_{\mathrm{N(1Ga)}} &= 2.39x10^{-5}y^2 - 0.0064y + 1.8384 \\ E_{\mathrm{N(2Ga)}} &= 2.82x10^{-5}y^2 - 0.0067y + 1.7808 \\ E_{\mathrm{N(3Ga)}} &= 3.66x10^{-5}y^2 - 0.0071y + 1.7258 \\ E_{\mathrm{N(4Ga)}} &= 3.96x10^{-5}y^2 - 0.0074y + 1.6700 \end{aligned} \tag{17.3}$$

In the above y is the In composition. In obtaining the set of equations (17.3) we have an interpolation scheme of second order polynomial to the results presented in [24]. The C_{MN} parameter according to [24] is approximately 2 for the 4Ga NN configuration and about 1.35 for the 4In NN configuration. The set of equations (17.3) and the corresponding C_{MN} values provide the framework for the pair of E_{N}-C_{MN} values to be used in our calculations.

In the above y is the In composition. In obtaining the set of equations (2.3) we applied an interpolation scheme of second order polynomial to the results presented in [24]. The C_{MN} parameter according to [24] is approximately 2

for the 4Ga NN configuration and about 1.35 for the 4In NN configuration. The set of equations (17.3) and the corresponding C_{MN} values provide the framework for the pair of E_{N}-C_{MN} values to be used in our calculations.

17.2.3 Band Lineup

It is well established that the reduction of band gap when N is introduced in the GaInAs matrix is mainly accommodated in the conduction band, the exact percentage of which is usually introduced phenomenologically. This, however, raises the issue of hole confinement. Indeed early work suggested that the incorporation of N not only causes the lowering of the conduction band edge, but the valence band edge as well [26], which will effectively lead to *Type II* alignment. Further experimental [27] and theoretical studies [28] contradict these results and instead have shown that the valence band has the same type of alignment as the conduction band, namely *Type I*.

Typical values regarding the band offsets are 95% for the conduction band [17] and 5% for the valence band whereas other authors [29] have proposed 80% and 20%. Bearing in mind that material gain and related parameters are sensitive to the band offsets considered [30], the different band offset values reported in literature are confusing.

Klar and coworkers [31] have related the band offsets with band parameters derived from tight-binding calculations. Their approach consists of accounting for the band offsets of the matrix semiconductor in the context of model solid theory [32] and introducing a further shift to these depending on the nitrogen concentration. The modified matrix semiconductor energy levels are inserted in the band structure model, which will give the additional shifts. In particular, denoting the modified valence band edge energy of the matrix semiconductor by E_{Mv} and the modified conduction band edge energy by E_{Mc}, and assuming nitrogen content of x then, $E_{\mathrm{Mc}} = E_{\mathrm{co,GaInAs}} + \alpha x$ and $E_{\mathrm{Mv}} = E_{\mathrm{vo,GaInAs}} + \kappa x$ where, $\alpha \approx 1.55$ and $\kappa \approx 3.88$. $E_{\mathrm{co,GaInAs}}$ and $E_{\mathrm{vo,GaInAs}}$ are the unperturbed conduction and valence band edge energies of the matrix semiconductor. In the following we use the model of [31].

17.2.4 Implementation of the Band Structure Model

To develop a better understanding of the unusual electronic properties of GaInNAs, it is useful to decipher the effect of nitrogen on the band structure. For this reason we consider three different structures with In and N compositions tailored so that the emission wavelength is 1.3 μm. The band structure of these is shown in Fig. 17.1.

A straightforward observation is the nonparabolic nature of the GaInNAs conduction bands resulting from the admixture of the extended like states of the matrix semiconductor and the localized states of N. This remarkable feature is more obvious when compared to the parabolic conduction band of GaInAsP.

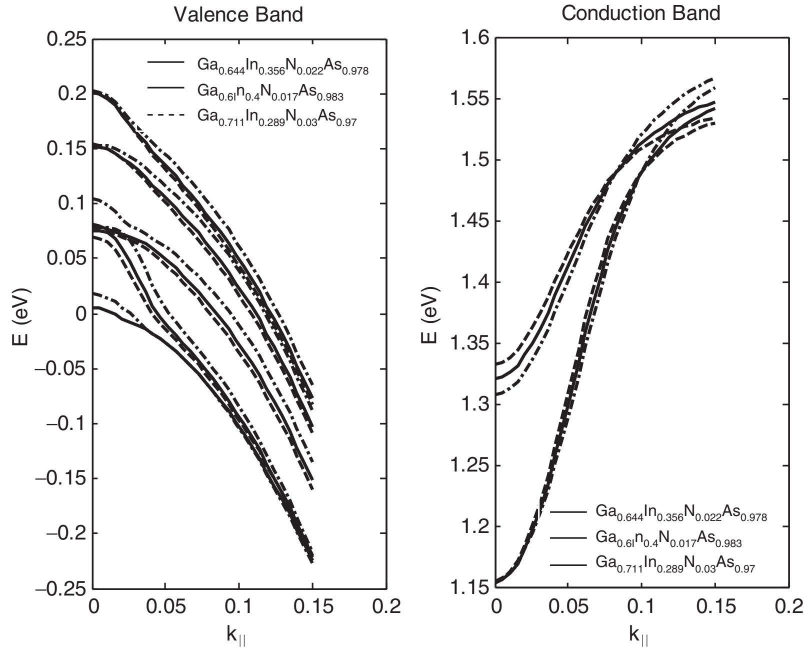

Fig. 17.1. Band structure of 7 nm GaInNAs/GaAs quantum well structures for three different N contents, as shown on the figure. $k_{||}$ is normalized with respect to the lattice constant of the well material

The valence bands, unlike the conduction band, do not exhibit any peculiar characteristics. This is expected since N primarily affects the conduction band [16]. Therefore, the valence bands are GaInAs-like (or matrix semiconductor-like). Another noticeable feature is that the parabolicity of the bands is restored with decreasing N content. It is reminded that the structures of interest emit at the same wavelength. The restoration of parabolicity with decreasing N content can be explained in terms of band repulsion, which is enhanced when the amount of compressive strain is increased, as is indeed the case for low N contents.

17.3 Optical Properties of GaInNAs Alloys

Having established the band structure in the previous section, here we proceed to calculate the material gain and related properties that characterize a GaInNAs-based laser, namely the differential gain, differential refractive index, and linewidth enhancement factor, emphasizing the effects of the band structure on these.

17.3.1 GaInNAs Material Gain

In Fig. 17.2 we plot the material gain for TE-polarization calculated for four different 7 nm GaInNAs/GaAs structures with compositions such that the emission wavelength is approximately 1.3 μm, for a carrier concentration of $2.5 \times 10^{18}\,\text{cm}^{-3}$.

The calculation is based on free carrier theory [33] while intraband relaxation effects are included via a lineshape broadening function [34].

The peak value and bandwidth of material gain are increasing with decreasing N content for a given carrier concentration, which is attributed to the N-induced modification of the conduction band density of states. The material gain for TM-polarization of the structures of Fig. 17.2 for the same carrier density is shown in Fig. 17.3. The TM gain attains considerably smaller values than TE gain, which is reasonable if we consider that TM-polarization couples to LH-states and these are repulsed from the top of the valence band because of compressive strain conditions, which results in low carrier population at the LH-states.

It is useful to remember that for the derivation of the band structure the assumption of 2Ga for the NN configurations is used. Adoption of a different NN configuration will alter the results presented above, since the band structure will be modified accordingly.

The bandwidth properties for TE and TM gain are the same. Gain bandwidth, i.e., the region defined by the range of energies over which the gain is positive, reflects the band structure properties and therefore for given carrier density it will be independent of the polarization. This does not hold for the

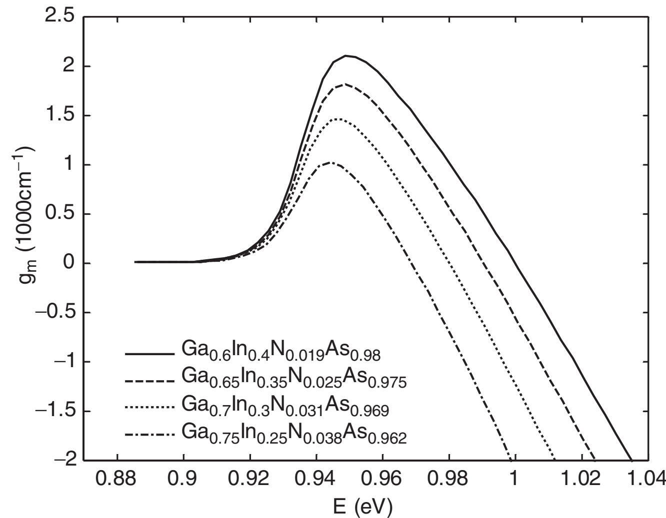

Fig. 17.2. TE material gain at carrier density of $2.5 \times 10^{18}\text{cm}^{-3}$ for various 7 nm GaInNAs/GaAs structures

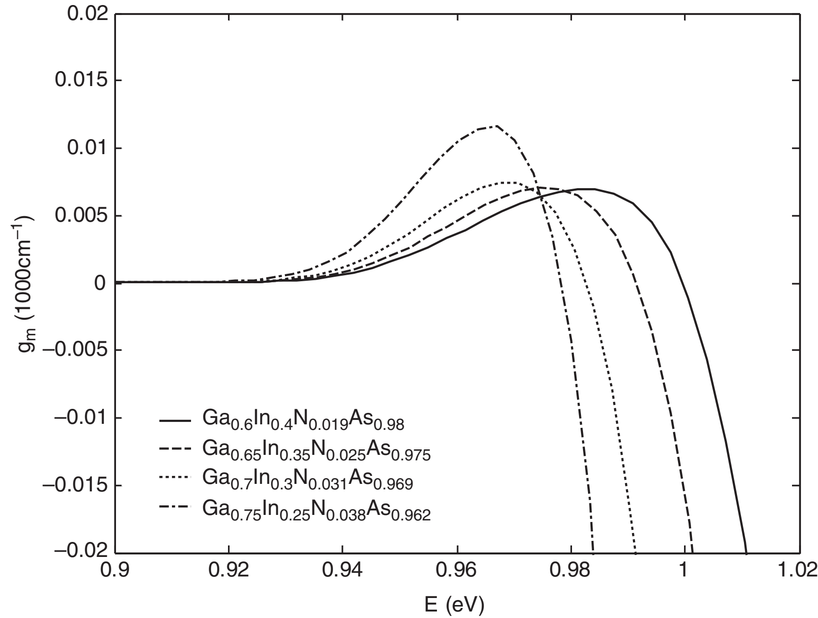

Fig. 17.3. TM material gain at carrier density of $2.5 \times 10^{18}\mathrm{cm}^{-3}$ for the structures of Fig. 17.2

peak gain wavelength and value for the two gain spectra. In particular, for TM gain the peak wavelength has the opposite trend than for TE gain. The red-shift of the peak gain wavelength of TM gain reflects in band structure terms an upward shift of the LH1 subband, which is indeed the case for increasing N content.

17.3.2 N-Positional Dependence of Material Gain

In the standard BAC model the electron associated with the N isoelectronic defect can be assumed to be strongly localized at the highly electronegative N defect site. In an effective mass type of picture this corresponds to a very large effective mass, $m_e{}^*$, and small orbit size, being associated with this electron. It follows naturally that the dispersion of this state can be taken as flat and that the N defect position within the quantum well is unimportant as the N electron wavefunction never feels the confining potential of the barrier. It also assumes that the N atoms are located randomly within the quantum well so that the concentration profile is uniform across the quantum well.

If the position of the N within the quantum well is not uniform this simple model breaks down. This may indeed be a more realistic situation as N may migrate to the edges of the quantum well to try to relieve strain effects. Qiu and Rorison [35] have investigated the role of the position of the N within the quantum well and have found that the strength of the conduction band

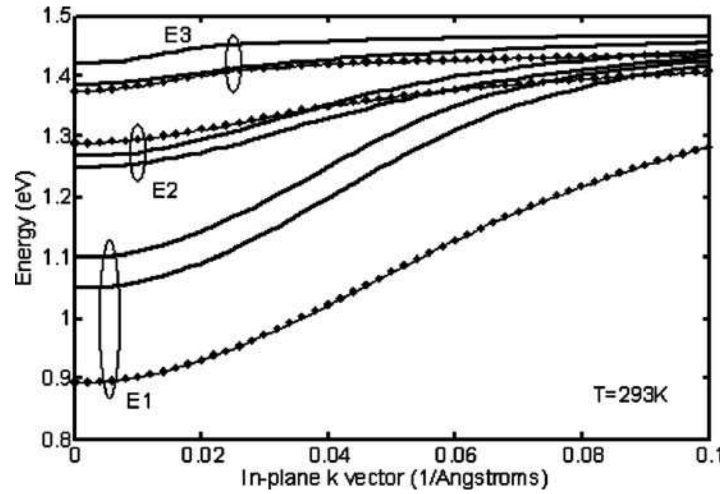

Fig. 17.4. The conduction band states for a $Ga_{0.35}In_{0.65}N_{0.01}As_{0.99}$/GaAs QW with three subbands (E1, E2, and E3). The solid lines show the N being distributed uniformly while the dotted lines show the N being distributed in a centralized peak and the dashed-lines correspond to the N being distributed at the two edges of the QW

probability with the localized N site determines the strength of interaction. Therefore, N atoms located at the center of the quantum well are more effective at pushing the conduction band down and decreasing the band gap than those N atoms located at the edge of the quantum well where the conduction band probability is low. Indeed this may also explain the blueshift if N atoms are migrating to the edges of the quantum well after annealing.

This model also predicts that the height of the quantum well barrier is important if N atoms are located at the edges with small barriers resulting in a larger conduction band probability at the edges and therefore a stronger interaction with the N atoms. Figure 17.4 shows the conduction band states in a GaInAs quantum well with three subbands when the added N is located at the center and the edges of the quantum well compared with the same concentration of N being uniformly distributed within the quantum well.

When the N is located at the center of the well it interacts spatially most strongly with the ground state and less with the first order state, whereas if N is located at the edges of the well it interacts spatially most strongly with the first excited state. This is reflected in the energy shifts seen in Fig. 17.4 where if N is in the center the splitting between the ground and first excited level is increased.

The gain is plotted in Fig. 17.5 where the increased strength of the interaction of the centrally positioned N with the lowest conduction band is observed as a red-shift in the wavelength of the *ee1-hh1* transition, which corresponds to the gain peak. In addition the magnitude of the gain is increased due to the increase in the splitting between the ground and first excited conduction states.

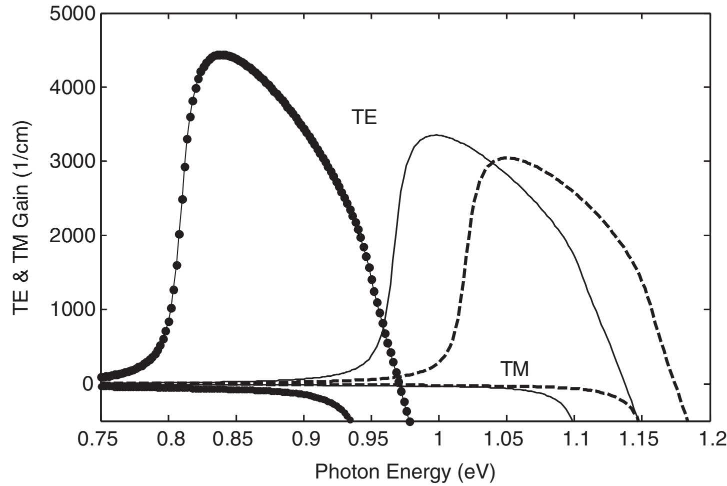

Fig. 17.5. The TE and TM gain for a $Ga_{0.35}In_{0.65}N_{0.01}As_{0.99}$/GaAs QW. The solid lines show gain for the N being distributed uniformly while the dotted lines show the N being distributed in a centralized peak and the dashed lines correspond to the N being distributed at the two edges of the QW

17.3.3 Comparison of GaInNAs and GaInAsP Material Gain

To establish the merits of this material system we compare the material gain with that of a GaInAsP/InP structure, a well-established solution for telecom optoelectronics. It must be emphasized though that the comparison can be misleading since one can vary strain parameters so as to alter particular attributes. Here, however, we feel that the comparison is valid since the structures chosen are such that the emission wavelength is approximately the same, as well as the peak gain value. The results for TE and TM polarization and details of the structures compared are shown in Fig. 17.6.

A general observation is that the material gain is comparable for the two material systems with the bandwidth being bigger for the GaInAsP material system. The bigger bandwidth of GaInAsP material gain is attributed to the smaller electron effective mass as compared to GaInNAs. This translates to smaller density of states and therefore the change of the Fermi levels with carrier injection is more efficient.

17.3.4 Differential Gain

Differential gain (DG), $\mathrm{d}g_{\mathrm{m}}/\mathrm{d}N$ enumerates the efficiency of the structure in using the pumped carriers for the amplification process of the EM wave. Mathematically, it describes the *rate* of change of the material gain under pumping conditions and can be calculated by differentiating the material gain with respect to carrier density [36].

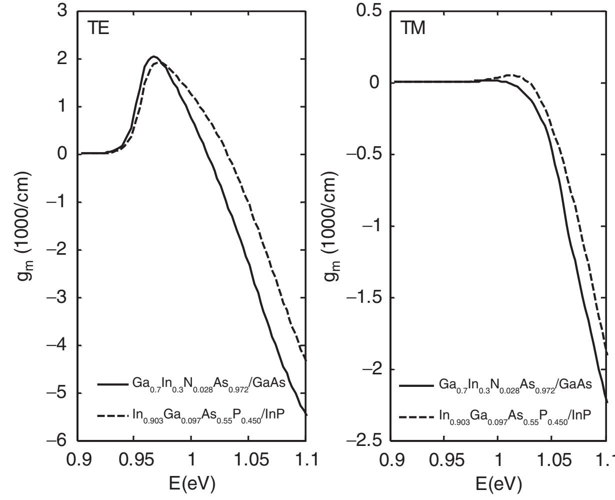

Fig. 17.6. Comparison of TE and TM material gain for 7 nm GaInNAs/GaAs and GaInAsP/InP structures as indicated in figure for carrier density of 3×10^{18} cm^{-3}

The importance of differential gain can be deduced from the very definition of it. The higher the value of the DG the bigger the change of the value of material gain with injected carriers and therefore positive gain is reached at lower carrier concentration. Hence, the threshold properties of a laser structure are governed by DG. In addition, DG determines the modulation properties of the laser [37], which is intuitively expected since DG quantifies the dynamics of the material. A key parameter that affects the modulation performance of a semiconductor laser is the *relaxation frequency* f_r, defined by [37];

$$f_{\mathrm{r}} = \frac{1}{2\pi}\sqrt{\frac{c}{n_{\mathrm{r}}}\frac{\mathrm{d}g_{\mathrm{m}}}{\mathrm{d}N}\frac{S_{\mathrm{o}}}{\tau_{\mathrm{p}}}} \tag{17.4}$$

where S_{o} is the photon density under steady state and τ_{p} is the photon lifetime in the cavity, and n_{r} is the refractive index. High values of f_{r} ensure improved modulation bandwidth and therefore high values of $\mathrm{d}g_{\mathrm{m}}/\mathrm{d}N$ are appealing for modulation applications.

Figure 17.7 shows the dispersion of the differential gain for the four GaInNAs/GaAs structures of Fig. 17.2. For each case the calculation is performed at transparency carrier concentration, i.e., at the lowest carrier density at which the material gain becomes positive. Structures with increased N content give smaller values of DG. This observation does not only apply for the peak value of DG, but extends over a considerable range of energies. At the low-energy side as well as in the high-energy side the DG curves converge. The reason for convergence near band gap energies is obvious, since at energies below band gap the material does not absorb radiation. For elevated energies, states with k-values away from the zone center participate in the transition.

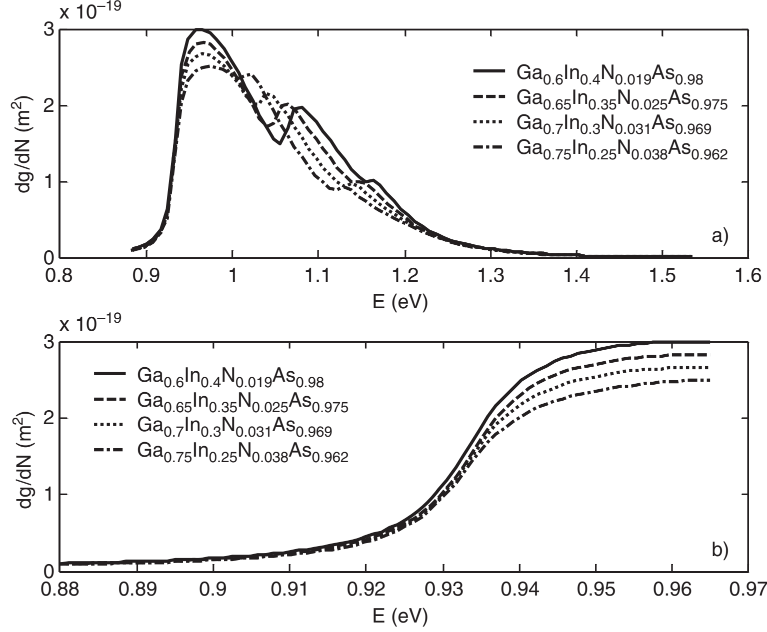

Fig. 17.7. (**a**) Differential gain for the four GaInNAs/GaAs structures of Fig. 17.2 calculated at transparency concentration for each structure; (**b**) detail of (**a**)

Energetically these states come closer because of the change of character of the bands due to band mixing, i.e., the HH-like bands near $k = 0$ develop a strong LH component for $k >> 0$ and vice versa.

In Fig. 17.7b we have plotted the detail of Fig. 17.6a that highlights the effects near the wavelength of interest, namely 1.3 μm or 0.954 eV. For the explanation of the trends identified, one has to consider that [36] the carrier gradient is depicted in the Fermi factors of the relation for DG; consequently the band structure will determine the spectral characteristics and peak gain value.

The results of Fig. 17.7 are in agreement with those reported by Chow and Harris [38] who have calculated for GaInNAs/GaAs under compressive strain ($\approx -2.5\%$) a value of $2.8 \times 10^{-19}\,\mathrm{m}^2$, which compares well with our calculation of $3 \times 10^{-19}\,\mathrm{m}^2$ for compressive strain of -2.48%. Tomic and O'Reilly [39] on the other hand have calculated a value of approximately $1.9 \times 10^{-19}\,\mathrm{m}^2$, whereas Yong and coworkers [40] have calculated $1.45 \times 10^{-19}\,\mathrm{m}^2$. The effect of the intraband relaxation time on the differential gain calculations was appreciated by Tomic and O'Reilly who calculated a difference in peak differential gain of the order of $0.6 \times 10^{-19}\,\mathrm{m}^2$, for intraband relaxation times ranging from 0.1 to 0.038 ps.

The band structure effect is manifested in the density of states of the bands, which in turn determines the "mobility" of the quasi-Fermi levels.

Elevated values of the density of states translate to bands with small curvature that makes the process of pushing the quasi-Fermi by carrier injection upwards (downwards) in the conduction (valence) band sluggish. Subsequently, harder carrier pumping is necessary to achieve the desired quasi-Fermi level. The above provide the explanation of reducing differential gain with increasing N content.

17.3.5 Differential Refractive Index

The interaction of the dense electron–hole plasma, created under pumping conditions in the semiconductor laser medium, with the EM radiation generates nonlinear effects, the strength of which depends on the carrier density. The deviation from the linear regime can be utilized to perform various schemes related to the manipulation of the signal.

Of particular importance for laser modeling is the nonlinear response of the refractive index change with injected carriers, the differential refractive index $\mathrm{d}n/\mathrm{d}N$. $\mathrm{d}n/\mathrm{d}N$ plays a pivotal role in phenomena that range from optical bistability (OB) [41], chirp [37], which describes the frequency displacement with injected carriers to frequency modulation (FM) [42]. These phenomena can be exploited to build optical devices [43, 44], hence it is useful to mention that OB and FM are enhanced for high values of $\mathrm{d}n/\mathrm{d}N$ whereas the detrimental effect of chirp is suppressed for low values of $\mathrm{d}n/\mathrm{d}N$.

In Fig. 17.8 we have plotted $\mathrm{d}n/\mathrm{d}N$ for the same structures as Fig. 17.7 for the corresponding transparency carrier concentrations. The band structure determines the spectral shape of $\mathrm{d}n/\mathrm{d}N$ through the carrier dependent Fermi factors. Same arguments hold for the behavior of $|\mathrm{d}n/\mathrm{d}N|$ as in the case of $\mathrm{d}g_\mathrm{m}/\mathrm{d}N$, regarding the modification of the DOS with N content and the consequent changes in quasi-Fermi levels.

17.3.6 Linewidth Enhancement Factor

It is well established that efficient carrier confinement in GaInNAs/GaAs quantum wells ensures excellent temperature characteristics of GaInNAs-based laser structures. However, carrier confinement is not a sufficient reason to switch from InP-based optoelectronics to dilute nitrides for emitters in the telecommunication window. Instead a number of issues need to be addressed, and we do this in Sect. 17.4. Here we will only deal with the spectral linewidth of GaInNAs structures.

The measure of the spectral linewidth of a semiconductor laser is the linewidth enhancement factor, α [45], and the functional form of the dependence is $\Delta v = \Delta v_\mathrm{ST}(1 + \alpha^2)$ [46] where α is the linewidth enhancement factor and Δv_ST is the linewidth predicted by the modified Schawlow–Townes formula. α is defined by the following formula:

$$\alpha(E) = \frac{2E}{\hbar c}\left(\frac{\mathrm{d}n(E)}{\mathrm{d}N}\bigg/\frac{\mathrm{d}g_\mathrm{m}(E)}{\mathrm{d}N}\right) \tag{17.5}$$

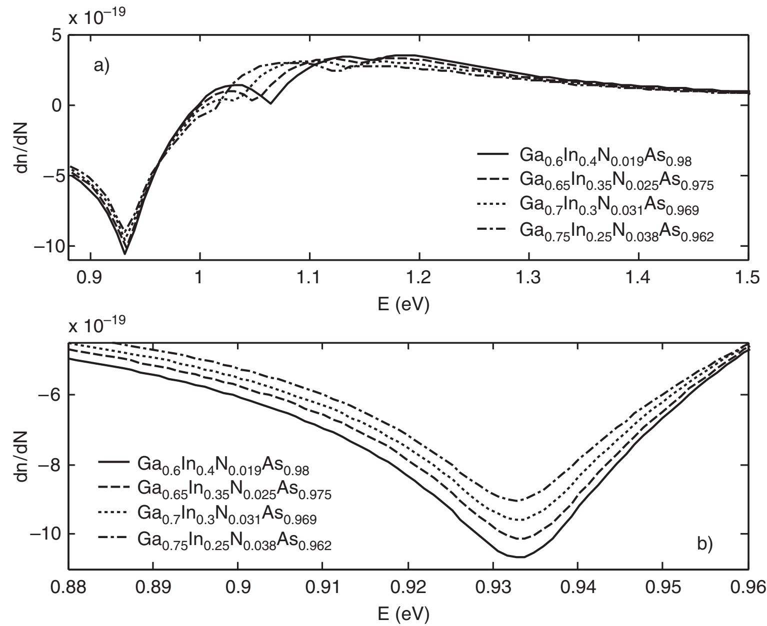

Fig. 17.8. (**a**) Differential refractive index for the four GaInNAs/GaAs structures of Fig. 17.2 calculated at transparency concentration for each structure; (**b**) detail of (**a**)

The results of the α factor calculation for the same structures as in Fig. 17.7 are shown in Fig. 17.9. The values of alpha for the four structures do not differ significantly over a wide range of energies (Fig. 17.9a) unlike $\mathrm{d}n/\mathrm{d}N$ and $\mathrm{d}g_{\mathrm{m}}/\mathrm{d}N$.

Apart from the effect of α on the linewidth of a semiconductor laser, in real device terms α is a useful tool for the design of high-speed lasers and the implementation of modulation schemes. For high-speed applications the device properties are tailored so that α is minimized with consequent suppression of chirp. Efficient amplitude modulation (AM) is also achieved with low values of α, whereas for FM applications the design should aim for high values of α.

Concentrating on a narrower range of energies that includes the emission energy (Fig. 17.9b), the values differ in the first decimal digit with the structure with less N content exhibiting the lowest $|\alpha|$. This is in accordance with published results regarding the effect of compressive strain on $|\alpha|$ [47]. As a measure of comparison it is noted that typical values of $|\alpha|$ are in the range of 2–4 [48]. For most laser applications it is usually desirable that the α factor has small values so that the linewidth is sufficiently narrow. Strategies for the minimization of $|\alpha|$ are discussed in [49].

A similar conclusion is reached in [50] when comparing GaInNAs and N-free GaInAs. Their findings suggest that the balance between the differential

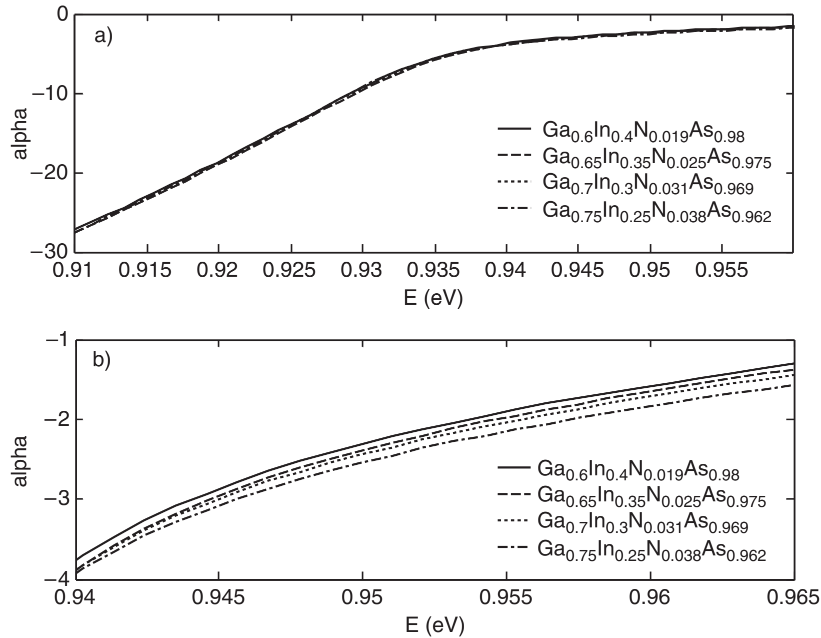

Fig. 17.9. (**a**) α factor for the four GaInNAs/GaAs structures of Fig. 17.2 calculated at transparency concentration for each structure; (**b**) detail of (**a**)

gain and differential refractive index quenches the band structure effect, thus making the α factor nearly N-independent. Experiment and theory on the α factor can be found in [50] and [51]. While the present study is in general agreement with the conclusions of [50] and [51], a strict comparison is not possible as the approach of [50] and [51] consists in studying the α factor at the gain peak.

While the band structure properties of GaInNAs exhibit many differences to InGaAsP, these are not manifested on the α values when comparing GaInNAs and InGaAsP structures [52]. This observation indicates the suitability of GaInNAs-based semiconductor lasers for transmitter applications in high-speed transmission systems.

17.4 Laser Design Considerations

In this section we will produce the composition mapping for 1.3 μm emission and derive some basic design rules not only from the viewpoint of the transition wavelength but also in terms of parameters related to laser performance.

The motivation for elaborating on the design lies in the observation that both the incorporation of In and the incorporation of N lead to a redshift

of the GaInNAs band gap [1]. Hence, the obvious routes for 1.3 μm emission are either to favor large In compositions and low N or the other way around. Therefore, it is necessary to distinguish these cases and explore the optimal route that will ensure not only the desirable emission wavelength but also enhanced laser performance. The gauges of this evaluation are the peak differential gain, the transparency concentration, and the momentum matrix element. Ideally for a laser structure one requires the maximum possible differential gain and the lowest possible transparency concentration, so that the carrier concentration required to reach the maximum gain and the carrier concentration necessary to reach positive material gain are minimized, respectively. In addition, high differential gain enhances the modulation bandwidth of laser structures and also influences the saturation power of semiconductor optical amplifiers. Differential refractive index at the wavelength of interest should be sufficiently low to ensure low values for the α factor, for applications that involve intensity or amplitude modulation, whereas for applications that utilize frequency modulation it should be high. The momentum matrix element quantifies the overlap between the electron wavefunction and the hole wavefunction. Hence maximum possible values are desired since the wavefunction overlap is then more efficient, which leads to higher values of gain.

17.4.1 Effect of In and N Composition on the Transition Wavelength

In Fig. 17.10, we plot the In and N compositions required to achieve 1.3 μm emission wavelength for various well widths. The E_{N} is taken to vary with In assuming that the NN environment is 2Ga, and C_{MN} is taken as the mean value of the two endpoint values, namely 1.675 [53]. Any combination of In and N composition that falls on the curve for the same well width will emit at 1.3 μm. The quantum confinement effect in the lasing wavelength is quite straightforward and exhibits the usual trend. For increasing well width the transition energy is shifted downwards and therefore less In and N are required to achieve an output wavelength of 1.3 μm (Fig. 17.10).

In Sect. 17.2 we underlined the importance of the parameterization of the band structure and we presented the NN approach for the determination of the E_{N} and C_{MN} values. Here, we elaborate on this aiming to show how different NN environments affect the calculations, given the strong dependence of the functional form of the E_{N} with In composition on the NN configuration. We plot in Fig. 17.11 the In and N compositions for a 7 nm GaInNAs/GaAs QW that emits at 1.3 μm for three cases, the two extremes 4Ga and 4In, and the mean approach, that is 2Ga.

Figure 17.11 provides an explanation of the plethora of values of the combinations of compositions found in the literature (a review of these can be found in [55]), for a given wavelength. It is easily seen that according to the approach of [24] for the $C_{\mathrm{MN}} - E_{\mathrm{N}}$ pairs, the compositions of In and N

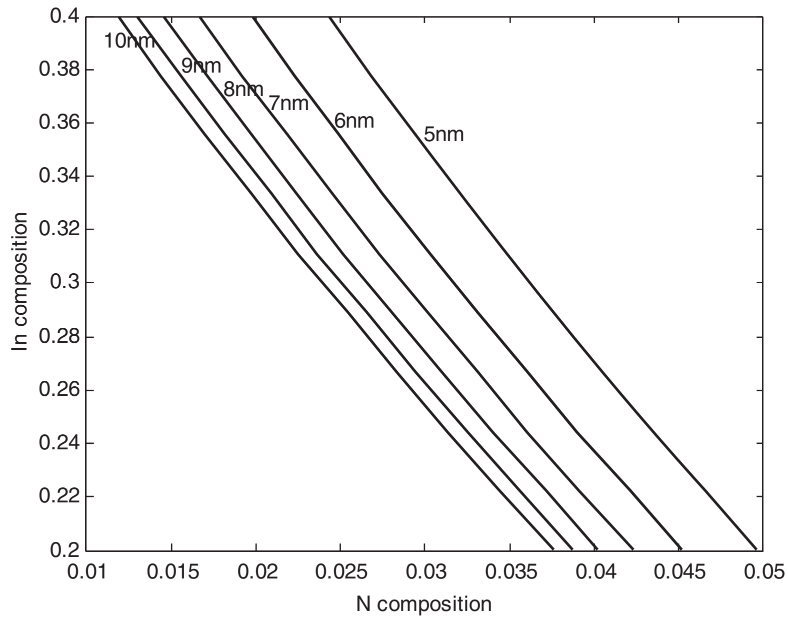

Fig. 17.10. Composition requirements for 1.3 μm of GaInNAs/GaAs QWs for the well widths shown (Taken from [54] © IET)

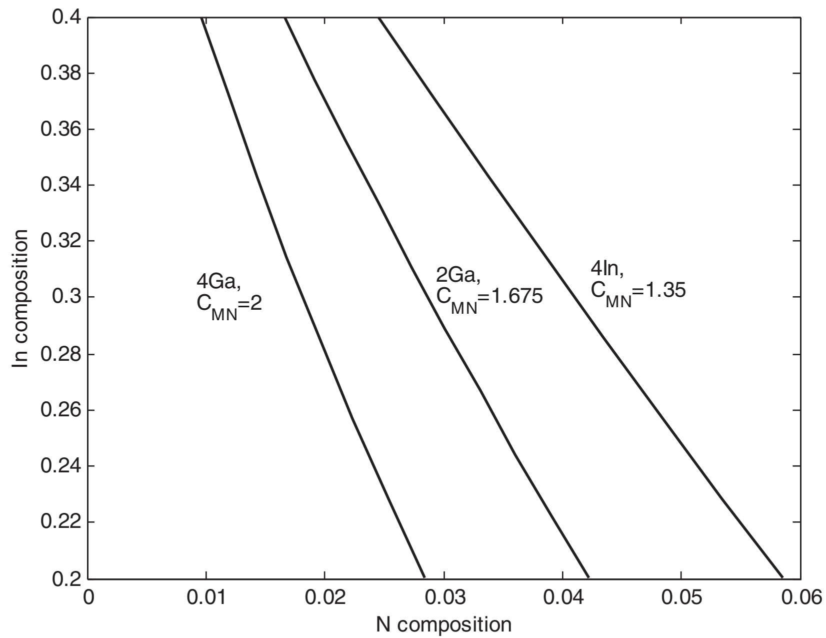

Fig. 17.11. Composition requirements for 1.3 μm of a 7 nm GaInNAs/GaAs for three different NN environments: 4Ga, 2Ga, and 4In (Taken from [54] © IET)

required for 1.3 μm emission vary substantially, depending on the microscopic configuration. In the light of these results, the differences in reported values arise from the different post-growth treatments that induce different microstructural changes and hence favor different NN configuration to dominate the transitions. Figures 17.10 and 17.11 serve also as a verification of our band structure model: comparison of these with published design curves for a 7 nm GaInNAs/GaAs structure produced from a 10×10 Hamiltonian [39] shows very good agreement.

17.4.2 Effect of In and N Composition on the Optical Properties

Figure 17.12 shows the transparency carrier concentration, that is, the concentration at which the material gain becomes positive, for different N compositions and well widths. The In composition is such that for the N composition, the emission wavelength is 1.3 μm. The corresponding peak differential gain at these transparency concentrations is shown in Fig. 17.13. The calculation of the peak differential gain is performed in the context of the free carrier theory allowing for lineshape broadening of 0.1 ps. In Fig. 17.14, we plot the differential refractive index at the transparency concentration at 1.3 μm. Finally we have calculated for the same conditions as above the normalized

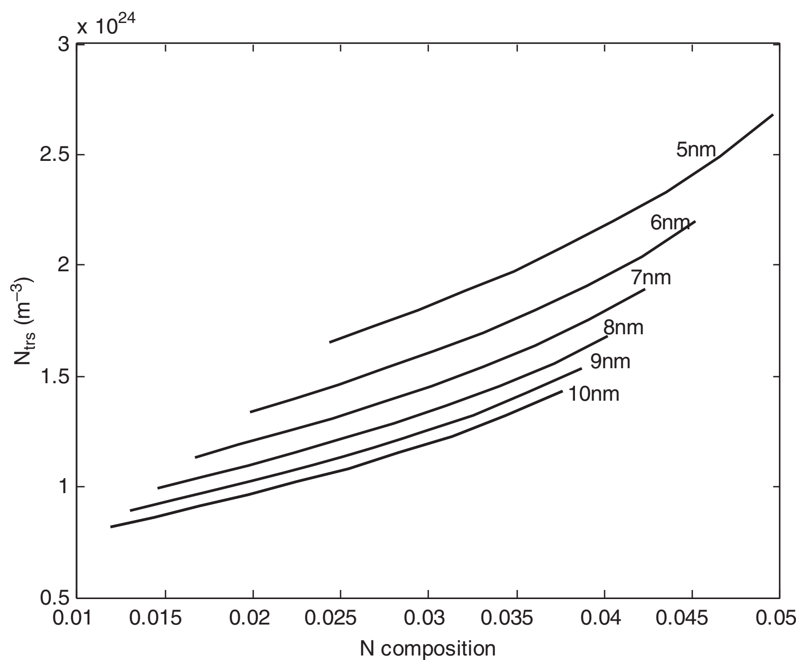

Fig. 17.12. Transparency concentration against N content for various well widths and In content such that the emission wavelength is 1.3 μm (Taken from [54] © IET)

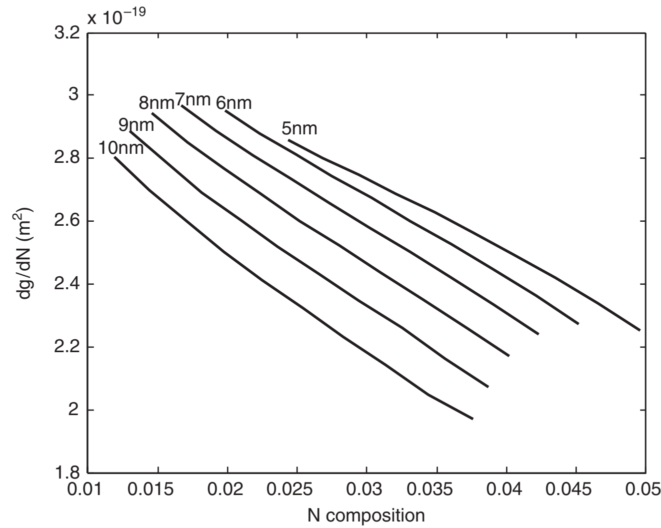

Fig. 17.13. Peak differential gain at the transparency concentration shown in Fig. 17.12 against N content for various well widths (Taken from [54] © IET)

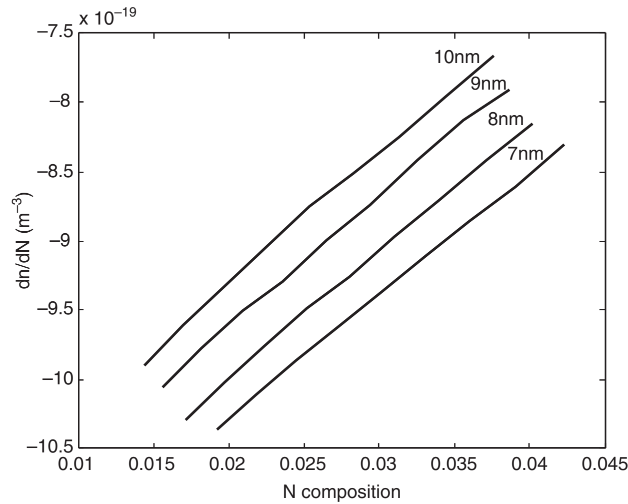

Fig. 17.14. Differential refractive index at transparency concentration at 1.3 μm against N content for various well widths (Taken from [54] © IET)

value of the TE momentum matrix element (MME), namely MME_{TE}/M_b and this is shown in Fig. 17.15. M_b is the bulk momentum matrix element with units of $(kg \times eV)^{-1/2}$.

Given that the emission wavelength is fixed at 1.3 μm, for any given N concentration the decrease of the peak differential gain with increasing well width

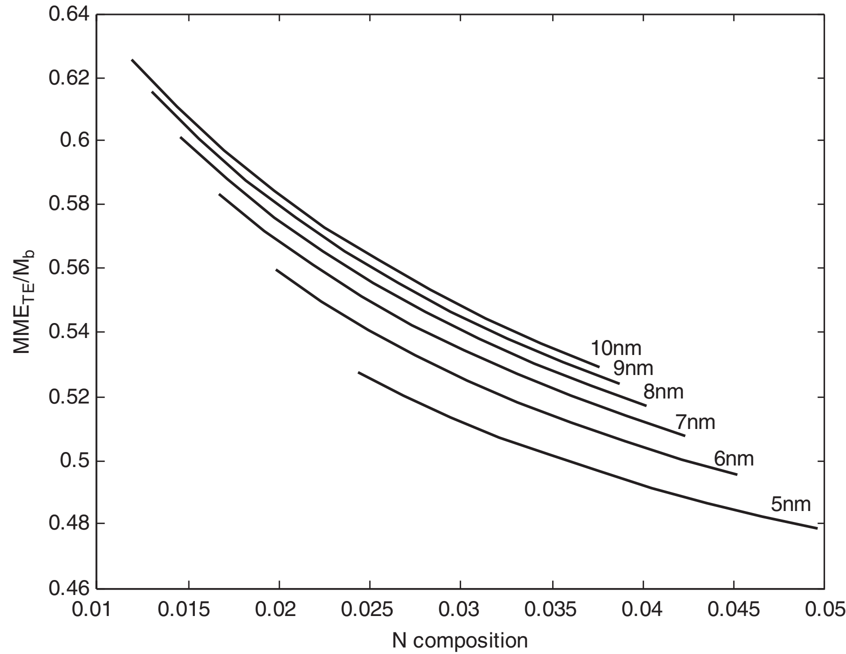

Fig. 17.15. MME for TE polarization for $CB1 \rightarrow HH1$ for various well widths against N composition (Taken from [54] © IET)

(Fig. 17.13) can be interpreted in terms of the amount of compressive strain. Indeed for increasing well width the In fraction necessary for 1.3 μm emission decreases and hence the compressive strain decreases, which translates to an increase of the density of states. This, however, is in competition with the quantum confinement effect on the density of states, but the differential gain behavior is primarily determined by the strain effect. The dependence of $|\mathrm{d}n/\mathrm{d}N|$ (being the Kramers–Kroning transform of $\mathrm{d}g/\mathrm{d}N$) on well width (Fig. 17.14) is also dominated by the band structure effect.

On the other hand, in the case of the transparency concentration (Fig. 17.12) the quantum confinement effect dominates, and the decreasing trend with increasing well width is attributed to the quantum size effect induced modification of density of states. Similar arguments hold for the momentum matrix element's dependence on the well width (Fig. 17.15). For decreasing well width thickness the electron envelope function spreads over the well leading to a decrease in the electron and hole overlap.

Next we discuss the effect of N on the value of the optical properties shown in Figs. 17.13–17.15 bearing in mind the prerequisites for optimal laser performance set in Sect. 17.4.1. The effect of increasing N composition for fixed well width on the optical properties is detrimental. This can be understood in view of the band structure of GaInNAs alloys. To make the discussion more transparent we make a short summary of the main conclusions of Sect. 17.2.

The band structure of GaInNAs alloys results from the hybridization of the extended-like states of the matrix semiconductor, i.e., GaInAs, and the N localized states, and the resulting electron bands have pronounced nonparabolicity. Because of the N induced nonparabolicity the electron effective mass exhibits unusually large values. Large values of effective mass translate to large values of conduction band density of states. Based on this framework, the transparency concentration is expected to increase with increasing N content as shown in Fig. 17.12. The effect on the transparency concentration is clearer considering the dependence of the quasi-Fermi levels on the carrier concentration. Since the density of states is higher with increasing N content, the electron Fermi level moves slowly with injected carriers.

The same reasoning can be used to explain the dependence of the peak differential gain (Fig. 17.13) on N and subsequently $|\mathrm{d}n/\mathrm{d}N|$. However, the effect of N content is not manifested only through the increased density of states but also through the momentum matrix element. Increasing the N content, the localized part of the electron wavefunction is enhanced at the expense of the extended part, which has the maximum overlap with the hole wavefunction. Hence, the MME is reduced with a consequent reduction of the peak differential gain.

17.5 GaInNAs Based Semiconductor Optical Amplifiers

An important optoelectronic function that will benefit from the use of GaInNAs is optical amplification by SOAs. The scope of this section is to explore the potential of GaInNAs in edge emitting semiconductor optical amplifiers.

For the SOA modeling we use a multisectioning approach [11] to the rate equation to approximate the length dependence of the gain and carrier concentration, accounting for amplified spontaneous emission (ASE) to calculate the amplifier gain, the amplifier bandwidth, the noise figure, and the output saturation power. The band structure effects are reflected on the material gain (discussed in Sect. 17.3) used in the SOA calculation.

17.5.1 Polarization Sensitive GaInNAs Semiconductor Optical Amplifiers

We have modeled four GaInNAs/GaAs structures with 7 nm quantum wells and 15 nm GaAs barriers. The structures are listed in Table 17.1. Each structure contains 4 QWs and the In and N contents are such that the peak gain wavelength is approximately 1.3 μm. The N compositions that we have chosen span the range of experimentally demonstrated values [56, 57]. It is noted that limitations are imposed on growth of GaInNAs with high N contents as crystalline quality deteriorates for increasing N. For all cases, the optical confinement is enhanced by 30 nm AlGaAs cladding layers, and the confinement factor is calculated following the averaging procedure outlined in [58].

Table 17.1. List of the structures used here. The quantum well width in each case is 7 nm

Structure	Strain
$Ga_{0.60}In_{0.40}N_{0.019}As_{0.981}/GaAs$	−2.42%
$Ga_{0.65}In_{0.35}N_{0.025}As_{0.975}/GaAs$	−1.97%
$Ga_{0.70}In_{0.30}N_{0.032}As_{0.968}/GaAs$	−1.49%
$Ga_{0.75}In_{0.25}N_{0.038}As_{0.962}/GaAs$	−1.01%

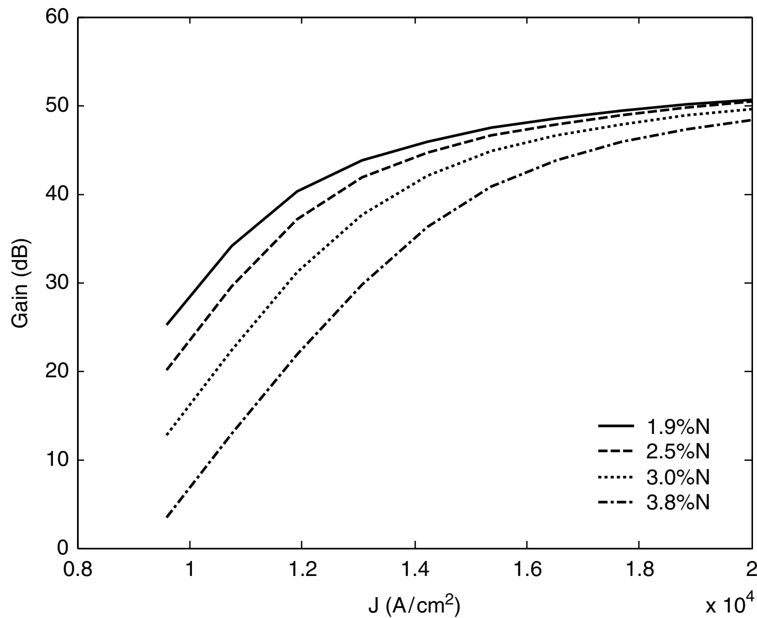

Fig. 17.16. Amplifier gain for the structures of Table 17.2 against current density (Taken from [11] © IEEE)

The results of the amplifier calculations are shown in Fig. 17.16. Figure 17.17 shows the output saturation power while the noise figure and amplifier bandwidth are depicted in Figs. 17.18 and 17.19, respectively. In all cases the calculations are performed for various injection currents and nitrogen contents. The input power is set to be constant at −35 dBm. The parameters of the SOA are listed in Table 17.2.

A first observation is that the magnitudes of the physical quantities calculated have no distinctive differences compared to published results concerning other material systems [59]. This is explicable, since the material gain, unlike the band structure, does not exhibit any unusual features. The amplifier gain (Fig. 17.16) is improved for relatively low nitrogen composition, in other words for compositions that favor compressive strain environment. The material gain in these cases is enhanced due to the lower effective masses and higher

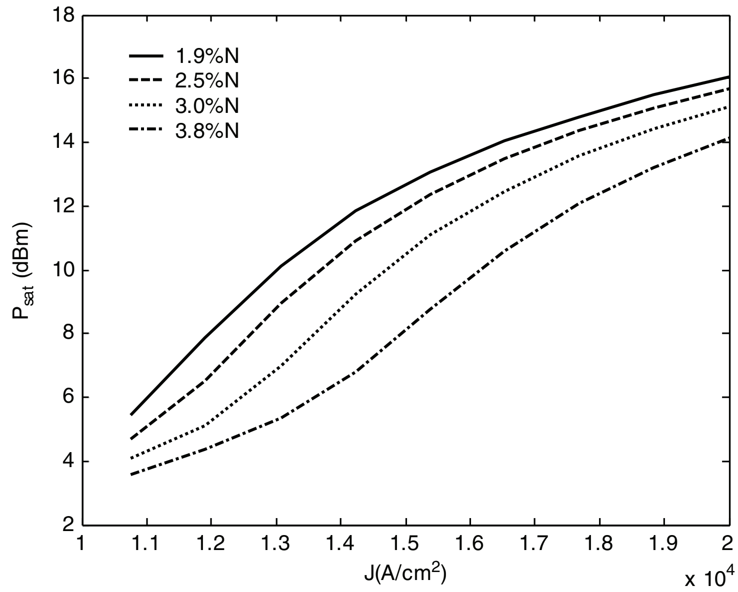

Fig. 17.17. Output saturation power against current density (Taken from [11] © IEEE)

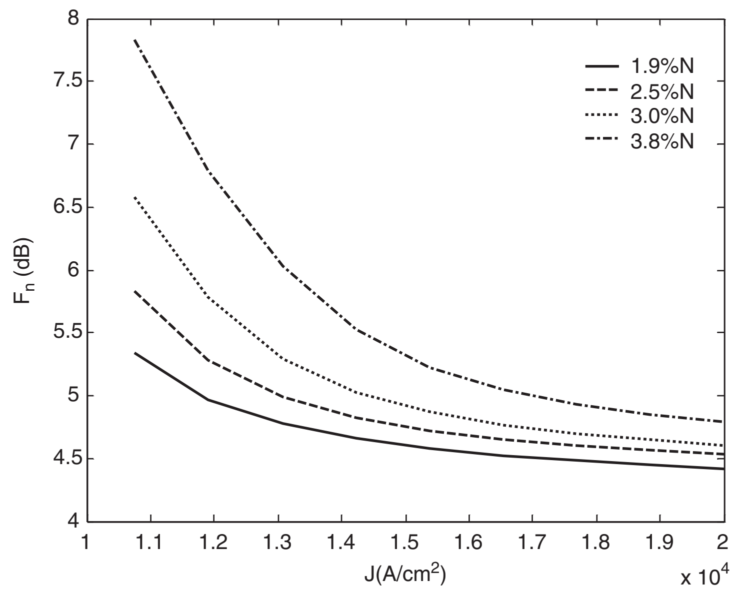

Fig. 17.18. Noise figure against current density (Taken from [11] © IEEE)

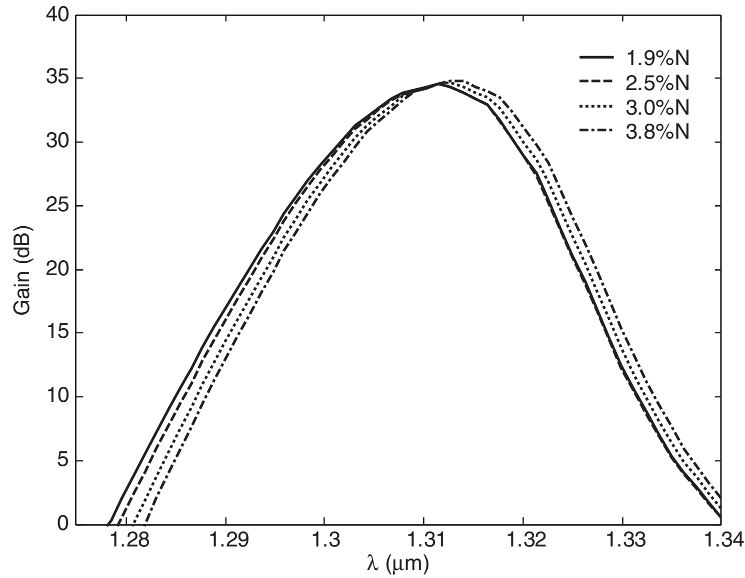

Fig. 17.19. Amplifier gain against wavelength, for the four different nitrogen concentrations as indicated in the figure (Taken from [11] © IEEE)

Table 17.2. List of the parameters used in the computations. Typical values for dimensions and losses have been used

L (cavity length)	500 μm
W (active region width)	2 μm
α_c (cladding loss)	30 cm^{-1}
α_a (active layer loss)	22 cm^{-1}
R_1 (front mirror reflectivity)	0
R_2 (back mirror reflectivity)	0
N_g (effective group refractive index)	4
A (monomolecular recombination coefficient)	$2 \times 10^8\ s^{-1}$
C (Auger recombination coefficient)	$4 \times 10^{-29}\ cm^6\ s^{-1}$

transition matrix elements. The four amplifier gain curves converge for high pumping. All the results are calculated for TE polarization as the TM is sufficiently suppressed due to compressive strain. Therefore, in applications where the amplification is required to be independent of the signal polarization, GaInNAs/GaAs QWs are unsuitable since the strain conditions do not allow the equalization of TE and TM gains. In particular, if the aim is the 1.3 μm window then the lattice constant relations will always lead to compressive strain and hence, the dominant polarization of GaInNAs/GaAs QWs will always be TE. If polarization insensitivity is a crucial issue in the application then alternative barrier material should be used. We discuss this in more detail in the following section.

The output saturation power (Fig. 17.17) has the same trend as the amplifier gain. This is, again, a consequence of strain effects. Indeed, from the early work of Yamamoto and coworkers [60], it is established that the input saturation power of an amplifier is inversely proportional to the differential gain. The direction towards reduced compressive strain reduces the differential gain and therefore increases the input saturation power with a consequent reduction of the output saturation power.

The effect of the current density on the output saturation power for given nitrogen composition can be understood if we first consider the effect of current density on the input saturation power: for increasing currents the amplifier gain for low input powers increases and the amplifier reaches saturation for lower input powers since the input signal depletes faster than the available carriers for recombination. Bearing in mind that $G(\mathrm{dB}) = 10\log_{10}(P_{\mathrm{out}}) - 10\log_{10}(P_{\mathrm{in}})$, the output saturation power follows the opposite trend from the input saturation, hence the trends identified in Fig. 17.17.

The decrease in the output saturation power with the inverse nitrogen content is accompanied by an increase in the noise figure (Fig. 17.18). Both the former and the latter are detrimental for the SOA performance, a fact that implies a simple design rule. Indeed this is the case for the samples with relatively high N content. In terms of band structure, the incorporation of N leads to the enhancement of the electron effective mass. At the same time, for given well width, the In content necessary to achieve the 1.3 μm emission wavelength is decreased, which affects the hole effective mass. Both cases have as a consequence the increase of the density of states and therefore the reduction of the quasi-Fermi separation ΔE_{f} for given carrier concentration. Given that the analytical expression of the noise figure is [61],

$$F_n = 2n_{\mathrm{sp}}\frac{G-1}{G}, \tag{17.6}$$

where G is the amplifier gain and n_{sp} is the population-inversion factor given by

$$n_{\mathrm{sp}}(E) = \left[1 - \exp\left(\frac{E - \Delta E_{\mathrm{F}}}{k_{\mathrm{B}}T}\right)\right]^{-1}, \tag{17.7}$$

reduction of ΔE_{F} results in the deterioration of the noise figure. On the other hand, as more carriers are pumped into the SOA operating in the unsaturated regime, the ΔE_{F} is increased with subsequent improvement of the noise figure as shown in the figure.

The amplifier gain bandwidth is calculated for −35 dBm input signal power and for current densities such that the four structures have the same maximum gain (Fig. 17.19). The current densities for which the bandwidth is calculated are 10^4, 1.05×10^4, 1.14×10^4, and $1.26 \times 10^4\ \mathrm{A\ cm^{-2}}$ for 1.9% N, 2.5% N, 3% N and 3.8% N, respectively. The amplifier gain, for given N content, for different input wavelengths follows the trends in the material gain, and therefore the same arguments hold in the case of the amplifier bandwidth

as in the case of the material gain. The bandwidth in all four is comparable and the differences are only slight. The two determining factors are strain conditions and carrier concentration. The interplay of the two cancels out their effects, resulting in practically the same bandwidth.

17.5.2 Polarization Insensitive GaInNAs SOAs

In this section we elaborate on the work presented in Sect. 17.5.1 to address the issue of polarization. The compressive strain conditions between the GaInNAs well material and the GaAs barrier material dictate TE polarization.

Given that the TE polarization couples to HH whereas TM couples to LH, for polarization insensitivity the relevant band structure engineering aims at the equalization of the contributions of HH and LH to the material gain.

It is possible to achieve this by introducing the GaInAs as the barrier. The motivation for this is that in this case GaInNAs is grown on GaInAs under tensile strain conditions (or close to lattice matching). For this scheme, the growth of a metamorphic buffer layer that will change the lattice constant from that of the substrate (GaAs) to that of the barrier (GaInAs) is necessary. The use of the GaInAs material as a buffer layer has been demonstrated before with In compositions in the range of 0.2–0.35 and buffer layer thickness varying from 0.4 to 3 μm [61–64].

To verify this we model the structures listed in Table 17.3. The compositions are chosen such that the emission wavelength is in the 1.3 μm window. The well width of the GaInNAs/GaInAs QWs in all cases is 7 nm.

In Fig. 17.20 the TE and TM material gain is plotted for these and for the sake of comparison we include in the same figure the material gain for a 7 nm $Ga_{0.7}In_{0.3}N_{0.028}As_{0.972}$/GaAs QW. The calculation in all cases is performed for $3 \times 10^{18}\,cm^{-3}$ carrier concentration.

It is evident that the TM component of the material gain is enhanced for the GaInNAs/GaInAs QWs as opposed to the material gain in GaInNAs/GaAs QW, where the TM component is suppressed. The material gain characteristics of the pz2 are intermediate between pz1 and pz3. Figure 17.20 serves as proof of our argument of the feasibility of polarization equalization of TE and TM gain using GaInAs barrier material.

In Fig. 17.21, the amplifier gain for a SOA based on structure pz2 with 4 QWs, is plotted against wavelength of the input signal for an input power of −30 dBm and a drive current of 85 mA. The calculated confinement factor

Table 17.3. List of the structures used here. The quantum well width in each case is 7 nm

Structure	Strain	Name
$Ga_{0.79}In_{0.21}N_{0.03}As_{0.97}/Ga_{0.79}In_{0.21}As$	0.62%	pz1
$Ga_{0.78}In_{0.22}N_{0.03}As_{0.97}/Ga_{0.8o}In_{0.2o}As$	0.43%	pz2
$Ga_{0.77}In_{0.23}N_{0.03}As_{0.97}/Ga_{0.81}In_{0.19}As$	0.36%	pz3

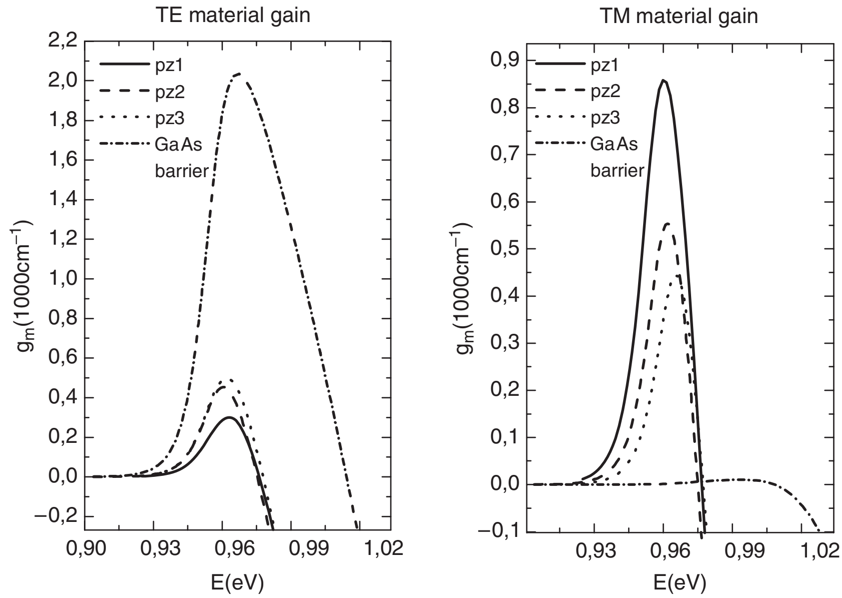

Fig. 17.20. TE and TM material gain for the structures of Table 17.3 and for a 7 nm $Ga_{0.7}In_{0.3}N_{0.028}As_{0.972}/GaAs$ QW (denoted as "GaAs barrier"), calculated for carrier density of $3 \times 10^{18}\ cm^{-3}$ (Taken from [12] © IEEE)

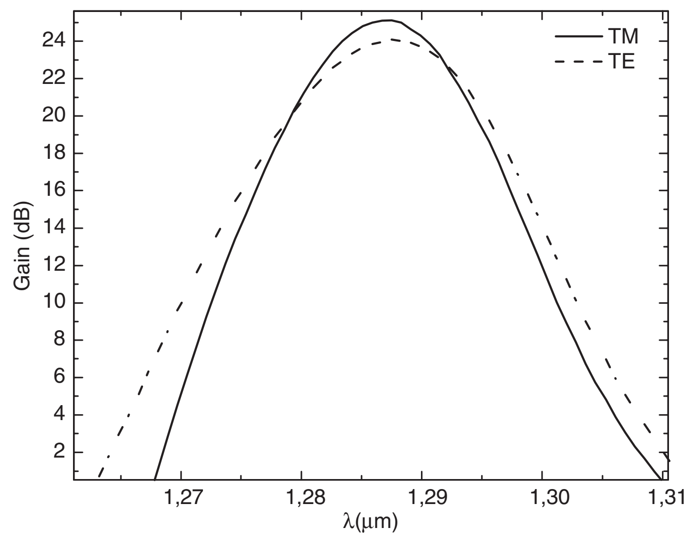

Fig. 17.21. TE and TM amplifier gain of a SOA based on structure pz2 for −30 dBm input signal and 85 mA drive current (Taken from [12] © IEEE)

for this structure is 0.04, following the averaging procedure of [58]. Details of the structure and various parameters involved in the calculations are tabulated in Table 17.2. Figure 17.21 confirms that the balanced band mixing of structure pz2 enables the equalization of TE and TM amplifier gain. Further optimization of the structure in terms of waveguide properties is needed to improve the polarization insensitivity, to match state-of-the art SOAs based on the InP technology [65].

17.6 Conclusion

We studied the optical properties of GaInNAs for laser and SOA applications. For the former it was established that the route of high In and low N ensures optimal device performance. The same applies for GaInNAs SOAs where polarization sensitivity is not an issue.

If on the other hand the application dictates polarization insensitive elements, the use of GaInAs barrier for GaInNAs QWs is necessary. This complicates the growth procedure as it entails growth of GaInAs on GaAs metamorphically but it manages in equalizing the gain response to both polarizations. Overall GaInNAs appears to be a viable candidate for the near future telecom optoelectronics covering both telecommunication windows.

References

1. M. Kondow et al., Jpn. J. Appl. Phys. **35**, 1273 (1996)
2. V.M. Ustinov, A.E. Zhukov, Semicond. Sci. Technol. **15**, R41 (2000)
3. M. Hugues et al., Appl. Phys. Lett. **88**, 091111 (2006)
4. H.D. Sun et al., Appl. Phys. Lett. **85**, 4013 (2004)
5. D. Gollub et al., IEEE J. Quantum Electron. **40**, 337 (2004)
6. S. Smith et al., Electron. Lett. **40**, 935 (2004)
7. D. Gollub et al., Electron. Lett. **40**, 1181 (2004)
8. J.B. Heroux et al., Appl. Phys. Lett. **75**, 2716 (1999)
9. S. Calvez et al., Electron. Lett. **39**, 100 (2003)
10. J. Hashimoto et al., Jpn. J. Appl. Phys. **43**, 3419 (2004)
11. D. Alexandropoulos, M.J. Adams, IEEE J. Quantum Electron. **39**, 647 (2003)
12. D. Alexandropoulos et al., IEEE J. Quantum Electron. **41**, 817 (2005)
13. A. Rutz et al., Electron. Lett. **41**, 321 (2005)
14. S. Wei, A. Zunger, Phys. Rev. Lett. **76**, 664 (1996)
15. A. Lindsay, E.P. O'Reilly, Solid State Commun. **112**, 443 (1999)
16. W. Shan et al., Phys. Rev. Lett. **82**, 1221 (1999)
17. W. Shan et al., J. Appl. Phys. **86**, 2349 (1999)
18. S.L. Chuang, Phys. Rev. B. **43**, 9649 (1991)
19. C.Y. Chao, S.L. Chuang, Phys. Rev. B **46**, 4110 (1992)
20. J.M. Luttinger, W. Kohn, Phys. Rev. **97**, 869 (1955)
21. G.E. Pikus, G.L. Bir, Sov. Phys. Solid State **1**, 1502 (1960)
22. C. Chang, S.L. Chuang, IEEE. J. Select. Top. Quantum Electron. **1**, 218 (1995)

23. D. Alexandropoulos, M.J. Adams, IEE Proc. Optoelectron. **150**, 40 (2003)
24. P.J. Klar et al., Phys. Rev. B. **64**, 121203(R) (2001)
25. V. Lordi et al., Phys. Rev. B. **71**, 125309 (2005)
26. S. Sakai et al., Jpn. J. Appl. Phys. **32**, 4413 (1993)
27. I.A. Buyanova et al., Phys. Rev. B **63**, 033303 (2001)
28. L. Bellaiche et al., Phys. Rev. B **56**, 10233 (1997)
29. J. Hader et al., Appl. Phys. Lett. **77**, 630 (2000)
30. J. Hader et al., Appl. Phys. Lett. **76**, 3685 (2000)
31. P.J. Klar et al., Phys. Stat. Sol. (b) **223**, 163 (2001)
32. C.G. Van De Walle, Phys. Rev. B. **39**, 1871 (1989)
33. S.L. Chuang, *Physics of Optolectronic Devices*, (Wiley Interscience, New York, 1995)
34. W.W. Chow, S.W. Koch, *Semiconductor Laser Fundamentals: Physics of the Gain Materials*, (Springer, Berlin Heidelberg New York, 1999)
35. Y.N. Qiu, J.M. Rorison, Appl. Phys. Lett. **87**, 081111 (2005)
36. Y. Arakawa, A. Yariv, IEEE J. Quantum Electron. **21**, 1666 (1982)
37. G.P. Agrawal, N.K. Dutta, *Long-Wavelength Semiconductor Lasers*, (Van Nostrand Reinhold, New York, 1986)
38. W.W. Chow, J.S. Harris, Appl. Phys. Lett. **82**, 1673 (2003)
39. S. Tomic, E.P. O'Reilly, IEEE Photon. Technol. Lett. **15**, 6 (2003)
40. J.C.L. Yong et al., IEEE J. Quantum Electron. **38**, 1553 (2002)
41. M.J. Adams et al., IEEE J. Quantum Electron. **21**, 1498 (1985)
42. R. Nagarajan, J.E. Bowers, in *Semiconductor Lasers I: Fundamentals*, ed by E. Kapon (Academic, New York, 1999)
43. H. Kawaguchi, *Bistabilities and Nonlinearities in Laser Diodes*, (Artech House, Boston, 1994)
44. M.J. Adams et al., Optic. Quantum Electron. **27**, 1 (1995)
45. C.H. Henry, IEEE J. Quantum Electron. **18**, 259 (1982)
46. A. Yariv, *Quantum Electronics*, 3rd edn. (Wiley, New York, 1989)
47. M. Mullane, J.G. McInerney, IEEE Photon. Technol. Lett. **11**, 776 (1999)
48. M. Osinski, J. Buus, IEEE J. Quantum Electron. **23**, 9 (1987)
49. T. Yamanaka et al., IEEE J. Quantum Electron. **29**, 1609 (1993)
50. A. Thranhardt et al., Appl. Phys. Lett. **86**, 201117 (2005)
51. N.C. Gerhardt et al., Appl. Phys. Lett. **84**, 1 (2004)
52. D. Alexandropoulos, M.J. Adams, J. Phys. Condens. Matter. **14**, 3523 (2002)
53. S. Tomic, E.P. O'Reilly, Physica E **13**, 1102 (2002)
54. D. Alexandropoulos, M.J. Adams, IEE Proc. Optoelectron. **150**, 105 (2003)
55. R. Potter et al., Superlattices and Microstructures **29**, 169 (2001)
56. M.O. Fischer et al., IEEE J. Select. Topics Quantum Electron. **7**, 149 (1997)
57. J.S. Harris, Semicond. Sci. Technol. **17**, 880 (2002)
58. W. Streifer et al., Appl. Opt. **18**, 3547 (1979)
59. H. Ghafouri-Shiraz, *Fundamentals of Laser Diode Amplifiers*, (Wiley, New York, 1996)
60. Y. Yamamoto et al., IEEE J. Quantum Electron. **19**, 47 (1983)
61. G.P. Agrawal, *Fiber-Optic Communication Systems*, (Wiley Interscience, New York 1997)
62. E.S. Semenova et al., Nanotechnology **15**, S283 (2004)
63. A.E. Zhukov et al., Semiconductors **37**, 1119 (2003)
64. A. Bosacchi et al., J. Cryst. Growth, **175**, 1009 (1997)
65. A.E. Kelly et al., Electron. Lett. **33**, 536 (1997)

18

Dilute Nitride Quantum Well Lasers by Metalorganic Chemical Vapor Deposition

N. Tansu and L.J. Mawst

We present and review the physics and device characteristics of high-performance strain-compensated metalorganic chemical vapor deposition grown 1,200 nm GaInAs and 1,300–1,400 nm GaInNAs quantum well lasers. Utilizing the GaAsP barriers surrounding the highly strained GaInNAs quantum well active regions, high-performance quantum well lasers have been realized from 1,170 nm up to 1,400 nm wavelength regimes. The design of the GaInNAs quantum well active region utilizes an In-content of approximately 40%, which requires only approximately 0.5–1% N-content to realize emission wavelengths up to 1,300–1,410 nm. Threshold current densities of only 65–90 A cm^{-2} were realized for GaInAs quantum well lasers, with emission wavelength of 1,170–1,233 nm. Room temperature threshold and transparency current densities of 210 and 75–80 A cm^{-2}, respectively, have been realized for 1,300 nm GaInNAs quantum well lasers. Despite the utilization of the highly strained GaInNAs quantum well, multiple quantum wells lasers have been realized with excellent lasing performance. Methods to extend the lasing emission wavelength up to 1,400 nm with GaInNAs quantum-well lasers are also presented. Theoretical analysis and experiments also show suppression of thermionic carrier leakages in GaInNAs quantum-well systems lead to high performance lasers operating at high temperature. Approaches based on dilute nitride quantum-wells to extend the emission wavelength up to 1,550 nm on GaAs substrate will also be discussed.

18.1 Introduction

The demand for higher bandwidth and longer transmission distance has led the pursuit of low cost single-mode 1,300–1,550 nm transmitter sources. Transmitters based on 1,300 nm edge emitters or vertical cavity surface emitting lasers (VCSELs) operating at a modulation bandwidth of 10 Gbs^{-1}, for the metro application using single mode fibre, allow data transmission up to a distance of 20–30 km [1, 2]. To realize low cost (uncooled) 1,300–1,550 nm-based

optical communications systems, high-performance (i.e., temperature insensitive) diode lasers (either in-plane or VCSELs) are needed, which operate up to 85°C. However, conventional InP-based long wavelength diode lasers, at λ = 1,300–1,550 nm, are inherently highly temperature sensitive, due to strong Auger recombination, large carrier leakage from the active layer, intervalence band absorption, and a strongly temperature-dependent material gain parameter [1, 2].

Another major factor motivating the development of 1.3–1.55 μm GaAs-based diode lasers is the ease in forming high quality (Al)GaAs/AlAs distributed Bragg reflectors (DBRs) on GaAs substrates [1, 2]. The ability to fabricate very high quality AlGaAs-based DBRs has allowed the GaAs-based VCSELs to have performance comparable to GaAs-based in-plane diode lasers.

An attractive approach for achieving long wavelength laser emission on GaAs substrates is the use of highly strained GaInNAs [1–19] or GaInAs [20–27] quantum wells (QWs). The use of a highly strained GaInAs QW active layer to extend the emission wavelength to 1.20-μm was pioneered by Sato et al. [20] and Kondo et al. [22]. The reduction in the band gap of the GaInNAs materials, pioneered by Kondow et al. [1], due to the existence of the N, is also followed by reduction in the compressive strain of the material due to the smaller native lattice constant of the GaInN compound. Since then, many promising results have been demonstrated for 1.3 μm GaInNAs-active lasers [1–19].

Similar to 1.3 μm lasers on InP, recent studies on recombination mechanisms in GaInNAs/GaAs lasers, at 1.3 μm, suggest that Auger recombination may also be a dominant recombination processes in this material system [28]. Other studies identify the role of carrier leakage as well as the material gain parameter in the device temperature sensitivity [29,30]. At present, a detailed understanding of recombination mechanisms, the material gains, and carrier leakage in this material system is still lacking.

The early development of GaInNAs QW lasers employed nearly lattice-matched low-In content and high N-content GaInNAs QW active regions [1,2]. Because of the smaller native lattice constant of the GaInN compound, the incorporation of N into the compressively strained GaInAs material system can result in a nearly lattice-matched GaInNAs QW. Unfortunately, the performance of the early 1,200–1,300 nm GaInNAs QW lasers were significantly inferior to the N-free GaInAs-active lasers as well as the conventional 1,300 nm InP-based lasers.

Sato and coworkers proposed the approach of utilizing very high In-content GaInNAs QW active regions [3] grown by metalorganic chemical vapor deposition (MOCVD). The idea proposed was to utilize as high an In-content as possible in the GaInNAs QW, such that only a minimum amount of N is required to push the peak emission wavelength to 1,300 nm. By utilizing this approach, Sato and coworkers were able to realize 1,300 nm GaInNAs QW lasers with reasonable threshold current density in the order of 0.9–1 kA cm^{-2}.

Prior to the year of 2001, the best-published 1,300 nm GaInNAs QW lasers [4] have been realized with molecular beam epitaxy (MBE), resulting in superior lasing performance in comparison to those of MOCVD-grown 1,300 nm GaInNAs QW lasers [3,5]. Only recently, MOCVD-grown 1,300 nm GaInNAs QW lasers [6–14] have been realized with performance comparable to the best MBE-grown devices.

This chapter deals with various aspects of the lasing characteristics of GaInAs-QW and GaInNAs-QW lasers, grown by low-pressure MOCVD with AsH_3 as the As-precursor. The GaInAs and GaInNAs QW lasers studied here cover emission wavelengths from 1,170 nm up to 1,410 nm. The detail of the MOCVD growth process and issues are discussed in Sect. 18.2. The lasing characteristics of 1,200 nm regime GaInAs QW are discussed in Sect. 18.3. The GaInNAs QW active structures investigated include both single QW and multiple QWs designs with strain compensation from GaAsP tensile-strained barriers, as discussed in Sects. 18.4 and 18.5, respectively. The effect of increased N-content on device performance is also discussed in Sect. 18.6. The first method to extend the emission wavelength up to 1,320 nm by utilizing GaNAs barriers to reduce the quantum confinement effects of GaInNAs QW is discussed in Sect. 18.7. To clarify the benefits of the GaInNAs QW active region, comparisons with conventional InP-technology is also discussed in Sect. 18.8. Continuous wave lasing characteristics of 1,300 nm GaInNAs QW single-mode ridge-guide lasers are discussed in Sect. 18.9. The second method to extend the emission wavelength of GaInNAs QW lasers up to 1,400 nm regimes by utilizing a higher N-content GaInNAs QW gain media is discussed in Sect. 18.10. The temperature analysis of the lasing characteristics of GaInNAs QW lasers with increasing N-content is also discussed in Sect. 18.11. Sections 18.12 and 18.13 discusses on the theoretical and the experimental evidence, respectively, of the impact of thermionic emission processes on the high-temperature lasing performances of GaInNAs QW lasers. Section 18.14 discusses on the novel nanostructure approaches with dilute nitride semiconductors to extend the emission wavelength to 1,550 nm regime on GaAs.

18.2 Metalorganic Chemical Vapor Deposition-Grown GaIn(N)As Quantum Well

All the lasers structures studied here were grown by low-pressure MOCVD. Trimethylgallium (TMGa), trimethylaluminium (TMAl), and trimethylindium (TMIn) are used as the group III sources and AsH_3, PH_3, and U-dimethylhydrazine (U-DMHy) are used as the group V sources. The dopant sources are SiH_4 and dielthylzinc (DEZn) for the n- and p-dopants, respectively.

A schematic diagram of the laser structure used for both GaInAs and GaInNAs QW active devices is shown in Fig. 18.1. The growth of the QW, barrier regions, and the optical confinement regions are performed at a temperature

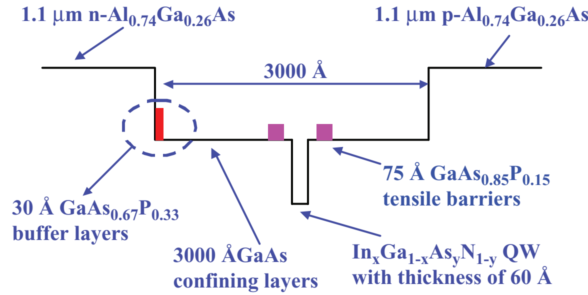

Fig. 18.1. Cross-sectional schematic conduction band diagram of the $Ga_{1-x}In_x N_{1-y}As_y$ QW lasers with tensile-strained $GaAs_{0.67}P_{0.33}$ buffer and $GaAs_{0.85}P_{0.15}$ barrier layers

of 530°C. The active regions typically consist of GaInAs and GaInNAs QWs with an In-content of approximately 40% and thickness of 60 Å. The lower and upper cladding layers of the lasers consist of $Al_{0.74}Ga_{0.26}As$ layers with doping levels of $1 \times 10^{18}\,cm^{-3}$ for both the n and p cladding layers, respectively. The growth temperatures of the n and p $Al_{0.74}Ga_{0.26}As$ are 775 and 640°C, respectively. The annealing of the GaInNAs QW is accomplished during the growth of the top cladding layer at a temperature of 640°C, with duration of approximately 27 min. The GaInNAs QW is surrounded by tensile-strain barriers of $GaAs_{0.85}P_{0.15}$, which are spaced 100 Å on each side of the QW. The tensile-strained buffer layer consists of a 30 Å $GaAs_{0.67}P_{0.33}$, which we found to be crucial for the growth of the highly strained GaIn(N)As QW materials on top of a high Al-content lower cladding layer [8, 9].

One of the challenges in growing GaInNAs QWs with an In-content of 40% by MOCVD is due to the difficulties in incorporating N into the GaInAs QW, while maintaining a high optical quality film. The low purity of the N-precursor used in MOCVD (U-DMHy) is also suspected as a possible reason for the low optical quality of MOCVD-grown GaInNAs QWs. To incorporate sufficient N into the GaInNAs QW, very large [DMHy]/V (as high as 0.961 or high) is required. Because of the high-cost and the low-purity of the DMHy precursor, lowering the $[AsH_3]$/III to achieve large [DMHy]/V would be the preferable option to increasing the DMHy flow. Large [DMHy]/V ratio requires the $[AsH_3]$/III ratio to be rather low. Takeuchi et al. [7, 26] has demonstrated that the growth of GaInAs QW ($\lambda = 1{,}200$ nm) with the very low $[AsH_3]$/III ratio is significantly more challenging compared to the case in which tertiary butyl arsine (TBA) is utilized as the As-precursor. As the $[AsH_3]$/III ratio is reduced, the luminescence of the GaInAs QW reduces rapidly for low $[AsH_3]$/III (below 15–20), which is however required for achieving sufficiently large [DMHy]/V. These challenges have resulted in difficulties in realizing high performance MOCVD-GaInNAs QW lasers with AsH_3 as the As-precursor until recently [3, 8, 9]. In our approach, the design of the active region is based on strain-compensated GaInNAs QW,

with very high In content (In ∼ 40%) and minimum N content (N ∼ 0.5%), to achieve 1,300 nm emission. Minimum N content in the GaInNAs QW allows us to grow the active region with an optimized AsH_3/III ratio. The growth rates for both $In_{0.35}Ga_{0.65}As_{0.992}N_{0.008}$ and $In_{0.4}Ga_{0.6}As_{0.995}N_{0.005}$ QW active regions are approximately 1.182 and 1.278 μm h^{-1}, respectively. The [AsH_3]/III, V/III, and [DMHy]/V ratios for $Ga_{0.6}In_{0.4}N_{0.005}As_{0.995}$ QW (and $Ga_{0.65}In_{0.35}N_{0.008}As_{0.992}$ QW) active regions are kept at approximately 12 (and 13), 403 (and 437), and 0.969 (and also 0.969), respectively.

All our GaInAs QW [23–25] and GaInNAs QW [8–14] lasers utilize strain-compensation techniques that are based on GaAsP-tensile barrier layers. The utilization of larger band gap barrier materials will potentially lead to suppression of thermionic carrier leakage, which will in turn lead to a reduction in the temperature sensitivity of the threshold current density of the lasers, in particular at high temperature operation [38].

18.3 Lasing Characteristics of 1,200 nm GaInAs

The early pursuit of the GaInNAs material systems focuses on the lattice-matched QW materials, which requires relatively large N-content in the range of 2.5–3%, for achieving emission in the 1,300–1,550 nm wavelength regimes [1].

Unfortunately, the early GaInNAs QW lasers suffer from poor lasing performance due to the utilization of nearly lattice-matched GaInNAs [1, 2]. Recently various groups utilizing In-content as high as 30–40% have been able to realize high-performance GaInNAs QW lasers in the wavelength regime of 1,280–1,300 nm [3–17].

In our previous work, GaInNAs QW lasers with an In-content of 40% and N-content of only 0.5% have been realized with threshold current densities of only 210 A cm^{-2} at an emission wavelength of 1,295 nm [9]. From studies on GaInNAs QW lasers with In-content of 35–43% [8,14], we also observe a trend toward reduction in the threshold current densities for 1,300 nm GaInNAs-QW lasers with increasing In content. Therefore, it is extremely important to realize high-performance GaInAs QW lasers with very long emission wavelength, such that it requires a minimal amount of N in the QW to push the emission wavelength to 1,300 nm.

Here we present high-performance GaInAs QW lasers with an emission wavelength beyond 1,230 nm, utilizing GaAsP tensile-strained buffer and barrier layers. The high Al content AlGaAs lower cladding layer introduces a slight compressively strained template prior to the growth of the highly strained active region. The tensile-strained GaAsP buffer layer (Fig. 18.1) acts to partially strain-compensate the QW growth template, leading to an improved optical quality for the highly strained GaIn(N)As QW. High optical luminescence intensity from the highly strained GaIn(N)As QW is only obtained with the utilization of the tensile buffer layer [8, 9].

All of the laser structures reported here are realized by low-pressure MOCVD. TMGa, TMAl, and TMIn are used as the group III sources. The group V precursors used here are AsH_3 and PH_3. The dopant sources are SiH_4 and DEZn for the n and p dopants, respectively. The composition of the QW is characterized by high-resolution X-ray diffraction experiments, and has been elaborated in our earlier work [24].

The schematic band diagram of the 1,200 nm laser structure is shown in Fig. 18.1, which is identical with that of the laser structure previously studied for 1,300 nm GaInNAs QW lasers [9] except for the active region. The active region is based on the 60 Å $In_{0.4}Ga_{0.6}As$ QW, sandwiched by barrier regions of 100 Å GaAs on each side. The strain compensation of the active region is provided by the 75 Å $GaAs_{0.85}P_{0.15}$ tensile barriers, which are grown before and after the GaAs barrier regions. The optical confinement factor for the GaInAs QW is calculated as approximately 1.7%. The growths of the active region and the optical confinement regions utilize $[AsH_3]/III$ ratio in excess of 100, at a reactor temperature of approximately 530°C. The n-cladding and p-cladding layers are based on $Al_{0.74}Ga_{0.26}As$ material system, grown at 775 and 640°C, respectively. Both cladding layers are designed with doping level of approximately $1 \times 10^{18}\,cm^{-3}$. The tensile buffer layer consists of a 30 Å $GaAs_{0.67}P_{0.33}$, which we found to be crucial for the growth of the highly strained GaInAs(N) QW material system on top of a high Al-content lower cladding layer [8, 9].

The room-temperature photoluminescence of the 60 Å $In_{0.4}Ga_{0.6}As$ QW active material is presented in Fig. 18.2, along with that of an 80 Å $Ga_{0.65}In_{0.35}As$ QW for comparison. The peak emission wavelength of the $Ga_{0.6}In_{0.4}As$ QW is measured at approximately 1,210–1,215 nm, which is 50–60 nm longer than that of the $Ga_{0.65}In_{0.35}As$ QW. The reduction in the

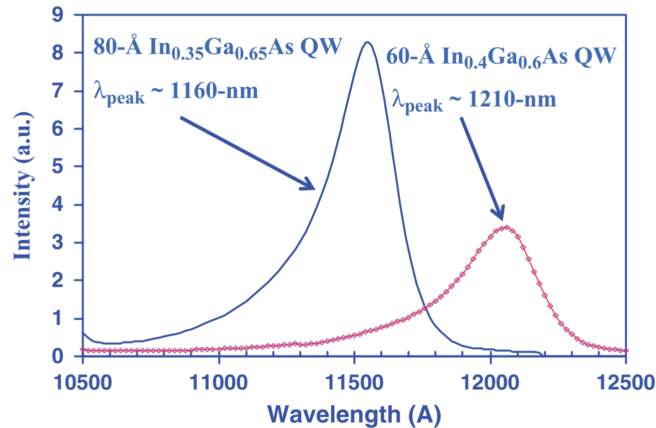

Fig. 18.2. PL spectra of 1,170 nm $Ga_{0.65}In_{0.35}As$ QW and 1,210 nm $Ga_{0.6}In_{0.4}As$ QW

optical luminescence of the $Ga_{0.6}In_{0.4}As$ QW ($\Delta a/a = 2.78\%$), in comparison to that of $Ga_{0.65}In_{0.35}As$ QW ($\Delta a/a = 2.45\%$), is presumably a result of a slight degradation in the crystal quality due to the higher strain of the 1,210 nm GaInAs QW.

The first step in developing high performance GaInNAs lasers is to establish an optimized growth process for high In-content GaInAs active devices operating near the 1,200 nm wavelength region. The addition of small quantities (<1%) of nitrogen can then be used to extend the emission wavelength to 1,300 nm.

The $Ga_{0.6}In_{0.4}As$ QW laser structure studied here uses strain compensation by $GaAs_{0.85}P_{0.15}$ tensile-strained barriers, as shown in Fig. 18.1. The laser utilizes an active region consisting of a 60 Å $Ga_{0.6}In_{0.4}As$ QW. From our earlier studies [8, 9], the existence of a slightly tensile-strained buffer layer is found to be essential for the realization of this laser structure. Broad area lasers with a stripe width of 100 μm are fabricated to characterize the device performance under pulsed conditions (pulse width of 5 μs, and duty cycle of 1%). The intrinsic physical device parameters can then be extracted from length-dependent studies performed on these lasers.

The room-temperature ($T = 20°C$) lasing spectrum for the 60 Å $Ga_{0.6}In_{0.4}As$ QW devices with cavity length of 1,000 μm is measured to be 1,233 nm, as shown in Fig. 18.3. The lasing emission wavelengths range from 1,216 to 1,233 nm, with little variation in threshold current densities (J_{th}). As shown in Fig. 18.3, the threshold current density of these $Ga_{0.6}In_{0.4}As$ QW lasers is found to be 90–92 A cm^{-2} for measurements at a heat-sink temperature of 20°C. The total external differential quantum efficiency (η_d) of the devices is measured as approximately 52%.

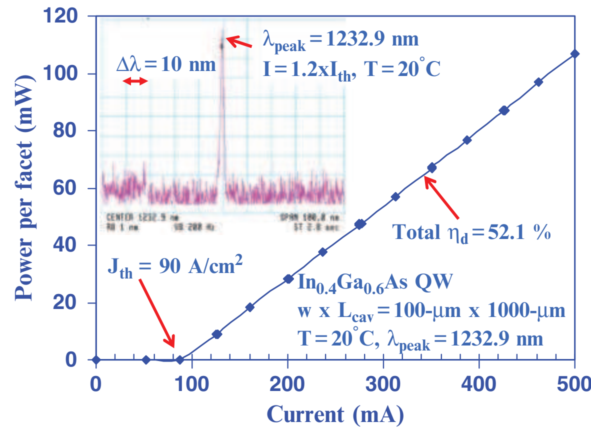

Fig. 18.3. Threshold current density (J_{th}) and external differential quantum efficiency (η_d) of 1,233 nm $Ga_{0.6}In_{0.4}As$ QW lasers ($L_{cav} = 1{,}000$ μm) as a function of temperature

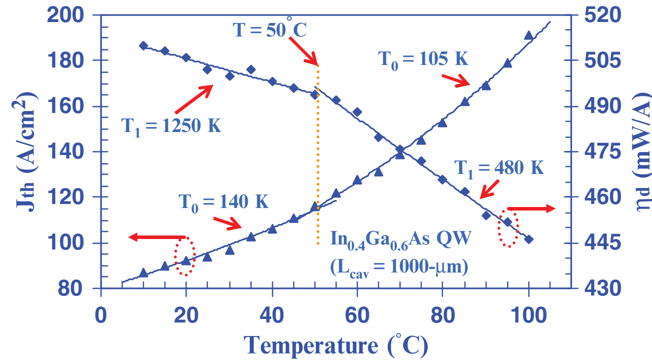

Fig. 18.4. The relation of output power per facet (P) and the total injected current (I) for $Ga_{0.6}In_{0.4}As$ QW lasers with a cavity length of 1,000 μm at a temperature of 20°C. The inset shows the lasing spectrum at 20°C.

The temperature characterization of these 1,233 nm GaInAs QW lasers, as shown in Fig. 18.4, is conducted from a temperature of 10°C up to a temperature of 50°C, with temperature steps of 5°C. In the temperature range of 10–50°C, the slope efficiency (η_d) hardly decreases with temperature, resulting in a T_1 value $(1/T_1 = (-1/\eta_d)\,d\eta_d/dT)$ of approximately 1,250 K based on our best fit. It is important to note that T_1 values of 1,250 K are significantly larger than those of 1,300 nm GaInNAs QW lasers. For 1,300 nm GaInNAs QW lasers with the same separate confinement heterostructure as the GaInAs active lasers and cavity length of 1,000 μm, we previously reported T_1 value of 255 K for measurements in temperature range of 20–60°C. The T_0 values $(1/T_0 = (1/J_{th})\,dJ_{th}/dT)$ are measured as 140 K. These reasonably high T_0 and T_1 values for $Ga_{0.6}In_{0.4}As$ QW lasers result in very low threshold current densities of only 160 and 190 A cm^{-2} are achieved for devices with cavity length of 1,000 μm at temperatures of 85 and 100°C, respectively.

Previously, we have reported room temperature threshold current densities of 65 and 100 A cm^{-2} for GaInAs QW lasers with emission wavelength of 1,170 and 1,190 nm, respectively [23, 24]. The transparency current densities for the 1,170 and 1,190 nm GaInAs QW lasers were measured as 30 and 58 A cm^{-2}, respectively, at room temperature [23, 24]. The material gain parameters (g_{oJ}) for both the 1,170–1,190 nm GaInAs QW lasers had previously been measured as 1,600–1,900 cm^{-1} [23, 24].

The comparison of the J_{th} of any QW laser is slightly more challenging, and at times could be deceptive when comparing various laser structures. Threshold current density of a QW laser typically depends on various factors, ranging from the quality of the QW active materials, the gain properties of the QW, the design of the separate confinement heterostructure (SCH) region, the choice of the compositions and doping levels of the cladding layers, and the modal threshold gain. Nevertheless, the comparison of the device performance

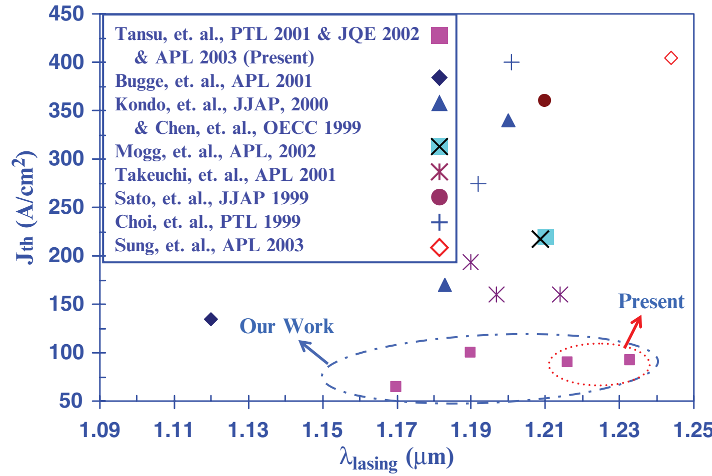

Fig. 18.5. Comparison of J_{th} of GaInAs QW lasers in the 1,100–1,250 nm wavelength regimes

in term of threshold current density is still of extreme importance, as this is generally the parameter of practical interest for laser diodes.

A comparison of the threshold current density of our GaInAs QW lasers with other published results [20–27,31,32,69] is shown in Fig. 18.5. The threshold current densities of the 1,233 nm $Ga_{0.6}In_{0.4}As$ QW (L_{cav} = 1,000 μm) and 1,170 nm $Ga_{0.65}In_{0.35}As$ lasers (L_{cav} = 1,500 μm) are approximately 90 and 65 A cm^{-2}, respectively. To the best of our knowledge, these results represent the lowest reported J_{th} values for any QW laser in the wavelength regime of 1,170–1,233 nm. It is also interesting to note that the J_{tr} and J_{th} of approximately 30 and 65 A $^{-2}$ for our 1,170 nm $Ga_{0.65}In_{0.35}As$ QW lasers is comparable with some of the best reported results realized by quantum dot (QD) active lasers in this wavelength regime. Recently, QD lasers at an emission wavelength of 1.15 μm with J_{th} and transparency current density (J_{tr}) of approximately 100 and 20 A cm^{-2}, respectively, are reported. [33]. The transparency current density in QD lasers is smaller as a result of the smaller active volume of the quantum dots. Although the J_{tr} is smaller, the threshold current density of the QD lasers is not significantly lower than the quantum well laser, from the fact that the QD active materials have a low material gain parameter. The relatively low g_o values of QD active material as a result of gain saturation leads to a modal material gain parameter (Γg_o) of approximately 4.5–9 cm^{-1} per QD stage [34,35], which is significantly lower than that of the typical Γg_o for a GaInAs QW laser (Γg_o = 30–45 cm^{-1} for a GaInAs QW).

18.4 Lasing Characteristics of GaInNAs Quantum Well Lasers

The structure of the GaInNAs laser is shown in Fig. 18.1, which is identical with the structure of GaInAs laser except for the active region. The active region utilized here consists of a 60 Å $Ga_{0.6}In_{0.4}N_{0.005}As_{0.995}$ QW. By utilizing this structure, low threshold and transparency current density, strain-compensated $Ga_{0.6}In_{0.4}N_{0.005}As_{0.995}$ QW lasers with high current injection efficiency (η_{inj}) were realized.

In characterizing the laser performance of the GaInNAs QW, broad area lasers with stripe widths of 100 µm are fabricated. The multilength studies of various broad area devices, with cavity lengths (L) ranging from 720 to 2,000 µm, are utilized to extract the intrinsic device parameters. All the measurements of these broad area devices were performed under pulsed conditions with a pulse width of 6 µs, and 1% duty cycle.

The measured threshold current density, at room temperature (20°C), for the GaInNAs QW lasers, is shown in Fig. 18.6 for various cavity length devices. The threshold- and transparency-current density is measured as low as 211 and 79–84 A cm^{-2}, respectively, for devices with cavity length of 2,000 µm, with an emission wavelength of 1.295 µm. Even for shorter cavity devices of 500, 720, and 1,000 µm, threshold current densities are measured as low as 450, 361, and 253 A cm^{-2} respectively. To the best of our knowledge, these data represent the lowest threshold and transparency current densities reported for GaInNAs QW lasers in the wavelength regime of 1.28–1.32 µm, as shown in Fig. 18.7 and Table 18.1.

The external differential quantum efficiency (η_d) of the GaInNAs QW lasers is as high as 57% for devices with cavity lengths of 720 µm. The lower η_d for the longer cavity devices is attributed to the relatively large internal loss ($\alpha_I = 10.3\,cm^{-1}$) for these unoptimized structures. The internal loss of the lasers may result from the combination of the narrow SCH region and

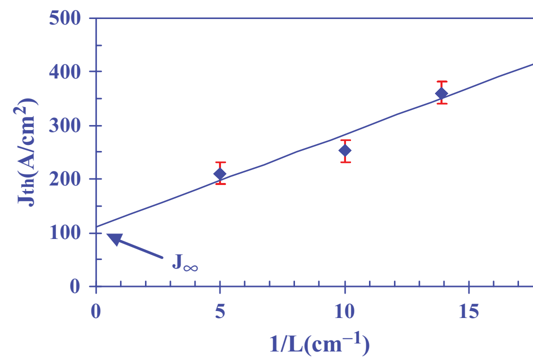

Fig. 18.6. The room-temperature J_{th} of the $Ga_{0.6}In_{0.4}N_{0.005}As_{0.995}$-$GaAs_{0.85}P_{0.15}$ QW as functions of inverse cavity length ($1/L$)

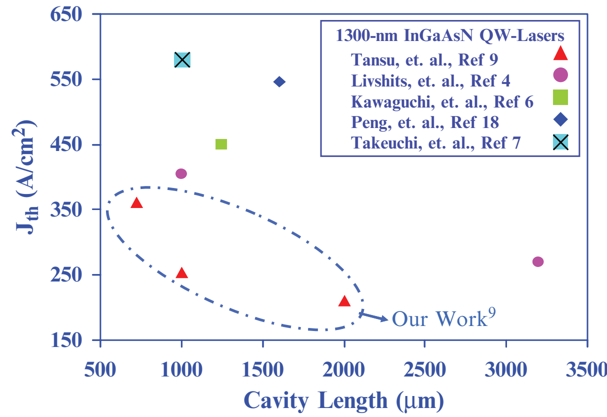

Fig. 18.7. Comparison of the threshold current density vs. cavity length for our 1,300 nm GaInNAs QW lasers with those from published results

Table 18.1. Threshold current densities comparisons for 1,300 nm regime GaInNAs QW lasers

	Growth	L (μm)	J_{th} ($\mathrm{A\,cm^{-2}}$)	J_{tr} ($\mathrm{A\,cm^{-2}}$)	η_{d} (%)	η_{inj} (%)	α_{i} ($\mathrm{cm^{-1}}$)	λ (μm)	T_{o} (K)	T_1 (K)
Livshits et al. [4]	MBE	3,200	270	110	45	93	4	1.3	75	–
		1,000	405	110	70	93	4	1.3	75	–
Ha et al. [17]	MBE	770	1,500	–	47	–	–	1.315	65	–
Peng et al. [18]	MBE	1,600	546	227	50	80	7	1.317	104	–
Wei et al. [15]	GS-MBE	3,000	1,150	–	23	82	9.76	1.3	122	–
Hohnsdorf et al. [5]	MOCVD	800	800	–	37	75	15	1.28	60	–
Sato et al. [3]	MOCVD	960	920	–	–	–	–	1.29	150	–
Kawaguchi et al. [6]	MOCVD	1,250	450	–	–	–	–	1.28	205	–
Takeucki et al. [7]	MOCVD	1,000	580	–	–	–	–	1.29	–	–
Tansu et al. [8]	MOCVD	750	400	110	51	72	6	1.29	110	416
		1,500	289	110	40	72	6	1.295	130	400
Tansu et al. [9]	MOCVD	720	361	75	57	97	13	1.29	82	360
	MOCVD	1,000	253	75	46	97	13	1.294	88	255
	MOCVD	2,000	211	75	33	97	13	1.295	90	200

relatively high doping level ($1 \times 10^{18}\,\mathrm{cm^{-3}}$) of the p-cladding of the laser. By utilizing a thin GaAsP buffer layer in place of GaInP/GaAsP buffer layer [8], improvement in the current injection efficiency ($\eta_{\mathrm{inj}} > 90$–95%) has been achieved as a result of removing the poor-interface between the InGaP-buffer and GaAs-SCH.

The material gain parameter, defined as $g_{\mathrm{oJ}} = g_{\mathrm{th}}/\ln(\eta_{\mathrm{inj}}J_{\mathrm{th}}/J_{\mathrm{tr}})$, is an important parameter in determining the threshold carrier density (n_{th}). Low

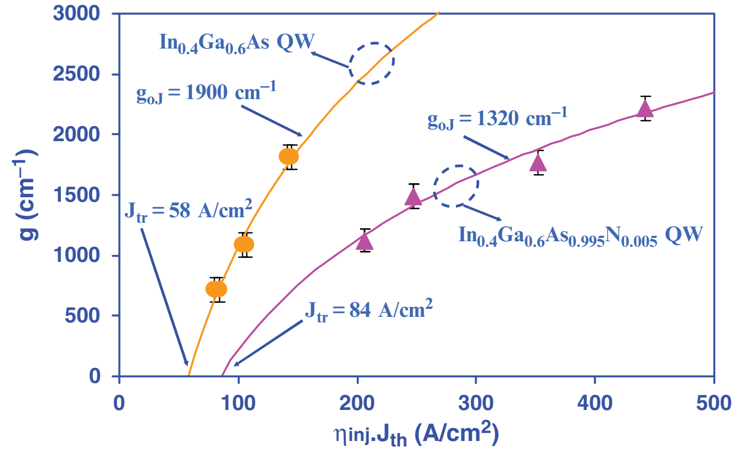

Fig. 18.8. Gain characteristics of GaInNAs QW and GaInAs QW lasers

$g_{\rm oJ}$ values for a QW laser lead to higher $n_{\rm th}$. Higher $n_{\rm th}$ will result in the possibility of an increase in Auger recombination, due to the $C{\rm n_{th}}^3$ behavior of the Auger recombination rate. Higher $n_{\rm th}$ will also lead to reduced current injection efficiency, due to a larger recombination in SCH and carrier leakage out of the QW. $g_{\rm oJ}$ and the differential gain $({\rm d}g/{\rm d}n)$ of the GaInNAs QW have been shown to decrease as nitrogen is introduced into the GaInAs QW [29,30]. As shown in Fig. 18.8, the $\rm g_{oJ}$ of the GaInNAs QW laser is measured as approximately 1,200–1,300 cm^{-1}, which is significantly lower than that ($g_{\rm oJ}$ = 1,600–1,900 cm^{-1}) of similar GaInAs QW lasers [22, 26] at λ = 1,170–1,190 nm. The GaInNAs active devices, with emission wavelengths of 1.29–1.295 µm, exhibit relatively low temperature sensitivity with T_0 values of 82–90 K for devices with cavity lengths of 720–2,000 µm. The T_1 values are measured to be in the range from 200–360 K for devices with L of 720–2,000 µm.

The continuous wave (CW) operation characteristics of the GaInNAs QW lasers were measured from laser devices with facet coatings of high reflective (HR) and antireflective (AR) layers. The HR layers consist of three pairs of Al_2O_3/Si with reflectivity in excess of 95%, and the AR layer was formed by a single layer of Al_2O_3 with reflectivity estimated to be in the range 7–10%. The devices were mounted junction down on copper heatsinks, and they were measured under CW operation for cavity lengths of 1,000–2,000 µm at temperatures in the range of 10–100°C.

The measured CW output-power ($P_{\rm out}$) characteristics, as a function of the injected-current (I) and the heat-sink temperature (T), are shown in Fig. 18.9. The CW measurements of the GaInNAs-QW lasers are measured up to a temperature of 100°C, limited by our equipment. The near threshold ($I \sim$ 1.2 $I_{\rm th}$) emission wavelengths of the GaInNAs QW lasers with cavity length of

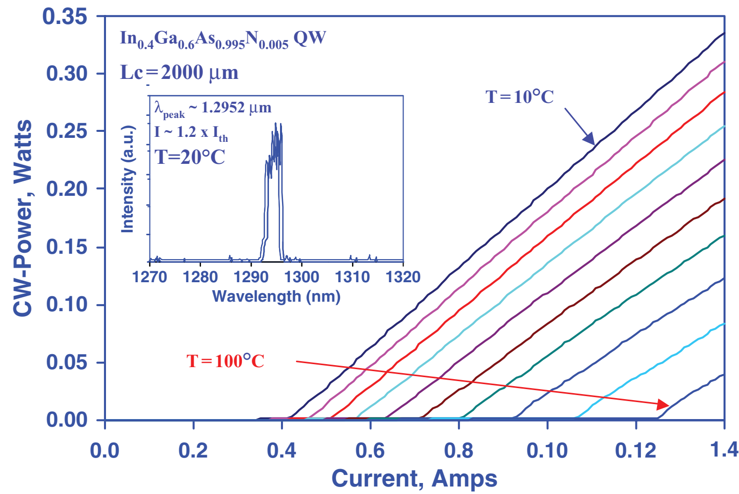

Fig. 18.9. CW P-I and spectrum of GaInNAs laser with $L_{cav} = 2{,}000\,\mu m$, as a function of temperature

2,000 µm are measured as approximately 1,295.2 and 1,331 nm, at temperature of 20 and 100°C, respectively.

The measured threshold current density of the HR/AR-coated GaINAs-QW laser devices under CW operation is very comparable with that of the as-cleaved GaInNAs QW laser devices with cavity length of 2,000 µm. Despite the large internal loss of our lasers (α_i is approximately 13 cm^{-1}), the threshold current density of the lasers with cavity length of 2,000 µm is measured as 210–220 A cm^{-2}, at a temperature of 20°C under CW operation. At elevated temperatures of 80 and 100°C, the threshold current densities of the HR/AR-coated ($L_{cav} = 2{,}000\,\mu m$) lasers are measured as only 455 and 615 A cm^{-2}, respectively, under CW operation.

The maximum CW output powers achievable from the 1,300 nm GaInNAs-QW lasers are approximately 1.8 W for cavity-lengths of both 1,000 and 2,000 µm, at heat-sink temperatures of 20°C. Figure 18.10 shows the measured output power characteristics for devices with $L_{cav} = 1{,}000\,\mu m$. This result represents the highest CW output power reported for 1,300 nm GaInNAs QW lasers grown by MOCVD at heat-sink temperatures of 20°C. The maximum wall plug efficiency for the cavity length of 1,000 µm is approximately 28%, limited by the large internal loss ($\alpha_I = 13\,cm^{-1}$). Further improvements in the external differential quantum efficiency of GaInNAs QW lasers can be achieved by utilizing a broad waveguide structure to minimize the internal loss.

To compare the lasing performance of the 1,300 nm GaInNAs QW lasers with those of the conventional InP technology, we list the published results that represent among the best performance 1,300 nm diode lasers based on conventional InP technology (GaInAsP-QW [36] and GaInAlAs-QW [37]), as shown in Fig. 18.11. Because of the low material gain parameter, carrier

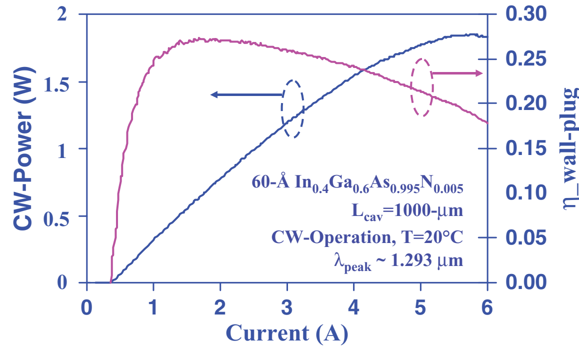

Fig. 18.10. CW output power characteristics for GaInNAs laser

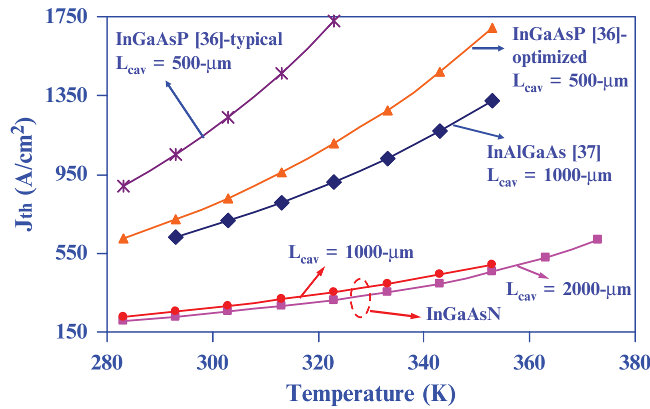

Fig. 18.11. Comparison of $J_{\rm th}$ for GaInNAs, AlGaInAs, and GaInAsP active lasers as a function of temperature

leakage, and Auger recombination, typically 1,300 nm GaInAsP-InP QW lasers require multiple QWs, ranging from 9–14 QWs [36]. The 1,300 nm GaInAlAs QW requires approximately 4–6 QWs for optimized structures [37]. For optimized 1,300 nm GaInAsP-QW structures, the threshold current densities of approximately 1,650–1,700 A cm^{-2} were achieved for devices with cavity length of 500 μm at operation temperature of 80°C, as reported by Belenky et al. [36]. The threshold current density of the 1,300 nm diode lasers based on the GaInAlAs QW on InP, with cavity length of 1,000 μm, has been reported as approximately 1,350 A cm^{-2} at temperature of 80°C [37]. The GaInNAs QW lasers require only a single QW active region for high temperature operation, owing to the larger material gain parameter and better electron confinement in the QW. Our 1,300 nm GaInNAs single QW as-cleaved diode lasers, with cavity-length of 500 and 1,000 μm, have threshold current densities of only 940 and 490 A cm^{-2}, respectively, at heat sink temperature of 80°C.

18.5 1,300 nm GaInNAs Multiple Quantum Well Lasers

Typically a single quantum well is sufficient for application in a conventional edge emitting diode laser. There are other types of devices that require a multiple quantum well structure as the active region for realizing higher threshold gains and improving the carrier injection efficiency. VCSELs are excellent examples of such devices that require higher gain active regions, due to the significantly higher mirror loss in VCSEL. A concern related to the high In content GaInAs(N) QW is related to the feasibility of implementing several quantum well (MQW) layers without material degradation due to the high strain.

The 1,300 nm GaInNAs double-QWs structure is shown schematically in Fig. 18.12. The laser structure studied here consists of a 60 Å GaInNAs double QW (DQW) active region, with strain compensation from $GaAs_{0.85}P_{0.15}$ tensile-strained barriers. The optical confinement and the cladding layers of this laser are kept identical to that of the SQW structure shown in Fig. 18.1. Similar to that of the single QW structure, thermal annealing of the GaInNAs double-QW structure is conducted at 640°C for 27 min.

The room temperature lasing spectrum of the GaInNAs-DQW devices with a cavity length of 1,500 μm was measured at 1,315 nm with a J_{th} of approximately 410 A cm^{-2}. The slightly longer emission wavelength of the DQW lasers, in comparison to that of the single QW lasers, can be attributed to smaller quasi-Fermi level separation at threshold. The J_{tr} and the g_{oJ} values for the GaInNAs double-QW lasers are measured as approximately 200 A cm^{-2} and 2,520 cm^{-1}, respectively, as shown in Fig. 18.13. The scaling of the J_{tr} and g_{oJ} values with number of quantum wells is in excellent agreement with theory, a good indication of the feasibility to implement highly strained GaInNAs DQWs for VCSELs structures.

The 1,300 nm GaInNAs triple QWs (3-QWs) structure is shown schematically in Fig. 18.14. The laser structure studied here consists of a 60 Å GaInNAs triple-QWs active region, with strain compensation from $GaAs_{0.85}P_{0.15}$ tensile

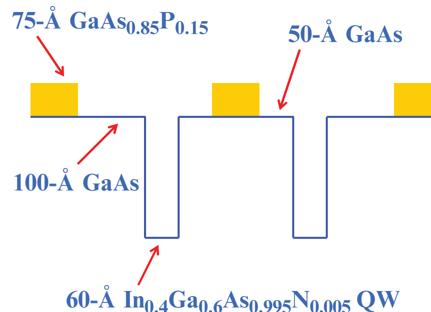

Fig. 18.12. Schematic energy diagram of the active region for the GaInNAs double QWs structures

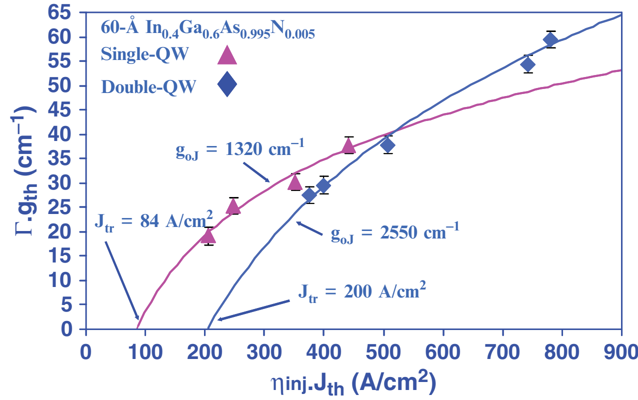

Fig. 18.13. Gain characteristics of the GaInNAs single QW and GaInNAs double-QWs

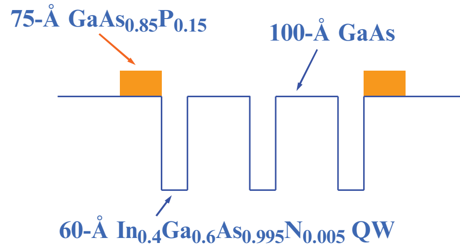

Fig. 18.14. Schematic energy diagram of the active region for the GaInNAs triple-QWs structures

strained barriers only surrounding the outer QWs. The optical confinement layer and the cladding layers of this laser are kept identical to that of the SQW structure shown in Fig. 18.1. Similar to that of the single QW and double QWs structures, thermal annealing of the GaInNAs triple-QWs structure is conducted at 640°C for duration of 27 min.

Threshold current density of only 505 A cm^{-2} was achieved for the GaInNAs triple-QWs laser devices (L_{cav} = 1,000 μm), with emission wavelength of 1,290 nm at room temperature. The measured T_0 values for the triple QWs lasers are approximately 110 K, for measurements in the temperature range of 20–60°C. The excellent lasing performance of the triple-QWs structures is a good indication of the feasibility of implementing these triple QWs structures into VCSELs structures.

18.6 1,300 nm GaInNAs Single Quantum Well Lasers with Higher N Content

The lasing characteristics of 1,300 nm GaInNAs QW lasers with higher N-content are fabricated and analyzed for comparison purposes. Higher N content (0.8%) GaInNAs QW lasers are fabricated using lower In-content

(35%) to keep the emission wavelength fixed at 1,300 nm. The thickness of the $Ga_{0.65}In_{0.35}N_{0.008}As_{0.992}$ single QW structure is adjusted to approximately 80 Å. The In and N compositions are calibrated with SIMS and XRD measurements. In our experiment here, only the active region of the structure, as shown in Fig. 18.1, is replaced with the 80 Å $Ga_{0.65}In_{0.35}N_{0.008}As_{0.992}$ single QW. The utilization of lower In content GaInNAs QW active region allows us to increase the thickness of the QW to 80 Å, which would lead to reduction of quantum size effect. Reduced quantum size effect in lower In content GaInNAs QW will also minimize its N-content requirement to achieve 1,300 nm emission wavelength.

The room temperature lasing spectrum of the $Ga_{0.65}In_{0.35}N_{0.008}As_{0.992}$ single QW devices with a cavity length of 1,500 μm was measured at 1,305 nm with a J_{th} of approximately 417 A cm^{-2}. As shown in Fig. 18.15, the transparency current density of the 1,300 nm $Ga_{0.65}In_{0.35}N_{0.008}As_{0.992}$ is estimated as approximately 144 A cm^{-2}, which is almost a factor of two higher in comparison to that of the 1,300 nm $Ga_{0.6}In_{0.4}N_{0.005}As_{0.995}$ single QW.

Approximately 25% of the increase in its J_{tr} value, in comparison to that of 60 Å $Ga_{0.6}In_{0.4}N_{0.005}As_{0.995}$ QW, can be attributed to the 25% thicker dimension of the 80 Å $Ga_{0.65}In_{0.35}N_{0.008}As_{0.992}$ QW. The remaining 70–75% increase in the J_{tr} value of $In_{0.35}Ga_{0.65}As_{0.992}N_{0.008}$ QW lasers, in comparison to that of $Ga_{0.6}In_{0.4}N_{0.005}As_{0.995}$ QW, can be attributed to several other factors, including increase in monomolecular recombination processes, carrier leakage, or other processes. The material gain parameter (g_{oJ}) of the $Ga_{0.65}In_{0.35}N_{0.008}As_{0.992}$QW is measured as 1,265 cm^{-1}, as shown in Fig. 18.15.

The T_0 and T_1 values of the $Ga_{0.65}In_{0.35}N_{0.008}As_{0.992}$ QW lasers are found to be significantly lower in comparison to those of the $Ga_{0.6}In_{0.4}N_{0.005}As_{0.995}$ QW lasers, as shown in Figs. 18.16 and 18.17, respectively. T_0 and T_1 values of only 75–80 K and 100–150 K, respectively, are measured for

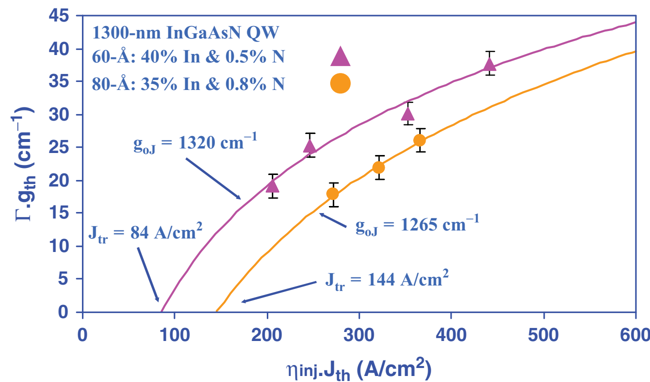

Fig. 18.15. Gain characteristics of the 60 Å $Ga_{0.6}In_{0.4}N_{0.005}As_{0.995}$ single QW and the 80 Å $Ga_{0.65}In_{0.35}N_{0.008}As_{0.992}$ single QW

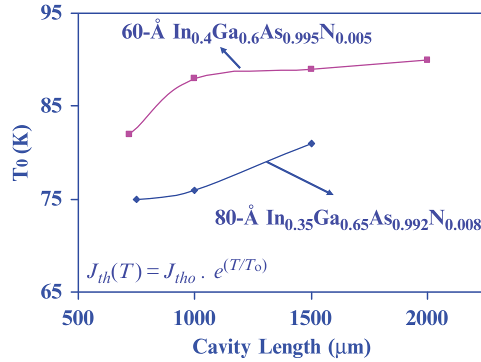

Fig. 18.16. The T_0 comparison for 80 Å $Ga_{0.65}In_{0.35}N_{0.008}As_{0.992}$ single QW and 60 Å $Ga_{0.6}In_{0.4}N_{0.005}As_{0.995}$ single QW lasers, for temperature range of 20–60°C

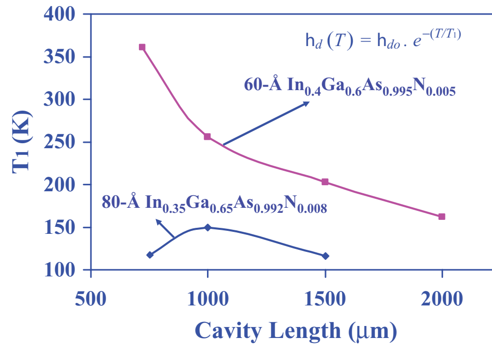

Fig. 18.17. The T_1 comparison for 80 Å $Ga_{0.65}In_{0.35}N_{0.008}As_{0.992}$ single QW and 60 Å $Ga_{0.6}In_{0.4}N_{0.005}As_{0.995}$ single QW lasers, for temperature range of 20–60°C

$Ga_{0.65}In_{0.35}N_{0.008}As_{0.992}$ QW lasers with cavity lengths from 750 to 1,500 μm. Careful studies are still required to clarify the mechanisms that lead to the lower T_0 values in these higher N content GaInNAs QW lasers, in spite of their higher J_{th}. Possible mechanisms of the lower T_0 and T_1 values include the increase in carrier leakage from a reduction in the hole confinement for higher N-content GaInNAs QW lasers, which would also lead to a more temperature sensitive current injection efficiency.

18.7 1,320 nm GaInNAs Quantum Well Lasers with GaNAs Barriers

In earlier sections, promising results [4, 6–19] have shown tremendous potential for GaInNAs QW lasers as an alternative material system to replace the conventional technology in the wavelength regime of 1,300 nm. GaInNAs

QW lasers have demonstrated impressive results for devices with emission wavelength slightly below or at 1,300 nm [4, 6–19].

Only few results of 1,300 nm GaInNAs QW lasers with GaNAs barriers grown by MBE have been realized with reasonably good lasing performance at emission wavelengths beyond 1,315 nm [17–19]. The utilization of GaNAs barriers surrounding the GaInNAs QW has been pursued previously by several other groups utilizing MBE technology [17–19]. Most of these pursuits have the intention of achieving slightly longer emission wavelength beyond 1,300 nm, by reducing the quantum confinement effect. An additional benefit from the utilization of tensile strained GaNAs barriers is the strain compensation of the highly compressively strained GaInNAs QW.

The method that we pursue here is to utilize a GaInNAs QW lasers with GaNAs barriers grown by MOCVD. In addition to a reduction in the quantum confinement effect, we also find improvements in the lasing characteristics at elevated temperatures, presumably as a result of stronger hole confinement.

All the laser structures reported here are realized by low pressure MOCVD, similar with the growth processes and conditions described in Sect. 18.2. The design of the laser structure is shown in Fig. 18.18, with the active region composed of a 60 Å $Ga_{0.6}In_{0.4}N_{0.005}As_{0.995}$ QW surrounded by 35 Å $GaN_{0.03}As_{0.97}$ tensile strained barriers on each side. The composition of the GaInNAs QW and GaNAs barriers was determined using HR-XRD and SIMS. The active region and GaNAs barrier regions are embedded symmetrically inside a 3,000 Å undoped-GaAs optical confinement region and $Al_{0.74}Ga_{0.26}As$ cladding layers, resulting in an optical confinement factor of 1.7% similar with that of structure in Fig. 18.1. Broad area lasers are fabricated with a stripe width of 100 μm, with similar structures and fabrications steps with those of the laser structures described in earlier sections.

As-cleaved laser devices are characterized under pulsed conditions, with a pulse width of 5 μs and duty cycle of 1%, for various cavity lengths ranging from 750 to 2,000 μm at room temperature ($T = 20°C$). The room temperature ($T = 20°C$) threshold current density and near threshold lasing spectrum of a GaInNAs-GaNAs QW laser with a cavity length of 750 μm are

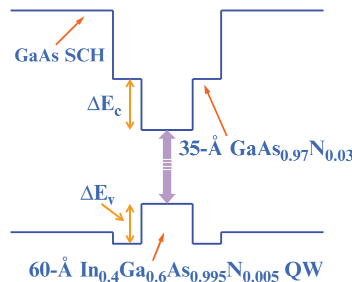

Fig. 18.18. Schematic band diagram of the $Ga_{0.6}In_{0.4}N_{0.005}As_{0.995}$ QW active region with $GaN_{0.03}As_{0.97}$ barriers

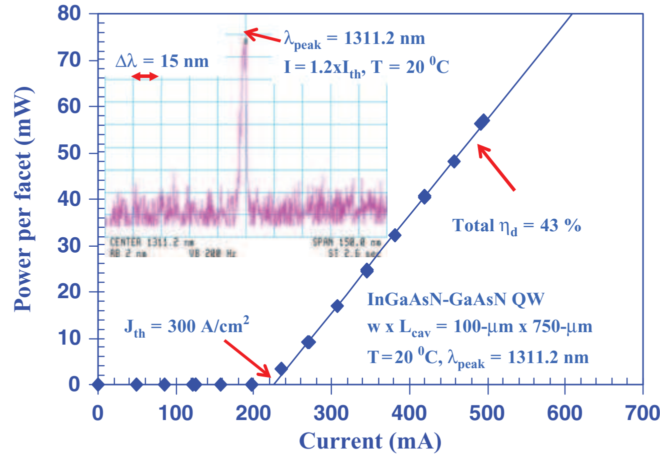

Fig. 18.19. The relation of output power per facet (P) and the total injected current (I) for $Ga_{0.6}In_{0.4}N_{0.005}As_{0.995}$ QW lasers with $GaN_{0.03}As_{0.97}$ barriers (L_{cav} = 1,500 μm) at a temperature of 20°C. The inset shows the lasing spectrum at 20°C

measured as 300 A cm^{-2} and 1,311 nm, respectively, as shown in Fig. 18.19. A redshift of approximately 20–25 nm in emission wavelength was observed for the GaInNAs-GaNAs QW lasers compared to those of our previously reported GaInNAs-GaAs structures [9], resulting in emission wavelength of 1,317 nm for devices with a cavity length of 1,500 μm. Threshold current densities of only 270, 230, and 210 A cm^{-2} are measured for devices with cavity lengths of 1,000, 1,500, and 2,000 μm, respectively. Total external differential quantum efficiency as high as 43–46% (420–430 mW A^{-1}) was also obtained for devices with a cavity length of 750 μm. The internal loss and the above threshold current injection efficiency of the GaInNAs-GaNAs QW lasers are measured as approximately 9 cm^{-1} and 70%, respectively.

The gain characteristics of the GaInNAs QW lasers in these studies are assumed to follow the conventional semi-logarithmic relation of $g_{th} = g_{oJ} \ln(\eta_{inj} J_{th}/J_{tr})$, with g_{oJ} defined as the material gain parameter. From measurements of devices with various cavity lengths, the material gain parameter (g_{oJ}) and the transparency current density (J_{tr}) have been determined to be approximately 1,320 ± 50 cm^{-1} and 75 ± 5 A cm^{-2}. The measured g_{oJ} and J_{tr} of the GaInNAs-GaNAs QW lasers reported here are comparable to those of GaInNAs QW lasers with GaAs barriers ($g_{oJ} \sim$ 1,150–1,200 cm^{-1} and $J_{tr} \sim$ 75–80 A cm^{-2}) [9]. We find, the choice of the barrier material surrounding the GaInNAs QW is very important, affecting primarily the threshold characteristics of the lasers at elevated temperatures.

The characteristics of the GaInNAs-GaNAs QW lasers are measured from temperatures of 10–100°C, with temperature steps of 5°C. In the temperature range from 10 to 50°C, the T_0 values ($1/T_0 = (1/J_{th})\,\mathrm{d}J_{th}/\mathrm{d}T$) of these

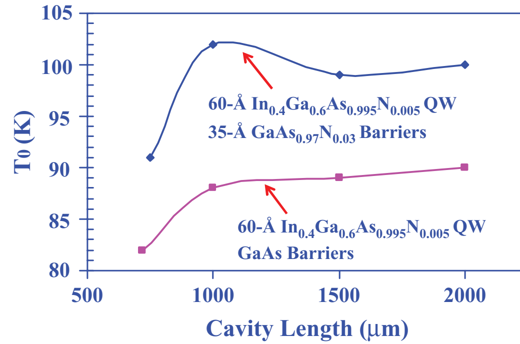

Fig. 18.20. The comparison of T_0 values, measured from temperature of 10–50°C, for $Ga_{0.6}In_{0.4}N_{0.005}As_{0.995}$ QW lasers with $GaN_{0.03}As_{0.97}$ barriers and GaAs barriers, for various cavity lengths

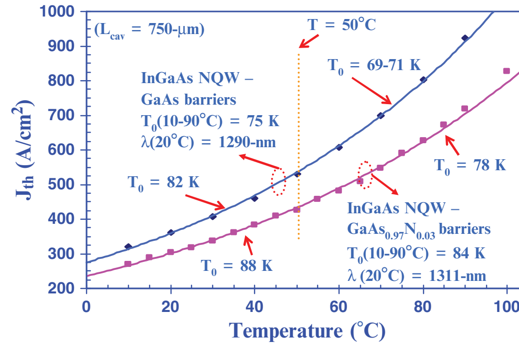

Fig. 18.21. Threshold current densities of $Ga_{0.6}In_{0.4}N_{0.005}As_{0.995}$-$GaN_{0.03}As_{0.97}$ QW and $Ga_{0.6}In_{0.4}As_{0.995}N_{0.005}$ – GaAs QW lasers devices with cavity length of 1,000 μm, as functions of temperature in the range of 10–90°C

lasers are measured as high as 100 K for devices with cavity lengths of 1,000 and 2,000 μm, as shown in Fig. 18.20. From our measurements on devices with various cavity lengths, the threshold characteristics of these 1,311–1,317 nm GaInNAs-GaNAs QW lasers is less temperature sensitive in comparison to the 1,290–1,295 nm GaInNAs QW lasers with GaAs barriers [9]. The increase in T_0 values for the GaInNAs-GaNAs QW lasers, in comparison to those of GaInNAs-GaAs QW lasers, is not accompanied by any increase in threshold current, as shown in Fig. 18.21. Very low threshold current densities of only 550 (and 520) A cm^{-2} and 715 (and 670) A cm^{-2} are also achieved for GaInNAs-GaNAs QW lasers with cavity-lengths of 1,500 and 750 μm, respectively, at a temperature of 90°C (and 85°C). The lasing wavelength shift with temperature is found to be a linear function with a rate ($d\lambda/dT$) of approximately 0.39 nm K^{-1}, resulting in emission wavelengths beyond 1,340–1,345 nm for devices with a cavity length of 1,500 μm at a temperature of 90°C.

In earlier works [17–19], aside from strain compensation, the motivation for using GaNAs barriers surrounding the GaInNAs QW is to reduce the quantum confinement effect, which in turn results in a redshifting of the emission from the QW. We demonstrate here that, in addition to the wavelength redshift, the utilization of GaNAs barriers surrounding the GaInNAs QW may also improve hole confinement in the QW, as evident from the improved temperature performance. The slight type-II alignment of the GaNAs material system to the GaAs material system has been previously reported with a very small negative valence band offset (ΔE_v) of 15–20 meV/%N [39–41], which would lead to a slight increase in the heavy hole confinement (ΔE_v) in GaInNAs QW, as shown schematically in Fig. 18.18.

To place the results reported here in perspective, we plot the best-reported threshold current densities for various GaInNAs QW lasers [4, 6–19] in Fig. 18.22. The previous lowest reported threshold current density of 546 A cm^{-2} for GaInNAs QW lasers with a cavity length of 1,600 μm at an emission wavelength of 1,317 nm was realized by utilizing MBE technology [18, 19]. To the best of our knowledge, the MOCVD-grown GaInNAs-GaNAs QW lasers reported here represent the lowest threshold current densities for wavelengths beyond 1,300 nm. Note that the threshold current densities plot (in Fig. 18.22) for our various GaInNAs QW lasers are taken from devices with cavity lengths of 1,000–2,000 μm, which exhibit slightly lower values in comparison to the shorter cavity devices (shown in Fig. 18.21, for $L_\mathrm{cav} = 750\,\mu\mathrm{m}$).

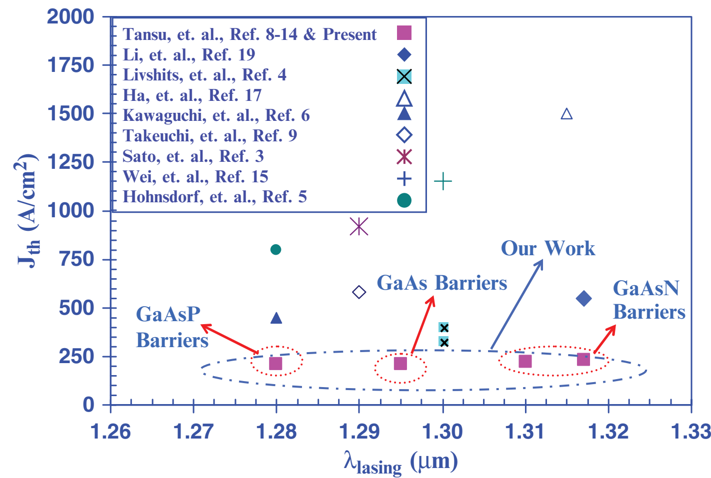

Fig. 18.22. Comparison of threshold current densities of GaInNAs QW lasers in the wavelength regimes of 1,260–1,330 nm

In summary, we have realized $Ga_{0.6}In_{0.4}N_{0.005}As_{0.995}$ quantum well lasers employing $GaN_{0.03}As_{0.97}$ barriers, with room-temperature emission wavelength of 1,311–1,317 nm. Threshold current density of approximately 300, 270, 230, and 210 A cm^{-2} are measured for these devices for cavity lengths of 750, 1,000, 1,500, and 2,000 μm, respectively. By changing only the barrier material from GaAs to GaNAs, we find improved device temperature characteristics in addition to a redshift in the emission wavelength. This improvement may be accounted for by the improved heavy-hole confinement in the GaNAs barrier structures. The weak dependency of the threshold current densities with emission wavelength for the range of 1,280–1,317 nm also indicates potential for high performance GaInNAs QW lasers with emission wavelength even beyond 1,320 nm.

18.8 Comparison of Metalorganic Chemical Vapor Deposition GaInNAs with Other GaInNAs in 1,300 nm Regimes

In the past several years, there has been a significant progress in the development of MOCVD-grown 1,300 nm GaInNAs QW lasers. The progress in the MOCVD-grown GaInNAs QW lasers is of extreme importance, due to its importance in realizing manufacturability GaInNAs QW VCSELs devices. The MOCVD growth technology is more compatible for realizing VCSELs devices, attributing to its higher growth rates. MOCVD technology also offers better compositional grading and doping control in the hetero-interfaces, which are essential for realizing low-resistive DBRs layers. The threshold current density comparisons of various GaInNAs QW lasers is shown in Table 18.1. The results presented here represent the best results for GaInNAs QW lasers in the wavelength regime of 1,300 nm. Our results of the 1,300 nm GaInNAs QW lasers are taken from the strain-compensated $Ga_{0.6}In_{0.4}N_{0.005}As_{0.995}$ QW active materials. Our 1,300 nm GaInNAs QW lasers are realized with transparency current densities of approximately 75–85 A cm^{-2} and 200–250 A cm^{-2}, respectively.

The transparency and threshold current densities of these 1,300 nm GaInNAs QW lasers that we realized here still represent the lowest transparency current densities ever reported for this wavelength regime. The best reported lasing performances of MBE-grown GaInNAs QW lasers are realized by Livshits et al. [4] and Peng et al. [18]. It is important to note that our reported results here still represent the only high-performance 1,300 nm GaInNAs QW lasers grown with conventional technology of AsH_3 as the As-precursor. Other MOCVD works with high performances, realized by Takeuchi et al. [26] and Kawaguchi et al. [6], utilized TBA as the As-precursor.

18.9 Single-Mode Ridge Waveguide 1,300 nm GaInNAs Quantum Well Lasers

Over the past several years, improved single-mode GaInNAs ridge waveguide (RWG) laser performance has been realized by MOCVD and MBE [42–46]. Illek and coworkers demonstrated MBE-grown lasers emitting at 1.28 μm with a threshold current of 11 mA under pulsed operation and a high-reflective coated facet (HR/as-cleaved) [42]. For MOCVD-grown GaInNAs RWG lasers, 1.295 μm emitting double quantum well devices with threshold currents of 75 mA under pulsed operation were reported by Sato and coworkers [45]. By utilizing strain-compensation technique of GaAsP barriers [9], we successfully achieve high-performance MOCVD-grown single-mode GaInNAs QW as-cleaved RWG lasers at 1.292 μm. The CW threshold current around 15 mA at room temperature is currently the best result reported by MOCVD growth technique and comparable to the best MBE result.

The laser structure and growth conditions here are similar with that described in Sect. 18.2 and 18.3, as shown in Figs. 18.1 and 18.23. It consists of a 6 nm $Ga_{0.6}In_{0.4}N_{0.005}As_{0.995}$ QW under a growth temperature of 530°C, with its composition calibrated by SIMS measurement. The growth rate of the QW is approximately 1.28 μm h^{-1}. On both sides of the GaInNAs QW, 75 Å $GaAs_{0.85}P_{0.15}$ tensile strain layers were employed for strain compensation with 100 Å GaAs setback layers. SCH consists of 300-nm undoped GaAs, with both n- and p-type cladding layers consisting of 1.1 and 0.9 μm thick $Al_{0.75}Ga_{0.25}As$ layers, respectively. The width and height of the ridge structure are 4 and 1 μm, respectively, formed by standard photolithography techniques and chemical wet etching with $NH_4OH : H_2O_2 : H_2O = 3 : 1 : 50$ solution. The lateral effective index step is calculated to be 0.023 using the effective index approximation and transition matrix method. A 1,000 Å thick SiO_2 layer was deposited by plasma enhanced chemical vapor deposition (PECVD) for current confinement and surface passivation. Alloys of Ti/Pt/Au and Ge/Ni/Au

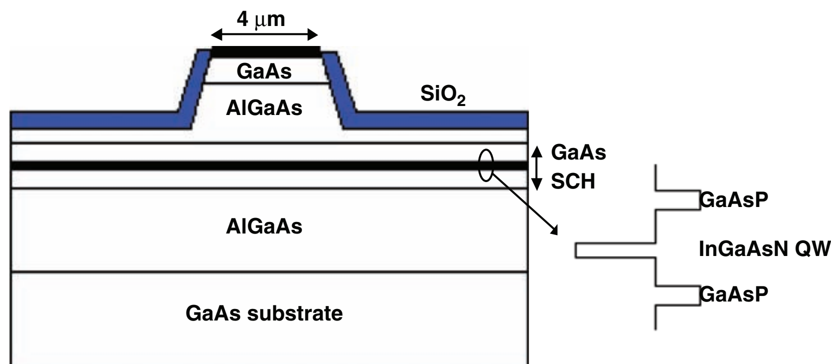

Fig. 18.23. Schematic device structure of the GaInNAs-GaAs RWG lasers

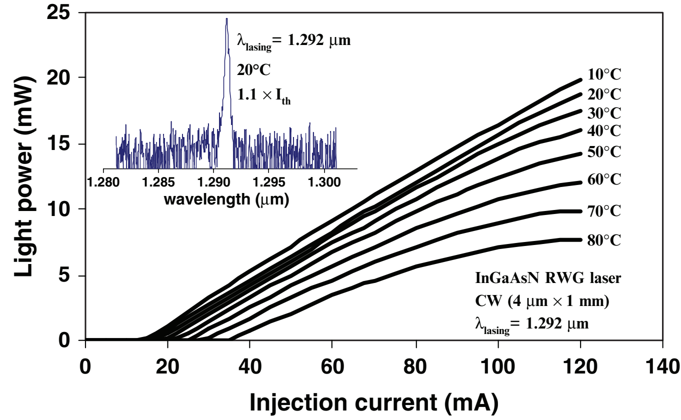

Fig. 18.24. Continuous-wave light–current characteristics of 4 μm × 1 mm single quantum well GaInNAs ridge waveguide lasers at various heat sink temperatures. *Inset*: Lasing spectrum at 20°C of 1 mm long as-cleaved devices. The peak wavelength is at 1.292 μm

for p- and n-type contact layers were deposited by e-beam evaporator and rapidly annealed at 370°C for 30 s under forming gas. The device schematic structure is shown in Fig. 18.23. The cleaved devices were mounted p-side up on copper heat sinks without facet coating for the light–current (P-I) and far field measurements under CW conditions.

Figure 18.24 shows the CW P-I curves of 1 mm long GaInNAs ridge waveguide lasers over a temperature range from 10 to 80°C. The threshold current is only 15.5 mA at 20°C, corresponding to threshold current density of 388 A cm^{-2}. This represents the lowest value reported for GaInNAs ridge waveguide lasers emitting at 1.3 μm, and is at comparable with conventional GaInAsP-InP QW lasers, showing promise for this material system [47–49]. The higher threshold current density compared to broad area devices (253 A cm^{-2}) with an identical structure is possibly due to lateral current spreading. With a shorter cavity length of 800 μm, the threshold current is only 14 mA. The maximum output power per facet is 24 mW at 20°C and reduces to 8 mW at 80°C limited by device heating. The turn-on voltage and device resistance were measured to be 1.15 V and 12 Ω, respectively. The relatively large series resistance (possibly a result of the high Al-content cladding layers) results in strong Joule heating in the junction and deteriorates laser maximum CW output power. The lasing spectrum is shown in Fig. 18.24 and the peak wavelength is 1.292 μm at 20°C. At 80°C, the lasing wavelength shifts to 1.32 μm with a wavelength temperature dependence $\lambda_{\text{lasing}}(T)$ of 0.5 nm°C^{-1}.

The GaInNAs RWG laser threshold current (I_{th}) and external differential quantum efficiency (η_{d}) characteristics as a function of heat sink temperature are shown in Fig. 18.25 for 1 mm long devices from 10 to 80°C. At 60°C, the

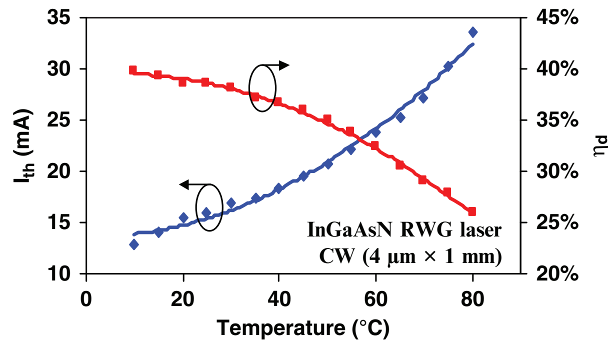

Fig. 18.25. Temperature dependence of threshold current and external differential quantum efficiency. The characteristic temperatures T_0 and T_1 are 93 and 227 K (20–60°C), respectively

threshold current increases to 23.8 mA and the measured T_0 is 93 K (20–60°C). Comparing η_d at 20 and 60°C, it decreases from 39 to 32% and the T_1 value is 227 K. The temperature dependence of the GaInNAs laser characteristics shows inferior performance compared to 1.23 µm emitting GaInAs RWG laser with an identical device structure, where T_0 and T_1 of 143 and 357 K were obtained. Nevertheless, a T_0 value of 93 K is significantly greater than the typical value of 50 K for conventional 1.3 µm emitting GaInAsP-InP ridge waveguide lasers [9, 47, 48] and quite comparable to AlGaInAs-InP QW lasers [50, 51].

At a heat sink temperature of 25°C, far field patterns (FFP) of the laser beam in the lateral direction have a full width half maximum (FWHM) of 20.7° for $I = 20$ mA and 22.2° for $I = 80$ mA. The field pattern indicates single mode operation for these RWG devices at low output power levels. At higher drive currents, multimode operation or beam instabilities occur. Utilization of a smaller ridge width (<3 µm) is expected to stabilize the optical mode to higher output powers.

In these experiments, low threshold single mode GaInNAs SQW as-cleaved ridge-waveguide lasers were achieved by metalorganic chemical vapor deposition. The threshold current is only 15.5 mA under continuous-wave operation for as-cleaved devices with 4 µm ridge width and 1 mm cavity length. For 800 µm long RWG lasers, the threshold current is only 14 mA. The lasing wavelength is 1.292 µm with a maximum output power of 24 mW at 20°C. T_0 and T_1 values of 93 and 227 K were obtained and show improved high-temperature characteristics compared to conventional InP-based ridge waveguide lasers. The lateral far field pattern indicates single mode operation near laser threshold.

18.10 Extension of GaInNAs Quantum Well Lasers Beyond 1,320 nm

Recent promising results [1–19] have shown tremendous potential for GaInNAs QW lasers with impressive results for devices emitting in the emission wavelength around 1,300 nm [1–19], as shown earlier in Sect. 18.3 up to Sect. 18.8, which indicate the feasibility of this material system as a promising alternative to replace the conventional InP-technology in the wavelength regime of 1,300 nm. Few results on GaInNAs QW lasers with emission wavelength around 1,370–1,400 nm have been published with reasonable lasing performance [5, 15, 17, 52, 53]. Threshold current densities of approximately 1.85–2.5 kA cm^{-2} [5, 15, 17, 52, 53] have been reported for GaInNAs QW lasers, grown MBE and MOCVD, in the wavelength regime of 1,370–1,400 nm. Several MOCVD-grown GaInNAs QW lasers have been demonstrated with threshold current densities of 2.5 and 2.2 kA cm^{-2} for emission wavelengths of 1,370 nm [52] and 1,380 nm [5], respectively. Recent effort, utilizing chemical beam epitaxy (CBE), has also resulted in 1,400 nm GaInNAs QW lasers with threshold current density of approximately 8.9 kA cm^{-2} [54]. Realization of low threshold current density and temperature-insensitive 1,400 nm diode lasers is essential for high-performance and low-cost pump lasers for Raman amplifiers.

Here we report high performance GaInNAs QW lasers on GaAs with emission wavelength ranging from 1,360 to 1,382 nm, by utilizing low-pressure MOCVD. The design of the active region utilizes a highly compressive, very high In-content (40%), GaInNAs QW, with a minimal N content of approximately 1%, to achieve emission wavelengths at 1,360 and 1,382 nm. Tensile-strained barriers of GaAsP are utilized to partially strain-compensate the QW active region.

The laser structures studied here, as shown in Fig. 18.1, consist of a 60 Å ($\Delta a/a = 2.7\%$) $In_{0.4}Ga_{0.6}AsN$ single QW active layer with GaAs layers bounding the QW. Partial strain compensation of the highly strained GaInNAs QW is achieved by utilizing $GaAs_{0.85}P_{0.15}$ tensile-strained layers offset from the QW [8, 9], and a tensile-strained buffer layer of $GaAs_{0.67}P_{0.33}$ [9] as shown in Fig. 18.1. The benefit and purpose of the various strain compensating layers have been demonstrated and elaborated on in our earlier studies discussed in Sects. 18.2 and 18.3. The lower- and top-cladding layers of the lasers consist of 1.1 μm thick $Al_{0.74}Ga_{0.26}As$ layers with doping levels of 1×10^{18} cm^{-3} for both the n- and p-cladding layers, respectively. The growth temperatures of the n- and p-$Al_{0.74}Ga_{0.26}As$ are 775 and 640°C, respectively. The annealing of the GaInNAs QW is accomplished during the growth of the top cladding layer at a temperature of 640°C, with duration of approximately 27 min.

From our prior work described in Sect. 18.2, we found that a DMHy/V ratio of 0.961 is required to realize 60 Å $In_{0.4}Ga_{0.6}As_{0.995}N_{0.005}$-GaAs QW active regions with an emission wavelength of 1,300 nm. The extension of the

emission wavelength of the GaInNAs QW laser is achieved by increasing the N-content in the GaInNAs QW, while maintaining the In-content and the QW thickness constant at 40% and 60 Å, respectively. The incorporation of N in the GaInAs material system is a very strong function of the DMHy/V ratio. By increasing the DMHy/V ratio, larger N-content GaInNAs QW can be realized. Utilizing DMHy/V ratios of 0.975 and 0.980, the lasing emission wavelengths of the 60 Å $In_{0.4}Ga_{0.6}AsN$ QW active regions are extended up to 1,360 and 1,382 nm, respectively. The N contents in the 1,360 and 1,382 nm GaInNAs QWs are estimated as approximately 0.8 and 0.85%, respectively, as calibrated from the growth conditions.

Broad area lasers, with a stripe-width (w) of 100 μm, were fabricated utilizing the GaInNAs QW active regions for emission wavelengths at 1,360 and 1,380 nm. The lasing characteristics are measured under pulsed currents with a pulse width of 5 μs and duty cycle of 1%. The measurements are performed on as-cleaved broad area laser devices, with an oxide-defined stripe-width of 100 μm. The metal contacts are realized with 250 Å Ti/500 Å Pt/1,500 Å Au and 200 Å Ge/1,000 Å GeAu/500 Å Ni/3,000 Å Au for p-contact and n-contact, respectively. The contact annealing of the devices is accomplished under forming gas (10% H_2 + 90% N_2) at a temperature of 370°C for duration of 30 s.

The pulsed lasing characteristics of the 1,360 nm GaInNAs QW lasers with a cavity length (L_{cav}) of 1,000 μm are shown in Fig. 18.26. A room temperature threshold current density (J_{th}) of only 520 A cm^{-2} is achieved for GaInNAs QW lasers with L_{cav} of 1,000 μm, at an emission wavelength of 1,357 nm. An external differential quantum efficiency of approximately 43.2% is also measured. The threshold current density of longer cavity devices

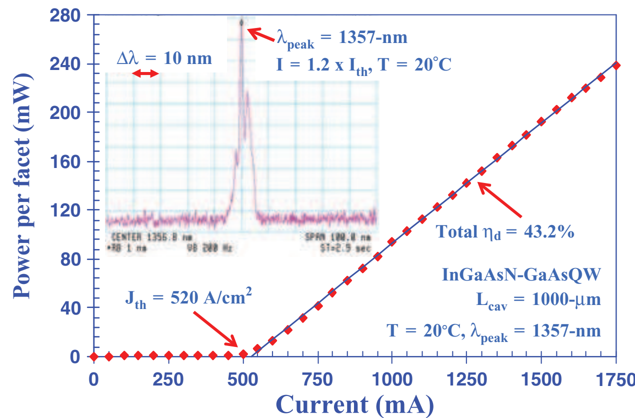

Fig. 18.26. The measured output power vs. current (P-I) characteristics of the 1,360 nm GaInNAs QW lasers with $L_{\text{cav}} = 1{,}000$ μm at a temperature of 20°C. The inset shows the near-threshold lasing spectrum at a heat-sink temperature of 20°C

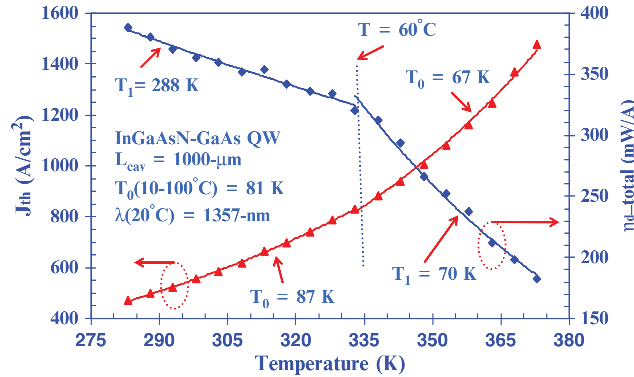

Fig. 18.27. The measured J_{th} and η_{d} of 1,360 nm GaInNAs QW lasers as a function of temperature

(L_{cav} = 1,500 μm) is measured as only 450 A cm^{-2} at a temperature of 20°C. Accompanying the large shift in the emission wavelength from 1,300 to 1,360 nm, the threshold current density of the 1,360 nm GaInNAs QW is increased by approximately a factor of two [9].

The temperature dependence of the threshold current density of the 1,360 nm GaInNAs QW lasers with a cavity length of 1,000 μm is shown in Fig. 18.27. The characteristic temperature coefficients of the threshold current density (T_0 values, with $1/T_0 = 1/J_{\mathrm{th}}\,[\mathrm{d}J_{\mathrm{th}}/\mathrm{d}T]$) of 87 and 67 K are measured in the temperature ranges of 10–60°C and 60–100°C, respectively. A threshold current density of 1,480 A cm^{-2} is measured at a heat sink temperature of 100°C, with an emission wavelength of approximately 1,400 nm.

The dependence of the external differential quantum efficiency of the 1,360 nm GaInNAs QW lasers as a function of temperature is shown in Fig. 18.27. At elevated temperatures, the slope efficiency of this laser is extremely temperature sensitive, reflected by the low T_1 value ($1/T_1 = -1/\eta_{\mathrm{d}}\,[\mathrm{d}\eta_{\mathrm{d}}/\mathrm{d}T]$) of only 70 K for the temperature range of 60–100°C. By comparison, optimized 1,233 nm emitting $\mathrm{Ga_{0.6}In_{0.4}As}$ QW lasers typically exhibit T_1 values of 1,250 K [25].

The pulsed lasing characteristics of the 1,382 nm GaInNAs QW lasers are shown in Fig. 18.28, for a device with a cavity length of 750 μm. By increasing the DMHy/V ratio to 0.980, emission wavelength up to 1,382 nm was realized for laser devices with a cavity length of 750 μm at a heat sink temperature of 20°C. Threshold current densities of approximately 900, 1,010, and 1,800 A cm^{-2} are achieved for GaInNAs QW lasers at heat-sink temperature of 10–20, and 60°C, respectively.

One of the interesting characteristics of the 1,382 nm GaInNAs QW lasers is the fact that its external differential quantum efficiency exhibits a very strong temperature sensitivity. The T_1 value of the 1,382 nm GaInNAs QW lasers is only 82 K in the temperature range of 10–40°C, which is extremely

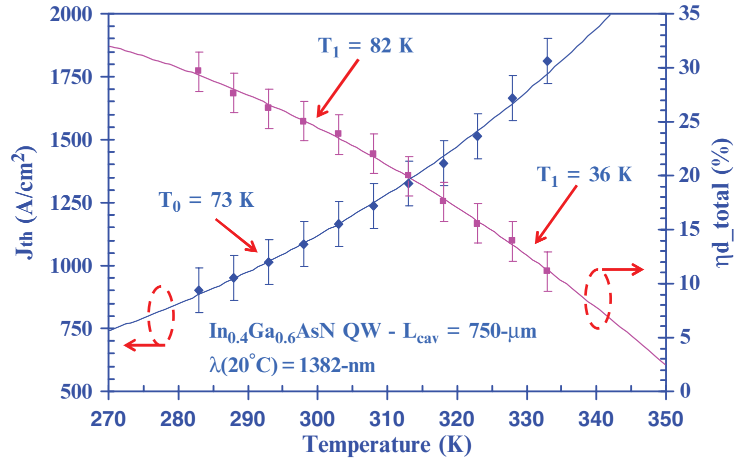

Fig. 18.28. The measured J_{th} and η_{d} of 1,382 nm GaInNAs QW lasers as a function of temperature

low in comparison to that ($T_1 = 360\,\mathrm{K}$ for temperature range of 10–60°C, [9]) of the 1,300 nm GaInNAs QW lasers. As we increase the N content in the GaInsNA QW to extend the emission wavelength, severe carrier leakage may occur from the QW as a result of a significant reduction in the hole confinement for larger N content GaInNAs QW [38].

Even though the threshold current density of the MOCVD-grown 1,360 and 1,382 nm GaInNAs QW lasers reported here are higher than lower N content 1,300 nm GaInNAs QW lasers, these results still represent the best reported threshold current densities in the wavelength regime of 1,360–1,400 nm as shown in Fig. 18.29. In Fig. 18.29, we plotted the best reported threshold current densities of GaInNAs QW lasers for the wavelength range from 1,360 to 1,400 nm [5, 14, 15, 17, 52, 53]. Some of the best reported J_{th} for MOCVD-grown GaInNAs QW lasers with emission wavelengths of 1,370 and 1,380 nm were realized with threshold current densities in the range of 2,200–2,500 A cm^{-2} [52, 53] by utilizing TBA as the As-precursor. The MOCVD-grown GaInNAs QW lasers reported here exhibit record low threshold current densities (at $T = 20°\mathrm{C}$) of only 450–520 and 1010 A cm^{-2} for emission wavelengths at 1,360 and 1,382 nm, respectively. These efforts demonstrate that high-performance 1,360 and 1,382 nm GaInNAs QW lasers can be realized with AsH_3 as the As-precursor.

In Fig. 18.30, we listed the summary of the best reported GaInAs-QW and GaInNAs-QW lasers on GaAs from emission wavelength of 1,100 up to 1,400 nm. As shown in the Fig. 18.30, we realized recently GaInNAs QW lasers with threshold current density of only approximately 500 A cm^{-2} for emission wavelength up to 1,370 nm. Our reported J_{th} for 1,370 nm GaInNAs QW lasers is extremely low in comparison to some of the published results for

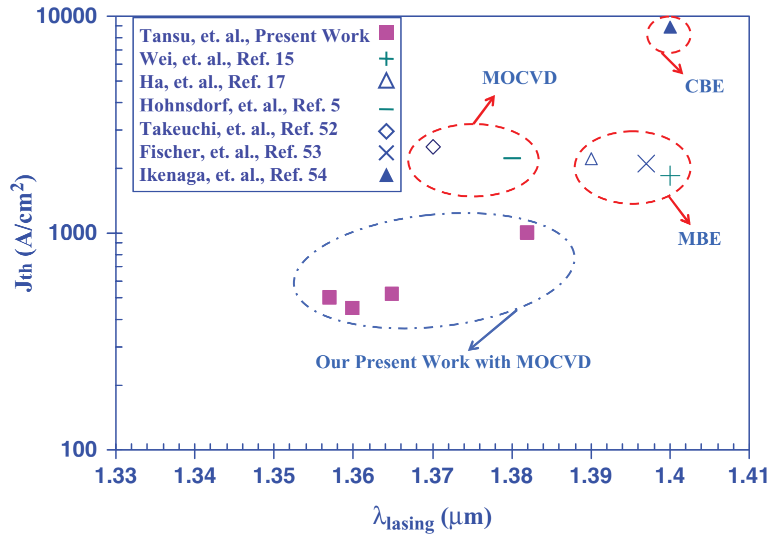

Fig. 18.29. Comparison of the threshold current densities for various GaInNAs QW lasers with emission wavelengths of 1,350–1,410 nm

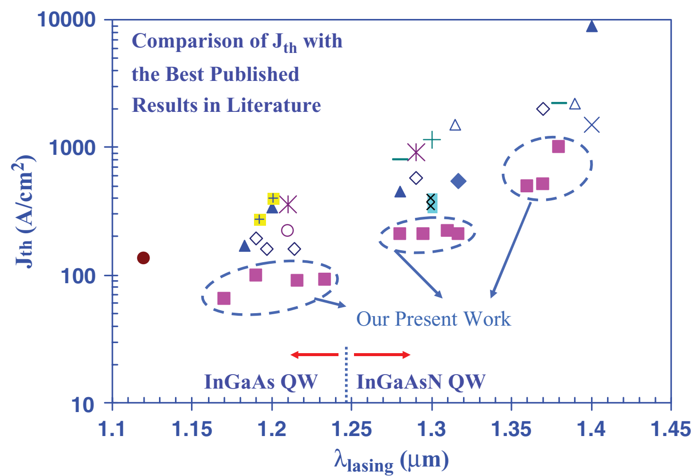

Fig. 18.30. Comparison of threshold current densities for various GaInNAs QW lasers with emission wavelengths from 1,170 up to 1,400 nm

GaInNAs QW in the wavelength of 1,370–1,400 nm. The fact that low J_{th} GaInNAs QW lasers have been realized with MOCVD technology indicates the large potential to push this material system for application beyond 1,400–1,550 nm. One of the main challenges in pushing the MOCVD-grown GaInNAs QW system is the difficulty in incorporating more N into the high In-content GaInAs to push the emission wavelength beyond 1,400–1,550 nm.

18.11 Temperature Analysis of the GaInNAs QW Lasers

Recent temperature analyses of GaInNAs diode lasers in the 1,300 nm wavelength region indicate that Auger recombination [28] and hole leakage [29, 30, 38] may play a significant role in the observed temperature sensitivity of the threshold current density and external differential quantum efficiency. To achieve emission wavelengths beyond 1,300 nm, higher N content GaInNAs active regions have been reported by various growth techniques such as MBE [6, 15, 17], MOCVD [6,52, and our work in Sect. 18.9], and CBE [54]. With much higher threshold current density and lower external differential quantum efficiency than 1,300 nm emitting lasers, these devices also showed severe temperature sensitivity of the laser characteristics. However, no study has yet focused on the strong temperature dependence of GaInNAs QW lasers beyond 1,300 nm and the underlying mechanism is still uncertain.

In this work, we present a temperature analysis of GaInAs(N) QW lasers over a wide emission wavelength range from 1,230 to 1,360 nm by simply adjusting the nitrogen composition in the QW. It was found that incorporation of higher nitrogen content significantly deteriorated the laser characteristics and temperature performance. Furthermore, we conclude that this behavior can be attributed to the highly temperature sensitive current injection efficiency and material gain parameter for GaInNAs QW lasers with higher N-content.

The GaInAs QW and GaInNAs QW laser structures were similar to the ones studied earlier, as shown in Fig. 18.1. In this study, we focused on three MOCVD-grown GaInAs(N) QW lasers with lasing wavelengths of 1.230 μm (laser A) [25], 1.295 μm (laser B) [9], and 1.360 μm (laser C) [see Sect. 18.9] for 2 mm long devices, respectively, and the schematic band diagrams are shown in Fig. 18.31. A high In content of 40% was utilized in the QW grown under a temperature of 530°C for all three laser bases. The only distinction

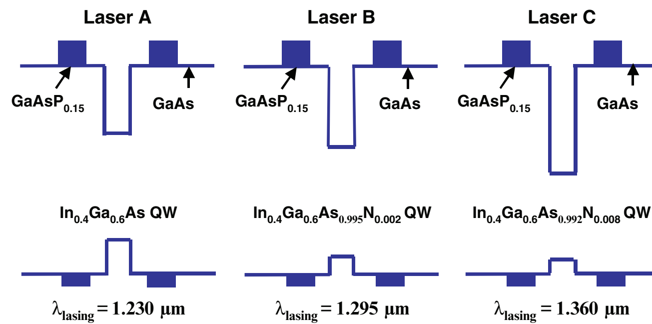

Fig. 18.31. Schematic band diagram of the GaInNAs QW laser structures with N content of 0, 0.5, and 0.8% for 1,230 nm $Ga_{0.6}In_{0.4}As$ (laser A), 1,295 nm $Ga_{0.6}In_{0.4}N_{0.005}As_{0.995}$ (laser B), and 1,360 nm $Ga_{0.6}In_{0.4}N_{0.008}As_{0.992}$ (laser C) QW lasers, respectively

of these laser structures was the nitrogen composition x of the 60 Å thick $Ga_{0.6}In_{0.4}N_xAs_{1-x}$ QW, which was determined to be 0% and 0.5% for laser A and B, calibrated by SIMS measurements, and 0.8% for laser C, which was estimated by extrapolating the growth parameters. The calculated strain of the GaInAs(N) QW are −2.79, −2.69, and −2.64%, for laser A–C, respectively. Minimum strain variation of the active regions utilized here should not result in any significant difference in laser characteristics contributed from strain difference. The detailed laser structure had been previously described in the earlier sections. The optical confinement factor (Γ) of 1.7% was calculated for all three structures by using the transmission matrix method.

As-cleaved broad-area lasers were fabricated with a stripe width of 100 µm and lasing characterization was conducted at a heat sink temperature range from 10 to 100°C with a pulse width of 5 µs (1% duty cycle). No heating was observed during the optical power vs. injection current measurement under the experimental condition. The threshold current density (J_{th}) was 110, 266, and 513 A cm^{-2} and external differential quantum efficiency (η_d) was 48, 46, and 43% at 20°C for 1 mm cavity length devices of laser A, B, and C, respectively. Figures 18.32 and 18.33 show the detailed temperature dependence of J_{th} and η_d as well as the characteristic temperature T_0 and $T_1(1/T_0 = 1/J_{th}(dJ_{th}/dT)$ and $1/T_1 = -1/\eta_d(d\eta_d/dT)$ at a temperature range of 10–50°C and 50–100°C. These data indicate that the 1,230 nm $In_{0.4}Ga_{0.6}As$ QW lasers (laser A) have both the lowest J_{th} and the largest η_d as well as higher T_0 and T_1 values compared with the 1,295 nm $Ga_{0.6}In_{0.4}As_{0.995}N_{0.005}$ (laser B) and 1,360 nm $Ga_{0.6}In_{0.4}As_{0.992}N_{0.008}$ (laser C) QW lasers. T_0 values from 20 to 60°C were characterized to be 120, 98, and 88 K and T_1 are 631, 333, and 227 K for laser A–C, respectively, indicating a trend of a reduction in T_0 and T_1 for

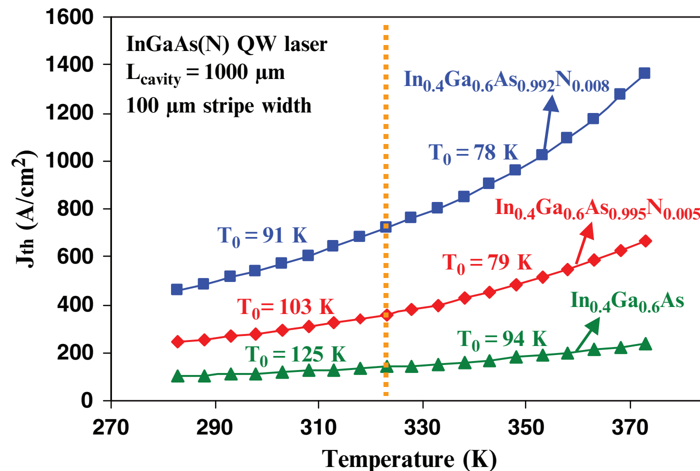

Fig. 18.32. The J_{th} as a function of temperature for lasers A–C with 1,000 µm cavity-length

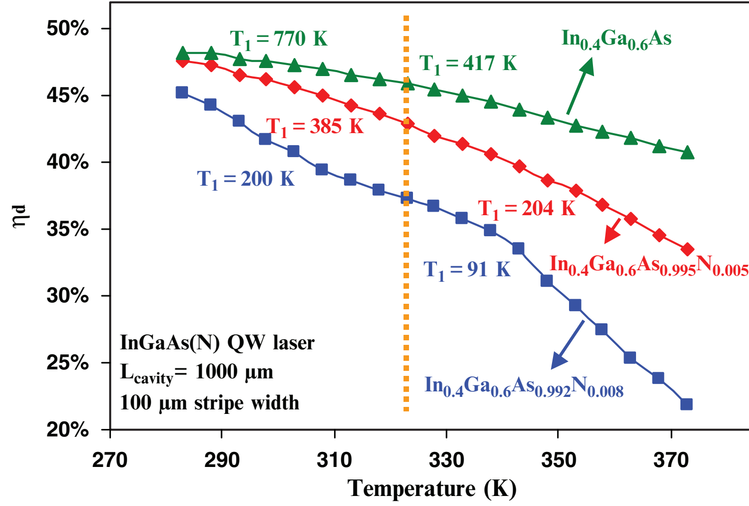

Fig. 18.33. The η_{d} as a function of temperature for lasers A–C with 1,000 µm cavity-length

the lasers with higher N content in QW. At 100°C, the GaInAs QW lasers exhibited a very low J_{th} of 237 A cm^{-2} and high η_{d} of 41%. It is concluded that with an increasing N content GaInNAs QW, the lasers show degraded lasing characteristics and, more importantly, significantly higher temperature sensitivity, although an extension of lasing wavelength can be achieved.

The characteristic temperature T_0 and T_1 have been shown that they can be expressed as (18.1) and (18.2) by assuming that J_{th}, transparent current density (J_{tr}), and internal loss (α_{i}) exponentially increase with temperature while η_{d}, current injection efficiency (η_{inj}), and material gain parameter ($g_{0\mathrm{J}}$) exponentially decrease. The relations can be written as [24, 29]

$$\frac{1}{T_{\mathrm{o}}(L)} = \frac{1}{T_{\mathrm{tr}}} + \frac{1}{T_{\eta\mathrm{inj}}} + \frac{\alpha_{\mathrm{i}} + \alpha_{\mathrm{m}}(L)}{\Gamma g_{\mathrm{oJ}}}\frac{1}{T_{\mathrm{goJ}}} + \frac{\alpha_{\mathrm{i}}}{\Gamma g_{\mathrm{oJ}}}\frac{1}{T_{\alpha\mathrm{i}}}, \tag{18.1}$$

$$\frac{1}{T_1(L)} = \frac{1}{T_{\eta\mathrm{inj}}} + \frac{\alpha_{\mathrm{i}}}{\alpha_{\mathrm{i}} + \alpha_{\mathrm{m}}(L)}\frac{1}{T_{\alpha\mathrm{i}}}, \tag{18.2}$$

where T_{tr}, $T_{\eta\mathrm{inj}}$, T_{g0J}, and $T_{\alpha\mathrm{i}}$ are the characteristic temperatures of J_{tr}, η_{inj}, $g_{0\mathrm{J}}$, and α_{i} and $\alpha_{\mathrm{m}}(L) = (1/L) \times \ln(1/R)$ is the mirror loss as a function of cavity length where R is the facet reflectivity and L is the cavity length. To distinguish the dominant mechanism for the poor temperature performance of the long wavelength 1,360 nm GaInNAs QW lasers, temperature characteristics of J_{tr}, η_{inj}, and $g_{0\mathrm{J}}$ were obtained from a series of temperature-dependent length studies. By deducing the slope and intercept of the $1/\eta_{\mathrm{d}}$ vs. L data

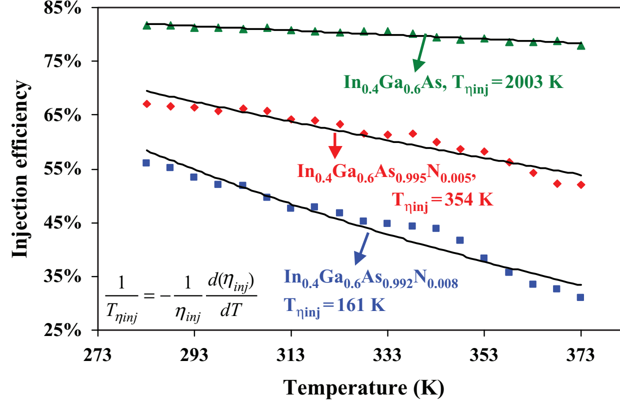

Fig. 18.34. Relation between current injection efficiency η_{inj} and temperature for the three laser structures. A higher $T_{\eta\text{inj}}$ was observed for the structure with less nitrogen in the QW

line, one can calculate the laser intrinsic parameters of α_{i} and η_{inj} based on the equation as follows:

$$\eta_{\text{d}} = \eta_{\text{inj}} \times \frac{\alpha_{\text{m}}(L)}{\alpha_{\text{i}} + \alpha_{\text{m}}(L)} \tag{18.3}$$

Also from the logarithmic relation of the threshold gain (g_{th}) and threshold current density shown in (18.4), $g_{0\text{J}}$ and J_{tr} can be extracted.

$$g_{\text{th}} = g_{\text{oJ}} \times \ln\left(\frac{\eta_{\text{inj}} J_{\text{th}}}{J_{\text{tr}}}\right) \tag{18.4}$$

The result of length studies for these three laser structures is shown in Fig. 18.34, where η_{inj} is expressed as a function of heat sink temperature from 10 to 100°C. Current injection efficiency (η_{inj}) values of 81, 66, and 53% at room temperature and $T_{\eta\text{inj}}$ of 2,000, 354, and 161 K were observed for the GaInAs(N) QW lasers with 0, 0.5, and 0.8% N content, respectively. The strong temperature dependence of the injection efficiency indicates a much stronger carrier leakage process for the high N content GaInNAs QW lasers. At 100°C, the η_{inj} of laser C reduces to 31% while the η_{inj} of laser A is still as high as 78%. The second term in (18.2) represents the contribution from internal loss temperature sensitivity. Values of $T_{\alpha\text{i}} \times (\alpha_{\text{i}} + \alpha_{\text{m}})/\alpha_{\text{i}}$ were measured and calculated to be 640, 1,153, and 2,132 for laser A–C, respectively, and $T_{\alpha\text{i}}$ values are 260, 360, and 400 K. According to (18.2), we can determine that the factor that limits T_1 for GaInAs QW laser is the internal loss (the second term) since $T_{\eta\text{inj}}$ hardly affects T_1 due to its large value of 2,000 K. On the contrary, the dominant factor resulting in the highly temperature sensitive η_{d} (a much lower T_1) of the 1,295 nm and 1,360 nm GaInNAs QW lasers is the

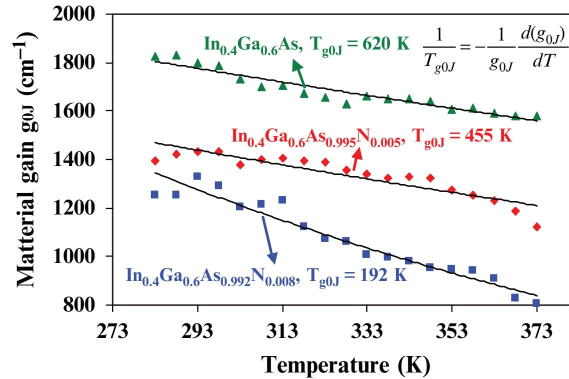

Fig. 18.35. Material gain parameter $g_{0\mathrm{J}}$ vs. temperature in a range of 10–100°C. Higher N content results in both lower $\mathrm{g}_{0\mathrm{J}}$ and $T_{g0\mathrm{J}}$

current injection efficiency $\eta_{\mathrm{inj}}(T)$ (the first term). The observed poor η_{inj} and $T_{\eta\mathrm{inj}}$ values could be presumably explained by a hole leakage mechanism in GaInNAs QW lasers [11,29,38] with a reducing valence band offset as nitrogen composition increases [55].

Unlike in (18.2) where $T_{\eta\mathrm{inj}}$ is the dominant factor, the more complicated dependence of (18.1) leads to difficulty in analyzing the dominant mechanism responsible for the degraded T_0 of GaInNAs QW lasers with increasing N content. For the analysis of T_0, the first three terms in (18.1) are considered important and need to be carefully examined. In Fig. 18.35, the measured $g_{0\mathrm{J}}$ values vs. temperature are shown over a range of 10–100°C. The $g_{0\mathrm{J}}$ values at room temperature are measured to be 1,800, 1,432, and 1,330 cm^{-1} and T_{g0J} values are 620, 456, and 192 K for laser A–C, respectively. The 1,360 nm GaInNAs QW lasers exhibit inferior gain characteristics compared with the other two structures and with such a low T_{goJ}, the $g_{0\mathrm{J}}$ value drops rapidly as temperature elevates and reaches a very low value of 800 cm^{-1} at 100°C. Possible mechanisms accounting for this behavior are possibly nonradiative Auger recombination, nitrogen-induced change of band structure, and temperature sensitive carrier leakage process below threshold for lasers with higher N-content. To improve understanding, $g_{0\mathrm{J}}$ and T_{g0J} of $\mathrm{Ga_{0.65}In_{0.35}N_{0.008}As_{0.992}}$QW lasers are compared with $\mathrm{Ga_{0.6}In_{0.4}N_{0.005}As_{0.995}}$ QW lasers for which the lasing wavelengths are designed to be 1.3 μm for both cases. With identical band gap energy, the contributions from Auger recombination are considered to be similar for these two laser structures. However, the results of lower $g_{0\mathrm{J}}$ of 1,251 cm^{-1} (at 20°C) and T_{g0J} of 330 K (from 10–60°C) of $\mathrm{Ga_{0.65}In_{0.35}As_{0.992}N_{0.008}}$ QW lasers indicate that mechanisms other than Auger recombination are also crucial to explain the degradation of $g_{0\mathrm{J}}$ and T_{g0J}. From these data, it can be concluded that increasing N content in GaInNAs QW not only significantly reduces η_{inj} and $T_{\eta\mathrm{inj}}$, but also seriously deteriorates g_{oJ} and T_{goJ}. Based on this study, it is believed that the observed low T_0 and T_1 of GaInNAs QW lasers with

increasing N content can be explained by the combination of a more severe carrier leakage process and stronger temperature dependence of g_{0J} [29, 30].

In the Sect. 18.10, the studies demonstrate that the N content in the GaInNAs QW dramatically affects the temperature sensitivity of η_{inj} and g_{0J}. The strong temperature dependence of η_{inj} and g_{0J} leads to low values of T_0 and T_1 for the GaInNAs QW lasers with higher N content. The current injection efficiency of GaInNAs QW lasers with increasing N content exhibits increasing temperature sensitivity, which could result from a reduction of the heavy hole confinement. In the following sections, theoretical calculations and careful experiments demonstrate that suppression of thermionic heavy hole escape from the GaInNAs QW systems lead to significantly improved lasing performances at high temperature.

18.12 Thermionic Emission Lifetime of GaInNAs Quantum Wells Lasers

As presented in the studies in Sect. 18.11, the stronger temperature sensitivity of the current injection efficiency of GaInNAs QW lasers with increasing N content lead to GaInNAs QW lasers with lower T_0 and T_1 values. In our earlier work [19, 30], the reduced T_0 and T_1 ($1/T_1 = -(1/\eta_d)\,d\eta_d/dT$, η_d = external differential quantum efficiency) values of the 1,300 nm GaInNAs QW lasers, compared to 1,190 nm GaInAs QW lasers, has been linked primarily to an increase in the carrier/current leakage processes. Despite the deeper quantum well structure in the GaInNAs QW lasers, the experimentally measured current injection efficiency (η_{inj}) of 1,300 nm GaInNAs QW reduces more rapidly with temperature compared to that of the 1,200 nm GaInAs QW lasers [19]. As N is added into the QW to push the emission wavelength longer, experiments have indicated that the η_{inj} of GaInNAs QW lasers decreases as a function of increasing N content [8, 15]. The reduction in η_{inj} can result for active layer carrier leakage. Here we identify a carrier leakage process in GaInNAs QW lasers [19] as heavy-hole leakage due to poor active layer hole confinement.

The thermionic carrier lifetime (τ_e) in QW lasers is an important factor in determining the current injection efficiency (η_{inj}) of a laser [56, 57]. A large thermionic lifetime of the carriers in the QW indicates a minimal escape rate of the carriers from the QW to the separate confinement heterostructure (SCH) [56, 57]. Minimal thermionic carrier escape rate out of the QW will lead to an increase in η_{inj} and a reduction in the temperature sensitivity of η_{inj} [56, 57]. The conventional method to express the thermionic lifetime is based on the model by Schneider et al. [58], which utilizes the bulk (3D) density of states (DOS) and a simple parabolic band model. However, this model [58] has been shown to be insufficient to explain experiments [59], and has a tendency to significantly over-estimate the hole-lifetime and to underestimate the electron lifetime [59]. The thermionic lifetime model that we employ in this study is

based on the model proposed by Irikawa et al. [59], that has been applied to the study of 1,500 nm GaIn(Al)As/InP QW lasers.

The thermionic current leakage, from the edge of the QW to one side of the SCH, J_{ee_i}, is related to the thermionic emission carrier lifetime to one side of the SCH τ_{ee_i} as follows

$$J_{ee_i} = NqL_z N_{QW}/\tau_{ee_i} \tag{18.5}$$

in which *i, N, q*, L_z, N_{QW}, represents the type of carriers (electrons or holes), the number of QWs, the electron charge, the QW thickness, and the carrier density in QW, respectively. It is important to note that the thermionic leakage current here is not the same as the total current leakage in QW laser devices, as the leaked carriers into the SCH region will have the probability of being recaptured back and recombine in the QW [56,57,59]. The relationships of the total threshold current density and the current injection efficiency with the thermionic carrier lifetime are more complex, and are interrelated by the total recombination lifetime in the QW and barrier regions and carrier capture time into the QW [56,57,59]. The leakage current J_{ee_i} has been described in [58, 59] with the standard thermionic emission theory as follows

$$J_{ee_i} = \frac{4\pi q(k_B T)^2}{h^3} m_i^* \exp(-\frac{E_{bi} - F_i}{k_B \cdot T}) \tag{18.6}$$

where m_i^*, E_{bi}, and F_i are the effective masses of the electrons or holes in the QW, the effective barriers and the quasi-Fermi levels for the electrons or holes in QW, respectively. The constants k_B and h represent the Boltzmann and Planck constant, respectively. The carrier density in the QW is calculated by taking into consideration the 2D DOS of the strained-QW, strain effects in band gap of the QW, and the Fermi-Dirac statistics [60]. The thermionic escape lifetime (τ_{ee_i}) can be extracted by relating the thermionic leakage current (J_{ee_i}) and the carrier density in the QW (N_{QW}), with consideration of the structure. The total current leakage from the SQW to both sides of the SCH, contributed by carrier i (electrons or holes), is $J_{e_i} = J_{ee_i_right} + J_{ee_i_left}$. The total thermionic escape lifetime of carrier i (τ_{e_i}) can be expressed as $1/\tau__e_i = 1/\tau_{ee__i_right} + 1/\tau_{ee_i_left}$. For the case of symmetrical barriers ($J_{ee_i_right} = J_{ee_i_left}$), the expression $1/\tau_{e_i} = 2/\tau_{ee_i}$ will be obtained.

In this study, the τ_{ee_i} values are analyzed for the case of the 1,190 nm emitting GaInAs-QW and 1,300 nm emitting GaInNAs-QW lasers. These 1,190–1,300 nm GaInAs(N) QW lasers, shown schematically in Fig. 18.1, are similar with the lasers that have been published previously [8, 9], in which a very high In-content (∼40%) and minimum N-content (∼0.5%) GaInAs(N) QW is utilized to achieve high-performance $\lambda = 1,190$–1,300 nm emitting lasers with GaAs as the direct barrier to the QW. Large band gap $Al_{0.74}Ga_{0.26}As$ layers are utilized as the n- and p-cladding layers, to ensure minimal carrier leakage from SCH region to cladding layers. The existence of the small N content (∼0.5–2%) in the GaInNAs QW mainly affects the

conduction band, which allows for the approximation of many of the material parameters of the $Ga_{1-x}In_xN_yAs_{1-y}$ QW with those of the $Ga_{1-x}In_xAs$ QW [61]. The compilation of the parameters used here follows the treatment in [55, 61] for the effective masses of the electrons, band gap energy, and conduction (ΔE_c) and valence (ΔE_v) band offsets.

We determine the appropriate band offset values by fitting the theory with the measured values from the experiments. The conduction band offset ratio ($Q_c = \Delta E_c/\Delta E_g$) for highly strained (In $> 20\%$) GaInAs-GaAs materials have been predicted to be in the range 60–65% [60, 62–64]. For the case of the GaInNAs QW, experimental studies [1, 55] show that Q_c is as high as 77–80% for the case of $Ga_{0.62}In_{0.38}N_{0.015}As_{0.985}$. Additional recent work [65] has also demonstrated experimentally the reduction in the valence band offset (ΔE_v) in GaInNAs QW as a result of N incorporation into GaInAs QW. We found very good agreement in emission wavelength and QW composition between theory and experiment with Qc values of 65%, and 82% for 63 Å $Ga_{0.57}In_{0.43}As$ QW, and 63 Å $Ga_{0.57}In_{0.43}N_{0.0062}As_{0.9938}$ QW, respectively. The compositions, the QW thickness, and the emission wavelengths of both the 60 Å $Ga_{0.6}In_{0.4}As$ QW and 60 Å $In_{0.4}Ga_{0.6}As_{0.995}N_{0.005}$ QW are measured experimentally [8, 24]. The $m_e{}^*$ for GaInAs QW and GaInNAs QW here are calculated as $0.047m_o$ and $0.069m_o$, respectively, with m_o as mass of electron. The $m_{hh}{}^*$ for both GaInAs and GaInNAs QW utilized in calculation is $0.457m_o$. Because of the large strain of the GaInAs and GaInNAs QW, the hole band structure consists of only heavy hole (*hh*) subbands in the 2D states, with light hole (*lh*) states having bulk like (3D) properties.

By utilizing the parameters listed in [58–64] and Fig. 18.36, the thermionic escape lifetime τ_{ee_i} can be calculated for electrons and holes for both GaInAs and GaInNAs QW's, as shown in Fig. 18.37. For the case of a GaInAs QW, the τ_{ee}(∼50–160 ps) of electrons is comparable to that (∼55–60 ps) of heavy-holes, for typical threshold carrier density of interest ($N_{QW} \sim 1.5\text{–}4 \times 10^{18}\,cm^{-3}$). In the case of a GaInNAs QW, the τ_{ee} of the heavy-hole is significantly smaller

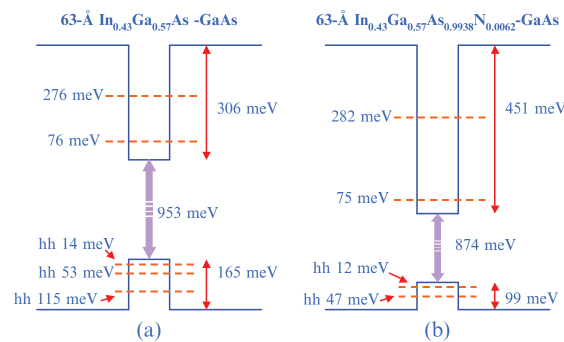

Fig. 18.36. Band line-up for conduction and valence bands of (**a**) 1,190 nm $In_{0.43}As$-QW and (**b**) 1,295 nm $Ga_{0.57}In_{0.43}N_{0.0062}As_{0.9938}$ QW lasers, with GaAs barriers

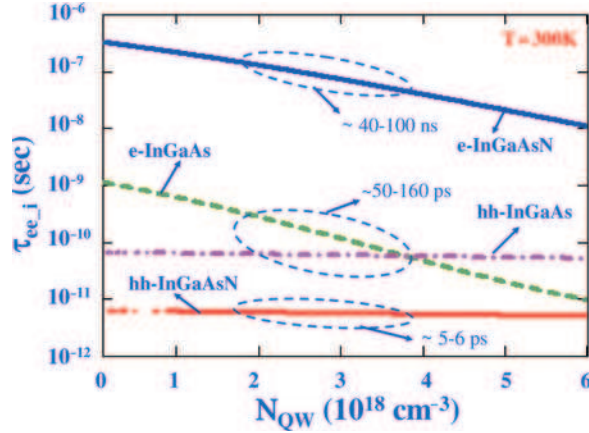

Fig. 18.37. The electron and hole thermionic escape lifetimes of 1,190 nm $Ga_{0.57}In_{0.43}As$-QW and 1,295 nm $Ga_{0.57}In_{0.43}As_{0.9938}N_{0.0062}$ QW lasers with GaAs barriers, at temperature of 300 K, as functions of carrier density

than τ_{ee} of the electron. The electrons are very well confined in GaInNAs QW, as indicated by the large τ_{ee}($\sim$40–100 ns) of the electron for typical threshold conditions. This large τ_{ee} of electrons in GaInNAs QW is expected, owing to its large conduction band-offset ($\Delta E_c \sim 450$ meV). On the other hand, the heavy-hole is very poorly confined due to the large disparity of the ΔE_c and ΔE_v. The small valence band-offset ($\Delta E_c \sim 99$ meV) in GaInNAs QW results in picosecond-range τ_{ee} of approximately 5–6 ps, for typical threshold conditions. Because of the significantly smaller τ_{ee} of the hole in GaInNAs QW, the heavy-hole leakage is the dominant leakage mechanism for the GaInNAs QW. Severe thermionic carrier leakage leads to a reduction in the current injection efficiency at threshold [56, 57], which is distinct from the above threshold η_{inj} [66], and will in turn lead to an increase in the threshold current density of the QW laser.

The thermionic carrier escape lifetimes for the GaInAs and GaInNAs QWs are shown in Fig. 18.38a,b. At elevated temperature (T = 360K), τ_{ee} of the heavy-hole reduces to only 3 ps. In the case of the GaInAs QW, the lowest τ_{ee} is approximately 21 ps at an elevated temperature of 360 K. The severe heavy-hole leakage at elevated temperature for GaInNAs QW lasers serves as one of the contributing factors that leads to the highly temperature-sensitive ($T_0 \sim$ 70–90 K) threshold-current of high-performance 1,300 nm GaInNAs QW lasers. Although the hole-leakage processes may dominate the high temperature sensitivity of GaInNAs QW lasers, Auger recombination, and other processes in the GaInNAs QW cannot be ruled out as contributing factors.

To achieve suppression of hole leakage from the GaInNAs SQW, larger band gap materials of tensile-GaAsP or GaInAsP can also be utilized as the direct barrier or SCH regions. As shown in Fig. 18.39, the τ_{ee} of holes in a GaInNAs QW are calculated for structures with various barrier regions.

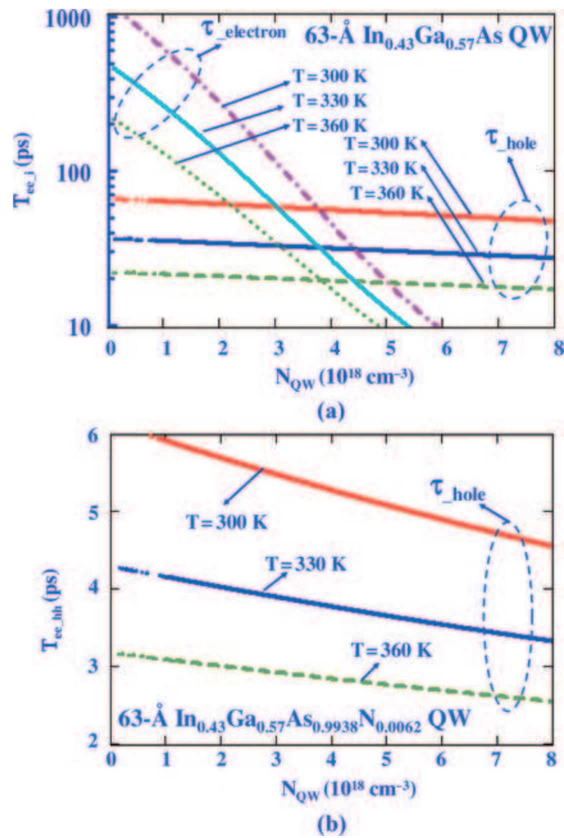

Fig. 18.38. The electron and hole thermionic escape time of the (**a**) 1,190 nm GaInAs-QW and (**b**) the 1,295 nm GaInNAs QW lasers with GaAs barriers, as functions of carrier density and temperature

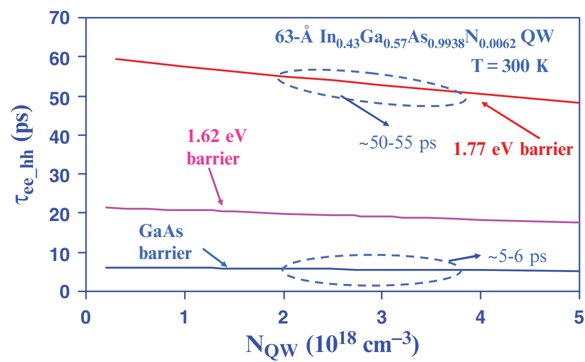

Fig. 18.39. The electron and hole thermionic escape lifetimes of the 1,295 nm GaIn-NAs QW lasers with various barriers, at temperature of 300 K, as functions of carrier density

By utilizing the 1.77 eV GaInAsP lattice-matched barriers, with the assumption of a band-offset ratio ($\Delta E_c : \Delta E_v$) of 82:18, the thermionic escape rate ($1/\tau_{ee_holes}$) of the heavy hole in GaInNAs QW is reduced significantly by approximately 10–12 times, in comparison with that of the GaInNAs-GaAs case.

The hole leakage process is identified as the main mechanism in the leakage process in 63 Å $Ga_{0.57}In_{0.43}As_{0.9938}N_{0.0062}$ SQW lasers with GaAs barriers. At a typical room temperature threshold carrier density ($N_{QW} = 1.5\text{–}3 \times 10^{18}\,cm^{-3}$), the estimated τ_{ee} for the heavy-hole in 1,300 nm emitting GaInNAs QW lasers is predicted to be around 5–6 ps, which is approximately 10 times smaller than that of the 1,190 nm emitting GaInAs QW lasers. Reduction in the hole leakage, by utilizing large band gap barriers in a SQW, should allow the realization of high-lasing-performance and high-temperature-operation 1,300 nm GaInNAs SQW lasers, comparable to that achieved with 1,190 nm emitting GaInAs SQW lasers. Utilization of multi-QW GaInNAs active regions will also allow reduction in the thermionic carrier escape rate, which will be beneficial for high-temperature operation.

Because of the complexity in determining the parameters for GaInNAs materials, the intent of this section is not to provide the most accurate values of the thermionic carrier escape time from GaInNAs QW. Rather it is to point out the significance of the thermionic carrier escape processes in 1,300 nm GaInNAs QW lasers, which have been neglected in previous analysis under the assumption of strong electron confinement [28]. Further analysis utilizing a self-consistent-computation [67], with consideration of thermionic carrier leakage, would allow improved and more accurate understanding of the physics of temperature sensitivity of GaInNAs QW lasers.

18.13 Experimental Evidence of the Existence of Carrier Leakages

Our previous studies presented in Sect. 18.10 have suggested carrier leakage and a more temperature sensitive material gain are also contributing factors that lead to a stronger temperature sensitivity of the GaInNAs QW lasers in comparison to that of the optimized 1,200 nm GaInAs QW lasers. In Sect. 18.11, we have also calculated theoretically that the thermionic carrier escape rate for 1,300 nm GaInNAs QW lasers is larger by one or two order of magnitude in comparison to that of 1,200 nm GaInAs QW lasers, as a result of poor heavy holes confinement in the GaInNAs QW.

In Sect. 18.12, we demonstrate experimental evidence for the existence of temperature induced carrier leakage in GaInNAs QW lasers. This work shows experimentally that carrier leakage in GaInNAs QW cannot be neglected, despite its deep electron confinement. Experiments are designed, in which the choice of the barriers surrounding an identical 60 Å $Ga_{0.6}In_{0.4}N_{0.005}As_{0.995}$ QW ($\Delta a/a \sim 2.8\%$, compressive) are modified from the conventional GaAs

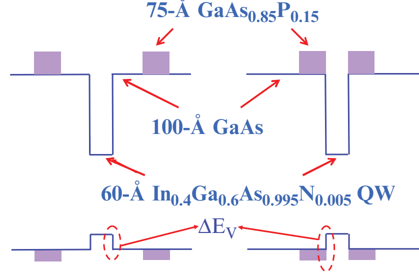

Fig. 18.40. Schematic band diagram of the $Ga_{0.6}In_{0.4}N_{0.005}As_{0.995}$ QW active regions with direct barriers of (**a**) GaAs and (**b**) $GaAs_{0.85}P_{0.15}$

barriers to higher band gap ($E_g \sim 1.55$eV) $GaAs_{0.85}P_{0.15}$ barriers ($\Delta a/a \sim -0.54\%$, tensile), as shown in Fig. 18.40. By replacing the direct barrier material, the thermionic escape lifetime of the carriers in the QW will be altered as a consequence of changes in the band offsets (ΔE_b). By utilizing the GaAsP-direct barriers, significant suppression of the carrier leakage phenomena at elevated temperature is observed, resulting in the realization of GaInNAs-QW lasers with low J_{th} and improved T_0 values at elevated temperatures. It is also important to note that the improvement in T_0 values in the GaInNAs-GaAsP laser structure is not a result of an increase in the J_{th}.

The J_{th} of QW lasers can be expressed as a function of device parameters, which include transparency current density (J_{tr}), current injection efficiency (η_{inj}), material gain parameter (g_{oJ}), and internal loss (α_i), as follows [24, 29]

$$J_{th} = \frac{J_{tr}}{\eta_{inj}} \exp(\frac{\alpha_i + (1/L)\ln(1/R)}{\Gamma g_{oJ}}) \tag{18.7}$$

The η_{inj} is defined as the fraction of the injected current that recombines in the QW active region. An expression for η_{inj} at threshold [56, 57], with the assumption of low photon density (S), can be expressed as follows

$$\eta_{inj}(S \to 0) \cong \frac{1}{\left[1 + \frac{\tau_{bw}}{\tau_b}(1 + \frac{\tau_{QW_total}}{\tau_e})\right]} \tag{18.8}$$

with τ_{bw} as the total carrier transport time, τ_b as the total recombination lifetime in the SCH region, τ_{QW_total} as the total recombination lifetime in the QW active region, and τ_e as the thermionic carrier escape lifetime. The expression in (18.8) can be derived from the conventional rate equation for QW lasers [56,57]. The τ_{bw} and τ_b are assumed as unchanged in all our experiments, as the design and the choice of material systems of the SCH region are identical for all structures investigated here. From the fact that the compositions and dimensions of the GaInNAs QW active regions in both experiments are kept identical, the total recombination lifetime in QW τ_{QW_total} can also be assumed as unchanged.

The thermionic escape lifetime ($\tau_{\mathrm{e_e,h}}$ for electrons and holes, respectively) of the carriers in the QW can also be expressed as follows [38, 57, 59]

$$\frac{1}{\tau_{\mathrm{e_e,h}}} \propto \frac{1}{N_{\mathrm{QW}} L_z} T^2 \exp(-\frac{\Delta E_{b_\mathrm{e,h}}}{k_{\mathrm{B}} T}) \qquad (18.9)$$

with k_{B} as the Boltzmann constant, T as the temperature, N_{QW} as the carrier density in QW, L_{z} as the thickness of QW, and $\Delta E_{\mathrm{b_e,h}}$ as the carrier confinement energy in QW (for electrons and holes, respectively). As the dimension (L_{z}) and composition of the GaInNAs QW active regions in both experiments are identical, the threshold carrier density in the QW ($N_{\mathrm{QW_th}}$) can also be assumed as identical for both lasers with similar confinement and cladding layer designs. The total thermionic carrier escape time of QW (τ_{e}) can be expressed as functions of the $\tau_{\mathrm{e_electron}}$ and $\tau_{\mathrm{e_holes}}$ as $1/\tau_{\mathrm{e}} = 1/\tau_{\mathrm{e_electron}} + 1/\tau_{\mathrm{e_holes}}$. The escape phenomenon is dominated by the escape rate of the carriers with the fastest escape time. Once the carriers escape, the carriers in the QW and SCH will redistribute themselves to maintain charge neutrality in the QW and SCH due to the high mobility of the carriers [56]. The differences in the τ_{e} of GaInNAs-GaAs and GaInNAs-GaAsP structures can be attributed solely to the differences in their respective ratios of $\Delta E_{\mathrm{b_e,h}}$/kBT. The ratios of the electron and hole confinement energy ($\Delta E_{\mathrm{c}} : \Delta E_{\mathrm{v}}$, with $\Delta E_{\mathrm{c}} = \Delta E_{\mathrm{b_e}}$, $\Delta E_{\mathrm{v}} = \Delta E_{\mathrm{b_h}}$) in GaInNAs-GaAs structures is approximately 80:20 [38, 55], resulting in extremely strong electron confinement and extremely poor heavy hole confinement. The calculated escape lifetime of the electrons and holes from GaInNAs QW is approximately 30–50 ns and 5–10 ps, respectively, for near-threshold conditions [38]. By utilizing the large band gap material surrounding the GaInNAs QW, the confinement energy of both the electrons and holes in the QW will be increased. As no studies has been reported on the GaInNAs-GaAsP structures, the $\Delta E_{\mathrm{c}} : \Delta E_{\mathrm{v}}$ ratio is assumed as similar with that of GaInNAs-GaAs case. The calculated increase in ΔE_{v} (without taking into account the tensile strain of GaAsP) of approximately 22–35 meV can be achieved for the GaInNAs-GaAsP structures, which is approximately 25% larger than that of GaInNAs-GaAs structures ($\Delta E\mathrm{v} \sim 99$ meV, [38]). Slight increase in ΔE_{v} leads to significant suppression of hole escape rate ($1/\tau_{\mathrm{e}}$) from the GaInNAs-GaAsP QW structures due to its exponential relation (from (18.9)), which will in turn lead to improved η_{inj} and J_{th} at elevated temperatures (from (18.7) and (18.8)). In the absence of any carrier leakage, by contrast, an increase in ΔE_{v} will not lead to any reduction in J_{th} at elevated temperatures or any improvement in the T_0 values. The tensile strain of GaAsP barriers could potentially lead to even further improved confinement of heavy holes in GaInNAs QW, due to the strain-induced lowering of the heavy-hole band edge of tensile strain material.

Both laser structures studied here, shown in Fig. 18.40, were grown and fabricated with similar methods as described in Sect. 18.2 and 18.3. The detail of the MOCVD growth of GaInNAs QW materials utilizing GaAs barriers

and larger band gap materials of GaAsP has been discussed elsewhere in [13] and [68].

As-cleaved broad area lasers, with oxide-defined stripe width of 100 µm were fabricated for both active regions shown in Fig. 18.40. The lasing characteristics were measured under pulsed conditions with a pulse width and a duty cycle of 5 µs and 1%, respectively. Room temperature threshold current densities of 320, 260, and 220 A cm^{-2} were measured for GaInNAs-GaAsP QW lasers for cavity lengths of 775, 1,000, and 2,000 µm, respectively. At room temperature ($T = 20°$C), threshold characteristics of both the GaInNAs-GaAs are measured as approximately 350–360 A cm^{-2}, 250 A cm^{-2} and 210–220 A cm^{-2}, for devices with cavity lengths of 720, 1,000, and 2000 µm, respectively. The emission wavelength of the GaInNAs-GaAsP lasers is approximately 1,280 nm ($L_{\mathrm{cav}} = 2{,}000$ µm), which is approximately 150 Å shorter than that of the GaInNAs-GaAs QW structures. Calculations considering the band gap, strain, and effective masses predict a blue-shift of the emission wavelength of approximately 100–120 Å for GaInNAs-GaAsP QW structures, in good agreement with experiments.

The temperature characterizations of both GaInNAs-GaAsP and GaInNAs-GaAs QWs lasers are performed over the range of 10–100°C. The characteristics of J_{th} with temperatures for both laser structures ($L_{\mathrm{cav}} = 2{,}000$ µm) are plotted in Fig. 18.41. The measurement is conducted for devices with long cavity to minimize the effect from the temperature sensitivity of material gain [24, 29].

Threshold current densities of both lasers are nearly identical in the temperature regime below 20°C. As the temperature increases, the J_{th} of the GaInNAs with GaAsP barriers increases at a significantly slower rate. The suppression of carrier leakage is also evident from the fact that the T_0 and T_1 ($1/T_1 = -(1/\eta_{\mathrm{d}})\,\mathrm{d}\eta_{\mathrm{d}}/\mathrm{d}T$, η_{d} = external differential quantum efficiency) values of the GaInNAs-GaAsP structures are significantly improved for devices with various cavity lengths, as shown in Figs. 18.42 and 18.43.

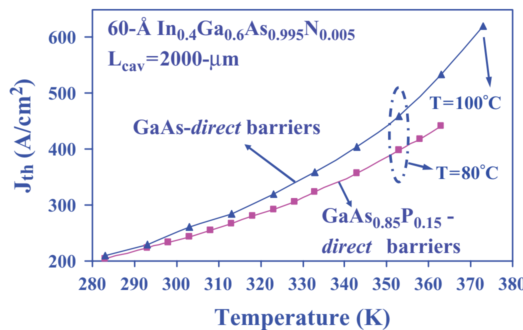

Fig. 18.41. The measured threshold current densities of GaInNAs-GaAs QW and GaInNAs-GaAsP QW lasers as function of temperature, for as-cleaved with $L_{\mathrm{cav}} = 2{,}000$ µm

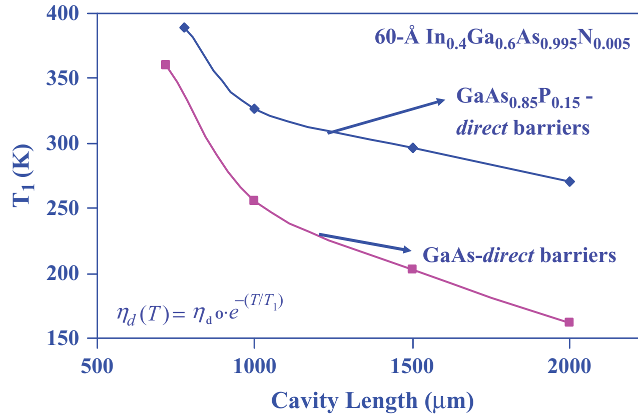

Fig. 18.42. The comparison of T_1 values, measured from temperature of 10–60°C, for $Ga_{0.6}In_{0.4}As_{0.995}N_{0.005}$ QW lasers with $GaAs_{0.85}P_{0.15}$ barriers and GaAs barriers, for various cavity lengths

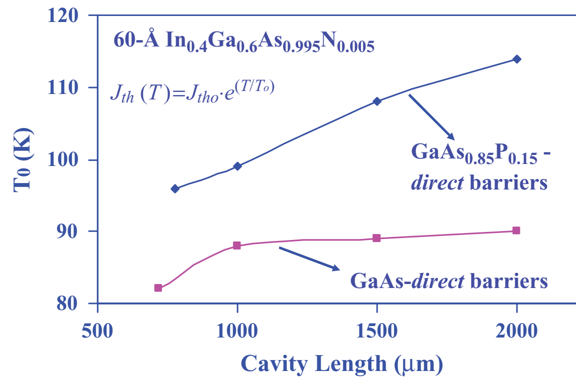

Fig. 18.43. The comparison of T_0 values, measured from temperature of 10–60°C, for $Ga_{0.6}In_{0.4}N_{0.005}As_{0.995}$ QW lasers with $GaAs_{0.85}P_{0.15}$ barriers and GaAs barriers, for various cavity lengths

Threshold current densities of only 390 and 440 A cm^{-2} were also measured for GaInNAs-GaAsP QW lasers ($L_{\mathrm{cav}} = 2{,}000\,\mu$m) at temperatures of 80 and 90°C, respectively. As electrons are very well confined in both GaInNAs QW laser structures, the reduction of the J_{th} of the GaInNAs-GaAsP QW structures at elevated temperatures as well as their improved T_0 and T_1 values are results of suppression of heavy hole leakage from the GaInNAs QW due to the lower hole escape rate ($1/\tau_{\mathrm{e_hole}}$).

The existence of carrier leakage in GaInNAs QW lasers has been demonstrated experimentally as one of the contributing factors influencing the temperature sensitivity of GaInNAs lasers. It is important to note that while these experiments demonstrate the existence of a carrier leakage processes in

GaInNAs QW lasers, they do not rule out Auger recombination as an additional contributing factor for the device temperature sensitivity. Suppression of carrier leakage in GaInNAs QW lasers with larger band gap barrier material of GaAsP leads to a reduction in the J_{th} at elevated temperature, accompanied by the increase in the T_0 and T_1 values. The J_{th} of the GaInNAs QW lasers (L_{cav} = 2,000 µm, as-cleaved), with $GaAs_{0.85}P_{0.15}$ direct barriers, have been measured as only 220 and 390 A cm^{-2}, for measurements at temperature of 20 and 80°C, respectively.

18.14 Extending the Emission Wavelength to 1,550 nm Regimes

The advancement of dilute nitride semiconductor materials and devices, in particular GaInNAs quantum wells, has progressed significantly during the last several years, leading toward realization of high performance diode lasers on GaAs substrate emitting at 1,300–1,400 nm wavelength regime [1–21, 70]. MOCVD-grown GaInNAs QW lasers have resulted in excellent lasing characteristics of 1,280–1,320 and 1,365–1,370 nm GaInNAs QW with threshold current density of only 200–220 A cm^{-2} [9–14, 70] and 450–540 A cm^{-2} [70], respectively. Although our GaInNAs QW lasers [9–14, 70, 71] have demonstrated excellent performance at 1,300–1,410 nm, extension of the emission wavelength up to 1,550 nm with only GaInNAs QW on GaAs is rather challenging [72–74]. Several promising approaches for realizing high-performance 1,550 nm diode lasers on GaAs substrate include InAs quantum dots (QD) [75–92], GaInNAsSb QW [93–105], GaAsSb-GaInAs type-II QWs [106, 107], and GaAsSb-(In)GaAsN type-II QWs [108–112].

High performance 1,150–1,380 nm InAs QD lasers had been realized by several groups [75–80, 84, 89, 92]. The lowest threshold current density of InAs QD lasers emitting in the 1,460 nm regime was reported as 2.3 kA cm^{-2} [75]. As the emission wavelength of InAs QD lasers is pushed beyond 1,460 nm, its threshold current density suffers. The existence of large strain and quantum size-effects in the InAs QD on GaAs leads to significant challenges in pushing its emission wavelength beyond 1,550 nm.

GaInNAsSb QW had been demonstrated utilizing MBE [93–103], for emission at 1,200–1,500 nm, with very good lasing performances. Recent works on MBE-grown GaInNAsSb has resulted in $J_{th} < 0.5$–1 kA cm^{-2} at 1,500 nm [93]. However, MOCVD-growth of GaInNAsSb QW is challenging, due to very different optimum growth conditions that Sb- and N-containing compounds require. To circumvent the challenges in MOCVD epitaxy condition for SbN-based QW, recent approach utilizing interdiffused GaInAsSbN QW had been proposed [104, 105]. The interdiffused SbN-based QW approach utilizes the large disparity of the diffusivities of Sb- and N-species in GaAs lattice, that allows the formation of SbN-based QW layers applicable for 1,550 nm. The details of the interdiffused GaInNAsSb QW will be discussed in Chap. 19.

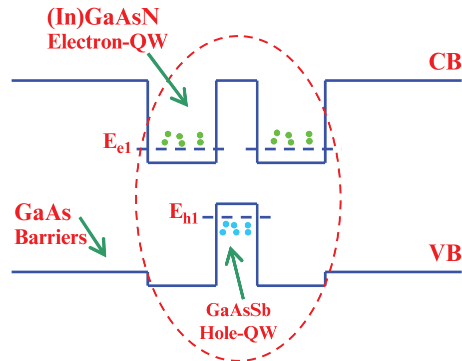

Fig. 18.44. Dilute nitride GaAsSb-GaNAs type-II QWs on GaAs for 1,550 nm emission

Novel approach based on GaAsSb-(In)GaNAs type-II quantum well gain media [108–112] had also been recently proposed as a method to achieve high performance 1,550 nm diode lasers on GaAs substrates, as shown in Fig. 18.44. Figure 18.44 shows the energy band diagram for the GaAsSb-(In)GaNAs type-II QWs [108–110]. Taking advantage of the deep electron confinement in the GaNAs layer and the deep holes confinement in the GaAsSb layer, type-II QW can be formed from these material systems. In this structure, the electron wells consist of (In)GaNAs layers and the hole well consist of GaAsSb layer. Strain-compensated structures with compressively-strained GaAsSb and tensile-strained GaNAs also allow the growth of multiple QW stages to achieve the necessary optical gain for lasers. Material optical gain as a function of radiative current density at 300 K for optimized 1,550 nm lasers based on GaAsSb-(In)GaNAs type-II QWs has also been analyzed, and it indicates large optical gain and low radiative threshold current density devices can be achieved [109]. Energy dispersion, wavefunctions, and optical matrix elements were calculated using 10-band $\boldsymbol{k}\cdot\boldsymbol{p}$ formalism, with band anti-crossing model employed to take into account the N-like band in the dilute nitride layers [109]. Recent experimental work on this novel dilute nitride type-II QW gain media grown on GaAs substrate has also resulted in PL peak luminescence emitting with low-temperature (T = 30K) photoluminescence wavelength at 1,600-nm [112]. The envisioned GaAsSb-(In)GaNAs type-II QW edge-emitters and VCSELs are expected to be a competitive alternative approach to achieve a high-performance GaAs-based 1,550 nm diode lasers.

18.15 Conclusions

High-performance GaInAs and GaInNAs QWs lasers, with emission wavelengths ranging from 1,170 to 1,320 nm, have been realized by MOCVD growth using AsH_3 as the As-precursor. Low threshold current density and

high temperature operation was obtained from 1,300 nm GaInNAs single-QW lasers, resulting in superior performance in comparison to conventional 1,300 nm InP-based lasers. Despite the high-strain of the GaInNAs QW, multiple-QWs lasers have been demonstrated with excellent scaling in transparency current and material gain. The utilization of a higher N-content GaInNAs QW has indicated possible increased carrier leakage, in comparison to the structures with lower N content GaInNAs QW active regions. Remaining issues concern the reliability of these active layer materials as well as the extension to longer wavelengths. In addition to the success of 1,300 nm GaInNAs QW lasers, we have demonstrated excellent lasing characteristics from GaInNAs QW lasers within the emission wavelength range of 1,360–1,382 nm, by utilizing MOCVD with AsH_3 as the As-precursor. These results represent among the lowest-reported threshold-current-densities of GaInNAs QW lasers for emission wavelengths at 1,360 and 1,382 nm. We observe a strong dependence of the device temperature sensitivity (T_0 and T_1) on the nitrogen content of the QW. The reasonably-low J_{th} of the 1,360 and 1,382 nm GaInNAs QW lasers also indicate the feasibility of pushing the GaInNAs QW technology beyond emission wavelength of 1,400 nm.

Detailed analysis of the temperature characteristics of GaInNAs QW lasers indicated the importance of suppression of thermionic carrier leakage to realize low threshold lasers. Here we have calculated theoretically and demonstrate experimentally that by suppressing the carrier leakage out of the GaInNAs QW, high performance lasers can be realized up to very high temperature.

Extension of the emission wavelength up to 1,550 nm with only GaInNAs QW remains challenging. Several approaches based on GaInAs QDs, GaInNAsSb QWs, dilute nitride GaAsSb-GaNAs type-II QWs have shown promising results for achieving 1,550 nm diode lasers on GaAs. The area of research for dilute-nitride lasers remains a very active field, in particular for achieving high-performance 1,550 nm diode lasers and understanding the physics of the QW and low-dimensional structures based on these novel materials.

Acknowledgements. The authors acknowledge helpful technical discussions with Dr. Jeng-Ya Yeh (University of Wisconsin-Madison), and Dr. M.R.T. Tan, Dr. D.P. Bour, Dr. S.W. Corzine, Dr. T. Takeuchi, Dr. Y.L. Chang (Agilent Technologies Laboratories, Palo Alto, CA), Dr. Jerry Meyer, Dr. Igor Vurgaftman (Naval Research Lab).

References

1. M. Kondow, T. Kitatani, S. Nakatsuka, M.C. Larson, K. Nakahara, Y. Yazawa, M. Okai, K. Uomi, IEEE J. Sel. Top. Quantum Electron. **3**, 719 (1997)
2. J.S. Harris Jr., IEEE J. Sel. Top. Quantum Electron. **6**, 1145 (2000)
3. S. Sato, Jpn. J. Appl. Phys. **39**, 3403 (2000)

4. D.A. Livshits, A.Yu. Egorov, H. Riechert, Electron. Lett. **36**, 1381 (2000)
5. F. Hohnsdorf, J. Koch, S. Leu, W. Stolz, B. Borchert, M. Druminski, Electron. Lett. **35**, 571 (1999)
6. M. Kawaguchi, T. Miyamoto, E. Gouardes, D. Schlenker, T. Kondo, F. Koyama, K. Iga, Jpn. J. Appl. Phys. **40**, L744 (2001)
7. T. Takeuchi, Y.L. Chang, M. Leary, A. Tandon, H.C. Luan, D.P. Bour, S.W. Corzine, R. Twist, M.R. Tan, in *IEEE LEOS 2001 Post-Deadline Session*, San Diego, USA, 2001
8. N. Tansu, L.J. Mawst, IEEE Photon. Technol. Lett. **14**, 444 (2002)
9. N. Tansu, N.J. Kirsch, L.J. Mawst, Appl. Phys. Lett. **81**, 2523 (2002)
10. N. Tansu, A. Quandt, M. Kanskar, W. Mulhearn, L.J. Mawst, Appl. Phys. Lett. **83**, 18 (2003)
11. N. Tansu, J.Y. Yeh, L.J. Mawst, Appl. Phys. Lett. **83**, 2112 (2003)
12. N. Tansu, J.Y. Yeh, L.J. Mawst, Appl. Phys. Lett. **83**, 2512 (2003)
13. N. Tansu, J.Y. Yeh, L.J. Mawst, Appl. Phys. Lett. **82**, 3008 (2003)
14. N. Tansu, J.Y. Yeh, L.J. Mawst, IEEE J. Sel. Top. Quantum Electron. **3**, 1220 (2003)
15. J. Wei, F. Xia, C. Li, S.R. Forrest, IEEE Photon. Technol. Lett. **14**, 597 (2002)
16. K.D. Choquette, J.F. Klem, A.J. Fischer, O. Blum, A.A. Allerman, I.J. Fritz, S.R. Kurtz, W.G. Breiland, R. Sieg, K.M. Geib, J.W. Scott, R.L. Naone, Electron. Lett. **36**, 2000 (2000)
17. W. Ha, V. Gambin, M. Wistey, S. Bank, S. Kim, K.M. Harris Jr., IEEE Photon. Technol. Lett. **14**, 591 (2002)
18. T. Peng, P. Jouhti, E. Laukkanen, M. Pavelescu, J. Konttinen, W. Li, M. Pessa, IEEE Photon. Technol. Lett. **14**, 275 (2002)
19. W. Li, T. Jouhti, C.S. Peng, J. Konttinen, P. Laukkanen, E.M. Pavelescu, M. Pessa, Appl. Phys. Lett. **79**, 3386 (2001)
20. S. Sato, S. Satoh, Jpn. J. Appl. Phys. **38**, L990 (1999)
21. W. Choi, P.D. Dapkus, J.J. Jewell, IEEE Photon. Technol. Lett. **11**, 1572 (1999)
22. T. Kondo, D. Schlenker, T. Miyamoto, Z. Chen, M. Kawaguchi, E. Gouardes, F. Koyama, K. Iga, Jpn. J. Appl. Phys. **40**, 467 (2000)
23. N. Tansu, L.J. Mawst, IEEE Photon. Technol. Lett. **13**, 79 (2001)
24. N. Tansu, Y.L. Chang, T. Takeuchi, D.P. Bour, S.W. Corzine, M.R.T. Tan, L.J. Mawst, IEEE J. Quantum Electron. **38**, 640 (2002)
25. N. Tansu, J.Y. Yeh, L.J. Mawst, Appl. Phys. Lett. **82**, 4038 (2003)
26. T. Takeuchi, Y.L. Chang, A. Tandon, D. Bour, S. Corzine, R. Twist, M. Tan, H.C. Luan, Appl. Phys. Lett. **80**, 2445 (2002)
27. F. Bugge, G. Erbert, J. Fricke, S. Gramlich, R. Staske, H. Wenzel, U. Zeimer, M. Weyers, Appl. Phys. Lett. **79**, 965 (2001)
28. R. Fehse, S. Tomic, A.R. Adams, S.J. Sweeney, E.P. O'Reilly, A. Andreev, H. Riechert, IEEE J. Sel. Top. Quantum Electron. **8**, 801 (2002)
29. N. Tansu, L.J. Mawst, IEEE Photon. Technol. Lett. **14**, 1052 (2002)
30. N. Tansu, L.J. Mawst, IEEE Photon. Technol. Lett. **16**, 741 (2004)
31. Z.B. Chen, D. Schlenker, F. Koyama, T. Miyamoto, A. Matsutani, K. Iga, in *Proceedings of APCC/OECC'99*, vol. 2, Beijing, China, 1999, p. 1311
32. S. Mogg, N. Chitica, R. Schatz, M. Hammar, Appl. Phys. Lett. **81**, 2334 (2002)
33. R.L. Sellin, Ch. Ribbat, M. Grundmann, N.N. Ledentsov, D. Bimberg, Appl. Phys. Lett. **78**, 1207 (2001)

34. A. Stintz, G.T. Liu, H. Li, L.F. Lester, K.J. Malloy, IEEE Photon. Technol. Lett. **12**, 591 (2000)
35. P.M. Smowton, E. Hermann, Y. Ning, H.D. Summers, P. Blood, Appl. Phys. Lett. **78**, 2629 (2001)
36. G.L. Belenky, C.L. Reynolds Jr., D.V. Donetsky, G.E. Shtengel, M.S. Hybertsen, M.A. Alam, G.A. Baraff, R.K. Smith, R.F. Kazarinov, J. Winn, L.E. Smith, IEEE J. Quantum Electron. **35**, 1515 (1999)
37. P. Savolainen, M. Toivonen, P. Melanen, V. Vilokkinen, M. Saarinen, S. Orsila, T. Kuuslahti, A. Salokatve, H. Asonen, T. Panarello, R. Murison, M. Pessa, in *Proceedings of 11th IPRM*, Davos, Switzerland, 1999
38. N. Tansu, L.J. Mawst, Appl. Phys. Lett. **82**, 1500 (2003)
39. J. Wu, W. Shan, W. Walukiewicz, K.M. Yu, J.V. Ager III, E.E. Haller, H.P. Xin, C.W. Tu, Phys. Rev. B. **64**, 85320 (2001)
40. B.Q. Sun, D.S. Jiang, X.D. Luo, Z.Y. Xu, Z. Pan, L.H. Li, R.H. Wu, Appl. Phys. Lett. **76**, 2862 (2000)
41. T. Kitatani, M. Kondow, T. Kikawa, Y. Yazawa, M. Okai, K. Uomi, Jpn. J. Appl. Phys. **38**, 5003 (1999)
42. S. Illek, A. Ultsch, B. Borchert, A.Y. Egorov, H. Riechert, Electron. Lett. **36**, 725 (2000)
43. M. Fischer, M. Reinhardt, A. Forchel, in *Device Research Conference*, Denver, CO, 19–21 June 2000, p. 19
44. B. Borchert, A.Y. Egorov, S. Illek, M. Komainda, H. Riechert, Electron. Lett. **35**, 2204 (1999)
45. S. Sato, S. Satoh, IEEE Photon. Technol. Lett. **11**, 1560 (1999)
46. K. Nakahara, M. Kondow, T. Kitatani, M.C. Larson, K. Uomi, IEEE Photon. Technol. Lett. **10**, 487 (1998)
47. P.J.A. Thijs, L.F. Tiemeuer, J.J.M. Binsma, Van T. Dongen, IEEE J. Quantum Electron. **30**, (1994)
48. N. Yokouchi, N. Yamanaka, N. Iwai, A. Kasukawax, Electron. Lett. **31**, 104 (1995)
49. J.P. Donnelly, S.H. Groves, J.N. Walpole, R.J. Bailey, J.D. Woodhouse, L.J. Missaggia, A. Napoleone, F.J. O'Donnell, R.E. Reeder, in *Conference Proceedings of LEOS*, vol. 2, 1994, p. 406
50. C.E. Zah, R. Bhat, B.N. Pathak, F. Favire, W. Lin, M.C. Wang, N.C. Andreadakis, D.M. Hwang, M.A. Koza, T.P. Lee, Z. Wang, D. Darby, D. Flanders, J.J. Hsieh, IEEE J. Quantum Electron. **30**, 511 (1994)
51. S.R. Selmic, T.M. Chou, J. Sih, J.B. Kirk, A. Mantle, J.K. Butler, D. Bour, G.A. Evans, IEEE J. Sel. Top. Quantum Electron. **7**, 340 (2001)
52. T. Takeuchi, Y.L. Chang, M. Leary, A. Tandon, H.C. Luan, D.P. Bour, S.W. Corzine, R. Twist, M.R. Tan, in *Proceedings of the SPIE Photonics West 2003, Novel In-Plane Semiconductor Lasers 2003*, San Jose, CA (2003)
53. M. Fischer, M. Reinhardt, A. Forchel, Electron. Lett. **36**, 1204 (2000)
54. Y. Ikenaga, T. Miyamoto, S. Makino, T. Kageyama, M. Arai, F. Koyama, K. Iga, Jpn. J. Appl. Phys. **41**, 665 (2002)
55. M. Hetterich, M.D. Dawson, Yu A. Egorov, D. Bernklau, H. Riechert, Appl. Phys. Lett. **76**, 1030 (2000)
56. R. Nagarajan, J.E. Bowers, IEEE J. Quantum Electron. **29**, 601 (1993)
57. N. Tansu, L.J. Mawst, J. Appl. Phys. **97**, 054502 (2005)
58. H. Schneider, K.V. Klitzing, Phys. Rev. B **38**, 6160 (1988)

59. M. Irikawa, T. Ishikawa, T. Fukushima, H. Shimizu, A. Kasukawa, K. Iga, Jpn. J. Appl. Phys. **39**, 1730 (2000)
60. S.L. Chuang, *Physics of Optoelectronic Devices* (Wiley, New York, 1995)
61. W.W. Chow, E.D. Jones, N.A. Modine, A.A. Allerman, S.R. Kurtz, Appl. Phys. Lett. **75**, 2891 (1999)
62. B. Jogai, Appl. Phys. Lett. **59**, 1329 (1991)
63. J.J. Coleman, in *Quantum Well Lasers*, chap. 8, ed. by P.S. Zory (Academic, New York, 1993)
64. S. Niki, C.L. Lin, W.S.C. Chang, H.H. Wieder, Appl. Phys. Lett. **55**, 1339 (1989)
65. J.B. Heroux, C. Yang, W.I. Wang, J. Appl. Phys. **92**, 4361 (2002)
66. P.M. Smowton, P. Blood, IEEE J. Sel. Top. Quantum Electron. **3**, 491 (1997)
67. J. Piprek, P. Abraham, J.E. Bowers, IEEE J. Quantum Electron. **36**, 366 (2000)
68. J.Y. Yeh, N. Tansu, L.J. Mawst, J. Cryst. Growth **262**, 5 (2004)
69. L.W. Sung, H.H. Lin, Appl. Phys. Lett. **83**, 1107 (2003)
70. N. Tansu, J.Y. Yeh, L.J. Mawst, J. Phys. Condens. Matter **16**, S3277 (2004)
71. J.Y. Yeh, N. Tansu, L.J. Mawst, IEEE Electron. Lett. **40**, 739 (2004)
72. M. Fischer, M. Reinhardt, A. Forchel, Electron. Lett. **36**, 1208 (2000)
73. D. Gollub, S. Moses, M. Fischer, A. Forchel, Electron. Lett. **39**(10), 777 (2003)
74. Y. Ikenaga, T. Miyamoto, S. Makino, T. Kageyama, M. Arai, F. Koyama, K. Iga, Jpn. J. Appl. Phys. **41**, 664 (2002)
75. N.N. Ledentsov, A.E. Kovsh, A.E. Zhukov, N.A. Maleev, S.S. Mikhrin, A.P. Vasil'ev, E.S. Semenova, M.V. Maximov, Yu.M. Shernyakov, N.V. Kryzhanovskaya, V.M. Ustinov, D. Bimberg, Electron. Lett. **9**, 1126 (2003)
76. O.B. Shchekin, D.G. Deppe, Appl. Phys. Lett. **80**, 3277 (2002)
77. A.R. Kovsh, N.A. Maleev, A.E. Zhukov, S.S. Mikhrin, A.R. Vasil'ev, Yu.M. Shemyakov, M.V. Maximov, D.A. Livshits, V. Ustinov, Zh.I. Alferov, N.N. Ledentsov, D. Bimberg, Electron. Lett. **38**, 1104 (2002)
78. V. Tokranov, M. Yakimov, A. Katsnelson, M. Lamberti, S. Oktyabrsky, Appl. Phys. Lett. **83**, 833 (2003)
79. R.L. Sellin, I. Kaiander, D. Ouyang, T. Kettler, U.W. Pohl, D. Bimberg, N.D. Zakharov, P. Werner, Appl. Phys. Lett. **82**, 841 (2003)
80. J. Tatebayashi, N. Hatori, H. Kakuma, H. Ebe, H. Sudo, A. Kuramata, Y. Nakata, M. Sugawara, Y. Arakawa, Electron. Lett. **39**, 1130 (2003)
81. D.L. Huffaker, G. Park, Z. Zou, O.B. Shchekin, D.G. Deppe, Appl. Phys. Lett. **73**, 2564 (2001)
82. P. Gyoungwon, B.S. Oleg, L.H. Diana, G.D. Dennis, IEEE Photon. Technol. Lett. **13**, 230 (2000)
83. P.G. Eliseev, H. Li, A. Stintz, G.T. Liu, T.C. Newell, K.J. Malloy, L.F. Lester, Appl. Phys. Lett. **77**, 262 (2000)
84. G.T. Liu, A. Stintz, H. Li, K.J. Malloy, L.F. Lester, Electron. Lett. **35**, 1163 (1999)
85. P. Gyoungwon, B.S. Oleg, C. Sebastion, L.H. Diana, G.D. Dennis, Appl. Phys. Lett. **75**, 3267 (1999)
86. V.M. Mikhail, V.K. Igor, M.S. Yuri, V.Z. Sergei, Y.G. Nikita, F.T. Andrew, V.S. Alexey, K. Igor, S.K. Petr, A. Zhores, N.L. Nikolai, D. Bimberg, O.K. Alexander, W. Peter, G.C. Ulrich, Jpn. J. Appl. Phys. **36**, 4221 (1997)
87. S.M. Kim, Y. Wang, M. Keever, J.S. Harris, IEEE Photon. Technol. Lett. **16**, 377 (2004)

88. D. Bimberg, N. Kirstaedter, N.N. Ledentsov, Zh.I. Alferov, P.S. Kop'ev, V.M. Ustinov, IEEE Sel. Top. Quantum Electron. **3**, 196 (1997)
89. K. Mukai, Y. Nakata, K. Otsubo, M. Sugawara, N. Yokoyama, H. Ishikawa, IEEE Photon. Technol. Lett. **11**, 1205 (1999)
90. A. Stintz, G.T. Liu, H. Li, L.F. Lester, K.J. Malloy, IEEE Photon. Technol. Lett. **12**, 591 (2000)
91. P. Bhattacharya, K.K. Kamath, J. Singh, D. Klotzkim, J. Phillips, H.T. Jiang, N. Chervela, T.B. Norris, T. Sosnowski, J. Laskar, M.R. Murty, IEEE Trans. Electron Devices **46**, 871 (1999)
92. S. Ghosh, S. Pradhan, P. Bhattacharya, Appl. Phys. Lett. **81**, 3055 (2002)
93. S.R. Bank, M.A. Wistey, L.L. Goddard, H.B. Yuen, V. Lordi, J.S. Harris Jr., IEEE J. Quantum Electron. **40**, 656 (2004)
94. S.R. Bank, M.A. Wistey, L.L. Goddard, H.B. Yuen, H.P. Bae, J.S. Harris, Electron. Lett. **40**, 1186 (2004)
95. W. Li, J.B. Heroux, W.I. Wang, J. Appl. Phys. **94**, 4248 (2003)
96. W. Ha, V. Gambin, S. Bank, M. Wistey, H. Yuen, S. Kim, J.S. Harris Jr., IEEE J. Quantum Electron. **38**, 1260 (2002)
97. X. Yang, J.B. Heroux, L.F. Mei, W.I. Wang, Appl. Phys. Lett. **78**, 4068 (2001)
98. X. Yang, J.B. Heroux, M.J. Jurkovic, W.I. Wang, Appl. Phys. Lett. **76**, 795 (2000)
99. X. Yang, M.J. Jurkovic, J.B. Heroux, W.I. Wang, Appl. Phys. Lett. **75**, 178 (1999)
100. X. Yang, J.B. Heroux, L.F. Mei, W.I. Wang, Appl. Phys. Lett. **78**, 4068 (2001)
101. H. Shimizu, K. Kumada, S. Uchiyama, A. Kasukawa, Electron. Lett. **37**, 28 (2001)
102. H. Shimizu, K. Kumada, S. Uchiyama, A. Kasukawa, Electron. Lett. **36**, 1701 (2000)
103. C. Setiagung, H. Shimizu, Y. Ikenaga, K. Kumada, A. Kasukawa, IEEE J. Sel. Top. Quantum Electron. **9**, 1209 (2003)
104. R.A. Arif, N. Tansu, in *Proceedings of the SPIE Photonics West 2005, Physics and Simulation of Optoelectronics Devices XIII*, San Jose, CA, 2005
105. R.A. Arif, N. Tansu, in *Proceedings of the MRS Fall Meeting 2005: Symposium EE: Progress in Semiconductor Materials V- Novel Materials and Electronic and Optoelectronic Applications*, Boston, MA, USA, 2005
106. P. Dowd, W. Braun, D.J. Smith, C.M. Ryu, C.Z. Guo, S.L. Chen, U. Koelle, S.R. Johnson, Y.H. Zhang, Appl. Phys. Lett. **75**, 1267 (1999)
107. P. Dowd, W. Braun, D.J. Smith, C.M. Ryu, C.Z. Guo, S.L. Chen, U. Koelle, S.R. Johnson, Y.H. Zhang, Appl. Phys. Lett. **75**, 1267 (1999)
108. N. Tansu, L.J. Mawst, IEEE J. Quantum Electron. **39**, 1205 (2003)
109. I. Vurgaftman, J.R. Meyer, N. Tansu, L.J. Mawst, Appl. Phys. Lett. **83**, 2742 (2003)
110. N. Tansu, L.J. Mawst, U.S. Patent 6,791,104, 14 September 2004
111. P.D. Dapkus, International Patent Application No. PCT/US00/14332 (WO01/29943), filed on 24 May 2000
112. J.Y. Yeh, L.J. Mawst, A.A. Khandekar, T.F. Kuech, J.R. Meyer, I. Vurgaftman, N. Tansu, J. Cryst. Growth **287**, 615 (2006)

19

Interdiffused GaInNAsSb Quantum Well on GaAs for 1,300–1,550 nm Diode Lasers

R.A. Arif and N. Tansu

Current state-of-the-art GaInNAsSb quantum well lasers emitting in the 1,550 nm regime can only be realized by molecular beam epitaxy due to the ease and efficient incorporation of Sb-species into the GaInNAs material system. The pursuit of GaInNAsSb materials systems by metalorganic chemical vapor deposition is still immature due to the challenges in incorporating Sb- and dilute-N-species into GaInAs layer simultaneously under optimum growth conditions. This chapter presents a novel approach to realize GaInNAsSb quantum well, which allows one to circumvent the challenges present in the metalorganic chemical vapor deposition epitaxy of this quinary material system. Our approach combines the already-established metalorganic chemical vapor deposition growth of GaInNAs and GaInAsSb quantum wells, with a postgrowth rapid-thermal annealing that leads to interdiffusion of Sb and N-species, resulting in high-quality interdiffused GaInNAsSb quantum well. Our studies indicated emission wavelength up to 1,550 nm is achievable from this interdiffused GaInNAsSb quantum well, obtained by rapid thermal annealing of the as-grown GaInAsSb sandwiched by GaInNAs layers at a temperature of 600–700°C. Strain-compensated interdiffused SbN-based quantum well on GaAs can also be achieved by conducting rapid thermal annealing of the GaInAsSb (compressive)-GaNAs (tensile) layers, leading to interdiffused GaInNAsSb quantum well with emission wavelength up to 1,500 nm. Both experimental and theoretical works are presented here, and our studies show that combination of metalorganic chemical vapor deposition and interdiffusion approach should allow realization of GaInNAsSb quantum well with emission wavelength up to 1,550 nm regime without having to grow the mixed SbN-based quinary compound directly by metalorganic chemical vapor deposition.

19.1 Introduction

Semiconductor lasers emitting in the 1,300–1,550 nm regime are of great interest for optical communications networks. Conventional InP-based lasers still have to deal with issues such as low-characteristic temperature due to small conduction band offset, large Auger recombination, and intervalence band absorption. In addition, challenges in realizing high-quality distributed Bragg reflectors (DBRs) on InP for vertical cavity surface emitting lasers (VCSELs), and the need for expensive electronics to maintain thermal stability, further spur the interest in developing long-wavelength GaAs-based gain media in the 1,300–1,550 nm regime. Long-wavelength lasers on GaAs may readily gain practical importance owing to the availability of high-quality AlAs/GaAs DBRs for VCSELs and its superior high-temperature performance to InP-based lasers.

Several promising approaches to realize 1,300–1,550 nm emission on GaAs have been attempted. These approaches include GaInNAs quantum wells (QWs) [1–17], InAs quantum dots (QD) [18–25], GaAsSb–GaInAs type-II QWs [26], GaAsSb–GaInNAs type-II QWs [27–29], GaAsSb–GaNAs type-II QWs [27–30], and GaInNAsSb QW [31–34]. Excellent GaInNAs QW lasing characteristics in the 1,300 nm regime [3,4,8–12] and high-performance 1,150–1,380 nm InAs QD lasers [18–20] have been demonstrated. However, as the emission wavelength is pushed beyond ~1,400 nm, threshold current density – for both GaInNAs QW and GaInAs QD lasers – suffers significantly. The existence of large strain and quantum size-effects in the InAs QD on GaAs lead to significant challenges in pushing the emission wavelength to 1,550 nm.

GaInNAsSb QWs have recently received a sizable interest as another alternative for 1,200–1,500 nm gain media on GaAs. However – as of today – GaInNAsSb QW lasers can only be realized by molecular beam epitaxy (MBE) [31–35] due to the ease of incorporating Sb species into the GaInNAs materials system. Recent works on MBE-grown GaInNAsSb has resulted in promising devices at 1,498 nm [31] and 1,466 nm [33]. Shimizu and coworker [35] reported significantly larger differential gain per well ($\mathrm{d}g/\mathrm{d}n$ per well) of GaInNAsSb QW in comparison to that of GaInAsP QW. The incorporation of Sb and N into GaInAs QW also offers a much improved electron and hole confinement, which leads to reduced thermionic emission and, in turn, improved carrier injection efficiency at high temperature [36].

The pursuit of GaInNAsSb materials systems by metalorganic chemical vapor deposition (MOCVD), however, is still immature due to the challenges in incorporating both Sb- and N-species into GaInAs simultaneously under optimum growth conditions. Optimum MOCVD growth of GaInNAs QW typically requires [DMHy]/[AsH_3] of ~20–25 resulting in [V]/[III] of ~180–200 [9]. In contrast, optimum growth of Sb-containing materials (with TMSb source) typically requires [V]/[III] in the order of ~3 [37]. This large discrepancy in the optimum growth requirements presents great difficulty in realizing high-quality GaInNAsSb QW grown directly by MOCVD.

Here, we present a novel approach to realize GaInNAsSb QW, which allows one to circumvent the challenges present in the MOCVD growth of this quinary compound. This novel approach combines the already-established MOCVD growth technique of GaInNAs and GaInAsSb QWs, with a post-growth annealing that leads to interdiffusion of Sb and N-species, resulting in high-quality interdiffused GaInNAsSb QW. As the GaInNAs and GaInAsSb are grown in separate layers, optimization of their individual MOCVD growth parameters can be achieved independently. High-quality GaInNAs [3, 4, 8–12] and (In)GaAsSb [37–40] QWs have also been previously realized independently by MOCVD. This interdiffused GaInNAsSb QW approach would allow the realization of GaInNAsSb QW emitting in the 1,300–1,550 nm regime without having to grow the SbN-based quinary compound directly by MOCVD.

19.2 Design of the Interdiffused GaInAsNSb Quantum Well

The novel concept is to realize interdiffused GaInNAsSb QW active region by utilizing MOCVD growth of GaInAsSb and GaInNAs layers followed by a postgrowth annealing, where Sb–N interdiffusion takes place, as shown in Fig. 19.1. This idea is made possible due to the large disparity between the

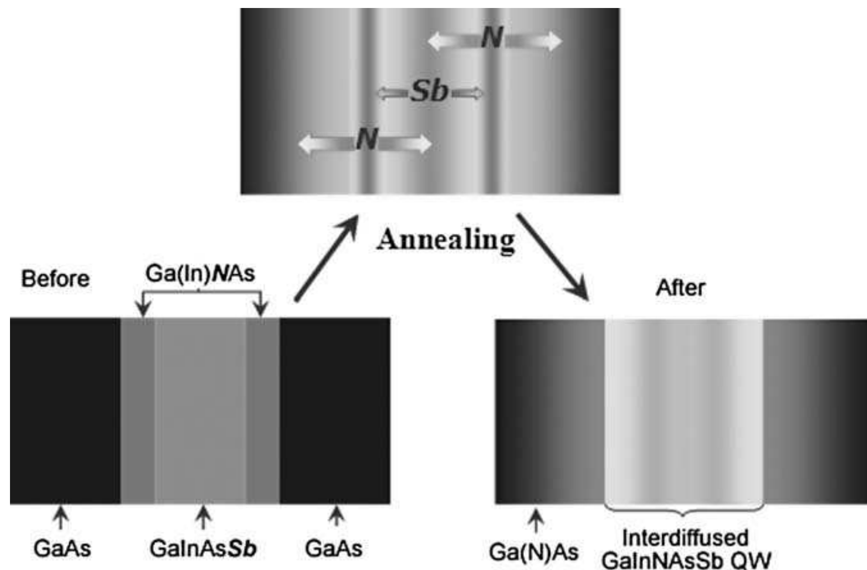

Fig. 19.1. Schematics of interdiffused GaInNAsSb QW by MOCVD and interdiffusion process, (**a**) as grown: GaInAsSb QW sandwiched by GaInNAs layers, (**b**) annealing: Sb–N interdiffusion, and (**c**) after: interdiffused GaInNAsSb QW

diffusion coefficients of N- and Sb-species in GaAs-based crystal lattice. The diffusion coefficient of Sb-species, D_{Sb} in GaAs lattice has been measured and can be expressed as a function of annealing temperature as [41]

$$D_{\mathrm{Sb}} = 2 \times 10^{-14} \exp\left(\frac{-0.62q}{k_{\mathrm{B}}T}\right), \tag{19.1}$$

where q is electron charge, k_{B} is Boltzmann's constant, and T is annealing temperature in Kelvin. Utilizing (19.1), D_{Sb} is estimated to give $\sim 5.3 \times 10^{-18} \mathrm{cm}^2\ \mathrm{s}^{-1}$ at 600°C. By extrapolating N-diffusion characteristics in GaAs lattice [42], the diffusion coefficient (D_{N}) of N-species can be expressed as

$$\log(D_{\mathrm{N}}) = 0.0142T - 27.4036. \tag{19.2}$$

Thus, the parameter D_{N} can then be extracted to give $9.84 \times 10^{-16} \mathrm{cm}^2\ \mathrm{s}^{-1}$ at an annealing temperature of 600°C.

Significant nitrogen diffusion out of GaNAs barrier layer into GaInAs QW (up to 90% of N in the barrier) had been recently reported experimentally [43]. Significant N out-diffusion of the GaInNAs QW had also been found experimentally through SIMS measurement as reported by Ha and coworkers [32]. At annealing temperature of 600°C, N-species diffuse at a rate approximately two orders of magnitude (>∼150) faster than their Sb counterparts, which effectively means that for certain annealing conditions, e.g., 2–5 min at 600°C, annealing multilayered structures with varying N and Sb contents across the layers causes significant N atoms out-diffusion from high N-content region to low N-content region, with only minimum diffusion of Sb-species, as shown in Fig. 19.2. The In and Ga atoms could be assumed as stationary – relative to N and Sb atoms – during annealing, due to their low-interdiffusion coefficients in

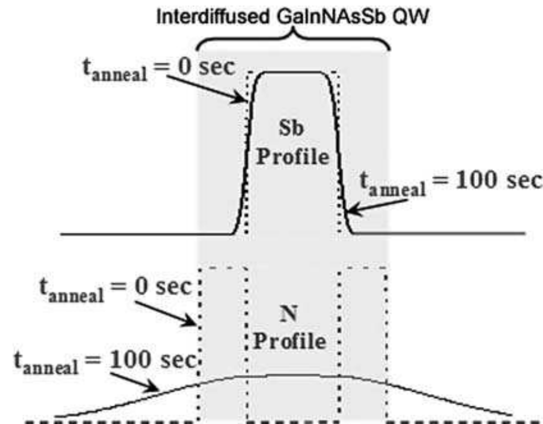

Fig. 19.2. Time evolutions of Sb-profile and N-profile in GaAs lattices during annealing process at temperature of 600°C, for initial condition ($t = 0$ s) and $t_{\mathrm{anneal}} = 100$ s

GaAs matrix (estimated from measurements to give values of $<10^{-20}\,\text{cm}^2\ \text{s}^{-1}$ at 600°C [44]). Recent work also showed that the In and Ga interdiffusion only start to be significant in the GaInAs–GaNAs heterostructure at annealing temperature around 950°C [43].

19.3 Band Lineups of GaInNAsSb Material Systems

The band lineups of GaInNAsSb strained-layer material systems on GaAs are shown in Fig. 19.3. Details of the calculation can be found in Sect 4.2. As Sb-content is increased, hole confinement in GaInAsSb QW is improved with very little penalty in the electron confinement reduction, while electron confinement in GaInNAs QW is improved significantly with increasing N-content. Hence, having both N and Sb in a QW, that is GaInNAsSb QW on GaAs, leads to a marked improvement in both electron and hole confinement, as shown in Fig. 19.3. Improved electron and hole confinement is desirable for high-temperature operation as it suppresses thermionic carrier leakage. The electron (ΔE_c) and holes (ΔE_v) confinement potentials of $\text{Ga}_{0.6}\text{In}_{0.4}\text{As}$–GaAs system are approximately 286 meV and 177 meV, respectively. By incorporating 5% Sb and 1.25% N in the $\text{Ga}_{0.6}\text{In}_{0.4}\text{As}_{1-x-y}\text{N}_y\text{Sb}_x$–GaAs, additional increase of 155 meV and 55 meV for ΔE_c and ΔE_v can be obtained, in comparison to those of the $\text{Ga}_{0.6}\text{In}_{0.4}\text{As}$–GaAs structure. Figure 19.4 gives a contour plot of constant emission wavelength for strained $\text{Ga}_{0.6}\text{In}_{0.4}\text{NAsSb}$ bulk layer (no quantum confinement) on GaAs substrate. Our studies indicate that incorporation of approximately 1.25% N and 5% Sb is sufficient to achieve 1.55 μm emission from GaInNAsSb QW. The GaInNAsSb material system also has

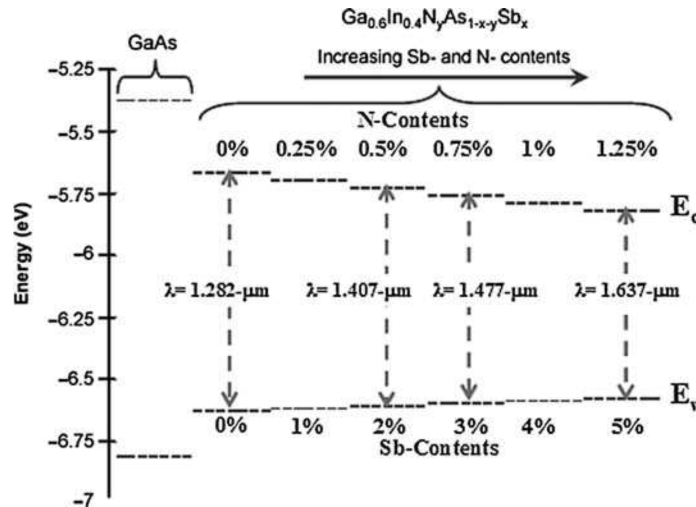

Fig. 19.3. Energy band lineup of strained GaInNAsSb bulk layer on GaAs for various Sb and N-content

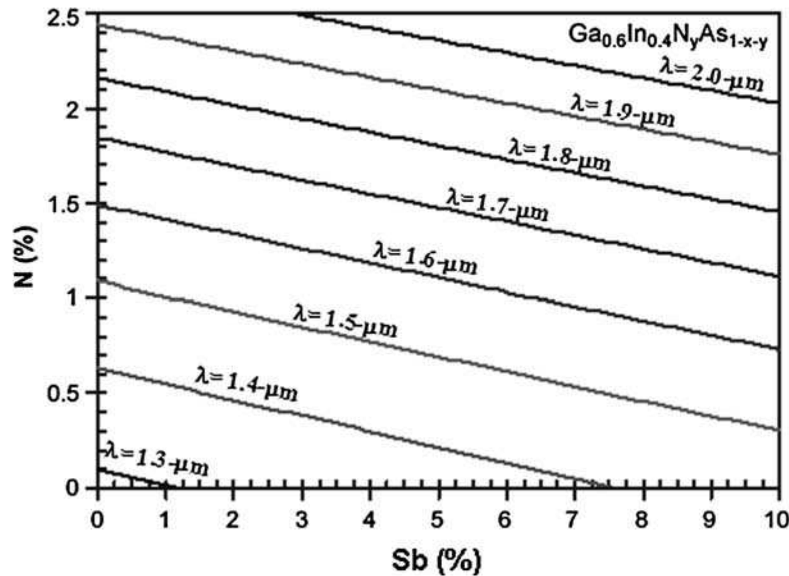

Fig. 19.4. Contour plot of constant emission wavelength ($\lambda_{\text{-emission}}$) of bulk GaInNAsSb strained layer on GaAs

the potential serving as active region for 2.0 μm emitting devices on GaAs substrates.

19.4 Computational Model of Sb–N Quantum Well Intermixing

A theoretical model based upon fundamental semiconductor properties and interdiffusion process is developed. We start with defining the concentration profiles of diffusing Sb- and N-species as functions of three variables: position along the growth axis, annealing temperature, and time. These profiles – time and position dependent Sb- and N-contents – are then incorporated into the energy band lineup calculation of our proposed structure. The effects of strain are also taken into account in the form of band edge energy shifts. Following that, quantum-confined energy levels of electron and hole are computed using effective mass approximation with propagation matrix approach for multilayer heterostructures. Transition energies and emission wavelengths, $\lambda_{\text{-emission}}$ can thus be obtained. Fundamental materials parameters used in our calculations are tabulated in Table 19.1 [45–47].

19.4.1 Sb–N Interdiffusion Model

Concentration profiles of Sb- and N-diffusing species as a function of position, annealing temperature, and time are obtained from solving Fick's diffusion

Table 19.1. Fundamental binary materials properties used in the calculation

Properties	GaAs	GaSb	InAs	InSb	GaN	InN
E_g (eV)	1.424	0.75	0.354	0.17	3.3	1.94
$E_{v,av}$ (eV)	−6.92	−6.25	−6.67	−6.09		
Δ (eV)	0.34	0.82	0.38	0.81	0.017	0.006
a (Å)	5.6533	6.09	6.0584	6.47	4.52	4.98
C_{11} (dyn cm^{-2})	11.879	8.842	8.329	6.847	2.93	1.87
C_{12} (dyn cm^{-2})	5.376	4.026	4.526	3.735	1.59	1.25
a_c (eV)	−7.17	−7.5	−5.08	−6.94	−2.2	−1.85
a_v (eV)	1.16	0.79	1	0.36	−5.2	−1.5
b (eV)	−1.7	−2	−1.8	−2	−2.2	−1.2

equation, and can be written by the following error function distribution [48]:

$$S(z,T,t) = \frac{S_0}{2}\left(\text{erf}\left(\frac{d_1 - z}{L_{\text{d_s}}}\right) + \text{erf}\left(\frac{d_2 + z}{L_{\text{d_s}}}\right)\right), \tag{19.3}$$

with S_0 is the initial (as-grown) species content in the layer of interest, $L_{\text{d_s}}$ as the diffusion length of the species, z as the position along the growth axis, and d_1 and d_2 as the spatial offsets for epitaxial layer definitions. Diffusion length $L_{\text{d_s}}$ is related to the diffusion coefficient (D_s) and the annealing time (t) as follow:

$$L_{\text{d_s}} = 2\sqrt{D_s t}, \tag{19.4}$$

where D_s is the diffusion coefficient of the diffusing species (D_{Sb} or D_N as given in (19.1) and (19.2), respectively). Figure 19.5a, b shows the Sb- and N-content profiles functions of position along the growth axis (z) for various annealing time (t_{anneal}) at a fixed annealing temperature (T_{anneal}) with as grown N and Sb content, $N_o = Sb_o = 3\%$. It is shown that at $T_{\text{anneal}} = 600°C$, at any calculated t_{anneal} (0, 30, 100, and 500 s), N-species outdiffusion due to concentration gradient is significantly larger than that of Sb-species, as shown in Fig. 19.5a, b.

19.4.2 Ga(N)As–GaInNAs–GaIn(N)AsSb Energy Band Lineup

In developing the computational model of this Sb–N materials system, we employ model solid theory, strain effect, and quantum confinement effect. Materials parameters of Sb-containing compounds obtained using correlated function expansion (CFE) method [49]. We divide the proposed structure into five layers composed of three different compounds: GaAs, GaInNAs, and GaInAsSb; with GaInAsSb layer sandwiched between GaInNAs layers on GaAs substrate. The impact on the band lineup of GaInNAs layer due to N incorporation is taken into account by using the phenomenological relation [50], as described in Sect. 4.2.3. The effect of strain on the band line up of the material system is taken into account in the form of energy band edge shifts.

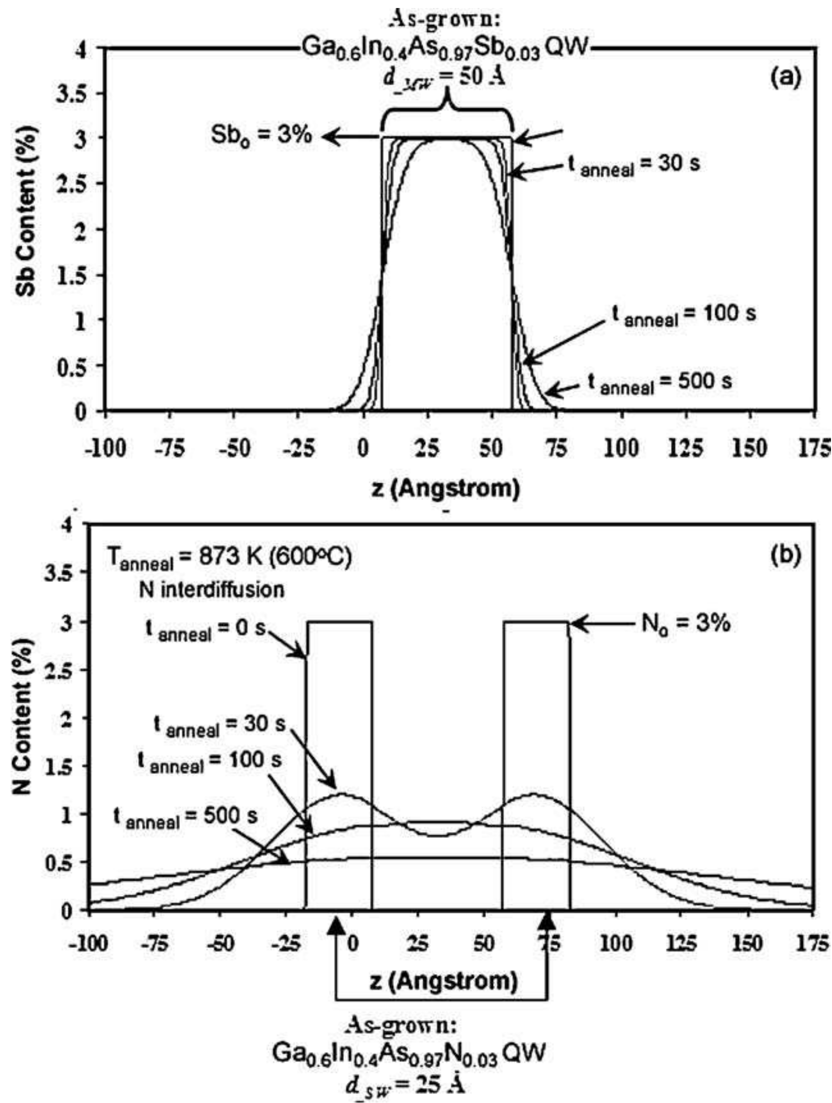

Fig. 19.5. (**a**) Sb-content and (**b**) N-content as a function of position along growth axis (z) and annealing time (t_{anneal})

Unstrained Band Lineup

Valence band edge energy levels of unstrained epitaxial layers can be calculated as follows [51]:

$$E_{\mathrm{vo}} = E_{\mathrm{v,av}} + \frac{\Delta}{3}, \tag{19.5}$$

Table 19.2. Expressions used for the energy gap of $Ga_{1-x}In_xAs_{1-y}Sb_y$, obtained from extrapolation of calculated CFE points

	Extrapolated expressions for E_g of $Ga_{1-x}In_xAs_{1-y}Sb_y$
$x = 0.1$	$E_g = 0.63y^2 - 1.5482y + 1.2711$
$x = 0.2$	$E_g = 0.4343y^2 - 1.3405y + 1.1185$
$x = 0.3$	$E_g = 0.5843y^2 - 1.2875y + 0.9794$
$x = 0.4$	$E_g = 08729y^2 - 1.3213y + 0.8552$
$x = 0.43$	$E_g = 0.7821y^2 - 1.2599y + 0.8203$

where $E_{v,av}$ is the average energy over three valence band edges (heavy hole, light hole, and spin–orbit split-off bands), and Δ is the spin–orbit split-off energy. To interpolate most of the ternary and quaternary compound parameters used in our calculation, e.g., $E_{v,av}$ and Δ, from their binary values, Vegard's linearity rule is used. The energy gap of GaInAs is widely available in literature and is given by [51]:

$$E_{g_GaInAs(x)} = 0.324 + 0.7(1 - x) + 0.4(1 - x). \tag{19.6}$$

GaInAsSb material systems, however, is not as widely studied. As a result, we extrapolate energy gap of GaInAsSb from points calculated using the CFE [49] method, as a function of Sb-content for various In-content, as listed in Table 19.2. Following that, the conduction band of unstrained layers (GaAs, GaInAs, and GaInAsSb) can be obtained by adding each compound's energy gap to its respective valence band edge energy levels:

$$E_{co} = E_{vo} + E_g \tag{19.7}$$

Strained Band Lineup

In the presence of strain, the strain tensors in the plane of GaInAs and GaInAsSb epitaxial layers can be expressed as

$$\varepsilon_{xx} = \varepsilon_{yy} = \frac{a_o - a}{a}, \tag{19.8}$$

where a_o is the lattice constant of GaAs substrate and a is the lattice constants of GaInAs or GaInAsSb epitaxial layers. The perpendicular strain tensors can be expressed as:

$$\varepsilon_{zz} = -2\frac{C_{12}}{C_{11}}\varepsilon_{xx}, \tag{19.9}$$

where C_{11} and C_{12} are the interpolated elastic stiffness constants of GaInAs and GaInAsSb.

The calculated valence band edge energy levels of GaInAs and GaInAsSb are then shifted to give their strained valence band edge energy levels:

$$E_v = E_{vo} - P_\varepsilon - Q_\varepsilon, \tag{19.10}$$

where P_ε and Q_ε are expressed as follows:

$$P_\varepsilon = -a_\mathrm{v}(\varepsilon_{xx} + \varepsilon_{yy} + \varepsilon_{zz}) \quad (19.11)$$

$$Q_\varepsilon = -\frac{b}{2}(\varepsilon_{xx} + \varepsilon_{yy} - 2\varepsilon_{zz}). \quad (19.12)$$

Similarly, the unstrained conduction band energy levels of GaInAs and GaInAsSb are also shifted to give their strained conduction band energy levels:

$$E_\mathrm{c} = E_\mathrm{co} + P_\mathrm{c}, \quad (19.13)$$

where P_c is expressed as follows:

$$P_\mathrm{c} = a_\mathrm{c}(\varepsilon_{xx} + \varepsilon_{yy} + \varepsilon_{zz}). \quad (19.14)$$

The parameters a_v and a_c are the hydrostatic deformation potentials for the valence band and conduction band, respectively, while b is the shear deformation potential.

N-Incorporation into Strained Band Lineup Calculation

N-incorporation into the GaInAs QW, to form the GaInNAs QW, is known to only mainly affect conduction band lineup of the structure. In this study, the out-diffusion of N species from the GaInNAs layer into the GaAs and GaInAsSb layers is assumed to only affect their conduction band edges as well. Here, we use the following phenomenological relationship to describe the change in energy gaps (in eV) due to N-species diffusion [50]:

$$E_{\text{g-N-containing_compound}} = E_{\text{g-N-free_compound}} - 69\Delta\varepsilon, \quad (19.15)$$

where $\Delta\varepsilon$ is the difference between the strain tensors calculated for N-free and N-containing compounds, e.g., GaInAsSb and GaInAsNSb. Equation (19.15) is originally extracted for GaInNAs material systems [50], and we assume the same expression could also be used to relate the energy gap of GaInAsSb and GaInNAsSb material systems with relatively low Sb-content (∼3–5% Sb). The uncertainty in some of the parameters used here should only affect the details and not the main qualitative trends/conclusions of this study.

The evolution of the conduction band and valence band profiles of the interdiffused GaInAsSb–GaInNAs QW structures as a function of t_anneal are shown in Fig. 19.6a, b. The change in the conduction band profiles of the interdiffused QW structure is attributed mainly to the large N-interdiffusion process into the center QW (from the surrounding as-grown GaInNAs layers), while minimal changes is observed in the valence band profile of the interdiffused QW structure.

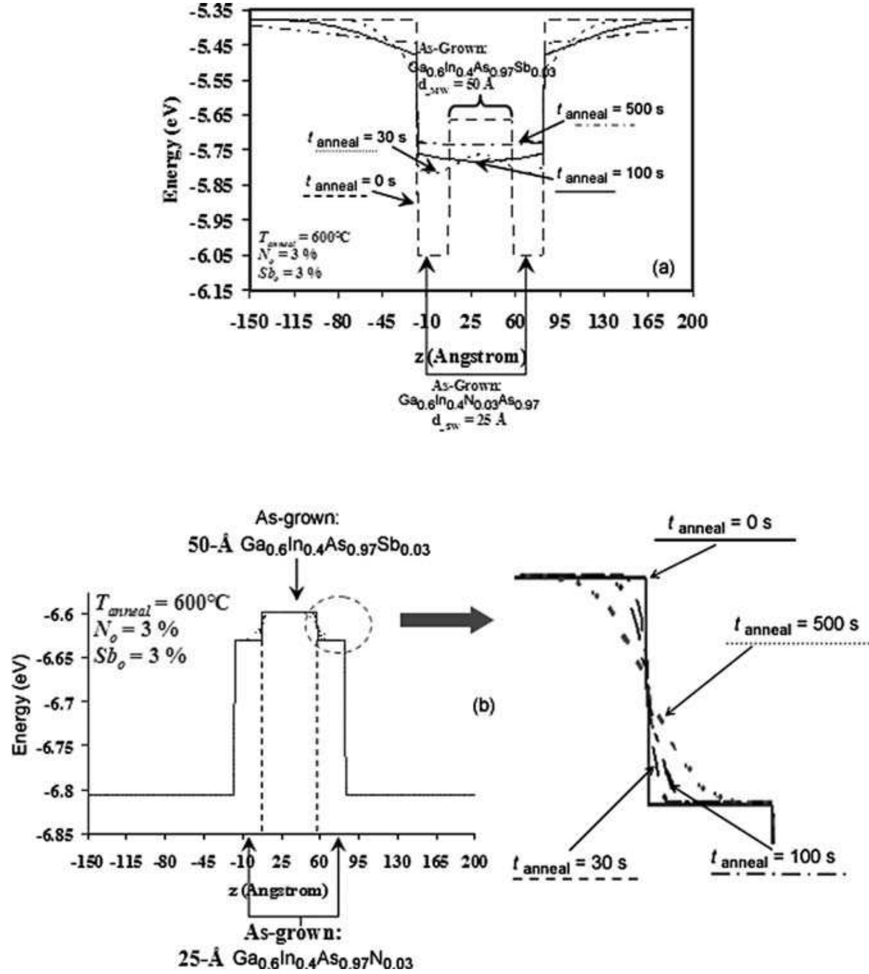

Fig. 19.6. (**a**) Conduction band edge and (**b**) valence band edge evolution due to Sb–N interdiffusion as function of annealing time (t_{anneal})

Quantum-Confined Energy Levels

For the calculation of emission wavelength, quantum confined energy levels must first be computed. We use the standard effective mass approximation with propagation matrix approach for multilayer heterostructures to obtain the confined energy levels of electron and hole [51].

Similar to the relation used to express energy gaps of N-containing compound, the N-induced changes in the electron effective masses for the N-containing compound at different regions can also be approximated using the phenomenological relation [50] as follows:

$$m_{\text{e_N-containing_compound}} = m_{\text{e_N-free_compound}} + 18.1667\ m_{\text{o}}\Delta\varepsilon, \qquad (19.16)$$

where m_o is the free electron mass. To ensure sufficient computational accuracy, the matrices were propagated for almost infinitesimal thickness elements of 2 Å each (final QW thickness after annealing ranges from 50–110 Å). Electron and hole wavefunctions are also plotted as means to verify the type-I transition for electron and hole ground states, i.e., $E_{e1} - E_{hh1}$.

19.5 Interdiffused GaInAsSb–GaInNAs Quantum Well Structure

In designing the GaInAsSb–GaInNAs QW emitting in the 1,500 nm regime, we utilize materials compositions that had been optimally realized by MOCVD growth technique. Prior MOCVD works had resulted in high-performance low-threshold GaInNAs QW lasers on GaAs with 40% In-content for emission wavelength at 1,280–1,380 nm [3, 4, 8–12]. Quantum well lasers based on GaInAsSb QW on GaAs with 40% In-content had also been realized by MOCVD, with emission wavelength at 1,270 nm [38]. In our studies, the composition of the In-contents is chosen as approximately 40% for both the GaInNAs and GaInAsSb QW layers. The dilute N-and Sb-contents in the range of 0–3% and 0–6% are utilized for the GaInNAs and GaInAsSb layers, respectively.

Figure 19.7 shows the emission wavelength ($\lambda_{_emission}$) of the interdiffussed $Ga_{0.6}In_{0.4}As_{1-x}Sb_x$–$Ga_{0.6}In_{0.4}N_y$ As_{1-y}QW structures with various Sb and N-contents, sandwiched by the GaAs barriers. The schema in Fig. 19.7 shows the as-grown cross-section of the GaInAsSb–GaInNAs QW structures with GaAs barriers. The dimensions of the as-grown GaInAsSb and GaInNAs layers

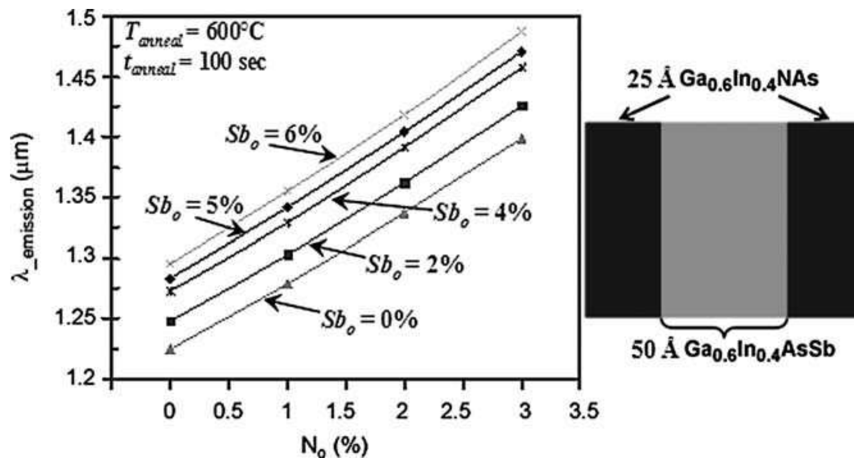

Fig. 19.7. Emission wavelength ($\lambda_{_emission}$) as function of as-grown Sb- and N-content

are kept at 50 Å and 25 Å, respectively. By annealing the GaInAsSb–GaInNAs QW structures at 600°C for 100 s, transition wavelength in the 1,300–1,500 nm regime can be achieved from the interdiffused GaInNAsSb QW structure, as shown in Fig. 19.7. Emission wavelength increases by approximately 50 nm and 12.5 nm are found for every percentage addition of the as-grown N- and Sb-contents, respectively, in the QW structures above.

It is important to note that (as shown in Fig. 19.6) the *as-grown* conduction and valence band profiles exhibit the type-II QW alignment. By annealing the QW structures, type-I interdiffused GaInNAsSb QW can be realized as shown in Fig. 19.6. The emission wavelength of the interdiffused QW structure is the longest when the N-distribution is maximal in the center region. It is important to note that further annealing beyond this point will lead to further out-diffusion of N from the center region of the GaInAsNSb QW, resulting in increase in the transition energy of the QW structure as shown in Fig. 19.8a. From Fig. 19.8b, we found that the typical range of the annealing time for the type-I QW formation starting with the structures above is approximately 80–120 s, at annealing temperature of 600°C.

19.6 Optimization for Interdiffused GaInNAsSb Quantum Well at 1,550 nm Regime

Extension of the emission wavelength of the interdiffused GaInAsSb–GaInNAs QW structures up to 1,550 nm regime can be achieved by increasing the thickness the as-grown GaInNAs layer ($d_{_SW}$), which in turn leads to reduced quantum confinement effect of the interdiffused QW structure. As shown in Fig. 19.9 for the case of 50 Å $Ga_{0.6}In_{0.4}As_{1-x}Sb_x$ surrounded by $Ga_{0.6}In_{0.4}N_yAs_{1-y}$ layers, the emission wavelength of the interdiffused QW structures monotonically increases as the thicknesses of the as-grown GaInNAs ($d_{_SW}$) increases. However, it is important to ensure the thickness of the GaInNAs layers to be kept below its critical thickness, for achieving high-quality materials.

Reducing the quantum confinement effect can also be achieved by increasing the thickness of the GaInAsSb layer ($d_{_MW}$). However, it is important to note that as the thickness of the GaInAsSb is increased beyond a certain value, the maximum N-content in the center region from the interdiffusion is reduced resulting in increase of the transition energy level. To illustrate this (as shown in Fig. 19.10), for as-grown QW structures consisting of $Ga_{0.57}In_{0.43}As_{0.95}Sb_{0.05}$ layer surrounded by 25 Å $Ga_{0.57}In_{0.43}N_{0.03}As_{0.97}$ layers, one observes that the emission wavelength reduces for the interdiffused GaInNAsSb QW with $d_{_MW} > 30$–40 Å, attributed to the decrease in the N-content in the QW center. Emission wavelength at 1,530 nm is achievable for the interdiffused QW structure above with $d_{_MW}$ at around 30 Å.

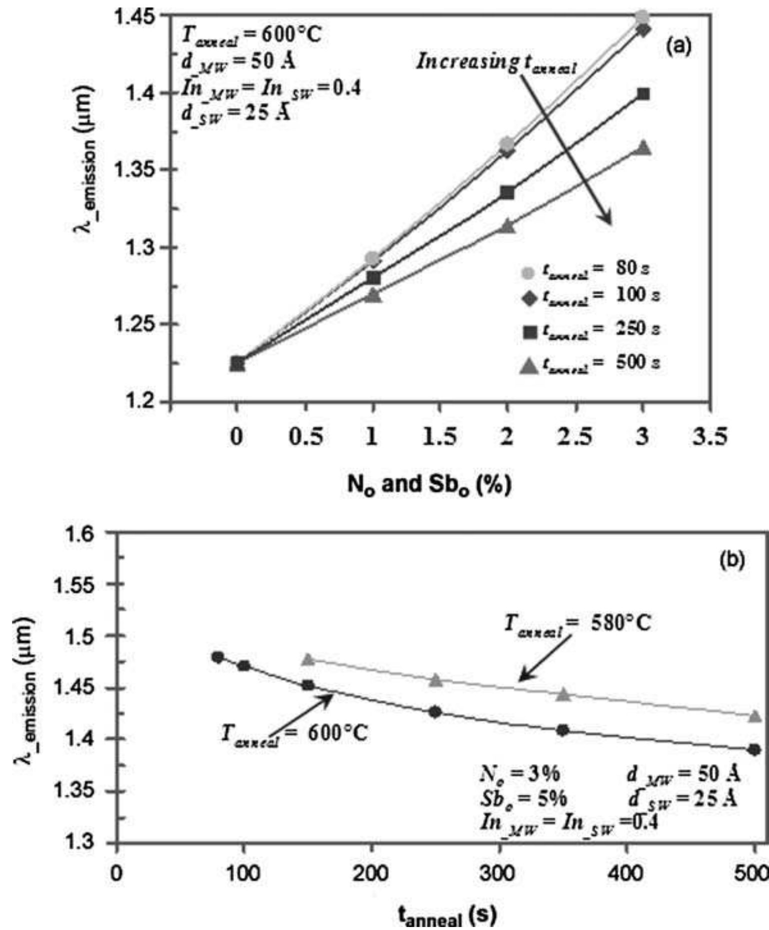

Fig. 19.8. (**a**) Emission wavelength is shown to decrease with increasing annealing time due to N-species out-diffusion of the GaInNAsSb QW center region, (**b**) the effect of overannealing on emission wavelength for various annealing temperature is also shown for a particular as-grown Sb- and N-content

19.7 Strain-Compensated Interdiffused GaInAsSb–GaNAs Quantum Well Structure

One of the potential challenges related to interdiffused GaInAsSb–GaInNAs QW structure is the need to realize as-grown GaInNAs layers with relatively-high N-content (2–3%), as described in earlier sections. However, the incorporation of relatively high (3%) N-content in the GaInNAs QW layers by MOCVD growth technique becomes increasingly challenging, as the In-content in the layer increases. An alternative approach to alleviate the challenges of N-incorporation in high In-content GaInNAs QW during the MOCVD growth,

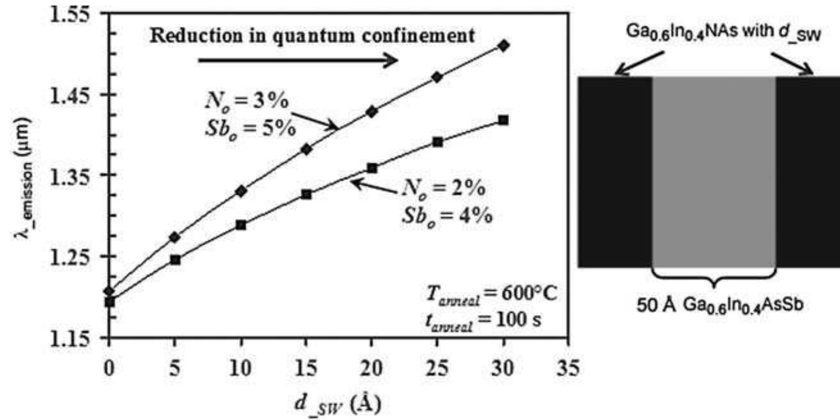

Fig. 19.9. Emission wavelength ($\lambda_{\text{_emission}}$) of interdiffused GaInNAsSb QW as function of GaInNAs layer thickness ($d_{\text{_SW}}$)

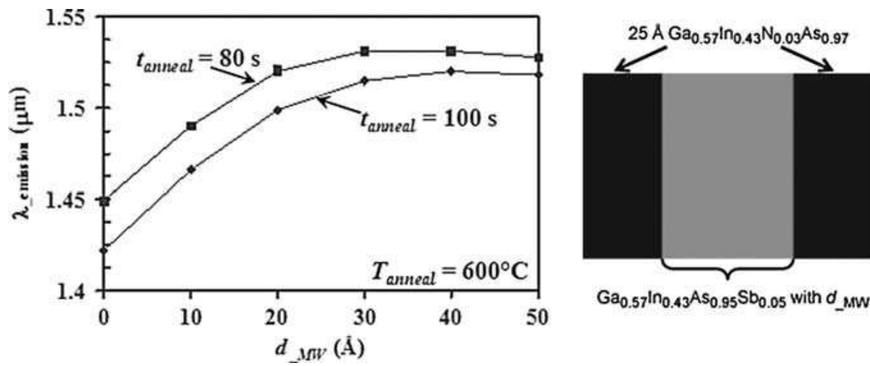

Fig. 19.10. Emission wavelength ($\lambda_{\text{_emission}}$) of interdiffused GaInNAsSb QW as function of GaInAsSb layer thickness ($d_{\text{_MW}}$)

is to replace the GaInNAs layers with the GaNAs layers to surround the GaInAsSb center QW, as shown in Fig. 19.11.

Utilizing the GaInAsSb–GaNAs QW structures leads to several advantages. The In-free GaNAs layers allow one to incorporate higher N-content in the layer, thus enabling post-interdiffused GaInAsSb–GaNAs QW structure with sufficiently long emission wavelength up to ∼1,500 nm even without the presence of In in the dilute-nitride layers. In addition, the tensile-strained GaNAs QWs and the compressively strained GaInAsSb QW allow strain compensation, leading to reduced effective net strain of the QW structures.

Figure 19.11 shows the emission wavelength of the interdiffused GaInAsSb–GaNAs QW structures as a function of GaInAsSb layer thickness ($d_{\text{_MW}}$), with various annealing conditions (annealing temperature at 600°C, for annealing times of 80 and 100 s). The interdiffused GaInAsSb–GaNAs QW

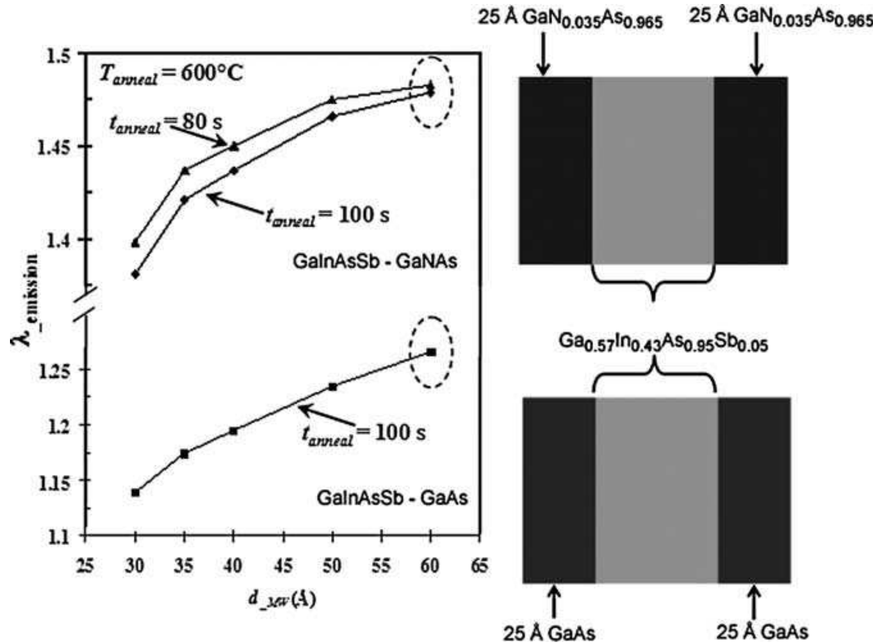

Fig. 19.11. Emission wavelength ($\lambda_{\text{_emission}}$) of strain-compensated interdiffused GaInAsSb–GaNAs QW structures and interdiffused GaInAsSb–GaAs QW, with annealing temperature at 600°C

structures on GaAs, with as-grown N- and Sb-contents of 3.5% and 5%, show the feasibility of achieving the emission wavelength in the 1,400–1,500 nm regimes. Emission wavelength of 1.483 μm is obtained for interdiffused $Ga_{0.57}In_{0.43}As_{0.95}Sb_{0.05}$-$GaN_{0.035}As_{0.965}$ QW structures after annealing condition at 600°C for 80 s. Thus, it is possible to achieve ~1.5 μm emission on GaAs with strain compensated, interdiffused GaInAsSb–GaNAs type-I QW structure. For comparison purpose, interdiffused $Ga_{0.57}In_{0.43}As_{0.95}Sb_{0.05}$–GaAs QW structures (annealing at 600°C for 100 s) only allows emission up to 1.266 μm for structures with thickness ($d_{\text{_MW}}$) of 60 Å.

19.8 Experiments on the Interdiffusion of Sb- and N-Species in GaAs

Preliminary experiments are conducted to understand the interdiffusion process in the Sb- and N-containing quantum well. The objective of these preliminary studies is to verify the minimum out-diffusion of the Sb species from Sb-containing QW, as well as to confirm the feasibility of realizing interdiffused SbN-based QW.

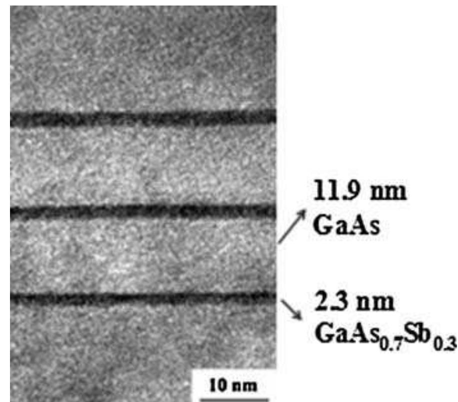

Fig. 19.12. Cross-sectional TEM images for 2.3 nm $GaAs_{0.7}Sb_{0.3}$ QW sandwiched by 12 nm GaAs barriers

Thus, experimental works utilizing rapid thermal annealing (RTA) of GaAsSb and GaNAs multiquantum well (MQW) samples on GaAs have been performed as a means to understand the diffusivities of these species in GaAs matrix. Photoluminescence (PL) measurements before and after annealing allows one to observe shifts in peak emission wavelength of the QW samples. By comparing the magnitude of these wavelength shifts for both types of samples, one is able to deduce the diffusivities of N- and Sb-species in GaAs matrix at a specific annealing temperature.

The preliminary Sb-interdiffusion experiments are conducted on MOCVD-grown $GaAs_{0.7}Sb_{0.3}$ multiple QWs structure, surrounded by GaAs barriers, as shown in Fig. 19.12. The dimensions of the GaAsSb QW and GaAs barriers are 2.3 nm and 11.9 nm, respectively. These values are obtained by XRD and TEM measurements. Sharp interfaces between GaAsSb QWs and GaAs barrier layers are observed via TEM measurements, indicating high-materials quality.

PL measurements at low temperature ($T = 77$ K) are conducted on the as-grown and annealed GaAsSb QW samples. The RTAs on the GaAsSb QW samples are conducted at annealing temperature of 700°C for 100 s and 200 s, using AG Associates Rapid Thermal Annealer.

In Figs. 19.13 and 19.14, low-temperature PL ($T = 77$ K) spectra and shifts in peak emission wavelengths of the as-grown and annealed samples are presented, respectively. Minimal shifts of only 6–11 nm in peak emission PL wavelength for the annealed samples (700°C for 100 s and 200 s), in comparison to that of the as-grown sample, are observed. The minimal peak wavelength blueshift for as-grown and postannealed spectra in the experiments presumably can be attributed to the minimal out-diffusion of Sb-species out of the QW due to the low diffusivity of the Sb-species in GaAs matrix, as predicted by the theory.

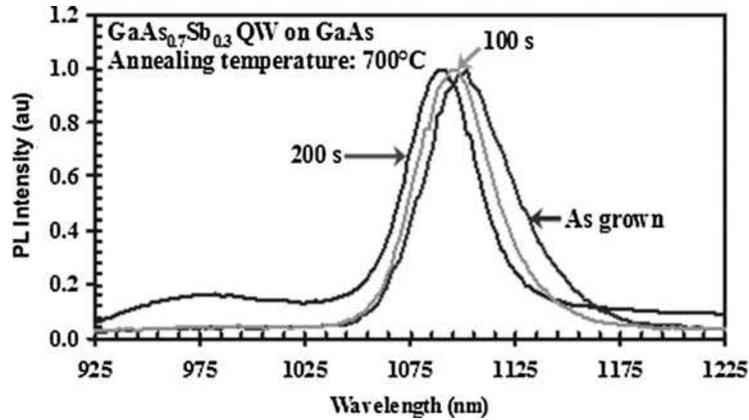

Fig. 19.13. Low-temperature (77 K) PL spectrum of $GaAs_{0.7}Sb_{0.3}$ QW samples. Minimum PL shift is observed between as-grown and annealed samples

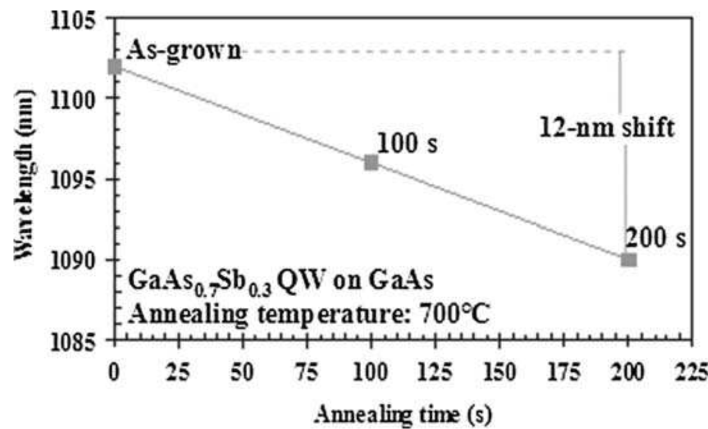

Fig. 19.14. PL shifts as a function of annealing time for as-grown and annealed $GaAs_{0.7}Sb_{0.3}$ samples

The preliminary N-interdiffusion experiments are also conducted on MOCVD-grown GaNAs multiple QWs structure, surrounded by GaAs barriers, as shown in Fig. 19.15. Similar RTA experiments are conducted on this MOCVD-grown GaNAs sample, consisting of four 7.3 nm $GaAs_{0.957}N_{0.043}$ QW separated by 16.7 nm GaAs barrier layers. The N-content in the GaNAs QW is measured at approximately 4.3% using high-resolution X-ray diffractometer.

Low-temperature ($T = 77$ K) PL measurements are conducted on the as-grown and annealed GaNAs QW samples. The annealing for the dilute nitride sample is done at a temperature of 700°C, which is identical with that of the Sb-interdiffusion experiment to allow direct comparison of both experiments. As shown in Fig. 19.15, the peak PL wavelength of the annealed GaNAs sample

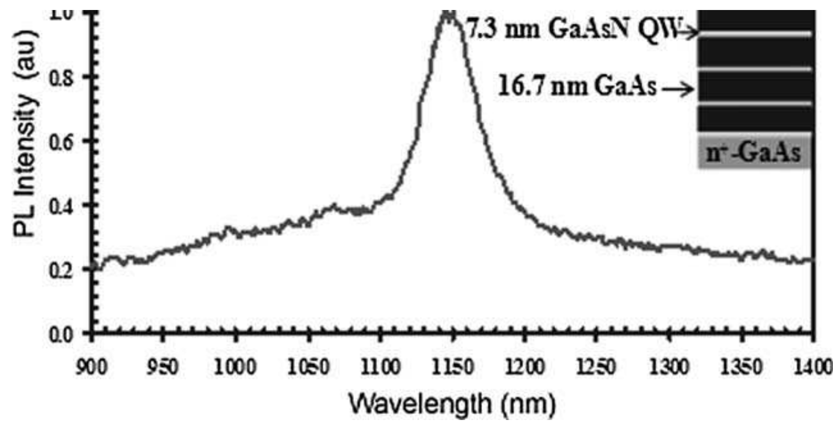

Fig. 19.15. Low-temperature PL spectrum of GaNAs sample after annealing at 700°C for 100 s. The schematic of the GaNAs–GaAs multiple quantum well structure is shown in the *inset*

(annealed at 700°C for 100 s) is measured at 1,150 nm, which corresponds to a significant blueshift of approximately 132 nm in comparison to that of the as-grown GaNAs sample. The significant blueshift in the annealed GaNAs QW can be presumably attributed to the large out-diffusion of N-species from the GaNAs QW, which is due to the large diffusivity of the N-species in GaAs matrix as predicted by theory. Our experimental findings of the large out-diffusion of N-species from the GaNAs QW structure is also in agreement with the recent experimental findings reported by other groups [32, 43], which reports significant nitrogen out-diffusion from Ga(In)NAs layers.

Our preliminary experimental findings show a good agreement with the theory, where the N-species diffuse at a rate approximately two orders of magnitude ($>\sim 150$) faster than their Sb counterparts in GaAs matrix (at 600–700°C). By annealing GaInNAs–GaInAsSb heterostructure, significant out-diffusion of N-species from the GaInNAs (high-N content region) will occur, with only minimal out-diffusion of Sb-species from GaInAsSb layer. Therefore, the Sb–N interdiffusion process is feasible for one to form the interdiffused GaInAsSb QW from MOCVD-grown GaInNAs–GaInSbAs heterostructures.

19.9 Summary

Here we present a novel approach to achieve interdiffused GaInAsNSb QW capable of emission wavelength in the 1,300–1,550 nm regimes on GaAs, utilizing the MOCVD growth epitaxy technology. This approach allows MOCVD growth of the Ga(In)NAs and GaInAsSb layers at their individually optimized epitaxy conditions, followed by an interdiffusion process to achieve quinary

GaInNAsSb QW structures. This interdiffused GaInNAsSb QW approach, which avoids challenges in growing the mixed SbN-based quinary compound directly by MOCVD, may provide an excellent alternative to the existing approaches for the pursuit of 1,550 nm emission on GaAs. An emission wavelength at the 1,500 nm could also be achieved from a strain-compensated interdiffused GaInAsSb–GaNAs QW structures. The large electron and hole confinements in the GaInNAsSb–GaAs QW systems allow suppression of thermionic carrier leakage, which is beneficial for high-temperature operations of semiconductor laser devices. Preliminary experimental findings have shown the feasibility of the method, indicated by a huge disparity between N- and Sb-species diffusivity in GaAs matrix.

Acknowledgments. The authors would like to acknowledge helpful technical assistances from Prof. Luke J. Mawst and Dr. Jeng-Ya Yeh of the Electrical and Computer Engineering Department at the University of Wisconsin-Madison (Madison, WI, USA), and helpful discussions with Prof. Boon-Siew Ooi of the Electrical and Computer Engineering Department at Lehigh University (Bethlehem, PA, USA).

References

1. M. Kondow, T. Kitatani, S. Nakatsuka, M.C. Larson, K. Nakahara, Y. Yazawa, M. Okai, K. Uomi, IEEE J. Select. Topic Quantum Electro. **3**, 719 (1997)
2. J.S. Harris Jr. IEEE J. Select. Topics Quantum Electron. **6**, 1145–1160 (2000)
3. N. Tansu, J.Y. Yeh, L.J. Mawst, IOP J. Phys.: Condens. Matter Phys. **16**, S3277 (2004)
4. D.A. Livshits, A. Yu Egorov, H. Riechert, Electron. Lett. **36**, 1381 (2000)
5. F. Hohnsdorf, J. Koch, S. Leu, W. Stolz, B. Borchert, M. Druminski Electron. Lett. **35**, 571 (1999)
6. M. Kawaguchi, T. Miyamoto, E. Gouardes, D. Schlenker, T. Kondo, F. Koyama, K. Iga, Jpn. J. Appl. Phys. **40**, sL744 (2001)
7. T. Takeuchi, Y.L. Chang, M. Leary, A. Tandon, H.C. Luan, D.P. Bour, S.W. Corzine, R. Twist, M.R. Tan, in *IEEE LEOS 2001 Post-Deadline Session*, San Diego, USA, 2001
8. N. Tansu, L.J. Mawst, IEEE Photon. Technol. Lett. **14**, 444 (2002)
9. N. Tansu, N.J. Kirsch, L.J. Mawst, Appl. Phys. Lett. **81**, 2523 (2002)
10. N. Tansu, A. Quandt, M. Kanskar, W. Mulhearn, L.J. Mawst, Appl. Phys. Lett. **83**, 18 (2003)
11. N. Tansu, J.Y. Yeh, L.J. Mawst, Appl. Phys. Lett. **83**, 2112 (2003)
12. N. Tansu, J.Y. Yeh, L.J. Mawst, Appl. Phys. Lett. **83**, 2512 (2003)
13. N. Tansu, J.Y. Yeh, L.J. Mawst, IEEE J. Select. Topic Quantum Electron. **3**, 1220 (2003)
14. J. Wei, F. Xia, C. Li, S.R. Forrest, IEEE Photon. Technol. Lett. **14**, 597 (2002)
15. K.D. Choquette, J.F. Klem, A.J. Fischer, O. Blum, A.A. Allerman, I.J. Fritz, S.R. Kurtz, W.G. Breiland, R. Sieg, K.M. Geib, J.W. Scott, R.L. Naone, Electron. Lett. **36**, 1388 (2000)
16. W. Ha, V. Gambin, M. Wistey, S. Bank, S. Kim, J.S. Harris Jr., IEEE Photon. Technol. Lett. **14**, 5 (2002)

17. C.S. Peng, T. Jouhti, P. Laukkanen, E.M. Pavelescu, J. Konttinen, W. Li, M. Pessa, IEEE Photon. Technol. Lett. **14**, 275 (2002)
18. N.N. Ledentsov, A.R. Kovsh, A.E. Zhukov, N.A. Maleev, S.S. Mikhrin, A.P. Vasil'ev, E.S. Semenova, M.V. Maximov, Yu. M. Shernyakov, N.V. Kryzhanovskaya, V.M. Ustinov, D. Bimberg, Electron. Lett. **39**, 1126 (2003)
19. O.B. Shchekin, Appl. Phys. Lett. **80**, 3277 (2002)
20. A.R. Kovsh, N.A. Maleev, A.E. Zhukov, S.S. Mikhrin, A.R. Vasil'ev, Yu. M. Shemyakov, M.V. Maximov, D.A. Livshits, V. Ustinov, Zh. I. Alferov, N.N. Ledentsov, D. Bimberg, Electron. Lett. **38**, 1104 (2002)
21. D.L. Huffaker, G. Park, Z. Zou, O.B. Shchekin, D.G. Deppe, Appl. Phys. Lett. **73**, 2564 (2001)
22. G.T. Liu, A. Stintz, H. Li, K.J. Malloy, L.F. Lester, Electron. Lett. **35**, 1163 (1999)
23. K. Mukai, Y. Nakata, K. Otsubo, M. Sugawara, N. Yokoyama, H. Ishikawa, IEEE Photon. Technol. Lett. **11**, 1205 (1999)
24. A. Stintz, G.T. Liu, H. Li, L.F. Lester, K.J. Malloy, IEEE Photon. Technol. Lett. **12**, 591 (2000)
25. S. Ghosh, S. Pradhan, P. Bhattacharya, Appl. Phys. Lett. **81**, 3055 (2002)
26. P. Dowd, W. Braun, D.J. Smith, C.M. Ryu, C.Z. Guo, S.L. Chen, U. Koelle, S.R. Johnson, Y.H. Zhang, Appl. Phys. Lett. **75**, 1267 (1999)
27. N. Tansu , L.J. Mawst, IEEE J. Quantum Electron. **39**, 1205 (2003)
28. I. Vurgaftman, J.R. Meyer, N. Tansu, L.J. Mawst, Appl. Phys. Lett. **83**, 2742 (2003)
29. N. Tansu, L.J. Mawst, US Patent No. 6,791,104, approved on September 14, 2004
30. P.D. Dapkus, International Patent Application No. PCT/US00/14332 (WO01/29943), filed on May 24, 2000
31. S.R. Bank, M.A. Wistey, L.L. Goddard, H.B. Yuen, V. Lordi, J.S. Harris Jr., IEEE. J. Quantum Electron. **40**, 656 (2004)
32. W. Ha, V. Gambin, S. Bank, M. Wistey, H. Yuen, S. Kim, J.S. Harris Jr., IEEE. J. Quantum Electron. **38**, 1260 (2002)
33. S.R. Bank, M.A. Wistey, L.L. Goddard, H.B. Yuen, H.P. Bae, J.S. Harris, Electron. Lett. **40**, 1186 (2004)
34. X. Yang, J.B. Heroux, L.F. Mei, W.I. Wang, Appl. Phys. Lett. **78**, 4068 (2001)
35. H. Shimizu, K. Kumada, S. Uchiyama, A. Kasukawa, Electron. Lett. **37**, 28 (2001)
36. J.Y. Yeh, N. Tansu, L.J. Mawst, Electron. Lett. **40**, 739 (2004)
37. J.G. Cederberg, M.J. Hafich, R.M. Biefield, M. Palmisiano, J. Cryst. Growth **248**, 289 (2003)
38. H.C. Kuo, H.H. Yao, Y.S. Chang, M.Y. Tsai, S.C. Wang, L.H. Laih, J. Cryst. Growth **272**, 538 (2004)
39. T. Kageyama, T. Miyamoto, M. Ohta, T. Matsuura, Y. Matsui, T. Furuhata, F. Koyama, J. Appl. Phys. **96**, 44 (2004)
40. S.W. Ryu, P.D. Dapkus, Electron. Lett. **36**, 1387 (2000)
41. V.V. Chaldyshev, N.A. Bert, G. Musikhin, A.A. Suvorova, V.V. Preobrazhenskii, M.A. Putyato, B.R. Semyagin, P. Werner, U. Gosele, Appl. Phys. Lett. **79**, 1294 (2001)
42. G. Bosker, N.A. Stolwijk, Phys. Rev. Lett. **81**, 3443 (1998)
43. M.O. Michael, G. Sridhar, S. Rubin, M.R. Jason, L.H. Archie Jr., Appl. Phys. Lett. **86**, 151903–1 (2005)

44. M.O. Manasrek (series Ed.), *Optoelectronic Properties of Semiconductors and Superlattices*, E. Herbert Li (Ed.), *Semiconductor Quantumwell intermixing*, (2000) Volume 8, Gordon and Breach Science Publishers, Singapore
45. I. Vurgaftman, J.R. Meyer, L.R. Ram-Mohan, J. Appl. Phys. **89**, 5815 (2001)
46. C.G. Van De Walle, Phys. Rev. B. **38**, 1871 (1989)
47. J. Piprek, *Semiconductor Optoelectronic Devices: Introduction to Physics and Simulation* (Academic Press, San Diego, 2003)
48. M.C.Y Chan, C. Surya, P.K.A Wai, J. Appl. Phys. **90**, 197 (2001)
49. K. Shim, H. Rabitz, P. Dutta, J. Appl. Phys. **88**, 7157 (2000)
50. W.W. Chow, E.D. Jones, N.A. Modine, A.A. Allerman, S.R. Kurtz, Appl. Phys. Lett. **75**, 2891 (1999)
51. S.L. Chuang, *Physics of Optoelectronic Devices.* (Wiley, New York, 1995)

20

Vertical Cavity Semiconductor Optical Amplifiers Based on Dilute Nitrides

S. Calvez and N. Laurand

This chapter presents a comprehensive report on our work on dilute nitride vertical cavity semiconductor optical amplifiers. It includes a presentation of a theoretical analysis of the components and a summary of the experimental assessment of monolithic and fibre-based tunable devices operated in the continuous-wave regime. In particular, it is shown how some material parameters can be extracted from this device continuous-wave characterization or from gain-dynamics experiments. Current investigations on the extension of the operation towards the 1,550 nm telecommunication band conclude this review.

20.1 Introduction

Semiconductor optical amplifiers (SOAs) are very attractive devices for a broad range of applications in advanced telecommunications systems – such as wavelength conversion and optical routing in passive network systems – because of their advantageous characteristics including their fast response and low threshold nonlinear behaviour. To meet the urgent requirement to bring high bandwidth telecommunications closer to the home, Metropolitan Area Networks require low-cost and high-functionality optical amplifier components around 1.3 μm. This cannot be done solely with fibre optic-based amplifier systems. The primary objective of the activity summarized below was to develop novel SOA components, which have two key distinguishing characteristics: (1) a vertical-cavity geometry and (2) monolithic formats facilitated by the advantageous GaAs-based active region material GaInNAs.

The choice of a vertical geometry in SOAs (*vertical cavity SOA's or VCSOAs*) brings advantages including: low drive powers, intrinsic polarization-insensitivity, efficient fiber coupling, compliance with wafer scale fabrication and testing and the potential for 2D-integration. Their in-built wavelength selection means that they are particularly suited for single channel operations

and can, therefore, provide different functionality within telecommunication networks.

In addition to these applications, monolithic and/or tunable VCSOAs are very useful devices in which to probe gain material properties by combining experimental characterization with theoretical analysis, as shown hereafter.

20.2 Device Description and Theory

20.2.1 Device Description

Vertical cavity SOAs exploit the advantages of the vertical geometry to provide compact devices or new functionalities for optical telecommunication networks. The choice of this geometry means that the length over which the signal interacts with the gain elements, here quantum wells (QWs), is much reduced (a few 10 s of nanometres instead of $\sim$250 µm) compared with conventional SOAs. To meet telecommunication system requirements (gain values >10 dB), it is thus natural to devise a scheme where by the signal goes through the active region several times. A practical means to achieve such recirculation is to exploit the resonance of a cavity built around the active region.

The typical architecture of a monolithic VCSOA operating at the wavelength λ_c consists, therefore, of an active region sandwiched between two mirrors as illustrated in Fig. 20.1. The mirrors are usually distributed Bragg reflectors (DBRs), i.e. stacks of N periodic repeats of alternating quarter wave-thick layers of low and high refractive index (n_{low} and n_{high}). As for the active region, it includes a set of N_{QW} QWs, positioned at or close to the anti-nodes of the electric-field established by the cavity to maximize the gain, a distribution known as resonant periodic gain [1]. The length of the active region is

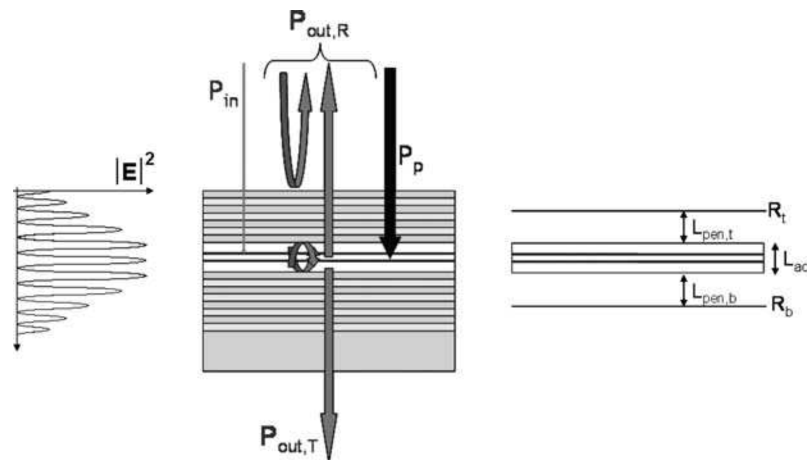

Fig. 20.1. Monolithic VCSOA structure, E-field pattern and simplified diagram

chosen so that it corresponds to a resonance of the Fabry-Perot cavity, i.e. is a multiple of half the wavelength of operation.

The reflectivity of each of the DBRs can be calculated using the transfer matrix method as commonly employed in thin-film software [2], but can more usefully be modelled as a fixed hard mirror positioned at a distance, L_{pen}, from the boundary with the incident medium and having an effective reflectivity, R_{DBR}, and bandwidth, $\Delta\lambda_{\mathrm{DBR}}$ [3]. The expressions for these parameters are summarized hereafter:

$$R_{\mathrm{DBR}} = \left(\frac{1 - aqp^{N-1}}{1 + aqp^{N-1}} \right)^2 , \tag{20.1}$$

$$\frac{\Delta\lambda_{\mathrm{DBR}}}{\lambda_{\mathrm{c}}} = \frac{4}{\pi} \arcsin \left(\frac{1-q}{1+q} \right) , \tag{20.2}$$

$$L_{\mathrm{pen}} = \frac{\lambda_{\mathrm{c}}}{2\left(n_{\mathrm{high}} + n_{\mathrm{low}}\right)} \frac{q(1 + a^2 p^{N-1})(1 - p^N)}{(1-p)(1 + q^2 a^2 p^{2N-2})}, \tag{20.3}$$

where $q = n_{\mathrm{lowI}}/n_{\mathrm{highI}}$, $a = n_{\mathrm{lowE}}/n_{\mathrm{highE}}$ and $p = n_{\mathrm{low}}/n_{\mathrm{high}}$ are refractive index ratios at the three types of interfaces characterizing the mirror (namely incident, exit and internal interfaces). For the evaluation of these expressions, the refractive indexes for the $\mathrm{Al}_x\mathrm{Ga}_{1-x}\mathrm{As}$ compounds are generally taken from [4].

As illustrated in Fig. 20.2 for an $\mathrm{Al}_x\mathrm{Ga}_{1-x}\mathrm{As}$/GaAs DBR with GaAs substrate and incident media, the number of repeats, N, controls the reflectivity of the mirrors. It will play an important role in the optimization of the device operation as we will see later. With a high-index-contrast ratio (small p factor), a smaller number of pairs is required to achieve a given reflectivity (see Fig. 20.2b) and the mirror has a broader bandwidth.

Furthermore, for a given $\mathrm{Al}_x\mathrm{Ga}_{1-x}\mathrm{As}$ micro-cavity structure, it can be shown that the DBR central wavelength and the cavity resonance shift towards longer wavelengths (redshift) at a rate of $0.11\,\mathrm{nm\,K^{-1}}$ as the temperature increases because of the alloy thermal expansion coefficient and refractive index temperature dependence.

As for the quantum wells, the choice of their thickness and composition can be based upon the simplified transition calculation formalism presented in ref. [5]. Figure 20.3 shows the ground-state transition energy for a square GaInNAs/GaAs QW at a set of indium (x) and nitrogen (y) contents.

The temperature-induced change in emission wavelength of a 1,300 nm GaInNAs/GaAs QW can be approximated above 0°C by a linear redshift at a rate of $0.33\,\mathrm{nm\,K^{-1}}$. Because the QW emission shifts faster than the cavity resonance with temperature, the QW peak emission wavelength at room temperature is chosen to be shorter than the cavity resonance wavelength to enable operation over a large temperature range.

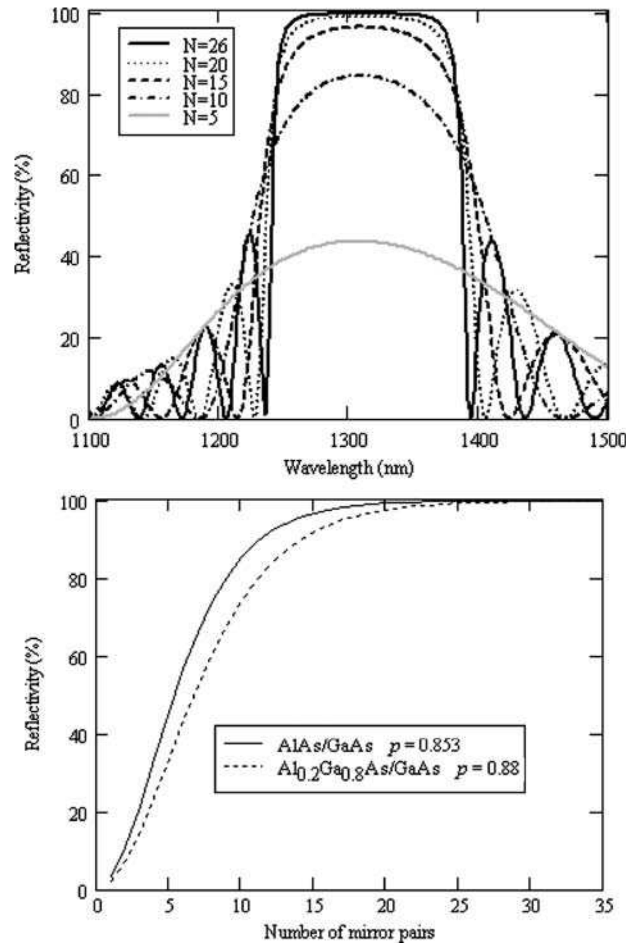

Fig. 20.2. Distributed Bragg reflectors: (**a**) Reflectivity spectra for an AlAs/GaAs DBR with different pair numbers, (**b**) Influence of the index contrast ratio

20.2.2 Amplification Analysis Using Rate Equations

Amplification is obtained when the device is pumped either optically or electrically and an input signal is provided. The component is said to be operated in reflection/transmission mode depending on the side of extraction of the output signal (same/opposite to the input), as shown in Fig. 20.1.

Following a standard Fabry-Perot analysis, it can be shown that the device gain for a component operated in reflection (respectively transmission) mode is given by $G_{\mathrm{R}}(G_{\mathrm{T}})$ [6]:

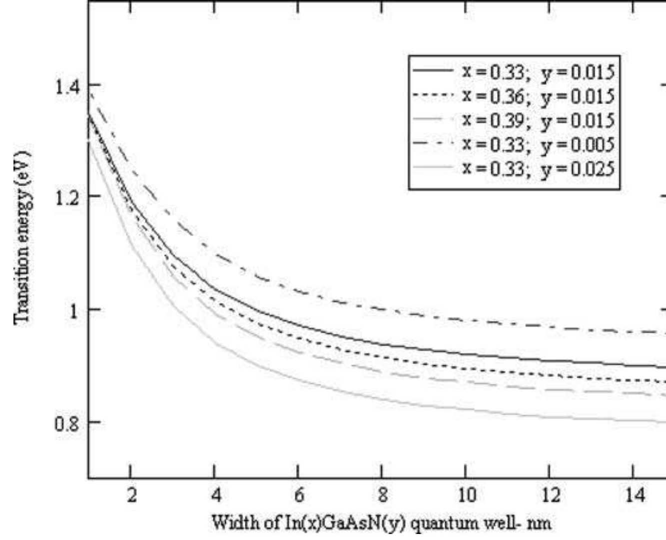

Fig. 20.3. Room-temperature ground-state energy transition for various GaIn-NAs/GaAs square quantum-wells at a set of indium (x) and nitrogen (y) contents

$$G_{\mathrm{R}} = \frac{P_{\mathrm{out,R}}}{P_{\mathrm{in}}} = \left| -\sqrt{R_{\mathrm{t}}} + (1-R_{\mathrm{t}})\sqrt{R_{\mathrm{b}}} g_{\mathrm{s}} e^{i\varphi} \sum_{k=0}^{\infty} (\sqrt{R_{\mathrm{b}} R_{\mathrm{t}}} g_{\mathrm{s}} e^{i\varphi})^k \right|^2 \tag{20.4}$$

$$= \frac{\left(\sqrt{R_{\mathrm{t}}} - \sqrt{R_{\mathrm{b}}} g_{\mathrm{s}}\right)^2 + 4\sqrt{R_{\mathrm{t}} R_{\mathrm{b}}} g_{\mathrm{s}} \sin^2\left(\frac{2\pi n L_{\mathrm{c}}}{\lambda}\right)}{\left(1 - \sqrt{R_{\mathrm{t}} R_{\mathrm{b}}} g_{\mathrm{s}}\right)^2 + 4\sqrt{R_{\mathrm{t}} R_{\mathrm{b}}} g_{\mathrm{s}} \sin^2\left(\frac{2\pi n L_{\mathrm{c}}}{\lambda}\right)}$$

$$G_{\mathrm{T}} = \frac{P_{\mathrm{out,T}}}{P_{\mathrm{in}}} = \frac{(1-R_{\mathrm{t}})(1-R_{\mathrm{b}}) g_{\mathrm{s}}}{\left(1 - \sqrt{R_{\mathrm{t}} R_{\mathrm{b}}} g_{\mathrm{s}}\right)^2 + 4\sqrt{R_{\mathrm{t}} R_{\mathrm{b}}} \sin^2\left(\frac{2\pi n L_{\mathrm{c}}}{\lambda}\right)}, \tag{20.5}$$

where n is the average refractive index, $L_{\mathrm{c}} = L_{\mathrm{act}} + L_{\mathrm{pen,t}} + L_{\mathrm{pen,b}}$ the effective cavity length, g_{s} is the single-pass gain, R_{t} (respectively R_{b}) is the effective reflectivity of the top (bottom, respectively) mirror, which can be evaluated using (20.1). It should be noted that n depends on pump and signal through carrier- and temperature-induced refractive index changes and that the sine terms vanish when the operation wavelength matches the resonance.

In telecommunications, device gain values are generally expressed in decibels with $G_{\mathrm{dB}} = 10Log(G)$. The overall device gain is limited by either the full inversion of the active region gain or by laser action for which the single-pass gain, $g_{\mathrm{s,th}}$, is given by:

$$g_{\mathrm{s,th}} \sqrt{R_{\mathrm{t}} R_{\mathrm{b}}} = 1. \tag{20.6}$$

One will further note that, in the reflection mode, the direct reflection from the top mirror and the contribution from the cavity are out of phase. Therefore, there exists a single-pass gain condition, $g_{\mathrm{s,AR}}$, called anti-resonance, for

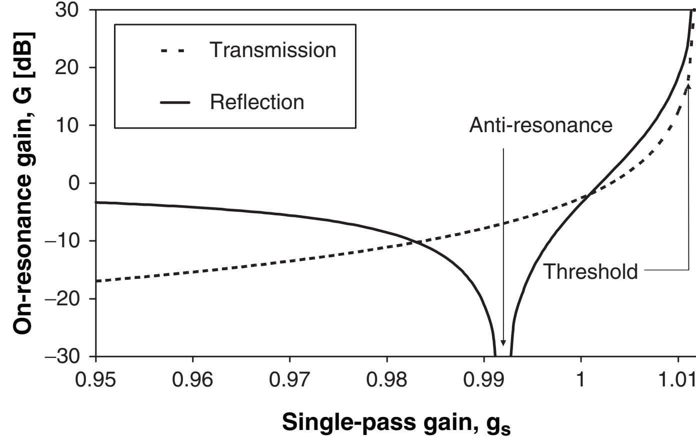

Fig. 20.4. On-resonance gain characteristics of a VCSOA ($R_\mathrm{t} = 98\%$; $R_\mathrm{b} = 99.6\%$; $L_\mathrm{c} = 6\lambda_\mathrm{c}$) operated in reflection and transmission modes

which these two contributions are of identical strength and the device gain is theoretically null. The expression for $g_{\mathrm{s,AR}}$ is:

$$g_{\mathrm{s,AR}} = \frac{\sqrt{R_\mathrm{t}}}{\sqrt{R_\mathrm{b}}}. \tag{20.7}$$

Figure 20.4 illustrates typical gain characteristics of a VCSOA in both reflection and transmission mode of operation, showing the anti-resonance feature.

In the remainder of this section, experimentally measurable quantities will be derived from the device characteristics.

The relation for g_s, taking into account the different level inversion of each QW as the injected pump is gradually absorbed in the structure, can be written as follows:

$$g_\mathrm{s} = \exp\left(\sum_{\mathrm{i}=1}^{N_{\mathrm{QW}}} \xi_\mathrm{i} \cdot g_{\mathrm{QW,i}} L_\mathrm{w} - \alpha_\mathrm{c} L_\mathrm{c}\right), \tag{20.8}$$

ξ_i is the relative overlap between the ith QW and the signal electric field, L_w is the QW thickness, $g_{\mathrm{QW,i}}$ is the material gain of the ith QW and α_c represents the cavity losses. The relative overlap coefficient can be obtained using the following equation:

$$\xi_\mathrm{i} = \frac{L_\mathrm{c} \int_{z_\mathrm{i}}^{z_\mathrm{i}+L_\mathrm{w}} |E(\lambda, z)|^2 \,\mathrm{d}z}{L_\mathrm{w} \int_{L_\mathrm{c}} |E(\lambda, z)|^2 \,\mathrm{d}z}. \tag{20.9}$$

It should be noted that this coefficient is wavelength dependent and is maximized when the QW is at the antinode of the field ($\xi_i \sim 2$).

Although the QW gain characteristics can be fully simulated as an additional step in a $\boldsymbol{k} \cdot \boldsymbol{p}$ band calculation, it is also standard practice to model the peak QW gain, $g_{\mathrm{QW,i}}$, using the following empirical expression:

$$g_{\mathrm{QW,i}} = g_0 \ln\left(\frac{N_\mathrm{i} + N_\mathrm{s}}{N_0 + N_\mathrm{s}}\right), \tag{20.10}$$

where N_i is the carrier density in the ith QW, N_0 is the carrier density at transparency, N_s is a carrier density fit parameter and g_0 is the gain parameter. Furthermore, when the carrier density is higher than the transparency carrier density, the QW gain spectral characteristic can be approximated by a parabolic function, while the influence of the temperature can be modelled as a linear decay [7]:

$$g_{\mathrm{QW,i}}(T) = g_0 \ln\left(\frac{N_\mathrm{i}+N_\mathrm{s}}{N_0+N_\mathrm{s}}\right)\left(1-2\left(\frac{\lambda(T)-\lambda_{\mathrm{QW,p}}(T)}{\Delta\lambda_{\mathrm{QW}}}\right)^2\right)\left(1-\frac{T-T_{\mathrm{ref}}}{T_0}\right), \tag{20.11}$$

where $\boldsymbol{\lambda}_{\mathrm{QW},p}(T)$ is the QW peak emission wavelength at the temperature T, $\Delta\boldsymbol{\lambda}_{\mathrm{QW}}$ the gain linewidth and T_0 describes the temperature-induced shrinking of the gain peak value. Finally, we can derive the carrier and photon conservation expressions for the structure to relate pump, signal injection and output signal power levels:

$$\frac{\mathrm{d}N_\mathrm{i}}{\mathrm{d}t} = \frac{j_{\mathrm{p,i}}}{eL_\mathrm{w}} - \left(AN_\mathrm{i} + BN_\mathrm{i}^2 + CN_\mathrm{i}^3\right) - \sum_{\mathrm{i}=1}^{N_{\mathrm{QW}}} \xi_\mathrm{i} g_{\mathrm{QW,i}} v_\mathrm{g} S, \tag{20.12}$$

$$\begin{aligned}\frac{\mathrm{d}S}{\mathrm{d}t} &= (1-R_\mathrm{t})\frac{\lambda}{h\,c}\frac{P_{\mathrm{in}}}{A_{\mathrm{in}}} + \beta\frac{L_\mathrm{w}}{L_\mathrm{c}}B\sum_{\mathrm{i}=1}^{N_{\mathrm{QW}}} N_\mathrm{i}^2 \\ &\quad + \left[\sum_\mathrm{i} \xi_\mathrm{i}\frac{L_\mathrm{w}}{L_\mathrm{c}} g_{\mathrm{QW,i}} - \left(\alpha_\mathrm{c} + \frac{\ln\left(1/\sqrt{R_\mathrm{t}R_\mathrm{b}}\right)}{L_\mathrm{c}}\right)\right] v_\mathrm{g} S,\end{aligned} \tag{20.13}$$

where e is the electron charge, c the speed of light and h Planck's constant. P_{in} is the signal input power, A_{in} the signal input area, S the photon density, ν_g the photon group velocity and β the fraction of spontaneously emitted photons that are coupled into the signal mode. A, B and C represents, respectively, the monomolecular, bimolecular and Auger recombination coefficients.

For an in-well pumped device i.e. a device for which the pump wavelength is selected in such a way that the pump is only absorbed into the QWs, and assuming a top-hat pump profile with single-pass absorption, the current density can be expressed as:

$$j_{\mathrm{p,i}} = \frac{P_\mathrm{p}\,\lambda_\mathrm{p}}{h\,c\,A_\mathrm{p}} \exp[-\alpha_\mathrm{w} L_\mathrm{w}(i-1)] T_\mathrm{p}(1-\exp(-\alpha_\mathrm{w} L_\mathrm{w})), \tag{20.14}$$

where α_{w} is the QW pump absorption coefficient, T_{p} the transmission of the top mirror at the pump wavelength, λ_{p} and A_{p} the excitation area.

In addition to the device gain, the other key characteristics of amplifiers are:

– The saturation input power, $P_{\mathrm{in,sat}}$, defined as the input power necessary to half the maximum device gain. This parameter can be obtained either by solving (20.11 and 20.12) numerically or by using the analytical solution as derived in ref. [6] for a device with uniformly-pumped QWs ($N_{\mathrm{i}} = N$ for $i = 1, \ldots, N_{\mathrm{QW}}$). The output power achieved when the input power is equal to or greater than $P_{\mathrm{in,sat}}$ is called the saturation output power, $P_{\mathrm{out,sat}}$. It is generally expressed in dBm, with

$$P_{\mathrm{dBm}} = 10Log\left(\frac{P}{1\,mW}\right). \tag{20.15}$$

– The gain-bandwidth, $\Delta f_{\mathrm{R}}(\Delta f_{\mathrm{T}})$, is the full frequency span within which the device gain is greater than half its maximum value. The analytical expressions for these gain-bandwidths are:

$$\Delta f_R = \frac{c}{\pi\, nL_{\mathrm{c}}} \arcsin\left[4\sqrt{R_{\mathrm{t}}R_{\mathrm{b}}}g_{\mathrm{s}}\left(\frac{1}{\left(1-\sqrt{R_{\mathrm{t}}R_{\mathrm{b}}}g_{\mathrm{s}}\right)^2} - \frac{2}{\left(\sqrt{R_{\mathrm{t}}}-\sqrt{R_{\mathrm{b}}}g_{\mathrm{s}}\right)^2}\right)\right]^{-1/2}, \tag{20.16}$$

$$\Delta f_T = \frac{c}{\pi\, nL_{\mathrm{c}}} \arcsin\left[\frac{\left(1-\sqrt{R_{\mathrm{b}}R_{\mathrm{t}}}g_{\mathrm{s}}\right)^2}{4\sqrt{R_{\mathrm{b}}R_{\mathrm{t}}}g_{\mathrm{s}}}\right]^{\frac{1}{2}}. \tag{20.17}$$

– The noise figure, *NF*, represents the signal-to-noise ratio degradation due to the noise added by the amplifier. This noise is caused by the spontaneous emission that is coupled into the cavity mode and is itself amplified, giving rise to what is called amplified spontaneous emission (ASE). On detection, the ASE cannot be distinguished from the signal and, therefore, two noise terms appear: the signal-spontaneous (sig-sp) and the spontaneous (sp-sp) beat noise. The latter depends on the ASE bandwidth and is reduced in a VCSOA because of the device filtering effect. The VCSOA also affects the shot noise because of the overall increase in optical power. In the gain regime, the spontaneous–spontaneous factor is negligible and the noise factor, F, can be written as follows [8]:

$$F = F_{\mathrm{excess}} + F_{\mathrm{shot}} = 2n_{\mathrm{sp}}\chi\frac{G}{G-1} + \frac{1}{G} = \frac{2\rho_{\mathrm{ASE}}}{Ghc} + \frac{1}{G}, \tag{20.18}$$

$$NF = 10Log(F), \tag{20.19}$$

where χ is the excess noise coefficient, n_{sp} is the inversion factor and $2\rho_{\mathrm{ASE}}$ corresponds to the ASE density as measured using an optical spectrum analyzer. For a reflection VCSOA, the former parameter is given by:

$$\chi = \frac{(1 + R_{\mathrm{b}} g_{\mathrm{s}})\,(g_{\mathrm{s}} - 1)}{(R_{\mathrm{b}} g_{\mathrm{s}}^2 - 1)}. \tag{20.20}$$

The importance of having an optimum cavity reflectivity and of using the device close to full inversion ($n_{\mathrm{sp}} = 1$) for low noise operation can, therefore, be understood from these equations.

The gain dependence of the output saturation power and of the optical bandwidth of a reflection-type VCSOA is represented in Figs. 20.5a and 20.5b, respectively, for a set of top mirror reflectivities. It can clearly be observed that there is a direct trade-off between the amplification optical bandwidth and the device gain and that the saturation power follows an S-shape evolution.

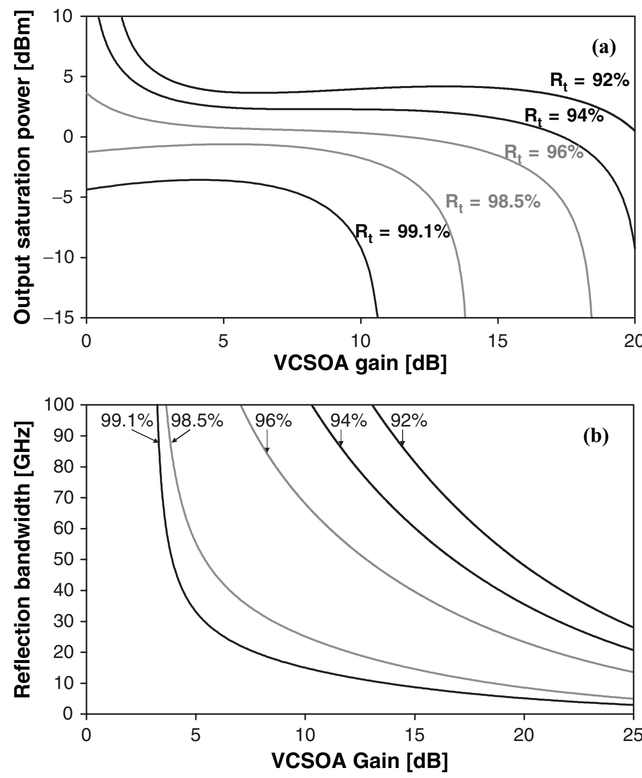

Fig. 20.5. Reflection-type VCSOA performance: (**a**) Output saturation power, (**b**) Optical bandwidth as function of device gain for a set of top mirror reflectivities ($R_{\mathrm{b}} = 99.6\%$; $L_{\mathrm{c}} = 6\lambda\mathrm{c}$)

It should also be noticed that using low top mirror reflectivities generally improves the gain, bandwidth and saturation characteristics of VCSOAs.

All the VCSOA characteristics described previously (gain, bandwidth, saturation power and noise figure) depend on the amplifier reflectivity and active region design. High-gain, high-saturation-power and low-noise performance are only obtained with an optimized cavity. For VCSOAs operated in reflection, low-noise considerations suggest the use of $R_b = 100\%$ and operation of the device close to full inversion.

The remaining optimization is a careful trade-off between two conflicting sets of desirable features:

- High-gain, high saturation power and wide bandwidth devices, which require high single-pass gain (high N_{QW}) and low top mirror reflectivity (see Fig. 20.5), and
- Low noise and low operating powers, which mean using components with a small number of QWs and a high top mirror reflectivity (see 20.5).

An illustration of an experimental optimization procedure for a given active region is provided in Sect. 3.4.

20.3 Continuous-Wave Experimental Demonstrations

20.3.1 Devices

Two types of devices have been studied: monolithically grown devices and fibre-based tunable VCSOAs for which the semiconductor part only included the gain and bottom mirror. All the semiconductor structures were grown by molecular beam epitaxy (MBE). The mirrors were grown at ∼600°C while the QWs where produced using a radio-frequency nitrogen plasma source and a growth temperature of 460°C. All the samples were in situ annealed to enhance their performance.

The monolithic device epilayer includes a 5/2-λ active-region containing six nominally 6.7-nm-thick $Ga_{0.64}In_{0.36}N_{0.014}As_{0.086}$/GaAs quantum wells positioned on five anti-nodes of the standing optical wave pattern (two wells in the central fringe) to facilitate resonant periodic gain. The quantum wells at the central fringe are separated by a 13-nm thick GaAs barrier. This active region is sandwiched between two 520 nm $Al_{0.3}Ga_{0.7}As$ separate confinement layers resulting in a total cavity length of 5-λ. The top mirror is a 19-pair GaAs/AlAs DBR and the bottom mirror a 20.5-pair GaAs/AlAs DBR, respectively.

The semiconductor part of the mirror-tunable VCSOA consists of a 25.5-pair GaAs/AlAs DBR, on top of which were successively grown a 3.25λ-thick GaAs section containing 513 nm-separated pairs of nominally 7-nm-thick $Ga_{0.63}In_{0.37}N_{0.012}As_{0.988}$/GaAs QWs, a 0.75λ-$Al_{0.3}Ga_{0.7}$As confinement window and a 10 nm GaAs cap. To complete the device, the top mirror is a nominally 99% reflective SiO_2/ZrO_2 mirror deposited commercially on the

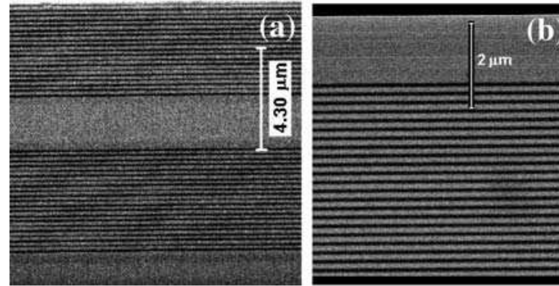

Fig. 20.6. Scanning electron microscope images of the semiconductor epilayers of (**a**) the fixed wavelength and (**b**) the tunable devices under investigation

fibre end, which is positioned in proximity of the semiconductor chip. The tunability of the device comes from the fact that the cavity includes an air-gap that can be adjusted by piezoelectric displacement of the fibre.

Scanning electron microscope (SEM) images of the semiconductor epilayers were taken and are presented in Fig. 20.6. Using the fact that the lighter alloys appear darker on these images, the DBR mirrors and cavities can clearly be identified.

Nondestructive testing of the structures was carried out to ensure that the grown structures match with the designs. Typically, temperature-dependent reflectivity and photoluminescence (PL) measurements are performed to do this assessment. The reflectivity measurement is based on the comparison with a silver mirror. The monolithic sample has a cavity that supports two resonances (longitudinal modes) within the DBR stopband as shown in Fig. 20.7a. Amplification will only occur at the longer-wavelength mode at room temperature and above because of the QW PL peak position (~1290 nm at 300 K). The absence of a top mirror from the epilayer of the tunable device results in a broader QW absorption feature in the reflectivity spectrum and a broader PL emission.

No transverse carrier or optical confinement schemes were employed i.e. all the devices were gain-guided. To allow better amplifier performance, part of the top mirror of the monolithic device has been etched-off by standard reactive ion etching methods utilizing end-point detection for process control. An additional dielectric single-layer anti-reflection coating was deposited on the tunable semiconductor chip to reduce the air-chip reflectivity to 4% and extend tuning range of the device.

20.3.2 Amplification Characterization Setup

The characterization of the monolithic devices was conducted under continuous-wave (CW-pumping) using the fibre-based system sketched in Fig. 20.8. The structures were mounted on a temperature-controlled heatsink fixed in a gimbal mirror mount. The common port (6.9 µm mode-field diameter

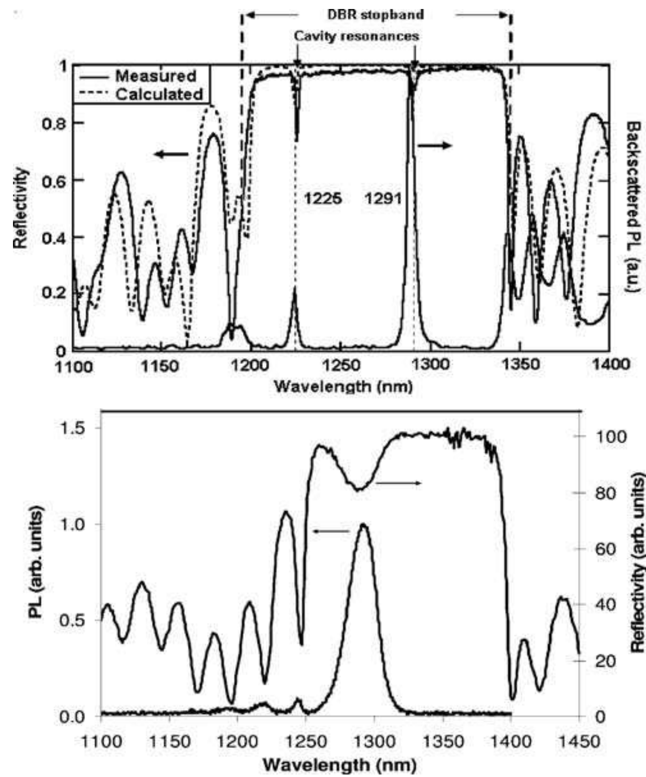

Fig. 20.7. Room-temperature reflectivity and photoluminescence of (**a**) the monolithic structure before etching and of (**b**) the semiconductor part of the tunable device

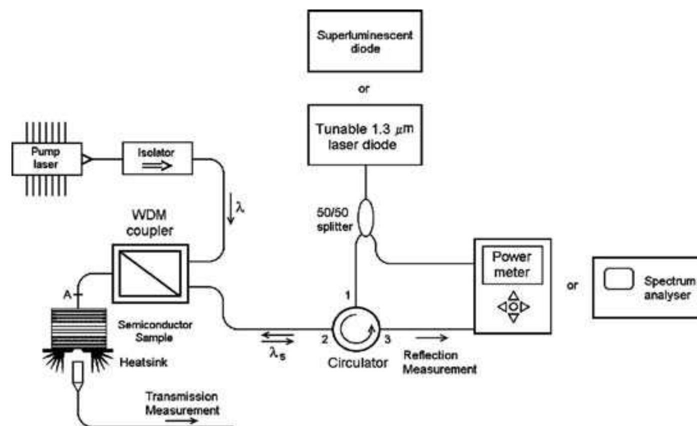

Fig. 20.8. Experimental setup for VCSOA assessment in continuous-wave operation

at 980 nm and 9 µm at 1,300 nm) of the WDM coupler was butt-coupled using a piezo-actuator to the device for signal (1,300 nm) and pump (980 nm) co-propagation.

The 1.3 µm input signal was provided, as required, either by a superluminescent diode (SLD) or a tunable laser. The circulator allowed separation of the amplified signal from the input signal and pump light. Amplified signal light was detected using either an optical spectrum analyzer or an optical power meter, both of which were fully calibrated industry-standard instruments. For the tunable device, the only modification was that the butt-coupled fibre was replaced by the mirror-coated fibre.

To determine fibre-to-fibre gain results that are independent of our testing arrangement, the losses incurred in going from the input port of the circulator to the APC connection of the patchcord (point A in Fig. 20.8) and from the APC connection of the patchcord to output port of the circulator were measured to be 2.8 dB and 2.3 dB, respectively.

20.3.3 Reflective 1,300 nm GaInNAs Vertical Cavity Semiconductor Optical Amplifier in Operation

In this section we present the typical characteristics of the above-described monolithic 1,300 nm GaInNAs VCSOA with an optimal 12-pair top mirror. The power transfer characteristic of the device in the absence of any 1,300 nm input signal was recorded to find the threshold condition, here achieved for a pump power of 238 mW. The SLD and a spectrum analyzer were used to record the fibre-to-fibre gain spectra of the structure for different pump powers. We can observe in Fig. 20.9 that initially the absorption shifts to shorter wavelengths (blueshifts from 1,287.3 to 1,286.7 nm as P_{p} varies from 0 to 45 mW)

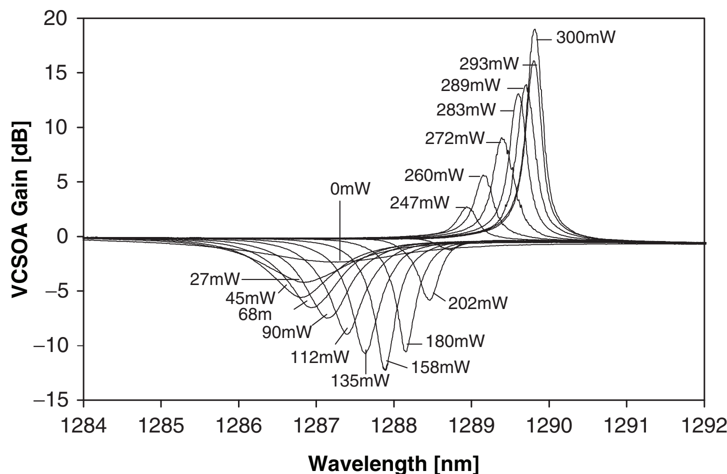

Fig. 20.9. Typical gain-spectrum evolution of a monolithic 1,300 nm GaInNAs VCSOA with pump power operated in reflection

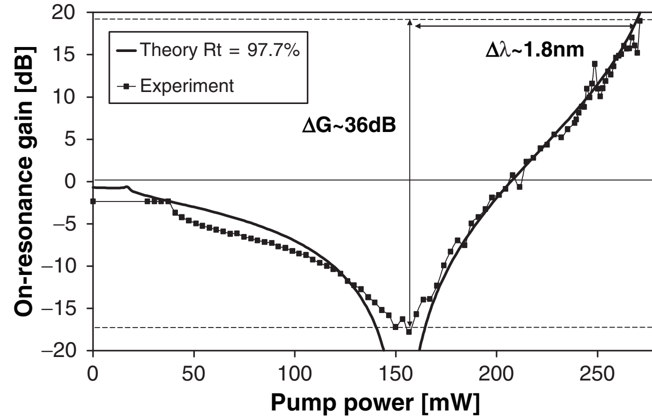

Fig. 20.10. Pump-power dependence of the gain on resonance of a monolithic 1,300 nm GaInNAs VCSOA operated in reflection

and then redshifts until threshold is reached. The blueshift corresponds to a situation where the carrier-induced refractive index change dominates over the thermal effects. The anti-resonance is reached around 158 mW of pump power where the gain is minimized. The observed gain is not $-\infty$dB as theoretically predicted because of the device noise. A maximum on-chip gain of 19 dB, or system gain of 13.9 dB, is achieved closed to threshold.

Because the major changes in the device response occur at the resonant wavelength, Fig. 20.10 plots the gain evolution at the resonant wavelength as the pump power is increased. It can be observed that the maximum to minimum gain contrast reaches 36 dB, a particularly attractive feature for application of these devices as modulators.

Since the spectrum analyzer resolution frequently limits the device characterization accuracy, detailed investigations of the amplification behaviour were conducted using the tunable laser source and a fibre-coupled, calibrated powermetre. For an input signal power of −25 dBm, the gain spectrum with peak gain value of 10.5 dB and a full –3 dB bandwidth of 22 GHz was measured and is shown in Fig. 20.11.

The amplification bandwidth was subsequently measured for different device gain values. The results are presented in Fig. 20.12 and experimentally demonstrate the VCSOA's inherent gain-bandwidth trade-off. The theoretical curve was obtained by fitting the data using the rate equations of Sect. 2 with the top mirror reflectivity value as the only fitting parameter. The value found for R_{t} was 97.5%, in good agreement with the calculated value of 97.7% using (20.1).

Investigations of the saturation characteristics were carried out by setting the wavelength of the tunable source to the peak gain wavelength and varying the input signal power. The results are represented in Fig. 20.13 together with

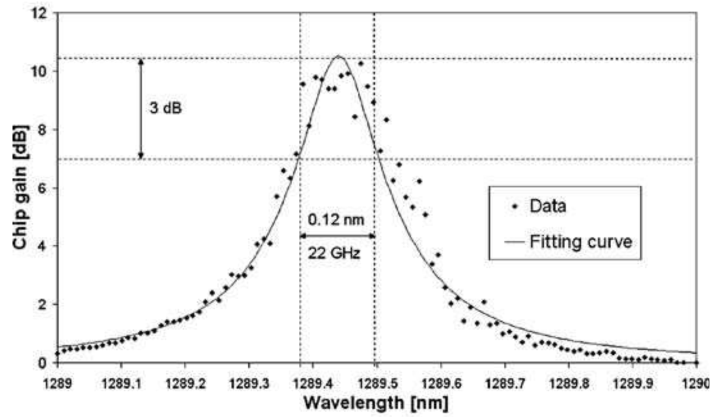

Fig. 20.11. Gain spectrum of a monolithic 1,300 nm GaInNAs VCSOA in reflection

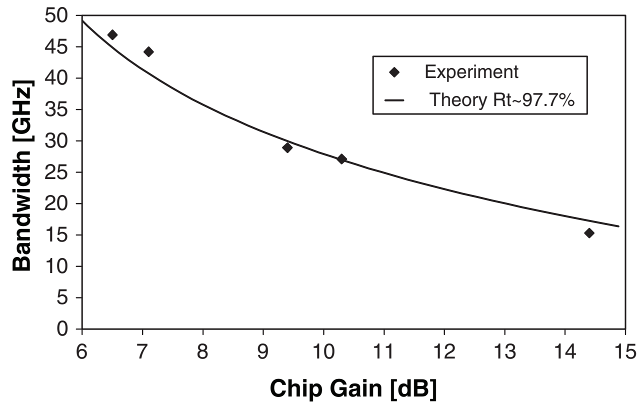

Fig. 20.12. Gain-bandwidth trade-off in a monolithic 1,300 nm GaInNAs VCSOA in reflection

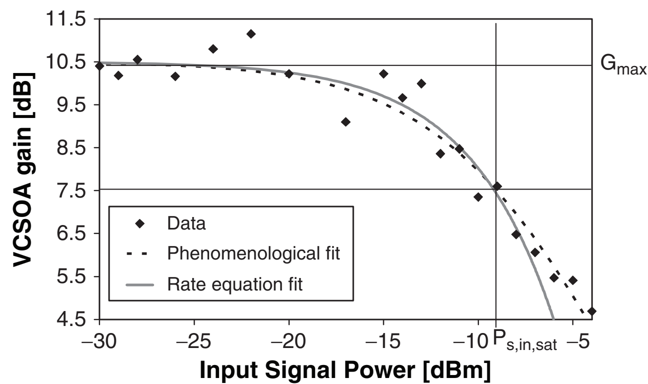

Fig. 20.13. Saturation characteristics of a monolithic 1,300 nm GaInNAs VCSOA in reflection for a small-signal device gain of 10.5 dB

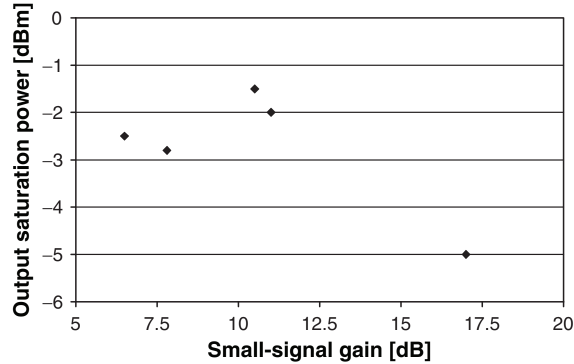

Fig. 20.14. Device gain dependence of the saturation output power for a monolithic 1,300 nm GaInNAs VCSOA in reflection

the theoretical plot and the fitting curve generated by the phenomenological equation:

$$G(P_{\mathrm{s,in}}) = G_{\mathrm{max}}/\,(1 + P_{\mathrm{s,in}}/P_{\mathrm{in,sat}}), \tag{20.21}$$

where $P_{\mathrm{s,in}}$ is the signal input power, and G_{max} the small-signal gain. The input saturation power is -9 dBm, which corresponds to an output saturation of -1.5 dBm.

The evolution of the saturation output power with device gain was also recorded. The dependence is shown in Fig. 20.14.

The device performance reported above compares very well with gain-guided InP-based VCSOAs at similar wavelengths [9]. It is interesting to note that similar gain values were obtained with a smaller number of QWs than for InP VCSOAs.

20.3.4 Optimization and Noise of 1,300 nm GaInNAs Vertical Cavity Semiconductor Optical Amplifiers

In this section, we discuss the optimization process that led to the results presented in Sect. 3.3. As we have seen in Sect. 2, good overall performance is only achieved for an optimized VCSOA. For reflection operation, the excess noise coefficient χ is minimized for an ideal back-reflectivity $R_{\mathrm{b}} = 100\%$. The bottom mirror of our structure, designed to provide $R_{\mathrm{b}} = 99.6\%$, ensures that a low noise figure is obtained for high gain amplification. The next step to reach high amplification, and therefore even lower noise, is to tailor the top mirror reflectivity. This is done by removing layers from the top-DBR. The VCSOA gain transfer functions for different top mirror reflectivities are represented in Fig. 20.15 (note that a lower number of DBR layers corresponds to a lower reflectivity as seen in Sect. 2).

Of special interest are the maximum and minimum gain values achieved and the power required to reach anti-resonance. Using (20.1) to evaluate the

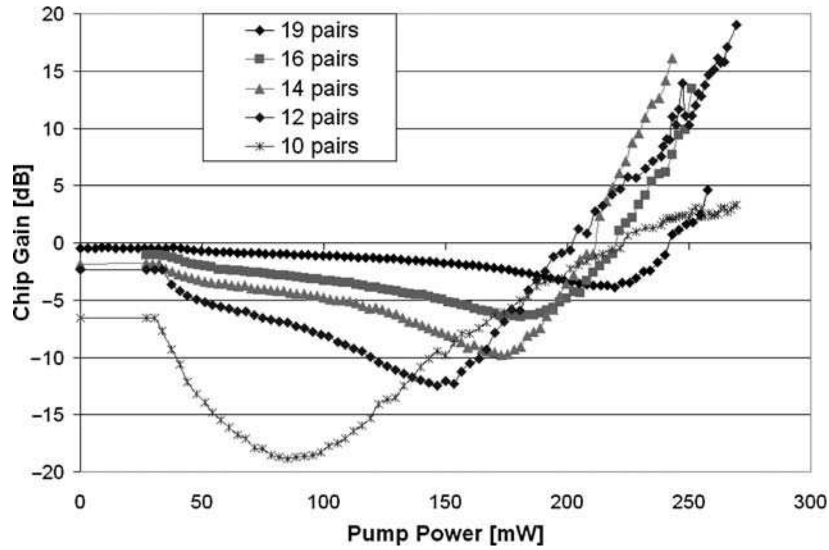

Fig. 20.15. Gain vs. optical pump power for a VCSOA with different top mirror layer pairs

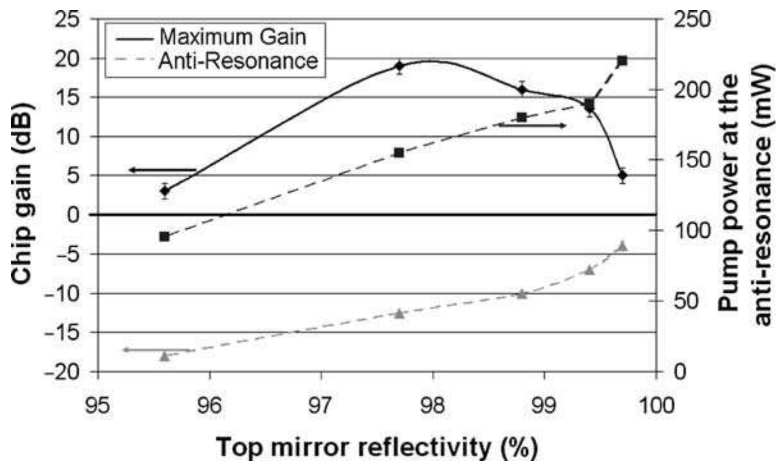

Fig. 20.16. Influence of the top mirror reflectivity on maximum chip gain and anti-resonance

top mirror reflectivities, we generated Fig. 20.16 to help with the analysis. It can clearly be seen that the optimum gain extraction is obtained for a reflectivity of $R_{\mathrm{t,opt}} = 97.7\%$ or equivalently a 12-pair top mirror device. For reflectivities higher than the optimum value, the maximum gain is restricted by laser action, while full-inversion of the QWs sets the limit for $R_{\mathrm{t}} < R_{\mathrm{t,opt}}$. It is also interesting to note that anti-resonance occurs at lower pump power

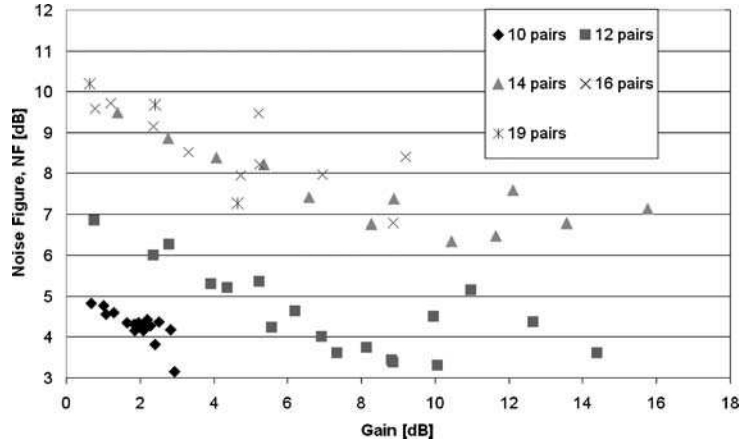

Fig. 20.17. Noise figure NF as a function of the VCSOA gain for different top mirror reflectivity

for lower reflectivity in agreement with (20.7). The recorded gain value at anti-resonance also decreases because of the associated reduction in ASE.

For the optimized cavity reflectivity, one would also expect to achieve low noise operation at high inversion (see Sect. 2). Figure 20.17 validates this statement by showing the noise figure for the different top mirror reflectivities. These values were obtained by measuring ASE and the gain under low signal input powers (~ -35 dBm) using an optical spectrum analyzer and applying (20.18).

For all reflectivities, the noise figure improves for increasing gain, i.e. as the inversion increases, in agreement with (20.18). At higher gains, we can see that for the highest reflectivity samples, the noise figure is limited to around 7–8 dB. For VCSOAs with a reflectivity close to, or below, the optimum value, the noise figure drops below 5 dB and tends towards 4 dB.

In summary, the optimum top mirror reflectivity of our structure for reflection mode amplification is obtained for a 12 layer-pairs DBR. The corresponding reflectivity has been calculated to be 97.7%. The maximum gain obtained in that configuration is 19 dB with $NF \sim 4$ dB. Taking into account the losses of the set-up (5.6 dB) in Fig. 20.8, the total module gain and NF are 13.4 dB and 6.8 dB respectively.

So far, we have shown the performance of VCSOAs in reflection. We also measured the transmission characteristics of the device with a 14-pair top mirror. Figure 20.18 shows the experimental on-resonance gain in both transmission and reflection operation together with theoretical fits based on a single set of parameters. The fibre-to-fibre transmission losses were evaluated to be ~ 8 dB, mainly attributed to non-optimum coupling optics and a poor substrate polish. It is interesting to note at this stage that while the reflection mode is particularly suited for modulation purposes because of the large

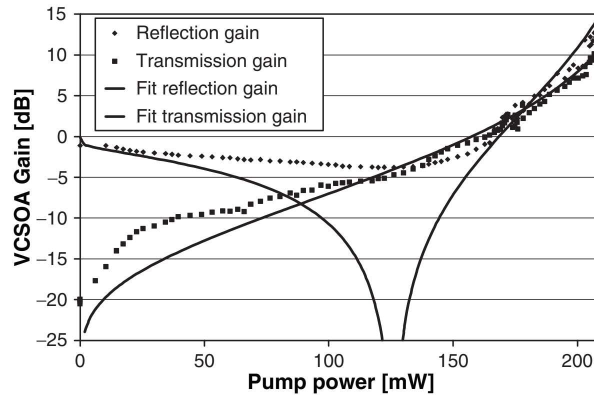

Fig. 20.18. Transmission and reflection characteristics

gain contrast, the transmission mode is favourable for loss-less highly selective filtering operations since there is no contribution outside the resonance feature.

20.3.5 Tunability

As we have seen, VCSOAs are characterized by a narrow amplification band resulting from the Fabry-Perot effect. The capability to dynamically change the operation wavelength of a VCSOA might prove useful in future multi-wavelength reconfigurable optical networks, and would make such an amplifier very versatile. Moreover, low-cost networks operating at 1.3 μm usually use uncooled laser sources. The wavelength of such sources varies quite considerably (compared to the VCSOA bandwidth) over time. VCSOAs that can be adjusted to match the source wavelength are, therefore, of great interest.

Two ways to tune the resonance have been investigated:

– Temperature tuning of the monolithic VCSOA
– Mirror-movable tunable devices

Temperature tuning is a simple technique to enable a single device to be used for the amplification of a selected channel among a set of wavelength division multiplexed (WDM) channels and to track its wavelength variations. Indeed, a change of device temperature leads to a change of the effective optical thickness of the cavity and thus leads to the wavelength tuning. However, as mentioned in Sect. 2, it also affects the spectral position and magnitude of the gain, and varies the non-radiative recombination rates. Figure 20.19-top represents, for a constant pump injection and temperature-independent losses, the overlay of the QW gain curves (solid lines) and corresponding cavity resonances (vertical lines) for six temperatures. Assuming a negative offset between the QW gain peak and the cavity resonance at low temperatures, as

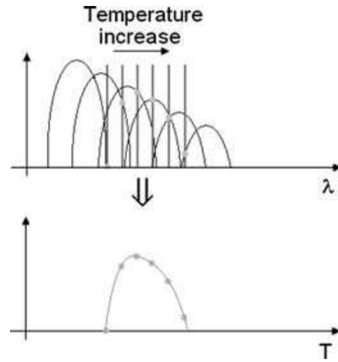

Fig. 20.19. Effects of temperature on the performance of a monolithic VCSOA

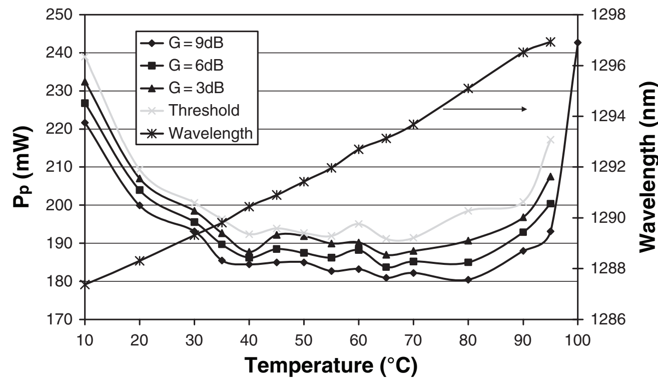

Fig. 20.20. Temperature dependence of the pump power required to reach fixed gain values and emission wavelength at threshold for a monolithic VCSOA

the temperature increases the device gain first improves as the QW gain curve, which redshifts at a faster rate, aligns with the cavity resonance. Subsequent heating leads to deterioration of the device gain because the QW gain curve and resonance walk away from each other. The resonance wavelength being proportional to the device temperature, a bell-shape dependence of the device gain with temperature is thus predicted (see Fig. 20.19-bottom).

Using the monolithic device described in Sect. 3.1 with a top mirror reflectivity of 99.1%, we investigated the influence of temperature on the performance of that particular component. The pump-power-dependent gain curves were recorded using a spectrum analyzer and a SLD for a set of temperatures between 10 and 100°C. Tunable operation over 9.5 nm with more than 9 dB of device gain was achieved as shown in Fig. 20.20. There is a sharp increase in the power required to achieve a given gain value at high temperatures that we attribute to enhanced Auger recombination. The relative temperature independence of the performance between 35 and 80°C suggests

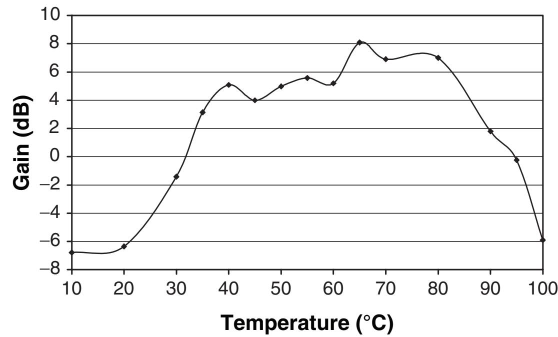

Fig. 20.21. Temperature-dependence of the gain of a monolithic VCSOA under constant pump injection (186 mW)

that the QW peak gain matches the resonance wavelength for a temperature of 55°C.

Keeping the injected pump power constant, the device gain is shown to possess a bell-shaped temperature dependence (see Fig. 20.21) as explained in Fig. 20.19. Though changes in the device temperature allow wavelength tuning of the amplification feature, the range is limited by the cavity mode-peak gain mismatch and the increase of losses at high temperatures. To extend the tuning range, reduce power consumption and obtain faster tuning speed, mechanical tuning methods are generally preferred. Since a lot of effort has previously been devoted to the realization of MEMS-based tunable Vertical-Cavity Surface-Emitting Lasers [10], and because of the device similarity, it would be natural to use a similar approach. However, to allow the separate optimization of each element of the cavity, we opted for the hybrid fibre-tunable device presented in Sect. 3.1, which also offers the additional benefit of providing direct fibre-coupling.

The mirror-coated fibre was brought in proximity to the chip to form a cavity whose total length was $\sim$4 µm including the mirror penetration depths. The maximum tuning range was thus limited to the 65 nm free-spectral range of the cavity. The device was then pumped using either an 980 nm-pump, which is only absorbed in the QWs (in-well pumping) or an 808 nm-pump whose absorption takes place over the full GaAs-based cavity length (in-barrier pumping). Laser action was achieved over a range of up to 23 nm (see Fig. 20.22) limited by the device gain bandwidth and the change of overlap between the QWs and the signal electric field as the fibre tip was displaced.

The better tuning performance under 980 nm pumping is to be treated with caution. Indeed, the use of in-barrier pumping offers reduced threshold power requirements (see Fig. 20.23) due to improved pump absorption efficiency (extended absorption length) at the expense of stronger temperature dependence because of the higher quantum defect.

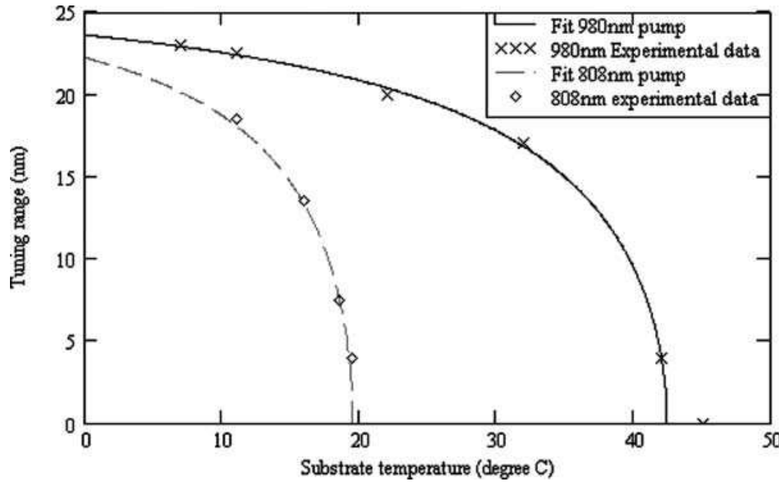

Fig. 20.22. Temperature-dependent tuning range of the mirror-tunable VCSOA for in-well and in-barrier pumping at threshold: experimental data and fit

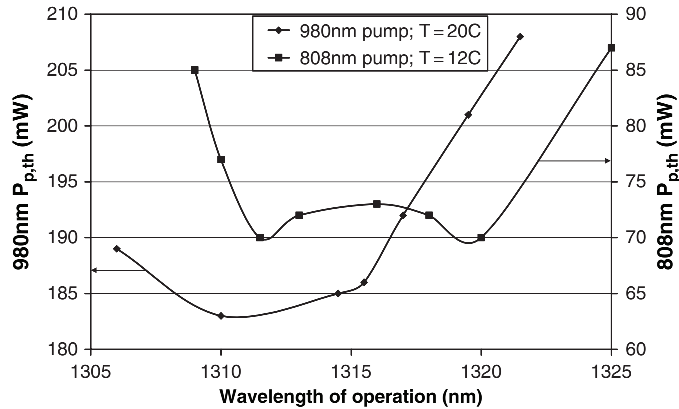

Fig. 20.23. Threshold requirements for the mirror-tunable VCSOA under in-well and in-barrier pumping

The amplification provided by the device below the lasing threshold was measured at room temperature using the 980 nm pump. A 6 dB gain was obtained over a range of greater than 17 nm (see Fig. 20.24). To keep the gain constant over the tuning range, it is necessary to adjust the pump power because of the change of overlap between the QWs and the signal electric field when the fibre is translated. The observed asymmetry of the amplification profiles is due to the close proximity of threshold.

The characteristics reported here are somewhat less impressive than the recent results around 1,550 nm with InP-based MEMS tunable VCSOAs [11]. Further optimization of the gain structure as well as a reduction of

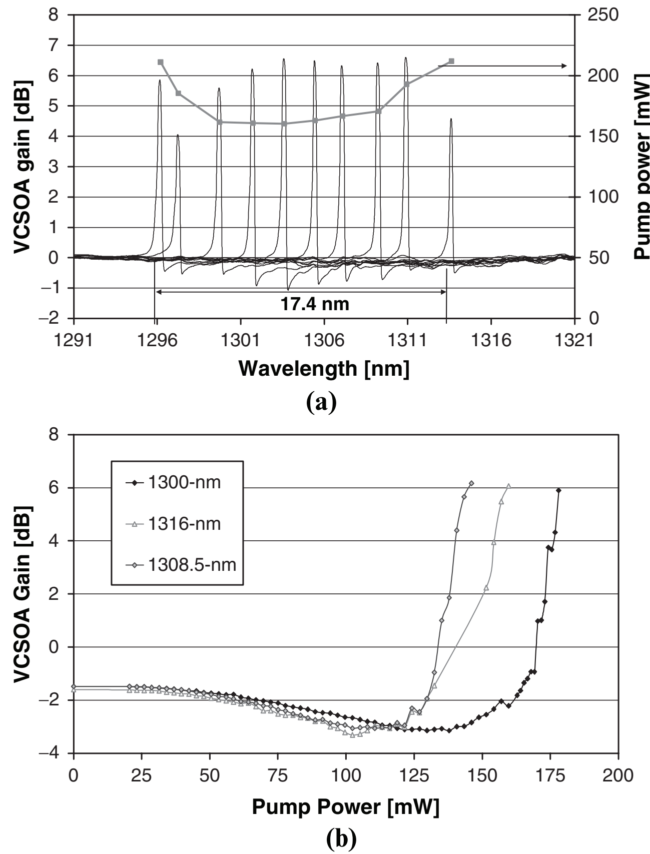

Fig. 20.24. Mirror-tunable VCSOA performance at room-temperature under 980 nm pumping. (**a**) Tuning, (**b**) Pump power dependence

the fibre-mirror reflectivity (<99%) should, however, enable GaInNAs-based devices to reach similar performance levels around 1,300 nm.

20.3.6 Material Parameter Extraction

So far, we have reviewed the performance of 1,300 nm GaInNAs VCSOAs under continuous-wave operation. Though this information is of direct relevance to component and network designers, the experimental data can be further exploited using the rate equation analysis presented in Sect. 2 to extract some material parameters. This is the object of this section.

First, we will look to find the values of g_0, N_0 and N_s. These parameters can be evaluated by fitting the on-resonance device gain of the optimum monolithic VCSOA using (20.4, 20.8, 20.10, 20.12 and 20.14). The experimental data used here were recorded with low input powers (SLD) to avoid

Table 20.1. Parameters used for the rate-equation analysis

Parameter	Meaning	Values
ξ	Total relative overlap factor	2
g_0	Gain parameter *Fitted*	4,200 cm^{-1}
N_0	Transparency carrier density	$1.8 \times 10^{18}\,\text{cm}^{-3}$
L_w	Quantum well thickness	6.7 nm
L_C	Cavity length	3.2 µm
A_P	Pumped area	$154\,\mu\text{m}^2$
A	Monomolecular recombination coefficient	$11 \times 10^8\,\text{s}^{-1}$
B	Bimolecular recombination coefficient	$8.2 \times 10^{-11}\,\text{cm}^3\text{s}^{-1}$
C	Auger recombination coefficient	$3.5 \times 10^{-29}\,\text{cm}^6\text{s}^{-1}$
N_S	Carrier density fit parameter *Fitted*	$-0.21 \times 10^{18}\,\text{cm}^{-3}$
α_C	Internal loss coefficient	$4\,\text{cm}^{-1}$
α_W	Pump absorption per quantum well	$6{,}000\,\text{cm}^{-1}$

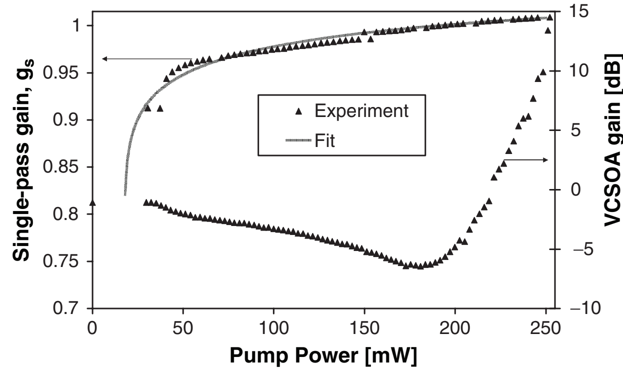

Fig. 20.25. Fit of single-pass gain data using rate equations for gain parameter extraction

gain compression and at the optimum temperature so that the gain peak and resonance were matched. The corresponding single-pass gain values were extracted using (20.4). Then, using the carrier density as a variable, one can easily calculate the single-pass gain of the device using (20.8 and 20.10) and also determine the incident pump power using (20.12) but neglecting the stimulated emission (last) term. In these calculations, the remaining parameters (listed in Table 20.1) were known from design (mirror reflectivities, cavity length and confinement factor) or based upon experimentally-validated coefficients taken from literature [12]. The result of the least-square fit to the data is shown in Fig. 20.25. The values found for g_0, N_0 and N_s are $4{,}200\,\text{cm}^{-1}$, $1.8 \times 10^{18}\,\text{cm}^{-3}$ and $-0.22 \times 10^{18}\,\text{cm}^{-3}$, respectively, and are consistent with the values calculated by $\boldsymbol{k} \cdot \boldsymbol{p}$ theory [13].

To further our knowledge of the GaInNAs material characteristics, we sought to determine the gain bandwidth, $\Delta\lambda_\text{QW}$, and temperature

compression factor, T_0. These parameters can be obtained by analyzing the tuning performance of the mirror-tunable device at threshold (see Fig. 20.22) using (20.6, 20.8 and 20.11) and assuming uniformly pumped QWs and temperature-independent carrier density for a given pump power i.e. temperature-independent recombination factors. The latter approximation is only valid over a small range of temperatures as considered here. Transfer matrix calculations of the total relative overlap factor, ξ, for our structure showed that the latter parameter had a parabolic wavelength dependence:

$$\xi = \sum_{i=1}^{N_\mathrm{w}} \xi_\mathrm{i} = \xi_\mathrm{max} \left(1 - 2\left(\frac{\lambda - \lambda_c}{\Delta\lambda_\mathrm{RPG}}\right)^2\right). \tag{20.22}$$

Furthermore, the active region temperature, T, depends on the substrate temperature, T_sub and the pump-induced heating via:

$$T = T_\mathrm{sub} + \Delta T = T_\mathrm{sub} + \frac{P_\mathrm{abs}}{R_\mathrm{th}}, \tag{20.23}$$

where P_abs is the absorbed power and R_th is the thermal resistance of the device.

A fitting procedure was performed to analyze simultaneously the tuning characteristics under in-well and in-barrier pumping. A single parameter was used for T_0 and $\Delta\lambda_\mathrm{QW}$ as the experiments were done with the same device while the peak gain coefficient $g_\mathrm{fit} = g_0 \ln\left(\frac{N+N_\mathrm{s}}{N+N_\mathrm{s}}\right) N_\mathrm{QW} L_\mathrm{w}$ and the fitted offset temperature, $T_\mathrm{fit} = T_\mathrm{ref} - \Delta T$, were taken to be different to account for the change in the pumping arrangements. The results of this fit are shown in Fig. 20.22 and the parameters listed in Table 20.2.

It is interesting to note that the difference in the fitted offset temperatures, which corresponds to the difference in pump-induced heating, is 29.4°C. This

Table 20.2. Fitting parameters found by the analysis of the temperature dependent tuning

Parameter	Meaning	Values
L_w	Quantum well thickness	7 nm
N_QW	Number of QWs	10
R_t	Top mirror reflectivity	99%
R_b	Bottom mirror reflectivity	99.90%
ξ_max	Maximum relative overlap coefficient	1.9
$\Delta\lambda_\mathrm{RPG}$	RPG bandwidth	83.4 nm
$g_\mathrm{fit,980}$	Peak gain for 980 nm pumping	8.7×10^{-3}
$g_\mathrm{fit,808}$	Peak gain for 808 nm pumping	14×10^{-3}
$T_\mathrm{fit,980}$	Offset temperature for 980 nm pumping	278.3 K
$T_\mathrm{fit,808}$	Offset temperature for 808 nm pumping	248.9 K
T_0	Gain compression factor	55.7 K
$\Delta\lambda_\mathrm{QW}$	QW gain linewidth	20.2 nm

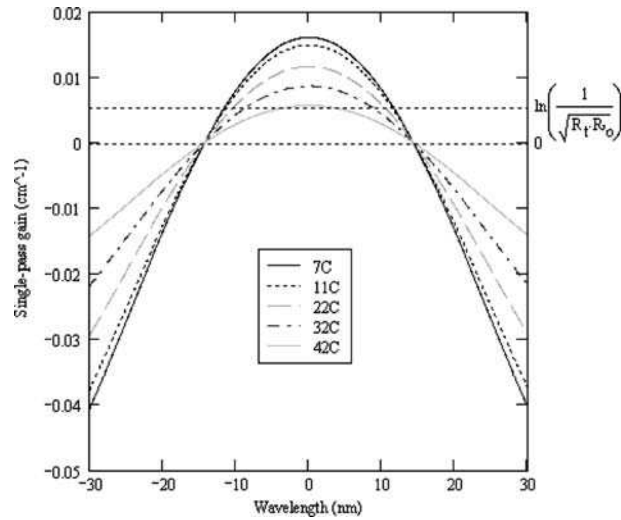

Fig. 20.26. Determined gain spectral characteristics for the 980 nm-pumped mirror-tunable VCSOA

observation is consistent with the fact that the device has stronger pump absorption and a worse quantum defect when barrier-pumped. This observation is also in agreement with the redshift of the centre of the tuning range that can be seen in Fig. 20.23.

Finally, Fig. 20.26 shows the evolution of the device single-pass gain as a function of temperature for the 980 nm-pumped device around its peak gain wavelength. It illustrates how the temperature dependence of the active region controls the tuning range of the device that corresponds to the part of the curves whose single-pass gain is greater than the mirror loss $\left(= \ln\left(1/\sqrt{R_{\mathrm{t}}R_{\mathrm{b}}}\right)\right)$.

20.4 Gain Dynamics

Because VCSOAs can potentially be used to provide amplification to data stream with 10–40 Gbs^{-1} bit rates in telecommunication systems, it is important to investigate the dynamic performance of these devices. Indeed, since both the gain and the refractive index of the gain region depend on the carrier density, pulsed signals can induce gain and phase variations. These changes in turn affect the amplification characteristics and could deteriorate the overall network performance. It is, therefore, important to determine the gain recovery and/or index response time of such components. Additionally, it will provide some further insight into the dynamics of GaInNAs material.

The remainder of this section will describe the pump-probe experiment conducted to investigate the dynamics of refractive index variation at

anti-resonance and gain recovery in the amplification regime for the optimized monolithic VCSOA discussed in Sect. 3.3.

20.4.1 Measurement Method and Associated Theoretical Remarks

To study the gain recovery and/or the refractive index dynamics in a component, it is common to use the pump-probe technique [14]. This method consists in sending two distinct ultrashort (∼150 fs long) pulses through the device and observing how the first pulse (the pump) modifies the device performance (here gain or wavelength shift) for the second pulse (the probe) as a function of their time separation. Generally, the pump is of greater intensity than the probe to enhance the effects being observed, while the probe power is kept small to avoid self-induced phenomena.

For example, when studying gain dynamics, as the pump pulse propagates through the device, its gain extraction depletes the carrier density and hence lowers the available gain. If the probe pulse follows immediately after, it experiences a reduced gain (see probe 1 in Fig. 20.27) while, for sufficiently long delays between the two pulses, the carrier density will have recovered to the same equilibrium condition as prior to the pump pulse and the probe pulse will have the same gain as the pump pulse (see probe 2 in Fig. 20.27). This phenomenon is illustrated in Fig. 20.27.

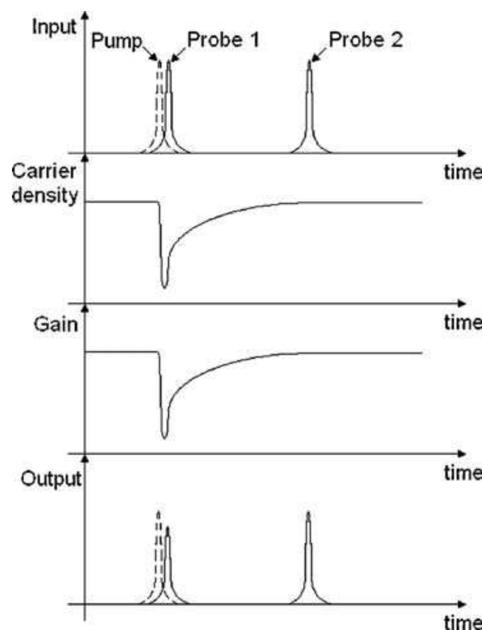

Fig. 20.27. Principle of gain-recovery measurement

As indicated earlier, the pump-probe method involves sending ultrashort pulses through the device. Assuming that these pulses are Fourier-transform limited, their spectral bandwidth is inversely proportional to their duration. While going through the VCSOA, they will be filtered, hence their spectral bandwidth will be narrowed and their duration increased. This means that the pump pulse is going to create a somewhat smeared carrier density change and that some measurable gain/refractive index variations will occur before the peak intensity of the pump pulse. Assuming that a square input pulse is injected into an active Fabry-Perot with constant single pass gain, we can estimate the intensity decay inside the cavity as the pulse leaves the cavity as follows [15]:

$$I_{\mathrm{m}} = I_0 \left[g_{\mathrm{s}}\sqrt{R_{\mathrm{b}}R_{\mathrm{t}}}\right]^{2(m-1)} \approx I \left[g_{\mathrm{s}}\sqrt{R_{\mathrm{b}}R_{\mathrm{t}}}\right]^{2m} = I \left[g_{\mathrm{s}}\sqrt{R_{\mathrm{b}}R_{\mathrm{t}}}\right]^{2t/\tau} = I(t), \tag{20.24}$$

where I_{m} is the intensity m round trips after the end of the input pulse (for which t is taken to be 0). In this formula, $\tau = c/2nL_c$ is the cavity round-trip time. By matching (20.24) with an exponential decay and approximating the pulse width by this fall time, we find that the pulse duration is given by:

$$\tau' = -\frac{\tau}{2\ln({g_{\mathrm{s}}}^2\sqrt{R_{\mathrm{b}}R_{\mathrm{t}}})} \tag{20.25}$$

Using $R_{\mathrm{t}} = 97.7\%$, $R_{\mathrm{b}} = 99.6\%$ and g_{s} value between 1 and 1.012, it is evaluated that τ' varies between 2 and 20 ps. This implies that effects induced by a 150 fs pump pulse will be recorded with delays up to 20 ps before reaching their maximum.

20.4.2 Experimental Setup

The setup used for the dynamic amplification characterization can be found in Fig. 20.28. Two orthogonally polarized trains of ultrafast pulses at the desired wavelength of around 1,290 nm were obtained from a Ti-Sapphire laser-Regenerative Amplifier system coupled to an optical parametric amplifier (OPA). The pulses had a repetition rate of 100 kHz and a typical temporal width of 150 fs for a bandwidth of 16 nm. The OPA system allowed us to tune the centre-wavelength of pulse spectrum to the VCSOA resonance, while an IR filter placed at the OPA output rejected the lower wavelengths generated by the system. The two trains of pulses were created from the initial OPA pulses using a 50/50 beam splitter (BS). The light was then reflected from mirrors that are represented in Fig. 20.28 by M1 and M2. A half-wave-plate was positioned along one of the optical paths with its axis at 22.5° to the incident polarization to ensure that the different pulse trains were of orthogonal polarizations. The pulses were then recombined at the beam splitter and coupled into a single-mode fiber connected to the VCSOA set-up described in

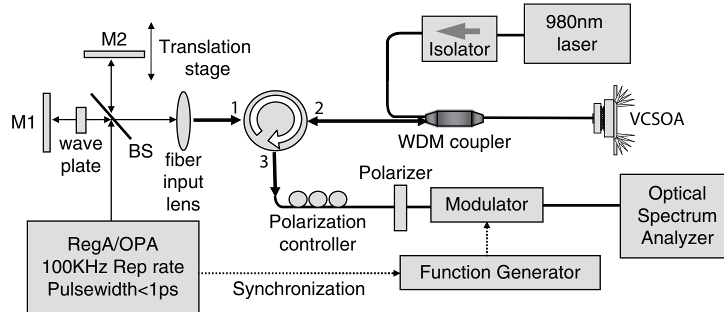

Fig. 20.28. Pump-probe experimental setup for the dynamic characterization of monolithic VCSOAs

Sect. 3.2. The fibre injection was adjusted to maximize the available power, whilst minimizing the self-phase modulation effects in the fiber; this was done by finding the highest coupling, whilst keeping an unbroadened pulse spectrum at the VCSOA input. To minimize the train of probe pulses own saturating effect on the gain medium, one of the mirror was slightly misaligned to induce a fiber-injection loss of 6 dB for the probe pulse beam. The averaged pump pulse power injected was around −16 dBm, while it was −22 dBm for the probe pulses. The mirror M2 was positioned on a motorized translation stage to vary the path length between the two trains of pulses and thus obtain variable delays ranging from −100 ps to +300 ps. The effect of the first pulse (pump pulse) on the VCSOA gain medium could, therefore, be studied by observing the evolution of the transmission of the second pulse (probe pulse) as a function of the delay.

At the detection side, the combination of a polarization controller and a polarizer enabled the selection of the probe pulses, while blocking the others with an extinction ratio of more than 15 dB. Furthermore, an intensity modulator synchronized to the laser pulses was added to increase the probe visibility by rejecting the ASE when the pulses were not present. The output was fed to an optical spectrum analyzer (OSA) for the measurement of the probe spectrum with a 0.02 nm wavelength resolution.

20.4.3 VCSOA Dynamics Measurement

We first investigated the refractive index dynamics of the device. The VCSOA was operated at the anti-resonance as this situation corresponds to the maximum visibility of the resonance shift.

By observing the output spectra, a shift of the VCSOA resonance could be observed for certain values of the pulse delay. The inset of Fig. 20.29 shows the recorded spectra for the two extreme situations. The maximum resonance shift was measured to be 0.3 nm and occurred for a delay of 13 ps. As explained

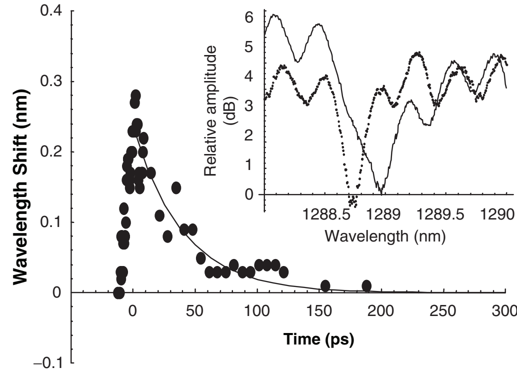

Fig. 20.29. Refractive index dynamics of a GaInNAs monolithic VCSOA operated at anti-resonance. *Inset*: Probe spectral characteristics at maximum (*solid*) and minimum (*dashed*) carrier depletion showing the maximal anti-resonance shift recorded

in the previous section, this wavelength shift is the greatest at the maximum carrier depletion and is equivalent to a refractive index variation of 9.3×10^{-4}. We then measured the spectra for different value of the delay from −20 ps up to 250 ps. The data was processed automatically, and the resonance peak shift plotted as a function of the delay in Fig. 20.29. A single exponential decay fit to the data gave an index recovery time τ_n at 1/e of $\tau_\mathrm{n} \sim 50\,\mathrm{ps} +/- 5\,\mathrm{ps}$. For higher delays, the anti-resonance returned to its original position. For small carrier density variations, which is the case here, the carrier recovery time τ_N can be approximated by the index recovery time τ_n, i.e., $\tau_\mathrm{N} \sim 50\,\mathrm{ps}$.

We then studied the VCSOA gain recovery when the device was biased to provide a small-signal gain of 15 dB. Measurement of the gain variations induced by the pump pulse was possible because the gain peak for the probe pulse was redshifted by approximately 0.3 nm with respect to the ASE peak, as can be seen in the dotted inset of Fig. 20.30. Saturation effects limited the gain of the probe pulses to 5 dB. In the presence of the pump pulse, the gain of the probe pulses was further reduced reaching a minimum value of −3 dB for a delay of about 10 ps. The spectrum of the probe corresponding to this maximum carrier depletion is shown in the solid line in the inset of Fig. 20.30. Recording the evolution of the probe pulse gain as a function of delay enabled the characterization of the gain recovery. However, cavity length instabilities with a magnitude of around 0.1 nm were present under these bias conditions and prevented us from measuring simultaneously the index recovery time. Figure 20.30 shows the evolution of the probe pulse gain as a function of the delay along with a $\tau_\mathrm{G} \sim 55\mathrm{ps} +/- 15\,\mathrm{ps}$ recovery fit. The τ_G is roughly equal to τ_N, which means that the carrier recovery time does not vary dramatically with the bias condition in our experiments. The measured

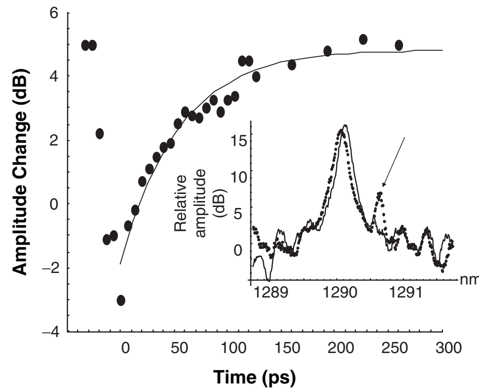

Fig. 20.30. Gain dynamics of a GaInNAs monolithic VCSOA biased to provide 15 dB of small-signal gain. *Inset*: Probe spectra at maximum (*solid*) and minimum (*dashed*) carrier depletion. The *arrow* indicates the wavelength at which the gain change occurs

value is also consistent with time-resolved photoluminescence measurements performed on other GaInNAs structures [16].

20.5 Extension to the 1,550 nm Band

Potential cost reduction and simpler manufacturing of telecommunication devices have been the major incentives to extend GaAs-based technology to the 1,300 and 1,550 nm wavelength bands. Up to this point, we have demonstrated that monolithically-grown VCSOAs based on GaInNAs compounds can deliver high performance single channel amplification at 1,300 nm. This section deals with current progress to push the operation wavelength of dilute nitride VCSOAs into the 1,550 nm window.

The main difficulty in achieving 1,550 nm operation is that the addition of nitrogen to InGaAs/GaAs QWs, which has constituted the main thrust of the extension to 1,300 nm, is associated with a dramatic reduction of PL efficiency. This degradation is believed to be due to phase separation during growth and/or an increased defect density. To date, the dilute nitride community has thus devised four strategies to overcome this issue:

- Finding particular growth conditions to avoid phase separation. This usually involves performing the growth at very low temperatures ($<400°C$) [17, 18], which generally leads to fairly high defect concentration.
- Reduction of the barrier band gap by using GaNAs or lattice-matched GaInNAs barriers [19]. The reduction in carrier confinement will, however, increase the temperature sensitivity of the devices.
- The use of InAs insertion layers inside GaNAs/GaInNAs superlattices [20]. Though this is effective in shifting the luminescence to 1550 nm, the growth

is very demanding as large composition changes every nanometre are required.

- The addition of antimony to the GaInNAs alloy forming the QWs [21–23]. Though the complexity associated with the growth of a quinary compound may seem off-putting, this technique is actually the most promising since the antimony acts as a surfactant for the dilute nitride growth, favouring 2D growth and high nitrogen content.

In the first instance, a temperature-dependent photoluminescence study of GaInNAsSb/GaNAs multi-quantum well (MQW) structures was carried out. A set of three double QW samples emitting at 1,550 nm, but having different conduction band profiles, were grown using MBE. All the structures consisted of a n^+-doped GaAs substrate, a 100 nm GaAs layer, a 20 period AlAs(2 nm)/GaAs(2 nm) superlattice, a 250 nm GaAs layer followed by two 7 nm-thick $Ga_{0.6}In_{0.4}$NAs(Sb) QWs embedded in 20 nm Ga(N)As barriers and further capped by 100 nm GaAs, followed by 50 nm $Al_{0.33}Ga_{0.67}As$ and 50 nm GaAs. The nitrogen concentrations were 4.5% (sample v0259), 2.9% (sample v0397), and 0 (sample v0398) in the barriers and 2.7%, 2.9% and 3.3% in the wells. Fig. 20.31a demonstrates that room-temperature photoluminescence at 1.5–1.55 μm was successfully achieved for all the samples, while Fig. 20.31b provides some insight into the influence of temperature on the emission properties of such QWs (sample V0397). The evolution of the ground state transition energy is fitted using the Varshni formula:

$$E_{\mathrm{g}}(T) = E_0 - \frac{\alpha T^2}{\beta + T}. \tag{20.26}$$

From the energy difference at low temperature between the measured value and the value given by (20.26), one can infer the localization depth E_{loc}. The QW peak wavelength redshifts at a rate of ~0.564 nm/K around room temperature. This figure is comparable to the 0.54 nm/K obtained for conventional 1,550 nm InGaAsP/InP material [24]. The temperature dependence of the integrated intensity was further analyzed using a dual-activation energy Arrhenius plot:

$$I(T) = \frac{I(0)}{[1 + c_1 \exp(-E_1/kT) + c_2 \exp(-E_2/kT)]}, \tag{20.27}$$

where, E_1 and E_2 represent the activation energies of two different thermal activation processes, and the pre-factors c_1 and c_2 represent the relative ratios of non-radiative recombination. The E_1 and E_2 were found to correspond respectively to the localization energy and energy difference in the valence band between the QWs and the barriers (~83 meV). The latter observation suggests that hole leakage might be a limiting factor in GaInNAs(Sb) QWs [25].

The work was extended to look at VCSOAs. The structure used in this instance included an epitaxially-grown semiconductor part completed by

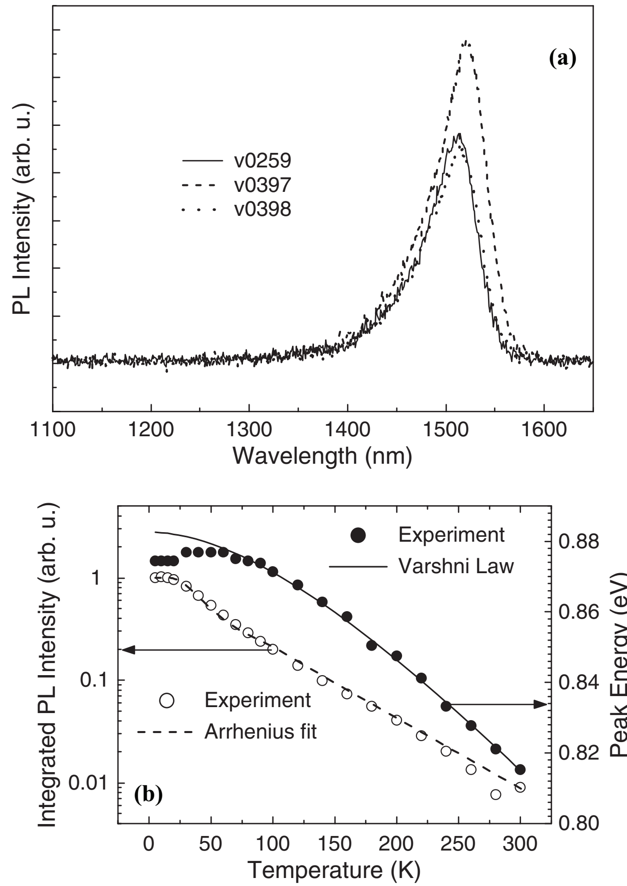

Fig. 20.31. Photoluminescence study of 1,550 nm emitting GaInNAsSb MQW structure. (**a**) Room-temperature photoluminescence spectrum; (**b**) Temperature-dependence of the photoluminescence characteristics

the subsequent deposition of a 1,550 nm dielectric (SiO_2/TiO_2) DBR with nominal reflectivity greater than 99.5%. The semiconductor epilayer design consists of a 25.5-pair AlAs/GaAs DBR, a GaAs active region and a 1λ-thick $Al_{0.3}Ga_{0.7}As$ confinement window capped with 10-nm of GaAs to prevent oxidation. The active region includes four sets of three nominally 7-nm-thick $Ga_{0.61}In_{0.39}N_{0.027}As_{0.962}Sb_{0.011}/GaAs_{0.956}N_{0.044}$ QWs with 20 nm between the wells. The target room-temperature photoluminescence of these quantum wells, 1,530 nm, is set to accommodate for pump-induced heating effects. The active region length and distribution of the groups of QWs is selected to achieve efficient and nearly uniform pumping using an 808 nm pump.

The sample was also grown using MBE with conventional thermal effusion cells for Ga, Al and In and radio frequency (rf) plasma sources with valved

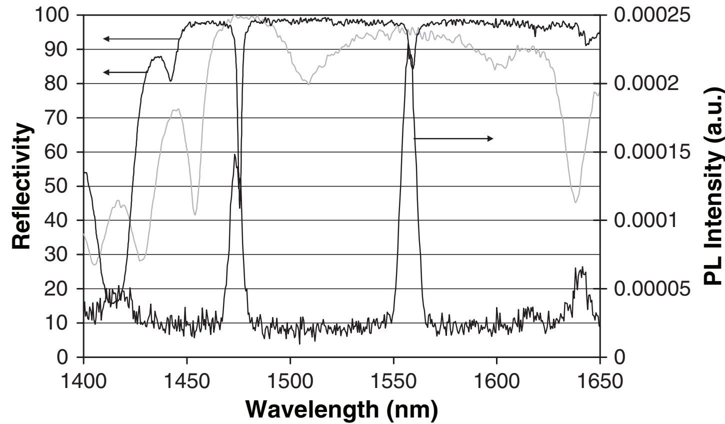

Fig. 20.32. Room temperature reflectivity before (*grey curve*) and after (*black curve*) dielectric coating deposition and photoluminescence of 1,550 nm GaIn NAsSb VCSOA

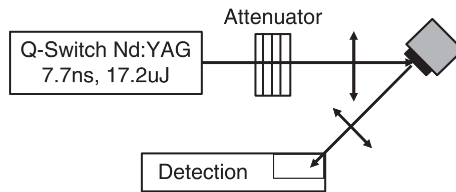

Fig. 20.33. Setup for pulsed laser assessment of the 1,550 nm VCSOA

cracker cells for As_2 and Sb_2. The growth was performed at 600°C apart from the groups of QWs for which the temperature was ramped down to 420°C. Details of the growth precision and monitoring techniques can be found in ref. [26, 27].

Static characterization of the wafer prior to and after dielectric mirror deposition was performed. Figure 20.32 shows typical results. It should be noted that there are two cavity modes, but that the short wavelength mode is very close to the edge of the semiconductor DBR stopband and thus the associated high loss level is likely to prevent amplification/laser action. Variation of the resonant wavelength from 1560 nm at the centre of the wafer to 1,540 nm at the edge was also recorded.

The laser characteristics of the sample were tested under pulsed condition using the setup of Fig. 20.33. The pump laser was a Q-switched Nd:YAG (1,064 nm) laser delivering 7.7 ns pulses with a 2 kHz repetition rate and up to 17.2 μJ per pulse. The pump beam propagated through an attenuating arrangement and was then focused on to the sample at ∼45 degrees incidence by a microscope objective, yielding a spot diameter of around 25 μm. The device output at 1.55 μm was collected, filtered (to eliminate any pump

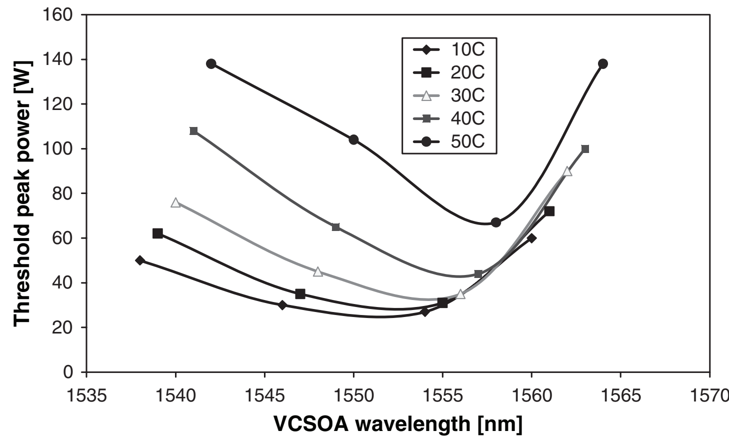

Fig. 20.34. Threshold characteristics of the 1,550 nm VCSOA under pulsed pumping for a set of temperatures and positions across the wafer

contribution) and focused onto a high-speed detector with a 5 ns rise time for measurement of the peak power or fibre-coupled to an optical spectrum analyser for spectral analysis.

The pulsed threshold was measured as a function of temperature at four different points on the wafer. The results are presented in Fig. 20.34 and show that both the cavity resonance and the minimum threshold shift at a rate of $\sim$0.15 nm/K. The latter observation suggests that the QW gain is broad and that the resonant periodic gain defines the maximum gain of the device. The recorded strong temperature dependence suggests that a high Auger recombination rate and/or carrier leakage impedes the device performance. A modification of the QW structure will be required to reduce these thermal limitations and demonstrate continuous-wave operation.

20.6 Conclusion

We have reviewed the performance of 1,300 nm GaInNAs-based VCSOAs under both continuous-wave and dynamic excitation. It has been demonstrated that monolithically grown GaInNAs-based devices can reach up to 19 dB of on-chip gain with noise figures as low as 4 dB and that these devices are suitable for single channel amplification of 10 Gb s^{-1} data streams. The suitability of these devices for metropolitan access networks has been enhanced by the demonstration of tunable operation using temperature changes or a fibre-based mirror-tunable embodiment achieving respectively 9.5 nm (23 nm) tuning with 10 dB (6 dB) of on-chip gain. It has also been shown that the experimental data can be further exploited, using a rate equation analysis, to provide information on the material gain characteristics. Finally, current material and device progress towards operation at

1,550 nm has been summarized. This is the next challenge for the dilute nitride compounds.

Acknowledgements. The authors acknowledge EPSRC for supporting this work under the grant GR/S59994/01. They thank Prof. M.D. Dawson for his support and encouragements throughout the duration of this project. They are obliged to Dr H.D. Sun for his help with the spectroscopic characterizations. They are also grateful to their colleague Dr A. Kemp for suggesting improvements and proof-reading the manuscript.

References

1. M.Y.A. Raja, S.R.J. Brueck, M. Osinski, C.F. Schaus, J.G. McInerney, T.M. Brennan, B.E. Hammons, IEEE J. Quantum Electron. **25**, 1500 (1989)
2. M. Born, E. Wolf, *Principles of Optics*, (Cambridge University Press, Cambridge, 1999)
3. D.I. Babic, S.W. Corzine, IEEE J. Quantum Electron. **28**, 514 (1992)
4. M. Hetterich, A. Grau, A.Y. Egorov, H. Riechert, IEE Proc. Optoelectron. **151**, 393 (2004)
5. M.A. Afromovitz, Solid State Commun. **15**, 59 (1974)
6. J Piprek, E.S. Bjorlin, J.E. Bowers, IEEE J. Quantum Electron. **37**, 127 (2001)
7. M.X. Jungo, D. Erni, W. Batchtold, IEEE J. Sel. Topics Quantum Electron. **9**, 939 (2003)
8. E.S. Bjorlin, J.E. Bowers, IEEE J. Quantum Electron. **38**, 61 (2002)
9. A. Karim, E.S. Bjorlin, J. Piprek, J.E. Bowers, IEEE J. Sel. Topics Quantum Electron. **6**, 1244 (2000)
10. C.J. Chang-Hasnain, *Vertical-Cavity Surface-Emitting Lasers: Technology and Applications*, (Gordon Breach Science Publishers, New York, 2000), p. 279
11. G.D. Cole, E.S. Bjorlin, Q. Chen, C.Y. Chan, S. Wu, C.S. Wang, N.C. MacDonald, J.E. Bowers, IEEE J. Quantum Electron. **41**, 390 (2005)
12. R. Fehse, S. Tomic, A.R. Adams, S.J. Sweeney, E.P. O'Reilly, A. Andreev, H. Riechert, IEEE J. Sel. Topics Quantum Electron. **8**, 801 (2002)
13. J.C.L. Yong, J.M. Rorison, I.H. White, IEEE J. Quantum Electron. **38**, 1553 (2002)
14. D.L. Andews, A.A. Demidov, *An Introduction to Laser Spectroscopy*, (Springer, Berlin Heidelberg New York, 2002)
15. A. Kastler, Nouv. Rev. Optique **5**, 133 (1974)
16. S. Calvez, J.M. Hopkins, S.A. Smith, A.H. Clark, R. Macaluso, H.D. Sun, M.D. Dawson, T. Jouhti, M. Pessa, K. Gundogdu, K.C. Hall, T.F. Boggess, J. Cryst. Growth **268**, 457 (2004)
17. G. Jaschke, R. Averback, L. Geelhaar, H. Riechert, J. Cryst. Growth **278**, 224 (2005)
18. M. Hughes, D. Damilano, J.Y. Duboz, J. Massies, Appl. Phys. Lett. **88**, 091111 (2006)
19. H.Y. Liu, M. Hopkinson, P. Navaretti, M. Gutierrez, N.S. Ng, J.P.R. David, Appl. Phys. Lett. **83**, 4951 (2003)

20. N.V. Kryzhanovskaya, A.Y. Egorov, V.V. Mamutin, N.K. Polyakov, A.F. Tsatsulnikov, Y.G. Musikhin, A.R. Kovsh, N.N. Ledentsov, V.M. Utsinov, D. Bimberg, Semicond. Sci. Technol. **20**, 961 (2005)
21. J.S. Harris Jr., J. Cryst. Growth **278**, 3 (2005)
22. J.A. Gupta, G.I. Sproule, X. Wu, Z.R. Wasilewski, J. Cryst. Growth **291**, 86 (2006)
23. L.H. Li, V. Sllet, G. Patriarche, L. Largeau, S. Bouchoule, L. Travers, J.C. Harmand, Appl. Phys. Lett. **83**, 1298 (2003)
24. J. Piprek, P. Abraham, J.E. Bowers, IEEE J. Quantum Electron. **36**, 366 (2000)
25. H.D. Sun, S. Calvez, H.D. Dawson, J. Gupta, G.C. Aers, G.I. Sproule, Appl. Phys. Lett. **89**, 101909 (2006)
26. N. Laurand, S. Calvez, H.D. Sun, M.D. Dawson, J. Gupta, G.C. Aers, Electron. Lett. **42**, 29 (2006)
27. J. Gupta, Z.R. Wasilewski, B.J. Riel, J. Ramsey, G.C. Aers, R.L. Williams, G.I. Sproule, A. Perovic, T. Garanzotis, A.J. Sprinthorpe, J. Cryst. Growth, **242**, 141 (2002)

21

Dilute Nitride Photodetector and Modulator Devices

J.B. Héroux and W.I. Wang

The application of the GaInNAsSb compound to the design and fabrication of photodetector and modulator devices for telecommunications is reviewed. An advantage of the material is that even though it is GaAs-based, operating wavelengths as long as 1.3 and 1.55 µm corresponding, respectively, to the minimum dispersion and attenuation in fiber optics can be reached. It is especially well suited for the growth of resonant cavity-enhanced devices because an active region can be incorporated between GaAs/AlAs distributed Bragg reflectors, with which a high reflectivity can be easily reached due to a large refractive index step. We present an overview of experimental results on: p–i–n resonant cavity-enhanced photodetectors; heterojunction phototransistors; avalanche photodiodes (APDs); quantum-confined stark effect modulators.

21.1 Introduction

High speed photodetectors and modulators are crucial components of optical telecommunication systems operating in the near infrared. As transmission rates become higher and the 1.3–1.55 µm wavelength range is increasingly used, the development of novel detectors with a high-quantum efficiency and of modulators with a high-absorption contrast is important.

The use of distributed Bragg reflectors (DBRs) to form a resonant cavity-enhanced (RCE) structure is a possible solution to address these issues. The optical and electrical path lengths can be decoupled to break the trade-off between bandwidth and quantum efficiency of standard p–i–n photodiodes, and the increased absorption allows to decrease the number of quantum wells and the operating voltage of modulators based on the quantum-confined stark effect (QCSE). The inherent wavelength selectivity of a resonant cavity is advantageous for demultiplexing receiver systems. Moreover, optical coupling normal to the surface makes RCE structures physically compatible

with vertical cavity surface emitting lasers. Various RCE devices have been demonstrated over the past 20 years [1].

Dilute nitride materials are well suited for the growth of GaAs-based heterostructures for devices operating in the 1.3–1.55 μm telecommunication window. With the GaInNAs compound, the replacement of a small fraction of arsenic by nitrogen atoms leads to a redshift of the bandgap and a decrease of the free lattice parameter, so that epitaxial layers can be grown on GaAs with a tolerable lattice mismatch and a narrow bandgap. Recent developments have shown that to obtain a good material quality, a fraction of Sb should also be incorporated to form the GaInNAsSb quinternary compound.

For photodetector and modulator applications, devices that are GaAs-based are advantageous not only due to a better-developed processing technology and lower overall fabrication costs, but also because the relatively high GaAs/AlAs refractive index step is benefic for the fabrication of RCE structures. Figure 21.1 shows a calculation of the peak quantum efficiency of a resonant cavity as a function of the normalized absorption coefficient. For high speed photodetectors, $\alpha d \sim 0.1$ is typically required so that a bottom DBR with a reflectivity close to 99% is essential for a near-unity quantum efficiency. GaAs/AlAs layers have a real refractive index step near 0.5 in the near infrared, so that the growth of only 20 periods is sufficient to obtain a DBR that fulfils this requirement. In contrast, on InP, the growth of DBRs is challenging due to the poor refractive index contrast between the $In_{0.53}Ga_{0.47}As$ and $In_{0.52}Al_{0.48}As$ alloys lattice matched to this substrate, and around 35 periods are needed to obtain a near-unity reflectance. Below 1.55 μm, absorption by the $In_{0.53}Ga_{0.47}As$ layers is also problematic.

In this chapter, an overview of the developments related to the use of dilute nitride materials for the fabrication of GaAs-based photodetector and

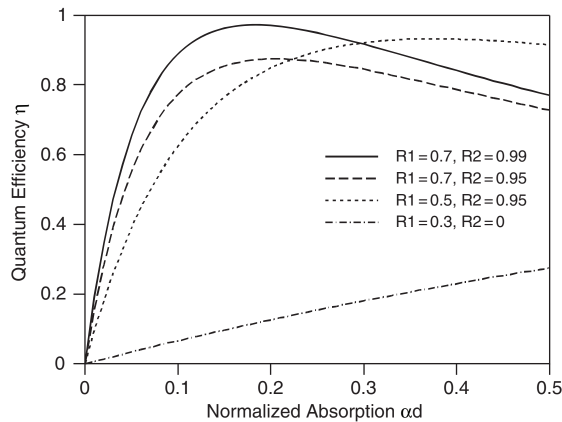

Fig. 21.1. Calculated peak quantum efficiency as a function of the normalized absorption of a resonant cavity for various top and bottom reflectivities R1 and R2. The standing wave effect is neglected

Table 21.1. Articles published on photodetector and modulator devices with dilute nitrides

Article title	λ (μm)	Structure	Function	Active region
GaInNAs resonant cavity-enhanced photodetector operating at 1.3 μm [4]	1.3	Bulk RCE	D	GaInNAs:Sb
GaNAs avalanche photodetector operating at 0.94 μm [5]	0.94	MQW	DG	GaNAs
GaNAs resonant cavity-enhanced avalanche photodetector operating at 1.064 μm [6]	1.06	MQW RCE	DG	GaNAs
MBE growth of Ga(In)NAs/GaAs heterostructures for photodiodes [7]	1.06	Bulk	DG	GaNAs
Optical investigation of InGaNAs structures for photodetector applications [8]	1.16	MQW	DG	GaInNAs:Sb
Electroabsorption and electrorefraction in InGaAsN quantum well heterostructures [9]	0.9	MQW	M	GaInNAs
GaAsSb resonant cavity-enhanced photodetector operating at 1.3 μm [10]	1.3	MQW	D	GaAsSb
Quantum confined stark effect in GaInNAs/GaAs MQWs [11]	1.3	MQW	M	GaInNAs:Sb
1.31 μm GaAsSb resonant cavity-enhanced separate absorption, charge, and multiplication avalanche photodiodes with low noise [12]	1.31	MQW RCE	DG	GaAsSb
Quantum-confined stark effect of GaInNAs(Sb) quantum wells at 1300–1600 nm [13]	1.3–1.6	MQW	M	GaInNAs:Sb
1.55 μm GaNAsSb photodetector on GaAs [14]	1.55	2 QW	D	GaNAsSb
1.55 μm GaInNAs RCE photodetector grown on GaAs [15]	1.55	6 QW RCE	D	GaInNAs

QW quantum well, *MQW* multiple quantum well, *D* detector, *DG* dectector with gain, *M* modulator, *RCE* resonant cavity-enhanced structure

modulator devices for long wavelength telecommunication applications is presented. Table 21.1 shows a list of the relevant articles published so far with the reference number, publication year, operating wavelength of the device, structure type, function of the device and material used for the active region. Closely related work on the GaAsSb compound has been included for completeness. In this chapter, experimental results obtained at Columbia University will be described in details, while those of other groups will be summarized. Dilute nitrides have also been studied for solar cell applications,

which present a completely different set of challenges and issues that are presented in [1–3] and Chapter 15 and will not be discussed further in this chapter.

A brief summary of the GaInNAsSb material properties will be given in Sect. 21.2 followed by results on p–i–n photodetectors in Sect. 21.3, where alternatives for high speed 1.3–1.55 μm detectors will also be shortly discussed. Devices with internal gain will be described in Sect. 21.4, and QCSE modulators in Sect. 21.5.

21.2 GaInNAsSb Material Properties for Detector and Modulator Devices

21.2.1 Material Growth

The incorporation of nitrogen into III–V compounds leads to a degraded material quality so that material growth is challenging and requires lengthy optimization. A high-purity radio frequency N source is typically used in a molecular beam epitaxy (MBE) system, with a growth temperature around 460°C.

The interface quality can be significantly improved by adding a slight antimony pressure background during growth to obtain a surfactant-like effect. Figure 21.2 shows photoluminescence spectra of $Ga_{0.7}In_{0.3}N_{0.008}$ $As_{0.992}$:Sb/GaAs multiple quantum wells (MQWs) [16]. Clearly, the emission intensity as well as the FWHM are improved with Sb, demonstrating that a higher quality dilute nitride compound is obtained.

The Sb flux can be further increased to form the quinternary compound GaInNAsSb to obtain a good material quality and emission wavelength near

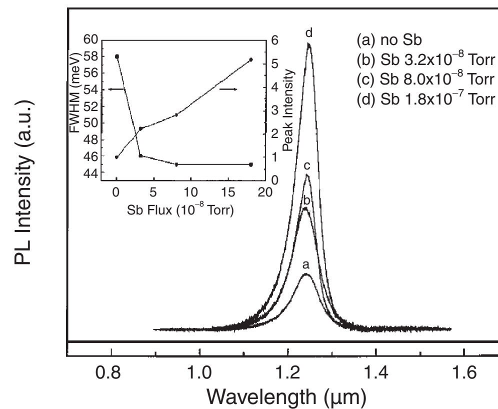

Fig. 21.2. Room temperature photoluminescence spectra of $Ga_{0.7}In_{0.3}N_{0.008}$ $As_{0.992}$:Sb/GaAs multiple quantum well structures. The nominal well width is 64 Å, and 10 periods are grown

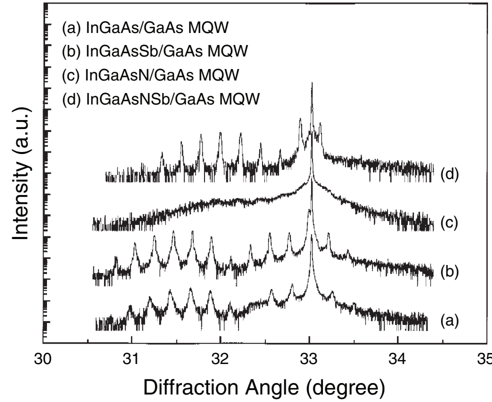

Fig. 21.3. X-ray diffraction spectra of MQW structures showing the effect of Sb incorporation

1.55 µm. Figure 21.3 shows X-ray diffraction spectra of 10-period MQW structures with 65 Å well and 180 Å barrier widths [17]. The N and Sb fractions were estimated to be around 3.5 and 1.5%, respectively. The addition of Sb prevents three-dimensional growth and phase separation, as seen from the presence of clear satellite peaks in curve (d) above. Progress for long wavelength devices with this novel compound is ongoing.

21.2.2 Band Structure

The virtual crystal approximation is not applicable to dilute nitride compounds due to the fact that nitrogen, although it is a column-V element, has a high electronegativity and a small atomic size. But even though the physical properties of dilute nitride heterostructures depend on the detailed arrangement of atom clusters, simple rules for device design can still be established. It has been known since the 1970s that nitrogen, an isoelectronic trap, leads to the formation of a deep level E_{N} in GaAs located approximately 200 meV above the bottom of the conduction band [18, 19], and other localized energy levels within and above the gap are also present due to the formation of different nitrogen pair complexes [20, 21].

Figure 21.4 summarizes the results obtained with the band anticrossing (BAC) model [[22], see also Chap 3]. The absolute position of E_{N} is fixed and independent of the surrounding crystal, while the extended energy level E_{M} is the bottom of the crystal conduction band in a nitrogen free compound. In GaInAs, the repulsion between E_{N} and E_{M} leads to the formation of two energy levels E_+ and E_- described by the equation

$$E_{\pm}(\mathrm{In}_x\mathrm{Ga}_{1-x}\mathrm{As}_{1-y}\mathrm{N}_y) = \frac{1}{2}\left([E_{\mathrm{M}}(x) + E_{\mathrm{N}}] \pm \sqrt{[E_{\mathrm{M}}(x) - E_{\mathrm{N}}]^2 + 4V_{\mathrm{NM}}^2} \right), \tag{21.1}$$

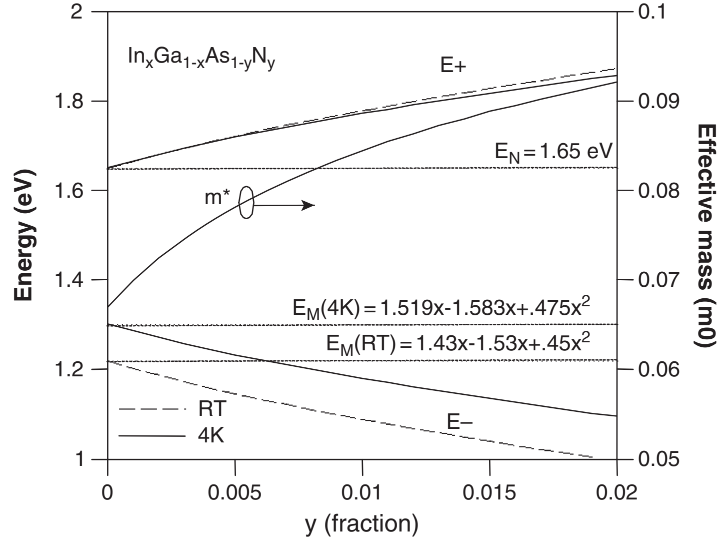

Fig. 21.4. Description of the band anticrossing model. The reference energy level is the valence band maximum of (In)GaAs (The numbers shown are for a 15% indium concentration.)

with $V_{\mathrm{NM}} = C_{\mathrm{NM}} y^{1/2}$ [23]. Assuming that the top of the valence band is used as reference energy and has a negligible variation, the position of the E_{-} level corresponds to the gap of the GaInNAs alloy. The conduction band effective mass is given by

$$\frac{1}{m^{*}_{\pm}} = \frac{1}{2m_{\mathrm{M}}} \left[1 \pm \frac{E_{\mathrm{M}} - E_{\mathrm{N}}}{\sqrt{(E_{\mathrm{M}} - E_{\mathrm{N}})^2 + 4V_{\mathrm{NM}}^2}} \right], \tag{21.2}$$

with m_{M} the effective mass of the extended E_{M} level [24].

As an illustrative example of the effect nitrogen incorporation on the band structure of III–V heterostructures, Fig. 21.5 shows low temperature transmittance spectra of GaInAsN:Sb/GaAs multiple quantum well structures. The different nitrogen fractions were determined by X-ray diffraction assuming a linear interpolation of the free lattice parameters [25]. The observed quantum confined optical transitions are noted as vertical arrows.

From the observation of three optical transitions for each sample, the properties of the heterostructures can be determined using an envelope function formalism and the BAC model. It has been postulated theoretically [26] and observed experimentally [1] that the gap of GaInNAs can vary by several tens of meV depending the detailed growth and annealing conditions of the samples. The variation of the gap with N can be usually well described with (21.1) using a value C_{NM} in the range 1.2–2 eV, and a good fit was obtained with $C_{\mathrm{NM}} = 1.45$ eV in the present case as shown in Fig. 21.6a.

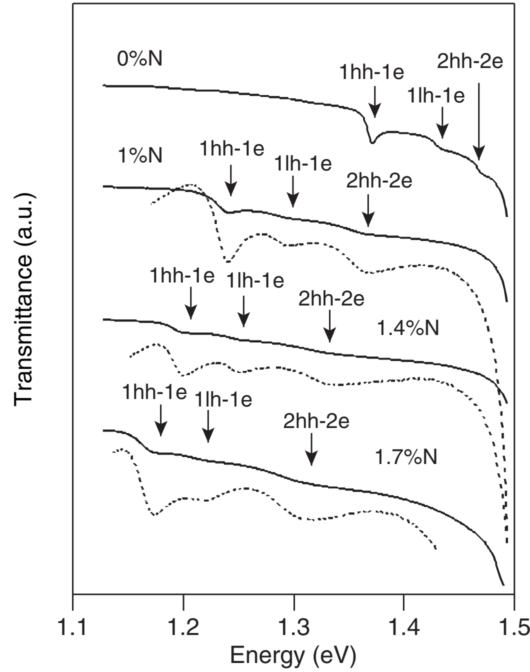

Fig. 21.5. Optical transmittance spectra of $Ga_{0.86}In_{0.14}N_xAs_{1-x}$:Sb/GaAs multiple quantum well samples with different nitrogen concentrations obtained at 4 K. *Solid lines* are the raw experimental curves. *Dashed lines* are an aid to the eye and show an expanded view along the vertical axis obtained after background subtraction. *Arrows* show the best estimate of the positions of the optical transitions found experimentally. *hh, lh*, and *e* indicate heavy hole, light hole, and conduction band quantum confined energies. Curves are vertically shifted for clarity

From photoreflectance spectroscopy measurements [27], the bandgap redshift due to N was found to decrease as the In fraction increases, and the conduction band effective mass increases to a value in the range 0.8–1.2 m_e. These trends are both also in accordance with the BAC model.

The incorporation of N into a III–V compound affects mostly the conduction band and has a negligible intrinsic effect on the valence band structure. However a decrease of the difference between the 1hh-1e and 1lh-1e optical transitions as the nitrogen fraction increases was observed experimentally. Figure 21.6(b) shows the strained and unstrained valence band offsets calculated for each sample based on the optical transitions shown in Fig. 21.5 (data points) using an envelope function formalism. Since the same conduction band energy level is involved in both transitions, the energy difference between the hh and lh valence band energy levels can be directly observed from this measurement and indicates a decrease of the valence band offset due the strain variation in the wells [25, 27]. Similar findings were also reported recently by

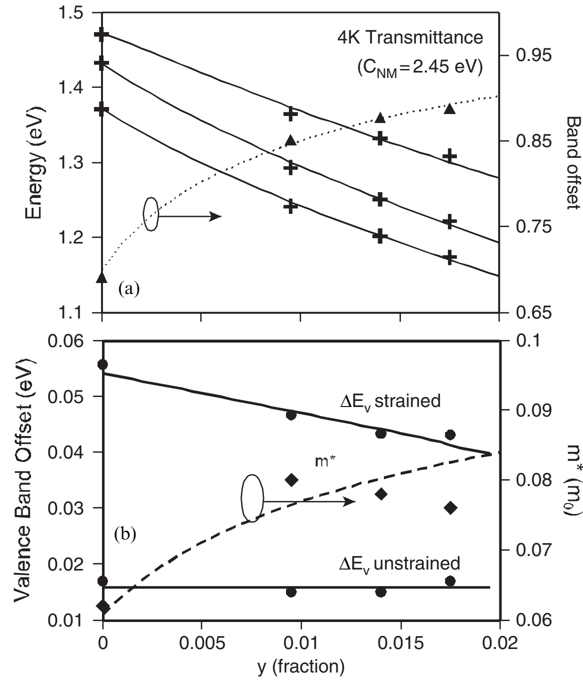

Fig. 21.6. (**a**) Experimental (*crosses*) and calculated (*lines*) transition energies of multiple quantum well structures as a function of the nitrogen fraction obtained at 4 K. The right scale is used to show the experimental (*triangles*) and calculated (*dash-dotted* line) strained conduction band offset ratio. (**b**) Experimental (*circles*, *diamonds*) and calculated (*solid*, *dashed lines*) values of the valence band offset and conduction band effective mass

another group [28, 29]. The unstrained band offset remains roughly constant as the nitrogen fraction varies, as shown in the bottom of Fig. 21.6b.

The effect of antimony on the band structure is neglected when a very small fraction is incorporated to improve material quality by a surfactant-like effect ($Ga_{1-x}In_xN_yAs_{1-y}$:Sb). In the case of a quinternary compound ($Ga_{1-x}In_xN_yAs_{1-y-z}Sb_z$), antimony can be taken into account using the virtual crystal approximation [30, 31].

21.3 p–i–n Photodetectors

21.3.1 GaInNAs:Sb Resonant Cavity-Enhanced Photodetector Operating at 1.3 μm

The interaction of light with an absorbing structure can be described with the simple equation $R + T + A = 1$, where the symbols R, T, and A are the power ratios of the reflected, transmitted, and absorbed light, respectively. With a

		Th (Å)
GaAs	p+	1547
GaAs	i	100
$In_xGa_{1-x}As_{.99}N_{.01}$:Sb	i	400
GaAs	i	1424
$In_xGa_{1-x}As_{.99}N_{.01}$:Sb	i	400
GaAs	i	1424
$In_xGa_{1-x}As_{.99}N_{.01}$:Sb	i	400
GaAs	i	100
GaAs	n+	595
GaAs buffer	n+	5000
GaAs subs	n+	

Fig. 21.7. Details of the p–i–n structure used for the design of a resonant cavity-enhanced detector. Two samples were grown with $x = 0.20$ and 0.25, respectively. The doping concentrations in the p^+ and n^+ regions is 2×10^{18} cm^{-3}

resonant cavity, the balance between these three variables can be altered so that the quantum efficiency η can be high even if a thin absorbing layer is used. In this section we describe the fabrication and characterization of the first RCE photodetector realized with a dilute nitride active region [4].

Bare p–i–n detector devices with a structure as shown in Fig. 21.7 were first grown and processed for characterization. The splitting of the bulk absorbing region into three parts allows to improve the material quality, and the GaInNAs:Sb layers can be positioned at the antinodes of a cavity to use to advantage the standing wave effect in an RCE structure. Two samples with indium concentrations of 20 and 25%, respectively were grown and processed using standard photolithography techniques, in which gold layers were evaporated on top of the mesas and onto the buffer layer to form ohmic contacts in a single liftoff step. The nitrogen fraction was estimated to be around 1% in both cases.

Figure 21.8 shows the reflectance, normalized absorption and quantum efficiency spectra of 1 mm diameter mesas obtained with a 2 V reverse bias. The responsivity of the devices was obtained using a Fourier transform spectrometer and a halogen light source with a calibrated Ge photodiode. By assuming a unity collection efficiency, a lower boundary value for the normalized absorption can be obtained [32]. Clearly, a 5% increase of the indium concentration decreases the bandgap and significantly increases the normalized absorption at 1.3 μm. The leakage current of 300 μm-diameter mesas was found to be comparable for the two samples, as shown in Fig. 21.9.

From the results shown above, the complex part of the GaInNAs:Sb refractive index could be estimated and the peak quantum efficiency of RCE structures can be simulated using the method of resultant waves [33, 34]. Figure 21.10 shows how the peak quantum efficiency of a complete RCE structure, calculated using the experimental results of Fig. 21.8, varies as a function of the reflectance of the bottom DBR. The number of periods of the top DBR

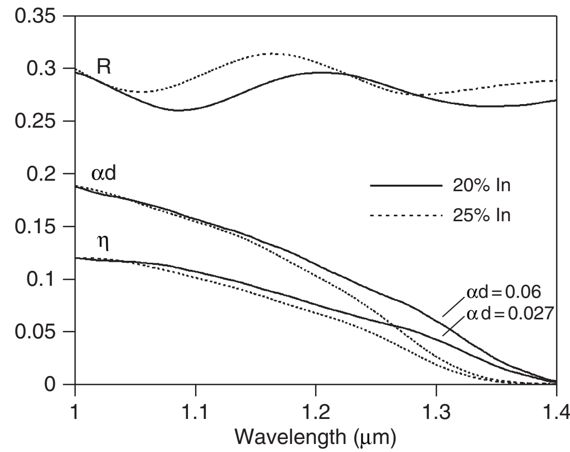

Fig. 21.8. Experimental reflectance (R), quantum efficiency (η), and normalized absorption coefficient (αd) of p–i–n photodiodes obtained at a 2 V reverse bias

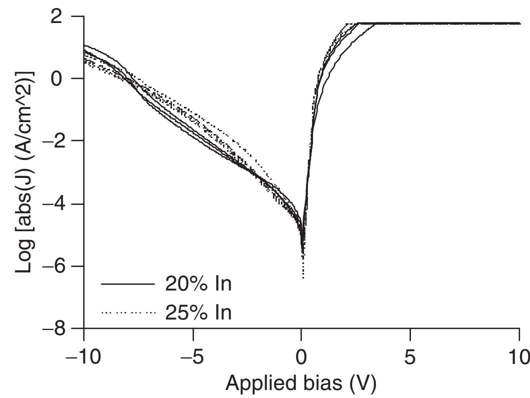

Fig. 21.9. I–V characteristics obtained with 300 μm diameter mesas

is chosen to provide a nearly optimal top reflectance. Even though the two samples should in theory have a peak quantum efficiency above 90% in ideal conditions, the sample with 20% In is much more sensitive to a slight drop in bottom reflectance. Therefore we adopted a structure with 25% In.

The growth of the complete resonant structure by MBE takes around 14 h. To calibrate a priori the optical thickness of the cavity, considering that the real part of the refractive index of the GaInNAs:Sb layers was not precisely known and that the growth rates can vary over time, p–i–n structures were grown on top of 5-period DBRs and a curve fitting procedure of the measured reflectance was performed using the method of resultant waves to estimate the required correction of the growth times. An example of this procedure is shown in Fig. 21.11.

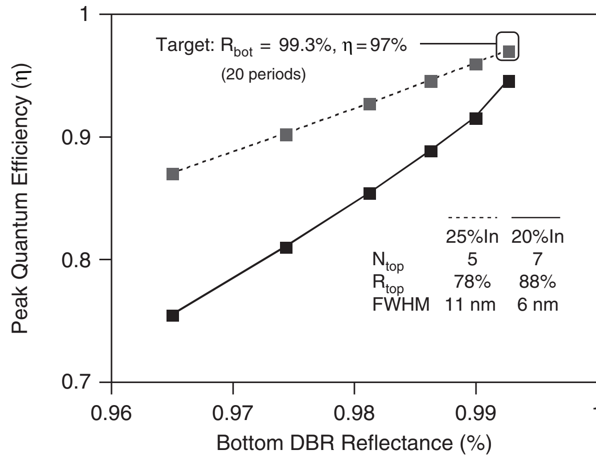

Fig. 21.10. Simulated peak quantum efficiency at 1.3 μm of a RCE p–i–n photodetector as a function of the bottom DBR reflectance. N_{top} is the number of periods of the top DBR. R_{top} and R_{bot} are the top and bottom DBR reflectance, respectively

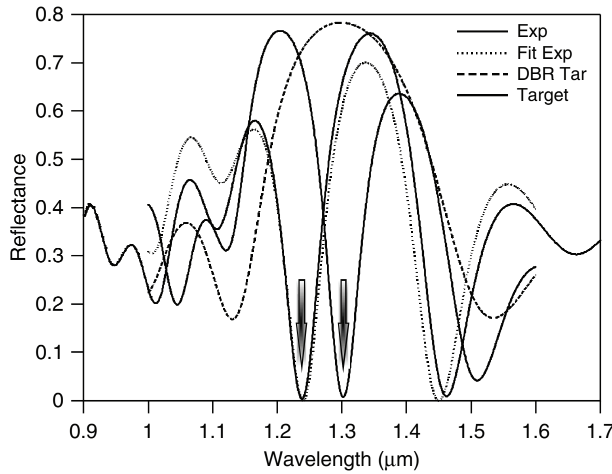

Fig. 21.11. Reflectance spectra of p–i–n structures grown on top of 5-period DBRs. Curves labeled "Exp" and "Fit Exp" show the measured and simulated spectra of a typical experimental structure with no prior thickness calibration. Curves labeled "DBR Tar" and "Target" show the simulated spectra of a DBR only and DBR + p–i–n structure assuming a correct calibration of all thicknesses. *Arrows* indicate the dip at the center of the reflectance spectra due to resonant absorption

The quantum efficiency, reflectance and dark current of the complete RCE detector, with bottom and top DBRs having 20 and 8 periods, respectively, are shown in Figs. 21.12 and 21.13. A 72% quantum efficiency was obtained at a wavelength of 1.292 μm with a reverse bias of 7 V and a 1 mm diameter

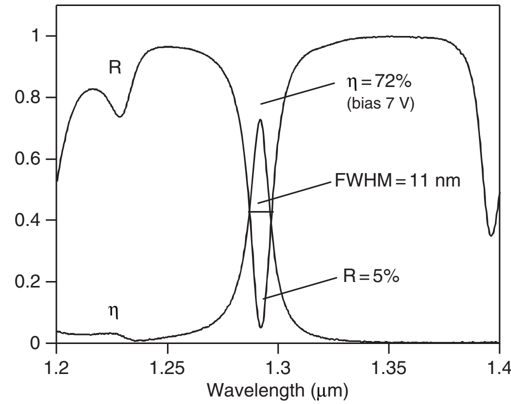

Fig. 21.12. Experimental reflectance and quantum efficiency spectra of a complete resonant cavity-enhanced p–i–n photodetector

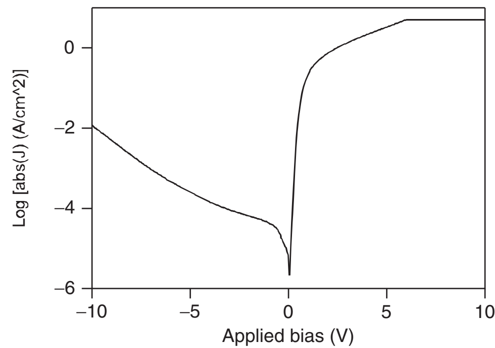

Fig. 21.13. Dark current of the resonant cavity-enhanced p–i–n photodetector

mesa. This peak quantum efficiency is slightly lower than the one predicted theoretically, but the reflectance drop to 5% at the resonant wavelength shows that the lower quantum efficiency is not due to a flaw in the design of the cavity but to an incomplete carrier collection. It is not uncommon, as we observe here, to obtain a lower than expected quantum efficiency even for structures grown using conventional, lattice-matched III–V materials [35].

21.3.2 Subsequent Results

The growth of GaAs-based RCE photodetectors using two multiple quantum well GaAsSb absorbing regions and a ZnSe/MgFe dielectric top DBR was subsequently reported [10]. An important difference with this compound is the nearly flat GaAs/GaAsSb conduction band offset, a situation that is nearly opposite to the GaInNAs:Sb/GaAs case and is favorable for the collection of the photogenerated electrons. A 54% quantum efficiency was obtained at

1.3 μm with an estimated leakage current at operating bias of the order of 10 μA cm^{-2}, which compares advantageously to the GaInNAs:Sb structure discussed in the previous section.

More recently, a monolithically grown GaInNAs/GaAs RCE photodetector operating at 1.55 μm with two multiple quantum well absorption regions was also demonstrated, and a 33% quantum efficiency was obtained [15]. A leakage current at operating bias below 40 μA cm^{-2} was measured, which is only slightly higher than maximum values reported for commercial, nitrogen-free high speed InGaAs photodiodes [36]. Speed measurements were performed, and an 800 ps risetime was reported. The low dark current obtained is especially promising for device applications.

A GaNAsSb p–i–n photodetector operating at 1.55 μm and grown on GaAs was also reported [14] with an absorption coefficient close to 10^4 cm^{-1}, which is suitable to obtain a high quantum efficiency with an RCE structure. The leakage current at operating bias was higher than for the case described in the previous paragraph, and may be improved with further growth optimization. Clearly, however, the replacement of a small fraction of As atoms with N atoms in GaAsSb is beneficial to decrease the lattice mismatch with GaAs and obtain a compound that is absorbing at 1.55 μm.

Further growth optimization using a quinternary InGaAsNSb compound for absorption could lead to better results and greater design flexibility. Another possibility for the growth of relatively thick active regions needed for a detector device would be a strain-compensated structure such as GaNAs/GaAsSb. An experimental and theoretical study on the absorption coefficient of GaInNAs quantum wires was also published recently [37] and may lead to novel detector devices.

21.3.3 Alternatives Devices

In this section we briefly mention other high quantum efficiency detector devices proposed for optical fiber applications. Wafer fusing was used in the mid-1990s to combine the advantages of an InP-grown active region with a high reflectivity GaAs/AlAs bottom DBR [38]. A 94% quantum efficiency was obtained at 1.3 μm using mesas with a $50 \times 50\,\mu m^2$ optical window. However the fabrication process, involving for example etching of the InP substrate, is relatively complex and dark current could be an issue.

InGaAs quantum dot RCE photodiodes have been grown on GaAs with an operating wavelength up to 1.27 μm [39–41]. Due the combined effect of the density of states with a resonant cavity, a spectral width as narrow as 3.3 nm near 1.3 μm can be obtained. With further growth optimization and better reproducibility, quantum dots could be a promising technology for detector applications.

A back-incidence, Si-based SiGe/Si multiple quantum well RCE detector with a SiO_2–Si top DBR has also been fabricated for operation at 1.3 μm [42]. Moreover, several solutions have been proposed to obtain on

InP substrates a high reflectivity, nonabsorbing bottom DBR to fabricate high quantum efficiency RCE devices operating near 1.55 μm. Those include Burnstein-shifted InGaAs/InP reflectors [43], the use of InP/air DBRs [44,45], or InAlAs/InAlGaAs DBRs [46, 47].

Planar devices such as RCE InGaAs metal-semiconductor-metal (MSM) detectors grown on InP have also been fabricated with operating wavelengths near 1.3 μm [48] and 1.55 μm [49] with 10 and 70 GHz bandwidth operations, respectively. Finally, InP-based edge-coupled waveguide photodiodes operating at 1.55 μm have been demonstrated [50, 51] and were shown to have a high operating bandwidth.

21.4 Photodetectors with Gain

21.4.1 Heterojuntion Phototransistors

Even though a nonconstant gain factor is a drawback of heterojunction phototransistors (HPTs), these devices are attractive to combine amplification and detection in a single structure with extremely low noise and a high sensitivity. Two- or three-terminal [52, 53] configurations can be designed, and a wide range of applications is possible [54]. Moreover integration into a resonant cavity to boost responsivity is straightforward, and a GaAs-based HPT with an InGaAs active region was one of the first RCE devices demonstrated. To obtain on GaAs an operating wavelength longer than 900 nm, HPTs with strain-relaxed InGaAs active layers have been experimentally investigated and at a wavelength up to 1 μm, a gain as high as 3,000 was obtained [55, 56].

The GaInNAs compound offers a straightforward solution to extend the operating wavelength of HPTs beyond 1 μm on GaAs, and in this section we present the growth and characterization of p–i–n MQW structures followed by a MQW HPT device with a 1.1 μm cutoff wavelength [8].

Figure 21.14 shows the structure of the complete HPT device. The normally incident light is transmitted through the emitter and base and is absorbed in the collector region. The photogenerated holes are swept through the base and accumulate at the emitter/base interface because of the large barrier height of the valence band. Hole accumulation in turn modifies the potential of the forward-biased emitter/base junction so that a large electron current flows from the emitter to the collector. The base and collector thicknesses and doping concentrations are chosen to avoid a punch-through effect and to ensure that the diffusion length of the minority carriers is larger than the width of the base to create a transistor action.

Figure 21.15 shows the normalized absorption coefficient of 10-period, 80/200 Å $Ga_{0.85}In_{0.15}N_yAs_{1-y}$:Sb/GaAs bare MQW structures obtained with an FTIR spectrometer. In all cases, the well width and period were estimated from X-ray diffraction measurements and found to be within two monolayers of their nominal value. A normalized absorption coefficient near 0.1 was obtained

			Doping (cm^{-3})		Th (μm)
Cap		GaAs	n+	2E+18	0.1
Emitter		$Al_{.3}Ga_{.7}As$	n	1.4E+18	0.1
Emitter		$Al_{.3}Ga_{.7}As$	n	5E+17	0.2
Base		GaAs	p	5E+17	0.1
	Spacer	GaAs	i		0.2575
Collector	Barrier	GaAs	i		0.015
	Well	$In_{.5}Ga_{.85}As_{.99}N_{.01}$:Sb	i		0.0085
20X	Barrier	GaAs	i		0.015
	Spacer	GaAs	i		0.2575
Subcollector		GaAs	n+	2E+18	1
Substrate		GaAs	n+		

Fig. 21.14. Structure of a heterojunction phototransistor

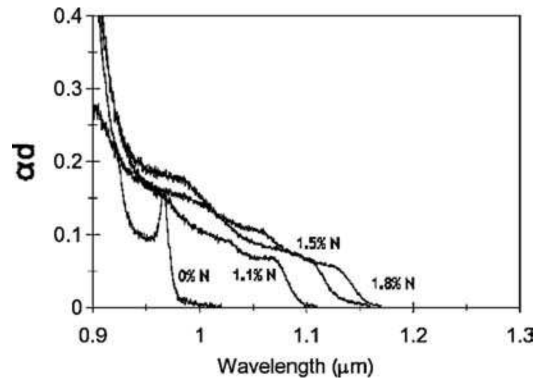

Fig. 21.15. Normalized absorption spectra of $Ga_{0.85}In_{0.15}N_yAs_{1-y}$:Sb/GaAs MQW samples with varying nitrogen concentrations

at the excitonic feature positions, so that the structures are suitable for high quantum efficiency RCE devices.

Partially strain-relaxed p–i–n structures as described in Fig. 21.14 but with the emitter part replaced by a 1,000 Å, $2 \times 10^{18}\,\text{cm}^{-3}$ p+ cap layer were grown for systematic studies. The growth of a 12-period, nitrogen-free sample as well as 12- and 20-period nitrogen-containing samples allowed a comparison with data previously published in the literature [57]. In all cases, the spacer thickness was adjusted so that the total thickness of the i region, and hence the built-in electric field, was constant but the degree of dislocations varied. Mesas with a 1 mm diameter were processed in a single lift-off step using gold ohmic contacts, and quantum efficiency spectra were obtained with an FTIR spectrometer and a calibrated Ge photodiode.

Figures 21.16 and 21.17 show, respectively, the quantum efficiency with a 10 V reverse bias and the dark current of the three samples. A comparison of the results for the two 12-period samples clearly shows that the addition of 1% nitrogen shifts the absorption threshold but has a small effect on the leakage current. The dark current is comparable to results presented by other

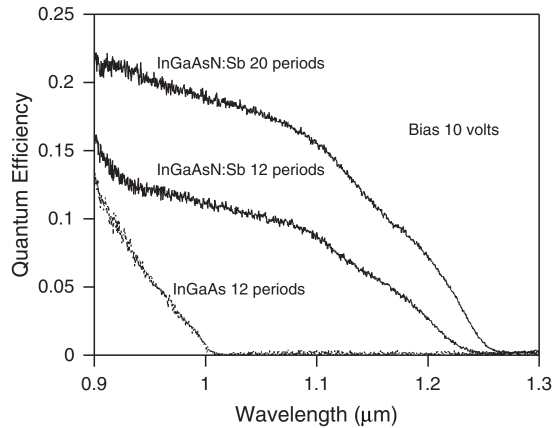

Fig. 21.16. Quantum efficiency of MQW p–i–n structures

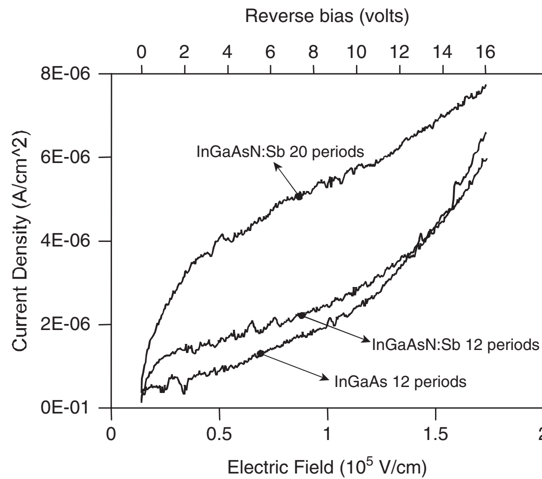

Fig. 21.17. Dark current of MQW p–i–n photodiodes as a function of the reverse bias and electric field in the intrinsic region

groups using nitrogen-free materials [57]. The material quality is degraded by nitrogen incorporation, but since the density of dislocations to which the dark current is highly sensitive does not vary significantly, the electrical properties are not greatly affected. In contrast, the 20-period sample has an almost threefold higher dark current, a fact that we can explain by the higher density of dislocations.

The dark current varies more or less exponentially with the reverse bias, a behavior different from what is observed experimentally for lattice-matched structures [58, 59] and not currently well understood [60]. It cannot be easily explained by the usual mechanisms of diffusion, generation–recombination and tunneling [61].

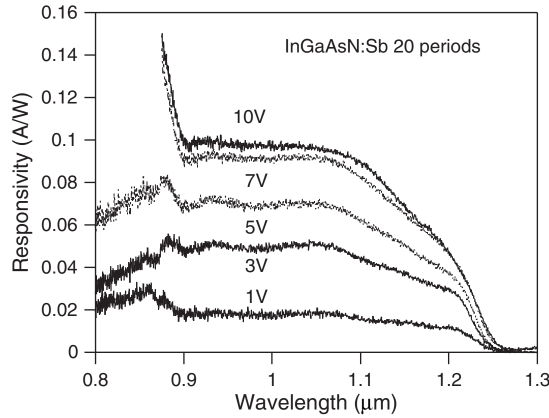

Fig. 21.18. Responsivity versus bias of a 20-period MQW photodiode

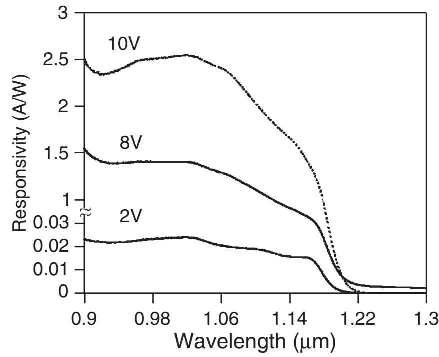

Fig. 21.19. Responsivity of a HPT with a 20-period MQW absorbing region under varying collector–emitter biases

Figure 21.18 shows the responsivity as a function of the applied reverse bias for the 20-period sample. A 10 V reverse bias is required to collect all the photogenerated carriers, which corresponds to a relatively high electric field around 100 kV cm^{-1}. This high value can be explained by the relatively large conduction band offset. It has been reported for InGaAsP/InP p–i–n structures, where the band offset is also large, that a reverse bias as high as 30 V could be required for a complete carrier collection if the structure is optimized for a high quantum efficiency and a low dark current [62].

Figure 21.19 shows responsivity spectra of a complete HPT structure with processed 300 μm diameter mesas. The responsivity obtained under a 10 V emitter–collector bias is above 1.5 A W^{-1} so that the device exhibits gain in a wavelength range above 1 μm.

Figure 21.20 shows how the collector current, I_C, varies as a function of the applied collector–emitter bias V_{CE} under different incident light powers.

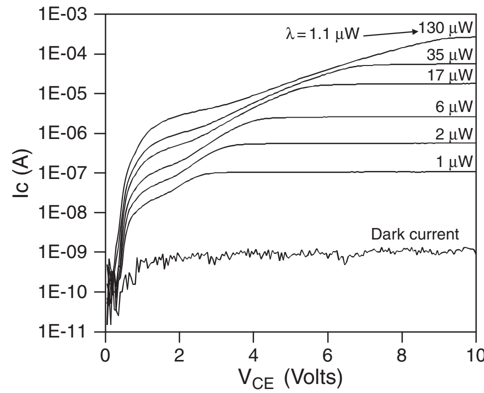

Fig. 21.20. Collector current I_C as a function of the collector–emitter voltage V_{CE} for different incident optical powers. The light source was a 1.1 μm wavelength laser diode

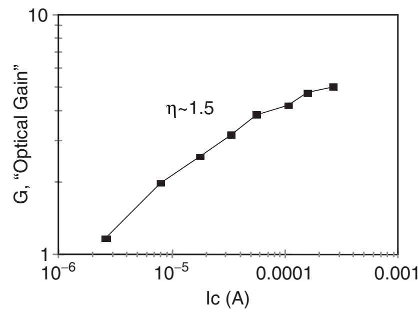

Fig. 21.21. Optical gain of the phototransistor device. η is the ideality factor

A clear saturation level is reached under all illumination conditions, and results compare advantageously with those of Ghisoni et al. [55, 56], who reported a current I_E continuously increasing with V_{CE} for strain-relaxed InGaAs/GaAs phototransistors and a nonconstant dark current. The optical gain of the device, however, is shown in Fig. 21.21 and is lower than the values between 20 and 200 reported by these authors. Better-optimized processing and characterization techniques should lead to InGaAsNSb HPTs with a higher gain. The growth of the MQW region could also be improved to obtain a lower degree of relaxation and the realization of high performance 1.3–1.55 RCE-HPT devices.

21.4.2 Avalanche Photodiodes

III–V compound APDs are being developed for telecommunication applications and are advantageous due to their very high sensitivity. Recently, new applications have also emerged [63].

A low dark current p–i–n GaNAs APD operating at 0.94 µm was first demonstrated in 2000 [5, 7], followed by a GaNAs APD RCE structure operating at 1.064 µm and exhibiting a gain up to 100 [6]. The growth of GaAsSb on GaAs is challenging [64], but a RCE APD with a peak external efficiency of 36% at 1.31 µm and a gain up to 40 [12] was fabricated with this compound. At a 1.06 µm wavelength, a 93% peak quantum efficiency was obtained [65].

21.5 Modulators

The quantum-confined stark effect (QCSE) in III–V heterostructures is used for the realization of standalone modulator devices [66], tunable photodetectors [67, 68] or for light output modulation in laser structures [69]. While it is well known that the high GaInNAs/GaAs conduction band offset is advantageous to improve the temperature characteristics of laser diodes by reducing electron overflow, this feature is also benefic in reverse-biased p–i–n structures to fabricate a modulator where the hole and electron wavefunction leakages are balanced. An ideal configuration for an efficient modulator has a band offset ratio given by $m_e V_e \approx m_h V_h$, where m_e (m_h) and V_e (V_h) are the conduction (valence) band effective mass and band offset, respectively. Moreover, a relatively low valence barrier height, typically around 50–70 meV, is desirable to improve the absorption contrast as a function of the applied bias [70, 71].

The effect of nitrogen incorporation on the band structure can be estimated with the formalism and experimental results described in Sect. 21.2. The increased conduction band offset and effective mass are advantageous for a reduced electron wavefunction leakage, while the slight decrease of the heavy hole band offset due to the reduced strain is also benefic for efficient modulation.

Figure 21.22 shows a calculation of the electron to hole tunneling probability ratio based on a transfer matrix method, taking into account the different effective masses in the GaInNAs wells and GaAs barriers. The well and barrier are assumed to have a 100 Å width, and 15 and 20% In compounds are shown. A nitrogen fraction in the 0.5–1% range allows to obtain a balanced structure corresponding to the ideal case where the tunneling probabilities are equal [11].

Electroabsorption with the GaInNAs/GaAs material system was first demonstrated experimentally by Jalili et al. [9]. A single quantum well structure was used, and a 4,000 cm^{-1} maximum absorption change was observed at 1.155 and 1.22 µm.

We investigated the effect of an applied reverse bias on MBE-grown p–i–n MQW structures by electroreflectance spectroscopy. A 5,000 Å n^+ doped (2×10^{18} cm^{-3}) GaAs buffer layer was grown on an n^+ GaAs substrate, followed by an intrinsic region composed of ten 89 Å GaInNAs:Sb quantum wells separated by 150 Å GaAs barriers positioned between two 3,500 Å GaAs layers. A 5,000 Å GaAs p-doped layer (5×10^{17} cm^{-3}) followed by a 1,000 Å GaAs p^+ doped

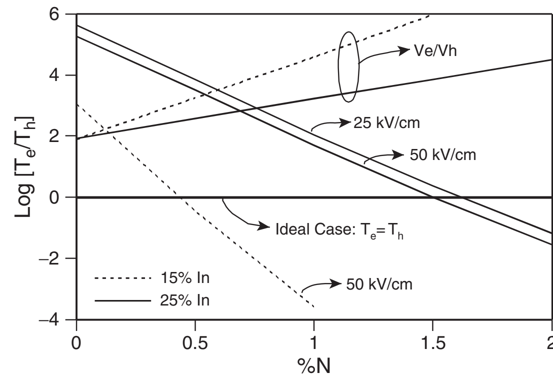

Fig. 21.22. Logarithm of the ratio of the electron to the heavy hole tunneling probabilities in a typical GaInNAs/GaAs multiquantum well structure as a function of the nitrogen fraction. The two lines with a positive slope show the ratio of the conduction to the heavy hole valence band discontinuities

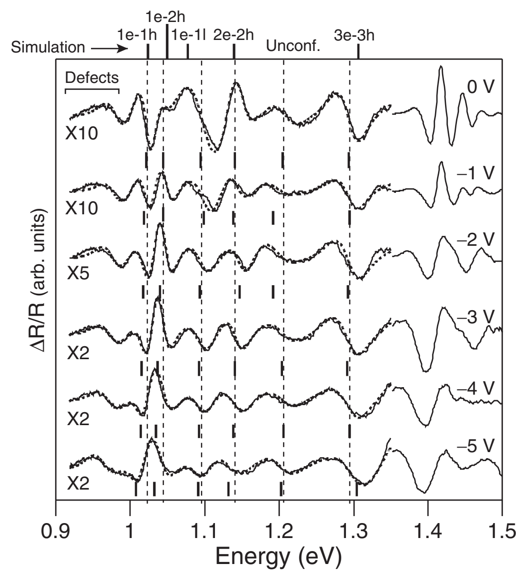

Fig. 21.23. Electroreflectance measurements of a $Ga_{0.84}In_{0.16}N_{0.02}As_{0.98}$:Sb/GaAs p–i–n multiquantum well structure under varying reverse biases. The *left portion of each curve* has been magnified for clarity. The *dashed vertical lines* are an aid to the eye showing the stark shift

$(2 \times 10^{18}\,\mathrm{cm}^{-3})$ layer were deposited on top of the i region. The quantum well layers were grown under a slight background pressure of antimony to improve material quality. One millimetre diameter mesas were etched, and gold ohmic contacts were formed.

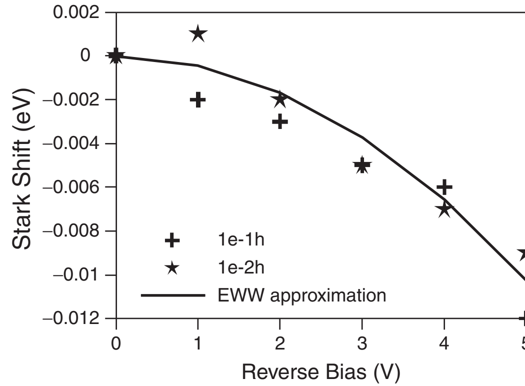

Fig. 21.24. Redshift of the 1*e*–1*h* and 1*e*–2*h* energy transitions as a function of the applied bias. The *solid line* is a calculation of the stark shift using the effective well width method

Figure 21.23 shows electroreflectance spectra obtained under different biases. The solid vertical lines show the position of the energy transitions found using a third derivative functional form curve fitting procedure (dashed lines superposed on top of the experimental curves). The energy transitions, noted at the top of the graph, were identified from an envelope function calculation. The forbidden 1*e*–2*h* transition can be seen, which is not surprising since the translation symmetry is broken by the applied electric field [72].

Figure 21.24 shows the stark shift obtained for the 1*e*–1*h* and 1*e*–2*h* transitions as a function of the reverse bias. If a low background doping in the intrinsic region and a uniform electric field are assumed, a 5 V reverse bias corresponds to a field around 60 kV cm^{-1}, a typical operating value for a modulator device. The solid line in the Fig. 21.24 shows a calculation of the stark shift using the effective well width method [73, 74], which reproduces relatively well the values obtained experimentally for the 1*e*–1*h* transition and only slightly underestimates the shift, as reported for other material systems [71]. The shift observed for the 1*e*-2*h* transition can also be observed but is somewhat lower, as expected theoretically.

More recently, the observation of QCSE in quantum wells made with the GaInNAsSb quinternary compound was reported in the 1.3–1.6 μm range with an absorption coefficient variation up to 10,000 cm^{-1} [13]. The high material quality along with the favorable band offset of the structure allowed the observation of exciton features and efficient modulation. Reported results are comparable to those obtained on InP with the added advantage of being compatible with a GaAs-based RCE structure.

Acknowledgments. The experimental work presented in this article was performed in collaboration with Dr X. Yang and was funded in part by IBM. J.B.H. acknowledges support from Tokyo University.

References

1. J.F. Geisz, D.J. Friedman, J.M. Olson, S.R. Kurtz, B.M. Keyes, J. Cryst. Growth **195**, 401 (1998)
2. D.J. Friedman, J.F. Geisz, S.R. Kurtz, J.M. Olson, J. Cryst. Growth **195**, 409 (1998)
3. S.R. Kurtz, A.A. Allerman, E.D. Jones, J.M. Gee, J.J. Banas, B.E. Hammons, Appl. Phys. Lett. **74**, 729 (1999)
4. J.B. Héroux, X. Yang, W.I. Wang, Appl. Phys. Lett. **75**, 2716 (1999)
5. G.S. Kinsey, D.W. Gotthold, A.L. Holmes Jr., B.G. Streetman, J.C. Campbell, Appl. Phys. Lett. **76**, 2824 (2000)
6. G.S. Kinsey, D.W. Gotthold, A.L. Holmes Jr., J.C. Campbell, Appl. Phys. Lett. **77**, 1543 (2000)
7. D.W. Gotthold, S. Govindaraju, J. Reifsnider, G.S. Kinsey, J.C. Campbell, A.L. Holmes Jr., Appl. Phys. Lett. **77**, 1543 (2000)
8. J.B. Héroux, X. Yang, W.I. Wang, Proc. SPIE **4288**, 238 (2001)
9. Y.S. Jalili, P.N. Stavrinou, J.S. Roberts, G. Parry, Elec. Lett. **36**, 343 (2002)
10. X. Sun, J. Hsu, X.G. Zheng, J.C. Campbell, A.L. Holmes, IEEE Photonics Techol. Lett. **14**, 681 (2002)
11. J.B. Héroux, X. Yang, W.I. Wang, IEE Proc.: Optoelectron. **150**, 92 (2003)
12. X. Sun, S. Wang, X.G. Zheng, X. Li, J.C. Campbell, A.L. Holmes Jr., J. Appl. Phys. **93**, 774 (2003)
13. V. Lordi, H.B. Yuen, S.R. Bank, J.S. Harris, Appl. Phys. Lett. **85**, 902 (2004)
14. H. Luo, J.A. Gupta, H.C. Liu, Appl. Phys. Lett. **86**, 211121 (2005)
15. Q. Han, X.H. Yang, Z.C. Niu, H.Q. Ni, Y.Q. Xu, S.Y. Zhang, Y. Du, L.H. Peng, H. Zhao, C.Z. Tong, R.H. Wu, Q.M. Wang, Appl. Phys. Lett. **87**, 111105 (2005)
16. X. Yang, M.J. Jurkovic, J.B. Héroux, W.I. Wang, Appl. Phys. Lett. **75**, 178 (1999)
17. X. Yang, J.B. Héroux, L.F. Mei, W.I. Wang, Appl. Phys. Lett. **78**, 4068 (2001)
18. A.A. Bergh, P.J. Dean, in *Light-Emitting Diodes* (Clarendon Press, Oxford, 1976)
19. D.J. Wolford, J.A. Bradley, K. Fry, J. Thompson, in *Physics of Semiconductors*, ed. by D.J. Chadi, W.A. Harrison (Springer, Berlin Heidelberg New York 1984), p. 627
20. X. Liu, M.E. Pistol, L. Samuelson, S. Schwetlick, W. Seifert, Appl. Phys. Lett. **56**, 1451 (1990)
21. X. Liu, M.E. Pistol, L. Samuelson, Phys. Rev. B **42**, 7504 (1990)
22. W. Shan, W. Walukiewicz, J.W. Ager III, E.E. Haller, J.F. Geisz, D.J. Friedman, J.M. Olson, S.R. Kurtz, Phys. Rev. Lett. **82**, 1221 (1999)
23. A. Lindsay, E.P. O'Reilly, Solid State. Commun. **112**, 443 (1999)
24. C. Skierbiszewski, P. Perlin, P. Wisniewski, W. Knap, T. Suski, W. Walukiewicz, W. Shan, K.M. Yu, J.W. Ager III, E.E. Haller, J.F. Geisz, J.M. Olson, Appl. Phys. Lett. **76**, 2409 (2000)
25. J.B. Héroux, X. Yang, W.I. Wang, J. Vac. Sci. Techol. B **20**, 1154 (2002)
26. A. Al-Yacoub, L. Bellaiche, Phys. Rev. B **62**, 10847 (2000)
27. J.B. Héroux, X. Yang, W.I. Wang, J. Appl. Phys. **8**, 4366 (2002)
28. M. Gallupi, L. Geelhar, H. Riechert, Appl. Phys. Lett. **86**, 131925 (2005)
29. M. Gallupi, L. Geelharr, H. Riechert, M. Hetterich, A. Grau, S. Birner, W. Stolz, Phys. Rev. B **72**, 155324 (2005)

30. R. Kudrawiec, H.B. Yuen, K. Ryczko, J. Misiewicz, S.R. Bank, M.A. Wistey, H.P. Bae, J.S. Harris Jr., J. Appl. Phys. **97**, 053515 (2005)
31. R. Kudrawiec, M. Motyka, M. Gladysiewicz, J. Misiewicz, H.B. Yuen, S.R. Bank, H. Bae, M.A. Wistey, J.S. Harris, Appl. Phys. Lett. **88**, 221113 (2006)
32. S.M. Sze, in *Physics of Semiconductor Devices* (Wiley, New York, 1981)
33. O.S. Heavens, *Optical Properties of Thin Solid Films* (Dover, New York, 1991)
34. R. Guenther, in *Modern Optics* (Wiley, New York, 1990)
35. S.S. Murtaza, R.V. Chelakara, R.D. Dupuis, J.C. Campbell, A.G. Dentai, Appl. Phys. Lett. **69**, 2462 (1996)
36. GPD Optoelectronics Corp., Salem, NH USA
37. A. Feltrin, A. Alemu, A. Freundlich, Phys. Rev. B **73**, 155310 (2006)
38. I. Tan, E.L. Hu, J.E. Bowers, B.E. Miller, IEEE J. Quantum. Electron. **31**, 1863 (1995)
39. J.C. Campbell, D.L. Huffaker, H. Deng, D.G. Deppe, Elec. Lett. **33**, 1337 (1997)
40. O. Baklenov, H. Nie, K.A. Anselm, J.C. Campbell, B.G. Streetman, Elec. Lett. **34**, 694 (1998)
41. H. Nie, O. Baklenov, P. Yuan, C. Lenox, B.G. Streetman, J.C. Campbell, IEEE Photonics Techol. Lett. **10**, 1009 (1998)
42. C. Li, Q. Yang, H. Wang, J. Yu, Q. Wang, Y. Li, J. Zhou, H. Huang, X. Ren, IEEE Photonics Techol. Lett. **12**, 1373 (2000)
43. S.S. Murtaza, R.V. Chelakara, R.D. Dupuis, J.C. Campbell, A.G. Dentai, Appl. Phys. Lett. **69**, 2462 (1996)
44. H. Huang, Y. Huang, X. Wang, Q. Wang, X. Ren, IEEE Photonics Techol. Lett. **16**, 245 (2004)
45. X. Ren, H. Huang, Y. Chong, Y. Huang, Micr. Opt. Tech. Lett. **42**, 133 (2004)
46. I. Kimukin, N. Biyikli, B. Butun, O. Aytur, S.M. Unlu, E. Ozbay, IEEE Photonics Techol. Lett. **14**, 366 (2002)
47. C. Chen, K. Tetz, Y. Fainman, Appl. Opt. **44**, 6131 (2005)
48. A. Strittmatter, S. Kollakowski, E. Droge, L.H. Bottcher, D. Bimberg, Elec. Lett. **32**, 1231 (1996)
49. E. Droge, E.H. Bottcher, D. Bimberg, O. Reimann, R. Steingruber, Elec. Lett. **34**, 1421 (1998)
50. G.S. Kinsey, J.C. Campbell, A.G. Dentai, IEEE Photonics Techol. Lett. **13**, 842 (2001)
51. S.T. Kollakowski, A. Strittmatter, E. Droge, E.H. Bolttcher, D. Bimberg, O. Reimann, K. Janiak, Appl. Phys. Lett. **74**, 612 (1999)
52. D.W.E. Allsopp, M.S. Stern, E. Strobel, IEEE Trans. Microw. Theory Tech. **47**, 1289 (1999)
53. S. Chandrasekhar, M.K. Hoppe, A.G. Dentai, C.H. Joyner, G.J. Qua, IEEE Electron. Dev. Lett. **12**, 550 (1991)
54. C. Lin, W. Martin, J.S. Harris Jr., F. Sugihwo, Appl. Phys. Lett. **76**, 1188 (2000)
55. M. Ghisoni, O. Sjolund, A. Larsson, S.M. Wang, Appl. Phys. Lett. **69**, 1773 (1996)
56. M. Ghisoni, O. Sjolund, A. Larsson, J. Thordsson, T. Andersson, S.M. Wang, IEEE J. Sel. Top. Quantum Electron. **3**, 768 (1997)
57. J.P.R. David, Y.H. Chen, R. Grey, G. Hill, P.N. Robson, P. Kightley, Appl. Phys. Lett. **67**, 906 (1995)
58. S.R. Forrest, M. Didomenico Jr., R.G. Smith, H.J. Stocker, Appl. Phys. Lett. **36**, 580 (1980)

59. S.R. Forrest, R.F. Leheny, R.E. Nahory, M.A. Pollack, Appl. Phys. Lett. **37**, 322 (1980)
60. J.P.R. David, P. Kightley, Y.H. Chen, T.S. Goh, R. Grey, G. Hill, P.N. Robson, Inst. Phys. Conf. Ser. **136**, 373 (1993)
61. S.R. Forrest, IEEE J. Quantum Electron. **QE-17**, 217 (1981)
62. J.C. Dries, M.R. Gokhale, K. Thomson, S. Forrest, R. Hull, Appl. Phys. Lett. **73**, 2283 (1998)
63. J.C. Campbell, S. Demiguel, F. Ma, A. Beck, X. Guo, S. Wang, X. Zheng, X. Li, J.D. Beck, M.A. Kinch, A. Huntington, L.A. Coldren, J. Decobert, N. Tscherptner, IEEE J. Sel. Top. Quantum Electron. **10**, 777 (2004)
64. X. Sun, S. Wang, J.S. Hsu, R. Sidhu, X.G. Zheng, X. Li, J.C. Campbell, A.L. Holmes, IEEE J. Sel. Top. Quantum. Electron. **8**, 817 (2002)
65. R. Sidhu, H. Chen, N. Duan, G.V. Karve, J.C. Campbell, A.L. Holmes Jr., Elec. Let. **40**, 6147 (2004)
66. M.G. Xu, T.A. Fisher, J.M. Dell, A. Clark, J. Appl. Phys. **84**, 5761 (1998)
67. A. Larsson, P.A. Andrekson, S.T. Eng, A. Yariv, IEEE J. Quantum Electron. **24**, 787 (1988)
68. S. Yan, J.H. Zhao, J. Sarathy, L. Hao, G.H. Olsen, IEEE Trans. Electron. Dev. **44**, 2167 (1993)
69. C. Gmachl, A. Golshani, N. Finger, A. Kock, E. Gornik, J.F. Walker, LEOS Proc. **95**, 431 (1995)
70. R.Y.F. Yip, R.A. Masut, J. Appl. Phys. **82**, 1976 (1997)
71. R.Y.F. Yip, P. Desjardins, L. Isnard, A. Ait-Ouali, H. Marchand, J.L. Brebner, J.F. Currie, R.A. Masut, J. Appl. Phys. **83**, 1758 (1998)
72. A. Dimoulas, K.P. Giapis, J. Leng, G. Halkias, K. Zekentes, A. Christou, J. Appl. Phys. **72**, 1912 (1992)
73. G. Bastard, E.E. Mendez, L.L. Chang, L. Esaki, Phys. Rev. B **28**, 3241 (1983)
74. D.A.B. Miller, D.S. Chemla, T.C. Damen, A.C. Gossard, W. Wiegmann, T.H. Wood, C.A. Burrus, Phys. Rev. B **32**, 1043 (1995)

Index

10 band $\boldsymbol{k}\cdot\boldsymbol{p}$ Hamiltonian, 343, 346, 496
3-band $\boldsymbol{k}\cdot\boldsymbol{p}$ model, 129

ab initio super-cell approach, 235
acoustic modes, 226
alloy fluctuations, 183, 333, 378
alloy scattering, 138, 256, 257, 275, 378, 404
amphoteric defect model, 17
Amplified Spontaneous Emission, 532
Anderson localization, 382
Anderson's many-impurity model, 258
antiphase boundaries, 406
antiphase domain, 319, 406
atomic nitrogen, 36, 38
Atomic-Spheres-Approximation, 94
avalanche photodiode, 580

band anticrossing (BAC) model, 2, 7, 13, 28, 67, 76, 77, 81, 108, 124, 127, 134, 256, 308, 334, 346, 358, 361, 364, 420, 421, 426
band tail states, 302
blueshift, 49, 53, 184, 188, 192, 214, 224, 229, 250, 303, 343, 351, 355, 357, 395, 396, 401, 409, 422, 519, 521
Bohr magneton, 297
Boltzmann equation, 257, 263
bond-orbital model, 235
Born-approximation, 378
Bose–Einstein relation, 184
bound exciton states, 310

CdO_xTe_{1-x} alloys, 22
coherent potential approximation (CPA), 68, 97, 258
composition fluctuations, 192, 203, 209, 215
contactless electroreflectance, 164, 355
correlated function expansion (CFE) method, 509
Coulomb interactions, 242
Coulomb scattering centre, 411
coupling matrix element C_{NM}, 7
crystalline Green's functions method, 234
cyclotron resonance, 125, 313

dark field scanning transmission electron microscopy, 208
deformation potential phonon scattering, 277
Delta Lattice Parameter (DLP), 210
density functional theory, 93, 390
density of states, 68, 70, 127, 183, 190, 259, 271, 274, 275, 277, 280
density of states (DOS) effective mass, 18
Differential gain, 428, 429, 434, 438, 504
diffusion coefficient, 214, 506, 509
Diffusion length, 509
diffusion mobility, 215
dispersion factor, 189
Drude model, 125

effective g-factors, 148
efficient amplitude modulation, 432

Electromodulated absorption, 354
Electromodulation spectroscopy, 164
electron energy loss spectroscopy (EELS), 208
electron spin memory, 287, 288
electronegativity, 66, 84, 86, 182, 567
empirical pseudopotential method, 142, 335
exciton localisation, 182, 183
exciton trapping, 188
exciton tunnelling, 350

Fabry–Perot oscillations, 126, 140
Fabry-Perot analysis, 528
Fabry-Perot effect, 543
Fick's diffusion equation, 509
First-principles local density approximation (LDA), 67
five-level $\boldsymbol{k}\cdot\boldsymbol{p}$ model, 149, 151, 153
Frequency Modulation, 431, 434
full pseudopotential calculations, 420
full-potential Linear Augmented Plane Wave (LAPW) method, 102

g^*-factors, 146, 151, 155, 156
gain-bandwidth, 532
Gourdon and Lavaillard's model, 190
Group II–VI dilute oxide (II–O–VI) semiconductors, 20

Hall mobility, 261
Hall transport, 370
Hartree–Fock approximation, 7, 68, 239
Hartree–Fock energy, 71
Hellmann-Feynman forces, 235
heterojunction phototransistors, 576
highly mismatched alloys, 1, 66, 86, 92
Hybridization, 24, 69, 70, 80, 82–84, 99, 439
hydrogenation, 384
hydrostatic deformation potentials, 512

II–O–VI alloys, 20
IBS technique, 3, 21
interdiffused GaInNAsSb QW, 505, 515, 522
interface roughness, 183
intermediate band solar cell IBSC, 26
internal quantum efficiencies, 400
Ion Implantation, 8–10, 413
ionization factor, 36
isoelectronic localised states, 283
isoelectronic trap, 226, 567
isolectronic impurity, 345
isovalent impurities, 66, 77
isovalent N, 18, 19, 29

Joule heating, 473

$\boldsymbol{k}$-selection rule, 183
kinetical model, 207
Koster–Slater model, 67
Kramers–Kronig relations, 166

ladder method, 255, 257, 263
Langmuir probe, 40
large atomistically relaxed supercells, 335
large-scale-integrated circuits, 405
LDA method, 67
light-emitting diode, 345, 405
Linear Combination of Isolated Nitrogen States, 359
linear-muffin-tin-orbital (LMTO), 129
linear-muffin-tin-orbital method (LMTO), 129
local density approximation, 67, 93
local vibrational mode, 350
Localization effects, 132, 302, 383, 386
localized vibrational modes, 226, 240, 387
Lorentz law, 262
Lorentzian line shape, 166, 167

magnetoresistance, 369, 370, 381
many-impurity Anderson model, 68
Metal Oxide Semiconductor Field Effect Transistors (MOSFET), 405
Mirror-movable tunable device, 543
mirror-tunable VCSOA, 534
modulator, 563
modulator device, 581
multijunction solar cells, 26
Mutual Passivation, 17, 81

near-band edge (NBE) emission, 302
nearest-neighbor (NN) configuration, 422

nitrogen plasma, 36, 38, 44
noise figure, 443, 532

Optical Emission Detector (OED), 36
optically detected cyclotron resonance (ODCR) measurement, 137, 313
optoelectronic-integrated circuits, 405

p–i–n Photodetectors, 570
paramagnetic centre, 283, 290, 293, 297
passivation of the N activity, 18
Peltier effect, 386
perturbation matrix, 236, 240, 244, 246
pesudopotential large-supercell calculations, 18
phase separation, 194, 199, 201, 209, 210, 217
phonon drag effect, 387
photoconductivity, 192
photodetectors, 563
photomodulated reflectance, 72, 164, 352
photovoltaic, 26, 369
Pikus–Bir Hamiltonian, 167, 421
PL up-conversion, 309
polar-optical phonon scattering, 256, 257, 266, 269, 279
potential fluctuations, 81, 132, 183, 194, 302
pseudo-potential method, 244
pseudopotential-supercell calculations, 104
pseudopotentials, 94, 102
pulsed-laser melting, 3, 8–10

quantum-confined stark effect, 563, 565, 581

Raman amplifiers, 475
Raman scattering, 229
rapid thermal annealing, 192, 225, 371, 409, 519
redshift, 176, 184, 335, 348, 352, 364, 527
Regular Solution (RS) model, 210
resonant cavity-enhanced photodetector, 565, 570

sp^3s^* tight-binding, 360
S-shape, 58, 184, 192, 302, 332, 386
scattering model, 256, 411
scattering rate, 266, 275, 278
second-order perturbation theory, 92
Seebeck coefficient, 386, 387
Semiconductor optical amplifier, 525
separate confinement heterostructure, 456, 485
Seraphin coefficients, 166
shear deformation potential, 168, 169, 512
single-mode GaInNAs ridge waveguide (RWG) laser, 472
six-level $\boldsymbol{k}\cdot\boldsymbol{p}$ model, 146, 149, 151
solar cell, 26, 328, 369, 400
space solar AM0-spectrum, 369
specific heat capacity, 211
spin dependent capture, 290, 296
Spin Dependent Recombination (SDR), 290
spinodal decomposition, 200, 210
Stranski–Krastanov growth mode, 37, 56, 208, 209, 324, 325
super-cell approach, 234, 235
super-shell tight-binding calculations, 420
Supercell method, 97, 101, 390

thermionic effect, 40
Thermionic Emission Lifetime, 485
Thermopower, 386
tight-binding calculation, 111, 137, 257, 353, 358, 420
Time-resolved photoluminescence (TR-PL), 188
transfer matrix method, 581
transparency current density, 457, 491
tunable Vertical-Cavity Surface-Emitting Lasers, 545
two-level band-anticrossing (BAC) model, 346, 358

valence band anticrossing (VBAC) model, 82
Valence Force Field, 321, 388
Varshni formula, 556
Varshni law, 184
Varshni model, 58

VCA approach, 66
Vegard's law, 168, 204, 373
Vegard's linearity rule, 511
vertical cavity SOA's or VCSOAs, 525
vibrational modes, 226, 230
virtual crystal approximation, 65, 92, 123, 145, 158, 275, 567

wavelength division multiplexed, 543

Springer Series in

MATERIALS SCIENCE

Editors: R. Hull R. M. Osgood, Jr. J. Parisi H. Warlimont

40 **Reference Materials in Analytical Chemistry**
A Guide for Selection and Use
Editor: A. Zschunke

41 **Organic Electronic Materials**
Conjugated Polymers and Low Molecular Weight Organic Solids
Editors: R. Farchioni and G. Grosso

42 **Raman Scattering in Materials Science**
Editors: W. H. Weber and R. Merlin

43 **The Atomistic Nature of Crystal Growth**
By B. Mutaftschiev

44 **Thermodynamic Basis of Crystal Growth**
P–T–X Phase Equilibrium and Non-Stoichiometry
By J. Greenberg

45 **Thermoelectrics**
Basic Principles and New Materials Developments
By G. S. Nolas, J. Sharp, and H. J. Goldsmid

46 **Fundamental Aspects of Silicon Oxidation**
Editor: Y. J. Chabal

47 **Disorder and Order in Strongly Nonstoichiometric Compounds**
Transition Metal Carbides, Nitrides and Oxides
By A. I. Gusev, A. A. Rempel, and A. J. Magerl

48 **The Glass Transition**
Relaxation Dynamics in Liquids and Disordered Materials
By E. Donth

49 **Alkali Halides**
A Handbook of Physical Properties
By D. B. Sirdeshmukh, L. Sirdeshmukh, and K. G. Subhadra

50 **High-Resolution Imaging and Spectrometry of Materials**
Editors: F. Ernst and M. Rühle

51 **Point Defects in Semiconductors and Insulators**
Determination of Atomic and Electronic Structure from Paramagnetic Hyperfine Interactions
By J.-M. Spaeth and H. Overhof

52 **Polymer Films with Embedded Metal Nanoparticles**
By A. Heilmann

53 **Nanocrystalline Ceramics**
Synthesis and Structure
By M. Winterer

54 **Electronic Structure and Magnetism of Complex Materials**
Editors: D.J. Singh and D. A. Papaconstantopoulos

55 **Quasicrystals**
An Introduction to Structure, Physical Properties and Applications
Editors: J.-B. Suck, M. Schreiber, and P. Häussler

56 **SiO_2 in Si Microdevices**
By M. Itsumi

57 **Radiation Effects in Advanced Semiconductor Materials and Devices**
By C. Claeys and E. Simoen

58 **Functional Thin Films and Functional Materials**
New Concepts and Technologies
Editor: D. Shi

59 **Dielectric Properties of Porous Media**
By S.O. Gladkov

60 **Organic Photovoltaics**
Concepts and Realization
Editors: C. Brabec, V. Dyakonov, J. Parisi and N. Sariciftci

61 **Fatigue in Ferroelectric Ceramics and Related Issues**
By D.C. Lupascu

62 **Epitaxy**
Physical Principles and Technical Implementation
By M.A. Herman, W. Richter, and H. Sitter

Springer Series in
MATERIALS SCIENCE

Editors: R. Hull R. M. Osgood, Jr. J. Parisi H. Warlimont

63 **Fundamentals of Ion-Irradiated Polymers**
By D. Fink

64 **Morphology Control of Materials and Nanoparticles**
Advanced Materials Processing and Characterization
Editors: Y. Waseda and A. Muramatsu

65 **Transport Processes in Ion-Irradiated Polymers**
By D. Fink

66 **Multiphased Ceramic Materials**
Processing and Potential
Editors: W.-H. Tuan and J.-K. Guo

67 **Nondestructive Materials Characterization**
With Applications to Aerospace Materials
Editors: N.G.H. Meyendorf, P.B. Nagy, and S.I. Rokhlin

68 **Diffraction Analysis of the Microstructure of Materials**
Editors: E.J. Mittemeijer and P. Scardi

69 **Chemical–Mechanical Planarization of Semiconductor Materials**
Editor: M.R. Oliver

70 **Applications of the Isotopic Effect in Solids**
By V.G. Plekhanov

71 **Dissipative Phenomena in Condensed Matter**
Some Applications
By S. Dattagupta and S. Puri

72 **Predictive Simulation of Semiconductor Processing**
Status and Challenges
Editors: J. Dabrowski and E.R. Weber

73 **SiC Power Materials**
Devices and Applications
Editor: Z.C. Feng

74 **Plastic Deformation in Nanocrystalline Materials**
By M.Yu. Gutkin and I.A. Ovid'ko

75 **Wafer Bonding**
Applications and Technology
Editors: M. Alexe and U. Gösele

76 **Spirally Anisotropic Composites**
By G.E. Freger, V.N. Kestelman, and D.G. Freger

77 **Impurities Confined in Quantum Structures**
By P.O. Holtz and Q.X. Zhao

78 **Macromolecular Nanostructured Materials**
Editors: N. Ueyama and A. Harada

79 **Magnetism and Structure in Functional Materials**
Editors: A. Planes, L. Mañosa, and A. Saxena

80 **Micro- and Macro-Properties of Solids**
Thermal, Mechanical and Dielectric Properties
By D.B. Sirdeshmukh, L. Sirdeshmukh, and K.G. Subhadra

81 **Metallopolymer Nanocomposites**
By A.D. Pomogailo and V.N. Kestelman

82 **Plastics for Corrosion Inhibition**
By V.A. Goldade, L.S. Pinchuk, A.V. Makarevich and V.N. Kestelman

83 **Spectroscopic Properties of Rare Earths in Optical Materials**
Editors: G. Liu and B. Jacquier

84 **Hartree–Fock–Slater Method for Materials Science**
The DV–X Alpha Method for Design and Characterization of Materials
Editors: H. Adachi, T. Mukoyama, and J. Kawai

85 **Lifetime Spectroscopy**
A Method of Defect Characterization in Silicon for Photovoltaic Applications
By S. Rein

86 **Wide-Gap Chalcopyrites**
Editors: S. Siebentritt and U. Rau

87 **Micro- and Nanostructured Glasses**
By D. Hülsenberg and A. Harnisch